The 39th Liège International Astrophysical Colloquium

The multi-wavelength view of Hot, Massive Stars

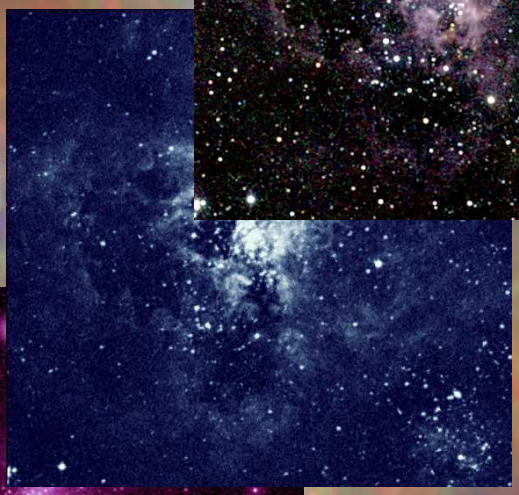

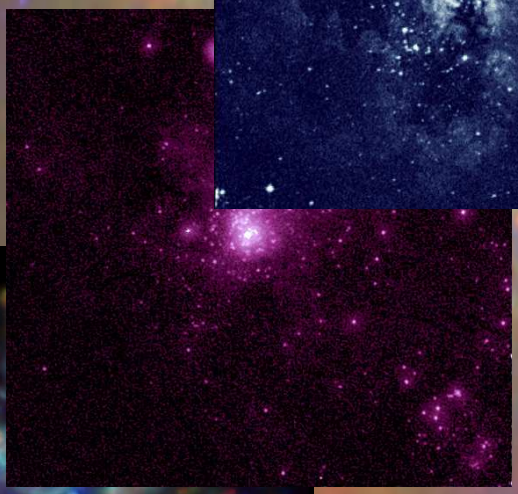

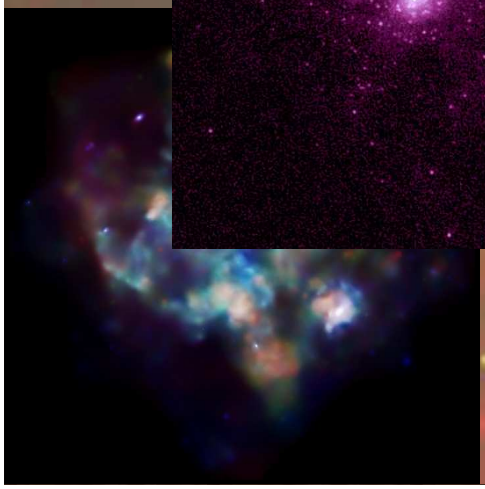

Liège,
12-16 July 2010

SOC:
Ronny Blomme, Rosie Chen, Michaël De Becker, Alex Fullerton, Doug Gies, Eric Gosset, Damien Hutsemékers, Yaël Nazé, Gregor Rauw - co-chair, Gustavo Romero, Dany Vanbeveren, Peredur Williams - chair

LOC:
Denise Caro, Michaël De Becker, Alain Detal, Eric Gosset, Sylvia Grandjean, Anne Lemaître, Thierry Morel, Yaël Nazé, Gregor Rauw, Jean-Pierre Swings, Jean-Marie Vreux

Contents

Foreword **13**

1 Stellar winds, diagnostics across the electromagnetic spectrum **15**

S. Owocki: *Theory of winds from hot, luminous massive stars* **16**

F. Martins: *UV, optical and near-IR diagnostics of massive stars* **29**

A. Lobel, J.A. Toalá & R. Blomme: *3-D radiative transfer modeling of structured winds in massive hot stars with Wind3D* **42**

J.O. Sundqvist et al.: *A proper description of clumping in hot star winds: the key to obtaining reliable mass-loss rates?* **48**

L.M. Oskinova et al.: *X-rays, clumping and wind structures* **54**

R. Blomme: *Radio observations of massive stars* **67**

J.L. Hoffman: *Massive stars in polarized light* **81**

S. Simón-Díaz: *Macroturbulent broadening in Massive Stars and its possible connection to Stellar Oscillations* **86**

G. Gräfener et al.: *On the mass-loss properties of the most massive stars* **92**

W.-R. Hamann et al.: *The most luminous stars in the Galaxy and the Magellanic Clouds* **98**

A.-N. Chené & A.F.J. Moffat: *Pulsations in Wolf-Rayet stars: Observations with MOST* **104**

Y. Nazé: *General X-ray properties of hot, massive stars* **109**

C. Aragona, M.V. McSwain & M.S.E. Roberts: *The Stellar Wind of LS 5039* **115**

M. Austin & R. Prinja: *Ion fractions and the weak wind problem* **120**

A. David-Uraz et al.: *Tracing WR wind structures by using the orbiting companion in the 29d WC8d + O8-9IV binary CV Ser* **125**

E.I. Doran & P.A. Crowther: *A VLT/UVES spectroscopy study of O2 stars in the LMC* **129**

S.M. Dougherty et al.: *Radio emission from the massive stars inWesterlund 1* **134**

C.A. Engelbrecht, F.A.M. Frescura & S. Moonsamy: *Observational signatures of rapidly rotating, pulsating B stars* **139**

M. Garcia, F. Najarro & A. Herrero: *Exploring the connection of weak winds and magnetic fields* **144**

S.R. Heap et al.: *Hot, Massive Stars in I Zw 18* **149**

A. Hervé & G. Rauw: *Effects of porosity on emergent synthetic spectra of massive stars in the X-ray domain* **155**

A. Liermann et al.: *High-mass stars in the Galactic center Quintuplet cluster* **160**

C.C. Lovekin & R.G. Deupree: *Mass loss in 2D Rotating Stellar Models* **165**

T. Morel et al.: *The Mons campaign on OB stars* **170**

M.-F. Nieva et al.: *Near-IR spectroscopy of OB stars with VLT/CRIRES* **175**

D. Pasemann, U. Ruehling & W-R. Hamann: *Spectral analyses of theWolf-Rayet stars in the Small Magellanic Cloud* **180**

A. Sander, W-R. Hamann & H. Todt: *Revised spectral analyses of Galactic WC stars* **185**

N. St-Louis et al.: *Spectroscopic Monitoring in the Optical Wavelength Region of Nine WC9 Stars* **190**

P.M. Williams: *Heated dust around the LMCWolf-Rayet system HD 36402 (BAT99-38)* **195**

2 Massive star formation, confronting theory and observation **199**

H. Beuther: *Formation and early evolution of massive stars* **200**

R. Kuiper: *Radiation pressure feedback in the formation of massive stars* **211**

R. Chini, V.H. Hoffmeister & D. Nürnberger: *Evidence for disks around young high-mass stars* **217**

J.S. Clark, B. Davies & M.A. Thompson: *Multiple stellar generations in massive star forming complexes* **223**

C.-H. R. Chen et al.: *Physical Properties and Evolutionary Stages of Massive Young Stellar Objects in the Large Magellanic Cloud* **229**

S.K. Ramsay et al.: *A near-infrared imaging survey of intermediate and high-mass young stellar object outflow candidates* **235**

C.A. Hummel: *Modeling the massive young stellar object NGC 3603 IRS 9A* **241**

E.R. Parkin et al.: *The interactions of winds from massive young stellar objects* **246**

R. Selier & M. Heydari-Malayeri: *A very young massive star-forming region in the Small Magellanic Cloud* **251**

S. Simón-Díaz et al.: *The chemical composition of the Orion star forming region: stars, gas and dust* **255**

D.J. van der Walt: *On the periodic class II methanol masers in the high mass star forming region G9.62+0.20E* **260**

3 Evolution and interaction of massive stars with their environment 265

G. Meynet et al.: *Red Supergiants, Luminous Blue Variables and Wolf-Rayet stars: the single massive star perspective* **266**

N. Przybilla et al.: *Mixing of CNO-cycled matter in massive stars* **279**

C. Martayan et al.: *Evolution of massive Be and Oe stars at low metallicity towards the Long Gamma Ray bursts* **285**

S. Wachter et al.: *Massive Stars with Circumstellar Shells Discovered with the Spitzer Space Telescope* **291**

Y.-H. Chu & R.A. Gruendl: *Feedback from Massive YSOs and Massive Stars* **297**

A.J. van Marle, R. Keppens & Z. Meliani: *3-D simulations of shells around massive stars* **310**

D.J. Stock & M.J. Barlow: *A search for Ejecta nebulae around Wolf-Rayet Stars in the SHS Hα survey* **316**

N. Smith: *Circumstellar Material Around Evolved Massive Stars* **322**

G. Umana et al.: *The nebulae around LBVs: a multiwavelength approach* **335**

D.J. Bomans & K. Weis: *The nature of the massive stellar transient in DDO 68* **341**

A.Z. Bonanos et al.: *The infrared properties of massive stars in the Magellanic Clouds* **346**

C. Buemi et al.: *Photometric monitoring of Luminous Blue Variables* **351**

B. Burggraf et al.: *Var C: (Semi-)Periodic Long-Term Variability* **356**

J.S. Clark et al.: *Investigating the properties of Galactic Luminous Blue Variables via IR observations* **361**

M.L. Edwards et al.: *A Near-Infrared Narrow-band Imaging Survey to Search for Massive Stars in Cl 1806-20* **366**

E.D. Grundstrom et al.: *Observations of Be Disk Building: Optical Spectra of NW Serpentis (HD168797) over 35 days* **371**

V. Hénault-Brunet et al.: *A Project to Study Stellar and Gas Kinematics in 30 Dor with the VLT-FLAMES Tarantula Survey* **376**

M. Garcia et al.: *In savvy pursuit of Local Group blue massive stars* **381**

B. Kumar et al.: *A photometric study of the Carina nebula region around WR22* **386**

J. Mackey & A.J. Lim: *Radiation-MHD models of elephant trunks and globules in* HII *regions* **391**

A. Marco & I. Negueruela: *The enigmatic open cluster NGC 7419* **396**

C. Martayan et al.: *X-shooter, NACO, and AMBER observations of the LBV Pistol Star* **400**

T. Morel: *Mixing in magnetic OB stars* **405**

E.W. Pellegrini et al.: *Escaping Radiation from Massive Star* HII *regions in the Magellanic Clouds* **410**

S. Ramírez Alegría et al.: *New Results from the Project MASGOMAS: Near-IR Study of the Stellar Population of Sh2-152* **415**

G.E. Romero et al.: *Non-thermal radiation from a runaway massive star* **420**

O.N. Sholukhova, A.F. Valeev & S.N. Fabrika: *Two New LBV Candidates in the M33 Galaxy* **425**

W.D. Taylor et al.: *The VLT-FLAMES Tarantula Survey* **430**

C. Vamvatira-Nakou et al.: *Herschel-PACS observations of Nebulae Ejected by Massive Stars* **435**

K. Weis: *Gone with the wind: Nebulae around LBVs* **440**

A. Wofford, R. Chandar & C. Leitherer: *FUV and UVIS observations of circumnuclear star clusters in M83* **445**

J. Zastrow, M.S. Oey & E.W. Pellegrini: *Single-Star* HII *Regions as a Probe of Massive Star SEDs* **450**

4 Future instrumentation and its application to massive star research **455**

C.J. Evans: *Massive stars in the era of ELTs* **456**

T. Eversberg: *Spectroscopic madness - A golden age for amateurs* **469**

G. Rauw & L. Oskinova: *Studying massive stars with the International X-ray Observatory* **475**

Y. Damerdji et al.: *Spectroscopic binaries as observed by the future Gaia space mission* **481**

M. De Becker, H. Le Coroller & J. Dejonghe: *Prospects for the multiplicity investigation of massive stars with the CARLINA interferometer* **486**

S.M. Dougherty & R. Perley: *The Expanded Very Large Array* **491**

T. Eversberg & K. Vollmann: *A focus for hot stars - The German STScI* **496**

A. Hervé et al.: *Study of a possible X-ray sensor based on the Plasmon Surface Resonance for the next generation of instruments* **500**

M. Palate et al.: *Massive binaries as seen with GAIA* **504**

S.K. Ramsay et al.: *CRIRES-POP: A library of high resolution spectra in the near-infrared* **509**

S. Simón-Díaz et al.: *The IACOB spectroscopic database of Northern Galactic OB stars* **514**

A. Sota et al.: *The Galactic O-Star Spectral Survey (GOSSS) Project status and first results* **519**

A. Willis, R. Prinja & D. Fenech: *The e-Merlin Cyg OB2 Radio Survey (COBRaS): Massive and Young Stars in the Galaxy* **524**

5 Massive binaries: interaction and evolution **529**

D. Vanbeveren: *Signatures of binary evolution processes in massive stars* **530**

S.E. de Mink, N. Langer & R.G. Izzard: *Binaries are the best single stars* **543**

I.I. Antokhin: *Solving light curves of WR+O binaries: the regularization approach* **549**

J. Pittard: *Theoretical Models of Interacting Winds in Massive Binaries* **555**

M.V. McSwain et al.: *A Multiwavelength Study of the Runaway Binaries HD 14633 and HD 15137* **565**

M. Kennedy et al.: *Cyg OB2 #5: When three stars are just not enough* **572**

M.F. Corcoran: *The Eta Carinae 2009 Campaign* **578**

J. Groh: *Multi-wavelength diagnostics of massive binary interaction in Eta Carinae* **590**

P. Williams: *Results from the 2009 campaign on WR 140* **595**

E.R. Parkin et al.: *3D modelling of the massive star binary systems Eta Carinae, WR 22, and WR 140* **610**

H.A. Kobulnicky & D.C. Kiminki: *Cygnus OB2: A Laboratory for Massive Binaries, Runaway Stars, and Triggered Star Formation* **616**

L. Mahy et al.: *The multiplicity of O-type stars in NGC 2244* **622**

B.W. Ritchie, J.S. Clark & I. Negueruela: *The massive binary population of the starburst cluster Westerlund 1* **628**

P. Blay & V. Reglero: *The peculiar O9.5V star BD+53 2790, the massive counterpart to the X-ray binary system 4U 2206+54* **634**

S.M. Caballero-Nieves et al.: *Cyg OB2 Unveiled: The Search for Astrometric Companions* **639**

J.A. Combi et al.: *Multiwavelength study of the intriguing massive star CPD−59 2629 (Tr 16-22)* **644**

M. De Becker, M.V. McSwain & C. Aragona: *First results on the optical campaign devoted to the gamma-ray binary candidate HD 259440* **648**

M. De Becker, J.M. Pittard & P.M. Williams: *The XMM-Newton view of the X-ray spectrum of WR 140 across periastron passage* **653**

S.M. Dougherty, V. Trenton & A.J. Beasley: *The Orbit and Distance of WR140* **658**

N.R. Evans: *Multiplicity in 5 $M_\odot$ Stars* **663**

R. Fahed et al.: *Spectroscopic follow-up of the colliding-wind binary WR140 during the 2009 January periastron passage* **668**

T. Fauchez, M. De Becker & Y. Nazé: *The X-ray emission of the colliding wind binary V444 Cyg* **673**

D. Gies et al.: *Combined Spectroscopic and Interferometric Orbits for HD 193322* **678**

E. Gosset et al.: *The X-ray emission of the WR+O binary WR79* **683**

J.R. Lomax & J.L. Hoffman: *Spectropolarimetry of Beta Lyrae: Constraining the location of the Hot Spot and Jets* **689**

T.I. Madura et al.: *Constraining the Properties of the Eta Carinae System via 3-D SPH Models of Space-Based Observations: The Absolute Orientation of the Binary Orbit* **694**

A.B. Mason et al.: *High-Mass X-ray Binaries in the NIR: Orbital solutions of two highly obscured systems* **699**

G. Montes et al.: *Thermal Radio Emission from Radiative shocks in Colliding Stellar Winds* **704**

Y. Nazé et al.: *A first orbital solution for the non-thermal radio emitter Cyg OB2 #9* **709**

K. Pavlovski et al.: *Observational approach to the chemical evolution of high-mass binaries* **714**

C.M.P. Russell et al.: *X-Ray Modeling of η Carinae and WR140 from SPH Simulations* **719**

Y. Sugawara et al.: *The variable X-ray spectrum of the Wolf-Rayet binary WR140 with Suzaku* **724**

F. Vilardell et al.: *The most massive eclipsing binary with apsidal motion* **729**

D. Volpi: *Modelling the synchrotron emission from O-star colliding wind binaries* **733**

Concluding Remarks **738**

D. Gies: *The multi-wavelength view of Hot, Massive Stars: Concluding remarks* **739**

Foreword

Massive stars are certainly among the most fascinating objects of stellar populations. They trigger many astrophysical processes from star formation to the chemical enrichment of the interstellar medium. Yet, their properties are still not fully understood and these objects are therefore at the core of many ongoing research activities.
With the advent of new, high-performance, ground-based and space-borne facilities, the multi-wavelength investigation of hot, massive stars has definitely been boosted over the last decade. It is indeed nowadays possible to study these objects over a wide part of the electromagnetic spectrum, all the way from radio waves to gamma-rays.
Motivated by this fact, we decided to organize a conference devoted to this topic in the framework of the well-established series of Liège International Astrophysical Colloquia (LIAC). The resonance in the community was extremely positive, with many proposals for high-quality contributions. During the week of 12 - 16 July 2010, 138 astrophysicists, from institutes in 21 countries all over the world, gathered in Liège to discuss how the multi-wavelength approach has revolutionized their research on massive stars[1].
The colloquium was organized into five thematic sessions, and the present proceedings are organized along the same chapters:

- stellar winds, diagnostics across the electromagnetic spectrum;
- massive star formation, confronting theory and observation;
- evolution and interaction of massive stars with their environment;
- future instrumentation and its application to massive star research;
- massive binaries: interaction and evolution.

The multi-wavelength view of Hot, Massive Stars was actually not the first Liège colloquium specifically dealing with the topic of massive stars. In 1996, the 33rd edition of the LIAC was devoted to *Wolf-Rayet Stars in the Framework of Stellar Evolution*, celebrating the 20th anniversary of the 'Conti scenario' proposed by Peter Conti at the 20th LIAC (*Astrophysique & Spectroscopie*) in 1975. In 2008, the 38th LIAC was dealing with *Evolution and pulsation of massive stars on the main-sequence and close to it*.
At this stage, it is our great pleasure to thank a number of people who helped us making this conference a success and who contributed to these proceedings. To start, we would like to thank our colleagues of the Scientific Organizing Committee who enthusiastically contributed to the scientific organization of the colloquium, as well the invited reviewers and conference participants who delivered many interesting and exciting contributions[2]. Our thanks go also to the numerous colleagues who agreed to review the

[1]This conference was one of the biggest events so far in the series of the Liège International Astrophysical Colloquia.
[2]The final programme featured 15 invited reviews, 33 contributed talks and 86 posters.

articles submitted to these proceedings and whose referee reports helped the authors to improve their papers. We gratefully acknowledge the support by the conference sponsors (the Liège University and its Science Faculty in particular; the Fonds de la Recherche Scientifique - FNRS; the AMOS company; the City of Liège; the European Space Agency - ESA; Rejouisciences, the Centre Spatial de Liège - CSL, Astronomy & Astrophysics). Last but not least, our warmest thanks go also to our colleagues of the Local Organizing Committee: our secretaries Denise Caro and Sylvia Grandjean for their invaluable help before, during and after the conference; our system manager Alain Detal for taking care of the conference webpage and solving the software issues during the conference; Eric Gosset, Thierry Morel and Jean-Pierre Swings for their advice, their efficient help (especially to track the discussions); and finally many of our Liège colleagues who spent some of their time to help us in the practical organization of this event.

The editors: Gregor Rauw,
Michaël De Becker,
Yaël Nazé,
Jean-Marie Vreux,
& Peredur Williams

Chapter 1

Stellar winds, diagnostics across the electromagnetic spectrum

Theory of Winds from Hot, Luminous Massive Stars

Stan Owocki[1]

[1] Department of Physics and Astronomy, University of Delaware, Newark, DE 19716 USA

Abstract: The high luminosities of massive stars drive strong stellar winds, through line scattering of the star's continuum radiation. This paper reviews the dynamics of such line driving, building first upon the standard CAK model for steady winds, and deriving the associated analytic scalings for the mass loss rate and wind velocity law. It next summarizes the origin and nature of the strong Line-Deshadowing Instability (LDI) intrinsic to such line-driving, including also the role of a diffuse-line-drag effect that stabilizes the wind base, and then decribes how both instability and drag are incorporated in the Smooth Source Function (SSF) method for time-dependent simulations of the nonlinear evolution of the resulting wind structure. The review concludes with a discussion of the effect of the resulting extensive structure in temperature, density and velocity for interpreting observational diagnostics. In addition to the usual clumping effect on density-squared diagnostics, the spatial *porosity* of optically thick clumps can reduce single-density continuum absorption, and a kind of velocity porosity, or *vorocity*, can reduce the absorption strength of spectral lines. An overall goal is to illuminate the rich physics of radiative driving and the challenges that lie ahead in developing dynamical models for the often complex structure and variability of hot-star winds.

1 Introduction

The strong stellar winds from hot, massive, luminous stars are driven by the scattering of the star's continuum radiation flux by line-transitions of metal ions (Lucy & Solomon 1970; Castor, Abbott & Klein 1975, hereafter CAK). The effectiveness of such line-driving depends crucially on the Doppler-shifted line-desaturation arising from the wind outflow; this gives the dynamics of such winds an intricate feedback character, in which the radiative driving force that accelerates the outflow depends itself on that acceleration. This leads to a strong, instrinsic Line-Deshadowing Instability (LDI) that is thought make such winds highly structured and variable. The review here summarizes the basic dynamics of such line-driven winds, with an emphasis on simulations of the nonlinear evolution of instability-generated wind structure, and its implications for interpreting wind diagnostics.

2 The CAK/Sobolev Model for Steady Winds

Consider a steady-state stellar wind outflow in which radiative acceleration g_{rad} overcomes the local gravity GM_*/r^2 at radius r to drive a net acceleration $v(dv/dr)$ in the radial flow speed $v(r)$. Since overcoming gravity is key, it is convenient to define a dimensionless equation of motion that scales all accelerations by gravity,

$$(1 - w_s/w)\, w' = -1 + \Gamma_{rad}\,, \tag{1}$$

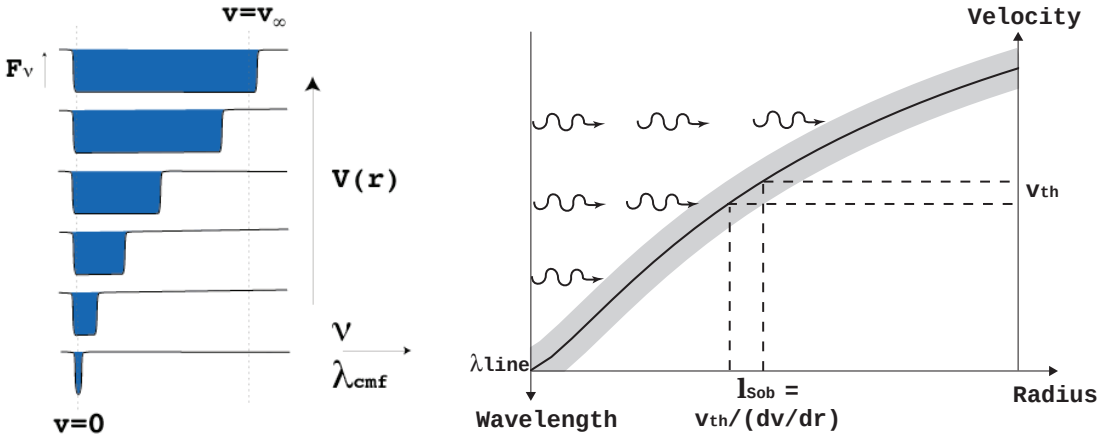

Figure 1: Two perspectives for the Doppler-shifted line-resonance in an accelerating flow. Right: Photons with a wavelength just shortward of a line propagate freely from the stellar surface up to a layer where the wind outflow Doppler shifts the line into a resonance over a narrow width (represented here by the shading) equal to the Sobolev length, set by the ratio of thermal speed to velocity gradient, $l_{Sob} \equiv v_{th}/(dv/dr)$. Left: Seen from successively larger radii within the accelerating wind, the Doppler-shift sweeps out an increasingly broadened line absorption trough in the stellar spectrum.

where $\Gamma_{rad} \equiv g_{rad}\, r^2/GM_*$, $w \equiv v^2/v_{esc}^2$, and $w' \equiv dw/dx$, with $x \equiv 1 - R_*/r$ and $v_{esc} \equiv \sqrt{2GM_*/R_*}$ the escape speed from the stellar surface radius R_*. Eqn. (1) neglects gas pressure terms on the right side, since for isothermal sound speed a these are of order $w_s \equiv (a/v_{esc})^2 \approx 0.001$ compared to competing terms needed to drive the wind.

For pure electron scattering opacity κ_e, the scaled radiative acceleration is just the usual Eddington parameter

$$\Gamma_e \equiv \frac{\kappa_e L_*}{4\pi G M_* c} = 2 \times 10^{-5} \frac{L_*/L_\odot}{M_*/M_\odot}\,. \tag{2}$$

Because typically $L_* \sim M_*^3$, stars with $M_* > 10M_\odot$ have $\Gamma_e > 10^{-3}$, with the Eddington limit $\Gamma_e \to 1$ perhaps even being central to setting a stellar upper mass limit of $M_* \sim 200M_\odot$. Eruptive mass loss from luminous blue variable (LBV) stars like η Carinae might in fact be continuum-driven during episodes of super-Eddington luminosity (Davidson & Humphreys 1997, Owocki, Gayley & Shaviv 2004).

But the *resonant* nature of line (bound-bound) scattering from metal ions leads to an opacity that is inherently much stronger than from free electrons, by a factor set by the "Quality" Q of the resonance, and fraction f_b of bound electrons in such metal lines (Gayley 1995). For allowed transitions in the UV, $Q \sim 2 \times 10^7$, and for solar metallicity, the total bound-electron fraction from all metal lines is $f_b \sim 10^{-4}$. Thus, in the, somewhat idealized, *optically thin* limit that all the line opacity could be illuminated with a flat, unattenuated continuum from the full stellar luminosity, the total line-force would exceed the free-electron force by a factor of order $\overline{Q} \sim Q f_b \sim 2000$. This implies line-driven winds can be initiated in even moderately massive stars with $\Gamma_e > 5 \times 10^{-4}$, while for more massive stars with $\Gamma_e \approx 1/2$, the net outward line acceleration in principle could be as high as $\Gamma_{thin} \approx \overline{Q}\Gamma_e \approx 1000$ times the acceleration of gravity!

In practice, self-absorption within strong lines limits the acceleration, with the mass loss rate $\dot{M}$ set at the level for which the line driving is just sufficient to overcome gravity. Indeed line-saturation keeps the dense, nearly static layers of the atmosphere gravitationally bound. But as illustrated by figure 1, within the accelerating wind, the Doppler shift of the line-resonance out of the absorption shadow of underlying material exposes the line opacity to a less attenuated flux. This effectively

desaturates the lines by limiting the resonance to a layer with width set by the Sobolev length, $l_{Sob} = v_{th}/(dv/dr)$, and with optical depth proportional to $t \equiv \kappa_e \rho c/(dv/dr) = \Gamma_e \dot{M} c^2/L_* w'$.

For the CAK line-ensemble with a power-law number distribution in line-strength, the cumulative force is reduced by a factor $1/(\overline{Q}t)^\alpha$ from the optically thin value,

$$\Gamma_{CAK} = \frac{\overline{Q}\Gamma_e}{(1-\alpha)(\overline{Q}t)^\alpha} = \Gamma_e k t^{-\alpha} = C(w')^\alpha \,, \tag{3}$$

where the second equality defines the CAK "force muliplier" $kt^{-\alpha}$, with[1] $k \equiv \overline{Q}^{1-\alpha}/(1-\alpha)$. The last equality relates the line-force to the flow acceleration, with

$$C \equiv \frac{1}{1-\alpha}\left[\frac{L_*}{\dot{M}c^2}\right]^\alpha \left[\overline{Q}\Gamma_e\right]^{1-\alpha} . \tag{4}$$

Note that, for fixed sets of parameters for the star (L_*, M_*, Γ_e) and line-opacity (α, $\overline{Q}$), this constant scales with the mass loss rate as $C \propto 1/\dot{M}^\alpha$.

Neglecting the small sound-speed term $w_s \approx 0.001 \ll 1$, application of eqn. (3) into (1) gives the CAK equation of motion,

$$F = w' + 1 - \Gamma_e - C(w')^\alpha = 0 \,. \tag{5}$$

For small $\dot{M}$ (large C), there are two solutions, while for large $\dot{M}$ (small C), there are no solutions. The CAK critical solution corresponds to a *maximal* mass loss rate, defined by $\partial F/\partial w' = 0$, for which the $C(w')^\alpha$ is tangent to the line $1 - \Gamma_e + w'$ at a critical acceleration $w'_c = (1-\Gamma_e)\alpha/(1-\alpha)$. Since the scaled equation of motion (5) has no explicit spatial dependence, this critical acceleration applies throughout the wind, and so can be trivially integrated to yield $w(x) = w'_c\, x$. In terms of dimensional quantities, this represents a specific case of the general "beta"-velocity-law,

$$v(r) = v_\infty \left(1 - \frac{R_*}{r}\right)^\beta , \tag{6}$$

where here $\beta = 1/2$, and the wind terminal speed $v_\infty = v_{esc}\sqrt{\alpha(1-\Gamma_e)/(1-\alpha)}$. Similarly, the critical value C_c yields, through eqn. (4), the standard CAK scaling for the mass loss rate

$$\dot{M}_{CAK} = \frac{L_*}{c^2}\,\frac{\alpha}{1-\alpha}\left[\frac{\overline{Q}\Gamma_e}{1-\Gamma_e}\right]^{(1-\alpha)/\alpha} . \tag{7}$$

These CAK results strictly apply only under the idealized assumption that the stellar radiation is radially streaming from a point-source. If one takes into account the finite angular extent of the stellar disk, then near the stellar surface the radiative force is reduced by a factor $f_{d*} \approx 1/(1+\alpha)$, leading to a reduced mass loss rate (Friend & Abbott 1986, Pauldrach, Puls & Kudritzki 1986).

$$\dot{M}_{fd} = f_{d*}^{1/\alpha}\dot{M}_{CAK} = \frac{\dot{M}_{CAK}}{(1+\alpha)^{1/\alpha}} \approx \dot{M}_{CAK}/2 \,. \tag{8}$$

Away from the star, the correction factor increases back toward unity, which for the reduced base mass flux implies a stronger, more extended acceleration, giving a somewhat higher terminal speed, $v_\infty \approx 3 v_{esc}$, and a flatter velocity law, approximated by replacing the exponent in eqn. (6) by $\beta \approx 0.8$.

[1] Here we use a slight variation of the standard CAK notation in which the artificial dependence on a fiducial ion thermal speed is avoided by simply setting $v_{th} = c$, where c is the speed of light. Backconversion to CAK notation is achieved by multiplying t by v_{th}/c and k by $(v_{th}/c)^\alpha$. The line normalization $\overline{Q}$ offers the advantages of being a dimensionless measure of line-opacity that is independent of the assumed ion thermal speed, with a nearly constant characteristic value of order $\overline{Q} \sim 10^3$ for a wide range of ionization conditions (Gayley 1995).

The effect of a radial change in ionization can be approximately taken into account by correcting the CAK force (3) by a factor of the form $(n_e/W)^\delta$, where n_e is the electron density, $W \equiv 0.5(1 - \sqrt{1 - R_*/r})$ is the radiation "dilution factor", and the exponent has a typical value $\delta \approx 0.1$ (Abbott 1982). This factor introduces an additional density dependence to that already implied by the optical depth factor $1/t^\alpha$ given in eqn. (3). Its overall effect can be roughly accounted with the simple substition $\alpha \rightarrow \alpha' \equiv \alpha - \delta$ in the power exponents of the CAK mass loss scaling law (7). The general tendency is to moderately increase $\dot{M}$, and accordingly to somewhat decrease the wind speed.

The above scalings also ignore the finite gas pressure associated with a small but non-zero sound-speed parameter w_s. Through a perturbation expansion of the equation of motion (1) in this small parameter, it possible to derive simple scalings for the fractional corrections to the mass loss rate and terminal speed (Owocki & ud-Doula 2004),

$$\delta m_s \approx \frac{4\sqrt{1-\alpha}}{\alpha}\,\frac{a}{v_{esc}} \quad ; \quad \delta v_{\infty,s} \approx \frac{-\alpha \delta m_s}{2(1-\alpha)} \approx \frac{-2}{\sqrt{1-\alpha}}\,\frac{a}{v_{esc}}\,. \tag{9}$$

For a typical case with $\alpha \approx 2/3$ and $w_s = 0.001$, the net effect is to increase the mass loss rate and decrease the wind terminal speed, both by about 10%.

An important success of these CAK scaling laws is the theoretical rationale they provide for an empirically observed "Wind-Momentum-Luminosity" (WML) relation for OB supergiants (Kudritzki, Lennon & Pauldrach 1995). Combining the CAK mass-loss law (7) together with the scaling of the terminal speed with the effective escape, we obtain a WML relation of the form,

$$\dot{M} v_\infty \sqrt{R_*} \sim L^{1/\alpha'} \overline{Q}^{1/\alpha' - 1} \tag{10}$$

wherein we have neglected a residual dependence on $M(1 - \Gamma_e)$ that is generally very weak for the usual case that α' is near $2/3$. Note that the direct dependence $\overline{Q} \sim Z$ provides the scaling of the WML with metalicity Z. Much current research aims also to understand deviations from this relation for the weak winds of cooler OB dwarfs, and for the strong winds of Wolf-Rayet stars (Puls et al. 2008).

3 Non-Sobolev Models of Wind Instability

The above CAK steady-state model depends crucially on the use of the Sobolev approximation to compute the local CAK line force (3). Analyses that relax this approximation show that the flow is subject to a strong, "line-deshadowing instability" (LDI) for velocity perturbations on a scale near and below the Sobolev length $l_{Sob} = v_{th}/(dv/dr)$ (MacGregor, Harmann & Raymond 1979, Owocki & Rybicki 1984, 1985). Moreover, the diffuse, scattered component of the line force, which in the Sobolev limit is nullified by the fore-aft symmetry of the Sobolev escape probability (see figure 2), turns out to have important dynamics effects on the instability through a "diffuse line-drag" (Lucy 1984).

3.1 Linear Analysis of Line-Deshadowing Instability

For sinusoidal perturbations ($\sim e^{i(kr-wt)}$) with wavenumber k and frequency ω, the linearized momentum equation (ignoring the small gas pressure) relating the perturbations in velocity and radiative acceleration implies $\omega = i\frac{\delta g}{\delta v}$, which shows that unstable growth, with $\Im\omega > 0$, requires $\Re(\delta g/\delta v) > 0$. For a purely Sobolev model (Abbott 1980), the CAK scaling of the line-force (3)

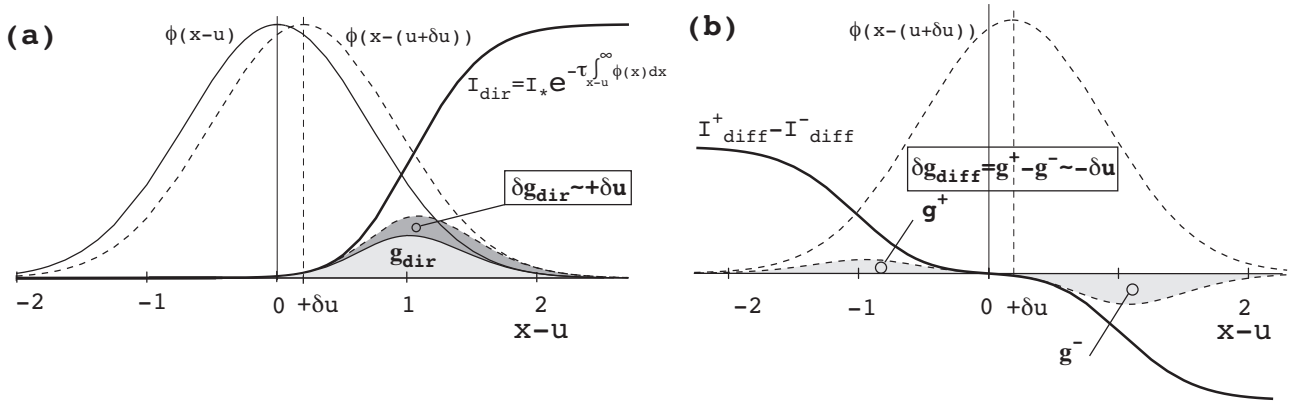

Figure 2: (a) The line profile ϕ and direct intensity plotted vs. comoving frame frequency $x - u = x - v/v_{th}$, with the light shaded overlap area proportional to the net direct line-force g_{dir}. The dashed profile shows the effect of the Doppler shift from a perturbed velocity δv, with the resulting extra area in the overlap with the blue-edge intensity giving a perturbed line-force δg that scales in proportion to this perturbed velocity $\delta u = \delta v/v_{th}$. (b) The comoving-frequency variation of the forward (+) and backward (-) streaming parts of the diffuse, scattered radiation. Because of the Doppler shift from the perturbed velocity, the dashed profile has a stronger interaction with the backward streaming diffuse radiation, resulting in a diffuse-line-drag force that scales with the negative of the perturbed velocity, and so tends to counter the instability of the direct line-force in part a.

with velocity gradient v' implies $\delta g \sim \delta v' \sim ik\delta v$, giving a purely real ω, and thus a stable wave that propagates inward at phase speed,

$$\frac{\omega}{k} = -\frac{\partial g}{\partial v'} \equiv -U \,, \tag{11}$$

which is now known as the "Abbott speed". Abbott (1980) showed this is comparable to the outward wind flow speed, and in fact exactly equals it at the CAK critical point.

As illustrated in figure 2a, instability arises from the deshadowing of the line by the extra Doppler shift from the velocity perturbation, giving $\delta g \sim \delta v$ and thus $\Im\omega > 0$. A general analysis (Owocki & Rybicki 1984) yields a "bridging law" encompassing both effects,

$$\frac{\delta g}{\delta v} \approx \Omega \frac{ik\Lambda}{1 + ik\Lambda} \,, \tag{12}$$

where $\Omega \approx g_{cak}/v_{th}$ sets the instability growth rate, and the "bridging length" Λ is found to be of order the Sobolev length l_{sob}. In the long-wavelength limit $k\Lambda \ll 1$, we recover the stable, Abbott-wave scalings of the Sobolev approximation, $\delta g/\delta v \approx ik\Omega\Lambda = ikU$; while in the short-wavelength limit $k\Lambda \gg 1$, we obtain the instability scaling $\delta g \approx \Omega \delta v$. The instability growth rate is very large, about the flow rate through the Sobolev length, $\Omega \approx v/l_{Sob}$. Since this is a large factor v/v_{th} bigger than the typical wind expansion rate $dv/dr \approx v/R_*$, a small perturbation at the wind base would, within this lineary theory, be amplified by an enormous factor, of order $e^{v/v_{th}} \approx e^{100}$!

3.2 Numerical Simulations of Instability-Generated Wind Structure

Numerical simulations of the nonlinear evolution require a non-Sobolev line-force computation on a spatial grid that spans the full wind expansion over several R_*, yet resolves the unstable structure at small scales near and below the Sobolev length. The first tractable approach (Owocki, Castor & Rybicki 1988) focussed on the *absorption* of the *direct* radiation from the stellar core, accounting now

for the attenuation from intervening material by carrying out a *nonlocal integral* for the frequency-dependent radial optical depth,

$$t(x,r) \equiv \int_{R_*}^{r} dr' \kappa_e \rho(r') \phi\left[x - v(r')/v_{th}\right] \,, \tag{13}$$

where ϕ is the line-profile function, and x is the observer-frame frequency from line-center in units of the line thermal width. The corresponding nonlocal form for the CAK line-ensemble force from this direct stellar radiation is

$$\Gamma_{dir}(r) = \Gamma_e \overline{Q}^{1-\alpha} \int_{-\infty}^{\infty} dx \, \frac{\phi\left(x - v(r)/v_{th}\right)}{t(x,r)^{\alpha}} \,. \tag{14}$$

In the Sobolev approximation, $t(x,r) \approx \Phi(x - v/v_{th})t$ (where $\Phi(x) \equiv \int_x^{\infty} \phi(x')\, dx'$), this recovers the CAK form (3). But for perturbations on a spatial scale near and below the Sobolev length, its variation also scales in proportion to the perturbed velocity, leading to unstable amplification. Simulations show that because of the inward nature of wave propagation implies an anti-correlation between velocity and density variation, the nonlinear growth leads to high-speed rarefactions that steepen into strong *reverse* shocks and compress material into dense clumps (or shells in these 1D models) (Owocki et al. 1988).

The assumption of pure-absorption was criticized by Lucy (1984), who pointed out that the interaction of a velocity perturbation with the background, *diffuse* radiation from line-scattering results in a *line-drag* effect that reduces, and potentially could even eliminate, the instability associated with the direct radiation from the underlying star. The basic effect is illustrated in figure 2. The fore-aft ($\pm$) symmetry of the diffuse radiation leads to cancellation of the g_+ and g_- force components from the forward and backward streams, as computed from a line-profile with frequency centered on the local comoving mean flow. Panel b shows that the Doppler shift associated with the velocity perturbation δv breaks this symmetry, and leads to stronger forces from the component opposing the perturbation.

Full linear stability analyses accounting for scattering effects (Owocki & Rybicki 1985) show the fraction of the direct instability that is canceled by the line-drag of the perturbed diffuse force depends on the ratio of the scattering source function S to core intensity I_c,

$$s = \frac{r^2}{R_*^2} \frac{2S}{I_c} \approx \frac{1}{1+\mu_*} \quad ; \quad \mu_* \equiv \sqrt{1 - R_*^2/r^2} \,, \tag{15}$$

where the latter approximation applies for the optically thin form $2S/I_c = 1 - \mu_*$. The net instability growth rate thus becomes

$$\Omega(r) \approx \frac{g_{cak}}{v_{th}} \frac{\mu_*(r)}{1+\mu_*(r)} \,. \tag{16}$$

This vanishes near the stellar surface, where $\mu_* = 0$, but it approaches half the pure-absorption rate far from the star, where $\mu_* \to 1$. This implies that the outer wind is still very unstable, with cumulative growth of ca. $v_\infty/2v_{th} \approx 50$ e-folds.

Most efforts to account for scattering line-drag in simulations of the nonlinear evolution of the instability have centered on a *Smooth Source Function* (SSF) approach (Owocki 1991; Feldmeier 1995; Owocki & Puls 1996, 1999). This assumes that averaging over frequency and angle makes the scattering source function relatively insensitive to flow structure, implying it can be pulled out of the integral in the formal solution for the diffuse intensity. Within a simple *two-stream* treatment of the line-transport, the net diffuse line-force then depends on the *difference* in the *nonlocal* escape probabilities $b_\pm$ associated with forward (+) vs. backward (-) *integrals* of the frequency-dependent

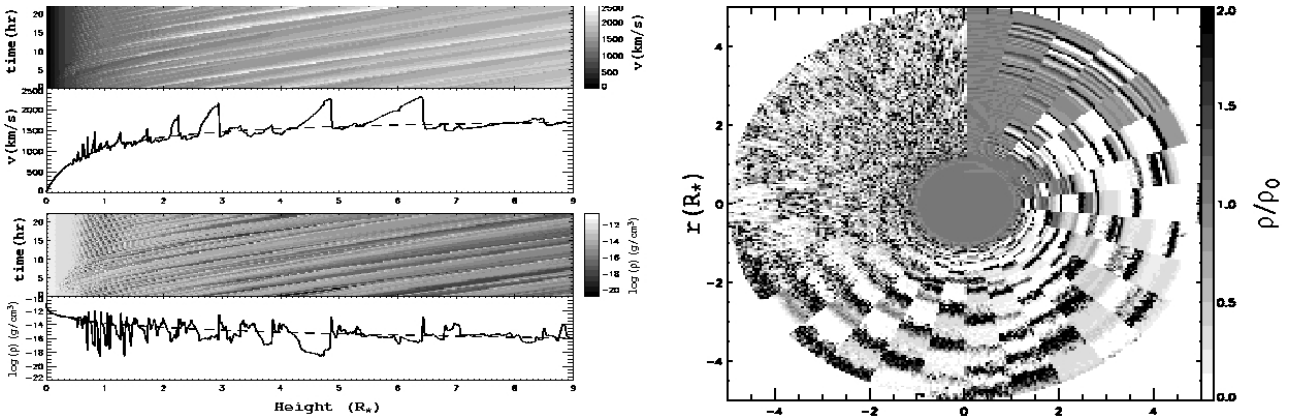

Figure 3: Left: Results of 1D Smooth-Source-Function (SSF) simulation of the line-deshadowing instability. The line plots show the spatial variation of velocity (upper) and density (lower) at a fixed, arbitrary time snapshot. The corresponding grey scales show both the time (vertical axis) and height (horizontal axis) evolution. The dashed curve shows the corresponding smooth, steady CAK model. Right: 2DH+1DR SSF simulation, greyscale representation for the density variations rendered as a time sequence of 2-D wedges of the simulation model azimuthal range $\Delta\phi = 12^o$ stacked clockwise from the vertical in intervals of 4000 sec from the CAK initial condition.

line-optical-depth (13). For a CAK line-ensemble, the net diffuse force can be written in a form quite analogous to the direct component (14),

$$\Gamma_{diff}(r) = \frac{\Gamma_e \overline{Q}^{1-\alpha}}{2(1+\mu_*)} \left[b_-(r) - b_+(r)\right] , \tag{17}$$

with

$$b_\pm(r) \equiv \int_{-\infty}^{\infty} dx \, \frac{\phi(x - v(r)/v_{th})}{[t_\pm(\pm x, r)]^\alpha} \tag{18}$$

where for t_- the integral bounds in (13) are now from r to the outer radius R_{max} (Owocki & Puls 1996) and the overall normalization for Γ_{diff} assumes the optically thin source function from eqn. (15). In the Sobolev approximation, both the forward and backward integrals give the same form, viz. $t_\pm(\pm x, r) \approx \Phi[\pm(x - v/v_{th})]t$, leading to the net cancellation of the Sobolev diffuse force. But for perturbations on a spatial scale near and below the Sobolev length, the perturbed velocity breaks the forward/back symmetry (figure 2b), leading to perturbed diffuse force that now scales in proportion to the *negative* of the perturbed velocity, and thus giving the diffuse line-drag that reduces the net instability by the factors given in (15) and (16).

The left panel of figure 3 illustrates the results of a 1D SSF simulation, starting from an initial condition set by smooth, steady-state CAK/Sobolev model (dashed curves). Because of the line-drag stabilization of the driving near the star (eqn. 16), the wind base remains smooth and steady. But away from the stellar surface, the net strong instability leads to extensive structure in both velocity and density, roughly straddling the CAK steady-state. Because the backstreaming component of the diffuse line-force causes any outer wind structure to induce small-amplitude fluctuations near the wind base, the wind structure, once initiated, is "self-excited", arising spontaneously without any explict perturbation from the stellar boundary.

In the outer wind, the velocity variations become highly nonlinear and nonmonotonic, with amplitudes approaching 1000 km/s, leading to the formation of strong shocks. However, these high-velocity regions have very low density, and thus represent only very little material. As noted for the pure-absorption models, this anti-correlation between velocity and density arises because the unstable

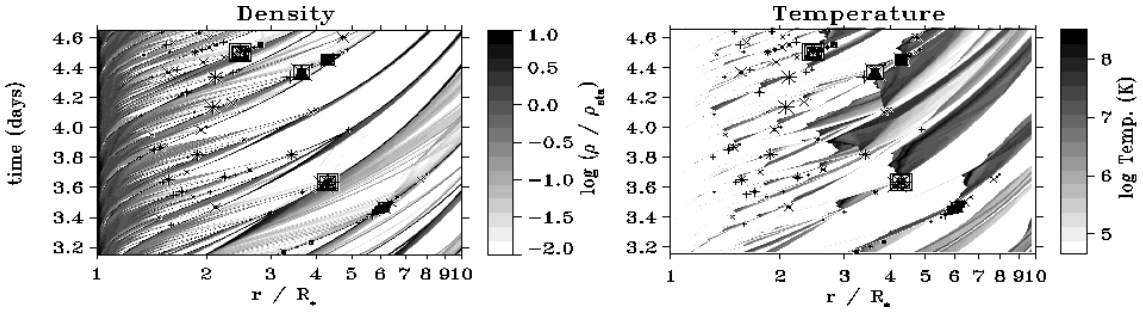

Figure 4: Greyscale rendition of the evolution of wind density and temperature, for time-dependent wind-instability models with structure formation triggered by photospheric perturbations. The boxed crosses identify localized regions of clump-clump collision that lead to the hot, dense gas needed for a substantial level of soft X-rays emission.

linear waves that lead to the structure have an *inward* propagation relative to the mean flow. For most of the wind mass, the dominant overall effect of the instability is to concentrate material into dense clumps. As discussed below, this can lead to overestimates in the mass loss rate from diagnostics that scale with the square of the density.

The presence of multiple, embedded strong shocks suggests a potential source for the soft X-ray emission observed from massive star winds; but the rarefied nature of the high-speed gas implies that this self-excited structure actually feeds very little material through the strong shocks needed to heat gas to X-ray emitting temperatures. To increase the level of X-ray emission, Feldmeier, Pauldrach & Puls (1997) introduced intrinsic perturbations at the wind base, assuming the underlying stellar photosphere has a turbulent spectrum of compressible sound waves characterized by abrupt phase shifts in velocity and density. These abrupt shifts seed wind variations that, when amplified by the line-deshadowing instabilty, now include substantial velocity variations among the dense clumps. As illustrated in figure 4, when these dense clumps collide, they induce regions of relatively dense, hot gas which produce localized bursts of X-ray emission. Averaged over time, these localized regions can collectively yield X-ray emission with a brightness and spectrum that is comparable to what is typically observed from such hot stars.

Because of the computational expense of carrying out nonlocal optical depth integrations at each time step, such SSF instability simulations have generally been limited to just 1D. More realistically, various kinds of thin-shell instabilites (Vishniac 1994) can be expected to break up the structure into a complex, multidimensional form. A first step to modelling both radial and lateral structure (Dessart & Owocki 2003) is to use a restricted "2D-H+1D-R" approach, extending the hydrodynamical model to 2D in radius and azimuth, but still keeping the 1D-SSF radial integration for the inward/outward optical depth within each azimuthal zone. The right panel of figure 3 shows the resulting 2D density structure within a narrow (12^o) wedge, with the time evolution rendered clockwise at fixed time intervals of 4000 sec starting from the CAK initial condition at the top. The line-deshadowing instability is first manifest as strong radial velocity variations and associated density compressions that initially extend nearly coherently across the full azimuthal range of the computational wedge.

But as these initial "shell" structures are accelerated outward, they become progressively disrupted by Rayleigh-Taylor or thin-shell instabilities that operate in azimuth down to the grid scale $d\phi = 0.2^o$. Such a 2DR+1DH approach may well exaggerate the level of variation on small lateral scales. The lack of *lateral* integration needed to compute an azimuthal component of the diffuse line-force means that the model ignores a potentially strong net lateral line-drag that should strongly damp azimuthal velocity perturbations on scales below the lateral Sobolev length $l_0 \equiv r v_{th}/v_r$ (Rybicki, Owocki & Castor 1990). Presuming that this would inhibit development of lateral instability at such scales, then

any lateral breakup would be limited to a minimum lateral angular scale of $\Delta\phi_{min} \approx l_0/r = v_{th}/v_r \approx 0.01\,\mathrm{rad} \approx 0.5^o$. Further work is needed to address this issue through explicit incorporation of the lateral line-force and the associated line-drag effect.

3.3 Clumping, Porosity and Vorosity: Implications for Mass Loss Rates

Both the 1D and 2D SSF simulations thus predict a wind with extensive structure in both velocity and density. A key question then is how such structure might affect the various wind diagnostics that are used to infer the mass loss rate. Historically such wind clumping has been primarily considered for its effect on diagnostics that scale with the square of the density, The strength of such diagnostics is enhanced in a clumped wind, leading to an overestimate of the wind mass loss rate that scales with $\sqrt{f_{cl}}$, where the clumping factor $f_{cl} \equiv \langle\rho^2\rangle \,/\, \langle\rho\rangle^2$, with angle brackets denoting a local averaging over many times the clump scale. For strong density contrast between the clump and interclump medium, this is just inverse of the clump volume filling factor, i.e. $f_{cl} \approx 1/f_{vol}$. 1D SSF simulations by Runacres & Owocki (2002) generally find f_{cl} increasing from unity at the structure onset radius $\sim 1.5R_*$, peaking at a value $f_{cl} \gtrsim 10$ at $r \approx 10R_*$, with then a slow outward decline to ~ 5 for $r \sim 100R_*$. These thus imply that thermal IR and radio emission formed in the outer wind $r \approx 10 - 100R_*$ may overestimate mass loss rates by a factor 2-3. The 2D models of Dessart & Owocki (2003) find a similar variation, but somewhat lower peak value, and thus a lower clumping factor than in 1D models, with a peak value of about $f_{cl} \approx 6$, apparently from the reduced collisional compression from clumps with different radial speeds now being able to pass by each other. But in both 1D and 2D models, the line-drag near the base means that self-excited, intrinsic structure does not appear till $r \gtrsim 1.5$, implying little or no clumping effect on $H\alpha$ line emission formed in this region. It should be stressed, however, that this is not necessarily a very robust result, since turbulent perturbations at the wind base, and/or a modestly reduced diffuse line-drag, might lead to onset of clumping much closer to the wind base.

If clumps remain optically thin, then they have no effect on single-density diagnostics, like the bound-free absorption of X-rays. The recent analysis by Cohen et al. (2010) of the X-ray line-profiles observed by Chandra from ζ-Pup indicates matching the relatively modest skewing of the profile requires mass loss reduction of about a factor 3 from typical density-squared diagnostic value. However, as discussed in the review by L. Oskinova et al. (2011) in these proceeedings, a key issue here is whether the individual clumps might become *optically thick* to X-ray absorption. In this case, the self-shadowing of material within the clump can lead to an overall reduction in the effective opacity of the clumped medium (Owocki, Gayley & Shaviv 2004; Oskinova, Feldmeier & Hamann 2006),

$$\kappa_{eff} = \kappa \frac{1 - e^{-\tau_{cl}}}{\tau_{cl}}\,, \tag{19}$$

where κ is the microscopic opacity, and the optical thickness for clumps of size ℓ is $\tau_{cl} = \kappa\rho\ell f_{cl}$. The product $\ell f_{cl} \equiv h$ is known as the *porosity length*, which also represents the *mean-free-path* between clumps. A medium with optically thick clumps is thus porous, with an opacity reduction factor $\kappa_{eff}/\kappa = 1/\tau_{cl} = 1/\kappa\rho h$.

However, it is important to emphasize that getting a significant porosity decrease in the *continuum* absorption of a wind can be quite difficult, since clumps must become optically thick near the radius of the smoothed-wind photosphere, implying a collection of a substantial volume of material into each clump, and so a porosity length on order the local radius. Owocki & Cohen (2006) showed in fact that a substantial reduction of the absorption-induced asymmetry of X-ray line profiles required large porosity lengths $h \sim r$. Since the LDI operates on perturbations at the scale of the Sobolev length $l_{sob} \equiv v_{th}/(dv/dr) \approx (v_{th}/v_\infty)R_* \approx R_*/300$, the resulting structure is likewise very small scale, as

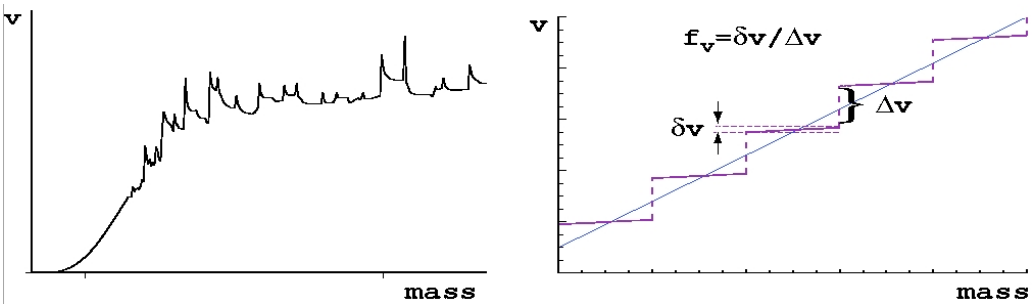

Figure 5: Left: Self-excited velocity structure arising in a 1D SSF simulation of the line-driven instability, plotted versus a mass coordinate, $M(r) = \int_R^r 4\pi\rho r'^2\, dr'$. Note the formation of velocity plateaus in the outer regions of the wind. Right: Velocity vs. mass in a wind seqment with structure described by a simplified velocity staircase model with multiple large steps Δv between plateaus of width δv. Here the associated velocity clumping factor $f_{vel} \equiv \delta v/\Delta v = 1/10$. The straight line represents the corresponding smooth CAK/Sobolev model.

illustrated in the 2D SSF simulations in figure 3. Given the modest clumping factor $f_{cl} \lesssim 10$, it seems clear that the porosity length is quite small, $h < 0.1r$, and thus that porosity from LDI structure is not likely to be an important factor [2] for continuum processes like bound-free absorption of X-rays.

The situation is however quite different for *line* absorption, which can readily be optically thick in even a smooth wind, with *Sobolev optical depth* $\tau_{sob} = \kappa_l \rho v_{th}/(dv/dr) = \kappa_l \rho l_{sob} > 1$. In a simple model with a smooth velocity law but material collected into clumps with volume filling factor $f_{vol} = 1/f_{cl}$, this clump optical depth would be even larger by a factor f_{cl}. As noted by Oskinova, Hamman & Feldmeier (2007), the escape of radiation in the gaps between the thick clumps might then substantially reduce the effective line strength, and so help explain the unexpected weakness of P V lines observed by FUSE (Fullerton et al. 2006), which otherwise might require a substantial, factor-ten or more reduction in wind mass loss rate.

But instead of *spatial* porosity, the effect on lines is better characterized as a kind of velocity porosity , or "*vorosity*", which is now relatively insensitive to the spatial scale of wind structure (Owocki 2008). The left panel of figure 5 illustrates the typical result of 1D dynamical simulation of the wind instability, plotted here as a time-snapshot of velocity vs. a *mass* coordinate, instead of radius. The intrinsic instability of line-driving leads to a substantial velocity structure, with narrow peaks corresponding to spatially extended, but tenuous regions of high-speed flow; these bracket dense, spatially narrow clumps/shells that appear here as nearly flat, extended velocity plateaus in mass. The right panel of figure 5 illustrates a simplified, heuristic model of such wind structure for a representative wind section, with the velocity clumping now represented by a simple "staircase" structure, compressing the wind mass into discrete sections of the wind velocity law, while evacuating the regions in between; the structure is characterized by a "velocity clumping factor" f_{vel}, set by the ratio between the internal velocity width δv to the velocity separation Δv of the clumps. The straight line through the steps represents the corresponding smooth wind flow.

The effect of the velocity structure on the line-absorption profile depends on the local Sobolev optical depth, which scales with the inverse of the mass derivative of velocity, $\tau_y \sim 1/(dv/dm)$, evaluated at a resonance location r_s, where the velocity-scaled, observer-frame wavelength $y = -v(r_s)/v_\infty$. In a smooth wind with Sobolev optical depth τ_y, the absorption profile is given sim-

[2] Okinova et al. (2004) argue that assuming clumps have a flattened 'pancake' shape with normal along the radial direction can allow greater transparency for X-rays passing near the star. But the above 2D SSF simulations suggest that Rayleigh-Taylor and thin-shell instabilities should break up such flattened pancakes into smaller, nearly spherical clumps.

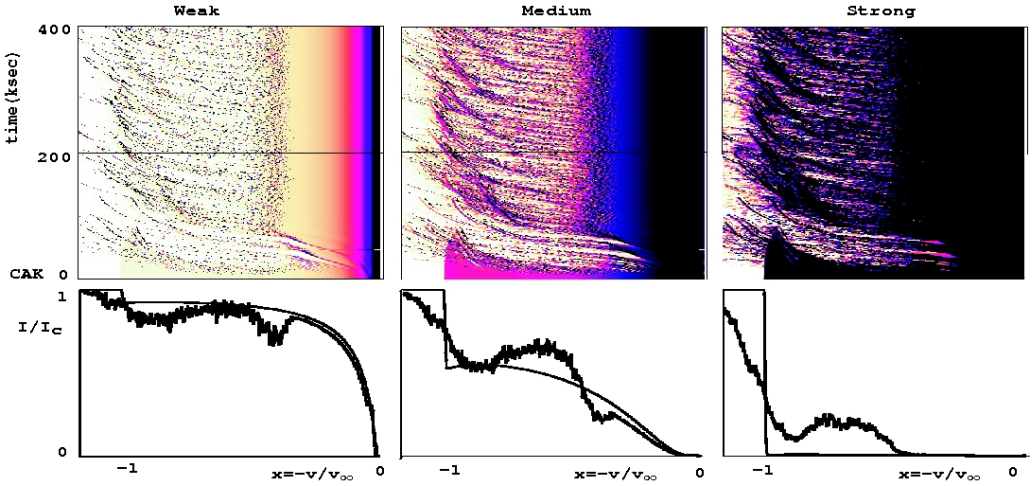

Figure 6: *Lower panels:* Absorption trough of time-averaged P-Cygni line profile plotted versus velocity-scaled observer wavelength $x = -v/v_\infty$ from line-center, for a weak, medium, and strong line. The smooth curves correspond to the smooth, CAK initial condition, while the jagged curves represent results for 1D dynamical instability simulations using the Smooth Source Function (SSF) method. *Upper panels:* Color-scale plots of the associated dynamical spectra, with time increasing vertically from the CAK initial condition.

ply by (Owocki 2008), $A_y = 1 - e^{-\tau_y}$. In the structured model, the optical thickness of individual clumps is increased by the inverse of the clumping factor $1/f_{vel}$, but they now only cover a fraction f_{vel} of the velocity/wavelength interval. The net effect on the averaged line profile is to *reduce* the net aborption by a factor (Owocki 2008),

$$R_A(\tau_y, f_{vel}) = f_{vel}\,\frac{1 - e^{-\tau_y/f_{vel}}}{1 - e^{-\tau_y}}\,. \tag{20}$$

Note that for optically thick lines, $\tau_y \gg 1$, the reduction approaches a fixed value, given in fact by the clumping factor, $R_A \approx f_{vel}$. If the smooth-wind line is optically thin, $\tau_y \ll 1$, then $R_A(\tau_y, f_{vel}) \approx (1 - e^{-\tau_y/f})/(\tau_y/f_{vel})$, which is quite analogous to the opacity reduction for *continuum* porosity (eqn. 19), if we just substitute for the clump optical depth, $\tau_c \rightarrow \tau_y/f_{vel}$.

But a key point here is that, unlike for the continuum case, the *net reduction in line absorption no longer depends on the spatial scale* of the clumps. Instead one might think of this velocity clumping model as a kind of velocity form of the standard venetian blind, with f_{vel} representing the fractional projected covering factor of the blinds relative to their separation. The $f_{vel} = 1$ case represents closed blinds that effectively block the background light, while small f_{vel} represent cases when the blinds are broadly open, letting through much more light.

3.4 Line-absorption profile from instability simulations

Figure 6 shows results for line-absorption spectra from a typical 1D-SSF instability simulation, wherein the intrinsic instabilty leads to extensive wind structure above a radius of about $r \approx 1.5R_*$. The upper panels of figure 6 show the corresponding effect on the dynamic spectra for a weak, medium, and strong line. The lower panels compare the associated time-average profile with that of the smooth CAK initial condition. The high level of velocity clumping leads to many tracks of enhanced, even saturated absorption, while at the same time exposing channels between the clumps that allow for increased transmission of the stellar surface flux. The time-averaged profiles in the

lower panels thus show a general *reduction* in the absorption compared to the smooth, CAK model, most notably at middle wavelengths ($-y = v/v_\infty \approx 0.3 - 0.8$) relative to the blue edge for the CAK terminal speed v_∞. On the other hand, the unstable flow faster than the CAK v_∞ extends the absorption beyond $y = -1$, leading to notable softening of the blue edge.

But a key result here is that even the strong, saturated line has a residual flux of 10-20%. This is qualitatively just the kind of absorption reduction needed to explain the observed moderate strength of the P V line reported by Fullerton et al. (2006). The contribution by Sundqvist et al. (2011) in these proceedings describes recent further efforts to account for unstable wind velocity structure in quantitative modeling of both UV resonance lines like P V, as well as recombination lines like $H\alpha$. While demonstrating again the importance of accounting for velocity and density structure for interpreting both diagnostics, the results suggest a need for further development in radiation hydrodynamical simulations to properly resolve the velocity structure of clumps, and to induce their onset closer to the wind base, where $H\alpha$ is formed.

References

Abbott, D.C. 1980, ApJ 242, 1183.
Abbott, D.C. 1982, ApJ 259, 282.
Castor, J., Abbott, D., & Klein, R. 1975, ApJ 195, 157 (CAK).
Cohen, D.H., Leutenegger, M.A., Wollman, E.E., Zsargó, J., Hillier, D.J., Townsend, R.H.D., & Owocki, S.P. 2010, MNRAS 405, 2391
Davidson, K., & Humphreys, R.M. 1997, Ann Rev Astr Astrophys 35, 1
Dessart, L., & Owocki, S.P. 2003, ApJ 406, 1.
Feldmeier, A. 1995, A&A 299, 523
Feldmeier, A., Puls, J., & Pauldrach, A. 1997, A&A 322, 878
Friend, D.B., & Abbott, D.C. 1986, ApJ 311, 701
Fullerton, A.W., Massa, D.L., & Prinja, R.K. 2006, ApJ 637, 1025
Gayley, K. 1995, ApJ 454, 410
Kudritzki, R. Lennon, D., & Puls, J. 1995, in *Science with the VLT*, eds. J. Walsh & I. Danziger, p. 246
Lucy, L.B. 1984, ApJ 284, 351
Lucy, L.B., & Solomon, P. 1970, ApJ 159, 879
MacGregor, K.B., Hartmann, L., & Raymond, J.C. 1979, ApJ 231, 514
Oskinova, L.M., Feldmeier, A., & Hamann, W.-R. 2006, MNRAS, 372, 313
Oskinova, L.M., Hamann, W.-R., & Feldmeier, A. 2007, A&A 476, 1331
Oskinova, L.M., Hamann, W.-R., Ignace, R., & Feldmeier, A. 2011, in Proceedings of the 39th Liège Astrophysical Colloquium, eds. G. Rauw, M. De Becker, Y. Nazé, J.-M. Vreux & P.M. Williams, BSRSL 80, 54
Owocki, S.P. 1991, in *Stellar Atmospheres - Beyond Classical Models*, NATO ASIC Proc. 341, 235
Owocki, S.P. 2008, in *Clumping in Hot-Star Winds*, eds. W.-R. Hamann, A. Feldmeier & L.M. Oskinova, Potsdam: Univ.-Verl., 121 URN: http://nbn-resolving.de/urn:nbn:de:kobv:517-opus-13981
Owocki, S.P., Castor, J.I., & Rybicki, G.B. 1988, ApJ 335, 914
Owocki, S.P., & Cohen, D.H. 2006, ApJ 648, 565
Owocki, S.P., Gayley, K., & Shaviv, N. 2004, ApJ 558, 802
Owocki, S.P., & Puls, J. 1996, ApJ 462, 894
Owocki, S.P., & Puls, J. 1999, ApJ 510, 355
Owocki, S.P. & Rybicki, G.B. 1984, ApJ 284, 337
Owocki, S.P. & Rybicki, G.B. 1985, ApJ 299, 265
Owocki, S.P., & ud-Doula, A. 2004, ApJ 600, 1004
Pauldrach, A., Puls, J., & Kudritzki, R.P. 1986, A&A 164, 86
Runacres, M.C., & Owocki, S.P. 2002, A&A 381, 1015
Puls, J., Vink, J., & Najarro, P. 2008, A&A Reviews 16, 209
Rybicki, G.B., Owocki, S.P., & Castor, J.I. 1990, ApJ 349, 274
Sobolev, V.V. 1960, *Moving Envelopes of Stars* (Cambridge: Harvard University Press)
Sundqvist, J.O., Puls, J., Feldmeier, A., & Owocki, S.P. 2011, in Proceedings of the 39th Liège Astrophysical Colloquium, eds. G. Rauw, M. De Becker, Y. Nazé, J.-M. Vreux & P.M. Williams, BSRSL 80, 48

Vishniac, E.T. 1994, ApJ 428, 186.

Discussion

G. Meynet: Is there any evidence for magnetic braking (spin down of rotation rate) of massive magnetic stars?
S Owocki: Yes, magnetic braking has been simulated recently by ud-Doula et al. (2008), who give a simple scaling law for the associated spindown time in terms of the inferred magnetic strength, mass loss rate, and stellar parameters, when applied to e.g. the B2 Vp star σ Orionis E, this predicts a spindown time of 1.2 Myr, in very good agreement with recent direct measurement from the timing of photospheric eclipse of magnetically trapped clouds (Townsend et al. 2010).

UV, optical and near-IR diagnostics of massive stars

Fabrice Martins[1]

[1] GRAAL-UMR5024, CNRS & Université Montpellier II
Place Eugène Bataillon, F-34095 Montpellier, France

Abstract: We present an overview of a few spectroscopic diagnostics of massive stars. We explore the following wavelength ranges: UV (1000 to 2000 Å), optical (4000–7000 Å) and near–infrared (mainly H and K bands). The diagnostics we highlight are available in O and Wolf–Rayet stars as well as in B supergiants. We focus on the following parameters: effective temperature, gravity, surface abundances, luminosity, mass loss rate, terminal velocity, wind clumping, rotation/macroturbulence and surface magnetic field.

1 Introduction

The development of sophisticated atmosphere codes combined with the regular access to multi–wavelength observational data (from the X–rays to the radio range) allow improved determination of stellar and wind parameters of massive stars. This in turn affects our understanding of these objects. Since massive stars play key roles in different fields of astrophysics (being the progenitors of long–soft GRBs, the producers of most metals heavier than oxygen, important contributors to the release of mechanical energy in the interstellar medium...) it is crucial to be able to accurately constrain their properties. Here, we present a non exhaustive overview of the main spectroscopic diagnostics used to determine the fundamental parameters of massive stars. We restrict ourselves to the UV, optical and near-infrared ranges. The diagnostics we present in the following apply to O and Wolf–Rayet stars as well as B supergiants.

2 Stellar parameters

In this section we present the main spectroscopic methods used to determine the stellar parameters: effective temperature, surface gravity, luminosity, surface abundances.

2.1 Effective temperature

The effective temperature of massive stars is usually derived using the ionization balance method. The principle relies on the computation of synthetic spectra from atmosphere models at different temperatures. Depending on the temperature, the ionization of the elements present in the atmosphere is different: the wind is more ionized for higher $T_{\rm eff}$. Consequently, the lines of ions of the same element but of different ionization states are also sensitive to the effective temperature. Comparing

the strength of synthetic lines to observed lines thus yields the star's temperature (e.g. Herrero et al. 1992, Puls et al. 1996, Martins, Schaerer & Hillier 2002). In practice, lines from successive ions of the same elements must be observed. The most reliable indicators for O and Wolf-Rayet stars are the He I and He II lines. The classical diagnostics are He I 4471 and He II 4542. They are the strongest photospheric lines in most stars (He II 4686 can be stronger than He II 4542 but it is more sensitive to wind contamination). An illustration of their behaviour with $T_{\rm eff}$ is given in Fig. 1. We see that increasing $T_{\rm eff}$ reduces the He I 4471 line strength and increases the He II 4542 absorption. A number of complementary lines can be used to confirm and refine the estimate based on the previously mentioned lines: He I 4026, He I 4388, He I 4712, He I 4920, He II 4200, He II 5412. Note that the He I singlet lines can be sensitive to subtle details of the modelling related to line–blanketing effects (e.g. Najarro et al. 2006). When the temperature drops below roughly 27000 K, helium is almost neutral in the atmosphere so that no He II lines are detected. This is the range of mid- and late-B stars. For those objects, one usually switch to the Si ionization balance traced by the following lines: Si II 4124-31, Si III 4552-67-74, Si III 5738, Si IV 4089, Si IV 4116 (e.g. Trundle et al. 2004). Depending on the temperature, either Si II and Si III , or Si III and Si IV lines are used. The temperatures derived from the optical have typical uncertainties of 500 to 2000 K depending on the quality of the observational data and on the temperature itself (uncertainties are larger when lines from one ionization state are weak).

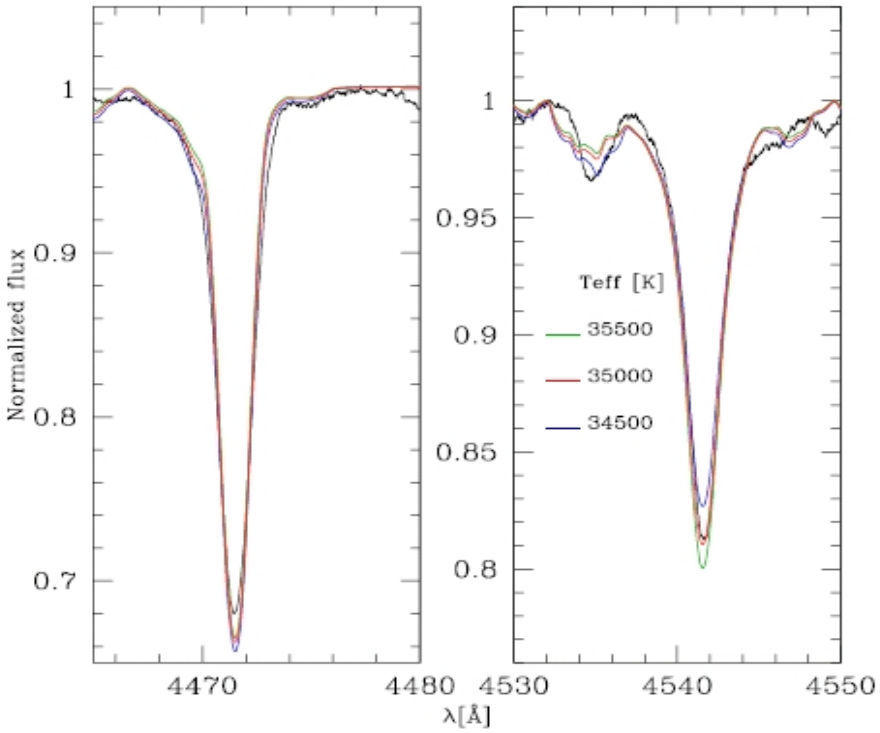

Figure 1: Dependence of the He I 4471 and He II 4542 line strength on the effective temperature. The synthetic spectra correspond to $T_{\rm eff}$ = 34500K (35000K, 35500K) and are shown by the blue (red, green) lines. The observed spectrum is the black line.

The ionization balance method can be applied to near-IR spectra of O stars. In the K–band, He I and He II lines are present above $\sim$ 30000 K (Hanson et al. 2005). The strongest He I line at 2.058μm must be used very carefully because of its extreme dependence on line-blanketing effects (Najarro et al. 1997, 2006). The use of He I 2.112μm is preferred although the line is weaker and can be blended with C III/N III emission. The only He II line in the K-band is He II 2.189μm. Repolust et al. (2005)

have analyzed the same sample of stars independently with optical and near–IR spectra and found that the derived temperatures were consistent within the uncertainties.

When only UV spectra are available, the determination of $T_{\rm eff}$ is more difficult. One usually relies on the iron ionization balance. Line forests from Fe IV (resp. Fe V, Fe VI) are indeed observed in the wavelength range 1600 - 1630 Å (resp. 1360 - 1380 Å, 1260 - 1290 Å). An illustration is given in Fig. 10 of Heap, Lanz & Hubeny (2006). The *relative* strength of these line forests provides the best $T_{\rm eff}$ indicator, although the uncertainties are usually larger than those of optical determination.

2.2 Surface gravity

The surface gravity is classically derived from optical spectroscopy. The wings of the Balmer lines are broadened by collisional processes (linear Stark effect) and are thus stronger in denser atmospheres, i.e. for higher $\log g$ (which causes larger pressure and thus more collisions). In practice Hβ, Hγ and Hδ are the main indicators, provided they are in absorption and/or their wings are not contaminated by wind emission. They are usually strong and well resolved.

In the near-IR, the Brackett lines can play the same role. Again, only the wings have to be considered since they are sensitive to collisional broadening. Repolust et al. (2005) showed that the behaviour of the Balmer and Brackett lines with gravity was similar only in the far wings, the line cores having different variations (see Repolust et al. for a thorough discussion). In practice Brγ is the best gravity indicator in the K–band. Br10 and Br11 (H–band) can be used as secondary indicators.

2.3 Luminosity

Until recently, bolometric luminosities were derived from optical (or near-IR) photometry and bolometric corrections. For instance, one could obtain $L_{\rm bol}$ from $log\frac{L_{\rm bol}}{L_\odot} = -0.4\times(M_V + BC(T_{\rm eff}) - M_\odot^{bol})$ where M_V is the absolute magnitude, BC($T_{\rm eff}$) the bolometric correction at temperature $T_{\rm eff}$ and $M_\odot^{bol}$ the Sun's bolometric magnitude. This method requires the use of calibrations of bolometric corrections. Another related method consists in comparing directly absolute magnitudes (usually in the V band) to theoretical fluxes in the appropriate band convolved with the filter's response.

Nowadays, spectral energy distribution (SED) fitting is becoming the standard way of deriving luminosities. In this process, spectrophotometry ranging from the (far)UV to the infrared is used to adjust the global flux level of atmosphere models. Since the full SED is used, there is no need for bolometric corrections. In addition, the reddening can be derived simultaneously. Any excess emission (due to dust for instance) can be identified and fitted with additional components. An example of such a fit is shown in Fig. 2.

For both methods briefly presented above, the distance to the star must be known independently.

2.4 Surface abundances

Once the effective temperature, gravity and luminosity have been constrained, it is possible to derive the surface abundance of several elements using photospheric lines. The classical spectroscopic method consists in comparing synthetic spectra with different abundances to key diagnostic lines.

Optical studies of OB stars allow the determination of abundances of C, N, O, Si, Mg. The main diagnostics are the following:

- carbon: C II 4267, C II 6578–82 / C III 4647–50, C III 5696 / C IV 5802–12
- nitrogen: N II 3995 / N III 4510-15 / N IV 4058, N IV 5200 / N V 4605-20
- oxygen: O II 4075, O II 4132, O II 4661 / O III 5592

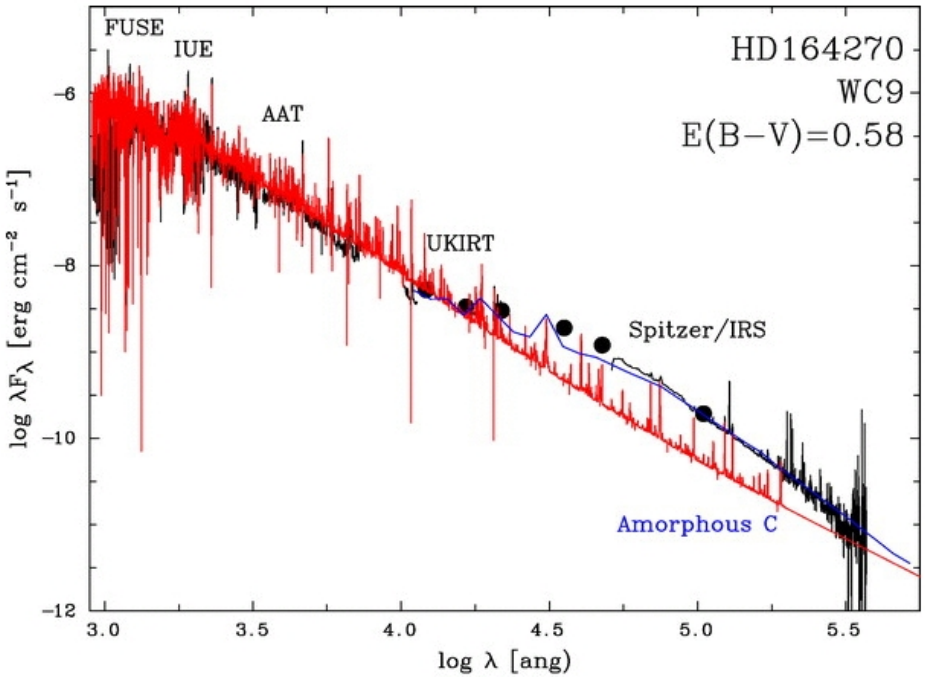

Figure 2: SED fitting of a WC9 star. The black line and symbols are the observational data. The red line is the synthetis stellar flux and the blue line is the synthetic dust emission. The infrared part of the spectrum shows an emission excess due to dust. Adapted from Crowther, Morris & Smith (2006a).

• silicon: Si II 4124–31 / Si III 4552–67–74, Si III 5738 / Si IV 4089, Si IV 4116
• magnesium: Mg II 4481
Several N III lines are also observed between 4630 and 4640 Å in O and early B stars. They are rather strong but their modelling is still difficult and they should be treated with care.

Low ionization lines are present in B stars while high ionization lines are observed in the earliest O stars. The same lines can be used to constrain the abundances of Wolf–Rayet stars. However, they are usually emitted in the wind and are observed in emission. The knowledge of the wind properties, especially the mass loss rate, is thus necessary to correctly derive stellar abundances.

In O and B stars, the determination of surface abundances requires the knowledge of the microturbulence velocity. It is usually constrained from a few metallic lines, either by direct comparison of synthetic spectra or by measurement of equivalent widths of synthetic profiles with different microturbulent velocity. The determination is usually done simultaneously with the abundance determination. The value of v_{turb} is chosen to minimize the spread in abundance derived from several lines of the same ion (e.g. Dufton et al. 2005).

In the UV range, lines from CNO and Si are usually formed in the wind and are used to constrain the mass loss rate and terminal velocity. A determination of the abundances from the optical lines is necessary to correctly derive the wind properties. There are several iron line forests (see also Sect. 2.1) that can be used to constrain the Fe content. If the relative strength of these line forests constrain T_{eff}, their absolute strength is an indication of the iron composition.

In the near-IR, the number of metallic lines is limited, especially in OB stars where the lines are weak. For stars with stronger wind (extreme O supergiants and Wolf-Rayet stars) a few features are available. In the K–band, the N III doublet at 2.247–2.251 μm is a valid indicator of the nitrogen content (Martins et al. 2008). The Mg II 2.138–2.144 μm doublet is detected in the coolest stars. In the hottest stars, C IV lines are observed at 2.070, 2.079 and 2.084 μm. In the H–band, Fe II 1.688 μm, Si II 1.691 μm and Si II 1.698 μm are used to constrain the iron and silicon abundances (Najarro

et al. 2009).

3 Wind parameters

We now turn to the wind parameters of massive stars. We first present the determination of terminal velocities, then the mass loss rates and finally review the spectroscopic diagnostics of clumping.

3.1 Terminal velocity

The terminal velocity is the maximum velocity reached by a stellar wind at the top of the atmosphere. If the wind density is high enough, P–Cygni profiles are observed in several lines. The strongest ones are UV resonance lines. The origin of the blueshifted part of the P–Cygni profile is the Doppler shift associated with the wind outflow in front of the photospheric disk. Consequently, the measure of the blueward extent of this absorption gives a direct access to the terminal velocity. The terminal velocity can be defined as the velocity leading to the absorption up to the point where the line profile reaches the continuum (the edge velocity) or as the velocity producing the bluest complete (i.e. zero flux) absorption (the black velocity). The former is usually affected by additional small-scale (microturbulence[1]) or large–scale (discrete absorption components) motions so that the latter is usually adopted (e.g. Prinja, Barlow & Howarth 1990). This definition is only valid for strong wind stars though: for thinner winds, the P-Cygni profiles are not saturated. The main UV diagnostics are the following: N V 1240, Si IV 1393–1403, C IV 1548–50, N IV 1718. Additional indicators are found in the *FUSE* range: O VI 1032-1038, C III 1176. Other P-Cygni profiles can be found below 1000 Å but they are usually blended with interstellar molecular and atomic hydrogen absorption.

When stars have strong winds ($\dot{M} \geq 10^{-5}$ M$_\odot$ yr^{-1}) but their UV spectra are not available, other diagnostics can be used. In the optical, the Balmer lines (Hα, Hβ, Hγ, Hδ) and sometimes some He I lines (e.g. He I 4471) can have pure emission or P-Cygni profiles. In the latter case, the same method as in the UV is applied. For pure emission lines, the line width is usually related to the wind terminal velocity. Fitting such profiles with synthetic spectra computed from atmosphere models with different terminal velocities will provide an indirect measure of the terminal velocity. Similarly, in the near-IR, He I 2.058μm and He I 2.112μm have P-Cygni profiles in late-type WR stars or LBVs, and emission profiles in other strong-wind massive stars. We can proceed as for the optical Balmer lines to estimate terminal velocities.

In case no spectroscopic diagnostic is available, the terminal velocity of a massive star can be estimated from the relation $v_\infty \approx 2.25\sqrt{(\frac{\alpha}{1-\alpha})}$ v$_{esc}$where v$_{esc}$ is the escape velocity and α the line force multiplier parameter of the CAK theory. In practice, $v_\infty \sim 3\times$ v$_{esc}$ for stars hotter than about 25000 K, and $v_\infty \sim 1.5\times$ v$_{esc}$ for stars cooler than this limit. This "bistability jump" is well known (Lamers, Snow & Lindholm 1995), although recent studies tend to show that it is more a gradual decrease than a real jump (Crowther, Lennon & Walborn 2006b, Markova & Puls 2008).

3.2 Mass loss rate

There are two main classes of spectroscopic diagnostics of mass loss rate: the P–Cygni resonance lines observed mainly in the UV range, and optical emission lines, mainly Hα.

UV P-Cygni profiles are sensitive to the wind density times the ionization fraction of the ion responsible for the observed line. Since the density is directly related to the mass loss rate (density $\propto$

[1]It is introduced as a proxy to represent a significant velocity dispersion which can be simulated by supersonic microturbulence.

$\frac{\dot{M}}{R^2 v_\infty}$) fitting such features provides constraints on $\dot{M}$. The strength of these P–Cygni features allows determinations down to very low values of $\dot{M}$ (typically down to 10^{-10} $M_\odot$ yr^{-1}). This is especially important for the so–called 'weak wind stars' (Martins et al. 2004, Marcolino et al. 2009). The main drawback is that it requires a good knowledge of the ionization structure. All physical processes affecting this structure have to be included in model atmospheres to ensure accurate determinations. The most common features used are: N V 1240, Si IV 1393–1403, C IV 1548–50, He II 1640, N IV 1718. P V 1118–28 can also be used provided X-rays and clumping are taken into account (see Sect. 3.3). An example of the fit of the C IV 1548-50 line is shown in Fig. 4. Other lines in the FUV range are available, but they are often contaminated by interstellar atomic and molecular hydrogen absorption (see also Sect. 3.1).

The other main diagnostics of mass loss rate is the Hα line in the optical (e.g. Puls et al. 1996). If the density is high enough, hydrogen recombination leads to Hα wind emission which adds to the underlying photospheric absorption. For strong winds, the emission completely dominates the line profile. Fig. 3 shows an example of fit for an SMC B supergiant (Trundle et al. 2004). Since it is a recombination line, it depends on the density square (as opposed to density for P–Cygni profiles). Consequently, its emission decreases quickly with density (and thus $\dot{M}$). Hα then turns rapidly into a pure photospheric absorption profile from which no $\dot{M}$ determination is possible. This happens below $\sim 10^{-8}$ $M_\odot$ yr^{-1}. Hα is however less sensitive to ionization issues since hydrogen is almost completely ionized in massive stars atmospheres. It is thus sometimes considered a better diagnostics (but again, only for strong wind stars). A secondary optical indicator is He II 4686. In the case of Wolf–Rayet stars, the other Balmer lines (Hβ, Hγ, Hδ) are also in emission and are complementary indicators.

In the near-IR range, the Brackett lines, especially Brγ, play the same role as the Balmer lines in the optical (Repolust et al. 2005, Martins et al. 2008). A rather strong line is Brα at 4.051 μm. Preliminary example of use of this line are shown in Puls, Vink & Najarro (2008).

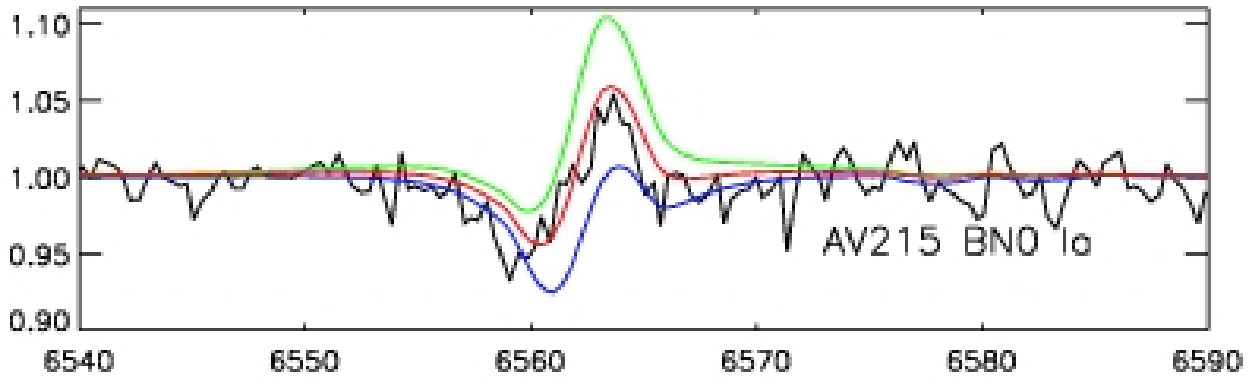

Figure 3: Hα fit for the SMC B supergiant AV215. The blue and green lines correspond to models with a mass loss rate changed by $\pm$15% compared to the best fit model (red line). Adapted from Trundle et al. (2004).

3.3 Clumping

Several pieces of evidence indicate that the winds of massive stars are not homogeneous. Spectroscopically, the first indirect proof came from Hillier (1991) who realized that the red electron scattering wing of strong emission lines of Wolf-Rayet stars was overpredicted in homogeneous models. The

inclusion of inhomogeneous winds by means of a volume filling factor approach led to a better agreement with observations. The electron scattering wings of emission lines are still used nowadays to constrain the degree of inhomogeneities in strong wind stars. The classical diagnostics are: He II 4686, He II 5412, Hβ (see Hillier 1991, Martins et al. 2009).

The presence of clumping in massive stars winds has two main effects: first, for a given atmospheric structure, it changes the shape of wind lines; second, due to the increased density in clumps, recombinations are stronger and thus the ionization structure is modified. The first effect can be explained as follows. For a recombination line, the line intensity is proportional to $\rho^2 \times V$ where ρ is the density and V the total volume of the wind. In the case of a volume filling factor f, the density in the clumped wind is $\rho_c = \rho_0/f$ where the indices 'c' and '0' refer to the clumped and unclumped models respectively. Similarly, the volume effectively containing the material is $f \times V_0$. Hence, the line intensity is proportional to ρ_0^2/f. Consequently, including clumping increases the line strength by $1/f$. Said differently, since $\rho_0 \propto \dot{M}$, the line intensity will be the same for similar $\dot{M}/\sqrt{f}$ ratios. Hα in the optical (e.g. Puls et al. 2006) and Br10/Br11 in the near–IR (Najarro et al. 2009) are the main ρ^2 diagnostics of clumping.

For scattering lines such as the UV P–Cygni profiles, the intensity depends linearly on the density, so that in principle there is no 'first effect' of clumping on these profiles[2]. But the second effect – the change of ionization structure – is present. This is illustrated in Fig. 4 and 5 – from Bouret, Lanz & Hillier (2005). In the former figure, UV P–Cygni profiles of an O4V((f)) star are shown for homogeneous (grey dashed line) and clumped (grey solid) models. The clumped models provide a much better fit to O V 1371 and N IV 1718. In Fig. 5, we see that adding clumping strongly reduces the fraction of O V in the atmosphere, leading to a weaker O V 1371 line. Another UV diagnostic of clumping is the P V doublet at 1118–1128 Å (e.g. Fullerton, Massa & Prinja 2006).

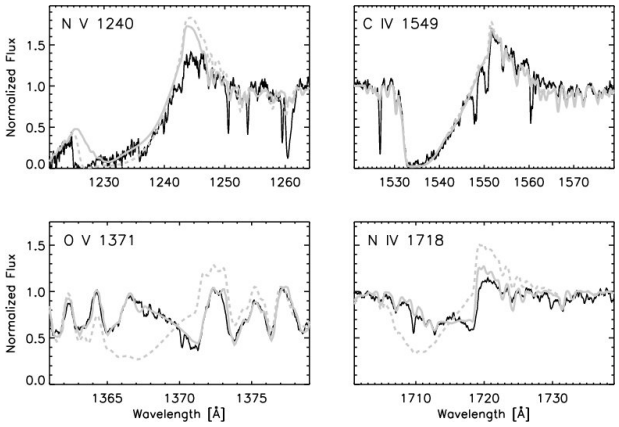

Figure 4: Observed P-Cygni profiles (black solid line) together with synthetic spectra from models with homogeneous wind (grey dashed line) and clumped wind (grey solid line). From Bouret et al. (2005).

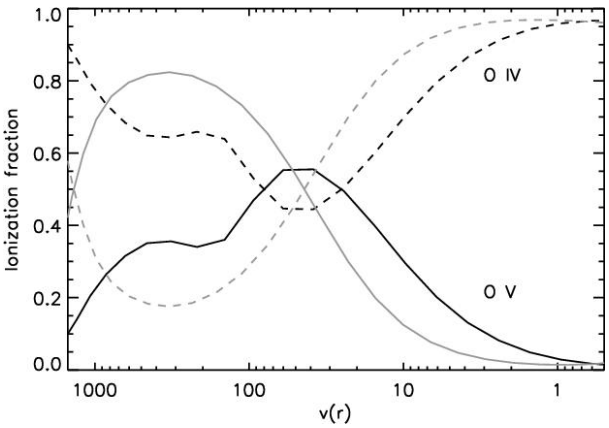

Figure 5: Oxygen ionization fraction of the homogeneous (grey) and clumped (black) models shown in Fig. 4. From Bouret at al. (2005).

More direct evidence for clumping comes from time series analysis of selected emission lines of O supergiants and Wolf-Rayet stars. The first study of Eversberg, Lépine & Moffat (1998) showed the presence of emission sub–peaks on-top of the main emission of He II 4686. These structures showed motions from the line center to the line wings. This is interpreted as the presence of clumps moving outward in the stellar atmosphere. Similar conclusions were subsequently reached for different types

[2]This is only true if clumps are optically thin in UV resonance lines (see e.g. Sundqvist, Puls & Feldmeier 2010).

of emission line stars, using C III 5696 and C IV 5802–12 in addition to the He II lines mentioned above (e.g. Lépine et al. 2000).

4 Rotation and magnetic field

We finally focus on two properties of massive stars: their rotation rates and the relation to macroturbulence, and their magnetic fields.

4.1 Projected rotational velocities and macroturbulence

The determination of projected rotational velocities (V sin$i$) has become a difficult task since it was realized that line profiles of O stars were also broadened by another mechanism dubbed macroturbulence. Its origin is not well constrained although a recent study by Aerts et al. (2009a) points to a probable role of stellar pulsations (see also Simón Díaz et al. 2010 for first observational evidence).

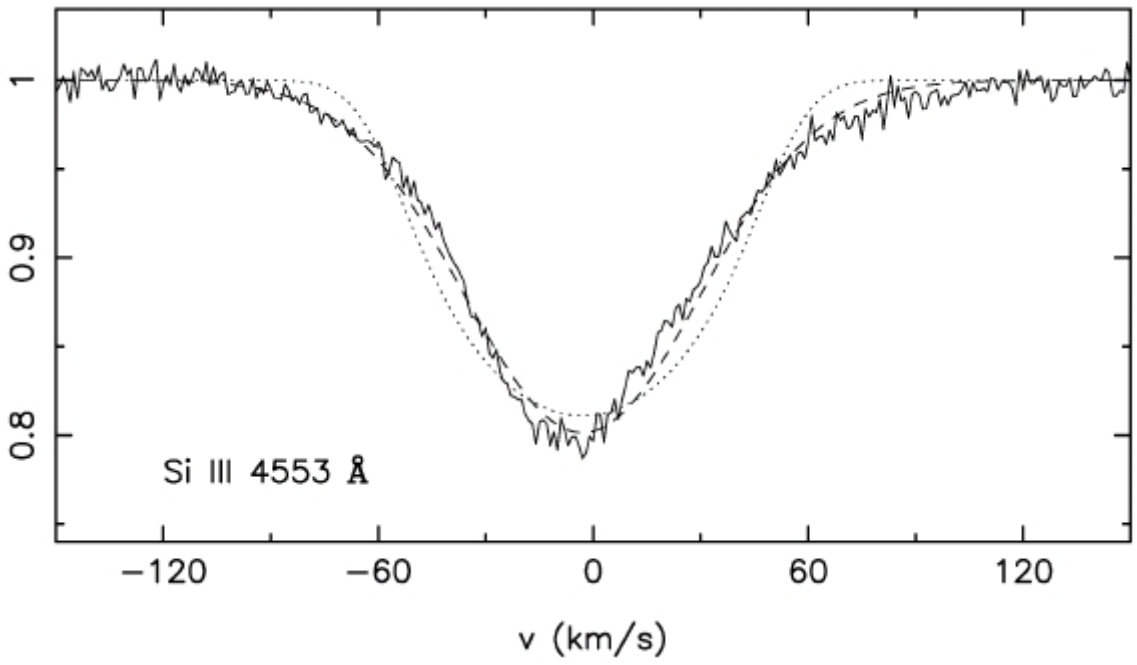

Figure 6: Observed profile (solid line) together with a synthetic spectrum including only rotational broadening (V sin$i$ = 57 km s^{-1}, dotted line) and rotational broadening + Gaussian macroturbulence (V sin$i$ = 5 km s^{-1}+ $v_{\rm mac}$ = 32 km s^{-1}, dashed line). The inclusion of macroturbulence leads to a much better fit of the observed profile. From Aerts et al. (2009b).

In absence of macroturbulence, two methods have been widely used to constrain V sin$i$:
• FWHM–V sin$i$: this method first developed by Slettebak et al. (1975) relies on the computation of synthetic line profiles at different rotational velocities from which the full width at half maximum (FWHM) is measured and subsequently compared to observational data. It was used by Herrero et al. (1992) and Abt, Levato & Grosso (2002) (among others) to derive V sin$i$ for O and B stars. It relies mainly on optical metallic lines.
• Cross-correlation: here, a low V sin$i$ template spectrum is convolved at different rotational velocities and is subsequently cross-correlated with observed spectra. The method has been particularly used in the UV range (e.g. Penny et al. 1996, Howarth et al. 1997) taking advantage of the large IUE database.

The direct comparison of synthetic line profiles to observational data revealed that the wings of photospheric lines did not show the classical "curved" shape of rotational profiles, but were wider and more "triangular". This is illustrated in Fig. 6 where we see that a pure rotational profile (dotted line) is a poor fit of the observed spectrum (see also Ryans et al. 2002). The addition of a macroturbulent profile, usually implemented by convolution with a Gaussian profile and thus mimicking isotropic turbulence, leads to a significant improvement. The consequence is a reduction of the derived V sin$i$ compared to studies ignoring macroturbulence (see Fig. 6). In practice, optical lines are well suited to constrain V sin$i$ and the amount of macroturbulence. Among the key lines, there is: C IV 5812, O III 5592, N IV 4057, He I 4712 (see Howarth et al. 2007, Martins et al. 2010). The main drawback of this method is that several combinations of V sin$i$/macroturbulence can give fits of similar quality, rendering the determination of projected rotational velocities uncertain.

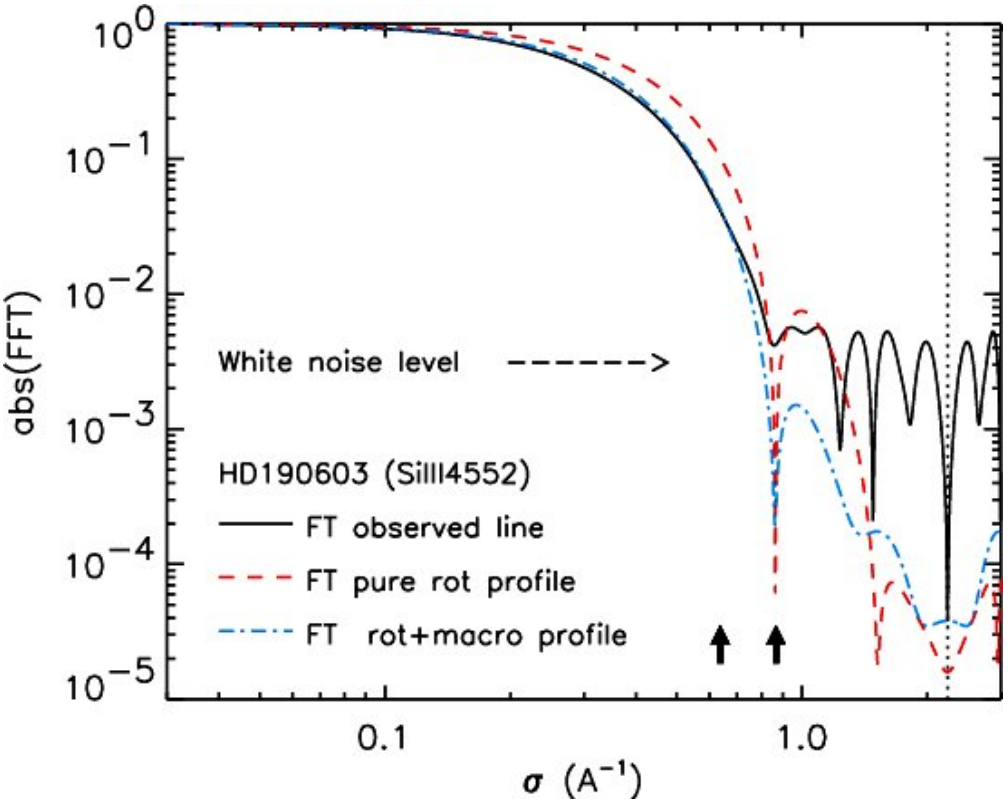

Figure 7: Fourier transform of observed and synthetic line profiles of Si III 4552. The synthetic profiles have the same projected rotational velocity (V sin$i$ = 45 km s^{-1}) but a different amount of Gaussian macroturbulence (0 for the dashed model, 50 km s^{-1} for the dot–dashed model). The position of the first zero is the same, independently of the amount of macroturbulence. From Simón Díaz & Herrero (2007).

A powerful method to break this degeneracy is the use of the Fourier transform (FT) of observed profiles. Provided the macroturbulence is well represented by a symmetric kernel (such as a Gaussian profile), the first zero of the FT is thus directly related to the projected rotational velocity by the relation: $\frac{\lambda}{c} v_{\rm sini} \sigma_1 = 0.66$ where λ is the wavelength of the line center and σ_1 the position of the first zero. An illustration is given in Fig. 7 where one can see that for a given V sin$i$, the position of the first zero is always the same, regardless of the amount of Gaussian macroturbulence included. Here again, optical metallic lines are well suited for this method: O II 4414, O II 4661, O III 5592, Si III 4553, Si IV 4089, N IV 4057, C IV 5812 (e.g. Simón Díaz et al. 2006). We stress that the conclusion about the relevance of the FT method to derive V sin$i$ relies on the assumption that macroturbulence was

represented by a symmetric function. If it is not the case (as for pulsations where macroturbulence results from the collective effects of hundreds of oscillations – see Aerts et al. 2009a), then the position of the first zero is affected. The recent study of Simón Díaz et al. (2010) favour a Gaussian radial–tangential macroturbulence profile over an isotropic Gaussian shape. More analyses are needed to characterize the origin and properties of macroturbulence in massive stars.

4.2 Surface magnetic field

The development of spectropolarimeters working in the optical range has led to the detection of surface magnetic fields in several O and B stars (e.g. Donati et al. 2002, 2006; Bouret et al. 2008, Grunhut et al. 2009). The principle of the detection relies mainly on the 'least square deconvolution' method (Donati et al. 1997). In practice, the idea is to detect Zeeman splitting in photospheric lines. Given the faintness of the polarized signal, a line mask made of several well understood lines is built and an average line profile is created from it (leading to the Stokes I parameter, see Fig. 8). The detection of a magnetic field is made from the Stokes V profile which is the difference between the right and left circular polarization signal created from the line mask. An example of unambiguous detection is displayed in Fig. 8. The photospheric lines used to build the line mask are usually the following: He I 4026, He I 4388, He I 4471, He I 4712, He II 4200, He II 4542, N III 4510, O III 5592, C IV 5812. Currently, there are no spectropolarimeters working in the infrared range nor in the UV.

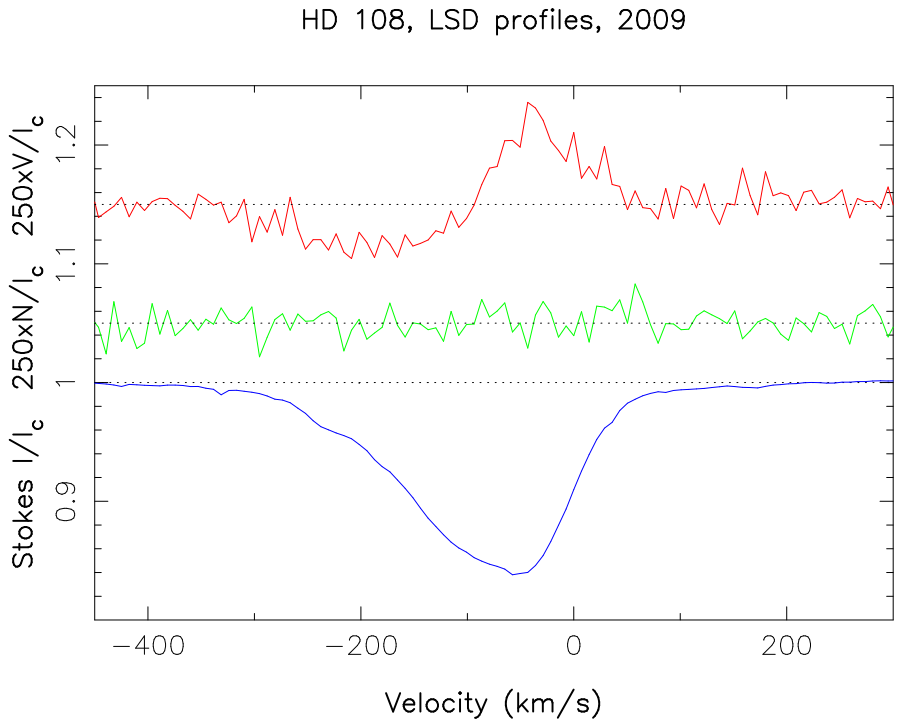

Figure 8: Stokes V, N and I profile (from top to bottom) for the Of?p star HD108. The presence of a clear signature in the Stokes V profile and the absence of feature in the null profile (middle) is a direct indication of the presence of the Zeeman effect and thus of a surface magnetic field. From Martins et al. (2010).

Table 1: Summary of the main diagnostic lines for several stellar and wind parameters

	UV	Optical	near-IR
$T_{\rm eff}$	Fe IV/V/VI	He I 4471 / He II 4542 Si II 4124 / Si III 4552 / Si IV 4116	He I 2.112 / He II 2.189
$\log g$	–	Hβ, Hγ, Hδ	Brγ
v_∞	N V 1240, Si IV 1393-1403 C IV 1548-1550, N IV 1718	Hα, Hβ, Hγ, He I 4471 *(if strong wind)*	He I 2.058, He I 2.112, Brγ *(if strong wind)*
$\dot{M}$	N V 1240, Si IV 1393-1403 C IV 1548-50, N IV 1718	Hα, He II 4686	Brγ
f (clumping)	O V 1371, N IV 1718 P V 1118-1128	Hα, He II 4686	Br10, Br11
Surface abundances	Fe IV/V/VI	C III 4637-40, C IV 5812, N III 4510-15, N IV 5200, O II 4661, O III 5592...	N III 2.247-2.251 Mg II 2.138-2.144 Si II 1.691-98 Fe II 1.688, Fe II 2.089
Magnetic field	–	He I 4026, He I 4712 He II 4200, He II 4542, O III 5592, C IV 5812	–

5 Summary

We have reviewed some of the main spectroscopic diagnostics of massive stars in the UV (1000–2000 Å), optical (4000-7000 Å) and near-infrared (H and K bands) wavelength ranges. The description was not exhaustive and was meant to give an overview of the most commonly used spectral lines and methods to derive the stellar and wind parameters of OB and Wolf–Rayet stars. A summary of the main diagnostics is given in Table 1.

Acknowledgements

FM acknowledges financial support from the french Pôle National de Physique Stellaire (CNRS/INSU). Comments by J. Puls helped to improve this contribution.

References

Abt, H.A., Levato, H., & Grosso, M. 2002, ApJ 573, 359
Aerts, C., Puls, J., Godart, M., & Dupret, M.-A. 2009a, A&A 508, 409
Aerts, C., Puls, J., Godart, M., & Dupret, M.-A., 2009b, CoAst 158, 66
Bouret, J.-C., Lanz, T., & Hillier, D.J. 2005, A&A 438, 301
Bouret, J.-C., Donati, J.-F., Martins, F., Escolano, C., Marcolino, W., Lanz, T., & Howarth, I.D. 2008, MNRAS 389, 75
Crowther, P.A., Morris, P. W., & Smith, J. D. 2006a, ApJ 636, 1033
Crowther, P.A., Lennon, D.J., & Walborn, N.R. 2006b, A&A 446, 279
Donati, J.-F., Semel, M., Carter, B.D., Rees, D.E., & Collier Cameron, A. 1997, MNRAS 291, 658
Donati, J.-F., Babel, J., Harries, T.J., Howarth, I.D., Petit, P., & Semel, M. 2002, MNRAS 333, 55
Donati, J.-F., Howarth, I. D., Bouret, J.-C., Petit, P., Catala, C., & Landstreet, J. 2006, MNRAS 365, L6

Dufton, P.L., Ryans, R.S.I., Trundle, C., Lennon, D.J., Hubeny, I., Lanz, T., & Allende Prieto, C. 2005, A&A 434, 1125
Eversberg, T., Lépine, S., & Moffat, A.F.J. 1998, ApJ 494, 799
Fullerton, A.W., Massa, D.L., & Prinja, R.K. 2006, ApJ 637, 1025
Grunhut, J.H., Wade, G.A., Marcolino, W.L.F., et al. 2009, MNRAS 400, L94
Hanson, M.M., Kudritzki, R.-P., Kenworthy, M.A., Puls, J., & Tokunaga, A.T., 2005, ApJS 161, 154
Heap, S.R., Lanz, T., & Hubeny, I. 2006, ApJ 638, 409
Herrero, A., Kudritzki, R.P., Vilchez, J.M., Kunze, D., Butler, K., & Haser, S., 1992, A&A 261, 209
Hillier, D.J. 1991, A&A 247, 455
Howarth, I.D., Siebert, K.W., Hussain, G.A.J., & Prinja, R.K. 1997, MNRAS 284, 265
Howarth, I.D., Walborn, N.R., Lennon, D.J., & Puls, J. 2007, MNRAS 381, 433
Lamers, H.J.G.L.M., Snow, T.P., & Lindholm, D.M., 1995, ApJ 455, 269
Lépine, S., Moffat, A.F.J., St-Louis, N., et al. 2000, AJ 120, 3201
Marcolino, W.L.F., Bouret, J.-C., Martins, F., Hillier, D.J., Lanz, T., & Escolano, C. 2009, A&A 498, 837
Markova, N., & Puls J. 2008, A&A 478, 823
Martins, F., Schaerer, D., & Hillier, D.J. 2002, A&A 382, 999
Martins, F., Schaerer, D., Hillier, D.J., & Heydari-Malayeri M. 2004, A&A 420, 1087
Martins, F., Hillier, D.J., Paumard, T., Eisenhauer, F., Ott, T., & Genzel, R. 2008, A&A 478, 219
Martins, F., Hillier, D.J., Bouret, J.C., Depagne, E., Foellmi, C., Marchenko, S., & Moffat A.F.J. 2009, A&A 495, 257
Martins, F., Donati, J.-F., Marcolino, W.L.F., Bouret, J.-C., Wade, G.A., Escolano, C., & Howarth, I.D. 2010, MNRAS 407, 1423
Najarro, F., Krabbe, A., Genzel, R., Lutz, D., Kudritzki, R.P., & Hillier, D.J. 1997, A&A 325, 700
Najarro, F., Hillier, D.J., Puls, J., Lanz, T., & Martins, F. 2006, A&A 456, 659
Najarro, F., Figer, D.F., Hillier, D.J., Geballe, T.R., & Kudritzki, R.P. 2009, ApJ 691, 1816
Penny, L.R. 1996, ApJ 463, 737
Prinja, R.K., Barlow, M.J., & Howarth, I.D., 1990, ApJ 363, 607
Puls, J., Kudritzki, R.-P., Herrero, A., et al. 1996, A&A 305, 171
Puls, J., Markova, N., Scuderi, S., Stanghellini, C., Taranova, O.G., Burnley, A.W., & Howarth, I.D. 2006, A&A 454, 625
Puls, J., Vink, J.S., & Najarro, F. 2008, A&ARv 16, 209
Repolust, T., Puls, J., Hanson, M.M., Kudritzki, R.-P., & Mokiem, M.R. 2005, A&A 440, 261
Ryans, R.S.I., Dufton, P.L., Rolleston, W.R.J., Lennon, D.J., Keenan, F.P., Smoker, J.V., & Lambert D.L. 2002, MNRAS 336, 577
Simón-Díaz, S., Herrero, A., Esteban, C., & Najarro, F. 2006, A&A 448, 351
Simón-Díaz, S., & Herrero, A. 2007, A&A 468, 1063
Simón-Díaz, S., Herrero, A., Uytterhoeven, K., Castro, N., Aerts, C., & Puls, J. 2010, ApJ 720, L174
Sundqvist, J.O., Puls, J., & Feldmeier, A. 2010, A&A 510, A11
Slettebak, A., Collins, G.W.II, Parkinson, T.D., Boyce, P.B., & White, N.M. 1975, ApJS 29, 137
Trundle, C., Lennon, D.J., Puls, J., & Dufton, P.L. 2004, A&A 417, 217

Discussion

C. Martayan: Usually the different parameters ($\dot{M}$,v_∞, etc) are determined in the UV, visible, or IR wavelength-ranges but not together. Do the measurements agree or do they show some discrepancies?
F. Martins: There are studies (Repolust et al.) comparing results of pure IR and pure optical analysis showing there is usually agreement. There are also others showing discrepancies (Bianci et al.) highlighting differences between UV and optical results.
Nowadays, more and more studies rely on multi-wavelength analyses. This helps to reduce the error bars on the fundamental parameters determinations.

L. Oskinova: How sensitive is L_{bol} determined from SED fitting to the stellar atmosphere model which is used? For example, could you, please, comment how L_{bol} would differ if the fitting is done by CMFGEN vs. Kurucz?

F. Martins: Fitting SEDs from the (E)UV down to the mid IR requires atmosphere models including winds because of the IR-mm excess. Hence Kurucz models are not appropriate for O/WR stars.
The uncertainty on luminosities derived by the SED fitting method is about 0.05-0.15 dex depending on the quality of the photometry.

S. Heap: Can you advise on determining v_∞ in very low-metallicity stars?
F. Martins: P-Cygni profiles are still observed in O supergiants at the SMC metallicity. It is not true for dwarfs. So in the MCs one should focus on the earliest O supergiants. There are studies by Urbaneja et al. and Evans et al. on that topic.

3-D Radiative Transfer Modeling of Structured Winds in Massive Hot Stars with Wind3D

A. Lobel[1], J. A. Toalá[2], and R. Blomme[1]

[1] Royal Observatory of Belgium, Ringlaan 3, B-1180, Brussels, Belgium
[2] Universidad Nacional Autónoma de México, Centro de Radioastronomía y Astrofísica, Campus Morelia, Michoacán, México

Abstract: We develop 3-D models of the structured winds of massive hot stars with the WIND3D radiative transfer (RT) code. We investigate the physical properties of large-scale structures observed in the wind of the B-type supergiant HD 64760 with detailed line profile fits to Discrete Absorption Components (DACs) and rotational modulations observed with IUE in Si IV λ1395.

We develop parameterized input models for WIND3D with large-scale equatorial wind density- and velocity-structures, or so-called 'Co-rotating Interaction Regions' (CIRs) and 'Rotational Modulation Regions' (RMRs). The parameterized models offer important advantages for high-performance RT calculations over ab-initio hydrodynamic input models. The acceleration of the input model calculations permits us to simulate and investigate a wide variety of physical conditions in the extended winds of massive hot stars.

The new modeling method is very flexible for constraining the dynamic and geometric wind properties of RMRs in HD 64760. We compute that the modulations are produced by a regular pattern of radial density enhancements that protrude almost linearly into the equatorial wind. We find that the modulations are caused by narrow 'spoke-like' wind regions. We present a hydrodynamic model showing that the linearly shaped radial wind pattern can be caused by mechanical wave action at the base of the stellar wind from the blue supergiant.

1 Introduction

Accurate mass-loss rates of massive hot stars determined from quantitative spectroscopy are important for understanding the physical properties of the radiative wind driving mechanism that is influenced by dynamic structures on both large and small length scales in the wind. Rotational modulations and Discrete Absorption Components are important tracers of large-scale structures in the highly supersonic winds of these stars. DACs are recurring absorption features observed in UV resonance lines of many OB-stars. They drift bluewards in the absorption portion of P-Cygni profiles. DACs are caused by spiral-shaped density- and velocity structures winding up in the plane of the equator over several tens of stellar radii (e.g., Cranmer & Owocki 1996). Lobel & Blomme (2008) demonstrated with 3-D RT modeling (combined with hydrodynamic simulations) of the detailed DAC evolution in HD 64760 (B0.5 Ib) that these wind spirals are extended density waves emerging from two bright equatorial spots that rotate five times slower than the stellar surface. Detailed hydrodynamic models of its structured wind with these large density waves (or CIRs) reveal only a very small increase of less than 1 % above the smooth (symmetric) wind mass-loss rate.

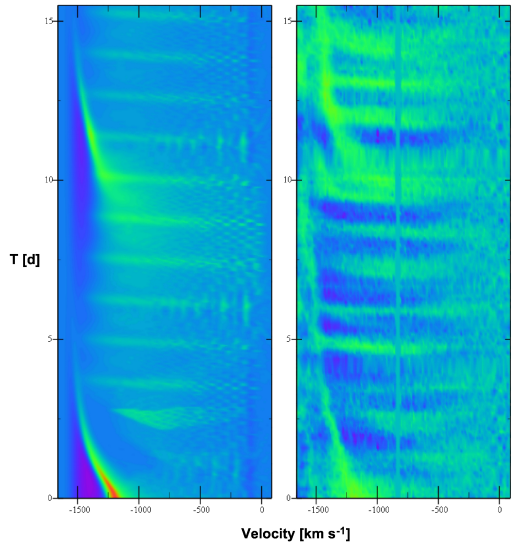

Figure 1: Dynamic spectrum of Si IV λ1395 observed during 15.5 d in HD 64760 (*right-hand panel*), compared to 3-D radiative transfer calculations (*left-hand panel*) with a parameterized structured wind model. Horizontal absorptions are the modulations we model in this paper.

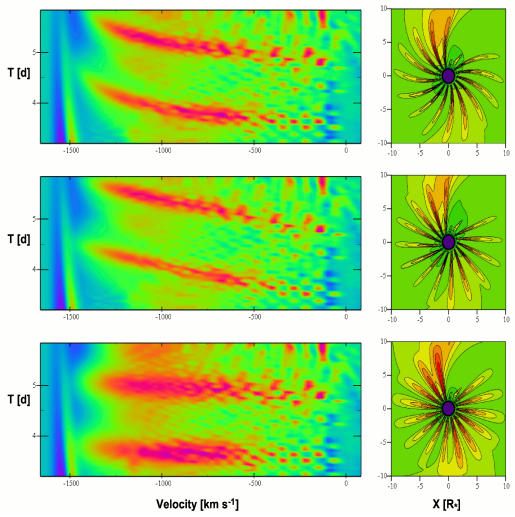

Figure 2: The curvature, incidence angle on the surface, and opening angle of the RMRs shown in the right-hand panels determine the acceleration (*upper panels*), inclination (*middle panels*), and duration (*lower panels*), respectively, of the RT calculated modulations (*left-hand panels*).

The bright surface spots produce the large-scale CIRs in the wind. The density enhancements and velocity plateaus of the CIRs yield migrating DACs with a recurrence period of 10.3 d in the UV line profiles of HD 64760. The modulations, on the other hand, show much shorter periods of $\sim$1.2 d and reveal a time-evolution that substantially differs from the rather slowly shifting DACs. The modulations are nearly-flat absorption features observed for only $\sim$0.5 d to 0.75 d with radial velocities that can range from $\sim$0 $\mathrm{km\,s^{-1}}$ to $\sim v_\infty$=1560 $\mathrm{km\,s^{-1}}$ (Massa et al. 1995; Prinja 1998). They can intersect the slowly drifting DACs and sometimes reveal a remarkable bow shape (Fullerton et al. 2006) with broad flux minima around $\sim$930 $\mathrm{km\,s^{-1}}$. In this paper we present a semi-empiric model of the large-scale wind structures based on detailed RT fits to the time-evolution of the modulations observed in HD 64760. We utilize the WIND3D code for performing non-LTE RT calculations (*Sect. 2*) of important diagnostic spectral lines, such as Si IV λ1395. We develop *parameterized* 3-D input models for Wind3D in Sect. 3 because they offer important advantages for high-performance RT calculations over ab-initio hydrodynamic input models. The acceleration of the input model calculations permits us to model and investigate a much broader range of 3-D physical conditions in the wind.

2 Parametrization of Wind3D Input Models

Wind3D computes the 3-D non-LTE transport of radiation for the 2-level atom in optically thick resonance lines formed in scattering-dominated extended stellar winds. It lambda-iterates the line source function on a Cartesian grid of 71^3 points. The radiative transfer equation is solved in parallel over a mesh of 701^3 voxels using the converged line source function. Typical computation times with WIND3D are $\sim$5 h for iterating the line source function, and $\sim$12 h for calculating the dynamic line profile variability at 90 viewing angles using 16 CPUs.

We develop a new software module in WIND3D for semi-empiric modeling of large-scale equatorial wind density- and velocity-structures. The computer code integrates the time-independent mo-

mentum balance equation of radiation-driven rotating winds following Castor, Abbott & Klein (CAK, 1975). First, we parametrize the large-scale density structures in a stationary model of the equatorial wind with:

$$\rho(x,y,\psi) = \rho_0(r) \left(1 + A(r) \sin^m \left(\psi\, n + 2\pi\, n\, f_c \left(\frac{\mathrm{R}_\star - \sqrt{(x-x_0)^2+y^2}}{\mathrm{R}_\star - \mathrm{R}_{\rm mod}}\right)\right)\right) , \qquad (1)$$

where r^2=x^2+y^2, $\mathrm{R}_{\rm cr} \leq r \leq \mathrm{R}_{\rm mod}$, $-\pi \leq \psi \leq \pi$, and $\mathrm{R}_{\rm mod}$ is the outer radius of the wind model. x_0=$\mathrm{R}_\star \sin(\psi_0)$, where ψ_0 is the incidence angle of the equatorial wind structures on the stellar surface, and $0 \leq \psi_0 \leq \pi/2$. $\rho_0(r)$ is the density of the smooth (unperturbed) equatorial wind. n denotes the number of large-scale wind structures with enhanced density in one hemisphere, and m is an even exponent of the sine function that sets the opening angle or the tangential width of the wind structures. In wind regions where the sine function vanishes the local wind density equals the smooth wind density. The term in Eq. (1) with f_c, where $0 \leq f_c \leq 1$, determines the curvature of the wind structures between $\mathrm{R}_\star$ and $\mathrm{R}_{\rm mod}$. If f_c=1, they turn completely around the star over $2\,\pi$ from the surface radius $\mathrm{R}_\star$ to $\mathrm{R}_{\rm mod}$. In case f_c=0, the structures do not curve at all and stay strictly radial (linear) in the wind, ordered in equal sectors around the star. We parametrize the density constrast of the large-scale wind structures with the function A in Eq. (1):

$$A(r) = c_1 \exp\left(-\left(\frac{r}{\mathrm{R}_\star} - c_2\right)^2 + c_3 \left(\frac{r}{\mathrm{R}_\star}\right)^2 + c_4\right) , \qquad (2)$$

where $c_{1,2,3,4}$ are constants. They determine the detailed density profile compared to $\rho_0(r)$. We vary the four constants until the parameterized density profile best fits the density contrast of the CIRs in the hydrodynamic wind model of HD 64760.

Next, with the parameterized radial wind density-structure we compute the corresponding radial wind velocity-structure for the α parameter of CAK theory set equal to 1/2 in hot stars with 20 kK $\leq T_{\rm eff} \leq$ 30 kK. We solve the CAK momentum balance equation in 1-D for many angles ψ, and include the centrifugal force in the equatorial plane due to the photospheric rotation velocity $v_{\rm rot}$. With the conservation of angular momentum the equatorial tangential wind velocity is $v_{\rm rot}\mathrm{R}_\star/r$, which becomes negligibly small in the highly supersonic outer regions of the parameterized wind models. We integrate the momentum equation together with the mass continuity equation towards the surface from a typical outer (reference) radius $r_{\rm ref}$ $\geq$30 $\mathrm{R}_\star$ with the boundary condition $v(r = r_{\rm ref}) = v_\infty$, down to the critical point $\mathrm{R}_{\rm cr}$ of the wind. The value of the mass-loss rate for calculating the CAK line force is computed with Eq. (5) of Lobel & Blomme (2008), but which typically increases the structured wind mass-loss rate by less than $\sim$1 % in the best-fit 2-spot model. We find that the radial wind velocity-structure computed with the CAK wind-momentum equation integration method, using parameterized stationary wind density models, compares very closely to the hydrodynamic wind velocity model of HD 64760 (Lobel & Toalá 2009).

3 Radiative Transfer Modeling of Rotational Modulations

Figure 1 compares the dynamic spectrum of Si IV observed over 15.5 d in HD 64760 (*right-hand panel*) and computed with WIND3D (*left-hand panel*) using a parameterized structured wind model. The slowly bluewards migrating upper and lower DACs result from two spiral-shaped CIRs shown in the right-hand panels of Fig. 2. The nearly horizontal absorption in the modulations is due to almost linearly shaped density enhancements and local wind velocity variations that radially protrude into the equatorial wind. The RMRs have maximum tangential widths of less than $\sim$1 $\mathrm{R}_\star$ across

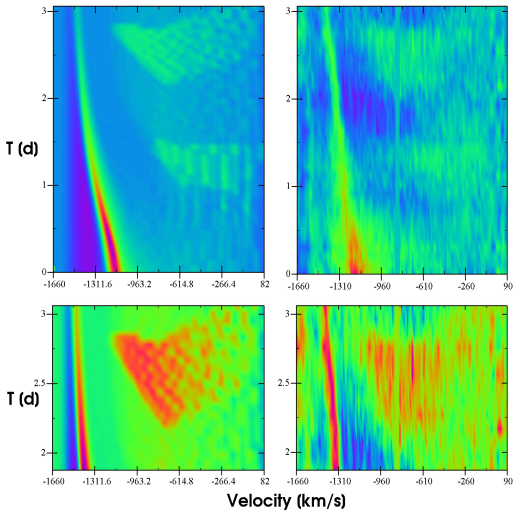

Figure 3: The upper panels show two modulations computed with Wind3D (*left-hand panel*) and observed over ∼3.1 d (*right-hand panel*) in Si IV λ1395 of HD 64760. The lower panels show the best fit (*left*) and the observed (*right*) upper 'bow shaped' modulation in more detail (*see text*).

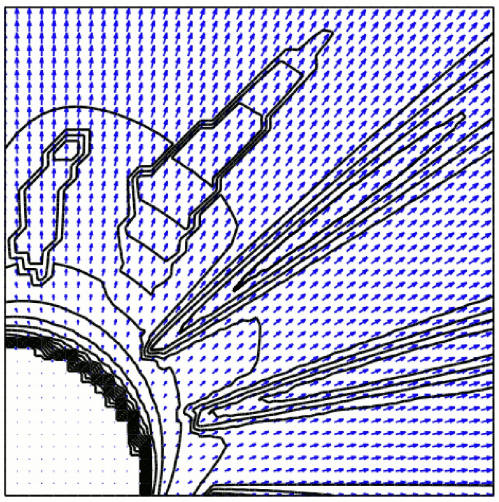

Figure 4: Parameterized model of the equatorial wind-density structure of HD 64760 computed with 3-D RT fits to the modulations in Fig. 3. The solid drawn lines show density contours of the modulations. The blue arrows mark the local wind velocity to ∼3 $\mathrm{R}_\star$ above the stellar surface.

the wind. Our parameterized RT modeling reveals that the RMRs are *linear* density enhancements through the wind because the modulations of HD 64760 stay flat beyond 1000 $\mathrm{km\,s^{-1}}$. The upper panels of Fig. 2 show that the (radial velocity) acceleration of the modulations is too slow (*left-hand panel*) in case the RMRs curve too quickly over ∼10 $\mathrm{R}_\star$ above the stellar surface (*right-hand panel*). Hence, the RMRs are large-scale density- and velocity-structures in the supersonically (radiatively) accelerating equatorial wind. The parameterized best-fit modeling method shows that the RMRs are centered around the star with small inclination angles of $\leq 6°$ from the radial direction (the rather narrow RMRs have small incidence angles on the stellar surface in the middle panel of Fig. 2). We also compute opening angles of $\leq 10°$ for the RMRs at the wind base to correctly fit the observed duration of the modulations.

Figure 3 shows a portion of the dynamic spectrum in Fig. 1 observed between 0 d and 3.1 d (*upper right-hand panel*). The lower DAC in Fig. 3 slowly shifts bluewards from ∼1100 $\mathrm{km\,s^{-1}}$ to ∼1400 $\mathrm{km\,s^{-1}}$, while two modulations are observed around 1.2 d (*lower modulation*) and 2.5 d (*upper modulation*). The upper modulation is observed during ∼0.7 d and reveals a somewhat curved shape, whereas the lower one occurs during ∼0.5 d showing a more irregular absorption pattern below ∼800 $\mathrm{km\,s^{-1}}$. We delineate the borders of the wind density enhancements in two RMRs above the stellar surface and compute the radial wind velocity structure of the parameterized model by integrating the CAK momentum equation (*Sect. 2*). The lower panels of Fig. 3 show the observed (*right-hand panel*) and best-fit (*left-hand panel*) dynamic flux profile of the upper modulation computed with WIND3D. We fit the peculiar wedge-like shape at its short-wavelength side in detail by decreasing the opening angle of the density enhancement borders of the RMR beyond 1 $\mathrm{R}_\star$ above the stellar surface, shown in Fig. 4. The radial wind velocity-structure of the upper modulation does not exceed ∼1200 $\mathrm{km\,s^{-1}}$ around 2.8 d, and it does not intersect the velocity of the lower DAC around ∼1400 $\mathrm{km\,s^{-1}}$. The wind density and velocity model of the upper modulation in Fig. 4 does therefore not exceed a distance of ∼2.5 $\mathrm{R}_\star$ above the stellar surface because the smooth-wind velocity exceeds ∼1200 $\mathrm{km\,s^{-1}}$ only beyond that radius. We therefore attribute the remarkable bow shape (called

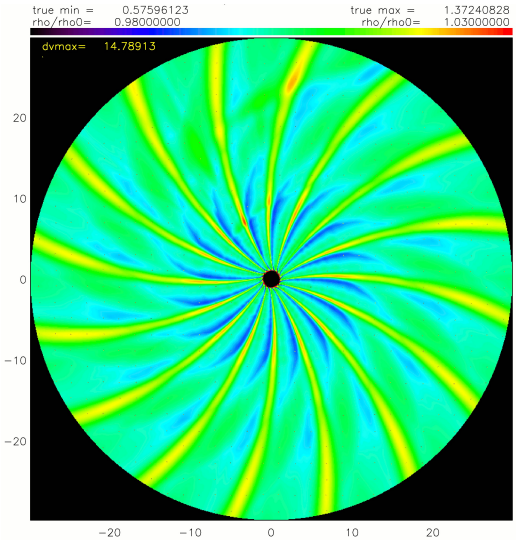

Figure 5: Yellow colors mark density enhancements in the hydrodynamic wind model for rotational modulations of HD 64760 (*see text*).

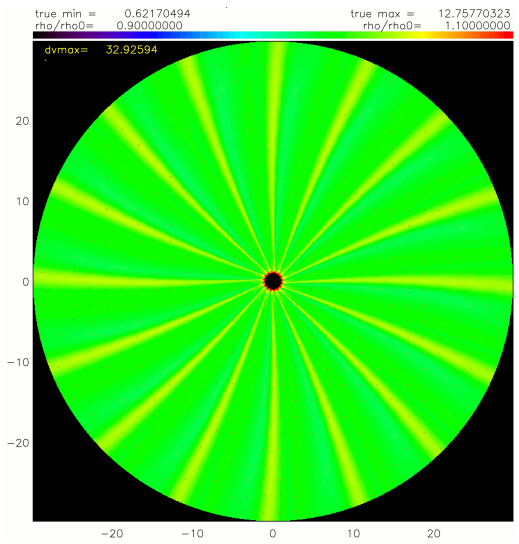

Figure 6: The RMRs in the hydro model are less curved for a horizontal wave at the wind base that rotates 5 times slower than the star.

'phase-bowing') observed in the upper modulation to the intrinsically curved shape of the front and backside borders of the RMR we model in detail in Fig. 4. Several modulations observed between 5.5 d and 9 d in Fig. 1 do not show a clear bow shape (they are in fact strictly flat), although their flux profiles compare closely to the modulations that show the bow shape in Fig. 3. The remarkable bow shape is rather peculiar and results from the slightly curved shapes of a number of RMRs in the model. Modulations without the bow shape are due to RMRs that protrude strictly radially into the wind. Best fits to the detailed flux profiles in the modulations show that the maximum density of the RMRs does not exceed the smooth-wind density by $\sim$17 %, or about half the maximum density contrast of $\sim$31 % in the CIR model of the lower DAC. Hence, the RMRs do not appreciably increase the wind mass-loss rate of HD 64760, also concluded for the CIR models in Lobel & Blomme (2008).

Owocki, Cranmer & Fullerton (1995) presented a kinematic model for the spiral density wind features that satisfies the time-dependent mass-continuity relation. We further investigate the results of the (time-independent) semi-empiric modeling method with time-dependent hydrodynamic models. We compute hydroynamic test models of RMRs in HD 64760 with ZEUD3D. We introduce a propagating pressure wave at the lower wind boundary near the stellar surface. The wave propagates horizontally over the stellar equator. It periodically alters the radiative wind acceleration due to mechanical momentum imparted upwards to the wind by wave action. Figure 5 shows the density contrast computed in the wind out to 30 $\mathrm{R}_\star$ for a wave with a radial velocity amplitude of $v_{\rm sound}/100$ at the stellar surface. The wavelength is set to 1/16 of the stellar circumference and it co-rotates counter-clockwise with the surface ($\omega_{\rm wave}$=$\omega_{\rm star}$). The density structure at the wind base is very intricate and converges into 16 rather narrow and stable density enhancements extending almost radially through the wind. The tangential width of the wind density enhancements (*in yellow color*) is $\leq 1\ \mathrm{R}_\star$, comparable to the parameterized model we find for the RMRs. The hydrodynamic model in Fig. 6 shows a decrease of the intrinsic curvature of these narrow wind features for a wave that rotates 5 times slower than the surface ($\omega_{\rm wave}$=$\omega_{\rm star}$ / 5). The velocity amplitude of the wave is increased to $2 \times v_{\rm sound}$, producing somewhat larger densities of $\sim$8 % above the smooth-wind density. The near-linear regular pattern in the hydrodynamic wind model is almost identical to the spoke-like RMRs we compute with parameterized models of the modulations in HD 64760. The maximum density contrast of the hydrodynamic wind pattern is however too small compared to $\sim$17 % of the RMRs to fit the

flux profiles observed in the modulations. Further hydrodynamic modeling is required to simulate the conditions of the best-fit parameterized wind model in more detail, and to investigate the formation physics of the large-scale wind pattern that causes the modulations observed in HD 64760.

4 Conclusions

We perform 3-D RT calculations with WIND3D of the rotational modulations observed in Si IV λ1395 of HD 64760. We find that the horizontal absorptions in the line are caused by a very regular pattern of almost linearly shaped radial density- and velocity-variations in the equatorial wind out to $\sim$10 $\mathrm{R}_\star$ above the stellar surface. The density in the RMRs does not exceed $\sim$17 % of the smooth-wind density, and hence they do not appreciably increase the stellar mass-loss rate. Hydrodynamic models computed with ZEUS3D show that RMRs can result from mechanical wave action at the base of the stellar wind producing the rather narrow 'spoke-like' wind regions in a regular geometric pattern centered around the star. We conjecture that the waves are caused by non-radial pulsations (for example discussed in Kaufer et al. 2006) of HD 64760.

References

Castor, J. I., Abbott, D. C. & Klein, R. I. 1975, ApJ, 195, 157
Cranmer, S. R., & Owocki, S. P. 1996, ApJ, 462, 469
Fullerton, A. W., Massa, D. L., Prinja, R. K., Owocki, S. P., & Cranmer, S. R. 1997, A&A, 327, 699
Kaufer, A., Stahl, O., Prinja, R. K., & Witherick, D. 2006, A&A, 447, 325
Lobel, A., & Blomme, R. 2008, ApJ, 678, 408
Lobel, A., & Toalá, J. A. 2009, in *Eta Carinae in the Context of the Most Massive Stars*, Proc. of XXVIIth IAU GA, Highlights of Astronomy 14, ed. I. F. Corbett, p. 20, arXiv:0910.3158v1
Massa, D., et al. 1995, ApJ, 452, L53
Owocki, S. P., Cranmer. S. R., & Fullerton, A. W. 1995, ApJ 453, L37
Prinja, R. K. 1998, in *Cyclical Variability in Stellar Winds*, eds. L. Kaper & A. W. Fullerton, 92, Springer-Verlag, Heidelberg

Discussion

S. Owocki: When you put the density structures to model the "phase bowing" of the periodic modulations, do you include the dynamical feedback of the enhanced density on the line-driving and flow speed? Steve Cranmer and I developed kinematic models that fit the phase bowing quite well but in dynamical models the effect of density on the velocity gradient led to very different line profiles, which did not fit the phase bowing very well at all.
A. Lobel: Yes. We compute the radial wind velocity structure from integrating the momentum equation for radiatively driven rotating winds with $\alpha = \frac{1}{2}$. Density enhancements of the periodic modulations do influence locally the flow speed and radial wind velocity gradient. Due to the geometrically narrow, almost "spoke-like" shapes of these periodically enhanced wind density regions, however, the changes of flow speed (from the smooth wind gradient) are geometrically also very confined (e.g., compared to the geometrically large and broad velocity gradients in and behind CIRs), and primarily in the radial direction. Note also that the "phase-bowing" is observed in a number of periodic modulations of HD 64760 but not in all of them. Some modulations are almost completely flat, without clear "banana shape" and require density enhancements and corresponding velocity gradients that are strictly radially oriented. The modulations resemble in fact a wave interference pattern in the equatorial wind.

A proper description of clumping in hot star winds: the key to obtaining reliable mass-loss rates?

Jon O. Sundqvist[1], Joachim Puls[1], Achim Feldmeier[2], and Stanley P. Owocki[3]

[1] Universitätssternwarte München, Scheinerstr. 1, 81679 München, Germany
[2] Institut für Physik und Astronomie, Karl-Liebknecht-Strasse 24/25, 14476 Potsdam-Golm, Germany
[3] University of Delaware, Bartol Research Institute, Newark, DE 19716, USA

Abstract: Small-scale inhomogeneities, or 'clumping', in the winds of hot, massive stars are conventionally included in spectral analyses by assuming optically thin clumps. To reconcile investigations of different diagnostics using this microclumping technique, very low mass-loss rates must be invoked for O stars.

Recently it has been suggested that by using the microclumping approximation one may actually drastically underestimate the mass-loss rates. Here we demonstrate this, present a new, improved description of clumpy winds, and show how corresponding models, in a combined UV and optical analysis, can alleviate discrepancies between previously derived rates and those predicted by the line-driven wind theory. Furthermore, we show that the structures obtained in time-dependent, radiation-hydrodynamic simulations of the intrinsic line-driven instability of such winds, which are the basis to our current understanding of clumping, in their present-day form seem unable to provide a fully self-consistent, simultaneous fit to both UV and optical lines. The reasons for this are discussed.

1 Introduction

The winds from hot, massive stars are described by the radiative line-driven wind theory (Castor, Abbott & Klein 1975), in which the standard model assumes the wind to be stationary, spherically symmetric, and homogeneous. Despite its apparent success (e.g., Vink, de Koter, & Lamers 2000), this model is probably oversimplified. In particular, much evidence for a time-dependent, small-scale inhomogeneous wind (that is, a 'clumped' wind) has over the past years accumulated, from the theoretical as well as the observational side (for an overview, see Hamann, Feldmeier & Oskinova 2008). In the following, we investigate and discuss the *indirect* evidence for wind clumping that has arisen from quantitative spectroscopy aiming to infer mass-loss rates from observations.

2 Deriving empirical mass-loss rates from hot star winds

The main mass-loss diagnostics of OB-star winds are UV resonance lines, Hα line emission (and other recombination lines), and infra-red and radio continuum emission. Recently, X-ray emission lines have also been added to the set (e.g., Cohen et al. 2010). Here we will focus on resonance

lines and Hα, discussing the influence of optically thick clumping on these diagnostics and using the well-studied Galactic O supergiant λ Cep as a test bed.

2.1 Smooth wind models and microclumping

When smooth wind models are used, mass-loss rates inferred for a given star, but from different diagnostics, can vary substantially. For example, in an analysis by means of the unified NLTE model atmosphere code FASTWIND (Puls et al. 2005), we find that the phosphorus V (P V) UV resonance lines suggest a mass-loss rate approximately 20 times lower than the one required for a decent fit of the Hα emission. That is, depending on which diagnostic is used, the inferred mass-loss rate of λ Cep can vary by more than an order of magnitude. This inconsistency has been interpreted as a consequence of neglecting clumping when deriving these rates.

Wind clumping has traditionally been included in diagnostic tools by assuming statistically distributed *optically thin* clumps and a void inter-clump medium, while keeping a smooth velocity field. The main result of this *microclumping* approach is that mass-loss rates derived from smooth models and diagnostics that depend on the square of the density (such as Hα in OB-star winds) must be scaled down by the square root of the clumping factor, $f_{\rm cl}({\rm r}) \equiv \langle\rho^2\rangle/\langle\rho\rangle^2$ with the angle brackets denoting spatially averaged quantities. On the other hand, processes that depend linearly on the density (such as the UV resonance lines) are not directly affected by microclumping. Thus, with such an optically thin clump model, the only way to reconcile the above large deviations in rates would be to accept the very low mass-loss rate indicated by P V, and so assume very high clumping factors (in this case $f_{\rm cl} \approx 400$!) to simultaneously reproduce Hα. Using this technique, we would derive a mass-loss rate for λ Cep that is roughly an order of magnitude lower than predicted by the line-driven wind theory (according to the mass-loss recipe in Vink et al. 2000). Similar results have been found by, e.g., Bouret, Lanz & Hillier (2005) and Fullerton, Massa & Prinja (2006).

Such low mass-loss rates would have enormous implications for massive star evolution and feedback, and of course also cast severe doubts on the validity of the line-driven wind theory. In addition, the extreme clumping factors we had to invoke to reproduce Hα are in stark contrast with theoretical predictions (e.g., Runacres & Owocki 2002, see also Fig. 2). A possible solution of this dilemma is that clumps are not optically thin for the diagnostic lines under consideration, which would lead to underestimated rates if microclumping were still assumed (Oskinova, Hamann & Feldmeier 2007; Owocki 2008; Sundqvist, Puls & Feldmeier 2010a).

2.2 Relaxing the microclumping approximation

Clump optical depths. The critical parameter determining the validity of the microclumping approximation is the *clump optical depth* (which of course is different for different diagnostics). Actually, for both resonance lines and Hα, we may quite easily obtain reasonable estimates for this quantity. In the following, all radii are given in units of the stellar radius and all velocities in units of the terminal speed. The *radial* clump optical depth for a resonance line may then, in the Sobolev approximation, be written as

$$\tau_{\rm cl}^{\rm res} \approx \frac{\tau_{\rm sm}^{\rm res}}{f_{\rm vel}} \approx \frac{\kappa_0 q f_{\rm cl}}{r^2 v {\rm d}v/{\rm d}r}, \tag{1}$$

where q is the ionization fraction of the considered ion and $f_{\rm vel}$ a *velocity* filling factor (Owocki 2008), defined as the ratio between the clump velocity span, δv, to their velocity separation, in full analogy with the traditional volume filling factor. $f_{\rm vel}$ largely controls how a perturbed velocity field affects the line formation, and may be approximated by $f_{\rm vel} \approx |\delta v/\delta v_\beta| f_{\rm cl}^{-1}$ (Sundqvist et al. 2010b), where δv_β is the clump velocity span of a corresponding model with a smooth velocity field. As seen from

the middle term in Eq. 1, $f_{\rm vel}$ also controls how the clump optical depth differs from the corresponding smooth one. κ_0 is a line-strength parameter proportional to the mass-loss rate and the abundance of the considered element, and taken to be constant within the wind (e.g., Puls, Vink & Najarro 2008). As an example, assuming a mass-loss rate $3.0 \times 10^{-6}\,{\rm M}_\odot/{\rm yr}$ and a solar phosphorus abundance, we get $\kappa_0 \approx 3.0$ for the blue component of P V in λ Cep. Note that Eq. 1 assumes that the clumps cover a complete resonance zone. This is reasonable for the wind's inner parts, but may be questionable for its outer, slowly accelerating parts (see Sundqvist et al. 2010b). For our discussion here, however, a Sobolev treatment suffices. For Hα, the analogy to κ_0 is the parameter A (Puls et al. 1996)[1], which is proportional to the mass-loss rate *squared* and to the departure coefficient of the lower transition level. We may write the radial Sobolev clump optical depth for Hα as

$$\tau_{\rm cl}^{\rm rec} \approx \tau_{\rm sm}^{\rm rec} \frac{f_{\rm cl}}{f_{\rm vel}} \approx A \frac{f_{\rm cl}^2}{r^4 v^2 {\rm d}v/{\rm d}r}. \qquad (2)$$

Assuming unity departure coefficients, and a mass-loss rate as above, $A \approx 1.5 \times 10^{-3}$ for Hα in λ Cep. Note the extra $f_{\rm cl}$ term in this expression, stemming from the ρ^2-dependence of this diagnostic. In Fig 1, we plot the Hα and P V clump optical depths, using κ_0 and A as just given and $f_{\rm cl} = 9$, which is a typical value. For simplicity, we also used $q = 1$ for the P V line formation and a smooth velocity field, $v = 1 - 0.99/r$ (i.e., a 'β=1' law), which gives $f_{\rm cl} = {f_{\rm vel}}^{-1}$, when calculating the clump optical depths displayed in the figure. Clearly, within these approximations the clumps remain optically thick for P V throughout the entire wind. For Hα, the ρ^2-dependence makes the optical depth decrease faster with increasing radii, so this line is optically thick only in the lower wind. Based only on these simple estimates, we may therefore expect that resonance lines such as P V should be sensitive to deviations from microclumping in the complete line profile, whereas recombination lines such as Hα should be affected only in the line core. We note also that even if we were to reduce the ion fraction of P V to, say, $q = 0.1$, the clumps would still be optically thick. This illustrates the necessity of relaxing the microclumping approximation for typical mass-loss line diagnostics of hot star winds.

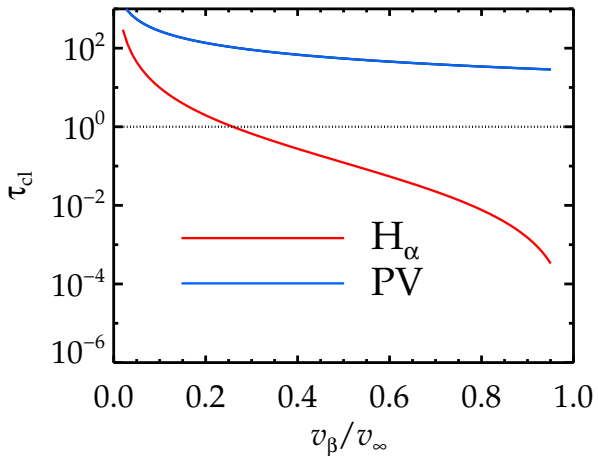

Figure 1: Clump optical depths for Hα and P V line formation as functions of wind velocity. Stellar and wind parameters as for λ Cep, see text.

Wind models. To investigate effects on the line formation from optically thick clumps, a non-void inter-clump medium, and a non-monotonic velocity field, we create (pseudo-)2D and 3D wind models, following the 'patch method' of Dessart & Owocki (2002). In this technique, the full wind is

[1] A may be readily modified to handle other recombination lines than Hα.

'patched' together by assembling inhomogeneous, spherically symmetric, wind-snapshots in radially independent slices. We construct winds using both self-consistent, time-dependent, radiation-hydrodynamic (RH) simulations (computed following Feldmeier, Puls & Pauldrach 1997) and empirical, stochastic models. Line synthesis of resonance lines is carried out using the Monte-Carlo method described in Sundqvist et al. (2010a), whereas for Hα we have developed a new radiative transfer code, in which we solve the 'formal integral' within our 3D winds, assuming that the departure coefficients are unaffected by optically thick clumping, which should be reasonable for the O-star winds discussed here (Sundqvist et al. 2010b). Hydrogen departure coefficients, and ionization fractions of P V, are calculated with FASTWIND, accounting for radially dependent microclumping. Stellar rotation is treated by the standard convolution procedure of a constant $v \sin i$ (thus neglecting differential rotation), set to 220 $\mathrm{km\,s^{-1}}$.

When creating our stochastic models, we take an heuristic approach and use a set of parameters to define the structured medium. If clumps are optically thick for the investigated diagnostic, the line formation will generally depend on more structure parameters than just $f_{\rm cl}$. These parameters (for a two component medium) were defined and discussed in Sundqvist et al. (2010a). They are the inter-clump medium density, the physical distances between the clumps, $v_\beta \delta t$, set by the time interval δt between the release of two clumps and in our geometry equal to the porosity length (Owocki, Gayley & Shaviv 2004), and finally the velocity filling factor, $f_{\rm vel}$ (see previous paragraph). We stress that these parameters are essential for the radiative transfer in an inhomogeneous medium with optically thick clumps, and not merely 'ad-hoc parameters' used in a fitting procedure. We notice also that in our stochastic models they are used to *define* the structured wind, and so are independent of the origin to the inhomogeneities. This should be distinguished from the RH simulations, in which the structure arises naturally from following the time evolution of the wind and stems directly from the line-driven instability. For these simulations then, the averaged structure parameters are an *outcome*.

3 Results from an exemplary study of λ Cep

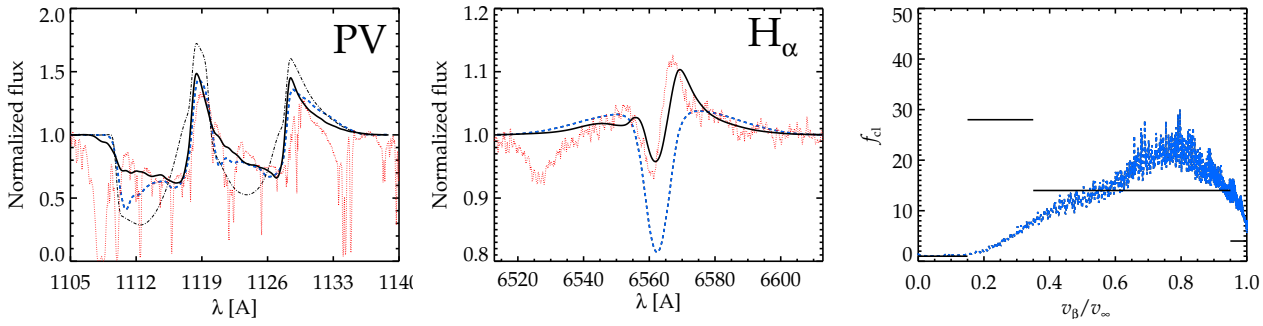

Figure 2: *Left and middle panels:* Observed and modeled P V and Hα line profiles in λ Cep. Solid black lines are calculated from empirical, stochastic wind models, and blue dashed ones from RH simulations. The dashed-dotted line in the left panel illustrates corresponding results using the micro-clumping approximation. Observations (red dotted lines) are from Fullerton, et al. (2006) (P V) and Markova et al. (2005) (Hα). *Right panel:* Corresponding clumping factors.

We have carried out a combined P V and Hα study, using both RH models and stochastic ones. We find that synthetic spectra computed directly from the RH models are unable to reproduce the diagnostic lines (Fig. 2). Two main problems are identified: i) the absorption toward the blue edge of P V is too deep, and ii) the core emission of Hα is much lower than observed. Note that changing the mass-loss rate for which the RH model is calculated ($\dot{M}$=1.5 $\times$ 10^{-6} $\mathrm{M_\odot/yr}$) does not resolve

these issues, or even alleviate them; if for example a higher rate is adopted, the wings of Hα become much too strong. Consequently, we apply our stochastic models, aiming to empirically capture the essence of the structured wind. By means of these models, we obtain consistent fits essentially by increasing the clumping in the lower wind, but also by adopting somewhat lower velocity spans of the clumps. The second point largely resolves the issue of reproducing the observed P V lines, and was extensively discussed in Sundqvist et al. (2010a). Regarding the first point, the observed Hα absorption trough followed by the steep incline to rather strong emission can only be reproduced by our models if clumping is assumed to start at a velocity only marginally lower than predicted by the RH models (see also Puls et al. 2006; Bouret et al. 2008), but with a much steeper increase with velocity (Fig. 2, right panel). Regarding the outermost wind, RH simulations by Runacres & Owocki (2002), which extend to much larger radii than those used here, indicate that the clumping factor there settles at approximately four. $f_{\rm cl} \approx 4$ is consistent with our derived mass-loss rate (see below) and the constraints from radio emission derived by Puls et al. (2006), suggesting that the outermost wind is better simulated than the inner by current RH models. However, let us point out that the use of the so-called smooth source function formalism in our RH models probably leads to overly damped perturbations in the inner wind (e.g., Owocki & Puls 1999), which might at least partly explain the discrepancies between theoretical clumping factors and those inferred from observations.

The basic expectations from the clump optical depth estimates in Sect. 2.2 are confirmed by our detailed analysis. The P V line profiles are clearly weaker than those calculated using microclumping (Fig. 2, left panel), whereas Hα is affected only in the line core (not shown). Finally, our derived mass-loss rate for λ Cep is the same as the one used in our RH simulations. It is approximately two times lower than predicted by the line-driven wind theory, but a factor of five higher than the corresponding rate derived assuming microclumping. This suggests that only moderate reductions of current mass-loss predictions for OB-stars might be necessary, and illustrates how a correct description of clumping is pivotal for obtaining consistent, reliable estimates of mass-loss rates.

Acknowledgements

J.O.S and J.P acknowledge a travel grant from the DFG cluster of excellence.

References

Bouret, J.-C., Lanz, T., & Hillier, D. J. 2005, A&A, 438, 301
Bouret, J., Lanz, T., Hillier, D. J., & Foellmi, C. 2008, in Clumping in Hot-Star Winds, ed. W.-R. Hamann, A. Feldmeier, & L. M. Oskinova, 31
Castor, J. I., Abbott, D. C., & Klein, R. I. 1975, ApJ, 195, 157
Cohen, D. H., Leutenegger, M. A., Wollman, E. E., Zsargó, J. Hillier, D. J., Townsend, R. H. D., & Owocki, S. P. 2010, MNRAS, 405, 2391
Dessart, L. & Owocki, S. P. 2002, A&A, 383, 1113
Feldmeier, A., Puls, J., & Pauldrach, A. W. A. 1997, A&A, 322, 878
Fullerton, A. W., Massa, D. L., & Prinja, R. K. 2006, ApJ, 637, 1025
Hamann, W.-R., Feldmeier, A., & Oskinova, L. M., eds. 2008, Clumping in hot-star winds
Markova, N., Puls, J., Scuderi, S., & Markov, H. 2005, A&A, 440, 1133
Oskinova, L. M., Hamann, W.-R., & Feldmeier, A. 2007, A&A, 476, 1331
Owocki, S. P. 2008, in Clumping in Hot-Star Winds, ed. W.-R. Hamann, A. Feldmeier, & L. M. Oskinova, 121
Owocki, S. P., Gayley, K. G., & Shaviv, N. J. 2004, ApJ, 616, 525
Owocki, S. P. & Puls, J. 1999, ApJ, 510, 355
Puls, J., Kudritzki, R.-P., Herrero, A., et al. 1996, A&A, 305, 171
Puls, J., Urbaneja, M. A., Venero, R., Repolust, T., Springmann, U., Jokuthy, A., & Mokiem, M. R. 2005, A&A, 435, 669

Puls, J., Markova, N., Scuderi, S., Stanghellini, C., Taranova, O. G., Burnley, A. W., & Howarth, I. D. 2006, A&A, 454, 625
Puls, J., Vink, J. S., & Najarro, F. 2008, A&A Rev., 16, 209
Runacres, M. C. & Owocki, S. P. 2002, A&A, 381, 1015
Sundqvist, J. O., Puls, J., & Feldmeier, A. 2010a, A&A, 510, A11
Sundqvist, J. O., Puls, J., Feldmeier, A., et al. 2010b, submitted to A&A
Vink, J. S., de Koter, A., & Lamers, H. J. G. L. M. 2000, A&A, 362, 295

Discussion

S. Owocki: Regarding your introduction of strong clumping in the inner wind, I should note that most instability simulations so far have been purposely conservative by allowing the instability to be self-excited, i.e. without external perturbations. Moreover, the damping from line-drag is estimated to completely cancel the strong instability near the base. But if this cancellation is not exact, and there is moderately strong net instability, then a model with base perturbations, e.g. from photospheric turbulence, could induce substantial wind clumping quite close to the surface.
J. Sundqvist: In our latest analysis we use the instability simulations by Feldmeier, which do include photospheric turbulence as base perturbations. But the clumping in the Hα forming regions is still too low to reproduce the observations. We do use the SSF formulation though. So in principle, I agree with you, and it should be made a high priority to try and develop self-consistent instability models that are able to reproduce the observed spectral features.

X-rays, clumping and wind structures

Lidia Oskinova[1]*, Wolf-Rainer Hamann[1], Richard Ignace[2], and Achim Feldmeier[1]

[1] Universität Potsdam, Germany
[2] East Tennessee State University, TN, USA

Abstract: X-ray emission is ubiquitous among massive stars. In the last decade, X-ray observations revolutionized our perception of stellar winds but opened a Pandora's box of urgent problems. X-rays penetrating stellar winds suffer mainly continuum absorption, which greatly simplifies the radiative transfer treatment. The small and large scale structures in stellar winds must be accounted for to understand the X-ray emission from massive stars. The analysis of X-ray spectral lines can help to infer the parameters of wind clumping, which is prerequisite for obtaining empirically correct stellar mass-loss rates. The imprint of large scale structures, such as CIRs and equatorial disks, on the X-ray emission is predicted, and new observations are testing theoretical expectations. The X-ray emission from magnetic stars proves to be more diverse than anticipated from the direct application of the magnetically-confined wind model. Many outstanding questions about X-rays from massive stars will be answered when the models and the observations advance.

1 Introduction

Two aspects in studies of X-ray emission from massive stars attract most attention: *i)* how X-rays are generated in massive stars, and *ii)* how X-ray emission can be used in analyzing stellar winds. In the basic concept, the wind has two components: a general cool wind with temperature of $T_{\rm w} \sim 10\,$kK which contains nearly all the wind mass, and a hot tenuous component with $T_{\rm X}$ ~few MK where the X-rays originate. The X-ray photons suffer continuum K-shell absorption in the cool wind and, in turn, can affect the wind ionization via the Auger process.

In this review we concentrate on X-ray emission from single stars. This is thermal emission from gases heated in the stellar wind shocks or in magnetically confined wind regions. Cassinelli & Olson (1979) proposed X-radiation from a base coronal zone plus Auger ionization in the surrounding cool wind to explain the superionization (e.g. N V, O VI) that was observed to be present in *Copernicus* UV spectra of OB stars. From the analysis of *Einstein* spectra of OB-stars, Cassinelli & Swank (1983) concluded that the base corona idea was not correct since soft X-rays were observed. The Si XIII and S XV line emission was detected in the SSS spectrum of the O-star ζ Ori. These ions correspond to high temperature and are located at an energy where the wind would be thin to X-rays. This led to a conclusion about two sources of X-ray emission, X-rays that arise from fragmented shocks in the wind and X-rays from very hot, probably magnetically confined loops, near the base of the wind. Furthermore since X-ray variability was already known to be less than about 1%, Cassinelli &

*lida@astro.physik.uni-potsdam.de

Swank (1983) suggested that there had to be thousands of shock fragments in the wind. Radiation hydrodynamic simulations of the nonlinear evolution of instabilities in stellar winds were performed by Owocki, Castor, & Rybicki (1988). They demonstrated that the X-rays can originate from plasma heated by strong reverse shocks, which arise when a high-speed, rarefied flow impacts on slower material that has been compressed into dense shells. Feldmeier, Puls, & Pauldrach (1997) assumed a turbulent seed perturbation at the base of the stellar wind and found that the shocks arising when the shells collide are capable of explaining the observed X-ray flux. These 1D hydrodynamical models predict plasma with temperatures 1–10 MK which is permeated with the cool wind. X-rays suffer absorption as they propagate outwards through the ensemble of dense, radially compressed shells.

Waldron (1984) calculated the opacity of O-star winds for the X-ray radiation. The absorption of X-rays in Wolf-Rayet (WR) star winds was investigated by Baum et al. (1992). They employed detailed non-LTE stellar atmosphere models and showed that since the WR wind opacity is very high, the observed X-rays must emerge from the far outer wind region. Hillier et al. (1993) computed the wind opacity of the O5Ia star ζ Pup. They found that the high opacity of the stellar wind would completely block the soft X-rays (< 0.5 keV) unless some significant fraction of hot plasma is located far out in the wind, at distances exceeding $100\,R_*$.

The shape of X-ray emission line profiles was predicted by MacFarlane et al. (1991). They considered the effect of wind absorption on the emission from an expanding shell of hot gas. When the cool wind absorption is small, the line is broad and has a box-like shape. For stronger wind absorption, the line becomes more skewed (see Fig. 7 in MacFarlane et al. 1991). The line shape is largely determined by a parameter τ_0:

$$\tau_0 = \kappa_\lambda R_* = \rho_{\rm w} \chi_\lambda R_* \tag{1}$$

where R_* [cm] is the stellar radius, and the atomic opacity κ_λ is the product of the mass absorption coefficient χ_λ [cm^2 g^{-1}] and the density of the cool wind ($\rho_{\rm w}$) as defined from the continuity equation $\dot{M} = 4\pi\rho_{\rm w} v(r) r^2 R_*^2$, where r is the radial distance in units of R_*, and $v(r)$ is the velocity law, that can be prescribed by the formula $v(r) = v_\infty(1 - 1/r)^\beta$. MacFarlane et al. notice that when τ_0 increases, the red-shifted part of the line ($\Delta\lambda > 0$) becomes significantly more attenuated than the blue-shifted part. They suggested that evaluating the line shape can be used to determine τ_0. The K-shell opacity varies with wavelength with the power between 2 and 3 (Hillier et al. 1993), therefore in the X-ray band τ_0 should change by orders of magnitude. Consequently, the X-ray emission line shape at shorter and longer wavelengths should be different. Waldron & Cassinelli (2001) expanded the single-shock model of MacFarlane et al. and considered emission from spherically symmetric shocks equally distributed between $0.4 v_\infty$ and $0.97 v_\infty$ with temperatures ranging from 2 to 10 MK. In similar spirit, Ignace (2001) provided a formalism that accounts for the emission from a flow that is embedded with zones of X-ray emitting gas. Owocki & Cohen (2001) calculated model X-ray line profiles for various combinations of the parameters β, τ_0, and onset radii for X-ray emission.

2 The high-resolution X-ray spectra of O-type supergiants

Waldron & Cassinelli (2001) obtained the first high-resolution X-ray spectrum of an O star. Their analysis of this *Chandra* spectrum of the O9.7Ib star ζ Ori revealed that the hot plasma is located relatively close to the stellar core and that the line profiles appear to be symmetric, and not skewed.

Subsequent analyses of X-ray spectra of single O-type stars are broadly consistent with these first results. The *XMM-Newton* RGS spectra of two O-type stars are shown in Fig. 1. The general properties of X-ray emission from massive stars are summarized in Waldron & Cassinelli (2007) and Güdel & Nazé (2009, see also Nazé 2011). The X-ray spectra of O-stars are well described by a thermal plasma with temperatures spanning between $\approx 2 - 10$ MK. The ratio between the fluxes

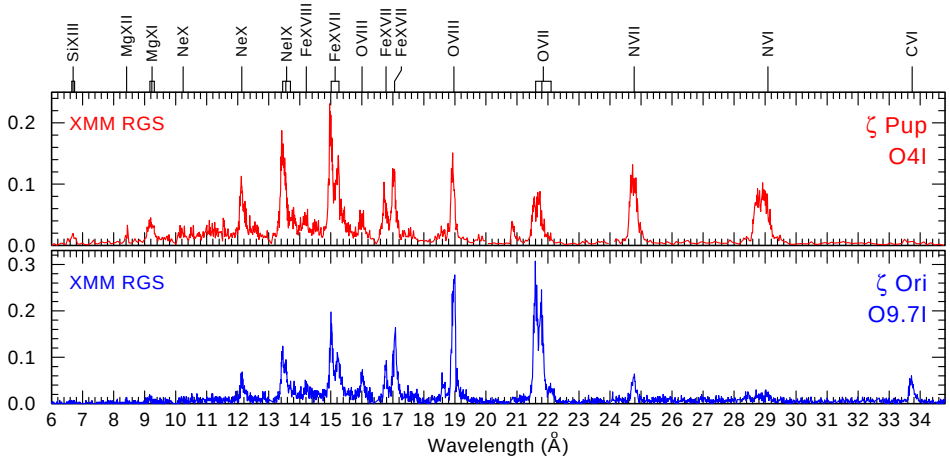

Figure 1: RGS spectrum of the O4Ief star ζ Pup (top panel) and of the O9.7Ib star ζ Ori (bottom panel), not corrected for interstellar absorption. The ζ Pup spectrum results from the combination of separate exposures accumulating about 530 ks of useful exposure time. In the case of ζ Pup, the strength of the nitrogen lines compared to the oxygen and carbon lines clearly indicates an overabundance of nitrogen.

in forbidden and intercombination lines of He-like ions indicates that the line formation region lies between $\approx 1.2-20\,R_*$ (e.g. Leutenegger et al. 2006). The line widths are proportional to the terminal wind speed as obtained from UV line diagnostics. The values of τ_0 (see Eq. 1) are small and the emission line profiles are similar across the X-ray spectrum.

3 How to reconcile theory and observations

The high-resolution X-ray spectra present two key problems. First, how to explain the origin of X-rays at a distance of a few tens of stellar radii from the photosphere? Second, how to explain the shape of the X-ray emission lines and their similarity across the spectrum?

The presence of magnetic fields may help to heat the plasma very close to the stellar surface (e.g. Cassinelli & Olson 1979). Recently, this idea was boosted by the direct measurement of magnetic fields on some massive stars (e.g. Bouret et al. 2008a). Waldron & Cassinelli (2007) pointed out a "high-ion near star problem": the radii of formation for the lines of ions with higher ionization potential ions are closer to the surface than those of lower ions. Their proposed explanation invokes magnetic fields. Unfortunately, the signal-to-noise ratio in the lines of He-like ions of Si, S, Ar, and Ca, which provide the diagnostics for the hottest plasma, is rather low. Better quality data are needed to pin-point the exact location of the hot plasma in massive star winds in order to verify the claim of Waldron & Cassinelli.

However, surface magnetic fields may not be required to explain the available measurements. The simulations of instabilities in stellar winds (Runacres & Owocki 2002, 2005) show that strong shocks may develop at the distances which agree well with those inferred from the analysis of He-like ions.

Below, we briefly consider some solutions proposed to explain the observed emission line profiles:

i) Line optical depth alters the line shape of X-ray emission profiles (Ignace & Gayley 2002);

ii) Reduction of the wind absorption column density implying a lower $\dot{M}$ (e.g. Waldorn & Cassinelli 2001; Cassinelli et al. 2001; Kramer, Cohen, & Owocki 2003);

iii) Macroclumping resulting in smaller effective opacity (e.g. Feldmeier, Oskinova, Hamann 2003; Oskinova, Feldmeier, Hamann 2006; Owocki & Cohen 2006; Cassinelli et al. 2008).

3.1 Optically thick X-ray emitting plasma

Ignace & Gayley (2002) calculated X-ray line profiles produced in an hot plasma that is optically thick. They found that the optically thick lines have nearly symmetrical shape. Leutenegger et al. (2007) used this formalism to show that the resonance lines of He-like ions of N and O in the X-ray spectrum of ζ Pup are better described under the assumption of resonant scattering.

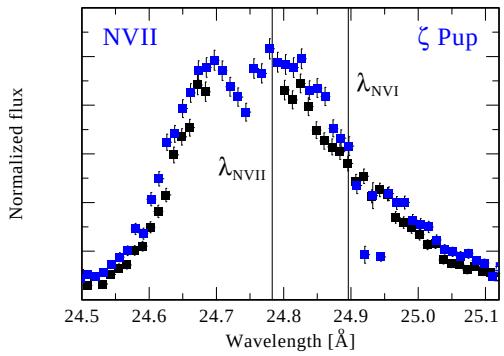

Figure 2: The N VII λ 24.758 and N VI λ 24.898 blend in the *XMM-Newton* RGS1 (blue symbols) and RGS2 (black symbols) spectra of ζ Pup. The central wavelengths of corresponding lines are indicated.

Further evidence that some X-ray lines can be optically thick comes from the characteristic shapes, e.g. the dip at the top of the N VII line in ζ Pup spectrum (Fig. 2). Such line structures are typical for optically thick emission lines in the optical spectra of WR stars, e.g. He II λ 5412 Å in WR3. As estimated by Ignace & Gayley (2002), the X-ray lines of leading ions in the most dense winds can indeed be optically thick. However, the lines of less abundant ions (such as S, Si, Ne, Fe) originating in the less dense winds cannot be explained by resonant scattering.

3.2 Reducing the wind absorption column density

The observed X-ray emission lines in O-star spectra are typically symmetrical and similar across the X-ray spectrum. Fitting observed lines with the MacFarlane et al. line model, generally yields low values of τ_0 and its weak dependence on wavelength (e.g. Cassinelli et al. 2001, Kahn et al. 2001, Miller et al. 2002, Kramer et al. 2003, Pollock 2007). Recalling that $\tau_0 \propto \kappa_\lambda = \chi_\lambda \rho_{\rm w}$, these empiric results can be explained by the weak wavelength dependence of opacity and by the reduced wind density $\rho_{\rm w}$.

The wind opacity for the X-rays is mainly due to K-shell ionization of metals. In O-stars κ_λ chiefly depends on the chemical composition, but little on other details of the wind models (Oskinova et al. 2006). Hence, knowing the metal abundances is prerequisite to calculate wind opacity.

The abundance in O-type stars are often non-solar (e.g. Lamers et al.1999). An example of a typical ON-type star with enhanced nitrogen abundance is ζ Pup. Using non-LTE wind atmospheres, Pauldrach, Hoffmann, & Lennon (2001) found that while N is overabundant in this star, C and O are depleted. They show that the N/C ratio is 20$\times$solar and the N/O ratio is 10$\times$solar in ζ Pup. Fig. 3 demonstrates our model fit to the UV spectrum of ζ Pup, assuming abundances as derived in Pauldrach et al.. The lines of C, N, and O are well reproduced.

The abundances obtained from the analysis of X-ray spectra of ζ Pup are in general agreement with those from Pauldrach et al. (e.g. Fig. 1, also Kahn et al. 2001). Leutenegger et al. (2007) estimate that nitrogen has twice the abundance of oxygen in ζ Pup. Krtička & Kubàt (2007) show that the use of new 3D solar abundances (Asplund, Grevesse & Sauval 2005) with lower metalicity improves the

agreement between observation and wind theory. Their calculations of κ_λ in ξ Per agree well with those in Oskinova et al. (2006).

At softer X-ray energies the large wind optical depth for the X-rays is largely determined by the CNO edges (see Fig. 20 in Pauldrach et al.). Selectively reduced metal abundance would lead to a drop in the jump heights in wind opacity due to the edges, leading to less pronounced wavelength dependence of optical depth. Recently, Cohen et al. (2010) assumed that in ζ Pup the abundance ratio of N/C is 60×solar and N/O is 25×solar, which resulted in the less steep jumps of wind optical depths at the wavelengths of the K-shell edges. They claimed that this wind optical depth agrees with the marginal wavelength dependence of τ_0 (on 68% confidence limits) which they found by fitting the lines in the *Chandra* spectrum of ζ Pup. For consistency, we calculated the Hα line adopting the same wind parameters as used by Cohen et al. (2010) for their X-ray line model. The resulting model Hα line shows a large discrepancy with the observed one. This points out that the parameters used by Cohen et al. (2010) to model the X-ray lines may not be realistic.

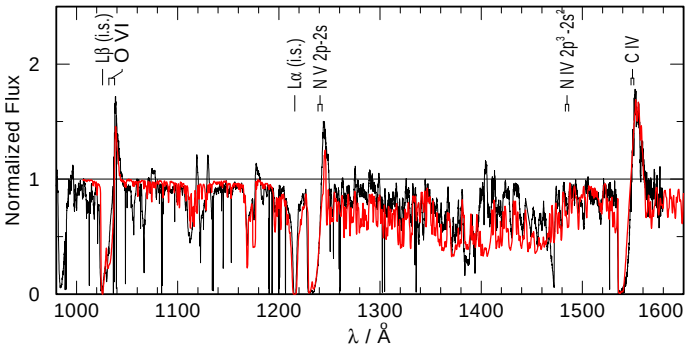

Figure 3: The EUV spectrum of ζ Pup, observed with FUSE (black line), compared to a PoWR model spectrum (red line). The resonance doublets of C IV, N V and O VI are well reproduced, as well as the forest of iron-group lines. The O VI doublet can only be fitted with models accounting for a diffuse X-ray field. (Adopted from Oskinova et al. 2006).

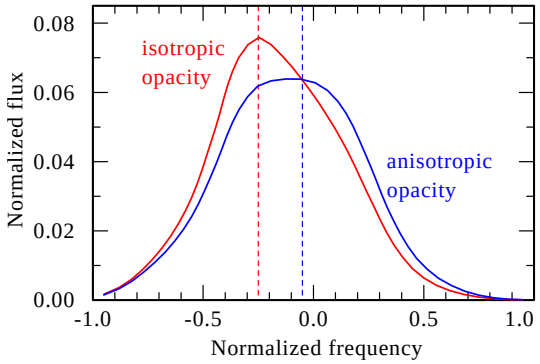

Figure 4: Two model lines calculated using the same wind parameters but assuming isotropic and anisotropic clumps. Isotropic opacity leads to a significantly more skewed line.

The observed nearly symmetric shapes of the X-ray emission lines can be explained if the wind density, $\rho_{\rm w}$, is small. The reduction of the density can be expected from atmosphere models that account for wind *clumping*.

The inhomogeneity of stellar winds has been established in the last decade (see reviews in Hamann, Feldmeier & Oskinova 2008). The mass-loss rates are empirically inferred from modeling recombination and resonance lines in the optical and UV. The recombination line strength depends on $\rho_{\rm w}^2$, while the resonance line strength depends on $\rho_{\rm w}$. Assuming that the interclump medium is void and that the density within the clumps is enhanced by a factor D, the $\dot{M}$ inferred from analysis of recombination lines has to be reduced by a factor $\sqrt{D^{-1}}$ compared to the values obtained under the assumption of a smooth wind.

Assuming that nearly all mass is in clumps, the volume filling factor is $f_{\rm V} \approx D^{-1}$. In order to fit recombination and resonant lines simultaneously, the wind models require very small filling factors (Fullerton, Massa & Prinja 2006). Consequently, these models require a reduction of empirically inferred $\dot{M}$ up to a factor of 100 compared to the unclumped models.

Waldron & Cassinelli (2010) proposed an alternative solution to the problem of the mass-loss rate discordance. They pointed out that the XUV radiation near the He II ionization edge originating in wind shocks would destroy P V ions. Consequently, the key diagnostic resonant line of P V would be

weakened and could be explained without the need to decrease $\dot{M}$. The source of the XUV radiation could be the bow-shocks around the wind clumps as proposed in Cassinelli et al. (2008).

The models with severely reduced mass-loss rates encounter substantial problems when one tries to explain the observed X-ray line spectra:

i) The low values of $\dot{M}$ do not explain why the shapes of X-ray lines show no significant wavelength dependence.

ii) Eq. 1 can be used to model the X-ray lines only assuming that the clumps are optically thin. This strong assumption (often referred to as *microclumping* approximation) is not always valid.

4 Macroclumping

4.1 On the size of optically thick clumps

There is no known reason why the microclumping approximation should apply. The optical depth of an isotropic clump (i.e. with the same dimensions in 3D) is

$$\tau_{\rm clump}(\lambda) = \rho_{\rm w}\chi_\lambda D d_{\rm clump} R_* \;=\; \frac{\dot{M}\chi_\lambda}{4\pi v_\infty R_*}\cdot\frac{d_{\rm clump}}{f_{\rm v}}\cdot\frac{1}{(1-\frac{1}{r})^\beta r^2} \;\equiv\; \tau_*(\lambda)\frac{d_{\rm clump}}{f_{\rm v}}\cdot\frac{1}{(1-\frac{1}{r})^\beta r^2}, \quad (2)$$

where $d_{\rm clump}$ is the geometrical size of the clump expressed in R_*. The strong wavelength dependence of χ_λ suggests that a clump may be optically thick at long wavelengths but thin at short ones.

It is convenient to express $\tau_*(\lambda)$ as

$$\tau_*(\lambda) \;\approx\; 722\frac{\dot{M}_{-6}}{v_\infty \mathcal{R}_*}\cdot\chi_\lambda, \quad (3)$$

where $\dot{M}_{-6}$ is the mass-loss rate in units $10^{-6}\,M_\odot\,{\rm yr}^{-1}$, v_∞ is the terminal velocity in [km s^{-1}], and $\mathcal{R}_* = R_*/R_\odot$. If at some radius r, the clump size is larger than $d^{\tau=1}_{\rm clump}$, such a clump is not optically thin for the X-ray radiation at λ. The size of a clump with optical depth $\tau = 1$ at wavelength λ is

$$d^{\tau=1}_{\rm clump} = \frac{f_{\rm V}}{\tau_*(\lambda)}\cdot\left(1-\frac{1}{r}\right)^\beta r^2. \quad (4)$$

The microclumping approximation is valid only for significantly smaller clumps.

It is a common misconception to assume that *macroclumping*, which allows for any clump optical depth, implies a geometrically large size of clumps. Let us estimate the geometrical size of a clump which has optical depth unity. We consider ζ Pup and use parameters from Zsargo et al. (2008): $\dot{M}_{-6} = 1.7$, $v_\infty = 2300$, $\mathcal{R}_* = 19$, $\beta = 0.9$. Thus, $\tau_*(\lambda) \;\approx\; 0.03\chi_\lambda$. Then a clump with optical depth unity has the size

$$d^{\tau=1}_{\rm clump}(\zeta\,{\rm Pup}) = \frac{f_{\rm V}}{0.03}\cdot\frac{1}{\chi_\lambda}\cdot\left(1-\frac{1}{r}\right)^{0.9} r^2. \quad (5)$$

For a sample of O-stars, Bouret et al. (2008b) find $0.01 < f_\infty < 0.08$, where f_∞ is the filling factor in wind regions where $v_{\rm w} = v_\infty$ (see Bouret et al. for details). For a rough estimate we adopt $f_{\rm V} = 0.03$. Then a clump of optical depth unity has the size $d^{\tau=1}_{\rm clump}(\zeta\,{\rm Pup}) = \chi_\lambda^{-1}\cdot(1-\frac{1}{r})^{0.9} r^2$. Zsargo et al. (2008) do not provide χ_λ values, and we are not aware of any consistent calculation χ_λ for the low values of $\dot{M}$. Adopting $\dot{M}_{-6} = 4.2$, Oskinova et al. (2006) derive $\chi_\lambda \approx 60$ [cm^2 g^{-1}] at 12Å and $\chi_\lambda \approx 180$ [cm^2 g^{-1}] at 19Å. To roughly account for the lower mass-loss rate, we reduce these values

Table 1: Estimate of the geometrical size of a clump with optical depth unity at wavelength λ in the wind of ζ Pup. The wind parameters are from Zsargo et al. (2008) $\dot{M}_{-6} = 1.7$, $v_\infty = 2300$, $\mathcal{R}_* = 19$, $\beta = 0.9$. Compared to Oskinova et al. (2006), χ_λ is scaled down by a factor of two to account for the smaller $\dot{M}$ adopted in Zsargo et al. (2008).

Wavelength λ	χ_λ	$d_{\rm clump}(\tau_\lambda = 1)\,[R_*]$	
Å	[cm^2 g^{-1}]	At R = $2R_*$ in the wind	At R = $5R_*$ in the wind
12	30	0.07	0.7
19	90	0.02	0.2

by a factor of two. The geometrical sizes of clumps which have optical depth unity at 12Å and 19Å in ζ Pup wind are shown in Table 1. Note that if $\dot{M}$ is higher, clumps with even smaller geometrical sizes will be optically thick.
It is possible that the clumps in the wind of ζ Pup have sizes similar to those shown in Table 1, and, thus, are optically thick at the corresponding wavelengths. Therefore the X-ray line profile fitting based on the microclumping approximation can lead to erroneous results.

4.2 Effective opacity

The idea that clumping may reduce the wind opacity and lead to more symmetric line profiles was briefly discussed in Waldron & Cassinelli (2001), Owocki & Cohen (2001) and Kramer et al. (2003). The effects of wind clumping on the X-ray lines were investigated in detail in Feldmeier et al. (2003), who solved the pure absorption case of radiative transfer in clumped winds and found that the emission lines are more symmetric than in the case of a smooth wind. In Oskinova et al. (2006) we employed a 2.5-D Monte-Carlo code (Oskinova, Feldmeier & Hamann 2004) to compute the emission line profile for a finite number of clumps and compared the results to the observed lines.

The effective opacity, $\kappa_{\rm eff}$, in a clumped wind is the product of:

- the average number of clumps per unit volume, $n(r)$ [cm^{-3}]
- the geometrical cross-section of a clump, $\sigma_{\rm clump}$ [cm^2]
- the probability that an X-ray photon of wavelength λ which encounters a wind clump gets absorbed, $\mathcal{P} = 1 - {\rm e}^{-\tau_{\rm clump}(\lambda)}$

Thus,

$$\kappa_{\rm eff} = n(r) \cdot \sigma_{\rm clump} \cdot \mathcal{P} = \frac{\rho_{\rm w}\chi_\lambda}{\tau_{\rm clump}} \cdot (1 - {\rm e}^{-\tau_{\rm clump}(\lambda)}), \qquad (6)$$

where we used Eq. (2) and expressed the filling factor as $f_{\rm V} = D^{-1} = n(r)V_{\rm clump}$ with $V_{\rm clump} = \sigma_{\rm clump} d_{\rm clump} R_*$. In the case of optically thin clumps ($\tau_{\rm clump} \ll 1$) the effective opacity is $\kappa_{\rm eff} = n(r) \cdot \sigma_{\rm clump} \cdot \tau_{\rm clump} = \rho_{\rm w}\chi_\lambda \equiv \kappa_\lambda$, recovering the microclumping approximation. In the case of optically thick clumps ($\tau_{\rm clump} \gg 1$), the absorption probability is $\mathcal{P} = 1$, yielding $\kappa_{\rm eff} = n(r)\sigma_{\rm clump}$. In this limit of porous wind, the opacity does not depend of the wavelength, but is "gray".

In general, the effective opacity is wavelength dependent. As can be seen from Eqs. (2) and (6), the dependence on wavelength enters via the clump optical depth: $\kappa_{\rm eff} \propto 1 - {\rm e}^{-\tau_{\rm clump}(\lambda)}$. This reduced dependence of effective opacity on wavelength agrees well with observations.

Evaluating the wind optical depth as an integral over effective opacity along the line-of-sight z:

$$\tau_{\rm w} = \int_{z_\nu}^{\infty} n(r)\sigma_{\rm clump}(1 - {\rm e}^{-\tau_\nu^{\rm clump}}){\rm d}z, \quad (7)$$

where z is the coordinate along the line of sight. Motivated by the results of the hydrodynamic simulations which predict radially compressed wind structures, Feldmeier et al. (2003) studied the case of radially compressed clumps, with $\sigma_{\rm clump} \propto |dr/dz|$. In this case, the integral in Eq. (7) transforms into an integral over r. As a result, the X-ray emission line profiles will be nearly symmetric (see Fig. 3), while in the case of isotropic clumps the line profiles are more skewed (see also Hervé & Rauw 2011). Therefore, fitting the observed lines under the assumption of spherically symmetric clumps can lead to unrealistically low values of τ_0.

4.3 The impact of clumping on empirical mass-loss rate estimates

Owocki, Gayley, & Shaviv (2004) studied the effects of porosity on the atmospheres of LBV stars. Massa et al. (2003) and Fullerton et al. (2006) discussed how porosity can affect the formation of P Cygni lines. Prinja & Massa (2010) found the spectroscopic signatures of wind clumping, and show that macroclumping must be taken into account to model the UV resonance lines. The effect of macroclumping on *line opacity* was studied for the first time in Oskinova, Hamann, & Feldmeier (2007). The macroclumping was incorporated in the state-of-the-art non-LTE atmosphere model PoWR (e.g. Gräfener, Koesterke & Hamann 2002). We have shown that accounting for clumps leads to empirical mass-loss rate estimates which are by a factor of a few higher than those obtained under the assumption of microclumping, but are still reduced compared to a smooth wind.

In the case of line opacity, an additional parameter, $v_{\rm D}$ is required, which describes the velocity field *within* the clump. The detailed UV line fits for O stars require a "microturbulence velocity" of 50 to 100 km s^{-1}, which, perhaps, can be attributed to the velocity dispersion within clumps. Figures 5 and 6 illustrate the effect of macroclumping on resonance lines. With a lower velocity dispersion within a clump, the Doppler broadening becomes smaller, and the line absorption profile is narrower but peaks higher. Thus, the clump optical depth becomes larger in the line core, but smaller in the line wings. In the statistical average, this leads to a reduction of the effective opacity and a weakening of the line (see also Sundqvist et al. 2011).

At present macroclumping is included in the non-LTE model atmosphere only as a first approximation. Even though the results are very encouraging because consistent mass-loss rates can be obtained simultaneously from the analysis of UV, optical, and X-ray spectra. As an example, our analyses of Hα, P V, and Si IV lines and the X-ray emission lines all agree with a value for the mass-loss rate of $\dot{M} \approx 2.5 \times 10^{-6}\, M_\odot\, {\rm yr}^{-1}$ in the wind of ζ Pup (Oskinova et al., 2006, 2011, in prep.).

5 The large scale structures in stellar winds and the X-rays

5.1 X-rays and Co-rotating Interaction Regions

In the previous section, we discussed the small-scale, stochastic wind inhomogeneities. Beside those, there is strong evidence for the presence of large-scale structures in stellar winds. Spectral lines formed in stellar winds are variable, e.g. discrete absorption components (DACs) are observed in the UV resonance lines of nearly all O stars (Prinja & Howarth, 1986). Cranmer & Owocki (1996) explained DACs as originating from co-rotating interaction regions (CIR), where high-density, low-speed streams collide with low-density, high-speed streams. The observed slow drift of DACs can be understood by considering the motion of the patterns in which the DAC features are formed (Hamann

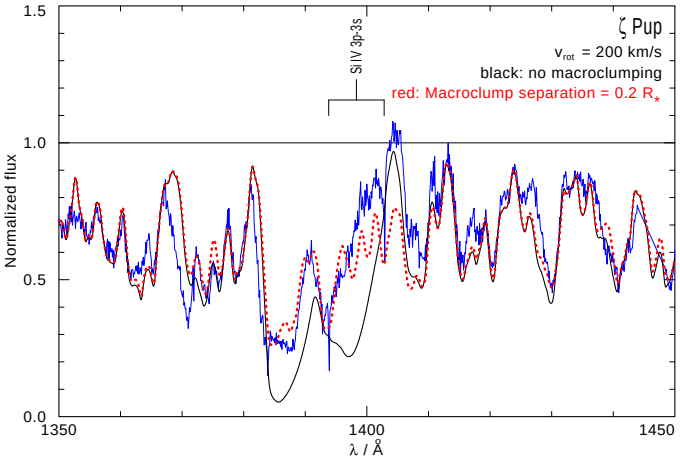

Figure 5: Effect of macroclumping on the Si IV doublet. The IUE spectrum of ζ Pup is shown in blue. The usual microclumping modeling yields P Cygni features that are too strong (black, continuous line). With our macroclumping formalism, the line features are reduced to the observed strength (red, dotted curve).

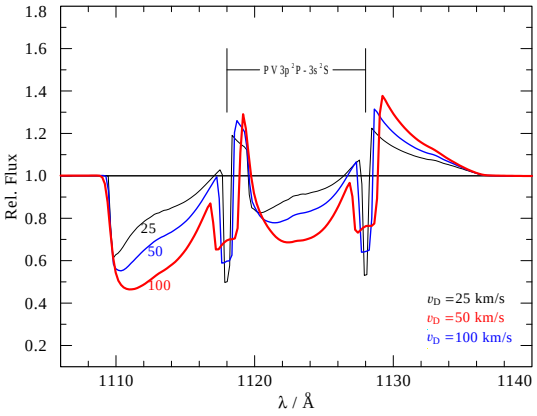

Figure 6: Synthetic P V resonance doublet at $\lambda\,1118/1128$ Å for different values of the microturbulence velocity $v_{\rm D}$ (labels). All other model parameters are kept fixed. When the velocity dispersion across the clumps is decreased, the macroclumping effect becomes more pronounced and leads to a weaker line profile.

et al. 2001). The hydrodynamics of stellar winds which can explain the DACs and the faster modulations are considered by Lobel, Toalá & Blomme (2011).

This complex wind geometry should affect the production and the propagation of X-rays in stellar winds: the wind can be shocked at the CIR surfaces (Mullan 1984). X-rays may suffer additional absorption in density enhanced CIRs.

The DACs recurrence time is on time scale of days. Oskinova, Clarke, & Pollock (2001) detected periodic X-ray variability with an amplitude of ∼20% in the ASCA passband (0.5-10 keV) of the O9Ve star ζ Oph. The detected period of $0\overset{\rm d}{.}77$ possibly indicates a connection with the recurrence time ($0\overset{\rm d}{.}875 \pm 0\overset{\rm d}{.}167$) of the DACs in the UV spectra of this star. In contrast, the analysis of $1\overset{\rm d}{.}175$ continuous ASCA observations of ζ Pup failed to confirm the previously reported variability at the 6% level with a period of 16.667 h found in earlier *ROSAT* data. The new, more sensitive analyses of X-ray observations of O-stars which will extend over the stellar rotational periods should shed more light on the connections between DACs, rotation, and X-ray emission.

5.2 X-ray emission from Oe-type stars

ζ Oph belongs to the rare class of Oe stars (Negueruela, Steele, & Bernabeu 2004). Oe-type stars display Balmer lines similar to those in the classical Be stars. The latter are fast rotating stars with decretion disks. Negueruela et al. point out that the Oe-phenomenon is restricted to the latest subtypes among the O stars, indicating that the building of disks is more problematic for the higher-mass stars.

Li et al. (2008) studied the X-ray emission from Oe/Be stars to test whether the disks of these stars could form by magnetic channeling of wind toward the equator (Cassinelli et al. 2002). In their model, X-rays can be produced by material that enters the shocks above and below the disk region. The model by Li et al. predicts an existence of a relation between $L_{\rm X}/L_{\rm bol}$ and the magnetic field strength in Oe/Be stars.

High-resolution X-ray spectra are only available for two Oe stars: ζ Oph (O9Ve) and HD 155806

(O7.5Ve). The X-ray properties of these stars are quite different. ζ Oph shows periodic modulations of the X-ray flux, has narrow X-ray emission lines. The bulk of its plasma is at a high temperature of 8 MK (Zhekov & Palla 2004). Nazé, Rauw & ud-Doula (2010a) do not detect a modulation of the X-ray flux in HD 155806 and report that its X-ray emission lines are broad. The bulk of its hot plasma has only 2 MK. The $\log L_{\rm X}/L_{\rm bol} = -6.75$ for HD 155806, while $\log L_{\rm X}/L_{\rm bol} = -7.4$ for ζ Oph (Oskinova et al. 2006, Nazé et al. 2010a). Clearly, larger observational samples are required to understand the link between the X-ray emission of Oe-type stars and their hypothetical circumstellar disks.

5.3 X-ray emission from O-stars with magnetic fields

Large-scale flow structures in stellar winds can result when a large-scale magnetic field confines the outflow of matter. Babel & Montmerle (1997) studied the case of a rotating star with a sufficiently strong dipole magnetic field. Collision between the wind components from the two hemispheres in the closed magnetosphere leads to a strong shock. Based on this magnetically confined wind shock model (MCWS), the presence of a magnetic field on the O-type star θ^1 Ori C had been postulated. Direct confirmation of the magnetic field in this star by Donati et al. (2002) proved that X-rays have large diagnostic potential in selecting massive stars with surface magnetic fields.

The MHD simulations in the framework of the MCWS model were performed by ud-Doula & Owocki (2002) and Gagné et al. (2005). Using as input parameters the characteristic values of the wind and the magnetic field strength of θ^1 Ori C, these simulations predict the plasma temperature, emission measure, and periodic X-ray flux modulation which compare well with observations.

This modeling success established the MCWS model as a general scenario for the X-ray emission from magnetic early type stars. The MCWS model makes predictions that can be directly compared with observations: *i)* the hottest plasma should be located at a few stellar radii from the stellar surface at the locus where the wind streams collide; *ii)* the X-ray emission lines should be rather narrow, because the hot plasma is nearly stationary; *iii)* magnetic stars should be more X-ray luminous than their non-magnetic counterparts of similar spectral type; *iv)* the X-ray spectrum of magnetic stars should be harder than that of non-magnetic stars, with the bulk of the hot plasma at temperatures $\sim$20 MK; *v)* the X-ray emission should be modulated periodically as a consequence of the occultation of the hot plasma by a cool torus of matter, or by the opaque stellar core. X-ray variability may be expected when the torus breaks up.

The X-ray observation of magnetic O-type stars led to perplexing results that are not always in agreement with the model predictions. ζ Ori A has a weak surface magnetic field, that may be responsible for the presence of hot plasma close to stellar surface (Waldron & Cassinelli 2007). But, in general, its X-ray properties are typical for an O-type star (Raassen et al. 2008). A strong magnetic field ($\sim$ 1 kG) is detected on HD 108 (O7I) (Martins et al. 2010). However, the emission measure (EM) of the softer spectral component, with a temperature of $\approx$ 2 MK, is more than one order of magnitude higher than the EM of the harder component $T_{\rm max} \approx 15$ MK, contrary to the expectation of the MCWS model (Nazé et al. 2004). HD 191612 also has a $\sim$ 1 kG strong magnetic field (Donati et al. 2006a). Recently, Nazé et al. (2010b) demonstrated that the large EM at $\approx$2 MK and the broad X-ray emission lines in the X-ray spectrum of this star do not compare well with the predictions of the MCWS model. The early-type B-star τ Sco has a complex magnetic field topology (Donati et al. 2006b) and a hard X-ray spectrum (Wojdowski & Schulz 2002, Mewe et al. 2003). A substantial modulation of the X-ray flux with stellar rotation period was expected, but indications for only marginal variability were found by Ignace et al. (2010).

Overall, considering the analysis of X-ray observations of magnetic O stars, it appears that only one star, θ^1 Ori C, displays the properties that are fully compatible with the MCWS model.

5.4 X-ray emission from WR stars

The X-ray emission from WR-type stars remains enigmatic – some WN-type stars are X-ray sources (Ignace, Oskinova & Brown 2003, Skinner et al. 2010), while others remain undetected despite low upper limits on $L_{\rm X}$ (Gosset et al. 2005). Oskinova et al. (2003) showed that WC-type stars are not X-ray sources, a result which they attribute to the very large wind opacity. WO-type star winds are even more metal enriched. However, a reduction in the mass-loss (a poorly constrained parameter) by a factor of only two and/or a higher effective stellar temperature result in a higher degree of wind ionization. In this case a fraction of X-rays could escape. Wind anisotropy can further mitigate wind attenuation.

Magnetic fields and large-scale distortions of stellar winds are invoked as possible explanations for the recently detected X-ray emission from the WO-type star WR 142 (Oskinova et al. 2009). WR 142 is a massive star in a very advanced evolutionary stage shortly before its explosion as a supernova or γ-ray burst. From qualitative considerations we conclude that the observed X-ray radiation is too hard to allow wind-shock origin of X-ray emission. The proposed explanation of its X-ray emission suggests surface magnetic field. Possibly related, WR 142 seems to rotate extremely fast, as indicated by the unusually round profiles of its optical emission lines. Our X-ray detection implies that the wind of WR 142 must be relatively transparent to X-rays, which could be due to strong wind ionization, wind clumping, or non-spherical geometry from rapid rotation.

6 Open questions

We find that incorporating macroclumping in the wind models allows to explain the shapes of X-ray emission lines in O-star spectra. However, many questions about X-rays from single massive stars remain. We list a subjective selection of these questions, which we think are the most promising ones to answer with new advances in theory and observations:

– Is there a correlation between $T_{\rm X}$ and $T_{\rm eff}$ as found by Walborn, Nichols, & Waldron (2009)?

– Is there a near star high ion problem? Is there a dependence of τ_0 on the radius of line formation?

– What is the origin of the $L_{\rm X} \propto L_{\rm bol}$ correlation and how to explain deviations from it?

– Does the MCWS model explains the different X-ray properties of magnetic OB-stars?

– Why X-rays from Oe/Be stars are not meeting the model expectations?

– How are X-rays produced in WR-stars?

Acknowledgements

Authors are grateful to J.P. Cassinelli for the insightful review which helped to improve this manuscript.

References

Asplund, M., Grevesse, N., & Sauval, A.J. 2005, ASP Conf. Ser., 336, 25

Babel, J., & Montmerle, T. 1997, A&A, 323, 121

Baum, E., Hamann, W.-R., Koesterke, L., Wessolowski, U., 1992, A&A, 266, 402

Bouret, J.-C., Donati, J.-F., Martins, F., Escolano, C., Marcolino, W., Lanz, T., Howarth, I. D., 2008a, MNRAS, 389, 75

Bouret, J.-C, Lanz, T., Hillier, D., Foellmi, C., 2008b, Clumping in Hot Star Winds, Universitatsverlag, Potsdam, p.31

Cassinelli, J.P. & Olson, G.L., 1979, ApJ 229, 304
Cassinelli, J.P. & Swank, J.H., 1983, ApJ 271, 681
Cassinelli, J.P., Miller, N.A., Waldron, W.L., MacFarlane, J.J., Cohen, D.H., 2001, ApJ, 554, 55
Cassinelli, J.P., Brown, J.C., Maheswaran, M., Miller, N.A., Telfer, D.C., 2002, ApJ, 578, 951
Cassinelli, J.P., Ignace, R., Waldron, W.L., Cho, J., Murphy, N.A., Lazarian, A. 2008, ApJ, 683, 1052
Cohen, D., Leutenegger, M. A., Wollman, E.E., Zsargó, J., Hillier, D. J., Townsend, R. H. D., Owocki, S. P., 2010, MNRAS, 405, 2391
Cranmer, S.R. & Owocki, S.P., 1996, ApJ, 462, 469
Donati, J.-F., Babel, J., Harries, T. J., Howarth, I. D., Petit, P., Semel, M., 2002, MNRAS, 333, 55
Donati, J.-F., Howarth, I. D., Bouret, J.-C., Petit, P., Catala, C., Landstreet, J., 2006a, MNRAS, 365, L6
Donati, J.-F., Howarth, I.D., Jardine, M.M., et al., 2006b, MNRAS, 370, 629
Gagné, M., Oksala, M.E., Cohen, D.H., Tonnesen, S. K., ud-Doula, A., Owocki, S. P., Townsend, R. H. D., MacFarlane, J. J., 2005, ApJ, 628, 986
Gosset, E., Nazé, Y., Claeskens, J.-F., Rauw, G., Vreux, J.-M., Sana, H. 2005, A&A, 429, 685
Güdel, M. & Nazé, Y., 2009, A&ARv, 17, 309
Gräfener, G., Koesterke, L.,& Hamann, W.-R, 2002, A&A, 387, 244
Feldmeier, A., Puls, J., & Pauldrach, A. W. A., 1997, A&A, 320, 899
Feldmeier, A., Oskinova, L.,& Hamann, W.-R., 2003, A&A, 403, 217
Fullerton, A. W., Massa, D. L., & Prinja, R. K. 2006, ApJ, 637, 1025
Hamann, W.-R., Brown, J.C., Feldmeier, A., Oskinova, L.M. 2001, A&A, 378, 946
Hamann, W.-R., Feldmeier, A., & Oskinova, L. M., 2008, *Clumping in Hot Star Winds*, Universitatsverlag, Potsdam
Hervé, A. & Rauw, G., 2011, in Proceedings of the 39th Liège Astrophysical Colloquium, eds. G. Rauw, M. De Becker, Y. Nazé, J.-M. Vreux & P. Williams, BSRSL, 80, 155
Hillier, D. J., Kudritzki, R.P., Pauldrach, A.W., Baade, D., Cassinelli, J. P., Puls, J., Schmitt, J. H. M. M., 1993, A&A, 276, 117
Ignace, R., 2001, ApJ, 549, 119
Ignace, R., Oskinova, L. M., & Brown, J. C., 2003, A&A, 408, 353
Ignace, R. & Gayley, K. G., 2002, ApJ, 568, 954
Ignace, R., Oskinova, L. M., Jardine, M., Cassinelli, J. P., Cohen, D. H., Donati, J.-F., Townsend, R. H. D., ud-Doula, A., 2010, ApJ, 721, 1412
Kahn, S.M., Leutenegger, M. A., Cottam, J., Rauw, G., Vreux, J.-M., den Boggende, A. J. F., Mewe, R., Güdel, M., 2001, A&A, 365, 312
Kramer, R.H., Cohen, D.H., & Owocki, S.P., 2003, ApJ 592, 532
Krtička, J. & Kubát, J., 2007, A&A, 464, 17
Lamers, H.J.G.L.M., Haser, S., de Koter, A., Leitherer, C., 1999, ApJ, 516, 872
Leutenegger, M.A., Paerels, F.B.S, Kahn, S.M., Cohen, D.H., 2006, ApJ, 650, 1096
Leutenegger, M.A., Owocki, S.P., Kahn, S.M., & Paerels, F.B.S. 2007, ApJ, 659, 642
Li, Q., Cassinelli, J.P., Brown, J.C., Waldron, W.L., Miller, N.A., 2008, ApJ, 672, 1174
Lobel, A., Toalá, J.A., & Blomme R., 2011, in Proceedings of the 39th Liège Astrophysical Colloquium, eds. G. Rauw, M. De Becker, Y. Nazé, J.-M. Vreux & P. Williams, BSRSL, 80, 42
MacFarlane, J.J., Cassinelli, J.P., Welsh, B.Y., Vedder, P.W., Vallerga, J. V., Waldron, W. L. 1991, ApJ 380, 564
Martins, F., Donati, J.-F., Marcolino, W.L.F., Bouret, J.-C., Wade, G. A., Escolano, C., Howarth, I. D., 2010, MNRAS, 407, 1423
Massa, D. Fullerton, A.W., Sonneborn, G., Hutchings, J. B., 2003, ApJ, 586, 996
Mewe, R., Raassen, A.J.J., Cassinelli, J.P., van der Hucht, K. A., Miller, N. A., Güdel, M., 2003, A&A, 398, 203
Miller, N.A., Cassinelli, J.P., Waldron, W.L., MacFarlane, J.J., Cohen, D.H., 2002, ApJ, 577, 951
Mullan, D.J., 1984, ApJ 283, 303
Nazé, Y., 2011, in Proceedings of the 39th Liège Astrophysical Colloquium, eds. G. Rauw, M. De Becker, Y. Nazé, J.-M. Vreux & P. Williams, BSRSL, 80, 109
Nazé, Y., Rauw, G., Vreux, J.-M., De Becker, M. 2004, A&A, 417, 667
Nazé, Y., Rauw, G., & ud-Doula, A., 2010a, A&A, 510, 59
Nazé, Y., ud-Doula, A., Spano, M., Rauw, G., De Becker, M., Walborn, N.R., 2010b, A&A, 520, 59
Negueruela, I., Steele, I.A., & Bernabeu, G., 2004, AN, 325, 749
Oskinova, L.M., Clarke, D., & Pollock, A.M.T., 2001, A&A, 378, L21
Oskinova, L.M., Ignace, R., Hamann, W.-R., Pollock, A.M.T., Brown, J.C., 2003, A&A, 402, 755
Oskinova, L.M., Feldmeier, A., & Hamann, W.-R., 2004, A&A, 422, 675
Oskinova, L.M., Feldmeier, A., & Hamann, W.-R., 2006, MNRAS, 372, 313

Oskinova, L.M., Hamann, W.-R., & Feldmeier, A., 2007, A&A, 476, 1331
Oskinova, L.M, Hamann, W.-R., Feldmeier, A., Ignace, R., Chu, Y.-H., 2009, ApJL, 693, 44
Owocki, S. P., Castor, J. I., & Rybicki, G. B., 1988, ApJ, 335, 914
Owocki, S.P. & Cohen, D. H., 2001, ApJ, 559, 1108
Owocki, S.P., Gayley, K.G., Shaviv, N.J., 2004, ApJ, 616, 525
Owocki, S.P. & Cohen, D. H., 2006, ApJ, 648, 565
Pauldrach, A.W.A, Hoffmann, T.L, & Lennon, M., 2001, A&A 375, 161
Pollock, A. M. T., 2007, A&A, 463, 1111
Prinja, R.K. & Howarth, I.D., 1986, ApJS, 61, 357
Prinja, R.K & Massa, D., 2010, A&A, 521, L55
Raassen, A.J.J., van der Hucht, K.A., Miller, N.A., Cassinelli, J.P., 2008, A&A, 478, 513
Runacres, M. C. & Owocki, S. P., 2002, A&A, 381, 1015
Runacres, M. C. & Owocki, S. P., 2005, A&A, 429, 323
Skinner, S.L., Zhekov, S.A., Güdel, M., Schmutz, W., Sokal, K.R., 2010, AJ, 139, 825
Sundqvist, J., Puls, J., Feldmeier, A., Owocki, S.P., 2011, in Proceedings of the 39th Liège Astrophysical Colloquium, eds. G. Rauw, M. De Becker, Y. Nazé, J.-M. Vreux & P. Williams, BSRSL, 80, 48
Walborn, N.R., Nichols, J. S., & Waldron, W.L., 2009, ApJ, 703, 633
Waldron, W. L., 1984, ApJ, 282, 256
Waldron, W. L. & Cassinelli, J. P., 2001, ApJ, 548, 45
Waldron, W. L. & Cassinelli, J. P., 2007, ApJ, 668, 456
Waldron, W. L. & Cassinelli, J. P., 2010, ApJ, 711, 30
Wojdowski, P.S & Schulz, N.S, 2002, ApJ, 627, 953
ud-Doula, A., & Owocki, S. P. 2002, ApJ, 576, 413
Zhekov, S.A. & Palla, F. 2004, MNRAS, 382, 1124
Zsargó, J., Hillier, D.J., Bouret, J.-C., Lanz, T., Leutenegger, M.A., Cohen, D.H., 2008, ApJ, 685, 149

Discussion

C. Martayan: About WR142, you indicate a $v \sin i$ of 4000 km/s. This velocity is above the critical velocity. Could you please comment on this result and tell us more about the stability of this star?
L. Oskinova: Our estimate of rotational velocity is based on a rather simple modeling and is, perhaps, an upper limit. But the star is a very fast rotator.

G. Romero: What is the role, you think, of magnetic reconnection at the base of the wind in heating the plasma and generating the X-rays?
Answer: Thank you. I think that in the stars with surface magnetic field, and in case the magnetic field configuration allows for the reconnection, the magnetic field may play a role in heating the plasma or leading to some kind of mass ejection. This was recently investigated by Waldron & Cassinelli (2009).

Radio observations of massive stars

Ronny Blomme

Royal Observatory of Belgium, Ringlaan 3, B-1180 Brussel, Belgium

Abstract: Detectable radio emission occurs during almost all phases of massive star evolution. I will concentrate on the thermal and non-thermal continuum emission from early-type stars. The thermal radio emission is due to free-free interactions in the ionized stellar wind material. Early ideas that this would lead to an easy and straightforward way of measuring the mass-loss rates were thwarted by the presence of clumping in the stellar wind. Multi-wavelength observations provide important constraints on this clumping, but do not allow its full determination.

Non-thermal radio emission is associated with binarity. This conclusion was already known for some time for Wolf-Rayet stars and in recent years it has become clear that it is also true for O-type stars. In a massive-star binary, the two stellar winds collide and around the shocks a fraction of the electrons are accelerated to relativistic speeds. Spiralling in the magnetic field these electrons emit synchrotron radiation, which we detect as non-thermal radio emission. The many parameters that influence the resulting non-thermal radio fluxes make the modelling of these systems particularly challenging, but their study will provide interesting new insight into massive stars.

1 Introduction

Radio emission in massive stars occurs in almost all stages of stellar evolution. It starts with the molecular clouds in which the stars are formed: these can be detected in the radio through their maser emission (Elitzur 1992, Chapt. 8; Van der Walt 2011). As the H II region forms, we can detect it in its atomic recombination lines, as well as in its thermal and non-thermal continuum emission (Rohlfs & Wilson 2000, Chapt. 10 & 13). In the red supergiant phase, molecular maser emission again dominates (Elitzur 1992, Chapt. 8). During the Luminous Blue Variable (LBV) phase, the ionized material in the nebula emits at radio wavelengths (Umana et al. 2010, 2011). At the end-phase of evolution, compact objects are responsible for the radio emission in pulsars, massive X-ray binaries and micro-quasars (Paredes 2009). Various interactions with the interstellar medium, such as bowshocks, bubbles and supernova remnants are also detectable in radio emission (Rohlfs & Wilson 2000, Chapt. 10; Cappa et al. 2002). The present review, however, will concentrate on the main-sequence evolutionary phase, as well as on the blue supergiant and Wolf-Rayet (WR) phases, where the radio emission is due to the thermal and non-thermal processes in stellar winds.

1.1 History

Historically, the first massive star detected at radio wavelengths was the LBV star P Cygni. Wendker et al. (1973) found fluxes of 9 ± 2 mJy[1] at 6 cm and 15 ± 3 mJy at 3 cm. Later, Wendker et al. (1975) were the first to detect a Wolf-Rayet star, WR 136, while studying its ejecta nebula NGC 6888. The first radio-detected O-type star was, not surprisingly, ζ Pup (Morton & Wright 1978).

In 1981, the 27-telescope Very Large Array (VLA[2]) became available, which presented a major step forward compared with the single-dish telescopes that had been used till that time. The 27 antennas not only provide a larger collecting surface area, but they are furthermore used as a radio interferometer. In such an interferometer, the spatial resolution is determined by the largest distance between two antennas. The positions of the VLA antennas are changed approximately every trimester, allowing astronomers to study the radio sky with different spatial resolutions. The high sensitivity of the VLA allowed Bieging et al. (1982) to make a survey of Wolf-Rayet stars (they detected 8 of the 13 stars studied). Later, Bieging et al. (1989) also surveyed OB stars, detecting 18 of the 88 stars studied.

1.2 Theory

In parallel, there were also theoretical developments in understanding and modelling the origin of the radio emission from these hot, massive stars. Within a very short time span various authors deduced that the emission is due to free-free processes in the ionized material of the stellar winds (Seaquist & Gregory 1973; Olnon 1975; Panagia & Felli 1975; Wright & Barlow 1975). Working out the details, a simple equation is found that relates the radio flux (S_ν) to the mass-loss rate ($\dot{M}$, in $M_\odot$ yr^{-1}):

$$S_\nu = 2.24 \times 10^{11} \frac{1}{D^2} \left(\frac{\dot{M}}{\mu v_\infty} \right)^{4/3} \left(\frac{\gamma g Z^2}{\lambda} \right)^{2/3} \quad [\mathrm{mJy}], \tag{1}$$

where D is the distance to the star (in kpc), v_∞ is the terminal wind velocity (km s^{-1}), λ is the radio wavelength (cm) and g is the Gaunt factor. The chemical composition of the wind is encoded in the μ factor, and the ionization state in the γZ^2 factors. Eq. 1 suggests that radio observations are an easy way to determine mass-loss rates: we do not need to know the detailed ionization balance of some trace species (as we need for the analysis of ultraviolet P Cygni profiles), but only the gross ionization properties of the wind. We also do not need to know the shape of the velocity law (as we do need for Hα, infrared and millimetre work), but only the terminal velocity.

The radio flux shows a near-power law dependence on the wavelength. Taking into account the weak wavelength dependence of the Gaunt factor, we have that $S_\nu \propto 1/\lambda^{+0.6}$, where the exponent $\alpha = +0.6$ is called the spectral index. It is also important to realize that the geometric region from which we receive the radio emission is quite extended. For an O-type star such as ζ Pup, the 6-cm formation region is beyond $\sim 100 R_*$. Furthermore, this region depends on the wavelength, because the optical depth for free-free absorption is proportional to λ^2. At longer wavelengths, the formation region is further away from the star.

1.3 Non-thermal emission

Although the radio emission for most early-type stars is due to free-free emission, it became clear already early on that a number of anomalies exist. Abbott et al. (1980) found that the radio mass-loss

[1] 1 mJy = 10^{-29} W m^{-2} Hz^{-1} = 10^{-26} erg cm^{-2} Hz^{-1} s^{-1}.

[2] `http://www.vla.nrao.edu/`

rate for the O4 V star 9 Sgr was a factor 40 higher than that derived from the ultraviolet or Hα line profiles. Such a difference is much higher than can be accounted for by the intrinsic errors. From spatially resolved observations, it is also possible to derive a brightness temperature (or a lower limit, if the source is unresolved). The brightness temperature of Cyg OB2 No. 9 was found by White & Becker (1983) to be higher than 300,000 K. It is very unlikely, however, that the electrons and ions responsible for the free-free emission would be at so high a temperature. Abbott et al. (1984) found flux variability in 9 Sgr and Cyg OB2 No. 9 which was too high to be attributed to changes in the stellar wind parameters. They also measured radio flux values that deviate significantly from the +0.6 spectral index, with values of $\alpha \approx 0.0$, or even negative in later observations (Bieging et al. 1989). All this indicates that, besides the free-free emission, a second mechanism is operating in these stars, which we call non-thermal emission.

2 Thermal radio emitters

Eq. 1 has been used to determine the mass-loss rates of hot, massive stars. One example is the large set of Wolf-Rayet mass-loss rate determinations by Cappa et al. (2004). The equation has also been used to study the mass-loss rate across the bi-stability jump (Benaglia et al. 2008). Theoretical modelling predicts a change in ionization around 21,000 K that substantially changes the mix of lines responsible for the radiative driving of the wind. The radio observations indeed indicate that around the bi-stability jump, stellar winds have a higher efficiency than expected from the general declining trend towards later spectral types.

2.1 Clumping

The major problem with Eq. 1, however, is that it does not include the effect of clumping or porosity. Many indicators show the presence of substantial clumping in stellar winds: the Phosphorus V discrepancy, X-ray spectroscopy, the electron scattering wings of WR emission lines, the presence of subpeaks on WR emission lines that are seen moving outward, ... (Crowther 2007; Puls et al. 2008). Also from a theoretical point of view, considerable clumping is expected due to the instability of the radiation driving mechanism of the stellar wind (Owocki & Rybicki 1984).

Because free-free emission is a process that depends on the density-squared, it is influenced by this clumping. Eq. 1 can be extended to include some simple model of clumping that assumes all the wind material is concentrated in clumps, with no interclump material. All clumps have the same clumping factor given by $f_{\rm cl} =< \rho^2 > / < \rho >^2$, where the angle brackets indicate an average over the volume in which the radio continuum at that wavelength is formed. The resulting equation is (Abbott et al. 1981):

$$S_\nu = 2.24 \times 10^{11} \frac{1}{D^2} \left(\frac{\dot{M}\sqrt{f_{\rm cl}}}{\mu v_\infty} \right)^{4/3} \left(\frac{\gamma g Z^2}{\lambda} \right)^{2/3} . \qquad (2)$$

Sometimes, in the literature, a volume filling factor f is used. With our assumption of no interclump material, there is a direct relation between f and the clumping factor: $f = 1/f_{\rm cl}$. In the above equation we have also assumed that the clumps are optically thin; optically thick clumps would result in porosity (Owocki et al. 2004).

Eq. 2 considerably changes the interpretation of an observed radio flux. All we can derive from the observations is the combined quantity $\dot{M}\sqrt{f_{\rm cl}}$. A given flux can thus correspond to a certain mass-loss rate assuming a smooth wind ($f_{\rm cl} = 1$), or to a lower mass-loss rate assuming a clumped wind ($f_{\rm cl} > 1$). This uncertainty in the mass-loss rates has important consequences for stellar evolution: if the

rates during the main-sequence evolution are too low, mass-loss episodes during other evolutionary phases need to be invoked to explain the existence of Wolf-Rayet stars (Smith & Owocki 2006).

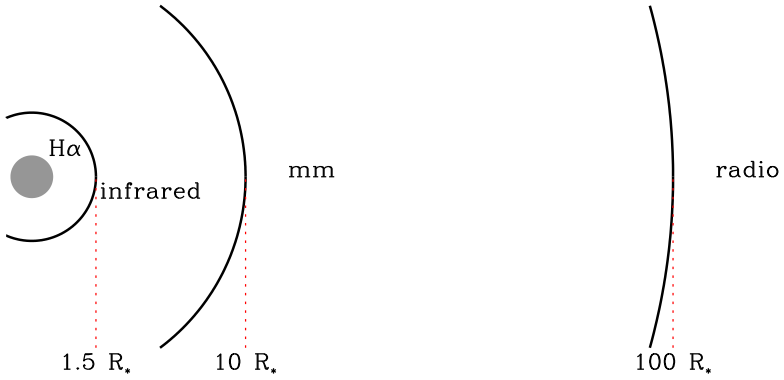

Figure 1: The formation regions of various density-squared observational indicators in the stellar wind of a typical O-type star.

2.2 Clumping gradients in OB stellar winds

From radio data alone, it is difficult to make a distinction between smooth and clumped winds. But a number of other observational indicators are also sensitive to clumping because they depend on density-squared processes (as does the radio emission). These indicators include the Hα spectral line, the infrared and the millimetre continuum. Interestingly, these different indicators are formed in different regions of the wind (Fig. 1). Very approximate values for an O-type star with a strong stellar wind are: Hα within $1.5\,R_*$ of star, infrared up to a few R_*, millimetre from about $10\,R_*$ and radio from $\sim 100\,R_*$.

This opens up the possibility to compare the clumping in different regions of the wind, and to see if there is a gradient in the clumping. Lamers & Leitherer (1993) were the first to attempt this, by comparing the mass-loss rate derived from the Hα line with that from the radio (assuming a smooth wind). They found no significant differences and therefore concluded that significant clumping in stellar winds was unlikely.

Runacres & Blomme (1996) compared the infrared, millimetre and radio fluxes with smooth wind models for a sample of 18 OB stars. The models were fitted through the observed visual and near-infrared continuum fluxes, which fixes the distance and interstellar extinction. They determined the mass-loss rate so that a good fit to the observed radio fluxes was also obtained. They then checked how well this smooth wind model agreed with the observed far-infrared and millimetre fluxes (which were not used in the fitting procedure). Four stars (α Cam, δ Ori A, κ Ori and ζ Pup) showed fluxes that are significantly higher than the smooth wind model.

Later, an even better example was found: for the bright B0 Ia star ϵ Ori, Blomme et al. (2002) combined new data with archival observations and applied the same technique. Fig. 2 shows the observed fluxes as a function of wavelength, covering the range from visual to radio wavelengths. The y-axis shows the observed flux divided by the smooth wind flux. Any significant excess above the y=1 line is interpreted as being due to clumping in the wind. A clear excess is seen at millimetre wavelengths, with a possible onset already in the far-infrared and a continuation in the radio region. This indicates the presence of more clumping in the geometric region where the millimetre flux is formed.

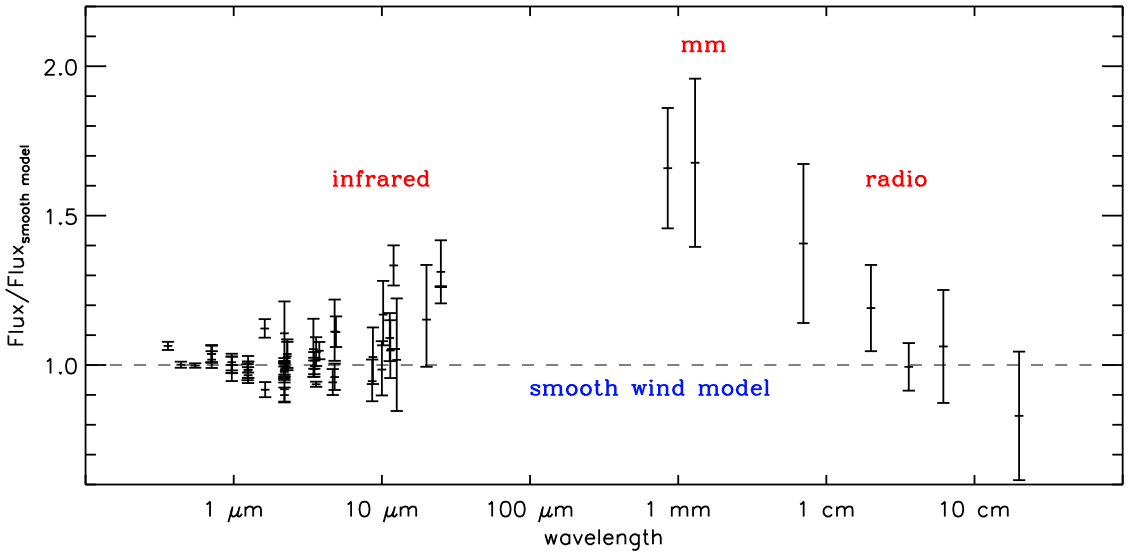

Figure 2: The ϵ Ori fluxes from visual to radio wavelengths, compared with a smooth wind model. The flux excess in the millimetre region is interpreted as indicating a higher clumping factor in the millimetre formation region. Based on Blomme et al. (2002), with some new radio data added.

It is important to realize that in this type of work we need to assume that the wind region where the radio emission is produced, is not clumped, otherwise we would just introduce another parameter on which we have no observational constraints. But it is of course quite likely that the radio formation region is also clumped. The downward gradient seen in the 7 mm to 20 cm radio fluxes (Fig. 2) is suggestive of some decrease of clumping in the radio formation region, as we go further out in the wind.

Puls et al. (2006) not only studied the continuum fluxes, but also included the Hα line, for a sample of 19 O-type supergiants and giants. The first thing they noticed is that the radio mass-loss rates (assuming a smooth wind) are in better agreement with the predicted wind-momentum luminosity relation (Vink et al. 2000) than the Hα mass-loss rates (again, assuming a smooth wind). A closer inspection reveals that it is mainly the stars with Hα in emission (i.e. those with a stronger stellar wind) that are most discrepant.

Puls et al. (2006) then introduced a clumped wind model. The wind was divided into 5 regions, and in each region a constant clumping factor was taken. These clumping factors were then adjusted to obtain a good fit to the observed Hα, infrared, millimetre and radio data. Because of the reason explained above, the radio region was assumed not to be clumped. A major result from their work is the behaviour of the clumping factor in the Hα formation region (their Fig. 10). For stars with low mass-loss rates, the clumping factors are not significantly different from 1. But for stars with higher mass-loss rates, the Hα clumping factors average around 4. This means that the geometric region where Hα is formed (i.e. close to the stellar surface) is more clumped than the radio formation region, at least for OB stars with strong winds.

2.3 Clumping gradients in Wolf-Rayet stellar winds

Such a gradient in the clumping factor might also exist in Wolf-Rayet stars. Nugis et al. (1998) studied the spectral index between the infrared and radio wavelengths for 37 WR stars. According to Eq. 1, this spectral index should be $\alpha = +0.6$ for a wind that has the same clumping everywhere. However,

Nugis et al. measured α values from $+0.66 \pm 0.01$ up to $+0.88 \pm 0.04$, with most spectral indices being larger than $+0.7$ (their Fig. 1). This again indicates more clumping in the inner part of the wind compared with the outer part. Nevertheless, the interpretation of these results is more complicated than for OB stars, because the ionization in a Wolf-Rayet wind can change sufficiently to influence the spectral index. Furthermore, for at least one WR star, Montes et al. (2011) ascribe the higher than $+0.6$ spectral index to thermal emission in the increased density region of a colliding-wind binary.

In summary, it is clear that OB stars with strong winds show a gradient in their stellar wind clumping, with stronger clumping in the inner part of the wind. Puls et al. (2006) also point out that these results are not in agreement with the hydrodynamical models of Runacres & Owocki (2005), which predict more clumping in the radio than in Hα. It is possible however that even minor changes in the input physics of these hydrodynamical models might change this conclusion. A similar clumping gradient probably also exists in the winds of Wolf-Rayet stars, with the important caveat that ionization changes also play a role and are not easy to distinguish from clumping.

3 Non-thermal radio emitters

In Sect. 1.3, we saw that some hot, massive stars also show non-thermal radio emission. This emission is characterized by a spectral index significantly smaller than the $+0.6$ value for thermal emission and by a high brightness temperature. It is also frequently associated with variability in the radio fluxes, though this characteristic in itself is not sufficient to identify non-thermal emission: e.g., the LBV P Cygni shows radio variability, but this is due to ionization changes in the wind, not to non-thermal emission (Exter et al. 2002).

In the literature, various values for the incidence of non-thermal emission are cited. Abbott et al. (1986) claim that 12 % of the Wolf-Rayet stars are non-thermal and Bieging et al. (1989) give at least 24 % of the OB stars. Later, much higher numbers were claimed: 20 – 30 % of the detected WR stars (Cappa et al. 2004); more than 40 % of the Wolf-Rayet stars (Leitherer et al. 1997; Chapman et al. 1999); up to 50 % of detected O-type stars (Benaglia et al. 2001). The reason for these differences is an observational bias: non-thermal emitters are intrinsically radio-brighter than thermal ones and therefore easier to detect. The higher percentages indicate the probability of finding a non-thermal emitter in a random sample of massive stars. The lower percentages by Abbott et al. (1986) and Bieging et al. (1989) refer to volume-limited samples, and therefore give a better indication of the incidence of non-thermal emission in massive stars.

3.1 Binary connection

Quite early on, it was clear that there was some connection between non-thermal emission and binarity. Moran et al. (1989) used the MERLIN radio telescopes to spatially resolve the emission from WR 147. They found a thermal radio emitting source at the position of the Wolf-Rayet star itself and also a well separated non-thermal source between the WR star and a close-by B-type star (this companion was discovered later in the infrared by Williams et al. 1997). The geometry of the situation suggests that the non-thermal region is positioned at the collision region between the wind of the Wolf-Rayet star and that of the B-type star.

A detailed theoretical explanation was provided by Eichler & Usov (1993). In a massive binary system, the stellar winds of both components collide (Fig. 3). This creates a contact discontinuity with a shock on either side. The position and shape of the contact discontinuity is determined by the relative strengths (ram pressure) of the two winds: the discontinuity is closer to the star with the weakest wind, and wraps around that star.

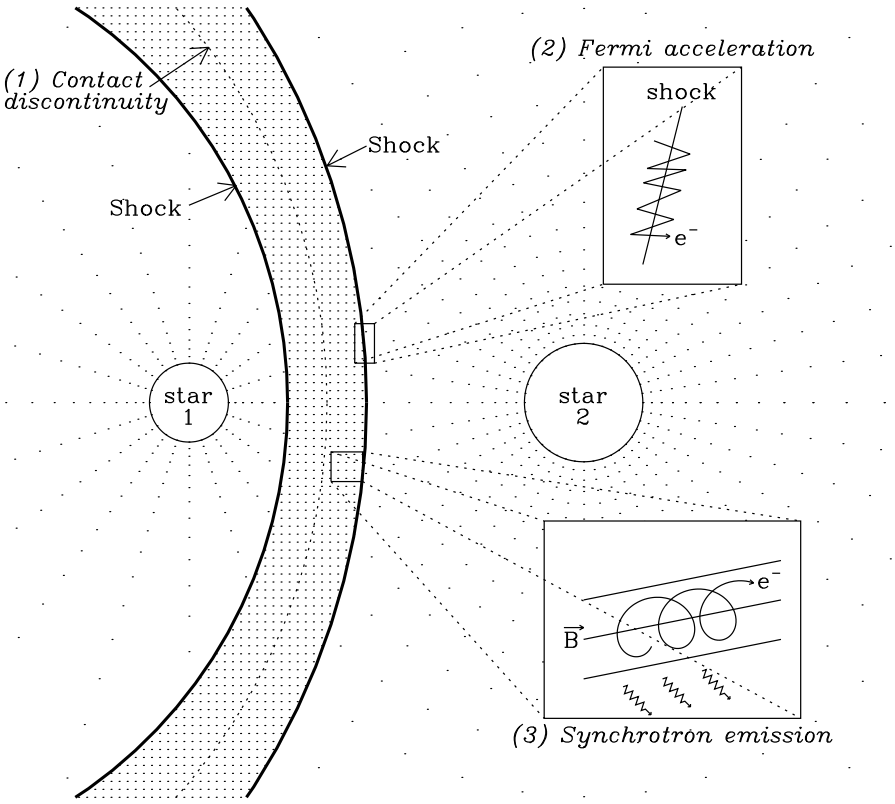

Figure 3: Synchrotron emission from colliding winds. *(1)* The winds of both components collide, creating a shock on either side of the contact discontinuity. *(2)* At each shock, the Fermi mechanism accelerates a fraction of the electrons to relativistic speeds. *(3)* These relativistic electrons spiral in the magnetic field and emit synchrotron radiation.

At each shock, a fraction of the electrons is accelerated up to relativistic speeds, through the first-order Fermi mechanism (Bell 1978). In this mechanism, electrons bounce back and forth across the shock and at each bounce gain some energy from the shock (Fig. 3). A fraction of the electrons make enough bounces to attain relativistic speeds. These electrons then spiral around in the magnetic field, emitting synchrotron radiation at radio wavelengths. It is this synchrotron radiation that we see as the non-thermal emission.

The synchrotron emission has a spectral index of -0.5 to -1.0 (Bell 1978; Pittard et al. 2006), explaining the observed spectral index. The emission is due to high-energy particles, which explains the high brightness temperature. Not all of the synchrotron emission is detected, however, because part of it (or in some cases, all of it) is absorbed by the free-free absorption in the stellar winds of both stars. The effect of the absorption depends on the orbital phase, because the sightline from the synchrotron emission region to the observer passes through different parts of the wind(s) as the positions of the stars change in their orbit. Furthermore, in an eccentric binary, the changing separation also generates variability in the intrinsic synchrotron emission as the ram pressure of the collision changes. The combination of both effects explains the variability seen in non-thermal radio emitters.

Van der Hucht et al. (1992) studied a number of Wolf-Rayet stars and found a good correlation between binarity and non-thermal emission. They also showed that these binaries are frequently associated with dust emission (detectable in the infrared) and with X-ray emission. They made the bold extrapolation *"... that all other non-thermal WR stars discussed in this paper, as well as all (variable) non-thermal radio OB stars (...), are actually long-period binaries..."*.

3.2 Wolf-Rayet binaries

An outstanding example of a colliding-wind binary is WR 140. It consists of a WC7 + O4-5 star in a 7.9-yr orbit with a high eccentricity ($e \approx 0.88$). White & Becker (1995) followed this system during more than one orbital period and determined the 2, 6 and 20 cm fluxes approximately every month. The detailed radio light curves (their Fig. 3) show substantial variability that is well correlated with orbital phase and that repeats from one orbit to the next. The light curves at different wavelengths are reasonably similar to one another, except that the shorter-wavelength curves start rising earlier and decline more slowly after maximum. The variability is due to the combined effect of changing synchrotron emission and free-free absorption as a function of orbital phase. Obtaining a good model fit to these data is still a considerable challenge (Pittard 2011).

More recently, Dougherty et al. (2005) have used the Very Long Baseline Array (VLBA) to spatially resolve the wind-collision region. They obtained data with a resolution of ~ 2 milli-arcsec at 23 epochs, covering orbital phases 0.74 to 0.97. These data reveal how the emission region changes orientation and size as a function of orbital phase. The continued popularity of WR 140 is shown by the many contributions about this system at this colloquium (Dougherty, Trenton & Beasley 2011; Fahed et al. 2011; Parkin et al. 2011; Russell et al. 2011; Sugawara et al. 2011; Williams 2011).

Although WR 140 is an outstanding example of the link between binarity and non-thermal emission, the link cannot be proven with only one, or a few, examples. A more statistical approach was taken by Dougherty & Williams (2000). From the 23 WR stars they studied, they selected 9 that had a non-thermal spectral index, or composite index (between thermal and non-thermal). Seven of these stars are known binaries (later, Marchenko et al. (2002) found WR 112 to have a dusty spiral, strongly suggesting it is also a binary). A plot of the spectral index vs. orbital period (Dougherty & Williams, their Fig. 1) shows an interesting correlation: short-period stars have a nearly-thermal index, while long-period stars have a non-thermal index. This effect is easily explained with the colliding-wind model: short-period binary components are so close to one another that all synchrotron emission is absorbed by the free-free absorption region in the stellar winds. Longer-period binaries have components that are further away from one another; the synchrotron emitting region is therefore largely outside the free-free absorption, and most of the synchrotron emission gets through to the observer.

3.3 Single O stars

While the link between binarity and non-thermal emission is quite strong for Wolf-Rayet stars, this was not the case for O-type stars. Some years ago, there were still a number of non-thermal O stars that were seemingly single. Before getting carried away by the binary explanation, it is therefore important to also investigate if single stars can produce non-thermal emission. After all, there are shocks in the winds of single stars, due to the instability of the radiative driving mechanism (Owocki & Rybicki 1984), and these shocks should be able to accelerate electrons and thus generate synchrotron emission.

Van Loo et al. (2006) investigated this possibility for a typical O-star non-thermal emitter, Cyg OB2 No. 9. They made a model containing a number of shocks in the stellar wind. The parameters of these shocks (mainly the shock jump velocity) were inspired by the Runacres & Owocki (2005) hydrodynamical model. They then calculated the number of relativistic electrons accelerated at each shock and followed them as they cooled down due to inverse Compton and adiabatic cooling. From this, the synchrotron emission was calculated, and – taking into account the free-free absorption – the emergent radio flux was determined. There is considerable synchrotron emission in the inner part of the wind, where the shocks are strong (high jump velocity). This emission, however, is completely absorbed by the free-free absorption. In the outer part of the wind, there is also synchrotron emission, but the shock jump velocity has reduced considerably there, so there is not enough emission to

explain the observations. The fact that the model cannot explain the Cyg OB2 No. 9 observations throws serious doubt on the single-star hypothesis.

3.4 O star binaries

More positive proof that Cyg OB2 No. 9 is a binary was provided by Van Loo et al. (2008). Using VLA archive data covering 20 years, they detected a 2.355-yr period in the radio data (see also Volpi 2011). The radio fluxes vary with orbital phase and the variations repeat very well from one orbit to the next. All this indicates that Cyg OB2 No. 9 is a binary. At the same time Nazé et al. (2008) also detected binarity in the spectroscopic data. Newer spectroscopic observations are presented in Nazé et al. (2010, 2011).

A similar technique was used on HD 168112 observations by Blomme et al. (2005). The amount of data is less than for Cyg OB2 No. 9, so the result is less certain. A period between 1 and 2 years is found, with P = 1.4 yr as the formally best value. There is as yet no spectroscopic confirmation of the binary status of this star.

As we did for the Wolf-Rayet stars, we need to proceed to a more statistical approach to show the link with binarity. Detailed statistics of non-thermal emission in O-type stars are provided by De Becker (2007) and by Benaglia (2010). De Becker (his Table 2) shows that many of the O-star non-thermal emitters are now confirmed, or at least suspected, binaries. Although a few stars have not yet been investigated for multiplicity, we can now confidently confirm the Van der Hucht et al. (1992) quote (Sect. 3.1) that all non-thermal O-star and Wolf-Rayet star radio emitters are indeed colliding-wind binaries.

3.5 Remaining problems

Although the link between non-thermal emission and binarity is now quite secure, that does not mean we understand everything about non-thermal radio emission. One interesting point is that quite a number of non-thermal emitters are actually multiple systems. A nice example is HD 167971, which consists of a 3.3-d eclipsing binary and a third light (Leitherer et al. 1987). It is not clear if this third component is gravitationally bound to the binary, or whether it is just a line-of-sight object. Blomme et al. (2007) studied the VLA archive data of this system. They did not find any radio variability on the 3.3-day time scale, as may be expected from such a short-period binary. But the data show a clear cycle of ~ 20 yrs, suggesting that the third component and the binary are gravitationally bound and orbit each other with a 20-yr period. Another example of a multiple system is Cyg OB2 No. 5 (Kennedy et al. 2010, 2011).

A further problem is posed by the short-period binary Cyg OB2 No. 8A (P = 21.9 d, De Becker et al. 2004). Although no synchrotron emission was expected from such a close binary, the VLA data do show orbit-locked variability (Blomme et al. 2010; see also Fig. 4, left panel). This radio variability is furthermore nearly anti-correlated to the X-ray variability. Blomme et al. develop a theoretical model for this system, starting from an analytical solution for the position of the contact discontinuity. At both shocks, relativistic electrons are injected and followed as they move away with the flow and as they cool down due to adiabatic and inverse Compton cooling. The resulting synchrotron emission is then included in a radiative transfer calculation, together with free-free absorption, giving the radio flux. By following the two components along their orbit, an artificial light curve is constructed. A first model that uses the wind parameters determined by De Becker et al. (2006) fails to explain the observations. By accepting stellar wind parameters that are different from those expected for single stars, however, we achieve a better agreement (Fig. 4, right panel). The model can qualitatively explain many of the observed features of the radio data, as well as the anti-correlation with the X-ray

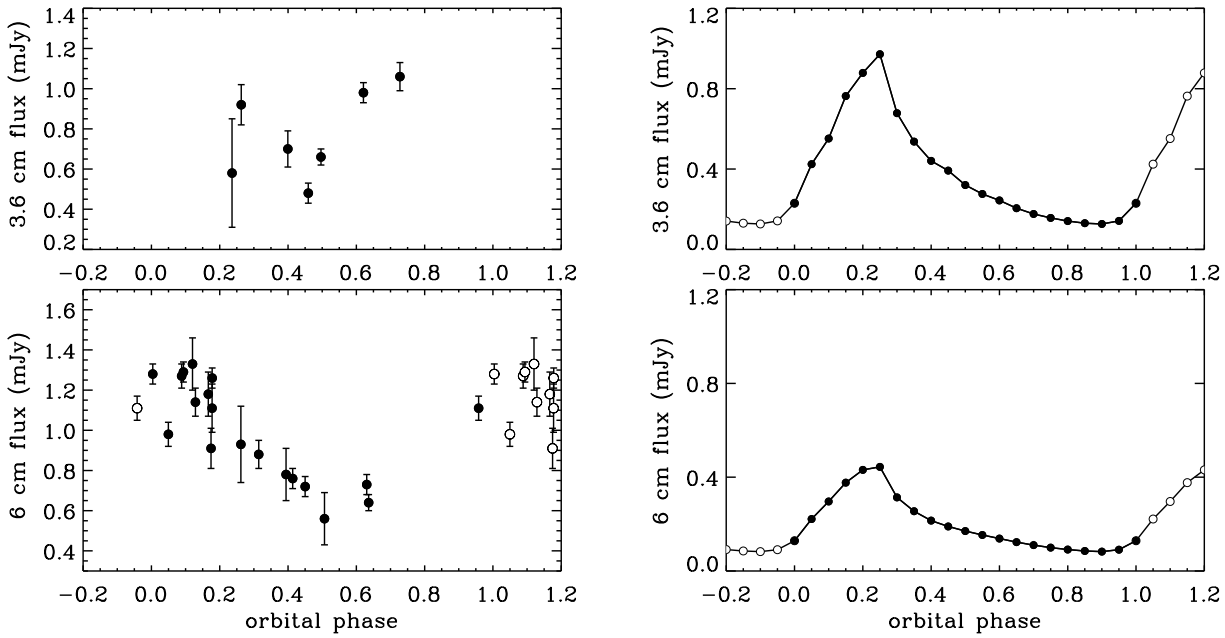

Figure 4: Observed (left panel) and calculated (right panel) radio fluxes for Cyg OB2 No. 8A. The phase range is extended by 0.2 on either side to provide a good overview of the variability. Open circles indicate duplication in this extended range. Phase 0.0 corresponds to periastron. From Blomme et al. (2010).

data. Problems remain with explaining the spectral index: the model values range between +0.75 and +1.5, while the observed value remains close to $\sim$ 0.0. Porosity is suggested as a possible solution for this problem.

Modelling these colliding-wind binaries can therefore tell us something about porosity in single-star winds. For this, we need detailed theoretical models, which is quite challenging work as the models need to explain not only the radio data, but also the X-ray and optical spectroscopy observations. A review of modelling colliding-wind binaries is given by Pittard (2011).

4 Future radio astronomy

A number of existing radio facilities are currently being upgraded. The VLA is being converted into the EVLA[3] (Dougherty & Perley 2011), resulting in an order of magnitude improvement in sensitivity and a very large wavelength coverage. The MERLIN instrument is also being upgraded to e-MERLIN[4]. One of the legacy programmes planned for e-MERLIN is a deep radio survey of the Cyg OB2 association (PI: R. Prinja; see Willis, Prinja & Fenech 2011). As Sect. 3 has made clear, Cyg OB2 has provided quite a number of colliding-wind binaries and these new data are expected to provide more examples, as well as many detections of thermal radio emission.

On the southern hemisphere, two interferometers are being constructed, one in South Africa (MeerKAT[5]) and one in Australia (ASKAP[6]). Both will start with a modest number of telescopes, but MeerKAT will later be extended to 80 antennas (in 2013-2016), and ASKAP to 36 antennas

[3] http://science.nrao.edu/evla/
[4] http://www.e-merlin.ac.uk/
[5] http://www.ska.ac.za/meerkat/
[6] http://www.atnf.csiro.au/projects/askap/index.html

(2013). Both instruments will allow much deeper radio observations of the southern sky than was hitherto possible.

On a longer time scale, the Square Kilometer Array (SKA[7]) will be built, providing a further order-of-magnitude improvement in sensitivity compared with the EVLA. SKA is expected to have 10 % of its capability in 2016-2019 with full capability by 2024. Much closer in time is the Atacama Large Millimeter Array (ALMA[8]), consisting of 66 antennas, covering the wavelength range 350 μm – 9 mm. Early science will start in 2011, with full operations in 2013.

5 Conclusions

The simple relation between thermal radio emission and mass-loss rate was thought to give us a reliable set of mass-loss rates for hot, massive stars. Unfortunately, the presence of clumping in the wind makes this impossible at the moment. The radio data are very useful however as a reference point to determine the amount of clumping in the inner wind. From this we learned that there is a clumping gradient in strong stellar winds, with the clumping decreasing as we move further away from the star. It is important to realize that, out of necessity, it is assumed there is no clumping in the radio formation region. It should be realized however that the radio region is probably clumped as well.

For the non-thermal radio emission, it is now clear that this is due to colliding-wind binaries, both for Wolf-Rayet and O stars. The variations in the observed radio light curve are due to a combination of intrinsically varying synchrotron emission (in an eccentric binary) and the varying free-free absorption along the sightline to the observer. The study of these colliding-wind systems is important for a number of reasons: we can learn more about the Fermi mechanism that accelerates the electrons, which is also relevant in other astrophysical contexts; colliding-wind binaries help in the binary frequency determination in clusters; and they can provide constraints on clumping and porosity in stellar winds. This last constraint depends on the development of good models for the observations. Such modelling work is quite challenging, as it has to explain not only the radio data, but also the X-ray and optical spectroscopy observations.

Finally, radio instrumentation is currently being upgraded and new facilities are planned for the near future. For the study of radio emission from hot, massive stars, this will provide a step forward that is at least as big as the introduction of the VLA was, some 30 years ago.

Acknowledgements

I would like to thank my colleagues who collaborated with me on this interesting subject of radio observation of massive stars, especially M. De Becker, R. K. Prinja, G. Rauw, M. C. Runacres, J. Vandekerckhove, S. Van Loo and D. Volpi.

References

Abbott, D. C., Bieging, J. H., Churchwell, E., & Cassinelli, J. P. 1980, ApJ, 238, 196
Abbott, D. C., Bieging, J. H., & Churchwell, E. 1981, ApJ, 250, 645
Abbott, D. C., Bieging, J. H., & Churchwell, E. 1984, ApJ, 280, 671
Abbott, D. C., Bieging, J. H., Churchwell, E., & Torres, A. V. 1986, ApJ, 303, 239
Bell, A. R. 1978, MNRAS, 182, 147

[7] http://www.skatelescope.org/
[8] http://www.almaobservatory.org/

Benaglia, P. 2010, ASP Conf. Proc., 422, 111
Benaglia, P., Cappa, C. E., & Koribalski, B. S. 2001, A&A, 372, 952
Benaglia, P., Vink, J. S., Maìz Apellàniz, J., et al. 2008, Rev. Mex. Astron. Astrofis. (Serie de Conferencias), 33, 65
Bieging, J. H., Abbott, D. C., & Churchwell, E. B. 1982, ApJ, 263, 207
Bieging, J. H., Abbott, D. C., & Churchwell, E. B. 1989, ApJ, 340, 518
Blomme, R., Prinja, R. K., Runacres, M. C., & Colley, S. 2002, A&A, 382, 921
Blomme, R., Van Loo, S., De Becker, M., et al. 2005, A&A, 436, 1033
Blomme, R., De Becker, M., Runacres, M. C., Van Loo, S., & Setia Gunawan, D. Y. A. 2007, A&A, 464, 701
Blomme, R., De Becker, M., Volpi, D., & Rauw, G. 2010, A&A, 519, A111
Cappa, C. E., Goss, W. M., & Pineault, S. 2002, AJ, 123, 3348
Cappa, C., Goss, W. M., & Van der Hucht, K. A. 2004, AJ, 127, 2885
Chapman, J. M., Leitherer, C., Koribalski, B., Bouter, R., & Storey, M. 1999, ApJ, 518, 890
Crowther, P. A. 2007, ARA&A, 45, 177
De Becker, M. 2007, A&AR, 14, 171
De Becker, M., Rauw, G., & Manfroid, J. 2004, A&A, 424, L39
De Becker, M., Rauw, G., Sana, H., et al. 2006, MNRAS, 371, 1280
Dougherty, S. M., & Williams, P. M. 2000, MNRAS, 319, 1005
Dougherty, S. M., Beasley, A. J., Claussen, M. J., Zauderer, B. A., & Bolingbroke, N. J. 2005, ApJ, 623, 447
Dougherty, S.M., & Perley, R. 2011, in Proceedings of the 39th Liège Astrophysical Colloquium, eds. G. Rauw, M. De Becker, Y. Nazé, J.-M. Vreux & P.M. Williams, BSRSL 80, 491
Dougherty, S.M., Trenton, V., & Beasley, A.J. 2011, in Proceedings of the 39th Liège Astrophysical Colloquium, eds. G. Rauw, M. De Becker, Y. Nazé, J.-M. Vreux & P.M. Williams, BSRSL 80, 658
Eichler, D., & Usov, V. 1993, ApJ, 402, 271
Elitzur, M. 1992, *Astronomical Masers*, Astrophysics and space science library Vol. 170, Kluwer, the Netherlands
Exter, K. M., Watson, S. K., Barlow, M. J., & Davis, R. J. 2002, MNRAS, 333, 715
Fahed, R., Moffat, A.F.J., Zorec, J., et al. 2011, in Proceedings of the 39th Liège Astrophysical Colloquium, eds. G. Rauw, M. De Becker, Y. Nazé, J.-M. Vreux & P.M. Williams, BSRSL 80, 668
Kennedy, M., Dougherty, S. M., Fink, A., & Williams, P. M. 2010, ApJ, 709, 632
Kennedy, M., Dougherty, S.M., Williams, P.M., & Fink, A. 2011, in Proceedings of the 39th Liège Astrophysical Colloquium, eds. G. Rauw, M. De Becker, Y. Nazé, J.-M. Vreux & P.M. Williams, BSRSL 80, 572
Lamers, H. J. G. L. M., & Leitherer, C. 1993, ApJ, 412, 771
Leitherer, C,, Forbes, D., Gilmore, A. C., et al. 1987, A&A, 185, 121
Leitherer, C., Chapman, J. M., & Koribalski, B. 1997, ApJ, 481, 898
Marchenko, S. V., Moffat, A. F. J., Vacca, W. D., Côté, S., & Doyon, R. 2002, ApJ, 565, L59
Montes, G., González, R.F., Cantó, J., Pérez-Torres, M.A., & Alberdi, A. 2011, in Proceedings of the 39th Liège Astrophysical Colloquium, eds. G. Rauw, M. De Becker, Y. Nazé, J.-M. Vreux & P.M. Williams, BSRSL 80, 704
Moran, J. P., Davis, R. J., Spencer, R. E., Bode, M. F., & Taylor, A. R. 1989, Nature, 340, 449
Morton, D. C., & Wright, A. E. 1978, MNRAS, 182, P47
Nazé, Y., De Becker, M., Rauw, G., & Barbieri, C. 2008, A&A, 483, 543
Nazé, Y., Damerdji, Y., Rauw, G., et al. 2010, ApJ, 719, 634
Nazé, Y., Damerdji, Y., Rauw, G., et al. 2011, in Proceedings of the 39th Liège Astrophysical Colloquium, eds. G. Rauw, M. De Becker, Y. Nazé, J.-M. Vreux & P.M. Williams, BSRSL 80, 709
Nugis, T., Crowther, P. A., & Willis, A. J. 1998, A&A, 333, 956
Olnon, F. M. 1975, A&A, 39, 217
Owocki, S. P., & Rybicki, G. B. 1984, ApJ, 284, 337
Owocki S.P., Gayley K.G., & Shaviv N.J. 2004, ApJ, 616, 525
Panagia, N., & Felli, M. 1975, A&A, 39, 1
Paredes, J. M. 2009, ASP Conf. Proc., 407, 289
Parkin E.R., Pittard J. M., Corcoran M. F., Hamaguchi K., Stevens I.R., Gosset E., Rauw G., & De Becker M., 2011, in Proceedings of the 39th Liège Astrophysical Colloquium, eds. G. Rauw, M. De Becker, Y. Nazé, J.-M. Vreux & P. Williams, BSRSL, 80, 610
Pittard, J.M. 2011, in Proceedings of the 39th Liège Astrophysical Colloquium, eds. G. Rauw, M. De Becker, Y. Nazé, J.-M. Vreux & P.M. Williams, BSRSL 80, 555
Pittard, J. M., Dougherty, S. M., Coker, R. F., O'Connor, E., & Bolingbroke, N. J. 2006, A&A, 446, 1001
Puls, J., Markova, N., Scuderi, S., et al. 2006, A&A, 454, 625
Puls, J., Vink, J. S., & Najarro, F. 2008, A&AR, 16, 209

Rohlfs, K. & Wilson, T. L. 2000, *Tools of radio astronomy*, 3rd ed., Astronomy and Astrophysics Library, Springer-Verlag, Berlin, Heidelberg, New York
Runacres, M. C., & Blomme, R. 1996, A&A, 309, 544
Runacres, M. C., & Owocki, S. P. 2005, A&A, 429, 323
Russell, C.M.P., Corcoran, M.F., Okazaki, A.T., Madura, T., & Owocki, S.P. 2011, in in Proceedings of the 39th Liège Astrophysical Colloquium, eds. G. Rauw, M. De Becker, Y. Nazé, J.-M. Vreux & P.M. Williams, BSRSL 80, 719
Seaquist, E. R., & Gregory, P. C. 1973, Nature, 245, 85
Smith, N., & Owocki, S. P. 2006, ApJ, 645, L45
Sugawara, Y., Maeda Y., Tsuboi Y., et al. 2011, in Proceedings of the 39th Liège Astrophysical Colloquium, eds. G. Rauw, M. De Becker, Y. Nazé, J.-M. Vreux & P.M. Williams, BSRSL 80, 724
Umana, G., Buemi, C. S., Trigilio, C., Leto, P., & Hora, J. L. 2010, ApJ, 718, 1036
Umana, G., Buemi, C.S., Trigilio, C., Leto, P., Hora, J.L., & Fazio, G. 2011, in Proceedings of the 39th Liège Astrophysical Colloquium, eds. G. Rauw, M. De Becker, Y. Nazé, J.-M. Vreux & P.M. Williams, BSRSL 80, 335
Van der Hucht, K. A., Williams, P. M., Spoelstra, T. A. Th., & De Bruyn, A. C. 1992, ASP Conf. Proc., 22, 249
van der Walt, D.J. 2011, in Proceedings of the 39th Liège Astrophysical Colloquium, eds. G. Rauw, M. De Becker, Y. Nazé, J.-M. Vreux & P.M. Williams, BSRSL 80, 260
Van Loo, S., Runacres, M. C., & Blomme, R. 2006, A&A, 452, 1011
Van Loo, S., Blomme, R., Dougherty, S. M., & Runacres, M. C. 2008, A&A, 483, 585
Vink, J. S., De Koter, A., & Lamers, H. J. G. L. M. 2000, A&A, 362, 295
Volpi, D. 2011, in Proceedings of the 39th Liège Astrophysical Colloquium, eds. G. Rauw, M. De Becker, Y. Nazé, J.-M. Vreux & P.M. Williams, BSRSL 80, 733
Wendker, H. J., Baars, J. W. M., & Altenhoff, W. J. 1973, Nature, 245, 118
Wendker, H. J., Smith, L. F., Israel, F. P., Habing, H. J., & Dickel, H. R. 1975, A&A, 42, 173
White, R. L., & Becker, R. H. 1983, ApJ, 272, L19
White, R. L., & Becker, R. H. 1995, ApJ, 451, 352
Williams, P.M. 2011, in Proceedings of the 39th Liège Astrophysical Colloquium, eds. G. Rauw, M. De Becker, Y. Nazé, J.-M. Vreux & P.M. Williams, BSRSL 80, 595
Williams, P. M., Dougherty, S. M.; Davis, R. J., et al. 1997, MNRAS, 289, 10
Willis, A., Prinja, R., & Fenech, D. 2011, in Proceedings of the 39th Liège Astrophysical Colloquium, eds. G. Rauw, M. De Becker, Y. Nazé, J.-M. Vreux & P.M. Williams, BSRSL 80, 524
Wright, A. E., & Barlow, M. J. 1975, MNRAS, 170, 41

Discussion

J. Sundqvist: Just a comment regarding clumping and thermal radio emission. All analyses so far (to my knowledge) that have considered clumping have used the so-called micro-clumping approach, which assumes optically thin clumps. It may be worth testing if also the radio emission indicates optically thick clumps, for example by using a porosity formalism.

W.-R. Hamann: You mentioned theoretical predictions of clumping in the radio-region of stellar winds. To which models do you refer? To my knowledge, the time-dependent hydrodynamic models with line driving do not extend to such large distances from the star.
R. Blomme: The Runacres and Owocki models (2005, A&A 429, 323) use a moving box that moves out with the wind. The equations solved inside the box are the gas dynamic equations. They do not include the line radiative driving anymore, as they showed this to have negligible effects at larger distances.

J. Pittard: Two comments. First, you mentioned the effect of clumping on the thermal radio emission. But of course, binarity can affect the thermal radio emission in interesting ways too. For instance, depending on the stellar separation and the relative mass-loss rates, the thermal flux from a binary system may be substantially greater than the expected single star value, or it could be significantly

less (see e.g. Stevens 1995 and Pittard 2010).
Second, you showed evidence for a lack of non-thermal emission from short period binaries, and attributed this to the significant circumstellar absorption in such systems. However, hot gas created in a wind-wind collision has a very low opacity. Now it is true that the wind interaction region in such systems will show strong curvature due to the orbital motion, which will limit to some extent the length of sight lines with low opacity, but I think one needs to investigate these competing effects, because if the NT emission can escape its lack would instead tell us something about particle acceleration and cooling in such systems.
R. Blomme: It shows the complexity of the modelling that is needed. On your first point, Montes et al. (2011) show how the spectral index in WR binaries is influenced by the thermal emission of the colliding-wind region.

S. Owocki: First regarding whether clumps can survive to the radio region at hundreds of stellar radii, I think a key issue regards the energy balance. If the clumps cool adiabatically, then I think the lack of thermal expansion will allow them to survive to quite large distances. On the other hand, if they are kept warm, e.g. by irradiation, then the thermal expansion will gradually smooth them out.
Regarding whether they can be optically thick, a key point is for a clump near the usual radio photosphere to become optically thick requires it to collect material from a scale comparable to the photospheric radius, i.e. $\sim 100\ R_*$ for radio. I think this is unlikely, as some radio clumps are probably not 'porous'.
R. Blomme: Assuming porosity in the radio formation region would also introduce other parameters, on which we have no observational constraints.

Massive Stars in Polarized Light

Jennifer L. Hoffman[1]

[1] University of Denver, Denver, CO, USA

Abstract: Polarimetry is an important observational technique in the study of hot stars. Practiced across the full range of wavelengths, polarimetry provides a window into a variety of stellar phenomena not accessible by other means. For example, polarimetry constrains the properties of circumstellar disks, unveils details of the magnetic fields in hot stars and their winds, and reveals the complex geometries of binary systems and YSOs.

I focus here on the applications of spectropolarimetry to the study of the atmospheres, winds, and circumstellar material of massive stars and their supernova descendents. When polarized light is produced by electron and dust scattering, spectropolarimetry allows mapping of clumpy and aspherical structures in the atmospheres, winds, and circumstellar surroundings of hot stars and core-collapse supernovae. When polarization arises from magnetic phenomena such as the Zeeman effect, spectropolarimetry probes the complex circumstellar magnetic fields threading the disks and winds of massive stars. I discuss recent results in both these areas and look to the near future, when the combination of polarimetry with interferometric and synoptic observations will open new frontiers in our understanding of massive stellar evolution.

1 Introduction

Astrophysical polarization is most often produced when light scatters in a gaseous or dusty environment. In the case of hot stars, which ionize their surroundings, electron scattering is a particularly important polarizing mechanism. The amount and orientation of polarization encodes information about the geometry and composition of the scattering region. Thus, polarimetric studies can reveal morphological details of stellar atmospheres, winds, and circumstellar material even for faraway, unresolved sources. Although spectral lines are often assumed to be depolarizing, they can acquire their own polarization via mechanisms such as resonance scattering and the Zeeman effect. Polarized lines often trace distinctive paths when plotted in the Stokes Q-U plane (e.g., Vink et al. 2002; Vink, Harries & Drew 2005; Magalhães et al. 2006). Analyzing these effects can lead to more detailed understanding of polarized objects by probing line formation and scattering regions.

Interstellar dust also produces polarization (ISP) via scattering, so stellar polarimetric measurements must be carefully corrected for this effect. An ISP contribution can change not only the amount but also the sense of polarization; for example, it can make polarized emission lines appear to be absorption lines in a polarized spectrum. A variety of methods exist to measure or estimate the ISP contribution to an observed polarization spectrum (e.g., Quirrenbach et al. 1997; Tran et al. 1997). However, the variation of ISP with wavelength is slow, smooth, and constant in time (Serkowski, Mathewson & Ford 1975; Whittet et al. 1992), so any line polarization effects or changes in polarization over time can be safely attributed to the target and not to the ISP.

In the past few years, polarimetric techniques have improved substantially, providing better resolution, better time coverage, longer-term monitoring, larger sample sizes, and more robust interpretation

via detailed modeling than was previously possible. In the rest of this contribution, I highlight some recent polarimetric results in the areas of young massive stars, Oe/Be stars, evolved massive stars, and supernovae and GRBs. The selection is necessarily limited and is meant to be representative, not comprehensive. Finally, I discuss the prospects for future developments in polarimetric techniques and combination of these techniques with others.

2 Young Massive Stars

Imaging polarimetry in the infrared and near-IR allows us to trace the circumstellar structures of massive young stellar objects (YSOs). The disk/outflow morphology seen in low-mass YSOs is relatively common in their high-mass counterparts (e.g., Jiang et al. 2008). However, at least some massive YSOs instead display evidence of episodic mass ejection and asymmetrical outflow structures, perhaps due to binarity (e.g., Simpson et al. 2009).

Imaging polarimetry can also reveal detailed structure within YSO accretion disks; for example, Wisniewski et al. (2008) found indications of self-shadowing and small enhancements in scale height in the disk of HD 163296. However, such data must be carefully interpreted. In the case of AB Aur, polarimetric images in the infrared initially suggested the existence of a gap in the circumstellar disk (Oppenheimer et al. 2008); however, higher-contrast images and detailed radiative transfer modeling subsequently revealed the "gap" to be a region of low polarization intensity likely caused by backscattered light (Perrin et al. 2009).

Line polarization measurements can measure the strength and and probe the detailed morphologies of magnetic fields in young massive stars. Zeeman signatures revealed that the magnetic field in τ Sco is not a simple dipole, but contains a warped torus that may help explain the unusual UV and X-ray properties of the star (Donati et al. 2006). Studies of the Stokes *V* line profiles in V380 Ori led to estimates of the strength and obliquity of the dipolar magnetic field in this binary system as well as the inclination of the system and the rotation period of the primary star (Alecian et al. 2009).

3 Oe/Be Stars

Polarimetry is especially powerful in combination with other observational and theoretical methods. One of the best recent examples of such combined techniques occurred in the case of the well-studied Be star ζ Tau. A pair of papers by Štefl et al. (2009) and Carciofi et al. (2009) combined quantitative radiative transfer modeling with long time-baseline photometric, spectroscopic, interferometric, and spectropolarimetric data to confirm the presence of a one-armed spiral density wave within the circumstellar disk of this object and to fix its inclination angle for the first time.

Other Oe/Be stars display long-term variations and can best be studied polarimetrically via monitoring on long timescales. Such spectropolarimetric monitoring illuminated the details of the transition between disk and non-disk phases in π Aqr and 60 Cyg (Wisniewski et al. 2010). These authors found that disk loss in these two objects occurs on a viscous timescale and proceeds in an "inside-out" fashion over several to many orbits of the companion. In addition, they detected both small and large outbursts causing disruption of disk symmetry, possibly in the form of disk warps or non-equatorial rings.

Line polarization in Oe/Be stars probes their envelope/wind structure. For example, theoretical modeling of Stokes *V* line shapes in hot star winds showed that a characteristic "heartbeat" profile can indicate the presence and strength of the winds' magnetic fields (Ignace & Gayley 2003; Gayley & Ignace 2010).

4 Evolved Massive Stars

Like Oe/Be stars, evolved massive stars possess complex circumstellar environments, due in large part to their strong winds and episodic mass loss. Evolved stars with companions may experience Roche lobe overflow, mass transfer, and wind collisions. Polarimetry has been an invaluable tool in disentangling the compound spectral signatures of such objects and enabling us to glimpse their detailed structures. For example, spectropolarimetry of the WR+O binary WR137 constrained the location of dust formation in the system (Harries, Babler & Fox 2000). In the case of another evolved binary, β Lyr, continuum and line polarization analysis revealed the location of the disk "hot spot" (Lomax & Hoffman 2011); similar analysis can be applied to other eclipsing systems (Hoffman et al. 2003).

Polarimetry of evolved massive stars can also probe the details of their evolution (Patel et al. 2008). A spectropolarimetric survey of nearby LBVs (Davies, Oudmaijer & Vink 2005) showed that their winds are aspherical and strongly clumped; depolarization across the Hα line is a signature of asphericity and correlates with strong Hα emission and wind variability.

5 Supernovae and Gamma-Ray Bursts

Complex polarimetric and spectropolarimetric behavior has been observed in more and more supernovae (SNe) in recent years, suggesting that the majority of core-collapse SNe are fundamentally aspherical (Chornock et al. 2010). In addition, SN ejecta can evolve over time from spherical to aspherical morphologies (Leonard et al. 2006) or vice versa (Wang & Wheeler 2008). Many SNe show polarimetric evidence for multiple misaligned axes (e.g., Kawabata et al. 2002; Hoffman et al. 2008) or axial rotation over time (e.g., Maund et al. 2007a, b). This behavior may hold clues to the nature of the pre-explosion mass loss of core-collapse progenitors. Emerging sophisticated line polarization models will help interpret high-resolution spectropolarimetric observations of SNe (e.g., Kasen et al. 2003; Hoffman 2007; Hole, Kasen, & Nordsieck 2010).

Polarimetry of gamma-ray bursts (GRBs) is a developing area of research that promises to reveal important information about the magnetic field structure of the expanding fireballs in these massive explosions (Mundell, Guidorzi & Steele 2010 and references therein). Detection of polarization at the 10% level in GRB 0901012 indicated that the relativistic outflow was threaded by large-scale ordered magnetic fields (Steele et al. 2009). Polarization measurements also probe the nature of GRB progenitor stars; Vink (2007) used line polarization measurements of Wolf-Rayet (WR) stars in the LMC and the Milky Way to investigate their rotational properties. However, he found no difference between the two populations, raising further questions about the identity of GRB progenitors.

6 Future Prospects

In the near future, advances in the study of massive stars using polarimetry will come from improvements in spectral resolution, expansion of the time domain, more sophisticated computational modeling, and a combination of polarimetric with interferometric and other techniques. A more comprehensive overview of upcoming advancements in stellar polarimetry was presented in the Astro2010 white paper *O/IR Polarimetry for the 2010 Decade (SSE)* (Hoffman et al. 2009).

Recent advances in very high-resolution spectropolarimetry promise to refine or even overturn our picture of the physical processes that drive and characterize massive stars. For example, data taken with the HiVIS and ESPaDOnS spectropolarimeters at R = 13,000 and 68,000 showed that Hα line polarization in many Be and Herbig Ae/Be stars is associated not with the emission peak but instead

with the absorptive components of the line, an effect that is not seen in lower-resolution data and is difficult to explain with current scattering theories (Harrington & Kuhn 2009). The MiMeS Project, a CFHT Large Programme using ESPaDOnS, discovered a new magnetic O star whose peculiar emission lines may arise from confined circumstellar material rather than a wind (HD57682; Grunhut et al. 2009). Both results hint at the wealth of new discoveries that such high-resolution spectropolarimetry can enable.

The combination of polarimetric capabilities with the high spatial resolution of interferometric observations promises to shed new light on the complex structures produced at many stages in the lives of massive stars, as well as to calibrate polarimetric signatures that can be observed in extragalactic sources where interferometry is impossible. First steps in this direction have been taken using VEGA/CHARA (Mourard et al. 2009).

New polarimetric instruments are being planned or considered for a variety of upcoming observational facilities. For example, the Robert Stobie Spectrograph (RSS) on the queue-scheduled Southern African Large Telescope will open new vistas in polarimetric studies of variable and transient objects with high time-resolution spectropolarimetric capabilities in the visible and NIR (Brink et al. 2010; Sheinis et al. 2010). RINGO2 (Steele et al. 2010) and GAP (Yonetoku et al. 2010) will expand our ability to detect and track GRB polarization. Meanwhile, advances in computing power will continue to drive new computational models that can predict the polarimetric and spectropolarimetric signatures that will be observed by the next generation of instruments (Hoffman 2007; Hole et al. 2010).

An upcoming topical conference in June 2011 (*Stellar Polarimetry: From Birth to Death*, Madison, WI, http://arwen.etsu.edu/starpol/) will highlight recent results in this field, encourage the formation of new collaborations, and provide opportunities for the community to prepare for new developments in stellar polarimetry. Researchers with interests in all aspects of massive stars are cordially invited to attend.

References

Alecian, E., Wade, G.A., Catala, C., et al. 2009, MNRAS 400, 354

Brink, J.D., Buckley, D.A.H., Nordsieck, K.H., & Potter, S.B. 2010, in *Ground-based and Airborne Instrumentation for Astronomy III*, eds. McLean I.S., Ramsay, S.K., Takami, H., Proc SPIE 7735, 773517

Carciofi, A.C., Okazaki, A.T., le Bouquin, J.-B., Štefl, S., Rivinius, T., Baade, D., Bjorkman, J.E., & Hummel, C.A. 2009, A&A 504, 915

Chornock, R., Filippenko, A.V., Li, W., & Silverman, J.M. 2010, ApJ, 713, 1363

Davies, B., Oudmaijer, R.D., & Vink, J.S. 2005, A&A 439, 1107

Donati, J.-F., Howard, I.D., Jardine, M.M., et al. 2006, MNRAS 370, 629

Gayley, K.G., & Ignace, R. 2010, ApJ 708, 615

Grunhut, J.H., Wade, G.A., Marcolino, W.L.F., et al. 2009, MNRAS 400, L94

Harries, T.J. 2000, MNRAS 315, 722

Harries, T.J., Babler, B.L., & Fox, G.K. 2000, A&A 361, 273

Harrington, D.M., & Kuhn, J.R. 2009, ApJSS, 180, 138

Hoffman, J.L. 2007, in *Circumstellar Media and Late Stages of Massive Stellar Evolution*, eds. García-Segura G., Ramirez-Ruiz, E., RMxAC 30, 57

Hoffman, J.L., Hines, D.C., Adamson, A., et al. 2009, *The Astronomy and Astrophysics Decadal Survey*, Science White Paper 128, arXiv:0902.4222

Hoffman, J.L., Leonard, D.C., Chornock, R., Filippenko, A.V., Barth, A.J., & Matheson, T. 2008, ApJ 688, 1186

Hoffman, J.L., Whitney, B.A., & Nordsieck, K.H. 2003, ApJ 598, 572

Hole, K.T., Kasen, D., & Nordsieck, K.H. 2010, ApJ 720, 1500

Ignace, R., & Gayley, K.G., 2003, MNRAS 341, 179

Jiang, Z., Tamura, M., Hoare, M.G., Yao, Y., Ishii, M., Fang, M., & Yang, J. 2008, ApJ 673, L175

Kasen, D., Nugent, P., Wang, L., et al. 2003, ApJ 593, 788

Kawabata, K.S., Jeffery, D.J., Iye, M., et al. 2002, ApJ 580, L39
Leonard, D.C., Filippenko, A.V., Ganeshalingam, M., et al. 2006, Nature 440, 505
Lomax, J.R., & Hoffman, J.L. 2011, in Proceedings of the 39th Liège Astrophysical Colloquium, eds. G. Rauw, M. De Becker, Y. Nazé, J.-M. Vreux & P.M. Williams, BSRSL 80, 689
Magalhães, A.M., Melgarejo, R., Pereyra, A., Carciofi, A.C. 2006, in *Stars with the B[e] Phenomenon*, eds. Kraus M., Miroshnichenko A.S., ASP Conference Series 355, 147
Maund, J.R., Wheeler, J.C., Patat, F., Wang, L., Baade, D., & Höflich, P.A. 2007a, ApJ 671, 1944
Maund, J.R., Wheeler, J.C., Patat, F., Baade, D., Wang, L., & Höflich, P.A. 2007b, MNRAS 381, 201
Mourard, D., Clausse, J.M., Marcotto, A., et al. 2009, A&A 508, 1073
Mundell, C.G., Guidorzi, C., & Steele, I.A. 2010, Advances in Astronomy 2010, article ID 718468
Oppenheimer, B., Brenner, D., Hinkley, S., et al. 2008, ApJ 679, 1574
Patel, M., Oudmaijer, R.D., Vink, J.S., Bjorkman, J.E., Davies, B., Groenewegen, M.A.T., Miroshnichenko, A.S., & Mottram, J.C. 2008, MNRAS 385, 967
Perrin, M.D., Schneider, G., Duchene, G., Pinte, C., Grady, C.A., Wisniewski, J.P., & Hines, D.C. 2009, ApJ 707, L132
Quirrenbach, A., Bjorkman, K.S., Bjorkman, J.E., et al. 1997, ApJ 479, 477
Serkowski, K., Mathewson, D.L., & Ford, V.L. 1975, ApJ 196, 261
Sheinis, A.I., Wolf, M.J., Bershady, M.A., Nordsieck, K.H., Doering, R.L., & Williams, T.B. 2010, in *Ground-based and Airborne Instrumentation for Astronomy III*, eds. McLean I.S., Ramsay, S.K., Takami, H., Proc SPIE 7735, 77354U
Simpson, J.P., Burton, M.G., Colgan, S.W.J., Cotera, A.S., Erickson, E.F., Hines, D.C., & Whitney, B.A. 2009, ApJ 700, 1488
Steele, I.A., Bates, S.D., Guidorzi, C., Mottram, C.J., Mundell, C.G., & Smith, R.J. 2010, in *Ground-based and Airborne Instrumentation for Astronomy III*, eds. McLean I.S., Ramsay, S.K., Takami, H., Proc SPIE 7735, 773549
Steele, I.A., Mundell, C.G., Smith, R.J., Kobayashi, S., & Guidorzi, C. 2009, Nature 462, 767
Štefl, S., Rivinius, T., Carciofi, A.C., et al. 2009, A&A 504, 929
Tran, H.D., Filippenko, A.V., Schmidt, G.D., Bjorkman, K.S., Jannuzi, B.T., & Smith, P.S. 1997, PASP 109, 489
Vink, J.S. 2007, A&A 469, 707
Vink, J.S., Drew, J.E., Harries, T.J., & Oudmaijer, R.D. 2002, MNRAS 337, 356
Vink, J.S., Harries, T.J., & Drew, J.E. 2005, A&A 430, 213
Wang, L., & Wheeler, J.C. 2008, ARA&A 46, 433
Whittet, D.C.B., Martin, P.G., Hough, J.H., Rouse, M.F., Bailey, J.A., & Axon, D.J. 1992, ApJ 386, 562
Wisniewski, J.P., Clampin, M., Grady, C.A., Ardila, D.R., Ford, H.C., Golimowski, D.A., Illingworth, G.D., & Krist, J.E. 2008, ApJ 682, 548
Wisniewski, J.P., Draper, Z.H., Bjorkman, K.S., Meade, M.R., Bjorkman, J.E., & Kowalski, A.F. 2010, ApJ 709, 1306
Yonetoku, D., Murakami, T., Gunji, S., et al. 2010, arXiv:1010.5305

Discussion

S. Owocki: Have you looked for linear polarization in any of the magnetic Bp stars, e.g. σ Ori E or some of the similar examples recently discovered by MiMeS. They are inferred to have rotating magnetospheres and so should show rotationally modulated linear polarization.
J. Hoffman: σ Ori E was studied polarimetrically by Kemp and Heman in the 1970's, and they did find linear polarization modulations. I don't know of any more recent polarimetry, so this would certainly be a good target for the revived HPOL. Linear polarimetry of HD108 obtained by Fox & Hines (1998) shows only random variations, not correlated with the rotation period. MiMeS will undoubtedly yield many more interesting targets for linear spectropolarimetry.

Macroturbulent broadening in Massive Stars and its possible connection to Stellar Oscillations

S. Simón-Díaz[1,2]

[1] Instituto de Astrofísica de Canarias, E-38200 La Laguna, Tenerife, Spain.

[2] Departamento de Astrofísica, Universidad de La Laguna, E-38205 La Laguna, Tenerife, Spain

Abstract: In this contribution, I review what we have learnt about macroturbulent broadening in the last decade and present first results of a long term observational project aimed at investigating the possible connection between this spectroscopic feature and the stellar variability phenomena and oscillations.

1 Introduction

1.1 Macroturbulent and rotational broadenings in OB stars

Macroturbulent[1] broadening is the name commonly assigned to a type of non-rotational broadening observed in the line profiles of B Supergiants (Sgs). It was first invoked to explain the lack of narrow line spectra in the first large spectroscopic databases of these objects (Slettebak 1956, Conti & Ebbets 1977). This was a puzzling result since the rotational velocity of a star is expected to decrease when it evolves from an O Main Sequence star to a B Sg due to the increase in stellar radius and mass loss rate. In addition, in a large enough sample, some of the B Sgs should have low $v \sin i$ values (from the statistical distribution of the inclination angle, i). From those observations it was concluded that an extra broadening (probably associated to macroturbulent motions in the outer layers of the star) was affecting the spectra of B Sgs.

The presence of this extra broadening, differing in shape from rotational broadening, can be perfectly identified in high resolution spectra (see Fig. 1). The figure presents the Si III 4552 line in the spectra of three stars: the left panel shows a narrow lined early B-type star in which the effect of the rotational broadening is very small, either because the star rotates slowly, or because the star is seen (almost) pole-on; the other panels show two stars selected to illustrate a case in which the rotational broadening dominates (middle panel) and a case in which a non negligible contribution of the *macroturbulent* broadening is present (right panel). It is important to remark that (i) the shape of the line profile of the stars at the far right in Fig. 1 is a consequence of the effect of both broadening contributions, and (ii) *macroturbulent* broadening must not be confused with microturbulent broadening (which is present in the three line profiles).

[1] From now on this word will be written in italics, to emphasize that macroturbulent broadening is unlikely related to large scale turbulence as explained in the text.

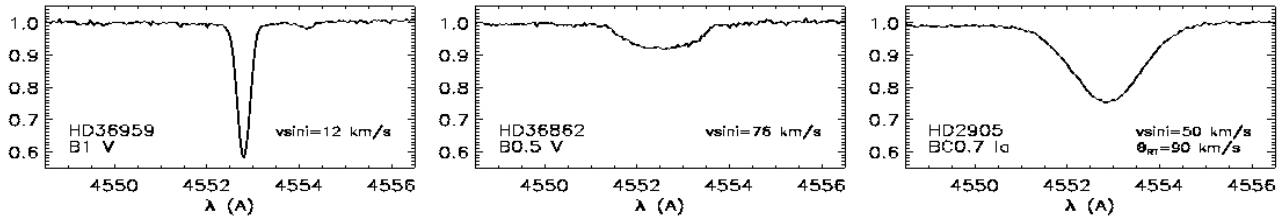

Figure 1: Three illustrative examples of Si III line profiles affected by different broadening mechanisms. The spectra are taken from the IACOB spectroscopic database.

1.2 Characterization of the macroturbulent broadening

The advent of high resolution spectroscopic observations of B Sgs enabled the development of methods to disentangle and measure relative contributions of rotation and extra broadening mechanisms. Two main techniques have been proposed. Ryans et al. (2002) applied a goodness-of-fit method to a sample of high quality spectra of B Sgs, and obtained acceptable results for a model in which the *macroturbulent* broadening dominates and rotation is negligible. However, the reliability of this method is limited by two facts: first, there is degeneration of line profiles for different pairs ($v \sin i$, $v_{\rm mac}$); and second, results depend on the type of profile considered for the *macroturbulent* broadening (e.g. Gaussian, radial-tangential; see Simón-Díaz et al. 2010). Simón-Díaz & Herrero (2007), following Gray (1976), investigated the applicability of the Fourier transform (FT) method in the case of OB-type stars. The strength of this method is that it can separate the rotational broadening from any other broadening mechanism using the FT of a line profile[2]. This method probed to be very powerful and has been increasingly used for the determination of projected rotational velocities in O and B stars ever since.

But the determination of $v \sin i$ is only half of the way; the size of the extra broadening still needs to be determined. The easiest way is to consider metal lines, not affected by other important broadenings (basically Stark broadening) as are the He I and He II lines. There are again two methods to do so (based on the goodness-of-fit method or on the fitting of the first lobe of the FT), but in both cases one has to decide the type of profile defining the extra broadening. Two cases have been investigated (see e.g. Dufton et al. 2006, Aerts et al. 2009, and Simón-Díaz et al. 2010): an isotropic Gaussian profile, and a radial-tangential Gaussian profile. Indirect arguments obtained by the comparison of the $v \sin i$ derived by means of the FT method and the goodness-of-fit method using both types of profiles allowed Simón-Díaz et al. (2010) to prefer the latter.

One can also use He I and He II lines, but in this case, appropriate stellar atmosphere code predictions for these lines need to be used to account for the Stark broadening. The determination of the stellar parameters and the extra broadening must be performed at the same time.

1.3 *Macroturbulent* broadening in B Sgs

In the past decade several studies using both the FT and goodness-of-fit methods have derived *macroturbulent* broadening from the Si III 4552 line profile in B Sgs (see Dufton et al. 2006, Lefever et al. 2007; Markova & Puls 2008, Fraser et al. 2010). These studies have taught us that (i) the size of this extra broadening increases from late- to early-B Sgs (see Fig. 1 in Simón-Díaz et al. 2010), and

[2]Two important remarks to keep in mind: (i) this argument is only valid under the hypothesis considered by the convolution method, which assumes that the effects of the different broadening mechanisms act independently to broaden the emergent flux profile; (ii) the $v \sin i$ provided by the FT method may differ from its actual value in the case of highly asymmetric profiles.

(ii) if interpreted as turbulent motions, *macroturbulent* broadening would represent highly supersonic velocities in most of the cases.

Since the extra broadening is present in photospheric lines and affects the whole profile, even wavelengths close to the continuum (i.e. whatever is producing this broadening has to be deeply rooted in the stellar photosphere, and possibly deeper, in layers where we do not expect any significant velocity field in these stars), the interpretation of this extra broadening as the effect of turbulent motion is quite improbable.

1.4 What is the physical origin of macroturbulent broadening in massive stars?

One physical mechanism suggested as the origin of this extra broadening relates to oscillations. Many OB Sgs show photometric and spectroscopic variability. Lucy (1976) postulated that this variability might be a pulsation phenomenon, and macroturbulence may be identified with the surface motions generated by the superposition of numerous non-radial oscillations. More recently, Aerts et al. (2009) computed time series of line profiles for an evolved massive star broadened by rotation and thousands of low amplitude non-radial gravity mode oscillations and showed that the resulting profiles could mimic the observed ones.

Stellar oscillations are hence a plausible explanation for the extra broadening in B Sgs, but this hypothesis needs to be confirmed observationally.

2 The project, observational data set and first results

2.1 Aim of the project

In 2008, we began a long term observational project aimed at investigating the macroturbulent broadening in O and B stars and its possible connection to spectroscopic variability phenomena and stellar oscillations. The project is a joint international collaboration between researchers in Spain (IAC: S. Simón-Díaz (PI), A. Herrero, N. Castro), France (CEA-Saclay: K. Uytterhoeven), Germany (USM: J. Puls), Belgium (KULeuven: C. Aerts) and Bulgaria (IA-NOA, N. Markova).

2.2 Observational data set

Our initial observational dataset is based on spectra obtained with FIES@NOT (see *The IACOB spectroscopic database of Northern Galactic OB stars*, Simón-Díaz et al. 2011). The IACOB database includes high resolution, high signal-to-noise ratio spectroscopic observations in the optical range of $\sim$100 O and B stars in our Galaxy, along with short time-series observations (two 4 nights campaigns in 2008 and 2009) for a selected sample of candidates.

The IACOB observations will continue in the next semesters. In addition, we have been awarded several additional nights to obtain new time series of spectra with the 1.2 m MERCATOR telescope at Roque de los Muchachos observatory (Spain) and the 2 m BG NAO telescope (Bulgaria).

2.3 First results

2.3.1 Macroturbulent broadening: also present in the O star domain

The investigation of *macroturbulent* broadening in massive stars has been constrained to B Sgs so far. The main reason is that there are many isolated, strong metal lines in the optical spectrum of this type of stars. The usual lines considered for this study are Si III 4552, Si II 4130, and/or C II 4267. In the

case of O stars, there are not many isolated, strong metal lines available, and the determination of *macroturbulence* broadening by means of He I and He II lines is not so straightforward.

A careful examination of the IACOB spectroscopic database has allowed us to identify one metal line appropiate for the determination of $v \sin i$ and the size of the extra broadening in the case O stars: the O III 5592 line. From the analysis of this line we have been able to confirm for the first time in a systematic way that the extra broadening is not only present in B Sgs, but also in O-type stars[3] of all luminosity classes (see Simón-Díaz et al. 2011). Interestingly, the increasing trend of the size of the extra broadening with spectral type previously found for B Supergiants continues in the O star domain. In addition, there is a clear separation between dwarfs, giants and supergiants.

2.3.2 Observational evidence for a correlation between macroturbulent broadening and line-profile variations in early B Sgs

In Simón-Díaz et al. (2010), we analysed the spectroscopic time series of the selected bright candidates obtained with FIES@NOT (13 early-B Sgs, complemented with 2 early-B dwarfs and 2 late-B Sgs). In agreement with earlier studies of spectroscopic variability in O and B Sgs (e.g. Howarth et al. 1993; Fullerton, Gies & Bolton, 1996; Prinja et al., 2004; Morel et al. 2004; Kaufer et al. 2006; Markova et al. 2008), we found clear signatures of line-profile variations (LPVs). To quantify these LPVs, we used the first and third moments of the line profiles ($\langle v \rangle$ and $\langle v^3 \rangle$, see Aerts, Christensen-Dalsgaard & Kurtz, 2010, for definitions).

We applied a combined FT + goodness-of-fit method to the Si III 4567 or O III 5592 lines in the time-series spectra, assuming a radial-tangential Gaussian definition to characterize the *macroturbulent* broadening, to obtain $v \sin i$ and the size of the extra broadening ($\Theta_{\rm RT}$). We then investigated the possible connection between *macroturbulent* broadening and the detected LPVs, finding a clear positive correlation between the average size of the macroturbulent broadening, $\langle \Theta_{\rm RT} \rangle$, and the peak-to-peak amplitude of $\langle v \rangle$ and $\langle v^3 \rangle$ variations. To our knowledge, this was the *first clear observational evidence for a connection between extra broadening and LPVs in early B and late O Sgs.* Interestingly, a similar trend can be obtained from the simulations by Aerts et al. (2009).

2.4 A *macroturbulent* broadening – stellar oscillations connection?

Non-radial oscilations have often been suggested as the origin of LPVs in photospheric lines in OB Sgs, as well as the driver of large scale wind structures; however, a firm confirmation (by means of a rigorous seismic analysis) has not been achieved yet. From a theoretical point of view g-mode oscilations can occur (e.g. Saio et al, 2006, Lefever et al. 2007). The latter results, along with our observational confirmation of a tight connection between macroturbulence and LPVs render stellar oscillations the most probable physical origin of macroturbulent broadening in B Sgs; however, it is too premature to consider them as the only physical phenomenon explaining the unknown broadening.

2.5 The future of the project

First results from our project are encouraging; however, there are still some things to be done before firmly concluding that *macroturbulent* broadening in massive stars should be actually called **pulsational broadening**. One of the tasks we plan to accomplish in the near future is the quantitative spectroscopic analysis of the stars included in the IACOB database to locate them in the ($\log T_{\rm eff}$, $\log g$) diagram. By overplotting the instability strips in this diagram, we want to investigate whether

[3]Similar results have been obtained from the analysis of a small sample of low luminosity O-type stars using model fitting (N. Markova, priv. comm.).

there is a correlation between candidates in which stellar oscillations are expected and the appearance of the *macroturbulent* broadening. We also plan to extend the type of study performed for early B Sgs to other candidates in the O star domain. Finally, with the time series of spectra we are gathering for selected candidates, we aim at investigating the temporal behaviour of the LPVs. From the preliminary analysis of the time-series spectra already obtained (see Simón-Díaz et al. 2009) we have found that the RV variations in the B Sgs suggest variabilities on two time-scales: variations of the order of half a day to several days, with amplitudes of the order of 1-9 $\mathrm{km\,s^{-1}}$, and a faster variation of tens of minutes at low amplitude ($< 2\ \mathrm{km\,s^{-1}}$). However, this analysis is limited by the severe aliasing resulting from the short time span of the time series. Therefore, to step forward in our project towards a pulsational analysis of selected targets, it is necessary to increase as much as possible the time span of our temporal series. This is needed to resolve the frequencies properly in order to interpret them in terms of stellar oscillations.

The confirmation of the macroturbulent-pulsation connection will open a bright future in the realm of massive stars, not only in terms of traditional, time-independent, spectroscopic analysis, but also from a seismic point of view. Both studies will provide independent observational constraints to models of stellar structure and evolution of massive evolved stars.

Acknowledgements

I'm really grateful for the help, support, and useful comments of the people in the collaboration.

References

Aerts, C., Christensen-Dalsgaard, J. & Kurtz, D. W. 2010, *Asteroseismology* (Berlin: Springer)
Aerts, C., Puls, J., Godart, M. & Dupret, M.-A. 2009, A&A, 508, 409
Conti, P. S. & Ebbets, D. 1977, ApJ, 213, 438
Dufton, P. L., Ryans, R. S. I., Simón-Díaz, S., Trundle, C. & Lennon, D. J. 2006, A&A, 451, 603
Fraser, M., Dufton, P. L., Hunter, I. & Ryans, R. S. I. 2010, MNRAS, 404, 1306
Fullerton, A. W., Gies, D. R. & Bolton, C. T. 1996, ApJS, 103, 475
Gray, D. F. 1976, *The Observations and Analysis of Stellar Photospheres*, 1st ed. (New York: Wiley)
Howarth, I. D., Bolton, C. T., Crowe, R. A., Ebbets, D. C., Fieldus, M. S., Fullerton, A. W., Gies, D. R., McDavid, D., et al. 1993, ApJ, 417, 338
Kaufer, A., Stahl, O. Prinja, R. K. & Witherick D. 2006, A&A, 447, 325
Lefever, K., Puls, J., & Aerts, C. 2007, A&A, 463, 1093
Lucy, L. B. 1976, ApJ, 206, 499
Markova, N., Prinja, R. K., Markov, H., Kolka, I., Morrison, N., Percy, J., & Adelman, S. 2008, A&A, 487, 211
Markova, N. & Puls, J. 2008, A&A, 478, 823
Morel, T., Marchenko, S. V., Pati, A. K., Kuppuswamy, K., Carini, M. T., Wood, E. & Zimmerman, R. 2004, MNRAS, 351, 552
Prinja, R. K., Rivinius, T., Stahl, O., Kaufer, A., Foing, B. H., Cami, J. & Orlando, S. 2004, A&A, 418, 727
Ryans, R. S. I., Dufton, P. L., Rolleston, W. R. J., Lennon, D. J., Keenan, F. P., Smoker, J. V. & Lambert, D. L. 2002, MNRAS, 336, 577
Saio, H., Kuschnig, R., Gautschy, A., Cameron, C., Walker, G. A. H., Matthews, J. M., Guenther, D. B., Moffat, A. F. J., et al. 2006, ApJ, 650, 1111
Simón-Díaz, S., Herrero, A., Uytterhoeven, K., Castro, N., Aerts, C. & Puls, J. 2010, ApJ, 720, L174
Simón-Díaz, S., Uytterhoeven, K., Herrero, A. & Castro, N., 2009, AIPC, 1170, 397
Simón-Díaz, S. & Herrero, A. 2007, A&A, 468, 1063
Simón-Díaz, S., Castro, N., Garcia, M., Herrero, A., & Markova, N. 2011, in Proceedings of the 39th Liège Astrophysical Colloquium, eds. G. Rauw, M. De Becker, Y. Nazé, J.-M. Vreux & P.M. Williams, BSRSL 80, 514
Slettebak, A. 1956, ApJ, 124, 173

Discussion

J. Sundqvist: About using the Fourier Transform (FT) method to infer $v \sin i$ when macrotubulence is important. It was shown by Aerts and colleagues that if indeed macroturbulence is due to pulsations, then the FT method may give you erroneous estimate of $v \sin i$. Can you comment on this?
S. Simón-Díaz: You are right; this conclusion arises from the analysis of the simulated profiles by Aerts et al., and it is also based on well established arguments (e.g. the FT technique must be used with care in the case of asymmetric profiles). This is something we are also investigating in our observational project. In the analysis of the time series observations we have found that the $v \sin i$ provided by the FT and goodness-of-fit methods (when a radial-tangential definition of macroturbulence is assumed) are in quite good agreement. In addition the dispersion of $v \sin i$ values, derived by both methods is similar, and not as large as the one found from the analysis of Aerts et al. simulations. Finally, we have found cases in which macroturbulence is quite large and the first zero of the FT from the time series profiles is quite stable.
We are planning to apply the FT technique in well known pulsators in which $v \sin i$ is derived independently by means of a seismic analysis. We are also investigating whether there is any correlation between the third moment of the line profile and the position of the first zero in the FT. Note that in case of $\langle v' \rangle = 0$ the line is symmetric and the FT should be giving right $v \sin i$ values.
J. Puls: This comment also refers to the talk by Fabrice Martins. It has to be noted that the positions of the first zero's in the Fourier Transform (FT) (related to $v \sin i$) remain unaffected from extra-broadening only if the broadening function can be described by certain functions, by a Gaussian (or related functions). When the broadening would be due to the collective effects from oscillations, this is not longer true, as shown by Aerts et al. (2009). In so far, the different positions of the first zero's in the FTs as a function of time (as shown by Sergio Simón-Díaz) are consistent with the hypothesis of a relation to pulsations.

I. Antokhin: In your fits of spectral line profiles, do you take into account gravitational darkening?
S. Simón-Díaz: No. In these stars the rotational velocities are not expected to be very large. So gravitational darkening is negligible.

On the mass-loss properties of the most massive stars

G. Gräfener[1], J.S. Vink[1], J.M. Bestenlehner[1],
and the VLT-FLAMES Tarantula Consortium

[1] Armagh Observatory, College Hill, Armagh BT61 9DG, United Kingdom

Abstract: The most massive stars are believed to form Wolf-Rayet like emission line spectra already on the main sequence. One goal of the new VLT-FLAMES Tarantula Survey is to understand the nature of such 'O stars on steroids', and to investigate the transition from normal O star to WR-type mass loss. The Tarantula nebula (30 Dor) hosts the closest starburst-like region in our neighborhood, with a cluster of 30-50 extremely massive stars in its center. In this paper we present a multi-wavelength program that includes integral field K-band spectra of the central region of 30 Dor with VLT/SINFONI. We discuss the prospects of this program in the context of our theoretical work on Γ-dependent mass-loss rates in the O-WR transition phase.

1 Introduction

Wolf-Rayet (WR) type mass loss fundamentally affects the evolution, the final fate, and the chemical yields of massive stars. The precise amount of mass loss in the WR phase determines whether a star ends its life as neutron star, or black hole (Heger et al. 2003). The nature of WR-type mass loss is however still poorly understood. E.g., stellar evolution models rely on empirical mass-loss relations (e.g., Nugis & Lamers 2000; Hamann et al. 2006), with the WR phase identified on the basis of observed WR surface abundances in our neighborhood. Clearly, for the modeling of stellar populations that cannot be observed locally, a more physical approach would be desirable.

In the present work we discuss such an approach, namely a mass-loss relation for WR stars that chiefly depends on the Eddington factor $\Gamma_{\rm e}$. Such a relation has been predicted by theoretical studies of radiatively driven winds close to the Eddington limit (Gräfener & Hamann 2005, 2008, Vink et al. in prep.). Notably, the proximity to the Eddington limit provides a natural explanation for the occurrence of WR mass loss. Large Eddington factors can be reached, on the one hand, by very young and massive stars on the main sequence because of their extremely high luminosities, and on the other hand, by less massive evolved (He-burning) stars due to the enhanced mean molecular weight in their cores. The occurrence of WR-type mass loss for young, luminous, hydrogen-rich stars (typically late WN subtypes), and evolved, hydrogen-free WR stars can thus be explained in the same way.

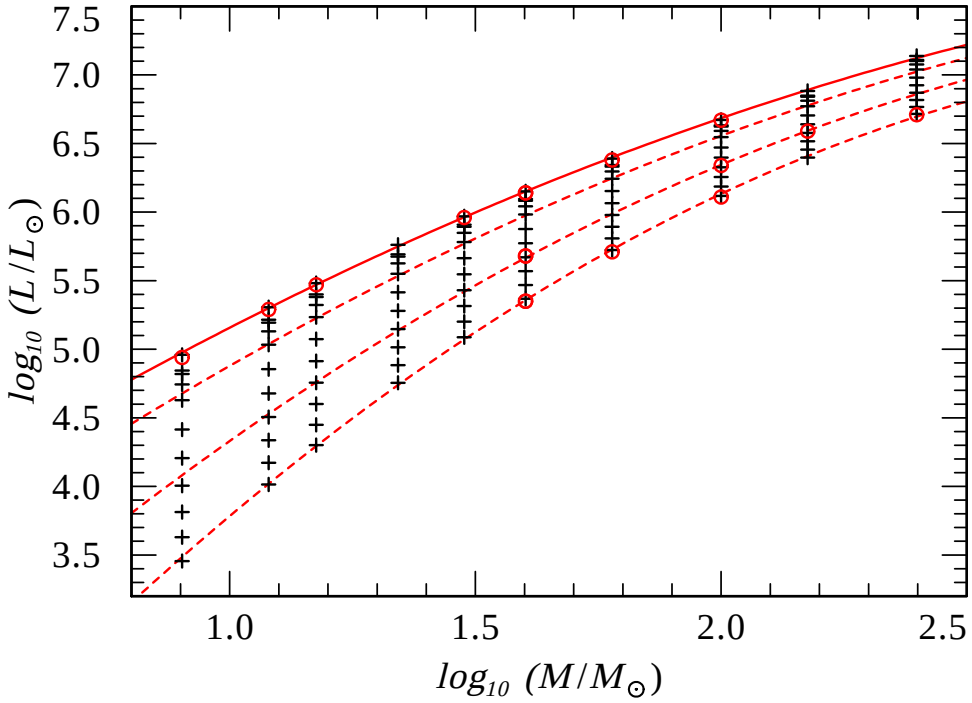

Figure 1: Homogenous stellar structure models for the mass range 8–250 $M_\odot$ (black symbols). The models are computed for hydrogen mass fractions $X_\mathrm{H} = 0.7$–0 (from bottom to top). Red lines indicate fitted M-L relations for H-burning models with $X_\mathrm{H} = 0.7$, 0.4, and 0.1 (dashed), and pure He-models (solid). For comparison, model computations from Ishii et al. (1999) are indicated by red symbols.

2 Mass loss predictions for very massive stars

Wind models for very massive stars close to the Eddington limit (Gräfener & Hamann 2008, Vink et al. in prep.) reveal a steep dependence on the Eddington factor Γ_e for the optically thick, WR-type winds of these objects. Moreover, Gräfener & Hamann (2008) find a very strong temperature dependence, with $\dot{M} \propto T_\star^{3.5}$. This strong sensitivity to stellar parameters offers the potential to provide very precise estimates of Γ_e for stars in this regime, based on the predicted mass loss relations. Using large stellar samples where parameters like $\dot{M}$, L, X_H, and Z are determined by spectral analyses, we can thus test the existence of such relations in an empirical way.

3 Mass–luminosity relations for very massive stars

To get a handle on the $\dot{M}$–Γ_e relation for observed stars we need to estimate the *expected* values of Γ_e for stars with observed stellar parameters L, and X_H. For this purpose we need to estimate the stellar mass M, and compute $\Gamma_\mathrm{e} = \chi_\mathrm{e} L/4\pi cGM = 10^{-4.813}(1+X_\mathrm{H})L/M$. The important dependence on $(1+X_\mathrm{H})$ enters this equation via the mass absorption coefficient χ_e, because, in a fully ionized gas, hydrogen provides one free electron per nucleon, in contrast to 0.5 for helium.

Because the internal structure of a single observed star is generally not known, we will concentrate here on the lowest and highest possible mass for a star with given parameters L, and X_H. The highest possible mass is given by the *chemically homogenous* case. Under this assumption, the star is characterized by one, constant hydrogen abundance X_H, which equals the observed surface abundance. The estimated stellar mass $M_\mathrm{hom}(L, X_\mathrm{H})$ is strongly dependent on the (observed) surface abundance X_H.

The lowest possible mass is given by the completely inhomogenous case, i.e., by a hydrogen-free stellar core. In this case the star is in the *core He-burning* phase. For the case of hot, massive stars with large convective cores the He-burning mass equals the mass of a pure He-star (Lauterborn et al. 1971), i.e., $M_{\rm Heb}(L) \equiv M_{\rm hom}(L, X_{\rm H} = 0)$. Note that, in contrast to the homogenous case, this mass estimate is completely independent of the observed surface abundance $X_{\rm H}$. In the following this difference will help to distinguish between samples of well-mixed, quasi chemically homogenous stars, and stars with a pronounced chemical profile. In Fig. 1 we illustrate the M–L relations as obtained from our own stellar structure computations for chemically homogenous stars.

4 The most massive stars in the Arches cluster

One of the biggest known samples of very massive stars is found in the Arches cluster, near the Galactic Center. Stellar parameters of these stars have been determined by Martins et al. (2008). In Figs. 2, and 3 we display semi-empirical mass loss relations, based on observed mass-loss rates, and mass estimates under the assumptions of homogeneity, and core He-burning. Only for the homogenous case (Fig. 3) we obtain a pronounced Γ-dependent mass-loss relation that compares well with theoretical predictions. Note that the qualitative difference between both plots arises from the dependence of $M_{\rm hom}(L, X_{\rm H})$ on the surface hydrogen abundance $X_{\rm H}$. For the homogenous case, this dependence puts the H-deficient WN stars on the same relation as the H-rich Of/WN stars. We interpret this as evidence 1) for the existence of a Γ-dependent mass-loss relation, and 2) for the H-burning nature of the Arches cluster stars.

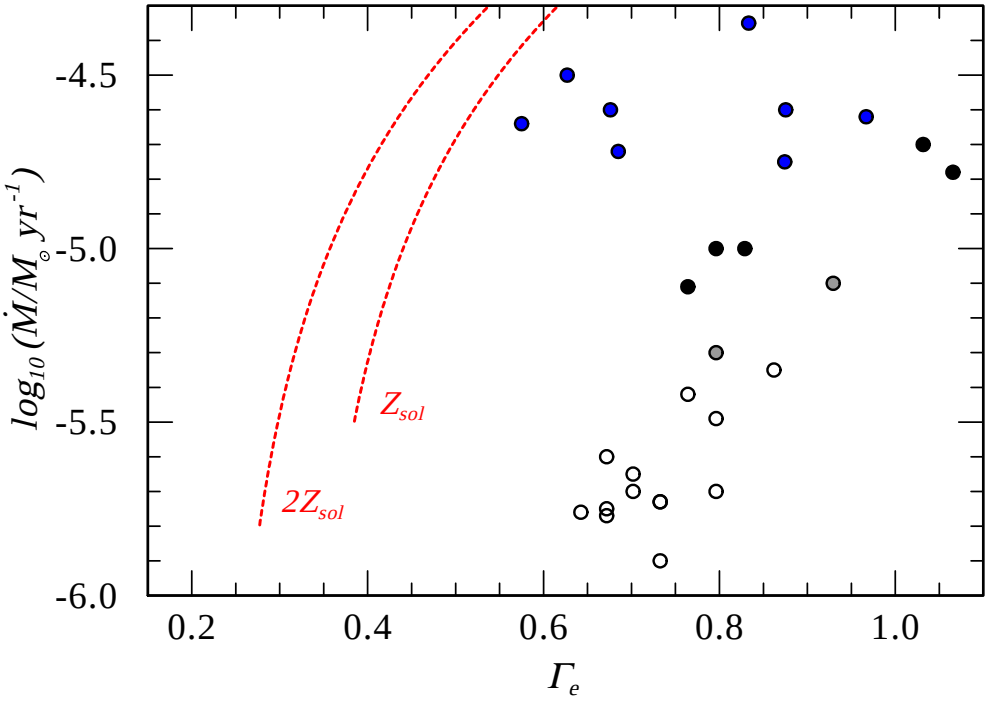

Figure 2: Under the assumption of central He-burning, the Arches cluster stars display no general Γ-dependence. Colored symbols indicate stars with spectral subtypes WNh (H-deficient blue, normal H abundance black), Of (grey), and O (white). We compare with mass loss relations by Gräfener & Hamann (2008) for $log(L) = 6.3$, $T_\star = 30$ kK, and $X_{\rm H} = 0.7$ (dashed red lines).

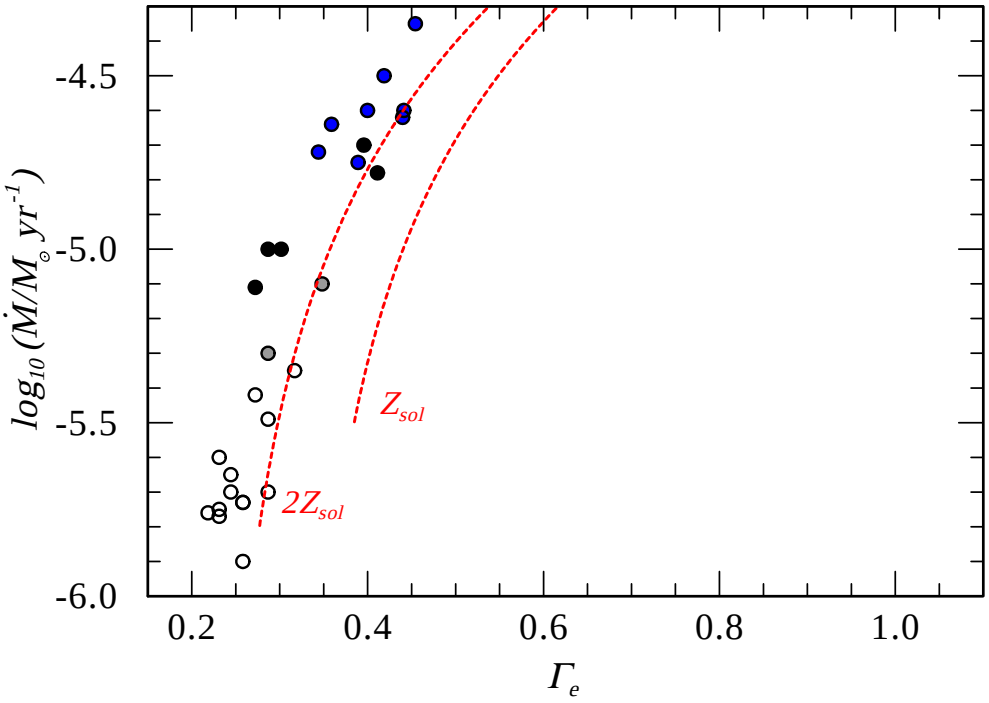

Figure 3: Under the assumption of chemical homogeneity, the Arches cluster stars display a pronounced Γ-dependent mass-loss relation. Symbols are the same as in Fig. 2.

5 The VLT-FLAMES Tarantula Survey

In the framework of the VLT-FLAMES Tarantula Survey we currently investigate the mass-loss properties of the most massive stars in the central part of 30 Dor in the LMC. This stellar sample will complement our previous investigation of the Arches cluster stars in an ideal way, as it represents very similar objects with different metallicity, and temperature. We will thus be able to investigate the important dependencies on these two parameters in an empirical way.

In Fig. 4 we illustrate the spatial coverage of the 30 Dor sample by different observational programmes. The FLAMES-MEDUSA fiber pointings are indicated in red. Due to crowding, the central part of the cluster is however largely omitted by this program. To obtain a homogenous dataset for the whole cluster we have secured SINFONI K-band spectra that cover the complete central cluster (yellow fields). These spectra provide the same mass-loss diagnostics as the previous IR studies, e.g., for the Arches cluster, and are augmented by existing HST data (blue).

6 Conclusions

In this work we have presented theoretical, as well as observational evidence for the existence of a Γ-dependent mass-loss relation for very massive stars.

For the most massive stars in the Arches cluster, we only find such a relation under the assumption of a chemically homogenous stellar structure. We interpret this as evidence for the H-burning nature of the WN stars in the Arches cluster. This is in line with the picture that WR-type mass loss is generally triggered by the proximity to the Eddington limit, for very massive stars as well as for 'classical' He-burning WR stars. Our ongoing work on the most massive stars in 30 Dor will help to investigate the stellar mass loss in this regime over a much broader range of temperatures and metallicities.

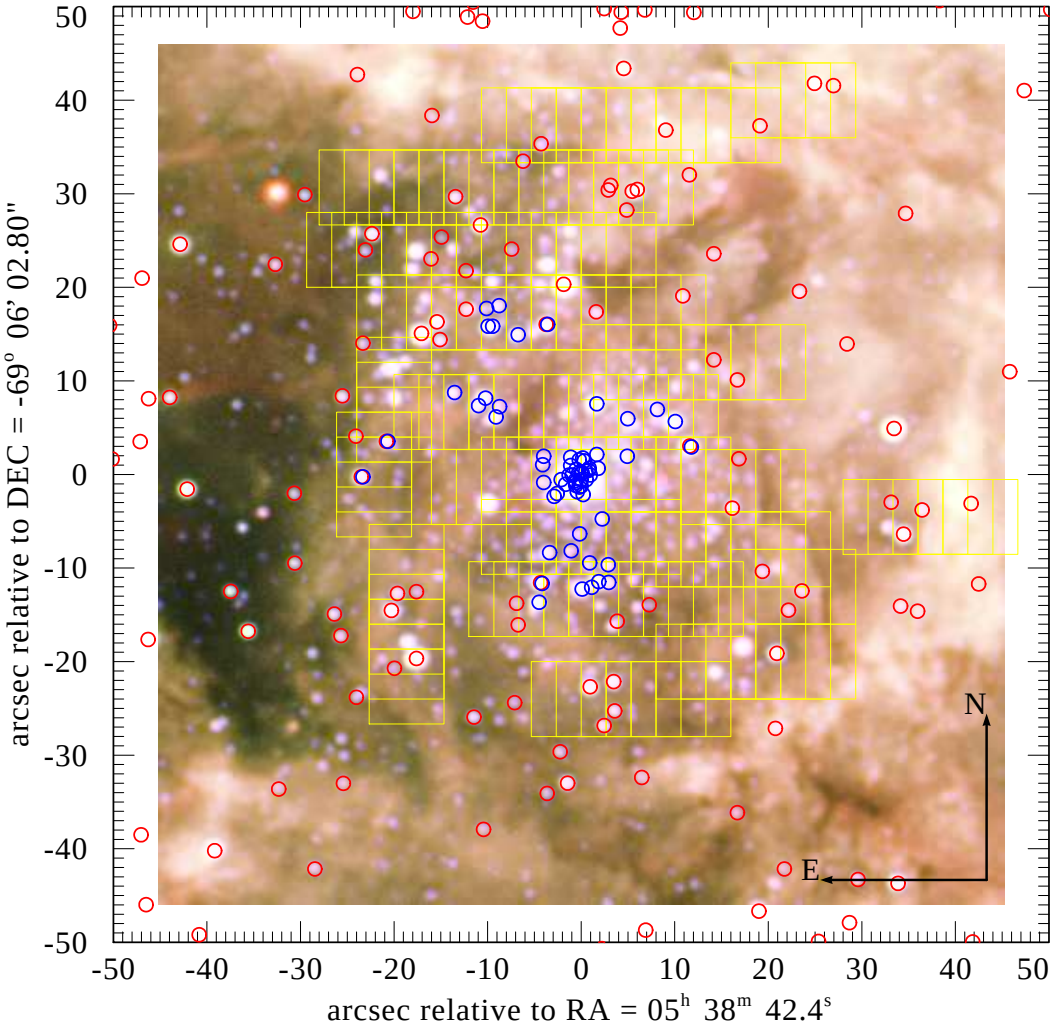

Figure 4: The VLT-FLAMES Tarantula Survey. The picture illustrates the central part of 30 Dor with pointings of the FLAMES-MEDUSA fiber spectrograph (red), existing HST spectra (blue), and SINFONI integral-field K-band spectroscopy.

References

Gräfener, G. & Hamann, W.-R. 2005, A&A, 432, 633
Gräfener, G. & Hamann, W.-R. 2008, A&A, 482, 945
Hamann, W.-R., Gräfener, G., & Liermann, A. 2006, A&A, 457, 1015
Heger, A., Fryer, C. L., Woosley, S. E., Langer, N., & Hartmann, D. H. 2003, ApJ, 591, 288
Ishii, M., Ueno, M., & Kato, M. 1999, PASJ, 51, 417
Lauterborn, D., Refsdal, S., & Weigert, A. 1971, A&A, 10, 97
Martins, F., Hillier, D. J., Paumard, T., et al. 2008, A&A, 478, 219
Nugis, T. & Lamers, H. J. G. L. M. 2000, A&A, 360, 227

Discussion

I. Brott: You compare your mass-loss rates to homogeneous stars of $2\times$ solar metallicity. Usually, homogeneity does not appear in evolutionary models of solar or higher metallicity.
G. Gräfener: We use homogeneous structure models to constrain Γ. This method is independent from evolutionary models.
Comment: In a later discussion it turned out that also high-Z evolution models evolve homogeneously. They only do not evolve to the blue because of an envelope inflation.

The most luminous stars in the Galaxy and the Magellanic Clouds

Wolf-Rainer Hamann, Andreas Barniske, Adriane Liermann,
Lidia M. Oskinova, Diana Pasemann, Ute Rühling

Universität Potsdam, Germany

Abstract: Some of the Wolf-Rayet (WR) stars are found to have very high bolometric luminosities ($\log L/L_\odot > 6$). We employ the Potsdam Wolf-Rayet (PoWR) model atmospheres for their spectral analysis, which yields the bolometric corrections. Distance and interstellar reddening also enter the luminosity estimates.

Among the Galactic stars, there is a group of very luminous WNL stars (i.e. WR stars of late subtype from nitrogen sequence with hydrogen being depleted in their atmospheres, but not absent). Their distances are often the major source of uncertainty. From K-band spectroscopy we found a very luminous star ($\log L/L_\odot = 6.5$) in the Galactic center region, which we termed the Peony Star because of the form of its surrounding dusty nebula. A similar group of very luminous WNL stars is found in the Large Magellanic Cloud (LMC). In the Small Magellanic Cloud (SMC) the majority of WR stars resides in binary systems. The single WNL stars in the SMC are not very luminous.

We conclude that a significant number of very luminous WNL stars exist in the Galaxy and the LMC. With initial masses above 60 $M_\odot$, they apparently evolved directly to the WNL stage without a prior excursion to the red side of the HRD. At the low metallicity of the SMC, the binary channel may be dominant for the formation of WR stars.

1 Introduction

Very luminous stars, with bolometric luminosities exceeding $10^6 L_\odot$, appear spectroscopically mainly as Wolf-Rayet (WR) types. However, hot stars emit most of their radiation in the extreme ultraviolet which is not accessible to observation. Hence the determination of their luminosity L must rely on adequate model atmospheres. Our "Potsdam Wolf-Rayet" code (PoWR – see Hamann & Gräfener 2003 and references therein) solves the non-LTE radiative transfer in a spherically symmetric expanding atmosphere. Detailed and complex model atoms are taken into account especially for H, He, and the CNO elements, while the iron-group elements are treated in the superlevel approximation. Wind inhomogeneities are accounted for in a first-order approximation ("microclumping"). The code has been applied mainly for the wind-dominated emission-line spectra of WR stars (see `http://www.astro.physik.uni-potsdam.de/PoWR.html` for grids of models), but can also be used for fitting photospheric absorption spectra. In the standard version of the PoWR code, mass-loss rate and velocity field are free parameters of the model, while they are determined consistently with the radiation pressure only in the hydrodynamical version (Gräfener & Hamann 2005, 2008). Another PoWR code option not used here is "macroclumping" (Oskinova et al. 2007).

2 How reliable are spectroscopic luminosities ?

In order to discuss the reliability of WR luminosities, we briefly describe the procedure of their spectroscopic determination. The first step is the fit of the normalized line spectrum. Spectra from stellar-wind models depend mainly on two parameters, the stellar temperature T_* and the so-called "transformed radius" $R_{\rm t}$. The terminal wind velocity v_∞ controls the widths of the profiles. Furthermore, the lines depend of course on the chemical abundance of their species.

The stellar temperature T_* is the effective temperature related to the luminosity L and the stellar radius R_* via the Stefan-Boltzmann law. R_* refers by definition to the point of the atmosphere where the Rosseland mean optical depth reaches 20.

The "transformed radius" is defined as $R_{\rm t} = R_* \left[\frac{v_\infty}{2500\,{\rm km\,s^{-1}}} \Big/ \frac{\dot{M}\sqrt{D}}{10^{-4}\,M_\odot\,{\rm yr^{-1}}} \right]^{2/3}$. Its name, historically coined by Schmutz et al. (1989), is actually misleading since $R_{\rm t}$ has not the meaning (although the units) of a radius. More suggestive is to consider $R_{\rm t}^{-3}$, which might be called a "normalized emission measure". Being proportional to the volume integral of the density squared, divided by the stellar surface, $R_{\rm t}^{-3}$ scales with the emission from recombination lines normalized to the continuum. This explains why different combinations of R_*, v_∞, and mass-loss rate $\dot{M}$ result in approximately the same normalized WR emission-line strengths as long as $R_{\rm t}$ (or $R_{\rm t}^{-3}$) is kept at the same value. (D is the clumping factor for which we assume $D = 4$ throughout the work described here.)

Taking advantage of this approximate parameter degeneracy, the analysis can start from models with an arbitrarily adopted luminosity (our grids are mostly calculated for $\log(L/L_\odot) = 5.3$) and find the optimum fit of the normalized line spectrum by varying T_* and $R_{\rm t}$ (using models of adequate v_∞ and chemical composition). The spectral fits that can be achieved are satisfactory (cf. Fig. 1), but also often leave characteristic discrepancies which we attribute mainly to deviations from wind symmetry and homogeneity. The fit parameters can be typically determined to an accuracy of ± 0.05 in $\log T_*$ and ± 0.1 in $\log R_{\rm t}$.

In a second step, the luminosity is determined from fitting the spectral energy distribution of the model to observations (flux-calibrated spectra or photometry) over the widest available range (see Fig. 2). The slope and form of the model SED is fitted by adjusting the color excess E_{B-V}, and by chosing an adequate reddening law (and its parameters). Sometimes the (circumstellar?) reddening is clearly anomalous, as demonstrated in the example of Fig. 2 by the weak 2200 Å feature. The absolute value is adjusted by scaling the model in luminosity (i.e. a vertical shift in the double logarithmic plot).

In order to discuss the error margins of the derived luminosity, we consider $M_{\rm bol} = 4.72 - 2.5 \log L/L_\odot$. This absolute bolometric magnitude follows from the observed apparent magnitude m_i in some band i (where i may stand for, e.g., the visual band V, or for the near-IR K band in case of

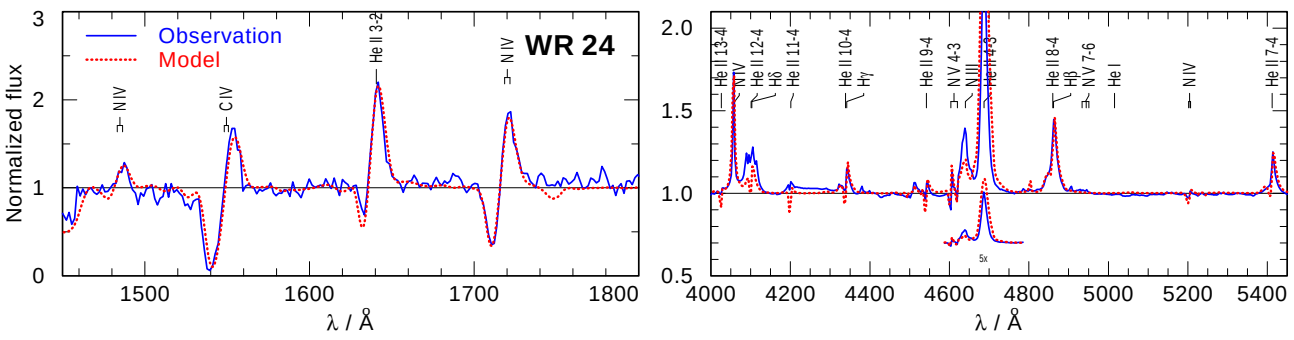

Figure 1: Example of line fit for the Galactic WN6h star WR 24, showing P Cygni type line profiles in the UV (*left panel*) and strong emission lines in the optical (*right*). Main parameters of the model (red-dotted) are T_* = 50 kK, $\log R_{\rm t}$ = 1.35, $X_{\rm H}$ = 0.44 and v_∞ = 2160 km/s (after Hamann et al. 2006).

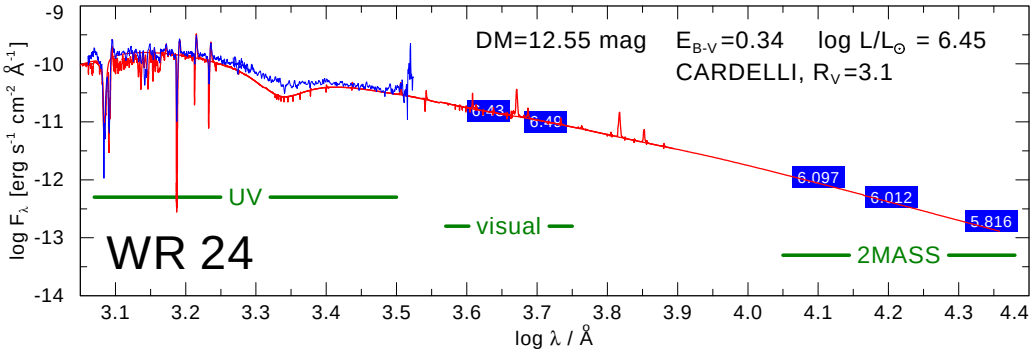

Figure 2: Example of a fit of the spectral energy distribution (SED) for WR 24 (red: model, blue: observation), using the model selected from the line fit (cf. Fig. 1). The distance modulus DM is known from cluster membership. Free parameters are the reddening and the luminosity scaling.

visually obscured objects), by applying the bolometric correction BC_i and the extinction A_i in the considered band, and the distance modulus DM (all in mag),

$$M_{\rm bol} = m_i - BC_i - A_i - DM \tag{1}$$

The bolometric correction is predicted by the model (see Fig. 3) and amounts to 3–5 mag for most WN stars, but can reach 6.5 mag for the hottest subtypes. Since the observed band lies in the Rayleigh-Jeans domain of the SED, the bolometric correction ($10^{0.4BC}$) scales roughly with T_*^3. Hence a typical fit uncertainty of ± 0.05 in $\log T_*$ propagates to ± 0.4 mag in BC or ± 0.15 in $\log L$.

The extinction can introduce a noticeable error especially when it is high. If the available wavelength basis is as long as in the example shown in Fig. 2, the color excess E_{B-V} can be determined from the spectral slope to a few hundredths of a magnitude. However, the extinction law itself can vary between different lines of sight. For the visual band, for instance, R_V may deviate considerably from 3.1 as the Galactic standard value, which affects the visual extinction $A_V = R_V\ E_{B-V}$.

For Galactic WR stars, the largest uncertainty often comes from the distance. Only when a star can be assigned to an open cluster or association, we can adopt the distance of the latter. Stars in

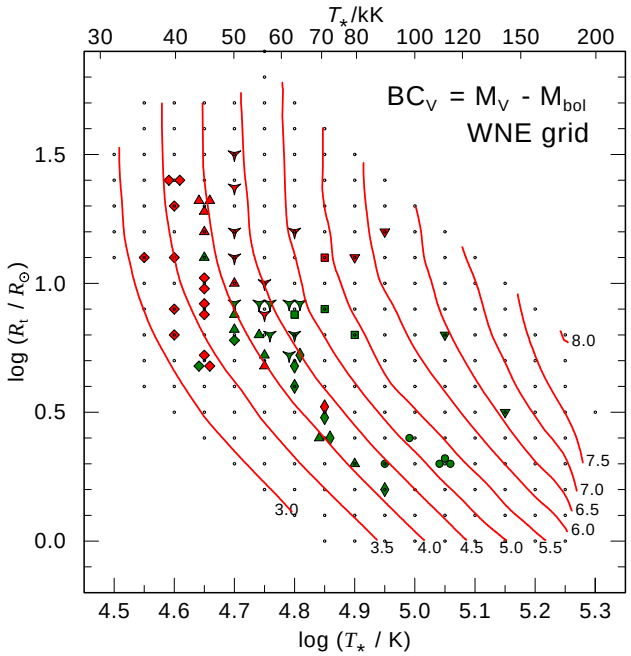

Figure 3: Contours of the same Bolometric Correction to the visual magnitude (labels: BC_V in mag) for PoWR models of hydrogen-free WN stars. Small dots mark the WNE grid models, and colored symbols show the parameters of Galactic WN stars from Hamann et al. (2006).

the Galactic Center, and especially objects in the LMC and SMC, have the clear advantage of a well-known distance.

Summarizing, the reliability of spectroscopically determined luminosities of WN stars depends very much on the individual circumstances. When the stellar temperature is well constrained from the line fit of different ions, the distance is known, and good photometry is available in spectral bands with not too high extinction, the error margins combine to ± 0.2 in $\log L$, typically.

3 Results

The empirical Hertzsprung-Russell-diagram (HRD) for the Galactic WN stars, analyzed with the methods described above, is displayed in Fig. 4 (left panel). Two groups of stars are clearly distinguished. The hydrogen-free stars, usually termed WNE ("E" for early subtypes), are pretty hot and located between the hydrogen and the helium main sequence. Their luminosities $\log L/L_\odot$ are between 5.3 and 5.8, typically. In contrast, the WNL ("L" for late subtypes) stars are less hot than the ZAMS and contain hydrogen. Most of them are very luminous ($\log L/L_\odot > 6$). They are not WR stars in the classical understanding, but rather very massive stars with strong winds which are still in the hydrogen-burning phase. However, for a couple of the WNL stars in this diagram the distance is actually not known (indicated by their smaller symbols). Their luminosity is basically adopted from

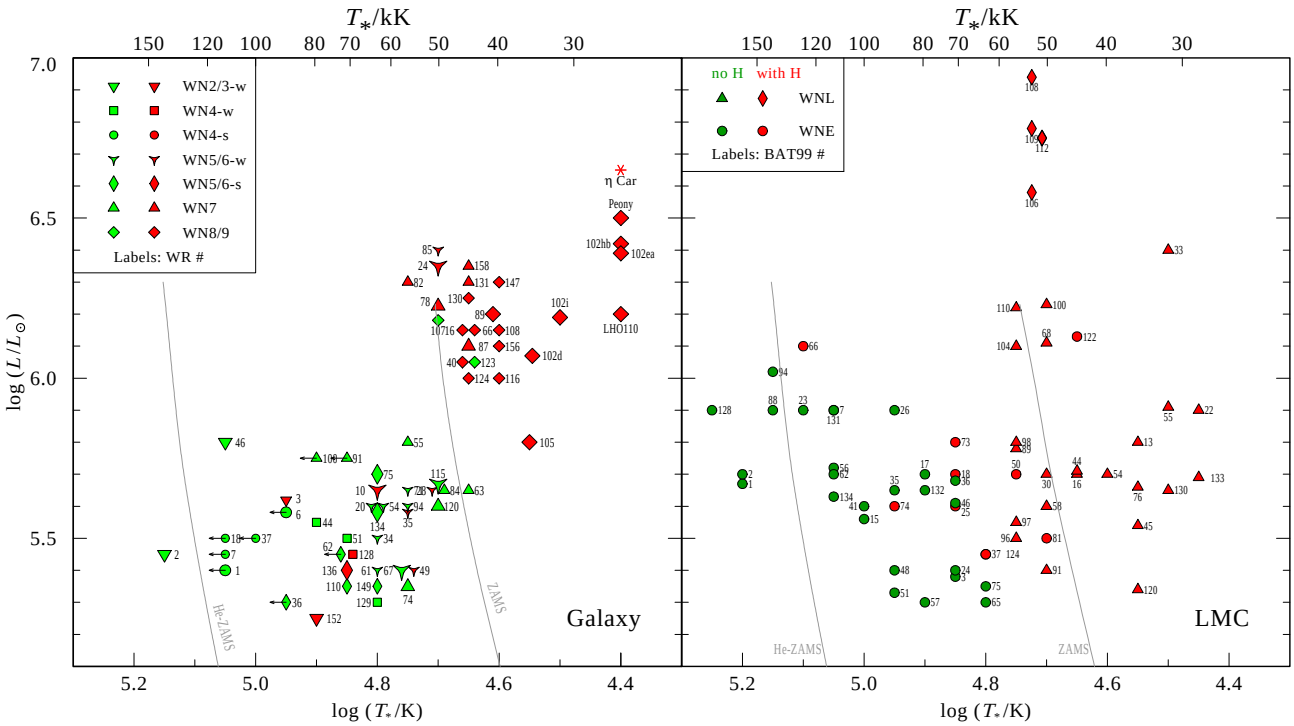

Figure 4: Empirical HRDs of WN stars in the Galaxy (*left*) and the LMC (*right*). The Galactic stars are from Hamann et al. (2006). Labels denote the WR catalog number, while red and green colors indicate whether photospheric hydrogen is detectable or not, respectively. The larger symbols refer to stars with independently known distances. Included are also the Galactic center stars WR 102hb, 102ea, 102i, 102d and LHO 110 analyzed by Liermann et al. (2010, 2011) and the Peony star (WR102ka) from Barniske et al. (2008). η Car (after Figer et al. 1998) is shown for comparison. The LMC stars in the right panel (identified by their BAT99 catalog number) are preliminary results from Rühling et al. (in prep.). The diamonds indicate four objects from the R136 cluster according to Crowther et al. (2010).

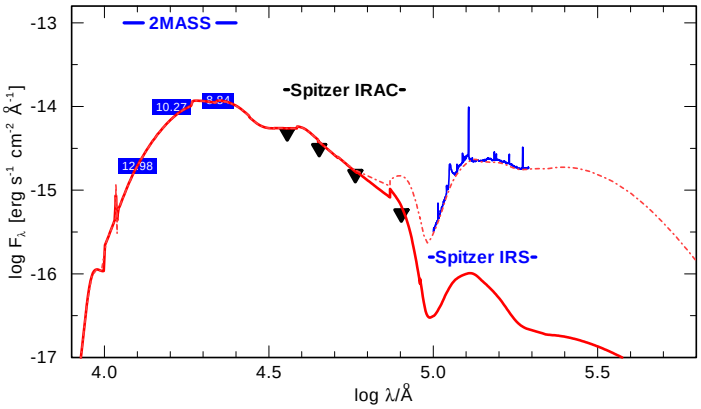

Figure 5: SED fit of the Peony star (WR 102ka) in the Galactic center region. Because of the strong interstellar extinction, the maximum of the observed flux is in the K band. The mid-IR excess observed with *Spitzer* indicates warm circumstellar dust (model: red dashed line), which was found here for the first time around a WN star. From Barniske et al. (2008)

similar stars of known distance. A couple of them might be in fact closer and less luminous.

Remarkable is the group of WNL stars from the Galactic center region. Being visually obscured, they have been analyzed only from their K-band spectra. Nevertheless, we believe that their luminosities are reliable. Figure 5 shows the SED fit for the Peony star. In the K band, the extinction A_K amounts only to about 3 mag. The analysis (Barniske et al. 2008) revealed that this star has the second-highest luminosity ($\log L/L_\odot$ = 6.5 $\pm$0.2) known in the Galaxy, after η Car.

In the LMC the group of very luminous WNL stars is less pronounced (Fig. 4, right panel). Instead there are many WNL stars with hydrogen, but moderate luminosities. It is not yet clear if we have missed such stars in the Galaxy because of the distance problem discussed above. The four extremely luminous stars represented in the figure by diamonds have been claimed recently by Crowther et al. (2010), and belong to the cluster R136 which we had avoided. The problem is to rule out accidental multiplicity in this very dense field of stars with identical spectral type.

The 12 WR stars (11 WN, 1 WO) known in the SMC are currently studied by Pasemann et al. (2011, and in prep.). Five of these stars appear to be single, while the remaining six are binaries for which we started to analyze the composite spectra. With $\log L/L_\odot < 6$ the single WN stars are not "very" luminous.

4 Conclusions

A couple of very luminous stars ($\log L/L_\odot > 6$) are found in the Galaxy and LMC. Apart from a few outstandingly bright LBVs, the most-luminous stars are of late WN type (WNL). Remarkable is the abundance of such stars in the Galactic center region. In the SMC, single WNL stars are also found despite of the low metallicity, but not with very high luminosities.

References

Barniske, A., Oskinova, L.M., & Hamann, W.-R. 2008, A&A 486, 971
Crowther, P.A., Schnurr, O., Hirschi, R., et al. 2010, MNRAS 408, 731
Figer, D.F., Najarro, F., Morris, M., et al. 1998, ApJ 506, 384
Gräfener, G., & Hamann, W.-R. 2005, A&A 432, 633
Gräfener, G., & Hamann, W.-R. 2008, A&A 482, 945
Hamann, W.-R., & Gräfener, G. 2003, A&A 410, 993
Hamann, W.-R., Gräfener, G., & Liermann, A. 2006, A&A 457, 1015
Liermann, A., Hamann, W.-R., Oskinova, L.M., Todt, H., & Butler, K., 2010, A&A 524, A82
Liermann, A., Hamann, W.-R., Oskinova, L.M., & Todt, H. 2011, in Proceedings of the 39th Liège Astrophysical Colloquium, eds. G. Rauw, M. De Becker, Y. Nazé, J.-M. Vreux & P.M. Williams, BSRSL 80, 160

Oskinova, L.M., Hamann, W.-R., & Feldmeier, A. 2007, A&A 476, 1331
Pasemann, D., Rühling, U., & Hamann, W.-R. 2011, in Proceedings of the 39th Liège Astrophysical Colloquium, eds. G. Rauw, M. De Becker, Y. Nazé, J.-M. Vreux & P.M. Williams, BSRSL 80, 180
Schmutz, W., Hamann, W.-R., & Wessolowski, U. 1989, A&A 210, 236

Discussion

P. Williams: In the different possible de-reddenings of the WR 24 SED, it seems none of them cancelled the 2200 Å feature - how is that?
W.-R. Hamann: You have correctly spotted that in the shown SED fit of WR24 the interstellar 2200 Å feature is not correctly reproduced. The standard reddening laws (Cardelli et al., Fitzpatrick et al.) that we use provide only one adjustable parameter, R_v. The actual reddening function A_λ may considerably deviate from these laws for an individual line-of-sight, especially with regard to the broad 2200 Å feature.

Pulsations in Wolf-Rayet Stars: Observations with *MOST*[*]

André-Nicolas Chené[1,2,3] and Anthony F. J. Moffat[4]

[1] Departamento de Física, Universidad de Concepción, Chile
[2] Departamento de Física y Astronomía, Universidad de Valparaiso, Chile
[3] National Research Council of Canada, Herzberg Institute of Astrophysics, Canada
[4] Département de Physique, Université de Montréal, Canada

Abstract: Photometry of Wolf-Rayet (WR) stars obtained with the first Canadian space telescope *MOST* (Microvariability and Oscillations of STars) has revealed multimode oscillations mainly in continuum light. The latter suggest stellar pulsations could be a significant contributing factor to the mass-loss rates. Since the first clear detection of a pulsation period of P = 9.8h in WR123, two other stars have also shown periods of a few days, which must be related to stellar pulsations.

1 Introduction

The wind momentum ($\dot{M}\,v$) of the Wolf-Rayet (WR) stars is a factor $\sim$10 times higher than the radiative momentum outflow rate (L/c); radiation pressure doesn't seem to be sufficient to initiate the strong winds. Hence, another driving mechanism should be present near, or at the surface of the star. Theoretical work suggest that strange-mode pulsations (SMPs) are present in the envelope of hot and luminous stars with a large luminosity-to-mass ratio, where the thermal timescale is short compared to the dynamical timescale, and where radiation pressure dominates (Glatzel, Kiriadikis & Fricke 1993). Hence, the most violent SMPs are expected in classical WR stars, where SMPs manifest themselves in cyclic photometric variability with periods ranging from minutes to hours (Glatzel et al. 1999). However, this variability is expected to be epoch-dependent, with small amplitude, therefore, very difficult to detect from the ground. That is why the study of WR stars became one of the primary science drivers of the space telescope *MOST* (Microvariability and Oscillations of STars, Matthews et al. 1999, Walker et al. 2003). The *MOST* photometry is non-differential, but given the orbit, its thermal and design characteristics, experience has shown that it is a very photometrically stable platform even over long timescales (with repeatability of the mean instrumental flux from a non-variable target with V$\sim$11-12 to within about 1 mmag over a month).

[*]Based on data from the *MOST* satellite, a Canadian Space Agency mission, jointly operated by Dynacon Inc., the University of Toronto Institute for Aerospace Studies and the University of British Columbia, with the assistance of the University of Vienna.

2 Three First Stars Observed With *MOST*

Since its launch, *MOST* has observed one WR star per year. The first one is the famous WN8 type WR 123 (Lefèvre et al. 2005). Its light curve has a total amplitude of 10 mmag and the periodogram shows a significant peak at $\sim$ 2.45 c d^{-1} (i.e. P$\sim$9.8 hours). Two quite different scenarios have been proposed to explain these observations. Townsend & MacDonald (2006) find that a deep, hot Fe opacity bump can lead to g-mode pulsations, but assumed a traditionally small stellar radius ($R_* \sim 2R_\odot$) compared to $R_* \sim 15R_\odot$, according to Crowther et al. (1995). As for, Dorfi, Gautschy & Saio (2006), they find that a cooler Fe opacity bump can produce SMPs, but had to assume significant hydrogen (X_H=0.35), compared to the observed value of 0.00. Both of these assumptions on the radius and on X_H contradict what we know about this star, thus casting some doubt on their applicability.
On the second year was observed WR 103, a dust-making WR star of the Carbon sequence. No clear period could be found although the light curve shows clear variations with an amplitude of $\sim$5 mmag (Marchenko et al. 2006). Simultaneous spectroscopy has shown that the changes are coming from the continuum light and not at all from the emission lines, formed further away in the expanding wind.
Finally, WR 111 (WC5) was observed in 2006. Moffat et al. (2008) have found no coherent Fourier components above the 50 part per million level over the whole interval for frequencies f$<$10 c d^{-1}. Simultaneous spectroscopic observations reveal a normal level of stochastic clumps propagating in the wind, which has no effect on period detection.

3 WR 124

WR 124 is a runaway star (e.g. Moffat et al. 1998) in the cool-nitrogen sequence with type WN8h (Smith, Shara & Moffat 1996). Fig. 1 shows the entire *MOST* light curve of WR 124 (*upper*) and a control star (*lower*), binned for each *MOST* orbit. Although significant variations are seen on timescales longer than $\sim$a day, no such variations are seen on shorter timescales and binning allows one to increase the photometric point-to-point *rms* precision from $\sim$3 mmag before binning to $\sim$0.5 mmag after. Using Period04 (Lenz & Breger 2005), we found three main frequencies present in the light-curve; ν_1=0.714$\pm$0.001 c d^{-1}, ν_2=0.375$\pm$0.001 c d^{-1} and ν_3=0.200$\pm$0.004 c d^{-1}. Fig. 1 shows a time-frequency plot with straddled 10-day sampling. In this figure, we see that the maximum power shifts from one of the main frequency to the other. However, the only frequency present for most of the observations if ν_1 (P$\sim$5.0 d). Simultaneous spectral monitoring gives a period of P$\sim$4.45 d. The spectral line-profile variability of WR 124 is very similar to the one observed for WR 123, although with a smaller amplitude. Since both these stars are of similar spectral types, the same type of pulsation may be present in each. Also, from previous ground-based observations, all the $\sim$10 relatively well-observed WN8 stars (and some other WNL) show a similar high degree of intrinsic variability (Antokhin et al. 1995, Marchenko et al. 1998), implying that all cool nitrogen-sequence WR stars may show similar behavior.

4 WR 110

WR 110 is in the mid-nitrogen sequence with type WN5-6b (Smith et al. 1996). Although to date it lacks any obvious binary signature, a comprehensive radial velocity search has not yet been carried out. However, WR 110 does have relatively high X-ray flux, with a significant hard component above 3 keV, compared to its lower-energy 0.5 keV emission, as seen in most WN stars (Skinner et al. 2002). The lower-energy component likely arises due to small-scale turbulent shocks in the wind, with velocity dispersion $\sim$100 km s^{-1}, as seen in virtually all WR-star winds (Lépine & Moffat

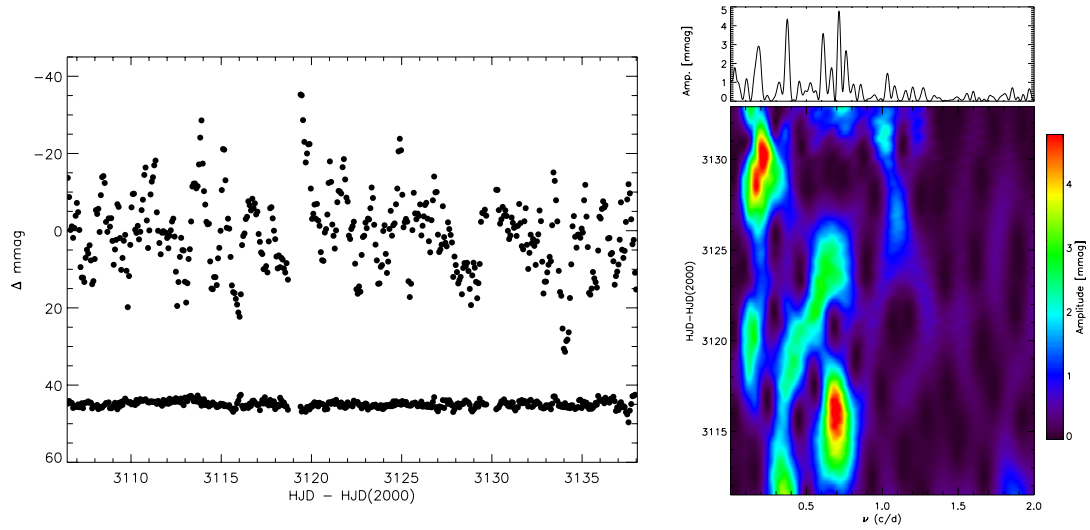

Figure 1: *Left*: *MOST* light curve of WR 124 in 101-minute MOST-orbit bins. *Right*: Fourier amplitude spectrum of the binned *MOST* light curve and Time-frequency Fourier plot with 10-day running windows in time.

1999) and other luminous hot stars (e.g. Eversberg, Lépine & Moffat 1998, Lépine & Moffat 2008). The former hard component implies velocities of at least 10^3 km s^{-1}, which are more difficult to explain, without invoking an additional mechanism to provide such high speeds (e.g. accretion onto a low-mass companion or colliding winds with a massive companion). However, WR 110 emits normal thermal radio emission from its wind (Skinner et al. 2002), which lends little support for its binary nature. Recently St-Louis et al. (2009) have examined a northern sample of 25 WR stars for the presence of Corotating-Interaction Regions (CIRs) via large-scale variations exhibited on broad, strong emission lines. Some 20% of these stars show clear signatures of such effects, with WR 110 situated at the limit between those stars that show CIRs and those that do not. As we show in this investigation, it is possible and even likely, that WR 110's hard X-rays arise in the shocks produced by its CIRs rotating at velocities of $\sim 10^3$ km s^{-1} relative to the ambient wind.

Fig. 2 shows the entire *MOST* light curve of WR 110 (*upper*) and a control star (*lower*), binned for each *MOST* orbit. Fig 2 also shows the Fourier spectrum for the *MOST* photometry (obtained using Period04; Lenz & Breger 2005). Here we see that the most significant peak occurs at a frequency of $\nu_1 = 0.245$ c d^{-1} (P = 4.08 d), with harmonics of this frequency at, or close to, $n \times \nu_1$, with $n = 2$, 3, 4, 5 and 6. Examination of the light curve in Fig. 2 shows relatively sharp cusps occurring on this time scale (i.e. P = 4.08 d, starting at t_0 = HJD 2 454 270.27) in all seven cases but one (the third case), although even then there is a rise in brightness, though not cusp-like. The cusps have typical widths at the base of $\sim$ a day. Such cusps are clearly non sinusoidal, requiring a series of successive harmonics to reproduce them, as observed. Fig. 2 also shows a time-frequency plot with straddled 8-day (double the best period) sampling. This plot reveals that the 4.08-day period stands out at all times except just before the middle of the run and at the ends (where edge effects come into play). The former is compatible with the apparently suppressed third cusp, as noted above.

The most likely scenario to explain the low-amplitude ($\sim$1 %) 4.08 d periodicity and cusp-like behavior in the *MOST* light curve, along with mostly unrelated spectral variations, appears to be large-scale, emitting over-density structure rotating with the wind. An attractive scenario for this are the CIRs (or their source at the base of the wind) proposed for O star winds by Cranmer & Owocki (1996). Since there is no model of the changes of light caused by CIRs available in the literature, we

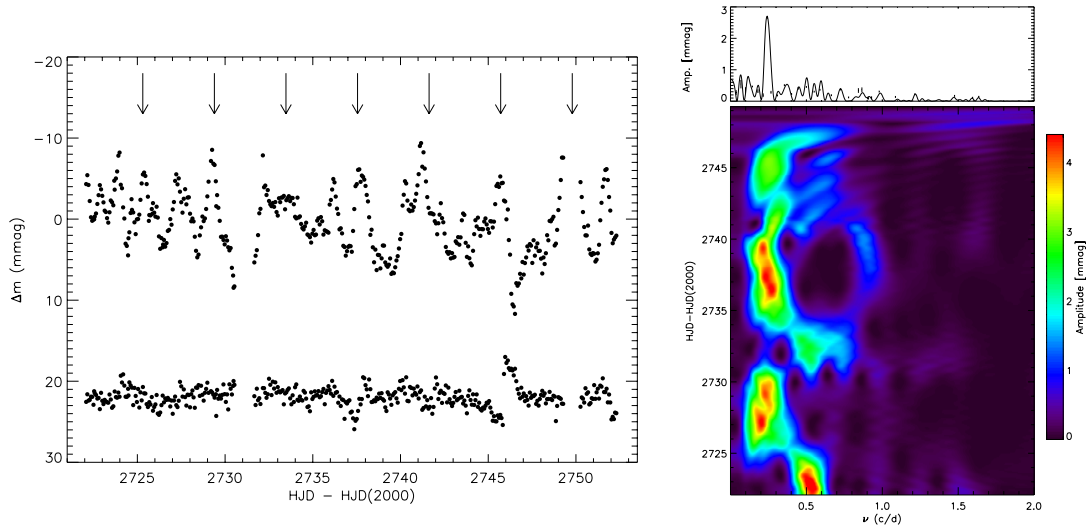

Figure 2: *Left*: *MOST* light curve of WR 110 in 101-minute MOST-orbit bins. The vertical lines indicate intervals of period 4.08 d starting at t_0 = HJD 2454270.31. *Right-Top*: Fourier amplitude spectrum of the binned *MOST* light curve. The highest peak refers to the adopted fundamental frequency corresponding to a period of P = 4.08 d. Harmonics are indicated at frequencies at multiples of 2 through 6 times fundamental. *Right-Bottom* : Time-frequency Fourier plot with 8-day running windows in time.

start with a very simplistic atmosphere model. First, we assume that the CIRs are continuum-emitting thermal sources, heated by the associated shock action created by a hot spot on the underlying rotating star with the ambient wind. Most of their emission must arise close to the star, where the ambient wind density is highest, as inspired by the simulations of Cranmer & Owocki (1996). Alternatively, the emission could arise in a hot spot at or close to the stellar surface, that produces the CIR. To simplify our calculations, we assume a point source located at some radius $R_s = \gamma R_*$ from the center of the star, with $\gamma > 1$ and R_* being the stellar core radius. For simplicity (and following Cranmer & Owocki 1996) we assume the CIR to initiate at the stellar rotation equator.
In this scenario, the changes in the light-curve are caused by the assumed CIR-associated point source attenuated by the wind and seen at different angles with the line of sight as it rotates on the near side of the WR star. In this study, we use a simple WR wind model derived by Lamontagne et al. (1996) in the context of wind eclipses for WR + O systems. Hence, the change in magnitudes is defined as :

$$\Delta m \; = \; constant \; - \; 2.5 \log_{10} \left(I_{WR} + I_s \mathrm{e}^{-\tau} \right), \tag{1}$$

with arbitrary constant and where I_{WR} is the intensity of the WR star and I_s, the intensity of the hot spot. Here the total opacity τ between the source and the observer, passing through the WR wind is :

$$\tau = k \int_{z_0}^{\infty} d\left(z/R_s\right) \left[r^2 \left(1 - R_*/r\right)^{\beta} \right]^{-1} \tag{2}$$

where $z_0 = -(R_s \sin i) \cos 2\pi\phi$, with R_s, the radial position of the hot spot (or the region of light emission) and i, the inclination of the rotation axis relative to the observer. We allow for a WR wind with a β velocity law, in which the actual β value will be fitted. Taking the second cusp in the light curve in Fig. 2 as the cleanest, most representative form of the hotspot light curve, we fit the Equation 1 to match the data best, for i = 90° (to give the maximum effect). We consider two cases: (a) an optically thin point source, whose emission is isotropic in direction, and (b) an optically thick

source whose emission is maximum when seen perpendicularly to the stellar surface, dropping to zero when seen parallel to the surface (i.e. like pancakes on or near the stellar surface). In case (b), the values of γ and β, which are always strongly coupled, tend to be slightly smaller than in case (a), since the projection factor in case (b) already provides a start (but only a start) to the correct form for the cuspy light curve, that requires less extended wind opacity to bring about the observed cuspy shape. All the best solutions for the thin and the thick cases are plotted in Fig. 3. Once again, this model is very simple, but its success is very encouraging. The next step would be to calculate the white-light emissivity of CIRs and to include their density distribution in the WR wind before calculating the light curve.

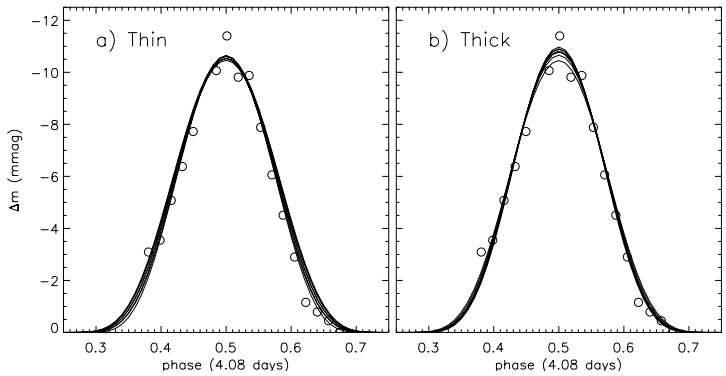

Figure 3: The data points refer to the second cusp indicated by a vertical line in Fig. 2. The curves indicate the best fits for (a) an optically thin point source and (b) an optically thick source (see text).

References

Antokhin, I.I., Bertrand, J.-F., Lamontagne, R., Moffat, A.F.J., & Matthews, J. 1995, AJ 109, 817
Cranmer, S.R., & Owocki, S.P. 1996, ApJ 462, 469
Crowther, P.A.C., Smith, L.J., Hillier, D.J. & Schmutz, W. 1995, A&A 293, 403
Dorfi, E.A., Gautschy, A., & Saio, H. 2006, A&A 453, L35
Eversberg, T., Lépine, S., & Moffat, A.F.J. 1998, ApJ, 494 799
Glatzel, W., Kiriakidis, M., & Fricke, K. J. 1993, MNRAS 262, L7
Glatzel, W., Kiriakidis, M., Chernigovskij, S., & Fricke, K.J. 1999, MNRAS 303, 116
Lamontagne, R., Moffat, A.F.J., Drissen, L., Robert, C., & Matthews, J. M. 1996, AJ 112, 2227
Lefèvre, L., Marchenko, S.V., Moffat, A.F.J., et al. 2005, ApJ 634, L109
Lépine, S., & Moffat, A.F.J. 1999, ApJ 514, 909
Lépine, S., & Moffat, A.F.J. 2008, AJ 136, 548
Lenz, P., & Breger, M. 2005, CoAst 146, 53
Matthews, J.M., Kuschnig, R., Walker, G.H.A., et al. 1999, JRASC 93, 183
Marchenko, S.V., Moffat, A.F.J., Eversberg, T., Morel, T., Hill, G.M., Tovmassian, G.H. & Seggewiss, W. 1998, MNRAS 294, 642
Marchenko, S., Lefèvre, L., Moffat, A.F.J., et al. 2006, AAS 208, 4601
Moffat, A.F.J., Marchenko, S.V., Bartzakos, P., et al. 1998, ApJ 497, 896
Moffat, A.F.J., Marchenko, S.V., Zhilyaev, B.E., et al. 2008, ApJ 679, L45
Skinner, S.L., Zhekov, S.A., Güdel, M., & Schmutz, W. 2002, ApJ 572, 477
Smith, L.F., Shara, M.M., & Moffat, A.F.J. 1996, MNRAS 281, 163
St-Louis, N., Chené, A.-N., Schnurr, O., & Nicol, M.-H. 2009, ApJ 698, 1951
Townsend, R.H.D., & MacDonald, J. 2006, MNRAS 368, L57
Walker, G.H.A., Matthews, J., Kuschnig, R., et al. 2003, PASP 115, 1023

General X-ray properties of hot, massive stars

Yaël Nazé[1*]

[1] GAPHE, Dépt AGO, ULg, Allée du 6 Août 17, Bât B5C, B4000-Liège, Belgium

Abstract: The recent X-ray observatories have not yet provided a large survey comparable (in sky coverage) to that based upon the *ROSAT* All-Sky Survey (RASS). However, two limited surveys exist : the 2XMM catalog for *XMM-Newton* (294 OB stars detected) and the Carina large-scale survey from *Chandra* (129 OB stars detected). Medium-resolution (CCD) spectra were analyzed and led to new results on the relationship between the X-ray luminosity and the bolometric luminosity, as well as on the typical properties (plasma temperature, variability) of these objects. This contribution thus presents the results of the first high-sensitivity investigation of the overall high-energy properties of a sizeable sample of hot stars.

1 Introduction

The X-ray emission of massive stars was serendipitously discovered 30 years ago in Cygnus OB2, Orion and Carina nebulae (Harnden et al. 1979, Ku & Chanan 1979, Seward et al. 1979). Very soon, a proportionality between the X-ray and optical/bolometric luminosities was detected (Harnden et al. 1979, Pallavicini et al. 1981). It is now called the 'canonical' relation ($L_X \sim 10^{-7} \times L_{BOL}$).

At first, such a relationship could appear surprising, as the X-ray emission of low-mass objects is rather related to rotation and/or age. However, for massive stars, most phenomena are linked to the presence of stellar winds, and the X-ray emission makes no exception. A short summary of the argument is: the winds are line-driven, thus depend on the stellar bolometric emission; this driving process is unstable, creating shocks throughout the wind; these shocks generate hot plasma, hence X-ray emission. Owocki & Cohen (1999) formally showed that the X-ray luminosity "naturally" scales with the wind density parameter $\dot{M}/v_\infty$. It then scales with the bolometric luminosity if there is "a delicate balance between X-ray emission and absorption" and "a special form for the radial distribution of wind shocks[1]" (for details see Owocki & Cohen 1999).

Observationally, the first global investigation of the $L_X - L_{BOL}$ relation was reported by Berghöfer et al. (1997). Cross-correlating the *ROSAT* All-Sky Survey (RASS) with the Yale bright star catalog, Berghöfer et al. (1997) found 216 detections of O and B stars, down to fluxes of 10^{-13} erg cm^{-2} s^{-1}, with a decreasing detection rate as one goes to later types (all O-stars earlier than O7 were detected whereas the fraction is only 6.5% for B2 stars). Using the RASS count rates and hardness ratios together with the interstellar column densities derived from the optical Yale photometry,

*Research Associate FNRS; the author acknowledges support from the FNRS (Belgium), the PRODEX *XMM* and *Integral* contracts, and the 'Action de Recherche Concertée' (CFWB-Académie Wallonie Europe).

[1]The X-ray filling factor should follow r^{-s} with s equal to 0.25–0.4. Note however that recent fitting of X-ray lines by embedded wind-shock models rather yields $s = 0$ (Cohen et al. 2006).

Berghöfer et al. (1997) evaluated the temperatures and unabsorbed X-ray luminosities for each star. The $L_X \sim 10^{-7} \times L_{BOL}$ relation was confirmed down to bolometric luminosities of 10^{38} erg s^{-1} (i.e. spectral types B1–1.5), but a large scatter (0.4 dex) was found around this relation. In addition, when comparing RASS and pointed observations, Berghöfer et al. (1997) detected no variations of the count rates of massive stars — note that this excludes only large variations, since the errors on the RASS count rates are quite large.

2 The $L_X - L_{BOL}$ relation revisited

2.1 Observations of clusters or associations

In the last decade, no further global X-ray survey was made, but the *XMM-Newton* and *Chandra* observatories have performed several sensitive observations of clusters and associations, some of these containing enough massive stars for a (limited) statistical study. In general, the $L_X \sim 10^{-7} \times L_{BOL}$ relation was once more confirmed. However, the scatter around the relation differs from that of the RASS study: when the properties of the massive star population were well known (i.e. deep photometric observations and spectral monitoring were available to assess both multiplicity and stellar parameters), the scatter was reduced to 0.1–0.2 dex (see the cases of NGC 6231, Sana et al. 2006; or Carina, Antokhin et al. 2008 or Nazé et al. 2010). The scatter remained large only when the stellar properties were known approximately (e.g. Westerlund 2, Nazé et al. 2008, or Cygnus OB2, Albacete Colombo et al. 2007). One could wonder where this difference in scatter comes from. Indeed, when comparing the two "philosophies" of these studies, clear differences appear (see Table 1) but it is unclear which one really explains the scatter problem.

It is important to note that, not considering the scatter, comparing recent studies with each other is not an easy task, as the effects of heterogeneous treatments can be surprisingly large. Indeed, the absolute value of $\log(L_X/L_{BOL})$ is always close to –7, but varies from one study to another. A good example is provided by the Carina studies: *XMM-Newton* data yielded $\log(L_X/L_{BOL}) = -6.58$ (Antokhin et al. 2008) whereas *Chandra* data led to $\log(L_X/L_{BOL}) = -7.26$ (Nazé et al. 2010). Crowding, as the cluster is seen with different spatial resolutions, does not seem to be the cause, nor the spectral fitting itself (similar models used); the main differences rather lie in the R_V, gas-to-dust ratio $N_H/E(B-V)$, and BCs (which are used to evaluate L_{BOL}). As a proof, using R_V of 3.1 rather than 4.0 yields $\log(L_X/L_{BOL}) = -6.99$ for the *Chandra* study, i.e. a reduction of the difference with the *XMM* study from 0.7 dex to 0.4 dex (Nazé et al. 2010).

2.2 The 2XMM survey

To really assess the origin of the scatter difference and search for potential cluster-to-cluster differences, one should combine both approaches. This has been made possible thanks to the 2XMM survey. With 220 000 X-ray sources, it is the largest X-ray catalog available at the present time. It consists of 4117 *XMM-Newton* archival datasets processed homogeneously by the SSC (Watson et al. 2009). Indeed, it is not an all-sky survey — it covers only 1% of the sky, biased to extragalactic fields — but it is still very useful for large, statistical studies. In the context of $L_X - L_{BOL}$ studies, it combines a high sensitivity (enabling detailed spectral/timing studies), an homogeneous treatment (single facility, single reduction of the data, single R_V,...), and a large sample (heterogeneous population like in RASS). The 2XMM catalog was cross-correlated with a recent catalog of O and B stars (Reed catalog, version of 2009 made available by the author) which includes the latest monitoring hence provides an up-to-date knowledge of the stellar properties: 294 O and B stars were detected in the X-ray range, down to fluxes of 10^{-14} erg cm^{-2} s^{-1}, and 128 sources display enough counts for a

Table 1: Comparison between RASS and *XMM/Chandra* studies of the $L_X - L_{BOL}$ relation.

RASS	*XMM/Chandra*
Survey (i.e. full sky)	A single cluster or association at a time
→ heterogeneous population (field+clusters)	→ homogeneous population
→ large sample, many spectral types	→ small sample, not all spectral types
→ short exp. times	→ deep exposure
Homogeneous treatment	Heterogeneous treatment
→ single instrument and reduction software	→ several instruments and reduction softwares
→ single R_V, BC,...	→ different R_V, BC,... for each cluster/ass.
Sp. types & photom. from general catalog	Sp. types & photom. from specific monitoring
L_X from count rates and HRs	L_X from detailed spectral fitting
Only ISM absorption	ISM + "wind" absorption

detailed spectral study (Nazé 2009). The distribution by subtype of the detected O-type stars closely follows that of the full Reed catalog: no bias is therefore detected. For B-type stars, however, there is a clear lack of detections of the late-type objects compared to early-type ones, and of giant stars compared with supergiants and main sequence objects. The former was already reported by Berghöfer et al. (1997), but the latter remains unexplained as such (but could be an artifact from the spectral type-luminosity class sampling). Variability was investigated at two levels: during exposures (provided there were enough counts) and between exposure (when several were available). Considering a 1% significance level, less than 1/10 of the O and B stars show variability during one exposure (and in the rare cases where it is detected, the lightcurves are compatible with PMS-like flares) but up to 70% of the stars display variability between exposures, with no obvious difference between O and B stars or single and binaries. It must be noted that, due to the high sensitivity of *XMM-Newton*, the changes reported here were well below the RASS detection threshold. While some variations are expected from the embedded-wind shock model, they should be rather stochastic, without long-term trends, and of very small amplitude. The detected variations therefore remain to be fully explained.

The spectral fitting was made using a model with two absorptions (one fixed to the interstellar value, the other let free to vary in order to represent a potential "wind" absorption) and a sum of optically-thin thermal plasma emissions (usually two, one only when the signal-to-noise was low). This is consistent with the models used in the cluster/associations studies mentioned above. An additional absorption (of the order of $\sim 0.4 \times 10^{21}$ cm^{-2}) is definitely needed to fit the spectra of O-type stars, while B-type stars rather show no absorption beyond the interstellar component. Concerning plasma temperatures, the dominant component always lies higher than 1 keV for B-type stars but amounts to only 0.2 or 0.6 keV for O-type stars, thereby confirming cluster studies (e.g. Sana et al. 2006). It is important to note, however, that the second thermal component often appears at $\sim$2 keV for O-type stars. This is not expected in the embedded-wind shock model, which predicts only soft X-ray emission. The origin of such a hard component must therefore be investigated: does it come from magnetic phenomena, from colliding wind emission (assuming therefore that most of these "single" stars actually are binaries), or from an entirely different direction? The question remains open.

Finally, the estimation of the $F_X/F_{BOL} = L_X/L_{BOL}$ ratios for the O-type stars shows a rather high dispersion, actually very similar to that of the RASS. It therefore seems that the observed scatter is not an artifact from the treatment itself (e.g. conversion of count rates vs. detailed spectral fitting) but is rather intrinsic to the massive star population. Considering subsamples of the 2XMM data indeed show hints of intercluster differences, but these differences are below or about the dispersion itself, hence not formally significant. Further investigation is needed to see which physical parameter,

beyond the bolometric luminosity, influences the X-ray emission. Studies of stars with different metallicities, in the Magellanic Clouds for example, would be invaluable in this context.

3 Additional information

Beyond the $L_X - L_{BOL}$ studies, the *XMM* and *Chandra* data yielded several additional results. One of them is a revision of our view on binaries. A decade ago, it was common wisdom to consider that a massive binary implies the presence of two winds which must collide and therefore leads to an enhanced (and harder) X-ray emission. The equality "binary$\Longleftrightarrow$X-ray overluminosity" is still quite popular, as exemplified by some recent papers (e.g. Crowther et al. 2010). However, the sensitive observations of *XMM* and *Chandra*, together with a better knowledge of the stellar population, have forced us to revise what now appears as an "urban legend"[2] (Oskinova 2005, Sana et al. 2006, Nazé 2009, Nazé et al. 2010). In NGC 6231, only two binary systems appear (slightly) overluminous (HD 152248 and CPD –41°7742, Sana et al. 2006), while in Carina, only one binary system is overluminous (HD 93403, Nazé et al. 2010). Binaries and single objects indeed appear mixed, i.e. at similar positions or $\log(L_X/L_{BOL})$ ratios, in $L_X - L_{BOL}$ diagrams. It must be noted, however, that these ratios are systematically larger for binaries whatever the energy band considered, but the difference is always below the dispersion of each sample (single or binary) around the $L_X - L_{BOL}$ relation (Nazé et al. 2010), e.g. $\log(L_X(0.5-10.keV)/L_{BOL}) = -7.26 \pm 0.21$ and -7.16 ± 0.21 for single stars and binaries in Carina, respectively. This implies that it is quasi-impossible to detect binarity by looking at the L_X/L_{BOL} ratio alone, since only few multiple systems show X-ray bright wind-wind emission. Detailed MHD modelling, as well as more observations of O+OB binaries (in order to study the influence of a single parameter, e.g. period, for otherwise similar stellar systems), should help pinpoint the cause of this rarity (effect of radiative braking, lack of ram pressure balance?).

In addition, it is also interesting to sample the O- to B-stars transition. Whatever the parameter envisaged (e.g. L_X/L_{BOL} ratio, medium-to-soft X-ray flux ratio), the earliest B-type stars always show properties close to those of the latest O-type stars. There thus seems to be a smooth transition from O- to B- stars, with a decreasing influence of the X-ray production by the embedded wind-shock process and another process growing in influence towards later B types (Nazé et al. 2010).

Finally, two additional parameters could be investigated thanks to the spectral fits: the average plasma temperature $< kT >= \sum kT \times norm_i / \sum norm_i$ and the medium-to-soft flux ratio $HR = F_X^{unabs}(1-2.5keV)/F_X^{unabs}(0.5-1keV)$. The average temperature is indeed well below 1 keV for O-type stars, except for a few peculiar systems. In a graph of L_X/L_{BOL} ratio vs. average temperature (e.g. Fig. 1), the "normal" O-type stars display low temperatures and L_X/L_{BOL} ratios and colliding wind binaries as well as objects with magnetically confined winds are expected to display both high temperatures and ratios. However, there appears to be a number of objects showing low temperatures but high ratios or high temperatures and low ratios: their nature is unknown, and both observational as well as theoretically follow-up studies are needed to understand them.

Considering the medium-to-soft flux ratio, it increases with average plasma temperature, as could reasonably well be expected, but there are also shallow increasing trends of this ratio with larger L_X/L_{BOL} (Fig. 1) or larger bolometric luminosities. These trends, which must be confirmed, could be related to two different effects, not mutually exclusive. One is that the plasma temperature could increase with bolometric luminosity (as possibly observed in the line ratio trends found by Walborn et al. 2009), another is that, at constant plasma temperature, the medium-to-flux ratio can change if the "additional absorption" varies (indeed, the L_X in the L_X/L_{BOL} ratio has been corrected only for

[2]For O+O systems at least, since evolved systems such as WR+O do appear overluminous, the question of the actual level of the intrinsic X-ray emission of (evolved) WRs stars being still debated.

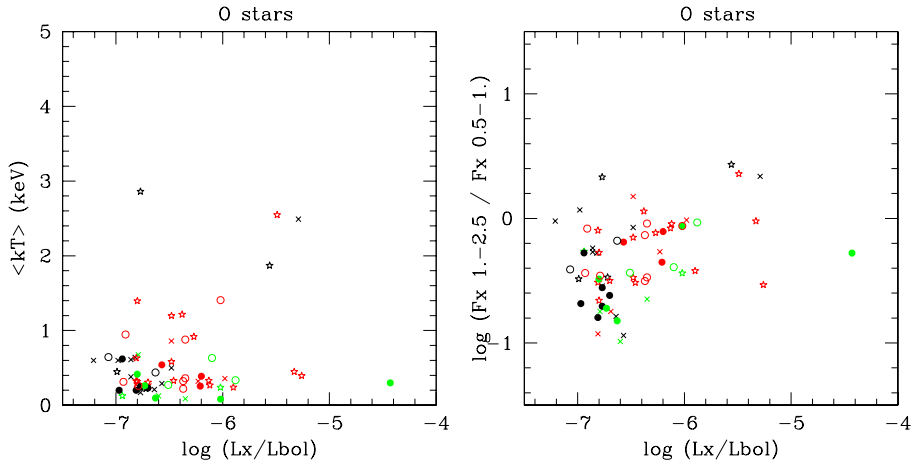

Figure 1: Average temperature (left) or medium-to-soft flux ratio (right) plotted against the L_X/L_{BOL} ratio. Crosses (resp. filled dots) correspond to single (resp. binary) stars showing no variation, stars (resp. open circles) to variable single (resp. binary) stars; black, red and green colors correspond to 1T, 2T and 3T spectral fits, respectively.

the interstellar absorption and, if the wind absorption is larger for larger bolometric luminosities, this could explain the observed shallow trend — note however that no obvious trend, not even a shallow one, of "wind" absorption vs. bolometric luminosity was detected in Carina (Nazé et al. 2010).

4 Conclusions

In the last decade, sensitive X-ray observations have led to several unexpected results. The scatter found in the RASS for the $L_X - L_{BOL}$ relation is not an effect from the poor X-ray data available back then, but a real phenomenon: cluster-to-cluster differences should exist. The X-ray variability of O and B stars is rare on short timescales but rather common on long timescales, though still unexplained. The spectral fits reveal a generally soft character of the X-ray emission of O-type stars, but a faint, hard component does exist in many cases — again of unknown origin. Finally, X-ray bright binaries are quite rare, though X-ray overluminosities are still a valid "binarity criterion" at the present time.

Acknowledgements

The author acknowledges support from the FNRS (Belgium), the PRODEX *XMM* and *Integral* contracts, and the 'Action de Recherche Concertée' (CFWB-Académie Wallonie Europe).

References

Albacete Colombo, J. F., Flaccomio, E., Micela, G., Sciortino, S., & Damiani, F. 2007, A&A, 464, 211
Antokhin, I. I., Rauw, G., Vreux, J.-M., van der Hucht, K. A., & Brown, J. C. 2008, A&A, 477, 593
Berghöfer, T.W., Schmitt, J.H.M.M., Danner, R., & Cassinelli, J.P. 1997, A&A, 322, 167
Cohen, D.H., Leutenegger M.A., Grizzard, K.T., Reed, C.L., Kramer R.H., & Owocki, S.P. 2006, MNRAS, 368, 1905
Crowther, P.A., Schnurr, O., Hirschi, R., Yusof, N., Parker, R. J., Goodwin, S.P., & Kassim, H.A. 2010, MNRAS, 408, 731
Evans, N.R. 2011, in Proceedings of the 39th Liège Astrophysical Colloquium, eds. G. Rauw, M. De Becker, Y. Nazé, J.-M. Vreux & P.M. Williams, BSRSL 80, 663

Harnden, F. R. Jr., et al. 1979, ApJ, 234, L51
Ku, W.H.M., & Chanan, G.A. 1979, ApJ, 234, L59
Nazé, Y., Rauw, G., & Manfroid, J. 2008, A&A, 483, 171
Nazé, Y. 2009, A&A, 506, 1055
Nazé, Y., et al. 2010, ApJS, submitted
Oskinova, L. 2005, MNRAS, 361, 679
Owocki, S.P., & Cohen, D.H. 1999, ApJ, 520, 833
Pallavicini, R., Golub, L., Rosner, R., Vaiana, G. S., Ayres, T., & Linsky, J. L. 1981, ApJ, 248, 279
Reed, B. C. 2003, AJ, 125, 2531
Sana, H., Rauw, G., Nazé, Y., Gosset, E., & Vreux, J.-M. 2006, MNRAS, 372, 661
Seward, F.D., et al. 1979, ApJ, 234, L55
Walborn, N.R., Nichols, J.S., & Waldron, W.L. 2009, ApJ, 703, 633
Watson, M. G., et al. 2009, A&A, 493, 339

Discussion

A. Willis: You mentioned that the O-binaries do not often show enhanced $L_X/L_{\rm Bol}$, as would be expected with CWB X-ray emission. Was there any evidence for these binaries of harder X-ray emission than for single O-stars?
Y. Nazé: No, the binaries showing no "peculiar" $L_X/L_{\rm Bol}$ do not show any significantly higher $< kT >$ ... Binaries in general have slightly higher average temperatures (cf. Carina analysis in Naz et al. 2010), but the dispersion is high for both single and binaries, and therefore binaries really lie amongst the "single" objects in terms of luminosity and temperature.

H. Zinnecker: I have a question on the X-ray emission of B-stars. People have suggested that their rather hard spectrum (≈ 2 keV) may be associated with T Tauri (low-mass) companions which are known to have coronal temperatures of 1-2 keV.
Have you followed this discussion and what is the current status? As an aside, would X-ray observations be sensitive enough to detect T Tauri companions to O-stars?
Y. Nazé:

1. Concerning B-type stars: hard emission, together with the reduced detection rate and an X-ray luminosity close to that of PMS stars, have indeed been seen as hints/evidence that the X-ray emission did not come from the B stars themselves. This is still considered as a good possibility — see, e.g., NGC 6231 (Sana et al. 2006) and Carina (Evans et al. 2011).

2. Concerning O-type stars: it is possible in principle if considering the late O-type stars and the most intense flares of PMS stars (otherwise, the X-ray luminosity of O stars is too high to detect the faint one from a PMS star).
   Additional note: some flares and PMS-like characteristics have been detected for some late O or early B stars (e.g. σ Ori E). These objects have been confirmed as magnetic, so that it is the same underlying phenomenon but truly linked to the massive stars.

N. Evans: In response to the question about whether X-ray sources associated with B-type stars could be due to T Tauri companions:

- it is not surprising that we do not identify (in general) T Tauri companions to O stars since the O-star X-ray luminosity is stronger than that of T Tauri stars;

- starting from the assumption that X-rays from B stars are from T Tauri companions, we (Evans 2011) derive a fraction of low mass companions (mid F through K-type stars) for B stars later than B3 in Trumpler 16.

The Stellar Wind of LS 5039

Christina Aragona[1] , M. Virginia McSwain[1], and Mallory S. E. Roberts[2]

[1] Department of Physics, Lehigh University, USA
[2] Eureka Scientific, Inc., USA

Abstract: LS 5039 is an unusual high mass X-ray binary that also exhibits $\gamma-$ray emission modulated with its orbital period. The system consists of an ON6.5V((f)) star and an unidentified compact companion. Using the Australia Telescope Compact Array (ATCA), we have measured radio fluxes at 20cm, 13cm, 6cm, and 3cm between 2008 February and 2009 July. We have observed the Hα line with the Goodman High Throughput Spectrograph on the Southern Astrophysical Research (SOAR) telescope from 2010 June $2-4$. Here we combine these multiwavelength data to examine the structure of the massive star wind.

1 Introduction

LS 5039 is a member of the recently discovered class of γ-ray binaries. It consists of an ON6.5 V((f)) primary and an unidentified compact companion in a tightly bound, eccentric orbit with an orbital period of 3.906 days (McSwain et al. 2004; Casares et al. 2005; Aragona et al. 2009). The photosphere shows evidence of carbon depletion and nitrogen enrichment, indicating that mass transfer likely occurred between the O star and the supernova progenitor (McSwain et al. 2004). The system has a runaway velocity of 150 km s^{-1}, likely imparted by an asymmetric supernova explosion that occurred about 1.1 Myr ago (Ribó et al. 2002; McSwain et al. 2004).

The system has a low X-ray flux modulated with the orbital period and a hard spectrum (Bosch-Ramon et al. 2005; Takahashi et al. 2009). Both Fermi (energies between 100 MeV to 300 GeV) and HESS (energies above 0.1 TeV) have detected LS 5039 (Abdo et al. 2009; Aharonian et al. 2005, 2006). Both data sets confirm variability in the γ-ray emission modulated with the orbital period of the system.

Ribo et al. (2008) observed the system using the VLBA. Their two observations were spaced 5 days apart and showed a 12° change in the position angle of the system. Observations in the low-frequency radio regime, using the GMT, showed evidence of a spectral turnover at $\sim$ 964 MHz (Godambe et al. 2008). Bosch-Ramon (2009) used this collection of data to constrain a model of the radio emission sources in the system. He concludes that the low-frequency radio emission originates several AU from the primary star. Emission was also detected at 234 MHz.

In this work, we present observations of the Hα line taken with the Southern Astrophysical Research Telescope (SOAR) in order to probe the stellar wind of LS 5039. From this data set, we are able to derive a mass loss rate for the system and search for signs of changing wind morphology. We also present preliminary results from radio observations taken using the Australia Telescope Compact

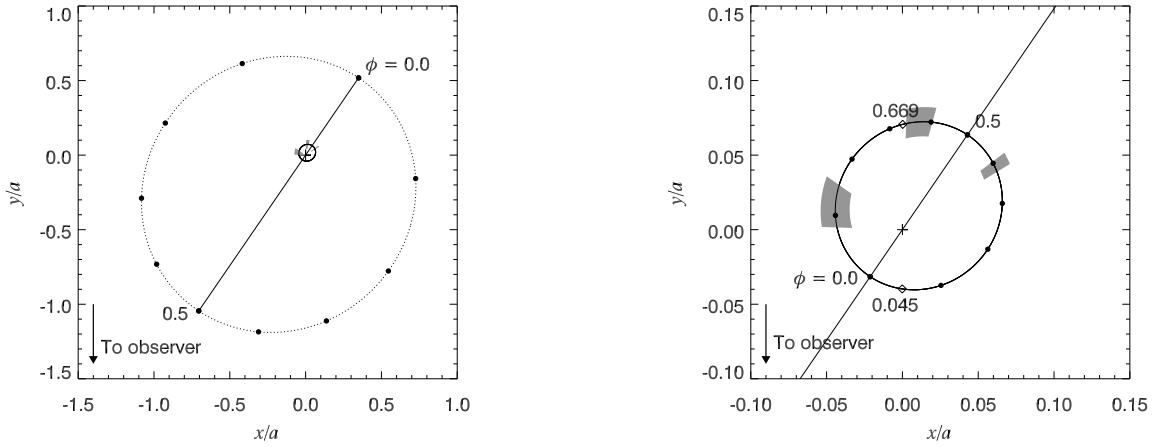

Figure 1: Left: the relative orbit of LS 5039 as seen from above. The black circles mark intervals of 0.1 phase. The dotted line represents the orbit of the compact object, which we assumed to have a mass of 1.4 $M_\odot$. The solid line represents the orbit of the O star, assumed to have a mass of 23 $M_\odot$ (Casares et al. 2005). Right: a close up view of the O star orbit, to highlight the orientation of the system during our SOAR observations. The gray shaded regions indicate the phases of our observations. The diamonds mark the phases of inferior and superior conjunction.

Array (ATCA). We compare these flux measurements with the expected thermal radio emission, calculated using the mass loss rates obtained from the Hα equivalent width, to confirm the fraction of the total radio emission due to non-thermal processes.

2 Observations

2.1 Optical

We observed LS 5039 using the Goodman High Throughput Spectrograph (GHTS) on SOAR from 2–4 June 2010. We used the 1200 l/mm grating in 1^{st} order to obtain a wavelength range of 5550–6850 Å and a resolving power, $R = \lambda/\delta\lambda$ = 6000–7000. Exposure times ranged from 10 to 15 minutes in duration. A flat field and a Ne comparison lamp spectrum were taken after each exposure, and spectra were zero-corrected, flatfielded, and wavelength calibrated using standard procedures in IRAF[1]. Our observations were taken between orbital phases 0.38–0.92 (see Figure 1, right), calculated using the orbital ephemeris from Aragona et al. (2009).

2.2 Radio

Radio observations were taken using the Australia Telescope Compact Array (ATCA) between 2008 February and 2009 July. Each observation spanned a 2–3 hour period. We switched between the 3cm/6cm back end and 13cm/20cm back end 2–3 times over each observation to ensure that the mid-exposure times at each wavelength were approximately the same. Data were reduced using standard procedures in MIRIAD. We defined the location of bright sources in our field and used the CLEAN algorithm to model the observed radio flux in each wavelength band. After five iterations of cleaning

[1]IRAF is distributed by the National Optical Astronomy Observatory, which is operated by the Association of Universities for Research in Astronomy, Inc., under cooperative agreement with the National Sciences Foundation

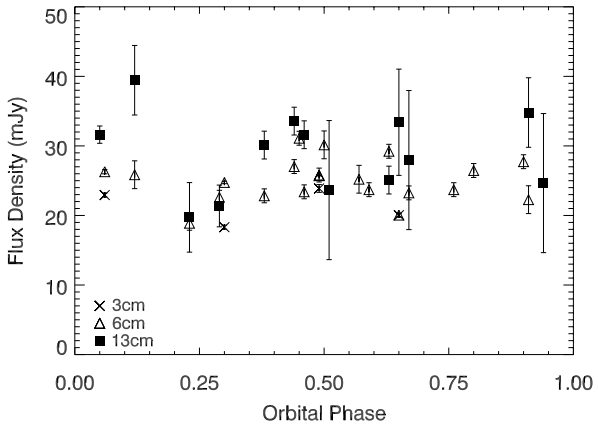

Figure 2: Radio flux measurements of LS 5039.

and self calibration, we used the *imfit* module to measure the flux from LS 5039. The results for the 3cm, 6cm, and 13cm data are plotted in Figure 2. The 20cm fluxes are still being reduced.

3 Hα Equivalent Widths and Mass Loss Rates

We coadded the spectra from SOAR in sets of two to improve the signal-to-noise, S/N, of the data and used the orbital ephemeris of Aragona et al. (2009) to shift the Hα line in each observation to the rest wavelength. Casares et al. (2005) noted blue-shifted points in their radial velocity data at phase 0.45. The radial velocity curved used to determine the orbital parameters in Aragona et al. (2009) showed additional blue-shifted points between phases 0.4 and 0.6. To investigate the source of these spurious points, we examined Hα for changing line profiles which would indicate the presence of large scale structures in the wind (such as a focused wind stream). The resulting plot is shown in Figure 3. The line profile does not show variation above the level of the noise.

We also determined the mass loss rate of the system (Figure 4) from the equivalent width of the Hα line, $W_{H\alpha}$, using the method of Puls et al. (1996) and assuming a β=1 velocity law. The measurements show considerable scatter but no significant variation correlated with orbital phase. We find an average mass loss rate of 1.9 x 10^{-8} $M_\odot$ yr^{-1}. Spectra from the Goodman spectrograph suffer from fringing near the Hα line. Thus far, we have not corrected for this effect. Once we correct for fringing, we will reexamine these spectra for small variations in the line profile which might indicate large scale structure in the wind.

4 Radio Emission from the Stellar Wind

Our preliminary optical results justify assuming a spherically symmetric stellar wind when modeling the radio emission. We calculated the free-free opacity due to ionized electrons in the wind and determined the optical depth, τ_ν, of the wind as a function of stellar distance using the method outlined in Lamers and Cassinelli (1999). The free-free optical depth is

$$\tau_\nu = 1.13 \times 10^{-4} \frac{g_\nu}{\mu^2} \nu^{-2} R^{-3/2} \left(\frac{\dot{M}}{v_\infty} \right)^2 R_\star^{-3} \int_r^\infty x^{-4} w^{-2} dr \qquad (1)$$

where μ is the mean atomic mass, ν is the frequency, g_ν is the gaunt factor, T is the temperature of the wind, $\dot{M}$ is the mass loss rate, v_∞ is the terminal wind velocity, $R_\star$ is the radius of the star, w is

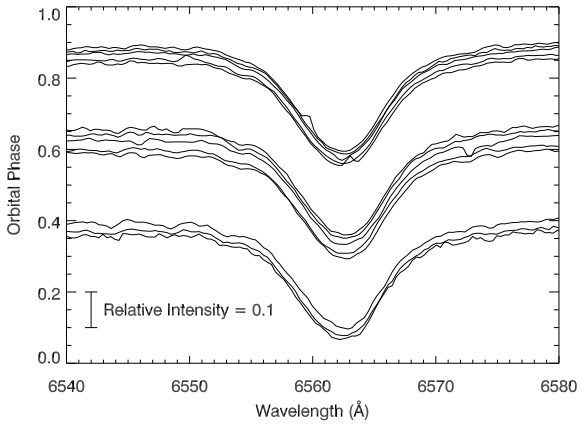

Figure 3: The Hα line from the SOAR observations. Consecutive pairs of spectra were coadded to improve S/N. We shifted each spectrum to the rest wavelength to highlight any variations in the line profile due to structure in the stellar wind.

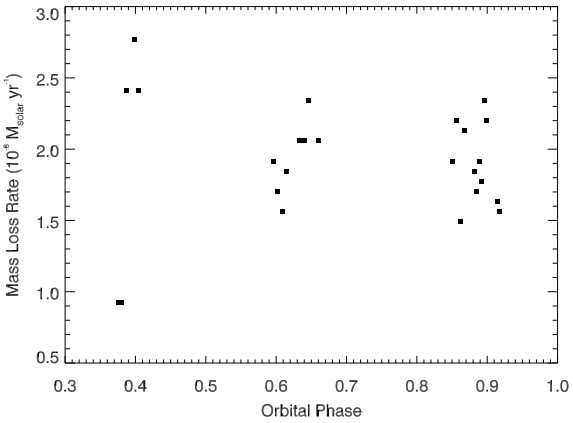

Figure 4: The mass loss rate of LS 5039 plotted as a function of orbital phase. We estimate an error of 0.5×10^{-8} $M_\odot$ yr^{-1} originating from measuring $W_{H\alpha}$ rather than any real variation in the mass loss rate of the system over the orbital period.

Table 1: Radio flux expected from a thermally emitting stellar wind compared to our measured fluxes.

λ (cm)	20	13	6	3
R(τ_ν = 1/3) ($R_\odot$)	223.3	167.4	102.3	65.1
$F_{predicted}$ (mJy)	0.00008	0.0002	0.0009	0.0034
$\langle F_{observed} \rangle$ (mJy)	–	29.0	25.0	21.3

the wind velocity divided by v_∞, and x is the distance from the star divided by $R_\star$. We assumed a fully ionized hydrogen wind following a β=1 velocity law. All values are in cgs units.

We calculated the distance from the star at which τ_ν=1/3, where the stellar wind becomes opaque to radio waves. We assumed that the wind would emit as a blackbody at this radius and used the Rayleigh-Jeans approximation to estimate the resulting radio flux predicted at 3cm, 6cm, 13cm, and 20cm. The results are shown in Table 1. The calculated radio flux expected from a thermally emitting stellar wind is on the order of μJy for each wavelength band. By contrast, our radio observations (Figure 2) show fluxes on the order of 10–40 mJy. Clearly the bulk of the radio flux in this system is not due to a thermally emitting stellar wind.

We performed a preliminary calculation of the spectral index using pairs of 3cm/6cm and 6cm/13cm fluxes that were observed simultaneously. Purely thermal radio emission from the stellar wind should have a spectral index, Γ, of -0.6, where $F_\nu \alpha \nu^{-\Gamma}$. For the 6cm/13cm points, values for α lie between 0.5 and -1.0, have error bars larger than the scatter in the points, and show no obvious trends with respect to orbital phase. For the 3cm/6cm fluxes, the values are between -0.2 and 0.6. However, the 3cm data set has proven more problematic to reduce, resulting in fewer reliable flux measurements at the time of these calculations. Consequently, we cannot draw any conclusions about the source of the emission at this time. We hope that improving the error bars on the observed radio fluxes and adding the 20cm data points will allow us to achieve better results in the future.

5 Conclusion

The error bars on the radio observations are fairly large, but there appears to be real variation in radio emission with respect to orbital phase, particularly between phase 0.0 and phase 0.25. The observed radio flux variations cannot be explained by pure free-free emission produced in the stellar wind of the primary, as this should be constant with respect to orbital phase. The emission is probably generated by the interaction between the stellar wind and the compact object. The correlation of the radio emission with orbital phase suggests a wind-wind interaction region: the variations in radio emission produced by a precessing jet should not depend on orbital phase. In the colliding wind scenario, a non-thermal distribution of particles is ejected into the shock region from the relativistic pulsar wind. This material will flow away from the shock region in a comet like tail, with emission dominated by synchotron losses. The radio emission expected from such a scenario would be modulated with orbital phase (Dubus 2006). Furthermore, a radio map of such a configuration would bear some resemblance to a microquasar jet (Dubus 2006), which is consistent with the observations of Paredes et al. (2000).

Due to the different optical depths for radio waves and Hα, we can assume that our observations probe two different regions of the stellar wind, with the Hα line carrying information about the wind closer to the star. Future work will include more detailed modeling of the interaction between the neutron star and the stellar wind.

Acknowledgements

We are grateful for support from NASA DPR Nos. NNX 08AV70G, NNX 09AT67G, and Lehigh University. We would like to thank Sean Points for aiding us with the use of the SOAR GHTS and data reduction, and P. Edwards and R. Wark for scheduling and aid in taking observations with ATCA.

References

Abdo, A. A., Ackermann, M., Ajello, M., Atwood, W. B., Axelsson, M., Baldini, L., Ballet, J., Barbiellini, G., et al. 2009, ApJ, 706, L56

Aharonian, F., Akhperjanian, A. G., Aye, K.-M., Bazer-Bachi, A. R., Beilicke, M., Benbow, W., Berge, D., Berghaus, P., et al. 2005, Science, 309, 746

Aharonian, F., Akhperjanian, A. G., Bazer-Bachi, A. R., Beilicke, M., Benbow, W., Berge, D., Bernlöhr, K., Boisson, C., et al. 2006, A&A, 460, 743

Aragona, C., McSwain, M. V., Grundstrom, E. D., Marsh, A. N., Roettenbacher, R. M., Hessler, K. M., Boyajian, T. S., & Ray, P. S. 2009, ApJ, 698, 514

Bosch-Ramon, V. 2009, A&A, 493, 829

Bosch-Ramon, V., Paredes, J. M., Ribó, Miller, J. M., Reig, P., & Martí, J. 2005, ApJ, 628, 388

Casares, J., Ribó, M., Ribas, I., Paredes, J. M., Martí, J., & Herrero, A. 2005, MNRAS, 364, 899

Dubus, G. 2006, A&A, 456, 801

Godambe, S., Bhattacharyya, S., Bhatt, N., & Choudhury, M. 2008, MNRAS, 390, L43

Lamers, H. J. G. L. M., & Cassinelli, J. P., 1999, *Introduction to Stellar Winds* (New York, NY: Cambridge University Press)

McSwain, M. V., Gies, D. R., Huang, W., Wiita, P. J., Wingert, D. W., & Kaper, L. 2004, ApJ, 600, 927

Paredes, J. M., Martí, J., Ribó, M., & Massi, M. 2000, Science, 288, 2340

Puls, J., Kudritzki, R.-P., Herrero, A., Pauldrach, A. W. A., Haser, S. M., Lennon, D. J., Gabler, R., Voels, S. A., et al. 1996, A&A, 305, 171

Ribó, M., Paredes, J. M., Moldón, J., Martí, J., & Massi, M. 2008, A&A, 481, 17

Ribó, M., Paredes, J. M., Romero, G. E., Benaglia, P., Martí, J., Fors, O., & García-Sánchez, J. 2002, A&A, 384, 954

Takahashi, T., Kishishita, T., Yasunobu, U, Tanaka, T., Yamaoka, K., Khangulyan, D., Aharonian, F. A., Bosch-Ramon, V., et al. 2009, ApJ, 697, 592

Ion Fractions and the Weak Wind Problem

Matthew Austin and Raman Prinja

Department of Physics and Astronomy, University College London,
Gower Street, London, WC1E 6BT, United Kingdom

Abstract: Some late-type O stars are observed to display anomalously weak winds. This issue and the uncertainty about the nature of wind clumping are challenges to line-driven wind theory and need resolving in order to fully understand hot stars. We describe the results from the computation of ion fractions for the various elements in O star winds using the non-LTE code CMFGEN, including parameterisations of microclumping and X-rays. Ion fractions can also be derived from fits to UV wind lines if a mass-loss rate is assumed. We discuss a project to fit unsaturated C IV lines in late O dwarfs, and show that the weak wind scenario could still be a major issue, with some values of $\dot{M}\langle q_{CIV}\rangle$ indicated to be more than an order of magnitude lower than theoretical predictions of mass-loss, and measurements from radio and optical diagnostics.

1 Introduction

There are several spectroscopic diagnostics available for measuring the mass-loss rate of O stars. Each of these has certain advantages and drawbacks, and often requires ill-determined information or parameter knowledge. In the ultraviolet, wind profiles can be matched using the SEI (Sobolev with Exact Integration) method of Lamers, Cerruti-Sola & Perinotto (1987) to yield the product of the mass-loss rate and the ion fraction of the element. The mass-loss results are therefore very dependent upon the wind ionization balance. We compiled a grid of O star models using the spherical non-LTE model atmosphere code CMFGEN (Hillier & Miller 1998), producing a variety of model types from O3 to O9.5, with different wind-clumping scenarios and with or without X-rays. These models have a large number of applications, but here we focus on the run of ion fraction with effective stellar temperature, which was derived for each clumping and X-ray scenario, to assess the possible effects of these two phenomena on the ionization balance in O star winds.

2 Model Ion Fractions

For each spectral type a set of mean ion fractions was calculated for each element, normalised to the range 0.2-0.9v_∞. This was done in order to ensure a direct comparison to empirical fits described in the section below, in which the very lowest and highest velocity positions are excluded so as to avoid any variable phenomena such as DACs.

Figure 1 shows the results for C^{3+} and C^{4+} for dwarfs, which are predicted to account for most of the total carbon population. N, O, Si, P and S were also processed but for brevity are not shown here;

they will be published separately. We focus discussion on carbon, which is pertinent to the project described in the next section. The clumping scenario is either unclumped (smooth wind, volume filling factor 1.0) or moderately clumped (with a volume filling factor of 0.1). The models with X-rays have an X-ray luminosity consistent with the relation $\log L_x/L_{bol} \sim -7$ from e.g. Nazé 2009. When changing to a clumped wind in the absence of X-rays, the higher ionization stage reduces in population at higher temperatures as recombination from higher local density forces the balance in favour of the lower stage. In general this balance appears more fragile when X-rays are implemented and the effect is greater. Bringing X-rays into the unclumped scenario shifts the balance strongly in favour of the upper stage but with a non-negligible portion still in the lower. The supposedly most detailed description of the wind (i.e. with both clumping and X-rays) yields a somewhat uncertain picture, in which it is unclear for much of the O star range whether either ion becomes dominant. A stark difference in the X-ray models is brought about by introducing moderate clumping. Whilst in the unclumped wind, the X-rays cause C^{4+} to be dominant for the whole O star range, the clumping then changes the ionization balance much more than in the non-X-ray models. In order to distinguish the most likely scenario, the profiles in the corresponding model spectra were examined and compared to observations (*IUE, Copernicus, FUSE*). For later type objects we find that it is crucial to include a treatment of X-rays to get realistic N V and O VI lines. The model profiles also seem to suggest a very low level of clumping to be most likely, implying that the bottom-left panel in Fig. 1 is that which should be used.

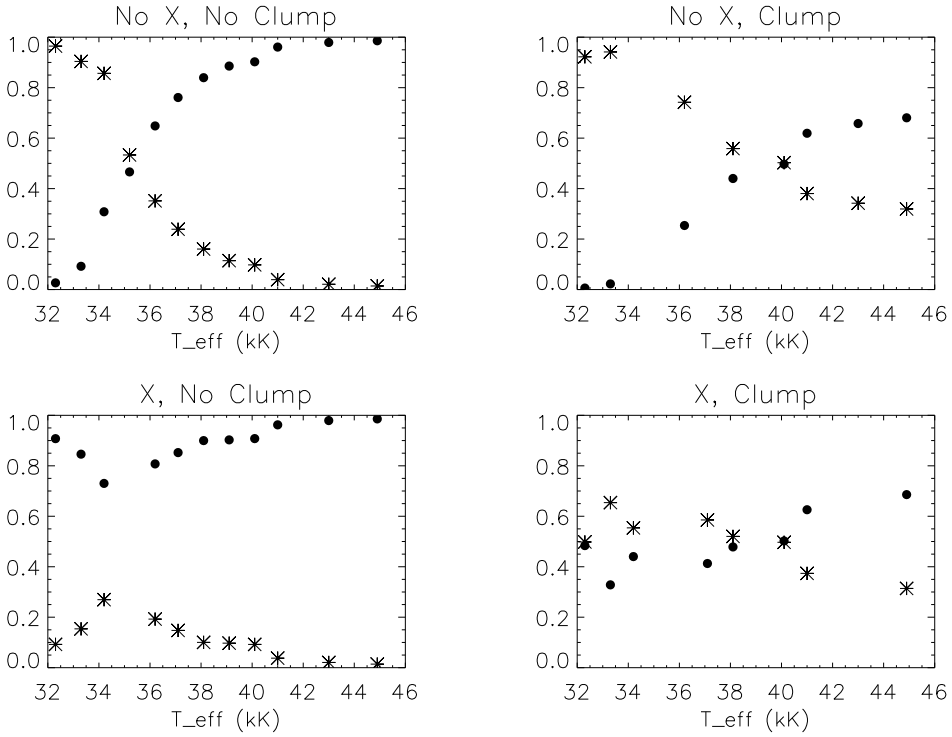

Figure 1: Ion fractions of carbon for different clumping and X-ray scenarios. Dots = C^{4+}, stars = C^{3+}.

3 Mass-loss determination

For later type dwarfs (O6-O9.5) the fraction of C^{3+} is predicted to be either $\sim$0.1 or $\sim$0.5, depending on which clumping scenario is preferred. However, if canonical mass-loss rates are assumed, the ion

fractions derived from empirical modelling are rather different. C IV profiles in a sample of 30 O dwarfs were fitted using the SEI method in order to determine their $\dot{M}\langle q_{C^{3+}}\rangle$. Fig. 2 displays an example fit; that of HD41161. For all objects under investigation the quantity $\dot{M}\langle q_{C^{3+}}\rangle$ is shown in Table 1, and was generally found to be between 2 and 3 orders of magnitude lower than the theoretical predictions of $\dot{M}$ of Vink, de Koter & Lamers (2000), which themselves are approximately in line with measures from other diagnostics (Hα, radio). Even employing the X-ray and unclumped scenario, this is too large a gap once the ion fraction is taken into account. To make up for the disparity between observation and theory, $\langle q_{C^{3+}}\rangle$ would need to be in the range 0.01-0.001, and this is clearly not the case in the CMFGEN models, which show an ion fraction for C^{3+} of 0.1 or more for later type O dwarfs. The remaining discordance could be partly to do with the lack of a treatment for optically thick clumping in the SEI method. This effect has the potential to change how we interpret UV line profiles, as optically thick clumps covering the disk will change the formation of profiles (e.g. Oskinova, Hamann & Feldmeier 2007 and Sundqvist, Puls & Feldmeier 2010), however it would take a highly porous wind to bring UV-derived mass-loss rates in line with theoretical values, if only a spatial porosity is considered. Optically thick clumps as considered by Sundqvist et al. (2010) have been shown to reduce profile sizes using only moderate clumping factors, and so this may be the most likely effect to reconcile the apparent discordance. In addition, Hα becomes insensitive to the mass-loss rate at later O types, and so may skew comparisons to other diagnostics. We believe there still exists a discordance between mass-loss measures, and that new diagnostics, a proper multi-wavelength approach, and a thorough treatment of optically thick clumping are required for O dwarfs.

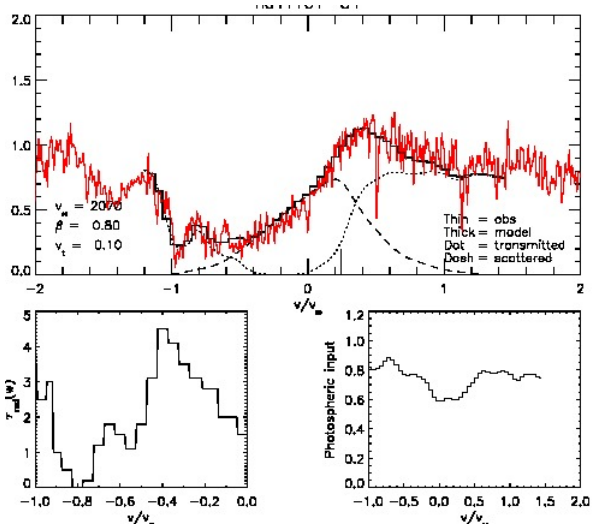

Figure 2: Fit to C IV in HD 41161. Bottom left shows the input radial optical depth; bottom right shows the photospheric contribution from TLUSTY (Hubeny & Lanz, 2003).

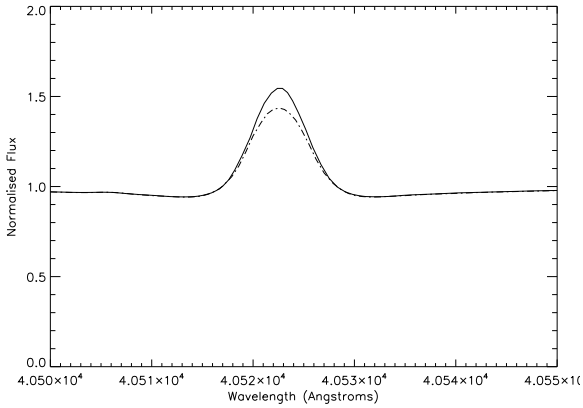

Figure 3: The region around Brα in two CMFGEN models from the grid, nominally of spectral type O9 V. Dotted: $\dot{M} = 1 \times 10^{-9}$; solid: $\dot{M} = 2 \times 10^{-9}$

To provide another diagnostic of mass-loss in weak-winded objects, we are currently gathering spectra of Brα in several Galactic O stars from the C IV investigation, using ESO-VLT/CRIRES. This line is proposed to be an excellent measure of mass-loss in weak-winded stars (Puls, Vink & Najarro 2008) and is far more sensitive in models (Fig. 3) for O dwarfs than its Balmer series counterpart. We plan to determine the Brα mass-loss rate using model atmospheres and compare it directly to the information we already have from C IV and other diagnostics, where possible.

Table 1: The product of C^{3+} fraction and mass-loss rate for the sample of O dwarfs, along with the implied ion fraction based on theoretical mass-loss rates. Effective temperatures are of equivalent CMFGEN models for the given spectral type.

HD/CPD	T_{eff} (kK)	$log(\dot{M}\langle q_i \rangle)$	$log\dot{M}$ (Vink)	Implied $q_i \times 10^{-3}$
5005	38.1	-9.25	-6.47	1.7
12993	38.1	-9.14	-6.36	1.7
17505	38.1	-8.86	-6.30	2.8
42088	38.1	-9.26	-6.33	1.2
54662	38.1	-9.21	-6.30	1.2
93146	38.1	-9.14	-6.42	1.9
93161B	38.1	-9.04	-6.30	1.8
101436	38.1	-9.00	-6.43	2.7
165052	38.1	-9.50	-6.30	0.6
206267	38.1	-8.99	-6.30	2.0
-59 2603	37.1	-9.96	-6.43	3.0
35619	37.1	-9.57	-6.46	0.8
36879	37.1	-9.39	-6.54	1.4
44811	37.1	-9.85	-6.43	0.4
46485	37.1	-9.17	-6.43	1.8
47839	37.1	-9.21	-6.55	2.2
48099	37.1	-9.06	-6.43	2.3
91824	37.1	-9.36	-6.43	1.2
152623	37.1	-9.07	-7.13	11.5
159176	37.1	-9.01	-6.62	4.1
41997	36.2	-9.07	-6.82	5.6
53975	36.2	-9.87	-6.50	4.3
152590	36.2	-9.63	-6.63	1.0
155806	36.2	-9.27	-6.80	3.4
14633	35.2	-10.22	-7.02	0.6
41161	35.2	-9.45	-6.62	1.5
46056	35.2	-9.98	-6.68	0.5
46966	35.2	-9.40	-6.94	3.5
48279	35.2	-8.20	-6.62	26.3
60848	35.2	-9.60	-7.02	2.6
93222	35.2	-8.99	-6.62	4.3
100213	35.2	-9.73	-6.62	0.8
101413	35.2	-9.50	-6.62	1.3
46149	34.2	-10.31	-6.86	0.4
73882	34.2	-9.34	-7.36	10.5
216532	34.2	-10.00	-6.86	0.7
75759	33.3	-10.14	-6.88	0.5
193322	33.3	-9.88	-6.88	1.0
209481	33.3	-9.78	-6.88	0.8
214680	33.3	-10.37	-6.88	0.3
34078	32.3	-10.51	-6.69	0.2
38666	32.3	-10.36	-7.05	0.5
93027	32.3	-10.24	-7.09	0.7
149757	32.3	-9.91	-6.88	0.9

Acknowledgements

MA acknowledges the use of the UCL Legion cluster for computation of models for this work, and help from John Hillier and Adam Burnley for consultation on using the code.

References

Hillier, D. J. & Miller, D. L., 1998 ApJ, 496, 407
Hubeny, I. & Lanz, T., 2003 ASPC, 288, 51
Lamers, H. J. G. L. M., Cerruti-Sola, M., Perinotto, M., 1987 ApJ, 314, 726
Nazé, Y., 2009 A&A, 506, 1055
Oskinova, L. M., Hamann, W.-R., Feldmeier, A., 2007 A&A, 476, 1331
Puls, J., Vink, J. S., Najarro, F., 2008 A&ARv, 16, 209
Sundqvist, J. O., Puls, J., Feldmeier, A., 2010 A&A, 510, 11
Vink, J. S., de Koter, A., Lamers, H. J. G. L. M., 2000 A&A, 362, 295

Tracing WR wind structures by using the orbiting companion in the 29d WC8d + O8-9IV binary CV Ser

Alexandre David-Uraz[1], Anthony F. J. Moffat[1],
André Nicolas Chené[2 3 4] and Nicholas Lange[2]

[1] Département de Physique, Université de Montréal, Canada
[2] Herzberg Institute of Astrophysics/National Research Council, Canada
[3] Facultad de Ciencias Físicas y Matemáticas, Universidad de Concepción, Chile
[4] Facultad de Ciencias, Universidad de Valparaíso, Chile

Abstract: We have obtained continuous, high-precision, broadband visible photometry from the MOST satellite of CV Ser over more than a full orbit in order to link the small-scale light-curve variations to extinction due to wind structures in the WR component, thus permitting us to trace these structures. The light-curve presented unexpected characteristics, in particular eclipses with a varying depth. Parallel optical spectroscopy from the Mont Megantic Observatory and Dominion Astrophysical Observatory was obtained to refine the orbital and wind-collision parameters, as well as to reveal line emission from clumps.

1 Introduction

The primary aim of our project was to probe the structures in the wind of the WR component in the CV Ser WR + O binary by using high-precision photometry. The basic idea is shown in Fig. 1. According to the phase, clumps with different sizes will go through the O star's line of sight, thus producing random dips in the light curve. We can then analyze these dips to find constraints on the sizes and shapes of the clumps.

In early studies (Hjellming & Hiltner 1963, Stepień 1970, Kuhi & Schweizer 1970, Cowley et al. 1971), CV Ser has proved to be a misbehaving binary system, with the depth of its eclipse varying with time. It was even reported to have stopped eclipsing. The most plausible explanation is that the wind of the dust-forming Wolf-Rayet component changed its structure between observations. However, for the first time, we show evidence for two consecutive eclipses with different depths, which might suggest a rapidly varying mass-loss rate.

1.1 Observations

The MOST space telescope observed CV Ser continuously for a period of approximately 45 days during summer 2009. The light curve includes 2 minima of the 29.7d binary. Curiously, both minima

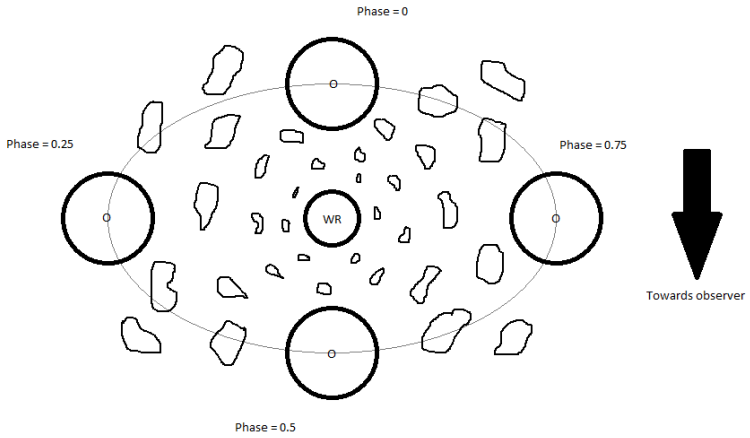

Figure 1: Intuitive model of the effects of clumps on the light curve. Seen here is the projection of the orbital plane along the observer's plane. This figure is not to scale.

have different depths. The light curve was binned to one data point per orbit (101 min) and a 3-sigma clipping was performed. The result is presented in the next section.

As for the spectroscopy, two Canadian observatories were used : Observatoire du Mont-Mégantic (OMM), as well as the Dominion Astrophysical Observatory (DAO). The observing campaigns were synchronous with MOST's, but due to poor weather, long gaps are present in the spectral data. Nevertheless, the RV points obtained from DAO were sufficient to determine that the orbit of CV Ser is circular and well-behaved, as can be seen in Fig. 2.

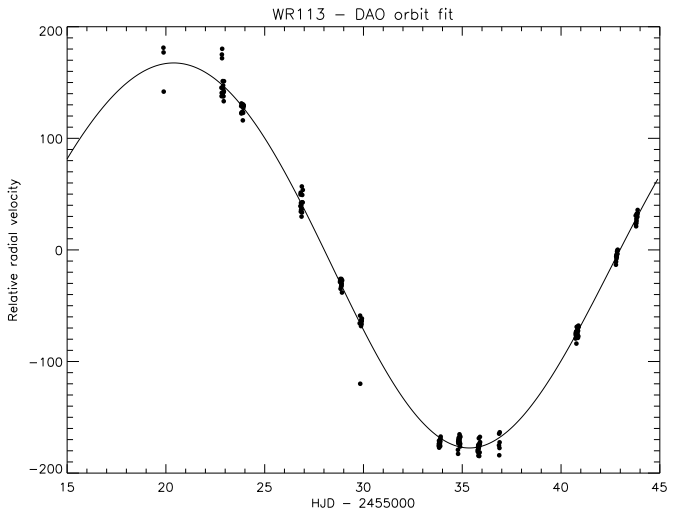

Figure 2: Elliptical fit to DAO radial velocity data yields e=0. The scatter of the data points about the fitted curve is due to a combination of the effects of the random instrumental error and stochastic clumps on the line profiles.

1.2 Theoretical background

Assuming an atmospheric eclipse, we use a first-order model for WR+O binaries, with a $\beta = 0$ wind (constant) velocity law, as described and justified (the $\beta = 0$ wind velocity law is shown to explain atmospheric eclipses of all observed WR+O systems) in Lamontagne et al. (1996):

$$\Delta m = \Delta m_0 + A \left(\frac{\pi/2 + \arcsin \epsilon}{\sqrt{1-\epsilon^2}} \right) \tag{1}$$

with $\epsilon = (\sin i) \cos(2\pi\phi)$, $A = \frac{(2.5 \log e)k}{(1+I_{WR}/I_O)}$ and $k = \frac{\alpha \sigma_e \dot{M}}{4\pi m_p v_\infty a}$, in which Δm_0 is a constant, i is the orbital inclination, I_{WR}/I_O is the intensity ratio of the 2 stars in the observed bandpass, $\alpha \simeq 0.5$ free electrons per He nucleus, σ_e is the Thomson electron-scattering cross section, $\dot{M}$ is the WR mass-loss rate, m_p is the proton mass, v_∞ is the terminal wind speed and a is the orbital separation.

Eq.1 only takes into account the electron scattering of the O star's light along the line of sight but it has revealed itself to be a powerful tool to derive the mass-loss rates of WR stars in close binaries.

2 Preliminary results

We tried to fit our light curve using the Lamontagne et al. model. However, since our two eclipses do not have the same depth, it was necessary to make a small adjustment. We let A vary linearly with time, which could indicate a change in the mass loss parameters (most probably $\dot{M}$ and/or v_∞). We also had to allow Δm_0 to vary linearly with time (with slope B_1, most likely due to detector drift):

$$\Delta m = B_0 + B_1 \cdot t + (A_0 + A_1 \cdot t) \left(\frac{\pi/2 + \arcsin \epsilon}{\sqrt{1-\epsilon^2}} \right) \tag{2}$$

The best fit is shown in Fig. 3. The scatter in magnitude around the fit is quite significant and may be related to intervening clumps in the WR wind.

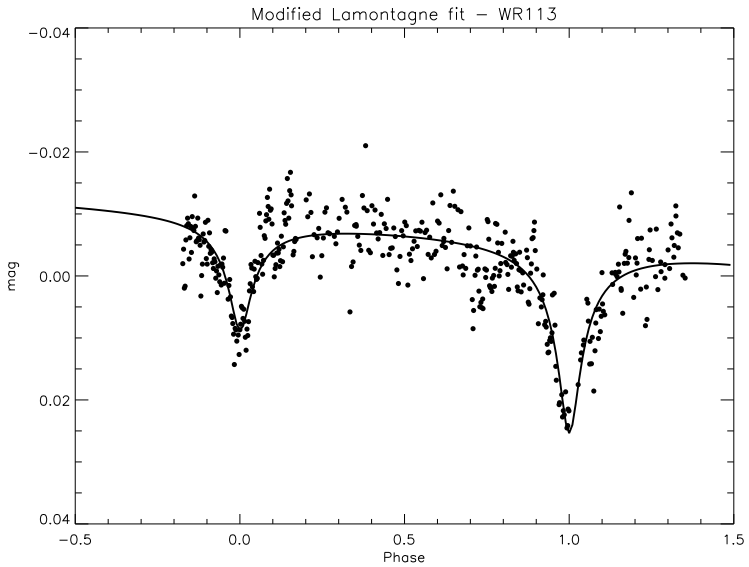

Figure 3: Best fit to the modified Lamontagne et al. model. The scatter in the light curve of CV Ser is most likely intrinsic (pulsations and/or intervening clumps).

Assuming the values given in Lamontagne et al. (1996) for most parameters for CV Ser except $\dot{M}$, the fit yields a mass-loss rate of about $2.9 \cdot 10^{-5}\,\mathrm{M}_{\odot}\,\mathrm{yr}^{-1}$ for the first eclipse. If we assume that the variation of the depth of the eclipse is entirely due to the variation of the mass-loss rate, we then find that the Wolf-Rayet mass-loss rate increases by 70% from the first eclipse to the second eclipse! However, it is possible that other parameters of the wind structure could change at the same time, thus probably setting a 70% increase as an upper limit to the change in $\dot{M}$.

The fit was also done through the average level of the lightcurve. This conservative approach was used since the nature of the scatter was not yet known. Indeed, we suspect that the clumps going through the O star's light path should produce an absorption signature, but there also might be features related to possible pulsations which cannot be ignored. If pulsations are not detected, then the fit might be biased to too low a level, although this should not affect the relative eclipse depths, since the bias is about constant for all phases.

3 What's next?

There is still much to be done with CV Ser. First, Fourier and wavelet analyses will help detect coherent or random variations in the light curve (which can hopefully be linked to clumps). The spectra of both components of the binary system can be separated using the "shift and add" method (Demers et al. 2002). We will also check for changes in the spectra which could be linked to variations in the properties of the WR wind (mass-loss rate, temperature, terminal velocity, ionisation, etc.). Lührs' model (Lührs 1997) can be applied to the excess emission to model the shock cone and compare the value of i obtained to the one given by Lamontagne's model. Ultimately, the goal of this project is to characterize the clumping phenomenon. New data (MOST and ground-based spectra) taken during summer 2010 will help us complete our analysis. A third eclipse was observed, which will be compared to the two obtained during summer 2009.

Acknowledgements

This research was made possible in part by the science team of the MOST space telescope, the OMM and DAO staffs as well as NSERC (Canada) and FQRNT (Quebec).

References

Cowley, A.P., Hiltner, W.A., Berry C., 1971, A&A, 11, 407
Demers, H., Moffat, A.F.J., Marchenko, S.V., Gayley, K.G., Morel, T., 2002, ApJ, 577, 409
Hjellming, R.M., Hiltner, W.A., 1963, ApJ, 137, 1080
Kuhi, L.V., Schweizer, F., 1970, ApJ, 160, 185
Lamontagne, R., Moffat, A.F.J., Drissen, L., Robert, C., Matthews, J.M., 1996, AJ, 112, 2227
Lührs, S., 1997, PASP, 109, 504
Stepień, K., 1970, AcA, 20, 13

A VLT/UVES spectroscopy study of O2 stars in the LMC

Emile I. Doran and Paul A. Crowther

Department of Physics and Astronomy, University of Sheffield
Hicks Building, Hounsfield Road, Sheffield, S3 7RH, United Kingdom

Abstract: We have analysed VLT/UVES spectra of six O2 stars within the Large Magellanic Cloud using the non-LTE atmospheric code CMFGEN. A range of physical properties was determined by employing a temperature calibration based upon N IV-N V diagnostics. Wind properties were also obtained from the Hα line, while CNO surface abundances were supplied through various diagnostics. Our results reveal effective temperatures in excess of $T_{\rm eff}$ $\sim$50 kK in all cases. We also addressed their evolutionary status and favour a mass dependent division. For lower masses $\leq$100 $M_{\odot}$, an O2 star follows the classical sequence, evolving from dwarf on to giant, through to supergiant. At higher masses, the dwarf phase may be circumvented and instead O2 stars begin their lives as giants or supergiants, evolving to the H-rich WN stage within $\sim$1.5 Myr.

1 Introduction

The O2 spectral type was introduced by Walborn et al. (2002). It was defined by the very weak/absent He I and N III lines and presented higher excitation via prominent N IV and N V lines. Their appearance suggests O2 stars have the highest effective temperatures of main-sequence stars. Temperature calibration of later O-star subtypes has always relied on the analysis of the helium lines, typically the ratio between He IIλ4541/He Iλ4471 (Gray & Corbally 2009). This becomes increasingly difficult for early O-stars due to the weakness of the He I line. Massey et al. (2005) studied seven O2 stars via this technique but concluded there was little benefit from the O2 type extension as the $T_{\rm eff}$ for O2-3.5 spectral types showed no strong correlation. Furthermore, they measured the equivalent width ratios of the N III/N IV and He I/He II lines but found neither to show a strong correlation with $T_{\rm eff}$. Mokiem et al. (2007) also studied 28 O-type and early B-type stars in the LMC, including two O2 dwarfs and two giants. They also employed the He lines diagnostic and, in contrast, found the O2 stars to be the hottest of their sample. However, due to the very weak He I line, uncertainties in $T_{\rm eff}$ were much larger ($\sim$ 10%) than the remainder of their sample ($\sim$ 3%). The need to refine the $T_{\rm eff}$ scale of O2 stars is evident and in turn, we establish more reliable stellar properties for this early subtype.

Ideally, one would seek to use the more prominent N IV and N V lines as a temperature diagnostic. However, they can be particularly difficult to model in comparison to hydrogen and helium lines given the much more complex atomic physics required. Nevertheless, developments to the latest stellar atmosphere codes such as CMFGEN and FASTWIND, have now made this approach possible and we applied the former code to six O2 stars in the LMC. Two of these stars were in common

with the Walborn et al. (2004) study where updated parameters are used. A selection of luminosity classes was chosen as indicated in Table 1. Subsequently, we used the derived stellar properties to obtain masses and ages, and identify any evolutionary sequences within the O2 subclass, as well as a possible link to the H-rich WN stars studied by Crowther et al. (2010).

2 Observations and Analysis

Spectral analysis was carried out on VLT/Ultraviolet and Visual Echelle Spectrograph (UVES) observations of six O2 stars. Data sets covered wavelengths 3300-10250 Å, at a resolving power of about 40,000 with the exception of Mk 42 and HDE 269810 which only spanned 3300-6650 Å. These were supplemented by UV spectra obtained from different instruments including HST/GHRS, FOS and STIS. Photometric data in the UBV bands were taken from Massey (2002) and Walborn et al. (2002), and the 2MASS All Sky Catalog for the JHK bands. Mk 42 was an exception to this, due to its location in the crowded 30 Dor region, for which higher spatial resolution VLT/MAD photometry from Campbell et al. (2010) was adopted.

The physical properties were derived using the CMFGEN atmospheric modelling code (Hillier & Miller 1998). This solves the radiative transfer equation in the co-moving frame, under the constraint of statistical equilibrium. The temperature structure follows from the assumption of radiative equilibrium. Our detailed approach closely mimics that set out by Evans et al. (2010a) except that a clumped wind model was applied for the two supergiants, using a volume filling factor, f, as described by Hillier et al. (2003), for which we select f=0.1. Effective temperatures were calculated in all cases from the N IV λ4058 and N V $\lambda\lambda$4604-4620 lines. Since the nitrogen abundance of each star was unknown, this was simultaneously derived.

Stellar luminosities were estimated by adopting an LMC distance of 49$\pm$4 kpc (distance modulus = 18.45$\pm$0.18 mag). The photometric data sets were then reproduced by varying amounts of extinction that accounted for foreground Galactic and LMC dust. Furthermore, Mk 42 featured an additional term allowing for the extinction within 30 Dor. These extinction values and absolute magnitudes, derived for the K-band, are given in Table 1. In this provisional study, the UV spectra did not serve as diagnostics but allowed a consistency check with optical results. The broad wings of the He II λ4686 line were overestimated in the supergiants but theoretical models showed good agreement with the supplementary UV spectra. However, for the giants and dwarfs, the C IV λ1550 line was predicted too strong and the O V λ1371 line was underestimated. Current surface abundances for H, He, C, N and O were also estimated through various optical diagnostics. Only the supergiants showed signs of depleted H abundance and in turn indicated N enrichment as high as N/N_{ISM} $\sim$35 in the case of Mk 42.

3 Results

Effective temperatures of T_{eff} $\gtrsim$ 50 kK were obtained in all cases, together with high luminosities, $10^{5.8-6.6}$ $L_{\odot}$. The giants presented the highest T_{eff}, with the dwarfs and then supergiants being progressively cooler. This can be seen in Figure 1, which plots the positions of the stars on a Hertzsprung-Russell diagram. The two supergiants, in particular, showed quite different physical properties. Stellar mass-loss rates were compared with those predicted by Vink, de Koter & Lamers (2001), using masses we derived from evolutionary models. Empirical mass-loss rates exceeded predictions in all cases (up to a factor of 3) although modest wind clumping for dwarfs and giants would reduce this discrepancy.

Table 1: Spectral types of our O2 stars taken from Walborn et al. (2004) and Massey et al. (2005). An updated classification scheme (Walborn & Crowther, in prep.) was favoured for Mk 42 and Sk -67 22. V and K-band photometry together with interstellar extinctions and absolute magnitudes in K-band, assuming distance modulus 18.45±0.18 mag (49±4 kpc)

Star	Spectral Type	m_V (mag)	m_K (mag)	A_K (mag)	M_K (mag)
BI 237	O2 V((f*))	13.89	14.04±0.07	0.08±0.04	-4.49±0.19
BI 253	O2 V((f*))	13.76	13.68±0.05	0.09±0.04	-4.86±0.20
HDE 269810	O2 III(f*)	12.28	12.88±0.04	0.04±0.04	-5.61±0.19
LH 10-3061	ON2 III(f*)	13.68	13.52±0.05	0.12±0.04	-5.05±0.20
Mk 42	O2 If*	12.71	12.19±0.08	0.12±0.04	-6.38±0.20
Sk -67 22	O2 If*/WN 5	13.44	13.78±0.06	0.05±0.04	-4.73±0.19

Our nitrogen-derived results are consistent with the work by Mokiem et al. (2007) who also studied BI 237 and BI 253, based on their H and He lines. Massey et al. (2005) also studied these two stars, along with Sk -67 22 but in some cases could only set a lower temperature limit owing to the weakness of the He I λ4471 line. By utilising the N IV and N V lines, our results did not suffer from such ambiguity. Table 2 compares the various temperature estimates from previous studies with the present sample of O2 stars.

Table 2: Comparison of past studies on O2 star sample with respect to this work. Differences in analysis techniques along with resulting effective temperatures are given.

		Puls et al. (96)	Massey et al. (05)	Mokiem et al. (07)	This Work
Spectral Observations		ESO/Caspec	CTIO/RC Spec	VLT/UVES	VLT/UVES
Atmospheric Code		Various	FASTWIND	FASTWIND	CMFGEN
Temperature Diagnostic		H/He	He I/He II	He I/He II	N IV/N V
Star	Spectral Type	T_{eff} (kK)			
BI 237	O2 V((f*))	–	48	53.2	52.1
BI 253	O2 V((f*))	–	>48	53.8	52.8
HDE 269810	O2 III(f*)	60	–	–	54.3
LH 10-3061	ON2 III(f*)	–	–	–	54.7
Mk 42	O2 If*	50.5	–	–	49.8
Sk -67 22	O2 If*/WN 5	–	>42	–	49.3

In an attempt to establish ages, masses and a possible evolutionary sequence for O2 stars, their properties were compared to the latest main-sequence rotating and non-rotating evolutionary tracks of the Geneva group (R. Hirschi, private communication). These were based on the models from Hirschi, Meynet & Maeder (2004) at LMC metallicity (0.4 $Z_\odot$) and ranged from 60-200$M_\odot$. They used theoretical mass-loss rates from Vink, de Koter & Lamers (2001) during the main sequence phase and an initial to critical (maximum) rotational velocity ratio of v_{init}/v_{crit}=0.4 for the rotating case. Comparisons to our derived parameters, including predicted H and CNO abundances, favoured the rotating models in all cases. Figure 1 overlays these main-sequence evolutionary tracks on the H-R diagram.

The two dwarfs showed very little enhancement in N and within the uncertainties of our parameters, closely matched the zero-age main-sequence (ZAMS) predictions. Masses of 75 $M_\odot$ and 85 $M_\odot$ for BI 237 and BI 253, respectively, were in agreement with the typical mass ($<$100 $M_\odot$) of O2 dwarfs found by Walborn et al. (2002). The giants had more enhanced N, especially LH 10-3061 and although both lay close to the ZAMS, we favoured a more evolved status for LH 10-3061. We therefore estimated HDE 269810 as a young $M_{init}\sim$150 $M_\odot$ giant, no older than 1 Myr, while LH 10-3061 is a less massive and more evolved giant of $M_{init}\sim$75-80 $M_\odot$ at an age of 2.5 Myr. For the two supergiants Mk 42 is $\sim$5 times more luminous than Sk -67 22. This supported a very high mass of $M_{init}\sim$180 $M_\odot$ for Mk 42, allowing it to achieve its greatly enriched nitrogen surface abundance through mixing at a relatively young age of $\sim$1.5 Myr. Meanwhile Sk -67 22 represented a star of much lower mass, $M_{init}\sim$60 $M_\odot$, at a later age, of at least 2.5 Myr.

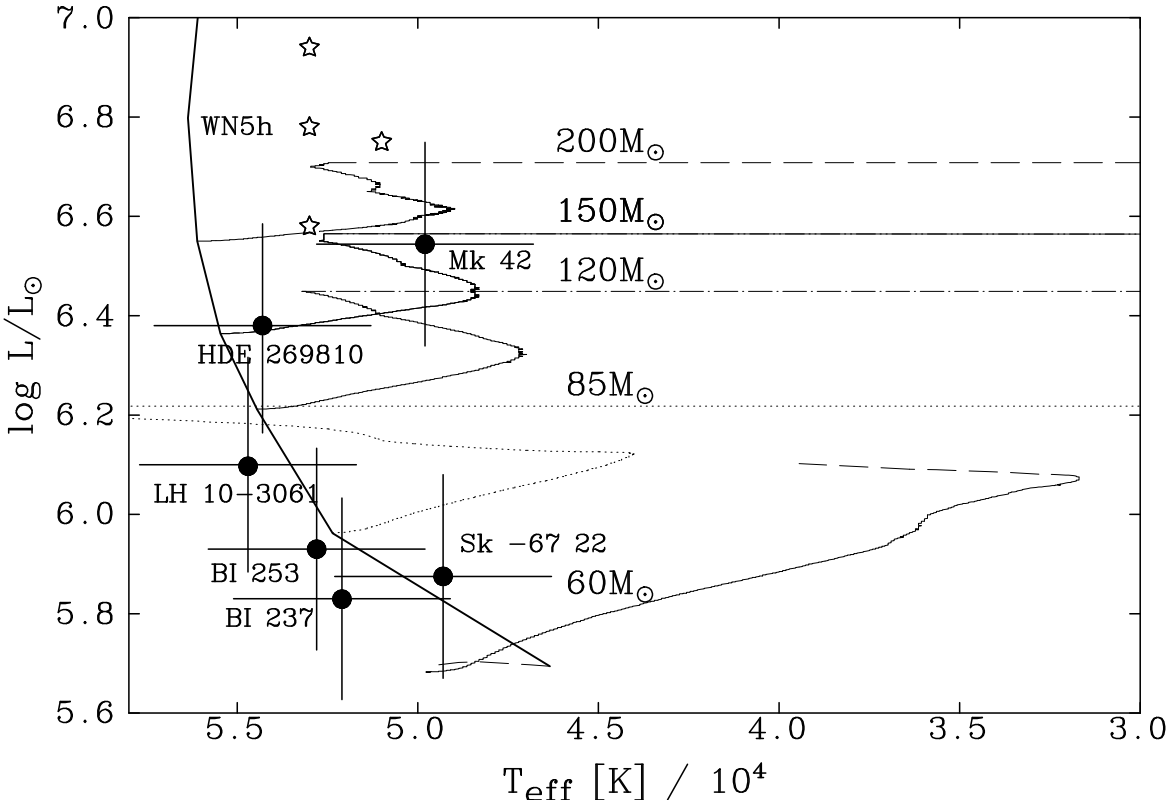

Figure 1: H-R diagram of O2 stars (filled circles) overlaid on Geneva evolutionary rotating models 60 $M_\odot$ (dashed-solid), 85 $M_\odot$ (dotted), 120 $M_\odot$ (dot-dashed), 150 $M_\odot$ (solid) and 200 $M_\odot$ (dashed). The thick solid line represents the ZAMS. R136 WN5h stars from Crowther et al. (2010) have also been included (hollow stars).

In summary, the O2 stars we have analysed all showed some of the highest known effective temperatures for main-sequence stars, ($T_{eff} \gtrsim 50$ kK), determined using the N IV and N V lines. A typical evolutionary sequence could be followed for O2 stars with M$<$100 $M_\odot$ starting from dwarfs such as BI 253, passing through a giant phase like LH 10-3061 and ending up as as supergiant in a similar mass regime to Sk -67 22. The high luminosities of stars with M$\gg$100 $M_\odot$ naturally produce strong winds at the outset so we favour an O2 giant ZAMS stage for very high mass stars (eg. HDE 269810),

rapidly followed by a supergiant stage (eg. Mk 42). These are likely precursors to massive H-rich WN stars studied by Crowther et al. (2010) at the core of the NGC 3603 and R136 clusters.

The parameters presented here are currently only initial values, having only been based on our analysis of the optical spectra. Our aim is to extend the modelling into the UV domain, thereby extending available diagnostics. Future targets, including W-R stars, from the FLAMES Tarantula Survey (Evans et al. 2010b) will help enhance our study of the earliest O-stars and allow better constraints to be placed on the evolutionary sequence of the most massive stars.

Acknowledgements

We are grateful to Raphael Hirschi for providing the high-mass Geneva evolutionary tracks required for this study. EID would like to thank the STFC for its financial support.

References

Campbell, M.A., Evans, C.J., Mackey, A.D., Gieles, M., Alves, J., Ascenso, J., Bastian, N., Longmore, A.J., 2010, MNRAS, 405, 421
Crowther, P.A., Schnurr, O., Hirschi, R., Yusof, N., Parker, R.J., Goodwin, S.P., Kassim, H.A., 2010, MNRAS, 408, 731
Evans, C.J., Walborn, N.R., Crowther, P.A., et al., 2010a, ApJ, 715, L74
Evans, C.J., Bastian, N., Beletsky, Y., et al., 2010b, IAUS, 266, 35
Gray, R.O., & Corbally, C.J., 2009, Stellar Spectral Classification, Princeton University Press
Hillier, D.J., Lanz, T., Heap, S.R., Hubeny, I., Smith, L.J., Evans, C.J., Lennon, D.J., Bouret, J.C., 2003 ApJ, 588, 1039
Hillier, D.J., & Miller, D.L., 1998, ApJ, 496, 407
Hirschi, R., Meynet, G., Maeder, A., 2004, A&A, 425, 649
Massey, P., 2002, ApJS, 141, 81
Massey, P., Puls, J., Pauldrach, A.W.A., Bresolin, F., Kudritzki, R.P., Simon, T., 2005, ApJ, 627, 477
Mokiem, M.R., de Koter, A., Evans, C.J., et al., 2007, A&A, 465, 1003
Puls, J., Kudritzki, R.-P., Herrero, A., et al., 1996, A&A, 305, 171
Vink, J.S., de Koter, A., Lamers, H.J.G.L.M., 2001, A&A, 369, 574
Walborn, N.R., Howarth, I.D., Lennon, D.J., et al., 2002, AJ, 123, 2754
Walborn, N.R., Morrell, N.I., Howarth, I.D., Crowther, P.A., Lennon, D.J., Massey, P., Arias, J.I., 2004, ApJ, 608, 1028

Radio emission from the massive stars in Westerlund 1

S.M. Dougherty[1,2], J.S. Clark [3], I. Negueruela[4], T.W. Johnson[1,5] and J.M. Chapman[6]

[1] NRC-HIA, Penticton, Canada
[2] Institute for Space Imaging Science, University of Calgary, Canada
[3] Open University, Milton Keynes, UK.
[4] University de Alicante, Alicante, Spain
[5] University of Victoria, Victoria, BC, Canada
[6] Australia Telescope National Facility, Sydney, Australia

Abstract: The diverse massive stellar population in the young massive cluster Westerlund 1 (Wd 1) provides an ideal laboratory to observe and constrain mass-loss processes throughout the transitional phase of massive star evolution. A set of high sensitivity radio observations of Wd 1 leads to the detection of 18 cluster members, a sample dominated by cool hypergiants, but with detections among hotter OB supergiants and WR stars. Here the diverse radio properties of the detected sample are briefly described. The mass-loss rates of the detected objects are surprisingly similar across the whole transitional phase of massive star evolution, at $\sim 10^{-5}$ M$_\odot$ yr^{-1}. Such a rate is insufficient to strip away the H-rich mantle in a massive star lifetime, unless the stars go through a period of enhanced mass-loss. The radio luminous star W9 provides an example of such an object, with evidence for two eras of mass-loss with rates of $\sim 10^{-4}$ M$_\odot$ yr^{-1}.

1 Introduction

Mass-loss is a fundamental property of stars with masses in excess of $\sim 30\ M_\odot$, important to stellar evolution and feedback to the ISM. Mass-loss rates of massive main sequence stars are insufficient to remove H-rich mantles to produce WR-type stars. There must be epochs of enhanced mass-loss rate in their evolution to WR stars, through phases that include hot supergiant B[e], Luminous Blue Variables (LBV), cool Yellow Hypergiant (YHG) and Red Supergiant (RSG) stars.

Westerlund 1 (Wd 1) is one of the most massive clusters in the Milky Way ($M_{\rm total} \sim 10^5\ M_\odot$), directly comparable to Super-Star Clusters in other galaxies such as M82. Hence Wd1 represents a nearby example of one of these clusters, providing a valuable opportunity to study the properties, evolution and interaction of massive stars.

Wd 1 contains a unique population of cool and hot supergiants, with a large population of post-MS stars that represent all phases of massive star evolution: OB supergiants and hypergiants, RSGs, YHGs, and WR stars (Clark & Negueruela 2002; Clark et al. 2005).

Radio observations are a long established tool for estimating mass-loss rates. Clark et al. (1998) discovered two unusually radio luminous stars in Wd 1 - the supergiant B[e] star W9 and the RSG

W26. Motivated by the possibility of detecting emission from stars across a broad range of evolutionary stages, more sensitive radio observations of Wd 1 were obtained with the Australian Telescope Compact Array to establish radio characteristics of cluster members, particularly their mass-loss rates. These observations have been used in conjunction with optical, IR and X-ray observations from the literature to elucidate the nature of the radio sources.

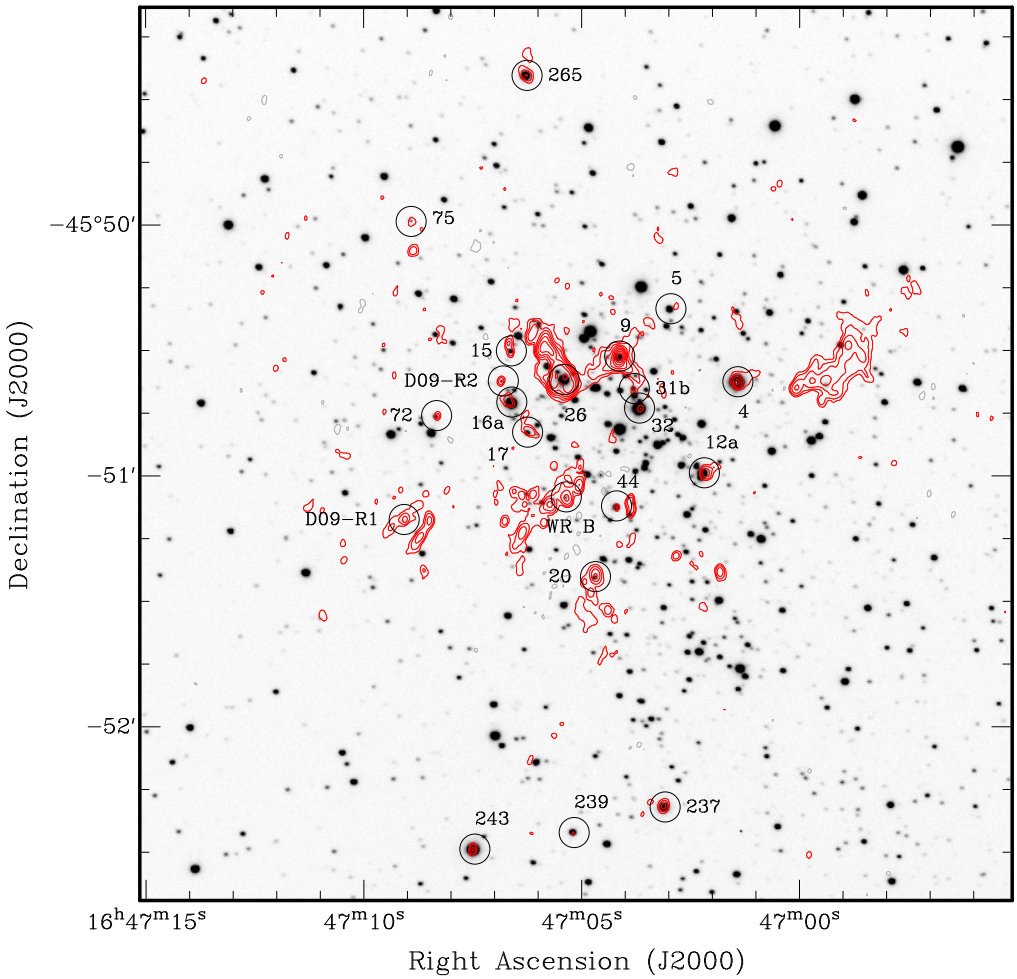

Figure 1: 8.6-GHz map of Wd 1 overlaid on a FORS R-band image, with limiting magnitude 17.5 mag. The radio sources with putative optical counterparts are identified by circles and Westerlund numbers.

2 Results

- 18 cluster members were detected, dominated by cool hypergiants, though with detections among hotter OB supergiants and WR stars (see Table 1).
- The sources are a diverse population of point-like, unresolved sources and extended, resolved sources with spectral indices corresponding to thermal, non-thermal and composite thermal and non-thermal emission.
- The radio observations in conjunction with X-ray and IR observations provide striking evidence for a high fraction of binaries among the massive stars in Wd 1, strongly supporting previous

Table 1: Number of radio emitters of given spectral type

Spec. Type	No. radio emitters	Source ID	Cluster total
OB SGs	3(4?)	15, 17, D09-R1, (D09-R2?)	∼150
sgB[e]	1	9	1
BHGs	1	243	4
YHGs	4(5?)	4, 12a, 32, 265 (16a?)	6
RSGs	4	20, 26, 75, 237	4
WN9-10	1 (2?)	44, (5?)	2
WN5-8	3	WR B, 31b, 72	14
WC	1	239	8

estimates of high binary fractions, in excess of 40% (Clark et al. 2008; Ritchie et al. 2009).

- The derived mass-loss rates determined for YHG W4, LBV W243 and WR L, which form an evolutionary sequence in some schemes, are all closely the same.
- Mass-loss rates of $\leq 10^{-5} M_{\odot} yr^{-1}$ are likely insufficient to remove the H-rich mantle unless stars remain in the transitional phase for significantly longer than expected. This implies an additional mechanism is required to shed the requisite mass, with short-lived episodes of greatly enhanced mass loss. Indeed mass-loss rates $> 10^{-4} M_{\odot} yr^{-1}$ have already been inferred for RSGs e.g. VY CMa (Smith et al. 2001) and directly observed for the YHG ρ Cas (Lobel et al. 2003). The nebulae around the RSGs W20, 26 and 236 already indicate that significant mass loss has occurred for some stars within Wd 1, while the mass-loss rate inferred for W9, over a magnitude greater than any other transitional star in Wd 1, is of obvious interest.

2.1 W9 - a luminous radio source

W9 is the brightest radio source in Wd 1, with a total flux at 8.6 GHz of 55.4 mJy, which implies a luminosity of 1.6×10^{21} erg s^{-1}. This makes W9 one of the most luminous radio stars, being a factor of a few less luminous than the extreme LBV η Car at radio minimum (Duncan & White 2002).

The radio structure of W9 is a compact radio source surrounded by an extended emission region. The spectral index of the compact source ($+0.68 \pm 0.08$) is consistent with thermal emission from a stellar wind. The extended region is essentially flat ($+0.16 \pm 0.07$) and arguably consistent with optically-thin thermal emission. Assuming a radial ion distribution in the extended region goes as r^{-2}, the lack of a turnover in its continuum spectrum implies that the region is optically-thin down to at least 1.4 GHz, with an inner radius to the region larger than the $\tau_{\nu} = 1$ surface at 1.4 GHz. We believe this is from an earlier epoch of mass loss, prior to the start of the current stellar wind phase.

Modelling the envelope as a stellar wind surrounded by an optically thin shell-like wind from an earlier phase of mass loss gives mass-loss rates of $(9.2 \pm 0.4) \times 10^{-5} (v_{\infty}/200 \text{ km s}^{-1}) f^{1/2}$ and $(33 \pm 10) \times 10^{-5} (v_{\infty}/200 \text{ km s}^{-1}) f^{1/2}$ M$_{\odot}$ yr^{-1} respectively, where f is the volume filling factor (see Dougherty et al. 2010 for modelling details).

The structure of the envelope is similar to some LBVs, with W9 having a current mass-loss rate similar to galactic examples e.g. Pistol star. The rate deduced for the extended shell is close to the limit expected for line-driven winds (Smith & Owocki 2006), and comparable to several other galactic LBV's during outburst, though orders of magnitude less than for P Cygni and η Car during outburst (Clark et al. 2009). Nevertheless, the question of whether W9 is undergoing an 'eruptive' event remains.

The X-ray properties imply W9 is a binary system, being too hard ($kT \sim 3$ keV) and bright ($L_{\rm X} \sim 10^{33}$ erg s^{-1}) to come from a single star. However, it is not possible to constrain the properties of a putative companion star from current observations. Given the unusually high radio luminosity and concomitant high mass-loss rates, W9 is clearly an object for further study.

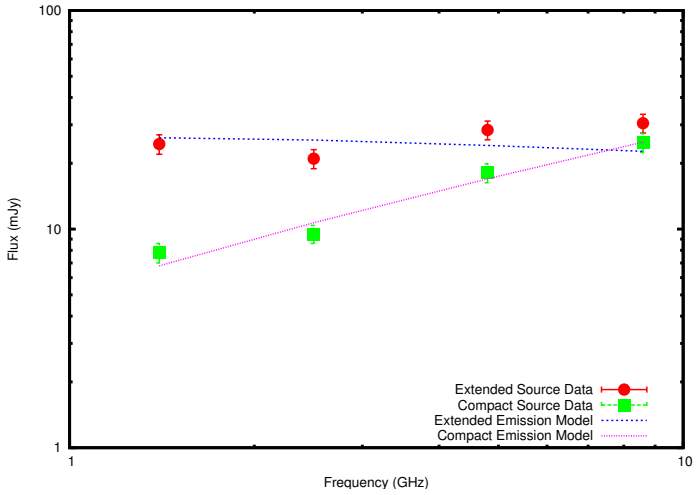

Figure 2: Model fits to the observations of W9, using a partially optically-thick compact source from a current stellar wind, and a flat spectrum extended region due to optically-thin emission from an earlier epoch of mass loss via a stellar wind.

2.2 OB stars

Surprisingly, three of the > 100 evolved OB stars are detected, with radio fluxes larger than an order of magnitude higher than expected for stellar winds at these types. These may be colliding-wind binaries based on potentially composite spectra (both thermal and non-thermal components) but there are neither X-ray emission nor RV variations associated with these three objects to support the claim. Alternatively, the high level of radio emission may be influenced by extended radio emission in which they are embedded.

2.3 Red Supergiants

All four RSGs are detected, three of them associated with large nebulae with masses up to $\sim 0.3\ M_{\odot}$. The nebulae around W20 and W26 have a pronounced cometary morphology, suggesting significant interaction with either the intracluster medium or cluster wind.

W237 shows less evidence for such interaction and has a kinematic age of ∼3,600 yr and a *time averaged* mass-loss rate of $2 \times 10^{-5} (\mathrm{v}_{\infty}/30 \mathrm{km\,s^{-1}}) f^{1/2}$ M$_{\odot}$yr^{-1}. This is consistent with other field RSGs, although it is substantially lower than inferred for NML Cyg and VY CMa during the formation of their nebulae.

2.4 Yellow Hypergiants

The YHG W4 has a stellar wind with a mass-loss rate of $10^{-5} (\mathrm{v}_{\infty}/200 \mathrm{km\,s^{-1}}) f^{1/2}$ M$_{\odot}$yr^{-1}, consistent with the few estimates available for other field YHGs. The extended nebulae associated with W4, W12a and W265 are significantly less massive than those associated with the RSGs in Wd 1, and likely arise from quiescent mass loss rather than outburst episodes.

Neither the YHGs nor RSGs are hot enough to ionize their own stellar winds and/or more extended nebulae, and the requisite ionizing photons must arise from either an unseen companion or the cluster radiation field.

2.5 B Hypergiants

Of the extreme B-type hypergiants, only LBV W243 was detected, with a spectral index consistent with thermal emission. The corresponding mass-loss rate is comparable to YHG W4, as expected given the similarity in current spectral type and radio flux. Upper limits for the three other B hypergiants were found to be $2 \times 10^{-6}(\mathrm{v}_{\infty}/200\mathrm{km\,s^{-1}})f^{1/2}$ $\mathrm{M_{\odot}yr^{-1}}$, consistent with mass-loss rates amongst field stars of these types

2.6 Wolf-Rayet stars

Five of the 24 WRs in Wd 1 were detected. WR L has a partially optically-thick wind, with a mass-loss rate consistent with stars of identical spectral type in the Galactic Centre cluster and the general field population i.e. $\dot{M} = 2 \times 10^{-5}(\mathrm{v}_{\infty}/1000\mathrm{km\,s^{-1}})f^{1/2}$ $\mathrm{M_{\odot}yr^{-1}}$. The remaining three (WR A, B and V) are identified as having composite spectra from a CWB. The optical and X-ray properties of WR A and WR B have previously indicated these to be binaries, while this is the first hint of binarity in WR V.

Acknowledgments

We thank Paul Crowther, Ben Davies, Simon Goodwin, Rene Oudmaijer, Julian Pittard, Ben Ritchie and Rens Waters for many stimulating discussions related to this work. A special thanks to Rob Reid for advice on smear fitting, the deconvolution method used. The Australia Telescope Compact Array is part of the Australia Telescope which is funded by the Commonwealth of Australia for operation as a National Facility managed by CSIRO. This work was partially supported by a UK Research Council (RCUK) Fellowship and by the Spanish Ministerio de Ciencia e Innovación (MICINN) under grants AYA2008-06166-C03-03 and Consolider-GTC CSD2006-70.

References

Clark, J. S., Crowther, P. A., Larionov, V. M., Steele, I. A., Ritchie, B. W. & Arkharov, A. A. 2009, A&A, 507, 1555

Clark, J. S. & Negueruela, I. 2002, A&A, 396, L25

Clark, J. S., Fender, R. P., Waters, L. B. F. M., Dougherty, S. M., Koornneef, J., Steele, I. A. & van Blokland, A. 1998, MNRAS, 299, L43

Clark, J. S., Negueruela, I., Crowther, P. A. & Goodwin, S. P. 2005, A&A, 434, 949

Clark, J. S., Muno, M. P., Negueruela, I., Dougherty, S. M., Crowther, P. A., Goodwin, S. P. & de Grijs, R. 2008, A&A, 477, 147

Dougherty, S. M., Clark, J. S., Negueruela, I., Johnson, T. & Chapman, J. M. 2010, A&A, 511, A58

Duncan, R. A. & White, S. M. 2002, MNRAS, 330, 63

Lobel, A., Dupree, A. K., Stefanik, R. P., Torres, G., Israelian, G., Morrison, N., de Jager, C., Nieuwenhuijzen, H., et al. 2003, ApJ, 583, 923

Ritchie, B. W., Clark, J. S., Negueruela, I. & Crowther, P. A. 2009, A&A, 507, 1585

Smith, N., Humphreys, R. M., Davidson, K., Gehrz, R. D., Schuster, M. T. & Krautter, J. 2001, AJ, 121, 1111

Smith, N. & Owocki, S. P. 2006, ApJ, 645, L45

Observational signatures of rapidly rotating, pulsating B stars

Chris Engelbrecht[1], Fabio Frescura[2] and Sashin Moonsamy[2]

[1] Department of Physics, University of Johannesburg, South Africa
[2] School of Physics, University of the Witwatersrand, Johannesburg, South Africa

Abstract: The effects of the geometric distortion of a rapidly rotating star on the relative amplitudes of radial velocity and luminosity variations are modelled. The possibility of determining the inclination angle of the rotation axis of a rapidly rotating star, from observations of its radial velocity and luminosity variations, is then explored and the nature of these effects for a model of an early B main-sequence star are presented. It is found that this approach holds sufficient promise that more detailed calculations should be embarked upon.

1 Introduction

Three phenomena contribute to the observed light variability of a star:

1. The changing direction of the unit vector normal to the stellar surface, relative to the observer;
2. The changing projected area of a light-emitting element of surface, as seen by the observer;
3. The changing surface brightness of the surface element, due to a change in its temperature.

Both pulsation and rotation contribute to the Lagrangian displacement of elements of stellar material from their positions in a spherically symmetric equilibrium configuration. Buta & Smith (1979) derived expressions for the light variability of a pulsating star in the absence of rotation. Subsequent work has explored various aspects of the observational signatures of pulsating stars that are due to rotation (see, for example, Townsend 2003). Some studies of rotational effects on stellar pulsation ignore the distortion of the stellar surface due to rotation. This is usually justified by arguing that these effects are proportional to the square of the rotation velocity Ω, and thus are second-order effects. We investigate whether the role of the inclination of the rotation axis (to the line of sight from the observer) might be identified by taking these second-order effects into account.

2 Light variations

We model the light curve for a star by superposing first order pulsational effects on a second order rotational geometry. This assumes that there is no coupling of pulsation modes with the rotation. Since

our interest here is in the geometric effects of rotation, and not the temporal effects, this approximation is acceptable. The luminous power emitted at wavelength λ by an element of stellar surface is given by

$$L_0 = (F_\lambda d\vec{A}) \cdot \hat{n} \tag{1}$$

while the power detected by an observer is given by

$$L = (hF_\lambda d\vec{A}) \cdot \hat{z} \tag{2}$$

where

$$\begin{aligned} F_\lambda &= \text{radiative flux through element at wavelength}\lambda \\ d\vec{A} &= \text{vector area of surface element, i.e. } d\vec{A} = |d\vec{A}|\hat{n} \\ \hat{n} &= \text{unit normal to surface element} \\ h &= \text{limb darkening function at wavelength } \lambda \text{ at position of surface element} \\ \hat{z} &= \text{unit vector in direction from star to observer.} \end{aligned}$$

Buta & Smith (1979) write the Lagrangian displacement of an element on the stellar surface, due to pulsation, as

$$\delta R_{pul}(\theta, \phi, t) \;=\; a(R) Y_{lm}(\theta, \phi) e^{i\sigma t}. \tag{3}$$

This assumes that the tangential motion of the stellar material is negligible. The effect of rotation is to distort the stellar surface. We model the distortion by a Clairaut-Legendre expansion, as suggested by Tassoul (1978):

$$R \;=\; R_0 \left(1 - \sum_{n=1}^{\infty} \epsilon_{2n}(R_0) P_{2n}^0(\cos\theta) \right). \tag{4}$$

We have established that, for small distortion amplitudes, terms with n $>$ 1 can be neglected even for equatorial rotation speeds as high as 400 km/s. We may therefore express the rotational distortion with the single term

$$\delta R_{rot} = R - R_0 = -R_0 \epsilon_r P_2^0(\cos\theta). \tag{5}$$

Adding the pulsational distortion to the rotational one, we get:

$$\delta R \;=\; \delta R_{pul} + \delta R_{rot}. \tag{6}$$

In the Cowling approximation, a change in radius of the star causes a change in pressure given by

$$\frac{\delta P}{P} \;=\; \left[\frac{\ell(\ell+1)}{\omega_{\rm nd}^2} - 4 - \omega_{\rm nd}^2 \right] \frac{\delta R}{R} \;=\; f_p(\ell, \omega_{\rm nd}^2)\, \frac{\delta R}{R} \tag{7}$$

where $\omega_{\rm nd}$ denotes the dimensionless pulsation frequency. Assuming that surface elements distort adiabatically:

$$\frac{\delta T}{T} \;=\; \frac{\Gamma_2 - 1}{\Gamma_2}\, \frac{\delta P}{P} \;=\; \frac{\Gamma_2 - 1}{\Gamma_2}\, f_p(\ell, \omega_{\rm nd}^2)\, \frac{\delta R}{R} \;=\; f_T(\ell, \omega_{\rm nd}^2)\, \frac{\delta R}{R}. \tag{8}$$

In the blackbody approximation, a temperature change effects the following change in the radiative flux at wavelength λ:

$$\frac{\delta F_\lambda}{F_\lambda} \;=\; \frac{xe^x}{e^x-1}\,\frac{\delta T}{T} \;=\; \frac{xe^x}{e^x-1}\,f_T(\ell,\omega^2_{\rm nd})\,\frac{\delta R}{R} \;=\; f_\lambda(\ell,\omega^2_{\rm nd},T)\,\frac{\delta R}{R} \tag{9}$$

where $x = hc/kT$. We choose values for the arguments of f_λ that are appropriate for an early B-type p-mode pulsator. A practical reference frame, from the observer's point of view, is one that has its origin at the centre of the star and its z-axis pointing in the direction of the observer. We denote the coordinates in this frame by

$$(r,\vartheta,\varphi) \tag{10}$$

We now employ the limb-darkening law

$$h(\cos\vartheta) \;=\; \frac{6}{3-u}\,(1-u+u\cos\vartheta) \tag{11}$$

with

$$\cos\vartheta = \hat{n}\cdot\hat{z}. \tag{12}$$

We choose a value of u appropriate for early B stars, using the tables in Al-Naimiy (1978). The total limb-darkening function, including the distortion of the stellar surface, is given by Buta & Smith (1979).

$$h+\delta h \;=\; \frac{6}{3-u}\,[1-u+u(\hat{n}+\delta\hat{n})\cdot\hat{z}] \;=\; \frac{6}{3-u}\,\left[1-u+u\left(\frac{d\vec{A}+\delta d\vec{A}}{\left|d\vec{A}+\delta d\vec{A}\right|}\right)\cdot\hat{z}\right]. \tag{13}$$

The term in round brackets on the right hand side represents a change in direction of the surface normal due to the distortion of the surface. We can now calculate the total flux emitted by the star in the direction of the observer. We explore the utility of this approach by executing the explicit calculation of this flux for a rotationally distorted early B star pulsating in a single p-mode, as a first test case. In our calculation, we ignore all the terms which were established (algebraically) to contribute negligibly to the flux. The explicit formulae are complicated, containing large numbers of terms, and cannot be displayed here. Once we have calculated the variation in luminosity of the model star, the variation in its magnitude is readily obtained.

3 Radial velocity variations

'Radial velocity' means the velocity of the stellar surface in the direction ($\hat{z}$) pointing towards the observer. The Eulerian variation in the velocity of a given surface element of the star due to pulsation is given by

$$\vec{v}\,' \;=\; \delta\vec{v} - \vec{\xi}\cdot\nabla\vec{v} \;=\; i(\omega+m\Omega)\vec{\xi} - \Omega(\xi_\phi\sin\theta\,\hat{r} + \xi_\phi\cos\theta\,\hat{\theta}) \tag{14}$$

where $\vec{\xi}$ denotes the Lagrangian displacement of an element of the stellar surface due to pulsation. We use a second-order rotational modification for the pulsation frequency:

$$\omega \;\approx\; \omega_0 - (1-C_1)m\Omega + C_2\,\frac{\Omega^2}{\omega_0^2} \tag{15}$$

and calculate the radial velocity projected towards the observer:

$$\overline{v}_{rad} \;=\; \int v_{obs}(\theta,\phi)\frac{dL(\theta,\phi)}{L} \tag{16}$$

where v_{obs} denotes the total velocity of a surface element towards the observer, i.e.

$$v_{obs} = \vec{v}\cdot\hat{z} \tag{17}$$

with

$$\vec{v} = \Omega r\sin\theta\,\hat{\phi} + \vec{v}\,'. \tag{18}$$

4 Results

We now illustrate the effects of the rotational distortion of a pulsating star's geometry on its observational signatures. The first four figures deal with radial ($\ell = 0$) and dipole sectoral ($\ell = 1, m = 0$) modes respectively. Figures 1 and 2 display our calculated ratios of radial velocity variation to variation in B magnitude, as a function of equatorial rotation speed, when the geometric distortion is *not* taken into account. The numbers appearing on the right hand side of the curves, inside the plots (0, 22.5, 45, etc.), denote the inclination angles used in the calculations. Figures 3 and 4 display the calculated ratios when the geometric distortion *is* taken into account. Figures 5 and 6 display the corresponding comparison for a quadrupole tesseral mode. The clear dependence of the ratios on the inclination angle of the rotation (and pulsation) axis only becomes apparent when the geometric distortion is included in the calculation.

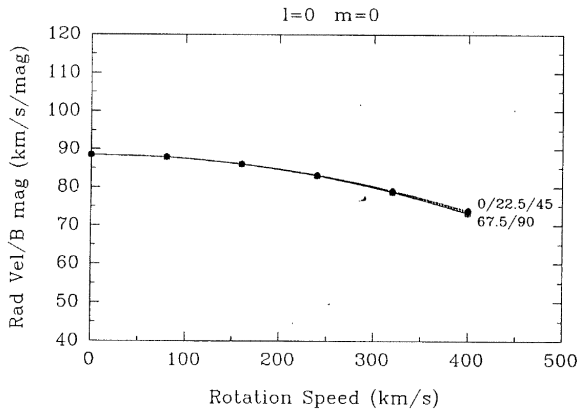

Figure 1: Amplitude ratios calculated without rotational distortion, for a radial mode.

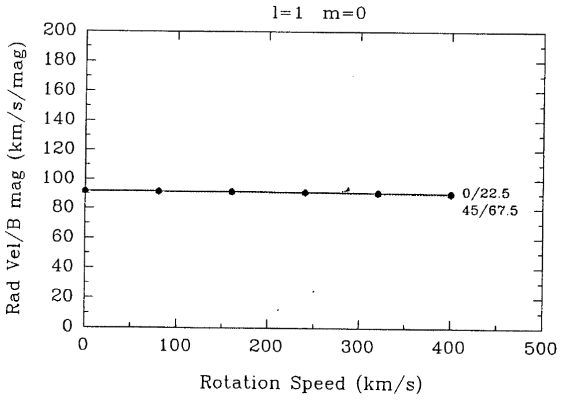

Figure 2: Amplitude ratios calculated without rotational distortion, for a dipole sectoral mode.

References

Al-Naimiy, H.M. 1978, ApSS 53, 181

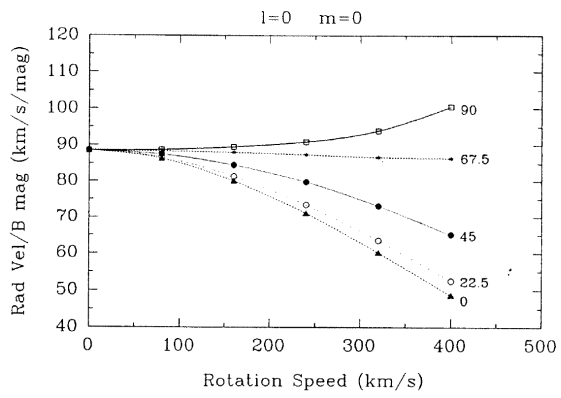

Figure 3: Amplitude ratios calculated with rotational distortion, for a radial mode.

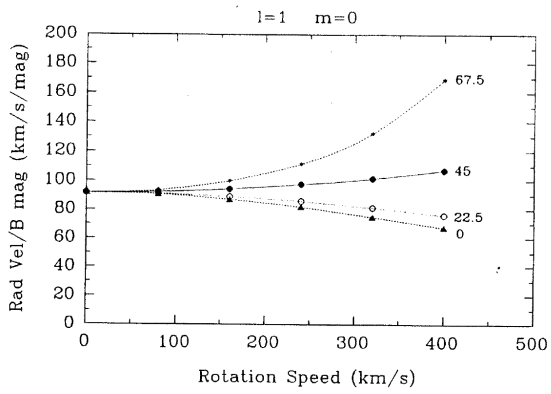

Figure 4: Amplitude ratios calculated with rotational distortion, for a dipole sectoral mode.

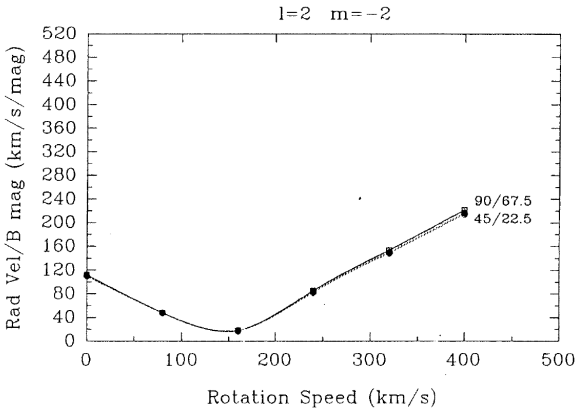

Figure 5: Amplitude ratios calculated without rotational distortion, for a quadrupole tesseral mode.

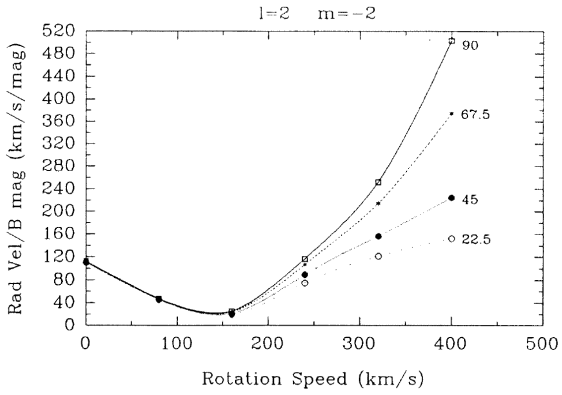

Figure 6: Amplitude ratios calculated with rotational distortion, for a quadrupole tesseral mode.

Buta, R.J., & Smith, M.A. 1979, ApJ 232, 213
Tassoul, J.-L. 1978, *Theory of Rotating Stars*, Princeton University Press
Townsend, R.H.D. 2003, MNRAS 343, 125

Exploring the connection of weak winds and magnetic fields

Miriam Garcia[1,2], Francisco Najarro[3] and Artemio Herrero[1,2]

[1] Instituto de Astrofísica de Canarias, La Laguna, Spain
[2] Universidad de La Laguna, La Laguna, Spain
[3] Centro de Astrobiología (CSIC-INTA), Torrejón de Ardoz, Spain

Abstract: The theory of radiatively driven winds successfully explains the key points of the stellar winds of hot massive stars. However, there is an apparent break-down of this paradigm at $\log L/L_{\odot}$ <5.2: the stellar wind momentum is smaller than predicted for low luminosity early-type stars from metal poor environments, and there are also some Galactic examples. We present a preliminary analysis of a small sample of stars of this luminosity regime in the Orion Nebula region and evaluate whether magnetic fields may play some role in the weak wind problem.

1 Introduction

There is an apparent breakdown of the theory of radiation driven winds at $\log L/L_{\odot}$ <5.2 and spectral type ∼O9 V, where the wind-momentum derived from the observations is smaller (beyond error bars) than predicted by theory. This was first thought a metallicity effect since it was detected in stars from metal-poor environments like the SMC (Bouret et al. 2003, Martins et al. 2004). However, there are also some Galactic cases (Martins et al. 2005, Marcolino et al. 2009).

We still lack an explanation but current hypothesis include a metallicity-dependent threshold luminosity to start the wind, an early evolutionary state previous to wind onset, decoupling of the driving ions from the plasma or magnetic fields.

We study a sample of O9-B0 young dwarfs in the Orion star forming region, together with τ Sco, a known magnetic star. Our first analysis of ultraviolet (UV) spectra (1150-1800Å) with WM-basic models revealed that all targets have smaller wind momentum than predicted by the theory (Garcia & Herrero 2010), although τ Sco's was larger and closer to the theoretical relation. However, this analysis was not conclusive, as the photospheric properties ($T_{\rm eff}$ and $\log$ g) were adopted from optical studies. We present here first results from an improved multiwavelength analysis (from UV to the optical range) for the same sample of stars, using CMFGEN synthetic spectra to fit the observations, where stellar and wind parameters are determined consistently. We also discuss qualitatively that magnetic fields may provide a solution for the weak wind problem.

2 Previous work: analysis with WM-basic models

We derived the wind properties of a sample of O9-B0.5V stars from their UV spectra. The sample includes four O9-B0 stars in the Orion Nebula, 10 Lac and τ Sco (Garcia & Herrero 2010).

The UV spectra were observed with the International Ultraviolet Explorer (IUE) and downloaded from the INES archive (Wamsteker et al. 2000). The spectra did not display any wind features in the IUE range with the exception of C IV 1550 (and perhaps N V 1240) in some stars in the sample.

To analyze the UV data, we built for each star a grid of spherical hydrodynamical line-blanketed non-LTE synthetic spectra calculated with the WM-Basic code (Pauldrach, Hoffmann, & Lennon 2001). WM-Basic provides a very detailed treatment of the spectral lines in the UV range, however, it lacks an appropriate treatment of the Stark broadening and is not suitable for analysis of photospheric lines in the optical range.

Consequently, the grid was run with photospheric ($\mathrm{T_{eff}}$, $\log$ g) parameters derived for these stars by Simón-Díaz et al. (2006) from detailed quantitative analysis of optical spectra using FASTWIND (Puls et al. 2005). The observed Hα line did not exhibit a wind profile, indicating a low mass loss rate. The Hα profiles of the synthetic spectra calculated with the derived photospheric parameters were in fact insensitive to variations of the wind parameters. Therefore, Simón-Díaz et al. could only set upper limits for the wind-strength Q-parameter ($Q = \dot{M}/(v_\infty R_\star)^{1.5}$, $\dot{M}$ being the mass loss rate, v_∞ the terminal velocity and $R_\star$ the stellar radius).

Each object's customized grid has the following varying parameters:

- Mass loss rate. Starting from Simón-Díaz et al. upper limit of Q as first value, $\dot{M}$ was decreased until it reproduced the observed weak UV features.
- Terminal velocity. The traditional method to derive this parameter could not be used, as the UV stellar spectra did not display any saturated lines. The values of v_∞ considered in the grid were estimated from the escape velocity (see Lamers, Snow, & Lindholm 1995). Additional models with $v_\infty \pm 500\,\mathrm{km\,s^{-1}}$ were also calculated.
- Shocks in the wind, parametrized by the X-ray luminosity released in the shock cooling zone. This parameter could not be constrained since observations of the O VI 1033 doublet in the Far-UV were not available for all stars. The adopted values for this parameter were: $\log L_X/L_{bol}$ =-6.5, -7.0, -7.5, -8.0 and shocks off.

We found that the grid models predicted strong P Cygni profiles of C III 1176, C IV 1550, N V 1240 and Si IV 1398 not seen in the observations, unless mass loss rate was extremely small. Moreover, the models could not reproduce the observed strength of all these lines simultaneously. Only upper limits for $\dot{M}$ could be set.

The subsequent upper-limits for the Wind momentum-Luminosity Relation (WLR) are systematically smaller than the theoretical prediction. Only τ Sco and HD 37020 are close to Vink, de Koter, & Lamers (2000)'s relation (see Fig. 1). τ Sco is a known magnetic star and HD 37020 has been recently reported a candidate based on its X-ray behaviour (Stelzer et al. 2005) and its non-thermal radio-emission (Petr-Gotzens & Massi 2007), hinting that magnetic fields may be somehow related to the weak wind problem.

How this connection works is not clear yet. The recently discovered magnetic star HD 57682 has very small mass loss rate (Grunhut et al. 2009) although the authors find that the profile of Hα varies with time and $\dot{M}$ determinations should therefore be monitored. Conversely, recent observations (to be confirmed) have yielded a possible magnetic field detection for 10 Lac (Schnerr et al. 2008) whose wind momentum we find under the theoretical expectations.

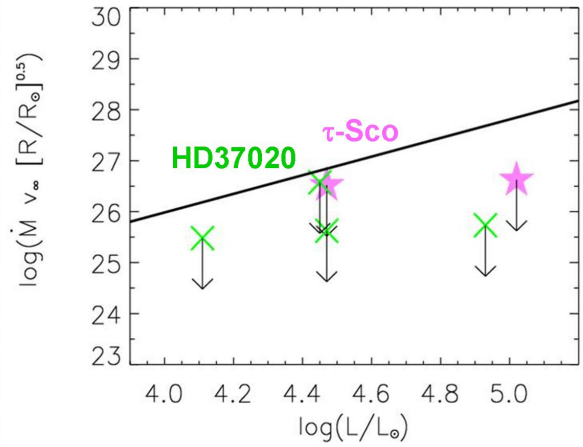

Figure 1: Wind-momentum Luminosity Relation (WLR) for the stars analyzed in Garcia & Herrero (2010). We include the theoretical relation of Vink et al. (2000) as reference .

3 The interplay of magnetic fields and X-ray luminosity

Magnetically confined wind shocks, colliding loops and reconnection events may produce strong, hard X-ray emission in the lower wind (see for instance Puls et al. 2009). This leads to increased ionization; since ions have less lines, the radiative line-acceleration is weaker. To reproduce the observed wind features, models with enhanced $\dot{M}$ are required. This could explain why τ Sco and HD 37020 are closer to the theoretical WLR.

3.1 A word of caution

Schulz et al. (2006) found that the X-ray emission of HD 37041 may be produced as close as less than 1 stellar radius from the photosphere (see also Cohen 2011).

X-rays in the expanding atmospheres of O stars alter the ionization balance of elements, shifting it towards higher values, thus mimicking the effects of higher temperature (Garcia 2005). This effect should not affect photospheric line diagnostics, nor the effective temperature derived from photospheric lines, as shocks were thought to be produced further out in the atmosphere. However, if produced close enough to the photosphere, X-rays may impact the $\mathrm{T_{eff}}$determinations (Najarro et al. 2011, in prep.). The derived $\dot{M}$ would also change, as wind indicators are also sensitive to $\mathrm{T_{eff}}$.

4 Panchromatic analysis with CMFGEN models

The complexity of this problem requires that all stellar (photospheric+wind) parameters must be derived jointly and consistently, to properly take into account the interplay of the different contributing factors. We have embarked on a project to re-analyze the same sample of stars, using better observations and a more suitable model atmosphere code. The analysis will be subsequently extended to about a dozen O9-B0 dwarfs observed for the IACOB database (see S. Simón-Díaz et al. 2011).

We will use the IUE UV spectra, combined with high resolution echelle spectra from the IACOB database. By fitting simultaneously the UV and optical lines, tighter constraints are set on the temperature and velocity structure of the atmosphere, leading to a better characterization of the ion-stratification and the wind.

We used the CMFGEN code (Hillier & Miller 1998) to calculate synthetic spectra covering from

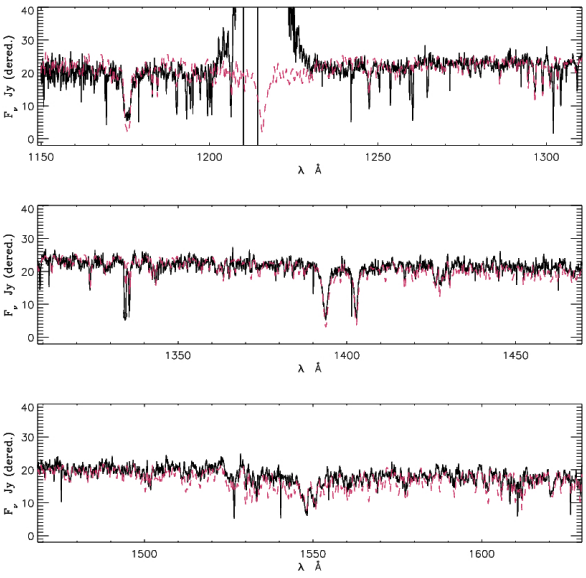

Figure 2: CMFGEN fit (red,dashed) to the IUE flux-calibrated spectrum (black, solid) of HD 37020. The CMFGEN model has $\dot{M}$ =1 $\times$ 10^{-10}M$_\odot$ yr^{-1} and $\log L_X/L_{bol}$ =-9.0 (lower than detected for the star, but needed to reproduce the Si IV 1400 lines). The observed wind signatures are very weak. The synthetic spectrum reproduces well the C III 1176 and C IV 1550 lines, and the iron-nickel continuum.

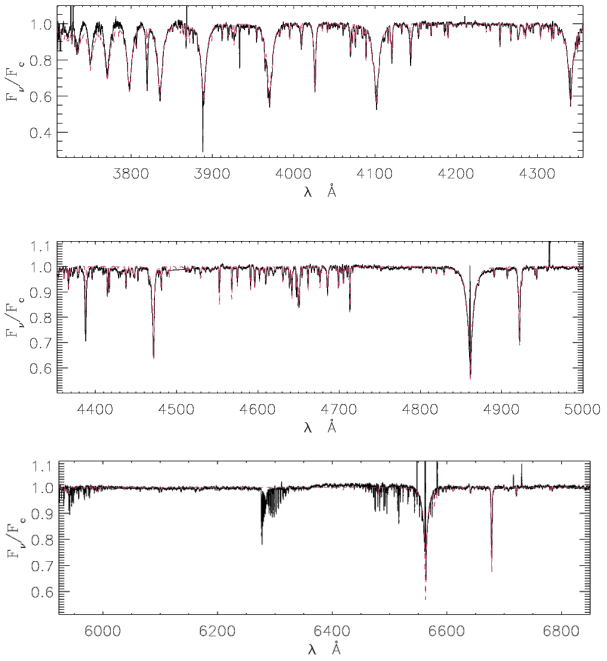

Figure 3: Same as Fig. 2, normalized spectra in the optical range. The CMFGEN model reproduces well the photospheric features observed in these wavelengths. This indicates a correct consistent determination of photospheric and wind parameters. Hα (bottom panel) exhibits no clear wind feature.

the UV to the optical range. CMFGEN solves the spherically expanding non-LTE atmosphere in the co-moving frame, providing a consistent solution for the processes in the photosphere and the wind. In addition, the code includes a simulation of shocks, allowing the user to set up the temperature of the shock region and the wind-depth where they form.

We present in Figs. 2 and 3 our first fits to the spectrum of HD 37020. Results are preliminary, but CMFGEN model reproduces simultaneously the photospheric and [weak] wind features, and produces a good fit to the optical and UV spectra.

5 Conclusions

Our first results indicate that τ Sco and HD 37020, both in the weak-wind luminosity and spectral type regime, have a wind momentum close to the theoretical prediction. Since HD 37020 may have some magnetic activity, and τ Sco is a confirmed magnetic star, this hints that stars with magnetic fields may not experience weak winds. The enhanced X-ray activity due to magnetic fields would change the ionization of elements, and stronger mass loss rates are needed to reproduce the observed wind profiles. Systematic studies of magnetic and non-magnetic stars, including several shock diagnostics (X-ray observations and Far-UV spectra of the O VI 1033 doublet) and mass loss indicators (mostly UV lines) are needed to establish a connection between stellar wind momentum and magnetic activity. The use of CMFGEN models will also be determinant for the problem of weak winds.

Starting from the stars in Orion, we will model the UV and optical spectra of the O9-B0 dwarfs included in the high-resolution, high-S/N IACOB spectroscopic database. New results in the X-ray

domain from Chandra (see for instance Stelzer et al. 2005) will be essential. Results on this relatively large sample, which includes young stars, known magnetic rotators and X-ray emitters will help us disentangle the role played by each of these factors in the weak wind problem.

Acknowledgements

Funded by Spanish MICINN under CONSOLIDER-INGENIO 2010, program grant CSD2006-00070, and grants AYA2007-67456-C02-01 and AYA2008-06166-C03-01.

References

Bouret J.-C., Lanz, T., Hillier, D. J., Heap, S. R., Hubeny, I., Lennon, D. J., Smith, L. J., & Evans, C. J., 2003, ApJ, 595, 1182

Cohen, D., 2011, in *IAU Symposium 272: Active OB stars*

Garcia, M., 2005, *PhD Thesis*

García, M., & Herrero, A., 2010, in *VIII Scientific Meeting of the Spanish Astronomical Society*, Highlights of Spanish Astrophysics V, 407

Grunhut, J. H., Wade, G. A., Marcolino, W. L. F., et al., 2009, MNRAS, 400, L94

Hillier, D. J., & Miller, D. L., 1998, ApJ, 496, 407

Lamers, H. J. G.. L. M., Snow, T. P., & Lindholm, D. M., 1995, ApJ, 455, 269

Marcolino, W.L.F , Bouret, J.-C., Martins, F., Hillier, D. J., Lanz, T., & Escolano, C., 2009, A&A, 498, 837

Martins, F., Schaerer, D., Hillier, D. J., & Heydari-Malayeri, M., 2004, A&A, 420, 1087

Martins, F., Schaerer, D., Hillier, D. J., Meynadier, F., Heydari-Malayeri, M., & Walborn, N. R., 2005, A&A, 441, 735

Pauldrach, A.W.A., Hoffmann, T. L., & Lennon, M., 2001, A&A, 375, 161

Petr-Gotzens, M. G., & Massi, M., 2007, MmSAI, 78, 362

Puls, J., Urbaneja, M. A., Venero, R., Repolust, T., Springmann, U., Jokuthy, A., & Mokiem, M. R., 2005, A&A, 435, 669

Puls, J., Sundqvist, J. O., Najarro, F., & Hanson, M. M., 2009, AIPC, 1171, 123

Simón-Díaz, S., Herrero, A., Esteban, C., & Najarro, F., 2006, A&A, 448, 351

Simón-Díaz, S., Castro, N., Garcia, M., Herrero, A., & Markova, N. 2011, in Proceedings of the 39th Liège Astrophysical Colloquium, eds. G. Rauw, M. De Becker, Y. Nazé, J.-M. Vreux & P. Williams, BSRSL, 80, 514

Schnerr, R. S., Henrichs, H. F., Neiner, C., et al., 2008, A&A, 483, 857

Stelzer, B., Flaccomio, E., Montmerle, T., Micela, G., Sciortino, S., Favata, F., Preibisch, T., & Feigelson, E. D., 2005, ApJSS, 160, 557

Schulz, N. S., Testa, P., Huenemoerder, D. P., Ishibashi, K., & Canizares, C. R., 2006, ApJ, 656, 636

Vink, J., de Koter, A., & Lamers, H. J. G. L. M., 2000, A&A, 362, 295

Wamsteker, W., Skillen, I., Ponz, J. D., de la Fuente, A., Barylak, M., & Yurrita, I., 2000, Ap&SS, 273, 155

Hot, Massive Stars in I Zw 18

Sara R. Heap[1], Ivan Hubeny[2], Thierry Lanz[3], Wayne Landsman[1,4], Don Lindler[1,5], Eliot Malumuth[1,6]

[1] NASA's Goddard Space Flight Center, Mail Code 667, Greenbelt MD, USA
[2] University of Arizona, Tucson AZ, USA
[3] University of Maryland, College Park MD, USA
[4] Adnet Systems, Inc., Rockville MD, USA
[5] Sigma Space, Inc., Lanham MD, USA
[6] Wyle Information Systems, McLean VA, USA

Abstract: We present the far-ultraviolet spectrum of the northwest component of I Zw 18, a blue compact galaxy having a very low metallicity. The spectrum is compatible with continuous star-formation over the past ~ 15 Myr (CSF age), and a very low metallicity, $\log Z/Z_{\odot} \sim -1.7$, although the stellar surface may be enhanced in carbon. Stellar winds are very weak, and the edge velocity of wind lines is very low (~ 250 km/s).

1 Introduction

Blue, compact, dwarf galaxies (BCD's) are primitive galaxies: they are low-mass galaxies that have converted only a small fraction of their gas mass into stars; some are only minimally chemically evolved, with oxygen abundances as low as $1/40^{\rm th}$ that of the sun (Thuan 2008). Their blue, compact appearance arises from prominent star-forming regions containing massive stars. BCD's are starting to receive due attention as they are the closest analogues to the $z \geq 7$ galaxies being discovered by the Hubble Space Telescope (e.g. Finkelstein, Papovich, Giavalisco, et al. 2010). The proximity of BCD's allows us to observe them over a wide spectral band, from X-rays to radio wavelengths, and at high spatial resolution; some have even been resolved into individual stars.

One of the most primitive and best studied BCD is I Zw 18. The ionized gas in I Zw 18 has a low oxygen abundance ($O \sim 1/30\ O_{\odot}$) and nitrogen abundance ($N \sim\ 1/100\ N_{\odot}$) (Pequignot 2008). Metal abundances in the surrounding H I envelope are even lower (Aloisi et al. 2003; Lecavelier des Etangs et al. 2004). HST optical imagery indicates that the two massive star clusters making up the main body of I Zw 18 contain young, massive but apparently normal stars (Hunter & Thronson 1995). Optical spectra of both northwest and southeast clusters revealed the presence of WC stars (Legrand et al. 1997; Izotov et al. 1997), and two WC star-like objects were identified on STIS low-resolution, long-slit UV spectrograms (Brown et al. 2002).

2 Observations

In April 2010, we obtained a far-UV spectrum of the northwest massive star cluster of I Zw 18 using Hubble's Cosmic Origins Spectrograph (COS). The spectrum covers the wavelength region, $\lambda \sim 1130 - 1760$ Å. As the northwest cluster more or less fills the COS 2.5-arc second aperture, the effective resolving power, $R \sim 3500$, is lower than the nominal (point-source) resolving power of COS. The signal-to-noise ratio of the observed spectrum, S/N=15-30 per 7-pixel resolution element, is on the low side for analysis of weak lines. We plan to obtain longer-exposure spectra later this year. Nevertheless, this S/N and resolution (0.4 Å) of the spectrum in hand are sufficient to identify and measure the major stellar features in the UV spectrum.

Not surprising for a low-metallicity galaxy, the stellar features are weak. To help gain an appreciation of how weak, Figure 1 compares the far-UV spectrum of I Zw 18-NW to that of a single star in the Small Magellanic Cloud, NGC 346-113 (OC6 Vz), a metal-deficient star near the zero-age main

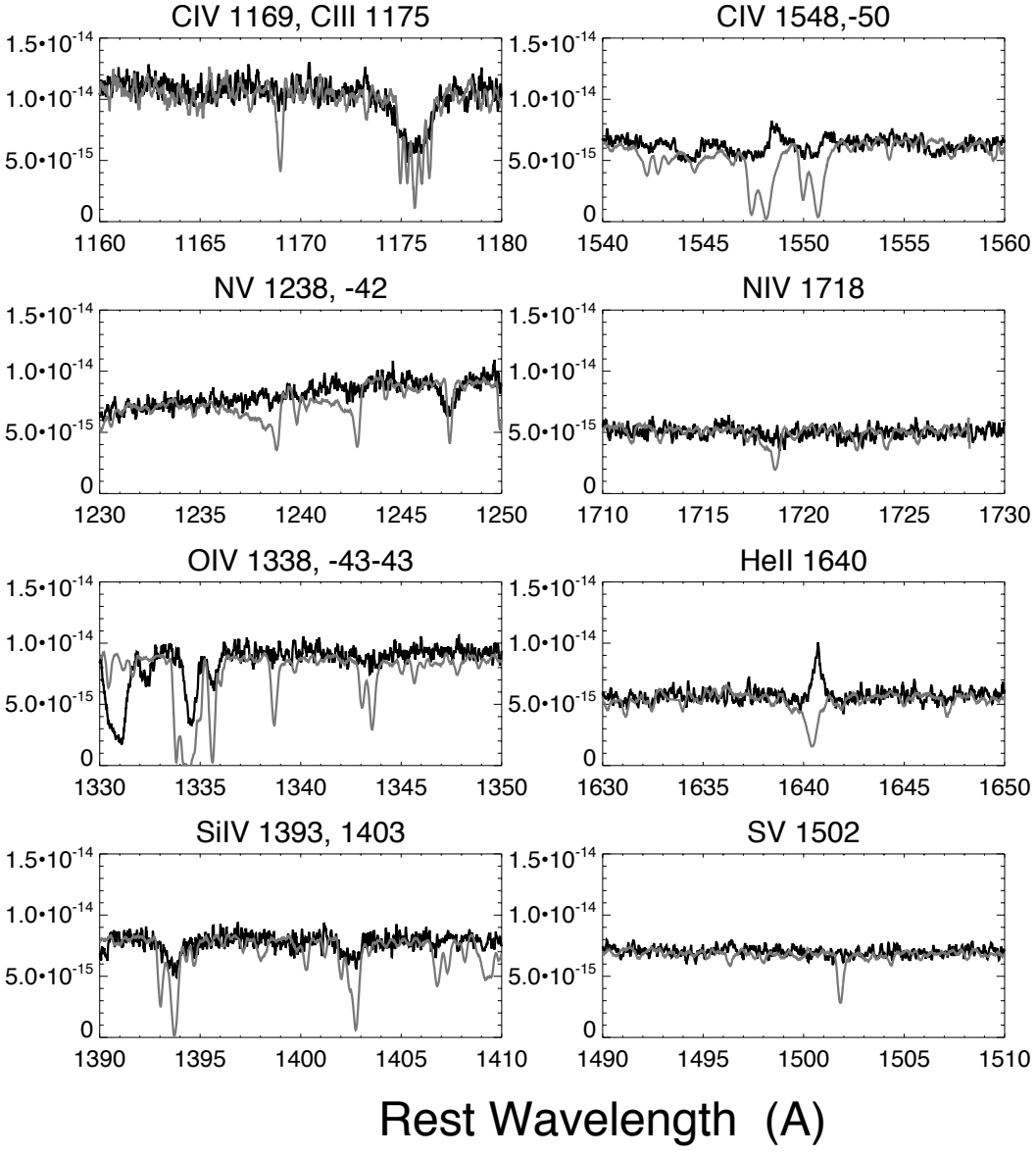

Figure 1: Comparison of the COS spectrum of I Zw 18 (black) with the STIS spectrum of NGC 346-113 (gray) scaled to the flux of I Zw 18 and smoothed to match the resolution of COS.

sequence (Heap, Lanz & Hubeny 2006). In the spectrum of I Zw 18, C III 1175 is moderately strong, the C IV 1549 resonance doublet has a weak P Cygni profile, O IV 1342-3 is present (although too difficult to measure because of the low S/N), and He II 1640 is a strong emission line – all features consistent with a stellar population containing WC stars. Since many of the brighter stars must be O-type stars, it was expected that the N V 1240 doublet and N IV 1718 would also be present, but they are only marginally detected if at all. The Si IV 1400 doublet appears to be purely photospheric rather than having P Cygni profiles, no doubt a consequence of very low metallicity.

3 Observed Properties of the Stellar Population

Figure 2 shows an ultraviolet color-magnitude diagram of stars in the COS aperture derived from HST/STIS images obtained by Brown et al. (2002). Geneva isochrones for $\log Z/Z_\odot = -1.7$ (Lejeune & Schaerer 2002) scaled to a distance of 14.1 Mpc are superposed. The CMD indicates a spread in ages, compatible with continuing star formation. The very blue stars brighter than $m_{FUV} = 20$ have masses of 150 $M_\odot$ or more. They are likely unresolved binaries or multiple systems. The brightest star-like object has a WC spectrum according to Brown and colleagues. The spectra of the other bright blue stars in I Zw 18 vary widely, especially in the strength of Ly-α absorption; some show unidentified emission lines. One caution: the distance to I Zw 18 is not a settled matter; e.g. Izotov & Thuan (2004) obtain D=14.1 Mpc, while Aloisi et al. (2007) estimate D=18 Mpc. If the longer distance is adopted, the luminosities and masses will be even higher than inferred from Fig. 2.

We have estimated the age and metallicity of I Zw 18-NW from the COS spectrum itself. Fig-

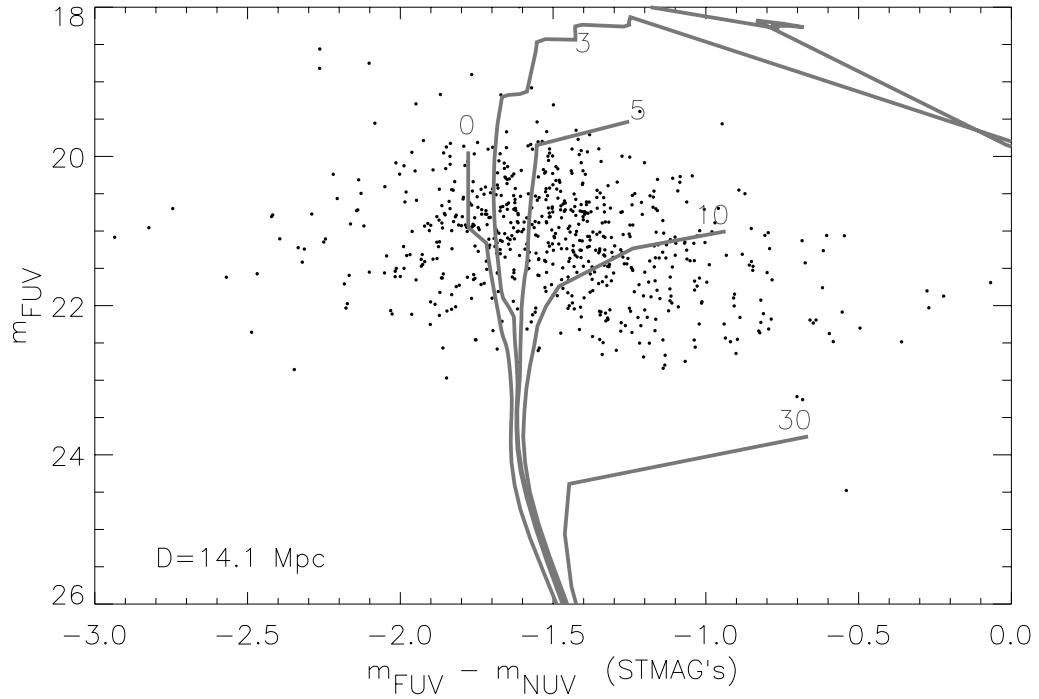

Figure 2: UV color-magnitude diagram of I Zw 18-NW stars in the COS aperture (black dots) and Geneva isochrones for $\log Z/Z_\odot = -1.7$, mass range, $M = 0.8 - 150\,M_\odot$, and age of continuing star-formation = 0, 3, 5, 10, and 30 Myr, as labeled. The magnitudes and colors were measured by Malumuth et al. (in preparation) via PSF-fitting photometry. Corrections for Galactic extinction, E(B-V)=0.032, have been applied.

ure 3 compares the observed spectrum of I Zw 18-NW to a spectral population synthesis model of stars having formed over the past 15 Myr (CSFR=0.055 $M_\odot$/yr) and with a scaled-solar metallicity, $\log Z/Z_\odot = -1.7$. The stellar population synthesis models are based on NLTE photospheric spectral models of Lanz & Hubeny (2003, 2007) and Geneva evolutionary tracks (Lejeune & Schaerer 2002). The main age/metallicity diagnostics are C IV 1169 and C III 1175. (The nitrogen lines are too weak to be measurable and clearly have a very low abundance, the Si IV 1400 doublet does not vary significantly in the age/metallicity range of interest, and the C IV 1549 doublet, and He II 1640 emission are formed at least partially in the wind, where the photospheric models are invalid.) The closest agreement (least disagreement) between model and observation is at an age$\sim$15 Myr, and a metallicity, $\log Z/Z_\odot = -1.7$ (the lowest metallicity in the Geneva grid of evolutionary tracks). At a younger age, e.g. 3 Myr, C IV 1169 and O IV 1342-43 are too strong, while C III 1175 is too weak. At an older age, e.g. 30 Myr, the C IV and O IV lines are too weak. At a higher metallicity, e.g.

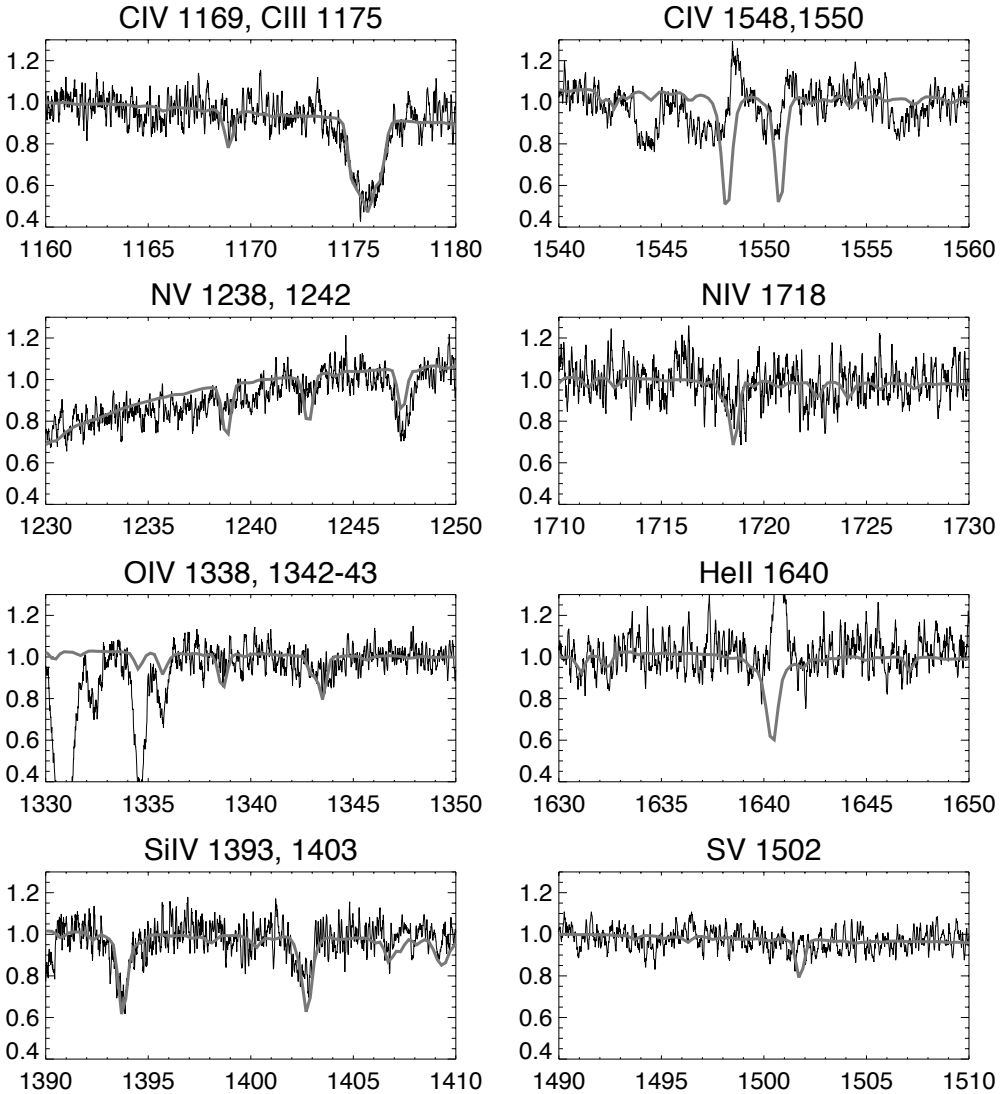

Figure 3: Comparison of the COS spectrum of I Zw 18 (black) with NLTE model photospheric spectrum (gray) of a stellar population with a continuing star-formation age=15 Myr and a scaled-solar metallicity, $\log Z/Z_\odot = -1.7$.

$\log Z/Z_\odot = -1.3$ of the evolutionary model, all the diagnostic C and O lines in the model are too strong. For comparison, a CSF age, $\sim 15 - 27$ Myr, was derived by Martin (1996) from dynamical considerations.

4 Star Formation and Evolution at Very Low Metallicity

Perhaps the massive stars in I Zw 18-NW are not as normal as originally thought –"normal" being stars like massive stars in the Galaxy except in having a lower metal content than galactic stars and thus, weaker winds. Symptoms of abnormality – more probably, symptoms of our lack of understanding of star formation and evolution at very low metallicity – include the following issues.

Abundances. Studies of galactic halo stars (i.e. low mass, low metallicity) (Bonifacio et al. 2009, Fabbian et al. 2009) find that [C/O] first decreases with decreasing oxygen abundance but then rises when [O/H] ≤ -1. This upturn in [C/O] at very low metallicity is interpreted as due to the contribution of carbon in the winds of WR stars. The stellar [C/O] in I Zw 18-NW is consistent within the observational errors with this interpretation.

Nitrogen is synthesized in the CNO cycle operating in H-burning layers of the stellar interior. Nitrogen is said to be "primary" or "secondary" in origin depending on whether the seed C and O are synthesized in the star during helium burning, or were present in the material from which the star formed. Primary N is thought to be produced mainly by intermediate-mass stars ($M/M_\odot = 4 - 7$) on the asymptotic giant branch and is released back to the ISM only after about 250 Myr (Henry, Edmunds & Köppen 2000), well after O was ejected in Type II supernova explosions. But if massive stars are also major contributors of nitrogen, then there would be no time lag between the release of O and N. The low stellar N/O ratio in I Zw 18 favors intermediate-mass stars as the main source of N and a young age of the current star-formation episode.

Stellar Winds at Low Metallicity. The C IV 1549 wind feature has a surprisingly low edge velocity, $v_{edge} \sim 250$ km/sec, compared to predictions ($v_\infty \sim 1050$ km/sec) based on the relation, $v_\infty \propto Z^{0.13}$ (Leitherer, Robert & Drissen 1992; Vink, de Koter & Lamers 2001). Why is it so low? One possibility is that the density of C^{3+} ions is so low that the observed absorption comes from the denser base of the wind where the velocity is much lower than the terminal velocity. A second possibility is that the dependence of the terminal velocity on metallicity is much steeper than usually assumed,. A third possibility, the one we favor, is that the most massive stars producing the bulk of the C IV 1549 wind feature are close binaries, in which the wind of one star is affected by "radiative braking" by a close companion (Owocki 2007).

Crowther & Hadfield (2006) were the first to investigate the spectral properties of Wolf-Rayet stars at low metallicities, and they made specific predictions about the population of WC stars in I Zw 18. They pointed out that the luminosities of WR emission lines should be lower in low-metallicity stars, in qualitative agreement with the weak C IV 1548, 1550 and He II 1640 emission observed in I Zw 18. The lower line luminosities mean that it will take a higher number of WC stars (they estimate at least 30) to match the observed strengths of wind lines. Detailed modeling will be needed to reproduce the observed spectrum of I Zw 18-NW accounting for all contributors – O and B-type stars as well as WR stars.

Rotation-enhanced mass-loss vs. mass transfer in close binaries. Wolf-Rayet stars are the stellar cores of massive stars whose H-rich envelopes have been removed either by strong stellar winds or by mass transfer in close binaries. Not long ago, it was thought that single stars of low metallicity could not enter the WR phase of evolution, because radiatively-driven mass-loss in the lines would be too low to remove the H-rich outer layers characteristic of O-type stars. Then in 2005, Meynet & Maeder showed that when rotation is included in evolutionary models, massive, low-metallicity stars such as

those in the SMC can indeed have a WR phase. Rotation favors the WR phenomenon by lowering the mass limit for entry into the WR phase and lengthening the WR phase. It appears, however, that rotation cannot explain the presence of only WC stars in I Zw 18-NW, because the computed lifetime in the WC phase is always shorter than in the WN phase, so I Zw 18-NW should show both WN and WC characteristics, in contradiction to the observations.

WR stars can also be formed via mass transfer through Roche Lobe Overflow in close binaries. To our knowledge, the binary hypothesis has not yet been developed and applied to very massive ($M/M_{\odot} > 60$), very low-metallicity stars such as those in I Zw 18 but is well deserving of future study. Not only could mass transfer in close binaries explain the presence of WC stars in I Zw 18, but it might also help to understand the low apparent terminal velocity inferred from the C IV 1549 resonance doublet through the mechanism of radiative inhibition.

Acknowledgements

This research was supported by a grant from the COS Science Team at the University of Colorado.

References

Aloisi, A., Clementini, G., Tosi, M., et al., 2007, ApJ, 667, 151
Aloisi, A., Savaglio, S., Heckman, T., Hoopes, C., Leitherer, C., Sembach, K., 2003, ApJ, 595, 760
Bonifacio, P., Spite, M., Cayrel, R., et al., 2009, A&A 501, 519
Brown, T., Heap, S., Hubeny, I., Lanz, T., Lindler, D., 2002, ApJ, 579, L75
Crowther, P. & Hadfield, L., 2006, A&A 449, 711
Fabbian, D., Nissen, P., Asplund, M., Pettini, M., Akerman, C., 2009, A&A 500, 1143
Finkelstein, S., Papovich, Giavalisco, M. et al., 2010, ApJ 719, 1250
Heap, S., Lanz, T., Hubeny, I., 2006, ApJ 638, 409
Henry, R.B.C., Edmunds, M., Köppen, J., 2000, ApJ 541, 660
Hunter, D. & Thronson, H., 1995, ApJ 452, 238
Izotov, Y., Foltz, C., Green, R., Guseva, N., Thuan, T., 1997, ApJ, 487, L37
Izotov, Y, & Thuan, T., 2004, ApJ 616, 768
Lanz, T. & Hubeny, I. 2003, ApJS, 146, 417
Lanz, T. & Hubeny, I. 2007, ApJS 169, 83
Lecavelier des Etangs, A., Désert, J.-M., Kunth, D., et al., 2004, A&A 413, 131
Legrand, F., Kunth, D., Roy, J.-R., Mas-Hesse, J., Walsh, J., 1997, A&A 326, 17
Leitherer, C.. Robert, C., Drissen, L., 1992, ApJ 401, 596
Lejeune, T. & Schaerer, D., 2001, A&A 366, 538
Martin, C., 1996, ApJ 465, 680
Meynet, G. & Maeder, A., 2005, A&A 429, 581
Owocki, S., 2007, in "Massive Stars in Interacting Binaries", ASP Conf. Ser., Vol 367, p. 233
Thuan, T., 2008, in "Low-Metallicity Star Formation", IAU Symp 255, p. 348
Pequignot, D., 2008, A&A 478. 381
Vink, J., de Koter, A., Lamers, H., 2001, A&A 369, 574

Effects of porosity on emergent synthetic spectra of massive stars in the X-ray domain

Anthony Hervé and Gregor Rauw

GAPHE, AGO, Université de Liège, Allée du 6 Août 17, Bât. B5c, 4000 Liège, Belgium

Abstract: Massive stars possess powerful stellar winds. Studies over the last decade, including the analyses of X-ray emission-line profiles, revealed the importance of wind fragmentation and clumping and led to a downwards revision of the mass-loss rates. We present the first results of our code that allows to compare two models of wind fragmentation, and their consequences on the emergent X-ray spectra of massive stars.

1 Introduction

The concept of fragmentation of stellar winds is now widely admitted (Eversberg, Lépine & Moffat 1998, Bouret et al. 2005). Different formalisms exist to describe the absorption of X-rays by fragmented winds. We have developed a code to simulate X-ray spectra in order to compare the porosity formalism involving spherical clumps (Owocki & Cohen 2006) with the fragmentation frequency theory where the clumps are oblate (Oskinova et al. 2006) and allowing for any clump optical depth in both cases. In this contribution, we present a brief overview of some of our results. More details will be given in a forthcoming paper (Hervé et al. 2011, submitted). After a brief description of our method, we show the impact of anisotropy on line profiles and, finally, we explore the impact of a presence of a tenuous interclump medium.

2 Physics and geometry of the model

We adopt the ATOMDB[1] model for the X-ray emissivity as a function of plasma temperature and composition. For the absorption by clumped stellar winds, we compare two different formalisms. We consider the X-ray emitting plasma, defined by an inner and outer radius to be embedded in the wind and moving outwards along with the latter. We discretize the plasma into small cells and analyse the absorption of the photons by the wind along the direction towards the observer. We assume that the wind is homogeneous close to the star and becomes fully fragmented due to the hydrodynamical instabilities at around 1.5 R_*. Optionally, we can add a tenuous smooth interclump medium. Finally we sum up the emission of all the cells accounting for their Doppler shift due to the line-of-sight velocity of the emitting matter as well as for their absorption by the cool wind material (see Sect. 2.1 and 2.2) and we construct the synthetic X-ray spectrum (Hervé et al. 2011).

[1]For more details see the website of Atomdb at the url http://www.atomdb.org/

2.1 Porosity length formalism

The absorption of X-rays by a stellar wind is mainly due to the bound free transitions from the K and L energy levels. Let us consider a model where the individual clumps are spherically symmetric and optically thick. In this case, the geometrical properties of the clumps determine the effective opacity which can be written (Owocki & Cohen 2006):

$$\kappa_{eff} = \frac{l^2}{m_c} = \frac{\kappa}{\tau_c} \tag{1}$$

with $\tau_c = \kappa\langle\rho\rangle\frac{l}{f}$ and where l is the size of the clump, m_c its mass, $\langle\rho\rangle$ the mean density of the stellar wind, f the volume filling factor, and κ the mass absorption coefficient.
The generalisation of the effective opacity accounting for the optically thin and thick limit and the hypothesis that the effective clump absorption in the optically thick limit is given by the geometric cross section lead to a simplified scaled effective opacity:

$$\frac{\kappa_{eff}}{\kappa} = \frac{1}{1+\tau_c} \tag{2}$$

Using this result in a steady state (i.e. non variable) wind, Owocki & Cohen (2006) obtain the wind optical depth:

$$\tau(p,z) = \tau_* \int_z^\infty \frac{R_* dz'}{r'(r'-R_*) + \tau_* h(r')} \tag{3}$$

where $r' = \sqrt{p^2+z'^2}$, $\tau_* \equiv \frac{\kappa\dot{M}}{4\pi v_\infty R_*}$ is a typical measure of the optical depth of the wind, $\dot{M}$ is the mass loss rate, v_∞ is the terminal velocity of the wind, R_* is the radius of the star and $h(r') \equiv \frac{l}{f}$ the so-called porosity length (Owocki & Cohen 2006). In the following we adopt $h(r') = h \times r'$.

2.2 Fragmentation frequency formalism

Alternatively, we now assume that the wind consists of an ensemble of flattened broken-shell-like fragments. Let us consider a flattened fragment of the wind at reference radius r. Its optical depth along the line of sight can be written:

$$\tau_j = \frac{\tau_j^{rad}}{|\mu_j|} = \frac{\kappa_\nu \dot{M}}{4\pi}\frac{1}{r^2}\frac{1}{n_0}\frac{1}{|\mu_j|} \tag{4}$$

with κ_ν the mass absorption coefficient at the frequency ν, τ_j^{rad} the average radial optical depth of a fragment located at distance r and $\mu(r) = \frac{z}{\sqrt{z^2+p^2}}$ its orientation (Oskinova et al. 2004). The number n_0 corresponds to the number of fragments passing through some reference radius and is also called the *fragmentation frequency*. In the case of an isotropic opacity (i.e. spherically symmetric clumps), as for instance in the Owocki & Cohen (2006) formalism, μ is taken equal to unity (i.e. the line of sight crosses each clump along a radial direction). Generalising the opacity of a flattened fragment to all the clumps of the wind, the wind opacity can be written in the general case for the non-spherical fragments as:

$$\tau(p,z) = n_0 \int_z^{z_{max}} (1-e^{-\tau_j})|\mu(r')|\frac{dz'}{v(r')} \tag{5}$$

(see Oskinova et al. 2004), where $v(r)$ is the velocity at radial position r, which is described by a so-called β-law, $v(r) = v_\infty(1-\frac{R_*}{r})^\beta$ with $\beta = 1$.

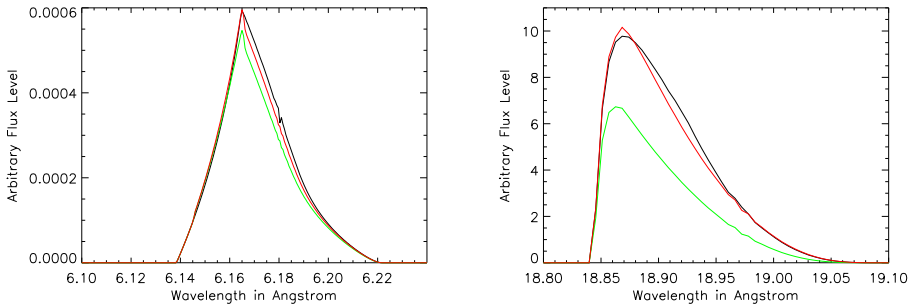

Figure 1: Impact of porosity ($h = 0.07$ in red) on the profiles of two representative X-ray lines, (see Table 1 & 2). The profiles are compared with those computed in the fragmentation formalism for $n_0 = 1.7 \times 10^{-4} s^{-1}$ (in black) and for a homogeneous wind model (in green).

Table 1: Lines considered in this study and associated wind opacity corresponding to the model parameters listed in Table 2.

Line	Wavelength (Å)	τ_*
Si XIV	6.18	1.8
O VIII	18.97	21.89

Table 2: Stellar and wind parameters used in our model corresponding to the wind parameters of ζPup as in Oskinova et al. (2006)

R_*	R_{inner}	R_{outer}	v_∞	$\dot{M}$	n_0	kT
18.6 $R_\odot$	1.5 R_*	10 R_*	2250 km s^{-1}	4.2×10^{-6} M$_\odot$ yr^{-1}	1.7×10^{-4} s^{-1}	0.287 keV

3 Results

To begin, we present the differences between the two formalisms by comparing single X-ray lines with different τ_* in the case of an isotropic opacity ($\mu = 1$ in the fragmentation frequency theory, see Fig.1). As can be seen on Fig. 1, in the case of isotropic fragments, it is possible to find a value of h that yields line profiles that match those for a given value of n_0 rather well, although the value of h is not constant over the entire spectrum, but rather depends on wavelength, especially if we consider lines from a wider wavelength range than illustrated in Fig. 1 (see Hervé et al. 2011). Next, we show the impact of the anisotropy of opacity in the case of flattened clumps ($\mu \neq 1$) on the line profiles (Fig. 2). As can be seen from this example, assuming flattened fragments leads to a lower effective wind opacity and hence a less depressed red shoulder of the X-ray line profiles. We then present the impact of porosity on emergent flux spectra (Fig. 3). Finally, we explore the impact of a tenuous interclump medium on the line profiles (Fig. 4) and global spectra (Fig. 5). More details will be given in a forthcoming paper (Hervé et al. 2011, submitted).

4 Conclusions

In general, the observable flux of X-rays is higher in a fragmented stellar wind than in an homogeneous one. An anisotropic opacity further reduces the absorption by the stellar wind compared to an isotropic one. The profiles of X-ray lines are also modified compared with an homogeneous model. We can find a porosity length to reproduce the X-ray profile simulated in the fragmentation frequency

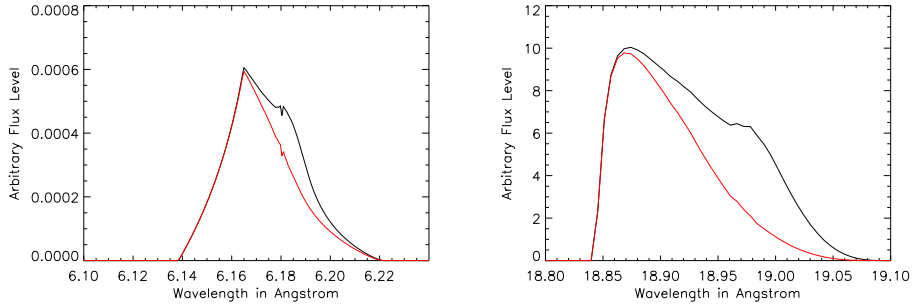

Figure 2: Impact of the anisotropy of the opacity (in black) (fragmented shells seen under a direction cosine μ) on the emergent line profile for two representative X-ray lines lines, (see Table 1 & 2), compared with the line profiles computed for an isotropic opacity ($\mu = 1$; in red) with $n_0 = 1.7 \times 10^{-4} s^{-1}$.

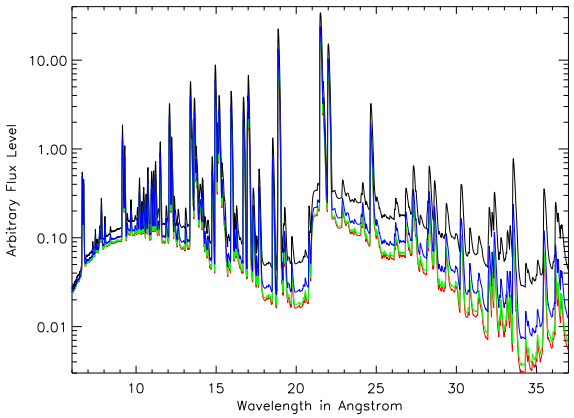

Figure 3: Effect of porosity on the global spectrum. In red, the results for a homogeneous wind, in green, blue and black the spectra for different porosity lengths (0.01, 0.05 and 0.15 respectively).

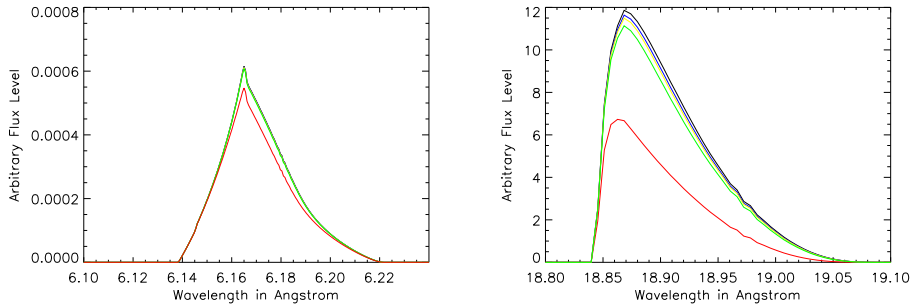

Figure 4: Impact of the presence of an interclump medium. The black line profiles correspond to a fully porous wind (with $h = 0.10$), whilst the red profiles yield the results for a fully homogeneous wind. The blue, yellow and green profiles display the situation for three different mixed models with respectively 97%, 95% and 90% of the wind material in clumps.

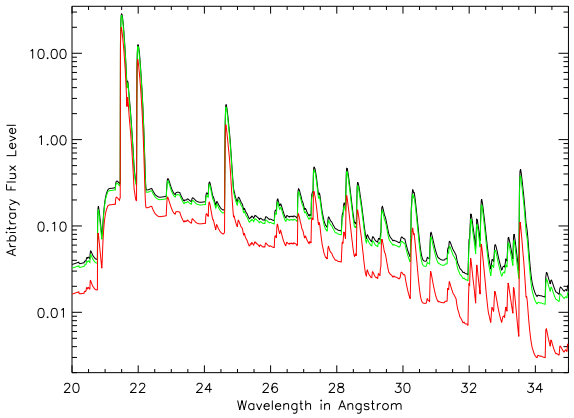

Figure 5: Impact of the presence of an interclump medium on the spectrum between 20 and 35 Å. The black line profiles correspond to a fully porous wind (with $h = 0.10$), whilst the red profiles yield the results for a fully homogeneous wind. The green spectrum displays the situation for a mixed model with 90% of the wind material in clumps.

formalism in the case of an isotropic opacity. However, in general, the porosity length parameter needed to match the profiles computed for a given value of n_0 varies with wavelength. The strongest impact on the global X-ray spectra is expected in the low energy band where the stellar wind opacity is the largest (see Figs. 3 and 5). A mixed model (clumps with a tenuous interclump medium) has a lower emerging X-ray flux than a totally clumped model with the same porosity length, but is equivalent to a less porous model.

Acknowledgements

This research is supported by the FNRS (Belgium) and by the Communauté Française de Belgique - Action de recherche concertée (ARC) - Académie Wallonie–Europe and XMM+INTEGRAL PRODEX contracts.

References

Bouret, J.-C., Lanz, T., & Hillier, D.J. 2005, A&A 438, 301
Eversberg, T., Lépine, S., & Moffat, A.F.J. 1998, ApJ 494, 799
Hervé, A., Rauw, G., Forster, A., & Nazé,Y. 2011, A&A submitted
Oskinova, L.M., Feldmeier, A., & Hamann, W.-R. 2006, MNRAS 372, 313
Oskinova, L.M., Feldmeier, A., & Hamann, W.-R. 2004, A&A 422, 675
Owocki, S.P., & Cohen, D.H. 2006, ApJ 648, 565

High-mass stars in the Galactic center Quintuplet cluster*

Adriane Liermann[1,2], Wolf-Rainer Hamann[2], Lidia M. Oskinova[2] and Helge Todt[2]

[1] Max-Planck-Institut für Radioastronomie, Bonn, Germany
[2] Universität Potsdam, Potsdam, Germany

Abstract: The Galactic center region is heavily obscured by dust in the ultra-violet and visual. Recently, a catalog with near-infrared K-band spectra of massive stars located in the Quintuplet cluster at about 35 pc projected distance of the GC was presented. Among several O stars the cluster hosts a number of massive stars in their late evolutionary stages, i.e. Wolf-Rayet stars of the nitrogen (WN) and carbon (WC) sequence. Tailored analyses with the Potsdam models for expanding atmospheres (PoWR) are presented for the WN stars. We find that the stars belong to a group of rather cool ($T_* \approx 25 - 36$ kK) but very luminous WNL stars ($\log(L/L_\odot) > 6.0$). The derived stellar parameters are discussed in the context of stellar evolution and it is shown that the stars are descendants from massive stars with initial masses of $M_{\rm init} \geq 60\,M_\odot$.

1 Introduction

With the discovery of three massive star clusters within 35 pc projected distance to the Galactic center (GC), this region turned out to be unique to study star formation and evolution. The clusters host a large fraction of the known Galactic massive stars also in late evolutionary stages, e. g. luminous blue variables (LBVs) and Wolf-Rayet (WR) stars.

While the Arches cluster is found to be the youngest cluster with about 2.5 Ma old (Figer et al. 2002) containing basically OB and WR stars of the nitrogen sequence (WN), the Central cluster and Quintuplet cluster are slightly older with ages of 6 and 4 Ma (Figer et al. 1999a, Paumard et al. 2006) and contain carbon enriched WR stars (WC) as well. For the Quintuplet, the Pistol star LBV (Figer et al. 1999a, b), and further LBV candidates (Geballe et al. 2000, Barniske et al. 2008) are found in the neighborhood of the cluster.

The combination of quantitative spectral analysis and comprehensive stellar model atmospheres allows the stellar parameters to be determined. In comparison of stellar evolution models with the stellar parameters the initial masses and ages of the sample stars can be estimated. Thus, the evolution of the stellar population of massive stars in the Galactic center can be discussed.

*Based on observations with the ESO VLT-SINFONI

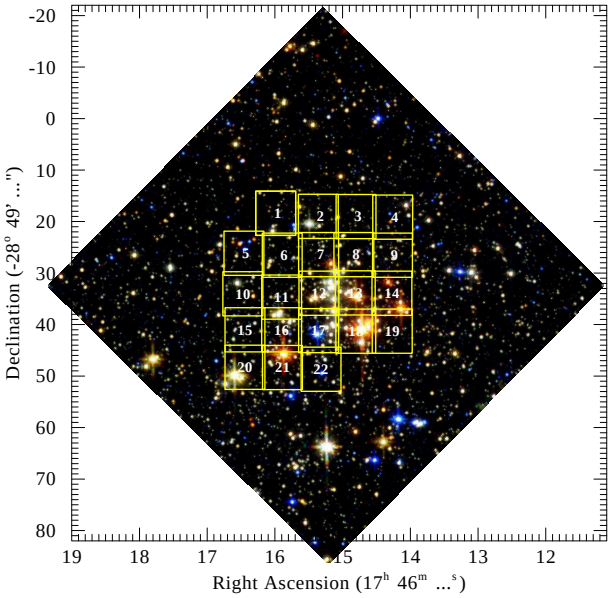

Figure 1: Fields observed with SINFONI in the Quintuplet central regions shown on an HST image (STScI-PRC1999-30b).

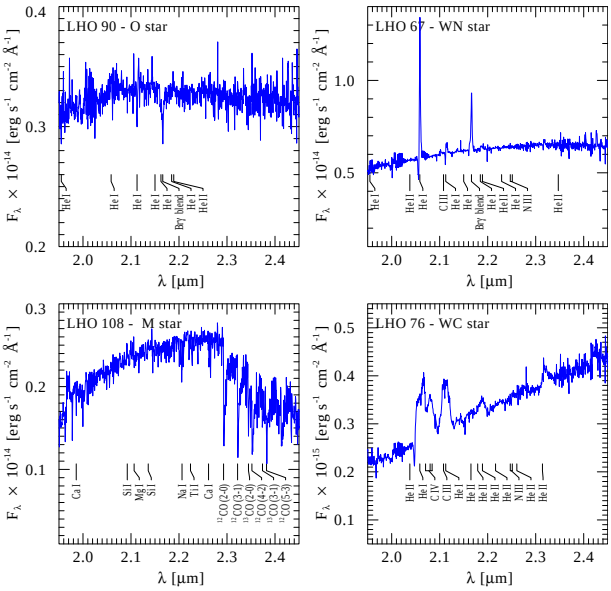

Figure 2: Example spectra from the LHO catalog with line identifications used for spectral classification.

2 Analysis

2.1 Observations

The high extinction in the direction of the GC ($A_V \approx 28$ mag) prohibits observations in the ultraviolet and optical range. Therefore, infrared spectroscopy is the prime tool to study massive stars in this region of the Milky Way. We used the ESO-VLT Spectrograph for INtegral Field Observation in the Near-Infrared (SINFONI) to observe the central parts of the Quintuplet cluster in 22 fields of 8×8 arcsec field of view, see Fig. 1 with a background composite HST image (HST program 7364, PI D. Figer, NICMOS F110W, F160W, and F205W). A spectral catalog of the point sources with 160 flux-calibrated K-band spectra was presented by Liermann et al. (2009, hereafter LHO catalog). Example spectra are shown in Fig. 2. For details on data reduction and flux-calibration, please refer to the catalog paper.

Among the 13 WR stars listed in the LHO catalog four are of WN and nine are of WC type. First, we concentrate on the analysis of the WN stars as described in Liermann et al. (2010). The sample comprises WR 102d, WR 102i, WR 102hb, and WR 102ea. Additionally, the star LHO 110 was included in the sample, which was classified as Of/WN candidate in the LHO catalog. However, the spectrum of this star strongly resembles spectra of typical WN stars.

2.2 PoWR models

The Potsdam Wolf-Rayet non-LTE model atmospheres (PoWR) are described in a number of publications and we refrain from repeating the details here. For further reading we suggest the reader to have a look in Hamann & Gräfener (2004).

To determine the stellar parameters we fit the spectral energy distribution (SED) of the stars by adjusting the extinction to match the observed 2MASS J, H, and K-band magnitudes (Fig. 3, upper panel). Simultaneously, the model continuum is used to normalize the observed flux-calibrated spectrum which then can be fitted with a synthetic emission line spectrum (Fig. 3, lower panel). To obtain

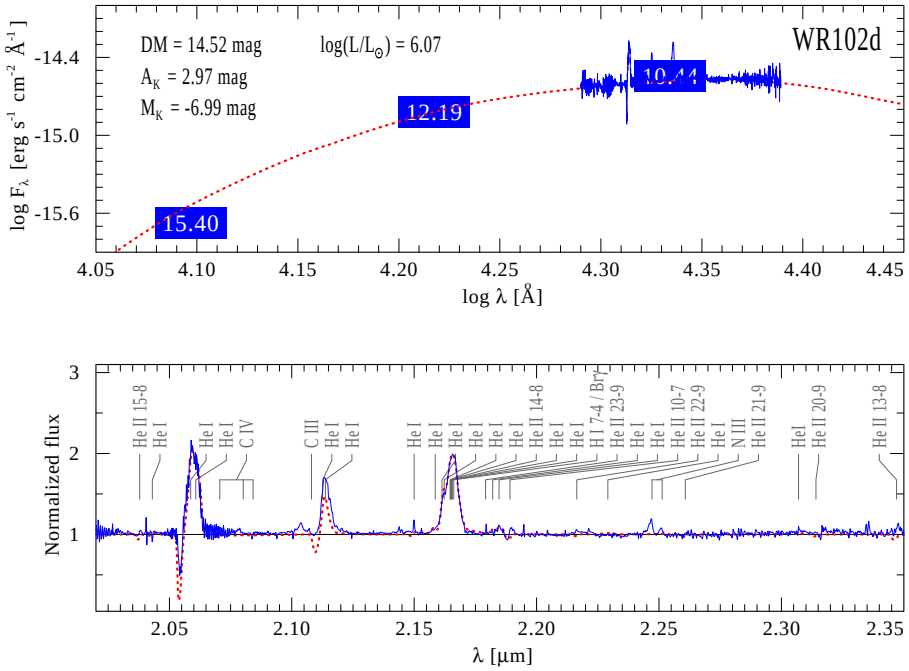

Figure 3: *upper panel*: SED and 2MASS J, H and K-band magnitudes (blue solid line and boxes) fitted with PoWR model (red dotted line) to determine the extinction and luminosity of the star. *lower panel*: Normalized emission line spectrum (blue solid line) and PoWR model (red dotted line) to derive the stellar and wind parameters.

the best fitting model these steps are an iterative process.

We find that all Quintuplet WN stars are of late type (WN9h) still having a significant amount of hydrogen (up to 45%) in their atmospheres, and that they are descendants from initially very massive ($M_{\rm init} \geq 60\,M_{\odot}$) stars. Further details on the models and the spectral analysis of the individual stars can be found in Liermann et al. (2010). In the following, we will focus on the aspect of the initial mass of the sample stars and their position in the HRD compared with Geneva stellar evolution tracks.

3 Discussion

Massive stars with initial masses above $20\,M_{\odot}$ are supposed to pass the WR phase after they left the main sequence. In dependence of the initial stellar mass, different evolutionary scenarios are possible, which might exclude specific phases such as the blue or red supergiant (BSG/RSG) or LBV phase completely, e. g. Crowther (2007) and Maeder et al. (2008). However, in any evolutionary sequence the luminous late-type WN stars (WNL) are an interphase between O stars leaving the main-sequence and WR stars of the carbon sequence (WC), before these massive stars explode as supernova (SN).

As shown in the HRD (Fig. 4) the WNL stars in the Quintuplet form a group of relatively cool but very luminous stars to the right of the zero-age main sequence. Other Galactic WNL stars (open symbols, Hamann, Gräfener & Liermann 2006) and the WNL stars from the Arches cluster (light grey filled symbols, Martins et al. 2008) support the idea of two distinct groups with the hydrogen containing WNL and hydrogen-free WNE stars.

The cool temperatures in combination with the extreme luminosities make it quite difficult to compare the position of the stars with stellar evolution models. Fig. 5 shows the HRD again, with tracks including the effects of rotation (solid lines) and without (dashed lines) by Meynet & Maeder (2003, Geneva tracks). The tracks were calculated for solar metallicity and different initial masses. It

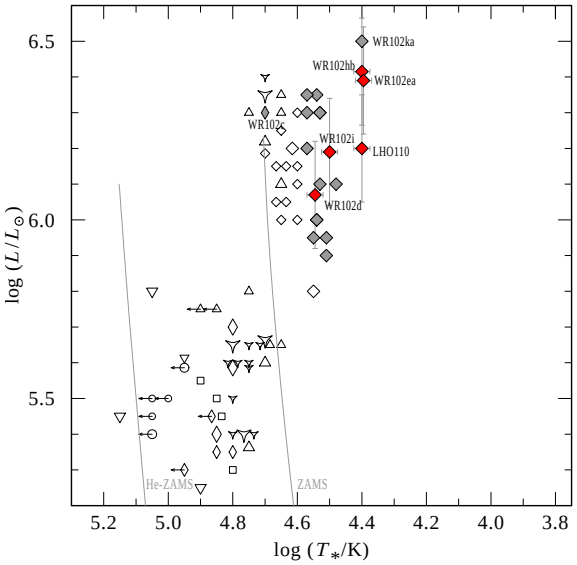

Figure 4: HRD placing the Quintuplet WN stars (red with error bars) in a group of cool but luminous stars: Galactic WN (open symbols, Hamann et al. 2006), Arches WN stars (filled grey, Martins et al. 2008), and WR 102c and WR 102ka (Barniske et al. 2008).

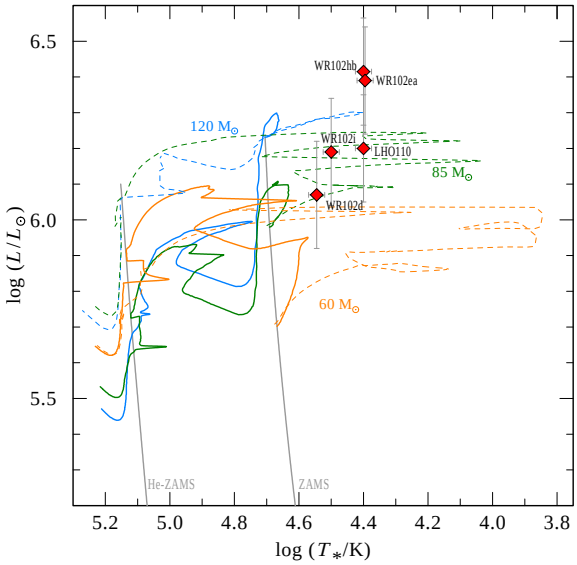

Figure 5: Similar to Fig. 4, the Quintuplet WN stars are shown in comparison with stellar evolution models (Meynet & Maeder 2003). Tracks are for initial masses of 60, 85, and 120 $M_\odot$ and include for the effects of rotation (solid) or not (dashed).

can clearly be seen, that the tracks with rotation don't reach into the cool domain the stars are located in and that only the very high-mass tracks $\geq 60\,M_\odot$ initial stellar mass can be considered for their origin. As already noticed by Hamann, Gräfener & Liermann (2006) stellar evolution tracks without rotation extend further into the cool domain and thus fit better to the HRD positions of the stars. This might only imply that the initial equatorial rotational velocity might be lower than the 300 km/s assumed in the stellar evolution models.

The stars WR 102d, WR 102i and LHO 110 fall in the domain of the tracks with initial masses of 60 $M_\odot$ and 85 $M_\odot$. We assume a range of luminosities and stellar temperature for each star according to the error margins (see Liermann et al. 2010) to determine present-day masses and ages for the stars. Additionally, we keep an eye on the surface hydrogen abundance and mass-loss rate to be comparable to the one we derived with the PoWR models; this helps to overcome the slight degeneracy that, within their error margins, most of the sample stars can be assigned to either of the two tracks. In the corresponding part of the Geneva tracks, the models are still the the phase of central hydrogen burning.

But WR 102hb and WR 102ea lie far above the track with the highest initial mass of 120 $M_\odot$. Since we cannot apply the Geneva models, their position in the HRD is compared with stellar evolution tracks by Langer et al. (1994) shown by Figer et al. (1998, Fig. 15a). This leads to an initial mass of > 100 and 150 $M_\odot$ with an age estimate of > 1.9 and 2.1 million years for WR 102ea and WR 102hb, respectively.

We obtained present-day stellar masses from comparison with the Geneva tracks for the three stars of "lower" initial mass in our sample, WR 102d, WR 102i and LHO 110, see Table 1. But we cannot easily provide the numbers for the two most-luminous stars of our sample, WR102hb and WR102ea. However, we notice that the mass-luminosity-relation by Langer (1989), which was actually calculated for core-helium-burning stars, yields similar values for the three stars for which we had obtained $M^{\mathrm{Geneva}}_{\mathrm{present}}$ from the tracks; although our stars have hydrogen abundances up to 45% left in their atmospheres. Thus, we use the Langer relation as a proxy to estimate the present-day masses of WR 102hb

Table 1: Age, initial mass ($M_{\rm init}$), and present-day mass ($M_{\rm present}^{\rm Geneva}$) for the Quintuplet WN stars determined from the Geneva tracks (Meynet & Maeder 2003). The last column lists masses derived with the mass-luminosity relation by Langer (1989, $M_{\rm present}^{\rm Langer}$).

star	age [Ma]	$M_{\rm initial}$ [$M_\odot$]	$M_{\rm present}^{\rm Geneva}$ [$M_\odot$]	$M_{\rm present}^{\rm Langer}$ [$M_\odot$]
WR102hb	2.1	150	-	61
WR102ea	>1.9	>100	-	58
WR102i	3.1	85	45	43
WR102d	3.6	60	28	36
LHO 110	3.1	85	43	44

and WR 102ea (Table 1, last column).

4 Conclusion

We analyzed the WNL stars in the Quintuplet cluster by means of stellar atmosphere models (PoWR) and determined their fundamental parameters. In the cases where the stars could be properly assigned to evolutionary tracks, they show ages older than 3 million years which is in agreement with the cluster age of 4 million years. In addition, they are most likely still hydrogen-burning objects and their derived present-day masses reveal that the stars have already lost up to 50 % of their initial mass. This strongly emphasizes the importance of the mass loss for the stellar evolution.

References

Barniske, A., Oskinova, L. M. & Hamann, W.-R. 2008, A&A, 486, 971

Crowther, P. A. 2007, ARA&A, 45, 177

Figer, D. F., Najarro, F., Morris, M., McLean, I. S., Geballe, T. R., Ghez, A. M. & Langer, N. 1998, ApJ, 506, 384

Figer, D. F., McLean, I. S. & Morris, M. 1999a, ApJ, 514, 202

Figer, D. F., Morris, M., Geballe, T. R., Rich, R. M., Serabyn, E., McLean, I. S., Puetter, R. C. & Yahil, A. 1999b, ApJ, 525, 759

Figer, D. F., Najarro, F., Gilmore, D., Morris, M., Kim, S. S., Serabyn, E., McLean, I. S., Gilbert, A. M., et al. 2002, ApJ, 581, 258

Geballe, T. R., Najarro, F. & Figer, D. F. 2000, ApJ, 530, L97

Hamann, W.-R. & Gräfener, G. 2004, A&A, 427, 697

Hamann, W.-R., Gräfener, G. & Liermann, A. 2006, A&A, 457, 1015

Langer, N. 1989, A&A, 210, 93

Langer, N., Hamann, W.-R., Lennon, M., Najarro, F., Pauldrach, A. W. A. & Puls, J. 1994, A&A, 290, 819

Liermann, A., Hamann, W.-R. & Oskinova, L. M. 2009, A&A, 494, 1137

Liermann, A., Hamann, W.-R. & Oskinova, L. M., Todt, H. & Butler, K. 2010, A&A 524, A82

Maeder, A., Meynet, G., Ekström, S., Hirschi, R., & Georgy, C. 2008, in IAU Symposium, Vol. 250, IAU Symposium, 3–16

Martins, F., Hillier, D. J., Paumard, T., Eisenhauer, F., Ott, T. & Genzel, R. 2008, A&A, 478, 219

Meynet, G. & Maeder, A. 2003, A&A, 404, 975

Paumard, T., Genzel, R., Martins, F., Nayakshin, S., Beloborodov, A. M., Levin, Y., Trippe, S., Eisenhauer, F., et al. 2006, ApJ, 643, 1011

Mass loss in 2D Rotating Stellar Models

Catherine Lovekin[1*] and Robert G. Deupree[2]

[1] LESIA, Observatoire de Paris
5 Place Jules Janssen, 92195 Meudon, France
[2] Institute for Computational Astrophysics, Saint Mary's University
923 Robie St, Halifax, NS B3H 3C3, Canada

Abstract: Radiatively driven mass loss is an important factor in the evolution of massive stars. The mass-loss rates depend on a number of stellar parameters, including the effective temperature and luminosity. Massive stars are also often rapidly rotating, which affects their structure and evolution. In sufficiently rapidly rotating stars, both the effective temperature and radius vary significantly as a function of latitude, and hence mass loss rates can vary appreciably between the poles and the equator. In this work, we discuss the addition of mass loss to a 2D stellar evolution code (ROTORC) and compare evolution sequences with and without mass loss.

1 Introduction

Many massive stars start their lives as rapid rotators, and some remain rapidly rotating throughout their main sequence evolution. This will influence their structure and the course of their evolution. As a result of centrifugal forces, rapidly rotating stars become flattened, and the temperature, and hence the flux, varies as a function of co-latitude (von Zeipel 1924). Very massive OB stars are luminous enough to lose mass in a radiatively driven wind (Lucy & Solomon 1970; Castor, Abbott & Klein 1975). The amount of mass lost can be significant, as is the effect on the stellar evolution, as radiatively driven winds remove both mass and angular momentum from the surface of the star. The rate at which mass is lost is dependent on the temperature and the radius, so as these vary across the surface of a star, the mass loss rate can also be expected to vary (see, e.g. Owocki, Cranmer & Gayley 1998; Dwarkadas & Owocki 2002).

Rotation also changes the shape of the stellar surface, increasing the radius of the equator relative to the polar radius. This is thought to be the origin behind the $\Omega\Gamma$ limit, as described by Maeder & Meynet (2000). In stars sufficiently close to the Eddington limit, the critical velocity is reduced, such that

$$v_{crit} = v_{crit,1}(\frac{3}{2})^{1.25}(1-\Gamma)^{1/2}$$

when $\Gamma > 0.639$, and $v_{crit,1} = (2GM/3R_p)^{1/2}$ (Maeder & Meynet 2000). This is not expected to have a large effect on the total mass loss, but see the discussion in Section 3.

*Current Address: Los Alamos National Laboratory, P.O. Box 1663, T-2, MS-B283, Los Alamos, NM 87545

The variation in the mass-loss rate over the surface of the star will also affect the angular momentum loss. As the angular momentum depends on the distance from the rotation axis, variation in the mass-loss rates over the surface of the star will change the amount of angular momentum lost compared to spherically symmetric (1D) models of mass loss. Since rotation is also an important factor in determining the evolution of a star, changing the amount of angular momentum lost will influence the evolution. The change in angular momentum loss and the distribution of mass loss from a rotating star can be expected to affect the evolution of the star. In this work, we investigate these effects and attempt to determine their significance.

To determine the actual importance of these 2D effects on the evolution of rotating massive stars, we have added radiatively driven mass loss to a 2D stellar evolution code. We discuss the method used to model the mass loss, and the effects of 2D mass loss on both the structure and evolution of the models.

2 Models

We calculate mass loss-rates for 2D stellar structure models calculated using `ROTORC` (Deupree 1990, Deupree 1995). This code solves the equations for conservation of mass, energy and three components of momentum along with Poisson's equation on a two dimensional grid, defined by the angular coordinate (co-latitude) and the fractional surface equatorial radius. The equatorial radius is determined by requiring the integral of the density over the volume to produce the correct mass of the model. The surface is assumed to be an equipotential with the value set by the equatorial radius. Calculating the surface in this way, allows us to determine the surface location in rotating stars without assuming von Zeipel's law (von Zeipel 1924) holds.

The models discussed here use 581 radial and 10 surface zones. The mass loss rate is calculated locally for each of the 10 surface zones using the local effective temperature and a local luminosity in each zone. The local luminosity is calculated using the local flux, and corresponds to the luminosity in a spherically symmetric star with the local effective temperature and radius. The mass-loss rates are calculated using the prescription of Vink et al. (2001), which also depend on the mass and metallicity of the star. All of the models discussed here are 20 $M_{\odot}$ with solar metallicity. Once the mass loss rate in each zone has been calculated, the total mass lost from that zone is calculated by weighting the mass loss rate by the area of the zone. We have also included an option to calculate the mass loss using the overall effective temperature, calculated as the effective temperature of a sphere with the same luminosity, and luminosity of the model, which gives us a pseudo-1D mass loss calculation. In this case, the mass lost is divided evenly among the angular zones.

Regardless of the mass-loss prescription, once the mass-loss rates and the total mass loss has been calculated, the mass is removed from successive surface layers until the required amount of mass loss has been reached. The surface of the star is redefined to this new location, and the model is then allowed to relax to an equilibrium configuration, in which the surface is once again an equipotential and the model is in thermal and hydrostatic equilibrium, before the evolution continues.

3 Mass-Loss Rates

We compared the mass loss rates calculated using the 2D mass loss rates, based on the local effective temperature and local luminosity in each zone to the pseudo-1D calculation, based on the overall effective temperature and luminosity of the star. In both cases, the total amount of mass lost is the same. This is consistent with the results of Maeder & Meynet (2000), which indicate that rotation is not expected to have a significant effect on the total mass loss. However, while the amount of mass

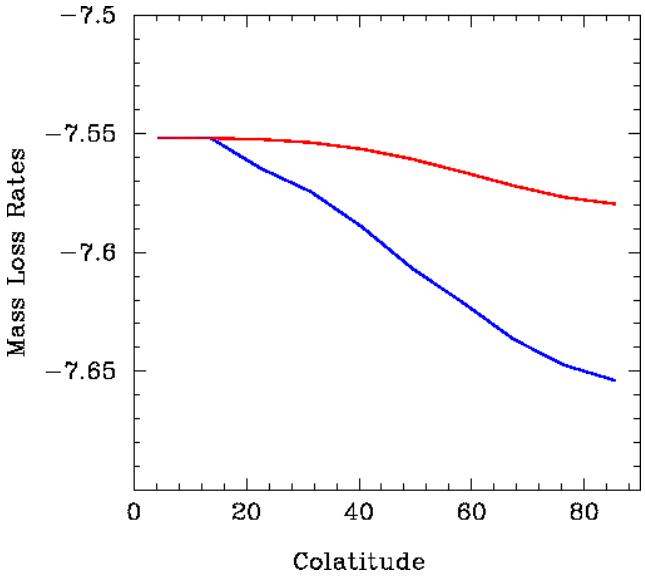

Figure 1: Calculated mass-loss rates for a 20 $M_\odot$ rotating at 275 km s^{-1} for the 2D case (blue) and the CAK predictions (red). The mass loss rates in the 2D calculation decrease towards the equator much more rapidly than the CAK predictions.

lost in both calculations is the same, the distribution of mass loss is not. The 2D calculation, using the local temperature and luminosity, has a much higher mass-loss rate at the pole than the 1D case, while the mass loss rate at the equator is lower. Our fully 2D calculations will allow us to calculate the evolutionary effects of the mass loss distribution and perhaps better understand the $\Omega\Gamma$ limit. Unlike previous calculations, we do not need to assume a Roche potential or a specific gravity darkening law when calculating the stellar structure.

Scaling laws for calculating the mass loss as a function of angle for 1D models exist, and have been used extensively. Using the Castor, Abbott & Klein (1975) (CAK) mass-loss rates and assuming a von Zeipel (1924) gravity darkening law, it can be shown that the mass loss rate as a function of angle is

$$\frac{\dot{m}(\theta)}{\dot{m}_o} = 1 - \Omega \sin^2 \theta$$

where $\Omega = V_{rot,eq}^2 R_{eq}/GM$ (Owocki, Cranmer & Gayley 1998). A comparison of our fully 2D calculation using the Vink et al. (2001) mass loss rates and the CAK predictions based on this formula is shown in Figure 1. The CAK mass loss rates are normalized to be the same as the Vink et al. (2001) mass loss rates at the pole. As shown in Figure 1, our calculated mass loss rates are considerably lower at the equator than the CAK predictions. Work is in progress to determine how much of this difference arises from the models, and how much arises from the different mass loss rates.

4 Structure

We have compared the interior structure of models that have had mass removed by both the 2D calculation and the pseudo 1D calculation. As discussed above, the type of calculation does not affect the total amount of mass removed, merely the distribution of this mass. We have found that even one mass loss event, corresponding to $\sim 10^{-4} - 10^{-5}$ $M_\odot$ is sufficient to affect the interior structure. A comparison of the 1D and 2D mass loss rates shows small differences throughout the star. In general, the density of the 1D model is larger than the 2D model, while the internal temperature is lower. After a single mass loss event, the differences are too small to have a significant effect on the star, but may

accumulate over the course of the main sequence evolution. As discussed below, the radius of the 1D model does not increase as rapidly as the other model, which would correspond to a larger density given the same rate of mass loss.

Changing the surface distribution of the mass loss also affects the surface structure, as might be expected. We compared mass loss in a model with an initial equatorial radius of 5.992 $R_\odot$. After a 2D mass-loss event, the equatorial radius was 5.997 $R_\odot$, while after a 1D mass-loss event the equatorial radius was 5.991 $R_\odot$. The surface shape was also affected. In both cases, the polar radius remained the same fraction of the equatorial radius, at 0.969 R_{eq}. Both models had slightly smaller radii at some intermediate latitudes, but the 1D model shrank at more latitudes than the 2D model. This is again consistent with the finding that the radius of the 1D model does not increase as rapidly as the 2D model, as discussed in the next section. The model under consideration here is rotating at only 200 $\mathrm{km\,s^{-1}}$, which gives $\Omega/\Omega_{crit} \sim 0.3$, and the temperature difference between pole and equator is only about 1000 K. Presumably, as this difference increases in more rapidly rotating models, the differences between 1 and 2D mass loss will also increase.

5 Evolution

To date, we have evolved models through the first 15 time steps of an evolution sequence, or approximately 1.5 Myr. Mass-loss events were calculated after the fifth and tenth time steps. We have found that relative to a rotating model with no mass loss, the effective temperature increases and the total luminosity decreases, as shown in Figure 2. The temperature difference is largest immediately after the mass loss event, and remains larger than that of a non rotating model. The differences in luminosity are smaller, but also smoother than the temperature differences. Interestingly, the temperature difference is larger in the pseudo-1D case, while the luminosity difference is slightly larger in the 2D case.

The origin of these differences is probably in the change in equatorial radius of each of these models. In all three models (1D, 2D, no mass loss) the equatorial radius increases and the surface rotational velocity decreases as the star evolves. Of the three models considered here, it is actually the model with no loss that expands and spins down the fastest. Although no angular momentum is removed by mass loss in this model, no mass is removed from any point on the star either. In the pseudo-1D case, a significant amount of mass is lost from the equator, taking angular momentum with it. The larger mass loss and angular momentum loss effectively shrink the equatorial radius in this model, such that the radius grows more slowly than in the other models, and the model spins down the least.

In effect, the temperature differences shown in Figure 2 are somewhat deceptive, as it is actually the pseudo-1D model that changes the least in temperature. What appears as a relatively large temperature difference is actually a result of the faster increase in radius, and hence faster decrease in temperature, of the model that does not lose mass. In the 2D model, less mass and angular momentum are lost from the equator than in the pseudo-1D case, and the model is intermediate between the other two cases. After only 1.5 Myr, the differences are small, but increase with time, and can be expected to accumulate over the course of the main-sequence evolution.

6 Conclusions

Preliminary results indicate that a full 2D calculation of mass loss using the local effective temperature and luminosity can significantly affect the distribution of mass loss in rotating main sequence stars. More mass is lost from the pole than predicted by 1D models, while less mass is lost at the

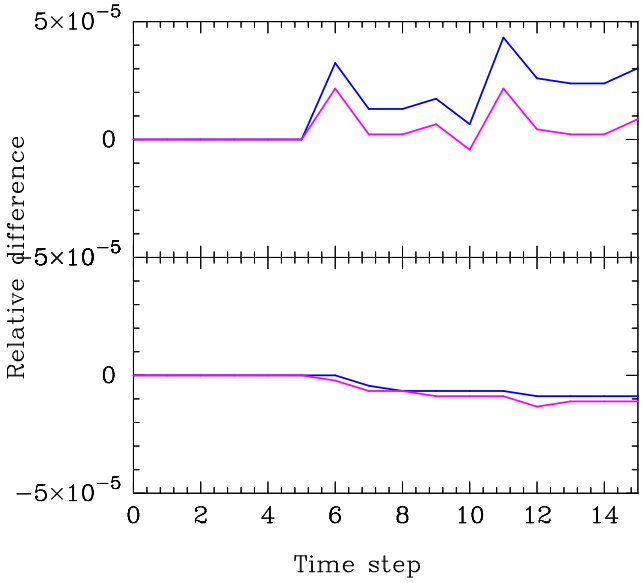

Figure 2: The effective temperature (top) and luminosity (bottom) relative to a model which is rotating but not losing mass. The differences are normalized by the effective temperture and luminosity of the non-rotating model. Shown are the differences for pseudo 1D (blue) and 2D (purple) mass loss.

equator. This change in the distribution of mass loss will affect the angular momentum loss, the surface temperature and luminosity, and even the interior structure of the star. After a single mass-loss event, these effects are small, but can be expected to accumulate over the course of the main sequence evolution.

Acknowledgements

This work was supported by the French National Research Agency (ANR) and the National Science and Engineering Research Council of Canada (NSERC). Computational facilities were provided through ACENet, which is funded by the Canada Foundation for Innovation (CFI) and agencies of the Atlantic Canadian provinces.

References

Castor, J.I., Abbott, D.C. & Klein, R.I. 1975. *ApJ*, 195, 157
Deupree, R.G. 1990. *ApJ*, 357, 175
Deupree, R.G. 1995. *ApJ*, 439, 357
Dwarkadas, V.V. & Owocki, S.P. 2002. *ApJ*, 581, 1337
Lucy, L.B. & Solomon, P.M. 1970. *ApJ* 159, 879
Maeder, A. & Meynet, G. 2000. *A&A*, 361,159
Owocki, S.P., Cranmer, S.R. & Gayley, K.G. 1998. *ApSS*, 260, 149
Vink, J.S., de Koter, A. & Lamers, H.J.G.L.M. 2001. *A&A*, 369, 574
von Zeipel, H. 1924. *MNRAS*, 84, 665

The Mons campaign on OB stars

T. Morel,[1] G. Rauw,[1] T. Eversberg,[2] F. Alves,[3] W. Arnold,[4] T. Bergmann,[5]
N. G. Correia Viegas,[6] R. Fahed,[7] A. Fernando,[8] L. F. Gouveia Carreira,[9]
T. Hunger,[10] J. H. Knapen,[11] R. Leadbeater,[12] F. Marques Dias,[13] A. F. J. Moffat,[7]
N. Reinecke,[14] J. Ribeiro,[15] N. Romeo,[16] J. Sánchez Gallego,[11] E. M. dos Santos,[6]
L. Schanne,[17] O. Stahl,[18] Ba. Stober,[19] Be. Stober,[19] K. Vollmann,[2]
M. F. Corcoran,[20] S. M. Dougherty,[21] K. Hamaguchi,[20] J. M. Pittard,[22]
A. M. T. Pollock[23] and P. M. Williams[24]

[1] Institut d'Astrophysique et de Géophysique, Université de Liège, 4000 Liège, Belgium
[2] Schnörringen Telescope Science Institute (STScI), Am Kielshof 21a, 51105 Köln, Germany
[3] Av. Portugal 616C - 2765–272 Estoril, Portugal
[4] Burggraben 3, 61206 Wöllstadt, Germany
[5] Eichendorffstrasse 8, 63538 Grosskrotzenburg, Germany
[6] Rua Nuno Ataide Mascarenhas, No. 47, 2.Esq. 8100–610 Loule, Portugal
[7] Département de Physique, Université de Montréal, Montréal (Québec) H3C 3J7, Canada
[8] Alto Ajuda, Rua 27 - No. 215 1300–581, Lisbon, Portugal
[9] R. Rego de Agua LT 24 RC Esq., Marrazes, 2400 Leiria, Portugal
[10] Normannenweg 39, 59519 Möhnesee-Körbecke, Germany
[11] Instituto de Astrofísica de Canarias, E-38200 La Laguna, Tenerife, Spain
[12] Three Hills Observatory, The Birches, Torpenhow CA7 1JF, UK
[13] Rua Almirante Campos Rodrigues, Edf. Girassol, 5F, 1500–036 Lisbon, Portugal
[14] Fontainegraben 150, 53123, Bonn, Germany
[15] R. Venezuela 29 3 Esq. - 1500–618 Lisbon, Portugal
[16] Virulylaan 30, 2267 BS Leidschendam, The Netherlands
[17] Hohlstrasse 19, 66333 Völklingen, Germany
[18] ZAH, Landessternwarte Königstuhl, 69117 Heidelberg, Germany
[19] Nelkenweg 14, 66907 Glan-Münchweiler, Germany
[20] Laboratory for High Energy Astrophysics, Goddard Space Flight Center, Greenbelt, USA
[21] Herzberg Institute for Astrophysics, Penticton, British Columbia V2A 6J9, Canada
[22] School of Physics and Astronomy, The University of Leeds, Leeds LS2 9JT, UK
[23] ESA XMM-Newton Science Operations Centre, Villafranca del Castillo, Spain
[24] Institute for Astronomy, University of Edinburgh, Royal Observatory, Edinburgh, UK

Abstract: In parallel with the monitoring of the periastron passage of the binary system WR 140, a number of B supergiants and Oe stars have been observed in the framework of a 4-month spectroscopic run using the Mons telescope at Teide observatory. We expose the motivations behind this campaign, present an overview of the Hα variations exhibited by the B supergiants and finally briefly discuss forthcoming developments in the data analysis.

1 The Mons project

The so-called Mons project is a collaboration between professional and amateur astronomers, which was primarily set up to monitor the periastron passage of the colliding-wind binary system WR 140 centred on January 12, 2009. A dedicated spectroscopic campaign was organised from December 2008 to March 2009 using the 50-cm Mons telescope at Teide Observatory, Canary Islands (see Eversberg 2011 and Fahed et al. 2011).[1] As WR 140 was observable for most of the run only close to sunset and sunrise, additional targets were required. We decided to focus on early B-type supergiants and Oe stars for which time-resolved observations of the Hα line can be used to investigate the properties of their large-scale wind structures and circumstellar material, respectively. The spectral coverage was 6360–6950 Å with a reciprocal dispersion of about 0.34 Å pixel^{-1}.

2 Motivations for this study

2.1 The B supergiants

Variability studies in the ultraviolet domain have shown that the winds of OB stars are likely made up of large-scale streams (the 'co-rotating interaction regions'; CIRs) whose formation may be triggered by the existence of non-uniform physical conditions at the stellar surface (as may be the case because of magnetic structures or pulsations; Cranmer & Owocki 1996). Establishing the incidence of anisotropic outflows is thus of relevance for issues related to pulsational and magnetic activity in early-type stars. In virtue of their density-squared dependence, optical recombination lines such as Hα are particularly good probes of the large density gradients expected to prevail in the CIRs. Revealing rotational modulation in these features would provide evidence that the CIRs extend relatively close to the star and are possibly directly emerging from the photosphere. Although previous campaigns have demonstrated that dramatic line-profile variability is widespread among OB supergiants, they generally suffered from a poor temporal sampling that hampered a detailed study of the line-profile variations on a rotational timescale (e.g., Ebbets 1982; Kaper et al. 1997).

Four bright B1–B3 supergiants were selected from Morel et al. (2004) based on previous indication of cyclical changes (HD 14134 and HD 42087 with a recurrence timescale of about 12.8 and 25 days, respectively) or unusually strong variations (HD 43384 and HD 52382). As discussed by Morel et al. (2004), three of these stars show evidence for a periodic behaviour in the *Hipparcos* photometric data: HD 14134 (12.823 days), HD 42087 (6.807 days) and HD 43384 (13.7 days). Further investigation is needed in the case of HD 42087 in view of the inconsistency between the spectroscopic and photometric periods, while the existence in HD 14134 of the same periodic signal both in the spectroscopic and in the photometric data makes it an especially attractive target.

[1] See also `http://www.stsci.de/wr140/index_e.htm`

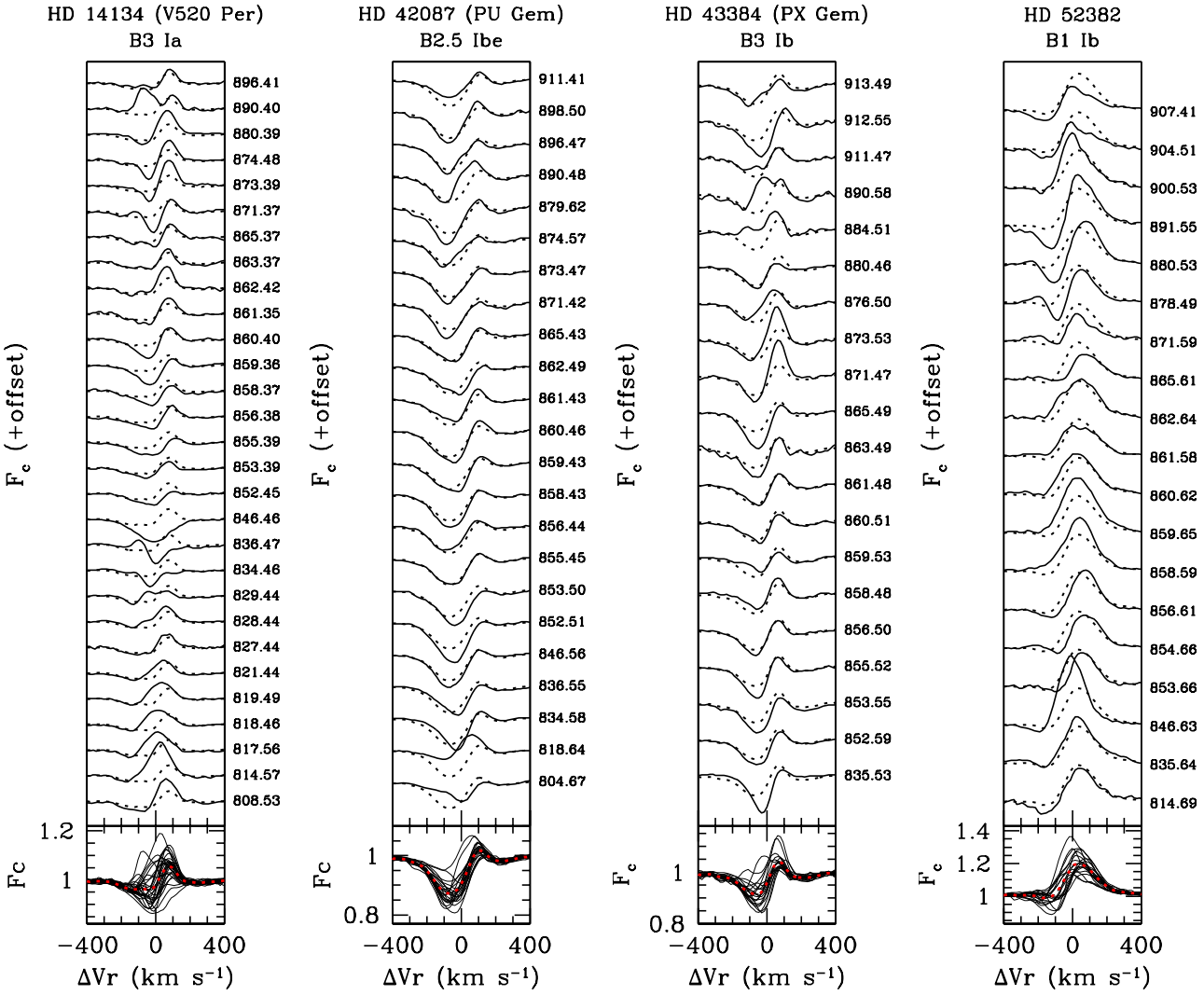

Figure 1: Hα time series for the B supergiants HD 14134, HD 42087, HD 43384 and HD 52382. Consecutive spectra are shifted by 0.15 continuum units, except in the case of HD 52382 (0.2 continuum units). The spectra are displayed in the stellar rest frame. The date of the observations at mid exposure (HJD–2,454,000) is indicated to the right of the panels. The bottom part of each panel shows a superposition of all the profiles. In all cases, the mean profile is overplotted as a dashed line for comparison.

2.2 The Oe stars

Another category of peculiar OB stars are the so-called Oe stars. In many respects, Oe stars are similar to Be stars. However, they are hotter and more massive than the latter and are very rare; only eight stars of this type are known in our Galaxy (Negueruela, Steele & Bernabeu 2004). These Oe stars have a spectrum that exhibits emission lines of the Balmer series of hydrogen as well as lower ionisation elements such as He I and Fe II, but do not display typical Of emission lines such as He II λ 4686 and N III λ 4634–40 (Conti & Leep 1974). As for Be-type stars, the emission lines of Oe stars frequently display a double-peaked morphology and the stars are often rapid rotators with equatorial rotational velocities that exceed 200 km s^{-1}. It is thus believed that the hydrogen emission lines arise in a disk-like outflow that surrounds the star, although this interpretation has been questioned because of the lack of a spectropolarimetric signature (Vink et al. 2009, but see Nazé, Rauw & ud-Doula 2011). Variability studies are crucial for a deeper understanding of these stars.

Indeed, their emission lines display strong variations that take the form of changing global intensities of the emission lines (by a factor of a few to about 10) and a change of the relative intensities of the violet and blue peak of the emissions (Rauw et al. 2007). The timescales of these variations are, however, poorly defined[2] and we thus selected two rather bright Oe stars, HD 45314 and HD 60848, for a spectroscopic monitoring in the framework of the Mons campaign.

3 Preliminary results

Here we present an overview of the Hα variations exhibited by the B supergiants (the data for the Oe stars are still being reduced). Strong line-profile variations operating on a daily timescale are observed in all the targets, as illustrated in the case of HD 14134 in Fig.1 by the great variety of profiles observed (strong emission/absorption, double peaked, classical or even inverse P-Cygni profile). This star is of particular interest because of the previous detection of a 12.8-d periodic signal both in photometry and in spectroscopy, with maximum light nearly coinciding with maximum wind emission (see Fig.2).[3] Although this clearly suggests a link between the development of extended wind structures and photospheric disturbances, unfortunately very little is known about the magnetic and pulsational properties of this star. A very similar correspondence between the photometric and spectroscopic behaviours (i.e., maximum Hα emission at maximum light) is observed in the O6.5f?pe–O8fp star HD 191612, whose wind is thought to be magnetically confined (Howarth et al. 2007, and references therein). Although a single circular polarization spectrum of HD 14134 obtained in 2003 with the MuSiCoS spectropolarimeter did not lead to the detection of a magnetic field (45$\pm$145 G; Morel et al. 2004), these data were unfortunately acquired at minimum Hα emission, i.e., when the longitudinal field is expected to be the lowest according to magnetically confined wind-shock models (e.g., Donati et al. 2002). Further observations with the much more sensitive instruments that are currently available may be warranted. On the other hand, to our knowledge no pulsation studies of this star have been conducted up to now. One of our objectives for the future is to fill this caveat (see below).

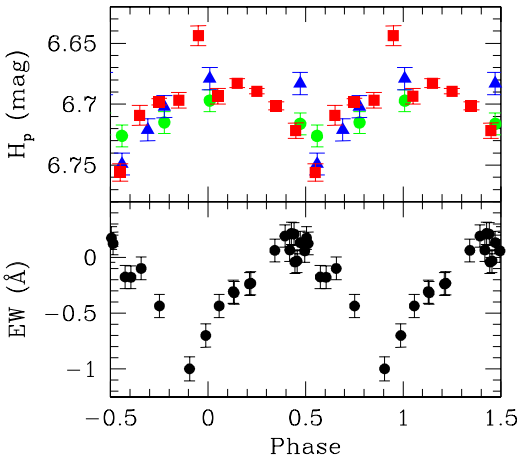

Figure 2: *Top panel: Hipparcos* light curve of HD 14134 binned to 0.1-phase resolution (squares). Our *B*- and *I*-band observations obtained in 2002 are overplotted as triangles and circles, respectively (the points are vertically shifted by a constant value to match the *Hipparcos* data). *Bottom panel:* EWs of the Hα line, as a function of phase. In all cases, the following ephemeris was used: $\mathcal{P}$=12.823 days and T_0=2,447,867.8 (zero phase arbitrarily set to maximum light). Adapted from Morel et al. (2004).

[2]Variations both on yearly (Rauw et al. 2007) and hourly timescales (Boyajian et al. 2007) have been reported, but there is a huge gap in our knowledge about timescales of weeks and months.

[3]A refined estimate of the period is needed to accurately phase together the *Hipparcos* and spectroscopic data, which were secured more than 10 years apart, and to assess the reality of the phase offset hinted at by Fig.2.

4 Conclusions and perspectives

Our efforts will now be directed towards the detection of a periodic behaviour that could allow us to identify the physical processes that drive the variations. For instance, a dipole magnetic field tilted with respect to the rotational axis in the Oe stars is expected to induce changes modulated by the rotational period, whereas the variations should take place on much longer timescales if they arise from some kind of disk instability. On the other hand, rotational modulation of the CIRs is expected to induce variations operating with a recurrence timescale of weeks in the B supergiants. The four B targets have already been intensively monitored over 36 nights in 2001–2002 (Morel et al. 2004). One of our main goals is to examine whether the pattern of variability remains coherent over such timescales and whether the 12.8- and 25-d periods detected in HD 14134 and HD 42087 are also present in this dataset.

We may expect a B3 supergiant such as HD 14134 to exhibit gravity-mode oscillations (Lefever, Puls & Aerts 2007). To obtain a more complete picture of the variability taking place in this star, high-resolution spectroscopic observations with SOPHIE are scheduled in November 2010 on the 193-cm telescope of the Observatoire de Haute Provence (OHP; France) to investigate the existence of pulsations and to eventually link the variations taking place in the photosphere to those in the wind. We wish in particular to examine whether the wind variability is the direct consequence of the interference of several pulsation modes with shorter periods, as might be the case in the B0.5 I star HD 64760 (Lobel & Blomme 2008).

Acknowledgements

T. M. acknowledges financial support from Belspo for contract PRODEX GAIA-DPAC. We wish to thank the observatory staff who helped make this campaign a success. Valuable suggestions from the anonymous referee and the editor, Yaël Nazé, were also very much appreciated.

References

Boyajian, T.S., Gies, D.R., Baines, E.K., et al. 2007, PASP 119, 742
Conti, P.S., & Leep, E.M. 1974, ApJ 193, 113
Cranmer, S.R., & Owocki, S.P. 1996, ApJ 462, 469
Donati, J.-F., Babel, J., Harries, T.J., Howarth, I.D., Petit, P., & Semel, M. 2002, MNRAS 333, 55
Ebbets, D. 1982, ApJS 48, 399
Eversberg, T. 2011, in Proceedings of the 39th Liège Astrophysical Colloquium, eds. G. Rauw, M. De Becker, Y. Nazé, J.-M. Vreux & P. Williams, BSRSL, 80, 469
Fahed, R., Moffat, A.F.J., Zorec, J., et al. 2011, in Proceedings of the 39th Liège Astrophysical Colloquium, eds. G. Rauw, M. De Becker, Y. Nazé, J.-M. Vreux & P. Williams, BSRSL, 80, 668
Howarth, I.D., Walborn, N.R., Lennon, D.J., et al. 2007, MNRAS 381, 433
Kaper, L., Henrichs, H.F., Fullerton, A.W., et al. 1997, A&A 327, 281
Lefever, K., Puls, J., & Aerts, C. 2007, A&A 463, 1093
Lobel, A., & Blomme R. 2008, ApJ 678, 408
Morel, T., Marchenko, S.V., Pati, A.K., Kuppuswamy, K., Carini, M.T., Wood, E., & Zimmerman, R. 2004, MNRAS 351, 552
Nazé, Y., Rauw, G., & ud-Doula, A., 2011, in *Active OB stars: structure, evolution, mass loss and critical limits*, proceedings of IAU Symp. 272, in press
Negueruela, I., Steele, I.A., & Bernabeu, G. 2004, AN 325, 749
Rauw, G., Nazé, Y., Marique, P.X., De Becker, M., Sana, H., & Vreux, J.-M., 2007, IBVS #5773
Vink, J.S., Davies, B., Harries, T.J., Oudmaijer, R.D., & Walborn, N.R. 2009, A&A 505, 743

Near-IR spectroscopy of OB stars with VLT/CRIRES*

Maria-Fernanda Nieva[1], Norbert Przybilla[2], Andreas Seifahrt[3,4], Keith Butler[5], Hans-Ulrich Käufl[6], Andreas Kaufer[7]

[1] Max-Planck-Institute for Astrophysics, Karl-Schwarzschild-Str. 1, D-85741 Garching, Germany
[2] Dr. Karl Remeis-Observatory & ECAP, Sternwartstr.7, D-96049 Bamberg, Germany
[3] Physics Department, University of California, Davis, CA 95616, USA
[4] Institut für Astrophysik, Georg-August-Universität Göttingen, Friedrich-Hund Platz 1, D-37077, Germany
[5] Universitätssternwarte München, Scheinerstr. 1, D-81679 München, Germany
[6] ESO Garching, Karl-Schwarzschild-Str. 2, D-85784 Garching, Germany
[7] ESO Santiago, Alonso de Córdova 3107, Casilla 19001, Santiago 19, Chile

Abstract: We have conducted a pilot observational programme in order to obtain very high resolution near-IR spectra ($R \sim 100\,000$) with wide wavelength coverage in the JHKL bands of early B-type stars with CRIRES on the VLT. The sample comprises a B0.2 V, a B0 III and a B1.5 III star, which have already been thoroughly analysed by us in previous work in the optical. The stars span a range of about 9000 K in effective temperature, thus covering different ions of several elements. A novel data reduction technique was carried out which facilitated telluric lines removal by precise modelling of the Earth's atmospheric spectrum. We investigate to what extent it is possible to derive atmospheric parameters and chemical abundances of early B-type stars from near-IR spectroscopy only. For this purpose we have extended our non-LTE spectral modelling to applications in the near-IR, based on our state-of-the-art model atoms that were thoroughly tested previously in the optical. Most H, He, C, N, O, Mg and Si lines in the near-IR (some of them resolved for the first time) could be reproduced, allowing atmospheric parameters and chemical abundances to be derived. Some remaining discrepancies between synthetic and observed strong lines, and some lines unidentified due to a lack of atomic data need to be investigated further. We have succesfully tested our modelling techniques and quantitative spectral analysis in the near-IR at high resolution and obtained excellent agreement with previous precision work in the optical. This will allow us to perform reliable spectral analyses of early B-type stars that suffer from strong optical extinction in the future, based on near-IR observations alone.

1 Introduction

The lifetimes of massive stars on the main sequence are so short ($\sim 10^6$–10^7 yr) that they are confined to their nursery[1]. Massive stars are expected to have the same chemical composition as their parent clouds, hence they are valuable metallicity indicators, a key to the understanding of star-formation processes, massive star evolution and galactic chemical evolution. Stars enshrouded by gas and dust

*Based on observations obtained at the European Southern Observatory, proposal 079.D-0810(A).
[1]Except for runaway or hypervelocity stars.

can suffer strong extinction of more than 10-20 mag in the visual. The dust and gas surrounding them becomes more transparent in the IR regime. Near-IR spectroscopy thus opens a new window to study stars in regions with high optical extinction.

Quantitative spectroscopic techniques make the derivation of stellar chemical abundances possible, however they rely on many model assumptions. Among the hot stars, less massive ($M \leq 20\,M_{\odot}$) and unevolved OB dwarfs and giants (luminosity class V to III) present much simpler radiative stellar atmospheres than hotter and more luminous stars. Weak stellar winds only affect the cores of the strongest spectral lines. Classical atmospheric models assuming plane-parallel geometry, homogeneity and even LTE have been shown to represent their atmospheric structure very well (see e.g. Nieva & Przybilla 2007, hereafter NP07). However, most of their spectral lines are still subject to non-LTE effects, nowadays well understood and constrained in the optical (see the review by Przybilla 2008) but still not thoroughly studied in the whole near-IR regime at high spectral resolution. Amplified non-LTE effects in the Rayleigh-Jeans tail of the stellar spectrum pose a challenge to the spectral modelling and analysis of the near-IR regime of massive stars (Lenorzer et al. 2004, Przybilla & Butler 2004). We concentrate here on early B-type stars, the least massive but potentially best-constrained objects among the massive stars in terms of quantitative spectral analysis.

So far, only a few groups have complemented the observational studies at lower resolution by implementing spectral modelling and quantitative analyses of massive stars in the near-IR. For example, Lenorzer et al. (2004) provided synthetic spectra based on the TLUSTY code for 9 H and 13 He lines for O-stars in the J, H and K bands. Repolust at al. (2005) analysed quantitatively 2 H and 8 He lines in OB main sequence to supergiant stars based on spectra of Hanson et al. (2005) by means of the FASTWIND code (Puls et al. 2005). Detailed chemical abundance studies and spectral modelling development require not only strong H and He but also weak metal lines to be resolved. For a slow-rotator like τ Sco, an $R = \lambda/\Delta\lambda \sim 75\,000$ is required. Hence, the detection of weak metal lines is not possible at intermediate or low spectral resolution. The advent of new and powerful instruments like CRIRES (CRyogenic high-resolution InfraRed Echelle Spectrograph, Käufl et al. 2004) on the Very Large Telescope allows us to study a large part of the spectrum ($\sim$1-5 μm) at extremely high resolution ($R = 100\,000$).

Our pilot observational programme aimed at obtaining very high resolution spectra of early B-type stars with wide wavelength coverage in the CRIRES range, similar to the objectives of the recent CRIRES-POP survey (Ramsay et al. 2011). The stars had already been carefully studied in the optical using FEROS spectra and our newest spectral modelling and analysis technique (NP07; Nieva & Przybilla 2006, 2008, hereafter NP06, NP08, respectively; Przybilla, Nieva & Butler 2008, PNB08). Our final goal is to derive atmospheric parameters and chemical abundances of early B-type stars in the near-IR regime only. We concentrate on the identification of all possible spectral indicators – H, He, C, N, O, Mg and Si lines – that are available in the cooler and hotter stars from different ions. We also test the capabilities of our spectral modelling technique to reproduce the spectral lines in the near-IR and test to what extent the quantitative analysis provides parameters and chemical abundances comparable to those from our previous precision analyses in the optical.

This work is of broader interest for current near-IR studies of hot stars in the Milky Way at lower spectral resolution than the one achieved in the present work because of the identification and modelling of many spectral features not observed so far. Further applications are e.g. for massive stars near the Galactic Centre, hot stars in ultra compact H II regions or reddened high-mass X-ray binary systems. The work also constitutes useful preparation for the science to be done with the next generation of extremely large telescopes (ELTs), which will apply adaptive optics techniques to resolve crowded fields of stars at near-IR wavelengths throughout the Milky Way and beyond. Moreover, the observational dataset will contribute to the upper HR diagramm of the spectral library CRIRES-POP (Lebzelter et al. 2010).

Table 1: Atmospheric parameters of the programme stars.

Parameter	τ Sco HD 149438	HR 3055 HD 63922	HR 3468 HD 74575
Sp.Type	B0.2 V	B0 III	B1.5 III
$T_{\rm eff}$ (K)	32000 ± 300	31200 ± 300	22900 ± 400
$\log g$ (cgs)	4.30 ± 0.05	3.95 ± 0.05	3.60 ± 0.05

2 The star sample

Three stars were selected for this study, one main sequence and two giant stars, spanning $\sim$9000 K in effective temperature. The sample size is constrained by telescope time because of the large spectral coverage selected for the study. The stars have been thoroughly analysed by us in the optical based on high quality FEROS spectra ($S/N \sim$ 500-800, R $\sim$ 48 000). They are a sub-sample of recent work that defines the present-day cosmic abundance standard locally (PNB08) and serve as reference to test model atoms for non-LTE line-formation calculations. They are located in OB associations and the field of the Solar Neighbourhood. Note that no massive star has so far been spectroscopically analysed to such an extent as the sample defining the present-day cosmic abundance standard. For the first time practically all observable H and He (NP07), carbon (NP06, NP08), nitrogen, oxygen, neon, magnesium, silicon and iron lines (PNB08) have been matched simultaneously in these stars in the visual by means of a hybrid non-LTE approach based on state-of-the-art model atoms. Some observed H and He lines have also been reproduced in the near-IR by NP07. The stellar parameters have been constrained to unprecedented accuracy by taking the Balmer and He lines and 5-6 independent ionization equilibria simultaneously into consideration. Table 1 provides ids, spectral types, effective temperatures $T_{\rm eff}$ and surface gravities $\log g$ of the stars as derived by NP08 and PNB08.

3 Data reduction of CRIRES spectra

The basic data reduction followed the standard recipes for long-slit infrared spectrographs. Observations were always performed in a single AB nodding pattern for all wavelength settings. Pairwise subtraction removed the atmospheric emission features and the individual A$-$B and B$-$A frames were divided by a normalized flatfield. The flatfielding step corrected the pixel-to-pixel gain variations of the chips but due to repeatability problems of the intermediate slit of CRIRES this step influenced the slope of the continuum which had to be corrected in a final step of the data reduction.

An ESOREX recipe of the CRIRES data reduction pipeline was used for optimal extraction of the 1D spectrum in each nodding position. The two 1D spectra of each setup and target combination were then cross-correlated to identify offsets in wavelength due to the slit curvature, shifted accordingly and co-added. In this step we removed the imprints of optical ghosts that are present in one of the two nodding positions in most J and H band settings and filtered cosmetic artefacts and outliers by an iterative procedure. The telluric absorption lines still contained in the processed 1D spectra could not be removed by dividing the spectrum by that of an early type standard star since this would have compromised the intrinsic features of our targets. Instead we have modelled the telluric features using the FASCODE algorithm (Clough et al. 1981, 1992), a line-by-line radiative transfer code for the Earth's atmosphere, and HITRAN (Rothman et al. 2005) as a database for molecular transitions. GDAS[2] atmospheric profiles were used as input for FASCODE and gave the necessary information for temperature, pressure, and humidity as a function of height in the atmosphere. The profiles were

[2]Global Data Assimilation System

retrieved from the NOAA website[3] for the two nights of observations. The amount of precipitable water vapour predicted by the models was adapted to achieve an optimal fitting in comparison to our measurements. The resulting spectra were smoothed with a Gaussian kernel to match the resolution of the science spectra. In a final step the telluric absorption features were then removed by dividing the science spectra by the model spectra. A more detailed discussion on the performance and limitations of using synthetic spectra to remove telluric absorption features is given in Seifahrt et al. (2010). The wavelength calibration is primarily based on the prediction of the physical instrument model implemented in the CRIRES data reduction pipeline. The initial wavelength calibration obtained with the pipeline was then refined by shifting the wavelength zero point and scaling the dispersion when fitting the telluric model to the observation. The final accuracy achieved for the majority of the settings is of the order of a 1/10 of a resolution element.

Continuum normalization is challenging for settings/chips in regions where broad hydrogen or helium lines are spread over 2-4 orders. Fortunately a sample of A supergiants (Przybilla et al., in prep.) that present sharper H lines and almost no He lines has also been observed in the same run. Division of the B-star spectra by the continuum derived from an A-supergiant around the broader lines allowed an improved normalization to be performed.

4 Stellar spectrum model calculation and analysis

The hybrid non-LTE approach solves the restricted non-LTE problem on the basis of prescribed LTE model atmospheres. Classical atmospheric models assuming plane-parallel geometry, homogeneity and even LTE are proven to represent very well the atmospheric structure of unevolved B-type stars (NP07). This approach also allows extensive non-LTE model atoms to be implemented, facilitating a highly detailed treatment of the atomic processes involved. We compute line-blanketed LTE model atmospheres using the ATLAS9 code (Kurucz 1993). Non-LTE population numbers and synthetic spectra are then obtained with recent versions of DETAIL and SURFACE (Giddings 1981; Butler & Giddings 1985). The coupled radiative transfer and statistical equilibrium equations are solved with DETAIL, employing the Accelerated Lambda Iteration (ALI) scheme of Rybicki & Hummer (1991). Synthetic spectra are calculated with SURFACE, using refined line-broadening theories. The non-LTE model atoms for hydrogen and He I/II adopted in the present work are described in detail by Przybilla & Butler (2004) and Przybilla (2005), respectively. Use of improved atomic data for electron impact excitations, in particular from *ab-initio* computations, allows consistent results from the hydrogen lines in the visual and near-IR to be derived throughout the entire range of early-A to O stars . The He I/II model atom has been successfully used to reproduce observed trends of the highly non-LTE-sensitive He I λ 10 830 Å transition in early-type main sequence stars (Przybilla 2005) and visual/near-IR spectra of extreme helium stars with B-type spectra (Przybilla et al. 2005, 2006b) and subluminous B stars (Przybilla et al. 2006a).

Photospheric lines in emission indicate the pure non-LTE nature of the transitions, i.e. the upper level is overpopulated due to the non-LTE effects. It is not possible to reproduce these lines with standard LTE techniques. So far two photospheric carbon lines in emission have been reported for the hotter stars and reproduced by us in the optical (NP06). An interesting result from this work is the finding of several photospheric lines in emission, which confirms the expected large non-LTE effects at these wavelengths. Direct application of existing non-LTE codes does not guarantee that all lines will be reproduced since the non-LTE effects are very sensitive to the choice of the input atomic data. Comparisons of model predictions based on stellar parameters and chemical abundances as derived in the visual to spectral line profiles in the near-IR are displayed in Fig. 1. The formation of some

[3] `http://www.ready.noaa.gov/ready/amet.html`

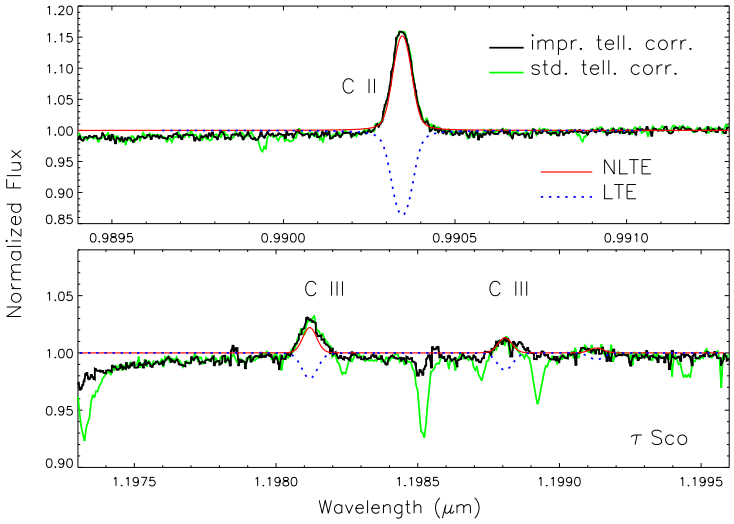

Figure 1: Example of observations vs. model predictions to C II/III lines. Our NLTE models agree very well with observation. LTE models are not able to reproduce the stellar spectrum. Different solutions for telluric line corrections are presented, one with standard values for parameters of the Earth's atmosphere (std.) and for the atmospheric conditions for the nights of the observations (improv.).

strong lines has to be investigated further in order to reproduce them by theory. Note that atomic data like line broadening parameters of some He lines in the near-IR are still not available. The strongest H lines may also be sensitive to stellar winds, unaccounted for in our approach. However, some lines like Brα in τ Sco pose a challenge, even when investigated with hydrodynamic non-LTE model atmosphere codes (see Przybilla & Butler 2004). More details can be found in a forthcoming paper (Nieva et al., in prep.)

References

Butler, K. & Giddings, J. R. 1985, in Newsletter of Analysis of Astronomical Spectra, No. 9 (Univ. London)
Clough, S. A., Kneizys, F. X., Rothman, L. S. & Gallery, W. O. 1981, Proc SPIE, 277, 152
Clough, S. A., Iacono, M. J. & Moncet, J.-L. 1992, Geophys. Res., 97, 15761
Giddings, J. R. 1981, Ph.D. Thesis, University of London
Hanson, M. M., Kudritzki, R.-P., Kenworthy, M. A., et al. 2005, ApJS, 161, 154
Käufl, H. U., Ballester, P., Biereichel, P., et al. 2004, Proc. SPIE, 5492, 1218
Kurucz, R. L. 1993b, CD-ROM No. 13 (Cambridge, Mass.: SAO)
Lebzelter, T., Seifahrt, A., Ramsay, S., et al. 2010, Messenger, 139, 33
Lenorzer, A., Mokiem, M. R., de Koter, A. & Puls, J. 2004, A&A, 422, 275
Nieva, M. F. & Przybilla, N. 2006, ApJ, 639, L39 (NP06)
Nieva, M. F. & Przybilla, N. 2007, A&A, 467, 295 (NP07)
Nieva, M. F. & Przybilla, N. 2008, A&A, 481, 199 (NP08)
Nieva, M. F. & Przybilla, N. 2010, ASP Conf. Ser., 425, 146
Przybilla, N. & Butler, K. 2004, ApJ, 609, 1181
Przybilla, N. 2005, A&A, 443, 293
Przybilla, N. 2008, Reviews in Modern Astronomy, 20, 323
Przybilla, N., Butler, K., Heber, U. & Jeffery, C. S. 2005, A&A, 443, L25
Przybilla, N., Nieva, M. F. & Edelmann, H. 2006a, Balt. Astron., 15, 107
Przybilla, N., Nieva, M. F., Heber, U. & Jeffery, C. S. 2006b, Balt. Astr., 15, 163
Przybilla, N., Nieva, M. F. & Butler K. 2008, ApJ, 688, L103 (PNB08)
Puls, J., Urbaneja, M. A., Venero, R., et al. 2005, A&A, 435, 669
Ramsay, S.K., Lebzelter, T., Seifahrt, A., et al. 2011, in Proceedings of the 39th Liège Astrophysical Colloquium, eds. G. Rauw, M. De Becker, Y. Nazé, J.-M. Vreux & P.M. Williams, BSRSL 80, 509
Repolust, T., Puls, J., Hanson, M. M., et al. (2005), A&A, 440, 261
Rothman, L. S., et al. 2005, Journal of Quantitative Spectroscopy and Radiative Transfer, 96, 139
Rybicki, G. B. & Hummer, D. G. 1991, A&A, 245, 171
Seifahrt, A., Käufl, H. U., Zängl, G., et al. 2010, A&A, 524, A11

Spectral analyses of the Wolf-Rayet stars in the Small Magellanic Cloud

Diana Pasemann, Ute Rühling and Wolf-Rainer Hamann

Universität Potsdam, Germany

Abstract: We have performed spectral analyses of all known Wolf-Rayet stars (single or binary) in the SMC. For this purpose, we have employed the Potsdam Wolf-Rayet (PoWR) model atmosphere code. For the 11 WR stars of the nitrogen sequence (WN), we calculated four grids of models with different hydrogen abundances. Furthermore, we established a series of O-star models, in order to construct the composite spectra of WN+O binaries. The only WO-type (i.e. oxygen-sequence WR) star in the SMC was also analyzed with the help of an adequate grid of models.

The preliminary results are in a rough agreement with the expectation, considering the lower mass loss in the SMC's metal-poor environment. In conflict with the evolutionary models is the high hydrogen abundance found in the single WN stars. The low luminosity of one WN star (SMC AB 2) is also not explainable.

1 Introduction

WR stars mark a late state of stellar evolution of the most-massive stars. Metallicity is one parameter that influences their evolution via the mass-loss rate. The theory of radiatively driven winds predicts a correlation between the mass-loss rate and the metallicity of a star, $\dot{M} = Z^{0.5}$ (Kudritzki et al. 1989). The metallicity in the SMC is about ten times lower than in the Milky Way. Consequently, the SMC stars may not develop a wind sufficiently strong to remove their hydrogen-rich envelope and to enter the Wolf-Rayet phase. There are two possible solutions to explain how WR stars can form at low metallicity. One possibility is that the WR stars in the SMC lose a lot of their mass via mass transfer (Roche-lobe overflow: RLOF) in close binary systems. Another solution is that only single O stars rotating the fastest can strip off their outer layers. In this study we focus on the binary assumption.

The evolution of massive binary systems can be very different from single-star evolution. Mass transfer via RLOF can dramatically influence the evolution of both components. Whether binary stars interact with each other depends on the physical parameters of the system, i.e. the initial orbital period, the initial distance between the components, and the initial mass ratio of the two stars.

Foellmi, Moffat & Guerrero (2003) searched for periodic radial velocity variations of the ten WN stars in the SMC at that time known and found that five of them are definitely binaries. A further WN star, SMC AB 11, also shows small radial velocity variations and highly blue shifted absorptions lines. However, Foellmi et al. (2003) argue that these lines come from the WR star itself and not from a companion and therefore classified the star as single. SMC AB 12 was discovered by Massey, Olsen & Parker (2003) after the study of Foellmi et al. (2003) and seems to be a single WR star. The WO star SMC AB 8 is a well-established binary (Moffat, Breysacher & Seggewiss, 1985).

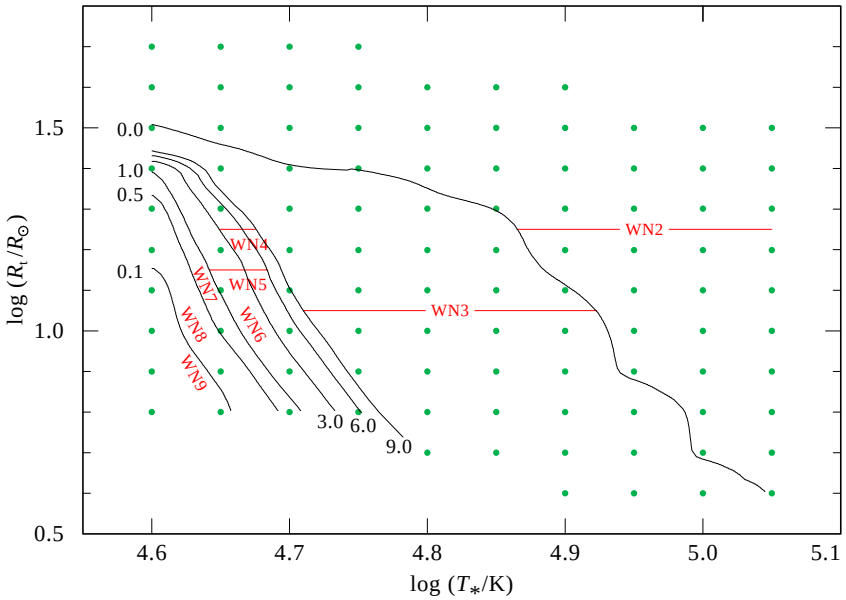

Figure 1: Calculated models (green dots) of the grid with 20% hydrogen in the R_t-T_*-plane. The domains of the WN subtypes after the classification of Smith, Shara & Moffat (1996) are labelled in red. The contour lines indicate the ratio of the equivalent width between He II (5412 Å) and He I (5875 Å).

2 Spectral analyses

For the spectral analyses we use the Potsdam Wolf-Rayet (PoWR) model atmosphere code which solves the non-LTE radiative transfer in a spherically expanding atmosphere in the co-moving frame. Complex model atoms of hydrogen, helium and the CNO elements are taken into account. The iron group elements are included in a super-level approximation. We establish four grids of models with different hydrogen content, reaching from 0%, 20%, 40% to 60 % H by mass fraction. The terminal wind velocity $v_\infty = 1600\,\mathrm{km/s}$, the clumping factor $D = 4$, the luminosity $\log\, L/\mathrm{L}_\odot = 5.3$ and the chemical composition are kept constant over all grids. Figure 1 shows one of the model grids. The main parameters of a model grid are the stellar temperature T_* and the so-called "transformed radius" R_t (see Hamann et al. 2011).

The WN subtypes are defined as an ionisation sequence, which is reflected by their location in the R_t-T_*-plane. Higher ionization is obtained by higher temperatures (T_*) and lower wind densities (i.e. higher R_t). The domains of the WN subtypes are defined by certain ranges of the ratio between the equivalent widths of the classification lines from He II and He I (see Fig. 1). The presence of hydrogen, if obvious from the strength of the Balmer-line blends with He II lines compared to the unblended members of the He II Pickering series, is indicated in the classification by the letter "h".

As a first step of our analyses, we identify the grid model which fits best to the observed line spec-

Table 1: Comparison of different spectral analyses of SMC AB 4

T_* [kK]	$\log\, L/\mathrm{L}_\odot$	v_∞ [km/s]	$\log \dot{M}$ [$\mathrm{M}_\odot$/yr]	Reference
42.0	5.70	1300	-5.05	Crowther (2000)
43.1	5.90	1000	-5.00	Martins et al (2009)
47.3	5.88	1000	-4.98	present study

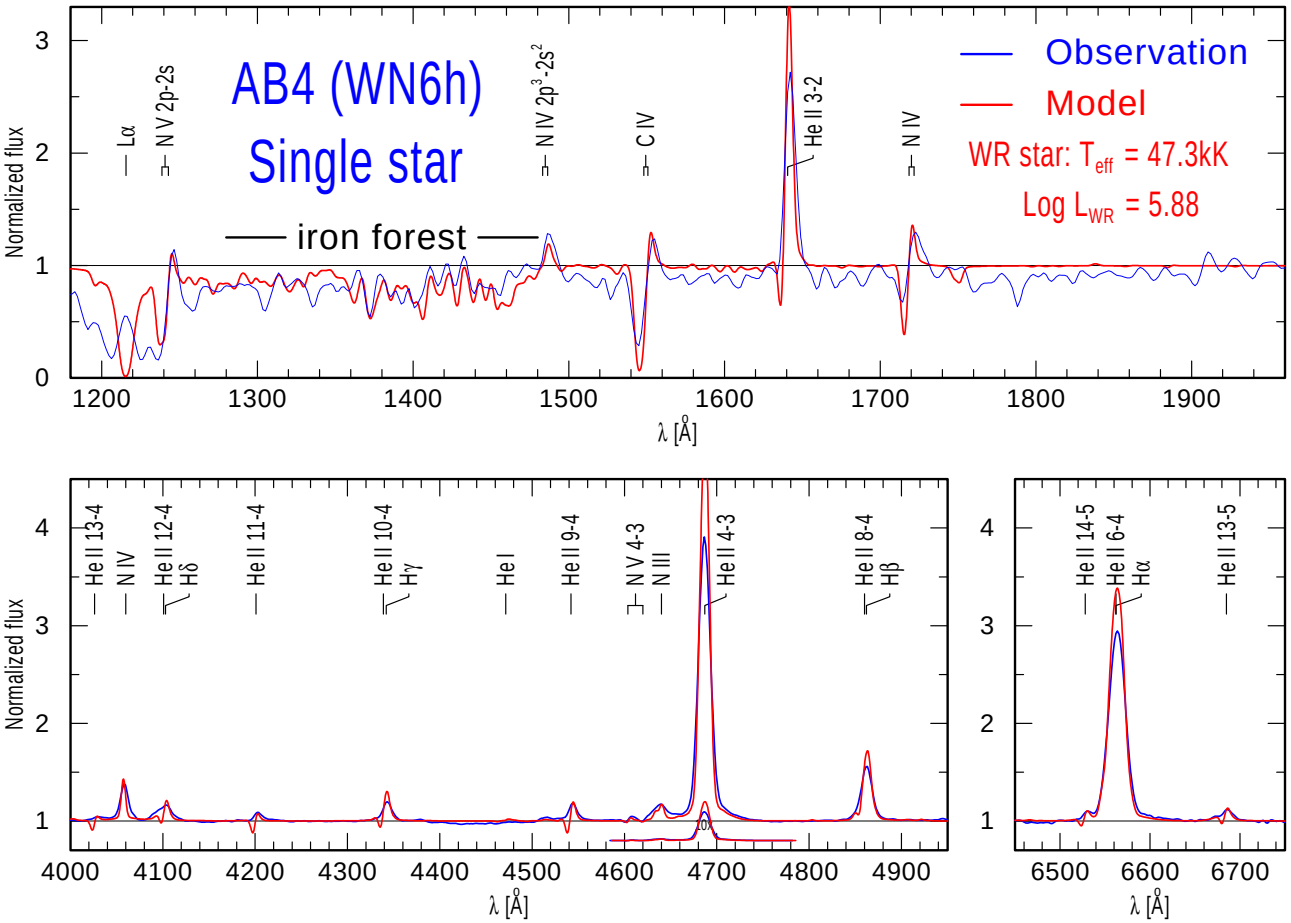

Figure 2: Model fit (red) to the observed spectrum (blue) of the WN6h single star SMC AB 4 in the UV and optical regime.

trum. Secondly, the spectral energy distribution is fitted by adjusting the luminosity and reddening. As an example, Fig. 2 shows the line fit for SMC AB 4, one of the six single WR stars in the SMC. The observed spectra are from Foellmi et al. (2003)[1] (optical) and IUE. The lines of all nitrogen ionisation stages are well reproduced. This star has been analyzed by other groups before. Our parameters are in good agreement with the results of Crowther (2000) and Martins et al. (2009). The results are listed in Table1.

To analyse the composite spectra of binaries we also calculated models for the O star companions. For example, SMC AB 6 is an SB2 binary, i.e. spectral lines from both stars are visible (see Fig. 3). The absorption features of He I 4471 Å and 5875 Å which are due to the O star, indicate an effective temperature between 30 and 35 kK. Secondly, we choose a suitable WN model which reproduces the emission lines. SMC AB 6 shows strong He II lines which are diluted by the continuum of the O-type companion. The ratio between the line strengths of He II 4686 Å and H α 6562 Å determines the hydrogen abundance. Finally, the two models spectra are added, while the luminosity ratio is adjusted such that the narrow absorption features from the O star and the broad emission lines from the WN star are reproduced simultaneously. Note that the flux in the optical and UV range of SMC AB 6 is dominated by the O star although both components have similar luminosities.

[1]We retrieved these data from http://wikimbad.obs.ujf-grenoble.fr/Home

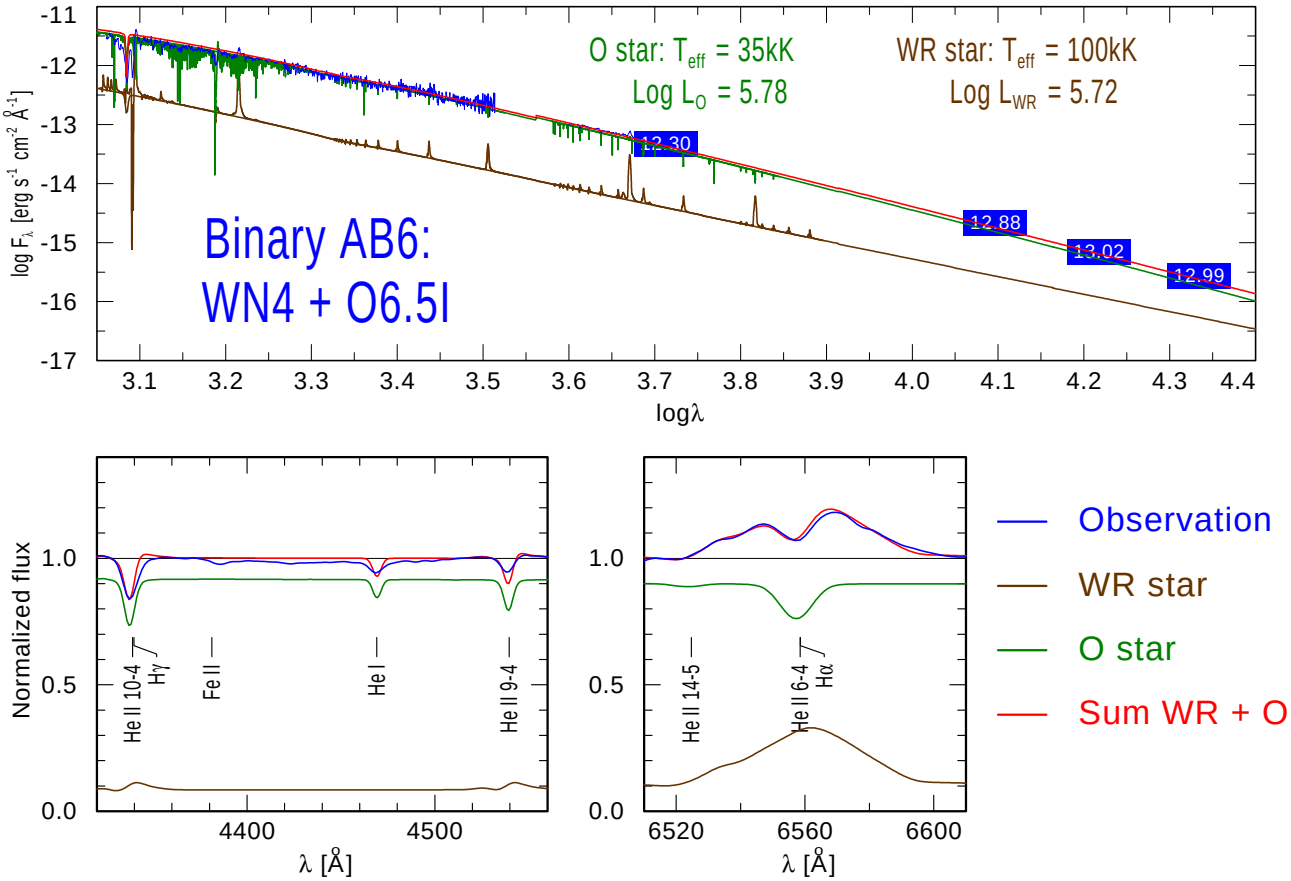

Figure 3: Composite spectrum of SMC AB 6, fitted by the sum of a WN and O star model (see text)

3 Results and conclusions

Figure 4 shows the Hertzsprung-Russell diagramm of all twelve WR stars in the SMC and their binary companions. It is remarkable that in contrast to the Galactic WR stars we do not find any hydrogen-free WNE stars at luminosities lower than $\log L/\mathrm{L}_\odot \approx 5.5$ in the SMC.

This can be explained as the effect of the low metallicity, which leads to smaller mass loss by radiation-driven winds. Indeed, we obtain $\dot{M} \approx 10^{-5.5}\mathrm{M}_\odot/\mathrm{yr}$ for the single WN stars in our sample. The evolutionary tracks predict that the minimum initial mass for single stars to return from the RSG branch and to reach the WR stage increases to $M_{\mathrm{init}} \approx 40\mathrm{M}_\odot$ at SMC metallicity, compared to the Galactic value of $M_{\mathrm{init}} \approx 22\mathrm{M}_\odot$ (with rotation).

Four of the five WN stars have high luminosities of $\log L/\mathrm{L}_\odot \geq 5.8$. This is compatible with the luminosity range where the tracks return to the hot side of the HRD. SMC AB 2, however, has a luminosity of only $\log L/\mathrm{L}_\odot = 5.5$ which is in contradiction to the evolutionary prediction. All single WN stars show hydrogen with mass fractions between 40 - 60%. This is significantly higher than predicted by the evolutionary tracks. For example, the $60\,\mathrm{M}_\odot$ track from Meynet & Maeder (2003) shows not more than 18% hydrogen at the surface when reaching a stellar temperature of $\log T_* = 4.9$.

For the binaries we obtained no or only little hydrogen (0 - 20%). These stars can lose their hydrogen envelopes via RLOF which is not metallicity dependent and therefore can explain the observed WN stars at lower luminosities ($\log L/\mathrm{L}_\odot = 5.5$). These stars are probably in the phase of core helium burning. With a lower mass than core hydrogen burning stars at same luminosity, they are closer to the Eddington limit. This can explain why we find higher mass-loss rates for the WN stars

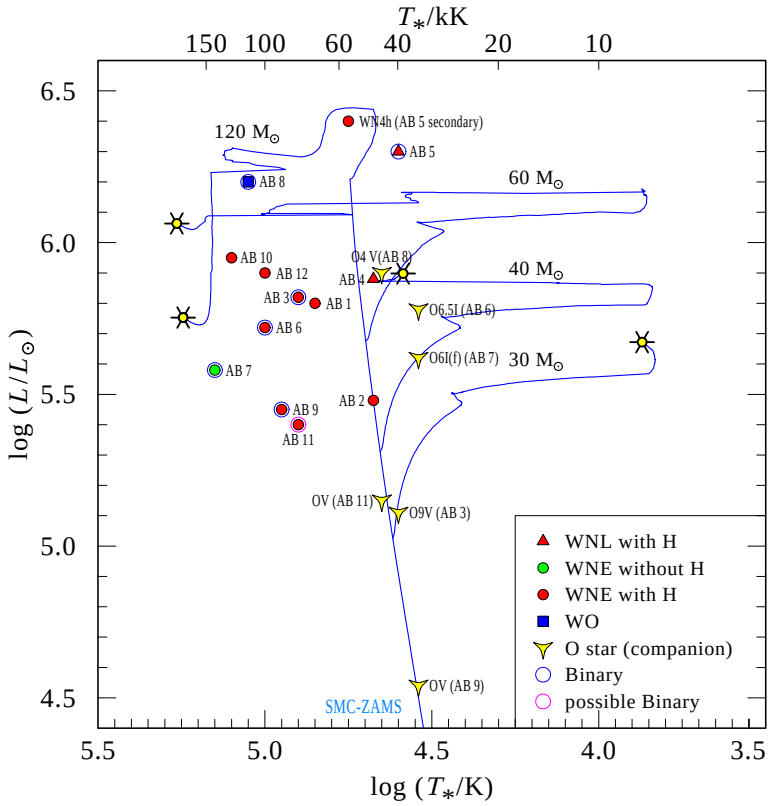

Figure 4: HRD with the WR stars of the SMC and their O-star companions compared to evolutionary tracks with rotation from Meynet & Maeder (2003)

in binary systems ($\dot{M} \approx 10^{-4.7} \mathrm{M}_\odot/\mathrm{yr}$) than for the single WN stars in our sample.

Acknowledgements

This research has made use of the SIMBAD database, operated at CDS, Strasbourg, France. UV spectra based on INES data from the IUE satellite. This publication makes use of data products from the Two Micron All Sky Survey, which is a joint project of the University of Massachusetts and the Infrared Processing and Analysis Center/California Institute of Technology, funded by the National Aeronautics and Space Administration and the National Science Foundation.

References

Crowther, P. A., 2000, A&A, 356, 191
Foellmi, C., Moffat, A. F. J., & Guerrero, M. A., 2003 MNRAS, 338, 360
Hamann, W.-R., Barniske, A., Liermann, A., Oskinova, L.M., Pasemann, D., & Rühling, U. 2011, in Proceedings of the 39th Liège Astrophysical Colloquium, eds. G. Rauw, M. De Becker, Y. Nazé, J.-M. Vreux & P.M. Williams, BSRSL 80, 98
Kudritzki, R. P., Pauldrach, A., Puls, J. & Abbott, D. C., 1989, A&A, 219, 205
Martins, F., Hillier, D. J., Bouret, J. C., Depagne, E., Foellmi, C., Marchenko, S. & Moffat, A. F., 2009, A&A, 495, 257
Massey, P., Olsen, K. A. G. & Parker, J. W., 2003, PASP, 115, 1265
Meynet, G. & Maeder, A., 2003, A&A, 404, 975
Moffat, A. F. J., Breysacher, J., & Seggewiss, W., 1985, ApJ, 292, 511
Smith, L. F., Shara, M. M., Moffat & A. F. J., 1996, MNRAS, 281, 163

Revised spectral analyses of Galactic WC stars

Andreas Sander, Wolf-Rainer Hamann and Helge Todt

Institut für Physik und Astronomie, Universität Potsdam, Germany

Abstract: A grid of models for Wolf-Rayet stars of the carbon sequence (WC) has been established with the Potsdam Wolf-Rayet (PoWR) model atmosphere code. In contrast to earlier versions, clumping and iron line blanketing are now taken into account. The spectra of more than 50 Galactic WC stars with subtypes ranging from WC4 to WC9 have been analyzed by finding the best-fitting model from the grid.

While the spectra of Wolf-Rayet stars of the nitrogen sequence (WN) can be nicely reproduced by a PoWR model fit, the WC spectra show a couple of features that cannot be consistently reproduced by a single model. Nevertheless, the models can be applied for their spectral analysis. The obtained parameters clearly reflect the sequence of WC spectral subtypes. From the positions of the WC stars in the Hertzsprung-Russell diagram we conclude that WC stars descend from stars with initial masses between 20 $M_\odot$ and 40 $M_\odot$ while stars with higher masses do not reach the WC stage.

1 Introduction

The Wolf-Rayet stars are divided into two main subtypes, depending on the dominance of nitrogen (WN) or carbon (WC) lines. The WC stars are evolved stars, with strong emission lines from helium, carbon and oxygen, that lost their outer hydrogen layers. However, their basic parameters are still uncertain and very different temperatures and mass-loss rates have been obtained in earlier analyses, such as Koesterke & Hamann (1995), Hamann, Gräfener & Koesterke (2003) or Gräfener & Hamann (2005). Spectral analyses of these stars require detailed modeling of their expanding atmospheres. The Potsdam Wolf-Rayet (PoWR) code can handle the non-LTE radiative transfer and account for the complex atoms required to reproduce the situation in the stellar atmosphere. Following the efforts of Barniske, Hamann & Gräfener (2006) we established a model grid to perform a coarse analysis of over 50 Galactic WC single stars ranging from the "early" subtype WC4 to the "late" WC9. In addition a few WN/WC transit type stars, the two WO stars WR 102 and WR 142 and six WC binaries have been analyzed.

2 Model Grid

In order to analyze a larger number of stars, a model grid has been established with the PoWR code, taking microclumping and iron line blanketing into account. The grid parameters are the stellar tem-

perature T_* and the so-called "transformed radius"

$$R_\mathrm{t} = R_* \left[\frac{v_\infty}{2500\,\mathrm{km/s}} \Big/ \frac{\dot{M}\sqrt{D}}{10^{-4}\mathrm{M}_\odot/\mathrm{yr}} \right]^{\frac{2}{3}}. \tag{1}$$

Luminosity, clumping factor and terminal wind velocity as well as the chemical composition have been kept fixed over the whole grid, using $\log L/L_\odot = 5.3$, $D = 4$, $v_\infty = 2000\,\mathrm{km/s}$ and mass fractions of 55% Helium, 40% Carbon and 5% Oxygen. For iron group elements we set the mass fraction to 0.16%. Additional models with different abundances and with different velocities have been calculated for comparison and for reproducing the WC9 and WO spectra. The WC9 stars require models with lower terminal wind velocities ($v_\infty = 1000$-$1600\,\mathrm{km/s}$) than the earlier subtypes.

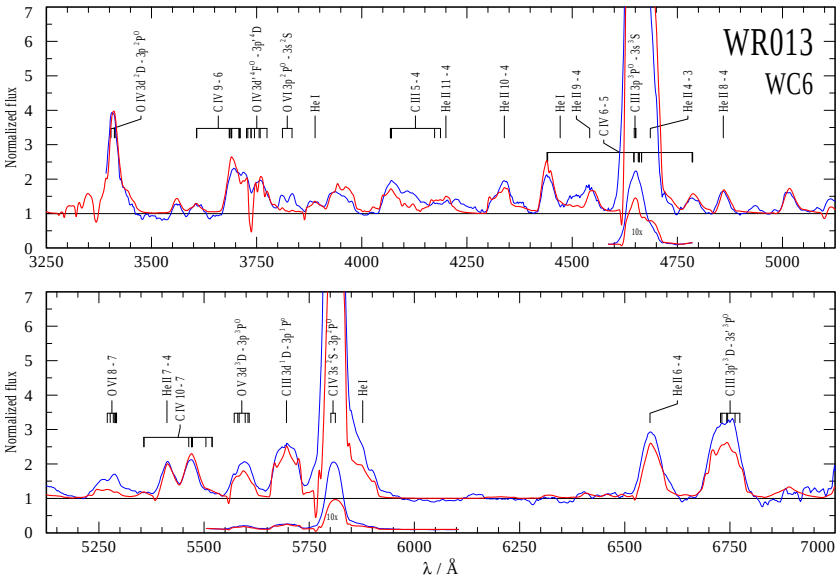

Figure 1: Optical spectrum of the WC6 representative WR 13 (blue) compared to the best-fitting PoWR model (red). The model reproduces most of the spectral features but underestimates the peak height of the prominent C IV line at 5808 Å. The same model fits to most of the Galactic WC6 single stars, although some of the peak heights do not match.

As an example of the fitting results, Fig. 1 shows the best fitting model for WR 13 compared to the observed spectrum by Torres & Massey (1987). The model reproduces most of the spectral features, although it tends to underestimate the peak heights of the most prominent lines. The good fit of the diagnostic line pair He II 5412 Å and C IV 5470 Å verifies the carbon-to-helium mass ratio of 40:55 as adopted for the model grid. There seems to be no difference in the chemical composition between the subtypes.

The locations of the analyzed Galactic WC stars in the $\log R_\mathrm{t}$-$\log T_*$-plane are shown in Fig. 2. In contrast to the WN stars, the WC stars form a one-dimensional sequence. From the subtypes WC8 to WC4, the stars align along a linear relation $\log R_\mathrm{t} \propto -2\,\log T_*$, while only the WC9 stars are lying apart. For the model grid with fixed L, v_∞ and D, this linear relation implies that the mass-loss rate is the same, as can be seen from combining Eq. (1) with $L \propto R_*^2\,T_*^4$.

The actual luminosities of the individual stars are obtained by scaling the spectral energy distribution of the grid models to photometric observations, which requires an independently known distance (cf. Sect. 3). With these individual luminosities, the constant mass loss from the linear relation in the model grid (Fig. 2) turns into the mass loss-luminosity relation

$$\dot{M} \propto L^{\frac{3}{4}} \tag{2}$$

provided that one adopts the same v_∞ and D for all stars. The empirical mass-loss rates of our sample range between $10^{-4.5}$ and $10^{-5}\,M_\odot/\mathrm{yr}$.

All stars located above the sequence in Fig. 2 are known to be binaries. Due to the neglection of the composite nature of their spectrum, they appear as stars with lower mass-loss rates and slightly lower temperatures. It turns out that the so-called "diluted emission line" (d.e.l.) criterion works indeed as a binary tracer for WC stars. A WC-s and WC-w classification as introduced by Koesterke & Hamann (1995) is not necessary.

The two WO2 stars WR 102 and WR 142 do not align with the rest of the sequence but require completely different models with 30% oxygen and a temperature of $T_* = 200\,\mathrm{kK}$ to reproduce the prominent oxygen lines. Their extremely broad lines require a wind velocity of $v_\infty = 5000\,\mathrm{km/s}$.

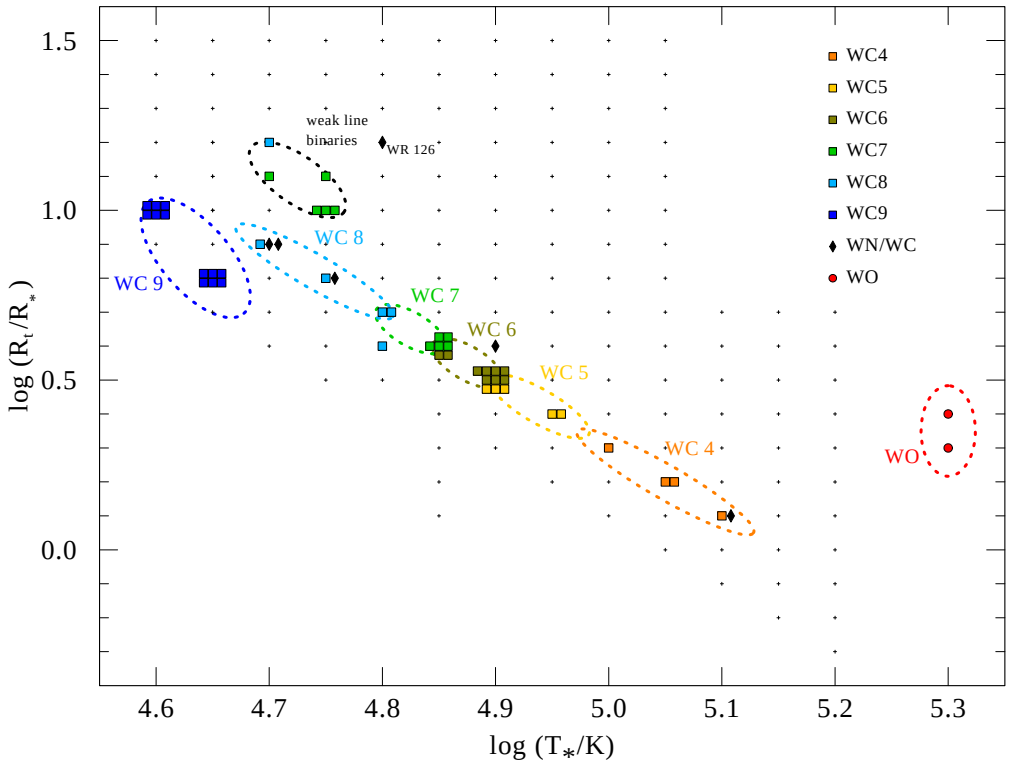

Figure 2: Location of the analyzed Galactic WC stars (colored symbols) in the $\log R_\mathrm{t}$-$\log T_*$-plane. The subtypes form a one-dimensional sequence from the cooler WC9 to the hotter WC4 subtypes with a slight offset for the WC9 stars. The stars above the sequence turn out all to be binaries where the neglection of the composite nature of their spectra leads to an underestimate of their mass-loss rates.

A few stars show a spectral appearance in between the WN and WC type, termed WN/WC. Their spectral appearance and chemical composition is similar to the hydrogen-free WN stars, but with enhanced traces of carbon. We calculated small model grids with carbon abundances of 0.1% and 5%, keeping nitrogen at 1.5% and iron group elements at 0.16% mass fraction with the rest being left for helium. The positions in the $\log R_\mathrm{t}$-$\log T_*$-plane for the WN/WC stars show that they are close to the WC sequence, with the exception of WR 126, which stands completely apart. However, the spectrum of WR 126 resembles a WC rather than a WN spectrum and is therefore classified as WC/WN (van der Hucht 2001).

The WN/WC stars may represent the standard evolutionary transition phase from the WNE to the WC stage. Alternatively, the enhanced carbon fraction in the WN/WC stars might come from dragged up material in some WNE stars having a special mixing process.

3 HR diagram and evolutionary models

To obtain the positions of the WC stars in the Hertzsprung-Russell diagram, luminosities have been determined by fitting the spectral energy distribution using flux-calibrated spectra and additional photometric observations from 2MASS. The stellar temperature T_* is given by the best fitting model. Of course the luminosity values also depend on the adopted stellar distance. Only some of the Galactic WC stars can be assigned to clusters or OB associations, from which we can infer the distance. For the other ones we adopt a subtype-magnitude calibration, assuming that all stars of the same WC subtype have more or less the same absolute magnitude. As this might not be close to reality, these stars are represented by smaller symbols, while those with known distances and therefore more trustworthy luminosities are represented by larger symbols in the HRD (Fig. 3).

With luminosity and temperature being determined we can obtain the position of the Galactic WC stars in the HR diagram and compare our results with evolutionary models. It turns out that the luminosities of the WC stars are mostly between $\log L/L_\odot = 4.8$ and $\log L/L_\odot = 5.5$, much lower than expected. Fig. 3 shows the evolutionary tracks with rotation by Meynet & Maeder (2003) compared to the obtained positions. Evolutionary models without rotation would lead to even more luminous tracks, enhancing the discrepancy between models and observations. In any case, most of the obtained luminosities are much lower than predicted by the tracks. Only the two WO stars seem to fit with the tracks, although they appear a bit more compact than predicted by the SN endpoint.

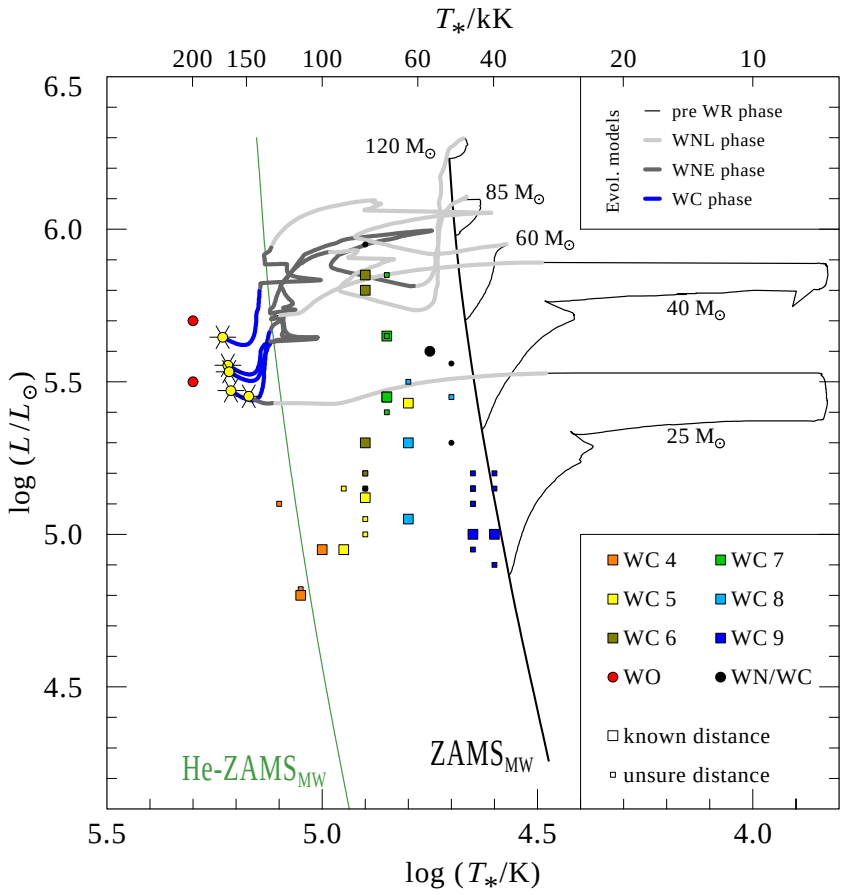

Figure 3: Hertzsprung-Russell diagram with the analyzed Galactic WC stars compared to the evolutionary tracks with rotation by Meynet & Maeder (2003). The part of the tracks which corresponds to the WC phase are drawn as thick blue lines, short prior to the SN explosion. The observed WC stars are less luminous and cooler than expected.

Interestingly the obtained WC positions in the HR diagram are close to the WNE positions (Hamann, Gräfener & Liermann, 2006), with the WNE luminosities being slightly higher than the WC values. The stellar temperatures T_* for the subtypes WC5 to WC9 are lower than the He-ZAMS where we would expect to find these helium burning stars without hydrogen. This can be explained with a stellar photosphere that is more extended than the hydrostatic stellar core. Only for WC4 and WO stars the stellar wind seems to be footed close to the core. Note that we plot the evolutionary models in Fig. 3 with respect to the effective temperature $T_{\rm eff}$ which refers to the radius of the hydrostatic core, without any correction for an extended stellar atmosphere.

The HRD positions question the scenario that WC stars evolve only or mostly from very massive progenitors. Instead it seems likely that these high-mass stars do not enter the WNE and WC stage after their WNL phase, but explode directly as supernovae. The WNE and WC stars instead evolve from lower initial masses in a post-RSG scenario. Vanbeveren et al. (1998) showed that higher mass-loss rates during the RSG branch can strip off the outer hydrogen layers, so that stars with an initial mass of $15\,M_\odot$ can make it to the WR stage. To enter the WC stage an initial mass of around $25\,M_\odot$ is required, sticking to the scenario from Vanbeveren et al. (1998). The luminosities for their tracks are lower than the ones from Meynet & Maeder (2003), leading to a better agreement with the obtained values.

4 Conclusions

The Galactic WC stars form a one-dimensional sequence in the $\log R_{\rm t}$-$\log T_*$-plane implying $\dot{M} \propto L^{3/4}$. They are less luminous and cooler than predicted by evolutionary models. The low effective temperatures might be explained by an extended layer under the photosphere. We find most WC stars at $\log L_{\rm WC}/L_\odot \leq 5.5$ and none above $\log L_{\rm WC}/L_\odot > 5.9$. The low observed luminosities contradict the common paradigm that WC stars evolve only from very massive stars. Instead our results indicate that WC stars descend only from stars with a medium-high initial mass between 20 $M_\odot$ and 40 $M_\odot$. Stars with higher initial masses might not be able to get completely rid of their hydrogen layers and explode already during their hydrogen-rich WNL or LBV phase.

Acknowledgements

This research has made use of the SIMBAD database, operated at CDS, Strasbourg, France. UV spectra based on INES data from the IUE satellite. This publication also makes use of data products from the Two Micron All Sky Survey, which is a joint project of the University of Massachusetts and the Infrared Processing and Analysis Center/California Institute of Technology.

References

Barniske, A., Hamann, W. & Gräfener, G. 2006, in ASP Conf. Series, Vol. 353, 243
Gräfener, G. & Hamann, W. 2005, A&A, 432, 633
Hamann, W., Gräfener, G. & Koesterke, L. 2003, in IAU Symposium, Vol. 212, 198
Hamann, W., Gräfener, G. & Liermann, A. 2006, A&A, 457, 1015
Koesterke, L. & Hamann, W. 1995, A&A, 299, 503
Meynet, G. & Maeder, A. 2003, A&A, 404, 975
Torres, A. V. & Massey, P. 1987, ApJS, 65, 459
van der Hucht, K. A. 2001, New Astronomy Review, 45, 135
Vanbeveren, D., De Donder, E., van Bever, J., van Rensbergen, W. & De Loore, C. 1998, New Astronomy, 3, 443

Spectroscopic Monitoring in the Optical Wavelength Region of Nine WC9 Stars

Nicole St-Louis[1], Dominique Soutière [1], Simon Péloquin[1],
Antoine de la Chevrotière[1], Vincent Hénault-Brunet[2] and André-Nicolas Chené[3]

[1] Département de physique, Université de Montréal, Montréal, Canada
[2] Institute for Astronomy, University of Edinburgh, Edinburgh, UK
[3] Gemini Office, Dominion Astrophysical Observatory, Canada

Abstract: We present a preliminary report of a spectroscopic monitoring campaign in the optical wavelength region of nine WC9 stars that we have carried out at the El Leoncito Observatory in Argentina in May-June 2009. The stars in our sample are not known binaries but have been shown from previous studies to present short-term spectroscopic variability. We confirm that large-scale, line-profile variability is indeed present for several stars in our sample with timescales shorter than $\sim$1 day. A simple visual inspection of the shape of the line-profiles as a function of time does not allow us to conclude if the variations are periodic or not. A more thorough analysis of the data (measurements of the radial velocity, equivalent width, skewness, etc) will be required. Our ultimate goal is to determine the origin of the spectroscopic variability which could lead to new insight into the origin of the dust in presumably single WC9 stars.

1 Introduction

Near-infrared photometry of WC-type Wolf-Rayet (WR) stars has shown that most WC9 stars (14 out of a total of 17) and a large fraction of WC8 stars produce dust (Williams, van der Hucht & Thé 1987). Only 3 WC9 stars (WR81, WR88, WR92) have not yet shown evidence of dust. Cherchneff et al. (2000) have investigated the formation of carbon chains and molecular precursors to dust in WC winds. They find that large density enhancements are a pre-requisite for the formation of dust grains in the harsh UV radiation field.

For WC9 stars that are members of a WR+O binary system, such as WR140 (Williams et al. 2009) or WR137 (Williams et al. 2001), the origin of the required gas compression is relatively well understood. Indeed, in such a case, when the two stellar winds collide, a region of shocked gas forms between the two stars. In this shock zone, that roughly has the form of a cone, the gas density is naturally increased. However in the region immediately between the two stars it is also heated to X-ray emitting temperatures. The X-rays are seen to vary as a function of orbital phase as they are absorbed by varying amounts of gas column (e.g. Willis, Schild & Stevens 1995). As the gas flows along the shock cone, it cools and gradually recombines. Line emission is then produced and in the case in which the transition is normally known to occur in the WR wind, the cone emission can be observed superposed on the broad wind emissions. By studying its behavior as a function of phase

Table 1: Spectral type, v magnitude and number of spectra obtained for the stars in our sample.

Star	Spectral Type	v	Nb. of spectra
WR 53	WC8d	10.88	24
WR 69	WC9d	9.43	25
WR81	WC9	12.71	22
WR88	WC9	13.25	21
WR 92	WC9	10.43	23
WR 103	WC9d	8.86	24
WR 106	WC9d	12.33	17
WR 119	WC9d	12.41	17
WR 121	WC9d	12.41	20

(Doppler shift and width), one can gather information on the shock cone structure such as its opening angle or flow velocity along the shock (Luehrs 1997). As the gas reaches high distances from the star where it has sufficiently cooled and the UV radiation field has decreased significantly, dust is able to form.

But not all WC9 stars are known binaries. For single WC9 dust makers, the origin of the regions of compressed gas required to form dust is less clear. WR winds are known to be highly clumped (e.g. Lépine & Moffat 1999) and the inhomogeneities are possible regions in which the dust could form. Another possibility are Corotating Interaction Regions (CIRs). Hydrodynamical simulations by Cranmer & Owocki (1996) have shown that if a perturbation occurred at the base of the wind of a rotating star, either a dark or bright spot, an excess or deficit of radiative force would cause fast material to collide with slow material causing a compression or even a shock. As this compressed gas makes its way through the wind, it is wrapped around by stellar rotation forming a spiral-like structure.

From a systematic survey of optical spectroscopic variability of WR stars in the northern and southern hemispheres, St-Louis et al. (2009) and Chené & St-Louis (2010) have found evidence for short-scale (days) optical spectroscopic variability of WC9 stars thought to be single. Actually, *all* WC9 stars in their sample showed profile variability at a level of $\sim$10% of line flux. It is thought that clumping leads to lower amplitude variations ($\leq$ 5%) and that these changes with higher amplitudes have a different origin. Such a large fraction of stars showing large-amplitude spectral variability is not found for other WR spectral subtypes. Is it possible that some of these presumably single WC9 stars are in fact yet undetected binaries? Alternatively, some might have CIRs in their wind. The goal of this project is to search for binary or CIR-related spectroscopic variability of the WC9 line profiles in order to shed some light on the physical origin of the changes and to search for other clues as to the absence or presence of dust in such an inhospitable environment as a WR wind.

2 Observations

Our dataset was secured at the El Leoncito Observatory (CASLEO) in Argentina between the 15 May – 15 June 2009 using the 60-cm Helen Sawyer Hogg telescope and a grating giving a dispersion of 0.97 Å/pix. The typical S/N of the spectra we obtained is $\sim$100. The stars we observed with their spectral type, v magnitude and number of spectra obtained are listed in Table 1.

3 Preliminary Results

In Figures 1, 2 and 3, we show examples of line profiles from the spectroscopic dataset we secured. We present timeseries of the C IIIλ5696 transition for WR81, WR88 and WR103 respectively. The profiles have been shifted vertically for clarity and the separation between them reflects the time difference between exposures. The Julian Dates are indicated on the y-axis.

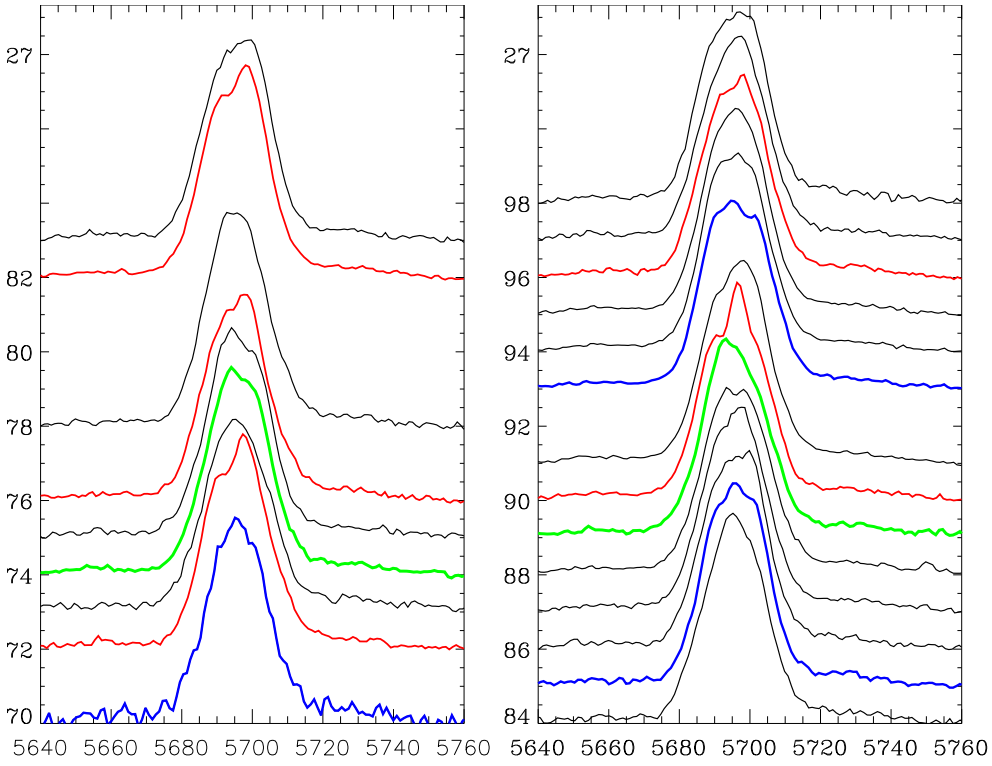

Figure 1: Series of CIIIλ5696 line profiles for WR 81.

Clear large-scale variability is present in the form of relatively large emission excesses superposed at various positions on the broad wind emissions. The changes can occur on relatively short timescales. For WR81 for example, the C III profile obtained on Julian Day 2 454 972 presents a large excess emission on the red side of the line while the spectrum obtained on day 2 454 973 shows a much more symmetric profile. The next day, an excess emission is developping on the blue side of the line. A similar pattern of variability is also seen $\sim$10 days later.

Note that the variability is found for well-known dust makers such as WR103 (Figure 3) but also for stars such as WR81 (Figure 1) and WR88 (Figure 2) for which no evidence for dust has been found in two decades of IR monitoring (van der Hucht 2001). For each plot, we have drawn in different colours, spectra showing similar line shapes. No clear period or timescale can of course be identified by simple visual inspection of the line profiles, but it is clear that lines with similar shapes do re-occur at various times in all three cases. The detailed nature of the changes remains to be determined. We will be able to characterize them by carrying out various measurements such as radial velocity, equivalent width, skewness and kurtosis of the profiles and studying their behavior as a function of time. Several questions remain to be answered. Is this variability related to binarity or to the presence of CIRs in the wind of the WR star? If so, is the fact that they occur even for dustless WC9 stars telling us something about the dust formation mechanism? Are some binaries too tight to harbor physical conditions favourable for dust production? We are confident that the present dataset will help us address at least some of the above questions.

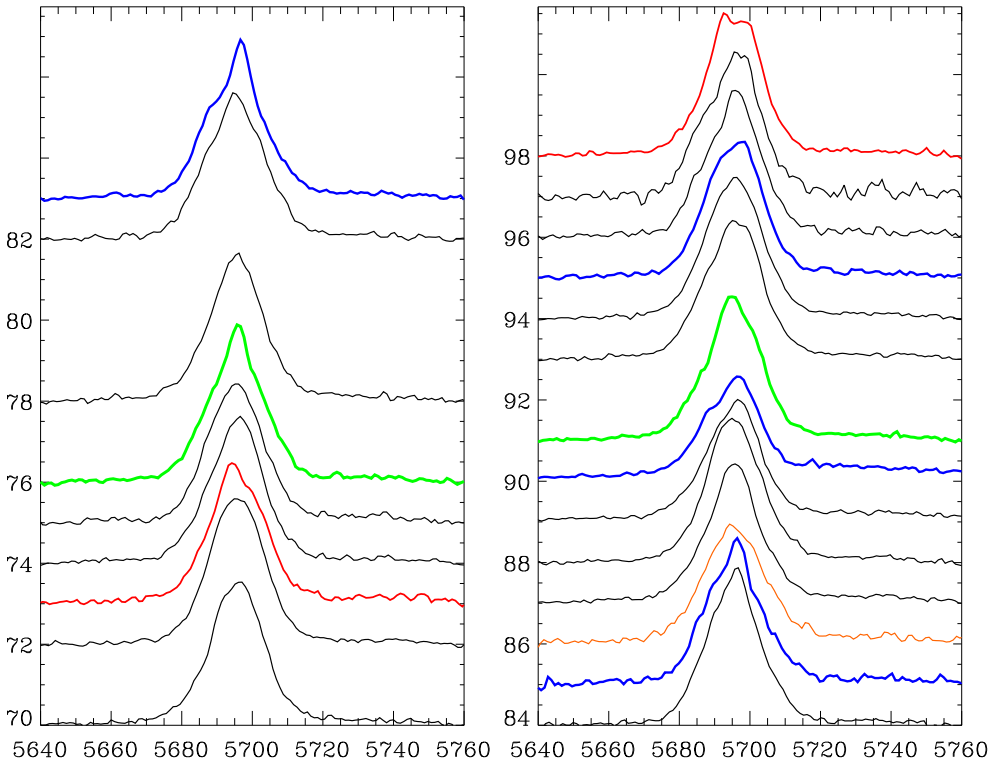

Figure 2: Series of CIIIλ5696 line profiles for WR 88.

Acknowledgements

NSL, DS and VHB acknowledge financial support from the Natural Sciences and Engineering Research Council (NSERC) of Canada. VHB and AdlC would like to thank the staff at the El Leoncito Observatory for support during the observing run.

References

Chené, A.-N. & St-Louis, N., ApJ, submitted
Cherchneff, I., Le Teuff, Y. H., Williams, P. M., & Tielens, A. G. G. M. 2000, A&A, 357, 572
Cranmer, S.R., & Owocki, S.P. 1996, ApJ, 462, 469
Lépine, S., & Moffat, A. F. J. 1999, ApJ, 514, 909
Luehrs, S. 1997, PASP, 109, 504
St-Louis, N., Chené, A.-N., Schnurr, O., & Nicol, M.-H. 2009, ApJ, 698, 1951
van der Hucht, K.A. 2001, New Astron. review, 45, 135
Williams, P. M., van der Hucht, K. A., & Thé, P. S. 1987, A&A, 182, 91
Williams, P. M., Kidger, M.R., van der Hucht, K.A. et al. 2001, MNRAS, 324, 156
Williams, P. M., Marchenko, S.V., Marston, A.P. et al. 2009, MNRAS, 395, 1749
Willis, A. J., Schild, H., & Stevens, I. R. 1995, A&A, 298, 549

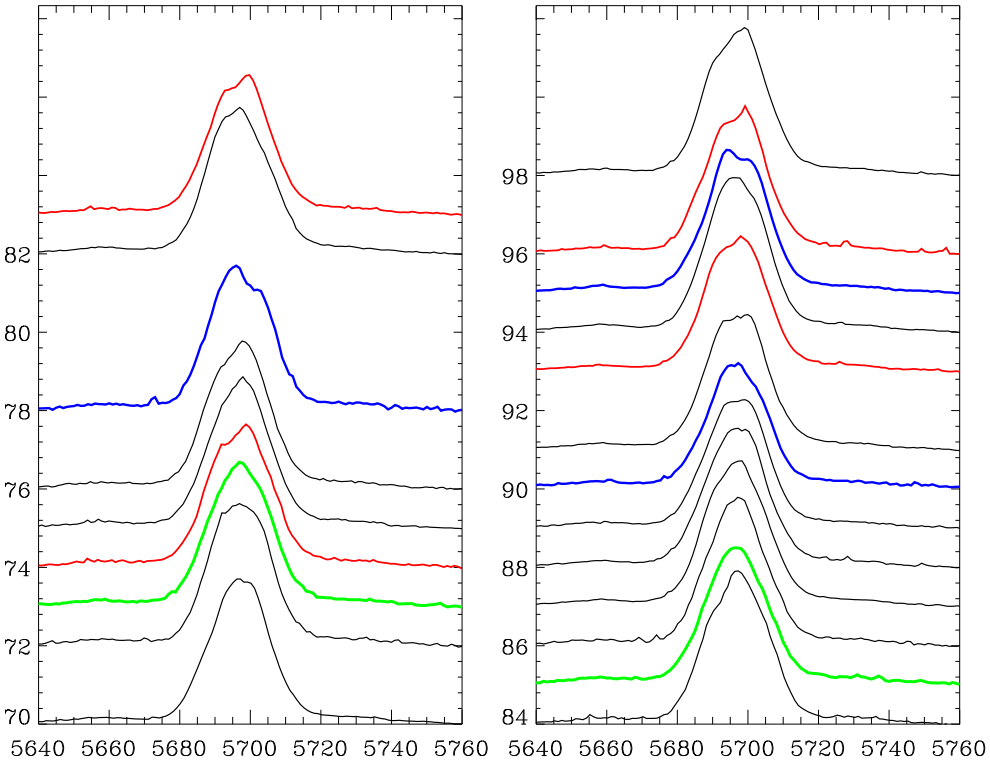

Figure 3: Series of CIIIλ5696 line profiles for WR 103.

Heated dust around the LMC Wolf-Rayet system HD 36402 (BAT99-38)

P. M. Williams

Institute for Astronomy, Royal Observatory, Edinburgh, U.K.

Abstract: Infrared photometry of the probable triple WC4 (+O?) +O8I: system HD 36402 (BAT99-38) in the LMC shows emission characteristic of heated dust. Although HD 36402 is close to two luminous YSOs, it is possible to distinguish its emission at wavelengths less than 10 microns. Simple modelling indicates a dust temperature near $800\ K$ and mass of about $1.5 \times 10^{-7} M_{\odot}$ amorphous carbon grains. The dust emission appears to be variable. It is apparent that Wolf Rayet dust formation occurs also in metal-poor environments.

1 Introduction

Infrared observations show the wide prevalence of dust formation by evolved stars of different types: red supergiants, AGB stars, Novae, LBVs, RCB stars – and some Population I Wolf-Rayet stars. Infrared photometric histories, some spanning decades, show properties ranging from persistent dust formation at apparently constant rates (e.g. WR 104 = Ve2-45) to brief episodes of dust formation at regular intervals (e.g. WR 140 = HD 193793, P = 7.94 y.), and these two stars are considered to be the prototypes of persistent and episodic dust makers respectively. A handful of systems show intermediate behaviour, forming dust persistently, but at a variable rate (e.g. WR 98a = IRAS 17380-3031). The persistent dust makers are nearly all WC9 stars and show a strong preference for the metal-rich region of our Galaxy, generally towards the Galactic Centre, while the smaller number of episodic dust makers have spectral types ranging from WC4 to WC8 and a less concentrated galactic distribution – but all of them are located within the Solar circle.

In the lower metallicity environments of the Magellanic Clouds, the fraction WR/O stars and distribution of WR spectral subtypes are very different from those in our Galaxy. In particular, there are no WC stars in the LMC having spectral subtypes 'later' than WC4. To date, the LMC WC4 stars have not been systematically observed for evidence of dust formation, but comparison of their data in the DENIS (Epchtein et al. 1999) and 2MASS (Skrutskie et al. 2006) surveys suggested that HD 36402 (BAT99-38, Brey 31) varied in K with an amplitude greater than that in J and could be a dust maker. This was supported by data in the IRSF Magellanic Clouds survey (Kato et al. 2007). The *SPITZER* SAGE photometry of massive stars in the LMC (Bonanos et al. 2009) allows us to examine the spectral energy distributions (SEDs) of LMC WC4 stars at longer wavelengths, and demonstrates that HD 36402 is indeed a dust-making WR star. Bonanos et al. tentatively identified HD 36402 with a 70- and 160-μm source but this has to be tested for confusion given the large beam sizes (18 and 40 arcsec respectively) at these wavelengths.

2 Infrared Photometry of HD 36402 from Surveys

Photometry and dates of observation of HD 36402 extracted from the DENIS, 2MASS and IRSF LMC surveys are collected in Table 1 and plotted in Fig. 1. These appear to be the only published near-IR photometry of HD 36402 but the star is most likely to have been observed in other studies. Hopefully, more photometry will become available, but the present data are sufficient to show that HD 36402 is variable in the near infrared. The amplitude in Ks is significantly greater than the uncertainties, σKs. It is also greater than that in J, arguing against a photospheric origin for the variation and suggesting variable emission by hot dust. Given that the data come from three different instruments, a Ks-band image of the field was searched for close companions which might introduce spurious variability through confusion. The closest is that marked 'a' in Fig. 2, 7″ west of HD 36402. This has 2MASS Ks = 14.76, which is $\sim$ 4 mag. fainter than the WR star and so not a significant contaminant to its near-IR photometry.

Table 1: Near-infrared photometry of HD 36402

Survey	Date	J	H	Ks	σKs
DENIS strip 4963	1996.92	11.63		10.55	0.02
2MASS all-sky	2000.08	11.76	11.62	10.97	0.02
2MASS 6X PSWDB	2000.98	11.73	11.47	10.82	0.02
2MASS 6X PSWDB	2001.09	11.69	11.46	10.73	0.02
IRSF LMC0525-6720A	2002.88	11.80	11.71	11.22	0.01

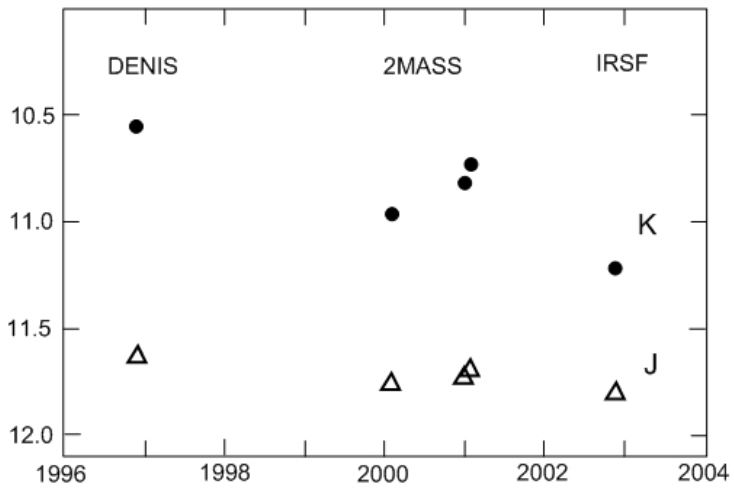

Figure 1: J (△) and Ks (•) magnitudes of HD 36402 from the DENIS, 2MASS and IRSF surveys.

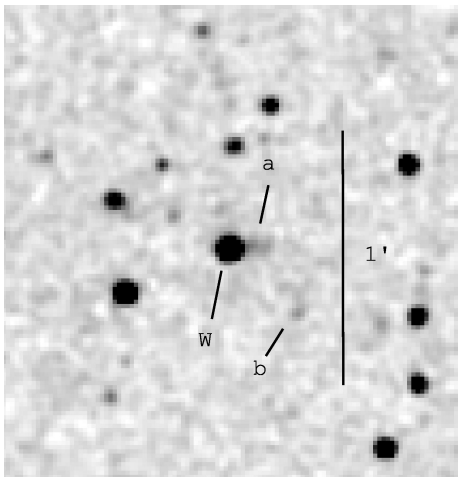

Figure 2: 2MASS Ks-band image (N top, E left) of the field of HD 36402 ('W'); see text for 'a', 'b'.

The *SPITZER* SAGE LMC catalogue gives multi-colour photometry, including *SPITZER* IRAC (3.6–8.0-μm) and MIPS (24-μm) data, for 17 WC4 stars. Of these, HD 36402 has the most convincing evidence for a Planckian spectrum, peaking near 3.6 μm, similar to those of dust-making Galactic WC stars (e.g. Williams, van der Hucht & Thé 1987, hereafter WHT). The photometry of HD 36402 was de-reddened using E_{b-v} = 0.09 (Smith, Shara & Moffat 1990) and the SED fitted by a simple stellar wind plus isothermal, optically thin, dust shell model following WHT. The dust was assumed to have the emissivity law of amorphous carbon. The fit gave $T_d \simeq 800\ K$ and $M_d \simeq 1.5 \times 10^{-7} M_\odot$, adopting

a distance of 50 kpc to the LMC. It is illustrated in Fig. 3. The dust temperature is somewhat lower than those ($\sim$ 1100 K) found for persistent dust makers but may result from the sensitivity of T_d to Ks–[3.6] and the fact that the $JHKs$ and IRAC 3.6–8.0-μm data are not contemporaneous.

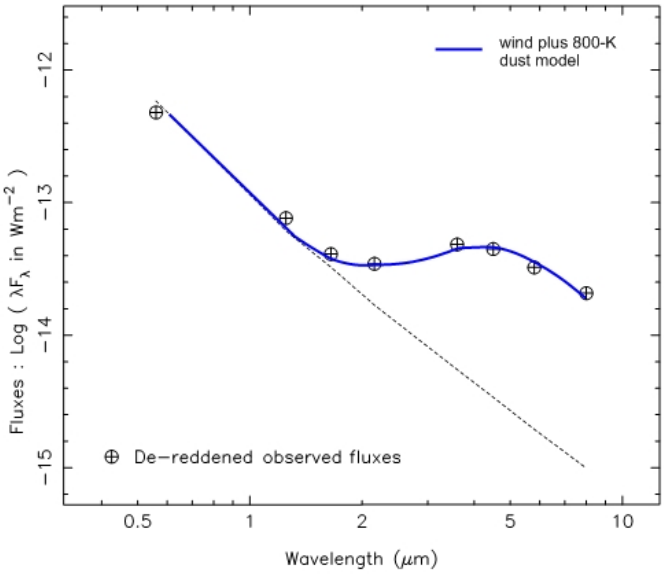

Figure 3: De-reddened optical to 8-μm fluxes of HD 36402 compared with those of a model (solid line) comprising a stellar wind (broken line) fitted to the v and J data plus emission from an isothermal dust shell.

Bonanos et al. (2009) tentatively identified HD 36402 with a 70- and 160-μm source, and suggested that its infrared excess might come from its associated ring nebula embedded in N51D (Dopita et al. 1994). The environs of HD 36402 are certainly complex. Chu et al. (2005) discovered two YSOs close to the WR star. One of them, their YSO-2, corresponding to 'a' in Fig. 2, is only 7″ from the WR star. The SED of YSO-2 formed from *SPITZER* data in Chu et al. and $JHKs$ magnitudes from 2MASS is compared with that of the WR star in Fig. 4. At 8 μm, YSO-2 is 1.7 mag. fainter than the WR star. At this wavelength, the IRAC beam is smaller than 2″ FWHM (Fazio et al. 2004), so we consider YSO-2 well separated from HD 36402 in the IRAC data too. At 8 μm, YSO-1 ('b' in Fig. 2) is almost as bright as the WR star (Fig. 4), but is much further (22″) away so the IRAC data can define the SED of HD 36402 in the mid-IR without fear of confusion.

At longer wavelengths, YSO-1 is even brighter (Fig. 4 and Chu et al.), and its fluxes at 70 and 160 μm given by Chu et al. are close to those tentatively ascribed to the WR star by Bonanos et al. Given the larger beam sizes (18″and 40″respectively) at these wavelengths, HD 36402 cannot be resolved from the YSOs and it is better to ascribe the long-wavelength emission to YSO-1 instead of the WR star. Similarly, we do not expect the *IRAS* or *MSX* observations to resolve the WR star from YSO-2.

A more recent observation is the *AKARI* IRC (Ishihara et al. 2010) photometry, which observed HD 36402 between 2006 May and 2007 August in the 9-μm band, giving S19W = 6.90 (97.9$\pm$6.8 mJy). The larger beam (5.″5 at 9 μm) could include some flux from YSO-2, which is rising in this wavelength region. From the IRAC and MIPS data, we estimate its flux to be 13.5 mJy at 9 μm, while extrapolation of the HD 36402 SED suggests its 9-μm flux would be about 43 mJy (cf. 48 mJy at 8 μm), three times brighter than YSO-2. Hence, the apparent two-fold brightening of HD 36402 at 9 μm between the IRAC observations in mid-2005 and the IRC observation 1–2 years later cannot be an artefact of confusion with YSO-2 but must result from changes in the WR dust cloud.

3 Conclusion: a WR dust maker in the LMC

Evidently, HD 36402 is a dust maker like those in the Galaxy. Moffat et al. (1990) deduced that it is a triple system: a 3-day binary and more distant O supergiant companion. The inner binary separation is probably too small for the O star wind to accelerate to its terminal value, and the colliding wind effects probably arise between it and the third component. The outer orbit deserves study and relation to the pattern of dust formation, which itself requires characterisation from further observations – some of which may already exist.

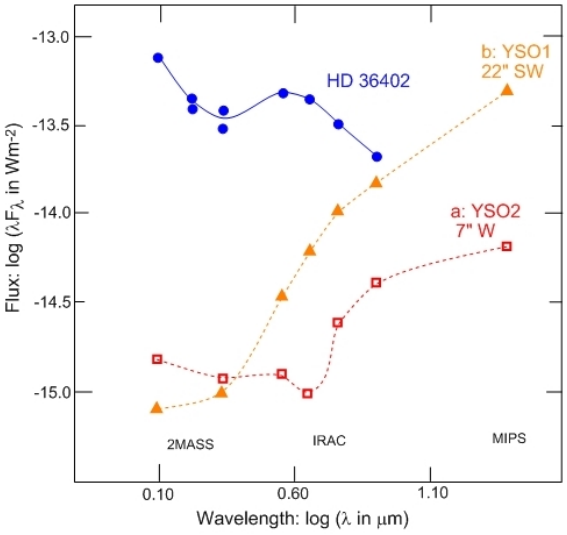

Figure 4: Spectral energy distributions of HD 36402 and the nearby YSOs discovered by Chu et al.

Acknowledgements

The author is grateful to the Institute for Astronomy for hospitality and continued access to facilities of the Royal Observatory, Edinburgh. This research has made use of the NASA / IPAC Infrared Science Archive, which is operated by the Jet Propulsion Laboratory, California Institute of Technology, under contract with the National Aeronautics and Space Administration; the Vizier database, operated by the CDS, Strasbourg, and the DARTS archive developed and maintained by C-SODA at ISAS/JAXA.
.

References

Bonanos, A.Z., Massa, D.L., Sewilo, M., et al. 2009, AJ 138, 1003
Chu, Y.-H., Gruendl, R.A., Chen, C.-H.R., et al. 2005 ApJ 634, L189
Dopita, M.A., Bell, J.F., Chu, Y.-H., & Lozinskaya, T.A. 1994, ApJS 93, 455
Epchtein, N., Deul, E., Derriere, S., et al. 1999, A&A 349, 236
Fazio, G.G., Hora, J.L., Allen, L.E., et al. 2004, ApJS 154, 10
Ishihara, D., Onaka, T., Kataza, H., et al. 2009, in *AKARI, A Light to Illuminate the Misty Universe*, eds T. Onaka, G.J. White, T. Nakagawa, I. Yamamura, ASPC 418, 9
Kato, D., Nagashima, C., Nagayama, T., et al. 2007, PASJ 59, 615
Moffat, A.F.J., Niemela, V.S., & Marraco, H.G. 1990, ApJ 348, 232
Skrutskie, M.F., Cutri, R.M., Stiening, R., et al. 2006, AJ 131, 1163
Smith, L.F., Shara, M.M., & Moffat, A.F.J. 1990, ApJ 348, 471
Williams, P.M., van der Hucht, K.A., & Thé, P.S. 1987, A&A 182, 91 (WHT)

Chapter 2

Massive star formation, confronting theory and observation

Formation and early evolution of massive stars

Henrik Beuther[1]

[1] Max Planck Institute for Astronomy, Königstuhl 17, 69117 Heidelberg, Germany

Abstract: The early evolutionary stages of high-mass star formation have been subject to intense research for more than a decade now. Because several comprehensive reviews exist, here I focus on a few results obtained in the last two years. Specific questions to be addressed are: What can we learn about the initial conditions of high-mass star formation from recent Herschel observations? How important are magnetic fields for high-mass star-forming clumps and cores? Do we find genuine massive accretion disks? Do high-mass stars form first, last or simultaneously with the low-mass stars during cluster formation?

1 Introduction

Since this conference deals with the birth, life and death of high-mass stars, it appears superfluous to stress the importance of them again. Therefore, I just like to point out that the formation and early evolution of high-mass stars has been one of the most important topics in star formation research over the last decade. This is also manifested in a loose series of conferences targeting this topic over recent years (e.g., Joint discussion at Manchester IAU 2000 "Massive Star Birth"; Boulder 2001 "The Earliest Phases of Massive Star Birth"; Sicily 2005 "Massive Star Birth: A Crossroads of Astrophysics"; Heidelberg 2007 "Massive Star Formation: Observations Confront Theory"; Townsville 2010 "Great Barriers in High-Mass Star Formation"). For more general reviews about the topic with extensive introductions and state-of-art discussions at the given time, I refer to two big reviews (Zinnecker & Yorke 2007; Beuther et al. 2007) as well as the conference proceedings from the 2005 and 2008 meetings aforementioned (Cesaroni et al. 2005; Beuther et al. 2008). Here, I like to concentrate on recent results obtained in that field over the last two years. In particular, I like to outline the progress made toward four sub-topics of that field: (a) the earliest evolutionary stages, in particular with respect to new Herschel results obtained toward infrared dark clouds (IRDCs), (b) the characterization of magnetic field structure by means of polarization and Zeeman measurements, (c) the properties of rotating toroids and/or potential massive accretion disks, and (d) discuss whether high-mass stars form first, last or simultaneously during the cluster formation process.

2 The earliest evolutionary stages of high-mass star formation

The initial conditions for, and the onset of the formation of massive stars has for a long time been largely elusive to observational research because already the identification of the right targets was difficult. This situation changed tremendously at the end of the last century when several mid-infrared

surveys became available allowing us to identify the youngest and coldest molecular clouds as dark shadows against the brighter background. While first ground-breaking work was conducted with the satellites *ISO* and *MSX* (e.g., Perault et al. 1996; Egan et al. 1998; Carey et al. 2000; Rathborne et al. 2005; Sridharan et al. 2005; Simon et al. 2006), the higher spatial resolution of *Spitzer* allowed additional great progress in that field (e.g., Vasyunina et al. 2009; Peretto & Fuller 2009). However, even with the *Spitzer* IRAC bands up to 8 μm as well as with MIPS in the 24 μm band, the peak of the spectral energy distribution was still out of reach, and any characterization of young massive star-forming regions had to be limited. The launch of *Herschel* in May 2009 again changed the picture considerably. The accessibility of all wavelength bands between 70 and 500 μm wavelength now allows us to study and characterize the birth sites and initial conditions of high-mass star formation in unprecedented detail.

There are several guaranteed and open time key projects which aim at characterizing these early evolutionary stages – e.g., EPOS, PI O. Krause; HiGAL, PI S. Molinari; HOBYS, PI F. Motte. While the first of the three mentioned projects is a targeted study toward a large sample of already well-characterized very young regions, the second aims at observing a large fraction of the Galactic disk (similar to GLIMPSE and MIPSGAL, Churchwell et al. 2009; Carey et al. 2009), and the third project targets most well-known regions within 3 kpc distance from the Sun, including all evolutionary stages.

Here, I like to focus on early results obtained within the EPOS project - The Early Phase of Star Formation. Within this guaranteed time key project, we observed a sample of 44 very young high-mass star-forming regions selected from different sub-samples. One third of the sources consists of 170 μm emission sources selected from the *ISO* Serendipity Survey (e.g., Krause et al. 2004; Birkmann et al. 2006; Hennemann et al. 2008), the second third is based on the sample identified by Sridharan et al. (2005) in the fields of high-mass protostellar objects (HMPOs), and the last third contains well-known IRDCs previously studied by, e.g., Carey et al. (2000). What all sources have in common is that they are already previously well characterized from ample observations at other wavelengths, and for most of the regions, we also have higher-spatial-resolution information from interferometer observations. Therefore, these regions allow us an in-depth study of the initial conditions important for the high-mass star formation processes. In the following, I will show a few early results.

2.1 The Snake or G11.11

One of the most famous IRDCs is the so-called Snake, a.k.a. G11.11. This region was previously observed by Carey et al. (2000) and has been subject to investigations since then (e.g., Johnstone et al. 2003; Pillai et al. 2006). Within the EPOS key project, the whole region was observed in all Herschel PACS and SPIRE continuum bands between 70 and 500 μm wavelengths (see Fig. 1 for a few example images, Henning et al. 2010). An image comparison allows us already interesting insights for the cloud being an absorption feature below 100 μm, then becoming nearly indistinguishable from the background at 160 μm, and turning into emission at longer wavelengths. More importantly, the data reveal many point-source-like protostars along the snake-filament. An SED analysis of these sources reveals dust temperatures below 20 K and masses usually of the order a few $M_\odot$, hence no massive protostars yet. It appears that most of the mass is still distributed over the cold envelopes and the entire filament. While for each individual sub-source, one cannot conclude whether it will be a high-mass star at the end of its evolution, it is a reasonable assumption that some will because the entire gas reservoir is sufficient to form massive stars. Furthermore, we detect an entirely new population of very young objects that was undetected even at 24 μm, but which become clear point-source emission features from 70 μm onwards. While the SED does not allow us to distinguish these sources from genuine starless cores, the fact that they appear as point sources in the 70 μm image with

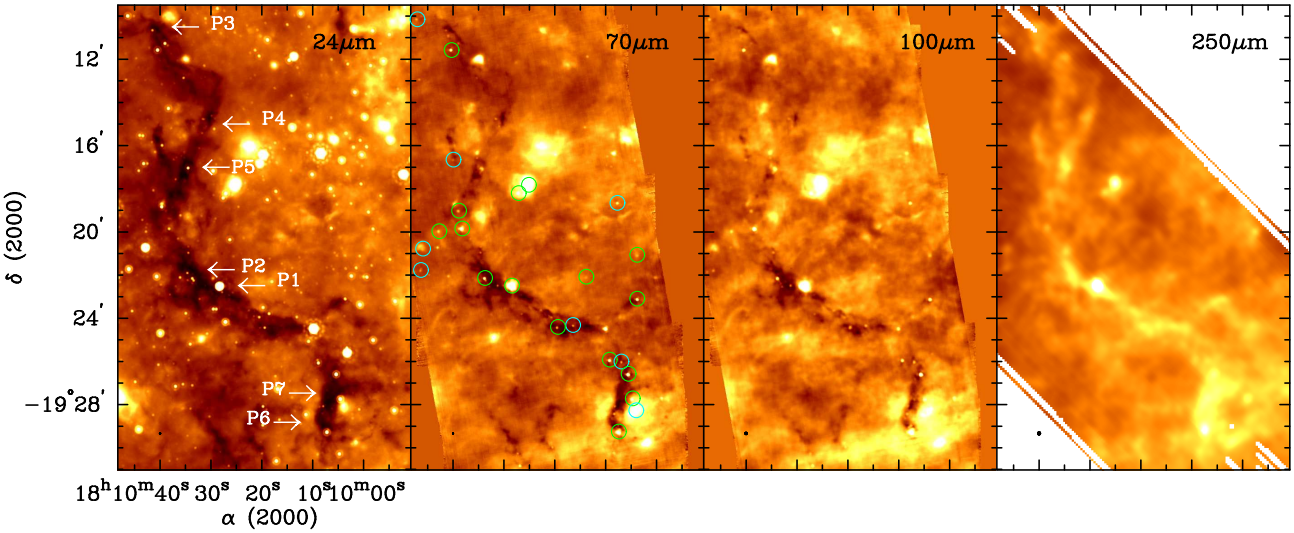

Figure 1: The Snake a.k.a. G11.11. The left panel shows the *Spitzer* 24 μm data, and the other three panels present different wavelengths bands from *Herschel* as marked (Henning et al. 2010). The labels in the left panel identify submm continuum sources from Johnstone et al. (2003), and the circles in the 2nd panel outline identified point sources.

a spatial resolution of $\sim$6″ ($\sim$21000AU) is indicative of an inner heating source already. Therefore, one may speculate whether these new detections may be the observational manifestation of the first hydrostatic cores in the star formation process.

2.2 The infrared dark cloud complex IRDC 18223

This cloud complex started to be investigated because of its IRAS identification as a high-mass protostellar object (HMPO) by Sridharan et al. (2002). However, it was quickly realized that not just the HMPO is interesting but that the whole complex presents a region with several evolutionary stages in close proximity (Fig. 2, Sridharan et al. 2005; Beuther et al. 2005; Beuther & Steinacker 2007). Right south of the strong IRAS source, one finds a dark filament that contains only weak 24 μm emission sources. These sources represent high-mass cores with embedded low-to intermediate-mass protostars that may (or may not) be destined to become massive at the end of their evolution. Further south, we identify another region that is dark at 24 μm, and now with Herschel also at 70 and 100 μm, but that becomes a strong emission source at longer wavelengths due to the cold dust emission. Hence, this region comprises all evolutionary stages ranging from high-mass starless cores up to HMPOs. The Herschel data now allow us a detailed evolutionary characterization of the different evolutionary stages. Fig. 2 presents spectral energy distributions (SEDs) for four different cores representing these stages and their properties (Beuther et al. 2010a). While the starless cores are only emission sources longward of 100 μm that can easily be fitted by single-component modified blackbody functions, as soon as an internal heating source starts modifying the environment, one finds excess emission at shorter wavelengths and additional warmer components are required to fit the data. The 70 μm emission source from that point of view is a borderline object, because it shows a clear point source at that wavelength but can still be fitted with a single component. That may again be a candidate source in an evolutionary stage of the first hydrostatic core, similar to the G11.11 case discussed above. While excess emission at 24 μm becomes evident early in the evolutionary sequence, it appears that for some time the luminosity of this warmer component remains still relatively low, from an observational point of view at least as long as the sources are infrared dark in the Spitzer IRAC

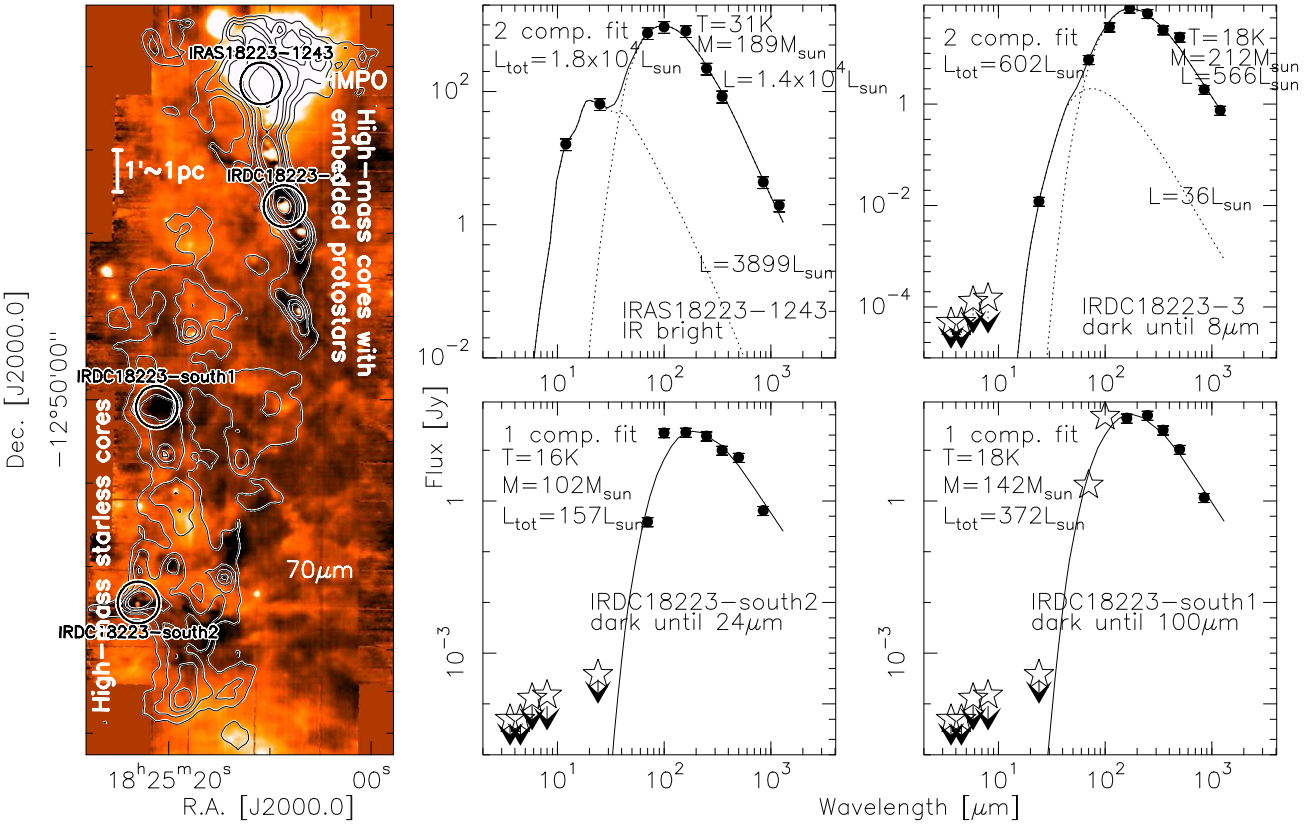

Figure 2: Composite of *Herschel* observations toward IRDC 18223 (Beuther et al. 2010a). The left panel presents in color the 70 μm continuum emission with the submm 850 μm contours on top. The evolutionary sequence as well as the four sources where spectra were extracted are marked. The other four panels show the corresponding SEDs and the associated fits. Fit parameters are given in each panel.

bands up to 8 μm. To quantify the time-scales of the different evolutionary stages will be one of the important questions in that field in the coming years. However, with the high-quality Herschel data available, a lot of progress is expected.

2.3 High-mass starless cores in the vicinity of a mini-starburst

The infrared dark clouds associated with the cloud complex IRDC 18454 are in the immediate vicinity of the galactic mini-starburst W43 (Motte et al. 2003; Sridharan et al. 2005). It is noteworthy in itself that one finds 70 μm dark extinction sources with masses of several 100 $M_\odot$ in such close proximity of one of the most active star-forming regions of our Galaxy (Fig. 3). Hence, it appears that the luminosity and energy output of W43 does not straight away trigger either the collapse or the dispersal of nearby cloud cores, but that some of them may stay around for some (unknown) amount of time. A detailed analysis of the Herschel dataset is currently being conducted (Beuther et al. in prep.). However, here we like to point out another curiosity of that region, namely some kinematic characteristics. It was early on recognized that some of the cores showed different velocity features in their spectra about 50 km s^{-1} apart. One component at $\sim$ 100 km s^{-1}, approximately the rest velocity of W43, and one component at 50 km s^{-1}. Is the latter just a chance alignment along the line of sight or may it be associated with the peculiar location of that region right at the interface of the inner Galactic bar and a spiral arm? Figure 3 also shows N_2H^+ emission maps integrated over the two velocity components. While the 100 km s^{-1} component clearly confirms the association of the

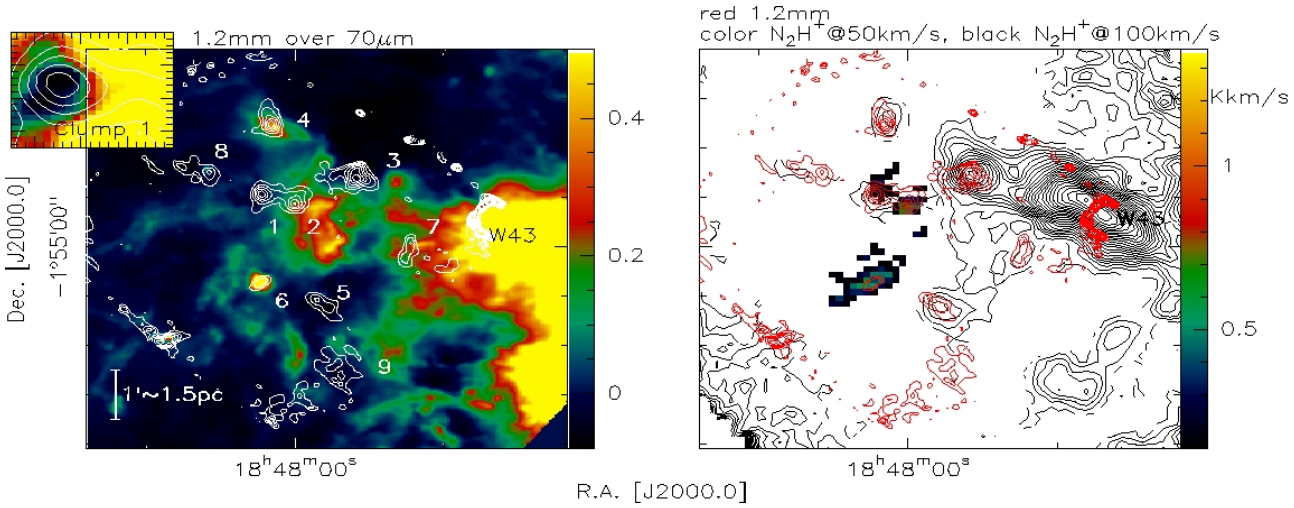

Figure 3: Composite of data toward the dark cloud complex IRDC 18454. The left panel shows in color the 70 μm emission with white contours of 1.2 mm continuum. The inlay presents a zoom into clump 1 (tick-marks there are arcseconds). The right panel shows the same region, this time the N_2H^+(1–0) and 1.2 mm continuum emission as labeled on top of the panel.

IRDC complex with the mini-starburst W43, the 50 km s^{-1} component is confined to only a few of the sub-sources. However, the nearly indistinguishable character of the submm sources between the different velocity components as well as the close spatial association let us speculate whether the two components may not be spatially interacting, maybe between the galactic bar and the spiral arm? The IRAM large program studying the whole region on much larger scales in ^{13}CO emission may shed more light on this question (PI F. Motte).

3 Magnetic field structure during high-mass star formation

The morphology of the magnetic field structure, in particular on the smallest spatial scales for high-mass star formation, has largely been elusive to observations. While Zeeman measurements with high-density tracers like CN or CH_3OH maser emission toward larger samples reveal magnetic field strengths on core scales (several 1000 to 10000 AU) of order mG (e.g., Falgarone et al. 2008; Vlemmings 2008), high-spatial-resolution polarization measurements of masers as well as the recent advent of polarization capabilities at mm interferometers has allowed us significant progress studying also the field morphology.

While VLBI OH maser observations revealed polarized emission at the edges of ultracompact HII regions, barely any evident morphological signature could be derived (e.g., Fish & Reid 2006). Vlemmings (2008) recently started exploring the polarization and Zeeman properties of the class II CH_3OH maser emission which traces the densest cores in high-mass star-forming regions. Toward the disk-outflow system Cepheus A, Vlemmings et al. (2010) were now able to trace the 3D morphology distribution of the maser polarization, and hence the magnetic field, via MERLIN VLBI observations at 6.7 GHz. They find that the magnetic field is predominantly aligned along the protostellar outflow and perpendicular to the disk (Fig. 4). A detailed analysis indicates that the core is collapsing and that the gas likely falls in along the magnetic field lines.

The advent of the submm continuum dust polarization capability at the Submillimeter Array (SMA) also opened the window to high-spatial-resolution magnetic field studies of the dense gas cores not just limited to the specific maser conditions. While early work revealed the predicted hour-

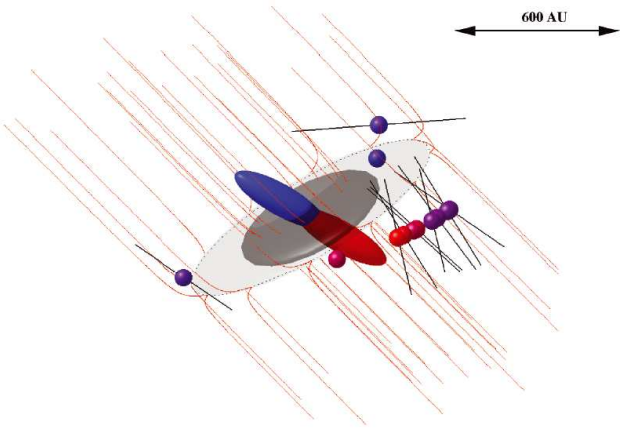

Figure 4: The three-dimensional magnetic field structure around the massive protostar CepheusA HW2 from Vlemmings et al. (2010). Spheres indicate the masers, with the black vectors indicating the true magnetic field direction. The grey region indicates the disk, and the blue and red cones the outflow. The red lines outline the magnetic field morphology.

glass shape magnetic field structure in low-mass cores (Girart et al. 2006), similar results were more recently also found in a few high-mass star-forming regions (e.g., Girart et al. 2009; Tang et al. 2009). Quantitative estimates from these data are difficult since the Chandrasekhar-Fermi method relies on the statistical spread of polarization angles in the data and is hence intrinsically prone to large error margins (Chandrasekhar & Fermi 1953). Nevertheless, current data indicate that magnetic fields are important, however, they do not seem to prevent the collapse of the cores.

Furthermore, the (sub)mm window also allows us studies of the Goldreich-Kylafis effect from molecular lines, in particular CO (Goldreich & Kylafis 1981, 1982). Since this effect relies on a combination of Zeeman-splitting and an anisotropic population of the different sub-levels, which can be achieved by anisotropic optical depth and radiation fields (for a qualitative description see Kylafis 1983), molecular outflows appear as particular promising candidates to study their magnetic field structure via this effect. Early work in this direction has been conducted by Girart et al. (1999); Lai et al. (2003); Cortes et al. (2005, 2008). Recently, we now also achieved the first spatially resolved Goldreich-Kylafis effect observations in CO(3–2) with the Submillimeter Array (SMA) toward the young massive disk-outflow region IRAS 18089-1732 (Fig. 5, Beuther et al. 2010b). Interestingly, we also find that the magnetic field structure appears to be approximately aligned with the outflow, similar to the maser data discussed above. One additional technical advantage of the CO polarization observations is that one obtains simultaneously the dust continuum polarized emission. Hence, within a single observation one can study the magnetic field of the dense core as well as that of the outflow.

One other recent very interesting magnetic field result is that Carrasco-Gonzales and co-workers measure the magnetic field of one high-mass jet via its synchrotron emission (presented in the Sept. 2010 “Great Barriers in High-Mass Star Formation” meeting in Townsville/Australia). They also find that the magnetic field is aligned with the jet. If one combines the maser, synchrotron and CO data, it appears that the magnetic field remains very organized over large spatial scales, down from the core center, along the jet and also within the entrained gas of the molecular outflow.

4 Rotation, infall and disks

The study of disks in high-mass star formation is considered as one of the cornerstones in this field. While there has been tremendous progress over the last decade (e.g., Cesaroni et al. 2007), we are

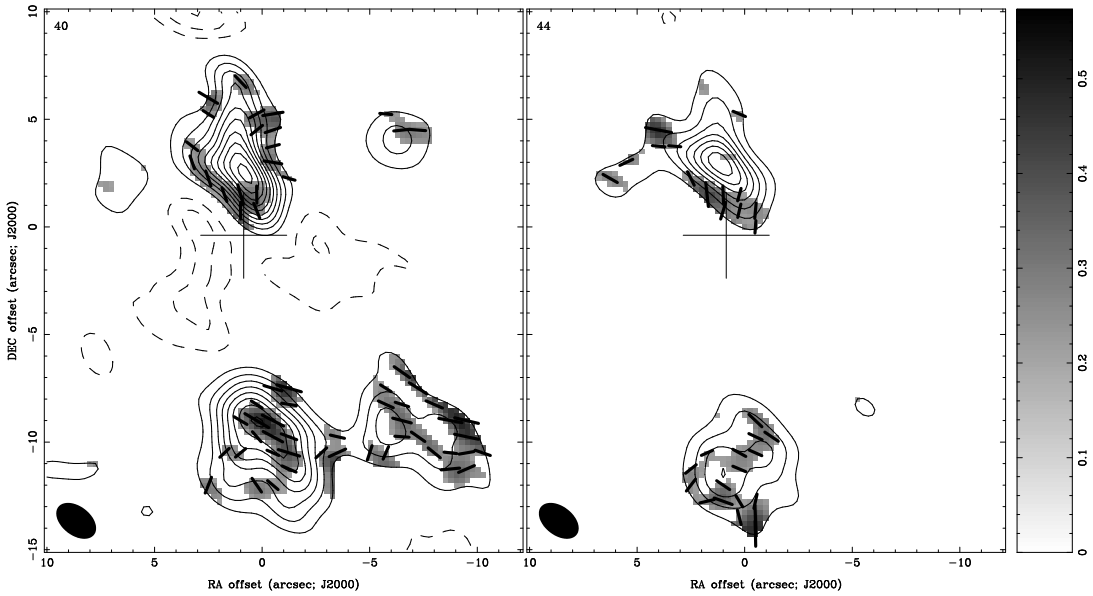

Figure 5: The grey-scale presents the linearly polarized CO(3–2) emission in two channels (central velocities are marked in the top-left corners) for the young high-mass disk-outflow system IRAS 18089-1732. The line-segments show the orientation of the polarized emission. The contours present the corresponding CO(3–2) Stokes I image. The cross marks the position of the submm continuum peak.

nevertheless still lacking a solid understanding of the properties of rotating structures, the infalling gas and the embedded disks. Among the best disk candidates are probably IRAS 20126 and CepA (e.g., Cesaroni et al. 2005; Jiménez-Serra et al. 2007), however, their inferred central stellar masses barely exceed $10\,M_{\odot}$. For more massive and more luminous regions, one usually finds rotating structures perpendicular to the outflows, but their sizes (several 1000 to 10000 AU) and non-Keplerian rotation curves preclude that these are genuine disks (e.g., Beltrán et al. 2004; Chini et al. 2004; Cesaroni et al. 2007; Beuther & Walsh 2008; Beuther et al. 2009). These structures are much more likely parts of rotating and infalling envelopes – sometimes also coined toroids – that may host more genuine accretion disks at the inner center.

Recent modeling work toward the prototypical high-mass disk candidate IRAS 20126 confirmed that both a warm, dense, rapidly-rotating disk and a cold, diffuse infalling envelope are required to reproduce all the available mm spectral line data. Work toward a younger source, the IRDC 18223-3 also revealed a rotating and flattened structure perpendicular to the outflow, however, the size is much larger of the order 25000 AU (Fallscheer et al. 2009). Furthermore, only a comparably small velocity difference of $\sim$3 km s^{-1} is found over the large region. These data are consistent with a large flattened, rotating and infalling envelope structure. However, since the region also exhibits a typical bipolar outflow, it is most likely that at the inner unresolved center one finds a more typical accretion disk. Going to more evolved regions, we recently observed a dozen hot core regions in the southern hemisphere identifying rotational signatures in 6 of them (Beuther et al. 2009). Again the velocity gradients are consistent with rotating and infalling envelopes but not yet real accretion disks. Taking the spatial resolution into account, if genuine accretion disks exist at the center of these rotating structures, they should not exceed $\sim$1000 AU. Going to even higher spatial resolution and more evolved sources that are detectable in the near-infrared, Kraus et al. (2010) recently presented the first near-infrared image of an accretion disk around a massive young stellar object obtained with the VLTI/AMBER instrument. This disk-like structure of warm and compact dust extends only about 20 AU and has a dust-free inner zone of less than 9.5 AU.

Although the statistical basis for toroid and disk studies is still small, current data indicate that there is an evolutionary trend for the rotating structures: They start with very large and extended toroidal infalling envelopes at the onset of collapse (size about 20000 AU), developing into rotating and infalling envelopes (size several 1000 AU) hosting likely accretion disks < 1000 AU at their centers, and continuing into smaller and compact disks (of order several 10 AU) during the continuing formation phase. A challenging task for future observations will be to connect the warm and compact dust disks seen in the near-infrared with the colder and more extended gas and dust disks usually observed at (sub)mm wavelengths.

5 Which stars form first/last?

One of the questions often discussed in high-mass star formation research is whether the high- and low-mass stars form simultaneously, or whether the massive stars form last or first during the early cluster evolution. Although perhaps not a very scientific approach, Zinnecker & Beuther (2008) conducted a poll during a panel discussion among leading theorists within that field, and even there no agreement was achieved.

To first order, one would argue that high-mass stars form last since their strong UV-radiation and winds should severely affect the surrounding gas reservoir that the maternal cocoons may get expelled shortly after the massive stars are actually born. This picture seems to be supported by observations where Kumar et al. (2006) detect already formed low-mass clusters around a sample of still actively accreting HMPOs. In contrast to this, numerical simulations show a larger degree of clumpiness and filamentary structure (e.g., Bonnell & Bate 2005), and within such an environment, the radiation from the massive stars may more easily escape without affecting the other cores in the environment too much. Another view is proposed by Joao Alves (priv. comm.), who, based on observations of the very luminous clusters within W49 (Alves & Homeier 2003; Homeier & Alves 2005), suggests that the massive stars form first and then trigger the formation of low-mass stars in the aftermath.

During a recent multi-wavelength study of the S255 star-forming complex from near-infrared to mm wavelengths, Wang et al. (subm. to A&A) dissected the different populations of the central forming cluster in detail. They find that the most massive cluster member drives an outflow with a dynamical age of the order 10^4 years. Although these dynamical ages are very uncertain, it is unlikely that this object is older than 10^5 years. In contrast to that, the near-infrared spectra reveal a cluster of low-mass stars in the direct environment of the central massive protostars. The spectral data allow Wang et al. to spectral type and then age date these sources via stellar evolution models. The derived age is $\sim 2 \pm 1$ Myr. While the actual age is again uncertain, it is unlikely that these sources are significant younger than 1 Myr. Therefore, taking into account the uncertainties, the data indicate that there is still an age difference of about 1 order of magnitude between the already formed low-mass cluster and the just forming high-mass protostar. Hence, these data are again support for the first scenario where massive stars form last.

But obviously, even with all these data at hand, this case is definitely not closed yet, and future studies may (or may not) shed more light on the order of star formation within young high-mass clusters.

6 Summary

While I could only address a few exciting new results here, it is obvious that much work remains to be conducted in this field. The ever evolving computational facilities promise great progress in the modeling part of high-mass star formation. In particular, there is hope that in the near future one will

self-consistently model the whole evolution from the cloud formation via the fragmentation to the collapse of massive gas clumps with full 3D magneto-hydrodynamic simulations including radiation transfer as well as chemical networks. On the observational side, Herschel already now shows that we will get a wealth of new results for the earliest formation times, whereas the advent of the Atacama Large Millimeter Array (ALMA) in 2011, and JWST in the mid of the starting decade, promises exciting new insights for the cold and warm dust and gas components at the highest possible spatial resolution. Combining these observational and theoretical approaches, it is likely that within the next decade we will establish a much better understanding of the high-mass star formation processes. Among the important questions to be tackled in the future are: How do disks fragment, do they form multiples or spiral-like structures? What are the actual accretion rates, and how variable are they? On what spatial scales is the initial mass function recovered, or is low-mass star formation suppressed at the cluster centers? Are disk-winds or stellar winds dominating in high-mass star formation? How can we relate our detailed local knowledge about high-mass star formation with the extragalactic more global views?

References

Alves, J. & Homeier, N. 2003, ApJ, 589, L45

Beltrán, M. T., Cesaroni, R., Neri, R., et al. 2004, ApJ, 601, L187

Beuther, H., Churchwell, E. B., McKee, C. F., & Tan, J. C. 2007, in Protostars and Planets V, ed. B. Reipurth, D. Jewitt, & K. Keil, 165–180

Beuther, H., Henning, T., Linz, H., et al. 2010a, A&A, 518, L78

Beuther, H., Linz, H., & Henning, T., eds. 2008, Massive Star Formation: Observations Confront Theory, ASP Conference Series 387

Beuther, H., Sridharan, T. K., & Saito, M. 2005, ApJ, 634, L185

Beuther, H. & Steinacker, J. 2007, ApJ, 656, L85

Beuther, H., Vlemmings, W. H. T., Rao, R., & van der Tak, F. F. S. 2010b, Accepted for ApJL, ArXiv e-prints, 1010.3635

Beuther, H. & Walsh, A. J. 2008, ApJ, 673, L55

Beuther, H., Walsh, A. J., & Longmore, S. N. 2009, ApJS, 184, 366

Birkmann, S. M., Krause, O., & Lemke, D. 2006, ApJ, 637, 380

Bonnell, I. A. & Bate, M. R. 2005, MNRAS, 362, 915

Carey, S. J., Feldman, P. A., Redman, R. O., et al. 2000, ApJ, 543, L157

Carey, S. J., Noriega-Crespo, A., Mizuno, D. R., et al. 2009, PASP, 121, 76

Cesaroni, R., Galli, D., Lodato, G., Walmsley, C. M., & Zhang, Q. 2007, in Protostars and Planets V, ed. B. Reipurth, D. Jewitt, & K. Keil, 197–212

Cesaroni, R., Neri, R., Olmi, L., et al. 2005, A&A, 434, 1039

Chandrasekhar, S. & Fermi, E. 1953, ApJ, 118, 113

Chini, R., Hoffmeister, V., Kimeswenger, S., et al. 2004, Nature, 429, 155

Churchwell, E., Babler, B. L., Meade, M. R., et al. 2009, PASP, 121, 213

Cortes, P. C., Crutcher, R. M., Shepherd, D. S., & Bronfman, L. 2008, ApJ, 676, 464

Cortes, P. C., Crutcher, R. M., & Watson, W. D. 2005, ApJ, 628, 780

Egan, M. P., Shipman, R. F., Price, S. D., et al. 1998, ApJ, 494, L199

Falgarone, E., Troland, T. H., Crutcher, R. M., & Paubert, G. 2008, A&A, 487, 247

Fallscheer, C., Beuther, H., Zhang, Q., Keto, E., & Sridharan, T. K. 2009, A&A, 504, 127

Fish, V. L. & Reid, M. J. 2006, ApJS, 164, 99

Girart, J. M., Beltrán, M. T., Zhang, Q., Rao, R., & Estalella, R. 2009, Science, 324, 1408

Girart, J. M., Crutcher, R. M., & Rao, R. 1999, ApJ, 525, L109

Girart, J. M., Rao, R., & Marrone, D. P. 2006, Science, 313, 812

Goldreich, P. & Kylafis, N. D. 1981, ApJ, 243, L75

Goldreich, P. & Kylafis, N. D. 1982, ApJ, 253, 606

Hennemann, M., Birkmann, S. M., Krause, O., & Lemke, D. 2008, A&A, 485, 753

Henning, T., Linz, H., Krause, O., et al. 2010, A&A, 518, L95

Homeier, N. L. & Alves, J. 2005, A&A, 430, 481

Jiménez-Serra, I., Martín-Pintado, J., Rodríguez-Franco, A., et al. 2007, ApJ, 661, L187

Johnstone, D., Fiege, J. D., Redman, R. O., Feldman, P. A., & Carey, S. J. 2003, ApJ, 588, L37
Kraus, S., Hofmann, K., Menten, K. M., et al. 2010, Nature, 466, 339
Krause, O., Vavrek, R., Birkmann, S., et al. 2004, Baltic Astronomy, 13, 407
Kumar, M. S. N., Keto, E., & Clerkin, E. 2006, A&A, 449, 1033
Kylafis, N. D. 1983, ApJ, 275, 135
Lai, S., Girart, J. M., & Crutcher, R. M. 2003, ApJ, 598, 392
Motte, F., Schilke, P., & Lis, D. C. 2003, ApJ, 582, 277
Perault, M., Omont, A., Simon, G., et al. 1996, A&A, 315, L165
Peretto, N. & Fuller, G. A. 2009, A&A, 505, 405
Pillai, T., Wyrowski, F., Menten, K. M., & Krügel, E. 2006, A&A, 447, 929
Rathborne, J. M., Jackson, J. M., Chambers, E. T., et al. 2005, ApJ, 630, L181
Simon, R., Jackson, J. M., Rathborne, J. M., & Chambers, E. T. 2006, ApJ, 639, 227
Sridharan, T. K., Beuther, H., Saito, M., Wyrowski, F., & Schilke, P. 2005, ApJ, 634, L57
Sridharan, T. K., Beuther, H., Schilke, P., Menten, K. M., & Wyrowski, F. 2002, ApJ, 566, 931
Tang, Y., Ho, P. T. P., Koch, P. M., et al. 2009, ApJ, 700, 251
Vasyunina, T., Linz, H., Henning, T., et al. 2009, A&A, 499, 149
Vlemmings, W. H. T. 2008, in ASP Conference Series, Vol. 387, Massive Star Formation: Observations Confront Theory, ed. H. Beuther, H. Linz, & T. Henning, 117
Vlemmings, W. H. T., Surcis, G., Torstensson, K. J. E., & van Langevelde, H. J. 2010, MNRAS, 404, 134
Zinnecker, H. & Beuther, H. 2008, in Astronomical Society of the Pacific Conference Series, Vol. 387, Massive Star Formation: Observations Confront Theory, ed. H. Beuther, H. Linz, & T. Henning, 438
Zinnecker, H. & Yorke, H. W. 2007, ARA&A, 45, 481

Discussion

Y.-H. Chu: The massive star community regards stars more massive than several tens of solar masses as 'massive stars'. What stellar mass range does your massive star formation correspond to?
H. Beuther: Most of the presented studies deal with stars in the 10-30 $M_{\odot}$ regime. The observational database of very young more massive regions is still relatively poor.

G. Romero: Is there any evidence for non-thermal emission in some of these SFR with strong magnetic fields?
H. Beuther: Yes, there are a few examples of non-thermal radio emission in young massive star-forming regions. The most prominent is maybe the synchrotron emission in W3 (H_2O) by Reid et al. (1995). This emission is usually associated with the jets. However, it should be stressed that thermal radio emission – from the jets and the protostars – is far more often observed.

D. Gies: Are high-mass star-formation regions usually associated with filamentary structures?
H. Beuther: Very often, yes. In particular, recent *Herschel* observations reveal filamentary structures in a very regular fashion.

R. Chini: The high-mass protostellar candidates that you find at FIR/submm wavelengths have typically a couple of hundred solar luminosities. A five-solar-mass protostar produces about thousand solar luminosities. What gives you the confidence to call them high-mass protostars if there are no additional hints like, e.g., high-mass or high-luminosity outflows?
H. Beuther: This is certainly an important point. For each individual source the answer is not easy. If we have a massive outflow with high outflow rates, that can be taken as an indirect indicator for a high-mass star-forming core. For larger samples, when we not always have such complementary data, the answer is more complicated, and one has to argue in a statistical sense. For each individual source one cannot be sure that the central object will form a massive star, it could remain low-mass star as you say. However, from a statistical point of view, some fraction is likely to form massive stars

in the end. Furthermore, an important criterion is that the mass reservoir has to be large enough to form a cluster, i.e., more than 500-1000 $M_\odot$ of gas.

H. Zinnecker: On sequential star formation in S 255-IR: in which direction is the sequence? S 255 and S 257 squeezing S 255-IR into massive star formation? Or perhaps is it the other way round: the semi-isolated B-stars powering the S 255 and S 257 H II regions could have been ejected from the S 255-IR forming cluster about 1 Myr ago, and are now pushing on their protocluster birth cloud? (cf. Zinnecker et al. 1993).
H. Beuther: While we cannot clearly exclude that idea, it still appears very unlikely to me. The age of these outer B-stars is ~ 2 Myrs, whereas the B-stars still forming in the center of S 255-IR should be younger than 10^5 years. Furthermore, the morphology is very suggestive of such a squeezing and sequential star formation.

Radiation pressure feedback in the formation of massive stars

Rolf Kuiper[1,2], Hubert Klahr[2], Henrik Beuther[2], and Thomas Henning[2]

[1] Argelander Institute for Astronomy, Bonn University, Auf dem Hügel 71, D-53121 Bonn, Germany
[2] Max Planck Institute for Astronomy, Königstuhl 17, D-69117 Heidelberg, Germany

Abstract: We investigate the radiation pressure feedback in the formation of massive stars in 1, 2, and 3D radiation hydrodynamics simulations of the collapse of massive pre-stellar cores. In contrast to previous research, we consider frequency dependent stellar radiation feedback, resolve the dust sublimation front in the vicinity of the forming star down to 1.27 AU, compute the evolution for several 10^5 yrs covering the whole accretion phase of the forming star, and perform a comprehensive survey of the parameter space. The most fundamental result is that the formation of a massive accretion disk in slowly rotating cores preserves a high anisotropy in the radiation field. The thermal radiation escapes through the optically thin atmosphere, effectively diminishing the radiation pressure feedback onto the accretion flow. Gravitational torques in the self-gravitating disk drive a sufficiently high accretion rate to overcome the residual radiation pressure. Simultaneously, the radiation pressure launches an outflow in the bipolar direction, which grows in angle with time and releases a substantial fraction of the initial core mass from the star-disk system. Summarized, for an initial core mass of 60, 120, 240, and 480 $M_\odot$ these mechanisms allow the star to grow up to 28.2, 56.5, 92.6, and at least 137.2 $M_\odot$ respectively.

1 Introduction

The understanding of massive stars suffers from the lack of a generally accepted formation scenario. If the formation of high-mass stars is treated as a scaled-up version of low-mass star formation, a special feature of these high-mass proto-stars is the interaction of the accretion flow with the strong irradiation emitted by the newborn stars due to their short Kelvin-Helmholtz contraction timescale (Shu, Lizano, & Adams 1987). Early one-dimensional studies (e.g. Larson & Starrfield 1971; Kahn 1974; Yorke & Krügel 1977) agree on the fact that the growing radiation pressure potentially stops and reverts the accretion flow onto a massive star.

But this radiative impact strongly depends on the geometry of the stellar environment (Nakano 1989). The possibility was suggested to overcome this radiation pressure barrier via the formation of a long-living massive circumstellar disk, which forces the generation of a strong anisotropic feature of the thermal radiation field. Earlier investigations by Yorke & Sonnhalter (2002) tried to identify such an anisotropy, but their simulations show an early end of the disk accretion phase shortly after its formation due to strong radiation pressure feedback. Krumholz et al. (2009) demonstrated the possibility to maintain the shielding property of the accretion disk by additional feeding due to the so-called '3D radiative Rayleigh-Taylor instability' in the outflow cavity.

2 Method

2.1 The aim

Aim of this study is to reveal the details of the radiation dust interaction in the formation of the most massive star during the collapse of a pre-stellar core (gravitationally unstable fragment of a molecular cloud). Due to the strong focus onto the core center, the physics in the outer core region have to be simplified, e.g. further fragmentation of the pre-stellar core is suppressed.

2.2 The code

For this purpose, we use our newly developed self-gravity radiation hydrodynamics code. The hydrodynamical evolution is computed using the open source code Pluto3 (Mignone et al. 2007), including full tensor viscosity. The frequency dependent hybrid radiation transport method is summarized by Kuiper et al. (2010a). The implementation of Poisson's equation, the viscosity prescription as well as the tabulated dust and stellar evolution model are presented in Kuiper et al. (2010b).

The simulations are performed on a time independent grid in spherical coordinates. The radially inner and outer boundary of the computational domain are semi-permeable walls, i.e. the gas can leave but not enter the computational domain. The resolution of the non-uniform grid is chosen to be $(\Delta r \times r\ \Delta\theta \times r\sin(\theta)\ \Delta\phi)_{\rm min} = 1.27$ AU $\times\, 1.04$ AU $\times\, 1.04$ AU in the midplane ($\theta = 90°$) around the forming massive star and decreases logarithmically in the radial outward direction. The outer core radius is fixed to $r_{\rm max} = 0.1$ pc. The accurate size of the inner sink cell was determined in a parameter scan presented in Kuiper et al. (2010b), Sect. 5.1.

2.3 The initial conditions

The basic physical initial conditions are very similar to the one used by Yorke & Sonnhalter (2002). We start from a cold ($T_0 = 20$ K) pre-stellar core of gas and dust. The initial dust to gas mass ratio is chosen to be $M_{\rm dust}/M_{\rm gas} = 1\%$. The model describes a so-called quiescent collapse scenario without turbulent motion ($\vec{u}_r = \vec{u}_\theta = 0$). The core is initially in slow solid-body rotation ($|\vec{u}_\phi|/R = \Omega_0 = 5 \times 10^{-13}$ Hz). The initial density slope drops with r^{-2} and the total mass $M_{\rm core}$ varies in the simulations from 60 up to 480 $M_\odot$.

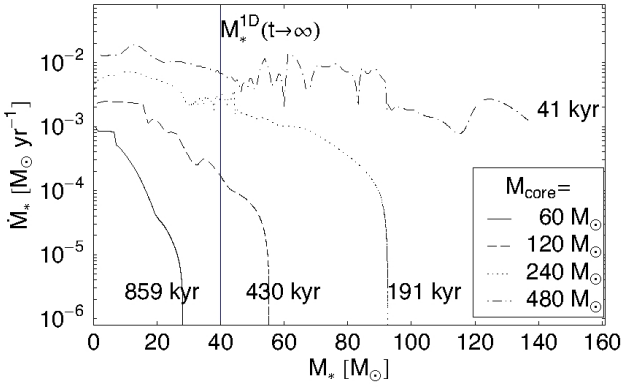

Figure 1: Accretion rate $\dot{M}_*$ as a function of the stellar mass M_* for varying initial core masses. The periods of accretion are mentioned for each run. The vertical line marks the upper mass limit for spherically symmetric accretion flows.

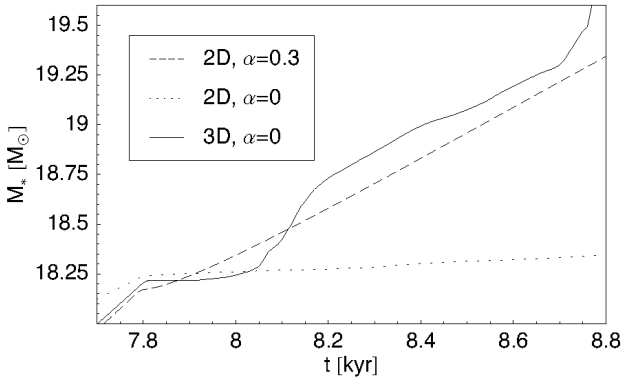

Figure 2: Accretion history of a three-dimensional run, driven by evolving torques in the self-gravitating massive accretion disk, compared with the axially symmetric viscous accretion models with and without α-viscosity ($M_{\rm core} = 120$ $M_\odot$).

3 Results

The presentation and discussion of the selective simulation results are divided in two subsections, which distinguish between the radiation pressure feedback onto the disk region and its interaction with the accretion flow (Sect. 3.1), and the feedback onto the region of the bipolar cavities yielding the launching of stable radiation pressure driven outflows (Sect. 3.2).

3.1 Radiation pressure in the circumstellar accretion disk

First, we performed pre-stellar core collapse simulations in axial symmetry for four different initial core masses $M_{\rm core} = 60\,{\rm M}_\odot$, $120\,{\rm M}_\odot$, $240\,{\rm M}_\odot$, and $480\,{\rm M}_\odot$. The resulting accretion histories as a function of the actual stellar mass are displayed in Fig. 1. Contrary to one-dimensional in-fall simulations (e.g. Larson & Starrfield 1971; Kahn 1974; Yorke & Krügel 1977; Kuiper et al. 2010b), the disk accretion scenario allows the formation of massive stars far beyond the upper mass limit of spherically symmetric accretion flows (the so-called 'radiation pressure barrier'). The reason for this strong dependence of the radiation pressure feedback on the geometry of the stellar environment is that the massive accretion disk results in a high anisotropy of the radiation field. Most of the radiation escapes perpendicular to the accretion flow. Consistently, all simulations performed so far (including resolution studies and different sizes of the inner sink cell) show that the accretion rate increases with a stronger suppression of the isotropic part of the thermal radiation field.

The difference between our simulations and the ones performed by Yorke & Sonnhalter (2002), which yield an early and abrupt end of the disk accretion phase directly after the formation of the circumstellar disk, is the fact that in our simulations the radiation dust interaction is resolved down to the dust sublimation front of the forming massive star. E.g. in contrast to the size of the inner sink cell of $r_{\rm min} = 80$ AU or 160 AU as well as a resolution of the inner core region of $(\Delta r)_{\rm min} = 80$ AU or 160 AU in the 60 $\rm M_\odot$ or 120 $\rm M_\odot$ collapse by Yorke & Sonnhalter (2002) respectively, we use an inner rim of the computational domain of $r_{\rm min} = 10$ AU with a maximum resolution of $(\Delta r)_{\rm min} = 1.27$ AU. For comparison: Radiation pressure becomes as strong as gravity for roughly a 20 $\rm M_\odot$ star (the so-called 'Generalized Eddington barrier') and its dust sublimation radius in the disk's midplane is about 20 to 30 AU. The short disk accretion phases by Yorke & Sonnhalter (2002) are reproduced, if we use the same huge inner sink cell radii they used (see Kuiper et al. 2010b).

Secondly, the validity of the standard α-shear-viscosity prescription based on Shakura & Sunyaev (1973), which we use in the axially symmetric disk simulations, is cross-checked in three-dimensional simulations without shear-viscosity, in which the angular momentum transport is self-consistently driven by evolving gravitational torques in the self-gravitating massive accretion disks. A comparison of the stellar mass growth after the onset of disk formation is shown in Fig. 2 for the collapse of a 120 $\rm M_\odot$ pre-stellar core. Although the three-dimensional run yields a more time dependent episodic accretion history than the viscous disk simulations, the mean accretion rates equal each other. We conclude that the self-gravity of massive accretion disks is a sufficient driver of angular momentum transport. The resulting accretion flow easily overcomes the remnant thermal radiation pressure, which is - deeply inside the disk - diminished by the shielding effect at the inner rim of the dust disk.

The difference between our simulations and Krumholz, Klein, & McKee (2007); Krumholz et al. (2009) is the fact that in the disk accretion scenario, which we propose here, the most massive stars can form consistently with standard accretion disk theories without the requirement of '3D radiative Rayleigh-Taylor instabilities' in the outflow region. We discuss the issue of the outflow stability in more detail in the following Sect. 3.2.

3.2 Radiation pressure in the bipolar outflow

The feedback of the radiation pressure onto the bipolar region differs strongly from the feedback onto the circumstellar disk region. The strong radiation pressure in the bipolar direction stops the in-fall and reverts the mass flow into a radiation pressure driven outflow with velocities of a few 100 km s^{-1}. Fig. 3 visualizes a slice through the three-dimensional density structure of such an outflow. The

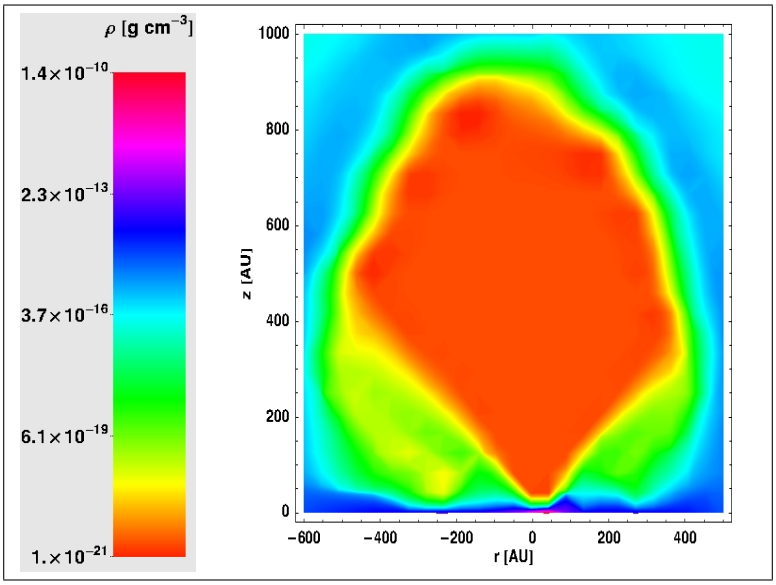

Figure 3: A slice through the three-dimensional density structure of a radiation pressure driven outflow during a 120 $M_\odot$ pre-stellar core collapse.

radiation pressure driven outflows in our axially symmetric simulations remain stable throughout the whole stellar accretion phase. As a result, the radiation pressure in the bipolar direction thrusts a substantial fraction (more than 40% during the stellar disk accretion phase) of the initial mass of the pre-stellar core into outer space, reducing the star formation efficiency of the massive star forming core. In contrast to Krumholz et al. (2009), the outflows in our three-dimensional simulations remain stable so far as well in spite of the strong non-axially symmetric features developing in the outflow region. The reason(s) for that disagreement can be manifold, and we briefly overview the most relevant explanations here:

1. It was supposed by Krumholz et al. (2009) that the instability requires non-axially symmetric modes, and this could explain why it is not seen in our two-dimensional simulations. In our three-dimensional runs, the outflow is stable during the launching and the first growth phase, but instability might appear at a later epoch. The instability in Krumholz et al. (2009) occurs when the outflow extends up to $r \sim 1000$ AU, and the outflow in our runs have propagated up to $r \leq 500$ AU so far. Our three-dimensional simulations are continuously running, and we will further report on their status in the near future.
2. Our simulations account for frequency dependent stellar irradiation instead of the frequency averaged (gray) approximation used in Krumholz et al. (2009).
3. We use a more accurate treatment (ray-tracing) of the first absorption of the stellar irradiation and the instability could be an artifact of the flux-limited diffusion approximation, which results in a wrong radiative flux at $\tau \sim 1$ directly in the cavity wall.
4. The disagreement could be due to the different numerical resolution of the diverse grid structures.

Conclusion: The details of the underlying physics of the '3D radiative Rayleigh-Taylor instability' are quite unknown so far and deserve further investigation.

4 Summary

We performed high-resolution radiation hydrodynamics simulations of monolithic pre-stellar core collapses including frequency dependent radiative feedback. The dust sublimation front of the forming star could be resolved down to 1.27 AU. The frequency dependent ray-tracing of our newly developed hybrid radiation scheme denotes the most realistic radiation transport method used in multi-dimensional hydrodynamics simulations of massive star formation by now. In axial symmetry, the whole accretion phase of several 10^5 yrs was computed. The comprehensive parameter studies reveal new insights of the radiative feedback onto the accretion flow during the formation of a massive star:

The massive accretion disk induces a strong anisotropy of the thermal radiation field. In contrast to the short disk accretion phases in Yorke & Sonnhalter (2002), the accretion disks reveal a persistent anisotropy also during their long-term evolution due to the fact that we resolve the dust disk down to the dust sublimation front of the forming star. Contrary to this explanation, Krumholz et al. (2009) stated that the much longer accretion phases in their own simulations compared to Yorke & Sonnhalter (2002) are a result of the so-called '3D radiative Rayleigh-Taylor instability' in the outflow cavity; in axially symmetric simulations sufficient feeding of the disk should therefore be impossible. But our axially symmetric collapse simulations show a stable radiation pressure driven outflow, while the circumstellar disk gains enough mass from the in-falling envelope to maintain its shielding property over several free fall times, in fact over a longer period ever simulated in previous research studies.

Our three-dimensional core collapse simulations support this accretion disk scenario consistently. Gravitational torques in the self-gravitating disk lead to a sufficiently high angular momentum transport to maintain accretion. The accretion history is stronger episodically compared to the viscous disk evolution in the axially symmetric runs, but adds up to a very similar mean accretion rate.

In the bipolar direction, the radiative feedback yields the launch of a stable radiation pressure driven outflow. No '3D radiative Rayleigh-Taylor instability' is identified yet. Although the three-dimensional simulations are still running, we can certainly conclude from the axially symmetric runs that additional feeding by an unstable outflow is not necessary to allow the formation of massive stars. On the other hand, a well-grounded conclusion on the stability of the outflow and its influence on the formation of massive stars clearly requires further investigation.

Summing up, the central stars in our simulations of the disk accretion scenario grow far beyond the upper mass limit found in the case of spherically symmetric accretion flows. For an initial mass of the pre-stellar host core of 60, 120, 240, and 480 $M_\odot$ the masses of the final stars formed add up to 28.2, 56.5, 92.6, and at least 137.2 $M_\odot$ respectively. Indeed, the final massive stars are the most massive stars ever formed in a multi-dimensional radiation hydrodynamics simulation so far.

References

Kahn, F. D. 1974, A&A, 37, 149
Krumholz, M. R., Klein, R. I., & McKee, C. F. 2007, ApJ, 656, 959
Krumholz, M. R., Klein, R. I., McKee, C. F., Offner, S. S. R., & Cunningham, A. J. 2009, Science, 323, 754
Kuiper, R., Klahr, H., Dullemond, C., Kley, W., & Henning, T. 2010a, A&A, 511, 81
Kuiper, R., Klahr, H., Beuther, H., & Henning, T. 2010b, ApJ, 722, 1556
Larson, R. B. & Starrfield, S. 1971, A&A, 13, 190
Mignone, A., Bodo, G., Massaglia, S., Matsakos, T., Tesileanu, O., Zanni, C., & Ferrari, A. 2007, ApJS, 170, 228
Nakano, T. 1989, ApJ, 345, 464
Shakura, N. I. & Sunyaev, R. A. 1973, A&A, 24, 337
Shu, F. H., Lizano, S., & Adams, F. C. 1987, in: Star forming regions, ed. M. Peimbert, J. Jugaku, 115, 417
Yorke, H. W. & Krügel, E. 1977, A&A, 54, 183
Yorke, H. W. & Sonnhalter, C. 2002, ApJ, 569, 846

Discussion

G. Romero: The outflows you are getting are not well-collimated. Do you expect that the inclusion of magnetic fields in your simulations would help to collimate the outflow producing a jet?
R. Kuiper: Yes, magnetic fields and radiation pressure have different effects on the jet and outflow region.

1. The momentum of the expelled material is $\gg \frac{L}{c}$ and therefore clearly a magnetic effect;
2. Magnetic fields tend to collimate the flow. This explains well collimated jets;
3. Contrary to point (2), radiation pressures broadens the bipolar cavity with time. This explains well the observed broadening of outflows in Massive Star Forming regions.

N. Smith: Just a couple of questions to clarify:

1. Is the radiation pressure exclusively the radiation pressure on dust grains in the envelope?
2. What provides the luminosity in the models - is it the stellar luminosity, accretion luminosity or both (and how important are they with time)?
3. Finally, could you say something about contributions from ionized gas pressure or stellar winds? Do you have plans to include these?

R. Kuiper:

1. As long as the absorption by dust grains dominates the opacity of the stellar environment, yes.
2. Both luminosities are accounted for. The accretion luminosity can be calculated directly from the hydrodynamic flow into the sink cell and the stellar radius. The stellar luminosity and the stellar radius are computed via fits to the pre-calculated stellar evolutionary tracks for accreting high-mass proto-stars by Hosokawa & Omukai (2009). Initially, at the onset of the collapse, the total luminosity is dominated by the accretion luminosity. Finally, the stellar luminosity dominates. The transition between both regimes is very sharp in time, see Hosokawa & Omukai (2009).
3. Massive stars have several feedback mechanisms on their environment. In descending order of their magnitude these are in fact radiation pressure, ionization, and stellar winds. In our studies we have analyzed the dominating effect of the radiation pressure so far. Our future tasks include studies of the other feedback mechanisms as well as an even broader parameter scan of the initial conditions.

N. Kumar: The radiation pressure eating off the disk region is interesting because there are ring-like structures around B stars that can be explained by this mechanism.
On what time scale does a 8-10 $M_\odot$ star disk totally gets eaten away?
R. Kuiper: In the lowest mass simulation (Mcore = 60$M_\odot$) finally a 26 $M_\odot$ star was formed. For an 8-10 M$M_\odot$ star, its radiation pressure is still not a big counterpart to its gravity, e.g. the equilibrium of both forces in the static limit (the generalized Eddington limit) is for a reasonable stellar evolution and dust model roughly given by $M_* \sim 20 M_\odot$. Therefore, a ring like structure with a non-keplerian rotation profile fits better to a large-scale torus such as formed at earlier epochs in the collapse simulations I have shown. To answer the questions at which timescale the forming star begins to push away the remnant disk mass: In our lowest mass simulation (Mcore = 60$M_\odot$) this process ends roughly at 14 free-fall times or 940 kyr (t_{ff} =67.6kyr) respectively. In a higher mass collapse where the massive star evolves faster, this process sets on earlier, see the parameter study of the initial core mass in Kuiper et al. 2010, ApJ 722.

Evidence for disks around young high-mass stars

Rolf Chini[1,2], Vera H. Hoffmeister[1] and Dieter Nürnberger[3]

[1] Astronomical Institute, Ruhr-Universität Bochum, Germany
[2] Facultad de Ciencias, Universidad Católica del Norte, Antofagasta, Chile
[3] European Southern Observatory, Santiago, Chile

Abstract: The formation of high-mass stars remains a poorly understood process despite growing observational evidence in favour of accretion from a circumstellar disk onto a protostellar core. The high fraction of multiple stellar systems among the most massive stars and the fact that these stars are usually born in dense clusters can alternatively be explained by merging of intermediate-mass stars. Here we review some observations that provide direct evidence for large ($\sim 10,000 - 20,000$ AU) disks and/or dusty envelopes seen in emission and absorption around high-mass stars. The objects are all members of the young cluster in M 17 and have been investigated by multicolor photometry and spectroscopy.

1 Introduction

M 17 is a region of active high-mass star formation at a distance of 2.1 kpc. It consists of a luminous H II region, a huge adjacent molecular cloud and an embedded young cluster with an age of about 5×10^5 years (Hoffmeister et al. 2008). About 74% of the investigated cluster members show infrared excess indicating the presence of dense circumstellar material. Spatially resolved images of circumstellar disks and shells have been obtained for a number of high-mass sources, suggesting the accretion scenario to work also in the high-mass regime. The present paper reviews two of the most outstanding high-mass sources with circumstellar dust and introduces a new candidate in M 17. Further similar sources exist in this young region and are subject to ongoing investigations.

2 IRS 15 - a B0.5 V star with an emission disk

Due to the rapid evolution of a new-born massive star and the early sublimation of circumstellar dust in the vicinity of these hot objects it is hard to find a high-mass star which is still surrounded by a remnant disk. Chini et al. (2006) reported on the rare case of such an optically visible star in the southwestern area of M 17, hereafter IRS 15, which is still associated with circumstellar dust.

Imaging from $0.4 - 2.2\,\mu$m shows a point-like object whose optical spectrum resembles type B0.5 V. Beyond 2.2 μm extended circumstellar emission becomes increasingly prominent around this high-mass star (Fig. 1). Eventually, at 10 μm the nebula attains its largest size of $17,400 \times 12,500$ AU. While usually, early embedded B stars are associated with blue reflection nebulae that disappear with increasing wavelengths, IRS 5 shows the opposite behavior, i.e. the extended emission becomes more

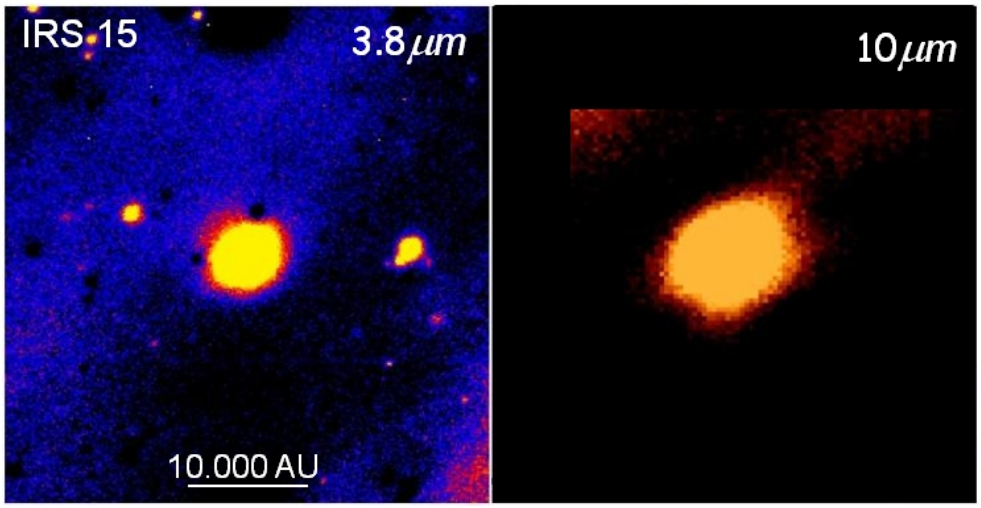

Figure 1: While at shorter wavelengths IRS 15 is point-like and its circumstellar neighborhood is inconspicuous, extended thermal emission of dust dominates at 3.8 and 10 μm; the disk has a total projected size of $17,400 \times 12,500$ AU (lowest 3σ intensity contour at 10 μm) and is seen under an angle of about 53 degrees with respect to the line of sight.

prominent at longer wavelengths. This indicates that the nebulosity is not due to scattering by micron-sized circumstellar dust grains but arises from their thermal emission. The photometric data at 3.8 and 10 μm (Chini et al. 2006), a 20 μm study by Nielbock et al. (2001) as well as the 8 μm data from the Spitzer archive, yield a mean color temperature of 220 K, indicative of warm dust.

The morphology of the dust distribution at 10 μm complies with two extreme cases: an oblate envelope seen edge-on (with a minimal axis ratio of about 2:1) or a flat disk seen under an inclination angle of about 53 degrees with respect to the line of sight. Adopting a disk-like configuration with a scale height ratio of 0.1, an inner radius of 130 AU, an outer radius of 10,000 AU and 0.1 μm-sized silicate dust particles, Chini et al. (2006) could reproduce the observed radial flux profiles at 3.8 and 10 μm fairly well. The dust density distribution displays a flattening in its inner part. Compared to standard accretion disk models a substantial fraction of the inner disk must have been already eroded. This may indicate a similar mass removal process as observed for older disks around lower-mass objects. Another argument in this direction comes from $K-$band spectra where the CO band-heads beyond 2.29 μm - usually arising at the inner disk from hot and dense material - are missing. The model requires a total dust mass of at least $5 \times 10^{-4}\,\mathrm{M}_{\odot}$.

IRS 15 is very likely a star on the main sequence which has stopped accretion. This is corroborated by the absence of typical accretion indicators like emission lines of Hα, Ca II and He I. On the other hand, IRS 15 must be extremely young because the time span during which a massive star can maintain a circumstellar disk that has not yet been completely destroyed by the strong stellar winds must be of the order of a few Myr. In summary, IRS 15 is a fortunate coincidence where the newly-born high-mass star is already optically visible while its circumstellar disk (or envelope) is not yet dispersed and still glowing at infrared wavelengths.

3 A hyper-compact H II region with a dark lane

M 17-UC1 was discovered as a cometary ultra-compact H II region displaying a shell structure with a diameter of 6.9×10^{15} cm. The number of stellar Lyman continuum photons of $\simeq 2 \times 10^{47}\,\mathrm{s}^{-1}$ requires a B0 - B0.5 V star as the ionising source. Meanwhile, M 17-UC1 is regarded as a hyper-compact H II

region (HCHII) with broad ($\geq 35\,\mathrm{km\,s^{-1}}$) radio recombination lines and a rising spectral index between 1.4 and 43 GHz. Numerous infrared studies have proven M 17-UC1 to be a strong source at $10\,\mu$m and beyond. Nielbock et al. (2007) presented deep NIR/MIR high-resolution imaging and spectroscopy as well as radio interferometry to study the morphology of M 17-UC1 with unprecedented detail.

While being extremely weak at short IR wavelengths, M 17-UC1 becomes prominent in the K band and beyond. Nielbock et al. (2007) resolved the source into two K band emission blobs, separated by 0.46" and a position angle of $54°$. A dark lane separates the two K band nebulae (Fig. 2). At L band the source attains a spherical shape with a radius of $\sim 1.0''$ corresponding to 2100 AU. The N band data show a similar – although less resolved – double structure as in the K band with a FWHM of 0.7×0.5; the brightness maximum is centred on the southwestern K band peak (Fig. 2). The total circumstellar emission ($\sim 10,500 \times 6300$ AU) is relatively complex with a noticeable extent to the northwest.

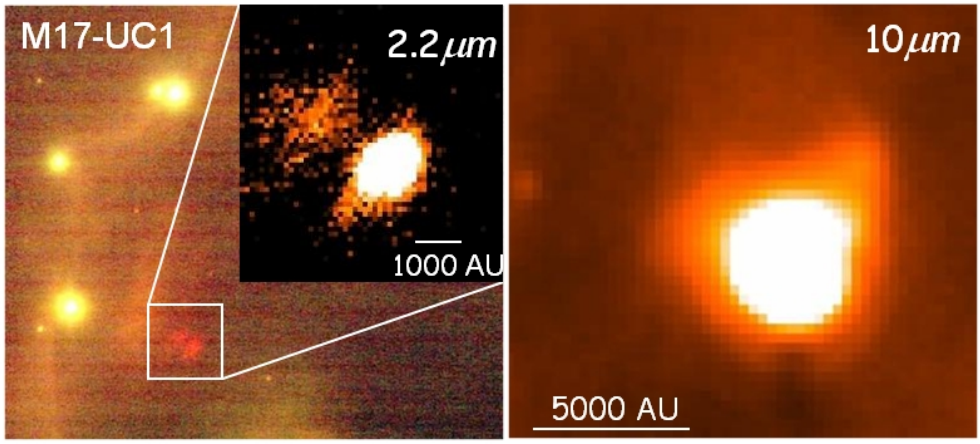

Figure 2: *Left:* Three-color image (*JHK*) of the Arc region in M 17. The inset at $2.2\,\mu$m shows the bipolar emission of M 17-UC1 and the associated absorption lane in between. Its symmetrical triangular shape on both sides resembles a circumstellar disk. *Right:* $10\,\mu$m image of the extended dust emission around M 17-UC1.

The $10\,\mu$m spectrum of M 17-UC1 displays a deep silicate feature indicating the presence of cold dust along the line of sight. The standard relation for converting optical depths of $\tau_V \sim 17{\cdot}\tau_{9.7}$ (Krügel 2003) yields a visual extinction of about 40 mag, consistent with the observed NIR spectral energy distribution of an embedded B0V star. Although the broad-band N image in Fig. 2 also includes the silicate feature, one can only see the warm emitting dust. The cool absorbing dust cannot be spatially resolved at $10\,\mu$m and is most likely located in the dark lane seen at $2.2\,\mu$m.

The absorption pattern of M17-UC1 with the scattered light nebulosities on both sides very much resembles the appearance of a young low-mass star with a circumstellar disk. Radiative transfer calculations can explain the K band image with the triangular absorption much better by a disk than by an unrelated dust filament in the foreground.

HCHIIs are very likely a transition state where the massive star has started to ionise its surroundings while the accretion process is still going on. From the results presented by Nielbock et al. (2007) it seems that a circumstellar disk can still be present during the HCHII stage and that M17-UC1 is the first example where such a disk could be directly observed.

4 IRS 5 – evidence for merging?

About 5.2" southwest of M 17-UC1 Chini & Wargau (1998) found an infrared source – hereafter IRS 5 – with a strong IR excess at wavelengths beyond 2.2 μm. It was subsequently imaged at *K, N, Q* (Nielbock et al. 2001) who presented a typical Class I SED from 1.2 to 20 μm with spectral indices of $\alpha_{K,N} = 2.5$ and $\alpha_{K,Q} = 2.4$. Kassis et al. (2002) obtained maps at 9.8, 10.53, 11.7 and 20.6 μm and performed radiative transfer code models that describe IRS 5 as a zero-age main-sequence (ZAMS) B0 type surrounded by a shell of 70 $M_\odot$ with an outer radius of 1 pc. Here we present deep NIR and MIR images which resolve M17-IRS 5 into several components. K and N-band spectroscopy helps to classify the stellar sources and probe the circumstellar environment.

Our NIR images resolve IRS 5 into six apparently stellar components (Fig. 3). From their location in the *JHK* color-color diagram at least three of them are heavily reddened and have IR excesses of various strengths. The brightest star (component *A*) has a visual extinction of 27 mag and displays X-ray emission. There is a fainter object *B* 0.9" west of component *A* with an extinction of 34 mag and a strong IR excess. An extremely red (component *C*) object with $K - L \sim 5$ is located 2.0" southwest of the main component; it is the only point source in the region that also shows up at 10 μm. Its visual extinction is about 34 mag – similar to that of component – *B* and it coincides with the H_2O maser No. 4 reported by Johnson (1998). The projected separations of this triple system are 2200 AU between components *A* and *B* and 4400 AU between *A* and *C*. Given that the visual extinction is fairly similar for all three stars we speculate that IRS 5 is a bound triple system of young objects.

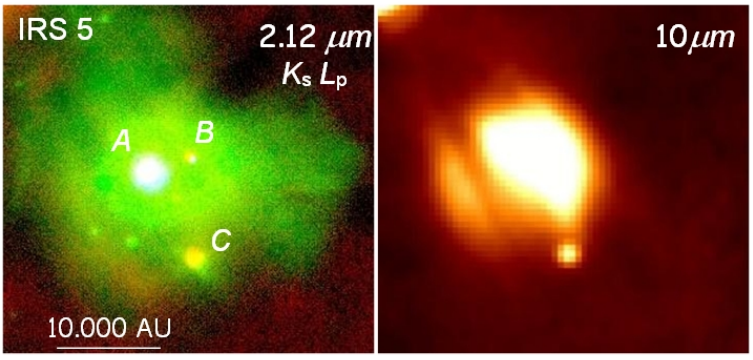

Figure 3: *Left:* Three-color image (NB 2.12 μm, *K*s, *L*p) of the IRS 5 region. The strong point source labeled "*C*" southwest of IRS 5 coincides with an H_2O maser. *Right:* 10 μm image of the extended dust emission around IRS 5; a faint dust lane (disk?) is visible in absorption.

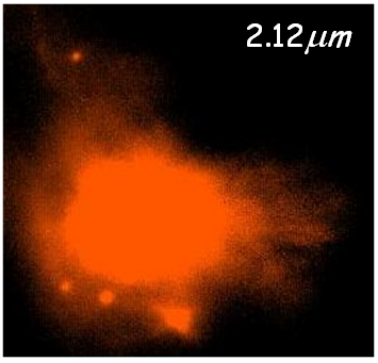

Figure 4: The H_2 emission around IRS 5 displays several filaments of shocked gas pointing away from the star.

Our K-band spectrum of IRS 5 A shows Brγ at 2.166 μm and He II at 2.188 μm in absorption. The absence of He I 2.112 μm suggests that the object is hot and probably equivalent to an O6.5 star.

As already indicated by earlier photometric data (Nielbock et al. 2001, Kassis et al. 2002) our MIR spectrum for component *A* displays silicate absorption at 9.7 μm. Converting the optical depth at 9.7 μm into a visual extinction yields $A_V \sim 30$ mag which is consistent with the NIR photometry above and with estimates from the X-ray emission (Broos et al. 2007). Obviously, there must be cool dust in front of the extended 9.7 μm dust emission seen in Fig. 3. This absorbing dust is indeed visible at L and N as a dark lane which is reminiscent of a circumstellar disk.

Bally & Zinnecker (2005) have made some qualitative predictions of how merging of intermediate stars may lead to the formation of a high-mass star. In the following, some of their statements are compared with the properties of IRS 5:

1. "*Protostellar mergers may produce high-luminosity IR flares lasting years ...*" – The $2.2\,\mu$m flux of IRS 5 has risen by a factor of 40 from $1993 - 1995$ and seems to fade slowly since then.

2. "*Mergers may be surrounded by thick tori of expanding debris, impulsive wide-angle outflows, and shock-induced maser and radio continuum emission.*" – Figs. 3 and 4 display several of these features including maser emission at the position of component *C*.

3. "*Collision products are expected to have fast stellar rotation and a large multiplicity fraction.*" – IRS 5 consists of several components of which at least four are sufficiently deeply embedded to form a young multiple system.

4. "*Massive stars growing by a series of mergers may produce eruptive outflows with random orientations; ... observable as filaments of dense gas and dust pointing away from the star.*" – Fig. 4 shows several "fingers" of shocked H_2 gas emerging from IRS 5.

Although one can argue that the observed properties of IRS 5 comply with the accretion scenario one may speculate whether it is a suitable candidate to study the merging scenario for high-mass stars.

5 Conclusions

In summary, M 17 is an ideal test bed to study the early evolution of high-mass stars. The examples in the present paper show three early evolutionary stages where a massive star is associated with circumstellar dust: i) The youngest object is M 17-UC1, a hypercompact H II region, which is probably still in the process of accretion. ii) An intermediate source, IRS 5, which is a heavily embedded O-star candidate with a disk and a maser source. iii) And the latest stage IRS 15, a B0.5 main sequence star that is still surrounded by a remnant disk. M 17 harbours a number of additional candidates where dust emission is associated with massive stars; these object are currently under investigation and seem to support the accretion scenario further.

Acknowledgements

This publication is supported as a project of the Nordrhein-Westfälische Akademie der Wissenschaften und der Künste in the framework of the academy program by the FRG and Nordrhein-Westfalen.

References

Bally J., Zinnecker H., 2005, AJ, 129, 2281
Broos P.S., Feigelson E.D., Townsley L.K., Getman K.V., Wang J., Garmire G.P., Jiang Z., Tsuboi Y., 2007, ApJS, 169, 353
Chini R., Wargau W.F., 1998, A&A, 329, 161
Chini R., Hoffmeister V.H., Nielbock M., Scheyda C.M., Steinacker J., Siebenmorgen R., Nürnberger D., 2006, ApJ, 645, L61
Hoffmeister V.H., Chini R., Scheyda C.M., Schulze D., Watermann R., Nürnberger D., Vogt N., 2008, ApJ, 686, 310
Johnson C.O., De Pree C.G., Goss W.M., 1998, ApJ, 500, 302
Kassis M., Deutsch L.K., Campbell M.F., Hora, J.L.; Fazio G.G., Hoffmann W.F., 2002, AJ, 124, 1636
Krügel, E. 2003, The Physics of Interstellar Dust, Series in Astronomy and Astrophysics (Bristol, UK: Institute of Physics Publishing)
Nielbock M., Chini R., Jütte M., Manthey E., 2001, A&A, 640, 382
Nielbock M., Chini R., Hoffmeister V.H., Scheyda C.M., Steinacker J., Nürnberger D., Siebenmorgen R., 2007, ApJ, 656, L81

Discussion

N. Smith: First a comment regarding these late O-type or early B-type stars which you interpreted as possible distorted disks. We found a number of similar sources in the Carina Nebula, and our analysis suggests that they are stand-off shocks between the stellar wind of the late O or early B star and a bulk flow of plasma in the H II region (see Smith et al. 2010). Also, Povich et al. found a few of these in M 17, but I'm not sure if they are the same sources you have discussed.
Also a question: regarding your potential massive merger source (I think IRS 5), which brightened by a factor of 40 over 2 years. Why do you think this is not a FU Ori outburst?
R. Chini: I agree that we cannot interpret them as remnant disks. What I wanted to show is that there exists dust close to late type O-stars. We don't find them with B-stars. I also agree that they are a result of the winds from the major ionizing sources in the center of M 17, because these rims are all pointing toward the central O4 Trapezium.
I would love to find a new FU Ori in its outburst. However, our IR spectra (with absorption lines of He and H) point toward an early type star.

H. Zinnecker: [The comment is that I did not bribe the speaker to find evidence for the Bally $\&$ Zinnecker (2005) merger scenario!]
Now the question, where did you get your O-star spectral-type vs. stellar mass calibration from? It seems to me that your mass estimates for a given spectral type are systematically too high (e.g. an O9 V star is closer to 20 $M_\odot$ than the 30 $M_\odot$ you quoted).
R. Chini: [I confirm that there was no contact before the talk between Hans and me about this paper.] I agree that the mass quotes are higher than what are published by e.g. Martins et al. (2005). However, I think that the uncertainties in this field are still much larger than the differences we are talking about here. I just learned from C. Hummel that they obtained a dynamical mass of about 27 $M_\odot$ for an O9.7 star which is close to the values we use.
J. Puls: I agree with Hans Zinnecker, that the typical masses of O9 dwarves should be below 20 $M_\odot$, and that the different calibrations should be fairly consistent.

N. Evans: The wide companions you discuss (~ 10000 AU) are very interesting. I would draw your attention to our recent Chandra observation of Polaris. X-ray observations are a very powerful way to identify low mass stars young enough to be massive stars' companions.
R. Chini: In fact, the young cluster in M 17 contains more than 800 Chandra sources. We use this information for disentangling cluster members from background stars. Interestingly, we find many X-ray sources to be associated with O- and B-type stars. Spectroscopy shows that these early-type X-ray sources are often close binaries. By the way, IRS 5 - the last source I was talking about - is coincident with ACIS 309 (Broos et al. 2007).

Multiple stellar generations in massive star forming complexes

J. S. Clark[1], B. Davies[2] and M. A. Thompson[3]

[1] Dept. Physics & Astronomy, Open University, Milton Keynes, UK
[2] School of Physics & Astronomy, University of Leeds, Leeds, UK
[3] Centre for Astrophysics Research, University of Hertfordshire, Hatfield, UK

Abstract: The formation of massive stars is an outstanding problem in stellar evolution. However, it is expected that they are (predominantly) born in hierarchical environments within massive young clusters, which in turn are located within larger star forming complexes that reflect the underlying structure of the natal molecular cloud. Initial observations of such regions suggest that multiple generations of stars and proto-stars are present, necessitating a multiwavelength approach to yield a full (proto-)stellar census; in this contribution we provide an overview of just such an observational approach for Galactic examples, focusing on the G305 complex.

1 Introduction

Imaging of external galaxies reveals that stellar formation yields large star cluster complexes of 10s-100s of parsec in size, and $>> 10^4 M_\odot$ in integrated mass. These are luminous across the electromagnetic spectrum; with emission at radio wavelengths from ionised gas, far-IR & submm from cold molecular material, IR from heated dust, optical-UV from the stellar population and X-rays from both pre-MS and massive stars. Therefore a multiwavelength approach is required to understand the ecology of such regions - and hence infer masses for unresolved regions from their integrated spectral energy distributions (SEDs) - as well as the evolution of massive ($>40 M_\odot$) stars from cold molecular cores through to the Main Sequence. The latter goal is particularly important, since our knowledge of this process suffers from few current observational contraints and yet very massive stars play an inordinate role in the excitation of their environment via their UV radiation field and wind energy. Consequently, in order to address these interelated issues we are undertaking such a study of several Galactic star forming regions, of which the G305 complex is of particular interest given current estimates for its stellar content (Clark & Porter 2004). In this contribution we briefly review the observational dataset acquired for it as a result of this program and highlight some initial results arising from it.

2 The G305 star forming complex

Located in the Scutum Crux arm at a distance of $\sim$4 kpc the G305 star forming complex appears to be one of the most massive such regions in the Galaxy, with the radio luminosity alone suggesting

the presence of >30 canonical O7 V stars (Clark & Porter 2004). Morphologically, it appears as a tri-lobed wind blown bubble with a maximal extent of ∼30 pc centred on the Young Massive Clusters Danks 1 & 2 (Fig. 1). Vigorous ongoing star formation is present on the periphery of the region as evidenced by significant IR-radio emission and the presence of numerous masers (Sect. 2.2).

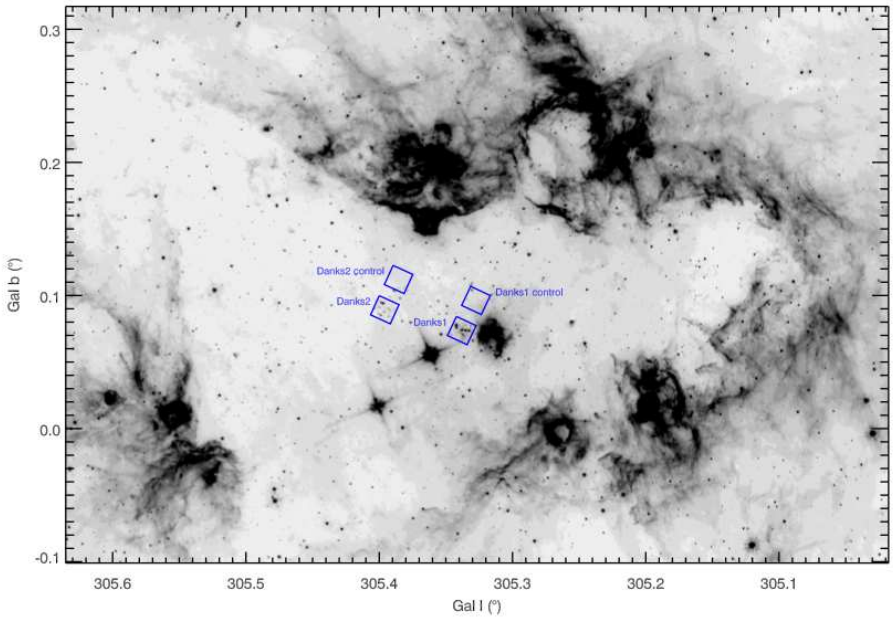

Figure 1: 5.8μm image of the G305 complex with the HST target fields for Danks 1 & 2 indicated.

2.1 The recent star formation history of G305

The location of ongoing star formation within the complex is indicative of triggered, sequential activity initiated by Danks 1 & 2. The presence of at least one Wolf-Rayet - the WC star WR48a - suggests that star formation must have been underway for at least ∼2.5 Myr while, following the arguments presented in Clark et al. (2009) for W51, the lack of a population of RSGs suggests an upper limit to the duration of the 'starburst' of ≤10 Myr. In order to more fully constrain the properties of Danks 1 & 2 and hence to determine whether they could have triggered the subsequent generations of star formation, we have undertaken near-IR imaging & spectroscopic observations of them with the HST & VLT/ISAAC and present a subset of the data focusing on Danks 1 in Figs. 2 & 3.

A full analysis of these data will be provided in Davies et al. (in prep.) but we highlight that both clusters appear to have integrated masses $>>10^3 M_\odot$. Surprisingly, given their apparent proximity (a *projected* separation of ∼3.5 pc) there appears to be a notable age difference (∼2-3 Myr) between them, evident in both the spectral types of cluster members and the location of the Main Sequence turn on. Focusing on Danks 1, we identify a number of emission line objects with spectra consistent with O Iafpe/WN7-9h stars; the cluster being reminiscent of the Arches in the Galactic Centre. The presence of such stars is of interest since they are expected to be massive core-H burning objects in which very high mass loss rates cause them to present a more evolved spectral type. Combined with their prodigious UV-fluxes, they are likely to be significant sources of feedback and detailed non-LTE model atmosphere analyses of these objects is currently underway in order to quantify this. In contrast such stars are absent in Danks 2, with the presence of a WC star and O supergiants of a later spectral type indicating an older spectral population.

However, massive (post-)MS objects are not restricted to these clusters. As well as the dusty WC star WR48a, recent IR observations have located a further 3 WC and 1 WN stars within the wind

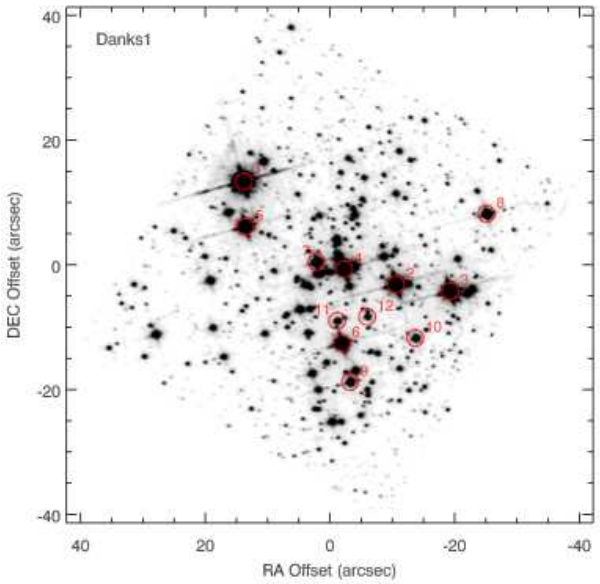

Figure 2: F160W mosaic of Danks 1

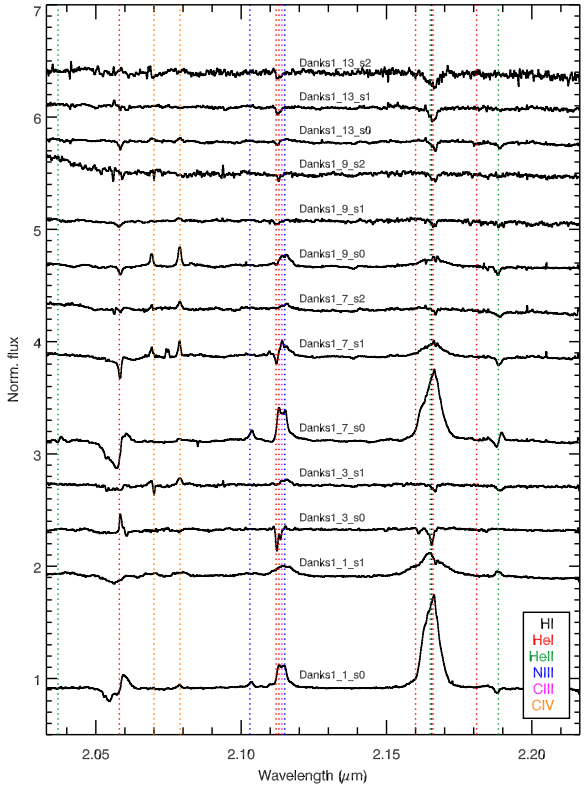

Figure 3: K band spectra of massive stars within Danks 1 (Davies et al. in prep.).

blown bubble (Shara et al. 2009, Mauerhan, van Dyk & Morris 2009), suggesting that an additional dispersed population is present within the complex, although their origin - e.g. ejected from a cluster or formed *in situ* - is uncertain. In this regard it closely resembles 30 Dor, which Walborn & Blades (1997) showed hosts a young central cluster and a diffuse, older population distributed across the wind blown cavity with an additional (pre-MS) component located on the periphery. Massive stars also appear present on the perimeter of G305, with Leistra et al. (2005) showing that the young cluster found within the cavity G305.254+0.204 contains at least one early O star. Moreover, early OB pre-MS stars are also found in the bubble PMN1308-6215 to the NW of the complex; the spectrum presented in Fig. 4 being dominated by H I line and CO bandhead emission, indicative of a hot ionising source surrounded by a cool accretion disc/torus, respectively. A full presentation and analysis of these and other data on the pre-MS population of G305 will be provided in Clark et al. (in prep.).

2.2 Earlier phases of (triggered) star formation

We next turn to the more deeply embedded massive protostars and the reservoir of cold molecular material. The former may be identified with ultracompact H II regions, very bright mid-far IR sources and H_2O & methanol maser emission, while the latter may be mapped via molecular tracers such as NH_3 or sub-mm continuum emission from cold ($\leq$50K) dust. Hill et al. (2006) presented a survey of cold dust for select regions within G305, finding a total of $\sim$23000 $M_\odot$ material located in clumps with masses up to $\sim$4500 $M_\odot$, although it is expected that these will comprise lower mass subclumps at higher spatial resolution. Recently, Hindson et al. (2010) undertook a molecular survey of the whole complex which revealed a total reservoir of cold gas of $\sim 6 \times 10^5 M_\odot$ (Fig. 5); even allowing for a relatively low star formation efficiency ($< 10\%$) this is sufficient to yield a substantial stellar

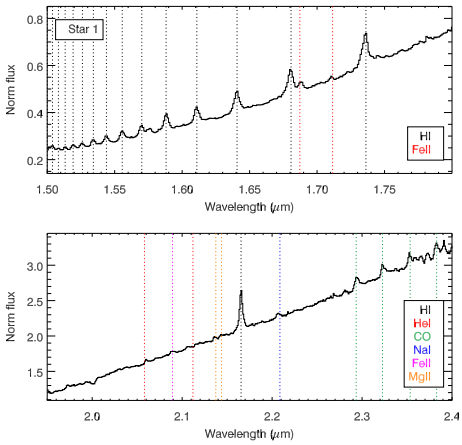

Figure 4: H and K band spectra of a pre-MS OB star in the star forming bubble PMN 1308-6215 to the NW of the complex proper.

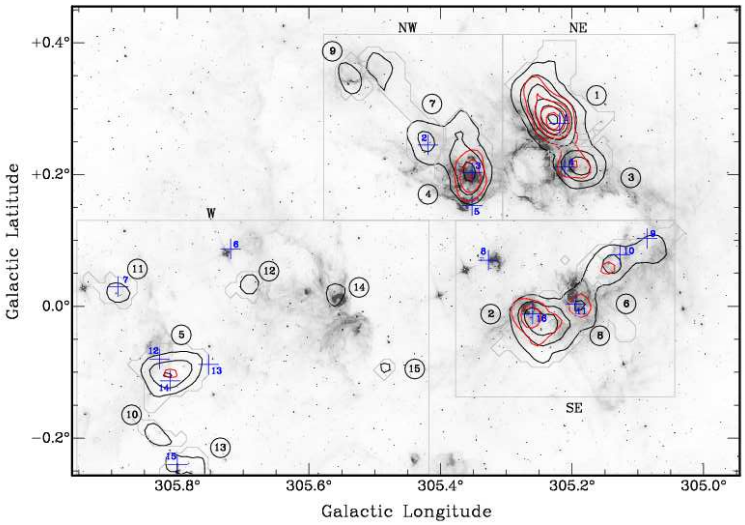

Figure 5: Overplot of NH_3 contours on a 5.4μm greyscale image. H_2O masers are indicated by crosses (Hindson et al. 2010).

population. In order to provide a higher resolution map of this material and to determine its properties such as clump mass function and temperature, we have obtained both APEX/LABOCA and Herschel far-IR - submm observations. A preliminary reduction of the 870μm LABOCA data is provided in Fig. 6, which shows the 'skeleton' of cold molecular material material upon which current star formation is occuring (see Clark et al. in prep. & Thompson et al. in prep. for a full analysis).

Finally, SEDs constructed from the full near-IR to sub-mm datasets allow the identification of Massive Young Stellar Objects (MYSOs) via their characteristic colours (e.g. Hoare et al. 2005), as well as a determination of their integrated bolometric luminosities. We show the location of such MYSOs in a subfield of G305 in Fig. 7 (as well as H_2O and methanol masers; Hindson et al. 2010). Clearly significant star formation that will result in a new population of massive stars is currently underway, and appears to be located on the surface of the molecular cloud adjacent to the nearby stellar cluster, suggesting that it has been triggered by the action of the OB stars contained within.

3 Concluding remarks

A multiwavelength approach to the study of star forming complexes allows us to locate the different stellar populations within these regions and hence determine the propagation (or otherwise) of star formation through the host GMC. Model atmosphere analysis of the massive stellar population constrains the feedback from such stars as well as helping date the onset of star formation via comparison to theoretical evolutionary tracks. Full analysis of the near-far IR SEDs of embedded sources yields their bolometric luminosity and hence an estimate of mass, while the far-IR - sub-mm SED will play a similar role for cold molecular cores - the first stage of massive star formation. Finally a synthesis of these data will provide a complete census of star formation within the cluster complex, an estimate of the efficiency of this process and - via comparison of the mass functions of the differing populations - constraints on the physics governing GMC fragmentation and subsequent cluster/star formation.

References

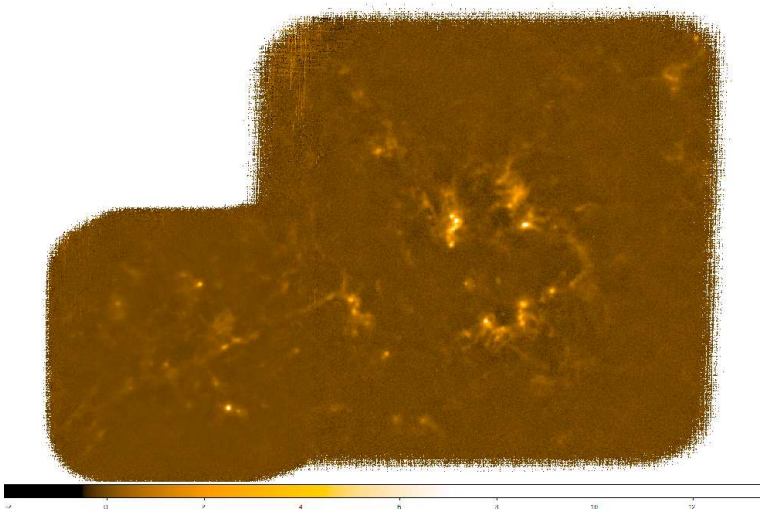

Figure 6: Preliminary reduction of APEX/Laboca 870μm continuum observations of the G305 complex.

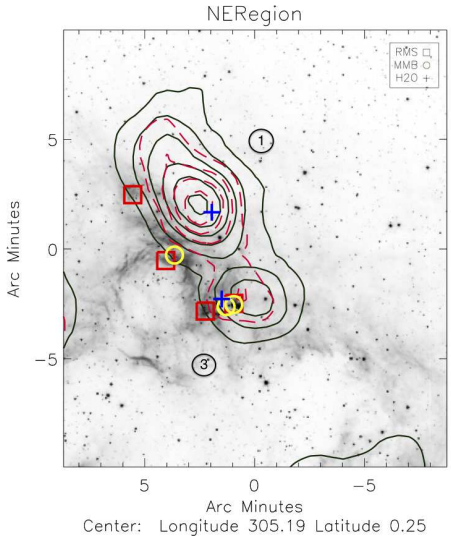

Figure 7: Blow up of the NE region of the complex from Fig. 5. Crosses and contours have the same meaning while squares represent MYSOs and circles methanol masers (Hindson et al. 2010).

Clark J., Porter, J., 2004, A&A, 427, 839
Clark J., Davies B., Najarro F., et al., 2009, A&A, 504, 429
Hill T., Thompson, M., Burton M., et al. 2006, MNRAS, 368, 1223
Hindson L., Thompson M., Urquhart, J., Clark, J., Davies B., 2010, MNRAS, 408, 1438
Hoare M., Lumsden S., Oudmaijer R., et al., 2005, IAUS 227, 370
Leistra, A., Cotera A., Liebert J., Burton M., 2005, AJ, 130, 1719
Mauerhan J., van Dyk S., Morris P., 2009, PASP, 121, 591
Shara M., Moffat A., Gerke J., et al., 2009, AJ, 138, 402
Walborn N., Blades C., 1997, ApJS, 112, 457

Discussion

L. Oskinova: When you estimate the ages of stellar population, do you use the evolutionary tracks for single stars only, or do you also account for binarity and e.g. rotation?
J.S. Clark: We used three different methods to estimate the age of the clusters: (i) fitting the MS turnoffs with both rotating and non-rotating Geneva isochrones, (ii) fitting the MS turnon with Schaller isochrones and (iii) a comparison of the (post-MS) stellar contents to other massive clusters with well defined ages. Neither of the first two methods accounted for binarity, but this will implicitly be addressed by method (iii) assuming a universal binary fraction.

M. Corcoran: Are there any X-ray observations with Chandra, and if so what do they show? Is there any evidence of diffuse emission?
J.S. Clark: X-ray observations have been made and are currently being analysed by Marc Gagné.

D. Bomans: A triggered SF claim is maybe too optimistic, yet, since you do not have an expansion velocity of the gas shell, therefore no proven causal connection of clusters, shell and young SF sites.
J.S. Clark: Forthcoming radio observations should provide an expansion velocity for the gas in the

region. However the location of various star formation diagnostics on the inner face of the wind evacuated cavity is certainly suggestive of triggered activity.

N. Smith: You mentioned possible evidence for triggered star formation at the edges of these regions (UCH II regions, protostars, etc). If you look nearby - i.e. interior to the edges of shells or outside - do you see evidence for recent star formation in the form of somewhat older YSOs (class II / T Tauri stars, etc)?
J.S. Clark: We are currently examining our data for this - and in particular are waiting for a new deep JHK imaging dataset from the VISTA/VVV survey to accomplish this (which will be significantly deeper than current 2MASS data).

Physical Properties and Evolutionary Stages of Massive Young Stellar Objects in the Large Magellanic Cloud

C.-H. Rosie Chen[1], Remy Indebetouw[1,2], Jonathan P. Seale[3], Leslie W. Looney[3], You-Hua Chu[3], Robert A. Gruendl[3] and Barbara A. Whitney[4]

[1] University of Virginia, Charlottesville, Virginia, U.S.A.
[2] National Radio Astronomical Observatory, Charlottesville, Virginia, U.S.A.
[3] University of Illinois, Urbana, Illinois, U.S.A.
[4] Space Science Institute, Boulder, Colorado, U.S.A.

Abstract: Massive stars drive the evolution of galactic interstellar media, yet their formation remains poorly understood. We use *Spitzer* Infrared Spectrometer (IRS) observations of 277 massive young stellar objects (YSOs) in the Large Magellanic Cloud (LMC) and combine them with multi-wavelength photometry from U to 70 μm to construct and model their spectral energy distribution (SED) and to deduce their mass and evolutionary stage. We also examine the immediate interstellar and stellar environment using high-resolution optical and near-IR images to assess the origin of dust emission and multiplicity of sources. Some of these YSOs are spatially coincident with known masers and ultracompact H II regions that can be used as an independent check on the feasibility of SED fits. Comparisons among YSOs' physical properties, immediate stellar and interstellar environment, and mid-IR spectral features are used to discuss evolution of massive YSOs in the LMC.

1 Introduction

Despite the fact that massive stars are one of the main energy sources of the interstellar medium (ISM) and hence play a key role in the evolution of their host galaxies, the processes of their formation remain not well understood. It has been challenging to observationally study these processes due to large distances, high extinction, and short timescales of critical evolutionary phases (e.g., Zinnecker & Yorke 2007). It is also difficult to model theoretically as the collapse timescale is so short that a massive star begins to produce high radiation pressure when it is still accreting, making accretion onto a star with mass $\geq 40 M_{\odot}$ difficult. Thus an alternate scenario such as mergers of lower-mass ones (Bonnell et al. 1997) or pressure release via outflow cavities (Krumholz et al. 2009) may be required.

High sensitivity *Spitzer* mid-IR observations make it possible for large surveys of massive YSOs to provide observational constraints such as relative timescales of evolutionary phases. This requires a well-defined classification system that can reflect the evolution of massive YSOs. The LMC, due to its proximity (50 kpc) and nearly face-on orientation, is an excellent laboratory as YSOs are at known, common distances and can be resolved. Its low metallicity (1/3 $Z_{\odot}$) also provides a chance to

investigate how that affects star formation. A large sample of massive YSOs has been detected in the LMC (Whitney et al. 2008; Gruendl & Chu 2009). Classifying these YSOs needs extra care as they can be multiples or small clusters unresolved by *Spitzer*'s 2″-resolution, i.e., 0.5 pc in the LMC. As demonstrated in our previous studies, the common method of comparing observed SEDs to predictions from single YSO models is a good approximation for YSOs that appear single or are dominant sources within the *Spitzer* resolution, but not for otherwise cases (Chen et al. 2009, 2010). We have then developed an empirical scheme using combined diagnoses of SEDs and immediate interstellar environment. Meanwhile, mid-IR spectral features are used to classify YSOs with *Spitzer* IRS observations (Seale et al. 2009). Each of these three schemes has its own perspectives in classifying YSOs. We thus use our large IRS sample to carry out a systematic study to examine how these classifications compare to one another and how they are linked to the evolutionary sequence of YSOs.

2 Data Reduction and Analysis

We use *Spitzer* IRS observations of 277 massive YSOs in the LMC, by far the largest mid-IR spectroscopic sample of confirmed extragalactic YSOs (Seale et al. 2009), to study their physical properties and evolutionary stages. To construct SEDs of these YSOs, we have used the IR catalog from Gruendl & Chu (2009), expanded it to include MCPS and IRSF catalogs in the optical and near-IR wavelengths (Zaritsky et al. 2004; Kato et al. 2007), and combined these photometric data with corresponding IRS spectra (Seale et al. 2009). To incorporate IRS spectra in the SED fitter (Robitaille et al. 2007), we extracted 11 data points at carefully selected wavelengths to delineate silicate feature and the underlying continuum (Chen et al. 2011, in prep.). Fig. 1 demonstrated that the model fits are better constrained with the SED composed of both photometric data and IRS spectrum than that of only photometric data. The inferred physical properties such as masses and evolutionary stages thus have smaller uncertainties for a critical examination. Each YSO is classified with three schemes summarized below.

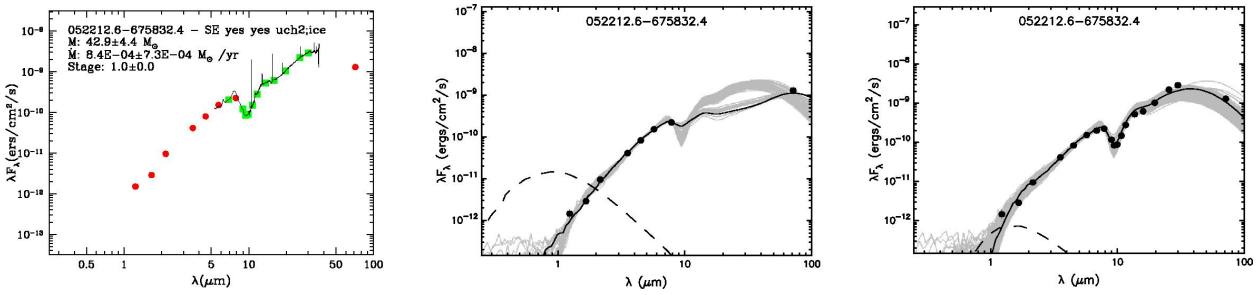

Figure 1: Left: An example of a YSO's SED with combined data of broadband photometry (red dots) and IRS spectra (solid lines). Data points extracted from the IRS spectrum for model fits are marked in green dots. Middle: Model fits (solid and gray lines) to the example YSO whose SED is composed of only photometric data (black dots). Right: Models fits (solid and gray lines) to the same YSO whose SED is composed of data points from both photometry and IRS data points (black dots). It is evident that the fits are better constrained with data points around the 10-μm silicate absorption.

Stage I/II/III – quantitative scheme using predictions from radiative transfer codes with dust distribution analogous to Class I/II/III (Robitaille et al. 2006). Classification is based on inferred envelope accretion rate ($\dot{M}_{\rm env}$) and disk mass ($M_{\rm disk}$) normalized to stellar mass ($M_\star$). Stage I YSOs have significant infalling envelopes and possibly disks and thus $\dot{M}_{\rm env}/M_\star > 10^{-6}$/yr. Stage II YSOs have optically thick disks and possibly remnant envelopes and thus $\dot{M}_{\rm env}/M_\star < 10^{-6}$/yr and $M_{\rm disk}/M_\star > 10^{-6}$. Stage III have optically thin disks and thus $\dot{M}_{\rm env}/M_\star < 10^{-6}$/yr and

$M_{\rm disk}/M_\star < 10^{-6}$. The scheme is physical but the applicability depends on geometry of dust distribution and relation between the observable envelope mass and $\dot{M}_{\rm env}$.

Type I/II/III – empirical scheme using SEDs and interstellar environments (Chen et al. 2009). Type I YSOs have SED with a steep rise from the near-IR to 24 μm as the radiation is mostly from their circumstellar envelopes; they are generally not visible at optical or J band, but visible in the K band and bright at 24–70 μm. Type II YSOs have SEDs with a low peak in the optical and a high peak at 8–24 μm corresponding to the stellar core and the circumstellar disk, respectively, after the envelope has dissipated; they are faint in the optical, but bright in the J band to 8 μm, and then faint again at the 24 μm. Type III YSOs have SEDs peaking in the optical with modest amounts of dust emission in the near- to mid-IR as they are largely exposed but still possess remnant circumstellar material; their brightness fades in the longer wavelength and they are often surrounded by H II regions.

Type S/SE/P/PE/E/F – empirical scheme using mid-IR spectral features: S – 10 μm silicate absorption, P – 5-10 and 10-13 μm polycyclic aromatic hydrocarbon (PAH) emission, and E – 10-20 μm ion fine-structure lines (Seale et al. 2009). YSOs are classified by their major spectral features into six groups: S, SE, P, PE, E, and F. S and SE groups have strong silicate absorption, indicating that they are highly embedded sources and most likely at earliest evolutionary stage. P, PE, and E groups have spectra dominated by UV-emitting central objects and are thus likely at later evolutionary stages. For YSOs in this sample, we adopted the classification results from Seale et al. (2009).

3 Toward a Consistent Evolutionary Picture of Massive YSOs

3.1 Physical Properties of YSOs vs. Formation of Ultracompact H II Regions

Massive stars inject energy into the surroundings even during their formation. They can ionize the circumstellar gas to form small, dense H II regions such as ultracompact H II regions (UCHIIs). Among the 277 YSOs in the sample, 20 are spatially coincident with UCHIIs identified by compact radio continuum sources (Indebetouw et al. 2004). The link between YSOs and UCHIIs allows us to compare the YSOs' evolutionary stages inferred from SED models to the circumstellar conditions required to form UCHIIs, providing an independent check for the feasibility of SED models.

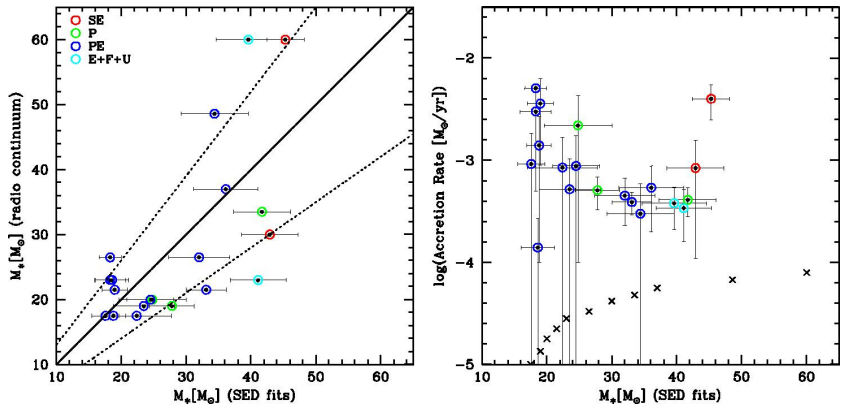

Figure 2: Left: Comparisons between masses inferred from SED fits and radio continuum (Indebetouw et al. 2004) for 20 YSOs that are counterparts of UCHIIs. Error bars from SED fits are marked. IRS spectral types of these YSOs are marked with additional circles in different colors (see legends). Masses estimated from these two methods are generally in good agreement within 30%, as indicated with dotted lines. Right: $\dot{M}_{\rm env}$ vs. $M_\star$ of YSOs inferred from SED fits (circles and error bars) compared to $\dot{M}_{\rm crit}$ of stars expected for certain masses (crosses; Churchwell 2002).

Masses of these 20 sources can be determined independently for YSOs and UCHIIs, providing a consistency check. For YSOs, masses are inferred from model fits to their SEDs. For UCHIIs, assuming the relationship for main-sequence stars, masses can be translated from spectral types implied by the ionizing fluxes determined from radio continuum emission. Fig. 2 shows that except a few outliers, agreement exists between masses estimated using these two methods within 30%. The discrepancies in outliers with masses $\geq 50 M_{\odot}$ from radio continuum are artificial since the upper mass limit in pre-calculated YSO models is 50 $M_{\odot}$. The discrepancies in the opposite cases likely indicate a non-negligible leakage of ionizing fluxes in UCHIIs.

The development of a UCHII depends not only on the ionizing flux provided by the central star, but also on the opacity of the circumstellar material. For infalling rates higher than some critical values, $\dot{M}_{\rm crit}$, the circumstellar medium will have such opacity that the ionized region will be too small and optically too thick to be detectable (Churchwell 2002). Fig. 2 shows that 70% (14 of 20) of the YSOs have inferred $\dot{M}_{\rm env} \gg \dot{M}_{\rm crit}$, similar to what was found in a smaller sample from our previous studies (Chen et al. 2009, 2010). Two possible causes have been suggested. One is that most of the infalling envelope material is used in forming an accretion disk as modeled by Yorke & Sonnhalter (2002), and the ionization radiation escapes in the polar directions. The other is that at the LMC distance, it is difficult to distinguish bound, circumstellar dust from the more distant but still heated interstellar dust. Several UCHIIs are Type III YSOs that have formed small H II regions visible in Hα images. Thus, their high $\dot{M}_{\rm env}$ mostly suggests that they still have abundant dust/gas in the surroundings. Lastly, compared to YSOs' IR spectral types, UCHIIs are found in all but the most embedded S-type, suggesting that they can form at very early stage and possibly accrete via hypercompact H II regions (Keto & Wood 2006). Confirmation would need higher resolution cm data and near-IR spectra.

3.2 Evolutionary Stages of Massive YSOs

The results of SED fits to YSOs are shown in Fig. 3. These YSOs are massive with $M_{\star}$ = 8–45$M_{\odot}$, and $\sim 90\%$ of them are Stage I sources with $\dot{M}_{\rm env}/M_{\star} \sim 10^{-6}$–$10^{-3}$/yr. These high $\dot{M}_{\rm env}/M_{\star}$ qualifies them as Stage I. However, as $> 50\%$ of them show optical counterparts or small H II regions, i.e., Types II or III YSOs using our empirical scheme, the inferred $\dot{M}_{\rm env}/M_{\star}$ appears more indicative of abundant dust than true accretion rates. Nonetheless, some of the Type I YSOs with high $\dot{M}_{\rm env}/M_{\star}$ are likely to be actively accreting. The highest $\dot{M}_{\rm env}/M_{\star} \sim 10^{-3}$/yr are found in YSOs with 10–20$M_{\odot}$ but not higher masses, suggesting that some of them might be younger counterparts in the process of accreting onto more massive ones. However the true accretion rates are yet to be estimated from independent methods such as outflow strengths. On the other hand, as aforementioned that $\sim 60\%$ of the YSOs are multiples, $\dot{M}_{\rm env}/M_{\star}$ for such sources are more relevant to accretion onto a compact (size < 0.5 pc) cluster. The high $\dot{M}_{\rm env}/M_{\star}$ is consistent with the accretion rate $\sim 10^{-3} M_{\odot}$/yr in models of cluster formation (Tan & McKee 2002). This small cluster mode of forming massive stars appears to be prevalent in both the Galaxy and the LMC, despite their metallicity difference.

Comparisons of IR spectral types to other classifications show that YSOs of S/SE-type or with ice absorption feature all have $\dot{M}_{\rm env}/M_{\star} \geq 10^{-5} M_{\odot}$/yr, qualitatively consistent with what is expected for massive, dense envelopes from which these spectral features arise. YSOs of P/PE-type have $\dot{M}_{\rm env}/M_{\star} \sim 10^{-6} - 10^{-3}$/yr, however, as more than half of them are Types II and III YSOs, the high $\dot{M}_{\rm env}/M_{\star}$ in some cases may have been raised due to inclusion of dust emission from H II regions. Examining IR spectral types of known masers and UCHIIs shows that only small fractions, i.e., 13% (=1/8) in masers and 15% (=3/20) in UCHIIs respectively, are embedded YSOs of SE-type or with ice absorption, while most of them are more evolved YSOs of P/PE-types. Masers and UCHIIs in the LMC appear to preferentially develop at later evolutionary stages.

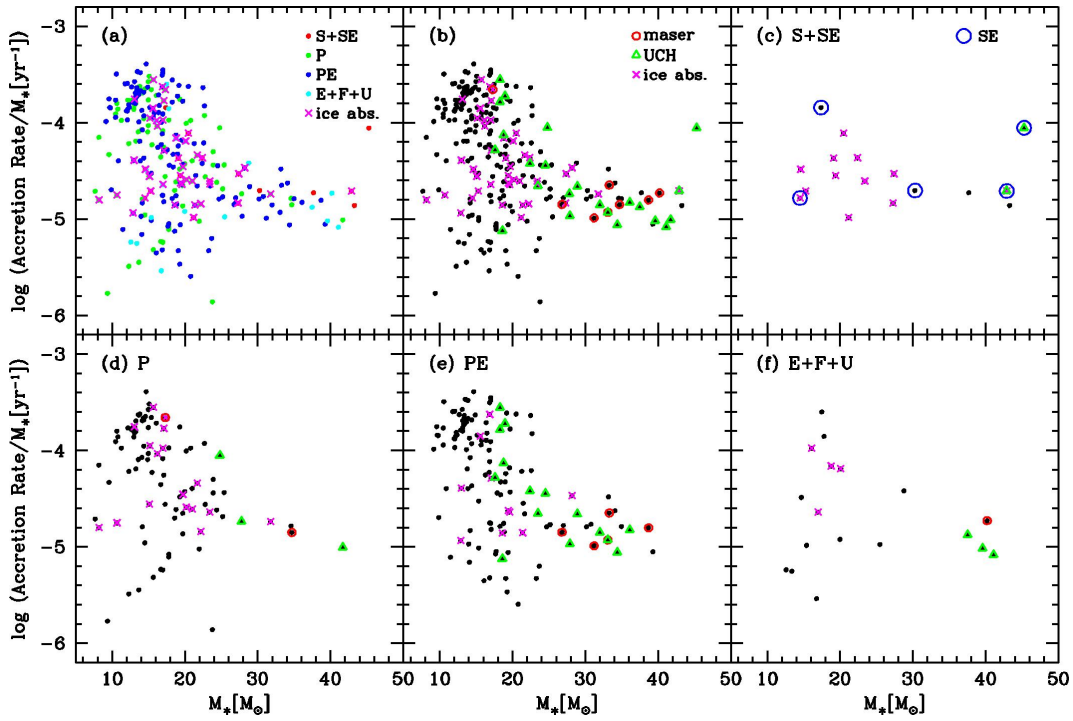

Figure 3: $\dot{M}_{\rm env}$ vs. $M_\star$ inferred from model fits to 277 YSOs with IRS spectra. (a) YSOs of different spectral classifications (Seale et al. 2009) are marked in different colors as shown in legends. YSO with ice absorption features are marked with additional crosses. (b) YSOs (black dots) that are counterparts of masers and UCHII (Green et al. 2008; Indebetouw et al. 2004) are marked with additional circles and triangles, respectively. (c-f) YSOs of different IR spectral types shown in separate panels for clarity. Symbols are the same as in (b) except extra blue circles for SE-type in (c).

Acknowledgements

This work is supported through NASA grants JPL 1282653 and 1288328.

References

Bonnell, I. A., Bate, M. R., Clarke, C. J. & Pringle, J. E. 1997, MNRAS, 285, 201
Chen, C.-H. R., Chu, Y.-H., Gruendl, R. A., Gordon, K. D. & Heitsch, F. 2009, ApJ, 695, 511
Chen, C.-H. R., Indebetouw, R., Chu, Y.-H., Gruendl, R. A., Testor, G., Heitsch, F., Seale, J. P, Meixner, M., et al. 2010, ApJ, 721, 1206
Churchwell, E. 2002, ARAA, 40, 27
Green, J. A., Caswell, J. L., Fuller, G. A., Breen, S. L., Brooks, K. Burton, M. G., Chrysostomou, A. Cox, J., et al. 2008, MNRAS, 385, 948
Gruendl, R. A., & Chu, Y. 2009, ApJS, 184, 172
Indebetouw, R., Johnson, K. E., & Conti, P. 2004, AJ, 128, 2206
Kato, D., Nagashima, C.; Nagayama, T., Kurita, M., Koerwer, J. F., Kawai, T., Yamamuro, T., Zenno, T., et al. 2007, PASJ, 59, 615
Keto, E., & Wood, K. 2006, ApJ, 637, 850
Krumholz, M. R., Klein, R. I., McKee, C. F., Offner, S. S. R. & Cunningham, A. J. 2009, Science, 323, 754
Robitaille, T. P., Whitney, B. A., Indebetouw, R., & Wood, K. 2007, ApJS, 169, 328
Robitaille, T. P., Whitney, B. A., Indebetouw, R., Wood, K. & Denzmore, P. 2006, ApJS, 167, 256
Seale, J. P., Looney, L. W., Chu, Y.-H., Gruendl, R. A., Brandl, B., Chen, C.-H. R., Brandner, W. & Blake, G. A. 2009, ApJ, 699, 150
Tan, J. C. & McKee, C. F. 2002, Hot Star Workshop III: The Earliest Phases of Massive Star Birth, 267, 267

Whitney, B. A., Sewilo, M., Indebetouw, R., Robitaille, T. P., Meixner, M., Gordon, K., Meade, M. R., Babler, B. L., et al. 2008, AJ, 136, 18
Yorke, H. W., & Sonnhalter, C. 2002, ApJ, 569, 846
Zaritsky, D., Harris, J., Thompson, I. B. & Grebel, E. K. 2004, AJ, 128, 1606
Zinnecker, H. & Yorke, H. W. 2007, ARAA, 45, 481

Discussion

H. Beuther: How can you be sure that some are single objects? At the given spatial resolution of $\sim$ 0.25 parsec, all objects should consist of at least small clusters...
R. Chen: We have examined the highest resolution of near-IR images, i.e. CTIO 4m or VLT NACO, available for these YSOs; those "single" sources appear as single point sources in these images. While we think it is possible that these "single" sources may have undetected low-mass young stars around them, or unresolved massive binary companion, the luminosities of these sources are dominated by one (or two in binary case) YSOs. The "multiple" sources have no obvious dominant YSOs and are considered as groups or clusters of massive YSOs. We focus on the contrast between these types of YSOs.

C. Martayan: At lower metallicity, it should be easier to form more massive stars. Do you have a mass-distribution for the YSOs in the LMC and MW? Are they different? I would expect some differences between the distributions with the metallicity.
R. Chen: I have made mass functions of massive YSOs in two H II regions in the LMC, N 44 & N 159, and found that in N 44 the slope of the mass function is consistent with the Salpeter value, while in N 159, the slope is more shallow. This shallow slope is likely to be biased by the higher detection limit of lower mass YSOs due to the bright background. We are working on getting physical properties of larger samples of YSOs in H II regions to examine whether there the IMF is shallower in the LMC.

A near-infrared imaging survey of intermediate and high-mass young stellar object outflow candidates

Suzanne K. Ramsay[1*], Watson P. Varricatt[2], Chris J. Davis[2] and Stephen Todd[3]

[1] European Southern Observatory, Karl-Schwarschild-Strasse, 2, 85748 Garching, Germany
[2] Joint Astronomy Centre, 660, N.A'ohuku Place, Hilo, HI 96720, USA
[3] UK Astronomy Technology Centre, Royal Observatory, Blackford Hill, Edinburgh, EH9 3HJ, UK.

Abstract: We present a new near-infrared imaging survey of 50 luminous young stellar outflow candidates. Using high spatial resolution observations in the v=1-0 S(1) line of H_2 we detect the outflows with a high success rate: 76% of the objects exhibit H_2 emission and 50% or more of the objects exhibit aligned H_2 emission features suggesting collimated outflows. Many of these are new detections. The young stellar objects responsible for the outflows are positively identified in many of our images based on their locations with respect to the outflow lobes, 2MASS colours and association with MSX, IRAS, millimetre and radio sources. The main results of our survey are as follows. The observations suggest that disk accretion is probably the leading mechanism in the formation of stars, at least up to late O spectral types. The close association of molecular outflows detected in CO with the H_2 emission features produced by shock excitation by jets from the young stellar objects suggests that the outflows from these objects are jet-driven. Towards strong radio emitting sources, H_2 jets were either not detected or were weak when detected, implying that most of the accretion happens in the pre-UCHII phase; accretion and outflows are probably weak when the YSO has advanced to its UCHII stage.

1 Why observe outflows from young high-mass stars?

The debate as to whether accretion or merger is the main mechanism for the formation of high ($>8M_{\odot}$) mass stars has been carried on for a number of years. Observational progress in understanding high mass star formation has been inhibited by a few well known factors. Massive stars are far fewer and have much shorter time scales for formation compared to low-mass stars. Hence, high-mass YSO candidates are rarer than their lower mass counterparts. Most regions of high-mass star formation are at distances of a few kpc or greater and since high-mass stars form in clusters, high spatial resolution is required to resolve the HMYSOs from other young stars in the region. Finally, observations at longer wavelengths are required to reduce the effect of extinction. Nevertheless, growing evidence for the accretion scenario as a method of forming high-mass stars has come from observations of small samples or individual objects. Evidence for disks has recently been reported by e.g. Wheelwright et al. (2010), Zapata et al. (2009) and Patel et al. (2005). Outflows have been observed by Zhang et al. (2005), Beuther et al. (2002a) and Wu et al. (2004) etc.

*sramsay@eso.org

Further proof requires work on statistically significant samples and a crucial contribution to the debate has come from the numerous observational programmes dedicated to identifying samples of high-mass YSO candidates and to searching for signposts of starformation by accretion associated with the HMYSOs (e.g. Molinari et al. 1996, 1998, 2000; Brand et al. 2001; Sridharan et al. 2002). This work has resulted in the identification of substantial numbers of well-characterised HMYSO candidates.

The survey presented here (Varricatt et al. 2010) is a search for the outflows associated with HMYSO outflow candidates in the v=1-0 S(1) line of H_2. This line is readily observed in the outflows associated with low-mass YSOs where it is excited by shocks from the outflows. Most previous studies of outflows from HMYSOs have been in CO at mm wavelengths using single dish telescopes with large beam sizes. One diagnostic of the formation scenario is the degree of collimation of the outflow: accretion generates highly collimated outflows, a merger would not. Observed high-mass outflows are often apparently poorly collimated, an effect which may be due to the low spatial resolution of the observations and the presence of multiple outflows in the beam. Using shock-excited H_2 as a tracer and exploiting the high spatial resolution and large field of infrared array cameras, sensitive observations of a substantial sample of sources could be carried out (see also Carratti o Garatti et al. 2008).

2 Target Selection and Observations

We selected candidates that are young, high-mass objects with evidence for outflows. Sources were selected that showed ammonia emission (Molinari et al. 1996) and also H_2O and CH_3OH maser emission (Sridharan et al. 2002), indicators of youth and high-mass. Those with high velocity CO, indicating outflows, from Shepherd & Churchwell (1996) and Beuther et al. (2002a) were included in the final list which totals 50 sources. The sources range in distance from $\sim 0.5 - 8$kpc and in measured bolometric luminosity from $\log(L/L_\odot) \sim 2.2 - 5.4$. The observations were carried out with the UKIRT Fast Track Imager (UFTI) on the UK Infrared Telescope (UKIRT). A 2.2×2.2arcmin^2 field was observed in the H_2 v=1-0 S(1) , Brackett-gamma and K band filters. In total, each source was observed for 15min.; the sensitivity reached was a 5σ limit of $K = 19$ for continuum sources and a per pixel sensitivity of 5σ at $1.3\times\ 10^{-18}\mathrm{Wm}^{-2}\mathrm{arcsec}^{-2}$ for the narrow band filters. The angular resolution obtained was limited by the seeing conditions to be from 0.5 to 1.0 arcsec. The data were reduced using standard infrared techniques to combine jittered images and remove instrumental effects. A continuum-subtracted H_2 image was produced following the method in Varricatt, Davis & Adamson (2005). Fits files of all of the images are available to download from http://cdsarc.u-strasbg.fr/ftp/cats/J/MNRAS/404/661/.

3 Results and Analysis

The immediate results from our survey were that many new embedded clusters were revealed in the K band images. Emission from H_2 was observed in 76% of our sources, many of these being new detections. An example of one source, IRAS22570+5912 is shown in Figure 1. Detailed comparison of each of the images with the published locations of the HMYSO candidates at other wavelengths was carried out, to identify the NIR counterpart of HMYSOs.

In the K band image (Figure 1) the location of the IRAS source is shown by a triangle and the MSX source by a cross. Our images reveal a cluster associated with IRAS 22570+5912, embedded in nebulosity. Five of the prominent sources in the cluster are labelled A–E. The 2MASS colours of these five sources show that D and E are the most deeply embedded. The asterisk shows the location of

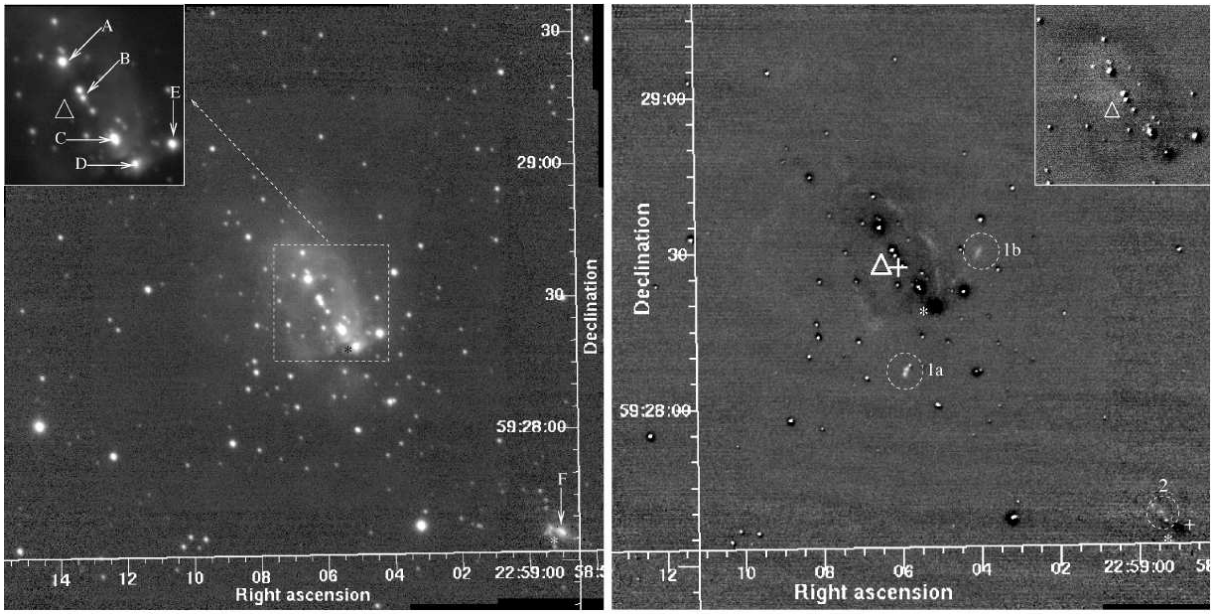

Figure 1: The K-band image of IRAS 22570+5912 (left) shows the central region at higher contrast in the inset. The H_2 line emission image of IRAS 22570+5912 (right) shows the Brackett-gamma image of the central region in the inset.

the 1.2mm peak observed by Beuther et al. (2002b) which coincides most closely with the embedded source, D. The location of a second 1.2mm peak can be seen just at the south-west edge of the field; this is associated with a source, or barely resolved cluster of sources, in the K band image. In the centre of the H_2 image, two prominent H_2 emission features (1a, 1b) are seen. We interpret these as part of the same outflow, centred on the sources D and E and on the 1.2mm peak. In the vicinity of source F and the second 1.2mm peak, further emission features from H_2 (labelled 2) are seen also with a linear geometry. The presence of two outflows in this region supports speculation that the CO velocity structure may be due to more than one outflow in this region (Shepherd & Churchwell 1996, Beuther et al. 2002a). The FIR luminosity estimated for this from the IRAS fluxes by Molinari et al. (1996) is $2.01\times10^4 L_\odot$. The ZAMS spectral type for a single source of this L_{bol} is O9 (from Panagia et al. 1973). The spatial resolution of the IRAS and MSX sources does not allow us unambiguously identify which of the sources A–E are contributing to this bolometric luminosity, and therefore this mass estimate is an upper limit. Deeper photometric studies of these regions would confirm absolutely the multiplicity of the sources and allow a more accurate determination of the mass of the driving YSOs. For this, as for all 50 sources in the sample, the 2MASS, MSX and IRAS colours were calculated and compared with the expected colours of HMYSOs. For IRAS 22570+5912, the MIR colours from IRAS place this source in the locus of UCHII regions, as given by Wood & Churchwell (1989).

Taking the sample as a whole, we find the following. H_2 emission features were detected in 38 (76%) of the 50 targets fields and in 25 (50%) of cases, aligned features were observed. The outflow collimation factors are typically in the range 4–8, with a maximum of 19 and minimum of 2, so are similar to those observed in low-mass YSOs. For sources with both H_2 and CO data, the direction and origin of the outflows are in good agreement. Based on the geometry of the sources, the strong similarity in appearance to low-mass YSO jets and the results from a few sources already followed up (Caratti o Garatti et el. 2008, Davis et al. 2004, Todd & Ramsay Howat 2006) we conclude that the H_2 emission is due to shock excitation and that the outflows are jet driven. Figure 2 shows the 2MASS colours for all the sources. Our outflow sources lie to the right of the reddening vectors for main

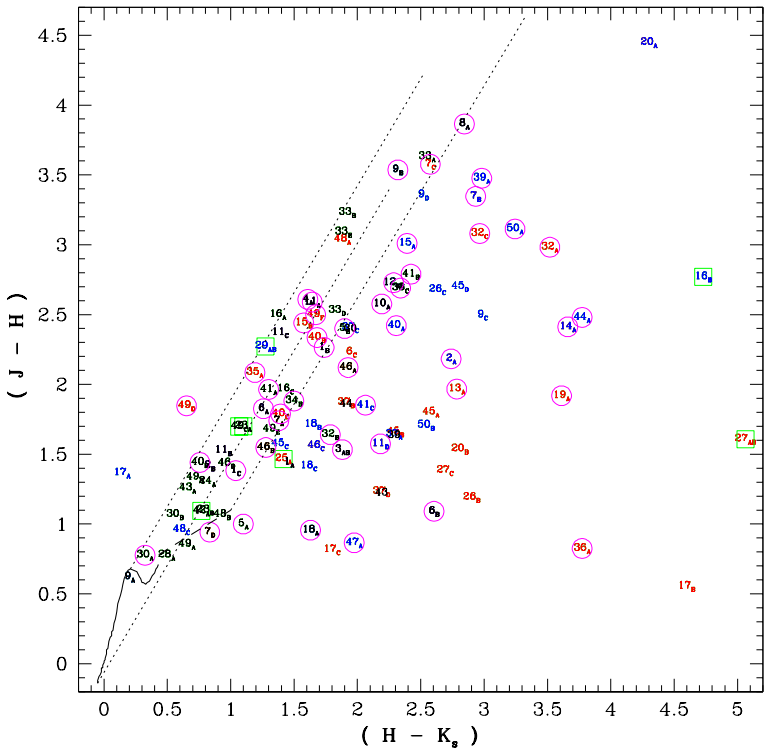

Figure 2: 2MASS colours for all the sources with source numbers from Varricatt et al. (2010). The sources of the outflows are circled, those which are confirmed as UCHII regions are enclosed in squares. The solid line shows the colours of MS stars, the dashed line shows the locus of CTTs and the dotted lines show the reddening vectors to A_v=30.

sequence stars, consistent with them being YSOs. The IRAS and MSX colours are treated similarly and the plots are shown in Figure 3. The confirmed UCHII sources are indicated with squares; they are seen to be well mixed with the other sources which are in a pre-UCHII phase. We therefore confirm the suggestion by Bik (2004) that the Wood & Churchwell (1989) colours for UCHII regions select both UCHII and pre-UCHII sources. Our sources are again consistent with the colours of HMYSOs and we believe that we have identified the NIR counterparts of the candidate HMYSOs. Following the method outlined in the case of IRAS 22570+5912, the observed bolometric luminosity for the YSOs from sub-mm or MIR data was used to estimate the single star ZAMS spectral type using the calculations of Panagia (1973) and Morton & Adams (1968). As already stated, this gives an upper limit to the mass of the YSO driving the outflow; if the source is multiple then the mass determined from the luminosity will be reduced. The single star ZAMS spectral types for the outflow sources are in the range from O7 to B3. Therefore we conclude that sources as massive as late O drive collimated outflows and disk accretion would be the main mechanism for their formation. Detailed discussion on each of the sources is presented in Varricatt et al. (2010). Strong radio emission is associated with 13 of the 50 sources: a notable result from the survey is that none of these is associated with an H_2 jet. Radio emission from the remaining 25 sources with jet-like H_2 emission is faint (in 12 cases) or not detected (in 9 cases) and, in 4 fields, clearly from a different source. It therefore appears that most of the accretion happens in the pre-UCHII phase.

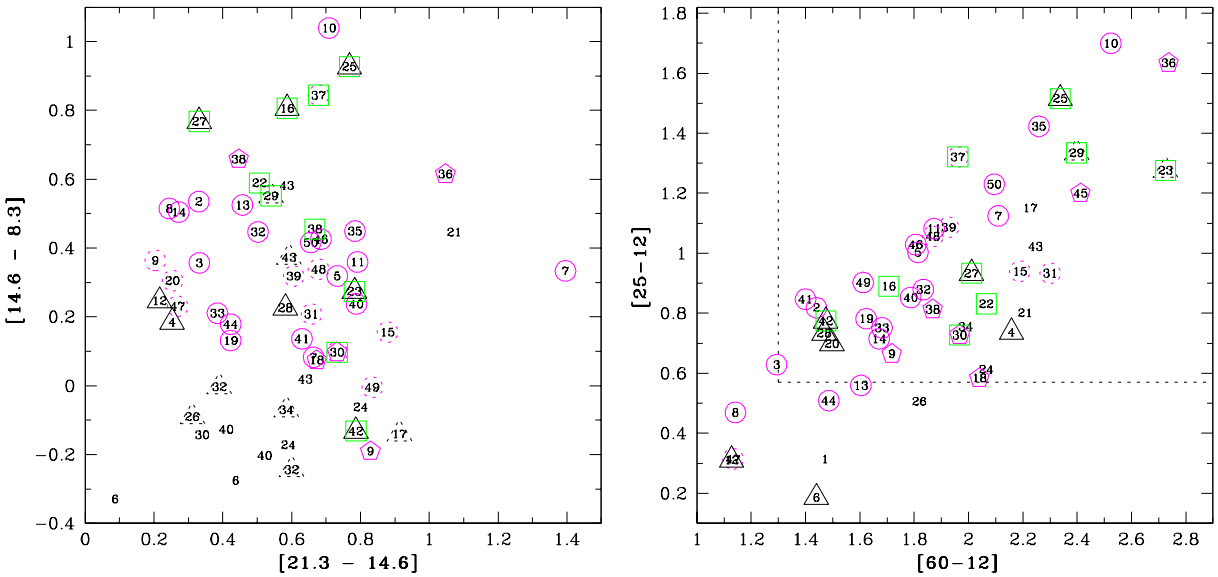

Figure 3: The MSX (left) and IRAS colours of the sources detected in our images are plotted. The dashed lines in the IRAS figure show the colour criteria for selecting UCHIIS from Wood & Churchwell (1989). Confirmed UCHII regions are shown as green squares and are seen to be well mixed with the other sources. Our candidate outflow sources have the colours of HMYSOs.

Acknowledgements

The UKIRT is operated by the JAC on behalf of the UK STFC. This paper makes use of data from 2MASS, a joint project of the University of Massachusetts and IPAC/CIT (funded by NASA and NSF) as well as *IRAS* and *MSX* data products and the SIMBAD database operated by CDS, Strasbourg.

References

Beuther, H., Schilke, P, Sridharan, T.K., Menten, K.M., Walmsley, C.M. & Wyrowski, F. 2002a, A&A, 383, 892
Beuther, H., Schilke, P, Menten, K.M., Motte, F., Sridharan, T.K. & Wyrowski, F. 2002b, A&A, 556, 945
Bik, A., 2004, PhD thesis, University of Amsterdam
Brand, J., Cesaroni, R., Palla, F. & Molinari, S. 2001, A & A, 370, 230
Caratti o Garatti, A., Froebrich, D., Eislöffel, J., Giannini, T. & Nisini, B. 1998, A&A, 485, 137
Davis, C.J., Varricatt, W.P, Todd, S.P. & Ramsay Howat, S.K. 2004, A&A, 425, 981
Molinari, S., Brand, J., Cesaroni, R. & Palla, F. 1996, A&A, 308, 573
Molinari, S., Brand, J., Cesaroni, R., Palla, F. & Palumbo, G.G.C. 1998, A&A, 336, 339
Molinari, S., Brand, J., Cesaroni, R. & Palla, F. 2000, 355, 617
Morton, D.C. & Adams, T.F. 1968, ApJ, 151, 611
Panagia, N. 1973, AJ, 78, 929
Patel, N.A., Curiel, S., Sridharan, T.K. et al. 2005, Nature, 437, 109
Shepherd, D. & Churchwell, E. 1996, ApJ, 472, 225
Sridharan, T.K., Beuther, H., Schilke, P., Menten, K.M. & Wyrowski, F. 2002, ApJ, 566, 931
Todd, S.P. & Ramsay Howat, S.K. 2006, MNRAS, 267, 238
Varricatt, W.P., Davis, C.J. & Adamson, A.J. 2005, MNRAS, 359, 2
Varricatt, W.P., Davis, C.J., Ramsay, S.K. & Todd, S.P. 2010, MNRAS, 404, 661
Wheelwright, H.E., Oudmaijer, R. D., de Wit, W. J., Hoare, M. G., Lumsden, S. L., & Urquhart, J. S. 2010, MNRAS, 408, 1840
Wood, D.O.S. & Churchwell, E. 1989, ApJ, 340, 265
Wu, Y., Wei, Y., Zhao, M., Shi, Y., Yu, W., Qin, S. & Huang, M. 2004, A&A, 426, 503
Zapata, L.A., Ho, P.T.P., Schilke, P., Rodriguéz, L.F., Menten, K., Palau, A. & Garrod, R.T., 2009, ApJ, 698, 1422

Zhang, Q., Hunter, T.R., Brand, J., Sridharan, T. K., Cesaroni, R., Molinari, S., Wang, J., & Kramer, M. 2005, ApJ, 625, 864

Discussion

L. Oskinova: Can you please comment : wouldn't H_2 emission be expected from the PDRs around UCH II regions?
S. Ramsay: Yes, certainly. My comments about the lack of H_2 emission around the UCH II regions were for the case of aligned H_2. Fluorescent H_2 emission could be expected and indeed may have been seen associated with the H II YSOs near IRAS20444+4629 and IRAS18174-1612. In other sources, H_2 from PDRs may fall below our detection limit.

Modeling the massive young stellar object NGC 3603 IRS 9A*

Christian A. Hummel

European Organization for Astronomical Research in the Southern Hemisphere,
Karl-Schwarzschild-Str. 2, 85748 Garching bei München, Germany

Abstract: We present results from our high angular resolution observations of the brightest high-mass young stellar object in NGC 3603, IRS 9A. Both MIDI at the VLTI and T-ReCS equipped with an aperture mask at Gemini South have resolved the mid-infrared dust emission on scales of 30 mas to 300 mas, corresponding to scales of 200 AU to 2000 AU. A flattened envelope or disk-like dust structure is the only way to explain why MIDI was able to detect a compact warm source in the presence of extended emission fully resolved even on 8 meter baselines. We have therefore described the structure using disks and envelopes based on models by Whitney et al., and can find reasonable agreement with the visibility measurements and the SED as measured by Spitzer.

1 Introduction

1.1 Motivation

Massive young stellar objects are usually deeply embedded in their natal environment which can be penetrated only at wavelengths long-ward of the near IR. In addition, sites of high-mass star formation are generally quite distant, hence require high angular resolution observations with interferometers. The MIDI instrument on the VLTI was therefore a perfect choice for us to study IRS 9A, at 7 kpc, in the star forming region of NGC 3603.

1.2 Environment

The molecular cloud from which IRS 9A was born has been largely eroded away by the radiation of the cluster of hot stars some 2.5 pc (projected on the sky) to the north-west. All obscuring gas and dust is gravitationally bound to the star and thus allows us to study the accretion in more detail. The foreground extinction is adopted to be $A_V = 4.5$ mag (Brandl et al. 1999).

*Based in part on observations collected at the European Southern Observatory and the Gemini South Observatory, Chile

Figure 1: JHK composite image taken with ISAAC at VLT-ANTU by Brandl et al. (1999). IRS 9A is the bright-orange source in the lower left. North is up, East to the left. The height of the image covers 1.9 arcminutes (3.5 pc).

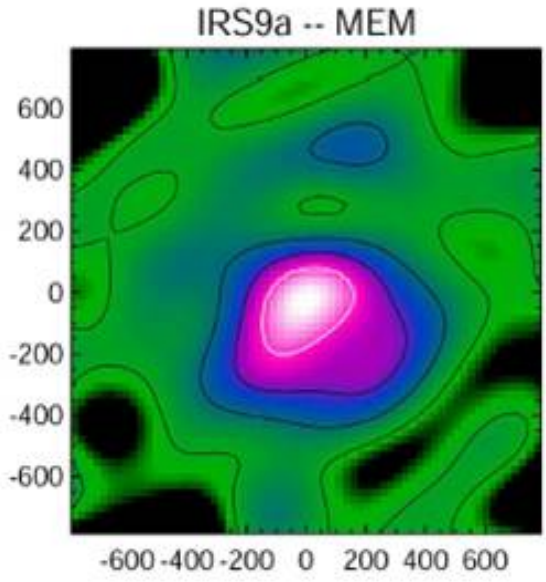

Figure 2: Image reconstructed from sparse-aperture masking observations at 11.7 microns at the Gemini South Telescope using the T-ReCS instrument (Vehoff et al. 2010). The scale is in milli-arcseconds, North is up and East to the left. Countours are at 30%, 15%, and 5% of the peak.

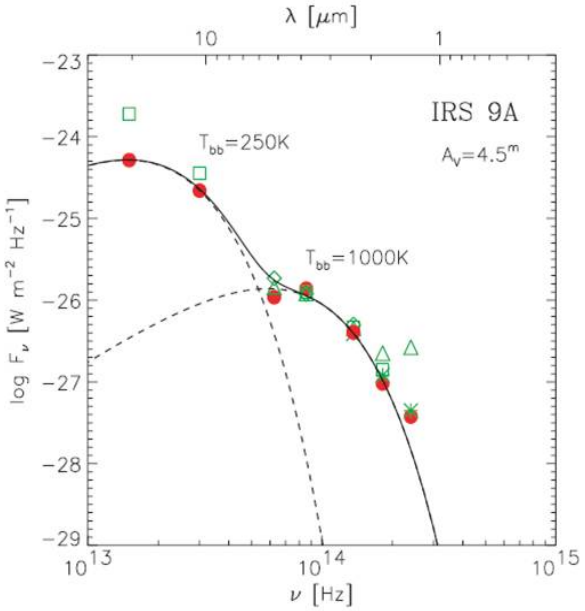

Figure 3: The SED of IRS 9A dereddened for the foreground extinction of $A_V = 4.5$ by Nürnberger (2003).

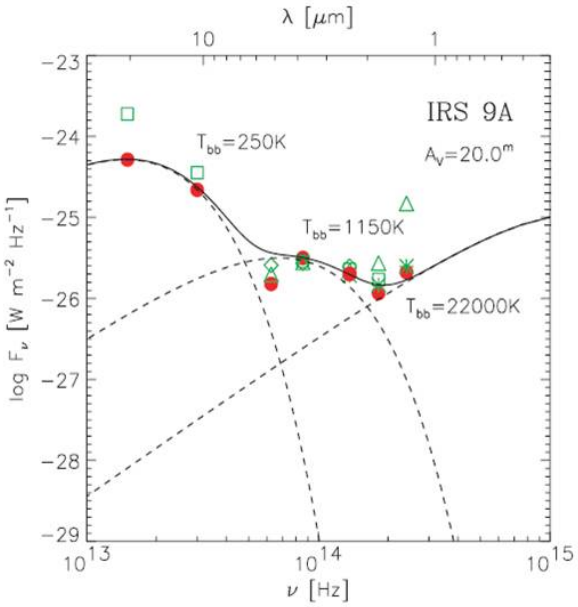

Figure 4: The SED dereddened by $A_V = 20$ mag, i.e. the combined foreground and intrinsic extinction, by Nürnberger (2003).

1.3 Emission components

The SED shows at least two components of different temperatures, the hotter one possibly corresponding to a dust evaporating inner edge of an accretion disk. If we correct the photometry for an adopted $A_V = 20$ mag, the photospheric spectrum of the central O-star is revealed. Moving the star in the $(J - K) - M_J$ diagram to the main sequence along the reddening vector indicates a mass of about 40 $M_\odot$ (Nürnberger 2003).

2 Observations and results

Observations were carried out with the MIDI mid-infrared beam combiner of the VLTI, and the aperture mask of the T-ReCS instrument at Gemini South. MIDI allows to measure the visibility as a function of wavelength between about 8 and 13 microns ($R = 35$), while T-ReCS allows to measure visibilities and (closure) phases for image reconstruction between all combinations of the 7-hole mask.

2.1 A compact hot component?

The MIDI visibility (46 m baseline) is near zero between 12 and 9 μm, but increases rapidly towards 8 μm. A simple geometrical model consisting of a hot (1000 K) ring component (57 mas diameter) and a warm (140 K) completely resolved component is shown in Figs. 5 and 6.

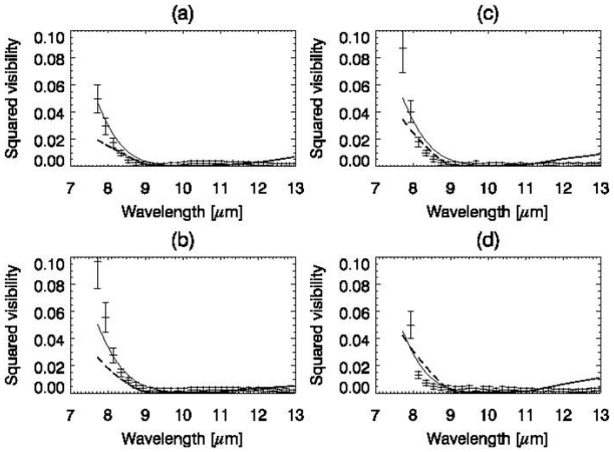

Figure 5: Visibility spectra measured at four epochs during the night of 2005, February 28, by MIDI. The solid line is a fit of a geometrical model, while the dashed line is a fit of the disk-envelope model # 3012790 of Robitaille et al. (2006).

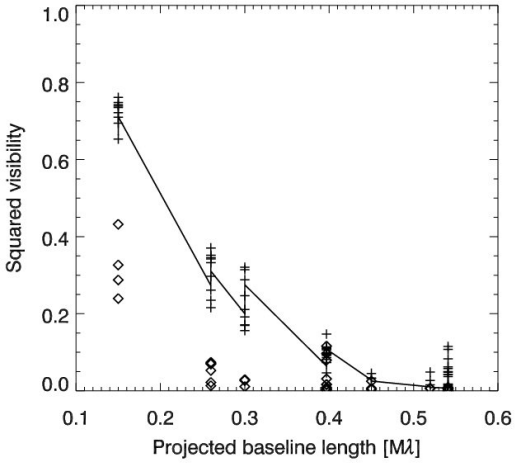

Figure 6: Visibility measurements as a function of baseline length measured with the aperture mask on Gemini South by the T-ReCS 11.7 micron camera. The solid line indicates the fit of the geometrical model, while the diamonds correspond to the physical disk-envelope model.

3 Modeling

3.1 Spherical dust distribution

Spherical dust distributions around MYSOs are very unlikely on theoretical grounds due to the fact that the very high luminosity of these stars would disperse the infalling envelope, preventing accretion to the final mass of the object. Despite of this, we attempted to fit a spherical dust envelope with a luminosity of 230 k$L_{\odot}$, $A_V = 29$ mag, and an inner radius $R = 170$ mas (1200 AU) where $T = 500$ K, and were able to reproduce the observed T-ReCS visibilities and the SED. The dust mass corresponds to one solar mass. However, this dust envelope would be completely resolved by MIDI. Only a flattened structure offers a direct view of the compact inner regions. Kraus et al. (2010) recently found evidence for such an accretion disk in another MYSO, while Krumholz et al. (2009) performed numerical simulations which indicate that disk accretion can overcome the Eddington limit.

3.2 An accretion disk at the center?

We are using the disk-envelope model of Whitney et al. (2003) to model the MIDI and T-ReCS visibilities, as well as the SED. Best-fitting models for the SED were selected from the grid published by Robitaille et al. (2006), and visibilities were computed. The best model is shown as a dashed line in the plots above. Only a disk model can explain the fact that significant correlated flux (from the hot inner regions) could be seen by MIDI despite the resolved envelope. A spherical model is excluded.

4 Conclusions and outlook

Our work can only be seen as a beginning of the investigation towards the unambiguous detection of a disk in the MYSO IRS 9A. Second generation VLTI instruments such as MATISSE will allow

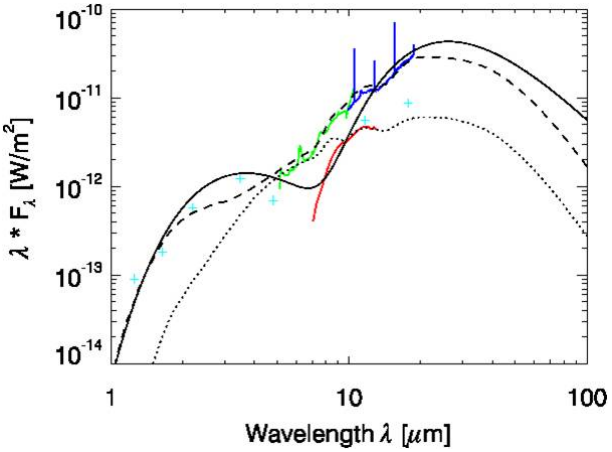

Figure 7: SED of model 3012790 for IRS 9A at 7 kpc distance (dashed line). The green and blue lines represent Spitzer SL and SH observations, respectively (Lebouteiller et al. 2008), while the red line is the MIDI spectrum. Solid line from the geometric model, dotted line for the MIDI aperture.

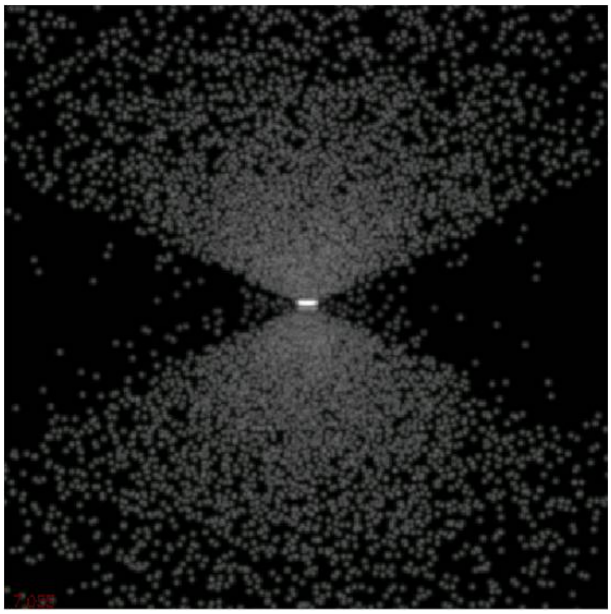

Figure 8: Image of the disk model with an envelope, inclined at 85 degrees.

imaging in the mid-infrared, dispensing with the need to use models to interpret the visibility data. We have shown that high angular resolution observations provide complementary information to mere modeling of the SED. A more comprehensive view should also include observations of outflows, indicative of ongoing accretion, and the possible Keplerian rotation of the flattened envelope or disk.

Acknowledgements

This work is the result of a collaboration with S. Vehoff, J.D. Monnier, P. Tuthill, D.E.A. Nürnberger, R. Siebenmorgen, O. Chesneau, and W. Duschl.

References

Brandl, B., Brandner, W., Eisenhauer, F., Moffat, A. F. J., Palla, F. & Zinnecker, H. 1999, A&A, 352, L69

Kraus, S., Hofmann, K., Menten, K. M., Schertl, D., Weigelt, G., Wyrowski, F., Meilland, A., Perraut, K., et al. 2010, Nature, 466, 339

Krumholz, M. R., Klein, R. I., McKee, C. F., Offner, S. S. R., & Cunningham, A. J. 2009, Science, 323, 754

Lebouteiller, V., Bernard-Salas, J., Brandl, B., Whelan, D. G., Wu, Y., Charmandaris, V., Devost, D. & Houck, J. R. 2008, ApJ, 680, 398

Nürnberger, D. E. A. 2003, A&A, 404, 255

Robitaille, T. P., Whitney, B. A., Indebetouw, R., Wood, K., & Denzmore, P. 2006, ApJS, 167, 256

Vehoff, S., Hummel, C. A., Monnier, J. D., Tuthill, P., Nürnberger, D. E. A., Siebenmorgen, R., Chesneau, O. & Duschl, W. J. 2010, A&A, 520, A78

Whitney, B. A., Wood, K., Bjorkman, J. E. & Cohen, M. 2003, ApJ, 598, 1079

The interactions of winds from massive young stellar objects

E. R. Parkin[1,2], J. M. Pittard[2], M. G. Hoare[2], N. J. Wright[3], J. J. Drake[3]

[1] Institut d'Astrophysique et de Géophysique, Université de Liège, Belgium
[2] School of Physics and Astronomy, The University of Leeds, UK
[3] Harvard-Smithsonian Center for Astrophysics, USA

Abstract: The supersonic stellar and disk winds possessed by massive young stellar objects will produce shocks when they collide against the interior of a pre-existing bipolar cavity (resulting from an earlier phase of jet activity). The shock heated gas emits thermal X-rays which may be observable by spaceborne observatories such as the Chandra X-ray Observatory. Hydrodynamical models are used to explore the wind-cavity interaction. Radiative transfer calculations are performed on the simulation output to produce synthetic X-ray observations, allowing constraints to be placed on model parameters through comparisons with observations. The model reveals an intricate interplay between the inflowing and outflowing material and is successful in reproducing the observed X-ray count rates from massive young stellar objects.

1 Introduction

Observational and theoretical advances have provided increasing evidence that massive star formation is not merely a scaled-up version of lower-mass star formation. However, there are some similarities. For instance, both involve outflows (Garay & Lizano 1999; Reipurth & Bally 2001; Banerjee & Pudritz 2006, 2007) and bipolar cavities are commonly observed around both high and low mass young stellar objects (Garay & Lizano 1999). The widths of IR recombination line emission observed from massive young stellar objects (MYSOs) indicates the presence of dense ionized outflows with velocities ranging from 100 to $> 340\ \mathrm{km\,s^{-1}}$ (Drew, Bunn, & Hoare 1993; Bunn, Hoare, & Drew 1995). Further confirmation of outflows has come from high angular resolution radio observations (e.g. Hoare et al. 1994; Hoare 2006; Curiel et al. 2006). One explanation would be a disk wind driven by radiation pressure at the surface of the disk (e.g. Drew et al. 1998).

X-rays have been detected from deeply embedded MYSOs in star forming regions by the *Chandra X-ray observatory* (hereafter *Chandra*; e.g. Broos et al. 2007; Wang et al. 2007). Preibisch et al. (2002) found that the X-ray emission from IRS3 A and C, with a count rate of $0.166 \pm 0.041\ \mathrm{ks^{-1}}$ for the former, could not be explained by the standard scenario for massive stars (i.e. wind embedded shocks produced by instabilities inherent in radiatively-driven winds - see Owocki, Castor, & Rybicki 1988), yet the estimated stellar masses of these objects implies they will have radiative outer envelopes which poses problems for the generation of X-rays through magnetic star/disk interactions.

A potential source of X-rays which has not been considered before is the collision between the stellar and disk winds and the infalling envelope. We explore this scenerio using hydrodynamical models and find that the interaction of the stellar and disk wind with the cavity wall produces shock heated plasma which emits X-rays in agreement with Chandra observations (Parkin et al. 2009).

The remainder of this work is structured as follows: in Sect. 2 we describe the winds-cavity model, in Sect. 3 we present the result of the hydrodynamic simulations and X-ray calculations, and in Sect. 4 we close with our conclusions.

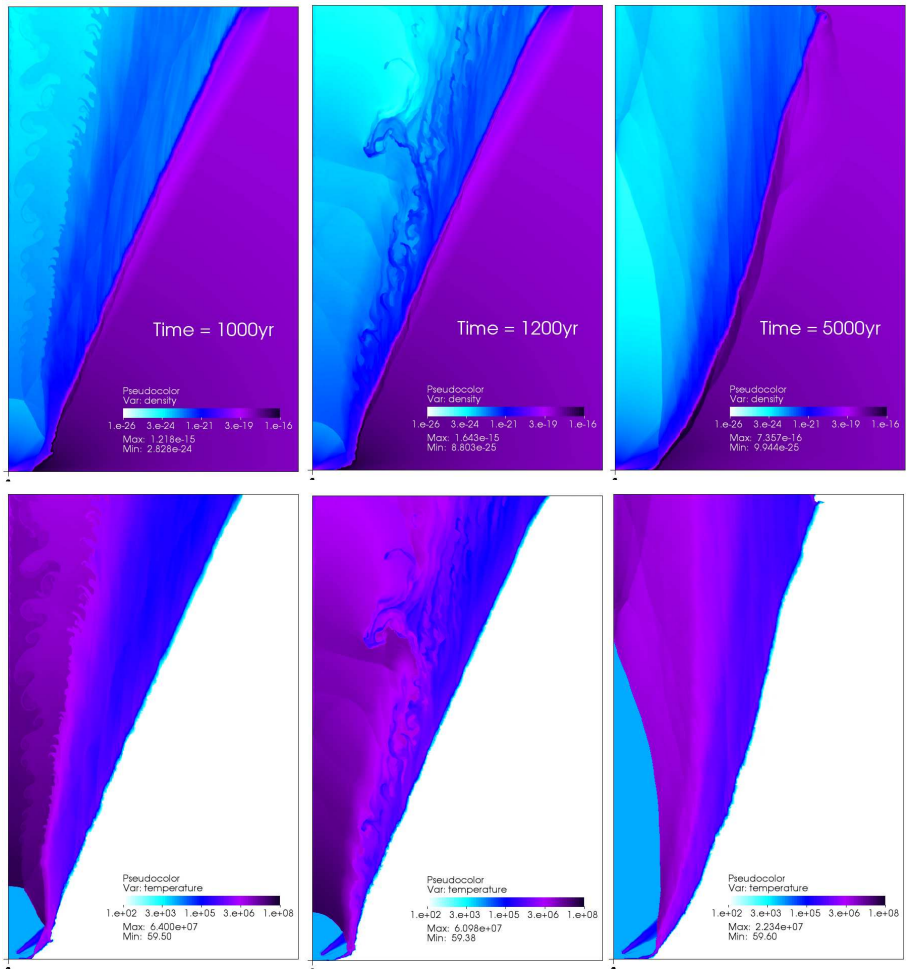

Figure 1: Density (top row) and temperature snapshots (bottom row) from our fiducial model at a simulation time of $t = 1000$ (left), 1200 (middle), and 5000 yrs (right). The grids extend to $x = 5 \times 10^{16}$ cm and $y = 8 \times 10^{16}$ cm. The central star is located in the bottom left corner. The reverse shock can be seen in the lower left of the grid, where the enclosed preshock wind has a temperature of $T = 10^4$ K.

2 The winds-cavity interaction model

The model consists of a MYSO situated at the centre of a previously evacuated bipolar cavity which is surrounded by infalling molecular cloud material. We include the stellar wind and a disk wind which emanates from the surface of the circumstellar accretion disk; both are assumed to be at terminal velocity. Due to the spatial scales under consideration we do not attempt to model the radiative driving of the winds as this requires high spatial resolution in the vicinity of the star/disk (e.g. Proga

et al. 1998). For simplicity we adopt an angle dependent wind prescription based on the models of Proga et al. (1998), Drew et al. (1998), and Sim et al. (2005), whereby the stellar wind occupies a region from a polar angle $0 - 60^{\circ}$ and the disk wind occupies the region from $60^{\circ} - 85^{\circ}$. The density and velocity distibutions for the infalling cloud material are described by the equations of Terebey et al. (1984), and a simple analytical prescription similar to that of Alvarez et al. (2004) is used to determine the morphology of the pre-existing outflow cavity. We model the winds-cavity interaction in 2D cylindrical symmetric coordinate system using VH-1 (Blondin et al. 1990). The code uses the piecewise-parabolic method of Colella & Woodward (1984) to solve the hydrodynamic equations on a fixed grid. Further details of the model can be found in Parkin et al. (2009).

We consider a 30 $\mathrm{M}_{\odot}$ O8V star with a mass-loss rate of 10^{-7} $\mathrm{M}_{\odot}$ yr^{-1} and terminal wind speed of 2000 $\mathrm{km\ s}^{-1}$. The disk wind has a mass-loss rate of 10^{-6} $\mathrm{M}_{\odot}$ yr^{-1} and a terminal wind speed of 400 $\mathrm{km\ s}^{-1}$. The unshocked winds are assumed to be at a temperature of 10^4 K. The mass infall rate for the cloud is 2×10^{-4} $\mathrm{M}_{\odot}$ yr^{-1} and the cavity opening angle is 30° . The winds-cavity interaction was followed for a simulation time of $t = 5000$ yrs.

To allow a comparison to be made between *Chandra* X-ray observations of MYSOs and the simulations we calculate attenuated X-ray fluxes. The emissivity values used are for optically thin gas in collisional ionization equilibrium obtained from look-up tables calculated from the MEKAL plasma code (Liedahl, Osterheld, & Goldstein 1995 and references there-in). Ray-tracing calculations are performed with an inclination angle (to the pole) of 60°.

In this work we only consider one set of parameters, and we refer the reader to Parkin et al. (2009) for a detailed parameter space exploration.

3 Results

Fig. 1 shows the spatial distribution of material in the simulation; the disk wind lines the cavity wall and separates the stellar wind from the infalling molecular cloud material. The winds in the simulation are supersonic, and their collision against the cavity wall generates a reverse shock close to the star (< 500 AU). Because the ram pressure of the inflow/outflow is angle dependent and the base of the cavity is subject to instabilities the position of the reverse shock oscillates, and its shape is often non-spherical. This is due to small fluctuations in the shape and size of the base of the cavity wall as inflowing material is ablated and incorporated into the outflow, and as new inflowing material replenishes it (see Fig. 1). The shear layer between the stellar and disk winds provides a site for the growth of ~ 700 AU (10^{16} cm) amplitude Kelvin-Helmholtz instabilities on timescales of $\sim$ a few years. By $t = 1200$ yrs an instability of this proportion can be seen driving a clump of disk wind material into the path of the stellar wind, which leads to mass-loading of the latter.

At a simulation time of $t = 1000$ yrs, the intrinsic X-ray emission comes mainly from disturbed cloud material ($L_{\mathrm{int_C}} \simeq 3.3 \times 10^{33}$ $\mathrm{erg\ s}^{-1}$), then the disk wind ($L_{\mathrm{int_D}} \simeq 4.3 \times 10^{32}$ $\mathrm{erg\ s}^{-1}$), and finally the stellar wind ($L_{\mathrm{int_S}} \simeq 5 \times 10^{30}$ $\mathrm{erg\ s}^{-1}$). The shock driven into the cloud is too slow to heat gas up to X-ray emitting temperatures, but large quantities of cloud material are ablated by the outflowing disk wind and mixed into this hotter flow[1]. This process heats the cloud material to temperatures where (soft) X-rays are emitted. However, the difference between the *attenuated* luminosities of the cloud and stellar wind components is very small ($L_{\mathrm{att_C}} \simeq 8 \times 10^{28}$ $\mathrm{erg\ s}^{-1}$ and $L_{\mathrm{att_S}} \simeq 7 \times 10^{28}$ $\mathrm{erg\ s}^{-1}$, respectively). The explanation is that the stellar wind emission is harder and extends to higher energies, and is less affected by attenuation. In contrast, the cloud material, which is heated to lower temperatures, emits prolifically at low energies and has a much higher intrinsic

[1]Note that some heating of the cloud material may occur due to numerical heat conduction between the hot postshock disk wind and the cooler cloud material (Parkin & Pittard 2010).

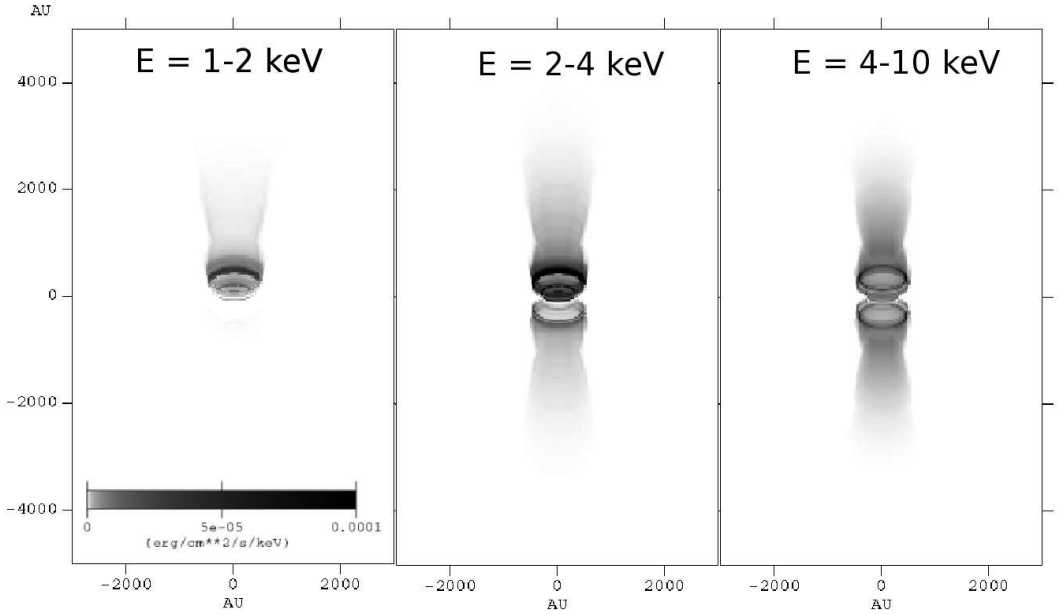

Figure 2: Ray-traced synthetic broadband X-ray images.

luminosity, but its emission is subject to considerable attenuation at $E < 1$ keV. Although some variation in X-ray emission occurs due to fluctuations in the position of the reverse shock, these values are indicative of the mean luminosities from the simulation.

The total attenuated luminosity from the model is $L_{\mathrm{att_{tot}}} \simeq 2 \times 10^{29}$ erg s^{-1} which, when placed at a distance of 1 kpc and convolved with the *Chandra* effective area, equates to a count rate of $\simeq 0.1$ ks^{-1}. Interestingly, this is in approximate agreement with X-ray count rates of 0.166 ± 0.041 ks^{-1} and 0.30 ± 0.11 ks^{-1} inferred from observations of Mon R2 IRS 3A by Preibisch et al. (2002) and for S106 IRS4 by Giardino, Favata, & Micela (2004), respectively.

Examining synthetic broadband X-ray images calculated from the simulation output one can see that the observable X-ray emission in the 1-2, 2-4, and 4-10 keV bands originates from similar regions of the cavity (Fig. 2). The peak in the intensity in the three bands have common origins near the reverse shock, and are mainly generated by shocked stellar and disk wind material. Importantly, the spatial extents of the detectable emission in all three energy bands (1-2, 2-4, and 4-10 keV) are just below the resolution limit of *Chandra* ($\sim 0.5''$) and so this model is consistent with the unresolved nature of real MYSOs.

4 Conclusions

The wind-cavity interaction around an embedded MYSO has been studied using hydrodynamic simulations and X-ray calculations. In summary, the collision of the winds against the cavity wall generates a reverse shock close to the star (< 500 AU). The shock heated gas produces X-ray emission with an integrated count rate ($\simeq 0.1$ ks^{-1}) and spatial extent ($< 0.5''$) in agreement with observations of MYSOs by *Chandra*.

We close with a note that future X-ray satellites, such as the International X-ray Observatory (IXO), may have the potential to resolve the spatial extent of the X-ray emission from the winds-cavity interaction. If this were the case, the winds-cavity model could be used in concert with detailed analysis at infra-red wavelengths to place unsurpassed constraints on the parameters of MYSO outflows.

Acknowledgements

ERP thanks The University of Leeds and PRODEX for funding.

References

Alvarez, C., Hoare, M. & Lucas, P. 2004, A&A, 419, 203
Banerjee, R. & Pudritz, R. E. 2006, ApJ, 641, 949
Banerjee, R. & Pudritz, R. E. 2007, ApJ, 660, 479
Blondin, J. M., Kallman, T. R., Fryxell, B. A. & Taam, R. E. 1990, ApJ, 356, 591
Broos, P. S., Feigelson, E. D., Townsley, L. K., Getman, K. V., Wang, J., Garmire, G. P., Jiang, Z. & Tsuboi, Y. 2007, ApJS, 169, 353
Bunn, J. C., Hoare, M. G. & Drew, J. E. 1995, MNRAS, 272, 346
Colella, P. & Woodward, P. R. 1984, J. Comput. Phys., 54, 174
Curiel, S., Ho, P. T. P., Patel, N. A., Torrelles, J. M., Rodríguez, L. F., Trinidad, M. A., Cantó, J., Hernández, L., et al. 2006, ApJ, 638, 878
Drew, J. E., Bunn, J. C. & Hoare, M. G. 1993, MNRAS, 265, 12
Drew, J. E., Proga, D. & Stone, J. M. 1998, MNRAS, 296, L6
Garay, G. & Lizano, S. 1999, PASP, 111, 1049
Giardino, G., Favata, F. & Micela, G. 2004, A&A, 424, 965
Hoare, M. G. 2006, ApJ, 649, 856
Hoare, M. G., Drew, J. E., Muxlow, T. B. & Davis, R. J. 1994, ApJ, 421, L51
Liedahl, D. A., Osterheld, A. L. & Goldstein, W. H. 1995, ApJL, 438, L115
Owocki, S. P., Castor, J. I. & Rybicki, G. B. 1988, ApJ, 335, 914
Parkin, E. R. & Pittard, J. M. 2010, MNRAS, 406, 2373
Parkin, E. R., Pittard, J. M., Hoare, M. G., Wright, N. J. & Drake, J. J., 2009, MNRAS, 400, 629
Preibisch, T., Balega, Y. Y., Schertl, D. & Weigelt, G. 2002, A&A, 392, 945
Proga, D., Stone, J. M. & Drew, J. E. 1998, MNRAS, 295, 595
Reipurth, B. & Bally, J. 2001, ARA&A, 39, 403
Sim, S. A., Drew, J. E. & Long, K. S. 2005, MNRAS, 363, 615
Terebey, S., Shu, F. H. & Cassen, P. 1984, ApJ, 286, 529
Wang, J., Townsley, L. K., Feigelson, E. D., Getman, K. V., Broos, P. S., Garmire, G. P. & Tsujimoto, M. 2007, ApJS, 168, 100

A very young massive star-forming region in the Small Magellanic Cloud

Romain Selier[1] and Mohammad Heydari-Malayeri[1]

[1] LERMA, Observatoire de Paris, CNRS, UPMC, F-75014 Paris, France

Abstract: We present a study of the compact H II region N 66A in the SMC starburst region N 66/NGC 346. This analysis is based on our ESO NTT observations coupled with archive HST ACS data. We obtain a number of physical characteristics of this compact H II region. Moreover we derive the spectral classification of the main exciting star of N 66A for the first time using spectroscopy. This compact object belongs to a rare class of H II regions in the Magellanic Clouds, called High-Excitation Blobs (HEBs). N 66A most probably represents a very young massive star formation event in the N 66 complex.

1 Introduction

N 66 is the most luminous H II region in the Small Magellanic Cloud (SMC). It is also the most active star-forming region in this neighboring galaxy. Indeed the star cluster NGC 346 located at its center hosts 33 O-type stars (Massey, Parker & Garmany 1989). Moreover it contains a large population of low-mass, pre-main-sequence stars (Gouliermis et al. 2006; Sabbi et al. 2007; Hennekemper et al. 2008).

N 66 displays an arc of dust that runs over some 60 pc from north-west to south-east below NGC 346, as can be seen on the high-resolution images of the region taken with HST/ACS (Nota et al. 2006). A bright and compact H II region, called N 66A, lies to the south-eastern end of the absorption lane. Our work was mainly focused on a detailed study of this compact H II region. We show that N 66A represents the youngest episode of massive star formation in the N 66 complex.

2 Results

2.1 The compact H II region N 66A

Figure 1 presents a high-resolution composite image of the compact H II region N 66A. It is $\sim 10''$ in diameter, corresponding to ~ 3 pc and is marked by a strong absorption lane. Interestingly, two bright stars are located towards the central part of the region, above the dust lane. Separated by $0''.7$ (~ 0.2 pc), they are the main exciting stars of the H II region (see also Sect. 2.2). The most extincted part of the region is the dust lane where A_V = 1.7 mag, as deduced from the optical Hα / Hβ ratio. Elsewhere the ratio is smaller, with an average value of 3.7 corresponding to A_V = 0.8 mag. N 66A also presents

a high degree of excitation, particularly at the north-eastern border where the [O III] λ 5007/Hβ ratio reaches its highest value of 5 (Heydari-Malayeri & Selier 2010).

Figure 1: A composite three-color image of SMC N 66A created using the *HST* ACS images in Hα (red), filter *I* (green), and filter *V* (blue). Field size : 26″ x 26″ ($\sim 7.5 \times 7.5$ pc). From Heydari-Malayeri & Selier (2010).

2.2 Stellar content

Figure 2 shows the spectrum of the main exciting star of N 66A, called N 66A-1. Spectral classification was performed using the criteria of Walborn & Fitzpatrick (1990). The spectral features used are the high absorption of He II λ 4686, and the predominance of He II λ 4541 over He I λ 4471. We classified N 66A-1 as O8 V (Heydari-Malayeri & Selier 2010).

We also evaluated the ionizing flux of the exciting star. First we calculated the total Hβ flux emitted by N 66A. Then we computed the reddening corrected Hβ intensity. It corresponds to a Lyman continuum flux of 3.4 x 10^{48} photons.s^{-1}, assuming that the H II region is ionization bounded (Heydari-Malayeri & Selier 2010). The exciting star needed to provide this flux is of spectral type about O7.5 V according to stellar atmosphere model results (Martins, Schaerer & Hillier 2005). This estimate agrees well with the spectral classification given above.

Note that the derived value of the stellar Lyman continuum is probably an underestimate. Indeed the H II region is not fully ionization-bounded, a part of the ionizing photons escape into the interstellar medium. Thus, the spectral classification based on spectroscopy is also an underestimate. This

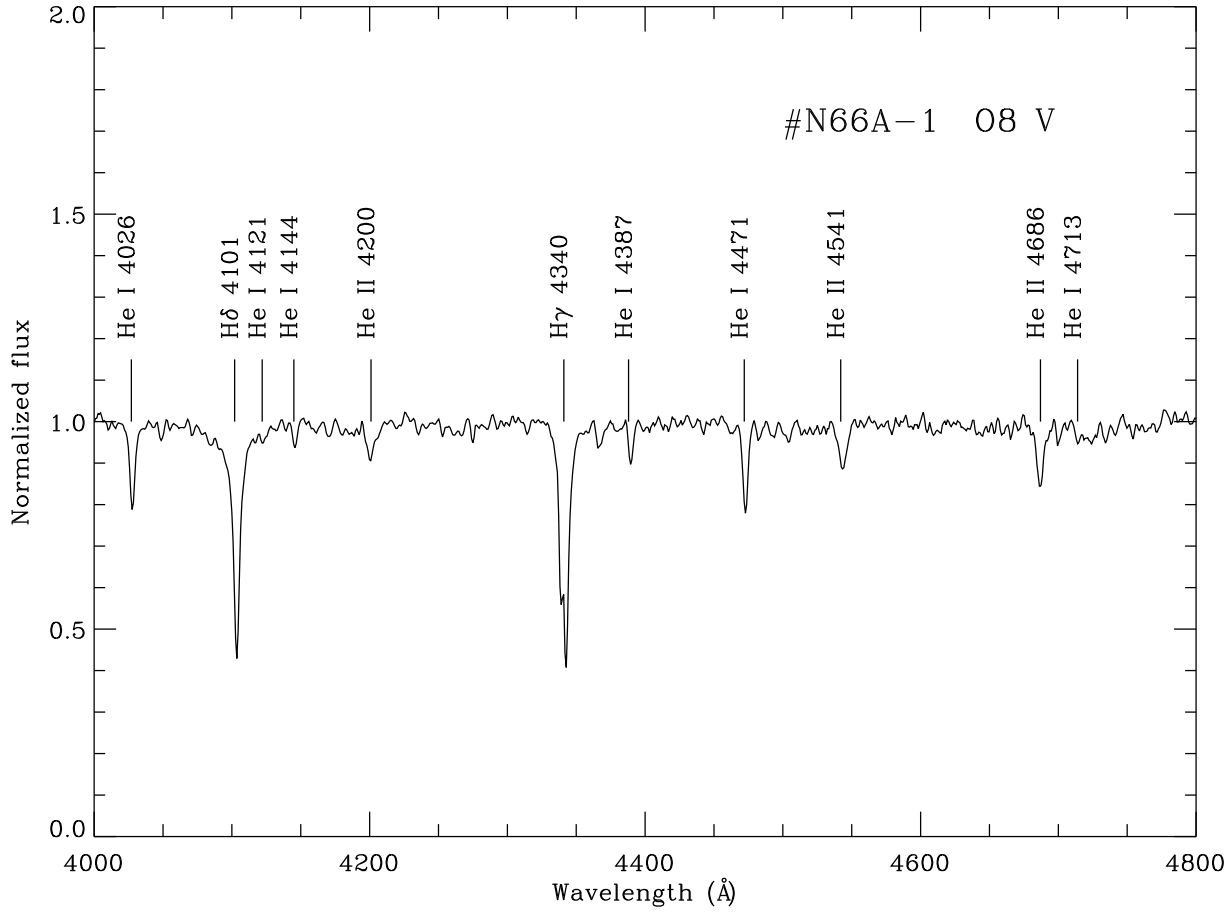

Figure 2: Spectrogram of N 66A-1 obtained with the spectrograph EMMI on the ESO NTT telescope (adapted from Heydari-Malayeri & Selier 2010).

is probably because the spectrum of N 66A-1 is contaminated by the closest neighboring star, called N 66A-2. If star #2 were of later type than star #1 the latter would be earlier than O8 V.

3 Discussion

The compact H II region N 66A is powered by a couple of massive stars, which represent a relatively younger generation in the N 66 complex. N 66A is associated with a compressed ionized front and an absorption lane. These observations suggest that its formation results from triggering by a previous generation of massive stars in the complex (Heydari-Malayeri & Selier 2010). This suggestion of a younger age for the exciting stars of N 66A agrees perfectly with other studies of this region. For example Gouliermis et al. (2008) note that the whole N 66 region may host younger star formation events induced from the east. Interestingly N 66A lies on this triggered formation arc.

N 66A is the most compact H II region of the N 66 complex in the optical. Moreover it presents a high excitation ratio and is marked by a prominent absorption lane of local dust (Sect. 2.1). These properties classify N 66A as a member of a rare class of H II regions in the Magellanic Clouds (MCs) called High-Excitation Blobs (HEBs). The two other known examples of HEBs in the SMC are N 88A and N 81 (Heydari-Malayeri et al. 1999a, b, 2002). These objects are very dense and small regions usually 5 to 10″in diameter ($\sim$ 1.5 to 3 pc) in contrast to the typical H II regions in the MCs. They

are characterized by a higher degree of excitation and are heavily affected by local dust. Although the formation mechanisms of these objects are not yet well understood, it seems sure that they represent the youngest massive stars reachable through IR and optical techniques. Therefore they offer a good compromise between massive stars "at birth", embedded in ultra-compact H II regions, and those in evolved, classical H II regions.

References

Gouliermis D. A., Dolphin A. E., Brandner W., Henning T., 2006, ApJS, 166, 549
Gouliermis D. A., Chu Y.-H., Henning T. et al. 2008, ApJ, 688, 1050
Hennekemper E., Gouliermis D. A., Henning T. et al. 2008, ApJ, 672, 914
Heydari-Malayeri M., Rosa M. R., Zinnecker H., Deharveng L., Charmandaris V., 1999a, A&A, 344, 848
Heydari-Malayeri M., Charmandaris V., Deharveng L., Rosa M. R., Zinnecker H., 1999b, A&A, 347, 841
Heydari-Malayeri M., Rosa M. R., Schaerer D., Martins F., Charmandaris V., 2002, A&A, 381, 951
Heydari-Malayeri M., Selier R., 2010, A&A, 517, A39
Martins F., Schaerer D., Hillier D. J., 2005, A&A, 436, 1049
Massey P., Parker J. W., Garmany C. D., 1989, AJ, 98, 1305
Nota A., Sirianni M., Sabbi E. et al. 2006, ApJ, 640, L29
Sabbi E., Sirianni M., Nota A. et al. 2007, AJ, 133, 44
Walborn N. R., Fitzpatrick E. L., 1990, PASP, 102, 379

The chemical composition of the Orion star forming region: stars, gas and dust

S. Simón-Díaz[1,2], M. F. Nieva[3], N. Przybilla[4] and G. Stasińska[5]

[1] Instituto de Astrofísica de Canarias, E-38200 La Laguna, Tenerife, Spain.
[2] Departamento de Astrofísica, Universidad de La Laguna, E-38205 La Laguna, Tenerife, Spain
[3] Max-Planck-Institut für Astrophysik, Karl-Schwarzschild-Str. 1, D-85741 Garching, Germany
[4] Dr. Karl Remeis-Sternwarte & ECAP, Sternwartstr.7, D-96049 Bamberg, Germany
[5] LUTH, Observatoire de Paris, CNRS, Université Paris Diderot, F-92190 Meudon, France

Abstract: We present a summary of main results from the studies performed in the series of papers *The chemical composition of the Orion star forming region*. We reinvestigate the chemical composition of B-type stars in the Orion OB1 association by means of state-of-the-art stellar atmosphere codes, atomic models and techniques, and compare the resulting abundances with those obtained from the emission line spectra of the Orion nebula (M42), and recent determinations of the Solar chemical composition.

1 Introduction

For many years, our knowledge about the chemical composition of early-B main sequence stars in the Solar vicinity has been characterized by two main results: (i) the derived abundances were highly inhomogeneous (with a dispersion of up to 0.5 dex), and (ii) the mean values indicated lower abundances than the standard set of Solar abundances (Grevesse & Sauval 1998, GS98) Some recent results have begun to change this situation. The Solar oxygen abundance traditionally considered as a cosmic abundance reference (GS98) was revised by Asplund et al. (2004) to a value of ϵ(O) = 8.66 dex, 0.17 dex lower than the standard value. This was the beginning of what has been called the epoch of the "solar crisis": between 2004 and 2008, several studies by different authors (see references in Simón-Díaz 2010) presented solar oxygen abundances derived by means of different approaches. The calculated values range from 8.63 dex (Socas-Navarro & Norton 2007) to 8.86 dex (Centeno & Socas-Navarro 2008). The debate about its actual value is still open[1]. Przybilla, Nieva & Butler (2008, PNB08) analyzed a representative sample of six unevolved early B-type stars in nearby OB associations and the field, and found a very narrow distribution of abundances, with mean values that are larger compared to previous works. PNB08 indicate the importance of properly determining the atmospheric parameters and using robust model atoms to avoid systematic errors in the abundance determination. The study by PNB08 shows that the chemical inhomogeneity previously found for B-type stars in the Solar vicinity may be spurious as a consequence of those systematic errors.

[1]The present solar O abundance indicated in Asplund et al. (2009) is 8.69 dex.

1.1 Orion OB1 and M 42

The Orion complex, containing the Orion molecular cloud and the Orion OB1 (Ori OB1) association, is one of the most massive active star-forming regions in the 1 kpc centered on the Sun. Blaauw (1964) divided Ori OB1 into four subgroups of stars, namely Ia, Ib, Ic, and Id, having different locations in the sky and different ages. Brown et al. (1994) derived mean ages of 11.4, 1.7, 4.6, and <1 Myr for subgroups Ia to Id, respectively. The youngest subgroup Ori OB1 Id is associated with the Orion nebula (M 42), the brigthest and most studied H II region and the closest ionized nebula to the Sun in which a high accuracy abundance analysis can be performed. The correlation between the ages of the stellar subgroups, their location, and the large scale structures in the interstellar medium around Ori OB1 have been interpreted as features of sequential star formation and Type-II supernovae (Reynolds & Ogden 1979, Cowie et al. 1979, Brown et al. 1994).

1.2 B-type star abundances in Orion

Cunha & Lambert (1992, 1994, CL92,94) obtained C, N, O, Si, and Fe abundances of 18 B-type main sequence stars from the four subgroups comprising the Ori OB1 association. They found a range in oxygen abundances of 0.4 dex, with the highest values corresponding to the stars in the youngest (Id and some Ic) subgroups. In this case, the inhomogeneity in stellar abundances (mainly oxygen and silicon) seemed to be real and coherent with a scenario of induced star formation in which the new generation of stars were formed from interstellar material contaminated by Type-II supernovae ejecta. The study by CL92,94 was based on a photometric estimation of $T_{\rm eff}$ and the fitting of the Hγ line computed from Kurucz (1979) LTE model atmospheres to derive $\log g$. In view of the results by PNB08 a reinvestigation of the chemical composition of B-type stars in Ori OB1 was warranted.

In the series of papers *The chemical composition of the Orion star forming region* we aimed at (i) investigating whether the inhomogeneity of B-type star abundances previously found is real, and (ii) comparing the derived abundances with recent determinations of the Solar chemical composition, abundances in other B-type stars in the Solar vicinity, and the nebular abundances derived from the emission line spectrum of the Orion nebula. We summarize here the main results from three papers in the series.

2 Homogeneity of O and Si abundaces in B-type stars

In Simón-Díaz (2010, Paper I) we investigated whether the inhomogeneity of abundances previously found in B-type stars in the Ori OB1 association is real or a consequence of intrinsic errors induced by the use of photometric indices to establish the stellar parameters prior to the abundance analysis. We obtained a high quality spectroscopic data set comprising 13 B-type stars in the various Ori OB1 associations (see Simón- Díaz et al. 2011), and performed a detailed, self-consistent spectroscopic NLTE abundance analysis by means of the modern stellar atmosphere code FASTWIND (Puls et al. 2005).

Main results of this study are summarized in Figure 1 and Table 1. We detected systematic errors in the stellar parameters determined previously which affected the derived abundances. Once these errors were accounted for, we find a high degree of homogeneity in the O and Si abundances for stars in the four Ori OB1 subgroups. The dispersion of abundances for the 13 stars is smaller than the intrinsic uncertainties (0.10 and 0.08 dex for O and Si, respectively).

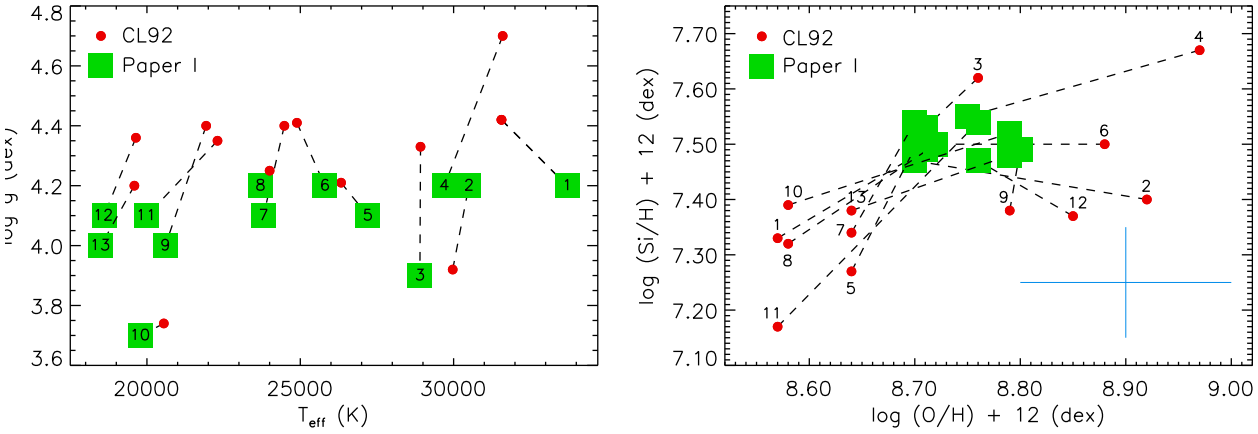

Figure 1: Comparison of stellar parameters, and O and Si abundances derived in Paper I and CL92. The cyan cross represents the mean intrinsic uncertainties for O and Si abundances. Numbering follows the order in Table 2 from the original paper.

Table 1: Mean O and Si abundances derived from stars in each of the subgroups in Ori OB1. The global mean abundances are also indicated (FASTWIND analysis, Paper I).

Group	ϵ(O)	ϵ(Si)
Ia	8.77±0.04	7.50±0.02
Ib	8.70±0.01	7.53±0.01
Ic	8.74±0.04	7.50±0.03
Id	8.72±0.04	7.51±0.06
Global	8.74±0.04	7.51±0.03

Table 2: Mean C, N, Ne, Mg and Fe abundances from B stars in Ori OB1 (ADS analysis, Paper III). Intrinsic uncertaintites from individual star analyses are indicated in parentheses.

Element	Mean abundance
C	8.35±0.03 (0.09)
N	7.82±0.07 (0.09)
Ne	8.09±0.05 (0.09)
Mg	7.57±0.06 (0.03)
Fe	7.50±0.04 (0.10)

The mean oxygen and silicon abundances agree with those resulting from a similar analysis of a representative sample of unevolved early B-type stars in the Solar neighbourhood (PNB08). Both results indicate that abundances derived from these stellar objects are more homogeneous and metal rich than previously thought.

We also compared the O and Si stellar abundance in Ori OB1 with those obtained for the Sun during the epoch of the "solar crisis". The O abundances in our sample of stars in Ori OB1 lay in the middle of all these values. In view of the present-day results the only thing we can say is that oxygen abundances in the Sun and B-type stars in the solar vicinity are the same within the uncertainties. However, we consider too premature to launch any firm conclusion or hypothesis about the chemical evolution of the local interstellar medium during the lifetime of the Sun. Silicon abundances are also very similar (contrarily to what was previously found from the study of B-type stars).

3 C, N, Ne, Mg, and Fe abundances in B-type stars revisited

In view of the results found in Paper I, a reinvestigation of other stellar abundances was warranted. In Nieva & Simón-Díaz (in prep., paper III) we derive C, N, Ne, Mg and Fe NLTE abundances for the stars analyzed in Paper I, following the procedure described in Nieva & Przybilla (2007, 2008). The strategy (ADS analysis) is based on a similar self-consistent spectroscopic analysis, but using

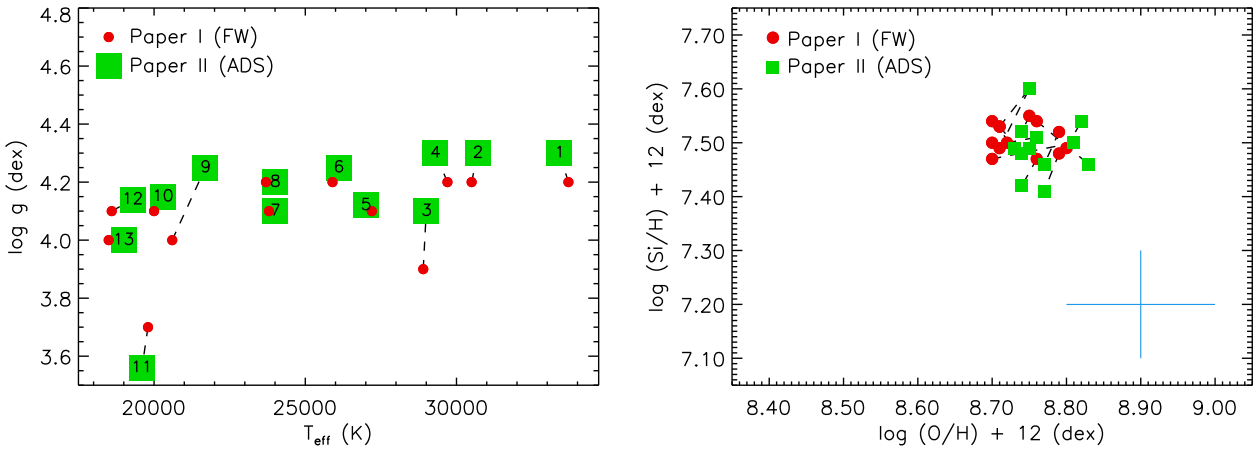

Figure 2: Comparison of stellar parameters, and O and Si abundances derived in Papers I and III (FW and ADS analyses, respectively). The cyan cross represents the mean intrinsic uncertainties for O and Si abundances. Same numbering as in Fig. 1.

ATLAS9 (Kurucz 1993) + DETAIL+SURFACE (Giddings 1981, Butler & Giddings 1985, plus recent updates).

We first compare the stellar parameters, O and Si abundances resulting from the FASTWIND (FW) and ADS analyses to be sure that both techniques provide similar results (see Figure 2). We find very good agreement within the uncertainties. Then we obtain abundances for C, N, Ne, Mg, and Fe by means of the ADS analysis (see final mean values from the analysis of 13 stars in the various subgroups from Ori OB1 in Table 2). Again, the dispersion of abundances for the 13 stars is smaller than the intrinsic uncertainties, indicating a high degree of homogeneity in the present-day abundances of these elements in the Orion star forming region (as derived from B-type stars).

4 Stars, gas and dust: the abundance discrepancy conundrum

In Simón-Díaz & Stasińska (2011, paper II), we re-examined the nebular abundance discrepancy problem which arises from the use of recombination lines (RL) on the one hand and collisionally-excited lines (CEL) on the other (see García-Rojas & Esteban 2007, and references therein) in the light of the high quality abundance determinations for B-type stars performed in Papers I and III. We reevaluated the CEL and RL abundances of several elements in the Orion nebula using the spectroscopic data set presented by Esteban et al. (2004) and ionization correction factors (ICFs) for unseen ions obtained by means of a photonization model suited for our purposes. The derived nebular abundances are compared with the mean stellar abundances obtained in Papers I and III (see Fig. 3). In particular, for the case of oxygen, we estimated the amount of oxygen trapped in dust grains for several scenarios for dust formation and compare the resulting gas+dust nebular abundances with the stellar abundances. Our study leads us to the conclusion that the oxygen abundances derived in the Orion nebula from CELs are incompatible with the abundances derived in the B stars (once the effects of depletion in dust grains are taken into account) while RL oxygen abundances are in better agreement (see Fig. 4).

References

Asplund, M., Grevesse, N., Sauval, A. J., et al. 2004, A&A, 417, 751

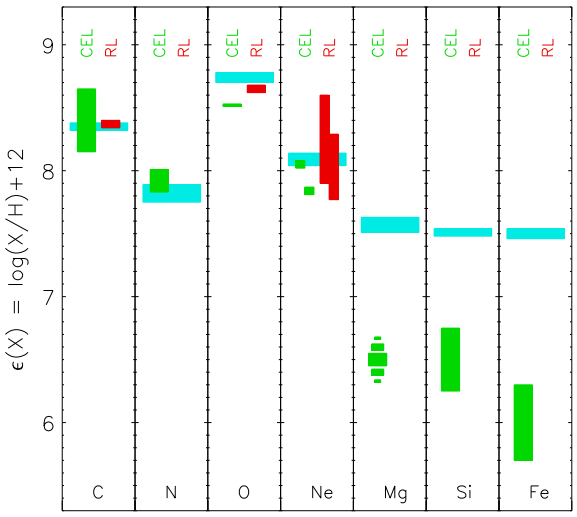

Figure 3: Comparison of C, N, O, Ne, Mg, Si and Fe abundances obtained from B-type stars (cyan), CEL (green), and RL (red). For Ne, there are two green boxes, corresponding to different ICFs (see paper II). The height of the boxes represents the uncertainties. Note that for Mg there is no evaluation of the uncertainty. A more detailed comparison (also including dust depletion) for oxygen is presented in Fig. 4.

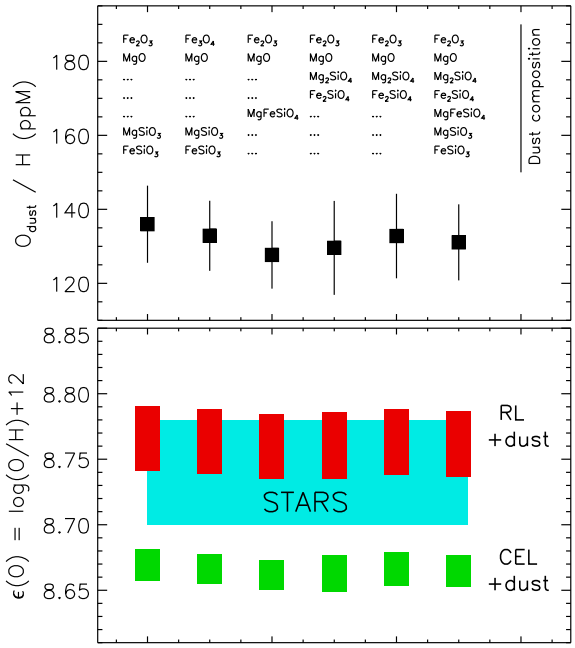

Figure 4: Upper panel: Amount of oxygen expected to be in solid form for various dust composition scenarios (see paper II). Lower panel: Comparison of the stellar oxygen abundance (wide cyan rectangle) with the gas+dust oxygen abundance in the nebula for the different dust scenarios. Green rectangles are obtained with CEL gas abundances, red rectangles are obtained with RL gas abundances.

Asplund, M., Grevesse, N., Sauval, A. J., Scott, P. 2009, ARA&A, 47, 481
Blaauw, A. 1964, ARA&A, 2, 213
Brown, A. G. A., de Geus, E. J., & de Zeeuw, P. T. 1994, A&A, 289, 101
Butler, K., & Giddings, J. R. 1985, in Newsletter of Analysis of Astronomical Spectra, No. 9 (Univ. London)
Cowie, L. L., Songaila, A., & York, D. G. 1979, ApJ, 230, 469
Centeno, R., & Socas-Navarro, H. 2008, ApJL, 682, L61
Cunha, K., & Lambert, D. L. 1992, ApJ, 399, 586
Cunha, K., & Lambert, D. L. 1994, ApJ, 426, 170
Esteban, C., Peimbert, M., García-Rojas, J., et al. 2004, MNRAS, 355, 229
García-Rojas, J., & Esteban, C. 2007, ApJ, 670, 457
Giddings, J. R. 1981, Ph.D. Thesis (Univ. London)
Grevesse, N., & Sauval, A. J. 1998, Space Sci. Rev., 85, 161
Kurucz, R. 1979, ApJS, 40, 1
Kurucz, R. 1993, CD-ROM No. 13 (SAO, Cambridge, MA)
Nieva M.F., Przybilla N. 2007, A&A, 467, 295
Nieva M.F., Przybilla N. 2008, A&A, 481, 199
Przybilla, Nieva & Butler 2008, ApJ, 688, L103
Puls, J., Urbaneja, M. A., Venero, R., et al. 2005, A&A, 435, 669
Reynolds, R. J., & Ogden, P. M. 1979, ApJ, 229, 942
Simón-Díaz, S. 2010, A&A, 510, A22
Simón-Díaz, S., & Stasińska, G. 2011, A&A 526, A48
Simón-Díaz, S., Castro, N., Garcia, M., Herrero, A., & Markova, N. 2011, in Proceedings of the 39th Liège Astrophysical Colloquium, eds. G. Rauw, M. De Becker, Y. Nazé, J.-M. Vreux & P.M. Williams, BSRSL 80, 514
Socas-Navarro, H., & Norton, A. A. 2007, ApJL, 660, L153

On the periodic class II methanol masers in the high mass star forming region G9.62+0.20E

DJ van der Walt*

Centre for Space Research, North-West University, Potchefstroom, 2520, South Africa

Abstract: Class II methanol masers are known to be exclusively associated with high mass star forming regions. The phenomenon of periodic methanol masers associated with a small number of star forming regions is now known for a number of years. The underlying process(es) responsible for the periodicity is not known however. In this paper I present a simple colliding-wind scenario to try explain the periodicity and the flare profiles of the periodic flaring of the class II masers in the high-mass star forming region G9.62+0.02E. It is found that the 12.2 GHz methanol maser time series as well as the profiles of individual flares are reproduced very well under the assumption that the observed flaring is due to changes in the free-free background emission from the H II region. A number of other properties of the masers can also be explained within the framework of this model. It is concluded that a colliding-wind binary is a possible underlying cause for the periodic class II masers in G9.62+0.20E and should be investigated further.

1 Introduction

A significant recent discovery in the field of astrophysical masers is that a small number of class II methanol masers show periodic or regular variability at 6.7, 12.2, and 107 GHz (Goedhart, Gaylard & van der Walt 2003; Goedhart, Gaylard, & van der Walt 2004; Goedhart, Gaylard & van der Walt 2007; Goedhart et al. 2009; van der Walt, Goedhart, & Gaylard 2009). Except also for the detection of quasi-periodic flaring of formaldehyde masers in IRAS 18566+0488 (Araya et al. 2010) no similar variability has yet been detected for other masing molecules associated with star forming regions. This suggests that for some reason yet unknown, the class II methanol masers in some high-mass star forming regions are sensitive to a periodic/regular phenomenon associated with these massive star forming regions. The underlying physical mechanism that drives the periodicity is, however, not yet known.

As for the maser variability, on the one hand, it might be due to changes in the physical conditions in the masing region itself which affect the population inversion. On the other hand the variability may be due to changes in the background radiation field that is amplified. Given the regularity of the flaring of these masers, it is reasonable to assume that only one of the above mechanisms is responsible for the observed behaviour of these maser. Whether it is the same mechanism that is responsible for the periodic flaring of the masers in all the periodic sources is not clear at all.

*johan.vanderwalt@nwu.ac.za

Recently van der Walt et al. (2009) presented an analysis of the periodic class II masers in G9.62+0.20E. In trying to find an underlying cause for the periodicity, these authors focused on the decay behaviour of the *average* profile of the 1.25 $\mathrm{km\,s^{-1}}$ feature of the 12.2 GHz masers. These authors excluded the variability of the masers being due to changes in the pumping infrared radiation field as a result of the heating and cooling of dust due to the short cooling time of dust. On the other hand, the decay time scale agrees very well with what can be expected of the recombination of a thermal hydrogen plasma with an electron density of about 5×10^5 $\mathrm{cm^{-3}}$. On the basis of this behaviour, van der Walt et al. (2009) suggested that the flaring of the masers might be due to changes in the free-free emission from those parts of the H II region against which the flaring maser features are projected. Periodic changes in the free-free emission are directly related to changes in the electron density which implies periodic changes in the ionization rate. The most likely cause for changes in the ionization rate is a change in the flux of ionizing photons, suggesting that a pulse of ionizing radiation periodically propagates into the H II region. As a possible source of the ionizing pulse a colliding-wind binary system seems to be a possible candidate.

As mentioned above, the suggestion by van der Walt et al. (2009) that the flaring of the masers in G9.62+0.20E might be due to the orbital modulation of the ionizing radiation emitted by the hot post-shock gas in a colliding-wind binary system, was based only on the decay of the flare. Here we investigate in somewhat more detail whether a colliding-wind binary can explain the full flare profile as well as the time series of the 12.2 GHz masers in G9.62+0.20E.

At present there is no explicit observational evidence indicating that G9.62+0.20E is a colliding-wind binary or even just a binary system. Also no observational data exists on wind and orbital parameters except for the association of the periodic methanol masers with a period of 244 days. Modelling of the system based on known values of physical quantities is therefore not possible. We show however, that the flare profiles as well as the time series can be explained in terms of a simple scenario where the maser flaring is due to changes in the free-free background seed photon flux following the passage of an ionization pulse through a partially ionized part of the H II region against which the masers are projected and where the time-dependence of the pulse is as expected for the adiabatic case for a colliding-wind binary.

2 Theory

The time-dependence of the electron density in a part of the H II region where the gas is partially ionized is given by

$$\frac{dn_e}{dt} = -\alpha n_e^2 + [\Gamma_\star + \Gamma_p(t)] n_{\mathrm{H^0}} \tag{1}$$

where $\alpha = 2.59 \times 10^{-13}\,\mathrm{cm^3 s^{-1}}$ is the hydrogen recombination coefficient, $\Gamma_\star$ the constant ionization rate at that particular position due to ionizing radiation either directly from the the star and/or the diffuse ionizing radiation from the H II region, $\Gamma_p(t)$ the time dependent ionization rate at the same position due to the ionization pulse alone, and $n_{\mathrm{H^0}}$ the neutral hydrogen number density also at the same position. The first term on the right gives the decrease of the electron density due to recombinations and the second term the production of electrons due to photoionizations. n_e and $n_{\mathrm{H^0}}$ are both time dependent and are related through $n_{\mathrm{H^0}} + n_e = n_{\mathrm{H}}$ with n_{H} the total hydrogen number density at that position in the H II region.

As for the time dependence of the ionization pulse we adopt the working hypothesis that the pulse is produced due to emission from hot post-shocked gas produced by the colliding winds in a binary system. As a starting point we furthermore assume that the shocked gas cools adiabatically implying that L_{shock}, the luminosity of the shocks, is inversely proportional to r, the distance between the two stars. The constant ionization rate $\Gamma_\star$ due to the stellar and diffuse nebular ionizing radiation at the

position of interest in the H II region is by definition given by $\Gamma_\star = \alpha n_e^2/n_{\rm H^0}$. The ionization pulse was normalized such that at apastron $\Gamma_p(t) = \beta\Gamma_\star$ with $\beta > 0$.

The time dependence of r^{-1} was calculated numerically using Kepler's second law in the form

$$r^2\frac{d\theta}{dt} = \frac{L}{\mu} \tag{2}$$

where $\mu = m_1 m_2/(m_1 + m_2)$ and $L = \mu\sqrt{G(m_1 + m_2)a(1 - \epsilon^2)}$ is the angular momentum. The time step was taken as one fifth of a day. The orbital parameters were calculated using stellar masses of 17 $\rm M_\odot$ and 8 $\rm M_\odot$ following van der Walt et al. (2009).

3 Results

The free parameters involved are $n_{\rm H}$, $n_{e,\star}$, β, and the eccentricity, ϵ, with $n_{e,\star}$ the equilibrium electron density at the position of interest in the H II region due to the stellar and diffuse ionizing radiation. To fit the time series it was first of all necessary to find combinations of the above parameters such that the relative amplitude (= $(S_{max} - S_{min})/S_{min}$) is equal to that of the observed flares which in the case of the 12.2 GHz 1.25 $\rm km\ s^{-1}$ feature in G9.62+0.20E is equal to 2.17. Exploration of parameter space showed that the solution is not unique but that a given relative amplitude can be produced by various combinations of $n_{\rm H}$, $n_{e,\star}$, β, and ϵ. Further exploration of parameter space and comparison of the model flare profiles with the data showed that $\epsilon \simeq 0.9$ is the best choice for the eccentricity.

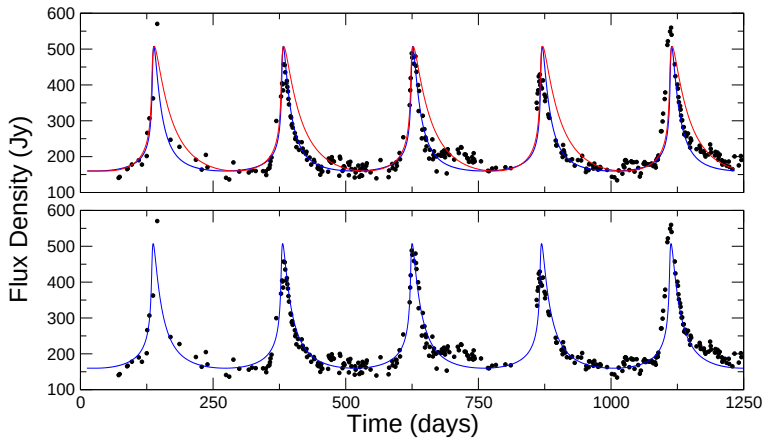

Figure 1: Comparison of the observed 12.2 GHz time series of the 1.25 $\rm km\,s^{-1}$ feature and the model time series. The relative amplitude is equal to 2.17. Top panel: $n_H = 7.5 \times 10^6$ $\rm cm^{-3}$. Blue: $\beta = 0.5$, $n_{e,\star} = 7.62 \times 10^5$ $\rm cm^{-3}$. Red: $\beta = 2$, $n_{e,\star} = 1.78 \times 10^5$ $\rm cm^{-3}$. Bottom panel: $n_H = 3.0 \times 10^6$ $\rm cm^{-3}$. Blue: $\beta = 1.35$, $n_{e,\star} = 7.62 \times 10^5$ $\rm cm^{-3}$.

We will not present all possible examples of the different combinations of parameter values that can reproduce the observed time series. Instead, in Fig. 1 we show just two examples of a good reproduction of the time series and one to indicate the effect of changing the equilibrium electron density, $n_{e,\star}$. The parameter values for the three cases are given in the figure caption. Comparison of the model results show that the rise times of the flares are similar and agree fairly well with the observed time series. The decay of the flare for $n_{e,\star} = 1.78 \times 10^5$ $\rm cm^{-3}$ is seen to be longer than for $n_{e,\star} = 7.62 \times 10^5$ $\rm cm^{-3}$. The difference in decay times simply reflects the fact that the recombination time for a higher density plasma is shorter than for a lower density plasma.

4 Discussion

The agreement of the "model" with the observed time series as shown in Fig. 1 is quite remarkable especially if its simplicity is considered. Given the agreement, a logical conclusion is therefore that the periodic flaring of the methanol masers in G9.62+0.20E might indeed be due to changes in the free-free emission from the H II region. As already mentioned above, a possible mechanism underlying this behaviour is that G9.62+0.20E is a colliding-wind binary system and the possibility of this being the case should be considered further.

Given the fact that the recombination rate of a hydrogen plasma depends on the equilibrium electron density, means that, at least in the case of G9.62+0.20E, the maser behaviour gives us an indication of the electron density at the distance the maser is projected from the core of the H II region. Applied to G9.62+0.20E it means that along the line of sight at a projected distance of about 5×10^{15} cm (using the distance of 5.2 kpc given by Sanna et al. 2009) from the core, the electron density is about 7.6×10^5 cm^{-3}. The total gas density is however not fixed by the fit. A lower limit can, however be set.

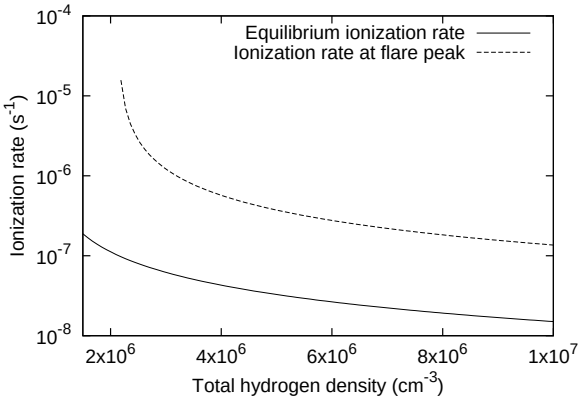

Figure 2: Required ionization rates as a function of total hydrogen density.

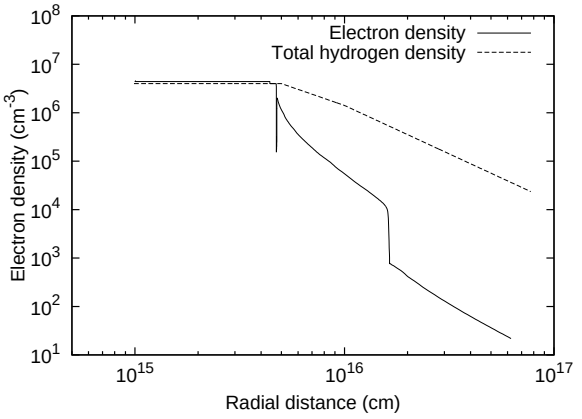

Figure 3: *Example* of the ionization structure of the H II region that may explain the flaring of the masers.

In the optically thin case we have that the free-free intensity $I \propto n_e^2$. Given that the relative amplitude of the flares is about 2.17 it follows that $S_{max}/S_{min} = 3.17$ and therefore that $n_{e,max}/n_{e,min} = \sqrt{3.17} = 1.78$. The minimum total gas density then is about 1.4×10^6 cm^{-3}. The ionization rate due to the star and the diffuse nebular emission required is thus 2.4×10^{-7} s^{-1}. In this case, it is then required that the gas be fully ionized at the peak of the flare in order for the free-free emission to increase by a factor of 3.17. However, the ionization rate required to raise the ionization level to 100% becomes too large to be realistic. In Fig. 2 are shown the ionization rate as a function of total hydrogen density for an equilibrium electron density of 7.6×10^5 cm^{-3} and the required ionization rate at the peak of the flare. The sharp increase in the required ionization rate toward lower total hydrogen densities is obvious.

As already mentioned above, if the interpretation of the maser flaring is correct, it implies that the electron density be about 7.6×10^5 cm^{-3} at a projected distance of about 5×10^{15} cm from the core of the H II region. This then also raises the question of the ionization structure of the H II region. Using the photoionization package Cloudy (Ferland et al. 1998), we briefly examined possible total hydrogen density distributions that will give rise to an electron density distribution such that at a distance of a few times 10^{15} cm the gas is partially ionized and that the electron density is such that the flaring of the masers can be explained. In Fig. 3 we show an *example* where the total hydrogen

density has constant value of 4×10^6 cm^{-3} up to 5×10^{15} cm after which it decreases following two power laws. The ionizing star was of spectral type O9.5 with $T_{\rm eff} = 36400$ K and $\log Q_{\rm H} = 48.26$ (Sternberg, Hoffmann & Pauldrach 2003). The gas is seen to be fully ionized up to about 5×10^{15} cm at which the electron density sharply drops and the ionized fraction falls to about 4%. It then rises again to a local maximum after which it decreases smoothly.

Within the framework of a colliding-wind binary system as the mechanism for producing a pulse of ionizing radiation, the ionization structure as shown in Fig. 3 seems to be what is needed. Since the H II region is basically fully ionized up to before the sharp drop in the ionization level, a pulse of ionizing photons can propagate almost unattenuated until it reaches the "wall" of non-ionized gas where it deposits its energy and temporarily raises the electron density.

We also note that in order to produce the ionization structure as shown in Fig. 3 it was necessary to assume that the ionizing star is of spectral type O9.5 and not B1 as given by Franco et al. (2000). Using a B1 type star simply cannot produce the sharp decrease in ionized fraction at 5×10^{15} cm but only at much smaller distances. Raising the total hydrogen density above 4×10^6 cm^{-3} will require an even earlier O-type star to produce a similar ionization structure.

5 Summary and Conclusions

We have shown that the observed 12.2 GHz maser time series in G9.62+0.20E can be reproduced very well by assuming that the flaring of the masers is due to changes in the background free-free emission produced by a pulse of ionizing radiation raising the electron density after which it decays to the equilibrium density as determined by the presence of the star and the diffuse nebular emission. The pulse has a time dependence expected for the change in luminosity in the adiabatic case from the post-shock gas in a colliding-wind binary system. This result strongly suggests the hypothesis that the maser flaring is due to changes in the free-free background emission from the H II region might be correct.

The following are some aspects that need further attention: (1) A more detailed investigation into whether a colliding-wind binary system can indeed produce the required change in ionization rate to explain the change in free-free emission at a distance of $5 - 7 \times 10^{15}$ cm from the core of the H II region. (2) Coupled to the above, it is necessary to explore other realistic density distributions to explain the partially ionized gas at a distance of about $5 - 7 \times 10^{15}$ cm from the core of the H II region and to link this with the microwave spectral energy distribution of this region. (3) It is necessary to revise the spectral type of the ionizing star associated with G9.62+0.20E

References

Araya, E.D., Hofner, P., Goss, W.M., et al. 2010, ApJ 250, 645
Ferland, G.J., Korista, K.T., Verner, D.A., et al. 1998, PASP 110, 761
Franco, J., Kurtz, S., Hofner, P., et al. 2000, ApJ 542, L143
Goedhart, S., Gaylard, M.J., & van der Walt, D.J. 2003, MNRAS 339, L33
Goedhart, S., Gaylard, M.J., & van der Walt, D.J. 2004, MNRAS 355, 553
Goedhart, S., Gaylard, M.J., & van der Walt, D.J. 2007, in IAU Symposium, 242, eds. J.M. Chapman, W.A. Baan, 97
Goedhart, S., Langa, M.C., Gaylard, M.J., & van der Walt, D.J. 2009, MNRAS 398, 995
Sanna, A., Reid, M.J., Moscadelli, L., et al. 2009, ApJ 706, 464
Sternberg, A., Hoffmann, T.L., & Pauldrach, A.W.A. 2003, ApJ 599, 1333
van der Walt, D.J., Goedhart, S., & Gaylard, M.J. 2009, MNRAS 398, 961

Chapter 3

Evolution and interaction of massive stars with their environment

Red Supergiants, Luminous Blue Variables and Wolf-Rayet stars: the single massive star perspective

Georges Meynet[1], Cyril Georgy[1], Raphael Hirschi[2], André Maeder[1],
Phil Massey[3], Norbert Przybilla[4], M.-Fernanda Nieva[5]

[1] Geneva Observatory, University of Geneva, Maillettes 51, 1290 Sauverny, Switzerland

[2] Astrophysics Group, EPSAM Institute, University of Keele, Keele, ST5 5BG, UK

[3] Lowell Observatory, 1400 W Mars Hill Road, Flagstaff, AZ 86001, USA

[4] Dr. Karl Remeis-Observatory & ECAP, Sternwartstr. 7, 96049 Bamberg, Germany

[5] Max-Planck-Institut fur Astrophysik, Karl-Schwarzschild-Str. 1, 85741 Garching, Germany

Abstract: We discuss, in the context of the single star scenario, the nature of the progenitors of Red Supergiants (RSG), of Luminous Blue Variables (LBV) and of Wolf-Rayet (WR) stars. These three different populations correspond to evolved phases of Main-Sequence (MS) OB stars. Axial rotation and mass loss have a great influence on massive star evolution in general and more specifically on the durations of these different phases. Moderate rotation and mass loss, during the MS phase, favor the evolution towards the RSG stage. Fast rotation and strong mass loss during the MS phase, in contrast, prevent the star from becoming a RSG and allow the star to pass directly from the OB star phase into the WR phase. Mass loss during the RSG stage may make the star evolve back in the blue part of the HR diagram. We argue that such an evolution may be more common than presently accounted for in stellar models. This might be the reason for the lack of type IIP SNe with RSG progenitors having initial masses between 18 and 30 $M_{\odot}$. The LBVs do appear as a possible transition phase between O and WR stars or between WNL and WNE stars. Fast rotation and/or strong mass loss during the Main-Sequence phase prevent the formation of LBV stars. The mechanisms driving the very strong ejections shown by LBV stars are still unknown. We present some arguments showing that axial rotation together with the proximity of the Eddington limit may play a role in driving the shell ejections. Rotation and mass loss favor the formation of Wolf-Rayet stars. The fact that WR stars and RSGs rarely occur in the same coeval populations indicates that the mass range of these two populations is different, WR stars originating from more massive stars than RSGs. Single star evolution models predict variations with the metallicity of the number ratios of Type Ibc to Type II supernovae, of Type Ib to Type II and of Type Ic to Type II, which are compatible with observations, provided that many stars leaving a black hole as a remnant produce an observable supernova event.

1 Introduction

Red Supergiants (RSG), Luminous Blue Variables (LBV) and Wolf-Rayet (WR) stars represent phases during which the star may lose large amounts of mass by stellar winds and/or strong shell ejections. These mass loss events are on the whole still not well understood. Our ignorance of their driving mechanisms, amplitudes, durations, metallicity dependence is in great part responsible for the uncertainties pertaining the results of stellar models. Very schematically, the evolutionary scenarios, at solar metallicity, for single massive stars follow the sequences shown below:

$M > 90 M_{\odot}$: O - Of - WNL - (WNE) - WCL - WCE - SN(SNIbc/BH/SNIIn)? (PCSN/Hypernova low Z?)
$60 - 90\ M_{\odot}$: O - Of/WNL⇔LBV - WNL(H poor)- WCL-E - SN(SNIbc/BH/SNIIn)?
$40 - 60\ M_{\odot}$: O - BSG - LBV ⇔ WNL -(WNE) – WCL-E - SN(SNIb)
- WCL-E - WO SN (SNIc)
$30 - 40\ M_{\odot}$: O - BSG - RSG – WNE - WCE - SN(SNIb)
OH/IR ⇔ LBV ?
$20 - 30\ M_{\odot}$: O -(BSG)- RSG – BSG (blue loop) – RSG – SN(SNIIb, SNIIL)
$10 - 20\ M_{\odot}$: O - RSG - (Cepheid loop, $M < 15\ M_{\odot}$) RSG – SN (SNIIP)

The sign ⇔ means back and forth motions between the two stages. The various types of supernovae are tentatively indicated. The limits between the various scenarios depend on metallicity Z and rotation.

We can classify the different scenarios in three families: below about 30 $M_{\odot}$, stars go through a red supergiant stage (RSG); above about 40 $M_{\odot}$, stars go through a Luminous Blue Variable (LBV) and a Wolf-Rayet (WR) phase[1]; in the intermediate mass range, between 30 and 40 $M_{\odot}$, stars can possibly (but not necessarily) go through the three phases, RSG, LBV and WR. As we shall discuss below, many very interesting questions remain to be solved before we can safely say that we understand massive star evolution. Among the challenges, which still remain before us, let us cite:

- The finding of a consistent explanation of the overall dependence with metallicity of the blue to red (B/R) supergiant ratio (see more below).
- The driving mechanism for the huge shell ejections undergone by LBV stars.
- The importance of the single and binary channels for explaining the WR and the different core collapse supernova types (II, Ib, Ic) at various metallicities.

In the following we discuss the importance of mass loss and rotation in the context of these questions and we propose some directions of research for future investigations. Very interesting and informative reviews on these topics have recently been written by Massey (2003), Crowther (2007) and Smartt (2009).

2 Red Supergiants: impact of mass loss and rotation

For a long time there was a mismatch between the observed positions of RSGs in the HR diagram and the predicted ones. Improvements in model atmospheres and in interior models allow now to obtain a good agreement, in particular Levesque et al. (2005) find that the upper luminosity of RSGs is around 5.2-5.3 (in log $L/L_{\odot}$ and taking the median value of the five most luminous RSGs). Interestingly, this upper luminosity presents no variation with the metallicity (Levesque et al. 2006). Red supergiants are found to be variable in the V band (not in K) with amplitude of 0.5 mag. in M31 and of 0.9 mag. in the Magellanic Clouds (Massey et al. 2009). Red supergiants are more reddened than the OB stars belonging to the same environment indicating that they are surrounded by local dust material.

If a star becomes a red supergiant at the very beginning of the core He-burning phase, then its red supergiant lifetime will be larger than the one of a star which will begin to transform its central helium already in the blue part of the HR diagram and enter its red supergiant stage in a more advanced evolutionary stage. Thus the red supergiant lifetimes depend on the way the star evolves into the red

[1]WN stars show at their surface the products of H-burning, WC and WO stars, the products of He-burning, see more details in Crowther (2007).

part of the HR diagram after the Main- Sequence phase. This redward evolution depends in turn on the extension of the intermediate convective zone associated with the H-burning shell. Let us recall that in a convective zone the density gradients are shallower. As a consequence, the larger the intermediate convective zone, the more compact the star and thus a blue position in the HR diagram is favored. On the contrary when this intermediate convective zone decreases in mass or even disappears, this favors the inflation of the star and a rapid evolution into the red part of the HR diagram. Mass loss (see e.g. Meynet 1993) and (rotational) mixing (Maeder & Meynet 2001) both reduce the extension of the intermediate convective zone and therefore favor an early entrance into the RSG stage during the core He-burning phase.

Let us illustrate this by looking at Figs. 1 and 2, where the structures of solar metallicity models for two 20 $M_\odot$ stars are shown. The models show the presence of an intermediate convective zone associated with the H-burning shell at the beginning of the core He-burning phase. This intermediate convective zone stays present for a much longer period in the non-rotating model than in the rotating one (time is in logarithm so it is not so apparent in the figures). Also the total mass of the non-rotating model is slightly larger than the total mass of the rotating one at the same stage. One expects thus that, at the end of the Main-Sequence phase, the non-rotating model will cross the HR gap more slowly. This is exactly what happens as can be seen in Fig. 3.

More important but similar effects are observed in metal poor models. It has been shown by Maeder & Meynet (2001) that rotation may be the reason for the large number of RSGs observed in the SMC cluster NGC 330. Also rotation may be a key ingredient for explaining the B/R ratio estimated in the galaxy Sextans A from HST imaging by Dohm-Palmer & Skillman (2002). They find that if the non-rotating stellar models of Schaller et al. (1992) well reproduce the shape of the variation of the B/R ratio as a function of age, the observed ratio is lower than the model by a factor two. Rotating models as those presented in Maeder & Meynet (2001) would allow to reproduce the observed value. The link between rotation and red supergiant is also indirectly supported by the observed positive correlation between the population of Be stars, which are fast rotating B-type star with an equatorial disk and the RSG populations (see Fig. 1b in Meynet, Eggenberger & Maeder 2007).

Once a red supergiant, the star can remain in this state until it explodes in a type IIP core collapse supernova[2]. But it is not necessarily the case. The star can also evolve back to the blue part of the HR diagram and end its life as a blue supergiant or even, in some probably rare cases (see below), as a Wolf-Rayet star. The important factor governing the blueward evolution from the red supergiant stage is the mass fraction occupied by the helium core (Giannone 1967). Typically, when the mass fraction of the He-core becomes greater than about 60-70% of the total actual mass, the star evolves back to the blue part of the HR diagram. This is what happens in the rotating 20 $M_\odot$ stellar model with $\upsilon_{\rm ini}$= 300 km s^{-1}, in which the He-burning core occupies more than 65% of the total mass. The non-rotating model has a core which occupies only about 25% of the total mass and remains in the red part of the HR diagram.

As it was the case for the first crossing of the HR gap, this second crossing of the HR diagram depends on mass loss (during the red supergiant stage) and mixing (during the previous evolutionary phases). Strong mass loss during the red supergiant phase favors a blueward evolution (Salasnich, Bressan & Chiosi 1999; Vanbeveren, Van Bever & Belkus 2007; Yoon & Cantiello 2010) since it makes the mass fraction of the core larger. Strong mixing during the previous phases also makes larger cores and thus favors an evolution from the red to the blue supergiant phase (Hirschi, Meynet & Maeder 2004).

Thus we see that the lifetime of the star in the red supergiant stage, as well as the possibility for the star to explode as a type II SN in that stage depend heavily on mass loss and mixing.

[2]Type IIP supernovae originate from exploding stars having kept a massive and extended hydrogen rich envelope.

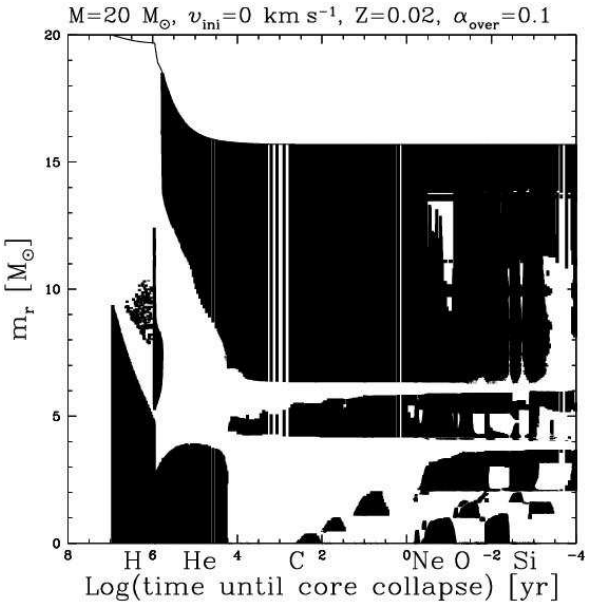

Figure 1: Evolution as a function of the remaining time until core collapse of the total mass and of the masses of the convective regions (in black) for a non-rotating solar metallicity 20 $M_\odot$ model. Figure taken from Hirschi et al. (2004).

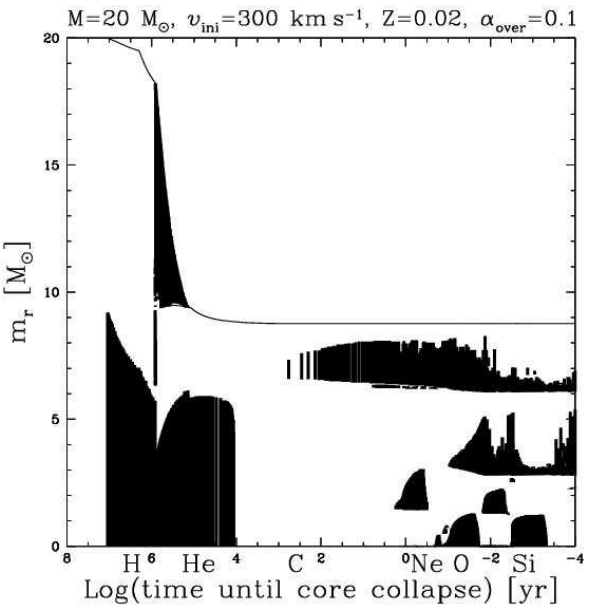

Figure 2: Evolution as a function of the remaining time until core collapse of the total mass and of the masses of the convective regions (in black) for a rotating solar metallicity 20 $M_\odot$ model. Figure taken from Hirschi et al. (2004).

Let us now recall a few observations which are relevant in that context:

- the number ratio of blue to red supergiants in clusters with ages between 6.8 and 7.2 (in logarithm of the age in years), or with masses at the turn off between about 12 and 30 $M_\odot$, increases when the metallicity increases (Meylan & Maeder 1983; Eggenberger, Meynet & Maeder 2002). This observed trend is exactly the opposite of what is expected from standard grids of models (see the discussion in Langer & Maeder 1995).

- An important number ratio is the relative number of RSGs to WRs. Massey (2003, see his Fig. 12) shows that this ratio decreases with increasing metallicity, by a factor of 100 over a range of 0.9 dex in metallicity. The strong decrease with the metallicity indicates that the mass range for the progenitors of WRs (RSGs) increases (decreases) when the metallicity increases.

These two important features emphasize the importance of metallicity in shaping the blue, red supergiants and Wolf-Rayet populations. Mass loss triggered by radiation increases with the metallicity (see the review by Kudritzki & Puls 2000) and this is probably one of the main factors responsible for the above observed trends. For instance, when the metallicity increases, stars enter at an earlier stage in the WR phase (making the duration of that phase longer), also stars of lower initial masses can become WR at the end of their lifetime. These two factors are exactly what is required to explain the trend of the relative number of RSGs and WRs with metallicity.

For the B/R ratio however this is not the case! Indeed, when the metallicity increases, mass loss rates increase at least during the MS phase and thus RSGs are favored at high metallicity, which is the contrary of what is observed. Thus the increase of the mass loss rate with the metallicity, expected for hot stars, cannot be the cause of the observed B/R trend. This is in fact a counteracting effect.

Now, we have mentioned that an increase of the mass loss rates *during the RSG phase* would shorten the RSGs lifeftime and lead to the formation of a blue supergiant, or even a WR star in some

cases. At the moment, mass loss rates used in current stellar models (de Jager, Nieuwenhuijzen & van der Hucht 1988) are too weak for producing this kind of evolution for stars in the mass range between 12 and 25-30 $M_\odot$ (at least for standard non-rotating models). However the uncertainties are large, actually, the determinations of the mass loss during the RSG phase is still more difficult than in the blue part of the HR diagram due in part to the presence of dust and to various instabilities active in red supergiant atmospheres (e.g. convection becomes supersonic and turbulent pressure can no longer be ignored). An illustration of the difficulty comes from the determinations of red supergiant mass loss rates by van Loon et al. (2005). Their study is based on the analysis of optical spectra of a sample of dust-enshrouded red giants in the LMC, complemented with spectroscopic and infrared photometric data from the literature. Comparison with galactic AGB stars and red supergiants shows excellent agreement for dust-enshrouded objects, but not for optically bright ones. Dust enshrouded objects show mass loss rates which are greater by a factor 3-50 than those deduced from optically bright ones! In this context the questions of which stars do become dust-enshrouded, at which stage, for how long, become critical to make correct prediction of the mass lost by stellar winds. One can also note a very interesting point deduced from the study by van Loon et al. (2005), that for dust-enshrouded objects mass loss appears to be independent of the metallicity! On the other hand the formation and duration of the dust enshrouded stage may be metallicity dependent! Thus one sees here that improvements are needed in order to clarify the situation. Let us just mention that stronger mass loss at high metallicity during the red supergiant phase would go in the right direction for explaining the observed B/R trend with metallicity. Indeed an increase of the mass loss rate during the red supergiant phase at high Z favors blueward evolution and thus reduces the RSG lifetimes.

We want now to discuss two other indirect arguments possibly supporting the view that red supergiants suffer important mass loss rates. The first one concerns an interesting point raised in the review by Smartt (2009). Using archive data, Smartt et al. (2009) searched for supernova progenitors of type IIP supernovae having occurred in a given volume-limited area of the Universe (28 Mpc) and in a given time-limited (10.5 yr) interval. They found 20 progenitors for type IIP supernovae. They deduced the mass of the progenitors using stellar models. They obtain that the mass range of the Type IIP supernova progenitors is comprised between 8.5 (+1/-1.5) $M_\odot$ and 16.5 (+/-1.5) $M_\odot$. Why did they not see progenitors with masses between 18 and 25 $M_\odot$, while red supergiants in this mass range are observed? According to the authors, this lack is significant. They estimate that the probability of no detection by chance is only 0.018 for a Salpeter IMF. The authors invoke two reasons for explaining this lack of massive Type IIP SNe progenitors: 1) the underestimate of the progenitor masses due to dust extinction; 2) the stars in the mass range between 18 and 25 $M_\odot$ do not produce type IIP SNe. If indeed, stars in the red supergiant stage lose more mass than currently accounted for in models then it may be that stars evolve back in the blue, ending their life either as blue supergiants, Wolf-Rayet stars or even red supergiants (if they return back to the red) but with a H-rich envelope too shallow for producing a type IIP SN.

The second argument is based on the strong helium enrichments observed at the surface of blue supergiants. In a recent work Przybilla et al. (2010, 2011) determined the He abundance at the surface of solar neighborhood blue supergiants with masses between $\sim$ 9 and 20 $M_\odot$. The enrichments are found to be in the range of 0.32-0.39 (in mass fraction), while rotating models would predict at most values in the range between 0.29 and 0.31 for stars entering the blue supergiant stage directly from the MS. Thus the predicted values are too low. In case the blue supergiants would be actually post red supergiant stars, then He-enrichments well in line with the spectroscopic values are obtained. Thus, like for the SN argument explained above, a blueward evolution after the red supergiant phase would overcome the difficulty.

When the star evolves back from the red to the blue, it may encounter instabilities (see e.g. de Jager et al. 2001). Typically when the effective temperature becomes greater than about 7000 K

on the blueward track, the main part of the photosphere becomes moderately unstable (de Jager & Nieuwenhuijzen 1997). Observations of yellow supergiants in that region indicate that the approach of this instability region may lead to phases of enhanced mass loss. These episodes of strong mass loss will help the star to evolve to the blue.

From the discussion above, we see that some interesting constraints would be obtained for stellar models if it would be possible to discriminate from observations, blue supergiants originating from MS stars, from blue supergiants originating from red supergiants. As indicated above helium surface abundances could be a way. But to prove it, we have to show that the He-rich blue supergiants are indeed post red supergiant stars! Is there any possibility, studying the circumstellar environment to find traces of a previous red or even yellow supergiant phase? In these phases some shell ejections might have occurred which may still be detectable around at least some blue supergiants. This remains to be investigated and is probably a very interesting line of research to address both from the theoretical and observational side. One can wonder also whether the vibrational properties of stars could be used to disentangle these two cases. This is a point which would also deserve some more theoretical thoughts.

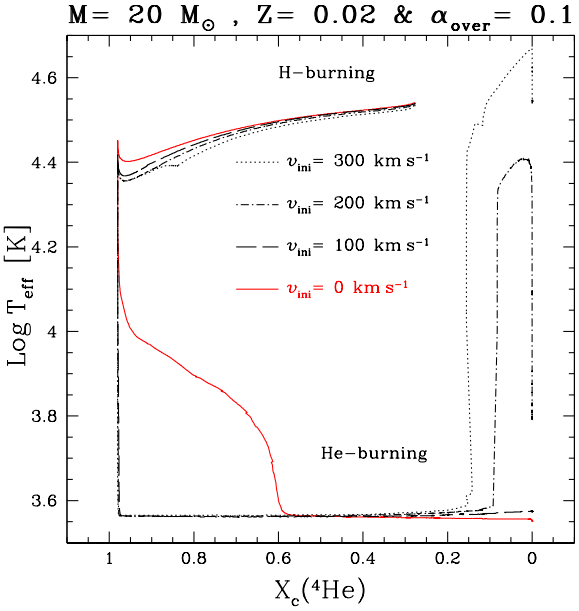

Figure 3: $T_{\rm eff}$ vs central helium mass fraction for 20 $M_{\odot}$ models: solid, dashed, dotted-dashed and dotted lines correspond respectively to $v_{\rm ini}$= 0, 100, 200 and 300 km s^{-1}. Figure taken from Hirschi et al. (2004)

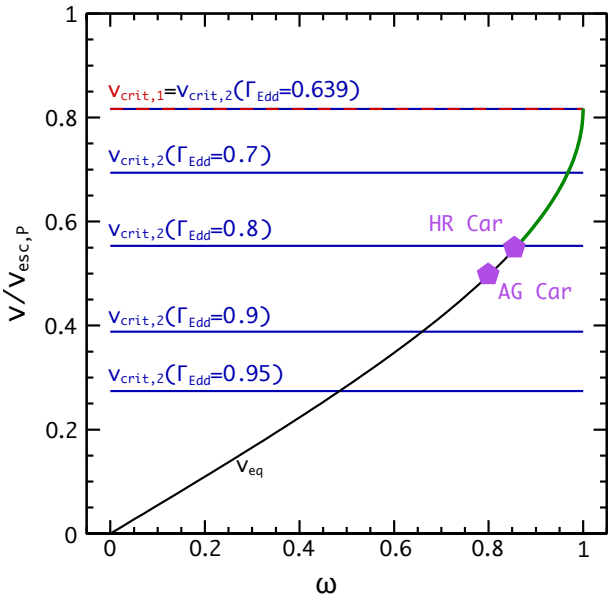

Figure 4: Variation of the linear velocity at the equator as a function of the angular velocity (see text). The horizontal lines show the critical velocities for different values of the Eddington factor. Figure taken from Georgy (2010).

To conclude this section, let us mention another new and interesting problem raised by yellow supergiants. Yellow supergiants are stars with effective temperatures between 4800 and 7500 K and initial masses above about 9 M$_{\odot}$. Recently Drout et al. (2009) and Neugent et al. (2010) have observed the yellow supergiant populations in M31 and in the SMC. In both cases, they find that rotating and non-rotating models of Maeder & Meynet (2001) and of Meynet & Maeder (2005) predict too many yellow supergiants in the mass ranges above 25 M$_{\odot}$ with respect to the observed number. It is difficult at the moment to invoke any precise physical cause to this discrepancy. Let us just make a few remarks: first since the same discrepancy appears in M31 and in the SMC, this means that metallicity and in particuliar the metallicity dependance of the mass loss rates probably does not play a role; 2) The models used have no blue loop above 12 M$_{\odot}$, thus this discrepancy is not related to a possible

blueward evolution after the red supergiant stage. The present models without blue loops already overestimate the time spent in the yellow supergiant stage originating directly from the MS phase. In case of a blue loop, the problem would become even more severe.

3 Luminous Blue Variable stars, transition phase or end point of the evolution?

The hydrogen surface abundances and the luminosity of the Luminous Blue Variables indicate that these stars have properties intermediate between O-type stars and WN stars. In the evolutionary scenarios recalled at the beginning of this paper, they are interpreted as a transition stage between these two types of stars and maybe between WNL (here defined as WN stars with hydrogen at the surface) and the WNE stars (interpreted here as WN stars with no hydrogen at the surface).

Recently however, the light curves of a few supernovae have been found to be consistent with SN ejecta interacting with dense circumstellar material containing a mass of 10-20 $M_{\odot}$, *i.e.* consistent with the ejected mass during the eruption of LBV stars (type IIn supernovae). This is the case of SN2006gy and 2006tf (Smith & McCray 2007; Smith et al. 2008). Also it has been found that the progenitor of SN 2005gl which was a Type IIn is consistent with a very luminous LBV star, not a RSG (Gal-Yam & Leonard 2009). These observations support the view that at least some luminous LBV stars are the end point of the evolution and not a transition phase. Can such a scenario be explained by single massive star evolution? It does not appear to be the case. LBVs originating from the most massive stars, as for instance η Car, lose so much mass in short intervals of time, that these stars will rapidly evolve away from their LBV stage for becoming a WR stars. Of course such a statement depends on the mass loss history of these stars, on the frequency with which they undergo strong LBV-type outbursts. Presently, computations modelling the LBV phase by accounting for an average mass loss rate of about 10^{-3} $M_{\odot}$ per year during a few tens of thousands years do not explode as LBV stars.

It may be that strong eruptions are not necessarily linked to LBV stars. For instance, Woosley et al. (2007) have invoked the possibility that massive stars could suffer at the end of their evolution giant eruptions caused by pulsational pair instability ejections. But this would occur only for initial masses above 100 $M_{\odot}$ and according to Smith (2011) these stars are too rare to account for all the observed Type IIn SNe. Are there other processes producing strong eruptions at the end of massive star evolution? This is of course an important question which needs to be addressed in order to make progress on this topic.

Let us now come back to one of the main characteristics of LBV stars: their eruptive nature. The physical cause of these eruptions is still subject of discussions. Maeder (1992) has shown that in the outer layers of these stars, the free fall time becomes longer than the thermal diffusion time. This means that during the dynamical ejection, the conditions which drive the ejection (producing e.g. the supra-Eddington luminosity) have time to move inside the star allowing a significant amount of mass to be ejected (geyser model).

What are the conditions which are needed for such processes to occur? The anisoptropies of the LBV nebulae support the view that rotation may play a role. In a fast rotating star, one expects polar ejections and this is quite in line with the peanut shape observed around η Car, HR Car and AG Car (Groh et al. 2009ab, 2010). In order for these anisotropies to be present the star must rotate at the surface with velocities not too far from the keplerian velocity also called sometimes the classical critical velocity. In the following, the surface angular velocity is noted Ω and the keplerian velocity $\Omega_{\rm Kep}$. Typically $\omega = \Omega/\Omega_{\rm Kep}$ should be greater than 80% for the mass flux at the pole be more than 1.65 times the mass flux at the equator (Georgy 2010). Maeder & Meynet (2000) have shown

that for luminous stars, i.e. stars sufficiently close to the Eddington limit, the critical velocity (i.e. a velocity such that the centrifugal acceleration at the equator plus the radiative acceleration plus the gravity becomes equal to zero) is no longer given by the classical expression but by a more complex expression involving the Eddington factor. The higher the Eddington factor, the smaller the critical velocity. In Fig. 4 the curve shows the relation between the surface angular velocity and the linear velocity (it would be a straight line for a rigid non-deformed body). The angular velocity is normalized to the classical critical velocity and the linear velocity to the escape velocity at the pole. These normalisations and the Roche approximation (for computing the gravitational potential) make this curve independent of the mass, age, metallicity of the star.

The horizontal lines correspond to critical velocities obtained for various Eddington factor $\Gamma = L/L_{\rm Edd}$. As long as the Eddington factor is inferior to 0.639, the top horizontal line is the critical velocity (note that the critical velocity is lower than the escape velocity. This reflects the fact that at the critical limit matter is launched in a disk and does not escape to infinity). For Eddington factors below 0.639, ω can take any value between 0 and 1. When the Eddington factor increases, the critical velocity decreases and ω can only take values between 0 and an upper value defined by the abscissa of the intersection between the horizontal line and the curve. For instance, when Γ is equal to 0.8, the maximum value of ω is around 0.85 . Using the data given by Groh et al. (2009ab, 2010), we have placed on the red curve the positions of the two LBV stars HR Car and AG Car. These two stars have Eddington factor in the range of 0.8. Thus we see that they rotate very near their critical limit. Interestingly they still present high enough values of ω for allowing significant anisotropies to appear which is in line at least qualitatively with the peanut shape of their nebulae. This supports the view that LBV stars may be at the $\Omega\Gamma$-limit as defined in Maeder & Meynet (2000).

4 Wolf-Rayet stars and type Ibc supernovae

Wolf-Rayet stars are the bare cores of initially massive stars, whose H-rich envelope has been removed by strong stellar winds or through Roche lobe overflow in a close binary system (see the review by Crowther 2007). Wolf–Rayet stars play a very important role in astrophysics, as signatures of star formation in galaxies and starbursts, as injectors of chemical elements and of the radioactive isotope ^{26}Al, as sources of kinetic energy into the interstellar medium and as progenitors of supernovae and, likely, as progenitors of long soft γ–ray bursts.

Rotational mixing favours the entry into the WR phase in two ways, firstly by allowing chemical species produced in the core to diffuse in the radiative envelope and, secondly, by making the mass of the convective core larger. In the non–rotating model, mass loss by stellar winds is the key physical ingredient which allows internal chemical products to appear at the surface and thus the formation of a WR star. The star becomes a WR star only when sufficiently deep layers are uncovered. In rotating models, the characteristic surface abundances of WR stars can be obtained through the effects of mass loss by stellar winds and of rotational mixing. The action of rotation allows WR stars to appear through the single star scenario even when the mass loss rates are reduced. To realize that, imagine a star rotating so fast that it would follow a homogenous evolution. Such a star can become a WR star, i.e. being a star with a log $T_{\rm eff}$ greater than about 4 and a mass fraction of hydrogen at the surface below ~ 0.4 without losing mass!

When models with a time-averaged rotation velocity during the MS phase in the range of the observed values are considered, then a reasonable number of WR stars can be produced through the single star scenario even using low mass loss rates (Meynet & Maeder 2003, 2005). Also the rotational models well reproduce the WN/WC ratio at low metallicity and the observed fraction of WR stars in the transition stage WN/WC (phase during which H- and He-burning products are simultaneously enhanced at the surface).

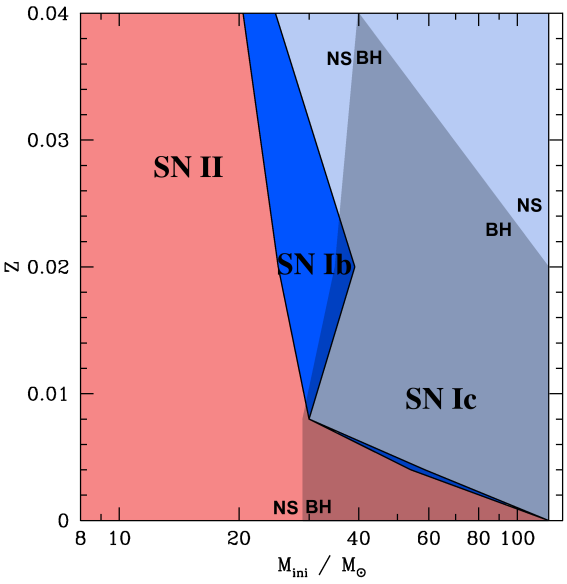

Figure 5: Ranges of masses of different types of SN progenitors at different metallicities. The type of progenitor is indicated in the figure. The shading on the right indicates the area where formation of a black hole (BH) is expected ; elsewhere, the remnant is a neutron star (NS). Figure taken from Georgy et al. (2009).

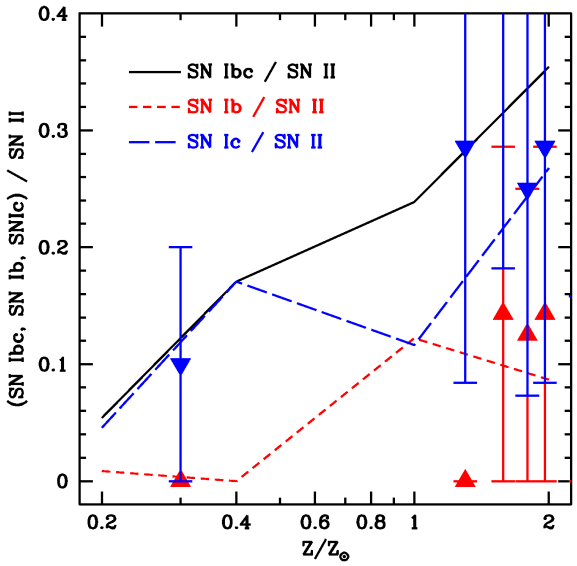

Figure 6: Rates of SN Ic / SN II (blue long–dashed line), SN Ib / SN II (red short–dashed line), and SN Ibc / SN II (black solid line) for the reference case. The points are extracted from the data of Prieto, Stanek, & Beacom (2008). Figure taken from Georgy et al. (2009).

The number of WC to WN stars increases with the metallicity (see the review by Massey 2003). Many attempts have been performed to reproduce this observed trend: for instance the enhanced mass loss rate models of Meynet et al. (1994) provided a good agreement for solar and higher than solar metallicity but produced too few WN stars in metal-poor regions. The inclusion of rotation together with reduced mass loss rates accounting for the effects of clumping improved the situation in the metal poor region, but produced too many WN stars at solar and higher metallicities (Meynet & Maeder 2005). Eldridge & Vink (2006) show that models that include the mass-loss metallicity scaling during the WR phase closely reproduce the observed decrease of the relative population of WC over WN stars at low metallicities. However such models severely underestimate the fraction of WR to O-type stars. In that case, to improve the situation, a high proportion of Wolf-Rayet stars originating from mass transfer in close binaries should be assumed at all metallicities. For instance at solar metallicity about 75% of the WR stars should be produced in close binary systems (Eldridge, Izzard & Tout 2008).

The WN/WC number ratio depends also on other factors, in particular on the evolutionary scenario. In Meynet & Maeder (2003), the most massive rotating stars enter into the WR regime already during the MS phase. This feature has good and bad effects. On one hand, it allows these models to well reproduce the variation of the number fraction of WR to O-type stars since it significantly increases the WR lifetimes. On the other hand, it produces very long WN phases since the star enters into the WR phase having still a huge H-rich envelope. As a consequence, too low values for the WC/WN ratio are obtained at solar and higher metallicities.

In Meynet & Maeder (2003,2005), the hypothesis has been made that when a star enters into the WR stage during the MS phase, it avoids the Luminous Blue Variable phase. Actually, stars may behave differently. It may well be that a star which becomes a WR star during the MS phase, enters

an LBV phase after the core H-burning phase, and then evolves back into the WR regime. When this evolutionary scenario is followed, reasonable values for both the WR/O and the WC/WN ratios are obtained. Indeed the ratios of WR/O and of WC/WN given by these models at the solar metallicity are 0.06 and 0.9 which compare reasonably well with the observed values of 0.1 and 0.9 respectively (Meynet et al. 2008). Both ratios are not reproduced by the non-rotating models to which a similar scenario is applied. This discussion illustrates the possible key role that the LBV phase may play in shaping the WC/WN ratio.

The nature of the supernova progenitor as a function of the mass and the metallicity can be deduced from stellar models. This has recently been studied by Georgy et al. (2009) using rotating stellar models (see Fig. 5). From the presupernova structure, it is also possible to deduce the nature of the supernova explosion and thus to obtain theoretical estimates for the frequency of the different types of core collapse supernovae as a function of metallicity. Supposing that any massive star, whether it produces a neutron star or a black hole, produces an observable supernova event, it is found that single stars can reproduce the variation with the metallicity of the number ratios of type (Ib+Ic)/II, Ib/II and Ic/II supernovae. Comparisons between observation and theory for the number ratios of Type Ib and Ic supernovae to Type II supernovae are shown in Fig. 6.

In case the most massive single stars produce black holes with no supernova event, then single stellar models produce too few Ibc supernovae at low metallicity and most Type Ibc supernovae might then be produced as a result of mass transfer in close binary systems (Podsiadlowski et al. 1992) . In close binaries, smaller initial mass stars can still give birth to small mass naked cores. These cores would then explode as type Ib or Ic supernova leaving behind a neutron star. If these naked cores are formed near the end of the evolution of the star, then their lifetime before explosion could be quite short and thus the objects may be very rare.

At the moment, it is quite difficult to chose between the single and binary scenario for the progenitors of Type Ibc supernovae, since both channels can reproduce the observed variation with the metallicity of the number ratios of Type Ibc to Type II supernovae. The question of the variation with the metallicity of the number ratios of Type Ib versus Type II and Type Ic versus Type II has not yet been studied in the framework of the binary scenario.

If the binary scenario is correct, this will decouple the WR populations from the Ibc supernovae. Smartt (2009) mentions the fact that 10 supernovae classified as Ibc have sufficiently deep pre-explosion images available. Curiously, none of them have a progenitor detected, although, the probability of no detection by chance would be only 11% (this estimate is obtained by comparing the broad band magnitudes of known WR stars with the magnitude limits for the progenitors of the 10 Ibc supernovae). This probably indicates that the progenitors of the type Ibc come at least in part from progenitors different from the known WR stars and/or that strong shell ejection occurs some time before explosion strongly reducing the magnitude of the progenitor. As we see important and interesting points remain to be clarified in order to know the final state of WR stars.

5 Conclusion

Let us recall the main three challenges that we mentioned at the beginning of this paper and let us see what we have learned from the present discussion.

- **the finding of a consistent explanation of the overall dependence with metallicity of the blue to red supergiant ratio:** rotation appears to play an important role at low metallicity while the interplay of rotation (mainly rotational mixing during the Main-Sequence phase) and mass loss during the red supergiant stage may be the most important physical mechanisms at solar and higher than solar metallicities. Let us recall here that there is no problem adjusting the

mass loss rates or rotation to reproduce the B/R ratio at a given metallicity. The real challenge is to reproduce the overall trend with a minimum number of hypothesis.

- **the driving mechanism for the huge shell ejection undergone by LBV stars:** there are some hints supporting the fact that LBVs are at the $\Omega\Gamma$ limit, i.e. that the physical conditions for the outbursts to occur involve both the proximity to the Eddington limit and to the critical velocity. It remains a big challenge for single star models to make a star explode in the LBV phase.

- **the importance of the single and binary channel for explaining the WR and the different core collapse supernova types (II, Ib, Ic) at various metallicities:** the initial mass range of stars becoming WR is different in the single star and the close binary scenario. In the close binary scenario, stars of smaller initial masses can become WR stars. Typically for instance a 12 $M_\odot$ could become a WR after having lost its H-rich envelope in a Roche Lobe overflow. This may occur on a timescale allowing single coeval massive stars to evolve into the RSG stage and thus, one would expect that in the close binary scenario for the formation of WR stars, we should obtain more frequently the simultaneous presence of RSGs and WR stars. The simultaneous presence of WR and RSG in coeval populations are quite rare. Known exceptions are the young clusters of the galactic centre (see e.g. Figer et al. 2004, Figer 2008). In that case, the high metallicity may explain the simultaneous presence of RSG and WR stars simply because lower initial mass stars can go through the WR stage. Another exception is Westerlund I (Clark et al. 2005). It is so massive that not all the stars may be coeval. Apart from these cases, RSGs and WR stars are not seen together in coeval populations. This may be an indication that formation of WR stars through Roche Lobe overflow from stars in the mass range between 9 and 25 $M_\odot$ is a relatively rare event.

References

Clark, J. S., Negueruela, I., Crowther, P. A., & Goodwin, S. P. 2005, A&A, 434, 949
Crowther, P. A. 2007, ARA&A, 45, 177
Dohm-Palmer, R. C., & Skillman, E. D. 2002, AJ, 123, 1433
Drout, M. R., Massey, P., Meynet, G., Tokarz, S., & Caldwell, N. 2009, ApJ, 703, 441
Eggenberger, P., Meynet, G., & Maeder, A. 2002, A&A, 386, 576
Eldridge, J. J., & Vink, J. S. 2006, A&A, 452, 295
Eldridge, J. J., Izzard, R. G., & Tout, C. A. 2008, MNRAS, 384, 1109
Figer, D. F., Rich, R. M., Kim, S. S., Morris, M., & Serabyn, E. 2004, ApJ, 601, 319
Figer, D. F. 2008, arXiv:0803.1619
Gal-Yam, A., & Leonard, D. C. 2009, Nature, 458, 865
Georgy, C. 2010, PhD thesis, Anisotropic Mass Loss and Stellar Evolution: From Be Stars to Gamma Ray Bursts, Geneva University
Georgy, C., Meynet, G., Walder, R., Folini, D., & Maeder, A. 2009, A&A, 502, 611
Giannone, P. 1967, ZAp, 65, 226
Groh, J. H., Hillier, D. J., Damineli, A., Whitelock, P. A., Marang, F., & Rossi, C. 2009a, ApJ, 698, 1698
Groh, J. H., Damineli, A., Hillier, D.J., et al. 2009b, ApJ, 705, 25
Groh, J. H., Madura, T. I., Owocki, S. P., Hillier, D. J., & Weigelt, G. 2010, ApJ, 716, L223
Hirschi, R., Meynet, G., & Maeder, A. 2004, A&A, 425, 649
de Jager, C., & Nieuwenhuijzen, H. 1997, MNRAS, 290, L50
de Jager, C., Nieuwenhuijzen, H., & van der Hucht, K. A. 1988, A&AS, 72, 259
de Jager, C., Lobel, A., Nieuwenhuijzen, H., & Stothers, R. 2001, MNRAS, 327, 452
Kudritzki, R.-P., & Puls, J. 2000, ARA&A, 38, 613
Langer, N., & Maeder, A. 1995, A&A, 295, 685
Levesque, E. M., Massey, P., Olsen, K. A. G., Plez, B., Josselin, E., Maeder, A., & Meynet, G. 2005, ApJ, 628, 973

Levesque, E. M., Massey, P., Olsen, K. A. G., Plez, B., Meynet, G., & Maeder, A. 2006, ApJ, 645, 1102
Maeder, A. 1992, Instabilities in Evolved Super- and Hypergiants, Royal Netherlands Academy of Arts and Sciences, p. 138
Maeder, A., & Meynet, G. 2000, A&A, 361, 159
Maeder, A., & Meynet, G. 2001, A&A, 373, 555
Massey, P. 2003, ARA&A, 41, 15
Massey, P., Silva, D. R., Levesque, E. M., Plez, B., Olsen, K. A. G., Clayton, G. C., Meynet, G., & Maeder, A. 2009, ApJ, 703, 420
Meynet, G. 1993, The Feedback of Chemical Evolution on the Stellar Content of Galaxies, 40
Meynet, G., & Maeder, A. 2003, A&A, 404, 975
Meynet, G., & Maeder, A. 2005, A&A, 429, 581
Meynet, G., Maeder, A., Schaller, G., Schaerer, D., & Charbonnel, C. 1994, A&AS, 103, 97
Meynet, G., Eggenberger, P., & Maeder, A. 2007, IAU Symposium, 241, 13
Meynet, G., Ekström, S., Maeder, A., Hirschi, R., Georgy, C., & Beffa, C. 2008, IAU Symposium, 250, 147
Meylan, G., & Maeder, A. 1983, A&A, 124, 84
Neugent, K. F., Massey, P., Skiff, B., Drout, M. R., Meynet, G., & Olsen, K. A. G. 2010, ApJ, 719, 1784
Podsiadlowski, P., Joss, P.C., & Hsu, J.J.L. 1992, ApJ, 391, 246
Prieto, J. L., Stanek, K. Z., & Beacom, J. F. 2008, ApJ, 673, 999
Przybilla, N., Firnstein, M., Nieva, M.-F., Meynet, G., & Maeder, A. 2010, A&A, 517, A38
Przybilla, N., Firnstein, M., Nieva, M.-F., Meynet, G., & Maeder, A. 2011, in Proceedings of the 39th Liège Astrophysical Colloquium, eds. G. Rauw, M. De Becker, Y. Nazé, J.-M. Vreux & P.M. Williams, BSRSL 80, 279
Salasnich, B., Bressan, A., & Chiosi, C. 1999, A&A, 342, 131
Schaller, G., Schaerer, D., Meynet, G., & Maeder, A. 1992, A&AS, 96, 269
Smartt, S. J. 2009, ARA&A, 47, 63
Smartt, S. J., Eldridge, J. J., Crockett, R. M., & Maund, J. R. 2009, MNRAS, 395, 1409
Smith, N. 2011, in Proceedings of the 39th Liège Astrophysical Colloquium, eds. G. Rauw, M. De Becker, Y. Nazé, J.-M. Vreux & P.M. Williams, BSRSL 80, 322
Smith, N., & McCray, R. 2007, ApJ, 671, L17
Smith, N., Chornock, R., Li, W., Ganeshalingam, M., Silverman, J. M., Foley, R. J., Filippenko, A. V., & Barth, A. J. 2008, ApJ, 686, 467
Vanbeveren, D., Van Bever, J., & Belkus, H. 2007, ApJ, 662, L107
van Loon, J. T., Cioni, M.-R. L., Zijlstra, A. A., & Loup, C. 2005, A&A, 438, 273
Woosley, S.E., Blinnikov, S., & Heger, A. 2007, Nature, 450, 390
Yoon, S.-C., & Cantiello, M. 2010, ApJ, 717, L62

Discussion

J. Puls: You showed the importance of mass-loss for the evolution of massive stars and the B/R ratio. However, you are using the theoretical rates by Vink and co-workers. I don't want to comment on the clumping problem discussed yesterday, but there is an additional problem. Vink et al. predict that $\dot{M}$ decreases strongly over the so-called bi-stability jump, a prediction which is in contrast to observations (e.g. Markova & Puls 2008). Have you checked what would happen if you keep the wind-momentum constant instead of increasing it?

G. Meynet: Changing from the rates of Vink et al. (2001) to those of for instance Kudritzki & Puls (2000) has impact on the results. As an example, the minimum rotation rate to obtain homogeneous evolution depends on the mass loss. Higher mass loss rates, lower the minimum initial rotation rate for obtaining a blueward evolution. Of course the impact would be the most important for the massive and luminous stars, likely less important for stars with initial masses between 8 and let's say 25 $M_{\odot}$. Note that results about the effect of rotation on the fraction of blue to red supergiants have been obtained with the rates of Kudritzki & Puls (2000).

S. Owocki: For hot stars we have a good predictive theory for wind mass loss driven by line-scattering of stellar continuum radiation, e.g. CAK or Vink $\dot{M}$. But mass loss in LBV and RSG phases are like critical limit, like spilling water from a nearby full glass. It depends a lot on subtle details of the pulsations or variations near the surface, and as such is much harder to make clear predictions. As such, there is a lot of uncertainty in the role of such LBV or RSG mass loss on stellar evolution.
G. Meynet: Yes, it is indeed quite challenging to obtain reliable mass loss rate prescriptions for LBVs and RSGs stars. A reasonable aim would be, thanks to good mass loss rate diagnostics, to obtain some kind of reliable mass loss rate prescriptions for these phases as well as to obtain some information about their metallicity dependence. In that respect it is interesting to mention that the "dust-enshrouded" RSG in the LMC and in the MW seem to present the same mass loss rates (Van Loon et al. 2005) indicating that at least these kinds of supergiants do seem to have metallicity independent mass loss rates in this metallicity range variations. On the other hand, we may expect that the formation and thus the frequency of dust-enshrouded red supergiants depends somewhat on the initial metallicity. It would be interesting for stellar evolution calculations to know better the circumstances leading to the formation of such dust-enshrouded RSG so to be able to account for their high mass loss rates in a proper way.

Mixing of CNO-cycled matter in massive stars

Norbert Przybilla[1], Markus Firnstein[1], Maria-Fernanda Nieva[2],
Georges Meynet[3] and Andre Maeder[3]

[1] Dr. Karl Remeis-Observatory & ECAP, Sternwartstr.7, D-96049 Bamberg, Germany
[2] Max-Planck-Institute for Astrophysics, Karl-Schwarzschild-Str. 1, D-85741 Garching, Germany
[3] Geneva Observatory, University of Geneva, Maillettes 51, CH-1290 Sauverny, Switzerland

Abstract: Anomalies in the light element abundances in massive stars on the main sequence and more pronounced in their evolved stages are known since long. These are explained by evolution models for rotating stars as the consequence of mixing of nuclear-processed matter into the stellar atmosphere. However, recent analyses of large star samples have challenged the concept of rotational mixing. We report on the abundances of helium, carbon, nitrogen and oxygen in a sample of Galactic massive stars covering the main sequence to the blue supergiant stage in the mass range $\sim$9 to 25 $M_{\odot}$. High-quality spectra are homogeneously analysed throughout the optical to near-IR using improved NLTE line-formation and comprehensive analysis strategies. Extremely tight trends among the light element abundances are found for the first time, tracing the nuclear paths of the CNO-cycles quantitatively. The improved observational constraints will facilitate model predictions to be tested in unprecedented detail and they may guide future improvements to the models.

1 Introduction

Energy production in massive stars is governed by the CNO-cycles throughout most of their lifetimes. While CNO-burning itself is catalytic, i.e. the total number of C, N and O nuclei is not changed, transmutations occur and lead to a buildup of nitrogen at the expense of carbon and (to much lower extent) oxygen, while the burning product, helium, is accumulated.

Observational evidence for the actions of the CNO-cycles is not only found in late stages of massive star evolution, as in the Wolf-Rayet stars of WN subtype, but also much earlier. Traces of mixing of CNO-cycled products from the stellar core to the stellar surface have been found in OB-type stars on the main sequence (MS) and their evolved progeny, the blue supergiants (BSGs, see e.g. Maeder & Meynet 2000, and references therein). A qualitative understanding of this early mixing could be achieved within the framework of evolution calculations for rotating stars, where meridional circulation and turbulent diffusion act as transport mechanisms (Maeder & Meynet 2000; Heger & Langer 2000). The interplay of rotation and a magnetic dynamo may enhance the transport efficiency even further (Maeder & Meynet 2005), or not (Heger, Woosley & Spruit 2005).

The only means to verify the models is via systematic comparison with observations. Here, we address the topic of early mixing of CNO-cycled products in massive stars from a fundamental perspective. We compare the model predictions for the relative changes within the C:N:O abundance ratios and the buildup of helium with observations.

2 Theoretical Considerations

At the centre of the present investigation are diagnostic plots of an abundance ratio vs. another one, such as N/C vs. N/O or helium vs. N/O. The predicted trends depend on both the changes produced by nuclear reactions and the dilution effects produced by mixing. We may estimate the slope $\frac{\mathrm{d}(N/C)}{\mathrm{d}(N/O)}$ produced by the nuclear effects at the beginning of CNO burning. Apart from the very massive stars ($M > 40\,M_{\odot}$), one may assume that, at the beginning of the burning, the ^{14}N enhancement comes from the ^{12}C destruction via the CN cycle, while oxygen remains about constant. Thus, one has $\mathrm{d}C = -\frac{6}{7}\mathrm{d}N$ (in mass fractions) since ^{14}N globally results from the addition of two protons to ^{12}C,

$$\mathrm{d}(N/O) = \mathrm{d}N/O\ ,$$
$$\mathrm{d}(N/C) = \frac{\mathrm{d}N}{C} - \frac{N}{C^2}\frac{\mathrm{d}C}{\mathrm{d}N}\mathrm{d}N = \frac{\mathrm{d}N}{C}\left[1 + \frac{6}{7}\frac{N}{C}\right]\ . \tag{1}$$

This gives the slope

$$\frac{\mathrm{d}(N/C)}{\mathrm{d}(N/O)} = \frac{(N/C)}{(N/O)}\left[1 + \frac{6}{7}\frac{N}{C}\right]\ , \tag{2}$$

which is determined by the initial CNO abundances solely. For initial ratios N/C and N/O of 0.31 and 0.11, respectively, it adopts a value of 3.77. The relation turns slightly upward as N/C is increasing owing to the term in brackets in Eq. (2). However, at some advanced stage in evolution, corresponding to WN stars not shown here, the curve will saturate and turn down slightly (Maeder 2009, p. 699), since the CN cycle is then at equilibrium, while ^{16}O is still turned to ^{14}N. Dilution mixes a fraction f of N + ΔN enriched and C depleted materials with a fraction $(1 - f)$ of the original N and C. Under the same assumptions as above, it is easy to show that, to the first order, the slope for the relative enrichments in the N/C vs. N/O plot behaves the same way as in Eq. (2) independently of f.

The value of f, however, determines the amplitudes of the departures from the cosmic ratios. Our models with rotational mixing (e.g. Meynet & Maeder 2003) or with rotation and magnetic fields (Maeder & Meynet 2005), as illustrated later in Fig. 2, have an initial slope $\frac{\mathrm{d}(N/C)}{\mathrm{d}(N/O)} \approx 4$, which is in excellent agreement with our estimate above. The amplitude f of the mixing depends on the various model assumptions, models that include both rotation and magnetic field predict the largest mixing.

Finally we consider the behaviour of the helium surface content Y_{s} vs. N/O. Strictly and only at the very beginning of the CN burning, and under the assumption of an initially constant oxygen, we get $\mathrm{d}Y_{\mathrm{s}} = \frac{2}{7}\mathrm{d}N$, since when 4 units of mass of helium are made, 14 units of mass of nitrogen are produced. The slope is $\frac{\mathrm{d}Y_{\mathrm{s}}}{\mathrm{d}(N/O)} = \frac{2}{7}\,O \approx 0.286 \times 0.009 = 0.0026$ i.e., it is essentially flat initially. Later in the evolution, both N and O change simultaneously, and one has to rely on numerical models. The resulting slope in the models can vary, see Fig. 2. This depends on whether the matter that arrives at the surface comes from inner regions that are at both CN and ON equilibria, or only at CN equilibrium. There is, of course, a range of intermediate cases.

3 Observational Constraints

Numerous studies of CNO abundances in massive stars of the Milky Way are available in the literature, mostly for early B-type stars close to the MS and for BSGs. Overall, a wide range of N/O–N/C combinations is found, scattering widely around the predicted trends, see Fig. 1 of Przybilla et al. (2010). However, error margins in the individual elements are typically about a factor 2 at 1σ-level. Consequently, such data are of limited use to draw *firm* conclusions on the quality of stellar evolution models. Improved modelling is required to reduce the uncertainties in the abundance determinations.

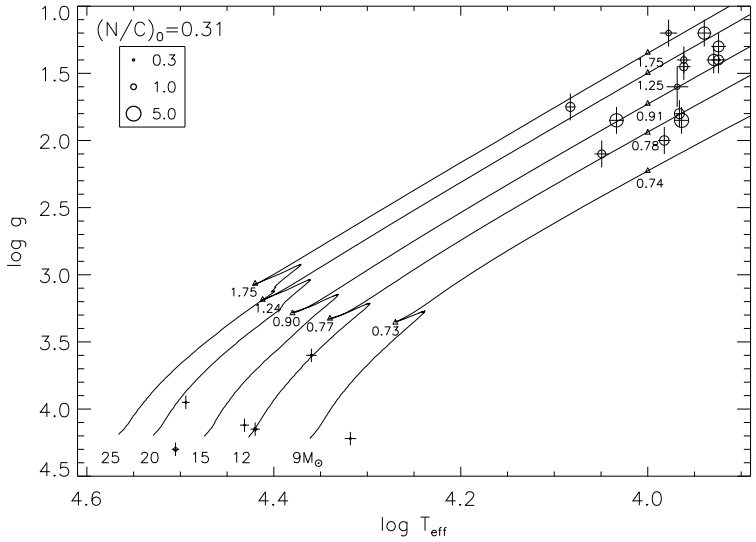

Figure 1: Sample stars in the $\log T_{\rm eff}$–$\log g$-plane. The symbol size encodes the N/C ratio (by mass), with typical values exemplified in the legend. Error bars correspond to 1σ-uncertainties. Evolutionary tracks for rotating stars of metallicity $Z = 0.02$ (Meynet & Maeder 2003) are shown. Predicted N/C ratios are indicated along the tracks (small triangles). From Przybilla et al. (2010).

We have published a series of high-accuracy studies of massive stars in the solar neighbourhood over the past years. Data on 6 slowly-rotating early B-type stars near the MS (Nieva & Przybilla 2006, 2007, 2008, Przybilla, Nieva & Butler 2008) and on 14 BA-type supergiants (Przybilla et al. 2006, Firnstein 2006, Schiller & Przybilla 2008) are available. The studies were based on high-resolution and high-S/N spectra ($S/N > 300$) with wide wavelength coverage (obtained with FOCES@Calar Alto Observatory and FEROS@ESO/La Silla). The analyses were performed homogeneously using a hybrid NLTE approach (Przybilla et al. 2006, Nieva & Przybilla 2007) and state-of-the-art atomic input data. In contrast to all previous work, multiple H lines, the He lines, multiple metal ionization equilibria and the stellar energy distributions were reproduced *simultaneously* in an iterative approach to determine the stellar atmospheric parameters. Chemical abundances were derived from analysis of practically the entire observable spectrum per element. The rewards of such a comprehensive, but time-consuming procedure are unprecedentedly small statistical error margins and largely reduced systematics. We reanalysed the supergiants for the present work, taking advantage of improved model grids. Our new results agree with the earlier ones within the uncertainties but are more accurate.

The sample is displayed in the $\log T_{\rm eff}$–$\log g$-plane and compared to evolutionary tracks in Fig. 1. The stars have initial masses between about 9 to 25 $M_{\odot}$. There is good qualitative agreement between the observations and predictions for the N/C ratios, finding low values close to the initial (solar) ratio on the main sequence and enhanced values in the supergiants. However, the observed N/C ratios reach much higher values than predicted by the models, provided these stars have recently left the main sequence and evolve now into red supergiants (RSGs).

The behaviour of light element abundances in the whole star sample is shown in Fig. 2. A clear and tight trend is found for the first time, confirming the predicted locus of N/O–N/C abundance ratios. However, as already indicated above, the models for rotating stars evolving towards the RSG stage (Meynet & Maeder 2003, solid line in Fig. 2) predict mixing that is too low, i.e. too low f (Sect. 2), in particular for most of the supergiants. The magnetic model (Maeder & Meynet 2005) fits observations better in this context. The observations are also compatible with first dredge-up values, which, however, are reached only after the stars have become red supergiants. Helium abundances provide further constraints (Fig. 2), which in the case of BA-type supergiants are determined for

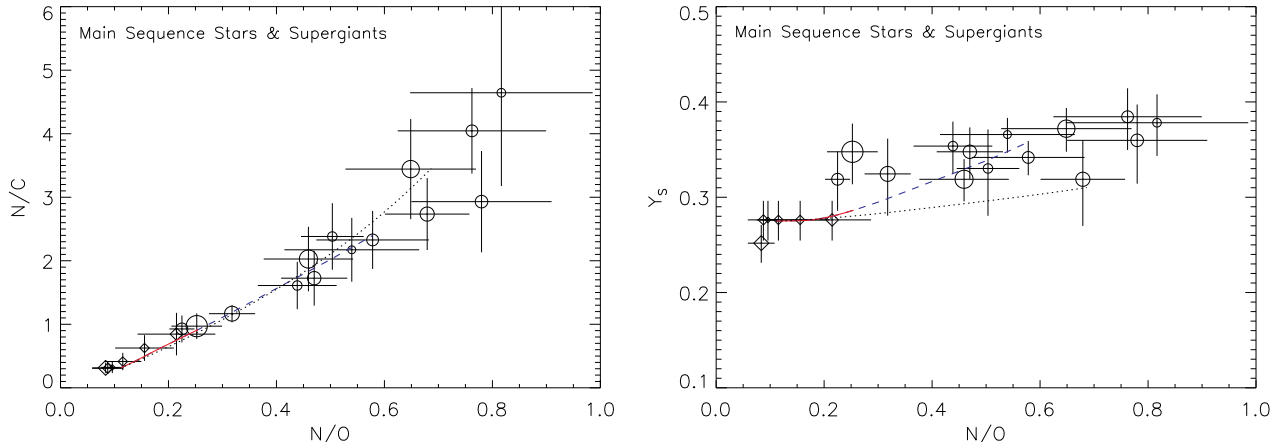

Figure 2: Left panel: N/C vs. N/O abundance ratios. Right panel: Surface helium abundance $Y_{\rm S}$ vs. N/O ratio (both by mass fraction) for our sample stars. B-type main sequence stars are displayed as diamonds, BA-type supergiants as circles. The symbol size encodes the stellar mass and error bars give 1σ-uncertainties. The different lines describe model predictions for 15 $M_{\odot}$ stars: for a rotating star ($v_{\rm ini} = 300\,{\rm km\,s^{-1}}$, Meynet & Maeder 2003; until the end of the MS: solid red line, until the end of He burning: dashed blue line) and for a model that in addition takes a magnetic dynamo into account (Maeder & Meynet 2005; until the end of the MS: dotted line). The predicted trends are similar for the entire mass range under investigation and they are independent of $v_{\rm ini}$ (except for the amount of mixed material). From Przybilla et al. (2010).

a significant number of stars for the first time in a self-consistent analysis. On the MS no helium surface enrichment is observed, as predicted in the models for stars with masses below about 20 $M_{\odot}$. He-enrichments at the level observed in the present supergiants are compatible with models having undergone a dredge-up in the RSG phase. Depending on the rotation velocity, the presence of a magnetic field or its absence, models will populate diverse parts of the region in the plane $Y_{\rm S}$ versus N/O after the RSG phase, as illustrated e.g. by the dashed and dotted lines in Fig. 2.

Actually, the interpretation of the BSG data can become really constraining only when we obtain additional hints on the previous evolution of the stars. Have the BSGs evolved directly from the MS, or have they evolved into that stage after going through a RSG stage? The problem is visualised in Fig. 3, which displays the evolution of the N/C-ratio as a function of $\log g$. The surface gravity decreases in general with increasing age of the star, except for blue-loop episodes like the one close to the end of the 9 $M_{\odot}$ track. The observed N/C-ratios are compatible with first dredge-up values (N/C $\approx$ 2-3) from a previous RSG stage for most of the BSGs, which is not predicted by the models (models with rotation do not predict blue loops for masses higher than $\sim$9 $M_{\odot}$). Moreover, given the extremely short period that the models predict the stars to spent in the BA-type supergiant regime (cf., however, Salasnich, Bressan & Chiosi 1999), there are way too many objects observed in this particular evolution stage. Magnetic models on the other hand may reach the observed N/C-ratios during their redward evolution from the MS, but they need to be computed further through core He-burning to facilitate detailed investigations.

Already from the small sample of stars on the MS it appears that other factors need to be considered in the models to explain some outliers (Fig. 3). An analysis of a larger sample of MS stars indicates that while the majority of objects is described well by evolution models for rotating stars, (fossil) magnetic fields may play a role in some cases, see Przybilla & Nieva (2010) for details.

Overall, our improved spectral modelling and the novel analysis techniques provide observational constraints of unprecedented accuracy and precision to stellar evolution models. Further investiga-

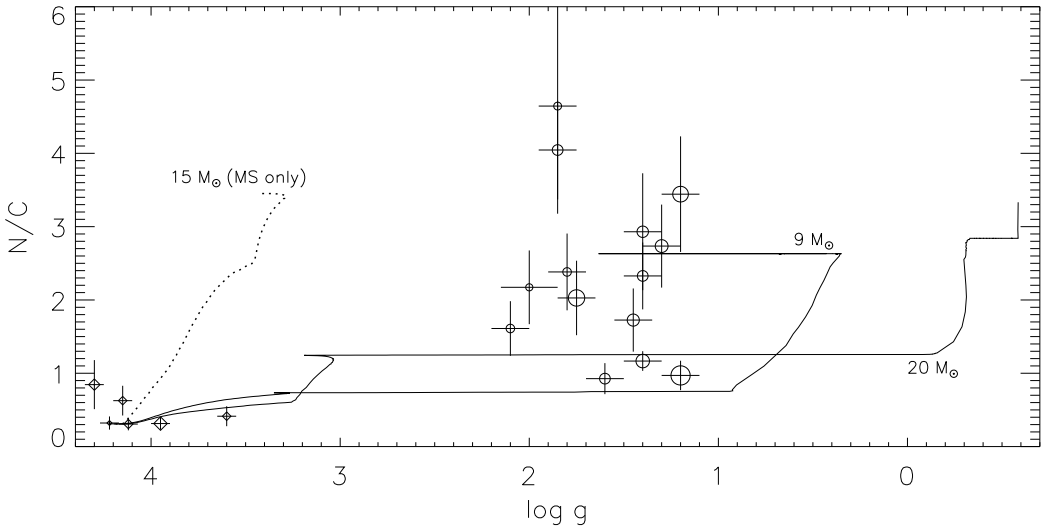

Figure 3: Sample stars in the $\log g$–N/C-plane. Symbol and line encoding as in Fig. 1. In addition, a magnetic model is displayed which has been evolved only to the end of H-burning (Maeder & Meynet 2005, dotted line). The symbol size is proportional to stellar mass. From left to right, the evolution proceeds from the MS over the BA-type supergiant regime to the RSG stage, potentially entering a blue loop (where $\log g$ develops towards higher values), like for the 9 $M_\odot$ model.

tions need to encompass larger sample sizes to cover all relevant quantities in the multi-dimensional parameter space (mass, age, rotational velocities, metallicity, etc.). This may finally lead to a deeper understanding of the fundamental processes governing the evolution of massive stars, single ones and those in close binary systems (e.g. Wellstein, Langer & Braun 2001).

Acknowledgements

NP and MFN would like to thank the staff at Geneva Observatory for their hospitality. MF acknowledges funding by the *Deutsche Forschungsgemeinschaft, DFG* under project number PR 685/3-1.

References

Firnstein, M. 2006, Diploma Thesis (Univ. Erlangen-Nuremberg)
Heger, A. & Langer, N. 2000, ApJ, 544, 1016
Heger, A., Woosley, S. E. & Spruit, H. C. 2005, ApJ, 626, 350
Maeder, A. 2009, *Physics, Formation and Evolution of Rotating Stars* (Springer Verlag, Berlin)
Maeder, A. & Meynet, G. 2000, ARA&A, 38, 143
Maeder, A. & Meynet, G. 2005, A&A, 440, 1041
Meynet, G. & Maeder, A. 2003, A&A, 404, 975
Nieva, M. F. & Przybilla, N. 2006, ApJ, 639, L39
Nieva, M. F. & Przybilla, N. 2007, A&A, 467, 295
Nieva, M. F. & Przybilla, N. 2008, A&A, 481, 199
Przybilla, N., Butler, K., Becker, S. R. & Kudritzki, R. P. 2006, A&A, 445, 1099
Przybilla, N., Nieva, M. F. & Butler, K. 2008, ApJ, 688, L103
Przybilla, N., Firnstein, M., Nieva, M. F., Meynet, G. & Maeder, A. 2010, A&A, 517, A38
Przybilla, N. & Nieva, M. F. 2010, in *Active OB stars – structure, evolution, mass loss, and critical limits*, IAU Symposium 272, eds. C. Neiner, G. Wade, G. Meynet, G. Peters (Cambridge University Press)
Salasnich, B., Bressan, A. & Chiosi, C. 1999, A&A, 342, 131
Schiller, F. & Przybilla, N. 2008, A&A, 479, 849
Wellstein, S., Langer, N. & Braun, H. 2001, A&A, 369, 939

Discussion

S. Owocki: Very interesting result about the anomalous high N/C for τ Sco, which as you note has a detected complex magnetic field. While your suggestion is that this might be explained by magnetic enhancement or internal mixing, it seems one should also consider atmospheric diffusion, which is understood to cause the peculiar abundance of magnetic A_p/B_p stars. Also, it would be interesting to look at the abundances of the emerging class of magnetic massive stars being detected by the MiMeS project.
N. Przybilla: Diffusion requires a very stable atmosphere to take place, in particular the absence of a wind, which is not the case for τ Sco. We have analyzed more magnetic stars and will report on the results soon.

J. Puls: Very nice work; your biggest discrepancies are in the supergiant range. Might it be that a certain part is due to neglected mass-loss in your models, though your objects have a decent mass-loss rate, as obvious from the Hα-spectra?
N. Przybilla: Most of the sample objects have negligible winds. The highest mass-loss rates in a few objects are of the order 10^{-7} M$_\odot$ yr^{-1}, which we don't expect to affect the photospheric line spectra.

Evolution of massive Be and Oe stars at low metallicity towards the Long Gamma Ray bursts*

C. Martayan[1,2], J. Zorec[3], D. Baade[4], Y. Frémat[5],
J. Fabregat[6], and S. Ekström[7]

[1] ESO, Alonso de Cordova 3107 Vitacura, Santiago, Chile

[2] GEPI, Observatoire de Paris, place Jules Janssen 92195 Meudon Cedex, France

[3] Institut d'Astrophysique de Paris, UMR7095 CNRS, Université P& MC,
98bis boulevard Arago, 75014 Paris, France

[4] ESO, Karl-Schwarschild-Str. 2, Garching bei Muenchen, Germany

[5] Royal Observatory of Belgium, 3 avenue circulaire, 1180 Brussel, Belgium

[6] Observatorio Astronomico de Valencia, 46980 Paterna Valencia, Spain

[7] Geneva Observatory, University of Geneva, Maillettes 51, 1290 Sauverny, Switzerland

Abstract: Several studies have shown recently that at low metallicity B-type stars rotate faster than in environments of high metallicity. This is a typical case in the SMC. As a consequence, it is expected that a larger number of fast rotators is found in the SMC than in the Galaxy, in particular a higher fraction of Be/Oe stars. Using the ESO-WFI in its slitless mode, the data from the SMC open clusters were examined and an occurrence of Be stars 3 to 5 times larger than in the Galaxy was found. The evolution of the angular rotational velocity at different metallicities seems to be the main key to understand the specific behavior and evolution of these stars. According to the results form the WFI study, the observational clues drawn from the WR stars and other massive stars in the SMC, and relying on the model predictions regarding the characteristics that LGRBs-progenitors should have on the ZAMS, we concluded that low metallicity Oe/Be stars are potential progenitors of LGRBs. In this document, we describe the different steps followed in these studies: determination of the number of Be/Oe stars at different metallicities, identification of the clues that lead to suppose the low metallicity Be/Oe stars as LGRB progenitors, comparison of models with observations.

1 Introduction

Let us recall that a Be star is a non-supergiant B-type star which spectrum has shown at least once emission-lines. Actually Be stars rotate very fast, in the Galaxy between 60 to 85% of the critical rotational velocity depending on their spectral type (Cranmer 2005; Huang, Gies & McSwain 2010). A similar result is found in the Magellanic Clouds (Martayan et al. 2006, 2007), where Be stars rotate in the LMC between 75 to 85% and in the SMC between 77 to 95% of the critical rotational velocity. With episodic matter ejection from the central star, a circumstellar decrection disk is formed. This phenomenon is not restricted to B type stars but can also occur in late O and early A stars in the

*Based on ESO runs 069.D-0275(A), 072.D-0245(A) and (C).

Galaxy. In the first part of this document the metallicity effects on the rotational velocities and on the ratios of Be to B stars are examined.

The second part of that document deals with the long soft gamma ray bursts (here type 2 bursts) and their possible relationship with the massive Be and Oe stars at low metallicity.

2 Ratios of Be stars with respect to the metallicity

Maeder, Grebel, & Mermilliod (1999) found that the ratio of Be stars to B stars in open clusters seems to increase as metallicity decreases. However, only 1 open cluster in the SMC was used. Wisniewski & Bjorkman (2006) found a similar result but the number of open clusters in the SMC/LMC remained small. The strong variation of the Be/B ratio from an open cluster to another prevents definite conclusions from these studies. It was thus needed to increase the samples (much more SMC open clusters) for improving the statistics, for better constraining the freedom degrees such as the age, the metallicity, the density, etc, and for quantifying the trend found with respect to the metallicity.

• The WFI Hα spectroscopic survey and Be stars ratios

Observations with the ESO-WFI in its slitless spectroscopic mode (Baade et al. 1999) were carried out on September 25, 2002 with the aim to map the LMC/SMC central parts for detecting the Hα emission-line stars and the Be stars. The WFI was used with a grism and a Hα filter insuring a bandpass of 7.4nm, a resolving power of 130 adapted to find the emission in the Hα line of Be stars. The exposure time was 600s. In the SMC 14 images and in the LMC 20 images were obtained (see Martayan, Baade & Fabregat 2010). Let us recall that this kind of instrumentation is not sensitive to the diffuse ambient nebulosity and is not sensitive enough to the weak emission, thus only lower estimates of the emission-line stars content can be provided. Finally 3 million spectra were obtained in the SMC (covering 3 square degrees), and 5 million in the LMC. In this first part of their survey, Martayan, Baade & Fabregat (2010) focused on 84 SMC open clusters. Once the emission-line stars and normal stars detected, the $\sim$4400 stars in SMC open clusters were classified in spectral types using the calibration of Lang (2001). In the SMC sample, the spectral type classification was possible from early O stars to late A stars in the main sequence for normal stars, while for Be stars it was mainly possible from O8e to B3e stars. For more details about the intermediate steps, see Martayan, Baade & Fabregat (2010). The SMC data were compared to the results from McSwain & Gies (2005) in the Galaxy.

At that step it is possible to compute the ratios of Be stars to B stars per spectral-type categories, i.e. for example B0e/(B0+B0e), etc, in the SMC and MW. Finally Martayan, Baade & Fabregat (2010) found that **the Be stars are 3 to 5 times more abundant in the SMC (at low metallicity) than in the MW.**

Studies by McSwain & Gies (2005) and Martayan, Baade & Fabregat (2010) are single-epoch surveys and in both cases, some Be stars in B phase were missed. According to McSwain & Gies (2008) 25 to 50% may go undetected in a single spectroscopic observation in the MW. Bonanos et al. (2010) showed that in the SMC, Be stars are also transient and they found that the ratio of early-Be stars to B stars in open clusters is about 32% (vs. 35% found by Martayan, Baade & Fabregat 2010).

• Metallicity (Z) and rotational velocities

Keller (2004), Martayan et al. (2006, 2007), Hunter et al. (2008) found that OBBe stars rotate faster at lower Z. The SMC OBBe stars rotate faster than LMC OBBe stars, which rotate faster than their Galactic counterparts. This is due to a lower mass-loss (the stellar winds are radiatively driven winds, see Bouret et al. 2003, Vink 2007) and lower angular momentum (Ω) loss at lower Z resulting in faster rotation (Maeder & Meynet 2001).

The ZAMS rotational velocities for SMC, LMC, and MW Be stars samples were determined by Martayan et al. (2007). Be stars at their birth rotate faster in the SMC than in the LMC, which rotate faster than in the MW. This is an opacity effect, at lower Z, the radii should be smaller, thus for an identical intial angular momentum, the stars rotate faster.

Theoretical tracks for Be stars at Z_{SMC} from Ekström et al. (2008) fairly agree with the mean $V \sin i$ and mean V_{ZAMS} of SMC Be stars (see Martayan et al. 2010).

3 Long soft Gamma Ray Bursts and relationship with Be/Oe stars

The gamma ray bursts (GRBs) are the most energetic events since the Big Bang. Among them, 3 classes are distinguished. Type 1 or short GRB (less than 2s) probably resulting from the collapse of 2 compact objects. Type 2 or long GRB (LGRB) is associated with the SNIc and is probably due to a massive fast rotating star that collapses into a black hole (Woosley 1993, Fryer 1997). The rare type 3, or pseudo LGRB, is not associated to a SN. New theoretical models (Hirschi, Meynet, & Maeder 2005, Yoon, Langer, & Norman 2006, Georgy et al. 2009) provide some information on the properties of LGRBs progenitors in the ZAMS: they must be massive fast rotators with low metallicity (Z) and weak magnetic field, in order to avoid huge mass- and angular momentum-losses. Thanks to an effective mixing unleashed by the fast rotation, these model-stars undergo a quasi chemically homogeneous evolution (Maeder 1987, Yoon et al. 2006; Woosley & Heger 2006).

Iwamoto et al. (1998, 2000) have found observationally that massive fast rotating stars are at the origin of the LGRBs. Thöne et al. (2008) found that the LGRB060505 was due to a $32M_{\odot}$ hosted in a low-Z galaxy having a high star-formation rate and a young environment (6 Myr). Campana et al. (2008) conclude that the LGRB060218 progenitor had an initial mass of $20M_{\odot}$, with Z=0.004$\sim Z_{(LMC,SMC)}$. Martins et al. (2009) observed several SMC WR stars whose evolutionary status and chemical properties can be understood if they are fast rotators undergoing quasi chemically homogeneous evolution.

• **Comparison of theoretical LGRBs-progenitor areas with observations**

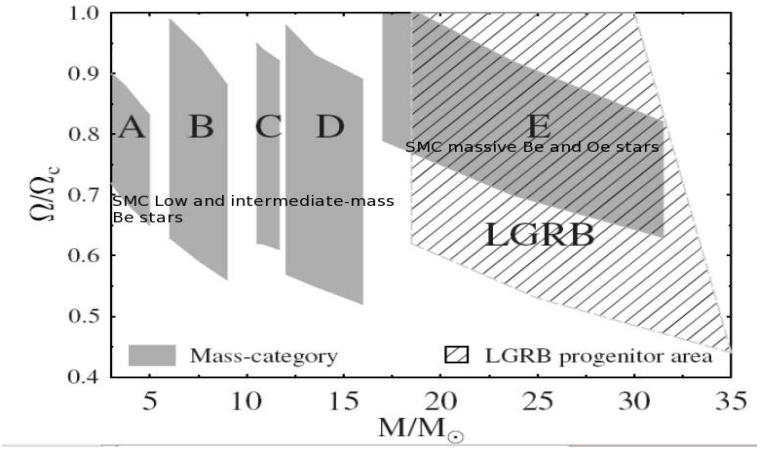

Figure 1: Comparison of LGRBs progenitors area (dashed) at Z_{SMC} at the ZAMS with categories of SMC Be/Oe stars (grey-plain ABCDE areas). This Figure was adapted from Martayan et al. (2010).

The models by Yoon et al. (2006) predict $(\Omega/\Omega_{\rm c}, M/M_{\odot})-$parameter domains that massive stars of low Z should have in the ZAMS to be progenitors of LGRBs. In Fig. 1 we compare them with the ZAMS-parameter-domains (ABCDE) of Oe/Be stars in the SMC derived by Martayan et al. (2010). The overlapping of the theoretical LGRBs-progenitor area with the observational E-zone suggests

that only massive Oe/Be stars with low Z could be progenitors of LGRBs. The rates of LGRB events based on the Oe/Be hypothesis also support this possibility:

• **Predicted LGRBs rates from the counting of Oe/Be stars with low Z**

The prediction of the number of LGRBs events is based on the following assumptions and treatments:

1) the SMC is a representative galaxy of Im type, which all are of low Z;

2) the fraction of Oe/Be stars over all O/B stars in each of them is the one determined by Martayan et al. (2010) for the SMC;

3) the total number N_{tot} of massive Oe/Be stars in the SMC is estimated from the counting carried out in the SMC OGLE-III catalogue, which is complete down to B9 spectral type;

4) binaries are removed from N_{tot} and the fraction of transient Oe/Be phenomena is taken into account;

5) the yearly base-rate of LGRBs events is obtained using N_{tot} and the rotation- and mass-dependent stellar evolutionary lifetime;

6) the observed rate at Earth is estimated using the LGRBs beaming angles distribution from Watson et al. (2006). This leads to the following average predicted LGRBs per year and average galaxy:

R_{pred}(LGRBs) = $(2-5)\times10^{-7}$ **LGRBs/year/galaxy**,

which has to be compared with the observed rate:

R_{obs}(LGRBs) = $(0.2-3)\times10^{-7}$ **LGRBs/year/galaxy** (Zhang & Mészáros 2004; Podsiadlowski et al. 2004; Fryer et al. 2007).

Then, one can predict the number of LGRBs events seen in the local universe based on the massive Oe/Be hypothesis by:

1) limiting the estimates to the redshift $z \leq 0.2$, where there are 17% of Im galaxies (Rocca-Volmerange et al. 2007);

2) taking into account the total number of galaxies with $z \leq 0.2$ determined by Skrutskie et al. (2006);

3) considering the above obtained $R_{pred}(LGRBs)$ rate.

Thus, we infer that in 11 years in $z \leq 0.2$ one should have had:

N_{pred} = 3-6 LGRBs,

while from 1998 to 2008 in $z \leq 0.2$ the GRBOX survey[1] has registered:

N_{obs} = 8 LGRBs.

From the above comparison of ZAMS parameters and predicted LGRBs rates, it can be concluded that massive Oe/Be with low Z can be a major link in the explanation chain of LGRBs.

4 Other issues and redshift evolution

In the plot above on the LGRB phenomenon still there are some open questions:

- The theory of stellar evolution with chemical mixing triggered by fast rotation at low-Z still conflicts with observations (Hunter et al. 2009).

- SN explosions of LBV stars without a WR phase (Smith et al. 2010) are not understood by the theory.

- Can GRB environments provide hints on the chemical evolution of fast rotators (Woosley & Heger 2006, Georgy et al. 2009), knowing that according to theory some SMC massive Be/Oe stars with $Vsini \sim 500$ km/s should display characteristics of chemically homogeneous evolution ?

[1] http://lyra.berkeley.edu/grbox/grbox.php

- Is the SMC fully representative of all Im, and its frequency of Be/Oe similar in all of them (Bresolin et al. 2007)?

- Are the surveys and counts of LGRB/SGRB events complete?

Finally, one can expect that at high redshift stars were extremely metal-poor and probably very fast rotators, like Be/Oe stars but also of other spectral types. Thus with the redshift the number of LGRBs should increase significantly as the number of LGRB progenitors should increase too (Martayan et al. 2010, and references therein).

References

Baade, D., Meisenheimer, K., Iwert, O., et al. 1999, The Messenger, 95, 15
Cranmer, S. R. 2005, ApJ, 634, 585
Bonanos, A. Z., Lennon, D. J., Köhlinger, F., et al. 2010, AJ, 140, 416
Bouret, J.-C., Lanz, T., Hillier, D. J., Heap, S. R., Hubeny, I., Lennon, D. J., Smith, L. J., & Evans, C. J. 2003, ApJ, 595, 1182
Bresolin, F., Urbaneja, M., Gieren, W., Pietrzynski, G., & Kudritzki, R.-P. 2007, ApJ, 671, 2028
Campana, S., Panagia, N., Lazzati, D., et al. 2008, ApJ, 683, L9
Ekström, , S., Meynet, G., Maeder, A., & Barblan, F. 2008, A&A, 478, 467
Fryer, C. L., Mazzali, P. A., Prochaska, J., et al. 2007, PASP, 119, 1211
Georgy, C., Meynet, G., Walder, R., Folini, D., & Maeder, A. 2009, A&A, 502, 611
Hirschi, R., Meynet, G., & Maeder, A. 2005, A&A, 443, 581
Huang, W. Gies, D. R. & McSwain, M. V. 2010 ApJ, 722, 605
Hunter, I., Lennon, D. J., Dufton, P. L., Trundle, C., Simón-Díaz, S., Smartt, S. J., Ryans, R. S. I., & Evans, C. J. 2008, A&A, 479, 541
Hunter, I., Brott, I., Langer, N., et al. 2009, A&A, 496, 841
Iwamoto, K., Mazzali, P. A., Nomoto, K., et al. 1998, Nature, 395, 672
Iwamoto, K., Nakamura, T., Nomoto, K., et al. 2000, ApJ, 534, 660
Keller, S. C. 2004, PASA, 21, 310
Lang, K. R. 1992, Astrophysical data, Planets and Stars (New York: Springer Verlag Eds)
Maeder, A. 1987 A&A, 178, 159
Maeder, A., Grebel, E. K., & Mermilliod, J.-C. 1999, A&A, 346, 459
Maeder, A., & Meynet, G. 2001, A&A, 373, 555
Martayan, C., Frémat, Y., Hubert, A.-M., Floquet, M., Zorec, J., & Neiner, C. 2006, A&A, 452, 273
Martayan, C., Frémat, Y., Hubert, A.-M., Floquet, M., Zorec, J., & Neiner, C. 2007, A&A, 462, 683
Martayan, C., Baade, D. & Fabregat, J. 2010, A&A, 509, A11
Martayan, C., Zorec, J., Frémat, Y., & Ekström, S. 2010, A&A, 516, A103
Martins, F., Hillier, D. J., Bouret, J. C., Depagne, E., Foellmi, C., Marchenko, S., Moffat, A. F. 2009, A&A, 495, 257
McSwain, M. V., & Gies, D. R. 2005, ApJS, 161, 118
McSwain, M. V., Huang, W, Gies, D. R., Grundstrom, E. D., & Townsend, R. H. D. 2008, ApJ, 672, 590
Podsiadlowski, P., Mazzali, P. A., Nomoto, K., Lazzati, D., & Cappellaro, E. 2004, ApJ, 607, L17
Rocca-Volmerange, B., de Lapparent, V., Seymour, N., & Fioc, M. 2007, A&A, 475, 801
Smith, N., Li, W., Filippenko, A., & Chornock, R. 2010, MNRAS, in press, arXiv1006.3899
Skrutskie, M. F., Cutri, R. M., Stiening, R., et al. 2006, AJ, 131, 1163
Thöne, C. C., Fynbo, J. P. U., Östlin, G., et al. 2008, ApJ, 676, 1151
Vink, J. 2007, AIPC, 948, 389
Watson, D., Hjorth, J., Jakobsson, P., Xu, D., Fynbo, J. P. U., Sollerman, J., Thöne, C. C., & Pedersen, K. 2006, A&A, 454, L123
Wisniewski, J. P., & Bjorkman, K. S. 2006, ApJ, 652, 458
Woosley, S.E. 1993, ApJ, 405, 273
Woosley, S. E., & Heger, A. 2006, ApJ, 637, 914
Yoon, S.-C., Langer, N. & Norman, C. 2006, A&A, 460, 199
Zhang, B., & Mészáros, P. 2004, Int. J. Mod. Phys. A, 19, 2385

Discussion

L. Oskinova: Is there evidence for circumstellar disks from afterglow observations?
C. Martayan: I am not a specialist of that topic but I do not think that there is an observational proof of the existence of circumstellar disks in GRB residual environment. Maybe the current XSHOOTER programs could bring some clues on it.
S. Owocki: Be disks are close to the star and relatively low mass, and so I expect they would be destroyed upon the SN shock breakout, without much evidence in the overall light curve.
C. Martayan: I agree, but I also expect that the circumstellar disk created during the MS by classical Be stars is destroyed in the post-MS phases.

Massive Stars with Circumstellar Shells Discovered with the Spitzer Space Telescope

Stefanie Wachter[1], Jon Mauerhan[2], Schuyler Van Dyk[2], D. W. Hoard[2] and Patrick Morris[3]

[1] IPAC, California Institute of Technology, Pasasdena, USA
[2] Spitzer Science Center, California Institute of Technology, Pasasdena, USA
[3] NASA Herschel Science Center, California Institute of Technology, Pasasdena, USA

Abstract: We report on our ongoing efforts to characterize the luminous central stars of circumstellar shell sources discovered with the Spitzer Space Telescope. The objects in our selection are highly symmetric, circular and elliptical shells, most prominent at 24μm, and the vast majority of the shells and central sources has never been studied previously. We obtained near-IR spectroscopic observations of the central stars and find the overwhelming number of these objects to be massive stars, including new Wolf Rayet stars and Luminous Blue Variable candidates.

1 Introduction

Massive stars play a key role in the chemical and mechanical evolution of the ISM in galaxies. These luminous stars with their strong winds and mass outflows are the dominating influence on their environment in terms of energetics and chemical modification of the ISM. Despite their importance, our knowledge about their formation and evolution is surprisingly limited. In particular, the post main sequence evolution of massive stars, where they shed most of their mass, is poorly understood. Observationally, this stage can be explored through the study of Wolf-Rayet stars (WRs), luminous blue variables (LBVs) and red supergiants.

Recently, a large population of obscured evolved massive stars has been revealed through their prominent circumstellar shells at 24 μm (Wachter et al. 2010, Mizuno et al. 2010, Gvaramadze et al. 2010) based on the data from the MIPSGAL legacy survey (Carey et al. 2009) conducted with the Spitzer Space Telescope. In Wachter et al. (2010), we selected a subsample of the 62 most well-defined, symmetrical shells with obvious central sources for an in depth follow-up study. A SIMBAD search within 2' of the shell locations revealed that most of these objects (90% of the shells, 80% of the central sources) had not been previously studied. The radii of our shells range from 0.14' - 2.4' with a formal average of 0.7'. Follow-up investigation utilizing the complementary data from the GLIMPSE Spitzer Legacy project (Benjamin et al. 2003), as well as 2MASS and the Digitized Sky Survey shows that about 60% of these shells are *only* detected at 24μm (the 8 and 24μm images of the shells are displayed in Wachter et al. 2010). This is somewhat unusual, as we generally expect a strong emission component due to polycyclic aromatic hydrocarbons (PAHs) at 8μm if we are simply observing warm dust continuum emission.

We report here on additional spectroscopic results for our sample of 24μm shell central sources.

2 Results

We summarize here the results of our newly acquired IR spectroscopy. Data were obtained on three nights in May 2010 on SOAR with OSIRIS, providing R $\sim$ 1200 JHK spectra, and on 19-20 June 2010 with Triplespec on the Palomar 200 inch telescope, with a slightly higher resolution of R $\sim$ 2700. In addition to the remaining targets from our sample detailed in Wachter et al. (2010), we also obtained data for the more asymmetric and/or bipolar shells included in the sample of Gvaramadze et al. (2010). A preliminary classification of all the newly observed central sources is presented in Table 1.

Table 1: Preliminary classification of newly observed shell central stars.

Name	Type		Name	Type
WMD 002	late type		MN 009	WN 8-9h
WMD 012	late type		MN 010	OB
WMD 015	B[e]/LBV		MN 013	B[e]/LBV
WMD 018*	B[e]/LBV		MN 018*	OB
WMD 019	B[e]/LBV		MN 031	OB
WMD 020*	Be		MN 039	B[e]/LBV
WMD 027	B[e]/LBV		MN 041*	B[e]/LBV
WMD 030	B[e]/LBV		MN 053	B[e]/LBV
WMD 032*	OB		MN 069	OB
WMD 035	OB		MN 079	B[e]/LBV
WMD 036*	B[e]/LBV		MN 092	OB
WMD 038	Be		MN 094	OB
WMD 039*	Be		MN 101	B[e]/LBV
WMD 041	WN 8-9h		MN 106	late type
WMD 042	B/A		MN 107	Be
WMD 047	WN 8-9h		MN 108*	OB
WMD 048	WN 8-9h		MN 109*	OB
WMD 050*	WN 3-4			
WMD 051	B[e]/LBV			
WMD 053	WN 9h			
WMD 054	B[e]/LBV/WN			
WMD 055	OB			
WMD 056	Be			

Targets labeled "WMD" correspond to the central stars of the shells of Wachter et al. (2010), targets designated as "MN" are from the sample of Gvaramadze et al. (2010). The * indicates sources which were already classified in Wachter et al. (2010) or Gvaramadze et al. (2010), but were reobserved to improve the S/N, search for variability, or cover a different wavelength range. A detailed comparison with existing data for these sources will be discussed in a future publication.

We discovered five new WR stars, namely the central sources of the shells WMD 041, 047, 048, 053, and MN 009. A detailed analysis for the twin WN stars at the center of the double shell complex WMD 047/048 is presented in Mauerhan et al. (2010), the remaining spectra of the WR sources are displayed in Figure 1. WMD 050 has previously been observed in the optical by Wachter et al. (2010). Curiously, the WR spectral type was determined to be WN6 from the optical spectrum, while

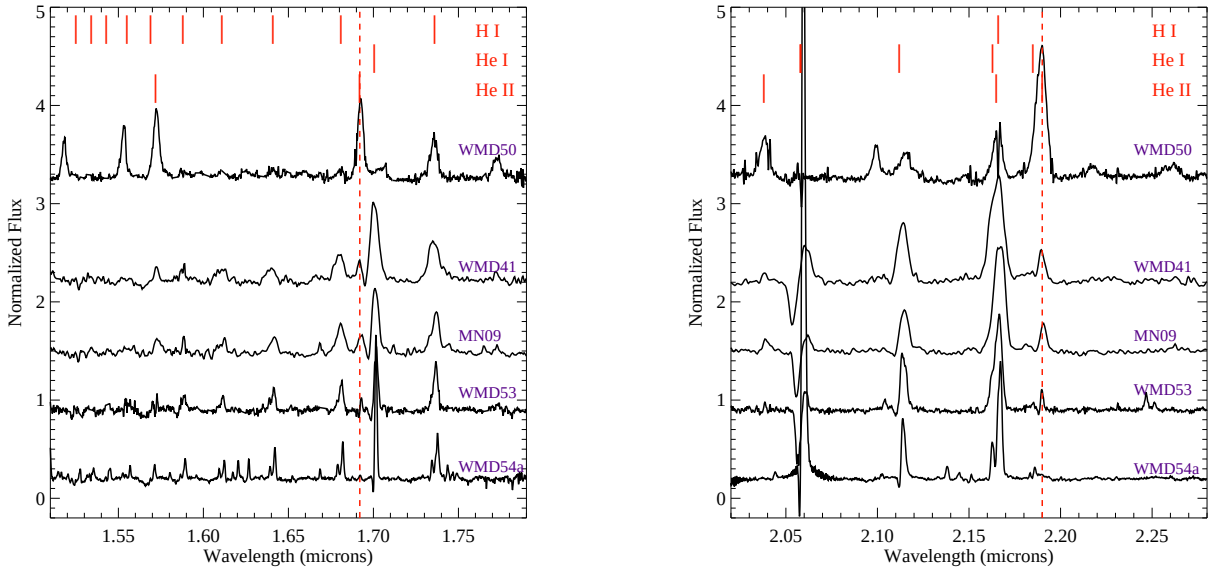

Figure 1: H and K band spectra of newly discovered WR stars.

the IR classification indicates an earlier type, WN3-4. We also find a treasure trove of potential LBV candidates, designated as B[e]/LBV in Table 1. An example of some of the spectra are shown in Figure 2. WMD 054 is an interesting source, as it exhibits emission features similar to both the WR and the B[e]/LBV group of sources (bottom spectrum of Figures 1 and 2), possibly even a hint of the He II 2.189μm line. Finally, we identify 11 OB type central stars, some of which are shown in Figure 3. More detailed analysis is needed to classify these stars in terms of luminosity class, but it is already apparent that OB central stars are preferentially located in shells with asymmetric or bipolar morphology.

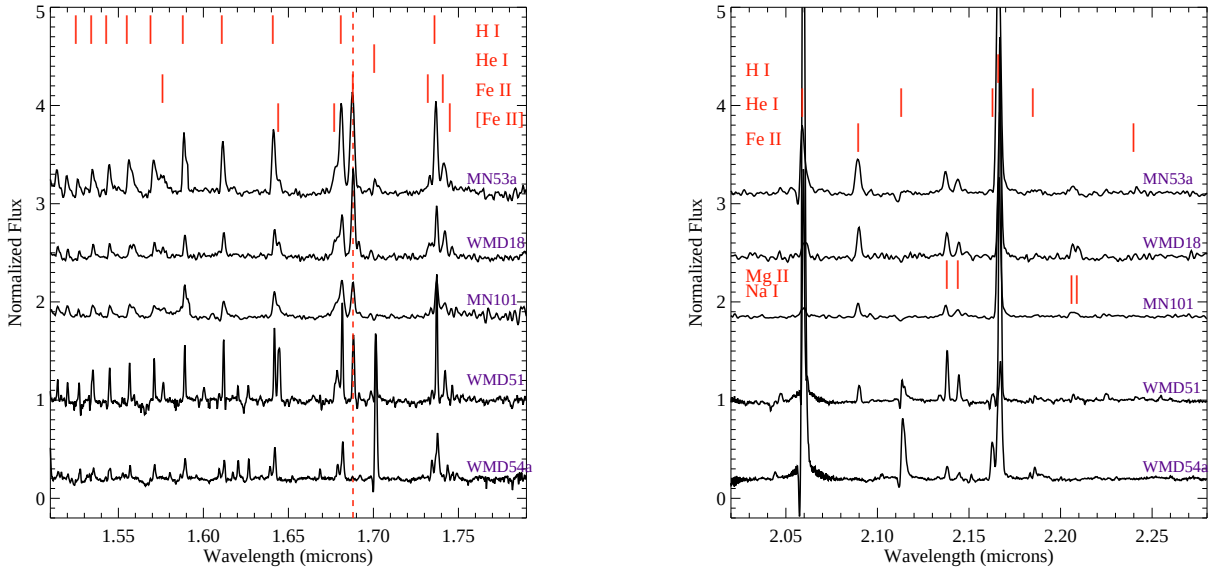

Figure 2: H and K band spectra of a subsample of the newly discovered B[e]/LBV type stars.

We assembled 2MASS and GLIMPSE photometry for each source and constructed a color-color diagram (Figure 4) following Mauerhan et al. (2009) and Hadfield et al. (2007). The various types of sources we have identified spectroscopically are indicated by different colors (see the caption of

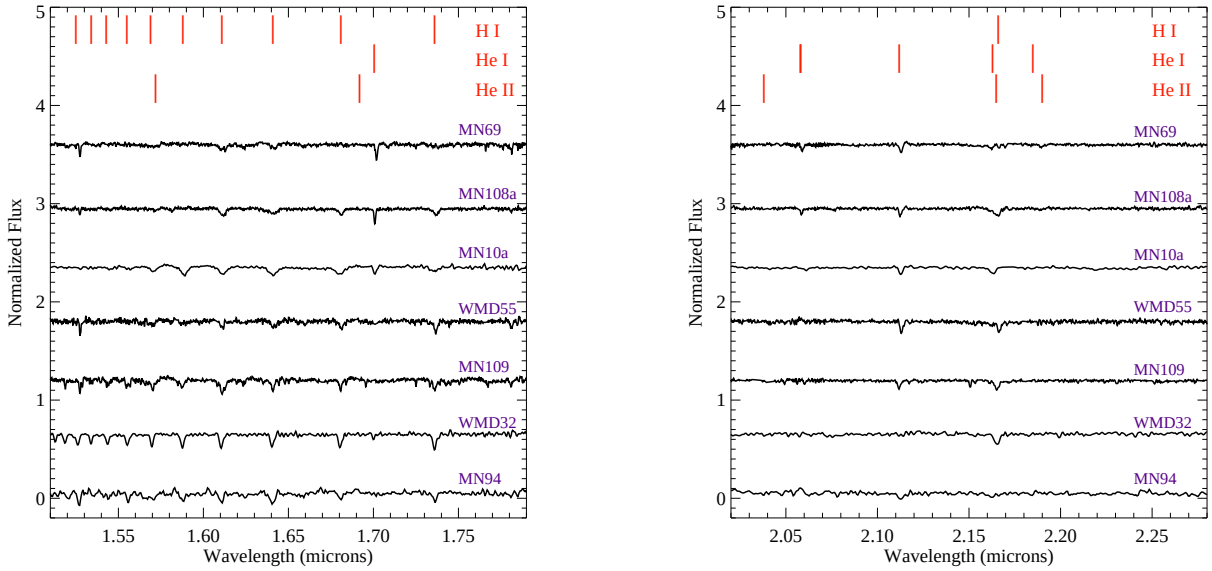

Figure 3: H and K band spectra of a subsample of the newly discovered OB type central stars.

Figure 4 for details). While there is clearly some overlap between the various types of sources, some general trends emerge. The WR stars (red points) in our sample separate quite cleanly from the main locus of field stars and form a surprisingly well-defined and tight sequence, roughly parallel to the reddening vector. The direction of the reddening vector at the locus of our WR stars is indicated by the dashed line. Compared to the analogous figure presented in Mauerhan et al. (2009), about half of our WR points have larger $J - Ks$ values, indicating a more heavily reddened population. B stars and LBV candidates appear to populate the locus in between the normal stars and the WR track. These photometric criteria can prove extremely useful in identifying additional transition stars *without* circumstellar nebulae in the vicinity of our shell sources. For example, we have spectroscopically identified a previously unknown WC and O7-8 star in the immediate environment of the double shell complex WMD 047/048 (Mauerhan et al. 2010) based on their position in the local color-color diagram. We are currently conducting similar searches around all the shell sources in our sample.

Overall, our sample of 62 sources contains 10 WR stars, eight of which are new identifications, as well as five OB type stars. Most strikingly, our study revealed a large number of new LBV candidates. Our sample of shells includes four known LBV type stars (one confirmed, three candidates) and we classified an additional twenty sources as LBV candidates based on the similarities between the spectra (we include both Be and B[e] stars in this group). We realize that the classification of a particular source as an LBV involves a host of criteria, including photometric and spectroscopic variability, that still need to be investigated for these new sources. However, given the small numbers of known LBVs, the presence of a shell combined with the spectroscopic characteristics make this relatively large sample of new candidates an exciting discovery.

Acknowledgements

This work is based in part on archival data obtained with the Spitzer Space Telescope, which is operated by the Jet Propulsion Laboratory, California Institute of Technology under a contract with NASA. Support for this work was provided by an award issued by JPL/Caltech. Based on observations obtained at the Hale Telescope, Palomar Observatory, as a part a continuing collaboration between the California Institute of Technology, NASA/JPL, and Cornell University. This publication makes use

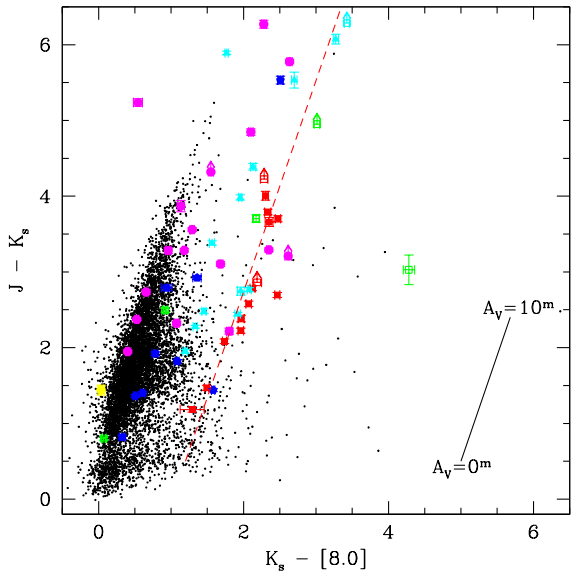

Figure 4: Color–color diagram for the sources in our sample. WR stars are indicated in red, LBVs / B[e]/LBV candidates in cyan, B stars in blue, planetary nebulae in yellow, and F-M stars in magenta. Green symbols indicate yet unclassified central sources. The comparison population of sources (black points) represents a 1 square degree "slice" of the Galactic plane from the GLIMPSE survey. The reddening vector was adapted from Indebetouw et al. (2005).

of data products from the 2 Micron All Sky Survey, which is a joint project of the University of Massachusetts and the Infrared Processing and Analysis Center/California Institute of Technology, funded by the National Aeronautics and Space Administration and the National Science Foundation. It also utilized NASA's Astrophysics Data System Abstract Service and the SIMBAD database operated by CDS, Strasbourg, France.

References

Benjamin, R.A., Churchwell, E., Babler, B.L., et al. 2003, PASP 115, 953
Carey, S.J., Noriega-Crespo, A., Mizuno, D.R., et al. 2009, PASP 121, 76
Gvaramadze, V.V., Kniazev, A.Y., & Fabrika, S. 2010, MNRAS 405, 1047
Hadfield, L.J., van Dyk, S.D., Morris, P.W., Smith, J.D., Marston, A.P., & Peterson, D.E. 2007, MNRAS 376, 248
Indebetouw, R., Mathis, J.S., Babler, B.L., et al. 2005, ApJ 619, 931
Mauerhan, J.C., van Dyk, S.D., & Morris, P.W. 2009, PASP 121, 591
Mauerhan, J., Wachter, S., Morris, P., Van Dyk, S.D., & Hoard, D. W. 2010, ApJ 724, L78
Mizuno, D.R., Kraemer, K.E., Flagey, N., et al. 2010, AJ 139, 1542
Wachter, S., Mauerhan, J.C., Van Dyk, S.D., Hoard, D.W., Kafka, S., & Morris, P.W. 2010, AJ 139, 2330

Discussion

D. Gies: Any evidence of more elliptical shapes among the Be star category?
S. Wachter: No. But the classification of the stars based only on IR spectra is difficult and I'm not sure these are truly classical Be stars. Also, the number of Be stars in our sample is quite small (most are B[e]/LBV types) so the statistics are not very meaningful.

S. Owocki: Why do you lump Be, B[e] and LBVs? The former should have a disk and asymmetric mass loss. The latter could well be mostly spherical.
S. Wachter: Be/B[e] and LBV stars exhibit very similar features in their IR spectra (as already noted by Morris et al. 1996). Based on their spectra (combined with the presence of a shell) we could classify all of the Be/B[e] stars in our sample as new LBV candidates. Of course we now have to study these sources in more detail to determine their luminosities, photometric + spectroscopic variability and the chemical composition and mass of their shells in order to explore this possibility further.

S. Dougherty: Were these objects picked out by eye since there seems to be a remarkable degree of symmetry in your sources - which suggests either a selection bias (by-eye detection) or that they are expanding symetrically into an evacuated medium?
S. Wachter: Yes, we assembled the original sample of > 200 shells by eye and then selected only the most symmetric shells (circular or slightly elliptical) for our in depth follow-up study presented here. So there is definitely a very strong selection bias for this sample. However, it is still a very interesting question of whether we find these circular shells in the first place because they happen to be in some preferred environment that doesn't destroy or impede the formation of the bubble.

N. Smith: Have you investigated what emission mechanism dominates the $24\mu m$ MIPS or IRAC filters? I.e. is it always dust continuum or line emission?
In cases where you have seen line emission, is it [O IV]?
S. Wachter: You can have both dust and/or line emission. We have a few spectra from Spitzer for a few of the shells. There are some with pure line emission and no sign of a dust continuum. In that case it is usually very strong [O IV] which makes the shell stand out at 24 μm. But there are also several that show a slowly rising dust continuum starting at $\sim 10\mu m$, sometimes with some emission lines (e.g. [Fe II]). These results should come out in Flagey et al. (2010) pretty soon.

M. Garcia: Do you have an estimate of the extinction caused by the dust structures?
S. Wachter: We only have an estimate of the combined extinction (interstellar and local) towards the central sources for which we can derive reliable spectral types (WR and late type stars). We don't have an estimate for the extinction in the shell structures.

W.-R. Hamann: You mentioned the need for spectroscopic data to establish the nature of the circumstellar nebulae around the WN star. I want to recall our work of the "Peony Nebula" (Barniske et al. 2008, A&A 486, 971) around WR102ka, for which we got a Spitzer spectrum in the mid-IR which revealed the whole combination of warm-dust emission, forbidden-line emission from an ionized nebula, and molecular hydrogen (H_2) emission from a photo-dissociation region (PDR).
S. Wachter: Absolutely, there are a few mid-IR spectra of known WRs and LBVs in the literature. However, I don't think we can simply assume that all of these newly discovered sources have the same SEDs and chemical composition, particularly given the differences in detection rate of the shells at $8\mu m$. All I'm saying is that it would be nice to get spectra of the shells to see if there are differences or common characteristics.

Feedback from Massive YSOs and Massive Stars

You-Hua Chu[1] and Robert A. Gruendl[1]

[1] Astronomy Department, University of Illinois, Urbana, IL 61801, USA

Abstract: Massive stars are powerful sources of radiation, stellar winds, and supernova explosions. The radiative and mechanical energies injected by massive stars into the interstellar medium (ISM) profoundly alter the structure and evolution of the ISM, which subsequently influences the star formation and chemical evolution of the host galaxy. In this review, we will use the Large Magellanic Cloud (LMC) as a laboratory to showcase effects of energy feedback from massive young stellar objects (YSOs) and mature stars. We will also use the Carina Nebula in the Galaxy to illustrate a multi-wavelength study of feedback from massive star.

1 Introduction

Massive stars generate large amounts of energy and are thus luminous. The energy leaves a star mainly in the form of radiation; only a small portion of the energy is imparted to the stellar wind through line scattering. For example, an O5 main sequence star has a luminosity of $\sim 10^6\ L_\odot$, or $\sim 4\times 10^{39}$ ergs s^{-1}, while the mechanical luminosity of its stellar wind is only $L_{\rm w} \sim 1.3\times 10^{35}$ ergs s^{-1}, assuming a typical mass loss rate ($\dot{M}$) of 10^{-7} M$_\odot$ yr^{-1} and a wind terminal velocity ($V_{\rm w}$) of 2000 km s^{-1}. As a massive star evolves and traces a nearly horizontal track in the theoretical HR diagram, its luminosity is nearly constant, but its varying effective temperature leads to different mass loss rates and stellar wind velocities. For example, a red supergiant has a higher $\dot{M}$, $\sim 10^{-4}$ M$_\odot$ yr^{-1}, but a lower $V_{\rm w}$, 10–50 km s^{-1}, and its $L_{\rm w}$ is even lower, $\sim 10^{34}$ ergs s^{-1}. A Wolf-Rayet (WR) star, on the other hand, has both a high $\dot{M}$ and a high $V_{\rm w}$, and thus the highest $L_{\rm w}$, 10^{37}–10^{38} ergs s^{-1}, which is still much lower than its luminosity.

At infancy, the radiation of a massive young stellar object (YSO) can heat and repel the ambient dust, photo-dissociate molecules, and photo-ionize atoms, while its stellar wind clears out the circumstellar material and further erodes the placental molecular cloud. During its adulthood, a massive star's radiation photo-ionizes and heats its ambient interstellar medium (ISM) to 10^4 K, and its stellar wind dynamically interacts with the ISM, blowing bubbles and generating turbulence. At the end of its life, a massive star explodes as a supernova, releasing $\sim 10^{51}$ ergs of kinetic energy into the ISM, forming a classical supernova remnant (SNR) in a dense medium, or merely heating its ambient medium further if it is in a hot low-density medium such as the interior of a superbubble.

Stellar energy feedback profoundly alters the structure of the ISM by producing interstellar shells up to 10^3 pc in size, injecting turbulence, creating multiple phase components with different physical conditions, and ejecting hot gas into the galactic halo. As stars are formed from the ISM, the physical changes of the ISM affect the future generation of star formation, either dispersing or compressing

the ISM to inhibit or enhance star formation. The mass loss from massive stars enriches the ISM and the intergalactic medium, contributing to the chemical evolution of a galaxy.

Sites of stellar energy feedback provide excellent laboratories for us to study a wide range of astrophysical processes, such as shocks, thermal conduction, turbulence, cosmic ray acceleration, etc. Observations of stellar energy feedback allow us to better grasp its ramifications on cosmic evolution. It is thus important to study stellar energy feedback. Unlike star formation, however, there is no simple recipe for stellar energy feedback because the ISM surrounding massive stars has diverse physical conditions, resulting in complex dynamical interactions.

2 The Large Magellanic Cloud as a Laboratory

The actions of energy feedback from massive stars are best observed in a galaxy where a clear, high-resolution view of both stars and the ISM for the entire galaxy can be obtained. The Large Magellanic Cloud (LMC) provides such an ideal laboratory to study massive stars acting on the ISM because of its nearly face-on orientation, small distance (50 kpc, where $1''$ corresponds to 0.25 pc), and low foreground extinction.

The LMC has been surveyed extensively for both stars and the ISM: $UBVI$ photometry of bright stars (MCPS, Zaritsky et al. 2004), emission-line survey of ionized gas (MCELS, Smith and the MCELS Team 1999), *ROSAT* X-ray mosaic image of the hot (10^6 K) ionized gas (made by S. Snowden), ATCA+Parkes 21-cm line survey of H I (Kim et al. 2003), *Spitzer* near- and mid-IR surveys of stars and dust (SAGE, Meixner et al. 2006), and CO surveys of molecular clouds (NANTEN, Fukui et al. 2008; MAGMA, Hughes et al. 2010). These surveys provide a detailed view of the distributions, physical conditions, and kinematics of the ISM and the underlying stellar population in the LMC.

Figure 1 displays some of the survey images to illustrate the full view of the LMC at different wavelengths: MCPS optical continuum, 2MASS K-band, *Spitzer* IRAC and MIPS composite, MCELS Hα, *ROSAT* PSPC mosaic in the 0.5–2.0 keV band, and ATCA+Parkes H I 21 cm line. These detailed surveys of stars and ISM enable many studies that are not possible in the Galaxy or in more distant galaxies. For example:

- The MCPS data have been used to determine the spatially-resolved star formation history of the LMC (Harris & Zaritsky 2009), and this star formation history combined with Starburst99 (Leitherer et al. 1999) can be used to estimate the history of stellar energy injected into the ISM.

- The actual stellar content of a superbubble can be observed to estimate the total stellar energy input, and the kinetic energy in the expanding shell and the thermal energy in the superbubble interior can be measured to determine the stellar energy retained in the ISM. It is found that the ISM retains much less energy than the total stellar energy injected (Cooper et al. 2004).

- The *Spitzer* survey of the LMC can be used to search for stars with IR excesses indicating circumstellar dust and to identify YSOs (Gruendl & Chu 2009). The power spectrum analysis of *Spitzer* images shows two power laws with different slopes joining at a scale of 100–200 pc, which may be a scale height of the dust disk of the LMC (Puerari et al. 2010).

- The stellar mass distribution assessed from the 2MASS survey and the gas distribution derived from the H I and CO surveys can be used to determine the gravitational instability map of the LMC, and it is found that $\sim$85% of the massive YSOs are located within the unstable regions (Yang et al. 2007).

- Star formation related to stellar energy feedback can be studied in detail around OB associations and superbubbles (Chen et al. 2009, 2010) as well as supergiant shells (Book et al. 2009).

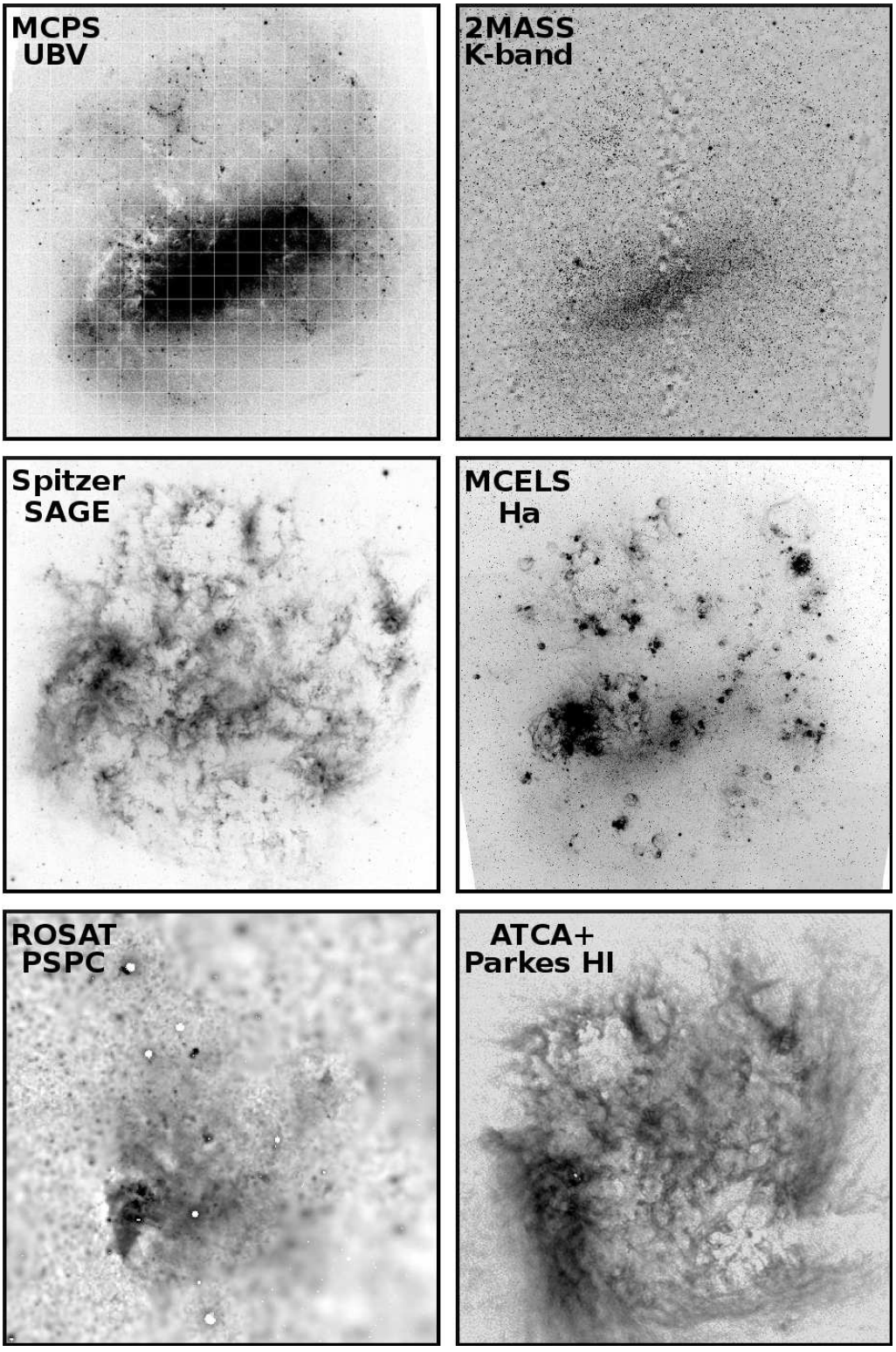

Figure 1: Multi-wavelength images of the LMC. The top row displays the MCPS composite image from Harris & Zaritsky (2009) and 2MASS K-band image, the middle row the *Spitzer* SAGE composite image from Meixner et al. (2006) and MCELS Hα image from Smith & the MCELS Team (1999), and the bottom row the *ROSAT* PSPC mosaic in the 0.5–2.0 keV band made by S. Snowden and ATCA+Parkes H I map from Kim et al. (2003). Note that these images do not have identical scales and orientation.

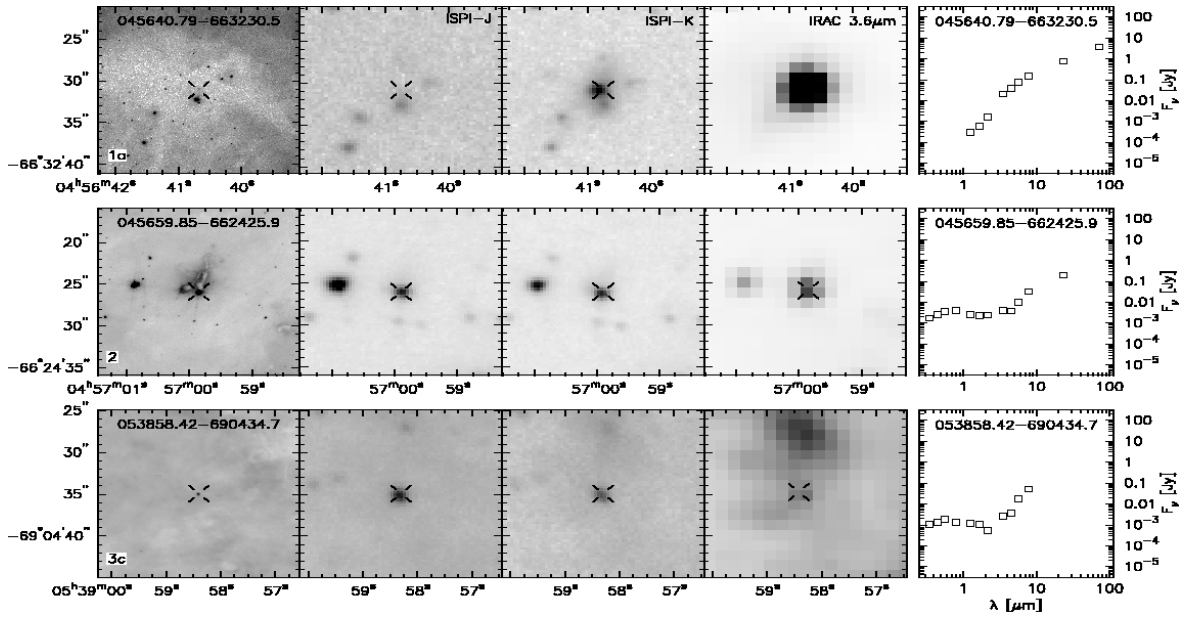

Figure 2: Images and SEDs of three YSOs with three different types of immediate environments: in a dark cloud (top row), in the tip of a bright-rimmed dust pillar (middle row), and in a small H II region (bottom row). The images from left to right are: *HST* Hα, CTIO 4m ISPI J and K, *Spitzer* IRAC 3.6 μm. The rightmost panel shows the SED.

It is impossible to review every stellar energy feedback topic. In this paper, we have selected a few obvious topics in which recent progress has been made: (1) dispersal of molecular clouds, (2) interstellar shells, (3) acceleration of cosmic rays, and (4) anatomy of the Carina Nebula.

3 Massive Star Formation and Dispersal of Molecular Clouds

To investigate the energy feedback of massive stars in their infancy, we can examine the immediate surroundings of massive YSOs. A large sample of massive and intermediate-mass YSOs have been identified in the LMC (Gruendl & Chu 2009). About 100 of these YSOs have archival *Hubble Space Telescope* (*HST*) Hα and continuum images available. These Hα images reveal three types of immediate environments of YSOs: in dark clouds, inside or on the tip of bright-rimmed dust pillars, and in small H II regions (Vaidya et al. 2009). Figure 2 shows images and spectral energy distributions (SEDs) of three exemplary YSOs. It is suggested that the three types of environments represent an evolutionary sequence, as the stellar wind clears out the ambient molecular cloud and reveals a small H II region. This evolutionary sequence is supported by the evolutionary stages of the YSOs indicated by their SEDs.

The dispersal of ambient molecular material by massive YSOs is also seen in direct observations of HCO^+, a tracer for dense molecular gas. Using the ATCA facility, HCO^+ has been mapped in two OB/H II complexes: N44 (Seale et al., in preparation) and N159 (Chen et al., in preparation). Many YSOs in these two complexes have *Spitzer* IRS spectra available. Based on the progressive presence of silicate absorption, PAH emission, and fine-structure atomic line emission, an evolutionary sequence of YSOs can be defined (Seale et al. 2009). It is observed that the youngest YSOs, those with silicate absorption, are still coincident with molecular cores indicated by HCO^+ peaks, while the intermediate-aged YSOs show offsets from molecular cores, and the most evolved YSOs are no longer associated with molecular cores. Both the aforementioned *HST* Hα observations and these HCO^+ observations suggest that massive YSOs quickly disperse their ambient molecular material,

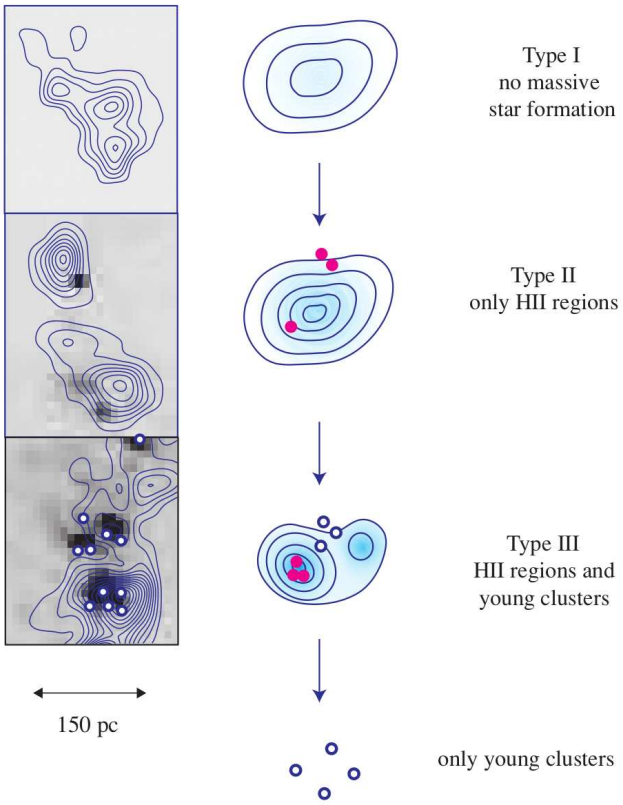

Figure 3: Evolutionary sequence of molecular clouds from Kawamura et al. (2009).

probably before they reach the main sequence.

On a larger scale, the dispersal of molecular clouds in the LMC has been studied by Kawamura et al. (2009). They find three types of molecular clouds: Type I has no massive star formation, as indicated by a lack of Hα emission; Type II has isolated massive star formation, as indicated by small discrete H II regions; and Type III has young clusters and prominent H II regions (see Figure 3). As 66% of LMC clusters younger than 10 Myr are associated with molecular clouds, Type III molecular clouds probably last for $\sim$7 Myr. If the three types of molecular clouds form an evolutionary sequence and the relative population of these three types is proportional to the time spent in these stages, then the population ratio of $N_{\rm I} : N_{\rm II} : N_{\rm III} = 1: 2 :1$ implies that the dispersal timescale of molecular clouds is $\sim$30 Myr.

4 Energy Feedback and Interstellar Shells

To study the energy feedback from massive stars, one ought to bear in mind that both stars and the ISM evolve, and that their evolutions are always intertwined, especially for a system like an OB association or a cluster. From birth to a few Myr old, massive O stars photo-ionize the ambient ISM to form an H II region. Starting at $\sim$5 Myr, O stars start to explode as supernovae. The combined action of fast stellar winds and supernova blasts sweeps the H II region into an expanding shell, i.e., a superbubble. At $\sim$10 Myr, O stars are gone and B stars start to explode as supernovae. Without ionizing sources, the superbubble recombines and becomes an H I shell. After $\sim$15 Myr, all massive stars are gone; the remaining lower-mass stars disperse, and the H I supershell coasts along. If the superbubble is not near dense molecular material, it will have a simple shell structure, such as N70. If the superbubble is in a molecular gas-rich environment, the expanding superbubble can compress

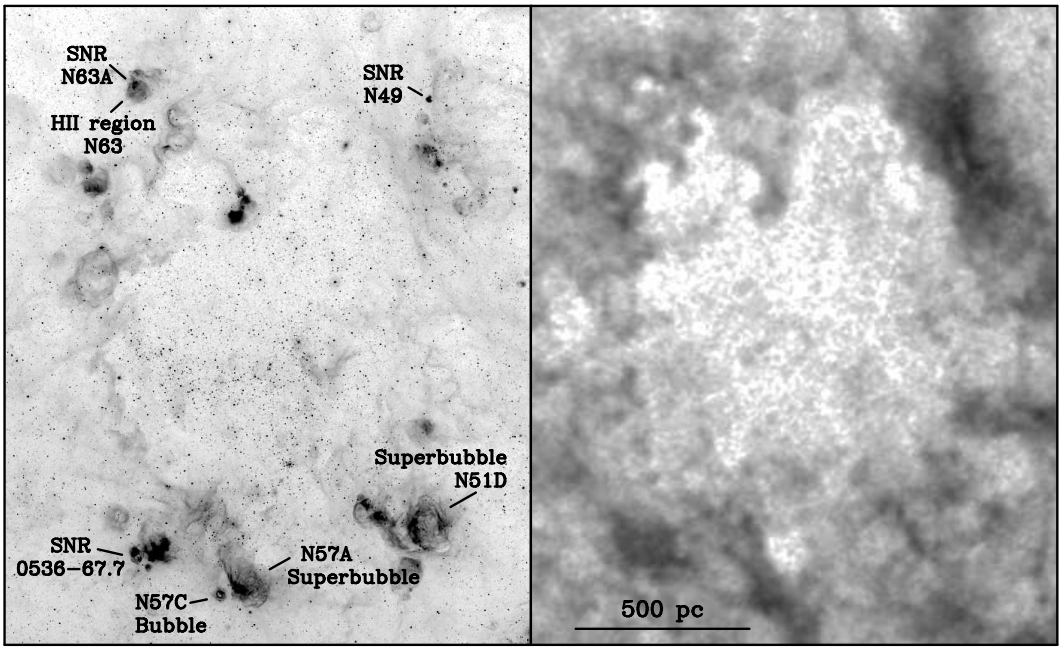

Figure 4: Hα image (left panel) and H I column density map (right panel) of supergiant shell LMC4 in the LMC. The two images have the same field-of-view. Superbubbles, SNRs, and a bubble are marked in the figure.

the ambient molecular clouds to form more stars along the shell rim, such as N11 and N44. Such sequential star formation can continue for more than 10^7 yr to form a supergiant shell reaching 1000 pc in size.

The most common product of stellar energy feedback is interstellar shells of various sizes, as illustrated in Figure 4. An isolated single massive star with a fast stellar wind can form an interstellar bubble during its main sequence stage, a circumstellar bubble (consisting of stellar material previously lost via a slow wind) during the WR star stage, and a SNR after its final explosion. The sizes of bubbles and SNRs can grow up to a few 10's of pc before dissipating and merging into the ISM. OB associations can blow superbubbles with sizes up to a few hundred pc. Multiple generations of propagated star formation over an extended period of time and space can form supergiant shells of sizes $\sim 10^3$ pc. The supergiant shell LMC4 in Figure 4 shows that the gas in this area has been cleared out, and that on-going star formation takes place along the supergiant shell rim where dense gas is present. As massive stars in LMC4 are concentrated in H II regions along the south and northeast rims, the bulk of gas associated with LMC4 is neutral, as seen in the H I column density map.

Studies of interstellar shells in recent years have provided answers to many puzzles, especially in the seeming lack of visible bubbles and rare detections of X-ray emission from bubbles. Massive O stars have fast stellar winds, and if an O star is in a reasonably dense ISM, it should blow an interstellar bubble (Weaver et al. 1977). However, bubbles are not commonly seen, and the Bubble Nebula is an exception rather than a rule. This "missing bubble" puzzle has been solved by studies of the young H II regions N11B and N180, where many O stars are present but no bubbles can be identified morphologically in optical images. Using high-dispersion, long-slit echelle spectra of N11B and N180, it has been shown that expanding shells are present around O stars, but the expansion velocities are only $\sim$20 km s^{-1}. Such weak shocks cannot compress the ambient medium to produce pronounced limb-brightening to be identifiable as a bubble (Nazé et al. 2001). When the central star evolves off the main sequence and loses its ionizing power, the bubble and the ambient medium will recombine. The isothermal sound speed of H I is low, and strong shocks and compression will be

produced by a bubble expanding at 20 km s^{-1}; therefore, H I bubbles are routinely detected around massive stars.

The difficulty in detecting diffuse X-ray emission from shocked stellar winds can be illustrated by the study of the Orion Nebula. The Orion Nebula hosts an O6 star (θ^1 Ori C) with a fast stellar wind, so it is expected to blow a bubble and the hot gas in the bubble interior should emit in X-rays. Diffuse X-ray emission from the Orion Nebula was first reported by Ku & Chanan (1979) using *Einstein* observations, but the diffuse emission was resolved into stars by *ROSAT* observations (Caillault, Gagné & Stauffer 1994). It was not until 2008 that the diffuse X-ray emission from shocked fast winds in the Orion Nebula was truly detected for the first time using *XMM-Newton* observations (Güdel et al. 2008). The *Spitzer* IRAC 8 μm image of the Orion Nebula region shows that the Orion cluster has blown a blister-like cavity, and the *XMM-Newton* observations show diffuse X-ray emission in the cavity, at the far end from the cluster. The plasma temperature determined from the X-ray spectral fits is $\sim 2\times10^6$ K. Future searches for diffuse X-ray emission from shocked stellar winds should bear in mind that IR images may be better at revealing bubble cavities in a complex environment and that shocked stellar wind may be located far away from the massive stars.

Many circumstellar bubbles blown by WR stars are known, but diffuse X-ray emission has been detected from only two – NGC 6888 and S 308. The plasma temperature of NGC 6888 is $\sim 2\times10^6$ K (Wrigge, Wendker & Wisotzki 1994) and S 308 $\sim 1\times10^6$ K (Chu et al. 2003). X-ray emission from such low plasma temperatures is extremely soft and the interstellar absorption is high for soft X-rays. The soft X-ray emission from S 308 can be detected because it is nearby and at a high galactic latitude, and thus its foreground absorption column density is low. If S 308 were in the Galactic plane and at a larger distance, it would not have been detected. Therefore, the higher interstellar absorption is responsible for the low X-ray detection rate of WR bubbles.

The biggest unanswered question is still the discrepancy between the observed bubble dynamics and theoretical predictions. Bubbles are observed to be too small or expand too slowly compared with those expected from bubble models using realistic stellar energy input. X-ray observations of WR bubbles, superbubbles, and planetary nebulae all show X-ray luminosities much lower than model predictions. The clumpiness of stellar winds can reduce the stellar mass loss rate by a factor of a few, but cannot fully remove the discrepancy between observations and model expectations. Artificially changing the heat conduction coefficient does not alleviate the discrepancy. Dynamically mixing cold nebular material with fast stellar wind (i.e., mass-loading) may lower the hot gas temperature, and thus raise the cooling rate. Recent models by Freyer, Hensler & Yorke (2003, 2006), Pittard, Dyson & Hartquist (2001), Pittard, Hartquist & Dyson (2001), and Arthur (2008) have grown more sophisticated. Detailed modelling for a specific bubble with accurate observations are needed for critical tests of bubble models.

It is worth noting that three cases of nonthermal X-ray emission from LMC superbubbles have been reported, but two of them are not confirmed by more careful analyses. *XMM-Newton* observations of N51D (Cooper et al. 2004) and *Suzaku* observations of N11 (Maddox et al. 2009) have been reported to show nonthermal diffuse X-ray emission from the superbubble interior. However, Yamaguchi, Sawada & Bamba (2010) have analyzed both *XMM-Newton* and *Suzaku* observations of N11 and N51D with a careful background subtraction, and found that neither show nonthermal X-ray emission. They conclude that 30 Dor C is the only LMC superbubble that shows bona fide nonthermal X-ray emission (Bamba et al. 2004; Yamaguchi et al. 2010).

5 Acceleration of Cosmic Rays

Cosmic rays can be accelerated in astronomical shocks (Bell 1978; Bykov 2001). While observations of some young SNRs have shown evidence of production of cosmic rays, the origin of Galactic cosmic

rays has been largely an unresolved mystery. The production and diffusion of cosmic rays can be traced by γ-rays, because collisions between interstellar protons and cosmic ray protons produce pions and each pion decays into two γ-rays. It is difficult to associate γ-ray emission with interstellar structures in the Galaxy because of the confusion in the Galactic plane. This is not a problem for the LMC because of its nearly face-on orientation.

Recently the *Fermi Gamma-Ray Space Telescope* detected γ-ray emission from the LMC, and provided the first spatially-resolved global view of γ-rays from a nearly face-on galaxy. Analyses of the first year's *Fermi* LAT observations of the LMC find (1) the brightest γ-ray emission appears to be centered near the 30 Dor giant H II region, but not its central R136 cluster; (2) fainter γ-ray emission is detected in the northern part of the LMC; (3) γ-ray emission shows little correlation with the total column density of the interstellar gas; and (4) γ-ray emission appears to be confined to massive star forming regions. These findings indicate that cosmic rays are accelerated in massive star forming regions and that the diffusion length of GeV cosmic ray protons is relatively short (Abdo et al. 2010).

The distribution of γ-ray emission can be compared with the underlying stellar and interstellar components. We have extracted the contours from the integrated $>$100 MeV emissivity map of the LMC (the left panel of Figure 10 of Abdo et al. 2010), assuming that all γ-rays are diffuse in origin, and plotted these contours in Figure 5 over the Hα image, H I column density map (Kim et al. 2003), *ROSAT* PSPC X-ray mosaic (made by S. Snowden), and star formation rates 6.3, 12.5, and 25 Myr ago (Harris & Zaritsky 2009).

Figure 5 shows that the $>$100 MeV emissivity is well correlated with the star formation within the last 6–12 Myr not only for the two γ-ray peaks, but also for the faint extension to the west. No correlation is seen for star formation at 25 Myr or earlier. Massive-star progenitors of supernovae have a lifetime ranging from a few to $\sim$15 Myr; thus, the correlation of γ-ray emissivity with the 6.3 and 12.5 Myr star formation rates indicates that supernovae play a major role in the acceleration of cosmic rays.

Less than 10% of massive stars are formed in isolation (Zinnecker & Yorke 2007) and produce classical SNRs. The great majority of massive stars are formed in groups, such as OB associations and clusters in single bursts of star formation, or star clouds in propagated star formation. OB associations and clusters a few Myr old produce superbubbles up to $\sim$200 pc across, while propagated star formation over 10^7 yr produce supergiant shells $\sim$1000 pc in size (Chu 2008). The Hα image and H I column density map of the LMC (Figure 5) indeed show superbubbles and supergiant shells in areas where the star formation rate was high within the last $\sim$12 Myr. Therefore, the γ-ray emission is also well correlated with superbubbles and supergiant shells. Within the brightest γ-ray peak, many superbubbles exist in the 30 Dor region; the second brightest γ-ray peak corresponds to the supergiant shell LMC4 whose periphery is dotted with superbubbles; and the faint western extension of diffuse γ-rays corresponds to the supergiant shell LMC8 (cataloged by Meaburn 1980).

It is not possible that uncataloged point sources, such as pulsars, contribute to the diffuse emission because the γ-ray emission is well correlated with the diffuse soft X-ray emission (Figure 5c) and *ROSAT* HRI observations have demonstrated that the diffuse X-ray emission is truly diffuse (Chu & Snowden 1998). Therefore, it may be concluded that the collective, interacting SNR shocks within superbubbles and supergiant shells produced by massive stars formed in the last $\sim$15 Myr have accelerated the cosmic rays in the LMC that are responsible for the $>$100 MeV γ-rays detected by *Fermi*.

6 Anatomy of the Carina Nebula

The Carina Nebula, at $\sim$2 kpc, is the nearest, most unobscured, giant H II region in our Galaxy. As a site of active star formation, it hosts the highest concentration of the earliest O stars in the Galaxy

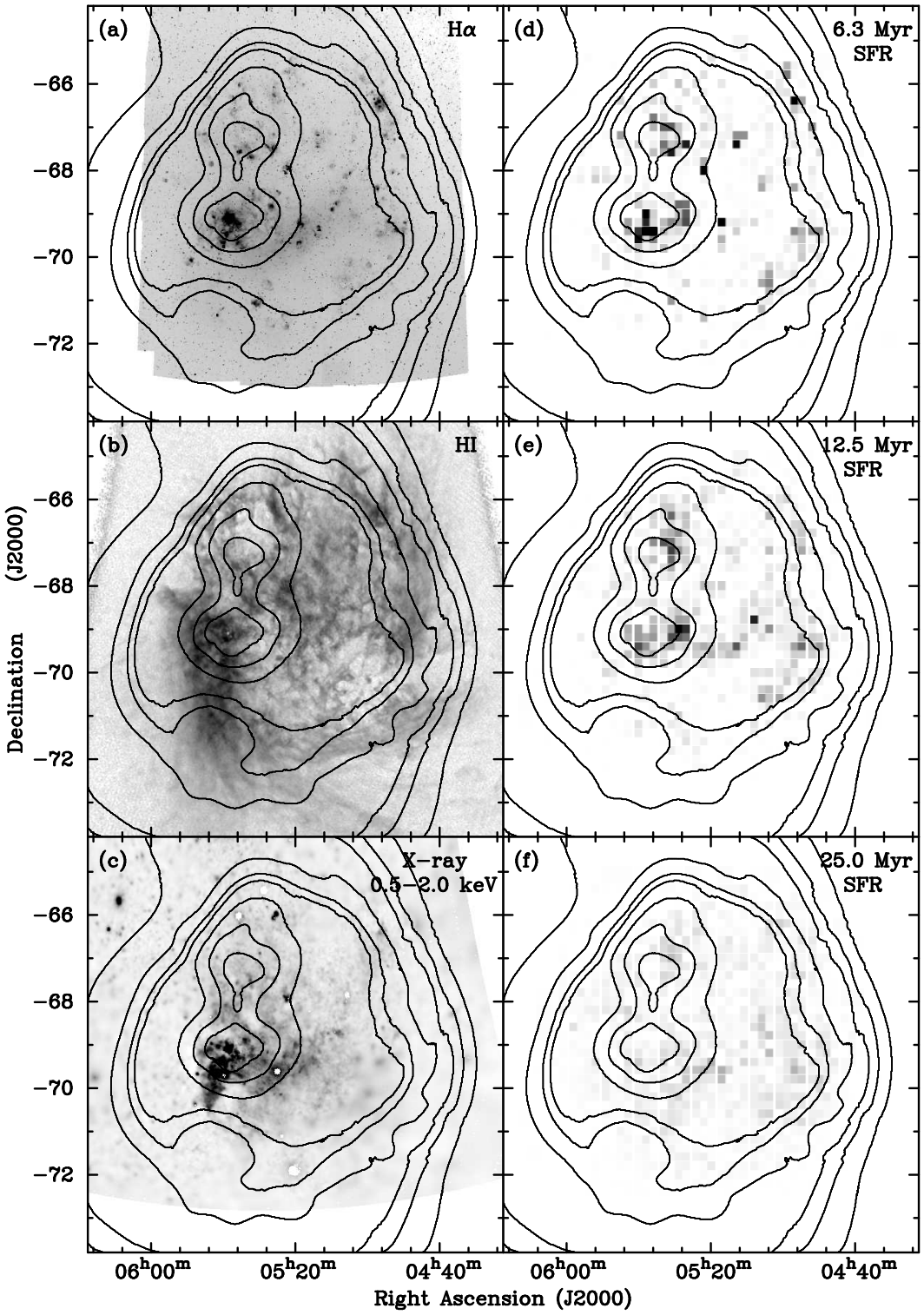

Figure 5: *Fermi* integrated >100 MeV emissivity contours overplotted on (a) MCELS Hα image, (b) H I column density map from Kim et al. (2003), (c) *ROSAT* PSPC mosaic in 0.5-2.0 keV made by S. Snowden, (d-f) maps of star formation rate at ages of 6.3, 12.5, and 25 Myr from Harris & Zaritsky (2009). The Hα, H I, and *ROSAT* X-ray images have been re-cast to the same projection scheme as the *Fermi* emissivity map and the star formation rate maps. The 30 Dor giant H II region is near the brightest γ-ray peak.

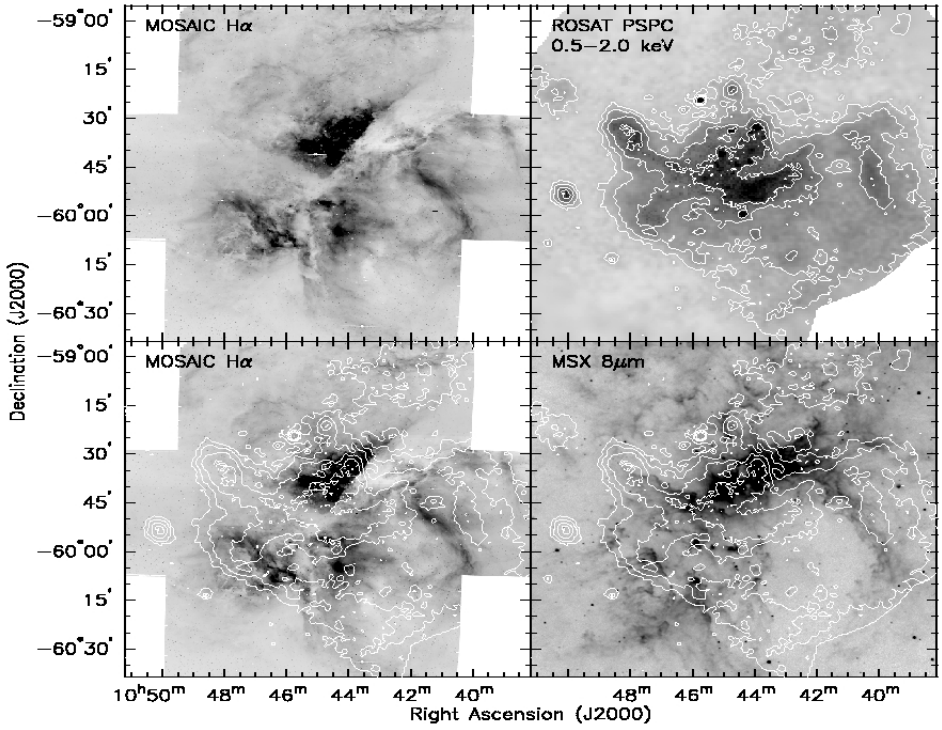

Figure 6: The top left panel shows the Hα emission from the Carina Nebula imaged using the MOSAIC II camera on the CTIO Blanco 4m. The top right panel shows the X-ray emission in the 0.5-2.0 keV band as seen by the *ROSAT* PSPC (courtesy S. Snowden). The bottom left panel shows the *ROSAT* X-ray emission contours overlaid on the Hα image, while the bottom right panel shows the X-ray contours overlaid on the *MSX* observations at 8μm.

as well as one of the most massive luminous blue variable, η Car (e.g., Walborn 1971; Walborn et al. 2002). As shown in Figure 6, the Hα image of the Carina Nebula reveals non-uniform extinction over the face of the H II region, particularly the V-shaped dust lane running through its waist.

Ever since the first detection of X-ray emission by the *Einstein X-ray Observatory* (Seward & Chlebowski 1982), the nature of the energy source has been debated. An O5 star with $L_{\rm w} \sim 10^{35}$ ergs s^{-1} injects 2×10^{49} ergs into the ambient ISM during its 5 Myr lifetime, and a WR star can inject 2×10^{50} ergs during 0.5 Myr. A supernova can deposit 10^{50} – 10^{52} ergs of explosion energy into the ISM. Thus, both fast stellar winds and supernovae could be important energy sources for the ISM in the Carina Nebula. Based on the absence of nonthermal radio emission and the presence of massive stars with powerful stellar winds, Seward & Chlebowski (1982) suggested that the hot, X-ray-emitting gas is powered by the stellar winds. The only evidence for recent supernovae are an anomalously high column density ratio of N(Mn)/N(Fe) observed toward HD 93205 in the Tr 16 cluster at the heart of the Carina Nebula (Laurent et al. 1982) and the recent discovery of a neutron star candidate in the region (Hamaguchi et al. 2009).

The *ROSAT* PSPC X-ray image of the Carina Nebula (Figure 6) shows diffuse emission in the vicinity of the cluster Tr16, roughly along the V-shaped dust lane, and extending to the southwest. This diffuse X-ray emission is confirmed by deeper, higher-resolution *Chandra* ACIS-I observations in a recent Msec campaign (Townsley et al. 2010). The southwest extension of the diffuse X-ray emission is coincident with a superbubble revealed by the *MSX* 8 μm image (Figure 6). The 8 μm emission detected by *MSX* suffers much less from the local extinction; thus the *MSX* 8 μm image can reveal the true underlying interstellar structure of the Carina Nebula. A second supershell to the

northeast of Tr16 is also seen in the 8 μm image, but diffuse X-ray emission is detected only near its base where the brightest Hα emission is seen.

Recently, we have obtained high-dispersion spectroscopic observations of the Hα and [N II] lines at positions throughout the Carina Nebula (Figure 7). These observations show line-splitting indicating expansion velocities of $\sim$15–30 km s^{-1} at positions that correspond to the *MSX* cavities and centered on Tr 16. Higher-velocity components with typical blue-shifted velocity offsets up to -180 km s^{-1}, and in a few cases red-shifted velocity offsets up to +130 km s^{-1} are observed at some positions in and around the dust lane that bisects the Carina Nebula. The higher velocity components appear to be associated with faint "frothy" emission from clumps with linear sizes as small as 0.05 pc extending over areas up to 1-3 pc. These higher velocity components may result from wind-ablated material from the dense gas along the waist of Carina. A more detailed analysis will be presented in Gruendl et al. (in preparation).

Acknowledgements

YHC would like to thank the generous support of the meeting organizers. Some of our research work has been supported by a number of NASA grants through JPL and STScI and an NSF grant.

References

Abdo, A. A., Ackermann, M., Ajello, M., et al. 2010, A&A, 512, 7
Arthur, S. J. 2008, IAUS, 250, 355
Bamba, A., Ueno, M., Nakajima, H., & Koyama, K. 2004, ApJ, 602, 257
Bell, A. R. 1978, MNRAS, 182, 147
Book, L. G., Chu, Y.-H., Gruendl, R. A., & Fukui, Y. 2009, AJ, 137, 3599

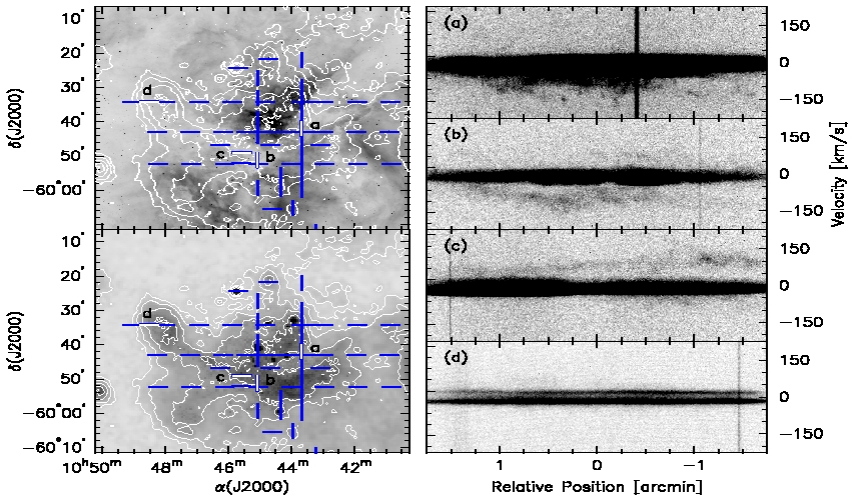

Figure 7: (Top Left) An Hα image of the central portion of the Carina Nebula overlaid with contours to show the X-ray emission. The horizontal and vertical marks show the positions of our echelle spectra. (Bottom left) The *ROSAT* PSPC X-ray image in the 0.5–2.0 keV energy band with the same slit positions overlaid. (Right) Each panel shows an echellogram for the [N II] λ6584 emission line. The position of each long-slit is highlighted and marked in the panels to the left.

Bykov, A. M. 2001, Space Science Reviews, 99, 317
Caillault, J.-P., Gagné, M., & Stauffer, J. R. 1994, ApJ, 432, 386
Chen, C.-H. R., Chu, Y.-H., Gruendl, R. A., Gordon, K. D., & Heitsch, F. 2009, ApJ, 695, 511
Chen, C.-H. R., Indebetouw, R., Chu, Y.-H., et al. 2010, ApJ, 721, 1206
Chu, Y.-H. 2008, IAUS, 250, 341
Chu, Y.-H., Guerrero, M. A., Gruendl, R. A., García-Segura, G., & Wendker, H. J. 2003, ApJ, 599, 1189
Chu, Y.-H., & Snowden, S. L. 1998, AN, 319, 101
Cooper, R. L., Guerrero, M. A., Chu, Y.-H., Chem, C.-H. R., Dunne, B. C. 2004, ApJ, 605, 751
Freyer, T., Hensler, G., & Yorke, H. W. 2003, ApJ, 594, 888
Freyer, T., Hensler, G., & Yorke, H. W. 2006, ApJ, 638, 262
Fukui, Y., Kawamura, A., Minamidani, T., et al. 2008, ApJS, 178, 56
Gruendl R. A. & Chu Y.-H. 2009, ApJS, 184, 172
Güdel, M., Briggs, K. R., Montmerle, T., Audard, M., Rebull, L., & Skinner, S. L. 2008, Science, 319, 309
Hamaguchi, K., Corcoran, M. F., Ezoe, Y., et al. 2009, ApJ, 695, L4
Harris, J., & Zaritsky, D. 2009, AJ, 138, 1243
Hughes, A., Wong, T., Ott, J., et al. 2010, MNRAS, 406, 2065
Kawamura, A., Mizuno, Y., Minamidani, T., et al. 2009, ApJS, 184, 1
Kim, S., Staveley-Smith, L., Dopita, M. A. 2003, ApJS, 148, 473
Ku, W. H.-M., & Chanan, G. A. 1979, ApJ, 234, L59
Laurent, C., Paul, J. A., & Pettini, M. 1982, ApJ, 260, 163
Leitherer, C., Schaerer, D., Goldader, J. D. 1999, ApJS, 123, 3
Maddox, L. A., Williams, R. M., Dunne, B. C., & Chu, Y.-H. 2009, ApJ, 699, 911
Meaburn, J. 1980, MNRAS, 192, 365
Meixner, M., Gordon, K. D., Indebetouw, R. 2006, AJ, 132, 2268
Nazé, Y., Chu, Y.-H., Points, S. D., Danforth, C. W., Rosado, M., & Chen, C.-H. R. 2001, AJ, 122, 921
Pittard, J. M., Dyson, J. E., & Hartquist, T. W. 2001, A&A, 367, 1000
Pittard, J. M., Hartquist, T. W., & Dyson, J. E. 2001, A&A, 373, 1043
Puerari, I., Block, D. L., Elmegreen, B. G. & Bournaud, F. 2010, presented at "Galaxies and their Masks" (2010arXiv1008.1044P)
Seale, J. P., Looney, L. W., Chu, Y.-H., et al. 2009, ApJ, 699, 150
Seward, F. D., & Chlebowski, T. 1982, ApJ, 256, 530
Smith, R. C., & the MCELS Team 1999, IAUS, 190, 28
Townsley, L. K., Broos, P. S., Chu, Y.-H., et al. 2010, ApJS, submitted
Vaidya, K., Chu, Y.-H., Gruendl, R. A., Chen, C.-H. R., & Looney, L. W. 2009, ApJ, 707, 1417
Walborn, N. R. 1971, ApJ, 167, L31
Walborn, N. R., Danks, A. C., Vieira, G., & Landsman, W. B. 2002, ApJS, 140, 407
Weaver, R., McCray, R., Castor, J., Shapiro, P., & Moore, R. 1977, ApJ, 218, 377
Wrigge, M., Wendker, H. J., & Wisotzki, L. 1994, A&A, 286, 219
Yamaguchi, H., Sawada, M., & Bamba, A. 2010, ApJ, 715, 412
Yang, C.-C., Gruendl, R.A., Chu, Y.-H., Mac Low, M.-M., & Fukui, Y. 2007, ApJ, 671, 374
Zaritsky, D., Harris, J., Thompson, I. B., & Grebel, E. K. 2004, AJ, 128, 1606
Zinnecker, H., & Yorke, H. W. 2007, ARAA, 45, 481

Discussion

I. Stevens: Can you comment on whether there is any non-thermal X-ray emission in the Carina Nebula?
Y.-H. Chu: There is no obvious diffuse hard X-ray emission of non-thermal origin. It is possible to include a power-low component in the spectral fitting, but that does not necessarily mean the existence of non-thermal X-ray emission.

S. Owocki: I would like to amplify your comment on the role of ablation and mixing in X-ray emission. If the interaction region has turbulent mixing, then the post-shock heated gas mixes with the cooler material and then radiates much more efficiently at UV-EUV- wavelengths, which is hard to detect. I think this could be a key factor in reducing X-ray emission from bubbles, but it's difficult to

quantify because of the unknown level of turbulent mixing in the interaction layer. Perhaps J. Pittard will discuss this further in his talk.
Y.-H. Chu: The 10^5K component cools the fastest. At the interface region and where cool material is mixed into the hot gas, cooling would cause energy loss. This should be considered seriously, but the effects can vary from case to case depending on how much mass-loading has occured.

N. Smith: You mentioned the issue of diffuse X-ray luminosity in giant H II regions being lower than what one expects for a standard wind-blown bubble. It seems probable that one reason for this discrepancy is that H II regions are not necessarily dominated by a pressure-driven stellar wind bubble... Instead it seems likely that radiation pressure and the rocket effect are also very important in driving the expansion of H II regions. As discussed before, mixing and cooling may also help to weaken the X-ray emission.
Y.-H. Chu: This is true in H II regions. There are other objects, such as WR circumstellar bubbles and planetary nebulae, that cannot be explained completely although they have well observed physical properties. Mass-loading from clumps indeed may be very important.

E. Pellegrini: The contribution to the expansion of bubbles due to radiation pressure will be almost equal to the wind energy plus momentum, as seen in a number of high mass star forming regions.
Y.-H. Chu: Well, yes ... in some cases, but it depends on the age and size of the H II region.

3-D simulations of shells around massive stars

Allard Jan van Marle[1] , Rony Keppens[1] and Zakaria Meliani[1]

[1] Centre for Plasma Astrophysics, K.U. Leuven,Celestijnenlaan 200B,
B-3001 Heverlee, Belgium

Abstract: As massive stars evolve, their winds change. This causes a series of hydrodynamical interactions in the surrounding medium. Whenever a fast wind follows a slow wind phase, the fast wind sweeps up the slow wind in a shell, which can be observed as a circumstellar nebula.

One of the most striking examples of such an interaction is when a massive star changes from a red supergiant into a Wolf-Rayet star. Nebulae resulting from such a transition have been observed around many Wolf-Rayet stars and show detailed, complicated structures owing to local instabilities in the swept-up shells.

Shells also form in the case of massive binary stars, where the winds of two stars collide with one another. Along the collision front gas piles up, forming a shell that rotates along with the orbital motion of the binary stars. In this case the shell follows the surface along which the ram pressure of the two colliding winds is in balance.

Using the MPI-AMRVAC hydrodynamics code we have made multi-dimensional simulations of these interactions in order to model the formation and evolution of these circumstellar nebulae and explore whether full 3D simulations are necessary to obtain accurate models of such nebulae.

1 Introduction

The winds of massive stars create complicated structures in the circumstellar medium. The morphology of these structures, known as circumstellar nebulae, is determined by the parameters of the progenitor stars, such as wind velocity, mass loss rate, orbital period and eccentricity as well as the evolutionary sequence of the stars. In this paper we explore two ways in which the wind of a massive star can create a shell.

1) By sweeping up an earlier, slower wind, as has been observed in e.g. NGC 6888 (Treffers & Chu 1982; Marston 1991), BR 48 (Chu, Weis & Garnett 1999) and Sh 2-308 (Gruendl et al. 2000).

2) Through collision with the wind of a massive binary companion. Such shells can not be observed directly, due to their much smaller scale, but their presence can be inferred through variability in the lightcurve as in the case of eta-Carinae (Okazaki et al. 2008) or through dust related IR emission along the tail of the resulting spiral structure as in the case of WR 104 (Monnier et al. 2002)

There are other sources for circumstellar shells, such as outbursts in which mass is ejected in a single, explosive event, rather than through a steady wind, but those fall outside the scope of this paper.

Rather than assuming a symmetry axis, we use the `mpi-amrvac` code (Meliani et al. 2007) to make 3-D models of the wind interactions. The single star scenario, in which a fast wind sweeps up

its slower predecessor has been explored numerically before by García-Segura, Langer & Mac-Low (1996); van Marle, Langer & García-Segura (2005); Freyer, Hensler & Yorke (2006); Dwarkadas (2007) and others. However, such simulations have been limited to 2-D models which, though they provide a great deal of insight, cannot fully describe the fundamentally 3-D structure caused by the instabilities in the shell. Because a binary system has no intrinsic symmetry axis it cannot be modelled in 2-D, although pioneering work was done by Stevens, Blondin & Pollock (1992). 3-D simulations of the interaction of massive star binary winds have been produced by, among others, Folini & Walder (2000); Parkin & Pittard (2008) and Pittard (2009). We add to this by studying the morphology of the shell and how it is influenced by stellar wind and orbital parameters for two different binaries: a luminous blue variable (LBV)+O-star and a hydrogen rich Wolf-Rayet (WNL)+O-star.

2 Numerical method

We use the `mpi-amrvac` code (Meliani et al. 2007), which solves the conservation equations of hydrodynamics on an adaptive mesh refinement (AMR) grid. The use of AMR as well as extensive parallellization allows us to do large scale, 3-D computations. In our simulations we ignore the effect of gravity and radiative driving, since the stellar winds are moving at their terminal velocity. We include the effect of optically thin radiative cooling, using the solar metallicity cooling table from Mellema & Lundqvist (2002). Because hot stars stars radiate strongly in the UV, we assume that the wind material is photo-ionized out to a distance of several parsec as predicted by Eq. 5.14 from Dyson & Williams (1997) for constant density. In an expanding wind the ionization will go to even larger distances (van Marle et al. 2005; Freyer et al. 2006). Hence, we enforce a minimum temperature of 10 000 K. In any case, temperature in the wind is largely irrelevant since the kinetic energy dominates the thermal energy by several orders of magnitude.

2.1 Single star wind interaction

For the single star simulation we use a spherical grid that covers a radius of 5 pc, with opening angles of $22.5^{\rm o}$ in both the equatorial and latitudinal plane. At the lowest level we use a grid of $400 \times 64 \times 64$ grid points and allow a maximum of two additional levels of refinement for a maximum effective resolution of $1600 \times 256 \times 256$. Refinement is done dynamically based on local density variations.

As input parameters we use the stellar evolutionary sequence in which a red supergiant (RSG) becomes a Wolf-Rayet (WR) star. This involves a transition from a high mass loss ($10^{-4}\,{\rm M_\odot\,yr^{-1}}$), low velocity ($10\,{\rm km\,s^{-1}}$) wind to a lower mass loss rate ($10^{-5}\,{\rm M_\odot\,yr^{-1}}$) with a much higher velocity ($2000\,{\rm km\,s^{-1}}$). The RSG wind parameters are similar to those used in previous 2-D simulations by e.g. García-Segura et al. (1996) and van Marle et al. (2005). The WR wind has a somewhat lower mass loss rate than in previous models as it has been observed that WR mass loss rates were over-estimated due to clumping (Vink & de Koter 2005). We initialize the simulation by filling the grid with the slow RSG wind and starting the fast WR wind at the inner radial boundary.

2.2 Binary wind interaction

We run the binary simulation by calculating the positions of the individual stars as a function of time according to Kepler's law, specifying the direction of motion (counter-clockwise in the XY-plane), the orbital period, stellar masses and eccentricity. Round each of these positions we define a sphere, 5×10^{12} cm in radius, which is filled with free-streaming wind material. For the binary parameters we use two different scenarios: a WNL+O binary, the other a LBV+O binary. The parameters of the stellar winds, masses and orbital motion are given in table 1, based on values from Vink & de Koter

Table 1: Binary parameters. Primary star: subscript 1, secondary: subscript 2.

Simulation	Mass_1 [$M_\odot$]	Mass_2 [$M_\odot$]	$\dot{M}_1$ [$M_\odot\,\text{yr}^{-1}$]	$\dot{M}_2$ [$M_\odot\,\text{yr}^{-1}$]	v_1 [$\text{km\,s}^{-1}$]	v_2 [$\text{km\,s}^{-1}$]	Period [yr]	eccentricity
WNL+O	50	30	5×10^{-6}	5×10^{-7}	1500	2000	1	0
LBV+O	50	30	1×10^{-4}	5×10^{-7}	200	2000	1	0

(2002; 2005). We do not include the variability of the LBV wind, but only the steady wind in between outbursts. This is possible, because we only look at a relatively short timeframe (1 year), over which the LBV wind can be expected to be steady.

The binary star simulation is done on a Cartesian grid, spanning 2.5×10^{14} cm in the XY-plane (orbital plane) and 2.5×10^{13} cm along the Z-axis. At its lowest resolution the grid measures $240 \times 240 \times 20$ points. We allow two additional levels of refinement. The first is dynamically adjusted based on local density variations, creating an effective resolution of $480 \times 480 \times 40$. The second is enforced only around the two stars, creating high resolution zones in the regions where the stellar winds are initialized.

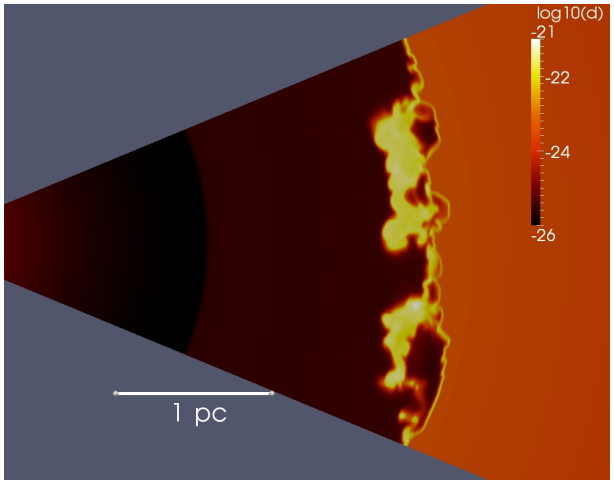

Figure 1: Density in $\text{g\,cm}^{-3}$ for a WR wind sweeping up its RSG predecessor after 40000 yr. This figure shows a 2D slice through the 3D data set. The swept-up shell is thin and shows thin-shell instabilities of the linear type.

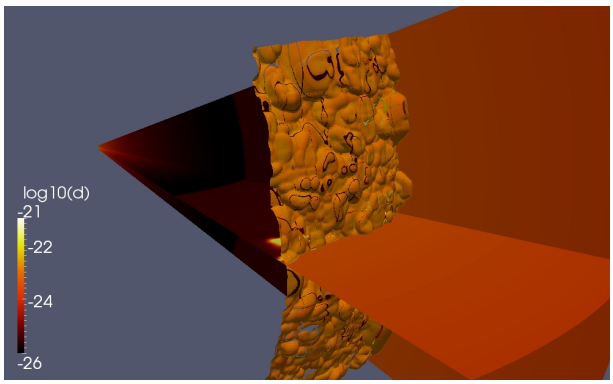

Figure 2: Density in $\text{g\,cm}^{-3}$ for a WR wind sweeping up its RSG predecessor. The shell is shown as an iso-surface at 30 $\text{km\,s}^{-1}$, which follows the front of the shell. The 3-D structure of the instabilities is clearly visible.

3 Single star circumstellar shell

The shell of swept-up RSG wind material (Figs. 1 and 2) after 40000 yr shows a complicated structure resulting from a combination of thin-shell and Rayleigh-Taylor instabilities as was found in 2-D simulations (García-Segura et al. 1996). The shell itself is highly compressed because of the radiative nature of the forward shock, which lowers the thermal pressure of the shocked RSG wind material. Note that the resolution of the grid places a limit on the compression factor, which may influence the

results. Although the 2-D representation (Fig. 1) strongly resembles earlier results from 2-D simulations, the actual nature of the instabilities is best modeled in 3-D to fully understand their morphology (Fig. 2). The density plot shows a difference in cross-section of about an order of magnitude between the clumps and the shell. García-Segura et al. (1996) show only a variation of a factor 2 before the shell breaks out of the RSG wind. Since emission of matter depends on the density squared, such structures show up clearly in observations of circumstellar nebulae such as NGC 6888.

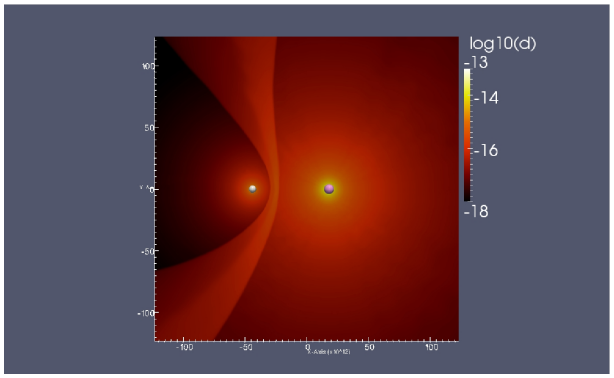

Figure 3: Density in g cm^{-3} in the orbital plane of a WNL+O binary, after one full orbit (1 yr). The binary stars rotate in counter-clockwise direction. This simulation produces a smooth shell because the wind collisions on both the O-star (white sphere) side and the WNL (violet sphere) side are adiabatic in nature. The resulting shell is thick and not subject to thin-shell instabilities.

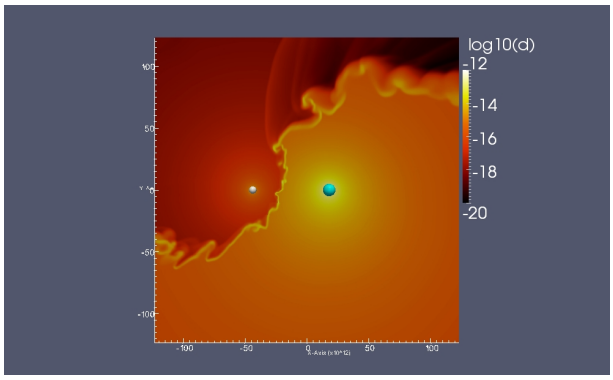

Figure 4: Density in g cm^{-3} in the orbital plane of an LBV+O binary, after one full orbit (1 yr). Since the wind collision is radiative on the LBV (blue sphere) side of the collision, the shell is thin and subject to instabilities. The trailing end of the shell (top) lags behind due to the low velocity of the LBV wind .

4 Massive binary shells

The two binary simulations show completely different results (Figs. 3 and 4, which show slices in the orbital plane through the 3-D dataset). The WNL+O binary has a smooth shell that follows the bowshock curve along which the ram pressure of the two winds is equal, with only a small deviation resulting from the orbital motion. The LBV+O binary has a thin, clearly unstable shell. The leading edge of the shell, which advances into the LBV wind, follows a general shape similar to that of the WNL+O binary, but the trailing edge (top of Fig. 4) deviates strongly from the bowshock shape, trailing behind the counter-clockwise orbital motion. The difference is caused by the wind parameters, which determine whether the wind collision shock is radiative or adiabatic in nature (Stevens et al. 1992). Owing to the high velocity and (relatively) low density of the WNL and O-star winds, the radiative cooling at the collision is inefficient making the collision nearly adiabatic. The result is a thick shell. On the other hand, the LBV wind, with its low velocity and high density creates a radiative shock. Therefore, the resulting shell is compressed and susceptible to thin-shell instabilities (Vishniac 1983, 1994). The strong deviation from symmetry in the global shape of the LBV+O shell is caused by the relatively low velocity of the LBV wind, relative to the orbital velocity (v_w = 200 km s^{-1} for the LBV wind versus $v_{\rm orbit}$ = 40 km s^{-1}). Because of its low velocity, the LBV wind cannot push the bowshock ahead fast enough to keep up with the orbital motion of the binary at larger radii. As a result the trailing end of the bowshock starts to fall behind leading to the asymmetric shape (Parkin & Pittard 2008, van Marle, Keppens & Meliani 2010). The WNL wind, which is 7.5 times faster than

the LBV wind can push the shell much faster. Consequently, the shell can maintain a near symmetric shape, co-rotating with the orbital motion of the binary stars.

Comparison with observations is difficult for these systems, because the shells cannot be observed directly. Their properties have to be inferred from indirect observation, such as dust trails and variations in the lightcurve.

5 Conclusions

In order to fully understand the structure end evolution of circumstellar shells, high resolution, 3-D hydrodynamics are necessary. For the single star scenario, 2-D models can be used in many applications, but cannot fully capture the details of the unstable shell. For the binary scenario 3-D simulations are unavoidable, due to the lack of a symmetry axis. Although the colliding winds can be simulated in 2-D using cylindrical symmetry, orbital motion would have to be neglected.

In both cases radiative cooling plays a crucial part in the shape of the shell as it determines the compression factor of the shock, which in turn determines whether the shell becomes thick and smooth, or thin and subject to instabilities. Since we assume photo-ionization, which sets a minimum temperature for the gas, the compression factor is limited. Should we allow the gas to recombine and cool further, which may occur if clumps of gas becomes dense enough to shield themselves from the ionizing radiation than the shells would be compressed even further.

In the future we will explore a larger parameter space of both single star and binary wind interactions in 3-D.

Acknowledgements

A.J.v.M. acknowledges support from FWO, grant G.0277.08 and K.U.Leuven GOA/09/009. Simulations were done at the Flemish High Performance Computer Centre, VIC3 at K.U. Leuven and on the CINECA SP6 at Bologna, Italy We thank the DEISA Consortium (www.deisa.eu), funded through the EU FP7 project RI-222919, for support within the DEISA Extreme Computing Initiative

References

Chu, Y.-H., Weis, K, & Garnett, D.R. 1999, AJ 117, 1433
Dwarkadas, V.V. 2007, ApJ 667, 226
Dyson, J.E., & Williams, D. 1997, *The physics of the interstellar medium*, 2^{nd} Edition, (Institute of Physics Publishing)
Folini, D., & Walder, R. 2000, AP&SS 274, 189
Freyer, T., Hensler, F., & Yorke, H.W. 2006, ApJ 638, 262
García-Segura, G., Langer, N., & Mac-Low, M.M. 1996, A&A 316, 133
Gruendl, R.A., Chu, Y.-H., Dunne, B.C., & Points, S.D. 2000, AJ 120, 2670
Marston, A.P. 1991, ApJ 366, 181
Meliani, Z., Keppens, R., Casse, F., & Giannios, D. 2007, MNRAS 376, 1189
Mellema, G., & Lundqvist, P. 2002, A&A 394, 901
Monnier, J.D., Greenhill, L.J., Tuthill, P.G., & Danchi, W.C. 2002, ApJ 566, 399
Okazaki, A.T., Owocki, S.P., Russel, C.M.P., & Corcoran, M.F. 2008, MNRAS 388, L39
Parkin, E.R., & Pittard, J.M. 2008, MNRAS 388, 1047
Pittard, J.M. 2009, MNRAS 396, 1743
Stevens, I.R., Blondin, J.M., & Pollock, A.M.T. 1992, ApJ 386, 265
Treffers, R.R., & Chu, Y.-H. 1982, ApJ 254, 569
van Marle, A.J., Langer, N., & García-Segura, G. 2005, A&A 444, 837
van Marle, A.J., Keppens, R., & Meliani, Z. 2010, accepted by A&A, arXiv:1011.1734

Vink, J.S., & de Koter, A. 2002, A&A 393, 543
Vink, J.S., & de Koter, A. 2005, A&A 442, 587
Vishniac, E.T. 1983, ApJ 274, 152
Vishniac, E.T. 1994, ApJ 428, 186

Discussion

J. Hoffman: Is there a way to make a quantitative comparison between, for example, your RSG → WR model and observed filamentary circumstellar structures? I am wondering whether you can tell if your models are "in the ballpark" of what we observe.
A.J. van Marle: It is becoming possible. We could estimate the luminosity from recombination in the shell. Also, it might be possible to do radiative transfer on our models. X-ray's are more difficult, as that part of the shock is very difficult to resolve.

N. Smith: Following that point, I'm wondering about how/if these simulations can help us with more quantitative analysis of images of nebulae. For example, can we use the size scale of the instabilities or the density enhancement (thickness) of the shell as a diagnostic of the relative wind density and velocity? I get the impression, though, that these properties depend strongly on the cooling prescription. Any thoughts on the prospects for this type of analysis?
A.J. van Marle: I think we are now reaching the point where our resolution is high enough to make such an attempt, as the instabilities are quite well resolved. The cooling curve is certainly an issue and we may have to explore how much it affects the result. Also, we don't include photo-ionization, which can change the shape of the instabilities considerably, if the shell is only partially ionized.

A. Lobel: One can test the validity of 3-D hydrodynamic simulations with multi-D line radiative transfer calculations. I am looking forward seeing results from such tests. Would you think that Balmer Hα is a good spectroscopic indicator with regards to the Hα images you show for WR nebulae?
A.J. van Marle: Doing radiative transfer through the simulation results would be great. I'm not very knowledgeable about spectral fitting, so the choice of the lines is difficult to judge. The most radiative parts of the shell have temperatures of about 10000-50000 K, so that Hα should work.
N.B.: the code does not account for ionization, so that value may change a bit.

A search for Ejecta nebulae around Wolf-Rayet Stars in the SHS Hα survey

D. J. Stock[1*] and M. J. Barlow[1]

[1] Department of Physics and Astronomy, University College London,
Gower Street, London, UK, WC1E 6BT

Abstract: Using the Southern Hα Survey (SHS), we have visually inspected every catalogued WR star in the Milky Way and the Magellanic Clouds for the presence of nebulosity suggesting an origin as stellar ejecta with the Southern Hα Survey (SHS) . Our survey revealed one new nebula around the star HD 62910 (WR 8) along with some correlations regarding binarity and WR nebulae progenitors.

1 Introduction

Since the suggestion that some Wolf-Rayet stars could be creating nebulae via mass loss (Johnson & Hogg 1965), efforts to detect more examples have been ongoing. The first attempt to morphologically categorise nebulae presumed to have been created by the influence of WR stars was performed by Chu (1981), who devised three broad categories for possible nebulae: W, R & E.

Our interest lies with the E type nebulae, which were defined to be those which were likely to contain processed ejecta from the progenitor star. These were suggested by Chu to have been formed by a violent mass loss episode recently in the star's history, which may not have been isotropic or homogeneous. The nebulosity can therefore be very clumped and irregular. Chu (1991) modified the scheme to refine the definition of E type nebulae, splitting the category into Stellar Ejecta nebulae and Bubble/Ejecta (W/E) nebulae: the former covering pure E type nebulae as defined above, the latter introduced to cover the case of ejecta shells having merged with the swept up shell.

Recent publicly available Hα surveys (like the SHS Parker et al. 2005) allow re-inspection of the environs of all known WR stars with a view to identifying new E type nebulosities which can provide constraints on the nucleosynthetic effects of WR stars. In contrast to this approach, several new WR nebulae and WR stars have been found recently by searching for rings in IR data, e.g. Mizuno et al. (2010), Wachter et al. (2010), Gvaramadze et al. (2010).

2 Morphology of Confirmed Ejecta Nebulae

For the two nebulae which Chu (1981) regarded as E type (M 1-67 and RCW 58) the nebulosities were found to be enriched relative to the ISM in nitrogen and helium but depleted in oxygen (Kwitter 1984,

*dstock@star.ucl.ac.uk

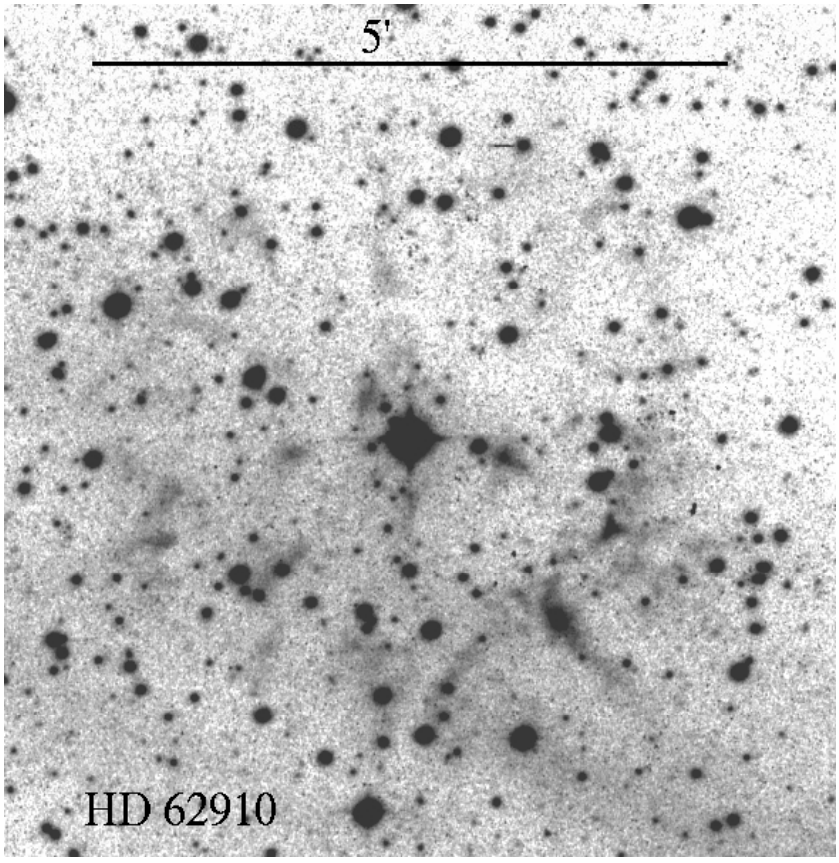

Figure 1: The SHS Hα image of the field around HD 62910 (WR 8, WCE+) shows newly revealed nebulosity. North is up, east is to the left.

Esteban et al. 1991). The anonymous nebula surrounding WR 16 was also shown to be comprised of material with a very similar abundance pattern to those of M1-67 and RCW 58 (Marston et al. 1999). The detection of processed material in these nebulae was a major success for the categorisation scheme, as this showed that it is possible to infer likely patterns in the chemical composition of a WR nebula by studying its morphology.

However, material displaying the same patterns of enrichment was also detected in NGC 6888 - a nebula Chu had initially classified as W type (Esteban & Vilchez 1992, Moore et al. 2000). This showed clearly that the lines between the inital Chu classes can be blurred: NGC 6888 appears to be a mixture of different kinds of nebulosity. The edge looks like a wind-blown shell, whilst there is evidence of flocculent nebulosity in the central regions, suggesting ejected material. NGC 6888 was later re-classified as a W/E nebulae by Chu (1991).

These spectroscopic results lead to the conclusion that the morphological criteria for ejecta nebulae presented by Chu (1981) may be too stringent, a problem addressed by the introduction of the Bubble/Ejecta (W/E) class (Chu 1991). Wind-blown bubbles can also contain ejecta in their filamentary nebulosities (e.g. NGC 6888). This suggests the following, revised criteria: ejecta nebula candidates must have either a highly flocculent structure, as in Chu's scheme or, alternatively, possess flocculent structure within their wind-blown shells, similar to that shown by NGC 2359, NGC 6888 & NGC 3199.

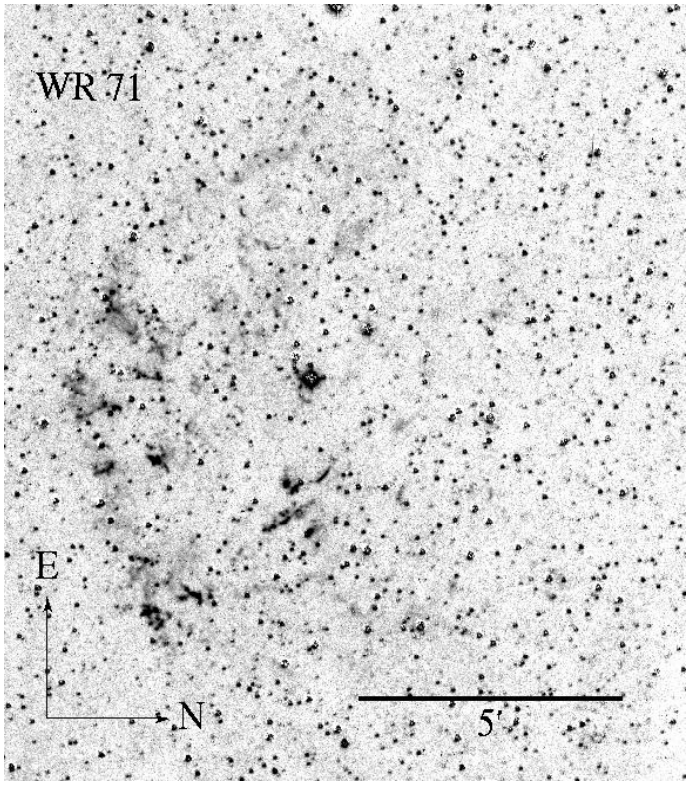

Figure 2: SHS image of the field around WR 71 (WN6) (Hα-red subtraction). The tenuous flocculent nebulosity to the south strongly suggests stellar ejecta, as noted by Marston et al. (1994).

3 Results

In the SHS imagery of the region around WR 8 (Figure 1) one can clearly discern nebulosity that appears to be associated with the star. It is aligned along radial "spokes" with an especially prominent example to the south-west. These spokes define a circular structure approximately 5 arcminutes in diameter, internal to which there are several prominent clumps of nebulosity.

The spectral type of the host star is listed by van der Hucht (2001) as WN7/WC4. Its spectrum places WR 8 neatly between those of WN and WC stars (Crowther et al. 1995). This was initially interpreted as a sign of binarity - a system comprising both WC and WN stars - however Crowther et al. (1995) showed that the wind properties were the same for both the N and C components - implying a single star origin.

The SHS image, shown in Figure 2, confirms the tenuous nebula around WR 71 first noted by Marston et al. (1994) and later classified as an E type nebula by Marston (1997). It appears similar to RCW 58 and anon (WR 8), in that it has highly clumped nebulosity to the south, although much fainter than either of the above. The SHS subtracted (Hα-R) image (Figure 2) also shows some arcs to the west while improving on the detail of the flocculent structure to the south. The progenitor is a runaway star and as such is significantly out of the plane ($z = 1190$ pc) suggesting that this object may have unique kinematics due to the low ISM density at this z distance.

Along with the detection of a new nebula around WR 8 and confirmation of an E type nebula around WR 71, several nebulae in the LMC were identified as WR ejecta nebula candidates.

Table 1: WR Nebulae with Binary Central Stars

	Isolated WR	Binary WR	All WR
Milky Way[a]			
Ejecta Nebulae	13	0	13
All WR Stars	142	85	227
Ratio	0.09	0.00	0.06
LMC[b]			
Candidate Ejecta Nebulae	4	0	4
All WR Stars	102	32	134
Ratio	0.04	0.00	0.03

a: Not including WR stars discovered by Wachter et al. (2010) as they were discovered by examining progenitor stars of detected IR ring nebulae.
b: Counting all O3If*/WN6-A stars as isolated WN type.

4 Discussion

From our sample of ejecta nebulae a curious fact emerges: none of the nineteen WR Ejecta nebula central stars listed here are binaries. In Table 1 we summarise the binary fractions for the WR populations in the MW and LMC along with the fraction that we have identified as ejecta nebulae for each case. The binarity classifications of van der Hucht (2001) and Breysacher et al. (1999) were adopted for the Galactic and LMC populations respectively. It is striking that the fraction of binary WR stars having ejecta nebulae is so low.

If the fraction of WR stars with ejecta nebulae were the same for binaries as single WR stars we would expect $\sim 7 - 8\%$ of WR binary stars to possess ejecta nebulae, which translates to around 6 expected in the MW compared to none observed. In the LMC we might expect ~ 4 LMC binary WR stars to possess ejecta nebulae.

It has long been speculated that there are two methods of creating WR stars, mass transfer between binary partners and mass loss of an isolated star (e.g. Smith & Payne-Gaposhkin 1968). A possible reason for the relative absence of ejecta nebulae around binary WR stars is that mass transfer onto a companion inhibits the mechanism that produces an ejecta nebulae around single WR stars.

The nebulosity surrounding WR 71 (see Figure 2) is possibly an exception to the previous discussion. The progenitor star is of spectral type WN6+? (van der Hucht 2001). Isserstedt et al. (1983) suggested that WR 71 has a binary partner that is a low-mass evolved stellar remnant - either a neutron star or a black hole - and that the supernova which created the collapsed object likely occured when the system was in the disk of the MW. However this finding has been disputed, and WR 71 is now normally thought to be an isolated star (Hamann et al. 2006), its runaway status probably coming about not through binary interactions, but rather dynamical cluster interactions leading to ejection (as it is very unlikely that a WR star could form in the low density environment 1000 pc above the galactic plane).

The nebulosity appears to be physically much larger than counterparts in the plane (although this is heavily dependent on the distance adopted) while retaining the appearance of a pure E type nebula. This may be caused by the size of the ISM cavity created by stellar winds being larger than those created by counterparts in the plane due to lower local ISM density beyond the galactic plane.

References

Breysacher, J., Azzopardi, M. & Testor, G. 1999, A&AS, 137, 117
Chu, Y.-H. 1981, ApJ, 249, 195
Chu, Y. H. 1991, in K. A. van der Hucht & B. Hidayat ed., Wolf-Rayet Stars and Interrelations with Other Massive Stars in Galaxies Vol. 143 of IAU Symposium, Ring Nebulae around Massive Stars (review), 349
Crowther, P. A., Smith, L. J. & Willis, A. J. 1995, A&A, 304, 269
Esteban, C. & Vilchez, J. M. 1992, ApJ, 390, 536
Esteban, C., Vilchez, J. M., Manchado, A. & Smith, L. J. 1991, A&A, 244, 205
Gvaramadze, V. V., Kniazev, A. Y. & Fabrika S. 2010, MNRAS, 405, 1047
Hamann, W., Gräfener, G. & Liermann A. 2006, A&A, 457, 1015
Isserstedt, J., Moffat, A. F. J. & Niemela V. S. 1983, A&A, 126, 183
Johnson, H. M. & Hogg, D. E. 1965, ApJ, 142, 1033
Kwitter, K. B. 1984, ApJ, 287, 840
Marston, A. P. 1997, ApJ, 475, 188
Marston, A. P., Welzmiller, J., Bransford, M. A., Black, J. H. & Bergman P. 1999, ApJ, 518, 769
Marston, A. P., Yocum, D. R., Garcia-Segura, G. & Chu, Y.-H. 1994, ApJS, 95, 151
Mizuno, D. R., Kraemer, K. E., Flagey, N., Billot, N., Shenoy, S., Paladini, R., Ryan, E., Noriega-Crespo A., et al. 2010, AJ, 139, 1542
Moore, B. D., Hester, J. J. & Scowen P. A. 2000, AJ, 119, 2991
Parker, Q. A., Phillipps, S., Pierce, M. J., Hartley, M., Hambly, N. C., Read, M. A., MacGillivray, H. T., Tritton, S. B., et al. 2005, MNRAS, 362, 689
Smith, L. F. & Payne-Gaposhkin, C. 1968, in K. B. Gebbie & R. N. Thomas ed., Wolf-Rayet Stars The Features of the System of Wolf-Rayet Stars. pp 21
van der Hucht, K. A. 2001, New Astronomy Reviews, 45, 135
Wachter, S., Mauerhan, J. C., Van Dyk, S. D., Hoard, D. W., Kafka, S. & Morris, P. W. 2010, AJ, 139, 2330

Discussion

E. Pellegrini: Why not use the MCELS Survey for the LMC?
D. Stock: I had not previously been aware of MCELS. However it does sound like an invaluable ressource for this kind of work.

S. Wachter:

1. Have you looked at the Spitzer observations for your LMC shells? Do you see any 24 μm emission?

2. What was your input WR list? Just the van der Hucht catalog or also the more recent newly discovered WRs by Shara, or Mauerhan, or Hadfield?

D. Stock:

1. I have not yet examined the Spitzer $24\mu m$ images, although that is a good idea.

2. I used the van der Hucht (2001) catalog along with its 2006 annex. In the Magellanic Clouds I used the Breysacher, Azzopardi & Testor Catalog of 1999.
   As far as I know most new WR discoveries are in clusters or bubbles and hence would be discounted anyway.

N. Smith: Regarding the WNh stars at the center of these nebulae, I suppose this is expected in either the post-RSG or post-LBV stage because new-born WN stars may still need to get rid of a small amount of H. Also, quiescent LBVs are sometimes seen with spectral types of Ofpe/WN9 or WN11

(with H), so there is a connection there as well.

S. Wachter: A comment on the idea that shell #16 from my sample shows streamers and special structure: There are a couple of similar looking shells like this in my sample and my interpretation from looking at the multiwavelength data is that these might just be in a denser environment, they have much more diffuse edges than most of the other shells.

A.J. van Marle: A comment on the remark by N. Smith: "Streamers" in WR nebulae may result from partial photo-ionization by the central star. If purely hydrodynamic, they can give very good indications of wind properties.

Circumstellar Material Around Evolved Massive Stars

Nathan Smith[1,2]

[1] Steward Observatory, University of Arizona, 933 N. Cherry Ave., Tucson, AZ, 85721, USA
[2] Astronomy Department, University of California, 601 Campbell Hall, Berkeley, CA 94720, USA

Abstract: I review multiwavelength observations of material seen around different types of evolved massive stars (i.e. red supergiants, yellow hypergiants, luminous blue variables, B[e] supergiants, and Wolf-Rayet stars), concentrating on diagnostics of mass, composition, and kinetic energy in both local and distant examples. Circumstellar material has significant implications for the evolutionary state of the star, the role of episodic mass loss in stellar evolution, and the roles of binarity and rotation in shaping the ejecta. This mass loss determines the type of supernova that results via the stripping of the star's outer layers, but the circumstellar gas can also profoundly influence the immediate pre-supernova environment. Dense circumstellar material can actually change the type of supernova that is seen when it is illuminated by the supernova or heated by the blast wave. As such, unresolved circumstellar material illuminated by distant supernovae can provide a way to study mass loss in massive stars in distant environments.

1 Introduction and Scope

There is a great variety of circumstellar material around massive stars. In the interest of brevity, I will restrict myself to discussing stars with detectable circumstellar *nebulae*, as distinguished from steady stellar *winds* or *disks* where the primary observable signature is seen in the spectrum and generally arises within several stellar radii (this was discussed in detail during the first session of this conference; see Owocki 2011 and Martins 2011). By virtue of their high luminosity and radiation-driven winds, all massive stars shed mass in stellar winds, except perhaps at near zero metallicity. However, not all stars are surrounded by detectable circumstellar nebulae.

Furthermore, I will discuss only *circumstellar* material and not *interstellar* material (i.e. H II regions, photodissociation regions, giant molecular clouds). Similarly, I will not delve into circumstellar accretion disks and outflows associated with the earliest formation phases of massive stars, as these were also discussed earlier in this conference (Beuther 2011), nor will I discuss the phenomena of pulsar winds or black hole accretion disks. The main focus here is the circumstellar matter that results from the mass loss from massive stars in the course of their evolution up to core collapse.

It is surprisingly difficult to directly detect circumstellar gas and dust around extremely luminous central stars, and in part of this contribution I will review some of the tricks observers use to see circumstellar material in spite of the bright photospheric continuum light. In general, circumstellar nebulae can only be detected if the material is extremely dense and located relatively far from the glare of the star. This requires densities several orders of magnitude higher than the densities of stellar winds at the same radius. Such high densities, in turn, imply that the nebulae are created by

large amounts of matter ejected by the star. That is the chief reason they are of interest; namely, circumstellar nebulae provide a fossil record of the most important mass-loss phases experienced by stars.

Mass loss plays a critical role in the evolution of massive stars (e.g., Chiosi & Maeder 1986; Maeder & Meynet 2000; Meynet et al. 2011), and profoundly impacts the eventual supernova explosion (e.g., Woosley et al. 1993). Whether the mass loss that leads to Wolf-Rayet stars and stripped envelope supernovae (i.e. Types Ib and Ic) is due to steady winds, eruptions, or binary Roche lobe overflow (RLOF), and at exactly what initial masses this occurs, is still debated. In a recent paper, I have reviewed the connection between mass loss of progenitor stars and the types of observed supernovae more extensively (Smith et al. 2010b).

Most importantly, the observational determination of the physical parameters of circumstellar nebulae — mass, composition, expansion age and kinetic energy, as well as global geometry and detailed structure — provide critical constraints for some of the most prodigious mass-loss phases of massive stars. This is particularly instructive for illuminating cases when the mass loss was strongly enhanced for a short time, and is therefore rarely observed directly (such as in brief giant LBV eruptions), or when the duration (and hence the cumulative mass-loss budget) is not well known. The chemical abundances of this ejected material tell us about the recent evolutionary phases of the star.

2 Types of Stars with Circumstellar Nebulae

As noted above, in order for a circumstellar nebula to be detectable, it must be very dense, with densities far exceeding those of normal stellar winds. Extremely high densities at large radii from the star can be achieved in two basic ways: (1) A dense shell can result from a sudden eruption or explosion that ejects a large amount of material from the star. This may happen, for example in an LBV eruption or in a red supergiant pulsation. The ejection of extremely dense shells may be accompanied by strong cooling to make dense clumps, or even dust grain formation, both of which may enhance the ability to be detected. (2) A dense shell nebula can result at the interface when a faster wind sweeps into a slow dense wind. In either case, the presence of a nebula requires a substantial change in the mass-loss behavior of the star on a relatively short timescale. For this reason, nebulae tend to be associated with stars in late transitional phases of evolution off the main sequence or immediately before a supernova. We do not generally see circumstellar nebulae around main sequence stars.[1] Some of the key types of stars that are normally associated with substantial circumstellar nebulae are outlined below, proceeding from cool to hot temperatures. I will try to highlight a demonstrative example of each.

2.1 Red Supergiants

Red supergiants have slow, dense, dusty winds. How the winds are driven from the stars is not completely understood, but it is likely that a combination of pulsations and radiation force on dust grains is at work, although there is also evidence for strongly enhanced episodes of mass loss as in the case of extreme red supergiants like VY CMa (Smith et al. 2001; 2009). Circumstellar material can sometimes be seen around red supergiants, but most notably in very nearby or very extreme cases. The detectability of circumstellar material is enhanced by the fact that the winds are slow and clumpy, giving rise to high density regions.

[1] Incidentally, the fact that observable signatures of dense circumstellar material are absent around main-sequence O-type stars indicates that these stars quickly clear away all natal disk material associated with the star formation process.

Betelgeuse is an extremely nearby example of a relatively normal red supergiant, but even at such close distances of only 150–200 pc (Harper et al. 2008), its circumstellar material is difficult to detect because its stellar wind mass-loss rate is only about 10^{-6} $M_\odot$ yr^{-1} (Harper et al. 2008; Smith et al. 2009). Emission from its dusty wind has been resolved with mid-IR nulling interferometry (Hinz et al. 1998), and its circumstellar shell has been spatially resolved in emission lines like K I (Plez & Lambert 1994, 2002) and infrared CO bandhead emission (Smith et al. 2009).

VY CMa is a much more striking case, where the recent mass-loss rate is about 10^3 times stronger than Betelgeuse, and is thought to be due to an enhanced mass-loss episode in the last 1 000 yr (Smith et al. 2001, 2009). This results in a dramatic circumstellar reflection nebula that is easily detected in visual-wavelength images with *HST* (Smith et al. 2001), polarized light (Jones et al. 2007), IR continuum emission from dust (Monnier et al. 1998), and in various spectral lines like K I (Smith 2004), infrared CO bandhead emission (Smith et al. 2009), and rotational lines of CO (Decin et al. 2006). Smith et al. (2009) have noted the stark difference between Betelgeuse and VY CMa, using the same techniques to observe circumstellar material around both stars. Schuster et al. (2006, 2009) have discussed the search for circumstellar material around other cool hypergiant stars using *HST*.

2.2 Yellow Hypergiants

Like red supergiants, the yellow hypergiants (YHGs) have slow and dense, dusty winds which can give rise to detectable nebulae. These cases are rare, however, and most YHGs do not have easily detectable circumstellar nebulae. One dramatic example of a YHG with an observable nebula is IRC+10420 (see Oudmaijer 1998, Oudmaijer et al. 1996; Humphreys et al. 1997, 2002; Davies et al. 2007), which seems to be cruising across the top of the HR diagram, transitioning from a spectral type of late F to early A in just a few decades. If a YHG is seen to have a spatially resolved nebula, it is thought to result because the YHG is in a post-RSG phase. In the case of IRC+10420 this may be following a phase of enhanced RSG mass loss like VY CMa. Otherwise it would be quite difficult to explain the presence of OH masers (e.g., Bowers 1984) around such a warm star. These nebulae are dusty, seen in scattered starlight or thermal-IR emission, as well as in molecular transitions at longer wavelengths (Tiffany et al. 2010; Castro-Carrizio et al. 2001, 2007).

2.3 Luminous Blue Variables

LBVs are perhaps the best known examples of circumstellar nebulae around massive stars, exemplified in memorable *HST* images like those of η Carinae (Morse et al. 1998) and the Pistol star (Figer et al. 1999). They are reminiscent of planetary nebulae in their complex structure and geometry, although LBV nebulae can be much more massive (see Vamvatira-Nakou et al. 2011, Weis 2011, Clark et al. 2011, and Wachter et al. 2011). Smith & Owocki (2006) noted several cases of luminous LBVs with nebulae of 10–20 $M_\odot$. These extremely massive shells – ejected relatively recently (typical ages of roughly 10^4 yr or less) – indicate an extremely violent history of mass ejection, when these stars can potentially shed a large fraction of their initial mass in a disruptive event that lasts only a few years. This eruptive mass loss endures as one of the chief mysteries of stellar astrophysics, despite its importance in determining the fate of massive stars. Not all LBV nebulae are so massive, of course. Many are only of order 0.1 $M_\odot$. This is sometimes even seen in the same star: after ejecting $\sim$15 $M_\odot$ in its 1840s eruption, η Carinae subsequently ejected 0.1–0.2 $M_\odot$ in its smaller 1890 eruption (Smith 2005).

The chemical abundances of LBV nebulae are generally nitrogen rich, indicating that nuclear material processed through the CNO cycle has risen to the surface of the star and has been ejected, therefore indicating that these stars are in an advanced phase of their evolution (Davidson et al. 1986;

Lamers et al. 2001; Smith & Morse 2004). In the case of η Car, this N enhancement is very recent, occurring in just the past few thousand years (Smith & Morse 2004; Smith et al. 2005).

The geometries of LBV nebulae are also interesting. LBV shells are often — although not always — bipolar. An obvious extreme example is η Carinae, where the bipolar shape of the nebula seems consistent with expectations of mass loss from a rapidly rotating star (Smith 2006; Owocki 2003; Owocki et al. 1996; Dwarkadas & Owocki 2002; Smith & Townsend 2007). Bipolarity of LBV nebulae has often been attributed to various degrees of asymmetry in the pre-existing ambient material (e.g., Frank et al. 1995), although the origin of that pre-existing asymmetry does not have a clear explanation. Recent imaging of the nebula around the LBV HD 168625 (Smith 2007) showed a triple-ring structure almost identical to the nebula around SN 1987A (Burrows et al. 1995), providing a tantilizing link between LBVs and supernova progenitors (see below). On the other hand, some LBVs are only mildy ellipsoidal, like AG Car (see Weis 2011), and some like P Cygni appear to be clearly spherical (Smith & Hartigan 2006). This suggests that we should avoid impulses to associate *all* LBV eruptions with stellar mergers or similar binary-induced effects.

2.4 B[e] supergiants and Equatorial Rings

The circumstellar material around B[e] stars was discussed in detail by Zickgraf et al. (1986, 1996; see also Bonanos et al. 2011). B[e] stars are thought to be surrounded by dusty equatorial tori with radii of order 10^3 AU, making them bright IR sources, while gas in these slowly expanding tori gives rise to their relatively narrow namesake forbidden emission lines. In many ways, the B[e] supergiants resemble less extreme versions of LBV nebulae. The spectral energy distributions of B[e] supergiants in the SMC and LMC look very similar to those of LBVs (Bonanos et al. 2009, 2010).

The origin of the equatorial circumstellar nebulae of B[e] stars remain unclear, but possibilities are that they arise from post-RSG evolution, equatorial mass loss from a recent RLOF phase, or that they arise from rapidly rotating stars. More detailed studies of B[e] stars and their circumstellar matter are certainly justified.

The dusty tori around B[e] supergiants with radii of $\sim 10^3$ AU may be related to an emerging class of early B supergiants with spatially resolved equatorial rings (see Smith et al. 2007; Smith 2007), including the progenitor of SN 1987A, SBW1 in the Carina Nebula, Sher 25 in NGC 3603, and HD 168625. Perhaps these equatorial rings are the expanding fossil remains of the B[e] tori (Smith et al. 2007).

2.5 Interacting Binaries

Although B[e] stars and LBVs are sometimes suspected to be binaries (and are indeed sometimes known to be binaries where the role of the companion star is unclear), there are also more clear-cut cases of binary-induced mass loss. Namely, there are very close interacting binaries that are sometimes even seen as eclipsing binaries, where we can see that they are in (or have recently been in) a RLOF phase of evolution.

One of the most interesting cases to mention is the massive, eclipsing, over-contact binary RY Scuti. To my knowledge, it is so far the only massive binary caught in the brief RLOF phase that also has a spatially resolved circumstellar nebula. This is interesting, because the nebula is not only torroidal (like those around B[e] supergiants), but also exhibits a bizarre double-ring structure (Smith et al. 2002; Gehrz et al. 2001). The properties of the nebula were discussed by Smith et al. (2002), while spectroscopy of the central binary system has been discussed recently by Grundstrom et al. (2007). RY Scuti is extremely interesting, since the originally more massive member is thought to be caught in a brief transition to a WR star. This system therefore provides the rare opportunity to

actually watch the stripping of the H envelope and the origin of a Type Ibc supernova progenitor in a binary system (e.g., Paczyński 1967). Smith et al. (2010b) have concluded that this channel probably dominates the production of Type Ibc supernovae.

2.6 Wolf-Rayet Stars

Although Wolf-Rayet (WR) stars are famous for their strong winds, they also sometimes exhibit circumstellar nebulae, which come in two main flavors. One is the large wind-blown bubble nebulae that are generally seen around younger WN stars (see Stock & Barlow 2010). A famous example is NGC 6888. The raw material for these nebulae probably is not from the WR wind itself, however. Rather, the dense nebular gas is probably slower material ejected in a previous LBV or RSG phase, which is then swept into a dense bubble or shell by the faster WR wind.

A very different type of circumstellar nebula seen around WR stars is the dusty nebulae associated with WC+O binaries, either appearing as so-called "pinwheel" nebulae in circularized systems like WR104, or as episodic puffs of asymmetric dust production in eccentric systems like WR140. Although the dusty nature of WC stars had been known since the early days of IR astronomy (Gehrz & Hackwell 1974), the spectacular structure of these WR nebulae was only revealed by special high-resolution aperture synthesis imaging at near-IR wavelengths pioneered on the Keck telescope (see Tuthill et al. 1999; Monnier et al. 1999, 2002). In these cases, the dense gas and dust – which is much denser than the material normally found in a WR star wind – arises as a result of the compression and cooling in the colliding-wind shock of the WC+O binary (see Williams et al. 1990, 2001). The formation of graphite grains is likely facilitated by the C-rich material in the WC wind.

3 Multiwavelength Diagnostics of Circumstellar Material

3.1 Visual Wavelengths

At visual wavelengths, the two chief ways to spatially resolve circumstellar material are with starlight scattered by dust, and with intrinsic emission lines in the nebula. Because the central stars are bright, simple optical continuum imaging is only successful in a few remarkable cases, like η Carinae, VY CMa, IRC+10420, etc. (see above), where the dusty nebula is very dense and the central star is partly obscured by the circumstellar dust. In other cases, polarimetric imaging or coronagraphy can help to suppress the direct light from the central star.

A more effective method is to use narrow-band imaging, long-slit spectroscopy, or IFU spectroscopy to detect extended emission lines from the circumstellar nebula. Concentrating on a forbidden emission line formed only in the nebula helps suppress the bright continuum radiation from the central star. The most common probe is [N II] λ6583, which arises in most circumstellar nebulae over a wide range in ionization level, and can be especilly bright in the N-enriched gas around evolved massive stars (Davidson et al. 1986; Lamers et al. 2001; Smith & Morse 2004). Forbidden lines like [N II] are usually better than Hα, since Hα is often an extremely strong emission line in the central star's spectrum as well. When high-resolution long-slit spectra are employed, lines like [N II] permit one to measure the expansion speed of a circumstellar shell (e.g., L. Smith 1994).

A lesser-known technique that has proven extremely useful for detecting nebulae around cooler stars (where N is neutral and [N II] cannot be seen) is the red resonance lines of K I. Extended K I λ7699 emission has been studied in detail around Betelgeuse and VY CMa, for example (Bernet & Lambert 1976; Bernet et al. 1978; Plez & Lambert 1994, 2002; Smith 2004). With high-resolution long-slit spectroscopy of K I λ7699, one can perform the same types of kinematic studies as with

[N II] around hotter stars. For nebulae around very hot stars, higher ionization lines like [Fe III] can also be useful, as in the case of RY Scuti (e.g., Smith et al. 2002).

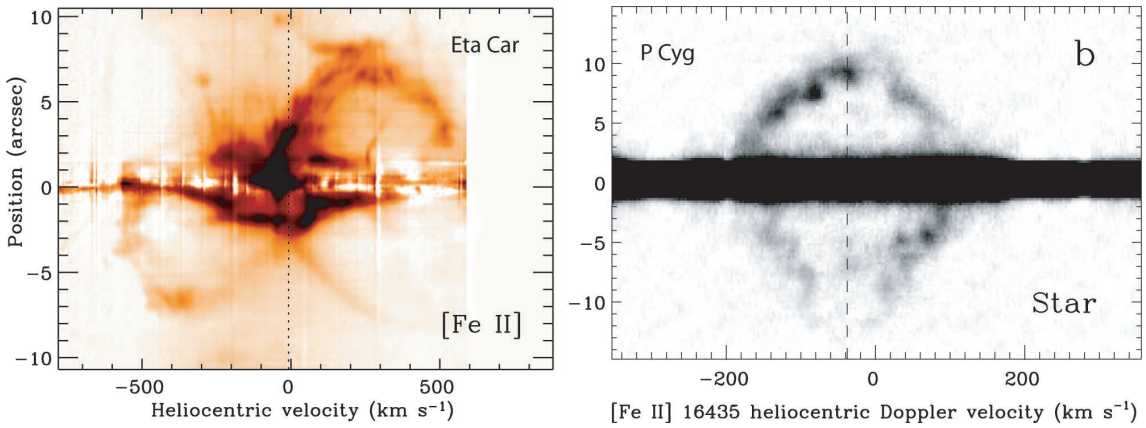

Figure 1: Long slit spectra of [Fe II] 1.644 μm around Eta Carinae (left; a) and P Cygni (right; b). The spectrum of Eta Car was taken with Phoenix on Gemini South (Smith 2006). The spectrum of P Cygni was taken with CSHELL on the IRTF (Smith & Hartigan 2006).

3.2 Near-IR

Near-IR wavelengths can provide a powerful probe of circumstellar material, especially in cases of massive stars that are obscured at visual wavelengths (in the Galactic Center, for example; Figer et al. 1999; Mauerhan et al. 2010). As with optical imaging, circumstellar shells can be resolved using scattered continuum starlight, although this is perhaps even more difficult than at visual wavelengths because of the lower scattering efficiency, unless the grains are large. However, with available technology, near-IR wavelengths have the advantage of adaptive-optics (AO) imaging or speckle-masking interferometry, as mentioned earlier. Again, polarimetric imaging and coronagraphy can help to suppress the bright central starlight.

Narrow-band imaging and long-slit spectroscopy are also used to resolve circumstellar material around massive stars in the near-IR, with H I lines such as Br γ or (from space with *HST*) Paα (e.g., Figer et al. 1999; Mauerhan et al. 2010). These lines are best around hotter stars where H is mostly ionized. In principle this is the same as Hα imaging in the optical, but it can be used for obscured sources in the Galactic plane.

One of the most powerful but underused near-IR probes of circumstellar gas around massive stars involves spectroscopy or narrow-band imaging of infrared [Fe II] emission lines. In particular, [Fe II] λ16435 and λ12567 are two of the brightest lines in the near-IR spectra of LBVs and similar stars (Smith 2002), due to the relatively low excitation and high density of the gas. These two bright lines arise from the same upper energy level, and so their observed ratio can serve as a reliable measure of the reddening and extinction toward a source (see Smith & Hartigan 2006 for the atomic data and intrinsic line ratios). Flux ratios of some other adjacent [Fe II] lines to [Fe II] λ16435 serve as density diagnostics, while high-resolution spectra can provide the expansion speed of a shell. Detailed studies of η Car and P Cygni have demonstrated the utility of these [Fe II] lines (Smith 2006; Smith & Hartigan 2006; see Figure 1).

Narrow-band imaging or spectroscopy of near-IR H_2 lines, like H_2 1–0 S(1) at 2.122 μm, are also common tracers of shocked gas or dense gas irradiated by moderately strong non-ionizing radiation. However, these lines are rarely seen around hot stars because the H_2 is destroyed, and they are rarely

seen in cooler supergiants because they are not sufficiently excited. An unusual exception is the extremely bright H_2 lines in the Homunculus of η Carinae (Smith 2006). In this source, the combination of a very young and dense nebula that is optically thick enough to be self-shielding allows the H_2 molecules to survive, while a surface layer of H_2 is struck by strong near-UV radiation from the luminous central star. As the Homunculus continues to expand and become more optically thin, the H_2 will be dissociated (see Smith & Ferland 2007 for details).

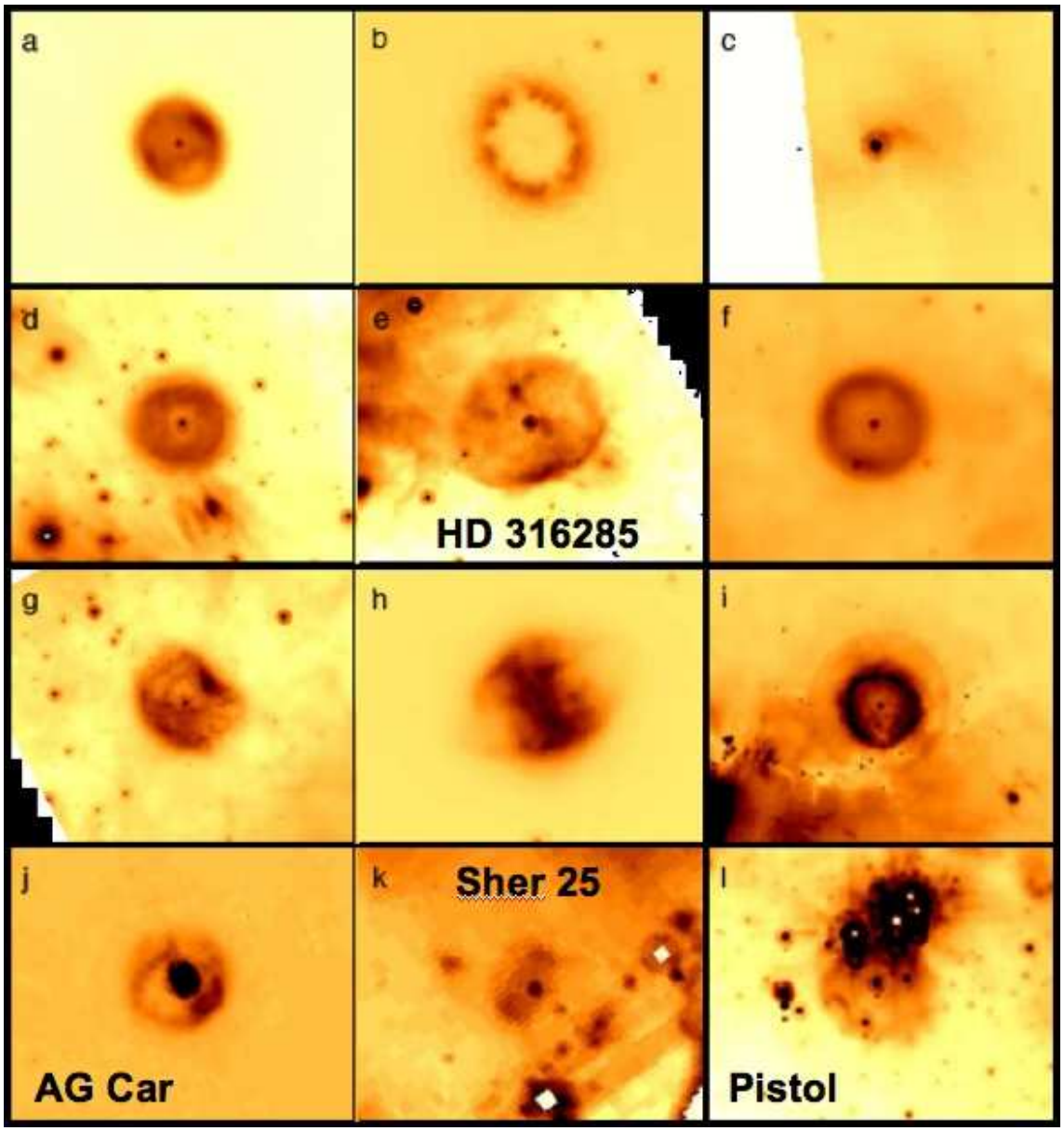

Figure 2: *Spitzer*/MIPS 24 μm images of shells around LBVs and related stars (reproduced from Gvaramadze et al. 2010 with permission).

3.3 Mid-IR/Far-IR

Moving into the mid-IR and far-IR, circumstellar shells of massive stars become more easily observed because the glare of photospheric emission from the central stars is no longer a problem, and because thermal-IR radiation from warm dust grains is substantial. Extreme red supergiants like VY CMa and

NML Cygni have been favorite targets of ground-based mid-IR observers for decades because their circumstellar dust is bright and spatially extended, while η Carinae is observed perpetually with every new mid-IR instrument that comes online in the southern hemisphere. Mid-IR observations played a special role in the history of our understanding of η Carinae, providing our first clue that it is an extremely luminous but self-obscured star (Westphal & Neugebauer 1969). The young dust shell of η Carinae acts as a calorimeter of the central star because it absorbs nearly all the star's UV radiation, and mid/far-IR observations provide our best estimates of the mass of the Homunculus (Smith et al. 2003).

Eta Carinae is an exceptional case, however, because its nebula is very young and very bright. For other LBVs, the shells are not so easy to detect in ground-based images because they are larger and more optically thin, and are therefore often too faint to detect in the mid-IR through the Earth's atmosphere. However, space-based IR telescopes have provided key information on a number of dusty shells around LBVs (e.g., Voors et al. 2000; Trams, Voors, & Waters 1998; Egan et al. 2002; Clark et al. 2003). In particular, recent surveys of the Galactic plane with the IRAC and MIPS instruments on *Spitzer* have revealed a large number of extended mid-IR shells around LBVs and related stars (see Fig. 2; Gvaramadze, Kniazev, & Fabrika 2010; Wachter et al. 2010; Smith 2007; Umana et al. 2009). This sample has the potential to tell us how much mass is typically ejected by an LBV, and to identify previously unrecognized LBVs and WR stars. We eagerly anticipate results on the far-IR emission from these shells with *Herschel* (e.g., Royer et al. 2010). Longer mid-IR and far-IR wavelengths are useful, because they have the potential to detect cooler dust in the shell, which may correspond to a large fraction of the total mass (e.g., Gomez et al. 2010).

In addition to very extended shell nebulae, the more compact dusty pinwheels and episodic ejections associated with colliding-wind WC+O binaries are also spatially resolved in the thermal-IR, as noted earlier (Tuthill et al. 1999; Monnier et al. 1999, 2002; Rajogopal et al. 2007), providing a powerful probe of a unique mass-loss phenomenon.

3.4 X-rays

The spatially resolved nebulae around massive stars are not often detected in X-rays, since strong shocks (and hence, strong differences in ejection velocity over a short period of time) are needed to produce sufficiently bright X-rays far from the star. The study of *diffuse* X-ray emission associated with massive stars is mainly concentrated toward SNe and SN remnants (see below). A notable exception, again, is the peculiar case of η Carinae, where a strong blast wave from the 19th century eruption is overtaking ejecta from a previous eruption (Smith 2008), giving rise to a spectacular soft X-ray shell made famous in *Chandra* images (e.g., Seward et al. 2001). The study of massive stars in X-rays is weighted heavily toward colliding wind binaries or unresolved soft X-ray emission from the winds of O-type stars.

3.5 Radio

At radio wavelengths, continuum free-free radiation traces the same photoionized gas around hot massive stars that can be observed with Hα emission, but without such strong continuum radiation from the central star, and free from line-of-sight extinction. This is particularly useful for studying the nebulae of hotter LBVs and WR stars (e.g., Duncan & White 2002; Lang et al. 2005; Umana et al. 2005, 2010; Dougherty et al. 2010; Buemi et al. 2010).

Radio wavelengths also provide unique probes of molecular shells around massive stars, most commonly seen around cooler supergiants. In particular, molecular masers like SiO, H_2O, and OH can be observed at very high spatial resolution with radio interferometers, and have yielded unique

and valuable information about the structure and expansion of shells around evolved cool stars (e.g., Bowers et al. 1993; Benson & Mutel 1979, 1982; Marvel 1997; Boboltz & Marvel 2000; Trigilio et al. 1998). One can actually follow the proper motion and Doppler velocity of individual maser spots, tracing out the structure, expansion, and rotation of the inner winds of these stars. Molecular shells are not generally observed around hot stars because they are quickly dissociated by UV radiation. However, they are seen in some cases of young WR stars or YHGs that are in a post-RSG phase, as noted earlier for IRC+10420. The N-enriched shells of LBVs may be detectable in ammonia, which has been detected in η Car (Smith et al. 2006), but has not been searched for extensively in other sources.

4 Supernova Blast Waves Crashing into Pre-Supernova Circumstellar Material

When a supernova (SN) explodes, it sends a flash of UV radiation and a strong blast wave out into the surrounding medium. In this way, SNe illuminate the circumstellar material that was ejected by the star *before* the SN. As the shock expands it can interact with either circumstellar or interstellar material, giving rise to a SN remnant. The posterchild for a SN remnant interacting with dense circumstellar material ejected by its progenitor is Cas A (e.g., Chevalier & Oishi 2003). Slow-moving N-rich "flocculi" (Fesen & Becker 1991; Chevalier & Kirshner 1978) indicate that the overtaken material was circumstellar rather than interstellar, and that the progenitor was at least a moderately massive evolved star with a fairly slow wind (Chevalier & Oishi 2003).

Perhaps the most famous case of a SN blast wave interacting with circumstellar material is SN 1987A. Almost immediately, the UV flash of the SN shock breakout photoionized the triple ring nebula seen in *HST* images (Burrows et al. 1995). After about 10 years, the SN blast wave began crashing into the equatorial ring seen in these images, and this collision is still unfolding (Michael et al. 2000; Sonneborn et al. 1998; Sugerman et al. 2002). The complex shock interaction is the focus of an ongoing multiwavelength campaign, and provides an enormous reservoir of information about shock physics as well as pre-SN mass loss of the progenitor star. Since the blue progenitor contradicted expectations of stellar evolution models, it has been suggested that the progenitor star underwent a binary merger event to produce the triple-ring nebula (e.g., Morris & Podsiadlowski 2007), but comparisons to LBV nebulae have also been made (Smith 2007).

Sometimes the interaction between the SN shock and circumstellar gas happens much sooner and is even more dramatic. In the case of Type IIn supernovae, this shock interaction with the nearest circumstellar gas can happen immediately, completely altering the apparent spectrum of the SN and in some cases markedly increasing the luminosity of the SN. The name "IIn" comes from the narrow H emission lines in the spectrum, arising from the slow shocked CSM gas. The dense circumstellar material decelerates the blast wave and thermalizes its kinetic energy. In some cases this thermal energy is radiated as visual light before adiabatic expansion can cool the gas, thus producing some of the most luminous SNe in the universe with $\sim 10^{51}$ ergs radiated in visual light alone (e.g., Smith & McCray 2007, Smith et al. 2007, 2010a; Woosley et al. 2007; van Marle et al. 2010; see Figure 3). By studying the time evolution of the luminosity and spectral properties of SNe IIn in the year or two after discovery, we can deduce the density and velocity of circumstellar matter at each radial position overtaken by the shock. An exemplary case concerns the spectral evolution and light echo of SN 2006gy, from which a circumstellar medium closely resembling that of η Carinae has been deduced (Smith et al. 2010a). We can therefore reconstruct the mass-loss rate and kinetic energy of pre-SN mass ejections as a function of time immediately before the SN explosion occurred. Aside from being lucky enough to be watching when an exceptional Galactic SN occurs, this is our most

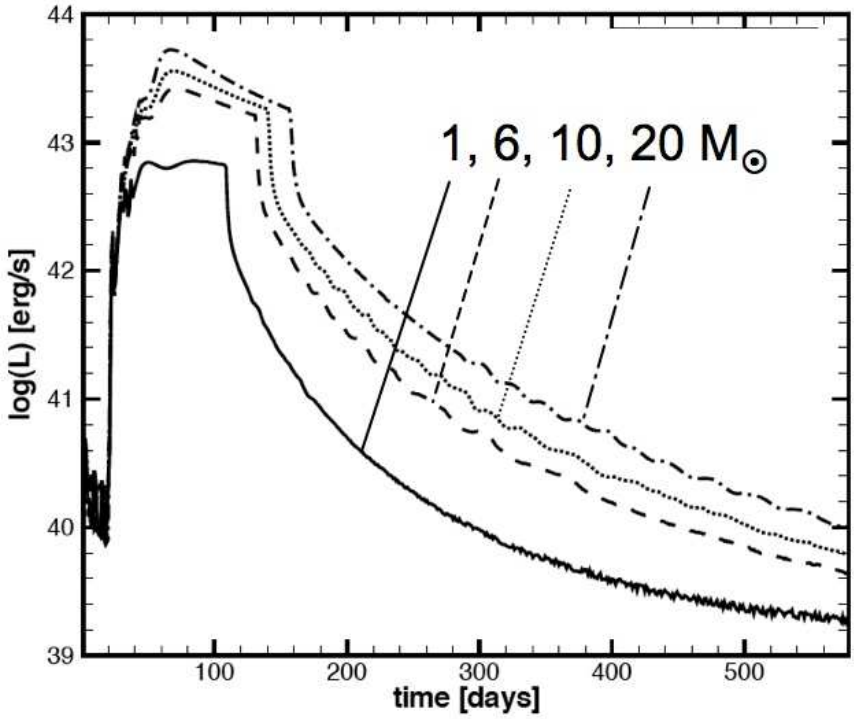

Figure 3: Theoretical light curves of a normal SN shock crashing into dense circumstellar gas with a range of masses from 1–20 $M_\odot$ (adapted from van Marle et al. 2010). A normal Type II-P supernova has a peak luminosity of about 10^{42} erg s^{-1}.

powerful tool for studying how massive stars behave in the rapid nuclear timescales immediately before they suffer core collapse.

The potential of using SNe IIn to learn about circumstellar structure and pre-SN evolution is extremely exciting. Not only does this shock interaction produce some of the most luminous SNe known, potentialy observable at high redshift, but it also can provide diagnostics of the detailed properties of circumstellar gas around a single (or binary) star at distances far beyond where we could ever hope to spatially resolve a circumstellar nebula.

Acknowledgements

I thank the conference organizers for covering part of my travel expenses at the conference.

References

Benson, J.M., & Mutel, R.L. 1979, ApJ, 233, 119
Benson, J.M., & Mutel, R.L. 1982, ApJ, 253, 199
Bernet, A.P., & Lambert, D.L. 1976, ApJ, 210, 395
Bernet, A.P., Honeycutt, R. K., Kephart, J. E., Gow, C. E., Sandford, M. T., II, & Lambert, D. L. 1978, ApJ, 219, 532
Beuther, H. 2011, in Proceedings of the 39th Liège Astrophysical Colloquium, eds. G. Rauw, M. De Becker, Y. Nazé, J.-M. Vreux & P. Williams, BSRSL, 80, 200
Boboltz, D.A., & Marvel, K.B. 2000, ApJ, 545, L149
Bonanos, A., Massa, D. L., Sewilo, M., et al. 2009, AJ, 138, 1003
Bonanos, A., Lennon, D. J., Köhlinger, F., et al. 2010, AJ, 140, 416

Bonanos, A., Lennon, D.J., Massa, D.L., et al. 2011, in Proceedings of the 39th Liège Astrophysical Colloquium, eds. G. Rauw, M. De Becker, Y. Nazé, J.-M. Vreux & P. Williams, BSRSL, 80, 346
Bowers, P.F. 1984, 279, 350
Bowers, P.F., Claussen, M.J., & Johnston, K.J. 1993, AJ, 104, 284
Buemi, C.S., Umana, G., Trigilio, C., Leto, P., & Hora, J.L. 2010, ApJ, 721, 1404
Burrows, C.J., Krist, J., Hester, J. J., et al. 1995, ApJ, 452, 680
Castro-Carrizo, A., Lucas, R., Bujarrabal, V., Colomer, F., & Alcolea, J. 2001, A&A, 368, L34
Castro-Carrizo, A., Quintana-Lacaci, G., Bujarrabal, V., Neri, R., & Alcolea, J. 2007, A&A, 465, 457
Chevalier, R.A., & Kirshner, R.P. 1978, ApJ, 219, 931
Chevalier, R.A., & Oishi, J. 2003, ApJ, 593, L23
Chiosi, C., & Maeder, A. 1986, ARAA, 24, 329
Clark, J.S., Egan, M. P., Crowther, P. A., Mizuno, D. R., Larionov, V. M., & Arkharov, A. 2003, A&A, 412, 185
Clark, J.S., Arkharov, A., Larionov, V., Ritchie, B., Crowther, P., & Najarro, F. 2011, in Proceedings of the 39th Liège Astrophysical Colloquium, eds. G. Rauw, M. De Becker, Y. Nazé, J.-M. Vreux & P. Williams, BSRSL, 80, 361
Davidson, K., Dufour, R., Walborn, N.R., & Gull, T.R. 1986, ApJ, 305, 867
Davies, B., Oudmaijer, R.D., & Sahu, K.C. 2007, ApJ, 671, 2059
Decin, L., Hony, S., de Koter, A., Justtanont, K., Tielens, A. G. G. M., Waters, L. B. F. M. 2006, A&A, 456, 549
Dougherty, S.M., Clark, J.S., Negueruela, I., Johnson, T., & Chapman, J.M. 2010, A&A, 511, 58
Duncan, R.A., & White, S.M. 2002, MNRAS, 330, 63
Dwarkadas, V.V., & Owocki, S.P. 2002, ApJ, 581, 1337
Egan, M., Clark, J. S., Mizuno, D. R., Carey, S. J., Steele, I. A., & Price, S. D. 2002, ApJ, 572, 288
Fesen, R.A., & Becker, R.H. 1991, ApJ, 371, 621
Figer, D., McClean, I.S., & Morris, M. 1999, ApJ, 514, 202
Frank, A., Balick, B., & Davidson, K. 1995, ApJ, 441, L77
Gehrz, R.D., & Hackwell, J.A. 1974, ApJ, 194, 619
Gehrz, R.D., Smith, N., Jones, B., Puetter, R., & Yahil, A. 2001, ApJ, 559, 395
Grundstrom, E., Gies, D. R., Hillwig, T. C., McSwain, M. V., Smith, N. Gehrz, R. D., Stahl, O., & Kaufer, A. 2007, ApJ, 667, 505
Gomez, H.L., Vlahakis, C., Stretch, C. M., Dunne, L., Eales, S. A., Beelen, A., Gomez, E. L., & Edmunds, M. G. 2010, MNRAS, 401, L48
Gvaramadze, V., Kniazev, A. Y., & Fabrika, S. 2010, MNRAS, 405, 1047
Harper, G., Brown, A., & Guinan, E. 2008, AJ, 135, 1430
Hinz, P.M., Angel, J. R. P., Hoffmann, W. F., McCarthy, D. W., McGuire, P. C., Cheselka, M., Hora, J. L., & Woolf, N. J. 1998, Nature, 395, 251
Humphreys, R.M., Smith, N., Davidson, K., et al. 1997, AJ, 114, 2778
Humphreys, R.M., Davidson, K., & Smith, N. 2002, AJ, 124, 1026
Jones, T.J., Humphreys, R. M., Helton, L. A., Gui, C., & Huang, X. 2007, AJ, 133, 2730
Lamers, H.J.G.L.M., Nota, A., Panagia, N., Smith, L. J., & Langer, N. 2001, ApJ, 551, 764
Lang, C.C., Johnson, K.E., Goss, W.M., & Rodriguez, L.F. 2005, AJ, 130, L2185
Maeder, A., & Meynet, G. 2000, A&A, 361, 159
Martins, F. 2011, in Proceedings of the 39th Liège Astrophysical Colloquium, eds. G. Rauw, M. De Becker, Y. Nazé, J.-M. Vreux & P. Williams, BSRSL, 80,
Marvel, K.B. 1997, PASP, 104, 1286
Mauerhan, J., Cotera, A., Dong, H., Morris, M. R., Wang, Q. D., Stolovy, S. R., & Lang, C. 2010, ApJ, 725, 188
Meynet, G., Georgy, C., Hirschi, R., Maeder, A., Massey, P., Przybilla, N., & Nieva, M.-F. 2011, in Proceedings of the 39th Liège Astrophysical Colloquium, eds. G. Rauw, M. De Becker, Y. Nazé, J.-M. Vreux & P. Williams, BSRSL, 80, 266
Michael, E., McCray, R., Pun, C. S. J., et al. 2000, ApJ, 542, L53
Monnier, J.D., Geballe, T.R., & Danchi, W.C. 1998, ApJ, 502, 833
Monnier, J.D., Tuthill, P., & Danchi, W.C. 1999, ApJ, 525, L97
Monnier, J.D., Tuthill, P., & Danchi, W.C. 2002, ApJ, 567, L137
Morris, T., & Podsiadlowski, P. 2007, Science, 351, 1130
Morse, J.A., Davidson, K., Bally, J., Ebbets, D., Balick, B., & Frank, A. 1998, AJ, 116, 2443
Oudmaijer, R.D. 1998, A&AS, 129, 541
Oudmaijer, R.D., Groenewegen, M.A.T., Matthews, H.E., Blommaert, J.A.D.L., & Sahu, K.C. 1996, MNRAS, 280, 1062
Owocki, S.P. 2003, in IAU Symp. 212, 281

Owocki, S.P. 2011, in Proceedings of the 39th Liège Astrophysical Colloquium, eds. G. Rauw, M. De Becker, Y. Nazé, J.-M. Vreux & P. Williams, BSRSL, 80, 16
Owocki, S.P., Cranmer, S.R., & Gayley, K.G. 1996, ApJ, 472, L115
Plez, B., & Lambert, D.L. 1994, ApJ, 425, L101
Plez, B., & Lambert, D.L. 2002, A&A,386, 1009
Paczyński, B. 1967, Acta Astron., 17, 355
Rajagopal, J., Menut, J.-L., Wallace, D., et al. 2007, ApJ, 671, 2017
Royer, P., Decin, L., Wesson, R., et al. 2010, A&A, 518, L145
Schuster, M.T., Humphreys, R., & Marengo, M. 2006, AJ, 131, 603
Schuster, M.T., Marengo, M., Hora, J.L., et al. 2009, ApJ, 699, 1423
Seward, F., Butt, Y. M., Karovska, M., Prestwich, A., Schlegel, E. M., & Corcoran, M. 2001, ApJ, 553, 832
Smith, L. 1994, ApSS, 216, 291
Smith, N. 2002, MNRAS, 336, L22
Smith, N. 2004, MNRAS, 349, L31
Smith, N. 2005, MNRAS, 357, 1330
Smith, N. 2006, ApJ, 644, 1151
Smith, N. 2007, AJ, 133, 1034
Smith, N. 2008, Nature, 455, 201
Smith, N., & Ferland, G.R. 2007, ApJ, 655, 911
Smith, N., & Hartigan, P. 2006, ApJ, 638, 1045
Smith, N., & McCray, R. 2007
Smith, N., & Morse, J.A. 2004, ApJ, 605, 854
Smith, N., & Owocki, S.P. 2006, ApJ, 645, L45
Smith, N., & Townsend, R.H.D. 2007, ApJ, 666, 967
Smith, N., Humphreys, R. M., Davidson, K., Gehrz, R. D., Schuster, M. T., & Krautter, J. 2001, AJ, 121, 1111
Smith, N., Gehrz, R. D., Stahl, O., Balick, B., & Kaufer, A. 2002, ApJ, 578, 464
Smith, N., Gehrz, R. D., Hinz, P. M., Hoffmann, W. F., Hora, J. L., Mamajek, E. E., & Meyer, M. R. 2003, AJ, 125, 1458
Smith, N., Morse, J.A., & Bally, J. 2005, AJ, 130, 1778
Smith, N., Brooks, K.J., Koribalski, B.S., & Bally, J. 2006, ApJ, 645, L41
Smith, N., Bally, J., & Walawender, J. 2007, AJ, 134, 846
Smith, N., Hinkle, K.H., & Ryde, N. 2009, AJ, 137, 3558
Smith, N., Chornock, R., Silverman, J. M., Filippenko, A. V., & Foley, R. J. 2010a, ApJ, 709, 856
Smith, N., Li, W., Filippenko, A. V., & Chornock, R. 2010b, MNRAS, in press, arXiv:1006.3899
Sonneborn, G., Pun, C. S. J., Kimble, R. A., et al. 1998, ApJ, 492, L139
Stock, D.J., & Barlow, M.J. 2010, MNRAS, 409, 1429
Sugerman, B.E.K. 2000, ApJ, 572, 209
Tiffany, C., Humphreys, R.M., Jones, T.J., & Davidson, K. 2010, AJ, 140, 339
Trams, N.R., Voors, R. H. M., & Waters, L. B. F. M. 1998, Ap&SS, 255, 195
Trigilio, C., Umana, G., & Cohen, R.J. 1998, MNRAS, 297, 497
Tuthill, P.C., Monnier, J.D., & Danchi, W.C. 1999, Nature, 398, 486
Umana, G., Buemi, C.S., Trigilio, C., Leto, P., & Hora, J.L. 2005 A&A, 437, L1
Umana, G., Buemi, C.S., Trigilio, C., Hora, J.L., Fazio, G.G., & Leto, P. 2009, ApJ, 694, 697
Umana, G., Buemi, C.S., Trigilio, C., Leto, P., & Hora, J.L. 2010, ApJ, 718, 1036
van Marle, A. J., Smith, N., Owocki, S. P., & van Veelen, B. 2010, MNRAS, 07, 2305
Vamvatira-Nakou, C., Royer, P., Hutsemékers, D., Rauw, G., Nazé, Y., Exter, K., Waelkens, C., & Groenewegen, M. 2011, in Proceedings of the 39th Liège Astrophysical Colloquium, eds. G. Rauw, M. De Becker, Y. Nazé, J.-M. Vreux & P. Williams, BSRSL, 80, 435
Voors, R.H.M., Waters, L. B. F. M., de Koter, A., et al. 2000, A&A, 356, 501
Wachter, S., Mauerhan, J. C., Van Dyk, S. D., Hoard, D. W., Kafka, S., & Morris, P. W. 2010, AJ, 139, 2330
Wachter, S., Mauerhan, J., Van Dyk, S., Hoard, D.W., & Morris, P. 2011, in Proceedings of the 39th Liège Astrophysical Colloquium, eds. G. Rauw, M. De Becker, Y. Nazé, J.-M. Vreux & P. Williams, BSRSL, 80, 291
Weis, K., et al. 2011, in Proceedings of the 39th Liège Astrophysical Colloquium, eds. G. Rauw, M. De Becker, Y. Nazé, J.-M. Vreux & P. Williams, BSRSL, 80, 440
Westphal, J.A., & Neugebauer, G. 1969, ApJ, 156, L45
Williams, P.M., van der Hucht, K. A., Pollock, A. M. T., Florkowski, D. R., van der Woerd, H., & Wamsteker, W. M. 1990, MNRAS, 243, 662

Williams, P.M., Kidger, M. R., van der Hucht, K. A., et al. 2001, MNRAS, 324, 156
Woosley, S.E., Langer, N., & Weaver, T.A. 1993, ApJ, 411, 823
Woosley, S. E., Blinnikov, S., & Heger, A. 2007, Nature, 450, 390
Zickgraf, F.J., Wolf, B., Leitherer, C., Appenzeller, I., & Stahl, O. 1986, A&A, 163, 119
Zickgraf, F.J., Kovacs, J., Wolf, B., Stahl, O., Kaufer, A., & Appenzeller, I. 1996, A&A, 309, 505

Discussion

G. Meynet: As you know, the fraction of Ibc to type II supernovae is observed to be different in different metallicity regions. For instance Prieto et al. (2008), Prantzos & Boissier (2003) show that the number fraction is about 10% at $Z \sim 0.3Z_{\odot}$ and about between 40 and 60% above solar metallicity. So my question is the following, are the statistics you showed deduced from a narrow range of metallicities? (Otherwise you may be in the danger to obtain a somewhat blurred picture, do you?).
N. Smith: Well, perhaps it is fair to say that we have a somewhat blurred picture because our supernova survey sampled galaxies with average metallicities of roughly 0.5-2 $Z_{\odot}$, dominated by $Z \approx 1Z_{\odot}$. However, this does not change the fact that at these metallicities, winds are far too weak to account for the large fraction of stripped envelope supernovae.
With regard to values of Ibc/II fractions, and their variation with metallicity, 2 points are important:

1. The ratio of observed type Ibc to type II can be misleading, since type IIb supernovae are actually more like type Ib but they have only a tiny amount of residual H. The fraction of IIb is $>$10%, so this is not a negligible effect. One should really consider the fraction of Type (Ib + Ic + IIb)/(II-P + II-L + IIn) with metallicity.

2. There are many observational selection effects in previous supernova statistics, so one must be careful. Considering only type Ibc supernovae, though, one would still expect strong metallicity effects even if all the H envelope is lost via metallicity independent mechanisms (i.e. LBV eruptions or RLOF in binaries). What I mean is that once the H envelope is removed, the further evolution is dominated by the line-driven WR wind which removes the He envelope and residual H. This is highly dependent on metallicity, of course.

W.-R. Hamann: In your considerations based on SN statistics you made the assumption - if I understood correctly - that the minimum stellar initial mass to reach the WR stage is 35 $M_{\odot}$ by single-star evolution. Our spectroscopic analyses e.g. of the Galactic WN sample (Hamann et al. 2006, A&A, 457,1015) and comparison with population synthesis showed that this mass limit is rather as low as 22 $M_{\odot}$, which also agrees with the Geneva tracks when rotational mixing is included. Would this change your conclusions?
N. Smith: The initial mass of 35 $M_{\odot}$ above which single stars are expected to shed their H envelopes at solar metallicity comes from standard stellar evolution models such as Heger et al. (2003), which adopt mass-loss rates that are already too high compared to current estimates of clumpy winds. I'm sure that one could construct stellar evolution models that make WR stars via single-star winds down to initial masses of 22 $M_{\odot}$ or perhaps even lower, but the critical question is whether one can do this adopting mass-loss rates that are realistic and in agreement with observational constraints. I think the answer is *no*.
Now, it may nevertheless be true that we have WR stars from initial masses of 22 $M_{\odot}$ or even lower (in fact, I am arguing that SN statistics require this), but the question is whether they have shed their H envelopes via winds, eruptions, or binary RLOF/binary mergers, etc. I think this question is more complicated, but the SN statistics suggest that it is very unlikely that single-star winds can dominate.

The nebulae around LBVs: a multiwavelength approach

Grazia Umana[1], Carla S. Buemi[1], Corrado Trigilio[1], Paolo Leto[1]
Joseph L. Hora[2] and Giovanni Fazio[2]

[1] INAF-Osservatorio Astrofisico di Catania, Via S. Sofia 78, 95123 Catania, ITALY
[2] Harvard-Smithsonian Center for Astrophysics, 60 Garden St. MS-65, Cambridge, MA 02138-1516, USA

Abstract: We present first results of our study of a sample of Galactic LBV, aimed to contribute to a better understanding of the LBV phenomenon, by recovering the mass-loss history of the central object from the analysis of its associated nebula. Mass-loss properties have been derived by a synergistic use of different techniques, at different wavelengths, to obtain high-resolution, multi-wavelength maps, tracing the different emitting components coexisting in the stellar ejecta: the ionized/neutral gas and the dust. Evidence for asymmetric mass-loss and observational evidence of possible mutual interaction between gas and dust components have been observed by the comparison of mid-IR (Spitzer/IRAC, VLT/VISIR) and radio (VLA) images of the nebulae, while important information on the gas and dust composition have been derived from Spitzer/IRS spectra.

1 Introduction

Luminous Blue Variables are luminous (intrinsically bright, $L \sim 10^4 L_{\odot}$) stars, which show different kinds of photometric and spectroscopic variabilities. They are massive ($M \sim 22-120 M_{\odot}$, Meynet & Maeder 2005), characterized by intense mass-loss rates ($10^{-6} - 10^{-4} M_{\odot}\mathrm{yr}^{-1}$), which can occur also in the form of eruptive events. LBVs are quite rare objects in our Galaxy. This is probably connected to their very short lifetime (some 10^4 yrs). The most recent census of Galactic LBVs counts 12 effective members and 23 candidates (Clark et al. 2005) and a few LBV (and candidates) have been also reported in some nearby galaxies.

LBVs represent a crucial phase in massive star evolution during which a star loses enough mass to become a $\sim 20 M_{\odot}$ WR star. To test evolutionary models, it is extremely important to quantify a key parameter: the total mass lost during the LBV phase, i.e. the gas (ionized, neutral, and molecular, if it exists) and the dust. Another important aspect of the study of circumstellar envelopes is to determine the mass-loss archeology of the central star and in particular how the mass-loss behavior (multiple events, bursts) is related to the physical parameters of the central object.

Figure 1: IRAC composite image of Wray 17-96 with north up and east to the left, $FOV = 5''$. Emission from the central star is evident at 3.6μm (blue), while the warm dust is well traced by the 8.5μm (red)

2 The project

A good understanding of the physical conditions in LBV ejecta requires multi-wavelength observations, tracing the different emitting components coexisting in the stellar ejecta: the ionized/neutral gas and the dust. The study of both components provides two kinds of information: current mass-loss, via direct observations of stellar winds (the gas component), and mass loss history of the central star, by analysis of the dust component/s. The detailed knowledge of the gas and dust distribution allows us to evaluate the total (gas+dust) mass of the nebula, the presence of different shells related to different mass-loss episodes, and thus the total mass lost by the central object during this critical phase of its evolution. Moreover, it could provide evidence for gas and dust mutual interactions which are a possible cause of the quite complex morphologies often observed in the LBV nebulae (LBVNs).

In the last few years we have started a systematic study of a sample of Galactic LBVs and LBV candidates aimed at deriving their mass-loss properties for a better understanding of the LBV phenomenon in the wider context of massive star evolution. Our approach is based on a synergistic use of different techniques, at different wavelengths, that allows us to analyze the several emitting components coexisting in the nebula. In particular, we performed a detailed comparison of mid-IR and radio maps, with comparable spatial resolution, to sort out the spatial differences in the maps in order to detect particular features which can be associated with mass-loss during the LBV phase: asymmetric winds versus symmetric winds in asymmetric environments; single events versus multiple events. In the framework of our LBV project, we obtained Spitzer/IRAC observations aimed at detecting and resolving the faint dust shells ejected from the central stars, and Spitzer/IRS observations to characterize the dust content of the nebula via mid-IR spectra. The ionised fraction of the nebulae has been mapped via high-angular resolution radio (VLA) observations. For the more compact nebulae, images in the mid-IR have been obtained by using VLT/VISIR in the N and Q mid-IR bands.

3 Results

Many interesting results have been obtained from our imaging and spectroscopic program. In particular, extended dusty shells have been detected around some of our targets (see Fig. 1) and evidence for asymmetric mass-loss and of possible mutual interaction between gas and dust components is suggested by the comparison of VLT/VISIR and VLA images of the more compact nebulae. The analysis of the mid-IR spectra has provided information on the gas and dust composition, allowing identification of the mineral composition of LBV ejecta and to discriminate between crystalline or amorphous dust components. Moreover, the presence of low-excitation atomic fine structure lines points out the existence of a photodissociation region (PDR), an extra component of neutral/molecular gas that should be taken into account when one determines the total budget of mass lost by the star during its LBV phase. We present examples of our results in the following sections. More details can be found in a series of papers devoted to the project.

Figure 2: Center: multi-configuration 6-cm VLA map (red) superimposed on the 11.26-μm VISIR map (blue) of IRAS 18576+0341. Both maps have north up and east to the left. The center image is $20''$ across. A zoomed (FOV $8''$) of the VLA map (left) and of the VISIR map (right) are also shown (adapted from Buemi et al. 2010).

3.1 IRAS 18576+034

This is the object which shows the most extreme difference between the ionized gas component (traced by free-free emission) and the dust component (Fig. 2). High spatial resolution and high sensitivity images of IRAS 18576+0341 were obtained using the mid infrared imager VISIR at the Very Large Telescope and the Very Large Array interferometer (see Buemi et al. 2010 for details) The approximately circularly-symmetric, mid-IR nebula strongly contrasts with the asymmetry that characterizes the ionized component of the envelope, as seen in the radio and [Ne II] line images. Among possible scenarios for the cause of the observed asymmetry in the ionized gas morphology are an unseen external ionizing source (either a companion or shocked gas) or holes in the dusty material. However, at the moment, it is not possible to discriminate amongst them.

The detailed mid-IR maps allowed us to determine the size of the dusty nebula (D_{dust}=7$''$), the dust temperature distribution, and the total dust mass. From the total dust mass (Buemi et al. 2010), assuming a gas to dust ratio of 100, a total nebular mass of $\sim 0.5 M_{\odot}$ is derived. LBVNs are believed to form from strong, eruptive episodes (Smith & Owocki 2006) even if the origin from more or less steady outflows cannot be ruled out (Nota et al. 1995; Voors et al. 2000). From the observed size of the dusty nebula, in the hypothesis that this material is expanding at constant velocity ($70\,\mathrm{km\,s^{-1}}$, Clark

et al. 2009), we derive a dynamical age of $\sim$ 3500 yrs and a mass-loss rate, averaged over the nebula formation, of $\sim 1 \times 10^{-4} M_{\odot}\mathrm{yr}^{-1}$. Moreover, the dust distribution in the nebula is consistent with a strong mass-loss episode that occurred $\sim$ 2000 years ago (Buemi et al. 2010), indicating the mass-loss is not constant, with different quantity of mass released during episodes of different duration. This result is corroborated by the current-day mass loss rate of $3.7 \times 10^{-5} M_{\odot}\mathrm{yr}^{-1}$ from the central object as measured in the radio (Umana et al. 2005), which is smaller than the average value necessary to fill up the circumstellar nebula.

3.2 HR Car

HR Car is surrounded by a faint, low-excitation nebula which is difficult to observe because of the high luminosity of the central object. One of the most striking properties of the nebula is the complete disagreement between the large scale optical structure, showing a SE-NW bipolar morphology (Weis et al. 1997) and the inner, strongly asymmetric, radio nebula (see White 2000). Our spectroscopic Spitzer/IRS observations of the inner nebula reveal a rich mid-IR spectrum showing both solid state and atomic gas signatures (Umana et al. 2009). The characteristic broad feature at 10μm indicates the presence of amorphous silicates, suggesting that dust formation occurred during the LBV outburst. This is in contrast to the detection of crystalline dust in other Galactic LBVs that are probably more evolved. The crystalline dust is similar to the dust observed in red supergiants that has been considered to be evidence of dust production during evolutionary phases prior to the outburst (Waters et al. 1998). Strong low-excitation atomic fine structure lines such as 26.0μm [Fe II] and 34.8μm [Si II] indicate, for the first time, the presence of a PDR around this object class. While the physics and chemistry of the low-excitation gas appears to be dominated by photodissociation, a possible contribution due to shocks can be inferred from the evidence of gas phase Fe abundance enhancement.

3.3 HD 168625

Our mid-IR spectroscopic observations (IRS) of this LBV candidate detected spectral features attributable to polycyclic aromatic hydrocarbons (PAHs), indicating the presence of a PDR around the ionized nebula. This result enlarges the number of LBV and LBV candidates where the presence of a PDR has been confirmed, implying the importance of such a component in the budget of total mass lost by the central object during this elusive phase of massive star evolution.

We have analyzed and compared the mid-IR and radio maps, and derive several results concerning the associated nebula (Umana et al. 2010). While the overall torus-like shape of the dust morphology is confirmed, the higher resolution and sensitivity of our images allow us to discern finer details of the dust distribution, most notably the highly structured texture of the nebula, and provide a better localization of the dust ring, with its north-west and south-east condensations (Fig. 3). There is also evidence for grain distribution variations across the nebula, with a predominant contribution from larger grains in the northern part of the nebula while PAH and smaller grains are more segregated in the southern part.

Besides via optical emission, the ionized part of the nebula can be traced by radio observations, without suffering of intrinsic extinction. We have obtained a 3.6-cm VLA map by using the interferometer in two configurations to determine the structure down to sub-arcsec scale without resolving out the more extended emission (Fig 4). The overall ionized nebula is reminiscent of the dust distribution, with one main difference: the brightest radio emission is located where there is a lack of thermal dust grains, corroborating the hypothesis of the presence of a shock in the southern portion of the nebula as consequence of the interaction of a fast outflow with the slower, expanding dusty nebula. Such a shock would be a viable means for PAH production as well as for changes in the

grain size distribution. Finally, from the detection of a central radio component, very probably associated with the wind from the central massive supergiant, we derive a current mass-loss rate of $\dot{M} = (1.46 \pm 0.15) \times 10^{-6} M_{\odot} \mathrm{yr}^{-1}$.

3.4 Future prospects

The study of the LBV phenomenon has been hampered by the lack of a significant sample of objects with associated nebulae. The presence of an extended, dusty circumstellar nebula can be identified by its IR/mid-IR fingerprints. Therefore, we can search among proposed candidates by assessing the presence of observational characteristics that define an LBV. A good possibility is offered by the more than 400 bubbles identified at 24μm by Mizuno et al. (2010) in the Galactic Plane survey conducted with MIPS on the Spitzer Space telescope (MIPSGAL). These small ($\leq 1'$) rings, bubbles, disks or shells are pervasive through the entire Galactic plane in the mid-infrared. Whatever the nature of these 24μm sources, the implications of such a large number in the Galactic plane is remarkable and they provide a powerful "game reserve" for evolved massive stars as already pointed out by Wachter et al (2011).

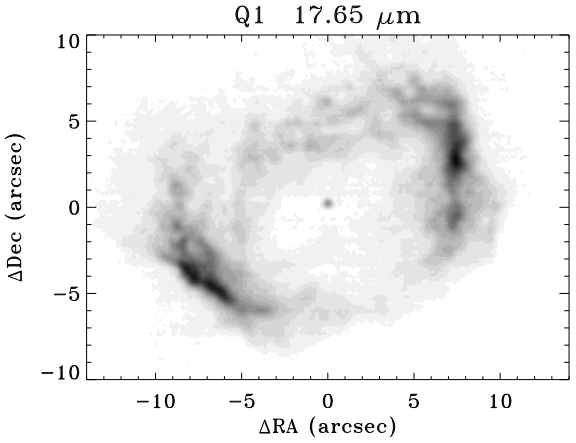

Figure 3: VISIR map of HD 168625 in the Q1 continuum filter. The brightness levels range from 0 to 8.06 Jy arcsec^{-2}.

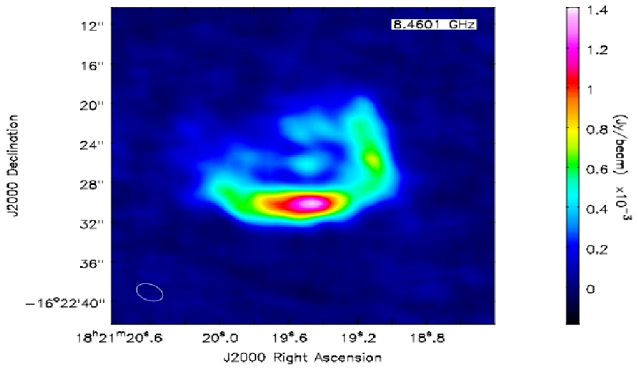

Figure 4: The multi-configuration 3.6-cm VLA map of HD 168625. The point-like central source, whose coordinates coincide with those of the central object, is probably related to the current-day stellar wind of the LBV.

Acknowledgements

This research is supported in part by ASI contract I/038/08/0 "HI-GAL" and by PRIN-INAF 2007.

References

Buemi, C. S., Umana, G.., Trigilio, C., Leto, P., Hora, J. L., 2010, ApJ, 721, 1404
Clark, J. S., Crowther, P. A., Larionov, V. M., Steele, I. A., Ritchie, B. W., Arkharov, A. A. 2009, A&A 507, 1555
Clark, J. S., Larionov, V. M., Arkharov, A., 2005, A&A, 435, 239
Meynet, G., Maeder, 2005, A&A, 581, 598
Mizuno, D. R., Kraemer, K. E., Flagey, et al. 2010, AJ 139, 1542
Nota A., Livio M., Clampin M., Schulte-Ladbeck R., 1995, ApJ, 448, 788
Smith N., Owocki S. P., 2006, ApJ, 645, L45

Umana, G.., Buemi, C. S., Trigilio, C., Leto, P., 2005, A&A , 437, L1
Umana, G.., Buemi, C. S., Trigilio, C., Hora, J. L., Fazio, G. G., Leto, P. 2009, ApJ, 694, 697
Umana, G.., Buemi, C. S., Trigilio, C., Leto, P., Hora, J. L., 2010, ApJ, 718, 1036
Voors R. H. M. et al. 2000, A&A, 356, 501
Weis, K., Duschl,W.J., Bomans, D.J., Chu, Y.H., Joner, M.D. 1997, A&A, 320, 568
Wachter, S., Mauerhan, J., Van Dyk, S., Hoard, D.W., & Morris, P. 2011, in Proceedings of the 39th Liège Astrophysical Colloquium, eds. G. Rauw, M. De Becker, Y. Nazé, J.-M. Vreux & P.M. Williams, BSRSL 80, 291
Waters, L. B. F. M., Morris, P. W., Voors, R. H. M., Lamers H. J. G. L. M., & Trams, N.R. 1998, AP&SS, 255, 179
White, S. M., 2000, ApJ, 539, 851

Discussion

F.J. Perez: Did you study the change in the structure of the dust grains, especially in the regions with a higher density?
G. Umana: Not yet. But we are going to do a more detailed modeling.

L. Oskinova: I would like to point out a paper by Barniske et al. (2008, A&A 486,971). The Spitzer IRS spectrum was modeled using the DUSTY code. The continuum of the IRS spectrum can be well modeled assuming a specific cut-off for the size of the grains.

The nature of the massive stellar transient in DDO 68

Dominik J. Bomans[1], and Kerstin Weis[1]

[1] Astronomical Institute, Ruhr-University Bochum, Germany

Abstract: When measuring the metallicity of several H II regions in the very low metallicity dwarf galaxy DDO 68, Pustilnik et al. (2008) noted a spectral change of one H II region within 2 years. The lines in the residual spectrum and the brightening of the continuum lead them to interprete this transient event to be due to a variable massive star. Using archival and new imaging and spectroscopy of DDO 68, we present a study of the variability of the transient. Using the derived photometric variability and the properties of its spectrum, we noted that the transient appears to the very similar to V1 in NGC 2366, an exceptional LBV-like object. Together with results on massive variable stars in other nearby, low metallicity galaxies, this indicate interesting twists for the evolution of massive stars at metallicities below that of the Magellanic Clouds. Based on our compilation of nearby, very metal-poor galaxies, there are several objects suitable for observational studies of massive stars at very low metallicities with the current ground and space based instrumentation. This opens the window to derive observationally parameters of stars and their feedback on the interstellar medium critical for analyzing the galaxies at high redshift up to the time of reionization.

1 Why is very low metallicity exciting?

It is long known from theory of stellar evolution and stellar atmospheres that there are significant changes when going to stars at low metallicity. These effects are already apparent in the Magellanic Clouds, which provide nice laboratories for massive stars at 0.4 and 0.2 of solar metallicity. Still, there is a significant gap between the metallicities of the Magellanic Clouds and the metallicities observed at high redshifts, despite a significant spread of metallicities observed in DLA and Lyman break galaxies. This is especially true for the epoch of galaxy formation to the end of reionization ($z > 6$) (Schaerer & de Barros 2010). Observational studies of massive stars at metallicities significantly below 1/10 of solar are therefore important for our understanding not only of galaxy formation but also stellar feedback at high redshift. Massive stars and subsequent supernovae provide the energy input driving galactic outflows and winds (Leitherer, Robert, & Drissen 1992), which are critical ingredients of galaxy formation and evolution. At very low metallicity, stellar evolution, stellar atmospheres, and the instabilities in stars should be very different. This effects stellar winds, late evolutionary phases, variability, (evolution of) rotation, convection, SN types, binary star evolution, and progenitors of long GRBs.

2 Nearby very low metallicity galaxies

To get a better handle on the stellar population and their time dependent energy input to their host galaxies in the early universe, observations of the best possible local proxies are mandatory. Unfor-

tunately, such extreme metal-poor galaxies (metallicities of less than ∼1/10 of solar) are quite rare objects (e.g., Kunth & Östlin 1999). The prototype for such galaxies is I Zw 18. Not surprisingly, it was repeatably observed with HST, but it turned out to be quite difficult to study due to high crowding, high and variable background and faintness of its stars. I Zw 18 has now a securely determined distance of 18 Mpc (Aloisi et al. 2007; Fiorentini et al. 2010), which places it beyond the reach for ground-based studies of its stars. The analysis of the HST data material showed that I Zw 18 does contain five periodic variables, 3 of them inside the Cepheid instability strip (2 of the Cepheids have periods $>$ 100 days), and 34 candidate/non-periodic variables (Fiorentino et al. 2010). Since the Meynet & Maeder (2005) rotation models imply an extension of the mass range of stars with LBV-like instabilities downward (e.g., Weis 2011), the location of the brightest and bluest of these candidate variables in I Zw 18 is consistent with the CMD location of rapidly rotating LBV-like stars. Additionally, 5 to 9 Wolf-Rayet stars appear to be present in I Zw 18 (de Mello et al. 1998).

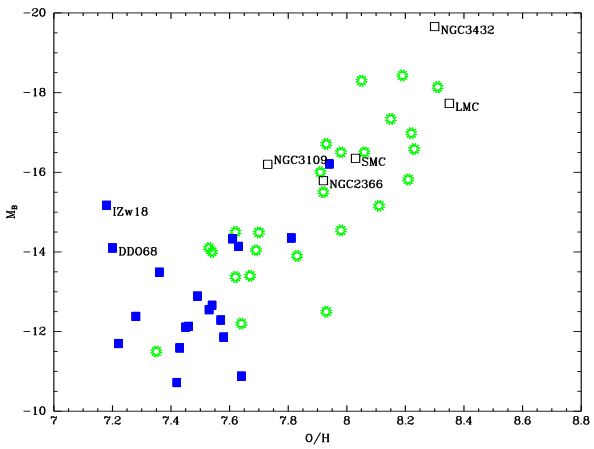

Figure 1: Metallicity-luminosity relation of the sample of local dwarf galaxies compiled by Lee et al. (2006) (green open sun symbols), several comparison galaxies (black open squares) and the nearby low metallicity star forming galaxies compiled by us (blue filled squares). It is potentially important to note that I Zw 18 and DDO 68 are both very luminous for their metallicity, which may imply that we catch them right in a significant burst of star formation, which leads to a temporary elevation of their B-band luminosity.

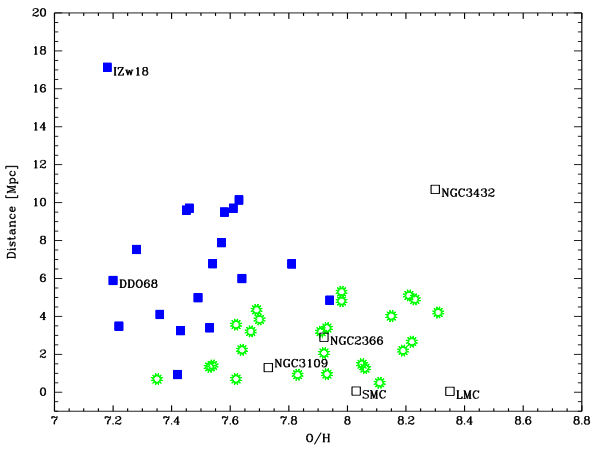

Figure 2: Metallicity-distance diagram of the same galaxy samples as plotted in Fig.1 and with the same symbols. It is clear that with its new, large distance, I Zw 18 is not the most ideal laboratory to perform observational studies of very low metallicity massive stars. Depending on the targets (e.g. extremely massive stars, Cepheids, red hyper- and supergiants, ...) there are several much closer objects. With its current high star formation rate, DDO 68 is definitely a prime target for the study of extremely massive stars at low metallicity.

Clearly, for detailed studies of massive stars at these metallicities, more targets at lower distances are important. The basic problem to reach this aim is that such low metallicities are found locally only in low mass galaxies (e.g., Lee et al. 2006). Therefore a significant recent star formation rate in these galaxies is needed to ensure useful sample sizes of (very) massive and therefore short lived stars. The short evolutionary time scales therefore imply that not every low metallicity dwarf galaxy will provide examples of all short lived, transitional phases. The recent star formation history enters as a critical parameter.

3 Very low metallicity galaxies in the local volume

Which are the galaxies with significant recent star formation at low metallicity and how many do exist in the Local Volume? As Local Volume we define here the sphere with 11 Mpc radius of the Milky Way. It is roughly the maximal volume in which massive single stars are accessible for detailed spectral analysis with 10 m class ground-based telescopes, e.g., Bresolin et al. (2001). A 10 or 11 Mpc definition of the "Local Volume" is also used for several survey projects recently, e.g. 11HUGS (Kennicutt et al. 2008) or LVHIS (Koribalski 2008). The problem for the study of single stars out to these distances is not only the faintness of the targets but also the spatial resolution. Dense groups and clusters of massive stars become unresolved, or just barely resolved, producing a significant light contamination to targets in or near them. In the case of luminous transients, like LBV outbursts, these problems are significantly reduced, as the star outshines its environment. In such a case the Local Volume may be even a conservative limit, see for example the LBV transient in NGC 3432 at a distance of 10.7 Mpc (Pastorello et al. 2010). In the case of very bright transients, time enters the problem. Due to their transient nature, they will unpredictively be bright enough for study. The other problem is that studying only these transient introduces a classical Malmquist bias to a lot of the analyses. We started to compile a data base of very low metallicity local galaxies, the current state of it is plotted in Fig.1 and 2. While I Zw 18 is clearly not the best target anymore, it is doable with the HST, and several more potentially useful targets within 8 Mpc are apparent.

4 Luminous transients at low metallicity

DDO 68 is an extremely low metallicity galaxy with an abundance of $\sim$1/40 solar. When taking a spectrum of a H II knot in 2008, Pustilnik et al. (2008) noted that it is significantly different from a spectrum taken 3 years earlier. The difference spectrum clearly showed P Cygni profiles in the Balmer lines and a blue continuum. The authors suggested that their finding is the brightening of an LBV, an interpretation later supported by Izotov & Thuan (2009).

Still, one should still be skeptical, since slight misalignment between the slit position of the observations in such a relatively distant (D $\sim$ 8 Mpc) and a complex background may lead to spurious results. To check the presence of a variable source, we compiled a ground-based light curve of the object using own and archival imaging data. The result is plotted in Fig.3. Clearly, the knot is variable by more than 1 mag over the last 50 years. If the measurement from 1988 defines the quiescent state of the most luminous star in the knot, than the star showed brightening by > 2 mag since then. For the interpretation one has to keep in mind that these measurements are integrated values for the unresolved (or barely resolved) ionizing cluster of an H II region. The age of the cluster should be below 3×10^6 yr to provide enough Lyman continuum photons. Our preliminary STARBURST99 (Leitherer et al. 1999) simulations even imply $\sim 1 \times 10^6$ yr (Bomans & Weis 2011).

All these pieces of evidence seem to be consistent with a very massive, highly variable star, dominating the luminosity and color of the cluster in its bright phases. Before jumping to the interpretation of an LBV, there are a few odd aspects: the brightening appears to be at constant or bluer color, which excludes a classical S Dor variability (e.g., van Genderen 2001). The wind terminal velocity estimated from the 2008 difference spectrum is $\sim$800 km s^{-1}, which looks more more like a wind than mass ejection event (a giant eruption).

In this context, it is interesting to look at NGC 2366, a strongly star forming (Lee et al. 2009) dwarf irregular galaxy at a distance of $\sim$ 3 Mpc and a metallicity of $\sim$ 1/10 solar. The massive stars are clearly driving material out into the halo of this galaxy (Martin 1998; van Eymeren et al. 2009), making it a good laboratory for stellar feedback studies. In NGC 2366, Drissen et al. (2001) noted the sudden appearance of a stellar source inside its brightest giant HII region. They found an increase

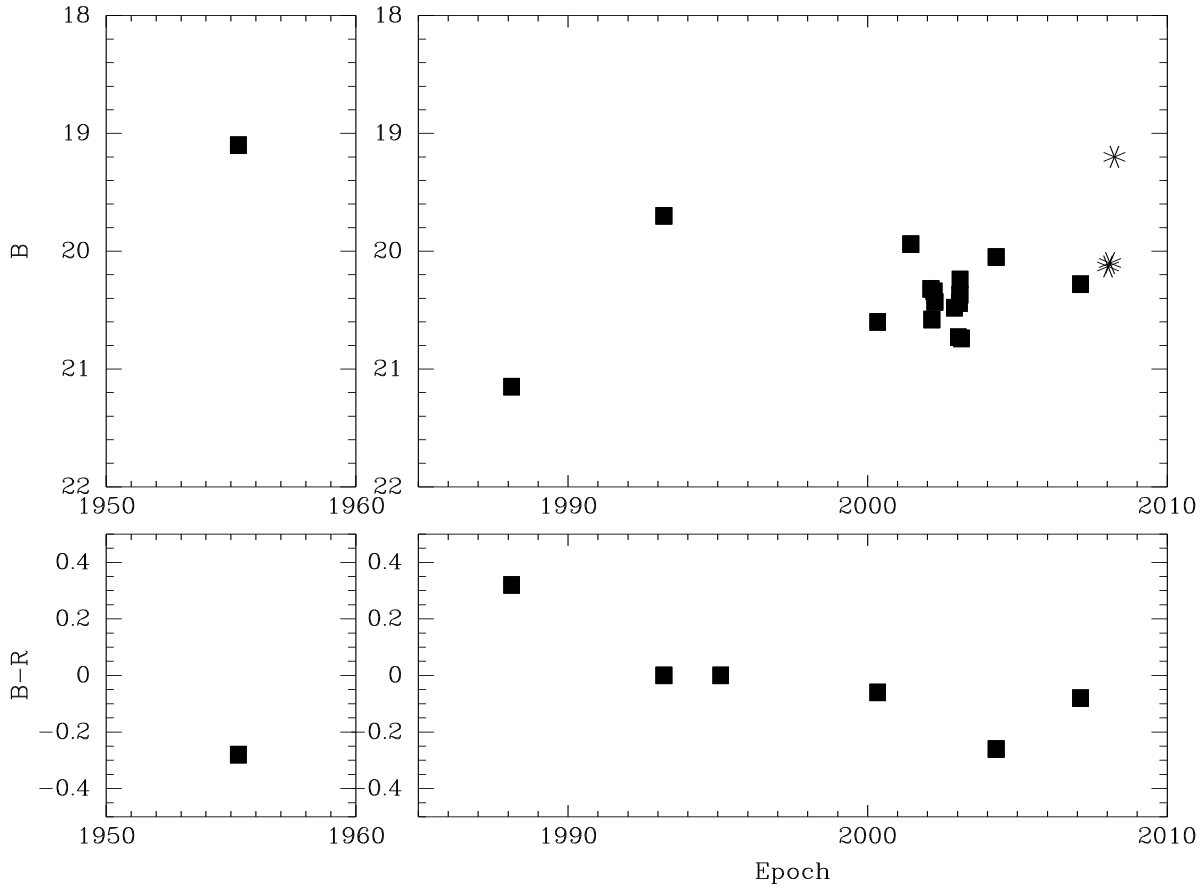

Figure 3: Lightcurve of the cluster plus transient source in DDO 68. Black squares are archival and our photometric data (mostly from CCD), asterisks denote spectroscopic fluxes converted to B band magnitudes. Clearly, there is a very luminous, variable star in the cluster.

by 3.1 mag to V ~ -10.2 mag and a rise in brightness while getting hotter (bluer colors). The spectra changed with time (Petit et al. 2006) and the early spectra are similar to the one of the DDO 68 transient. Again the spectra are more like wind instead of sudden mass ejection (giant eruption) with a wind terminal velocity $\sim 250\,\mathrm{km\,s^{-1}}$.

There appear to be similarities between the DDO 68 transient and NGC 2366 V1. One is tempted to speculate that we see a LBV-like variability, but somewhat different from classical S Dor cycle. Within that cycle the star should encounter the bistability jump, which is function of metallicity. This might lead to a less pronounced change in the star's spectrum (and the S Dor variability) and may yield a different spectroscopic behavior for LBVs like DDO 68 transient and NGC 2366 V1 (see e.g., Weis 2011).

5 Conclusions

So, what can be learned from the data collected up to now?

On the observational side, even if I Zw 18 is more of an HST (and in the future a (challenging) adaptive optics) target, there are several galaxies in the Local Volume with metallicities close to or only slightly higher than the one of I Zw 18, which enable us to observationally study the properties and evolution of massive very low metallicity stars.

Of these galaxies, DDO 68 is of special interest, not only because its metallicity is indeed very low, but also because it appears to contain a very luminous transient star. The information collected up to now appear to imply that it is similar in may aspects to V1 in NGC 2366, which was interpreted a a strange LBV-like star. NGC 2366 is a nearby, quite metal-poor starbursting dwarf galaxy itself (see e.g. Fig.2). The similarity between the transient source in DDO 68 and V1 in NGC 2366 may imply that the instabilities leading to LBV-like variability and/or eruptions work somewhat differently at low metallicity, or that different processes/instabilities are at work at these low metallicities.

The observational results on the transient in DDO 68, together with HST results on I Zw 18 (e.g. Fiorentino et al. 2010), and first results on massive variable stars in other low metallicity dwarfs (e.g. Hoessel, Saha, & Danielson 1998; Herrero et al. 2010; Bomans & Weis 2011) point at interesting differences of properties and evolution of these stars compared to stars in the Large and Small Magellanic Clouds, our "normal" template galaxies for low metallicity stars.

One can conclude, that there is a direct observational access to many parameters of interest for the stars and their feedback onto the interstellar medium and high redshift, maybe up into the age of the reionization.

References

Aloisi A., Clementini, G., Tosi, M., et al. 2007, ApJ, 667, L151

Bomans, D.J., & Weis, K. 2011, in: C. Neiner, G. Wade, G. Meynet & G. Peters, eds., IAU Symp. 272, Active OB stars: structure, evolution, mass loss, and critical limits, in press

Bresolin, F., Kudritzki, R.-P., Mendez, R. H., & Przybilla, N. 2001, ApJ, 548, L159

Drissen, L., Crowther, P. A., Smith, L. J., Robert, C., Roy, J.-R., & Hillier, D. J. 2001, ApJ, 546, 484

van Eymeren, J., Marcelin, M., Koribalski, B., Dettmar, R.-J., Bomans, D. J., Gach, J.-L., & Balard, P. 2009, A&A, 493, 511

Fiorentino G., Contreras Ramos, R., Clementini, et al. 2010, ApJ, 711, 808

van Genderen, A. M. 2001, A&A, 366, 508

Herrero, A., Garcia, M., Uytterhoeven, K., Najarro, F., Lennon, D. J., Vink, J. S., & Castro, N. 2010, A&A, 513, A70

Hoessel, J. G., Saha, A., & Danielson, G. E. 1998, AJ, 116, 1679

Izotov Y. I., Thuan T. X. 2009, ApJ, 690, 1797

Kennicutt, R. C., Jr., Lee, J. C., Funes, S. J., José G., Sakai, S., & Akiyama, S. 2008, ApJS, 178, 247

Koribalski, B. S. 2008, in: Galaxies in the Local Volume, eds. H. Jerjen and B.S. Koribalski, Springer Astrophysics and Space Science Proceedings, 41

Kunth, D., & Östlin, G. 2000, A&A Reviews, 10, 1

Lee, H., Skillman, E. D., Cannon, J. M., Jackson, D. C., Gehrz, R. D., Polomski, E. F., & Woodward, C. E. 2006, ApJ, 647, 970

Lee, J. C., Kennicutt, R. C., José G. Funes, S. J., Sakai, S., & Akiyama, S. 2009, ApJ, 692, 1305

Leitherer, C., Robert, C., & Drissen, L. 1992, ApJ, 401, 596

Leitherer, C., Schaerer, D., Goldader, J. D. et al. 1999, ApJS, 123, 3

Martin, C. L. 1998, ApJ, 506, 222

Meynet, G. & Maeder, A. 2005, A&A, 429, 581

de Mello, D. F., Schaerer, D., Heldmann, J., & Leitherer, C. 1998, ApJ, 507, 199

Pastorello, A., Botticella, M. T., Trundle, C., et al. 2010, MNRAS, 408, 181

Petit, V., Drissen, L., & Crowther, P. A. 2006, AJ, 132, 1756

Pustilnik, S. A., Tepliakova, A. L., Kniazev, A. Y., & Burenkov, A. N. 2008, MNRAS, 388, L24

Schaerer, D., & de Barros, S. 2010, A&A, 515, A73

Weis, K. 2011, in Proceedings of the 39th Liège Astrophysical Colloquium, eds. G. Rauw, M. De Becker, Y. Nazé, J.-M. Vreux & P. Williams, BSRSL, 80, 440

The Infrared Properties of Massive Stars in the Magellanic Clouds

A.Z. Bonanos[1] , D.J. Lennon, D.L. Massa, M. Sewilo, F. Koehlinger, N. Panagia, J.Th. van Loon, C.J. Evans, L.J. Smith, M. Meixner, K. Gordon and the SAGE teams

[1] National Observatory of Athens, IAA
I. Metaxa & Vas. Pavlou Street, Palaia Penteli GR-15236, Greece
Email: bonanos@astro.noa.gr

Abstract: We present highlights of our study of the infrared properties of massive stars in the Large and Small Magellanic Clouds (from Bonanos et al. 2009, 2010), which are based on the Spitzer SAGE surveys of these galaxies. We have compiled catalogs of spectroscopically confirmed massive stars in each galaxy, as well as photometric catalogs for a subset of these stars that have infrared counterparts in the SAGE database, with uniform photometry from 0.3 to 24 μm in the UBVIJHKs+IRAC+MIPS24 bands. These catalogs enable a comparative study of infrared excesses of OB stars, classical Be stars, yellow and red supergiants, Wolf-Rayet stars, Luminous Blue Variables and supergiant B[e] stars, as a function of metallicity, and provide the first roadmaps for interpreting luminous, massive, resolved stellar populations in nearby galaxies at infrared wavelengths.

1 Introduction

The *Spitzer Space Telescope* Legacy Surveys SAGE ("Surveying the Agents of a Galaxy's Evolution", (Meixner et al. 2006) and SAGE-SMC (Gordon et al. 2010) have for the first time made possible a comparative study of the infrared properties of massive stars at a range of metallicities, by imaging both the Large and Small Magellanic Clouds (LMC and SMC). In Bonanos et al. (2009, Paper I) and Bonanos et al. (2010, Paper II), we presented infrared properties of massive stars in the LMC and SMC, which we summarize below. The motivation was threefold: (a) to use the infrared excesses of massive stars to probe their winds, circumstellar gas and dust, (b) to provide a template for studies of other, more distant, galaxies, and (c) to investigate the dependence of the infrared properties on metallicity. Papers I and II were the first major compilations of accurate spectral types and multi-band photometry from 0.3$-$24 μm for massive stars in any galaxy, increasing by an order of magnitude the number of massive stars for which mid-infrared photometry was available.

Infrared excess in hot massive stars is primarily due to free-free emission from their ionized, line driven, stellar winds. Panagia & Felli (1975) and Wright & Barlow (1975) first computed the free-free emission from ionized envelopes of hot massive stars, as a function of the mass-loss rate ($\dot{M}$) and the terminal velocity of the wind (v_∞). The properties of massive stars, and in particular their stellar winds (which affect their evolution) are expected to depend on metallicity (Z). For example, Mokiem et al. (2007) found empirically that mass-loss rates scale as $\dot{M} \sim Z^{0.83\pm0.16}$, in good agreement with theoretical predictions (Vink et al. 2001). The expectation, therefore, is that the infrared excesses of

OB stars in the SMC should be lower than in the LMC, given that $\dot{M}$ is lower in the SMC. Furthermore, there is strong evidence that the fraction of classical Be stars among B-type stars is higher at lower metallicity (Martayan et al. 2007b). Grebel et al. (1992) were the first to find evidence for this, by showing that the cluster NGC 330 in the SMC has the largest fraction of Be stars of any known cluster in the Galaxy, LMC or SMC. More recent spectroscopic surveys (Martayan et al. 2010) have reinforced this result. We were also interested in quantifying the global dependence of the Be star fraction on metallicity. The incidence of Be/X-ray binaries is also much higher in the SMC than in the LMC (Liu et al. 2005), while the incidence of Wolf-Rayet (WR) stars is much lower; therefore, a comparison of infrared excesses for these objects was also of interest.

2 Spectral type and Photometric Catalogs

We compiled catalogs of massive stars with known spectral types in both the LMC and SMC from the literature. We then cross-matched the stars in the SAGE and SAGE-SMC databases, after incorporating optical and near-infrared photometry from recent surveys of the Magellanic Clouds. The resulting photometric catalogs were used to study the infrared properties of the stars. The LMC spectral type catalog contains 1750 massive stars. A subset of 1268 of these are included in the photometric catalog, for which uniform photometry from $0.3 - 24$ μm in the $UBVIJHK_s$+IRAC+MIPS24 bands is presented in Paper I. The SMC spectral type catalog contains 5324 massive stars; 3654 of these are included in the photometric catalog, for which uniform photometry from $0.3 - 24$ μm is presented in Paper II. All catalogs are available electronically.

3 Infrared properties of Massive Stars

Below we summarize some of our results on the following classes of massive stars:

3.1 O/Oe and early-B/Be stars

We clearly detect infrared excesses from free-free emission despite not having dereddened the stars, both in the LMC and SMC. In Figure 1, we plot J_{IRSF} vs. $J_{IRSF} - [3.6]$, $J_{IRSF} - [5.8]$ and $J_{IRSF} - [8.0]$ colors[1] for the 1967 early-B stars from our SMC catalog, respectively, denoting their luminosity classes, binarity and emission line classification properties by different symbols. We compare the observed colors with colors of plane-parallel non-LTE TLUSTY stellar atmosphere models (Lanz & Hubeny 2003, 2007) of appropriate metallicity and effective temperatures. For reference, reddening vectors and TLUSTY models reddened by $E(B-V) = 0.2$ mag are also shown. At longer wavelengths, the excess is larger because the flux due to free–free emission for optically thin winds remains essentially constant with wavelength. Fewer stars are detected at longer wavelengths because of the decreasing sensitivity of *Spitzer* and the overall decline of their spectral energy distributions (SEDs). We find that the majority of early-B supergiants in the SMC exhibit lower infrared excesses, when compared to their counterparts in the LMC (cf. Figure 10 in Bonanos et al. 2009), due to their lower mass-loss rates, although certain exceptions exist and deserve further study.

The color magnitude diagrams (CMDs) allow us to study the frequency of Oe and Be stars, given the low foreground and internal reddening for the Magellanic Clouds. Our SMC catalog contains 4 Oe stars among 208 O stars, of which one is bluer than the rest. There are 16 additional stars with $J_{IRSF} - [3.6] > 0.5$ mag and $J_{IRSF} < 15$ mag (including all luminosity classes), whose spectra appear normal (although the Hα spectral region in most cases was not observed). We refer to these

[1]Square brackets refer to *Spitzer* IRAC bands; IRSF to the survey of Kato et al. (2007).

as "photometric Oe" stars and attribute their infrared excesses to free-free emission from a short-lived, possibly recurrent circumstellar region, whose Hα emission line was not detected during the spectroscopic observations either because the gas had dispersed or because the region was optically thick to Hα radiation or the observation spectral range just did not extend to Hα. Given the expectation of lower $\dot{M}$ at SMC metallicity, we argue that such a region is more likely to be a transient disk rather than a wind. Assuming these are all Oe stars, we find a $10 \pm 2\%$ fraction of Oe stars among the O stars in the SMC. The error in the fraction is dominated by small number statistics. In contrast, there are 4 Oe and 14 "photometric Oe" stars (with $J_{IRSF} - [3.6] > 0.5$ mag and $J_{IRSF} < 14.5$ mag) out of 354 O stars in the LMC (despite the higher $\dot{M}$ at LMC metallicity), which yields a $5 \pm 1\%$ fraction of Oe stars among O stars in the LMC.

Turning to the early-B stars, the most striking feature in Figure 1 is a distinct sequence displaced by ~ 0.8 mag to the red. A large fraction of the stars falling on this redder sequence have Be star classifications, although not all Be stars reside there. Given that the circumstellar gas disks responsible for the emission in Be stars are known to completely vanish and reappear between spectra taken even 1 year apart (see review by Porter & Rivinius 2003, and references therein), the double sequence reported here provides further evidence for the transient nature of the Be phenomenon. A bimodal distribution at the $L-$band was previously suggested by the study of Dougherty et al. (1994), which included a sample of 144 Galactic Be stars. Our larger Be sample, which is essentially unaffected by reddening, and the inclusion of all early-B stars, clearly confirms the bimodal distribution. It is due to the much larger number of Be stars classified in the SMC, in comparison to the LMC, as well as the higher fraction of Be stars among early-B stars in the SMC, which is $19 \pm 1\%$ vs. $4 \pm 1\%$ in the LMC (see Bonanos et al. 2010) when considering only the spectroscopically confirmed Be stars (cf. $\sim 17\%$ for < 10 Myr B0–5 stars; Wisniewski et al. 2006). Excluding the targeted sample of Martayan et al. (2007a, 2007b) does not significantly bias the statistics, since the fraction only decreases to $15 \pm 1\%$. We caution that incompleteness in our catalogs could also affect the determined fractions, if our sample turns out not to be representative of the whole population of OB stars.

We proceed to define "photometric Be" stars as early-B type stars with an intrinsic color $J_{IRSF} - [3.6] > 0.5$ mag, given that a circumstellar disk or envelope is required to explain such large excesses. Including these "photometric Be" stars and using the same color and magnitude cuts as for the "photometric Oe" stars above, yields fractions of Be stars among early-B stars of $27 \pm 2\%$ for the SMC and $16 \pm 2\%$ for the LMC (cf. 32% from young SMC clusters; Wisniewski et al. 2006). We compare our results with the fractions determined by Maeder et al. (1999) from young clusters, i.e. 39% for the SMC and 23% for the LMC, finding ours to be lower, although the sample selections were very different.

These preliminary statistics (available for the first time for Oe stars) indicate that both Oe and Be stars are twice as common in the SMC than in the LMC. We emphasize the importance of including the "photometric Be" stars, which significantly increase the frequencies of Oe/O and Be/early-B stars determined and are crucial when comparing such stars in different galaxies. This novel method of confirming Oe and Be star candidates from their infrared colors or a combination of their optical and infrared colors, as recently suggested by Ita et al. (2010) is complementary to the detailed spectroscopic analyses by e.g. Negueruela et al. (2004) on individual Oe stars to understand their nature, although it is limited to galaxies with low internal reddening. We finally note that the spectral types of Oe stars in the SMC (O7.5Ve, O7Ve, O4-7Ve and O9-B0III-Ve) and the LMC (O9Ve (Fe II), O7:Ve, O8-9IIIne, O3e) are earlier than those of known Galactic Oe stars, which are all found in the O9-B0 range (Negueruela et al. 2004). Finally, we note that the brightest Be stars in the SMC ($J_{IRSF} \sim 13.2$ mag) are brighter than the brightest Be stars in the LMC ($J_{IRSF} \sim 13.4$ mag), i.e. there is a 0.7 mag difference in absolute magnitude, given the 0.5 mag difference in the distance moduli.

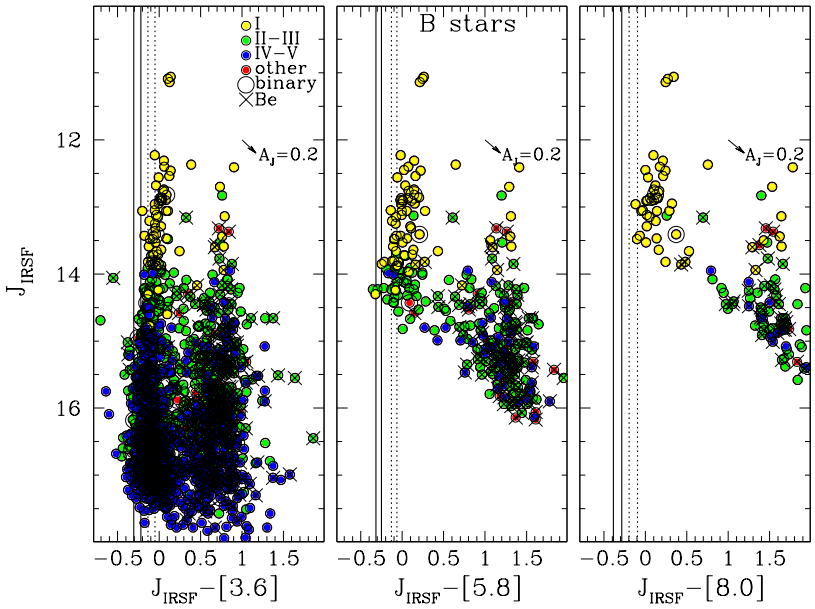

Figure 1: Infrared excesses (J_{IRSF} vs. $J_{IRSF} - [3.6]$, $J_{IRSF} - [5.8]$ and $J_{IRSF} - [8.0]$) for 1967 early-B stars in the SMC (from Bonanos et al. 2010). Supergiants are shown in yellow, giants in green, main-sequence stars in blue, stars with uncertain classifications ("other") in red, binaries with a large circle and Oe stars with an $\times$. The solid lines correspond to 30kK and 50kK TLUSTY models with $\log g = 4.0$. A reddening vector for $E(B-V) = 0.2$ mag is shown, as well as reddened TLUSTY models by this same amount (dotted lines). The more luminous stars exhibit larger infrared excesses, which increase with λ.

3.1.1 Supergiant B[e] stars

The sgB[e] stars are the most conspicuous group of stars in all infrared CMDs and two color diagrams: they are among the brightest and most reddened stars in both the LMC and SMC (Buchanan et al. 2006). In the LMC, 12 stars have been classified as sgB[e] stars (including LH 85–10, although it is not among the 11 stars listed in Zickgraf 2006). The 11 that were included in our catalog (S 22, S 134, R 126, R 66, R 82, S 12, LH 85-10, S 35, S 59, S 137, S 93) were all matched in the SAGE database. The SEDs of all the sgB[e] stars (except LH 85-10, which seems to be misclassified) are all very similar, with slowly decreasing flux in the optical, an inflexion point in the near-infrared and a "bump" starting at 2 μm and peaking near 5 μm. This peak corresponds to hot dust at $\sim$600 K. The slight change in the slopes of the SEDs between 8 and 24 μm from star to star suggests different contributions from cool dust (150 K).

In the SMC photometric catalog, we have detected 7 luminous sources with colors typical of sgB[e] stars, i.e. $M_{3.6} < -8$, $[3.6] - [4.5] > 0.7$, $J - [3.6] > 2$ mag. Five of these are previously known sgB[e] stars (with R50; B2-3[e] being the brightest in all IRAC and MIPS bands), while R4 (AzV 16) is classified as an LBV with a sgB[e] spectral type. In addition to these, we find that 2dFS1804 (AFA3kF0/B[e]) has a very similar SED (and therefore infrared colors) to the known sgB[e] 2dFS2837 (AFA5kF0/B[e]). Evans et al. (2004) also remarked on the similarity of their spectra. We therefore confirm the supergiant nature of 2dFS1804. The similarity of the SEDs of these sgB[e] stars, despite the various optical spectral classifications, implies that all are the same class of object. The cooler, composite spectral types indicate a lower mass and perhaps a transitional stage to or from the sgB[e] phenomenon. The only difference we find between the sgB[e] stars in the SMC vs. the LMC is that on average they are $\sim$1-2 mag fainter (in absolute terms).

3.1.2 Luminous Blue Variables

There are 6 confirmed LBVs (see review by Humphreys & Davidson 1994) in the LMC: S Dor, BAT99-83 or R127, R 71, R 110, BAT99-45, and R 85. The LBVs are not only among the most luminous sources at 3.6 μm, with [3.6]–[4.5] colors similar to AGB stars and intermediate between RSG and sgB[e] stars, but also at 8.0 μm and 24 μm. All 3 known LBVs in the SMC: R4 (AzV 16, B0[e]LBV), R40 (AzV 415, A2Ia: LBV) and HD 5980 (WN6h;LBV binary), were detected at infrared wavelengths. We find their SEDs to differ, given their very different spectral types. Moreover, we find evidence for variability, which can be confirmed from existing light curves in the All Sky Automated Survey (ASAS, Pojmanski 2002), as pointed out by Szczygiel et al. (2010), who studied the variability of the massive stars presented in Paper I in the LMC. The various SED shapes and spectral types observed depend on the time since the last outburst event and the amount of dust formed.

Acknowledgements

A.Z.B. acknowledges support from the Riccardo Giacconi Fellowship award of the Space Telescope Science Institute and from the European Commission Framework Program Seven under a Marie Curie International Reintegration Grant.

References

Bonanos, A. Z., Massa, D. L., Sewilo, M., et al. 2009, *AJ*, 138 , 1003
Bonanos, A. Z., Lennon, D.J., Koehlinger, F. et al. 2010, *AJ*, 140, 416
Buchanan, C. L., Kastner, J. H., Forrest, W. J., et al. 2006, *AJ*, 132, 1890
Dougherty, S. M., Waters, L. B. F. M., Burki, G., et al. 1994, *A&A*, 290, 609
Evans, C. J., Lennon, D. J., Trundle, C., et al. 2004, *ApJ*, 607, 451
Foellmi, C., Koenigsberger, G., Georgiev, L., et al. 2008, *RevMexAA*, 44, 3
Gordon, K. D., Meixner, M., Blum, R., et al. 2010, *AJ*, in preparation
Grebel, E. K., Richtler, T., & de Boer, K. S. 1992, *A&A*, 254, L5
Humphreys, R. M. & Davidson, K. 1994, *PASP*, 106, 1025
Ita, Y., Matsuura, M., Ishihara, D., et al. 2010, *A&A*, 514, 2
Kato, D., Nagashima, C., Nagayama, T., et al. 2007, *PASJ*, 59, 615
Lanz, T. & Hubeny, I. 2003, *ApJS*, 146, 417
Lanz, T. & Hubeny, I. 2007, *ApJS*, 169, 83
Liu, Q. Z., van Paradijs, J., & van den Heuvel, E. P. J. 2005, *A&A*, 442, 1135
Maeder, A., Grebel, E. K., & Mermilliod, J. 1999, *A&A*, 346, 459
Martayan, C., Floquet, M., Hubert, A. M., et al. 2007a, *A&A*, 472, 577
Martayan, C., Frémat, Y., Hubert, A., et al. 2007b, *A&A*, 462, 683
Martayan, C., Baade, D., & Fabregat, J. 2010, *A&A*, 509, A11
Meixner, M., Gordon, K. D., Indebetouw, R., et al. 2006, *AJ*, 132, 2268
Mokiem, M. R., de Koter, A., Vink, J. S., et al. 2007, *A&A*, 473, 603
Negueruela, I., Steele, I. A., & Bernabeu, G. 2004, *Astronomische Nachrichten*, 325, 749
Panagia, N. & Felli, M. 1975, *A&A*, 39, 1
Pojmanski, G. 2002, *Acta Astronomica*, 52, 397
Porter, J. M. & Rivinius, T. 2003, *PASP*, 115, 1153
Szczygiel, D. M., Stanek, K. Z., Bonanos, A. Z., et al. 2010, *AJ*, 140, 14
Vink, J. S., de Koter, A., & Lamers, H. J. G. L. M. 2001, *A&A*, 369, 574
Wisniewski, J. P. & Bjorkman, K. S. 2006, *ApJ*, 652, 458
Wright, A. E. & Barlow, M. J. 1975, *MNRAS*, 170, 41
Zickgraf, F.-J. 2006, in ASP Conference Series, Vol. 355, Stars with the B[e] Phenomenon, ed. M. Kraus & A. S. Miroshnichenko, 135

Photometric monitoring of Luminous Blue Variables

Carla Buemi[1], Elisa Distefano[1,2], Paolo Leto[1], Francesco Schillirò[3], Corrado Trigilio[1], Grazia Umana[1], Stefano Bernabei[4], Giuseppe Cutispoto[1], and Sergio Messina[1]

[1] INAF-Osservatorio Astrofisico di Catania, Catania Italy
[2]Dipartimento di Fisica e Astronomia, Universitá di Catania, Catania Italy
[3] INAF- Istituto di Radioastronomia, Noto, Italy
[4] Osservatorio astronomico, Bologna,Italy

Abstract: We present some preliminary results from our program of intensive near-infrared photometric monitoring of a sample of confirmed and candidate Luminous Blue Variables (LBVs) conducted from 2008 to 2010. Clear long-term variability has been observed for Wray 17-96 and V481 Sct, with overall brightness variation greater than 1 mag in the J band. Other sources, such as LBV 1806-20 showed detectable variability with amplitudes of few tenths of a magnitude with a time-scale of about 60 days.

1 Introduction

The class of Luminous Blue Variables (LBVs) consists of luminous and massive stars, that are believed to go through a short but violent transition phase of evolution from the main sequence towards the Wolf-Rayet stage (Humphreys & Davidson, 1994, Langer et al., 1994). LBVs are well known to show a combination of spectral and photometric variability (S-Doradus type variability and/or η-Car type eruptions), whose origin is not yet well understood, despite the crucial role that such objects play in the stellar evolution of massive stars (van Genderen 2001, Kotak & Vink 2006). A detailed analysis of the time scales of variability of LBV stars can provide useful insights in the understanding of the evolution of such objects and in the knowledge of the physical mechanisms that trigger the great giant eruption. Some objects, like η Car, P Cyg and AG Car, have been extensively monitored, but often fragmentary observations exist for others. We are thus conducting a long term multiwavelength photometric monitoring of a sample of confirmed and candidate LBVs. We present the most interesting results of the first two years of observations, performed by using the REMIR infrared imaging camera available at the REM (Rapid Eye Mount) telescope.

2 Observations and results

Here, we present observations taken with the 60 cm robotic Rapid Eye Mount (REM) telescope, located at the European Southern Observatory (ESO) (La Silla, Chile). Data were acquired in the V, R, I, J, H and K bands since April 2008 up to now with a time sampling of one measure per week, as part of a multiwavelength (optical and infrared) monitoring campaign of 25 LBVs and cLBVs, listed

Table 1: List of targets. The J magnitude are from the 2MASS catalog.

Name	α(2000)	δ(2000)	J mag	Name	α(2000)	δ(2000)	J mag
PV Vel	09:15:54.8	−49:58:24.6	*4.44*	V4375 Sgr	17:48:14.0	−28:00:53.1	*4.82*
HR Car	10:22:53.8	−59:37:28.4	4.56	LBV 1806−20	18:08:40.3	−20:24:41.1	13.66
GSC08958	10:53:59.6	−60:26:44.3	7.32	V4029 Sgr	18:21:14.9	−16:22:31.8	4.60
AG Car	10:56:11.6	−60:27:12.8	5.42	V4030 Sgr	18:21:19.5	−16:22:26.1	*5.14*
V432 Car	11:08:40.1	−60:42:51.7	7.96	V481 Sct	18:33:55.3	−06:58:38.7	8.36
Sher 25	11:15:07.8	−61:15:17.6	8.60	GAL025	18:37:05.2	−06:29:38.0	*15.80*
W243	16:47:07.5	−45:52:29.2	6.41	V452 Sct	18:39:26.1	−13:50:47.1	7.86
ζ Sco	16:53:59.7	−42:21:43.3	3.59	GAL026	18:39:32.2	−05:44:20.5	8.00
V1104 Sco	17:06:53.9	−42:36:39.7	6.71	V1672 Aql	19:00:10.9	+03:45:47.1	12.16
Wray17−96	17:41:35.4	−30:06:38.8	6.71	V1429 Aql	19:21:34.0	+14:52:56.9	6.09
V905 Sco	17:41:59.0	−33:30:13.7	3.55	W 51	19:23:42.3	+14:30:33.0	*14.32*
V4650 Sgr	17:46:18.0	−28:49:03.5	12.31	V1302 Aql	19 26 48.3	+11 21 16.7	5.47
WR102ka	17:46:18.1	−29:01:36.6	12.98				

in Table 1, dedicated to investigate their photometric variability. As the monitoring program is still ongoing, we present just the most interesting, although partial, results from the infrared light curves. Since our goal was to investigate variability of these objects, we carried out differential photometry of the candidates with respect to non-variable comparison stars in each target field, using the ensemble photometry technique (Gilliland & Brown 1988, Everett & Howell 2001) implemented in the software *ARCO* (Automatic Reduction of CCD Observation, developed by Distefano et al. 2007). This software allows to select the stars for the ensemble among those in common to all frames, iteratively rejecting stars that were found to have either a systematic variation in the instrumental magnitude or large errors. The NIR magnitudes were calibrated against magnitude in the 2MASS catalog.

The accuracy and time resolution of the monitoring allow us to detect even small amplitude variability. Photometric errors, as derived following the standard method described by Everett & Howell (2001), are about 0.01 mag on most of the individual measurements; thus the photometric data quality is good enough to distinguish photometric variations at close to 0.05 mag level.

Flux curves and observed color variations are presented for the clearest cases of both long and/or short term detected variability.

2.1 V481 Sct

Strong variation in amplitude has been observed in the light curves of this source (Fig. 1). The IR variability is large (ΔJ$\approx$1.0) and the rise seems to be faster between the first two runs, although the gap in the coverage does not allow us to follow the entire trend. The star further brightens up to a total magnitude variation of ΔJ$\approx$1.2 on a time scale of about two years. V481 Sct experienced a similar photometric variation between 2003-2004, as reported by Clark et al. (2005), suggesting a sort of cyclic photometric behavior. Smaller (ΔJ$\approx$0.3) and shorter (time scale of about 60 days) flux variations seems to be superimposed to the long term brightening. The infrared colors do not show a systematic trend but exhibit a quite irregular change, making it hard to derive the mechanism of the variability on the basis of the near-IR photometry alone. We note that the mean J-K and J-H seem to decrease during the first stellar brightening, suggesting a stellar blueing. However, the trend changes during the third run, suggesting that more than one process is acting.

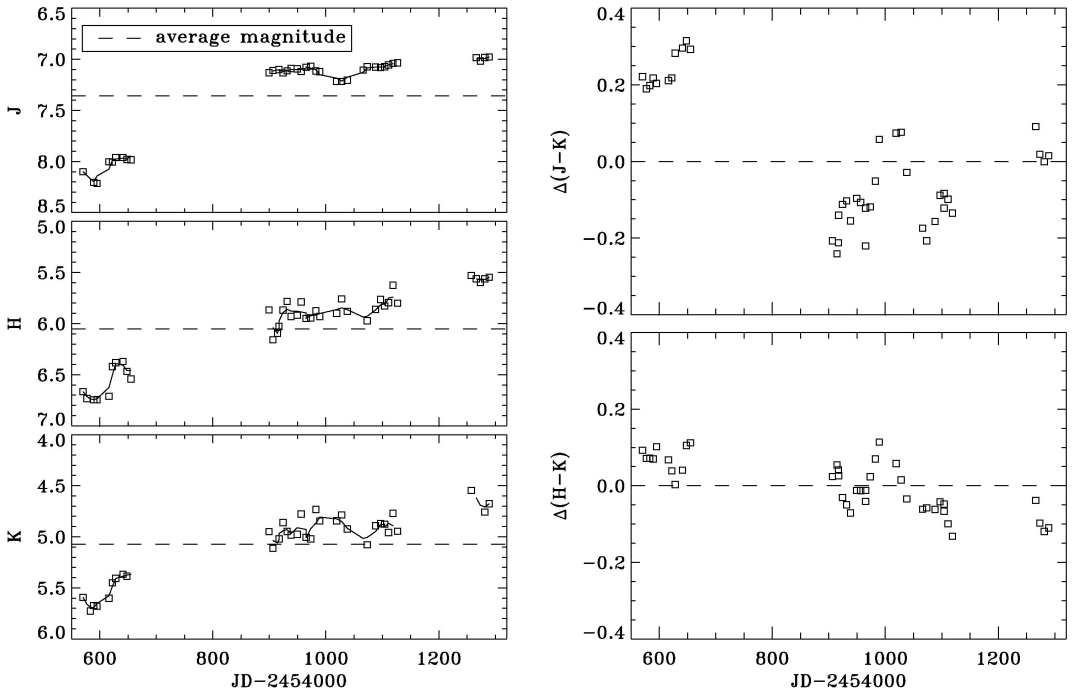

Figure 1: Light and color curves for V481 Sct. The solid lines represent the smoothed brightness.

2.2 Wray 17-96

As for V481 Sct, the brightness of Wray 17-96 varies significantly over the entire interval of our observations (Fig. 2). The total variation amplitudes tend to decrease with wavelength, spanning from 1 mag in the K band, to 1.45 mag in the J band, but clear small amplitude (ΔK$\approx$0.5) variability can be observed also on shorter time scales of about 60 days. As shown in the Figure 3, the infrared color became bluer as the flux rises, from the beginning to the end of our observations, indicating an increase of the stellar temperature. On the contrary, the short time variability is characterized by redder colors when the star becomes brighter. This behavior can be explained in terms of increasing mass loss or/and increased contribution from hot dust.

2.3 LBV 1806-20

As shown in Fig. 3, the observed light curves of this source show a long term rising trend, with total brightness variations having an amplitude of about 0.4 mag in all the bands from the beginning to the end of the observations. Short term variations with amplitude no larger than 0.2-0.25 mag are observed too. During the long term variation, the colors remain practically constant, with a weak blueing associated to the maxima of the short term flux oscillations, suggesting that both stellar temperature and radial changes could be present.

3 Summary

We are monitoring a group of LBV and cLBV to characterize the photometric variability changes as a star goes through these final stages of evolution. The aim of this monitoring program is to collect an as complete and homogenous as possible photometric dataset which helps to accurately estimate the

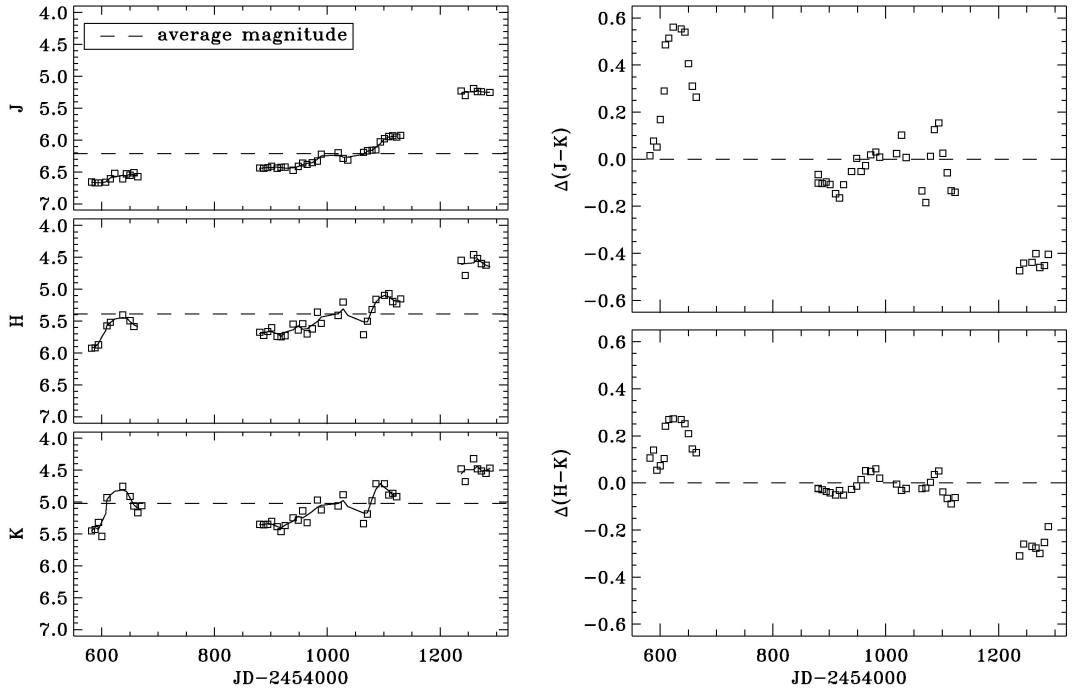

Figure 2: Light and color curves for Wray 17-96. The solid lines represent the smoothed brightness.

parameters of the photometric variability, as needed for a complete understanding of the properties of stars in this unstable regime.

We observed two time scales of variation in our dataset: long term light variation covering the entire interval of our observations (about 2 years) and a small amplitude (Δmag$\approx$0.2), short time ($\approx$60 days) oscillations. We found that about 40% of the sources in our sample are characterized by one or both such kinds of variations. Such preliminary results, support the need of a regular and homogeneous monitoring of such objects. A long term homogeneous monitoring of the objects in our sample could help to better define the distribution of the light curve parameters and to set limits on possible mechanisms generating such photometric behavior.

The complete results of our ongoing studies will be published in Buemi et al. (2011, in preparation), where the observed light curves from the entire sample will be discussed.

Acknowledgements

Based on observations made with the REM Telescope, INAF Chile. We wish to thank the REM team for technical support, and in particular Dino Fugazza, for their help in setting-up the observations. We acknowledge partial financial support from PRIN-INAF 2007 and the ASI contract I/038/08/0 “HI-GAL.

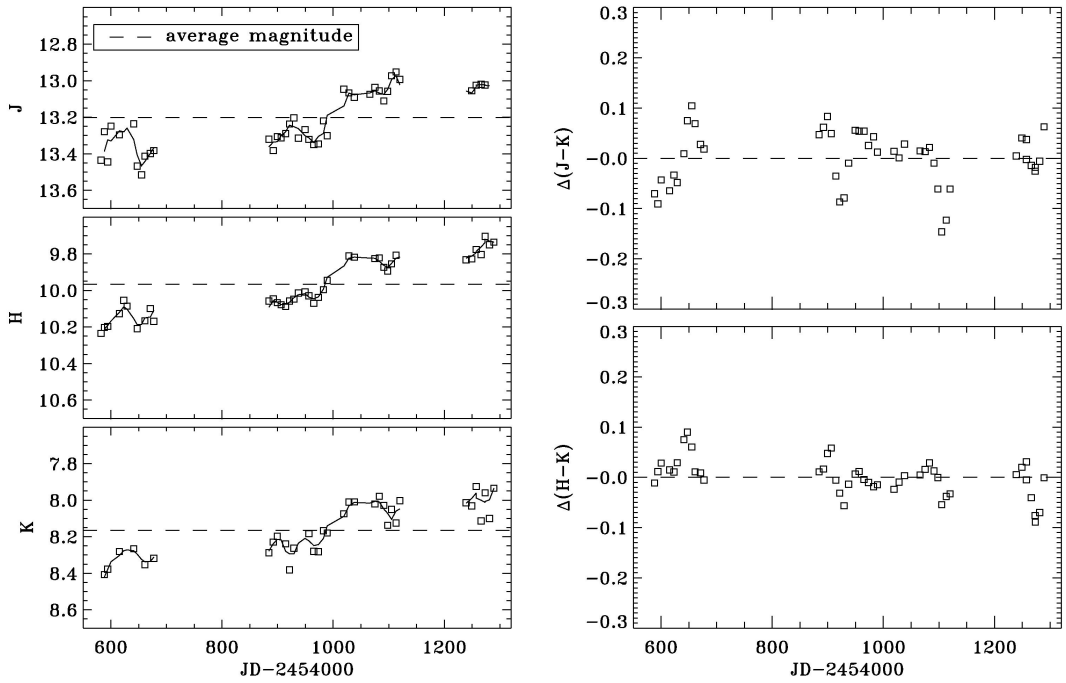

Figure 3: Light and color curves for LBV 1806-20. The solid lines represent the smoothed brightness.

References

Clark J.S., Larionov V. M., & Arkharov A. 2005, A&A, 435, 239.
Distefano E., Messina S., Cutispoto G., et al. 2007, EAS Publication Series, 25, 165
Everett, M. E., Howell, S. B. 2001, PASP, 113,1428.
Gilliland, R. L., Brown, T. M. 1988, PASP, 100, 754.
Humphreys R., Davidson K. 1994, PASP, 106, 1025.
Kotak, R., & Vink, J.S. 2006, A&A, 460, L5
Langer, N., Hamann, W.R., Lennon, M., Najarro, F., Pauldrach, A.W.A., Puls, J. 1994, A&A, 290, 819.
van Genderen, A.M 2001, A&A, 366, 508.

Var C: (Semi-)Periodic Long-Term Variability*†

B. Burggraf[1], K. Weis[1], D. J. Bomans[1], and M. Henze[2]

[1] Astronomisches Institut der Ruhr-Universität Bochum, Bochum, Germany
[2] Max-Planck-Institut für extraterrestrische Physik, Garching, Germany

Abstract: Luminous Blue Variables (LBVs) are characterised by irregular photometric and spectral variabilities. So far the underlying mechanism for these variations is not known. It is neither known under which circumstances massive stars become LBVs, nor what triggers the instabilities causing the variabilities, and if all massive stars in a certain mass range evolve into LBVs or not.

To find out more about the nature of the variabilities of LBVs, we investigated the long-term photometric and spectroscopic behaviour. One aspect of our analysis was the check for periodicity in the variations. Periodicity on smaller timescales in the order of approximately a few years is already known to occur in LBVs (van Genderen 2001). Detecting possible periodicity on larger scales (in the order of decades) was always difficult since most of the light curves do not reach back far enough and/or are much to fragmentary.

Combining historical and new data, we produced a light curve of significant length to perform a systematic search for long-term periodicity. We assume to have found long-term (semi-)periodicity of approximately 40 years being present in Var C. Seeing more than two full cycles gave us the possibility to make a prediction for the next maximum (2027$\pm$2).

1 Introduction

The LBV phase is a short (it only takes time in the order of 10^4 years) phase in the lifetime of evolved massive stars. LBVs belong to the most luminous (10^6 $L_\odot$) stars in the Universe.

As the name already indicates, LBVs are characterised by irregular photometric and spectral variabilities. These variations occur on quite different time scales, which range from months up to years or even decades, and with different amplitudes, ranging from some tenth of magnitudes up to $>$2 mag (Humphreys & Davidson 1994). Different kinds of variabilities can also be superimposed. The photometric variability intrinsic to LBVs, the so called S Dor variability, occurs on time scales of about 10-40 years and with amplitudes of 1-2 mag and can be subdivided into long ($>$20 years, L-SD) and short ($<$10 years, S-SD) S Dor variability (van Genderen 2001).

The photometric S Dor variabilities are caused by spectral variations. During phases of minimum visual light in this S Dor cycle LBVs show spectra of hot supergiants with H, He, Fe II and [Fe II] lines in emission, which often also show P-Cygni profiles. During a photometric maximum the spectrum

*Based on observations collected at the Centro Astronómico Hispano Alemán (CAHA) at Calar Alto, operated jointly by the Max-Planck Institut für Astronomie and the Instituto de Astrofísica de Andalucía (CSIC).

†Based on observations collected at the Thüringer Landessternwarte (TLS) Tautenburg.

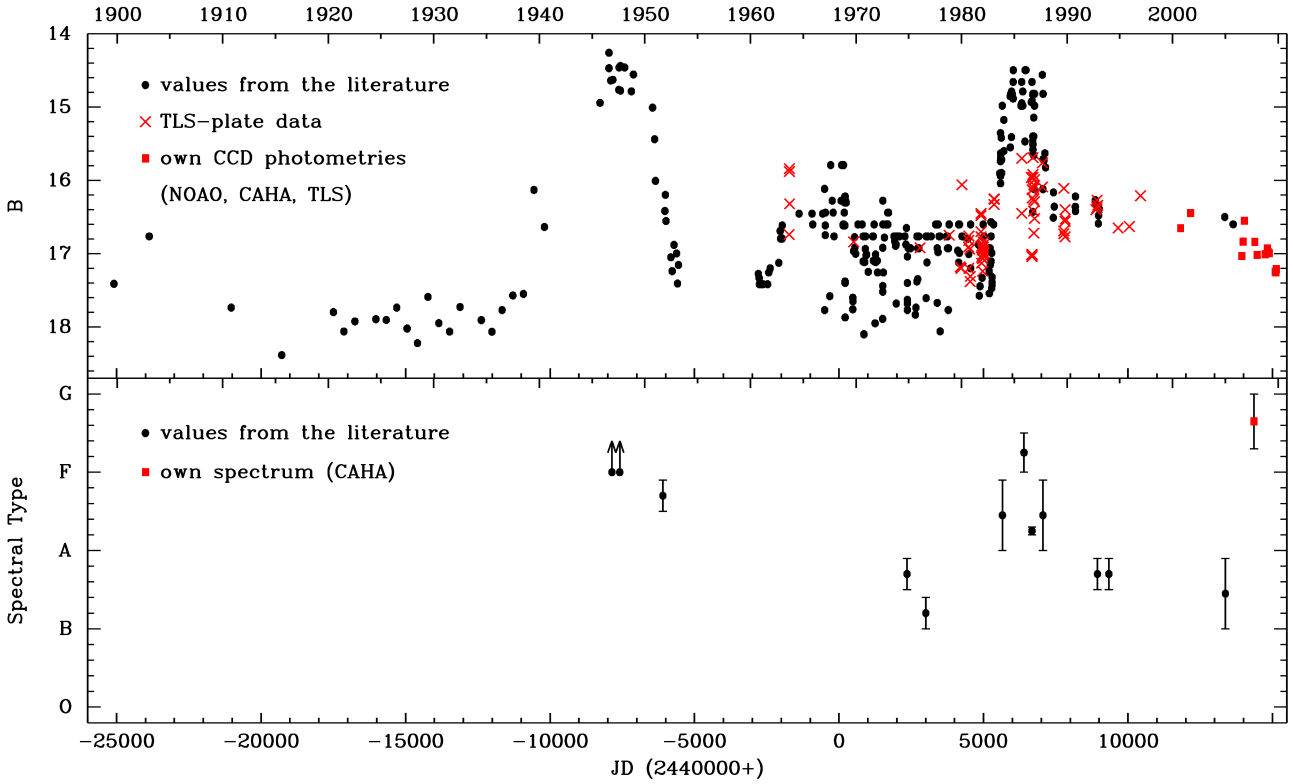

Figure 1: B Light curve (upper panel) and corresponding spectral type (lower panel) of Var C. Data points from our analyses are marked in red (red crosses: TLS-plate data, red squares: CCD photometries). Data points from the literature are marked with black dots (details will be presented in an upcoming paper).

turns into that of an A–F type star (Humphreys & Davidson 1994). These spectral changes lead to the star being brighter in the optical while it is cooler.

So far, the underlying mechanism that causes these variations is not known. It is still unclear under which circumstances massive stars become LBVs, what triggers the instabilities, and whether all massive stars in a certain mass range evolve into LBVs or not.

Var C (α=1:33:35.14, δ=30:36:00.55) is located about 5′ south-west of the centre of M33 (see Fig. 3). It was first noticed to be variable by Hubble & Sandage (1953). Var C is one of the classical LBVs in M33.

2 Data

To investigate the long-term photometric behaviour and to check for periodicity in the variations of Var C (Fig. 3), we generated a light curve of significant length. Therefore, we observed at the Centro Astronómico Hispano Alemán (CAHA) at Calar Alto (three data points) and at the Thüringer Landessternwarte (TLS) Tautenburg (ten data points). Additionally, we retrieved analyses on archival data from the National Optical Astronomy Observatory (NOAO) Local Group Survey (LGS) (Massey et al. 2001; two data points). For data from NOAO and TLS we carried out photometric analyses using IRAF/DAOPHOT. For CAHA data photometry, the analysis was performed using DOLPHOT (Dolphin 2000). Supplemental photometry was derived from several scanned archival photographic plates taken at the TLS between 1963 and 1996 (77 data points).

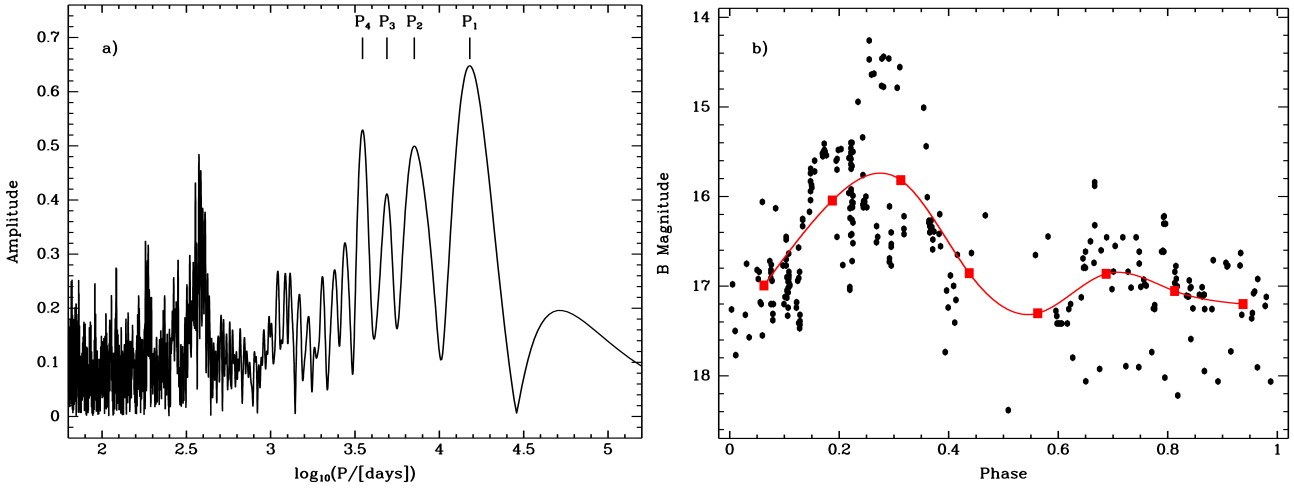

Figure 2: (a) Power spectrum derived for the B values given in Fig. 1. (b) Phase diagram corresponding to a frequency of $\nu_1 = 6.589 \cdot 10^{-5}$ 1/d ($P_1 = 15176$ d $= 41.5$ years). The data have been binned into eight bins (red squares) and a cubic interpolation of these binned values is given (red line).

In addition, we obtained a spectrum using the 2.2m-telescope at CAHA in order to further pinpoint the present evolutionary stage of Var C. Data reduction was carried out using IRAF.

To complete our own measurements, photometric and spectral data from the literature were gathered (all together 286 data points). Where necessary, we converted photographic and photoelectric data values into Johnson B magnitudes. For this purpose, we used the conversion given by Macri, Sasselov, & Stanek (2001), who derived a transformation between a photographic magnitude scale and CCD B magnitude in the standard system using comparison stars.

3 Periodicity of Var C

Periodicity on small timescales of the order of approximately one year is already known to occur in LBVs like e.g. AG Car (van Genderen 2001). Periodicity in the order of decades was only found to be a beat cycle as the result of these smaller periods. Detecting possible periodicity on lager scales (in the order of decades) was always difficult since most of the light curves do not reach back far enough and/or are much too fragmentary.

We combined historical and new data to produce a light curve (Fig. 1) of a significant length for Var C to analyse the long-term variability by carrying out a systematic search for long-term periodicities. Therefore, we performed Fourier transformation analysis (Fig. 2(a)) on our data set of B magnitudes by using the Period04 software (Lenz & Breger 2005). No weights were applied to the data but two data sets from the literature (100 data points) were excluded due to magnitude uncertainties equal to or larger than 0.5 mag.

In order to check whether the long-term variability occurred as a result of a beat cycle caused by variabilities on smaller timescales, a search for such smaller variabilities was performed on a homogeneous subsample of the data with an appropriate high data coverage.

Figure 1 shows the B Light curve between 1899 and 2009 (upper panel) and if measured the corresponding spectral type (lower panel) of Var C. Aside from two prominent maxima (around 1946 and 1986) and variations on smaller time scales, a secular trend of Var C getting brighter is seen in the light curve. Such a long-term trend of brightening was also found to be present in e.g. η Car (Humphreys, Davidson & Smith 1999).

Comparing the light curve with the changes of the spectral types shows that during maximum

light the star resembles an A or F type star. During phases of minimum light an O or B type star is seen. Such a behaviour is well in agreement with the S Dor cycle. Of special interest is the latest development of Var C. Even though the B light curve does not show an increase in luminosity, the spectrum in September 2007 of Var C resembles that of a quite cool star. Here the photometric and spectral behaviours of Var C seem not to follow the typical S Dor properties. However, recently gained additional data indicate irregular variations on smaller scales (in the order of months). Detailed analyses will be presented in an upcoming paper.

Figure 2(a) shows the power spectrum derived for the B magnitudes given in Fig. 1. The highest peak (at $\log(P_1) = 4.181$) corresponds to a period of $P_1 = 15176\,\mathrm{d} = 41.5\,\mathrm{years}$ ($\nu_1 = 6.589 \cdot 10^{-5}\,1/\mathrm{d}$). The peak around $\log(P) \approx 2.6$ corresponds to a period of approximately one year and is most probably due to the data sampling. The very broad and low amplitude peak around $\log(P) \approx 4.7$ reflects the secular trend of an overall increase of the luminosity. At least three more distinct peaks are present (at $\log(P_2) = 3.851$, $\log(P_3) = 3.689$, and $\log(P_4) = 3.545$ corresponding to periods $P_2 = 19.4\,\mathrm{years}$, $P_3 = 13.4\,\mathrm{years}$, and $P_4 = 9.6\,\mathrm{years}$).

The phase diagram corresponding to a frequency of $\nu_1 = 6.589 \cdot 10^{-5}\,1/\mathrm{d}$ ($P_1 = 15176\,\mathrm{d} \approx 41.5\,\mathrm{years}$ is displayed in Fig. 2(b). The data have been binned into eight bins (red squares) and a cubic interpolation of these binned values is given (red line). At least one pronounced maximum is seen, a second, smaller maximum at roughly half of the period might be assumed, but data scatter due to irregular variations on smaller time scales is large and renders it quite uncertain.

Together with an amplitude of approximately 1.5-2.5 mag for the major peak this puts Var C in the category of a strong-active S Dor member with a long S Dor cycle according to the subdivision as defined by van Genderen (2001).

With the last major maximum of Var C being around 1986 and a presumable period of $P \approx 41.5\,\mathrm{years}$, we predict the next bright maximum phase of Var C to occur around 2027 ± 2.

4 Conclusions

Combining historical and new data we produced a light curve of a significant length for Var C to analyse the long-term variability by carrying out a systematic search for long-term periodicity using a Fourier transformation analysis.

We assume a long-term (semi-)periodicity of 41.5 years being present in Var C. Seeing more than two full cycles gave us the possibility to make a prediction for the next maximum which should occur around 2027 ± 2. Var C is the first LBV to show a periodicity in the order of decades without periodicities on smaller time scales. This indicates that the long-term periodicity has to be a result of a different underlying mechanism, which is not yet understood.

Recent unexpected changes in Var C's spectrum (from a B to an F-G type star) make it necessary to further trace both the photometric and spectral behaviour of this LBV in order to fully understand Var C's evolutionary stage.

Acknowledgements

We thank Artie P. Hatzes, Helmut Meusinger, and Bringfried Stecklum from the Thüringer Landessternwarte (TLS) Tautenburg for service observations with the 2m-Alfred-Jensch-telescope. Thanks to Otmar Stahl for helpful comments on the classification of our spectrum of Var C. B. Burggraf is thankful for support by a stipend from the "Wilhelm and Günter Esser foundation".

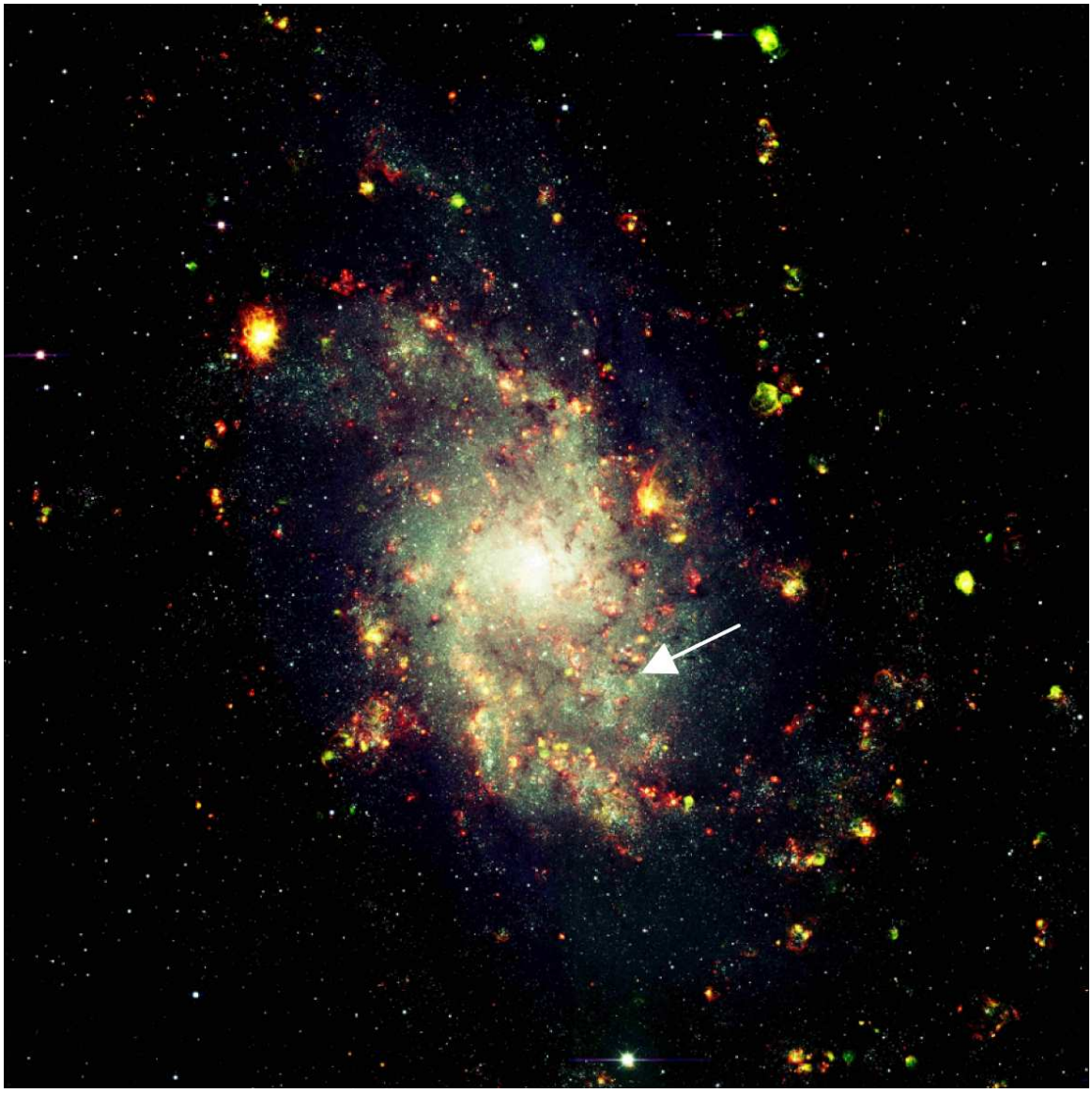

Figure 3: RGB (H_α, [O III], V) colour image of M33 produced by us using NOAO LGS data (Massey et al. 2001). North is up and east to the left. The image has a size of $\approx 36' \times 36'$. The position of Var C is marked with an arrow.

References

Dolphin, A. E. 2000, PASP, 112, 1383-1396
Hubble, E. & Sandage A. 1953, ApJ, 118, 353
Humphreys, R. M. & Davidson, K. 1994, PASP, 106, 1025-1051
Humphreys, R. M., Davidson, K. & Smith N. 1999, PASP, 111, 1124-1131
Lenz, P. & Breger, M. 2005, Communications in Asteroseismology, 146, 53-136
Macri, L. M., Sasselov, D. D. & Stanek K. Z. 2001, ApJL, 550, L159-L162
Massey, P., Hodge, P. W., Holmes, S., Jacoby, G., King, N. L., Olsen, K., Saha, A. & Smith C. 2001, Bulletin of the American Astronomical Society, 33, 1496
van Genderen, A. M. 2001, A&A, 366, 508-531

Investigating the properties of Galactic Luminous Blue Variables via IR observations

J. S. Clark[1], A. Arkharov[2], V. Larionov[3], B. Ritchie[1], P. Crowther[4], F. Najarro[5]

[1] Dept. Physics & Astronomy, The Open University, Milton Keynes, UK
[2] Pulkovo Astronomical Observatory, St Petersburg, Russia
[3] Astronomical Institute of St. Petersburg University, St Petersburg, Russia
[4] Dept. Physics & Astronomy, University of Sheffield, Sheffield, UK
[5] Dept. de Astrofísica, CAB, INTA-CSIC, Torrejón de Ardoz, Spain

Abstract: Recent IR surveys of the Galactic plane have revealed a large number of candidate Luminous Blue Variables. In order to verify these classifications we have been undertaking a long term spectroscopic and photometric monitoring campaign supplemented with tailored non-LTE model atmosphere analysis. Here we present a brief overview of selected aspects of this program, highlighting the prospects for identification, classification and quantitative analysis of LBVs in the near-IR spectral window.

1 Introduction

Luminous Blue Variables (LBVs) are massive post-Main Sequence stars that are experiencing a highly unstable phase of evolution that is characterised by dramatic photometric and spectroscopic variability and heavy mass loss. They have been the subject of much recent interest given the twin possibilities that their high mass-loss rates – particularly during transient outbursts – may be essential for the formation of H-depleted Wolf Rayet stars (e.g. Smith & Owocki 2006) and that they may be the immediate precursors of a subset of highly luminous Type II supernovae (e.g. Gal-Yam & Leonard 2009).

Historically, their rarity (e.g. Clark et al. 2005) has meant that their properties – particularly regarding their characteristic outbursts and eruptions (duration, duty cycle, associated mass loss rate and underlying physical cause) – have remained poorly understood. However, recent narrow- and broad-band infra-red surveys of the Galactic Plane have revealed a large number of new LBVs candidates (Clark et al. 2003, Gvaramadze et al. 2010, Mauerhan et al. 2010, Wachter et al. 2010) and it is hoped that studies of an expanded sample size will help elucidate the nature of the LBV phenomenon and its role in massive stellar evolution. However, given their location in the Galactic plane, observations of these stars must be undertaken in the (near)-IR due to significant line of sight extinction. In this contribution we preview the results of a long term spectroscopic and photometric campaign of recently identified candidate LBVs, supplemented with tailored model atmosphere analysis utilising the CMFGEN code (Hillier & Miller 1998); a full description of this program will be presented in Clark et al. (in preparation).

2 Data Reduction and Analysis

Since 2001, near-IR JHK broadband photometric observations of our targets have been obtained with the AZT-24 1.1m telescope in Campo Imperatore (Italy). Contemporaneous spectroscopy has been obtained from a number of facilities including the AZT-24 1.1m, UKIRT, the Mayall 4m and the VLT, while we have also made use of published spectroscopy and photometry. A full description of data collection and reduction will be presented in Clark et al. (in prep.).

Due to the numerous potential sources of near-IR variability – such as continuum emission from the stellar wind, emission/extinction due to circumstellar dust and changes in stellar temperature and bolometric luminosity – it is impossible to constrain the behaviour of LBVs from photometric observations alone. Consequently, where possible, we have undertaken quantitative modeling of the combined datasets; a description of the methodology employed is found in Clark et al. (2009).

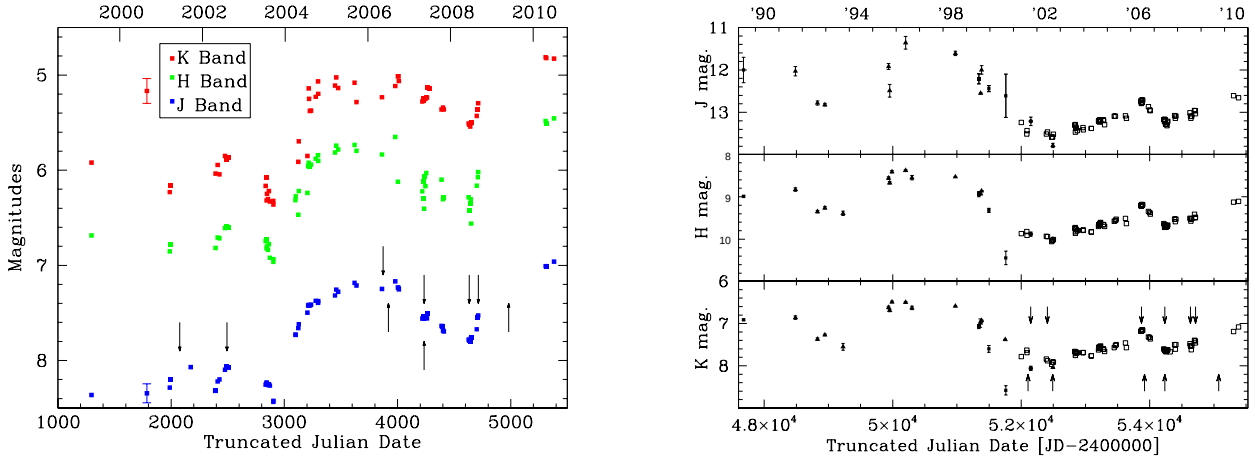

Figure 1: Long term JHK lightcurves of G24.73+0.69 (left panel; Clark et al. in prep) and AFGL 2298 (right panel; Clark et al. 2009). Times of spectral observations are indicated by arrows.

3 Selected Preliminary Results

In Fig. 1 we present sample lightcurves for two recently identified LBVs; AFGL 2298 and G24.73 +0.69 (Clark et al. 2005). Both are clearly variable over $\geq$decades, with $\Delta JHK \geq$1.5 mag. As such, the timescales and magntitudes of variability are entirely comparable to the results of optical monitoring although, as mentioned above, contemporaneous spectroscopy is required to interpret these data. In the case of AFGL 2298, analysis of such a dataset revealed that its bolometric luminosity varied by more than a factor of two over the course of the observations (Clark et al. 2009). This behaviour was driven by significant changes in the stellar radius, which were accompanied by relatively small changes in temperature (Fig. 2). Recent analysis by Groh et al. (2009) demonstrated that AG Car also varied in bolometric luminosity over the course of its photometric excursions, with a reduction in luminosity as the star expanded and cooled due to the energy required to support the extended outer layers of the star against gravity. However, unlike AG Car, the maximum luminosity of AFGL 2298 occured when its radius was also at a maximum rather than at a minimum; the 'pulsations' of both stars therefore appearing to be of a different character, with those of AFGL 2298 being more reminiscent of a (weak) 'Giant eruption' rather than a canonical 'S Dor' excursion.

A similar dataset also exists for G24.73+0.69 and the results of a comparable quantitative analysis will be presented in a future work, although preliminary comparison of spectra obtained in the

transition from photometric minimum (Clark et al. 2003) to maximum (Fig.2) suggests a cooling of the star in a manner analogous to AG Car.

A near-IR spectral classification scheme

Building on this approach, the identification and subsequent spectral follow up of numerous new LBV candidates enables us to define a classification scheme for LBVs in the near-IR as well as investigating the parameter space they occupy and their placement in an evolutionary scheme. We present a montage of K-band spectra of (candidate) LBVs/WN9-11h stars suitable for classification in Fig. 2, along with sample WN8 and Yellow Hypergiants (YHGs) spectra and the results of non-LTE model atmosphere analysis where available.

We highlight the diverse spectral morphology of (c)LBVs, as might be expected given that we sample stars with temperatures ranging from $\sim$8-20kK. Nevertheless, such stars are distinct from the 'normal' Blue Supergiants that also span this temperature range (Clark et al. in prep., Hanson et al. 1996) but which, as a result of their lower wind densities, lack the prominent emission lines of H I, He I and low excitation metals that characterise the spectra of (c)LBVs.

While unfortunately no luminosity dependent features are present in this wavelength range, the presence and line profiles of the various species do allow a gross, qualitative determination of stellar temperature, with the coolest (c)LBVs (T$<$10kK) demonstrating Na I doublet emission and critically lacking He I 2.112μm emission or absorption. At higher temperatures He I 2.112μm is intially observed in absorption, before being driven into emission along with He I 2.058μm and low excitation species such as Mg II and Fe II. At still higher temperatures these lines disappear, leaving a simple emission line spectrum dominated by Brγ and various He I lines. This process also seems to be accompanied by the development of a pronounced P Cygni profile in the He I 2.058μm line. Finally, we note that the He II 2.189μm line appears in emission for the WN8h-9h stars but is absent for the cooler early B supergiants such as P Cygni. It is observed to be weakly in emission in WN9h stars and to show a range of strengths in the WN8 stars due to the large temperature range spanned by this subtype (e.g. WR123 & 124; Crowther & Smith 1996, Crowther et al. 1999), hence it *may* also distinguish between these subtypes (e.g. Crowther et al. 2006). In this respect we note that LHO158, listed as WN8h by Liermann et al. (2009), could formally be classified as WN8-9h.

However, we caution that in the region of parameter space sampled by (c)LBVs and the closely related WN9-11h stars, the K band spectra of such stars can show a degeneracy whereby multiple combinations of stellar temperature, mass-loss rate and H/He ratio may result in similar spectral morphologies (e.g. Hillier et al. 1998). Indeed, this problem may be appreciated by noting the similarities between the spectra of P Cygni and HDE 316285 in Fig. 2 despite the significant difference in temperature between the two stars. We therefore emphasise that tailored, quantitative analysis of the spectra of individual stars over as broad a wavelength range as possible (due to the comparative lack of diagnostics in the K band) is required for the extraction of their physical properties. The Pistol star is a case in point, with Najarro et al. (2009) finding a downwards revision in luminosity by a factor of $>$2.5 over previous estimates following such modeling. Unfortunately, this requires both high S/N and, critically, spectral resolution, given the low terminal wind velocities – v$\leq$500kms^{-1} and typically $\leq$200kms^{-1} – of such stars.

Nevertheless, preliminary results from such analyses show an encouraging continuity in physical properties – and indeed spectral morphologies – with the WN8 stars, with a steady march to higher temperatures and wind velocities at relatively constant mass-loss rates. Such a connection has already been suggested by Langer et al. (1994) and latterly by Martins et al. (2007) based on the evolved population of the Galactic Centre cluster; indeed, analysis of the properties of the (evolved) stellar populations found within young massive clusters is a powerful tool in constraining the passage of

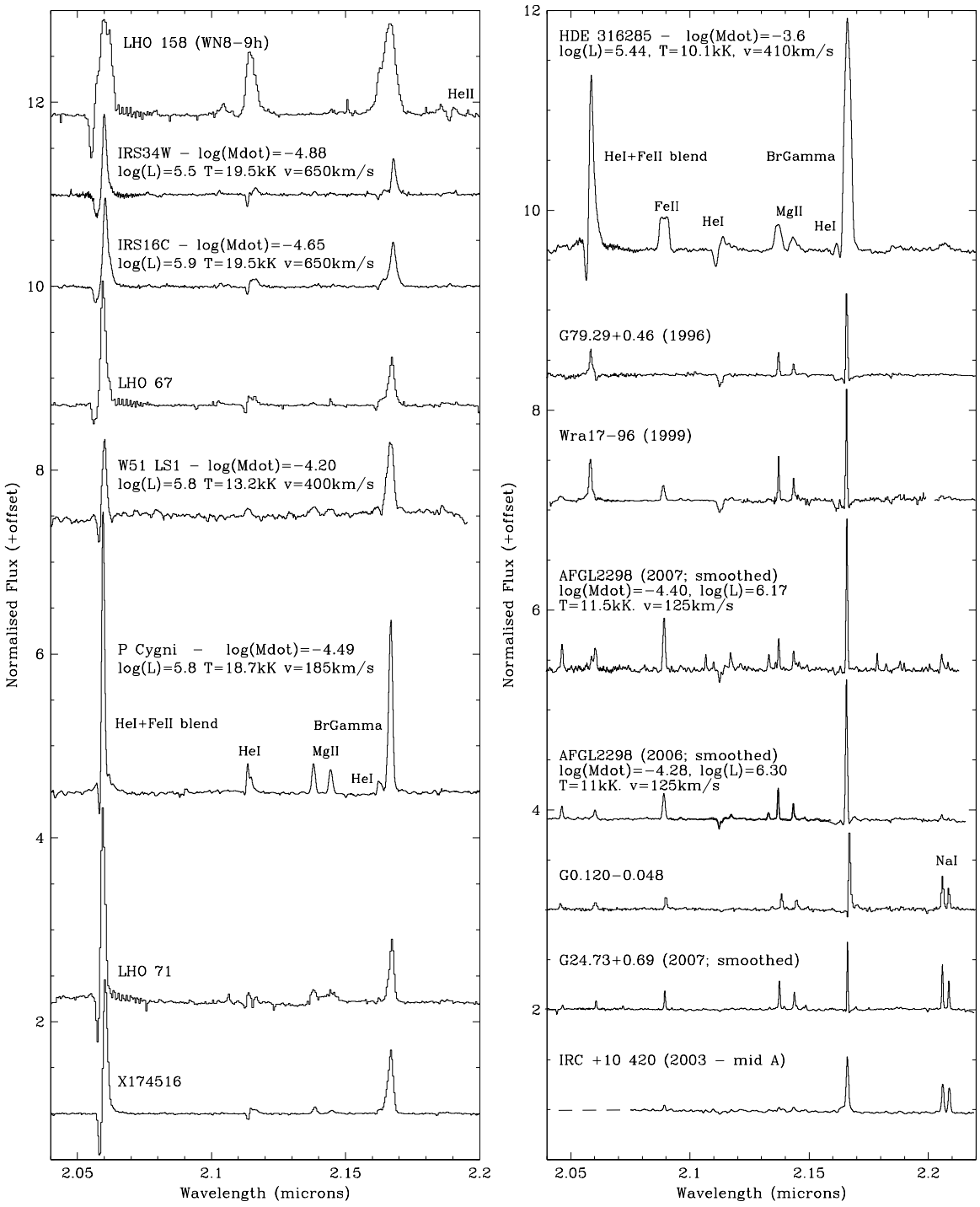

Figure 2: Montage of K band spectra of galactic LBVs demonstrating their diverse morphologies. For comparison the spectra of the Yellow Hypergiant IRC +10 420 and the WN8 Quintuplet member LHO 158 are also presented. For reasons of brevity the references to the origin of spectra and associated analyses have been omitted but are given in Clark et al. (in prep.).

stars from the Main Sequence through the 'transitional' zoo (e.g. Clark et al. 2010). At the other extreme there is a striking similarity between the YHG IRC+10 420 – which is currently evolving to higher temperatures – and LBVs in a cool phase such as G24.73+0.69 and G0.120-0.048. We do not claim that all LBVs evolve directly from YHGs, however; while this might be possible for low luminosity (and mass) stars such as G24.73+0.69, the lack of high luminosity cool super/hyper-giants clearly indicate that stars as luminous as G0.120-0.048 could not have evolved via such a pathway.

4 Concluding remarks and future prospects

While various lines of evidence suggest an important role for LBVs in the late evolutionary stages of massive stars – and by extention their death in SNe and the nature of the post-SNe relativistic remnants – the properties of this phase are still poorly understood, in large part due to the rarity of such stars. However, the recent identification of large numbers of new candidates within the Galactic plane and the viability of studying them via concerted spectroscopic and photometric monitoring supplemented with tailored non-LTE model atmosphere analysis will allow these issues to be directly addressed. Indeed, such work will greatly benefit from near-IR surveys such as VISTA/VVV and the advent of 1-2m class robotic facilities such as the Faulkes Telescopes. Likewise, the availability of multiplexing spectrographs and transient surveys such as PanSTARRS will permit similar studies in external galaxies over a range of metalicities. When combined with radiative transfer modeling of the spatially resolved gaseous & dusty ejecta associated with large numbers of galactic LBVs and which encodes their past mass loss histories, these programs have the potential to advance studies of this transient and violent phase of stellar evolution over the coming years.

Acknowledgements

AZT-24 observations made within an agreement between Pulkovo, Rome and Teramo observatories.

References

Clark, J. S., Egan, M. P., Crowther, P. A., et al., 2003, A&A, 412, 185
Clark, J. S., Larionov, V. M., Arkharov, A., 2005, A&A, 435, 239
Clark, J. S., Crowther, P. A., Larionov, V. M., et al., 2009, A&A, 507, 1555
Clark, J. S., Ritchie, B. W., Negueruela, I., 2010, A&A, 514, 87
Crowther, P. A., Smith, L. J., 1996, A&A, 305, 541
Crowther, P. A., Pasquali, A., DeMarco, O., et al., 1999, A&A, 350, 1007
Crowther, P. A., Hadfield, L., Clark, J. S., Negueruela, I., Vacca, W. D., 2006, MNRAS, 372, 1407
Gal-Yam, A.,Leonard, D. C., 2009, Nature, 458, 865
Groh, J. H., Hillier, D. J., Damineli, A., et al., 2009, ApJ, 698, 1698
Gvaramadze, V. V., Kniazev, A. Y., Fabrika, et al., 2010, MNRAS, 405, 1047
Hanson, M. M., Conti, P. S., Rieke, M. J., 1996, ApJS, 107, 281
Hillier, D. J., Miller, D. L., 1998, ApJ, 496, 407.
Hillier, D. J., Crowther, P. A., Najarro, F., Fullerton, A. W., 1998, A&A, 340, 483
Langer, N., Hamann, W.-R., Lennon, M., et al. 1994, A&A, 290, 819
Liermann, A., Hamann W.-R., Oskinova, L. M., 2009, A&A, 494, 1137
Martins, F., Hillier, D. J., Hillier, D. J., et al. 2007, A&A, 478, 219
Mauerhan, J. C., Morris, M. R., Cotera, A., 2010, ApJ, 713, L33
Najarro, F., Figer, D. F., Hillier, D. J., Geballe, T. R., Kudritzki, R. P., 2009, ApJ, 691, 1816
Smith, N., Owocki, S., 2006, ApJ, 645, L45
Wachter, S., Mauerhan, J. C., Van Dyk, S. D., et al., 2010, AJ, 139, 2330

A Near-Infrared Narrow-band Imaging Survey to Search for Massive Stars in Cl 1806-20

Michelle L. Edwards[1,2], Reba M. Bandyopadhyay[2], Stephen S. Eikenberry[2], Valerie J. Mikles[2,3], Dae-Sik Moon[4]

[1] Gemini Observatory, Southern Operations Center, La Serena, Chile

[2] Department of Astronomy, University of Florida, Gainesville, FL 32611

[3] Department of Physics and Astronomy, Louisiana State University, Baton Rouge, LA 70803

[4]Department of Astronomy and Astrophysics, University of Toronto, Toronto M5S3H8, Canada

Abstract: We survey the environment surrounding Cl 1806-20 using near-infrared narrow-band imaging to search for Brγ features indicative of massive stars. Using this technique, we successfully detect previously identified massive stars in the cluster. While we detect no new emission line stars, establishing a firm upper limit on the number of Wolf Rayets and Luminous Blue Variables, we do find several candidate OB supergiants, which likely represent the bulk of the heretofore undiscovered massive star population. Finally, we present spectroscopic evidence for emission-line variability in LBV 1806-20. Our results highlight the advantages of using narrow-band imaging to search for massive stars.

1 Introduction

Discovered by Fuchs et al. (1999), Cl 1806-20 is home to a variety of rare objects, including a candidate Luminous Blue Variable (LBV 1806-20), multiple Wolf Rayets (WRs), a soft-gamma repeater (SGR 1806-20), and several OB supergiants (Fuchs et al. 1999; Eikenberry et al. 2004; Figer et al. 2005). At a distance of either $\sim$ 15 kpc (Corbel & Eikenberry 2004) or $\sim$ 9 kpc (Bibby et al. 2008), the cluster spans $\sim$ 40 arcseconds (2.9 pc or 1.7 pc respectively) on the sky. It is located in a heavily crowded region of the Galactic Plane with $A_V \sim 29$ mag (Corbel & Eikenberry 2004).

Although individual members of Cl 1806-20 have been identified on a case-by-case basis with spectroscopy, no systematic effort to take a census of the cluster's massive stellar population exists in the literature. To better constrain the membership of Cl 1806-20, we performed near-IR broad- and narrow-band imaging to search for candidate massive cluster stars. We focused on Brγ emission indicative of stellar winds in massive stars (Hanson, Conti & Rieke 1996; Figer, McLean & Najarro 1997; Blum et al. 2001) and Brγ absorption found in OB supergiants (Hanson et al. 1996).

For our study, we applied a novel technique. We constructed a color-color diagram using J, K_s, 2.16μm Brγ, and 2.27μm K_{cont} photometry of sources in the vicinity of Cl 1806-20. We then identified stars with Brγ emission or absorption at the known $J-K_s$ color of the cluster. This method helped us to visually distinguish emission-line stars in the cluster from both massive field stars in the line-of-sight and bright late-type stars in the foreground.

2 Observations

On 2005 August 26-27, we used the Wide Field Infrared Camera (WIRC, Wilson et al. 2003) on the Palomar 200" telescope to obtain J, K_s, 2.16μm Brγ, and 2.27μm K_{cont} images of an 8.7$'$ $\times$ 8.7$'$ region around Cl 1806-20. The total exposure times were 13.5 minutes in Brγ and K_{cont}, 90s in K_s-band and 48s in J-band.

We reduced the data with FATBOY, a Python based data pipeline developed at the University of Florida, and performed astrometry on these images using KOORDS in the KARMA software package. We then completed PSF photometry on our science frames with DAOPHOT II and ALLSTAR (Stetson 1987, 1992) and calibrated the J and K_s magnitudes for our sources with 2-MASS photometry. Using TOPCAT, the Tool for OPeration on Catalogues and Tables (Taylor 2005), we matched our data across all four bands.

We used the position of the first object discovered in the cluster, SGR 1806-20, with an RA = 18^h 08^m 39.32^s and Dec = -20° 24$'$ 39.5" (Kaplan et al. 2002) as the cluster centre. We then created a $J - K_s$ versus $Br\gamma - K_{cont}$ diagram of objects within a 2$'$ radius from this position (Figure 1). We calculated the 2-D projected distance between each field star and the cluster centre.

3 Estimating Equivalent Widths

The color-color diagram that we constructed from our photometry offers a useful visual tool for identifying unknown massive stars in the cluster (see Sect. 5). However, the narrow-band photometry also provides a quantitative measure of the strength of a star's Brγ features, which we can compare to literature values. Since the 2.16μm Brγ filter detects both stellar continuum and Brγ emission or absorption, while the 2.27μm K_{cont} filter detects only stellar continuum, non-zero values of $Br\gamma - K_{cont}$ are indicative of Brγ features. Furthermore, the magnitude of the $Br\gamma - K_{cont}$ color difference is an estimate of the equivalent width (EW) of the line.

First, the instrumental $Br\gamma - K_{cont}$ values derived from our photometry must be calibrated to take into account differences in transmission and dust penetration by the two narrow-band filters. In Figure 1 there is a clear linear correlation between the $J - K_s$ and $Br\gamma - K_{cont}$ color of sources in the field. Using TOPCAT, we fit a line with slope (m) = 0.028 and y intercept (b) = -0.137 to the data points. For any given $J - K_s$ color, this line defines the expected value of $Br\gamma - K_{cont}$ for a star with neither Brγ absorption nor emission; a narrow-band "zeropoint".

To find the calibrated $Br\gamma - K_{cont}$ value, $(Br\gamma - K_{cont})_{cal}$, of an individual star in our data set, we first solved the equation of the line using the star's $J - K_s$ value. This gave us the $Br\gamma - K_{cont}$ "zeropoint" for that particular object. We then subtracted this value from the photometrically derived $Br\gamma - K_{cont}$ color. Finally, using this equation:

$$W = (1 - 10^{-\frac{(Br\gamma - K_{cont})_{cal}}{2.5}})d\lambda \quad (1)$$

where W is the equivalent width of the line and $d\lambda$ is the band-pass of the filters ($\sim$ 220 Å), we estimated the equivalent width for the stars in our study.

4 Comparison to Previous Results

For the remainder of the paper, we adopt the Eikenberry et al. (2004) nomenclature when an object has more than one designation.

Three of the four WR stars, B, 10, and 22 appear in our catalog; Star 3 is the exception. The location of Star 3 in the densest, most confused region of the cluster prevented an accurate measure

of its position or magnitude in one or more bands in our dataset. Star 22 has a reported Brγ excess of -0.20 $\pm$ 0.01 with a $J - K_s$ error = 0.02. We find an EW $\sim -45 \pm 2$Å, in agreement with the EW $= -42 \pm 3$Å previously reported (Eikenberry et al. 2004). We measure a $J - K_s \sim 5$ mag for Star 22, consistent with earlier measurements of this source (LaVine, *private communication*).

In some cases obvious discrepancies between our EW estimates and previous data do exist, however upon examination we found that they were indicative of physical processes in the stars in question. For instance, our photometry shows a Brγ absorption of 21 $\pm$ 2Å for Star B, seemingly at odds with its classification as a Wolf Rayet. However, comparison of our data with NIR spectra provided by Eikenberry et al. (2004) show that this result is consistent with the classification of Star B as a WCLd, a dust emission WR star with large NIR and MIR excess redward of 2.2μm. Since the K_{cont} band used in our observations is located at 2.27μm, we expect the flux in this narrow-band to be greater than the flux in the Brγ band. Thus, our apparent Brγ "absorption" is in fact a documented K_{cont} excess. We find a similar result for Star 10, also a WC9d. With a $J - K_s$ color $\sim$ 5.83 mag, this star is slightly redder than most stars in the cluster, likely indicative (as with Star B) of intrinsic reddening by circumstellar dust.

For many of the OB supergiants, we found that insufficient information in the literature prevented quantitative comparison. However, we note that it is easy to identify these sources as objects with Brγ absorption upon visual inspection of our color-color diagram.

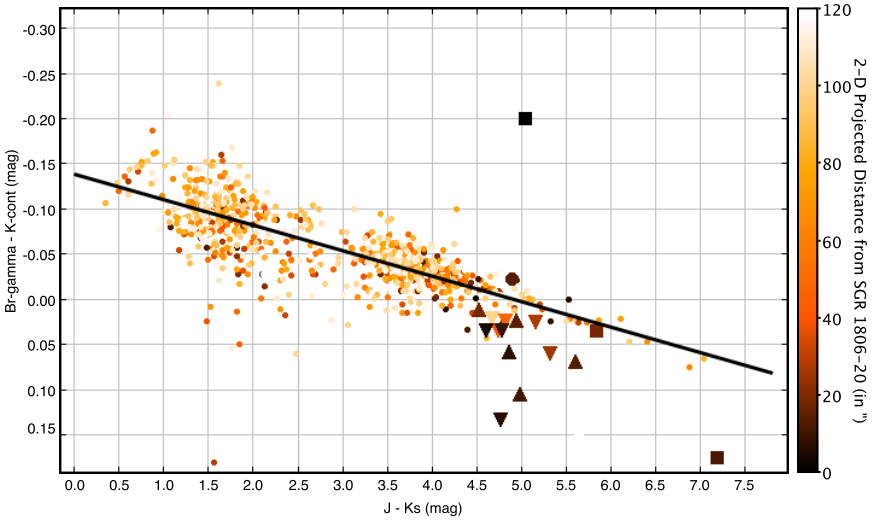

Figure 1: Color-color diagram of stars within a 2′ ($\sim$ 9 pc) radius of Cl 1806-20. OB supergiants are marked as triangles, WR stars as squares and the LBV as a circle. New OB supergiant candidates are marked as inverted triangles. The solid black line is the narrow-band zeropoint.

4.1 LBV 1806-20

Previously published spectra of LBV 1806-20 (Eikenberry et al. 2004, Figer, Najarro & Kudritzki 2004) reported a Brγ EW ~ -40Å. However, with the method described above, we found a Brγ EW $\sim -4 \pm 2$Å. To further investigate this result, we obtained spectra of LBV 1806-20 on 17 May 2004 and 2 July 2005 using the near-infrared spectrograph SpeX (Rayner et al. 2003) on the InfraRed Telescope Facility (IRTF). We reduced this data using standard SpeXTool procedure and produced flat-fielded, sky-subtracted, wavelength calibrated spectra for LBV 1806-20 for each of the two nights. Then, using Xcombspec (Cushing, Vacca & Rayner 2004) we combined the individual images of the

LBV to produce two, weighted-mean LBV spectra, one for 2004 and one for 2005. Finally, we divided the corresponding atmospheric standard from the program star, multiplied the LBV spectra by a 5600 K blackbody spectrum (the temperature of the standard), dereddened them using $A_v = 29$ mag and calculated the EW of all emission lines.

Our resulting K-band spectra appear in Figure 2. We find a Brγ EW $\sim -7.9 \pm 0.4$Å in May 2004 and -9.13 ± 0.6Å in July 2005 – substantially smaller than the EW found in the earlier observations by Eikenberry et al. (2004) and Figer et al. (2004), and much closer to the value derived from our narrow-band imaging – clearly indicating intrinsic variability in the Brγ emission line.

Our broad-band photometry reinforces that LBV 1806-20 was undergoing a notable variation. We find $K_s = 8.56 \pm 0.03$ and $J = 13.45 \pm 0.04$ for LBV 1806-20, compared to $K = 8.89 \pm 0.06$ and $J = 13.93 \pm 0.08$ found by Eikenberry et al. (2004). Taking into account the errors and slight difference between the K- and K_s- bands, LBV 1806-20 is significantly brighter during our observations.

Recent findings by Rahoui, Chaty & Lagage (2009) in the mid-IR also confirm the variable nature of LBV 1806-20. Between October 2004 and September 2005, the authors observed a significant increase in the MIR flux. The flux then decreased from September 2005 - April 2006, returning to October 2004 levels. Without finer time-resolution, it is difficult to correlate changes in the MIR flux discovered by Rahoui et al. (2009) with the variability of the NIR spectroscopy and photometry presented in this study. However, we can say with certainty that between 2001 - 2006, LBV 1806-20 manifested the variability and instability expected from a star of this type. Extended monitoring of this object is necessary to better track future episodes.

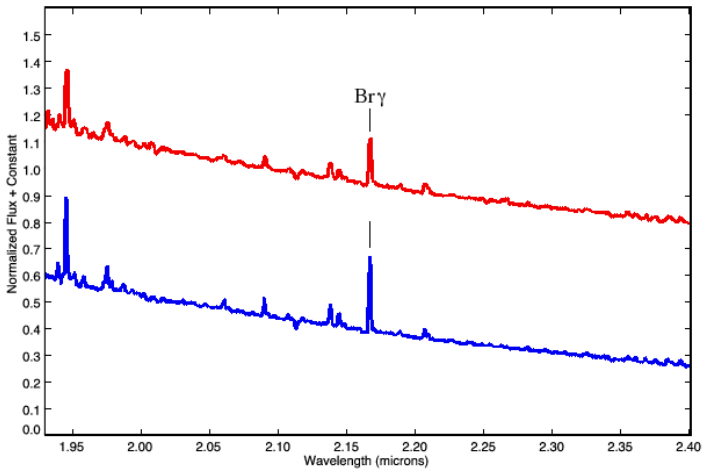

Figure 2: Spectra of LBV 1806-20 obtained with IRTF. The top spectrum was obtained in May 2004 and the bottom spectrum in July 2005. For clarity, each has been normalized by the last pixel and offset from each other by an arbitrary constant.

5 New Candidate Cluster Members

After confirming the efficacy of our method, we used the color-color diagram and our computed $Br\gamma - K_{cont}$ values to search for new massive stars in the cluster. We focused on objects with narrow-band emission or absorption that had the same $J - K_s$ color as known cluster members. Assuming $A_V = 29 \pm 2$ for Cl 1806-20, (Corbel & Eikenberry 2004) and $A_K = 0.112 A_V$ and $A_J = 0.282 A_V$

(Rieke & Lebofsky 1985) we calculated $A_K = 3.25 \pm 0.56$ and $A_J = 8.18 \pm 0.22$ for the cluster, yielding a $J - K_s = 4.93 \pm 0.34$ mag.

Using this criterion, we did not detect any previously unknown WR or LBV population in Cl 1806-20. This allows us to place a firm upper limit on the number of very massive stars in the cluster, which was the primary goal of this study. However, we did find a population of ~ 10 candidate OB supergiants that may represent the bulk of the heretofore undiscovered cluster population. We plan to perform follow-up spectroscopic observations of these targets.

Acknowledgements

MLE is grateful to Dave Clark and Maren Hempel for useful discussion. MLE is supported by the Gemini Observatory, which is operated by the Association of Universities for Research in Astronomy, Inc., on behalf of the international Gemini partnership of Argentina, Australia, Brazil, Canada, Chile, the United Kingdom, and the United States of America.

References

Bibby, J. L., Crowther, P. A., Furness, J. P., & Clark, J. S. 2008, *MNRAS*, L34

Blum, R. D., Schaerer, D., Pasquali, A., Heydari-Malayeri, M., Conti, P. S., & Schmutz, W. 2001, *AJ*, 122, 1875

Corbel, S., & Eikenberry, S. S. 2004, *A&A*, 419, 191

Cushing, M. C., Vacca, W. D., & Rayner, J. T. 2004, *PASP*, 116, 362

Eikenberry, S. S., Matthews, K., LaVine, J. L. et al. 2004, *ApJ*, 616, 506

Figer, D. F., McLean, I. S., & Najarro, F. 1997, *ApJ*, 486, 420

Figer, D. F., Najarro, F., & Kudritzki, R. P. 2004, *Ap. Lett*, 610, L109

Figer, D. F., Najarro, F., Geballe, T. R., Blum, R. D., & Kudritzki, R. P. 2005, *Ap. Lett.* , 622, L49

Fuchs, Y., Mirabel, F., Chaty, S., Claret, A., Cesarsky, C. J., & Cesarsky, D. A. 1999, *A&A*, 350, 891

Hanson, M. M., Conti, P. S., & Rieke, M. J. 1996, *ApJS*, 107, 281

Kaplan, D. L., Fox, D. W., Kulkarni, S. R., Gotthelf, E. V., Vasisht, G., & Frail, D. A. 2002, *ApJ*, 564, 935

LaVine, J., *private communication*

Rahoui, F., Chaty, S., & Lagage, P.-O. 2009, *A&A*, 493, 119

Rayner, J. T., Toomey, D. W., Onaka, P. M., Denault, A. J., Stahlberger, W. E., Vacca, W. D., Cushing, M. C., & Wang, S. 2003, *PASP*, 115, 362

Rieke, G. H., Lebofsky, M. J., & Low, F. J. 1985, *AJ*, 90, 900

Stetson, P. B. 1987, *PASP*, 99, 191

Stetson, P. B. 1992, Astronomical Data Analysis Software and Systems I, 25, 297

Taylor, M. B. 2005, Astronomical Data Analysis Software and Systems XIV, 347, 29

Wilson, J. C., Eikenberry, S. S. and Henderson, C. P., et al. 2003, Proceedings of the SPIE, 4841, 451

Observations of Be Disk Building: Optical Spectra of NW Serpentis (HD 168797) over 35 days

Erika D. Grundstrom[1,2], M. V. McSwain[3], C. Aragona[3],
T. S. Boyajian[4], A. N. Marsh[3], R. M. Roettenbacher[3*]

[1] Dept. of Physics & Astronomy, Vanderbilt University, Nashville, TN, USA
[2] Dept. of Physics, Fisk University, Nashville, TN, USA
[3] Dept. of Physics, Lehigh University, Bethlehem, PA, USA
[4] CHARA, Georgia State University, Atlanta, GA, USA

Abstract: The classical Be star NW Serpentis (HD 168797) is part of the CoRoT field and has long been studied photometrically and is known to have multi-periodic pulsational modes. Such pulsations are thought to be a way to generate the Be equatorial circumstellar disk. In an earlier survey, we identified this star as a possible non-radial pulsator and a known B←Be variable. During Fall 2008, we obtained 23 spectra over 35 nights in the Hα region. During this time, we observed Hα to go from purely photospheric absorption to double-peaked emission then "fade" back toward photospheric absorption. We present our determination of stellar parameters, our analysis of the circumstellar disk construction, and the possibility of a binary companion. These observations also suggest that frequent observations of Be stars known to be non-radial pulsators may yield more opportunities to study the disk-building phenomenon and thus assist in constraining theoretical models of disk generation.

1 Introduction

Be stars are rapidly rotating B-type stars that lose mass in an equatorial, circumstellar disk (Porter & Rivinius 2003) and cause Balmer and other line emission. Many Be stars exhibit short-term variability with a period range of a few hours to a couple of days. This short-term variability is detected in photometric studies (non-regular light curves) and in spectroscopic studies (line profile variability or *lpv*). While we do not yet know what causes the stellar material to actually leave the surface of the star, one of the prevailing theories is non-radial pulsation.

HD 168797 (NW Serpentis, HR 6873) is a $V = 6.14$ star with spectral type B2.5IIIe. It has an extensive photometric monitoring record spanning over two decades. It is also in the CoRoT field. During Grundstrom's (2007) spectroscopic survey of field Be stars, she identified HD 168797 as interesting on the basis of the variation in the Hα profile over two years. During the fall of 2008, we observed this star spectroscopically 23 times in a 35-day observing run and saw the growth of a double-peaked emission profile indicative of circumstellar disk growth.

*All were Visiting Astronomers, Kitt Peak National Observatory

2 Observations

We obtained 23 spectra in the Hα region (6370–7040 Å) of HD 168797 at the KPNO coudé feed telescope over 35 consecutive nights during 2008 October and November (HJD=2454756.6–2454791.7). We used grating B in second order with the OG550 order-sorting filter and the F3KB detector (for a resolution $\lambda/\triangle\lambda$ = 11400–12500). The spectra were wavelength-calibrated using Th-Ar comparison lamp spectra taken throughout the each night. These data do not appear to be coincident with any CoRoT observations.

The images were zero-corrected, flat-fielded, and wavelength-calibrated using standard procedures in IRAF.[1] The spectra were interpolated onto a log wavelength scale using a common heliocentric wavelength grid, and they were rectified to a unit continuum using line-free regions.

3 Physical Parameters from Spectral Models

In order to incorporate more recent research regarding determination of the physical parameters of B stars, we have found new values for $T_{\rm eff}$, $\log g$, and $V \sin i$. The method used by Frémat et al. (2006) of fitting metal lines to find effective temperature is not ideal as metallicity plays a role in the strength of such lines - one should use Hγ to get the most accurate estimates (Huang & Gies 2006).

We formed a mean blue spectrum using four spectra obtained between 2004–2006. Contemporaneous Hα spectra indicated that no emission was visible at these times, and furthermore no evidence of weak emission was present in the Hγ line. We omitted a fifth blue spectrum from the mean because its Hγ line profile was somewhat narrower than the others, suggesting that a weak emission disk was present at that time.

To measure the physical parameters of HD 168797, we used the new TLUSTY BSTAR2006 grid of metal line-blanketed, non-LTE, plane- parallel, hydrostatic model spectra (Lanz & Hubeny 2007). We used their models with solar metallicity and helium abundance and a microturbulent velocity of 2 km s^{-1}. We adopted the mean $V \sin i$ from Frémat et al. (2006), Abt, Levato & Grosso (2002), and Yudin (2001), using $V \sin i = 260$ km s^{-1} . We compared the Hγ line profile to the rotationally and instrumentally broadened model spectral line profiles at each value in the grid, minimizing rms^2 across the line region. We then refined our measurements to a higher precision using a linear interpolation between the available line profiles in the grid. Our best line fit indicated $T_{\rm eff} = 17650$ K and $\log g = 3.50$, shown in Figure 1. We determined the formal errors from the values above, however, we found that the placement of the continuum caused much larger errors than the formal errors from our line profile fits. Therefore, we adopted a lower limit for $T_{\rm eff}$ of 16000 K and an upper limit of 18000 K, and a range of acceptable $\log g$ between 3.3 – 3.5.

Rapidly rotating B stars may be distorted into an oblate spheroidal shape, so the surface gravity at the equator can be much lower than at the poles, and this $\log g_{polar}$ is a better indicator of the evolutionary state of the star. Huang & Gies (2006) performed detailed spectroscopic modeling of such distorted rotating stars to determine a statistical correction factor for $\log g$, averaged over all possible i, for a variety of stellar models. We made a bilinear interpolation between their models to convert our measured $\log g$ to $\log g_{\rm polar}$ for a more accurate comparison between slow and rapid rotators.

We also measured its mass, $M_\star$, and radius, $R_\star$, by interpolating between the evolutionary tracks for non-rotating stars from Schaller et al. (1992). The range of acceptable values of $M_\star$ and $R_\star$ correspond to our measured errors in $T_{\rm eff}$ and $\log g$. For simplicity, we assume the polar radius of

[1]IRAF is distributed by the National Optical Astronomy Observatory, which is operated by the Association of Universities for Research in Astronomy, Inc., under cooperative agreement with the National Science Foundation

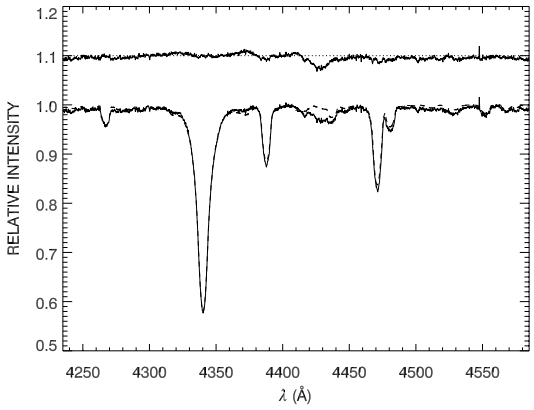

Figure 1: The mean blue spectrum of HD 168797 (from previous work by Grundstrom) compared to the best fit model derived from the Hγ data, with $V \sin i$ = 260 km s^{-1}, $T_{\rm eff}$ = 17650 K, and $\log g$ = 3.50. The residuals of the observed minus model spectrum are shown above (shifted by the value 1.1 for presentation). Note that the broad residual feature around $\lambda 4429$Å is a diffuse interstellar band.

Table 1: Newly Determined Stellar Parameters (numbers in parentheses are range of acceptable values)

$T_{\rm eff}$	17650 K (16000–18000 K)
$\log g$	3.5 (3.3–3.5)
$\log g_{polar}$	3.80
$M_\star$	6.63 $M_\odot$ (5.64–7.36)
$R_\star$	5.35 $R_\odot$ (4.88–6.32)
V_{crit}	397 km s^{-1} (324–438)
inclination	≈51° (39°–63°)

the star, $R_{\rm p}$ is equal to $R_\star$, and a rotationally distorted star has an equatorial radius $R_{\rm e} = 1.5R_{\rm p}$ in the Roche approximation. The resulting critical velocity is $V_{\rm crit} = (GM_\star/R_{\rm e})^{1/2}$. If we assume that the Be star is nearly critically rotating, with true rotational velocity $V_{\rm rot}$ equal to 90-95% of $V_{\rm crit}$ (Townsend, Owocki & Howarth 2004), we can constrain the inclination, i, of the rotation axis. Values for all parameters are summarized in Table 1.

We also found that by using these values, we obtained an excellent fit to the Hα line when it is purely photospheric as it was during our first three observations of this data set.

4 Preliminary Analysis

In looking at the Hα emission wings (Fig. 2,3) we notice that they are limited by approximately 260 km s^{-1} (the same as the projected rotation velocity of the star). The emission peaks are at slower speeds in our earlier observations, then these peaks slowly shrink as they move outward toward the faster regions as over the course of our observations. This implies that there was an outburst of material, with matter which escaped the surface of the star for a short period of time (and slowed as per Kepler's laws) but slowly fell back to the surface (and sped up). We note that it takes longer to dissipate this disk than it did to build it.

The height of the peaks changes over the course of our observations implying more material on one side (redward earlier, switching to blueward over the course of a few days). We can infer two

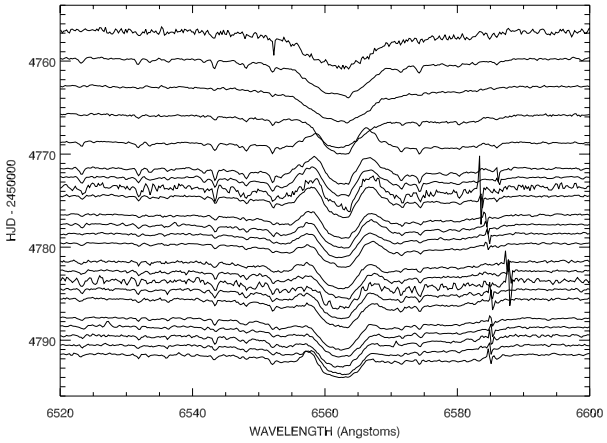

Figure 2: Time series plot of the 23 spectra in the Hα region over the 35 day observation period (time increasing down).

possible mechanisms for this observation: 1) the circularization of a blob (or several blobs) of material as it rotates around the star (as suggested for μ Cen by Rivinius et al. 1998); 2) the presence of a spiral density wave in this circumstellar disk (Okazaki 1991). This is the more unlikely as the timescales required are much longer ($\sim$years) than the few day timescales observed here.

4.1 Line Profile Variability

While some Be stars experience outbursts like this at periastron, our investigation of radial velocity variations (RVVs) is currently inconclusive. There do seem to be some RVVs between the peaks which may be indicative of spectroscopic evidence of non-radial pulsation. This star is known to have multiperiodic pulsations (from photometric studies by Gutiérrez-Soto et al. 2007) so perhaps we will be able to find such evidence in our data. We will investigate our data further. Also, we will undertake further work using the He I $\lambda 6678$ line - we do not trust it entirely as it is partially filled with emission and shows some evidence of non-radial pulsation signatures. However, discussions with conference attendees have caused us to look at it more closely.

5 Conclusions

Our serendipitous spectroscopic observation of the interesting Be star NW Serpentis (HD 168797) demonstrates the need for long term, consistent observation of certain stars - we were very fortunate to catch this very short-lived transition. We hope our observations will help provide constraints for models of Be stars and disks in general.

In general, we find that this star is just barely spinning fast enough to throw material off of the equator. We also find it can build a disk in three days (or less!) - perhaps the process is rather explosive (possibly like μ Cen - see Hanuschik et al. 1993)? Only further observations can answer that question. During our observations, we found that the disk falls back onto the star and only the material that is nearest the star (i.e. the fastest material) is emitting photons by the end of the observational period. We can provide no guidance at this time as to whether or not this system is a binary.

For future work, we are investigating further observations and an association with the resource of amateur astronomers with their own spectrographs - a collaboration will provide an unprecedented amount of data and hopefully we can catch NW Ser building another disk.

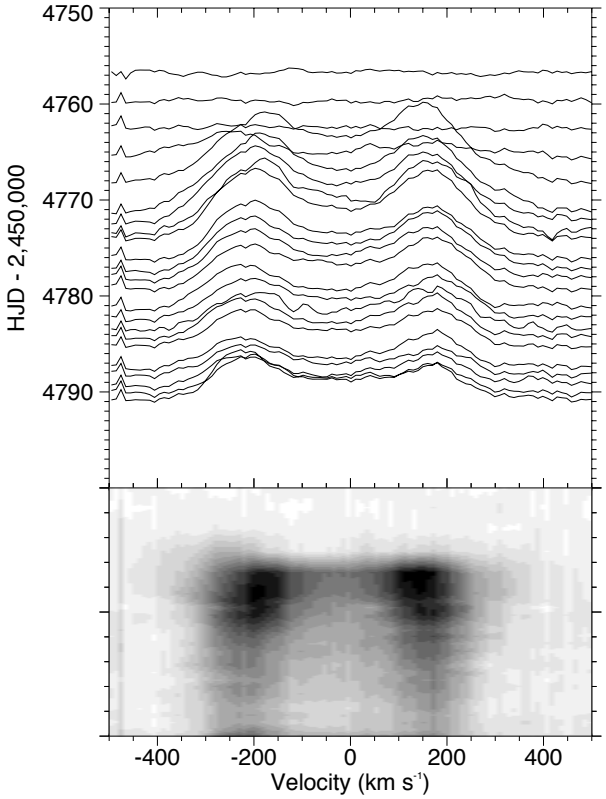

Figure 3: The upper plot shows the Hα line profile of NW Ser with the photospheric component removed over our continuous 35 nights of observation, sorted by HJD, and the lower plot shows a gray-scale image of the same line using the same chronological order. The intensity at each velocity in the gray-scale image is assigned one of 16 gray levels based on its value between the minimum (bright) and maximum (dark) observed values. The intensity between observed spectra is calculated by a linear interpolation between the closest observed phases.

Acknowledgements

This work has been supported in part by NASA grant #NNX08AV70G and NSF Career grant AST-0349075. EDG gratefully acknowledges travel support from the American Astronomical Society.

References

Abt, H. A., Levato, H., & Grosso, M. 2002, ApJ, 573, 359
Frémat, Y., Neiner, C., Hubert, A.-M., Floquet, M., Zorec, J., Janot-Pacheco, E., & Renan de Medeiros, J. 2006, A&A, 451, 1053
Grundstrom, E. D. 2007, Ph.D Dissertation, Georgia State Univ.
Gutiérrez-Soto, J., Fabregat, J., Suso, J., et al. 2007, A&A, 472, 565
Hanuschik, R. W., Dachs, J., Baudzus, M., & Thimm, G. 1993, A&A, 274, 356
Huang, W. & Gies, D. R. 2006, ApJ, 648, 591
Lanz, T. & Hubeny, I. 2007, ApJS, 169, 83
Okazaki, A. T. 1991, PASJ, 43, 75
Porter, J. M., & Rivinius, Th. 2003, PASP, 115, 1153
Rivinius, Th., Baade, D., Stefl, S., Stahl, O., Wolf, B. & Kaufer, A. 1998, A&A, 333, 125
Schaller, G., Schaerer, D., Meynet, G., & Maeder, A. 1992, A&AS, 96, 269
Townsend, R. H. D., Owocki, S. P., & Howarth, I. D. 2004, MNRAS, 350, 189
Yudin, R. V. 2001, A&A, 368, 912

A Project to Study Stellar and Gas Kinematics in 30 Dor with the VLT-FLAMES Tarantula Survey

Vincent Hénault-Brunet[1], Christopher J. Evans[2,1], William D. Taylor[1], Mark Gieles[3], & the VLT-FLAMES Tarantula consortium

[1] Institute for Astronomy, University of Edinburgh, Blackford Hill, Edinburgh, EH9 3HJ, UK
[2] UK Astronomy Technology Centre, Blackford Hill, Edinburgh, EH9 3HJ, UK
[3] Institute of Astronomy, University of Cambridge, Madingley Rd, Cambridge CB3 0HA

Abstract: The VLT-FLAMES Tarantula Survey offers a unique opportunity to study the stellar and gas kinematics of 30 Doradus in the Large Magellanic Cloud (LMC). Using the nebular emission lines in the fibre spectra of $\sim$1000 stars, we can map the radial velocity structure of ionized gas across the 30 Doradus region, enabling us to study the environment of massive stars. Multi-epoch ARGUS-IFU observations and MEDUSA/UVES fibre spectroscopy in the young massive cluster R136, at the core of 30 Dor, will allow us to quantify the effect of binaries on the velocity dispersion of the cluster. The true velocity dispersion will be measured from the radial velocities of the identified single stars, providing an essential ingredient to estimate the dynamical mass and probe the dynamical state of R136.

1 Introduction

High-quality spectra of large samples of O and B stars over a region more than 200 pc wide in 30 Doradus were obtained as part of the VLT-FLAMES Tarantula Survey (Evans et al. 2010a, Taylor et al. 2011). While it is primarily aimed at understanding the evolution of massive stars via detailed atmospheric analysis, this rich dataset also allows to address many other key questions about these stars and their environment. 30 Doradus is an intricate system and more than just a convenient region to sample a large number of massive stars. As the nearest extragalactic giant H II region, it is an ideal place to study the collective interactions between massive stars and the interstellar medium. The young ($\sim$2 Myr) dense star cluster R136, at its core, is a prime target to better understand the early evolution of young massive clusters (e.g. Portegies Zwart, McMillan & Gieles 2010).

In the following sections, we discuss ongoing efforts to analyze the gas and stellar kinematics in 30 Doradus and how this will improve our knowledge of feedback from massive stars and cluster dynamics.

2 Gas Kinematics in the 30 Doradus region

Nebular spectra have been extracted from the spectra of ∼1000 stars observed across the 30 Dor nebula and region as part of the survey (see Taylor et al. 2011 for a description of the data and fibre positioning). Several key nebular lines are covered (Hα, Hβ, Hγ, Hδ, [O III] 5007, [O III] 4959, [O III] 4363, [N II] 6549, [N II] 6583, [S II] 6717, [S II] 6731, He I 4471, He I 4922, He I 6678). Selected line ratios (corrected for reddening) will be measured to map the nebular gas properties (e.g. temperature, density) across the 30 Doradus nebula and out into the surrounding region, complementing the results obtained by Pellegrini, Baldwin & Ferland (2010) in the central 140×80 pc region of the nebula.

The spectral resolution of our data (R∼10000) is high enough to resolve the nebular line profiles, which are often complex and show multiple components. We fitted the strongest lines with multiple Gaussians (Fig. 1) to determine the radial velocity of the ionized gas. These measurements will be used to analyze the global dynamics of the gas and the associated feedback from stellar winds and supernovae. Previous studies of the kinematics of ionized gas in 30 Doradus, in particular the comprehensive echelle observations of Chu & Kennicutt (1994), have revealed a large number of expanding structures, ranging in size from ∼1 to ∼100 pc and with expansion velocities from about 20 to 300 km s^{-1}. Discrete high-velocity features ($\Delta v > 100$ km s^{-1}), sometimes isolated, have also been found. The high-velocity shells and structures are most likely associated to supernova remnants (SNRs). With the spectral coverage and resolution of the Tarantula Survey data, it will be possible to measure selected line ratios for the high-velocity component alone and see if they resemble those of LMC SNRs (see e.g. Meaburn et al. 2010), providing information on the role of supernovae in shaping the gas kinematics of 30 Dor.

The nebular spectra from the Tarantula Survey are also ideal to study the pervasive broad component (FWHM∼100 km s^{-1}) found by Melnick, Tenorio-Tagle & Terlevich (1999) in their long-slit spectra of the central region of the 30 Dor nebula. Such a broad component has been found in different starburst environments where it has been associated to emission from ionized gas within turbulent mixing layers caused by the impact of winds and radiation (e.g. Westmoquette et al. 2010). Preliminary analysis of the Tarantula Survey spectra shows that including a broad component is generally required in order to obtain a satisfying fit to the nebular line profiles (see Fig. 1).

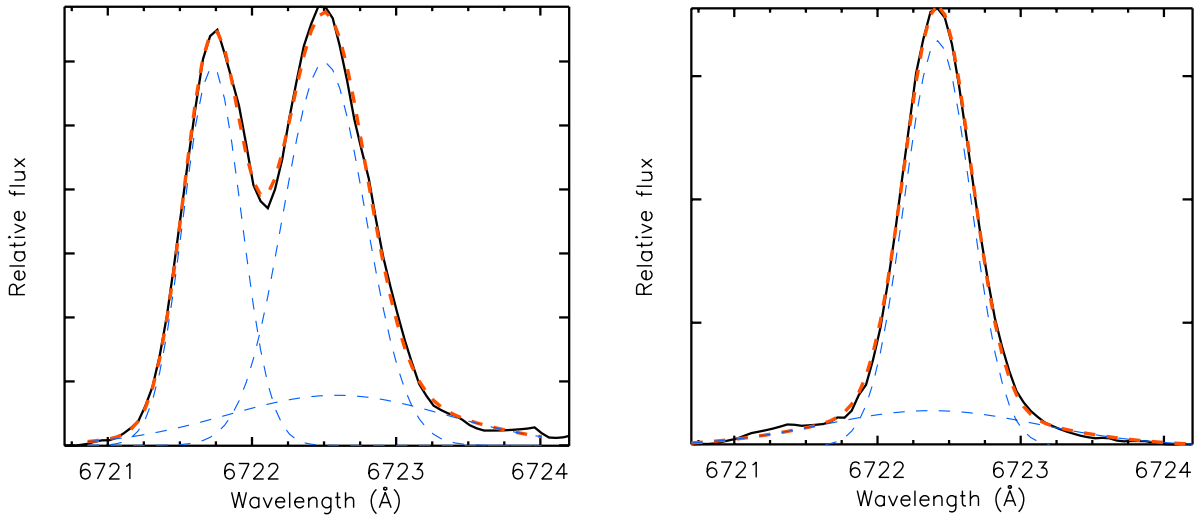

Figure 1: Examples of multiple-Gaussian fits to the [S II] 6717 line profile of two different MEDUSA targets. The fit is shown in red and the contribution of individual components in blue, illustrating the presence of a broad component.

Another application of the gas radial velocity measurements will be to serve as a reference frame to compare to the systemic stellar velocities obtained as part of the survey and see which stars have a discrepant radial velocity compared to the surrounding gas (e.g. Evans et al. 2010b). This is interesting, for example, to see if a star has formed in situ, or if it got to its current location after being ejected by dynamical interactions in a cluster or by the kick from the supernova explosion of a companion.

3 Stellar Kinematics in R136

To investigate the kinematics of stars in and around R136, five dense areas were observed with the ARGUS integral field unit (IFU) mode of FLAMES as part of the Tarantula Survey (see Fig. 2). The five pointings, each covering a $12'' \times 7''$ field of view, are located inside a radius of about 5 pc from the core of R136, with each observed at five different epochs. The observations were performed with the LR02 GIRAFFE setting, resulting in data cubes covering the spectral range from 3960 to 4560 Å with a resolving power of $\sim$10000. Sources were identified by comparison of the collapsed IFU images with the higher resolution HST-WFC3 image. The IFU spaxels are $0.52''$ wide and isolated sources generally extend over a few spaxels. By combining the signal of the appropriate adjacent spaxels, spectra were extracted for 41 sources, in addition to an integrated spectrum of the unresolved core. The typical signal-to-noise ratio of the spectra for a single epoch is around 90. In addition to the ARGUS spectra, it will also be possible to use for this analysis the fibre spectra obtained in the MEDUSA and UVES observing modes (see Taylor et al. 2011) for the targets located near R136. In total, more than 80 stars from the survey will be considered in the analysis of the stellar velocity dispersion of R136.

The mass of a star cluster can either be determined via its integrated luminosity and age-dependent mass-to-light ratio, or alternatively, from a combination of the radius containing half the light and the line of sight velocity dispersion. These quantities are respectively referred to as the photometric mass ($M_{\rm phot}$) and the dynamical mass ($M_{\rm dyn}$), and comparing them for a given cluster is a way to check the assumptions on which both estimates are based (i.e. the IMF for $M_{\rm phot}$ and virial equilibrium for $M_{\rm dyn}$). For example, a value of $M_{\rm dyn}$ that is found to be much larger than $M_{\rm phot}$ could mean that the cluster is not in virial equilibrium and instead dissolving. Such a comparison between $M_{\rm phot}$ and $M_{\rm dyn}$ is therefore useful to probe the dynamical state of clusters. In recent years, many young ($\sim$10 Myr) extra-galactic clusters were found to have $M_{\rm dyn}$ up to about 10 times larger than $M_{\rm phot}$ (e.g. Bastian et al. 2006), suggesting that they might be super-virial following gas expulsion (e.g. Goodwin & Bastian 2006). It was however realized that the dynamical timescale of these clusters is so short that they should have had time to reach a new equilibrium. Gieles, Sana & Portegies Zwart (2010) have shown that the discrepancy between $M_{\rm dyn}$ and $M_{\rm phot}$ in these young clusters can instead be explained by the excess velocity dispersion from the internal orbital motion of binaries. Taking binaries into account is therefore crucial to estimate $M_{\rm dyn}$ properly, and R136 should be no exception as it is young and its light is dominated by massive stars, for which the binary fraction is typically high (e.g. Sana & Evans 2010, Bosch,Terlevich & Terlevich 2009). However, given that the binary fraction of O stars in nearby open clusters is $\sim$50%, we can also expect to have a fair number single stars remaining (see Sana & Evans 2010).

The multi-epoch aspect of the Tarantula Survey makes it possible to disentangle binaries and single stars. The time sampling of the different ARGUS and UVES exposures is very similar to that of the MEDUSA data, with baselines of a few hours/days, $\sim$1 month, and $\sim$1 year. Monte-Carlo simulations of the detection probability as a function of period given the time sampling for one of the MEDUSA fields (e.g. Fig. 2 of Taylor et al. 2011) indicate that the survey should be fairly complete in detecting binaries with orbits of up to tens of days. Assuming a broken Öpik Law for the distribution of periods (see Sana & Evans 2010), the fraction of spectroscopic binaries missed by our

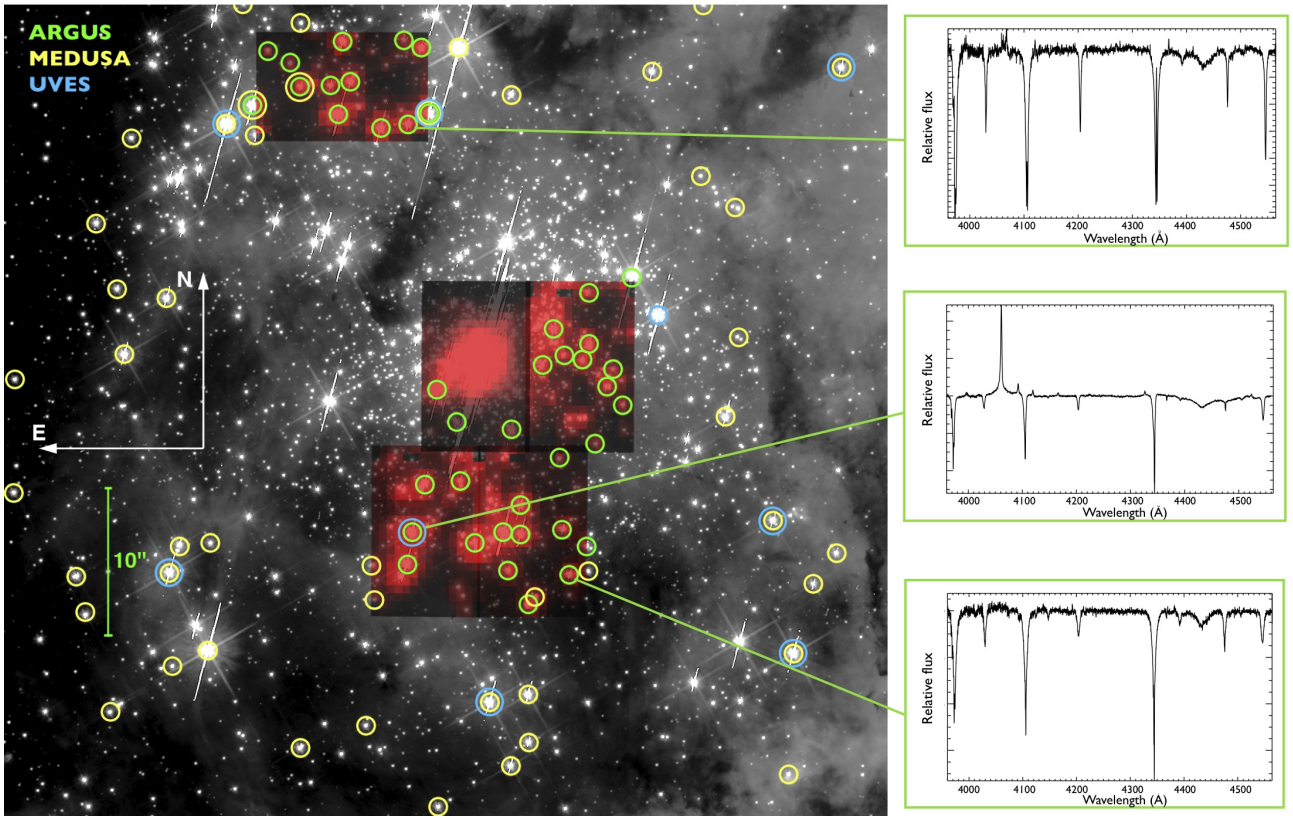

Figure 2: The five ARGUS-IFU pointings from the Tarantula Survey (in red) overlaid on the HST-WFC3 F555W image of the central region of 30 Doradus, with circles showing the distribution of ARGUS, MEDUSA, and UVES targets. Examples of spectra extracted from the ARGUS-IFU cubes are presented for three stars.

time sampling should not be significant. The binaries missed will be those with longer periods, for which the radial velocity amplitude is anyway smaller.

We will be able to quantify the effect of binaries on the measured velocity dispersion of R136. This will provide a clear observational illustration of the contribution of binary motions to the velocity dispersion of a young cluster, and an example to keep in mind when considering measurements of $M_{\rm dyn}$ from integrated light spectroscopy. The remaining single stars will be used to measure the true velocity dispersion of R136, a quantity which will then be essential in future efforts to estimate its dynamical mass and probe the dynamical state of the cluster.

With a resolving power of 10000 and a typical signal-to-noise in excess of 150 (when merging all epochs), our preliminary analysis using Gaussian fitting suggests that we can easily measure the radial velocity of single stars to a precision of a few km s^{-1}, and down to $\sim$1 km s^{-1} for the stars with narrower lines and higher signal-to-noise. These measurements will thus provide a meaningful constraint on the velocity dispersion, which we can expect to be of the order of several km s^{-1}.

4 Conclusion

The VLT-FLAMES Tarantula Survey will enable a detailed study of stellar and gas kinematics in 30 Doradus. Data reduction is now complete, giving us a rich dataset of $\sim$1000 nebular spectra across the region, and multi-epoch spectroscopy of more than 80 stars to analyze the stellar kinematics in R136. Future analysis will include studying feedback from massive stars and supernovae across the

broader 30 Doradus region, and measuring the stellar velocity dispersion of R136.

Acknowledgements

V. H.-B. acknowledges support from the Scottish Universities Physics Alliance (SUPA) and the Natural Sciences and Engineering Research Council of Canada (NSERC).

References

Bastian, N., Saglia, R. P., Goudfrooij, P., Kissler-Patig, M., Maraston, C., Schweizer, F., & Zoccali, M. 2006, A&A, 448, 881

Bosch, G., Terlevich, E., & Terlevich, R. 2009, AJ, 137, 3437

Chu, Y.-H., & Kennicutt, R. C., Jr. 1994, ApJ, 425, 720

Evans, C. J., Bastian, N., Beletsky, Y., et al. 2010a, in de Grijs & Lépine, eds, *IAUS266: Star Clusters: Basic Galactic Building Blocks Throughout Time & Space, Cambridge Univ. Press*, p. 35

Evans, C. J., Walborn, N. R., Crowther, P. A., et al. 2010b, ApJ, 715, L74

Gieles, M., Sana, H., & Portegies Zwart, S. F. 2010, MNRAS, 402, 1750

Goodwin, S. P., & Bastian, N. 2006, MNRAS, 373, 752

Meaburn, J., Redman, M. P., Boumis, P., & Harvey, E. 2010, MNRAS, 1206

Melnick, J., Tenorio-Tagle, G., & Terlevich, R. 1999, MNRAS, 302, 677

Pellegrini, E. W., Baldwin, J. A., & Ferland, G. J. 2010, arXiv:1009.4948, Accepted for publication in ApJS

Portegies Zwart, S. F., McMillan, S. L. W., & Gieles, M. 2010, ARA&A, 48, 431

Sana, H. & Evans, C. J., 2010, to appear in Neiner, Wade, Meynet & Peters, eds, *Proc. IAUS272: Active OB Stars: Structure, Evolution, Mass loss & Critical Limits*, Cambridge University Press; arXiv:1009.4197

Taylor, W.D., Evans, C.J., Hénault-Brunet, V., et al. 2011, in Proceedings of the 39th Liège Astrophysical Colloquium, eds. G. Rauw, M. De Becker, Y. Nazé, J.-M. Vreux & P.M. Williams, BSRSL 80, 430

Westmoquette, M. S., Slavin, J. D., Smith, L. J., & Gallagher, J. S., III 2010, MNRAS, 402, 152

In savvy pursuit of Local Group blue massive stars

Miriam Garcia[1,2], Artemio Herrero[1,2], Norberto Castro[1,2] and Luis José Corral[3]

[1] Instituto de Astrofísica de Canarias, La Laguna, Spain
[2] Universidad de La Laguna, La Laguna, Spain
[3] Instituto de Astronomía y Meteorología, Universidad de Guadalajara, México

Abstract: The important role of metallicity on massive star evolution and the combination of multi-object spectrographs and 10m class telescopes, have lead to numerous systematic studies of massive stars in Local Group galaxies. While color based quests of blue massive stars are relatively successful, they must be confirmed with spectroscopy and usually lead to lists dominated by B-type modest-mass stars. We have developed a friends of friends code to find OB associations in Local Group galaxies, presented in Garcia et al. (2009). One of the key points of the method is the photometric criterion to choose candidate OB stars from the reddening-free Q parameter, that could be easily extended to include from GALEX to near-IR photometry. While not a new idea, one of our code's strong advantages is the automatic determination of evolutionary masses for the members, enabling a quick and more insightful choice of candidates for spectroscopy, and the identification of potential advanced evolutionary stages. We present our work on the very metal-poor irregular galaxy IC 1613 (Garcia et al. 2010a). The association properties are not only a powerful aid towards finding the most interesting candidate massive stars, but also reveal the galaxy's structure and recent star formation history.

1 Introduction

Massive stars are chief agents of galactic-scale feedback, shaping the ISM with mighty winds throughout their evolution, and utterly disrupting their environment in the supernova explosion that puts their lives to an end.

Metallicity (Z) has a crucial two-fold role on blue massive star (BMS) evolution: (i) through the equations of stellar structure, and (ii) through the stellar wind (since $\dot{M} \propto Z^{0.8}$, Mokiem et al. 2007). BMSs must therefore be studied systematically as a function of metallicity.

In particular, we are in dire need to understand what happens at metallicities smaller than the Small Magellanic Cloud's, to make the connection with the early Universe first stars. The irregular galaxy IC 1613 is ideal to study the very-poor metallicity regime (Garcia et al. 2010b), located 714 kpc away (Dolphin et al. 2001) with metallicity 0.04 to 0.2 $Z_{\odot}$ (Talent 1980, Davidson & Kinman 1982, Dodorico & Dopita 1983, Peimbert, Bohigas, & Torres-Peimbert 1988, Kingsburgh & Barlow 1995, Tautvaišienė et al. 2007, Herrero et al. 2010). However, the required exposure times for quantitative spectroscopy of stars at this distance are long. It is therefore critical to build a good BMS candidate list.

2 What is AUTOPOP?

AUTOPOP is a highly customizable, modular code written in IDL. A detailed discussion of its use and the underlying theoretical concepts are given in Garcia et al. (2009).

Provided with a photometric catalogue of stars and user-defined target selection criteria for BMS, and isochrones, it automatically finds OB associations and analyzes their color-magnitude diagram. The final product is a list of candidate blue massive stars and their estimated evolutionary masses.

Here we present a brief description of the code and its application to IC 1613. For more details we refer the reader to Garcia et al. (2009, 2010a).

2.1 Input material

The code must be fed with: (i) a photometric catalog, (ii) user-defined criteria for target selection and extinction correction, and (iii) isochrones for age and mass determination.

The only requirement for the input catalog is to have coordinates, and the colors required for target selection/extinction correction. Since the code is modular the format is free, although in this case the user must also provide the reading routine.

At the moment, the target selection criteria is based on the reddening-free Q parameter:

$$Q = (U - B) - 0.72 \times (B - V) \tag{1}$$

This combination of colors is unaltered by interstellar extinction if the latter follows the mean galactic law. Q increases monotonically towards later spectral types in the interval $\mathrm{Q} \in [-1.0, -0.4]$, corresponding to O3-A0 types (see Fig. 1). In Fig. 5 of Garcia et al. (2009) we showed that most known OB stars in IC 1613 have $\mathrm{Q} \leq -0.4$.

However, following its versatility philosophy, the code allows to easily modify the target selection criteria. For instance, instead of using only optical photometry, the code could be changed to allow a linear combination of more colors including GALEX and 2MASS data. Alternatively, the selection criteria could be based on fits to the spectral energy distribution made, for instance, with CHORIZOS (Maíz-Apellániz 2004). The latter method has been applied to M31 by Kang et al. (2009).

Finally, the user is free to use the isochrones of his/her choice, with the only requirement that it is stored in an IDL structure storing all the fields used by AUTOPOP.

2.2 Code core

The code consists of two main modules: automatic finding of geometrical groups in the sky, which we shall call OB associations, and the isochrone analysis of such associations.

The search of groups in the sky follows the Friends-of-Friends philosophy or Path-Linkage criterion, after Battinnelli (1991): two stars belong to the same association if their apparent separation is less than a given search distance (D_S). Given a target, the program looks for other stars within the search distance and registers them as members of the same association. The search is repeated for all the new members until no star is found within D_S from any of the peripheral stars. Besides the list of points with spatial coordinates, the code must also be provided with the search distance and the minimum number of members for a group to be considered so. These parameters are specific for different galaxies (or input catalogs), as we found they may be strongly dependent on the instrumental set-up (Garcia et al. 2010a).

Because the search of groups is run on a BMS candidate list, the resulting geometrical groups are considered OB associations. One may argue that there are systematics on this kind of codes (see Bastian et al. 2007) and that OB associations are actually hierarchical groups, a subset of the

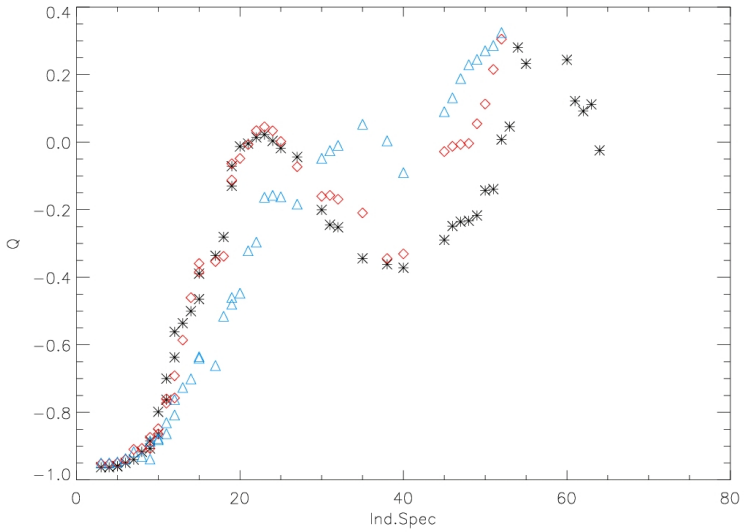

Figure 1: The variation of the reddening-free Q color with spectral type from O3 (Ind.Spec=3) to M0 (Ind.Spec=60) types. Colors were taken from Fitzgerald (1970). Different symbols represent different luminosity classes. For a given luminosity class, the relation between Q and spectral type is biunivocal up to Ind.Spec=20 (i.e., A0 types).

continuum of star formation only constrained by definition (see Elmegreen & Efremov 1998). This has been thoroughly discussed in Garcia et al. (2009, 2010a) and shall not be repeated here, but the conclusion is that physical or not, these groups are helpful in sorting out the content of blue massive stars in a galaxy.

The photometric analysis to derive masses and ages is made in the Q *vs* V_{dered} parameter space, V_{dered} being the observed stellar magnitude corrected from extinction. Such correction can be made thanks to the relation of Q with spectral type (therefore intrinsic color) for early-type stars. Massey, Waterhouse & DeGioia-Eastwood (2000) parametrized this relation for low-metallicity stars:

$$(B-V)_0 = -0.005 + 0.317 \times Q \tag{2}$$

using Kurucz' ATLAS9 Z=0.08$Z_\odot$ models (no such relationship exists for metallicity as low as IC 1613's). This equation will not hold if the reddening law deviates from the standard behaviour, but in this case a traditional correction in the B-V *vs* V diagram will not be valid either.

Even though photometric errors are larger in the Q *vs* V_{dered} parameter space compared to the traditional B-V *vs* V diagram because more colors are involved, we preferred the former because isochrones are more spread, and extinction is individually corrected towards each target. Finally, the code for automatic isochrone analysis basically finds which isochrones enclose the star and derives the evolutionary stellar properties from interpolation of the closest points of those isochrones.

3 Products from IC 1613 analysis

In short, AUTOPOP ingests a photometric catalog and returns a list of groups of likely OB stars, their ages, and masses for the members. The most direct application is a ready-to-use list for spectroscopy of the most massive members of a given galaxy. The output tables for OB association members and properties are VO friendly, hence can be easily cross-matched with lists of X-ray sources or other public catalogs, increasing the chances to find interesting targets.

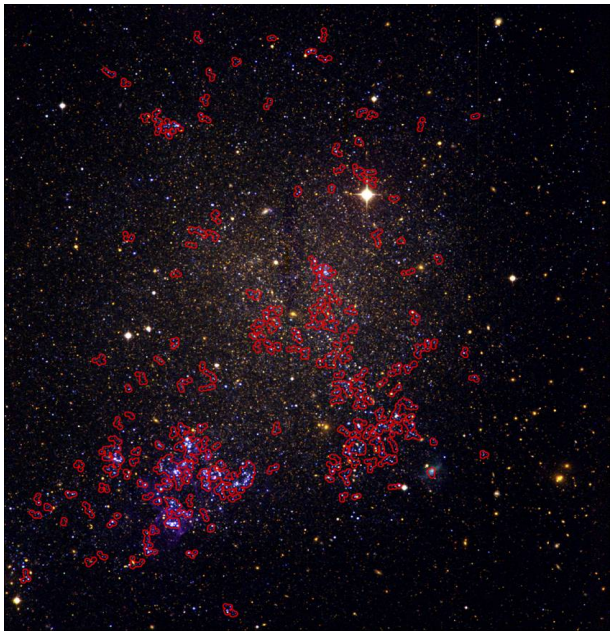

Figure 2: INT-WFC image of the optically brightest center of IC 1613. North is left and East is down. The RGB composition was made with the U- (blue), V- (green) and R-bands (red). The positions of the associations found in this work are marked in red.

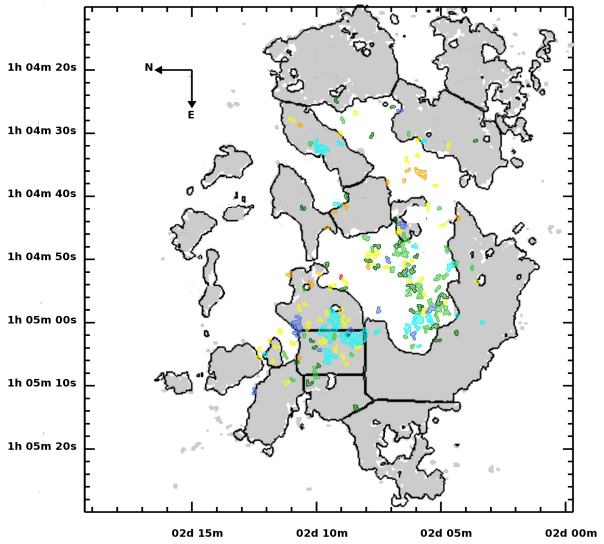

Figure 3: Relative distribution of neutral hydrogen and OB associations. The grey figures represent the distribution of H I in IC 1613 (adapted from Fig. 1 of Silich et al. 2006). Contours indicate the position of the associations, with colour indicating their ages (see text).

We have applied AUTOPOP to the analysis of the BMSs population of stars in IC 1613 (Garcia et al. 2009, 2010a). The input catalog of stars was built from observations of IC 1613 with the 2.5m Isaac Newton Telescope (INT) using the Wide Field Camera (WFC). The field of view ($34' \times 34'$) covers the whole galaxy with a resolution of 0.33"/pixel. The faint limit is V=25, and the maximum V-magnitude error for a V=23 star is 0.1mag. More details are provided in Garcia et al. (2009).

For the study of the association populations we used Lejeune & Schaerer (2001)'s basic grid of Z=0.004 ($0.2Z_{\odot}$) isochrones for single stars. The authors recalculated Charbonnel et al. (1993)'s stellar tracks with improved relations of photometric colors and stellar parameters.

The resulting OB associations are shown in Fig. 2. They group in the NE lobe of the galaxy, where IC 1613 displays spectacular giant H II shells. We find association ages ranging from $\log age[yr] =$ 5.9 to 7.7, usually with some spread. For each association, we provide its age as a colored contour in Fig. 3 (cyan $\log age[yr] = 5.9$, blue $= 6.2$, dark green $= 6.5$, light green $= 6.8$, yellow $= 7.1$, orange $= 7.4$, red $= 7.7$, violet $= 8.0$). There seems to be a galactic-scale age gradient following the NE direction, with the youngest members located in the NE lobe. This region, which also exhibits the largest age dispersion in the galaxy, is located in a density enhancement of neutral hydrogen (see Garcia et al. 2010a and Fig. 3). This fact suggests that star formation has proceeded in this region for an extended period of time, and that sequential star formation may be at work.

4 Summary and conclusions

The spectroscopic studies of OB stars in the Local Volume are now possible thanks to multi-object spectrographs on 10m-class telescopes. Such studies are driven by the need to understand the impact of metallicity on OB star evolution. It is necessary to optimize the selection of targets, since these observations are very expensive in observing time. AUTOPOP provides an optimal way of obtaining

potentially very interesting candidates.

Acknowledgements

Funded by Spanish MICINN under CONSOLIDER-INGENIO 2010, program grant CSD2006-00070, and grants AYA2007-67456-C02-01 and AYA2008-06166-C03-01.

References

Bastian, N., Ercolano, B., Gieles, M., Rosolowsky, E., Scheepmaker, R.A., Gutermuth, R., & Efremov, Y. 2007, MNRAS 379, 1302
Battinelli, P. 1991, A&A 244, 69
Charbonnel, C., Meynet, G., Maeder, A., Schaller, G., & Schaerer, D. 1993, A&AS 101, 415
Davidson, K., & Kinman, T.D. 1982, PASP 94, 634
Dodorico, S., & Dopita, M. 1983, in *Supernova Remnants and their X-ray Emission*, 101, 517
Dolphin, A.E., Saha, A., Skillman, E.D., et al. 2001, ApJ 550, 554
Elmegreen, B.G., & Efremov, Y.N. 1998, arXiv:astro-ph/9801071
Fitzgerald, M.P. 1970, A&A 4, 234
Garcia, M., Herrero, A., Vicente, B., Castro, N., Corral, L.J., Rosenberg, A., & Monelli, M. 2009, A&A 502, 1015
Garcia, M., Herrero, A., Castro, N., Corral, L., & Rosenberg, A. 2010a, A&A 523, A23
Garcia, M., et al. 2010b, in *The Ultraviolet Universe 2010*, eds. B. Shustov, A.I. Gomez de Castro and M. Sachkov, Ap&SS, in press
Herrero, A., Garcia, M., Uytterhoeven, K., Najarro, F., Lennon, D.J., Vink, J.S., & Castro, N. 2010, A&A 513, 70
Kang, Y., Bianchi, L., & Rey, S.-C. 2009, ApJ 703, 614
Kingsburgh, R.L., & Barlow, M.J. 1995, A&A 295, 171
Lejeune, T., & Schaerer, D. 2001, A&A 366, 538
Maíz-Apellániz, J. 2004, PASP 116, 859
Massey, P., Waterhouse, E., & DeGioia-Eastwood, K. 2000, AJ 119, 2214
Mokiem, M.R., de Koter, A., Vink, J.S., et al. 2007, A&A, 473, 603
Peimbert, M., Bohigas, J., & Torres-Peimbert, S. 1988, RMxAA 16, 45
Talent, D.L. 1980, Ph.D. Thesis
Tautvaišienė, G., Geisler, D., Wallerstein, G., Borissova, J., Bizyaev, D., Pagel, B.E.J., Charbonnel, C., & Smith, V. 2007, AJ 134, 2318

A photometric study of the Carina nebula region around WR 22

Brajesh Kumar[1,2], Jean Manfroid[1], Eric Gosset[1],
Gregor Rauw[1], and Manash R. Samal[2]

[1] Institut d'Astrophysique et de Géophysique, Université de Liège,
Allée du 6 Août 17, Bât B5c, 4000 Liège, Belgium
[2] Aryabhatta Research Institute of Observational Sciences, Manora Peak,
Nainital, 263 129, India

Abstract: We performed the first photometric observations of a field situated around WR 22 in the Carina nebula region. We present and discuss the preliminary results of the study.

1 Introduction

The Carina nebula (NGC 3372) in the Southern hemisphere, is one of the largest and brightest nebulae in our Galaxy. It provides a natural laboratory not only for the formation of the star clusters but also for the birth and the evolution of young and massive stars. To determine various properties of the stellar population in this region, extensive studies of several clusters and/or star concentrations have already been performed (Trumpler 14, 15 and 16; Collinder 228 and 232; Bochum 10 and 11, see Massey & Johnson 1993, Vazquez et al. 1996, Carraro & Patat 2001, DeGioia-Eastwood et al. 2001, Patat & Carraro 2001, Tapia et al. 2003, Carraro et al. 2004). This prominent structure is not as compact as some of the other galactic young clusters, but it provides a snapshot of the evolution of massive Population I stars and of their surroundings.

Here we deal with a less studied wide field ($34'$ x $33'$) around the very massive Wolf-Rayet binary WR 22 (α(J2000) = 10h 41m 17.5s, δ(J2000) = $-59^\circ\ 40'\ 36.9''$) located to the west side of the main part of the Carina nebula. Difficulties in the study of the Carina region arise from the differential extinction and the possibly peculiar reddening law (see Walborn 1995). This leads to some uncertainties on the derived distance. In this work, we adopt a distance of 2.7 kpc (DM = 12.15) and a colour excess E_{B-V} = 0.36 following Gosset et al. (2009).

2 Observations and data analysis

The photometric observations of the WR 22 field were obtained with the Wide Field Imager (WFI) instrument at the ESO/MPG 2.2m telescope at La Silla in May 2005 with a total exposure time of 3h 42m. The frames were taken through a set of U B V (R I)$_c$ Hα filters. The data were bias subtracted

and flat fielded using the IRAF `mscred` and `esowfi` packages. Zero points were estimated from the above mentioned photometric studies (Vazquez et al. 1996, DeGioia-Eastwood et al. 2001, Tapia et al. 2003, Carraro et al. 2004). To convert the WFI photometry into the standard Johnson-Cousins system, we used colour transformations derived from our observations of Landolt and Stetson standard fields, supplemented by the relations published by ESO on the WFI instrument website[1]. The Hα data were left in the natural system, with a zero-point arbitrarily defined by the R standards. To build the near-infrared (NIR) J, H, K colour-colour diagram, we have cross-correlated our photometric data with the 2MASS catalogue[2].

Figure 1: False colour image of the region around WR22. The RGB image was built by combining the U and B as the Blue channel, V as Green, and R, I, Hα as Red. The complex structure of the nebulosity is remarkable.

The same field was observed with the XMM-Newton observatory (Jansen et al. 2001) during seven

[1] http://www.eso.org/sci/facilities/lasilla//instruments/wfi/inst/zero-points/ColorEquations
[2] http://www.ipac.caltech.edu/2mass/index.html

pointings with exposure times of 10ks. In addition to the star WR 22 itself (see the study of Gosset et al. 2009), 42 X-ray sources were detected (Claeskens et al. 2011). Their positions have been cross-correlated with the list of sources detected in our photometric data in order to identify these X-ray sources.

3 Results

Figure 1 is a false color image that we built by combining the various WFI pointings. It illustrates the field covered by our photometry. Besides the large stellar population, the nebular component is particularly remarkable and highly structured.

In Fig. 2 we show the colour-magnitude diagram of all the sources in the field of view (having JHK counterparts), along with the main-sequence and pre-main sequence (PMS) isochrones from Siess, Dufour & Forestini (2000) for a distance of 2.7 kpc and an extinction giving E_{B-V} = 0.36. As can be seen many of the objects actually fall well above the main sequence, although there is probably a strong contamination by foreground stars. Most of the X-ray sources are found to be located above the main sequence, in agreement with the idea that these objects are most likely low-mass PMS stars with ages of a few million years or more distant objects. According to our photometry, the X-ray source #20 of Claeskens et al. (2010) has magnitudes V = 13.06, B−V = 1.41, U−B = −0.16, V−I = 1.86. These values are in good agreement with an O star reddened by $A_V \sim$ 4-5. This confirms the identification proposed by Claeskens et al. (2010). The identification for all the sources is in progress.

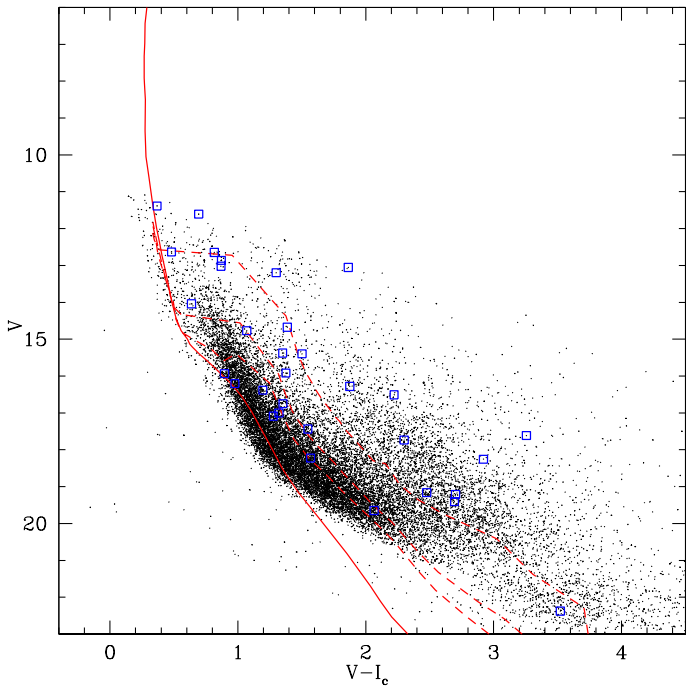

Figure 2: Colour-magnitude diagram of the WFI photometry for the region around WR22. The X-ray sources are highlighted by open square symbols. The PMS isochrones from Siess et al. (2000) are shown for the ages of 1Myr, 5Myr and 10Myr.

In Fig. 3 we show the R−Hα index as a function of the V−I_c colour. Large positive values of the R−Hα index indicate a strong emission in this line. To fix ideas, we draw a line representing the expected value of the index for main sequence stars (see Sung, Bessell & Lee 1997), but shifted by

about 0.3 magnitude. Therefore all the objects confirmed to belong to the Carina region, appearing over this line are almost surely Hα emitters. The red open square represents the location of the X-ray source #18 (Claeskens et al. 2010). Its R$-$Hα index amounts to 0.19 suggesting the source having Hα in emission; this confirms the identification reported by Claeskens et al. (2010) with an object exhibiting lines in emission from Hβ to Hδ.

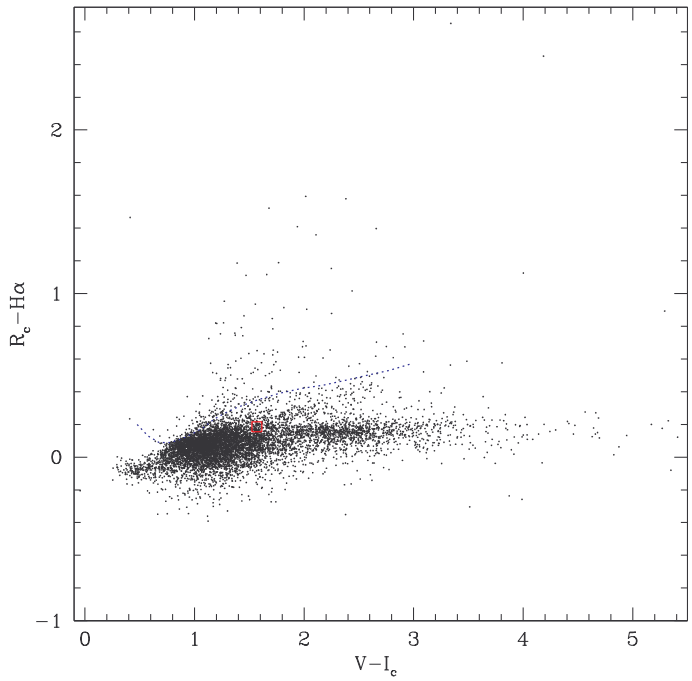

Figure 3: The R$_c-$Hα index is shown as a function of V$-$I$_c$. The dotted blue line (calibrated according to Sung et al. 1997) indicates the thresholds for Hα emitter candidates for the objects belonging to the Carina region. The counterpart of the X-ray source #18 (Claeskens et al. 2010) is highlighted by the red open square.

Fig. 4 shows the NIR colour-colour diagram for the studied region. This figure reveals a severe contamination of the cluster photometric data by the field stars. At the same time, it also shows a strong reddening gradient in the particular region. This suggests that we are observing a cluster at the edge of a molecular cloud, with some of the stars being located deeper inside the cloud. Whilst some of the X-ray sources have NIR counterparts that are consistent with a moderate reddening, a few X-ray selected objects are obviously subject to a rather substantial extinction.

4 Future work

As a next step, we will combine the NIR and WFI photometry to infer the reddening of individual sources and finally build a Hertzsprung-Russell diagram for the stellar population in this region allowing us to derive the age of the population and to identify the PMS stars. This photometry will further help in our on-going identification process of the different X-ray sources detected in this region.

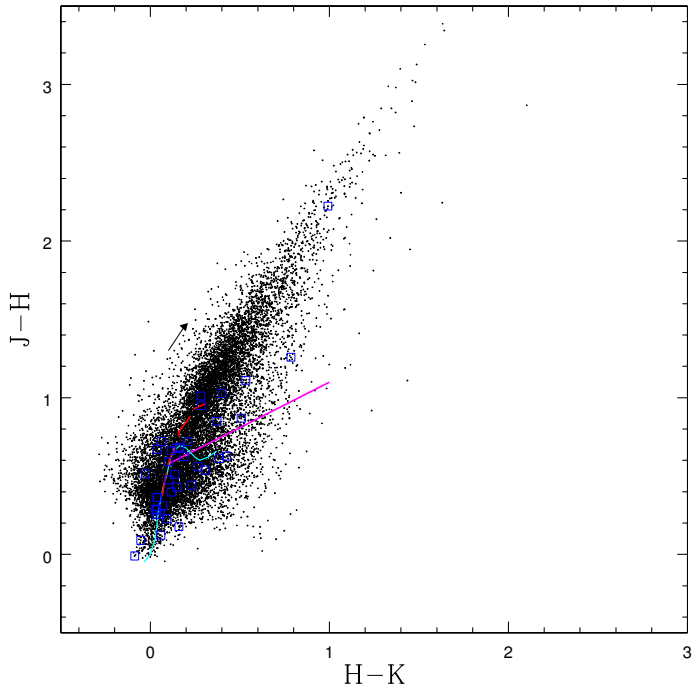

Figure 4: NIR colour-colour diagram of the studied region. The locus of the main-sequence and of the giant branch are shown by cyan and red curves, whilst the magenta straight line yields the locus of unreddened T Tauri stars as given by Meyer, Calvet & Hillenbrand (1997). The counterparts of the X-ray sources are highlighted by the blue open squares.

References

Carraro, G., & Patat, F. 2001, A&A, 379, 136
Carraro, G., Romaniello, M., Ventura, P., & Patat, F. 2004, A&A, 418, 525
Claeskens, J.-F., Gosset, E., Nazé, Y., Rauw, G., & Vreux, J.-M. 2011, A&A 525, A142
DeGioia-Eastwood, K., Throop, H., Walker, G., & Cudworth, K.M. 2001, ApJ, 549, 578
Gosset, E., Nazé, Y., Sana, H., Rauw, G., & Vreux, J.-M. 2009, A&A, 508, 805
Jansen, F., Lumb, D., Altieri, B., et al. 2001, A&A, 365, L1
Massey, P., & Johnson, J. 1993, AJ, 105, 980
Meyer, M.R., Calvet, N., & Hillenbrand, L.A. 1997, AJ, 114, 288
Patat, F., & Carraro, G. 2001, MNRAS, 325, 1591
Siess, L., Dufour, E., & Forestini, M. 2000, A&A, 358, 593
Sung, H., Bessell, M.S., & Lee, S.-W. 1997, AJ, 114, 2644
Tapia, M., Roth, M., Vázquez, R.A., & Feinstein, A. 2003, MNRAS, 339, 44
Vazquez, R.A., Baume, G., Feinstein, A., & Prado, P. 1996, A&A, 116, 75
Walborn, N.R. 1995, RevMexAA (Serie de Conferencias), 2, 51

Radiation-MHD models of elephant trunks and globules in H II regions

Jonathan Mackey[1,2*] and Andrew J. Lim[1]

[1] Dublin Institute for Advanced Studies, 31 Fitzwilliam Place, Dublin 2, Ireland

[2] Argelander Institut für Astronomie, Auf dem Hügel 71, 53121 Bonn, Germany

Abstract: We study the formation and evolution of pillars of dense gas, known as elephant trunks, at the boundaries of H II regions, formed by shadowing of ionising radiation by dense clumps. The effects of magnetic fields on this process are investigated using 3D radiation-magnetohydrodynamics simulations. For a simulation in which an initially uniform magnetic field of strength $|\mathbf{B}| \simeq 50\,\mu$G is oriented perpendicular to the radiation propagation direction, the field is swept into alignment with the pillar during its dynamical evolution, in agreement with observations of the "Pillars of Creation" in M16, and of some cometary globules. This effect is significantly enhanced when the simulation is re-run with a weaker field of $\simeq 18\,\mu$G. A stronger field with $|\mathbf{B}| \simeq 160\,\mu$G is sufficient to prevent this evolution completely, also significantly affecting the photoionisation process. Using a larger simulation domain it is seen that the pillar formation models studied in Mackey & Lim (2010) ultimately evolve to cometary structures in the absence of dense gas further from the star.

1 Introduction

The interstellar magnetic field in the Eagle Nebula (M16) was measured by Sugitani et al. (2007) using near infrared polarisation observations of background stars. They found that the field orientation within the massive pillars of gas and dust in M16 (Hester et al. 1996), known as the "Pillars of Creation", is aligned with the long axis of the pillars and with the UV radiation propagation direction, but misaligned with the ambient magnetic field (see Fig. 3 below). If the pillars have formed dynamically due to shadowing of ionising radiation (e.g. Williams, Ward-Thompson & Whitworth 2001; Lim & Mellema 2003) then it appears the field has been re-oriented by this process. Sugitani et al. (2007) suggest that this may constrain the ambient field strength in M16 because ionised gas pressure appears to dominate the dynamics. Here we test this suggestion and build on our earlier non-magnetised results (Macckey & Lim 2010, hereafter ML10) by using 3D radiation-magnetohydrodynamics (R-MHD) simulations to model the formation of pillars and globules due to shadowing of ionising radiation by pre-existing dense clumps.

A uniform grid, 2nd order accurate, finite volume code (see ML10) is used for the MHD calculations with a Roe-type Riemann solver (Cargo & Gallice 1997). The short characteristics ray-tracer is used to track direct monochromatic ionising radiation and the on-the-spot approximation for diffuse radiation. Radiative cooling is calculated explicitly for recombining hydrogen and using a cooling

*jmackey@astro.uni-bonn.de

Table 1: Simulation parameters for model R5, showing grid resolution (zones), domain coordinates in parsecs $(\mathbf{X}_{\rm min}, \mathbf{X}_{\rm max})$ relative to the radiation source which has monochromatic photon luminosity and photon energy as indicated. Clump positions, peak number density ($n_{\rm H}$), Gaussian scale radius (r_0) and total mass (M) are as indicated; the background magnetic field (in μG), number density ($n_{\rm H}$) and gas pressure (p_g) are similarly indicated.

Name	x	y	z	Further information.
Zones	384	256	256	Uniform Cartesian grid.
$\mathbf{X}_{\rm min}$	1.5	-1.5	-1.5	position in parsecs relative to the source.
$\mathbf{X}_{\rm max}$	6.0	1.5	1.5	position in parsecs relative to the source.
Source	0	0	0	$L_\gamma = 2 \times 10^{50}\,{\rm s}^{-1}$, $h\nu_0 - 13.6\,{\rm eV} = 5.0\,{\rm eV}$
Clump 1	2.30	0	0	$n_{\rm H} = 10^5\,{\rm cm}^{-3}$, $r_0 = 0.09\,{\rm pc}$, $M = 28.4\,{\rm M}_\odot$
Clump 2	2.75	0	0.12	$n_{\rm H} = 10^5\,{\rm cm}^{-3}$, $r_0 = 0.09\,{\rm pc}$, $M = 28.4\,{\rm M}_\odot$
Clump 3	3.20	0	-0.12	$n_{\rm H} = 10^5\,{\rm cm}^{-3}$, $r_0 = 0.09\,{\rm pc}$, $M = 28.4\,{\rm M}_\odot$
Background	$\mathbf{B}_0 = [0,$	$0,$	$53]$	$n_{\rm H} = 200\,{\rm cm}^{-3}$, $p_g = 1.38 \times 10^{-11}\,{\rm dyne\,cm}^{-2}$

curve for other elements, with neutral/molecular gas cooling treated very approximately by exponential cooling with cooling time $t_c = 10\,{\rm kyr}$ (see ML10, cooling model C2). This code has been extensively tested[1] and checked for consistency with previous work (e.g. Falle, Komissarov, & Joarder 1998; Lim & Mellema 2003; Mellema et al. 2006; Krumholz, Stone, & Gardiner 2007; Henney et al. 2009, ML10 and references therein).

2 Simulations

We have performed a number of 3D R-MHD simulations, to be presented in more detail in Mackey & Lim (2011). Here we present results from one of the simulations, denoted R5. This model consists of a monochromatic point source of ionising photons placed $2.3\,{\rm pc}$ from the nearest of three dense gas clumps (Gaussian density profiles) in a uniform background medium ($n_{\rm H} = 200\,{\rm cm}^{-3}$). Simulation parameters are described in Table 1; the same model was presented on a smaller simulation domain with zero field in ML10 but here a uniform magnetic field of $\mathbf{B} = [0, 0, 53]\,\mu{\rm G}$ is imposed in the initial conditions.

The evolution of dense gas over $400\,{\rm kyr}$ is shown in Fig. 1, where the initial field is horizontal and in the plane of the images. The evolution is broadly similar to that of the R-HD model in ML10 for the first $\sim 250\,{\rm kyr}$, but there are notable differences. Radiation-driven implosion ($t \sim 100\,{\rm kyr}$) is more pronounced along field lines than across them, leading to a flattened structure (cf. Henney et al. 2009); the narrow tail in the second panel is actually a sheet seen edge-on and the clumps are also flattened. Following this ($200 - 300\,{\rm kyr}$) magnetic pressure generates a stronger re-expansion and hence the pillar/globule is larger and has a lower density than the R-HD case. The re-expansion leads to fragmentation in this model ($t \gtrsim 400\,{\rm kyr}$), just beginning in the right-most panel. It is seen that the simulation ultimately evolves from being pillar-like (dense elongated structure) to a cometary globule (dense flattened head, low density neutral tail) in the absence of dense gas further from the star. We have confirmed that this is also true when the model is run with zero magnetic field (i.e. identical to model 17 in ML10 but with a larger simulation domain).

[1]For more information, including test results, see `http://www.astro.uni-bonn.de/~jmackey/jmac/`.

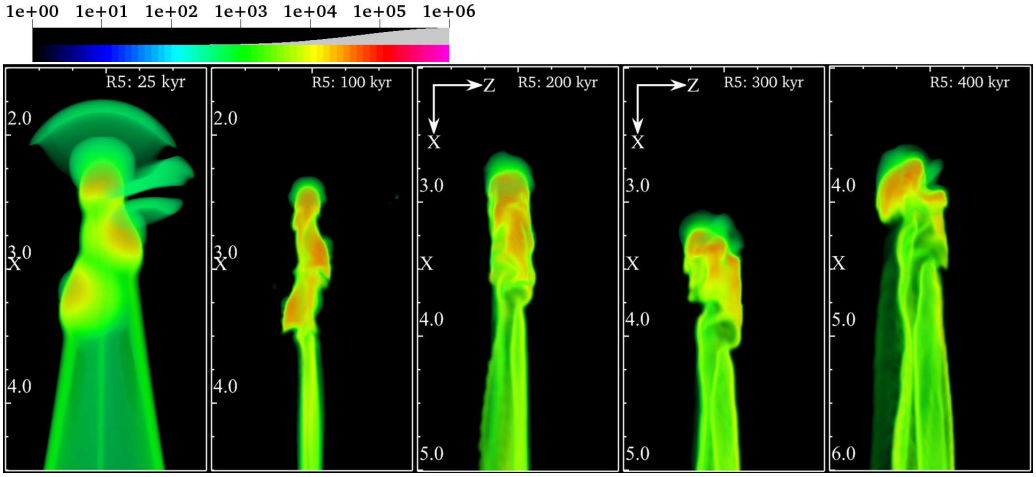

Figure 1: Volume-rendered images of gas density in the 3D R-MHD simulation R5 described above, shown at times $t = 25,\ 100,\ 200,\ 300,\ 400\,\mathrm{kyr}$. Tick-marks at $0.25\,\mathrm{pc}$ intervals show the physical scale (numbers refer to the tick-marks immediately below them). The logarithmic number density scale (cm^{-3}) is shown above, with the opacity function used for image generation as the grey curve (gas with $n_\mathrm{H} \lesssim 10^3\,\mathrm{cm}^{-3}$ is transparent). Only part of the simulation domain is shown in each panel.

3 Discussion

The projected magnetic field orientation was calculated by a density–weighted integration of "Stokes parameters" Q and U for the perpendicular magnetic field along the lines of sight (LOS) (cf. Arthur et al. 2010):

$$\langle Q \rangle = \int_{z=0}^{\infty} \min[n_\mathrm{H}(z), n_\mathrm{max}] \frac{B_x^2 - B_y^2}{\sqrt{B_x^2 + B_y^2}} dz\,, \quad \langle U \rangle = \int_{z=0}^{\infty} \min[n_\mathrm{H}(z), n_\mathrm{max}] \frac{2 B_x B_y}{\sqrt{B_x^2 + B_y^2}} dz\,, \quad (1)$$

with $n_\mathrm{max} = 2.5 \times 10^4\,\mathrm{cm}^{-3}$. Here $x - y$ is the image plane and z is distance along the LOS (i.e. observer rather than simulation coordinates). The projected field is then recovered from $\langle Q \rangle$ and $\langle U \rangle$ using trigonometric relations.

Formally this has units of $\mu\mathrm{G}\,\mathrm{cm}^{-2}$, but the normalisation is irrelevant for the orientation. The projected field orientation is over-plotted on column density maps in Fig. 2, projected such that the initial field is fully in the image plane and vertical. At $t = 250\,\mathrm{kyr}$ the clumps have undergone significant dynamical evolution and the pillar-like structure is slowly being flattened due to the rocket effect. The magnetic field, while relatively unaffected in ionised gas and the low density tail region, has clearly been dragged into alignment with the pillar in dense gas due to the pillar's acceleration away from the star. At $400\,\mathrm{kyr}$ only a flattened cometary globule remains, but the field is even more strongly aligned with the acceleration direction. This clearly shows that an initially perpendicular field is swept into alignment with the pillar during its dynamical evolution, and that this alignment remains once the structure evolves to a cometary morphology. This is in agreement with the observations of the pillars in M16 (reproduced here in Fig. 3, Sugitani et al. 2007) and some cometary globules (e.g. Bhatt, Maheswar, & Manoj, 2004) which also have the field aligned with the cometary tail.

The behaviour of the same simulation with a magnetic field $3\times$ weaker (R2) and $3\times$ stronger (R8) is rather different however (to be discussed in more detail in Mackey & Lim 2011). For R2 with $B \simeq 18\,\mu\mathrm{G}$ the field is more easily deformed by photoionisation–induced gas motions and the alignment is even stronger, whereas for R8 with $B \simeq 160\,\mu\mathrm{G}$ the field is dynamically dominant and barely changes from its initial perpendicular state. This is shown in the right panel of Fig. 3 where the ratio of the volume averaged field parallel and perpendicular to the radiation propagation

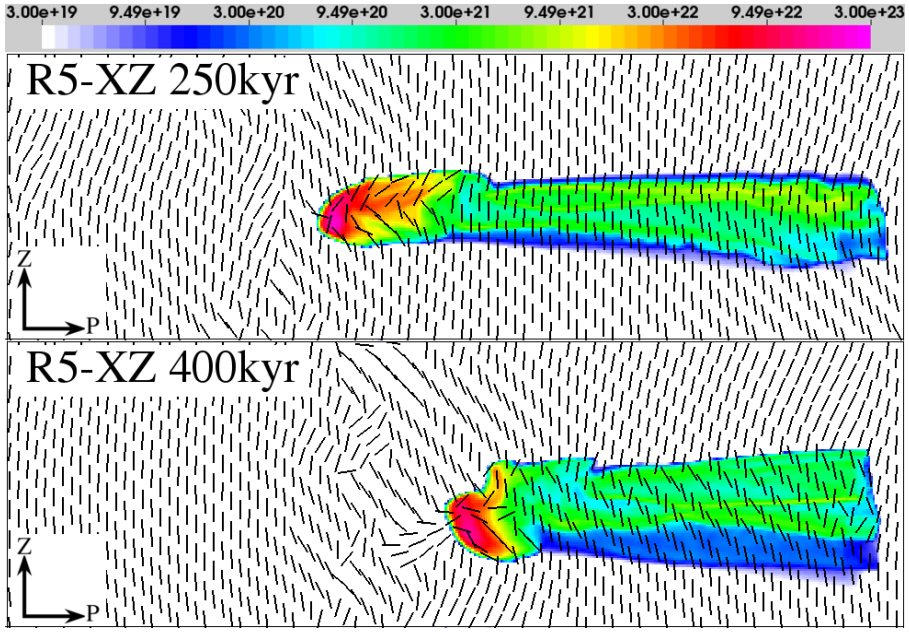

Figure 2: Column density (colour scale in cm^{-2}) and projected magnetic field (lines show orientation only) for the R5 simulation at $250\,\mathrm{kyr}$ (above) and $400\,\mathrm{kyr}$ (below). The projection LOS is $\hat{n} = \hat{x}\sin(20°)+\hat{y}\cos(20°)$ in the simulation coordinate system, so the initial magnetic field ($\mathbf{B} = 53\hat{z}\,\mu\mathrm{G}$) is vertical and $\perp$ to the LOS. The horizontal axis labelled $\mathbf{P}$ is therefore $\hat{P} = \hat{x}\cos(20°) - \hat{y}\sin(20°)$ i.e. a $20°$ rotation from the x-axis about the z-axis.

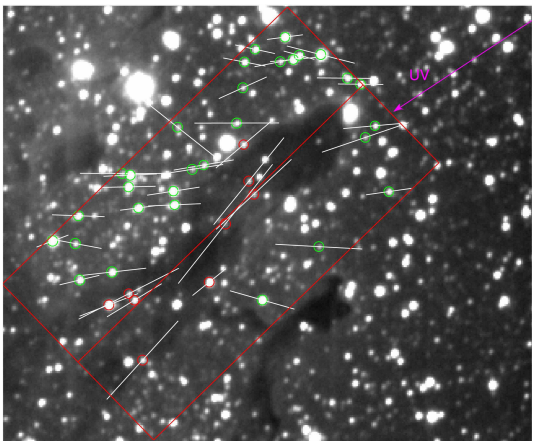

Figure 3: Figure 9b from Sugitani et al. (2007) showing near-IR absorption polarimetry observations of the magnetic field orientation in the central pillar in M16 (© the Astronomical Society of Japan; used with permission). North is to the top, East to the left, and the image width is $\simeq 2'.5$.

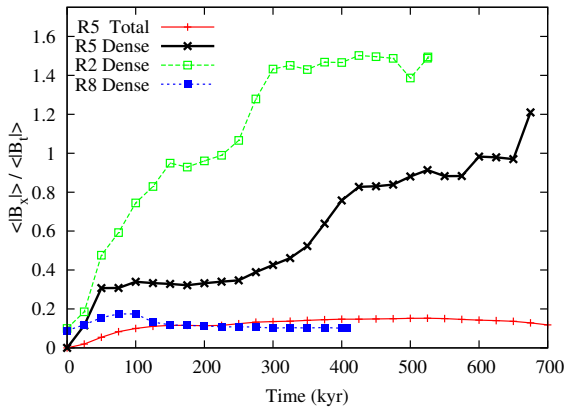

Figure 4: Ratio of volume-averaged parallel field $\langle|B_x|\rangle$ to perpendicular field $\langle\sqrt{B_y^2+B_z^2}\rangle$ as a function of time in simulations R2, R5, and R8. Red line: average of all cells (R5); Black: average of only dense cells with $n_\mathrm{H} > 5000\,\mathrm{cm}^{-3}$ (R5); Green: simulated with $|\mathbf{B}|$ $3\times$ weaker (R2); Blue: with $|\mathbf{B}|$ $3\times$ stronger (R8).

direction ($\hat{x}$) are plotted as a function of time for R2, R5, and R8. The evolution of dense gas with $n_{\rm H} > 5000\,{\rm cm}^{-3}$ is shown for all three models, and for the full simulation volume only for R5 (R2 and R8 are very similar). It is seen that while the ratio does not evolve significantly when averaged over the full simulation volume, in dense gas the situation is very different. For R5 the parallel field increases rapidly during the implosion phase and there is a subsequent slower increase during the acceleration phase to roughly equal field strength in both components. This trend is stronger for the weak field model R2, whereas for the strong field model R8 the field orientation remains almost constant throughout the simulation. This difference between the weaker and stronger field simulations is larger than was found by Henney et al. (2009) and deserves further investigation.

4 Conclusions

The results presented here show that both radiation-driven implosion and acceleration of clumps by the rocket effect tend to align the magnetic field with the radiation propagation direction in dense neutral gas. As was suggested by Sugitani et al. (2007), the effectiveness of this alignment is dependent on the initial field strength. For simulations which have similar gas densities and pressures to conditions in M16, we have shown that a magnetic field of strength $\sim 160\,\mu$G is sufficient to prevent any significant field reorientation. These results suggest that an ambient field of $|\mathbf{B}| < 160\,\mu$G (and more likely $|\mathbf{B}| \sim 50\,\mu$G) is required to explain the observed field configuration in the M16 pillars if the pillars formed via the mechanism we are modelling. Detailed R-HD models have recently been performed with dynamic initial conditions (Gritschneder et al. 2010) rather than the initially static models of ML10, allowing a potentially more realistic comparison with observations. Addition of magnetic fields to their simulations would be very useful to assess how significantly a non-uniform initial magnetic field will impact on the results presented here.

Acknowledgements

JM acknowledges funding for this work from the Irish Research Council for Science, Engineering and Technology; from the Dublin Institute for Advanced Studies; and from Science Foundation Ireland. AJL's work has been funded by a Schrödinger Fellowship from the Dublin Institute for Advanced Studies. The authors wish to acknowledge the SFI/HEA Irish Centre for High-End Computing (ICHEC) for the provision of computational facilities and support. Fig. 9b from Sugitani et al. (2007) © The Astronomical Society of Japan; reproduced with permission.

References

Arthur S. J., Henney W. J., Mellema G., De Colle F., Vázquez-Semadeni E., 2010, MNRAS, submitted.
Bhatt, H. C., Maheswar, G., & Manoj, P. 2004, MNRAS, 348, 83
Cargo, P., & Gallice, G. 1997, Journal of Computational Physics, 136, 446
Falle, S., Komissarov, S., & Joarder, P. 1998, MNRAS, 297, 265
Gritschneder, M., Burkert, A., Naab, T., & Walch, S. 2010, ApJ, 723, 971
Henney, W. J., Arthur, S. J., de Colle, F., & Mellema, G. 2009, MNRAS, 398, 157
Hester, J. J., Scowen, P. A., Sankrit, R., et al. 1996, AJ, 111, 2349
Krumholz, M., Stone, J., & Gardiner, T. 2007, ApJ, 671, 518
Lim, A., & Mellema, G. 2003, A&A, 405, 189
Mackey, J., & Lim, A. J. 2010, MNRAS, 403, 714
Mackey, J., & Lim, A. J. 2011, in preparation
Mellema, G., Iliev, I., Alvarez, M., & Shapiro, P. 2006, New Astronomy, 11, 374
Sugitani, K., Watanabe, M., Tamura, M., et al. 2007, PASJ, 59, 507
Williams, R., Ward-Thompson, D., & Whitworth, A. 2001, MNRAS, 327, 788

The enigmatic open cluster NGC 7419*

Amparo Marco[1] and Ignacio Negueruela[1]

[1] DFISTS. EPS. University of Alicante. Apdo.99. E-03080. Alicante (Spain)

Abstract: We determine the distance and the age of the open cluster NGC 7419 using accurate photometry and spectroscopy. We analyze spectra for a great number of members; concluding that NGC 7419 has one of the highest Be fractions among Galactic open clusters. We also confirm that the cluster contains five red supergiants but there are no blue supergiants. Both effects may be related to fast rotation, but high Be content and high RSG content do not always go together.

1 Introduction

The heavily reddened young open cluster NGC 7419 could hold the key to our understanding of the effects of rotation on the evolution of massive stars, as it is claimed to present several unusual characteristics.

Based on photometric searching techniques, Pigulski & Kopacki (2000) determined a Be fraction of $36 \pm 7\%$, which would be the highest for any Galactic open cluster. In addition, the cluster contains five red supergiants (Beauchamp, Moffat & Drissen 1994), though no blue object looks bright enough to be a supergiant. The red to blue supergiant ratio of $5/0$ is very different from expectations from current theoretical models and the observed ratios in other Galactic clusters. The very high fraction of Be stars and extremely low ratio of blue to red supergiants are predicted by current theoretical models to occur only in very low metallicity environments. Three previous photometric studies of NGC 7419 have used UBV photometry. The U magnitudes show average differences of several tenths of magnitude between the different works, rendering the parameters determined very insecure.

Here, we present Strömgren photometry and multi-epoch spectroscopy of NGC 7419. We are able to confirm the extremely high fraction of Be stars and the absence of any blue supergiant. Our extended dataset, which includes for the first time accurate spectral types for the brightest members, will allow a better determination of the extinction law and cluster parameters.

2 Observations

Observations of NGC 7419 were conducted with the 2.6-m Nordic Optical Telescope (La Palma, Spain), on 2004 October 2^{nd} to 4^{th} (poor weather), and again on 2005 October 3^{rd} to 5^{th} (photometric weather). The telescope was equipped with the imager and spectrograph ALFOSC. We obtained

*Partially based on observations collected at the Nordic Optical Telescope and the William Herschel Telesope (La Palma, Spain) and at the 1.93-m telescope at Haut Provence Observatory (France)

uvby observations of the cluster with a field of view of $6.3\,' \times 6.3\,'$ and secondary stars in several open clusters (Marco & Bernabeu 2001). We also took intermediate resolution spectra of the brightest early-type cluster members with ALFOSC grism #16 and low resolution spectra of other objects with grisms #7 and #14. We also obtained slitless spectroscopy of the field, by combining the low resolution grism #4 with the Bessell *R*-band filter. Slitless fields were taken at three different orientations, in order to minimise source overlapping. These observations were complemented by low resolution spectroscopy of some of the brightest Be candidates taken in July 2001 with the 1.93-m telescope at Haute Provence Observatory (France) and the Carelec spectrograph, and spectra of the red supergiants taken with William Herschel Telescope and ISIS. A preliminary report on the observations from 2001 and 2004 was presented in Negueruela et al. (2007).

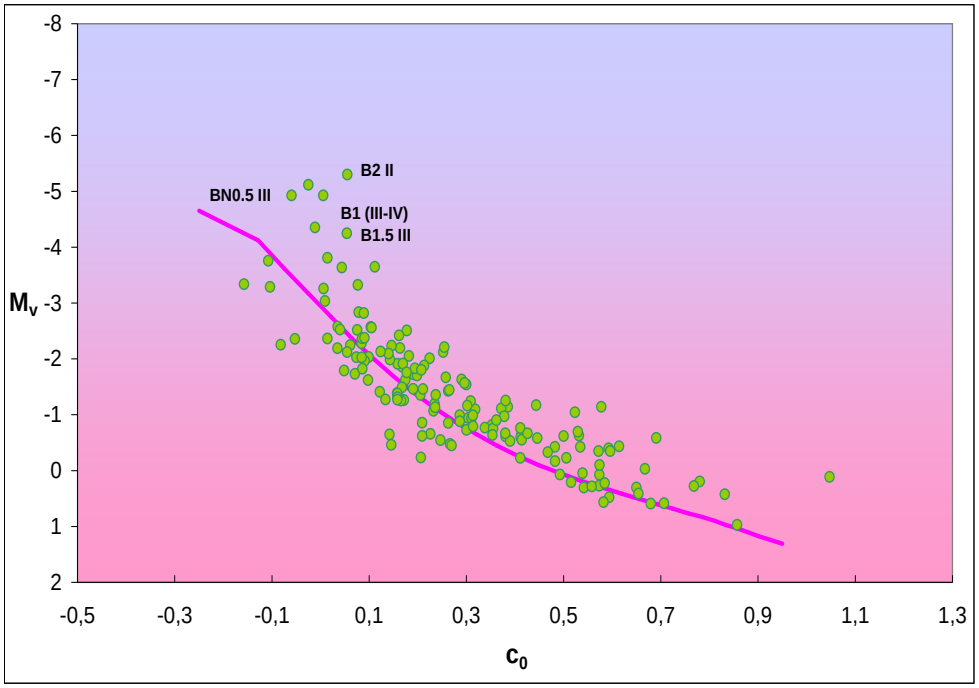

Figure 1: Observational HR diagram for the open cluster NGC 7419 based on our Strömgren photometry.

3 Results

We have carried a complete photometric and spectroscopic study of the open cluster NGC 7419. We have used Strömgren photometry for building the HR diagram. The use of this photometry which allows a more accurate determination of the parameters of the cluster, has never been tried at high reddenings. In spite of the $A_V \approx 5$ for NGC 7419, the transformation to the standard system seems to have worked. The M_V/c_0 diagram (Figure1) shows the expected shape and values. There is very good agreement between spectral types and position in the HR diagram. Objects close to the main-sequence turn-off have spectral types B1IV-V, suggesting an age in the $10-15$ Myr range. This is also

in good agreement with the determination of 14 ± 2 Myr by Beauchamp et al. (1994). The spectral types, however, are too early for the age of 22.5 ± 3.0 Myr given by Joshi et al. (2008). The fit of the ZAMS to our data gives a value of the distance modulus of 13.0 ± 0.2. In Figure 2 we display spectra of the brightest blue cluster members. The spectral types are in rather good agreement with those estimated by Caron et al. (2003) from *I*-band spectra. The most luminous stars have spectral types B2 II and BN0.5 III (this is likely a blue straggler).

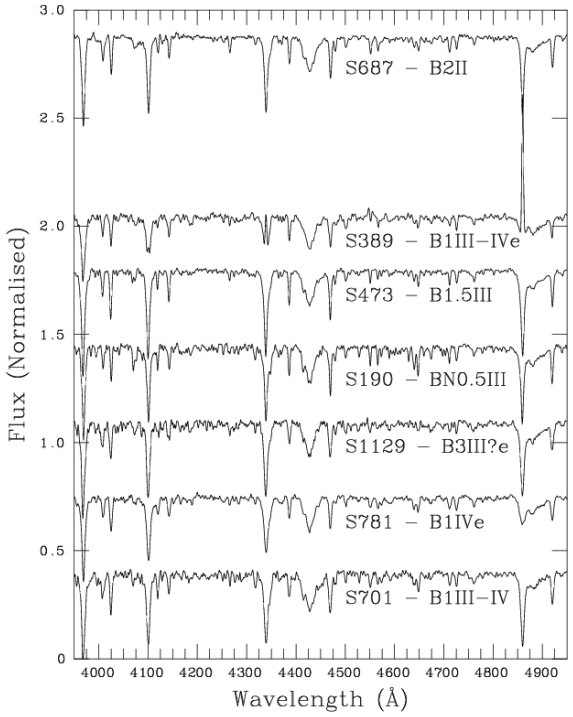

Figure 2: Classification spectra of the brightest blue cluster members. Nomenclature is taken from Beauchamp et al. (1994).

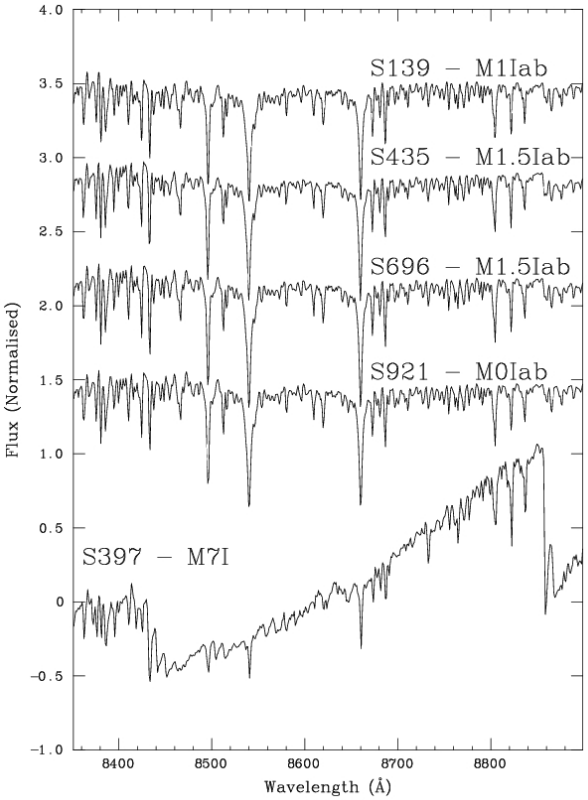

Figure 3: Spectra of the five red supergiants in NGC 7419, in the region of the Ca II triplet.

These values confirm that there are no blue supergiants in NGC 7419. Given the small number of blue stars above the main sequence turn-off, the presence of 5 red supergiants (Figure 3) represents a puzzle for evolutionary models, as the RSG phase is believed to be short.

We have detected 18 Be stars in NGC 7419. Among the photometric candidates of Pigulski & Kopacki (2000), we observe definitely in absorption two Be stars (one of them was losing its envelope in 2001). For the faintest candidates, we cannot confirm nor dismiss their Be status. These results confirm that NGC 7419 has one of the highest Be fractions among Galactic open clusters. We detect clear variability in the emission characteristics of several Be stars. In Figure 4, we show the spectra taken in different epochs for one Be star. This variability confirms that these objects are classical Be stars and not Herbig Be stars, as speculated by Subramaniam et al. (2006).

NGC 7419 is definitively younger ($10 - 15$ Myr) than the other two well known Be-rich clusters in the Galaxy, NGC 663 and NGC 3766, which are both 25 Myr old.

Several spectra seem to show evidence of nitrogen enhancement. This could be related to fast rotation. Unfortunately, our spectra lack resolution for model atmosphere fits and abundance determination. The high Be fraction may also be related to fast rotation. However, high Be content and high RSG content do not always go together. NGC 663 has five blue supergiants and no RSGs in its core.

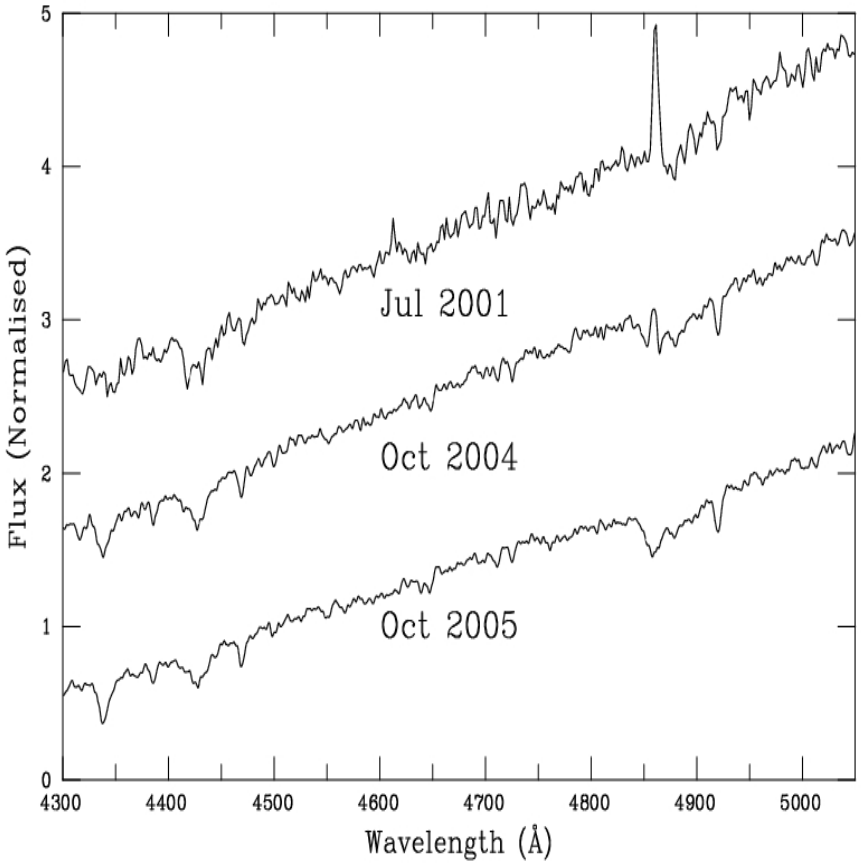

Figure 4: Spectra of the Be star S781 taken at different epochs and showing the progressive disappearence of emission characteristics.

Acknowledgements

This research is partially supported by the MEC under grants AYA2008-06166-C03-03 and CSD2006-70. This research has made use of the Simbad database, operated at CDS, Strasbourg (France) and the WEBDA database.

References

Beauchamp, A., Moffat, A.F.J., & Drissen L., 1994, ApJS, 93, 187
Caron, G., Moffat, A.F.J., St-Louis, N., Wade, G.A., & Lester, J.B. 2003, AJ 126, 1415
Joshi, H., Kumar, B., Singh, K.P., Sagar, R., Sharma, S., Pandey, J.C. 2008, MNRAS 391, 1279
Marco, A., & Bernabeu, G. 2001, A&A 372, 477
Negueruela, I., Marco, A., Motch, C., & Herrero, A. 2007, ASPC 361, 472
Pigulski, A., & Kopacki, G. 2000, A&AS 146, 465
Subramaniam, A., Mathew, B., Bhatt, B.C., & Ramya, S. 2006, MNRAS 370, 743

X-shooter, NACO, and AMBER observations of the LBV Pistol Star *

C. Martayan[1,2], R. Blomme[3], J.-B. Le Bouquin[4], A. Merand[1], G. Montagnier[1], F. Selman[1], J. Girard[1], A. Fox[1], D. Baade[5], Y. Frémat[3], A. Lobel[3], F. Martins[6], F. Patru[1], T. Rivinius[1], H. Sana[7], S. Stefl[1], J. Zorec[8], and T. Semaan[2]

[1] ESO, Alonso de Cordova 3107 Vitacura, Santiago, Chile

[2] GEPI, Observatoire de Paris, place Jules Janssen 92195 Meudon Cedex, France

[3] Royal Observatory of Belgium, 3 avenue circulaire, 1180 Brussel, Belgium

[4] Laboratoire d'Astrophysique de Grenoble, 38400 Saint-Martin d'Hères, France

[5] ESO, Karl-Schwarschild-Str. 2, Garching bei Muenchen, Germany

[6] GRAAL - UMR5024 Université de Montpellier II - CC 72 34095 Montpellier Cedex 05 FRANCE

[7] Universiteit van Amsterdam Sterrenkundig 1090 GE Amsterdam The Netherlands

[8] Institut d'Astrophysique de Paris, UMR7095 CNRS, Université P& MC, 98bis boulevard Arago, 75014 Paris, France

Abstract We present multi-instrument and multi-wavelength observations of the famous LBV star Pistol Star. These observations are part of a larger program on early O stars at different metallicities. The Pistol Star has been claimed to be one of the most massive star known, with 250 solar masses. We present preliminary results based on X-shooter spectra, as well as observations performed with the VLTI-AMBER and the VLT-NACO adaptive optics. The X-shooter spectrograph provides simultaneously a spectrum from the UV to the K-band with a resolving power of $\sim$15000. The preliminary results obtained indicate that Pistol Star has similar properties to η Car, including shells of matter, but is also a binary.

1 Introduction

LBV stars are exceptional transition objects in the stellar evolution of massive stars. η Car is the emblematic object of this category. It is now postulated that this kind of star could be a possible aborted supernova (SN). In all cases, they present a special interest for the stellar evolution theory and models because they have strong winds, and asymmetries in their structure, are very luminous at the Eddington limit or above. According to Groh et al. (2009), 2 kinds of "LBV-phases" could exist: the strong variable LBV with S-Dor variability that could be near critical rotators, and the group of dormant LBV with less variability like P-Cygni. Moreover, the progenitors of various supernova

*Based on ESO runs 85.D-0182A, 085.D-0625AC

were LBVs, including SN2006jc (Foley et al. 2007) and SN2006gy (Smith et al. 2007). This direct evolution from LBV to SN, without passing through the WR phase is not understood yet (Smith et al. 2007) but could lead to the ultra-powerful pair-instability SN.

2 Observations

The observations are spread over several months: 12/2009, 05-06-09/2010. Early O stars were observed with X-shooter: BRRG56, [ELS2006]N11-026, [ELS2006]N11-029 in the LMC. These stars were selected as they are expected to be among the earliest O stars in the LMC. BRRG56 is classified as an O2 star. They show few absorption lines and several emission lines. In the Galaxy, the brightest known O star [BSP2001]8 (Martins et al. 2008) and one of the most massive claimed stars, the LBV Pistol Star with 250 $M_{\odot}$, were observed with X-shooter. In addition, the Pistol Star was partially observed with the VLTI-AMBER using the UTs and with the VLT NACO-AO assisted imager.

2.1 Brief description of instruments

Three instruments were used to probe the environment of Pistol Star at different spatial scales, to study the nature of Pistol Star itself, and to obtain some parameters/properties of its surrounding nebula.

The VLT-X-shooter (D'Odorico et al. 2006): it is the first 2nd generation instrument and is a very efficient echelle spectrograph. It has a large simultaneous wavelength coverage from the near UV to the K-band, with three different arms. The UVB arm allows to make observations in the $\lambda\lambda$ 290 to 600nm range, the VIS arm from $\lambda\lambda$ 535 to 1050nm, and the NIR arm from $\lambda\lambda$ 980 to 2500nm. The resolving power of each arm is defined by the slits used, in the UVB arm from 3300 to 9100, in the VIS arm from 5400 to 19000, in the NIR arm from 3500 to 11500.

The VLT-NACO (Lenzen et al. 2003, Rousset et al. 2003) is an adaptive optics assisted imager in the wavelength range 1-5 microns. It allows the scan of spatial scales from several arcseconds down to 20-15mas. The observations were performed with the K, Lp, and NB4 filters.

The VLTI-AMBER (Petrov et al. 2007) is a near-infrared, multi-beam interferometric instrument, that combines up to 3 telescopes for the VLTI at ESO, sensitive to spatial scales from 20 to 3 mas. The observations of Pistol Star were challenging because this star (K$\sim$8 at the time of the observation) is the faintest object observed at the VLTI with a UTs triplet and at the limit of AMBER capabilities, while at this magnitude the fringe tracker FINITO cannot be used.

2.2 VLT-X-shooter spectroscopy for the Pistol Star

This section presents very preliminary results coming from X-shooter spectra. The data reduction and analysis are still in progress. The resolutions used are: R = 4000 in the UVB arm, R = 6700 in the VIS arm, and R = 11500 in the NIR arm. Two exposures of 3000s were taken in the UVB and VIS arms, and about 100 exposures of 50s in the NIR arm. A representative set of UVB, VIS, and NIR frames is shown in Fig. 1. The first quick-look at the spectra indicates that:

- in the last 2 orders of the UVB arm, a very faint object of V$\sim$27 is detected. Looking at the NACO image it could correspond to an object at 2.8" west-side of Pistol Star. This object will provide information about the extinction in that part of the sky.

- in the VIS arm, Pistol Star appears in the last 5 red orders, i.e at the 770-1050nm wavelength range. It is not visible in the bluest orders, because Pistol Star is highly extincted by its circumstellar nebulosity. Up to now no spectrum bluer than 1000nm has been obtained of Pistol Star. The study of the available lines in that range will help us to better understand/classify the star by providing more

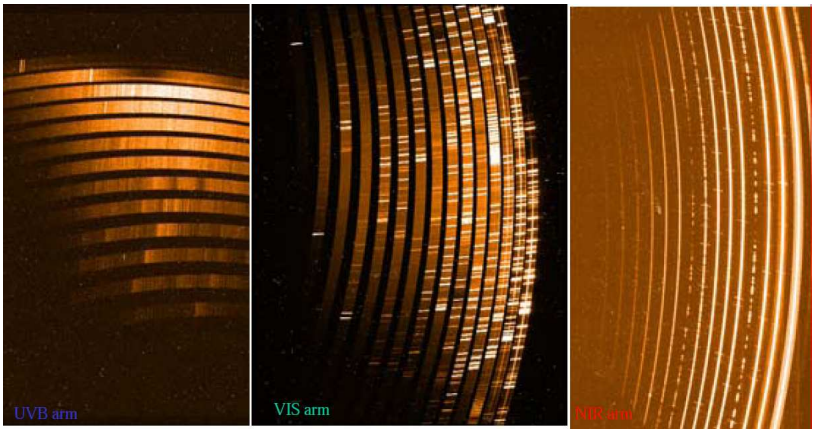

Figure 1: Snapshots of the 3 X-shooter arms of Pistol Star observations. Left: UVB arm (290-600nm), middle: VIS arm (525-1050nm), right: NIR arm (980-2500nm). One can see the spectra of Pistol Star mainly in the NIR arm as well as in the reddest orders of the VIS arm. Another very faint object can be seen in the UVB arm.

constraints on physical parameters such as the temperature. Some of the lines seem to show a double-peak profile. This could be related to a potential binarity or shell signatures. Some other lines also show P-Cygni profile.

- in the NIR arm, Pistol Star is easily seen in each order, and in the VIS arm, there are emission lines due to the nebulosity surrounding the central star. Some of them, such as Brγ show P-Cygni profile with a faint blue absorption component and a red strong emission peak corresponding to the shell of ejected matter. A small extract of the NIR spectrum near the Brγ line with lines of [Fe II], Fe II, Mg II, Na I and He I, is shown in Fig. 2. Several lines seem also to show a double-peaked structure indicating that possibly there is spherical expansion of the matter (as already reported by Figer et al. 1999) or/and a companion. Moreover, the EW of the lines are variable when they are compared with Figer et al. (1999) measurements, indicating a possible evidence of a variability cycle of Pistol Star. Is it related to the shells and matter-ejection, pulsations, and/or to a companion? Further observations and the study of the available lines in the VIS and NIR arms will help to obtain more information on the star(s) and on the circumstellar material/shell(s).

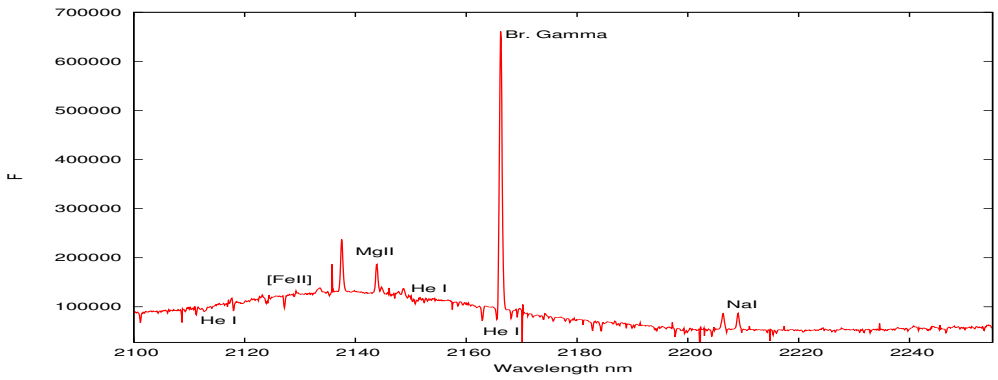

Figure 2: Small extract of the X-shooter NIR spectrum of Pistol Star in the region close to the Brγ line. One can see the P-Cygni profile of the Brγ line.

2.3 Pistol Star and the surrounding stars with the adaptive optics NACO.

The NACO images in Fig. 3 clearly show that the 2 “B” and “C” 2MASS stars are 2 groups of stars within few arcseconds. The “E” star corresponds to the Mira V4644 Sgr and seems to be surrounded by a shell. The “D” star corresponds to WR 102e. The “A” star corresponds to Pistol Star. The star in the right top of the bottom part of Fig. 3 shows the NACO PSF. One can see several stars close to the central system of Pistol Star at less than 0.4”. Moreover it seems that Pistol Star is surrounded by different concentric shells of matter. The largest one roughly measures 0.07pc (Pistol Star is at least at 7.7kpc). As explained in the previous section, the faint spectroscopic double-peaked profile could correspond to the ringlike signature of spherical expansion.

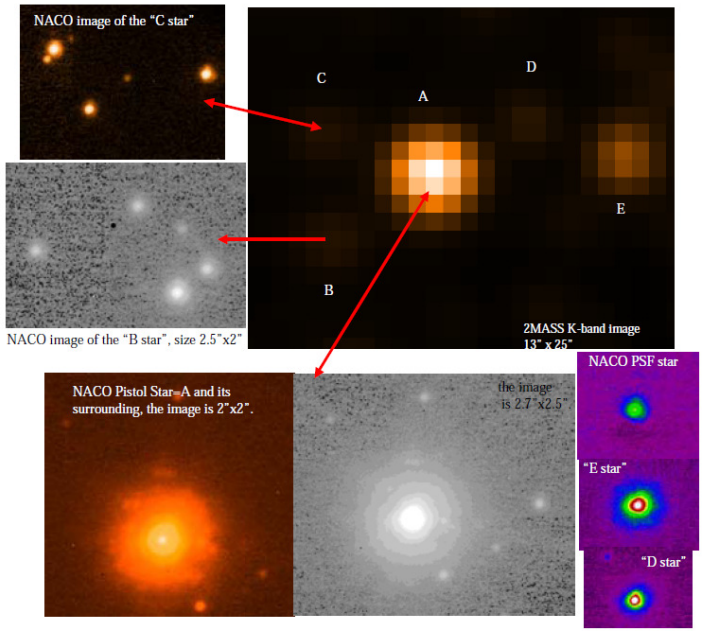

Figure 3: NACO observations of Pistol Star and the stars in its vicinity. The top panel shows the 2MASS image and extracts of the NACO K band image. The bottom panel shows Pistol Star with inner small shells of matter in K-band. The right column shows different stars including a PSF reference star.

2.4 Possible binarity of Pistol Star (VLTI-AMBER)

With these VLTI-AMBER observations we were able to scan smaller scales than with NACO. Moreover, the NACO, VLTI-AMBER, and X-shooter observations have the K-band in common that will be used to better understand/constrain the system of Pistol Star. From the VLTI-AMBER observations in K-band (the triplet UT-2-3-4 was used), it rises that there is a departure from single-star morphology. A companion of the Pistol Star has been detected with a rough separation of 10-50 mas ($\sim$80-400 AU). The visibility measurements are the best fitted by a model of a companion, while other models (disks, knot of the nebulosity) are not able to properly fit them. Figure 4 shows the corresponding $\chi 2$ map of the visibility of the VLTI-AMBER observations indicating in the framework of a companion-model, the companion position. The data reduction and analysis are in progress but this result suggests that as in the η Car case (Weigelt et al. 2007), the evolution and the understanding of the Pistol Star structure must go through a binary channel. Moreover, the VLTI observations suggest a minimum orbital period of several decades (unless, as in η Car, the eccentricity is large so that the

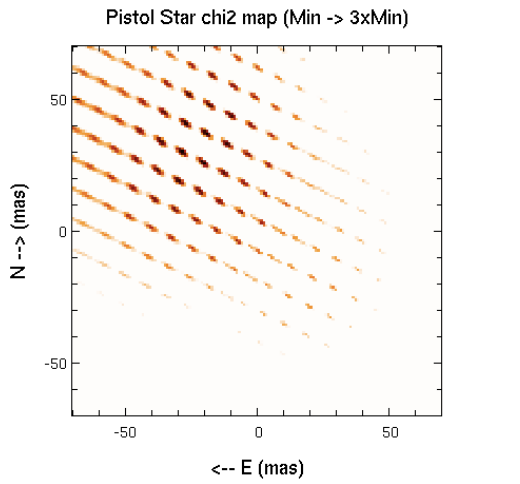

Figure 4: $\chi 2$ map of AMBER observations showing the possible positions of the Pistol Star companion. Pistol Star A is at (0,0).

current separation might not be representative of the orbit dimension at all). Long term monitoring of the system must be done in order to confirm the presence of the companion, to determine its location and its orbit to check its gravitational link, and finally determine the masses of the stars.

3 Conclusion

Combining multi-wavelength and multi-technique observations, one can better probe the nature of LBVs and better understand their properties. In the case of Pistol Star, it was found that it has a spectroscopic variability, that there are small inner shells of matter, and that the star is a possible binary. Together, these properties combine to make the Pistol Star a twin of the LBV η Car. A more detailed study will be published in a forthcoming article.

References

D'Odorico, S., Dekker, H., Mazzoleni, R., Vernet, J., Guinouard, I., Groot, P., Hammer, F., Rasmussen, P. K. et al. 2006, SPIE, 6269, 626933

Figer, D., Morris, M., Geballe, T., Rich, R. M., Serabyn, E., McLean, I. S., Puetter, R. C. & Yahil, A. 1999, ApJ, 525, 759

Foley, R., Smith, N., Ganeshalingam, M., Li, W., Chornock, R. & Filippenko, A. V. 2007, ApJ, 657, 105

Groh, J., Damineli, A., Hillier, D. J., Barbá, R., Fernández-Lajús, E., Gamen, R. C., Moisés, A. P., Solivella, G., et al. 2009, AJ, 705, L25

Lenzen, R., Hartung, M., Brandner, W., Finger, G., Hubin, N. N., Lacombe, F., Lagrange, A.-M., Lehnert, M. D., et al. 2003, SPIE 4841, 944

Martins, F., Hillier, D., Paumard, T., Eisenhauer, F., Ott, T. & Genzel, R. 2008, A&A, 478, 219

Petrov, R., Malbet, F., Weigelt, G., Antonelli, P., Beckmann, U., Bresson, Y., Chelli, A., Dugué, M., et al. 2007, A&A, 464, 1

Rousset, G., Lacombe, F., Puget, P., Hubin, N. N., Gendron, E., Fusco, T., Arsenault, R., Charton, J., et al. 2003, SPIE 4839, 140

Smith, N., Li, W., Foley, R., Wheeler, J. C., Pooley, D., Chornock, R., Filippenko, A. V., Silverman, J. M., et al. 2007, ApJ, 666, 1116

Weigelt, G., Kraus, S., Driebe, T., Petrov, R. G., Hofmann, K.-H., Millour, F., Chesneau, O., Schertl, D., et al. 2007, A&A, 464, 87

Mixing in magnetic OB stars

Thierry Morel

Institute for Astrophysics and Geophysics, Liège University, Allée du 6 Août 17, 4000 Liège, Belgium

Abstract: Recent observations have revealed the existence of a population of slowly-rotating, nitrogen-rich B dwarfs that are not predicted by evolutionary models including rotational mixing. However, as theoretical arguments suggest that magnetic processes may significantly increase the efficiency of the transport of the chemical elements, it is of importance to assess the extent of mixing in some known magnetic OB stars. We review our knowledge of the CNO abundance properties of these objects and present the first results of an NLTE abundance study of massive stars identified as being magnetic by the MiMeS collaboration. Although a nitrogen excess is often associated with the presence of a magnetic field, there is no evidence for a strict one-to-one correspondence between these two phenomena. This therefore suggests that other (still elusive) parameters may control the amount of mixing experienced by main-sequence OB stars.

1 Context

Magnetic fields are involved in a wide variety of phenomena associated to massive stars. A question that has recently been a focus of interest is the impact they may have on mixing of the internal layers. Evolutionary models incorporating magnetic fields generated through dynamo action generally predict a greater amount of mixing and hence higher CNO abundance anomalies (Maeder & Meynet 2005, but see Heger, Woosley & Spruit 2005). The detection of a sizeable population of slowly-rotating, yet N-rich, main-sequence B stars in the Magellanic clouds (Hunter et al. 2008) and in the Galaxy (e.g., Gies & Lambert 1992; Kilian 1992; Morel, Hubrig & Briquet 2008) challenges current rotational mixing theories (Brott et al. 2009) and urges the need to investigate this problem. The distribution of the N to C abundance ratio in nearby, main-sequence B stars appears to be bimodal with about 20–25% exhibiting values a factor 2–3 higher than the bulk of the sample (Fig.1). Guided by the theoretical results, one may be inclined to think that the relative proportion of magnetic stars could be higher in the N-rich group. Investigating the CNO abundance properties of magnetic OB stars thus appears not only warranted, but also timely in view of the rapidly growing number of magnetic field detections in massive stars. An indication for a higher incidence of a nitrogen excess in magnetic stars was inferred by Morel et al. (2008) who found 8 out of the 10 magnetic stars in their sample to be N rich by a factor $\sim$3. Here we re-address this result in the light of new spectropolarimetric observations that have questioned the magnetic status of some of these stars (Silvester et al. 2009) and first results of our NLTE abundance analyses of a number of main-sequence OB stars that have recently been shown to host a strong magnetic field by the MiMeS collaboration (Wade et al. 2011).

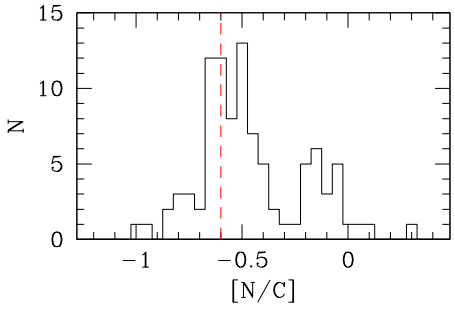

Figure 1: Distribution of the logarithmic N to C abundance ratio in nearby, main-sequence B stars (adapted from Morel 2009). The dashed line indicates the solar value (Asplund et al. 2009).

2 Analysis of the MiMeS stars

2.1 Observations and targets

High-resolution ($R \sim 46{,}000$) FIES spectra of four O9–B2 IV–V targets (NGC 2244 #201, Par 1772, NU Ori and HD 57682) were obtained in late 2009 in the framework of the 'fast-track service programme' of the Nordic Optical Telescope (NOT; Canary Islands). As can be seen in Fig.2, these stars span a wide range of $v \sin i$ values (from about 22 to 225 km s^{-1}).

Spectropolarimetric observations of NGC 2244 #201 by Alecian et al. (2008) indicate a longitudinal field strength of about 500 G with no variability of the Stokes V profile over 5 days. The star HD 57682 shows strong UV and optical line-profile variability. In particular, the Hα profile is atypical and modulated by the rotational period (Grunhut et al. 2011). The relatively sharp emission component filling in the absorption profile observed in our data is very similar to the case reported by Halbedel (1993). The field likely confines the stellar wind and has a polar strength of ∼1700 G assuming a dipole morphology (Grunhut et al. 2009). The polar field strengths under the same assumption are ∼1150 and ∼600 G in Par 1772 and NU Ori, respectively (Petit et al. 2008).

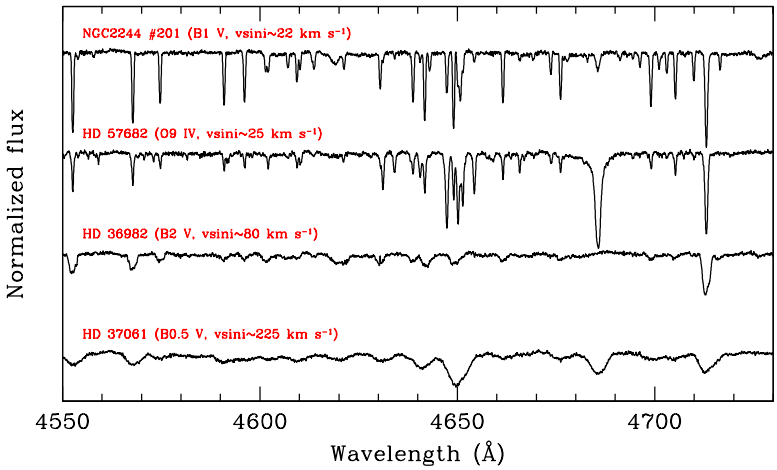

Figure 2: Spectra of the targets for the spectral range 4550–4730 Å.

2.2 Methods of analysis

The atmospheric parameters are derived purely on spectroscopic grounds: $\log g$ is determined from fitting the collisionally-broadened wings of the Balmer lines, $T_{\rm eff}$ from ionisation balance of various species (He I/II, N II/III, Ne I/II and/or Si III/IV) and the microturbulence, ξ, from requiring the abundances yielded by the O II features to be independent of their strength. The abundances are computed using Kurucz atmospheric models, an updated version of the NLTE line-formation codes

Table 1: Atmospheric parameters and elemental abundances of NGC 2244 #201 and HD 57682 (on a scale in which $\log \epsilon$[H]=12). The results of previous studies in the literature (Kilian 1992, 1994; Vrancken et al. 1997) and those obtained for τ Sco using exactly the same tools and techniques are shown for comparison (Hubrig et al. 2008). The number of lines used is given in brackets. A blank indicates that no value could be determined. The solar [N/C] and [N/O] ratios are –0.60±0.08 and –0.86±0.08 dex, respectively (Asplund et al. 2009).

	NGC 2244 #201		HD 57682		τ Sco
	This study	Vrancken et al. (1997)	This study	Kilian (1992, 1994)	Hubrig et al. (2008)
$T_{\rm eff}$ (K)	27000±1000	27300±1000	33000±1000	31800±200	31500±1000
$\log g$ (cgs)	4.20±0.15	4.3±0.1	4.00±0.15	3.85±0.10	4.05±0.15
ξ (km s^{-1})	3±3	4	5±5[a]	0^{+1}_{-0}	2±2
$v \sin i$ (km s^{-1})	22±2	22±1.5	25±4	35±3	8±2
He/H	0.072±0.023 (9)		0.106±0.030 (10)	0.085±0.008	0.085±0.027 (9)
$\log \epsilon$(C)	8.22±0.13 (6)	8.20± 0.23	8.20±0.19 (6)	8.75±0.06	8.19±0.14 (15)
$\log \epsilon$(N)	7.68±0.13 (20)	7.58±0.20	7.52±0.25 (8)	7.71±0.09	8.15±0.20 (35)
$\log \epsilon$(O)	8.63±0.18 (31)	8.59±0.19	8.31±0.21 (14)	8.10±0.08	8.62±0.20 (42)
$\log \epsilon$(Ne)	8.02±0.12 (7)		7.95±0.17 (1)	8.11±0.06[b]	7.97±0.10 (5)[c]
$\log \epsilon$(Mg)	7.29±0.20 (1)	7.38	7.37±0.18 (1)	7.33±0.07	7.45±0.09 (2)
$\log \epsilon$(Al)	6.20±0.13 (3)	6.15±0.15	6.07±0.21 (1)	6.23±0.06	6.31±0.29 (3)
$\log \epsilon$(Si)	7.41±0.25 (5)	7.28±0.30	7.47±0.32 (5)	7.24±0.06	7.24±0.14 (9)
$\log \epsilon$(S)	7.30±0.19 (1)			6.97±0.09[b]	7.18±0.28 (3)
$\log \epsilon$(Fe)	7.33±0.13 (20)			7.48±0.12[b]	7.33±0.31 (13)
[N/C]	–0.54±0.14	–0.62±0.31	–0.68±0.30	–1.04±0.11	–0.04±0.25
[N/O]	–0.95±0.21	–1.01±0.28	–0.79±0.19	–0.39±0.13	–0.47±0.29

[a]: Assumed value. [b] LTE values. [c] From Morel & Butler (2008).

DETAIL/SURFACE (Butler & Giddings 1985; Giddings 1981) and classical curve-of-growth techniques. The relatively low mass-loss rate of the O9 IV star HD 57682 ($\dot{M} \sim 1 \times 10^{-9}$ M$_\odot$ yr^{-1}; Grunhut et al. 2009) validates the use of a static model atmosphere for this star.

2.3 First results

In this contribution, we present the results for the two narrow-lined stars NGC 2244 #201 and HD 57682. The two fast rotators remain to be analysed using spectral synthesis techniques. The atmospheric parameters and elemental abundances are provided in Table 1 where they can be compared with previous results in the literature (Kilian 1992, 1994; Vrancken et al. 1997) and values obtained following exactly the same methodology for the magnetic, N-rich star τ Sco (Hubrig et al. 2008). Grunhut et al. (2009) obtained $T_{\rm eff}$=34500±1000 K and $\log g$=4.0±0.2 dex for HD 57682 from spectroscopic indicators using the NLTE, unified code CMFGEN (Hillier & Miller 1998).

There is no indication for a contamination of the surface layers of these two main-sequence stars by core-processed material. In the case of NGC 2244 #201, the CNO logarithmic abundance ratios ([N/C] and [N/O]) are consistent with the solar values, fully confirming the results of Vrancken et al. (1997). The results for HD 57682 are more uncertain owing to the weakness of the spectral lines and their strong $T_{\rm eff}$ sensitivity, but there is no indication for significant departures from the solar ratios either. Significant differences with the results of Kilian (1992, 1994) are found.

3 Discussion

These two apparently slowly-rotating, main-sequence stars do not show evidence for CN-cycled material at their surfaces and hence do not display the N excesses observed in other magnetic B stars. Figure 3a shows the positions of these two stars in the $\log T_{\rm eff}$-$\log g$ plane, along with those of other

late O/early B stars with or without a magnetic field detection analysed in exactly the same way (Morel et al. 2008). On average, stars in both groups have roughly similar masses, share about the same evolutionary status and are slow rotators. It is important to note that the distinction between magnetic and non-magnetic stars remains quite fuzzy: the detection in stars with weak fields is often disputed (see Hubrig et al. 2009 vs. Silvester et al. 2009), while non magnetic stars might be detected with more sensitive and intensive observations. For this reason, we also show in Fig.3b the results for the stars for which the (non) detection of a magnetic field can be regarded as more secure, either because it is (un)detected at a high degree of confidence or because it is confirmed by independent studies. Although magnetic and abundance studies of a larger sample are needed to draw firm conclusions, in both cases there is evidence for a higher incidence of an N excess in the magnetic stars.

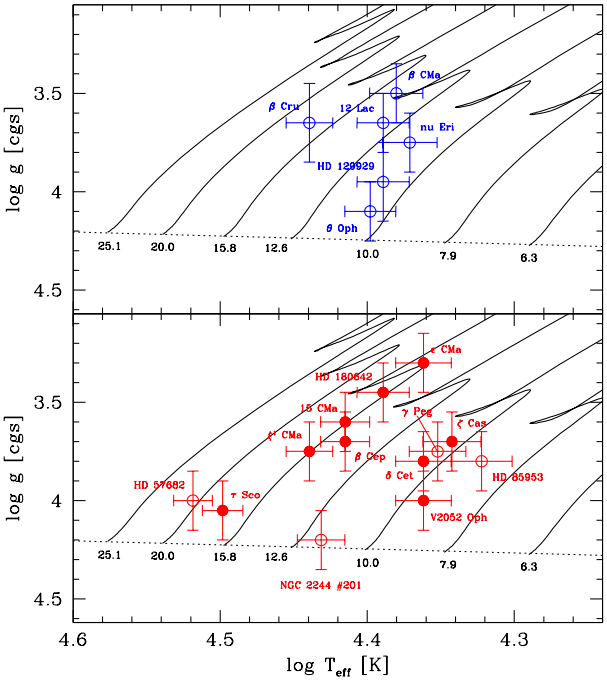

Figure 3a: Position in the $\log T_{\rm eff}$-$\log g$ plane of the OB stars without (*top panel*) and with (*bottom panel*) a magnetic field detection. Filled symbols denote stars showing an N excess (magnetic and abundance data from Morel et al. 2008 and this study). Evolutionary tracks from Claret (2004) for masses ranging from 6.3 to 25.1 $M_\odot$ are overplotted.

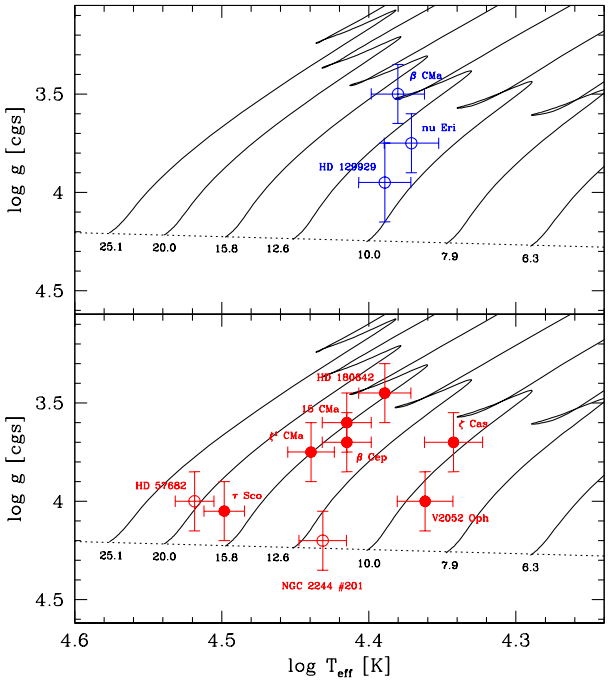

Figure 3b: Same as Fig.3a, but only taking into account the stars with a secure magnetic field (non) detection based on the spectropolarimetric observations of Alecian et al. (2008), Donati et al. (2001, 2006), Grunhut et al. (2009), Hubrig et al. (2009, 2010), Neiner et al. (2003a,b), Schnerr et al. (2006) and Silvester et al. (2009).

However, it is likely that this simple relationship is only statistical and that other (still elusive) parameters may play a role in the amount of mixing experienced. This is particularly well illustrated by the cases of HD 57682 and τ Sco. These two stars have only slightly evolved off the ZAMS, have about the same mass (Fig.3a) and are slow rotators (likely for HD 57682 unless it is seen nearly pole on, while τ Sco has a true rotational velocity as low as 6 km s^{-1}; Donati et al. 2006). Yet, the latter exhibits evidence for CN-cycled material dredged up to the surface (an N excess of a factor $\sim$3; see also Przybilla, Nieva & Butler 2008 who obtained [N/C]=–0.14$\pm$0.18), whereas the former does not.

We conclude by noting that several aspects may complicate a direct comparison between the observed CNO surface abundances and the predictions of evolutionary models. First, the models including magnetic effects consider a field created through shear instabilities, whereas it has a simple

morphology strongly indicative of a fossil origin in many stars. Second, many uncertainties about the evolution of the angular momentum along the main sequence still remain. For instance, while magnetic braking is unlikely to significantly spin down some of our magnetic targets (see, e.g., ud-Doula, Owocki & Townsend 2009 in the case of ζ Cas), the impact of g-mode pulsations in redistributing the angular momentum in the slowly pulsating B stars (SPBs) or hybrid β Cephei/SPBs in our sample might be dramatic (Townsend 2009).

Acknowledgements

The author acknowledges financial support from Belspo for contract PRODEX GAIA-DPAC. I am indebted to K. Butler for providing me with the line-formation codes DETAIL/SURFACE and S. Hubrig for having access to her unpublished magnetic data. Valuable suggestions from S. Simón-Díaz (the referee), P. Williams (the editor), K. Pavlovski and E. Tamajo were also very much appreciated.

References

Alecian E., Wade G. A., Catala C., et al., 2008, A&A, 481, L99
Asplund M., Grevesse N., Sauval A. J., Scott P., 2009, ARA&A, 47, 481
Brott I., Hunter I., de Koter A., Langer N., Lennon D., Dufton P., 2009, CoAst, 158, 55
Butler K., Giddings J. R., 1985, in Newsletter of Analysis of Astronomical Spectra, No.9 (Univ. London)
Claret A., 2004, A&A, 424, 919
Donati J.-F., Wade G. A., Babel J., Henrichs H. F., de Jong J. A., Harries T. J., 2001, MNRAS, 326, 1265
Donati J.-F., Howarth I. D., Jardine M. M., et al., 2006, MNRAS, 370, 629
Giddings J. R., 1981, Ph.D. Thesis, University of London
Gies D. R., Lambert, D. L., 1992, ApJ, 387, 673
Grunhut J. H., Wade G. A., Marcolino W. L. F., et al., 2009, MNRAS, 400, L94
Grunhut J. H., Wade G. A., Marcolino W. L. F., et al. 2011, in proceedings of IAU Symp.272, 'Active OB stars: structure, evolution, mass loss and critical limits', in press (arXiv:1009.3263)
Halbedel E. M., 1993, IBVS, #3850
Heger A., Woosley S. E., Spruit H. C., 2005, ApJ, 626, 350
Hillier D. J., Miller D. L., 1998, ApJ, 496, 407
Hubrig S., Briquet M., Morel T., Schöller M., González J. F., De Cat P., 2008, A&A, 488, 287
Hubrig S., Briquet M., De Cat P., Schöller M., Morel T., Ilyin I., 2009, AN, 330, 317
Hubrig S., Ilyin I., Schöller M., Briquet M., Morel T., De Cat P., 2010, ApJL, submitted
Hunter I., Brott I., Lennon D. J., et al., 2008, ApJ, 676, L29
Kilian J., 1992, A&A, 262, 171
Kilian J., 1994, A&A, 282, 867
Maeder A., Meynet G., 2005, A&A, 440, 1041
Morel T., Hubrig S., Briquet M., 2008, A&A, 481, 453
Morel T., Butler K., 2008, A&A, 487, 307
Morel T., 2009, CoAst, 158, 122
Neiner C., Geers V. C., Henrichs H. F., Floquet M., Frémat Y., Hubert A.-M., Preuss O., Wiersema K., 2003a, A&A, 406, 1019
Neiner C., Henrichs H. F., Floquet M., et al., 2003b, A&A, 411, 565
Petit V., Wade G. A., Drissen L., Montmerle T., Alecian E., 2008, MNRAS, 387, L23
Przybilla N., Nieva M.-F., Butler K., 2008, ApJ, 688, L103
Schnerr R. S., Verdugo E., Henrichs H. F., Neiner C., 2006, A&A, 452, 969
Silvester J., Neiner C., Henrichs H. F., et al., 2009, MNRAS, 398, 1505
Townsend R., 2009, in proceedings of 'Stellar pulsation: challenges for theory and observation', AIPC, 1170, 355
ud-Doula A., Owocki S. P., Townsend R. H. D., 2009, MNRAS, 392, 1022
Vrancken M., Hensberge H., David M., Verschueren W., 1997, A&A, 320, 878
Wade G. A., Alecian E., Bohlender D. A., et al. 2011, in proceedings of IAU Symp.272, 'Active OB stars: structure, evolution, mass loss and critical limits', in press (arXiv:1009.3563)

Escaping Radiation from Massive Star H II regions in the Magellanic Clouds

E.W. Pellegrini[1], M.S. Oey[1], P.F. Winkler[2], R.C. Smith[3] and S. Points[3]

[1] Department of Astronomy, University of Michigan, 500 Church St., Ann Arbor, MI, USA
[2] Department of Physics, Middlebury College, Middlebury, VT, USA
[3] CTIO, Casilla 603, La Serena, Chile

Abstract: We present a novel approach for distinguishing density-bounded vs radiation bounded H II regions based on [S II]/Hα and [S II]/[O III] ratio maps. We find most H II regions fall into one of three categories: radiation bounded, open blister type, and density bounded. Our approach directly diagnoses the existence of ionization fronts around massive stars, revealing a significant number of H II regions to be density bounded. Furthermore, we can place a lower limit on the fraction of ionizing photons escaping each region yielding values consistent with other methods, with direct implications for the ionization of the Warm Interstellar Medium and reionization of the universe at high redshift. We conclude that the three morphological classifications are correlated with the observed N(H I) column density and Hα luminosity, however a more filamentary structure of the LMC does not lead to higher H II escape fractions than in the SMC.

1 Introduction

It is critical that we determine the fate of ionizing radiation generated by massive stars. The optical depth to ionizing radiation, τ, and the fraction of ionizing radiation not immediately absorbed by H II regions, $f_{\rm esc} \equiv e^{-\tau}$, are of great importance to many fields of astrophysics, including the epoch of reionization. During this period bright quasars were less frequent than now, and alone were insufficient to reionize the universe (Sokasian, Abel & Hernquist 2003). If $f_{\rm esc}$ was large, young star forming galaxies would have generated enough ionizing radiation to make up the difference and ionize the universe by $z \sim 6$. A significant $f_{\rm esc}$ from H II regions will also have implications on the origin of the large scale, diffuse Warm Ionized Medium (WIM) of galaxies (Haffner et al. 2009), and derivations of star formation rates, stellar populations and IMF of high redshift galaxies using Hα observations. Therefore the value of $f_{\rm esc}$, and its dependence on environment is a fundamental parameter that must be better constrained.

Unfortunately, determining $f_{\rm esc}$ for individual H II regions is quite difficult, requiring indirect methods often with inconclusive results ranging between zero to unity. Giammanco et al. (2004) demonstrated that emission line ratios alone cannot differentiate between a density bounded (DB) or radiation bounded (RB) H II region in the case where the nebulae contain optically thick clumps. In their models, radiation escapes along low density lines of sight, free of clumps, resulting in a large

$f_{\rm esc}$. However, the spectrum is dominated by the high density clumps, each forming an individual ionization front (IF) with a spectrum similar to constant density RB models. A more promising approach to constrain $f_{\rm esc}$ relates the observed H II region Hα luminosity, L(Hα), to the expected rate of H ionizing photons (Q(H)) from a stellar population. Any discrepancy between the expected and observed L(Hα) is attributed to a non-zero value of $f_{\rm esc}$. With this method, uncertainties in Q(H) as large as a factor of 2, translate to values of $f_{\rm esc}$ ranging between 0 and 50%.

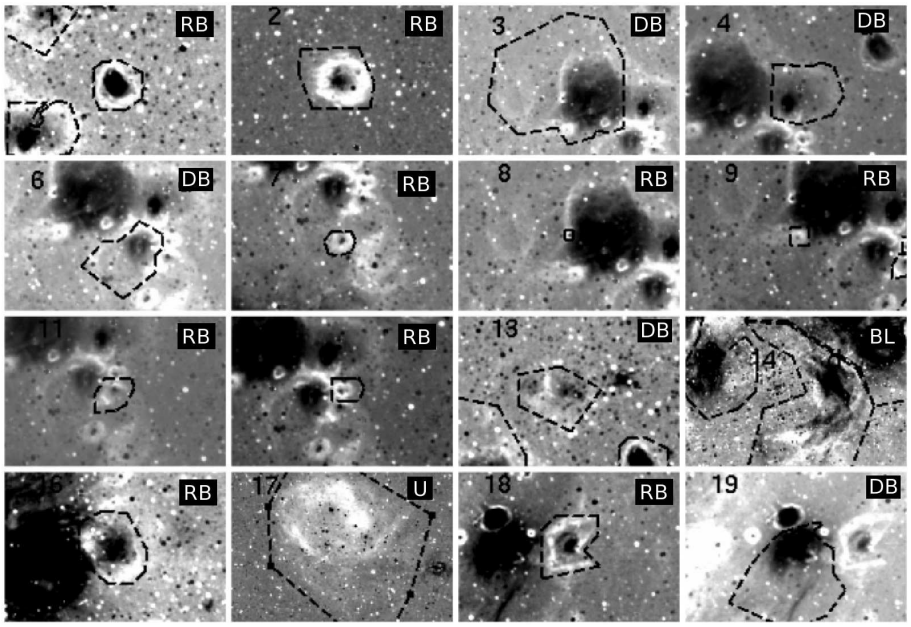

Figure 1: A sample of LMC H II regions from the MCELS survey as seen in [S II]/[O III]. The dashed contours represent the boundary of the aperture used to measure Hα fluxes and H I column densities. In the upper right corner of each individual panel the morphology of the object is indicated as RB, DB, BL or U (unknown).

2 Differentiating Radiation and Density Bounded Nebulae

To make progress in this important field we detect IFs unique to RB nebulae with [S II]/Hα and [S II]/[O III] ratio maps of the LMC and SMC which trace changes in gas ionization. For individual H II regions, seen in Figure 1, the different ionization potentials of S^0, H^0 and O^+ result in IFs appearing as limb-brightened [S II] enhancements (white). IFs in RB H II regions surround both the ionizing stars and the ionized gas (weak [S II]; black). In comparison, the DB H II regions are characterized by highly ionized gas with no surrounding IF, signaling a high $f_{\rm esc}$.

This method allows nearly all known H II regions in both the LMC and SMC to be separated into one of 3 empirically motivated categories: RB, DB or Blister type (BL) nebulae. BL type regions have IFs with only a partial covering factor, allowing radiation to escape the region in only certain directions. Using emission lines this way avoids many of the uncertainties inherent in previous studies.

We use data from the Magellanic Cloud Emission Line Survey (MCELS, Smith et al. 2005). Over 5 years, the MCELS collaboration obtained deep emission line images covering most of the LMC and SMC in Hα, [O III] and [S II] with a resolution of 5 arcsec. This survey was intended to provide data useful for research into the ionized gas of these galaxies. The data are ideal for our study because they are homogeneous and complete down to $L(\mathrm{H}\alpha) \simeq 10^{35}$ erg s^{-1}, which includes all known H II regions in both galaxies. We use these data to define a new set of physically motivated boundaries

for a complete sample of all H II regions in both galaxies. These boundaries are also used for our Hα photometry apertures. In some cases we find nebulae previously identified as distinct to be part of a larger single structure. In addition, some newly identified nebulae are detected within larger complexes.

3 Escape Fraction of Ionizing Radiation

We seek a diagnostic to quantize the global $f_{\rm esc}$, but the relative strengths of the emission lines we use depend on more parameters than just the local depth to ionizing radiation. These include the effective temperature of the ionizing stars $T_{\rm eff}$, and the ionization parameter U, defined as ratio of ionizing photon flux to hydrogen density. To constrain the possible values of $f_{\rm esc}$, we have used CLOUDY (Ferland et al. 1998) to simulate H II regions over a large range of $T_{\rm eff}$, U and $f_{\rm esc}$ characteristic of nebulae ionized by O-stars. Using 2D projections of the predicted surface brightness of emission lines we are able to make direct comparisons to our ionization maps. We find a general trend that the [S II] enhancement used to identify IFs at the edges of RB H II regions is absent in DB H II if $f_{\rm esc} \geq 0.6$. This also means that H II regions with signatures of an IF may have $f_{\rm esc}$ as large as 0.6, depending on $T_{\rm eff}$ and U.

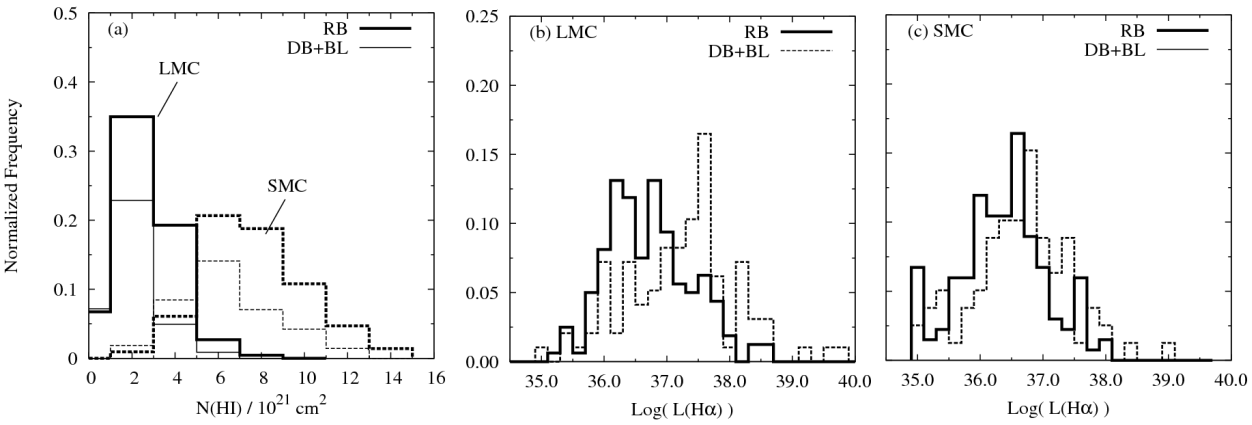

Figure 2: a) Distribution of N(H I) measured within the projected aperture used for the Hα photometry. RB(thick line) and DB+BL(thin) objects in both the LMC(solid) and SMC(dashed) are normalized by the total number of objects in each category; b) the LMC L(Hα) distribution with the same line types used in (a); c) same as plot (b) for the SMC.

To derive a global escape fraction from the entire H II region population, we first sum the observed H II region $L_{\rm H\,II}({\rm H}\alpha)$, proportional to $Q({\rm H})_{\rm absorbed}$. Then we estimate the rate of *ionizing* radiation escaping into and ionizing the WIM ($Q({\rm H})_{\rm esc}$) from $L_{esc}({\rm H}\alpha) = L_{\rm H\,II}({\rm H}\alpha) \times (f_{\rm esc}/(1-f_{\rm esc}))$, where $L_{esc}({\rm H}\alpha)$ is the Hα luminosity resulting from $Q({\rm H})_{\rm esc}$. Our simulations constrain RB regions to $f_{esc}({\rm RB}) \leq 0.6$ and DB to $0.6 \leq f_{esc}({\rm DB}) \leq 1.0$. For our calculations we assume $f_{\rm esc}(DB) = 0.6$, $f_{\rm esc}({\rm BL}) = 0.5 \times f_{\rm esc}(DB)$ and $f_{\rm esc}({\rm RB}) = 0.0$. In the LMC, we find a L(Hα) weighted average H II $f_{\rm esc} \geq 0.41$ and $L_{\rm esc}({\rm H}\alpha) = 1.2 \times 10^{40}$ erg s^{-1}. In the SMC we find $f_{esc} \geq 0.44$ and $L_{esc}({\rm H}\alpha) = 1.9 \times 10^{39}$ erg s^{-1}. A small number of weakly ionized and/or shocked regions are excluded from our sample, because they show no clear structure in ratio images. These account for no more than 20 % of the total Hα emission and will not affect the results. Assuming all escaping radiation is absorbed in the WIM, Kennicutt et al. (1995) approximated $f_{\rm esc}$ using $L({\rm H}\alpha)_{\rm WIM}/L({\rm H}\alpha)_{\rm H\,II}$, and found values in the LMC and SMC between $25-35\%$ and $34-40\%$ respectively. These are similar to our $f_{\rm esc}$'s,

and the idea that leaking photons from H II regions ionize the WIM (Haffner et al. 2009). Also, by correcting for $f_{\rm esc}$, we may more accurately derive the IMF of stellar populations from UV and Hα observations.

4 Results

To explore the link between local environment and $f_{\rm esc}$, we consider the H I column densities for all H II regions. The average LMC H I column in Figure 2a is half the SMC value, due in part to the projection of the flatter LMC compared to the irregular SMC. However, inclination will effect both RB and DB nebulae in the same way. Since a simple scaling can not bring the LMC H I distribution into agreement with the SMC, the distributions shown in (Fig. 2a) demonstrate a real difference between the LMC and SMC.

Independent of inclination, we find DB nebulae have lower values of N(H I) than RB nebulae in both galaxies. Figures 2b (LMC) and 2c (SMC) show the observed distribution in L(Hα) is bimodal. Without correcting for escaping radiation, we find the mean L(Hα) of DB H II regions to be $\approx$1 dex brighter than RB in the LMC, and 0.5 dex brighter in the SMC. In addition, we note the existence of objects with significant $f_{\rm esc}$ found near the outer regions of the SMC and LMC. The location of bright DB objects here may result in an unobstructed path for ionizing radiation to leave the galaxy.

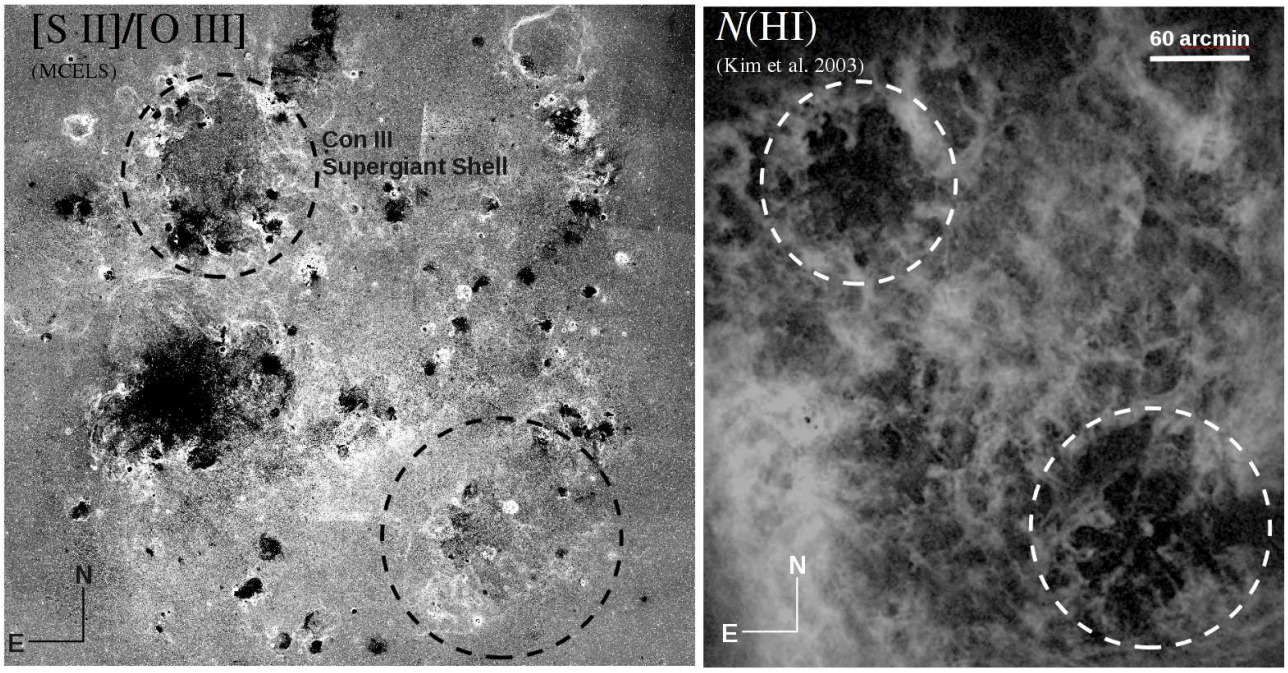

Figure 3: To the left is the ratio of [S II]/[O III] for the entire LMC galaxy. Black indicates lower ratios with a corresponding higher degree of ionization. The right is the H I column density map from Kim et al. (2003). Higher column densities are shown in white.

Figures 3 and 4 show striking differences in the large scale ionization and H I structures of the LMC and SMC. The LMC ISM is very filamentary and porous, with more highly ionized, low density bubbles surrounded by dense, weakly ionized shells. By contrast, the SMC ISM is more homogeneous, with less evidence of ionization gradients around localized ionization sources. Differences in Figures 2b and 2c are consistent with a scenario where massive star feedback and a higher star-formation rate has created a filamentary ISM in the LMC, allowing more radiation from lower luminosity nebulae to escape into the WIM and potentially out of the galaxy. However, both galaxies

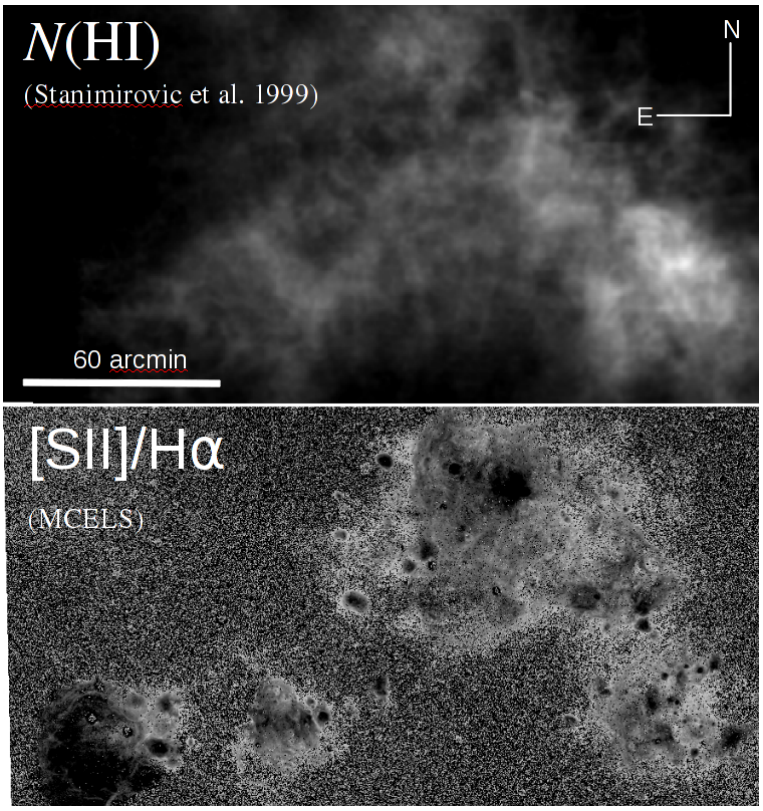

Figure 4: Similar to Figure 3, the top panel is the projected H I column density (Stanimirovic et al. 1999). Higher column densities are shown in white. The bottom panel shows the ratio of [S II]/Hα for the entire SMC. Black again indicates lower ratios with a corresponding higher degree of ionization.

have a similar escape fraction and further work is needed to understand the interplay between large scale structure and the escape fraction of ionizing radiation from H II regions.

Acknowledgements

This research is supported by NSF grant AST-0805476.

References

Ferland, G. J., Korista, K. T., Verner, D. A., Ferguson, J. W., Kingdon, J. B., & Verner, E. M., 1998, PASP, 110, 761
Giammanco, C., Beckman, J. E., Zurita, A., & Relaño, M. 2004, A&A, 424, 877
Haffner, L.M., Dettmar, R.J., Beckman, J.E., et al., 2009, RvMP, 81, 969
Kennicutt R.C., Bresolin, F., Bomans, D.J., Bothun, G.D., Thompson, I.B., 1995, AJ, 109, 594
Kim, S., Staveley-Smith, L., Dopita, M.A. Sault, R.J. Freeman, K.C., Lee, Y., Chu, Y.H., 2003, ApJS, 148, 473
Smith, R.C., Points. S.D., Chu, Y.H., Winkler, P.F., Augilera, C., Leiton, R., & the MCELS Team, 2005, AAS, 207, 2507
Sokasian, A., Abel, T., & Hernquist, L. 2003, MNRAS, 340, 473
Stanimirovic, S., Stavely-Smith, L., Dickey, J.M., Sault, R.J. & Snowden, S.L., 1999, MNRAS, 302, 417

New Results from the Project MASGOMAS: Near-IR Study of the Stellar Population of Sh2-152

Sebastián Ramírez Alegría[1,2], Artemio Herrero[1,2],
Antonio Marín-Franch[3,4], Elena Puga[5] and Francisco Najarro[5]

[1] Instituto de Astrofísica de Canarias, E-38205,Tenerife, Spain
[2] Universidad de La Laguna, E-38207, Tenerife, Spain
[3] Centro de Estudios de Física del Cosmos de Aragón (CEFCA), E-44001, Teruel, Spain
[4] Departamento de Astrofísica, Universidad Complutense de Madrid, E-28040, Madrid , Spain
[5] Centro de Astrobiología (CSIC-INTA), E-28850, Torrejón de Ardoz, Madrid, Spain

Abstract: We present a near-IR and optical spectrophotometric characterization of the stellar population of Sh2-152, as part of our MASGOMAS project. Using new broad band photometry (J, H and K_S) for the cluster and a control field, we have constructed CMD in order to select OB-candidates for H and K spectroscopy. Also, we have obtained the cluster mass function, with the disc population subtracted using the control field mass function. From the 13 spectroscopically observed stars, 6 were classified as B-dwarfs and with individual distance and extinction estimations. With these values we have obtained estimations for the distance (3.01 ± 0.11) kpc, mass (1.86 ± 0.83)$\cdot 10^3$ $M_\odot$ and age $<$8.1 Myr for Sh2-152. We also present a new optical spectrum for the central ionizing star of Sh2-152, showing some peculiarities associated to this central object and shed some light over the interesting star deeply embedded into the bright K_S nebulosity close to the IRAS source IRAS 22566+5828.

1 Introduction

Motivated by the discoveries of new massive stellar clusters, containing remarkable massive stellar populations (likes Arches and Quintuplet, Figer et al. 1999, RSGC1, Figer et al. 2006, RSGC3, Clark et al. 2009 or Alicante 8, Negueruela et al. 2010), the revelation of the massive natures of previously known stellar clusters (e.g. CygOB2, Knödlseder 2000; Westerlund1, Clark & Negueruela 2002) and the estimations of hundreds of galactic massive stellar clusters still unknown (Hanson & Popescu 2008), we have conceived the project MASGOMAS (MAssive Stars in Galactic Obscured MAssive clusterS, Marín-Franch et al. 2009, Puga et al. 2010), to characterize the stellar population of known massive clusters candidates and to discover new ones. Based on previous catalogues of galactic cluster candidates (Bica et al. 2003, Dutra & Bica 2001), we had completed a near-IR (J, H and K_S) photometric campaign for all our candidates and a spectroscopic follow up for 9 of them. One of these candidates is the star-forming compact H II region Sh2-152 (α(J2000)=$22^h58^m45^s$, δ(J2000)=+58°46′50″). Located in the Perseus (close to the Galactic plane; $l = 108.76$, $b = -0.95$), it contains two

IRAS sources (IRAS 22566+5828 and IRAS 22566+5830, Kleinmann et al. 1986), 6.7 GHz methanol (Szymczak et al. 2000), water and hydroxyl masers (Harju et al. 1998), indicating active massive star formation. This region has been the target of several near-IR observations but its stellar content has not been spectroscopically studied yet. We present a new near-IR spectrophotometric study and characterization of Sh2-152, using for first time information from several stellar sources from the cluster.

2 Observations

Our whole near-IR data set was obtained with LIRIS, an IR camera equipped with a Hawaii 1024×1024 HgCdTe array detector and a field of view of $4.2' \times 4.2'$. LIRIS has direct imaging, polarimetric and spectroscopic (single and multiobject) modes. Images were obtained with seeing around $0.6''$, while spectroscopy was acquired with seeing around $1.0''$. Thanks to the LIRIS near-IR image, we have been capable to resolve the central region of the cluster. The central ionizing star, previously classified as an O8.5 V star (Russeil et al. 2007), was spectroscopically observed at optical wavelength with the FIES cross disperser (R=46000) echelle spectrograph at NOT 2.5m (ORM-La Palma). Characteristic seeing for this observations was $1.5''$ and the final SNR for this optical spectra is less than 20. The images were reduced with FATBOY (Eikenberry et al. 2006) and the photometry was calibrated using 2MASS. The infrared spectra reduction was done with LIRISDR, while the telluric correction was completed with Xtellcor (Vacca et al. 2003) and telluric, an IRAF task. The optical spectrum was reduced with the FIEStool pipeline. A false colour image for Sh2-152 marking the position of the chosen stars for near-IR spectroscopy is presented in Figure 1.

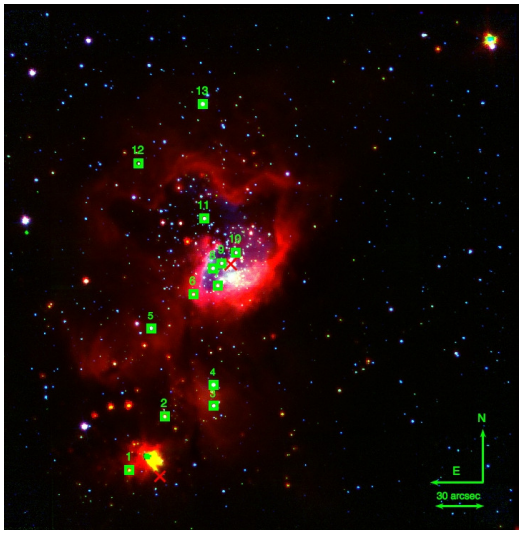

Figure 1: False colour image for Sh2-152, using LIRIS and Spitzer images (blue=J, green=K_S, red=Spitzer 3.6 μm). In this image, we mark the MOS stars with small green squares (numbered) and with red crosses, the IRAS regions IRAS 22566+5830 (central) and IRAS 22566+5828 (down).

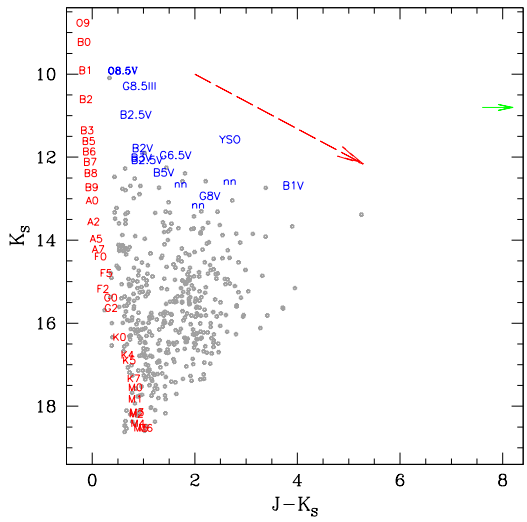

Figure 2: CMD for Sh2-152. The main sequence is located at 3.01 kpc. Spectral types in blue indicate the MOS stars and the origin of the green solid arrow shows the bluest position of the central star embedded into the bright nebulosity, associable with IRAS 22566+5828.

3 Results and Analysis

Using the derived CMD from our photometry, we selected OB-type candidates considering the LIRIS spectroscopic limit ($K_S \sim 12.5$) and its position in the cluster's field. Due to the differential reddening over the field, the cluster main sequence is spread to redder colours, following the reddening vector. To consider this effect, we also include as a selection criterion $J - K_S$ >0.5. The CMD for Sh2-152 is shown in Figure 2.

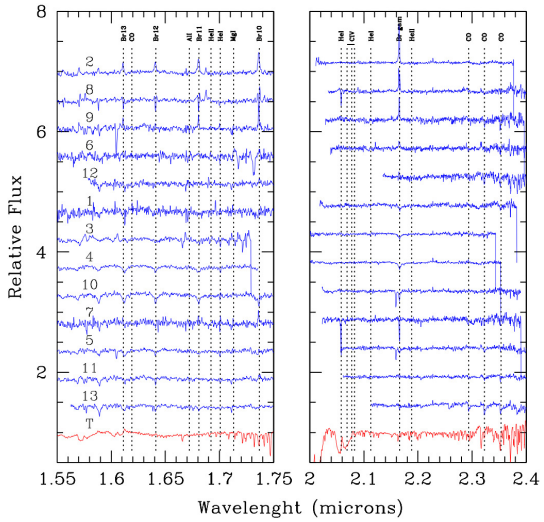

Figure 3: H and K spectra for MOS stars. In red are shown the respective telluric spectra.

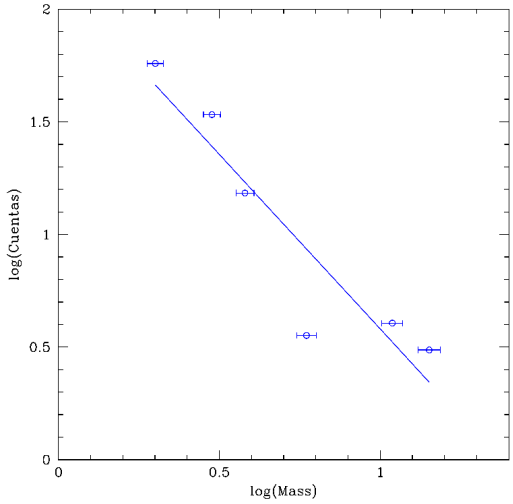

Figure 4: Mass function for Sh2-152. The solid blue line corresponds to the best fit to the data.

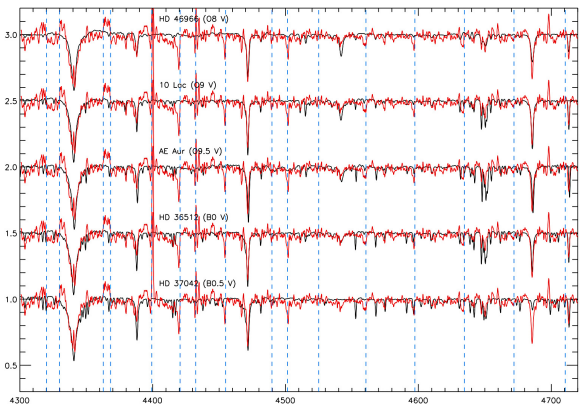

Figure 5: FIES optical spectra for the central star of the cluster (red) is compared with spectral type templates (O8 V to B0.5 V, in black). Remarkable are the depths of the helium lines and the non detection of Si III (4552Å and 4568Å).

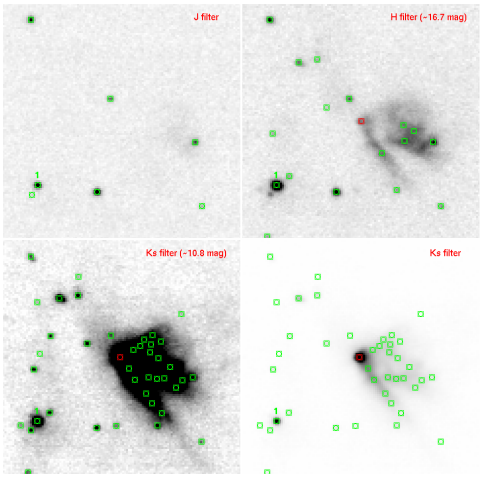

Figure 6: J, H and K_S image for IRAS 22566 +5828. Green squares mark the objects detected in our photometry. The red one, could be the central ionizing star of the nebulosity, marked with a blue arrow in the CMD. Star #1 corresponds to a MOS star.

ID	Spectral Type	A_{K_S}	Distance (kpc)
01	B1 V	2.60	3.35
03	B3 V	0.66	3.18
04	B2 V	0.50	2.92
05	B4 V	0.61	2.68
08	B3-5 V	0.65	2.96
10	B5-6 V	0.86	2.80

ID	Spectral Type
02	YSO
06	- (nebular)
07	- (nebular)
09	- (nebular)
11	G6.5 V
12	G8 V
13	G8-9 III

Table 1: Left: Early-type stars used for the distance determination. Central O8.5 V star was excluded due to saturated (LIRIS) or contaminated (2MASS) photometry. Right: Spectroscopically observed stars without determined spectral type or fore/background late-type stars.

3.1 Spectral Classification, Cluster Distance and Mass

Spectral classification was done using Hanson & Conti (1996), Wallace & Hinkle (1997), Hanson et al. (1998), Meyer et al. (1998), Ranade et al. (2004, 2007) near-IR stellar spectral catalogues. Adopting intrinsic colours (Ducati et al. 2001), absolute magnitudes (Cox 2000) and an extinction law with R=3.09 (Rieke & Lebofsky 1985), we have estimated a cluster distance of (3.01 ± 0.11) kpc, using for first time distance estimations for multiple sources in the field. The individual spectra are shown in Figure 3), and the stellar spectral types, extinctions and distance are summarized in Table 1. The cluster mass was obtained by substracting the stellar population from the Galactic disk, using J, H and K_S images from a control field. The cluster and control field histograms, previously corrected by completeness, were substracted leaving the mass function for the object, shown in Figure 4. The total mass of Sh2-152 derived with this method is $(1.86 \pm 0.83) \cdot 10^3$ $\mathrm{M}_\odot$.

3.2 Possible Ionizing Sources

Within the Sh2-152 field there are two interesting sources. First, the central star of the cluster, that has been classified as O8.5 V (Crampton et al. 1978, Russeil et al. 2007) and gives an upper limit for the clusters age of 8.1 Myr (using stellar models from Schaller et al. 1992, and stellar mass from Martins & Plez 2006). From our optical spectra (Figure 5, SNR$\sim$20 per pixel at R=46000) we derive the same spectral type but observing that the He II 4686Å line is deeper than He I 4388Å and He II 4542Å, and very similar to He I 4471Å. We can not determine which line, He II 4686Å or He I 4471Å is stronger, but we note that fulfilling the condition He II 4686Å >He I 4471Å at spectral type $\sim$O9 would indicate that this star is an OVz object. However a spectrum with a better SNR is required to clarify this point. Also is interesting the non detection of Si III 4552Å and 4568Å, setting the spectral type to earlier than O9 V. On the contrary, the Mg II line at 4481Å is detected. The relatively strong He II 4686Å and the lack of Si III at a relatively late O spectral type could also be due to contamination of a companion object (either physical or visual). A better spectrum is needed to solve this uncertainty. The second object is the star colocated with IRAS 22566+5828 (Helou & Walker 1988). This object was not selected as MOS candidate, due to its huge extinction ($J - K_S > 7$), being impossible to measure its J brightness (see Figure 6). With K_S=10.8 and assuming the distance of 3.01 kpc calculated for the cluster, the central star deeply embedded into the nebulosity would have a spectral type earlier than O4 V, being the most massive object of the cluster. Future K or mid-IR spectra for this object would clarify its spectral type and membership to Sh2-152. If this is confirmed, it would contribute to diminish the cluster age and increase the upper part of its mass function.

4 Conclusions

As part of our MASGOMAS project, we have studied the stellar content of the compact H II region Sh2-152. We have obtained a distance estimation of (3.01 $\pm$ 0.11) kpc for the cluster, in agreement with Russeil et al. (2007). It is remarkable that this estimation was obtained for first time using near-IR spectra for multiple sources in the field. Using the cluster luminosity function, corrected by the stellar population from the Galactic disk using a control field, we estimated the cluster's stellar total mass in (1.86 $\pm$ 0.83)$\cdot 10^3$ $M_\odot$. We also set an upper limit for the cluster's age of 8.1 Myr, based on the most massive early-type dwarf, which has not evolved into its giant phase. Future works include the near-IR observation and analysis of the possible ionizing stars of IRAS 22566+5830 and IRAS 22566+5828. The spectral classification of the last one, could improve the cluster age and mass determination.

Acknowledgments

Authors are members of the Consolider-Ingenio 2010 Program (CSD2006-00070). Financial support by the Spanish Ministerio de Ciencia e Innovación under the project AYA2008-06166-C03-01.

References

Bica, E., Dutra, C. M., Soares, J., & Barbuy, B. 2003, A&A 404, 223
Clark, J.S., & Negueruela, I. 2002, A&A 396, L25
Clark, J.S., Negueruela, I., Davies, B., et al. 2009, A&A 498, 109
Cox, A.N., ed. 2000, Allen's Astrophysical Quantities, fourth edition, Springer Verlag
Crampton, D., Georgelin, Y.M., & Georgelin, Y.P. 1978, A&A 66, 1
Ducati, J.R., Bevilacqua, C.M., Rembold, S.B., & Ribeiro, D. 2001, ApJ 558, 309
Dutra, C.M., & Bica, E. 2001, A&A 376, 434
Eikenberry, S., Elston, R., Raines, S.N., et al. 2006, SPIE 6269, 39
Figer, D.F., Kim, S.S., Morris, M., Serabyn, E., Rich, R.M., & McLean, I.S. 1999, ApJ 525, 750
Figer, D.F., MacKenty, J.W., Robberto, M., Smith, K., Najarro, F., Kudritzki, R.P., & Herrero, A. 2006, ApJ 643, 1166
Hanson, M., & Conti, P.S. 1996, ApJS 107, 281
Hanson, M., Rieke, G.H., & Luhman, K.L. 1998, AJ 116, 1915
Hanson, M., & Popescu, B. 2008, Proc. IAU Symp. 250, eds. F. Bresolin, P.A. Crowther & J. Puls, CUP, 307
Harju, J., Lehtinen, K., Booth, R.S., & Zinchenko, I. 1998, A&AS 132, 211
Helou, G., & Walker, D.W. 1988, IRAS, vol 7
Kleinmann, S.G., Cutri, R.M., Young, E.T., Low, F.G. & Gillet, F.C. 1986, SSC, C, 0
Knödlseder, J. 2000, A&A 360, 539
Marín-Franch, A., Herrero, A., Lenorzer, A., Najarro, F., Ramirez, S., Font-Ribera, A., & Figer, D. 2009, A&A 502, 559
Martins, F., & Plez, B. 2006, A&A 457, 637
Meyer, M., Edwards, S., Hinkle, K., & Strom, S. 1998, ApJ 508, 397
Negueruela, I., González-Fernández, C., Marco, A., Clark, J.S., & Martínez-Núñez, S. 2010, A&A 513, A74
Puga, E., Marín-Franch, A., Najarro, F., et al. 2010, A&A 517, A2
Ranade, A., Gupta, R., Ashok, N.M., & Singh, H. 2004, Bull. Astr. Soc. India 32, 311
Ranade, A., Singh, H., Gupta, R., & Ashok, N.M. 2007, Bull. Astr. Soc. India 35, 87
Rieke, G.H., & Lebofsky, M.J. 1985, ApJ, 288, 618
Russeil, D., Adami, C., & Georgelin, Y.M. 2007, A&A 470, 161
Schaller, G., Schaerer, D., Meynet, G., & Maeder, A. 1992, A&AS 96, 269
Szymczak, M., Hrynek, G., & Kus, A.J. 2000, A&AS 143, 296
Vacca, W., Cushing, M., & Rayner, J. 2003, PASP 115, 389
Wallace, L., & Hinkle, K. 1997, ApJS 111, 445

Non-thermal radiation from a runaway massive star

Gustavo E. Romero[1,2], Paula Benaglia[1,2], Cintia S. Peri[1,2],
Josep Martí[3], Anabella T. Araudo[1,2]

[1] Instituto Argentino de Radioastronomía, CCT-La Plata, CONICET,
C.C.5, (1894) Villa Elisa, Buenos Aires, Argentina
[2] Facultad de Ciencias Astronómicas y Geofísicas UNLP,
Paseo del Bosque S/N, B1900FWA La Plata, Argentina
[3] Departamento de Física (EPS), Universidad de Jaén, Campus Las Lagunillas s/n, 23071 Jaén, Spain

Abstract: We present a study of the radio emission from a massive runaway star. The star forms a bow shock that is clearly observed in the infrared. We have performed VLA observations under the assumption that the reverse shock in the stellar wind might accelerate charged particles up to relativistic energies. Non-thermal radio emission of synchrotron origin has been detected, confirming the hypothesis. We have then modeled the system and we predict a spectral energy distribution that extends up to γ-rays. Under some simplifying assumptions, we find that the intensity at high energies is too low to be detected by current instruments, but the future Cherenkov Telescope Array might detect the source.

1 Introduction

Runaway OB stars (Gies & Bolton 1986) can produce so-called stellar bow shocks on the surrounding interstellar medium. Bow shocks develop as arc-shaped structures, with bows pointing in the same direction of the stellar velocity, while the star moves supersonically through the interstellar medium (ISM). The stellar and shock-excited radiation heat the dust and gas swept by the bow shock. The dust, in turn, re-radiates the energy as mid to far IR flux.

Van Buren & McCray (1988) looked for bow-shaped features near high-velocity O stars and found an IR candidate close to the O supergiant BD+43°3654 (α, δ[J2000] = $20^{\rm h}33^{\rm m}36.077^{\rm s}, +43°59'07.40''$; $l, b = 82.41°, +2.33°$). Comerón & Pasquali (2007) related the star BD+43°3654 to a bow shock detected with the Midcourse Space eXperiment (MSX) at D and E bands. Also, data from the NRAO-VLA[1] NVSS Survey (Condon et al. 1998) revealed a coma-shaped source of ~ 7 arcmin spatially coincident with the MSX feature (Figure 1).

A radio study of the bow shock can shed light on the physical processes that give rise to high-energy emission from a stellar source, regardless of the history of the runaway star. The shock can accelerate particles up to relativistic energies by Fermi mechanism. Energetic electrons will cool through synchrotron radiation, producing a non-thermal radio source. We carried out radio observations at two frequencies to study the nature of the emission from the bow shock of BD+43°3654.

[1]National Radio Astronomy Observatory - Very Large Array (http://www.vla.nrao.edu/).

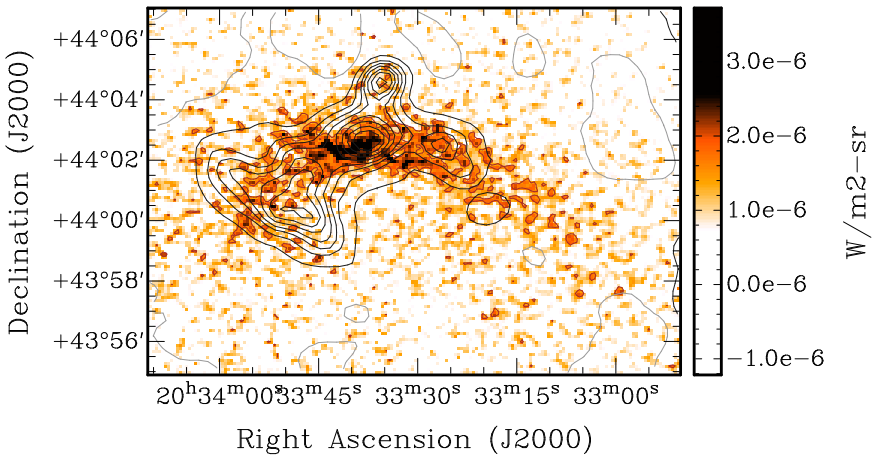

Figure 1: MSX-D band image (color scale) superposed to 1.4 GHz-NVSS contours. Levels are: -2, 2 (2σ), 5, 8, 11, 15, 19, 24, 29, 50, 70, and 90 mJy beam^{-1}.

2 Observations and results

Our continuum observations were carried out with the Very Lare Array (VLA) at 1.42 GHz (C config.) and at 4.86 GHz (D config.). Figure 2 presents the resulting images after primary beam correction, re-gridded with the same synthesized beam of 12". There is emission at both frequencies along the extension of the MSX source. The hypothesis of a physical association between the star and the radio/IR features is supported by the very good agreement of the residual proper motion of the star and the direction from the star to the apsis of the bow shock (Fig. 2). We used the continuum images

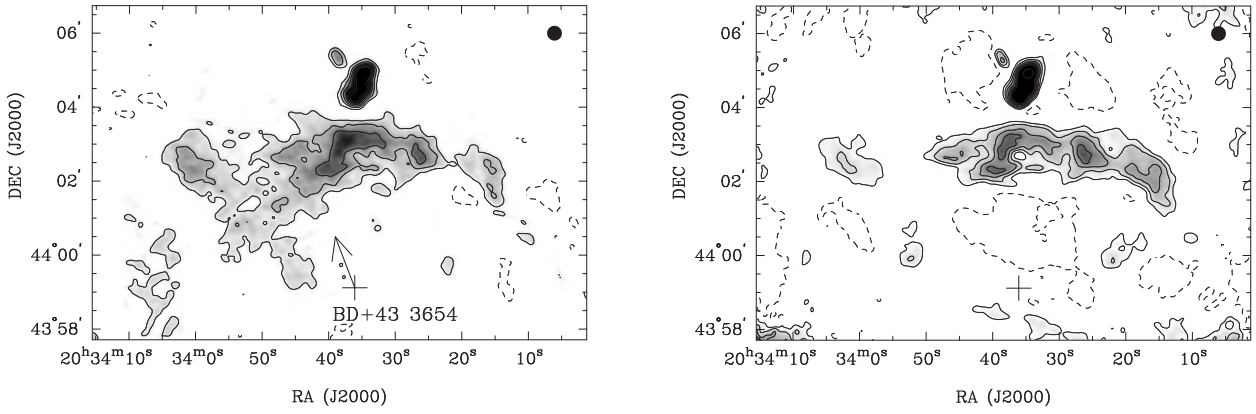

Figure 2: Continuum emission at 1.42 GHz (left), and at 4.86 GHz (right). Contour levels are -3, 3, 6, 10, 15, 20, 25, and 60 times the rms of 0.3 and 0.2 mJy beam^{-1}. BD+43° 3654 is marked with a cross. The arrow represents the velocity vector of the star, derived from proper motions corrected for local motion of the surrounding ISM (see text). Synthesized beams of $12'' \times 12''$ are shown in the top right corners.

at 1.42 and 4.86 GHz to build a spectral index distribution map. We only considered input pixels with a signal-to-noise ratio ≥ 4. Besides, the spectral index map was masked for a signal-to-noise ratio $\geq$ 10. Figures 3 and 4 show the spectral index distribution and corresponding noise maps.

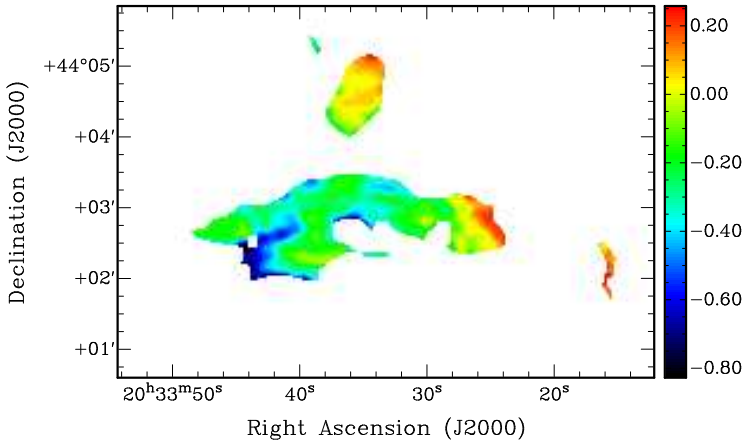

Figure 3: Spectral index distribution.

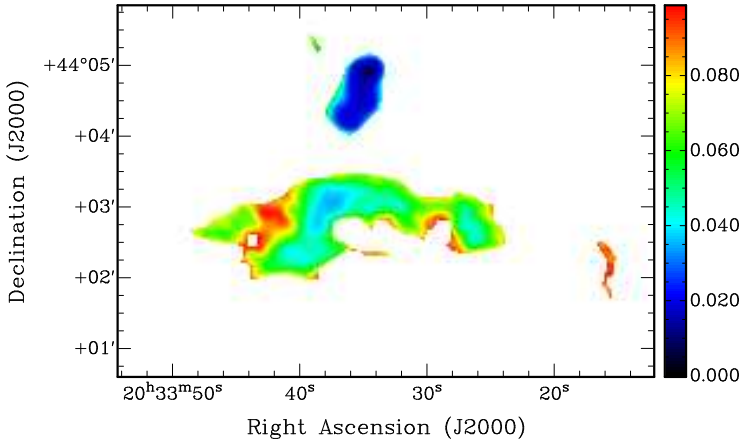

Figure 4: Spectral index error distribution.

3 Bow-shock emission

Most of the area shows a source of non-thermal radiation with index $< \alpha >= -0.5$ ($S_\nu \propto \nu^\alpha$), as obtained from the VLA data. We adopted a distance to the bow-shock of 1.4 kpc (Hanson 2003). The distance from the star to the bow-shock is $R = 5'$, or 2 pc. The volume occupied by the bow-shock is $\sim 4.6\,\mathrm{pc}^3$. We took a particle density of the ISM in the bow shock region of 100 cm^{-3} (see Kobulnicky et al. 2010).

The non-thermal radiation is expected from synchrotron emission generated by relativistic electrons accelerated either at the forward shock in the ISM or in the reverse shock in the stellar wind. We estimated the particle energy distribution (n) using the observed flux density and spectral slope, and assumed equipartition between magnetic and relativistic particles energy density.

We considered that the energy density of relativistic particles has three contributions:

$$u = u_{e_1} + u_p + u_{e_2} = \int E_{e_1} n_{e_1}(E_{e_1}) dE_{e_1} + \int E_p n_p(E_p) dE_p + \int E_{e_2} n_{e_2}(E_{e_2}) dE_{e_2}, \qquad (1)$$

where e_1, p, and e_2 stand for relativistic primary electrons, protons, and secondary electron-positron pairs (i.e. pairs coming from charged pion decays), respectively. The relation between primary electrons and protons energy density is $u_p = a u_{e_1}$, with $a \geq 0$. Three cases were considered: $a = 0$ (just electrons), $a = 1$ (equal energy density in both species), and $a = 100$ (proton-dominated case, as observed in the galactic cosmic rays). The magnetic field resulted $B \sim 5 \times 10^{-5}$ G.

The maximum energy of the particles was determined by balancing energy gains and losses. The loss mechanisms considered were *(i)* synchrotron radiation, *(ii)* relativistic Bremsstrahlung, *(iii)* particle escape from the radiation region due to convection by the stellar wind, and *(iv)* inverse Compton (IC) scattering of IR, stellar and cosmic microwave background photons. In the case of protons, the only relevant losses are proton-proton (pp) inelastic collisions and convective escape. Diffusion is negligible in comparison to convection in this situation (the respective timescales are $t_{\rm conv} \sim 6 \times 10^6$ s and $t_{\rm diff} \sim 10^{13}/(E/{\rm erg})$ s). Both primary electrons and protons reach energies up to $\sim 10^{13}$ eV, which is imposed by non-radiative losses, except for $a = 100$, where synchrotron losses dominate for electrons. Figure 5 shows the losses for electrons and protons in the case $a = 1$.

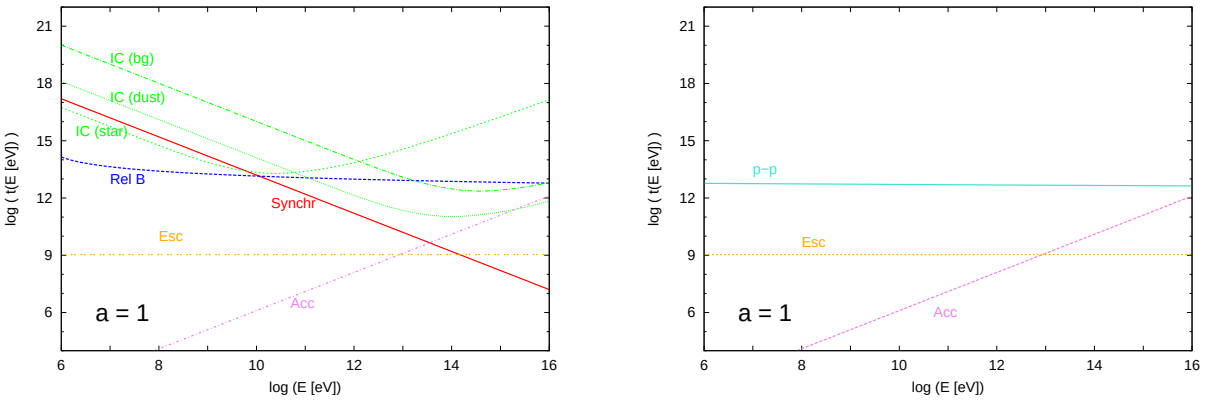

Figure 5: Left: acceleration ('Acc'), escape ('Esc'), and cooling times for electrons, due to synchrotron radiation ('Synchr'), IC scattering of dust photons ('IC (dust)'), stellar photons ('IC (star)'), and backgroud photons ('IC (bg)'). Cooling time for relativistic Bremsstrahlung radiation is indicated as 'Rel B'. The figure is for the case with equal energy density in electrons and protons ($a = 1$, see text). Right: acceleration, escape, and cooling time for protons due to the pp radiation process ('p-p').

4 Discussion and perspectives

The presence of highly relativistic particles in a dense medium with high photon density can result in the efficient generation of γ-rays. The corresponding γ-ray emissivity can be calculated using the delta-functional approximation (e.g. Aharonian & Atoyan 2000, Kelner et al. 2006).

In Fig. 6 we show the spectral energy distribution obtained for the case $a = 1$, with all contributions included (synchrotron self-Compton losses are negligible). The total luminosity from pp interactions is similar to that obtained from relativistic Bremsstrahlung of electrons. The IC upscattering of IR photons is the major contribution at high energies, with a peak around 100 GeV. The detectability of the source by the Fermi LAT[2] γ-ray observatory will depend on the actual particle density and the contribution related to the secondary electrons at large a. The pp contribution extends well into the TeV regime, but is weaker and will be difficult to detect with the current ground-based Cherenkov telescope arrays.

For the case $a = 100$, the relativistic particle content is proton-dominated and γ-rays from the pp process dominate the high energy spectrum. The CTA[3] North observatory might detect the source yielding information on the high enery cutoff.

[2]Fermi Large Area Telescope (http://www-glast.stanford.edu/).
[3]Cherenkov Telescope Array (http://www.cta-observatory.org/).

Observations of the spectral slope at high energies can be used to identify the proton content through the luminosity level, and the proton spectral index. Radio polarization data will provide additional information on B. X-ray observations will allow to determine the cutoff of the synchrotron spectrum, directly related to the maximum energy of the electrons[4]. This, in turn, would yield valuable information on the actual value of B and the correctness of the equipartition hypothesis.

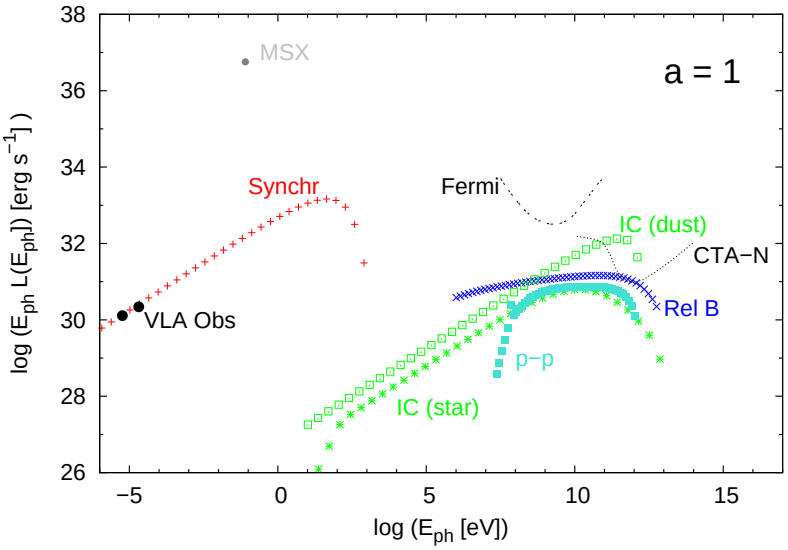

Figure 6: Spectral energy distribution for the case $a = 1$. Acronyms as in Figure 5. Measured radio fluxes from VLA observations ('VLA Obs') and MSX luminosity at D band are also represented. The contribution from secondary pairs is negligible in this case, so it is not shown here.

Acknowledgements

This work was supported by MinCyT - ANPCyT (PICT-2007-00848) and by CONICET (project ID 11220090100078). JM and GER acknowledge support by grant AYA2007-68034-C03-01 and -02 from the Spanish government and FEDER funds and Plan Andaluz de Investigación, Desarrollo e Innovación of Junta de Andalucía as research group FQM-322 and excellence fund FQM-5418.

References

Aharonian, F. A. & Atoyan, A. M. 2000, A&A, 362, 937
Comerón, F. & Pasquali, A. 2007, A&A, 467, L23
Condon, J. J, Cotton, W. D., Greisen, E. W., Yin, Q. F., Perley, R. A., Taylor, G. B. & Broderick, J. J. 1998, AJ, 115, 1693
Gies, D. & Bolton, C. T. 1986, ApJS, 61, 419
Hanson, M. M. 2003, ApJ 97, 957-969
Kelner, S. R., Aharonian, F. A. & Bugayov, V. V. 2006, Phys. Rev. D, 74, 4081
Kobulnicky, H. A., Gilbert, I. J. & Kiminki, D. C. 2010, ApJ, 710, 529
Van Buren, D. & McCray, R. 1988, ApJ, 329, L93

[4]Notice that the situation is quite different from that of colliding winds, where the particle acceleration occurs in a region of high photon density, with dominance of IC losses.

Two New LBV Candidates in the M 33 Galaxy

O. N. Sholukhova, A. F. Valeev and S. N.Fabrika

Special Astrophysical Observatory of the Russian AS, Nizhnij Arkhyz, Russia

Abstract: We present two new luminous blue variable (LBV) candidate stars discovered in M 33. We identified these stars (Valeev et al. 2010a, b) as massive star candidates at the final stages of evolution. The candidates were selected from the Massey et al. (2006) catalog based on the following criteria: emission in Hα, $V < 18\overset{\mathrm{m}}{.}5$ and $0\overset{\mathrm{m}}{.}35 < (B-V) < 1\overset{\mathrm{m}}{.}2$ (presumably reddened early stars). Based on our spectroscopy of the stars, we estimated their main parameters. Object N 45901 has a bolometric luminosity $\log(L/L_\odot)$ = 6.0 – 6.2 with the value of interstellar extinction $A_V = 2.3 \pm 0.1$. The temperature of the star's photosphere is $T_\star \sim 13000 - 15000$ K, its probable mass is M $\sim$ 60–80 $M_\odot$. The infrared excess in N 45901 corresponds to the emission of warm dust with a temperature $T_{warm} \sim 1000$ K. the bolometric luminosity of the second object, N 125093, is $\log(L/L_\odot)$ = 6.3 – 6.6, the value of interstellar extinction is $A_V = 2.75 \pm 0.15$. Its photosphere's temperature is $T_\star \sim 13000 - 16000$ K, the initial mass is M$\sim$ 90-120 $M_\odot$. The infrared excess in N 125093 amounts to 5–6 % of the bolometric luminosity. Its spectral energy distribution reveals two thermal components with temperatures $T_{warm} \sim 1000$ K and $T_{cold} \sim 480$ K. The [Ca II] $\lambda\lambda 7291, 7323$ lines, observed in LBV-like stars Var A and N 93351 in M 33, are also present in the spectrum of N 125093. The high bolometric luminosities of these stars and broad Hα emissions allow classifying the studied objects as LBV candidates.

1 Introduction

Apparently, most of the LBV stars without notable interstellar extinction in our Galaxy are already discovered. However, it is probably still possible to discover a few dozen more such objects in the Galaxy using modern infrared surveys (Gvaramadze et al. 2010a, 2010b). In M 33 almost all the LBV-like objects may be detected, as its fortunate orientation and a relatively close distance (950 kpc, Bonanos et al. 2006) allow detailed spectroscopy of its bright stars.

According to the catalog (Massey et al. 2006), M 33 contains 2304 stellar objects with $V < 18\overset{\mathrm{m}}{.}5$. If we assume that the mean interstellar extinction of the brightest stars in the galaxy is $A_V \approx 1\overset{\mathrm{m}}{.}0$ (see, e.g., Fabrika et al. (1999), where this value is estimated as $A_V \approx 0\overset{\mathrm{m}}{.}95 \pm 0\overset{\mathrm{m}}{.}05$), then with the distance modulus to M 33 of $(m-M)_0 = 24\overset{\mathrm{m}}{.}9$ (Bonanos et al. 2006), the stars with $V < 18\overset{\mathrm{m}}{.}5$ and $(B-V) < 0\overset{\mathrm{m}}{.}35$ will have the luminosity $M_V < -7\overset{\mathrm{m}}{.}4$ and color $(B-V)_0 \leq 0\overset{\mathrm{m}}{.}0$. In our paper (Valeev et al. 2010a) we obtained photometry in the Hα images of all the stars from the catalog of Massey et al. (2006) with the above restrictions on color and magnitude, and made a list of stars with an excess in Hα. These are bright supergiants of the Iab luminosity class and brighter, and the hottest Ib supergiants (with B0 spectra and earlier). We expected that all the potential LBV candidates will make it into our list. We hence isolated in Valeev et al. (2010a) 185 blue emission objects ($V < 18\overset{\mathrm{m}}{.}5$ and $(B-V) < 0\overset{\mathrm{m}}{.}35$), candidates for massive stars at the final stages of evolution.

Evidently, LBVs and similar objects may well have an extinction $A_V > 1\overset{m}{.}0$, for which reason an additional list of stars with $V < 18\overset{m}{.}5$ and $0\overset{m}{.}35 < (B-V) < 1\overset{m}{.}2$ with emission in Hα was made in Valeev et al. (2010a) containing 25 candidates. We have recently obtained spectra of 15 candidate stars from the supplementary list, among them we discovered two new LBV candidates (Fig. 1). In this paper we present the results of our study of these two objects.

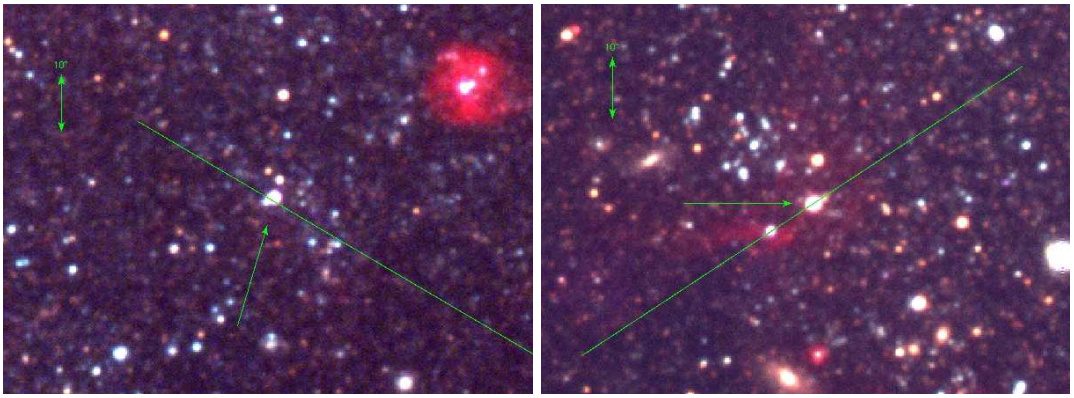

Figure 1: Finding charts in the B, V, Hα rgb image for the objects N 45901 (left) and N 125093 (right), the arrows mark their positions. The star numbers are according to nomenclature by Massey et al. (2006). The slit orientation during the observations is shown. North is at the top, west on the left.

2 Spectra and stellar parameters

The spectrum of **N 125093** is shown in Fig. 2 compared to the spectra of the known LBV stars in M 33, Var A, Var B, V 532 and a new quite firm LBV candidate in this galaxy, N 93351[1].

In the spectrum of N 125093 we see a broad Hα line with a width FWHM = 1000 km/s and equivalent width 36Å. The He I emissions in the spectrum of this star are very weak, but noticeable, the brightest line He I $\lambda\lambda 5876$ has a low intensity. The red region of the spectrum reveals weak Fe II emission lines, and several forbidden [Fe II] lines. There are nebular lines, [O I] $\lambda\lambda 6300, 6364$ as well as weak [N II] $\lambda\lambda 6548, 6384$ lines in the wings of the broad Hα emission. The [Ca II] $\lambda\lambda 7291, 7323$ lines are quite interesting, they indicate a recent gas eruption and linked dust activity (Valeev et al. 2009).

Absorption Fe II lines are visible in the blue region of the spectrum, some Ti II lines (like those in the spectrum of N 93351) and two Si II $\lambda\lambda 6347, 6371$ lines. However, the strongest metal line Fe II $\lambda 5169$ possesses emission components in the wings. In the spectrum of N 125093 diffuse interstellar bands (DIBs) are clearly visible, the Na I $\lambda\lambda 5890, 5896$ doublet is also strong. The Hβ emission of N 125093 is relatively weak and does not have broad wings at the given spectrum quality in the region.

We conducted the Gaussian analysis of the Hα emission, and found that a narrow component of this line has FWHM= 5.9 Å, which is not much different from our spectral resolution (5 Å), but its broad component has FWHM= 22.5 Å, which corresponds to the velocity dispersion in the outflowing wind of approximately 1000 km/s (after correcting for the spectral resolution). The narrow component of the Hβ line has FWHM= 4.4 Å.

[1]The spectrum of V 532 was kindly provided by Szeifert et al. (1994) and obtained with a resolution of 1.2 Å. All the remaining spectra were obtained with SCORPIO: the spectra of Var A, Var B with a spectral resolution of 12 Å, while the spectrum of N 93351 with a resolution of 5 Å. (Valeev et al. 2009)

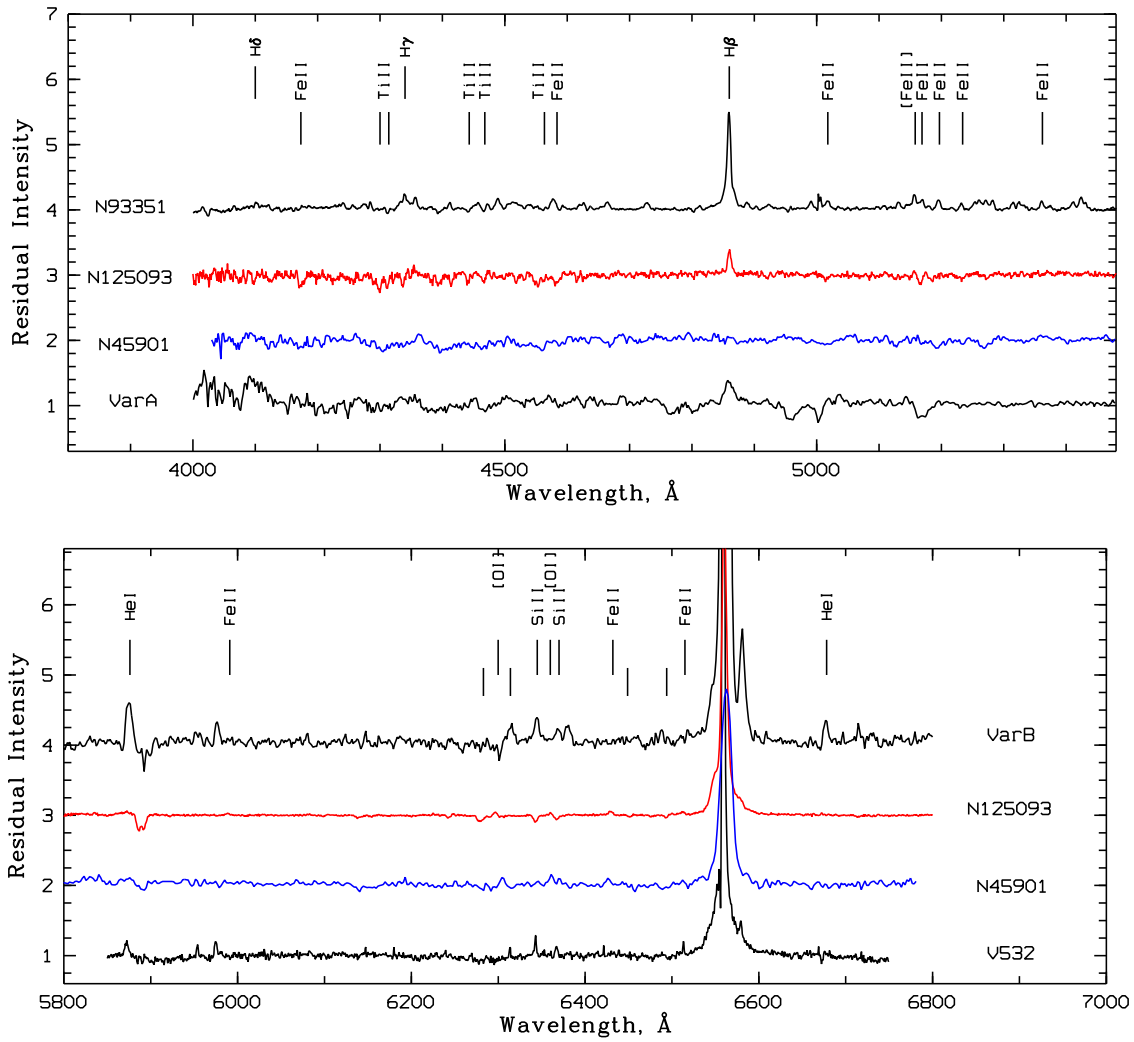

Figure 2: The normalized spectra of LBV candidates N 45901 and N 125093 in red and blue regions. The spectra of the two new LBV candidates were taken with the Russian 6-m telescope BTA with the SCORPIO focal reducer. For comparison we plot spectra of a known LBV in M 33, Var A (an LBV or a red hypergiant) and N 93351 (a firm LBV candidate) (top), Var B and V 532 (bottom). The main spectral lines detected in the spectra of our candidates are marked.

Faint and extended H II regions were captured by the slit. However around N 125093 the H II emission is very weak. To estimate the interstellar extinction, we used the Hα/Hβ line flux ratio for the emision extracted near the star. For the gaseous nebulae this ratio amounts to approximately 2.87 in a wide range of temperatures and densities (Osterbrock & Ferland 2006). We used the law of interstellar reddening from the work of O'Donnell (1994) at R_V=3.07. We obtained the value $A_V \leq 2.5$. A comparison of the spectrum of N 125093 with the spectra of relatively hot stars Var B and V 532 allows us to conclude that the temperature of the photosphere of N 125093 is certainly lower than 20000 K. On the other hand, based on the presence of deep Si II absorptions we can deduce that the temperature is definitely above 10000 K.

The spectrum of the star **N 45901** is shown in Fig. 2. We see a bright and broad Hα emission with extended wings. Gaussian analysis revealed a two-component line profile: a bright narrow line and broad wings. The widths of the narrow and broad components, corrected for spectral resolution, are equal to 140 km/s and 770 km/s, respectively. There is a [N II] λ6584 line in the broad Hα wing. The second line of the [N II] doublet, which should be 3 times weaker than the first, is probably lost in the bright blue Hα wing. We also found forbidden lines [O I] $\lambda\lambda 6300, 6364$, which are formed in the

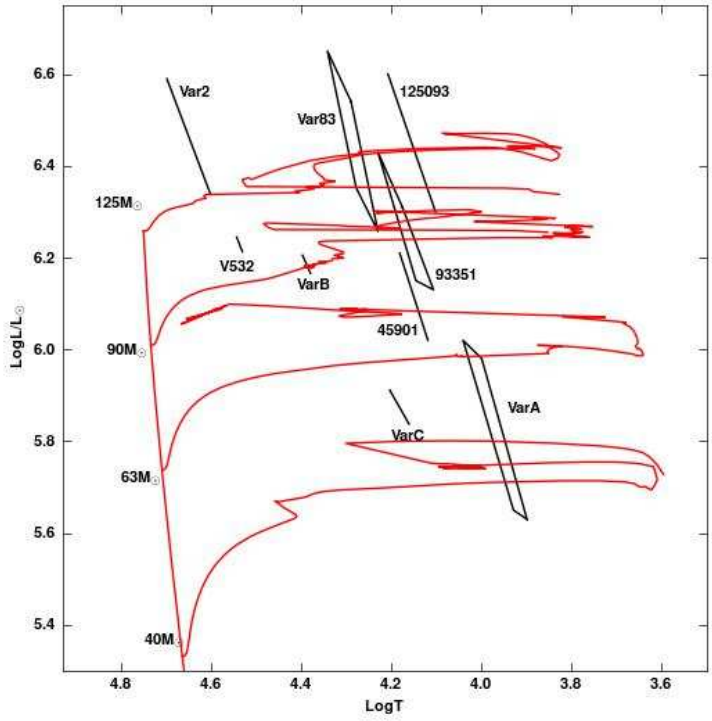

Figure 3: The temperature – luminosity diagram for all known LBV stars in M33 (Valeev et. al., 2009) with two new candidates N 45901 and N 125093 imposed. Error regions are shown. The evolution track are as calculated by Claret (2006) at metallicity Z=0.007 (M33 metallicity is 0.008).

unresolved region around the star which is smaller than 4–5 pc (at the distance of 950 kpc we adopted, the scale in M 33 is equal to 4.6 pc/arcsec). Despite the poor quality of the spectrum, especially in the blue region, the absorption lines Fe II and Ti II that are among the most intense lines of these ions, are visible in this range. In the red range, we may even suspect [Fe II] emission. The region shorter than the Hα line reveals signatures of two strongest Fe II emission lines.

Based on the presence of a broad and bright Hα emission, as well as the likely occurrence of Fe II and Ti II lines we can make a rough estimate that the temperature of the photosphere of N 45901 is above 10000–12000 K. We did not detect any He I lines, hence its temperature is below 15000 K.

2.1 Spectral energy distributions and stellar parameters

Here we present results of the spectral energy distributions (SED) of all known LBV stars in M33 and two new candidates N 45901 and N 125093 (for details see Valeev et al. 2010b). For N 125093 we find the optimal value of the interstellar extinction as $A_V = 2.75 \pm 0.15$. The temperature of the stellar photosphere is $T_\star \sim 13000 - 16000$ K, which is consistent with our estimate from the spectrum. The corresponding bolometric luminosity of N 125093 amounts to $\log(L/L_\odot)$ = 6.3 – 6.6. We find two thermal components in the spectrum, a warm component with $T_{warm} \sim 1000$ K, and a cold component with $T_{cold} \sim 480$ K. The infrared excess in N 125093 is 5–6 % of the bolometric luminosity.

In the case of N 45901 we deduced the interstellar extinction of $A_V = 2.3 \pm 0.1$. Accordingly, the temperature of the photosphere of N 45901 is estimated as $T_\star \sim$ 13000–15000 K, and its bolometric

luminosity amounts to $\log(L/L_\odot)$ = 6.0 – 6.2. Infrared excess in N 45901 corresponds to the warm dust radiation with the temperature of $T_{warm} \sim 1000$ K and amounts to 0.1 % of the bolometric luminosity.

Figure 3 illustrates the temperature–luminosity diagram for all the LBV stars known to date (Var B, Var C, Var 2, Var 83, V 532), as well as the stars Var A and N 93351 in M 33, the parameters of which were determined in our paper (Valeev et al. 2009). We show our two new candidates N 45901 and N 125093 and the evolutional tracks Claret (2006) computed for stars with metallicity 0.007, corresponding to M 33. From this diagram, we find the mass estimates for the stars on the ZAMS. The masses of N 45901 and N 125093 are estimated as approximately $60 - 80 M_\odot$, and $90 - 120 M_\odot$, respectively.

3 Conclusion

This paper presents a preliminary study of two new LBV candidates in the M 33 galaxy. The spectra of N 45901 and N 125093 are similar to the spectra of the stars at the LBV stage. They have strong and broad Hα, emissions, forbidden [O I] and [N II] lines. The spectrum of the second star reveals [Ca II], [Fe II] and Fe II emission lines, Ti II and Fe II absorptions. The spectrum of the first star has an insufficient quality for a reliable identification, however the [O I], Fe II and Ti II lines are present in its spectrum. Comparisons of brightness estimates from different catalogs indicate a probable variability of the object N 45901. We found an infrared excess in both stars. The temperatures of warm and cold dust components in the star N 125093 (it possesses the [Ca II] emissions), amount to 1400 K and 470 K, respectively. We estimate that the star N 45901 has a bolometric luminosity of $\log(L/L_\odot)$ = 6.0 – 6.2 and its probable mass on the initial main sequence is $M \sim 60 - 80\ M_\odot$. The luminosity of N 125093 amounts to $\log(L/L_\odot)$ = 6.3 – 6.6 and its initial mass is $M \sim 90 - 120 M_\odot$. In Valeevet al. (2010b) the possible variability of these stars is discussed. All the above properties of N 45901 and N 12509 allow us to classify them as LBV candidates.

4 Acknowledgements

This paper was supported by the grants of the Russian Foundation for Basic Research (N09-02-00163 and 10-02-00463), the grant "Leading Scientific Schools of Russia" N5473.2010.2 and The Federal Program "Scientific and educational cadre of innovating Russia 2009 -2013", N1244

References

Bonanos A.Z., Stanek K.Z., Kudritzki R.P. et al. 2006, ApJ, 652, 313
Claret A., 2006, A&A, 453, 769
Fabrika S. and Sholukhova O., 1999, A&AS, 140, 309
Gvaramadze V.V., Kniazev A.Y., and Fabrika S., et al. 2010a, MNRAS, 405, 520
Gvaramadze V.V., Kniazev A.Y., and Fabrika S., 2010b, MNRAS, 405, 1047
Massey Ph., Olsen K.A.G., Hodge P.W. et al. 2006, AJ, 131, 2478
O'Donnell J.E., 1994, ApJ, 422, 158
Osterbrock D.E.and Ferland G.J., 2006, Astrophysics of gaseous nebulae and active galactic nuclei, Univ. Sci. Books, Sausalite.
Szeifert T., Stahl O., Wolf B. et al., 1994, Astronomische Gesellschaft Abstract Series, 10, 36
Valeev A., Sholukhova O., and Fabrika S., 2009, MNRAS, 396, L21
Valeev A., Sholukhova O., and Fabrika S., 2010a, Astrophysical Bulletin, 65, 140
Valeev A., Sholukhova O., and Fabrika S., 2010b, Astrophysical Bulletin, 65, 360

The VLT-FLAMES Tarantula Survey

W. D. Taylor[1], C. J. Evans[2,1], V. Hénault-Brunet, N. Bastian, Y. Beletsky,
J. Bestenlehner, I. Brott, M. Cantiello, G. Carraro, J. S. Clark,
P. A. Crowther, A. de Koter, S. E. de Mink, E. Doran, P. L. Dufton, P. Dunstall,
M. Gieles, G. Gräfener, A. Herrero, I. D. Howarth, N. Langer,
D. J. Lennon, J. Maíz Apellániz, N. Markova, P. Najarro, J. Puls,
H. Sana, S. Simón-Díaz, S. J. Smartt, V. E. Stroud,
J. Th. van Loon, J.S. Vink and N. R. Walborn

[1] Institute for Astronomy, Royal Observatory Edinburgh, Blackford Hill, Edinburgh. EH9 3HJ, UK

[2] UK ATC, Royal Observatory Edinburgh, Blackford Hill, Edinburgh. EH9 3HJ, UK

Abstract: The VLT-FLAMES Tarantula Survey is an ESO Large Programme that has provided multi-epoch spectroscopy of over 1000 stars in the 30 Doradus region in the Large Magellanic Cloud. Armed with this unique dataset the assembled consortium is now addressing a broad range of fundamental questions in both stellar and cluster evolution. Here we give an overview of the survey and the observational strategy, which was designed to be very sensitive to massive binaries. We highlight the power of the multi-epoch approach with the discovery of a massive runaway O-type star which appears to be fleeing the core of the Tarantula region.

1 Introduction

The VLT-FLAMES Survey of Massive Stars obtained high-quality spectroscopy of $\sim$750 massive stars in fields centered on clusters in the Galaxy and the Magellanic Clouds (Evans et al. 2005, 2006). Key results from the project included evidence of the predicted dependence of stellar mass-loss rates on metallicity in O-type stars (Mokiem et al. 2007), and new insights into the role of rotational mixing in B-type stars (Hunter et al. 2008).

This second incarnation of the FLAMES consortium is now focussed on the oft-studied 30 Doradus region, also known as the Tarantula nebula. This is the largest nearby massive 'starburst' region, providing an excellent environment to study the physical properties and evolution of O- and early B-type stars. A broader range of scientific motivations will be discussed in the survey overview paper (Evans et al. in preparation), here we briefly describe two of the primary objectives.

- *The role of rotational mixing in O-type stars:* From analysis of B-type stars from the previous FLAMES survey, Hunter et al. (2008, 2009) found that the surface nitrogen abundances were not as well correlated with stellar rotational velocities as one might expect; work is still underway to reconcile these results with theory. One of the prime motivations for a large sample of high-quality spectroscopy of O-type stars is to undertake a similar analysis of nitrogen (and carbon/oxygen abundances where possible) to test the predictions of evolutionary models. Until

now we also have lacked the theoretical tools for such a large-scale analysis but, as described by Puls, Sundqvist & Rivero González (2011), work has been underway to include transitions from N III and N IV in the FASTWIND model atmosphere code (Puls et al. 2005)[1].

- *Detection and characterization of massive binaries:* There is increasing evidence that a significant number of massive stars are in binary systems. This has been observed in various clusters, both in the Galaxy and Magellanic Clouds, with an average binary fraction of 0.44 ± 0.05 from published studies of cluster populations (Sana & Evans 2011). To gain a true understanding of the evolution of massive-star populations, the effects of binarity need to be fully included in our theoretical models of stellar evolution. Identification of binaries is also important in the context of correct estimates of cluster velocity dispersions (e.g. Bosch, Terlevich & Terlevich 2009; Gieles, Sana & Portegies Zwart, 2010).

Other objectives include determining the evolutionary connections between the different subtypes of evolved O-type stars, dynamical measurements in the regions around R136 at the core of 30 Doradus, studying the feedback to the interstellar medium from stellar winds and the ionizing fluxes of the cluster stars, and investigating the dynamics of the associated nebular gas.

2 Observational data

FLAMES is a highly versatile multi-object instrument on UT2 of the VLT (Pasquini et al. 2002). The primary dataset for the Tarantula Survey was obtained with the Medusa mode of FLAMES, which uses deployable fibres to obtain simultaneous observations of up to 132 targets across a 25′ field-of-view; the fibres (each 1.″2 on the sky) feed the light from each target to the Giraffe spectrograph.

The Medusa observations comprise spectroscopy of exactly 1000 stars, which were selected from unpublished imaging of 30 Dor taken with ESO's Wide-Field Imager on the 2.2m telescope at La Silla. The targets were selected to sample not just the inner regions of the cluster, but also to extend out into the surrounding field stars and some of the nearby smaller associations/clusters, as shown in Figure 1. To avoid possible selection biases, no colour cuts were made, but a limiting magnitude was applied ($V < 17$, to ensure adequate signal-to-noise, S/N).

A total of nine fibre configurations (fields 'A' through to 'I') were used to build-up the sample of 1000 stars. Each target was observed at three of the standard Giraffe wavelength settings (LR02, LR03 and HR15N, as summarised in Table 1) thus providing coverage of the classical blue region used in the analysis of massive stars, combined with higher resolution observations of Hα, which provides a diagnostic of the intensity of the stellar winds. Each observation consisted of a pair of back-to-back exposures, with three pairs of observations at the LR02 and LR03 settings, and two pairs at HR15N, thus ensuring sufficient S/N ($\geq$50) in the combined spectra.

Table 1: Observational details of the Medusa component of the Tarantula Survey.

Setting	Wavelength	R	Exposures
LR02	3980-4525 Å	6500	$6 \times (2 \times 1815\text{s})$
LR03	4505-5050 Å	7500	$3 \times (2 \times 1815\text{s})$
HR15N	6470-6790 Å	17000	$2 \times (2 \times 2265\text{s})$

[1]For completeness we note that the CMFGEN code (Hillier & Miller 1998) includes models for the nitrogen ions, but is less well suited for analysis of large samples such as the new dataset from the Tarantula Survey.

2.1 Multi-epoch strategy

Three pairs of the LR02 exposures were obtained with no strong time constraints – in practise, these were often obtained consecutively, or on sequential nights. For detection of massive binaries, a further three pairs of LR02 exposures were obtained. The fourth and fifth epochs were constrained such that a minimum of 28 days had expired since the previous LR02 observation, while the final (sixth) epoch was obtained in the equivalent observing season one year later.

From the methods presented by Sana, Gosset & Evans (2009), it is possible to calculate the probabilities of detecting a binary companion around a star as a function of the orbital period, based on the time sampling of the observations. This is shown for one of the fields from the Tarantula survey in Figure 2. The black line shows the detection probabilities for the first five epochs, with the red line demonstrating how inclusion of the sixth, delayed, epoch significantly increases the chance for detecting binaries with periods greater than 100 days. The survey should be fairly complete for orbits of tens of days. Quantifying the potential selection biases is a critical component of the work to inform the binarity results from the survey.

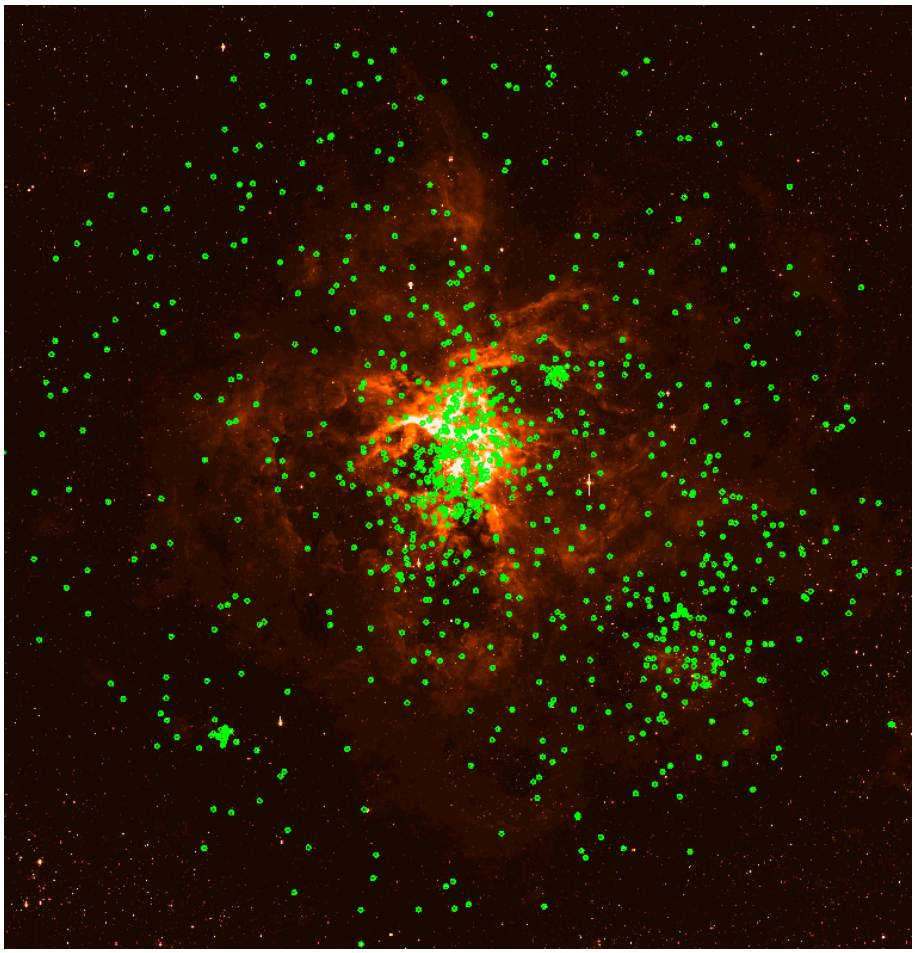

Figure 1: Positions of the FLAMES targets overlaid on a V-band mosaic from the Wide-Field Imager on the 2.2 m telescope at La Silla.

2.2 Spectral content

From the reduced LR02 frames and a first-pass analysis of the radial velocities, it has been possible to make an initial classification of all the Medusa objects. The sample contains around 300 O-type stars,

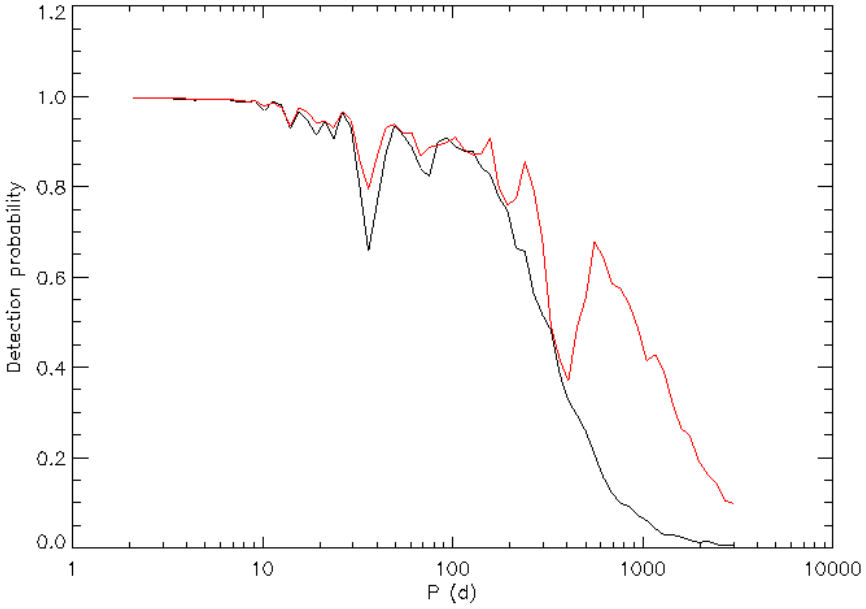

Figure 2: Detection probability of binary systems with different orbital periods given the observed time-sampling of one of the Tarantula fibre configurations. The black line shows the sensitivity for the first five LR02 observations, with the red line indicating the increased sensitivity to longer orbits given by inclusion of the sixth, delayed observation.

towards 500 B-type stars (also of significant interest in terms of multiplicity, chemical composition and the effects of rotational mixing), $\sim$20 Wolf-Rayet or 'slash' Of/WN emission-line stars, $\sim$90 cool-type (A-M) stars with radial velocities consistent with them being LMC members, and just over 100 foreground stars (rejected employing a radial velocity threshold of $\leq 100\,\mathrm{km\,s^{-1}}$).

2.3 Additional data

To expand our view of the 30 Dor stellar populations the survey also employs other modes of FLAMES, as well as being supplemented by other external sources:

- *ARGUS observations of R136:* Five ARGUS pointings were used to target the denser central regions in and around R136. For a fuller description of this aspect of the observing campaign, see Hénault-Brunet et al. (2011).

- *UVES observations:* In parallel to the ARGUS observations, a total of 25 stars were observed using the fibre-feed to the red arm of UVES. The λ5200 Å setting was used, which delivers a spectral resolving power of 47000. Of these 25 targets, five are unique to the UVES data, with the remaining 20 providing complementary information to targets also observed with Giraffe.

- *VLT-SINFONI K-band spectroscopy:* SINFONI has been used in a separate programme (PI: Gräfener) to obtain near-IR spectroscopy of the central arcminute around R136.

- *Faulkes Telescope South photometric monitoring:* Fields matched to our survey areas are being observed in the offline queue by the Faulkes telescope at Siding Spring, providing long-term photometric follow-up in the Bessel BV, SDSS i' and Pan-STARRS Y bands.

3 A massive runaway star from 30 Dor

On the western edge of the FLAMES field is the massive star #016 (numbered in the sequence of the FLAMES targets). Previous spectroscopy with the 2-degree Field (2dF) instrument at the Anglo-Australian Telescope had revealed this star as an O2-type star, with a radial velocity which is discrepant from its surroundings by $\sim 85\mathrm{kms}^{-1}$. Given its early spectral type, magnitude and location, the star was observed as one of the Servicing Mission Observy Verification targets of the *Hubble Space Telescope* Cosmic Origins Spectrograph (COS). Analysis of the P Cygni profiles in the UV spectrum from COS yielded an estimate of the terminal wind velocity of $3450 \pm 50\mathrm{kms}^{-1}$, one of the fastest winds observed for an O-type star (Evans et al. 2010).

The FLAMES observations showed no significant variation in the radial velocity and, using the methods discussed above, it was possible to rule out a massive binary companion to a confidence of 98%. Therefore, its highly discrepant velocity appears real, suggesting that the object has been kicked out the central regions of the cluster in the relatively recent past.

4 Current status

All the observations have been taken and the data have been reduced and released to the consortium. Work has begun in earnest towards the first papers, including classification of the different spectra, analysis of stellar radial velocities/binarity, and analysis of the nebular gas profiles.

Acknowledgements

Based on observations from ESO programme 182.D-0222 (PI: Evans).

References

Bosch, G., Terlevich, E. & Terlevich, R. 2009, AJ 137, 3437
Evans, C.J., Smartt, S.J., Lee, J.-K., et al. 2005, A&A 437, 467
Evans, C.J., Lennon, D.J., Smartt, S.J., & Trundle, C. 2006, A&A 456, 623
Evans, C.J., Walborn, N.R., Crowther, P.A., et al. 2010, ApJ 725, L74
Gieles, M., Sana, H. & Portegies Zwart, S.F. 2010, MNRAS 402, 1750
Hénault-Brunet, V., Evans, C.J., Taylor, W.D., & Gieles, M. 2011, in Proceedings of the 39th Liège Astrophysical Colloquium, eds. G. Rauw, M. De Becker, Y. Nazé, J.-M. Vreux & P.M. Williams, BSRSL 80, 376
Hillier, D.J., & Miller, D.L. 1998, ApJ 496, 407
Hunter, I., Brott, I., Lennon, D.J., et al. 2008, ApJ 676, L29
Hunter, I., Brott, I., Langer, N., et al. 2009, A&A 496, 841
Mokiem, M.R., de Koter, A., Vink, J.S., et al. 2007, A&A, 473, 603
Pasquini, L., Avila, G., Blecha, A., et al. 2002, Msngr 110, 1
Puls, J., Urbaneja, M.A., Venero, R., Repolust, T., Springmann, U., Jokuthy, A., & Mokiem, M.R. 2005, A&A 435, 669
Puls, J., Sundqvist, J.O. & Rivero González, J.G. 2011, in *Active OB Stars: Structure, Evolution, Mass loss & Critical Limits*, eds. Neiner, Wade, Meynet & Peters, Proc. IAUS272, Cambridge University Press, arXiv:1009.0364
Sana, H. & Evans, C.J. 2011, in *Active OB Stars: Structure, Evolution, Mass loss & Critical Limits*, eds. Neiner, Wade, Meynet & Peters, Proc. IAUS272, Cambridge University Press, arXiv:1009.4197
Sana, H., Gosset, E. & Evans, C.J. 2009, MNRAS 400, 1479

Herschel-PACS observations of Nebulae Ejected by Massive Stars *

Chloi Vamvatira-Nakou[1], Pierre Royer[2], Damien Hutsemékers[1,3], Gregor Rauw[1], Yaël Nazé[1,3], Katrina Exter[2], Christoffel Waelkens[2] and Martin Groenewegen[4]

[1] Institut d'Astrophysique et de Géophysique, Université de Liège, Belgium
[2] Instituut voor Sterrenkunde, Katholieke Universiteit Leuven, Belgium
[3] FRS-FNRS, Belgium [4] Royal Observatory of Belgium

Abstract: The study of the nebulae ejected from Luminous Blue Variables and the circumstellar bubbles around Wolf-Rayet stars, which radiate strongly in the infrared due to the heating of dust, is crucial for the understanding of the massive stars evolution. With Herschel we are able to observe these objects in the far-infrared region. In the context of the Mass-loss from Evolved StarS guaranteed time key program, we obtained imaging and spectroscopic observations of nebulae associated with Luminous Blue Variable and Wolf-Rayet stars using PACS, one of the three instruments on-board Herschel. A description of these observations, data analysis and preliminary results are presented.

1 Introduction

LBV stars represent a short stage ($\sim 10^4$ - 10^5 yr) in the evolution of massive stars with initial mass $>$40 $M_\odot$. An early-type O star evolves into a WR star by losing a significant fraction of its initial mass. One way to lose mass is through stellar winds. In the last few years the mass-loss rates of O stars have been revised strongly downwards (Fullerton et al. 2006, Puls et al. 2008). This highlights the key role played by episodes of extreme mass-loss in an intermediate evolutionary phase (LBV or Red Supergiant phase). The main characteristics of these stars are photometric variability, from giant eruptions, $\geq$2 mag, to small oscillations, $\sim$0.1 mag, high luminosity, $\sim 10^6$ $L_\odot$, and high mass-loss rate, $\sim 10^{-5}$ – 10^{-4} $M_\odot$ yr^{-1} (Humphreys & Davidson 1994). Most LBVs are surrounded by ejected nebulae (Hutsemékers 1994, Nota et al. 1995). Progressively, the outer layers of the star are removed revealing a bare core becoming a WR star which is a hot, luminous object with strong broad emission lines due to stellar winds. These winds have smaller mass-loss rates than LBV winds but higher velocities, up to 3000 km s^{-1}. They interact with the material ejected during the LBV phase, creating circumstellar bubbles observed around many WR stars. A significant fraction of the Galactic WR stars may be surrounded by nebulae (Marston 1997), but not all of them are ejecta nebulae.

There are many questions about the detailed evolution of these massive stars. We still do not know when and how these nebulae are formed, what causes the strong mass-loss phase to start and

*Herschel is an ESA space observatory with science instruments provided by European-led Principal Investigator consortia and with important participation from NASA.

what leads to the giant eruptions observed in some LBVs. Also, important quantities such as the nebular dust mass and the composition of the gas (CNO abundances) are very uncertain. Previous infrared studies of LBV nebulae have revealed that they contain dust and CO (McGregor et al. 1988, Hutsemékers 1997, Nota et al. 2002). With the ESA's Herschel Space Observatory (Pilbratt et al. 2010) we are able to study these nebulae in the far-infrared with high angular and spectral resolutions for the first time.

2 Our project with Herschel

As part of the Herschel Guaranteed Time Key Program entitled MESS - Mass-loss of Evolved StarS (Groenewegen et al. 2010, in preparation), we lead a project aiming at a detailed study of the gas and the dust in the circumstellar environments around LBVs and WR stars, so as to determine their properties. The accurate photometric maps of the far infrared emission provided by the instruments on-board Herschel will give us detailed information on the basic parameters of the dust shells. The combination of spectroscopic observations with optical data can provide accurate CNO abundances. Additionally, we can determine the properties of the neutral gas and of the photo-dissociation regions (PDR). Depending on the observed features, we will also be able to examine the dust mineralogy, estimate the mass and the location of the molecular gas and study the formation of dust in these nebulae. The list of our targets contains the LBVs AG Car, HR Car, WRA 15-751 and G79.29+0.46, the candidate LBVs He 3-519 and HD 168625 and the WR nebulae M 1-67 and NGC 6888. They will all be observed with the PACS photometer, while spectroscopic observations will be made for the brightest ones. In the following we present preliminary results for He 3-519 and WRA 15-751.

3 The LBV candidate He 3-519

He 3-519 is located in the Carina spiral arm of our Galaxy near some of the best known LBVs. Hoffleit (1953) discovered a shell nebula around it and Henize (1976) found that its spectrum was similar to that of AG Car. Stahl (1986, 1987) noted spectroscopic similarities to Ofpe/WN9 stars and published a [N II] λ 6584 CCD image of the nebula. Davidson et al. (1993) suggested that He 3-519 may be a post-LBV object and Smith et al. (1994) classified it as a WN 11 star, concluding that its nebula is a WR ring nebula.

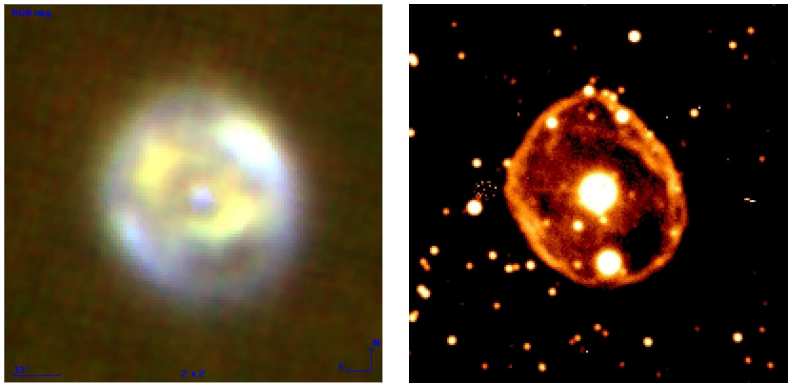

Figure 1: The nebulae around He 3-519. *Left*: morphology in the IR (RGB image with R being the PACS 100 μm image, G the PACS 70 μm image and B the Spitzer 24 μm image). *Right*: Hα image. The dimensions of both images are 2×2 arcmin. North is up and East is to the left.

The photometric observations were carried out using the Photo Array Camera and Spectrometer (PACS, Poglitsch et al. 2010). The scan map observing mode was used. For each of the two 'blue' filters (70, 100 μm), two orthogonal scan maps were obtained, so that our final data set consists in maps at 70, 100 and 160 μm. The data reduction was performed using Herschel Interactive Processing Environment (HIPE, Ott 2010) and following the basic data reduction steps. Figure 1 shows an RGB image of the nebula around He 3-519, which is a combination of two PACS scan maps at 70 μm (G) and 100 μm (R) with a Spitzer image at 24 μm from the archive (B), together with the nebula in the optical region (Hα). In the Hα image the nebula appears to be more elliptical with a thin shell structure, while the nebulae appears to have a more complicated structure in the infrared RGB image. Its diameter is approximately 80 arcsec in the IR images. In the Hα image the nebula has a diameter of about 62 arcsec.

4 The LBV WRA 15-751

WRA 15-751 was identified as a galactic LBV by Hu et al. (1990). Hutsemékers & Van Drom (1991) found that it is surrounded by a ring nebula of $\sim$22 arcsec in diameter. De Winter (1992) detected a cool dusty circumstellar shell around it with strong emission in the far-IR. Voors et al. (2000) derived many properties of the circumstellar dust around WRA 15-751 by modeling ground-based IR imaging around 10 μm and ISO spectroscopic observations: the dust shell is detached and slightly elongated, there is neutral gas outside the dust region and ionised gas only in the inner part of the dust region and the dust contains mostly large grains and a minor population of warm very small grains.

The PACS photometric observations were carried out in a similar way as those of He 3-519. For the spectroscopic observations, we used the SED observing template, providing a complete coverage between 52 and 220 μm. The PACS maps at 70 and 160 μm are shown in Figure 2, together with an Hα image. In the PACS images, the nebula surrounding WRA 15-751 has clearly a ring shape with a diameter of about 40 arcsec. Its central part, with a diameter of about 10 arcsec, is fainter than the outer ring area. The central star is not visible at these wavelengths. In the Hα image the morphology is different and the nebula diameter is about 25 arcsec.

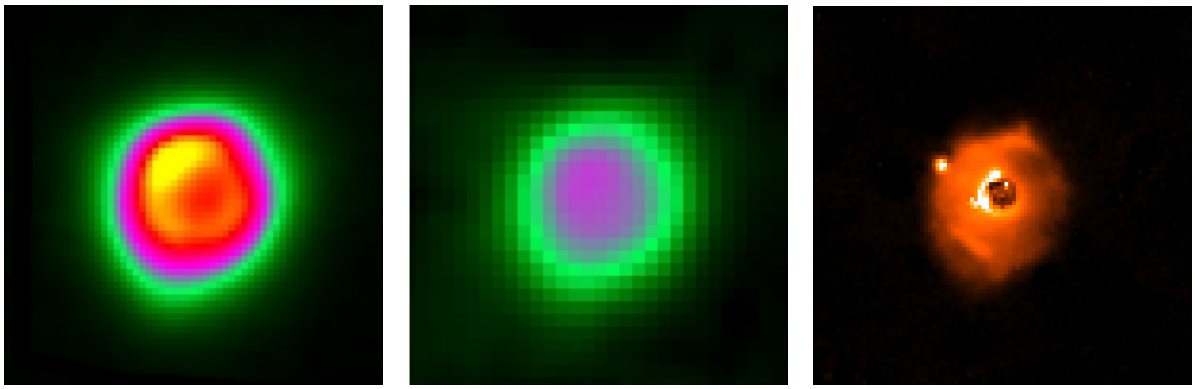

Figure 2: Images of WRA 15-751 obtained with PACS at 70 and 160 μm, together with an Hα image of the nebula (from left to right). The dimensions are 1×1 arcmin for each image. North is up and East is to the left.

Aperture photometry was performed on the IR images, providing a good measurement of the nebular flux. We plotted the results along with IRAS data (from the IRAS point source catalogue) in Figure 3 and we fitted a modified black body described by a function of the form $B_\nu\lambda^{-\beta}$ (for a grain

emissivity Q $\sim \lambda^{-\beta}$). The best fit gives a temperature of 104.9 $\pm$ 2.4 K and an emissivity index of 1.4 $\pm$ 0.1. This value is between amorphous carbon (β = 1) and silicates (β = 2). Voors et al. (2000) found an amorphous silicate emission feature and considered this as the main dust ingredient so as to model their spectrum, but finally they suggested also the presence of a small amount of very small carbon grains in order to explain a discrepancy of their model. Their model gave a temperature for small particles of 102 K at the inner and 82 K at the outer dust shell radius.

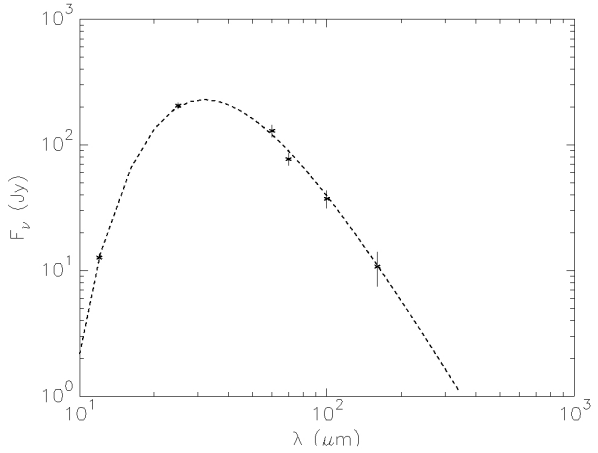

Figure 3: Modified black-body fit (T = 104.9 $\pm$ 2.4 K and β = 1.4 $\pm$ 0.1) to the derived fluxes from the PACS data of WRA 15-751 along with IRAS data.

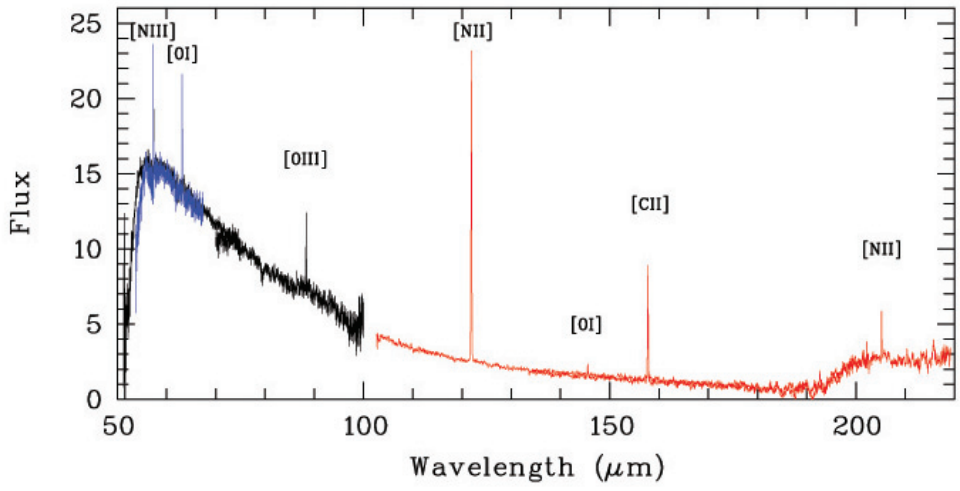

Figure 4: The PACS spectrum of WRA 15-751. Indicated are the lines [N III], [O I], [O III], [N II] and [C II]. The continuum shape below 55 μm results from a yet-imperfect spectral response function correction, while above 190 μm it results from a light leak, from the 2nd order (70-100 μm) to the 1st order (>100 μm).

The PACS spectrum is shown in Figure 4. The lines [N III] λ 57.3 μm, [O I] λ 63 μm and λ 145 μm, [O III] λ 88 μm, [N II] λ 122 μm and λ 205 μm and [C II] λ 158 μm are clearly visible with [N II] λ 122 μm being the strongest one. The presence of these lines shows that gas around WRA 15-751 is highly ionised. The [O I] λ 63 μm and [C II] λ 158 μm fine-structure lines may indicate the presence of a PDR region. Such regions have already been detected in LBV nebulae (Umana et al. 2009, Umana et al. 2010). Voors et al. (2000), using ISO data, detected only the two lines [O III]

λ 88 μm and [N II] λ 122 μm, in the waveband 40-140 μm. Apart from these nebular lines and the dust continuum, no other features are detected. More details will be given in Vamvatira-Nakou et al. (2010, in prep.).

5 Conclusion and future work

Although the results presented here are very preliminary, it is clear that Herschel data with their high spectral and angular resolution give us unique information about the structure and the composition of the nebulae around evolved massive stars. Future work consists of analysing the photometric and spectroscopic Herschel data for each one of our targets and combining them with data taken in other spectral regions, so as to identify where exactly the dust is located with respect to the gas and to derive accurate measurements of dust and gas properties. By comparing the results found for our targets we aim at answering important questions about the origin of the nebulae and the evolution of massive stars in general.

Acknowledgements

PACS has been developed by a consortium of institutes led by MPE (Germany) and including UVIE (Austria); KU Leuven, CSL, IMEC (Belgium); CEA, LAM (France); MPIA (Germany); INAF-IFSI/OAA/OAP/OAT, LENS, SISSA (Italy); IAC (Spain). This development has been supported by the funding agencies BMVIT (Austria), ESA-PRODEX (Belgium), CEA/CNES (France), DLR (Germany), ASI/INAF (Italy), and CICYT/MCYT (Spain). CVN, PR, DH, GR, YN and KE acknowledge support from the Belgian Federal Science Policy Office via the PRODEX Programme of ESA. The Liège team acknowledges also support from the FRS-FNRS (Comm. Franç. de Belgique).

References

Davidson K., Humphreys R.M., Hajian A. & Terzian Y., 1993, ApJ, 411, 336
Fullerton A.W., Massa D.L. & Prinja R.K., 2006, ApJ, 637, 1025
Henize K.G, 1976, ApJS, 30, 491
Hoffleit D., 1953, Ann. Harvard Coll. Obs., 119, 37
Hu J.Y., de Winter D., Thé P.S. & Pérez M.R., 1990, A&A, 227, 17
Humphreys R.M. & Davidson K., 1994, PASP, 106, 1025
Hutsemékers D., 1994, A&A, 28, 81
Hutsemékers D., 1997, ASPC, 120, 316
Hutsemékers D. & Van Drom E., 1991, A&A, 251, 620
Marston A.P., 1997, ApJ, 475, 188
McGregor P.J., Hyland A.R. & Hillier D.J., 1988, ApJ, 324, 1071
Nota A., Livio M., Clampin M. & Schulte-Ladbeck R., 1995, ApJ, 448, 788
Nota A., Pasquali A., Marston A.P., Lamers H.J.G.L.M., Clampin M. & Schulte-Ladbeck R., 2002, AJ, 124, 2920
Ott, S. 2010, in press, arXiv1011.1209
Pilbratt G.L. et al. 2010, A&A, 518, L1
Poglitsch A. et al. 2010, A&A, 518, L2
Puls J., Markova N. & Scuderi S. 2008, ASPC, 388, 101
Smith L.J., Crowther P.A. & Prinja R.K., 1994, A&A, 281, 833
Stahl O., 1986, A&A, 164, 321
Stahl O,. 1987, A&A, 182, 229
Umana G., Buemi C.S., Triglio C., Hora J.L., Fazio G.G. & Leto P., 2009, ApJ, 694, 697
Umana G., Buemi C.S., Triglio C., Leto P. & Hora J.L., 2010, ApJ, 718, 1036
Voors R.M.H. et al., 2000, A&A, 356, 501
De Winter D., Pérez M.R., Hu J.Y. & Thé P.S., 1992, A&A, 257, 632

Gone with the wind: Nebulae around LBVs

Kerstin Weis[1]

[1] Astronomisches Institut, Ruhr-Universität Bochum, Bochum, Germany

Abstract: The LBV phase is a short and active phase very massive stars may pass. Strong stellar winds and possibly giant eruptions of the stars in this phase lead to the formation of small (≤ 5 pc) circumstellar nebulae. A significant fraction (about 50%) of these nebulae show—to different degrees—a bipolar structure. Such a morphology, together with the presence of LBVs at lower bolometric luminosity, supports the newer stellar evolution models including rotation. Morphology, kinematics and the chemical composition of LBV nebulae are useful tracers to reveal the star's previous history, answer questions about the stellar interior and finally the stellar evolution of massive stars in general. A summary of our knowledge of the currently known LBV nebulae will be presented with a short special emphasis on a new analysis of the nebula around AG Carinae. Deep images and echelle spectra of this nebula show it to be much larger in size as known so far, and reveal in much more detail the—so far only hinted—highly bipolar structure of the nebula.

1 Luminous Blue Variables

Massive evolved stars—somewhat depending on their metallicity and rotation—do have a certain potential to enter an instable phase, as they turn into *Luminous Blue Variables* (LBVs, for details see e.g. Humphreys & Davidson 1994). LBVs, as the name indicates, are characterized by being luminous and blue stars, the latter however is no necessarily true all the time. LBVs are subject to photometric as well as spectral variabilities with various amplitudes (both in time and brightness/spectral type). A variability intrinsic to LBVs, is the S Dor variability. Depending on the direction of its evolution—redward or blueward in the HRD—the star gradually brightens, or gets fainter in the V band. This S Dor cycle (see e.g. van Genderen 2001, and Burggraf et al. 2011) draws back to the change of the stellar spectrum from a hot O-B to a cooler A-F star. The star is dimmer in the visual band in to the hot phase, and brighter while being cool. Balmer, He I and He II lines are seen in emission and often with P Cygni profiles. Therefore, LBVs can be found in the hot as well as in the cooler upper regime of the HRD. Nevertheless they are limited towards lower temperatures by the Humphreys-Davidson limit, which they may pass and violate for a short time. LBVs can exhibit so called *giant eruptions* in which the stars brightness increases significantly (several magnitudes), rapidly and only for a short time (several month to a few years, Humphreys et al. 1999). These LBVs are also dubbed *supernova impostors* (e.g. Van Dyke et al. 2000). While we have a good handle on the way stars loose mass by stellar winds, the underlying mechanism for the onset of the S Dor variability and the giant eruptions are still not fully understood. The star's proximity in the LBV phase to theoretical instability limits like the Γ- and or Ω-limit (e.g. Maeder & Meynet 2000), which roughly fall together with the observed Humphreys-Davidson limit, pose very likely scenarios. Initial mass, metallicity, stellar wind, and in particular rotation impact on the star's possible passage through an LBV phase, which is estimated to

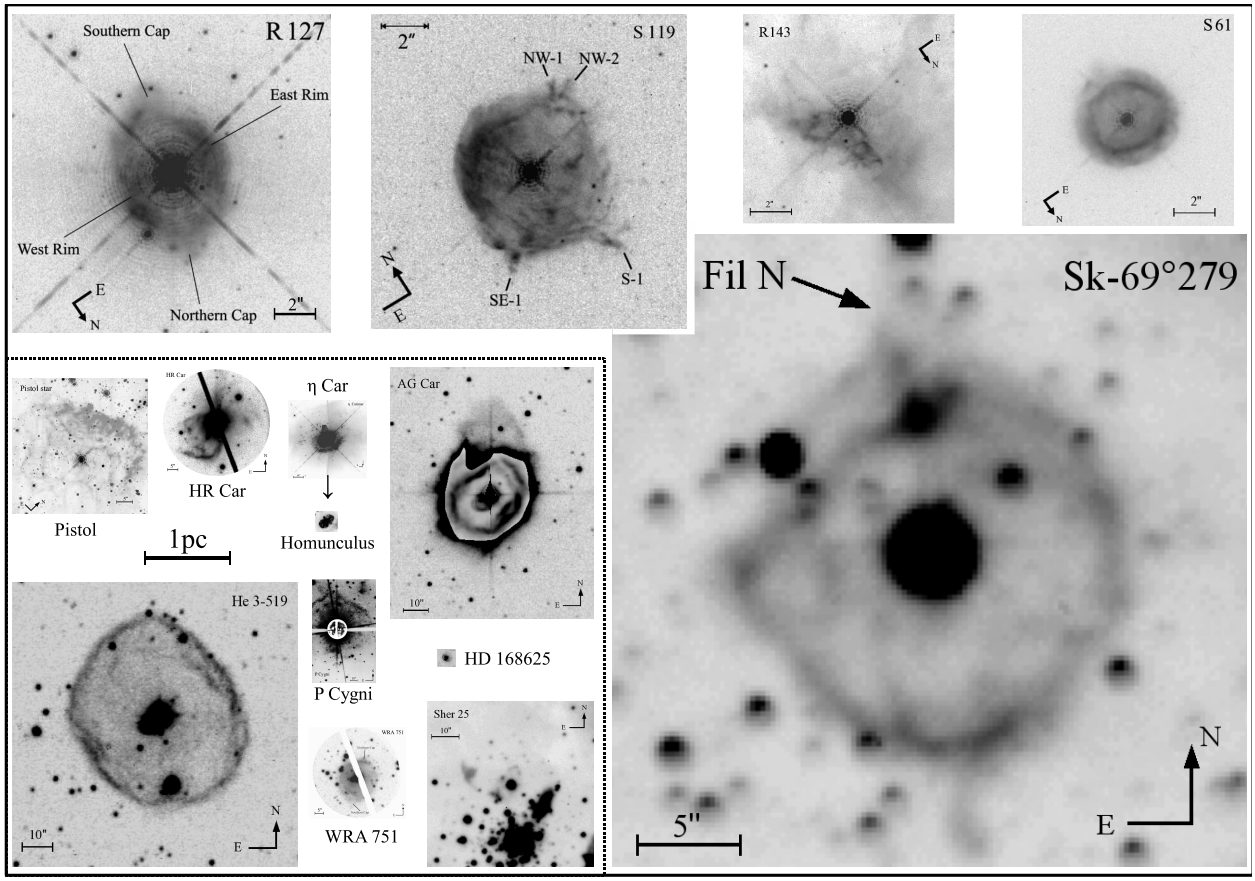

Figure 1: LBV nebulae of the Milky Way—concentrated in the lower left section within the dashed line—and the LMC on scale. Images taken from: Pistol (Figer et al. 1999), P Cygni (Barlow et al. 1994), S 119 (Weis et al. 2003, also published by Danforth & Chu 2001), HD 168625 (Weis 2000, also published by Pasquali et al. 2002). All other images are observed or published first by the author.

last several 10^4 yrs. Originally the lower limit of stars to enter the LBV phase used to be $50\,M_\odot$, stellar evolution model which include an initial rotation of $300\,km\,s^{-1}$ (Meynet & Maeder 2005) propose that stars with masses as low as $22\,M_\odot$ (for Z=0.02) may encounter the LBV phase. This matches better the observations for some low luminosity LBVs but at the same time poses that the number of LBVs we see should be higher, or the LBV phase must be shorter.

2 Nebulae around Luminous Blue Variables

Increased mass loss by stellar winds in the LBV phase (up to $10^{-4}M_\odot yr^{-1}$) and sometimes the massive giant eruptions provoke the formation of small circumstellar LBV nebulae (see e.g. Nota et al. 1995, Weis 2000). The nebulae are strong [N II] emitter, as CNO processed material is mixed up and carried away. Nebulae in the Milky Way and LMC which are resolved spatially (no SMC nebula is known) can be characterized further in morphology, size and kinematics (Tab. 1 and Fig. 1).

Morphology & Sizes: The morphologies in LBV nebulae are manifold, from quite spherical ring nebulae (e.g. S 61) and slightly elliptical structures (e.g. He 3-519), to one irregular object (R 143). A significant number of nebulae do show bipolarity or at least bipolar components. They are either of hourglass shape (η Car or HR Car) or show attached bipolar components dubbed caps (WRA 751 or R 127). A statistic of the morphologies (from Tab. 1) yields that about 50% of the nebulae show bipolarity (hourglass or caps), 40% are spherical and only 10% irregular. The frequency of bipolarity

Table 1: Parameters of LBV nebulae in the Milky Way and LMC. Slashes separate values for nebulae that consist of two distinct parts. Maximum size are either the largest extent as diameter or major and minor axes. For hourglass shaped bipolar nebulae, the radius and expansion velocities (marked with *) is given for one lobe. Table adapted from Weis (2001) and Weis (2003).

LBV	host galaxy	maximum size [pc]	radius [pc]	$v_{\rm exp}$ [km/s]	kinematic age [10^3 yrs]	morphology
η Carinae	Milky Way	0.2/0.67	0.05/0.335	$300^*/10-3200$		bipolar
AG Carinae	Milky Way	1.4×2	0.4	$\sim25^*$	~30	bipolar
HD 168625	Milky Way	0.13×0.17	0.075	40	1.8	bipolar ?
He 3-519	Milky Way	2.1	1.05	61	16.8	spherical/elliptical
HR Carinae	Milky Way	0.65×1.3	0.325	75^*	4.2	bipolar
P Cygni	Milky Way	0.2/0.84	0.1/0.42	$110-140/185$	0.7/2.1	spherical
Pistol Star	Milky Way	0.8×1.2	0.5	60	8.2	spherical
Sher 25	Milky Way	0.4×1	0.2×0.5	$30-70$	$6.5-6.9$	bipolar
WRA 751	Milky Way	0.5	0.25	26	9.4	bipolar
R 71	LMC	<0.1?	<0.05?	20	2.5 ?	?
R 84	LMC	<0.3 ?	<0.15?	24 (split)	6 ?	?
R 127	LMC	1.3	0.77	32	23.5	bipolar
R 143	LMC	1.2	0.6	24 (split)	49	irregular
S Dor	LMC	<0.25?	<0.13?	<40 (FWHM)	3.2 ?	?
S 61	LMC	0.82	0.41	27	15	spherical
S 119	LMC	1.8	0.9	26	33.9	spherical/outflow
Sk -69° 279	LMC	4.5×6.2	2.25	14	157	spherical/outflow

is higher among Galactic LBVs ($\sim$75%) than it is for LMC objects ($\sim$20%). Some nebulae have outflows like Sk -69° 279 (see Fil N in Fig. 1). In size LBV nebulae span a range from roughly 0.2 pc, the diameter of the nebula around HD 168625, to 4.5 pc for the ring around Sk -69° 279 (4.5 pc$\times$6.2 pc with the outflow). The LMC objects are generally larger, but note that with the lower resolution in the LMC (1 pc $\sim 4''$), small nebulae are overlooked more easily.

Kinematics: The expansion velocities of LBV nebulae range between 14 km s^{-1} (Sk -69° 279, Weis & Duschl 2002) to 185 km s^{-1} (P Cyg, outer nebula, Barlow et al. 1994). η Car is an exceptional case with velocities of 300 km s^{-1} for the Homunculus and some 3200 km s^{-1} (Smith & Morse 2004) detected in the outer ejecta. Typical values, however, are around 50 km s^{-1} for Galactic and about half of that for LMC nebulae. Morphologically identified bipolar nebulae are also detected kinematically. They exhibit a red and blue-shifted shell (two expansion ellipses in the spectra) or a bi-directional expansion of the attached caps with a red- one blueshifted side. Some nebulae have outflows (Sk -69° 279, S 119) or deformations (AG Car, see below) which are moving faster.

Origin & Bipolarity: LBV nebulae can be formed by continuous winds or during a short outburst (giant eruption). Given the small sample of well studied and observed eruption LBVs with nebulae (η Car and P Cyg) it is hard to identify any differences of the nebulae to those around non-eruptive LBVs. With the nebulae's large kinematic ages (Tab. 1) it cannot be excluded that other LBV nebulae might result from an eruption, which just has not been observed. Why do quite a number of nebulae show a bipolar shape? Several physical mechanism are conceivable to support bipolarity. Examples are fast stellar rotation, or a density gradient in the stellar wind (or the ISM) from the star's pole to the equator. This migh occur as the star passes the bistability jump and the wind changes from polar to equatorial. Bipolarity might result from a binary system, but with only two proposed LBV binaries (η Car, Damineli et al. 1997 and HD 5980, Hoffmann et al. 1978) seems not the dominant process.

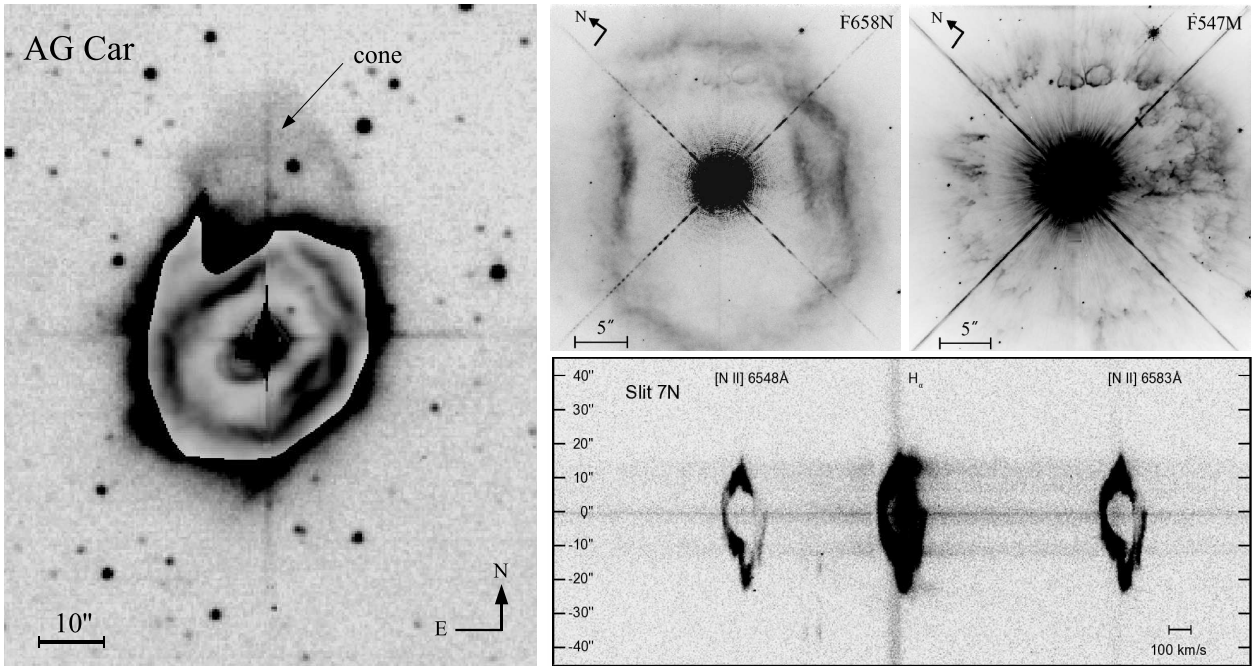

Figure 2: *Left:*Deep [N II] image of AG Car's nebula showing the fainter–and overlayed in the center the brighter–emission. To the north-east extends the cone-like structure. *Upper right:* HST-PC images of the central nebula taken in the F658N and the F547M filter (previouly published by Nota et al. 1995). *Lower right:* A long-slit echelle spectrum revealing two attached expansion ellipses.

3 The nebula around AG Carinae

AG Carinae is a classical LBV, it lies in the very upper part of the HRD, has a well documented S Dor cycle and a nebula. First pictures of its nebula date back to Thackeray (1950) and showed that it is an elliptically shaped ring slightly quenched in the middle with a size of $40'' \times 30''$ or $1.2\,\mathrm{pc} \times 0.9\,\mathrm{pc}$. In the south-west side an additional half-shell is present, in the north-east an arm like extension stretches out with a length of $20''$ (0.6 pc). First measurements of the expansion velocities ranged from $80\,\mathrm{km\,s^{-1}}$ (Johnson 1976), and line splits of 20-120 $\mathrm{km\,s^{-1}}$ (Thackeray 1977) to $70\,\mathrm{km\,s^{-1}}$ (Smith 1991). With new images and spectra, some of these nebula parameters can be updated.

Morphology: Deep [N II] ground based images of AG Carinae reveal that, taking the faintest emission into account, the dimension (with the current detection limit) of the nebula has increased to $70'' \times 48''$ or $2\,\mathrm{pc} \times 1.4\,\mathrm{pc}$ (Fig. 2), making it nearly twice the size reported before. This increase is in particular due to the discovery of a very faint cone shaped structure that extends to the north. The cone directly merges into the arm-like filament already reported by Thackeray. Taken together arm and cone have a total length of 1.4 pc (see Fig. 2). The same figure features two HST images of the central brighter part of the nebula. The F658N image shows the [N II] emission while the F547M frame shows scattered stellar light tracing the nebula's dust. Together with the kinematic data (see below), it was found that AG Car shows a two shell structure, the shells being superimposed in line of sight, with a marginal shift to the north-east of one shell. This shift is best seen in the south-west, here for about a length of $10''$ the bright rims of the shell are seen to be parallel.

Kinematics: Mapping the nebula the global expansion pattern was reconstructed. In the lower left section of Fig. 2, a typical echellogram of slit 7N ($7''$ north of the star, PA = 45°) is depicted. Two expansion ellipses are detected – one redshifted, one blueshifted – which are attached to each other. This further manifests the nebula's bipolar structure with an approaching and a receding shell. The shells are either connected to each other at the center (ellipses not closed) or the walls of the shells are

very thin and below our detection limit. The expansion ellipses yield a maximum expansion velocity of 20-30 km s^{-1} for each shell. Taken together that matches earlier measurements (remember the shells are superimposed in line of sight). The cone (Fig. 2) is part of the receding shell, moves about 75 km s^{-1} faster as the center of this shell and manifesting a larger dent or outflowing region.
Rotation & Bipolarity : It has been shown that AG Car is a fast rotating star, so is HR Car (Groh et al. 2006, 2009). Both do show bipolar nebulae. Therefore at least in these cases, rotation could be the explanation for bipolarity.

4 Summary or info to take home with!

Part I: LBV nebulae are formed by interaction of stellar winds and/or in giant eruptions. The morphology of the nebulae is, besides spherical (to some degree elliptical) and irregular, in many cases bipolar. Bipolarity is seen in hourglass shapes or as caps attached to the nebula's main body. The sizes of LBV nebulae range between 0.2 pc to about 5 pc. Their expansion velocities are typically several tenths to slightly above 100 km s^{-1}. LBV nebulae in the LMC (compared with the Galactic) are generally larger in size, have lower expansion velocities (factor two) and fewer bipolar nebulae.
Part II: AG Carinae has a nebula that is, including the faintest emission, with a size of 2 pc$\times$1.4 pc, significantly larger than previously reported. The nebula consists of two shells which expand bipolar with velocity between 20-30 km s^{-1}. A larger conical structure to the north (the cone) is a faster moving part of the redshifted shell and an extension of the arm reported by Thackeray (1950). The origin of the bipolar nebula might be linked to the star's fast rotation.

References

Barlow, M.J., Drew, J.E., Meaburn, J., & Massey, R.M. 1994, MNRAS 268, L29
Burggraf, B., Weis, K., Bomans, D.J., & Henze, M. 2011, in Proceedings of the 39th Liège Astrophysical Colloquium, eds. G. Rauw, M. De Becker, Y. Nazé, J.-M. Vreux & P.M. Williams, BSRSL 80, 356
Damineli, A., Conti, P.S., & Lopes, D.F. 1997 NewAstr 2, 107
Danforth, C.W., & Chu, Y.-H. 2001, ApJ 552, L155
Figer, D.F., Morris, M., Geballe, T.R., Rich, R.M., Serabyn, E., McLean, I.S., Puetter, R.C., & Yahil, A. 1999, ApJ 525, 759
Groh, J.H., Hillier, D.J., & Damineli, A., 2006, A&A 638, L33
Groh, J.H., Damineli, A., Hillier, D.J., et al. 2009, A&A 705, L25
Hoffman, M., Stift, M.J., & Moffat, A.F.J. 1978, PASP 90, 101
Humphreys, R.M., & Davidson, K. 1994, PASP 106, 1025
Humphreys, R.M., Davidson, K., & Smith, N. 1999, PASP 111, 1124
Johnson, H.M. 1976, ApJ 206, 469
Maeder, A., & Meynet, G. 2000, A&A 361, 159
Meynet, G., & Maeder, A. 2005, A&A 429, 581
Nota, A., Livio, M., Clampin, M., & Schulte-Ladbeck, R. 1995 ApJ 448, 788
Pasquali, A., Nota, A., Smith, L.J., Akiyama, S., Messineo, M., & Clampin, M. 2002, AJ 124, 1625
Smith, L.J. 1991, in *IAU Sym 143*, ed. K.A. van der Hucht, B. Hidayat, Kluwer Academic Publishers, 385
Smith, N., & Morse, J.A., 2004, ApJ 605, 854
Thackeray, A.D. 1950, MNRAS 110, 524
Thackeray, A.D. 1977, MNRAS 180, 95
Van Dyk, S.D., Peng, C.Y., King, J.Y., Filippenko, A.V., Treffers, R.R., Li, W., & Richmond, M.W. 2000, PASP 112, 1532
Weis, K. 2000, A&A 357, 938
Weis, K. 2001, in *Reviews in Modern Astronomy*, ed. R. E. Schielicke, 14, 261
Weis, K., & Duschl, W.J. 2002, A&A 393, 503
Weis, K., Duschl, W.J., & Bomans, D.J. 2003, A&A 398, 1041

FUV and UVIS observations of circumnuclear star clusters in M83

Aida Wofford[1], Rupali Chandar[2] and Claus Leitherer[1]

[1] Space Telescope Science Institute, 3700 San Martin Drive, Baltimore, MD 21218, USA

[2] University of Toledo, Department of Physics and Astronomy, Toledo, OH 43606, USA

Abstract: We analyze archival *HST*/STIS/FUV-MAMA imaging and spectroscopy of 13 compact star clusters within the circumnuclear starburst region of M83, the closest such example. We compare the observed spectra with semi-empirical models, which are based on an empirical library of Galactic O and B stars observed with *IUE*, and with theoretical models, which are based on a new theoretical UV library of hot massive stars computed with WM-Basic. The models were generated with Starburst99 for metallicities of Z=0.020 and Z=0.040, and for stellar IMFs with upper mass limits of 10, 30, 50, and 100 $M_\odot$. We estimate the ages and masses of the clusters from the best fit model spectra, and find that the ages derived from the semi-empirical and theoretical models agree within a factor of 1.2 on average. A comparison of the spectroscopic age estimates with values derived from *HST*/WFC3/UVIS multi-band photometry shows a similar level of agreement for all but one cluster. The clusters have a range of ages from about 2 to 20 Myr, and do not appear to have an age gradient along M83's starburst. Clusters with strong P-Cygni profiles have masses of a few $\times 10^4$ $M_\odot$, seem to have formed stars more massive than 30 $M_\odot$, and are consistent with a Kroupa IMF from 0.1-100 $M_\odot$.

1 Introduction

Determining the ages, masses, and stellar initial mass functions (IMFs) of individual OB star clusters in the circumnuclear regions of nearby disk galaxies, is important for understanding the relation between the origin of the clusters, and galaxy dynamics and interactions. Messier 83 (M83, NGC 5236), which is a southern nearly face-on grand-design barred spiral galaxy of morphological type SAB(s)c, located at a distance of 4.6$\pm$0.09 Mpc (mean from NED using various indicators), hosts the closest example of an arc-shaped circumnuclear starburst region. The region is $\sim$200 pc in length and $\sim$35 pc in thickness, and is composed of several dozen compact OB star clusters, located within 200 pc of the galaxy's optical nucleus. M83 has a close dynamical companion in the dwarf irregular galaxy NGC 5253 (Rogstad, Lockhart, & Wright 1974), which harbors a nuclear starburst (Calzetti et al. 1997). The two galaxies are part of the M81 group, including the dust-rich starburst proto-type, M82.

M83's circumnuclear starburst region has been observed at wavelengths ranging from the radio to the X-rays (for references, see Dopita et al. 2010). Based on the analysis of CO absorption and Brγ emission-line data, Puxley, Doyon, & Wardy (1997) found that the northwestern end of the starburst's arc is the youngest, while the southeastern end is the oldest. Based on the statistical analysis of the *HST*/WFPC2 photometry of Harris et al. (2001), Díaz et al. (2006) found that the oldest cluster in the

northwest is 5 Myr, and the oldest cluster in the southeast is 25 Myr, confirming the age gradient along the starburst. The above age gradient suggests that star formation occurs in an ordered manner, and supports the idea that the starburst is fed by the inflow of bar-driven material. If real, this gradient has profound implications for the formation and evolution of circumnuclear starbursts. For this reason, we re-visited M83's starburst's arc, and determined the ages and masses of 13 clusters within its northern portion, using three different techniques, i.e., by comparing archival *HST*/STIS FUV spectroscopy of the clusters with semi-empirical and new fully theoretical model spectra, and by deriving these properties from high spatial resolution *HST*/WFC3 multi-band optical photometry. We also studied the stellar IMFs of the clusters in our sample. Here, we focus on the analysis of the FUV spectroscopy, which is fully described in Wofford, Chandar, & Leitherer (2010), where we also studied field regions between the clusters. The description of the photometry and its analysis are summarized in the latter paper and presented in detail in Chandar et al. (2010), where the authors cover the entire field imaged by WFC3, which is larger than M83's circumnuclear region.

2 Model Spectra

We compared the observed FUV spectra with models generated with the widely used package Starburst99 (S99, Leitherer et al. 1999; Vázquez & Leitherer 2005). The main input parameters in S99 are 1) the star-formation law, 2) the IMF, 3) the metallicity and stellar evolution tracks, and 4) the stellar spectral library. Bresolin & Kennicutt (2002) ruled out continuous star formation within individual star clusters of M83's starburst region. Therefore, we fitted our cluster spectra with single stellar population (SSP) models. We tried IMFs with high mass limits of 10, 30, 50, and 100 $M_{\odot}$, and metallicities of Z=0.020 and Z=0.040, since the metallicity of M83 is intermediate between these two values (Bresolin & Kennicutt 2002). We used the stellar evolution tracks for non-rotating stars of Schaller et al. (1992) for masses M$<$12 $M_{\odot}$, and of Meynet et al. (1994) for masses M$\geq$12 $M_{\odot}$. Finally, we tried an empirical stellar library based on *IUE* observations of Galactic O and B stars (Robert et al. 1993), as well as a new high-resolution fully-theoretical UV library for massive stars, computed by Leitherer et al. (2010), with WM-Basic (Pauldrach, Hoffmann, & Lennon 2001). Figure 1 shows the age evolution from 1 to 20 Myr of models with a Kroupa IMF (Kroupa 2001), with Z=0.020, and based on the empirical and the theoretical stellar libraries, hereafter, the semi-empirical and the theoretical models, respectively.

The semi-empirical and theoretical models differ below 1240 Å because of the presence of Galactic interstellar Lyα but agree rather well in the range 1240-1700 Å, except for the O V 1370 Å line, which is stronger in the theoretical models at ages younger than $\sim$2 Myr, and the Si IV 1400 Å feature, which is stronger in the semi-empirical models at ages 3 and 4 Myr. Note that the empirical library is contaminated with interstellar lines.

3 Procedure

3.1 Reddening

We corrected the observed spectra for Galactic extinction based on the maps of Schlegel, Finkbeiner, and Davis (1998) and the extinction curve of Fitzpatrick (1999). We then fitted the FUV continuum with a power law of the form $F \sim \lambda^{\beta}$, and assumed that any deviation of β from the expected value for a dust free starburst (-2.6) was due to reddening. We used the obscuration law of Calzetti et al. (2000) to deredden the spectrum until $\beta = -2.6$ was reached.

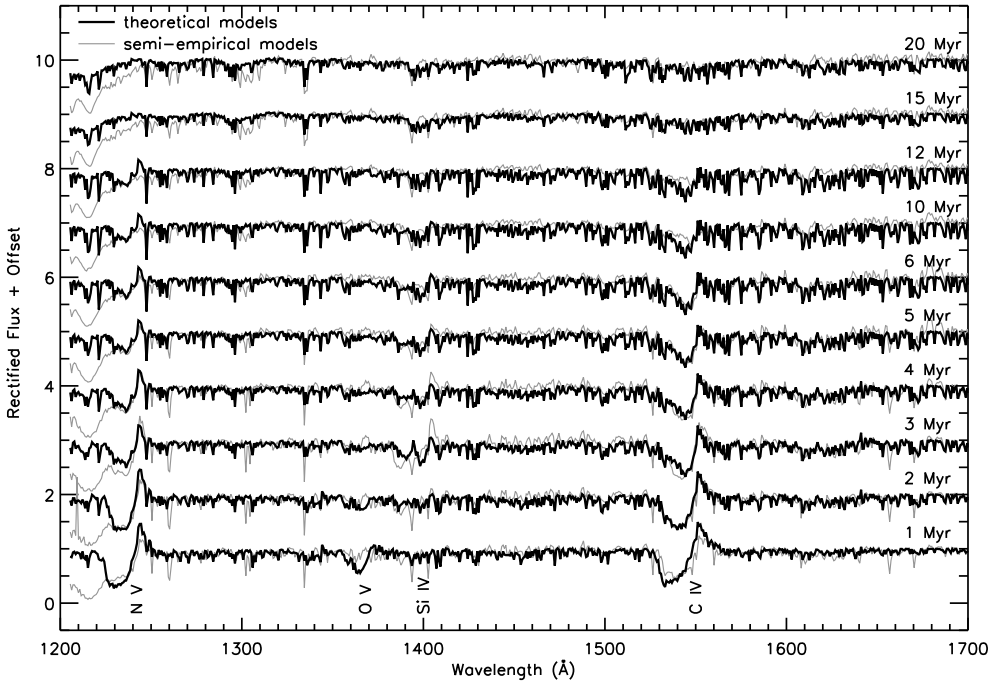

Figure 1: Evolution of SSP model spectra with time. The theoretical models are shown in black and the semi-empirical models are shown in grey. The models correspond to a metallicity of Z=0.020 and a Kroupa IMF from 0.1-100 $M_{\odot}$.

3.2 Spectroscopic Ages, Metallicity, and IMF

Figure 1 shows the sensitivity of the N V 1240, Si IV 1400, and C IV 1550 profiles to the age of the cluster. The metallicity of M83's starburst is intermediate between Z=0.020 and Z=0.040, but the age estimates from models corresponding to these two metallicities are very similar. Our clusters showing strong P-Cygni profiles in N V 1240, Si IV 1400, and C IV 1550 are consistent with having formed stars more massive than 30 $M_{\odot}$. This is illustrated in Fig. 2, where the observed spectra of two clusters (1 and 10) are compared against models having upper mass limits of 10, 30, 50, and 100 $M_{\odot}$. The presence of strong Si IV and C IV absorptions in the rest of clusters, suggests the presence of at least some B stars, assuming that the origin of these features is not mostly interstellar. We derived spectroscopic ages for the clusters in our sample by fitting their FUV spectra with models corresponding to a metallicity of Z=0.020 and a Kroupa IMF from 0.1-100 $M_{\odot}$. For this, we adopted the algorithm of Tremonti et al. (2001), which gives the most weight to the N V 1240, Si IV 1400, and C IV 1550 features and eliminates from consideration the interstellar lines. The goodness of the fit is characterized by χ^2, where $\chi^2 = (o_i - m_i)^2 w_i/\sigma_i^2$, and where o_i represents the observed data for the ith pixel, m_i the model data, σ_i the error in the observed spectrum, and w_i the assigned weight.

3.3 Spectroscopic Masses

The spectroscopic mass of each cluster was derived by comparing the mean luminosity of the best fit model to the data (corresponding to a stellar mass of 10^6 $M_{\odot}$), to the observed value.

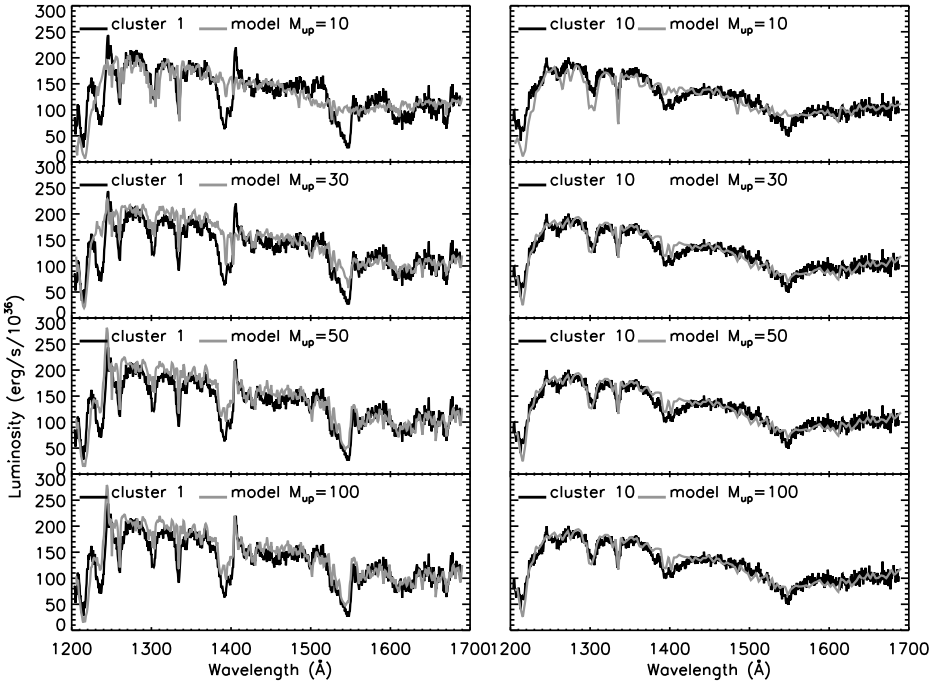

Figure 2: Observed spectra of clusters 1 and 10 (black curves) versus semi-empirical models corresponding to different upper mass limits to the IMF, M_{up}=10, 30, 50, and 100 $M_\odot$ (grey curves). The metallicity of the models is Z=0.020. The ages of clusters 1 and 10 are $\sim$4 Myr and $\sim$12 Myr, while their masses are $\sim 3\times10^4$ $M_\odot$ and $\sim 10^5$ $M_\odot$, respectively.

4 Cluster Properties

4.1 Masses

Optical photometry provides more leverage for determining the stellar mass than FUV spectroscopy. Therefore, our photometric masses (M_{phot}) are more reliable than our spectroscopic masses. Our most massive cluster has $M_{phot}=3.1\times10^5$ $M_\odot$, which is comparable to the virial mass of the ionizing cluster of 30 Doradus, NGC 2070 (4.5×10^5 $M_\odot$, Bosch, Terlevich, & Terlevich 2009). According to Larsen (2010), young star clusters with masses larger than 10^5 $M_\odot$ can last an age comparable or exceeding the age of the universe. Therefore the latter cluster could be a globular cluster progenitor, while two other clusters, which have $M_{phot}\approx10^5$ $M_\odot$, may also survive. One cluster has $M_{phot}=4\times10^3$ $M_\odot$. Unfortunately, its spectrum is too noisy to reliably say whether stars more massive than 30 $M_\odot$ have formed in it. The rest of clusters have M_{phot} of a few $\times10^4$ $M_\odot$.

4.2 IMF

Our clusters with strong P-Cygni profiles have M_{phot} $\sim10^4$ $M_\odot$, seem to have formed stars with masses > 30 $M_\odot$, and are consistent with a Kroupa IMF from 0.1-100 $M_\odot$. Clusters without P-Cygni profiles could be young clusters that did not form massive O stars, or older clusters whose O stars have died. The latter clusters are consistent with having formed at least some B stars.

4.3 Ages

The spectroscopic ages from semi-empirical and theoretical predictions are within a factor of 1.2 on average. The spectroscopic and photometric ages agree at a similar level. Our ages agree with those derived from *HST*/WFPC2 photometry by Harris et al. (2001), except for clusters 6, 7, and 10, which are older than 6 Myr in our case. Our ages for clusters 1-3 and 11-12 agree with the ages of regions A and B derived from STIS FUV spectroscopy by Bresolin & Kennicutt (2002). The clusters are $\sim$2-20 Myr old and were not all formed at the same time. We found no age gradient along M83's starburst, in disagreement with Puxley et al. (1997) and Díaz et al. (2006).

Acknowledgements

This work was supported by NASA grant N1317.

References

Bosch, G., Terlevich, E. & Terlevich R. 2009, AJ, 137, 3437
Bresolin, F. & Kennicutt Jr., R. C. 2002, ApJ, 572, 838
Calzetti, D., Meurer, G. R., Bohlin, R. C., Garnett, D. R., Kinney, A. L., Leitherer, C. & Storchi-Bergmann T. 1997, AJ, 114, 1834
Calzetti, D., Armus, L., Bohlin, R. C., Kinney, A. L., Koornneef, J. & Storchi-Bergmann, T. 2000, ApJ, 533, 682
Chandar, R., Whitmore, B. C., Kim, H., Kaleida, C., Mutchler, M., Calzetti, D., Saha, A., O'Connell, R., et al. 2010, ApJ, 719, 966
Díaz, R. J., Dottori, H., Aguero, M. P., Mediavilla, E., Rodrigues, I. & Mast D. 2006, ApJ, 652, 1122
Dopita, M. A., Blair, W. P., Long, K. S., Mutchler, M., Whitmore, B. C., Kuntz, K. D., Balick, B., Bond, H. E., et al. 2010, ApJ, 710, 964
Fitzpatrick, E. L. 1999, PASP, 111, 63
Harris, J., Calzetti, D., Gallagher III, J. S., Conselice, C. J. & Smith, D. A. 2001, AJ, 122, 3046
Kroupa, P. 2001, MNRAS, 322, 231
Larsen, S. S. 2010, RSPTA, 368, 867
Leitherer, C., Schaerer, D., Goldader, J. D., Delgado, R. M. G., Robert, C., Kune, D. F., de Mello, D. F., Devost, D., et al. 1999, ApJS, 123, 3
Leitherer, C., Ortiz Otálvaro, P. A., Bresolin, F., Kudritzki, R.-P., Lo Faro, B., Pauldrach, A. W. A., Pettini, M. & Rix S. A. 2010, ApJS, 189, 309
Meynet, G., Maeder, A., Schaller, G., Schaerer, D. & Charbonnel C. 1994, A&AS, 103, 97
Pauldrach, A. W. A., Hoffmann, T. L. & Lennon, M. 2001, A&A, 375, 161
Puxley, P. J., Doyon, R. & Wardy, M. J. 1997, ApJ, 476, 120
Rogstad, D. H., Lockhart, I. A. & Wright, M. C. H. 1974, 193, 309
Robert, C., Leitherer, C. & Heckman, T. M. 1993, ApJ, 418, 749
Tremonti, C. A., Calzetti, D., Leitherer, C. & Heckman, T. M. 2001, ApJ, 555, 322
Schaller, G., Schaerer, D., Meynet, G. & Maeder, A. 1992, A&AS, 96, 269
Schlegel, D. J., Finkbeiner, D. P. & Davis, M. 1998, ApJ, 500, 525
Vázquez, G. A. & Leitherer, C. 2005, ApJ, 621, 695
Wofford, A., Chandar, R. & Leitherer, C. 2010, ApJ, in press (arXiv:1011.4449)

Single-Star H II Regions as a Probe of Massive Star SEDs

Jordan Zastrow[1], M.S. Oey [1] and E.W. Pellegrini[1]

[1] Department of Astronomy, 500 Church Street, University of Michigan, Ann Arbor, MI, 48109, USA

Abstract: We critically examine stellar atmosphere models by exploiting the strong dependence of H II region optical spectra on the SED of the ionizing source. To accomplish this, we compare spatially resolved, longslit observations of LMC single-star H II regions to photoionization simulations based on observed nebular and stellar properties. We select stellar atmosphere models from the CoStar (Schaerer & de Koter, 1997), TLUSTY (Lanz & Hubeny, 2003), WM-basic (Pauldrach et al. 2001) and Smith et. al. (2002) grids to define the ionizing source in our simulations. Gas density fluctuations are necessary to simultaneously fit the emission from high and low excitation ions. We evaluate the atmospheres relative to each other and overall, find atmosphere models using the WM-basic code have the best agreement with our observations.

1 Introduction

Studies of massive star feedback, stellar populations and abundances, and star formation rate indicators depend on the spectral energy distributions (SED) and derived properties of massive stars. However, these stars emit a majority of their flux at wavelengths relatively inaccessible to observations. Thus, stellar atmosphere models are an important tool for understanding fundamental galaxy properties.

Modeling massive star atmospheres is complex. To accurately represent the SED, important physics such as non-LTE conditions, the effects of line-blanketing and, wind-blanketing effects need to be included. Incorporating all these processes in detail is computationally expensive. Therefore, research groups optimize computing time by using approximate treatments for different components. For example, CoStar (Schaerer & de Koter 1997) and WM-basic (Pauldrach, Hoffman & Lennon 2001) take into account expanding atmospheres while TLUSTY (Lanz & Hubeny 2003) uses a plane-parallel one. Additionally, the treatment of line-blanketing differs from code to code. These different approaches lead to differences in the predicted SEDs. Thus, it is crucial to understand how well these model atmospheres represent the actual SEDs of the stars.

The optical emission from an H II region depends primarily on the SED of the ionizing source, the metallicity (Z), and the ionization parameter (U) which depends on the rate of ionizing photons, the gas density and morphology. If the metallicity and ionization parameter can be constrained, we can use the line emission to constrain the SED of the ionizing star.

We can accomplish this with our sample of single-star H II regions in the Large Magellanic Cloud (LMC). The LMC is an ideal location for this study because it has a well measured metallicity, a known distance and does not have the extinction and crowding issues that a Galactic study would have. Additionally, the H II regions span 20″ - 30″ in diameter which allows us to obtain spatially

Table 1: Stellar and nebular properties.

Name	SpT	Log($\frac{L}{L_\odot}$)	Nebula	Filling	High Density		Low Density	
			Radius (pc)	Factor	n_H (cm^{-3})	Thickness (pc)	n_H (cm^{-3})	Thickness (pc)
DEM 08c	O5.5V	4.81 ± 0.05	6.8 ± 1	0.03	500	0.05	1	2.0
DEM 026	O8V	4.68 ± 0.05	6.1 ± 0.9	0.087	80	0.25	10	1.75
DEM 020	O8V	5.08 ± 0.05	8.5 ± 1.2	0.137	80	0.15	1	0.9

resolved spectra. The real strength of our data set lies in the single-star nature of the H II regions. With just one ionizing source, the morphology of the nebula is much simplified. Narrowband [O III], Hα, and [S II] images from the Magellanic Clouds Emission Line Survey (MCELS; Smith et al. 2005) of our objects show classical Strömgren sphere-like nebulae. This puts strong constraints on the gas density and morphology, thereby constraining *U*.

2 Observations

We report on the results obtained from three LMC H II regions: DEM L08c, DEM L026, and DEM L020. These objects are ionized by an O5.5V star, O8V star, and O8V star, respectively. Broadband (Bessell *B* and *V*) images and longslit spectra of these objects were obtained using the imaging spectrograph IMACS on the Magellan Baade Telescope at Las Campanas Observatory. The data were taken during the nights of 2008 January 29-31. The spectra have a spatial resolution of 0.44″ pixel^{-1} and a spectral resolution of 0.75 Å pixel^{-1} covering a total wavelength range of 3700 - 6740 Å. We used standard IRAF procedures for image and spectral reduction. The flux calibration was made using standard stars LTT 2415, LTT 3218, and LTT 1788 (Hamuy et al. 1994).

3 Models

Each H II region model is generated four times with the photoionization code CLOUDY (Ferland et al. 1998). Each time a different model atmosphere is used as the ionizing source. We then plot the ratio of predicted flux ($F_{\rm pre}$) to observed flux ($F_{\rm obs}$) for each emission line as a function of the ionization potential (IP) of that line. In this study we consider atmosphere models generated from different atmosphere codes: CoStar (Schaerer & de Koter 1997), TLUSTY (Lanz & Hubeny 2003), WM-basic (Pauldrach et al. 2001) and O star grid from Smith, Norris & Crowther (2002, hereafter SNC02). The models from SNC02 are generated using the WM-basic code with different fundamental stellar parameters for implementation into STARBURST99 (Leitherer et al. 1999).

To set up the model nebula, we need to specify the stellar luminosity, inner cloud radius, density, elemental abundance and stellar effective temperature ($T_{\rm eff}$). The observed and calculated nebular and stellar parameters are shown in columns 2-4 of Table 1. Column 2 lists the spectral type (SpT) determined from our IMACS spectra. Column 3 lists the stellar luminosity which is calculated from the observed magnitudes using the bolometric correction from Martins, Schaerer & Hillier (2005). Column 4 contains the radial size of the nebula as measured from the MCELS narrowband Hα image. Examining our objects in the MCELS images, the emission is consistent with gas close to the star. Therefore, we choose our inner cloud radius to be 0.1 pc for all models. A final size criterion is used to select successful models. We only consider models that reach the outer nebular radius measured with the MCELS data for comparison with our observations. Unfortunately, the gas densities of these

objects fall in the low density limit of the [O II] and [S II] density diagnostics. This means we only have an upper limit on the electron density of $n_e \leq 100$ cm^{-3}. Elemental abundances are drawn from Garnett (1999) except for that of nitrogen. The nitrogen abundance is calculated using the observed [N II] / [O II] line ratio and the relation from Pérez-Montero & Díaz (2005). The final input for the H II region models is the $T_{\rm eff}$ which we leave as a free parameter.

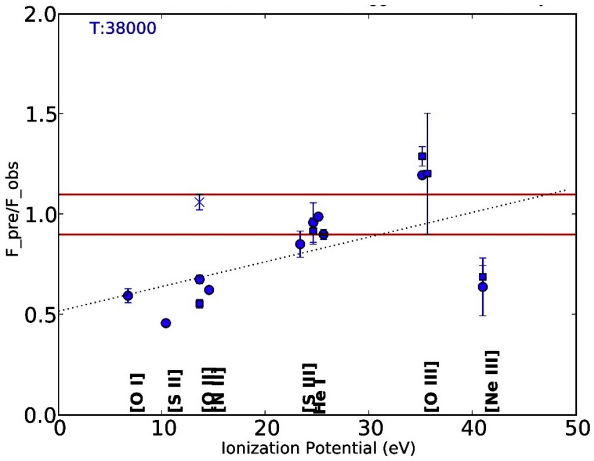

Figure 1: DEM L08c modeled as a constant density sphere with gas density of 40 cm^{-3} and using WM-basic. $F_{\rm pre}/F_{\rm obs}$ of emission lines is plotted as a function of IP. The red lines mark the $\pm 10\%$ allowance for agreement between the models and observations. Error bars represent the measurement error and do not include systematic error. The different symbols show $F_{\rm pre}/F_{\rm obs}$ for two different observations of the object and are representative of the observational scatter.

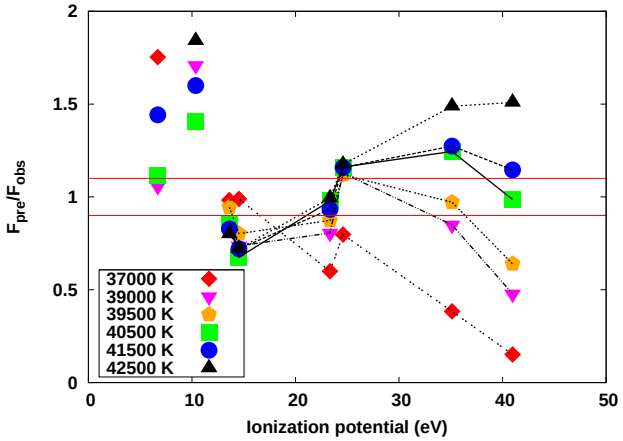

Figure 2: DEM L08c modeled using atmospheres from the SNC02 grid with 6 different $T_{\rm eff}$. This plot shows that moving from low to high $T_{\rm eff}$, the models first favor ions with low IP and then they favor ions with high IP.

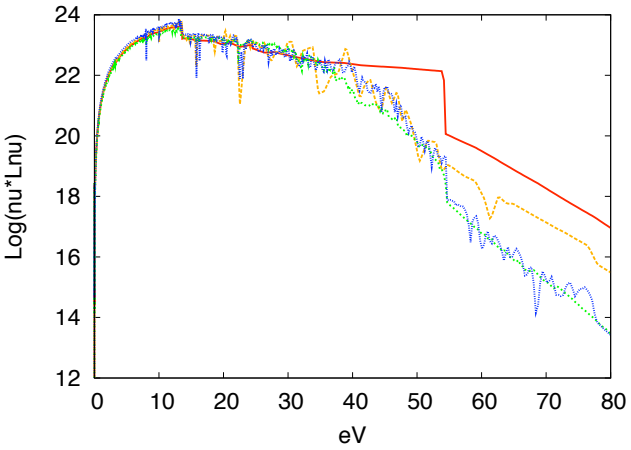

Figure 3: Comparison of the emergent SEDs from the atmospheres discussed in this paper for atmospheres with $T_{\rm eff} = 39000$. Red, green, blue, orange correspond to CoStar (Schaerer & de Koter 1997), TLUSTY (Lanz & Hubeny 2003), WM-basic (Pauldrach et al. 2001), and Smith et al. (2002) model atmospheres, respectively.

4 Results

In our initial suite of models, we model the H II regions as single-density Strömgren spheres. While it is possible to match the predicted emission to the observed one for ions with high IP, the models

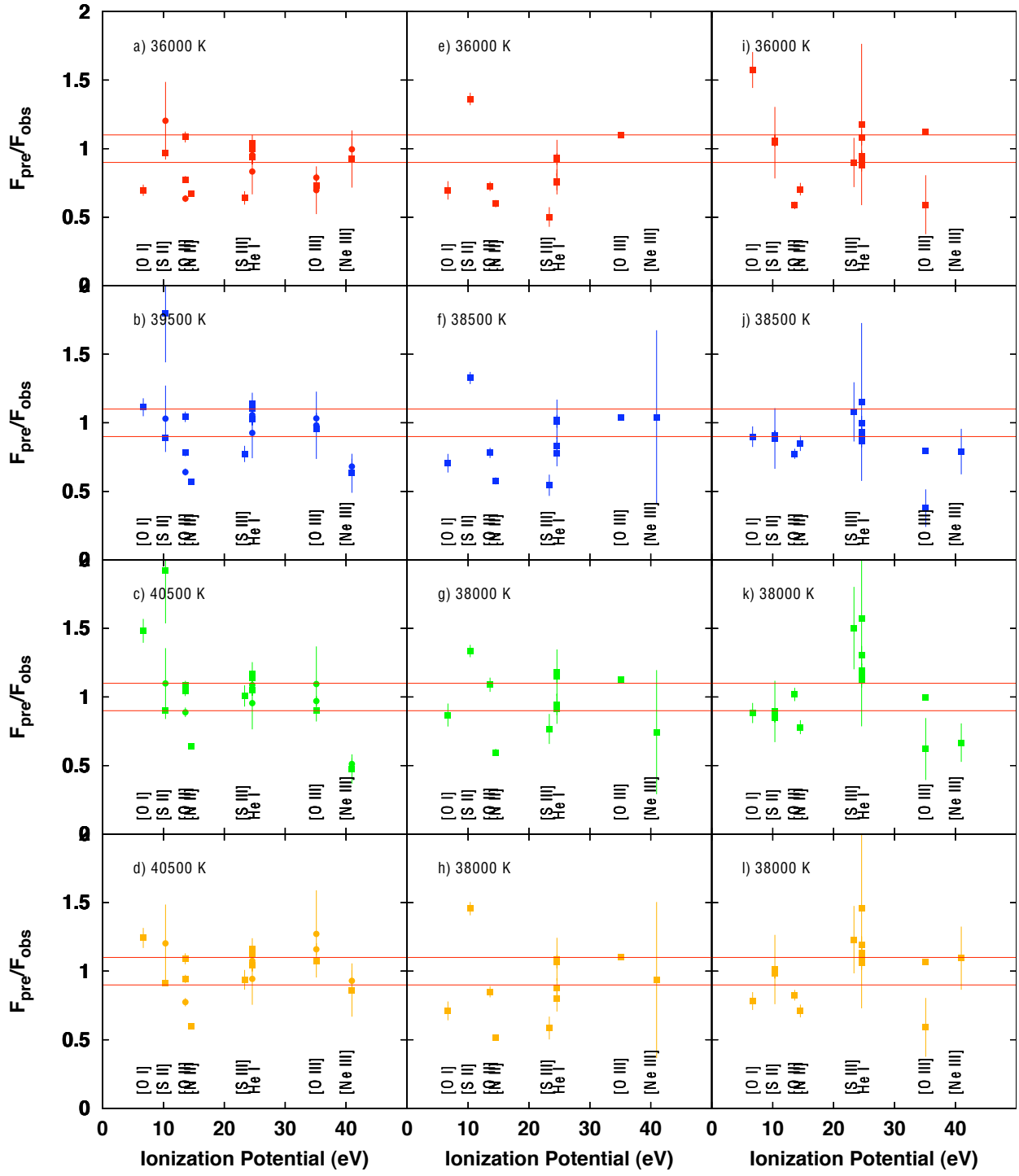

Figure 4: Same as Figure 1 except here, the each H II region is modeled as a nebula with density fluctuations. The T_{eff} of the model atmosphere is printed in the top left corner of each plot. Red, blue, green and orange points correspond to CoStar, WM-basic, TLUSTY, and SN02 model atmospheres, respectively. DEM L08c, ionized by an O5.5V, star is modeled in plots *a-d*; DEM L020, ionized by an O8V, star is modeled in plots *e-h*; DEM L026, ionized by an O8V, star is modeled in plots *i-l*.

consistently under-predict the ions with low IP (see Figure 1). This indicates the ionization parameter is too high. To reproduce the ions with low IP, we need a way to have dense gas further from the star to receive a weakened radiation field. At the same time we need to maintain the gas close to the star to reproduce the emission from ions with high IP. This is accomplished by a density distribution that has small high density clumps with a low density filler between.

The best models for our objects are shown in Figure 4. Each H II region is modeled as a uniform, low-density sphere with small regions of dense gas. The optimal model is determined by plotting the ratio of predicted to observed line flux ($F_{\rm pre}/F_{\rm obs}$) as a function of IP. For each atmosphere and object, we step through our grid in $T_{\rm eff}$ and density (see Figure 2). Most models favor either the ions with low or high IP. We choose the model that has the flattest slope, where most points have a ratio of 1. This indicates that the atmosphere model is radiating the appropriate amount of ionizing flux at both low and high energies. The model parameters are listed in columns 5-7 of Table 1. Column 5 contains the filling factor of the high density gas component. Columns 6a and 6b list the gas density and thickness, respectively, of the high density gas component. Column 7a lists the gas density of the low density component and column 7b lists the spacing between high density regions.

Generally, we find models using WM-basic and SNC02 atmospheres consistently come closest to observations. These model atmospheres have a very detailed treatment of line blanketing and include the effects of stellar winds. Models generated using the TLUSTY atmospheres also agree well for IP less than 40 eV. However, in these models [Ne III] is significantly under-predicted. This reflects the difference in SED between TLUSTY and the other models. At 40 eV, the IP of Ne^{+2}, the TLUSTY SED has lower flux than the other model atmospheres (Figure 3). The Figure also shows that the CoStar SED has a significant excess flux at high energies relative to the other atmosphere models. As a result, it is necessary to use a stellar atmosphere model with an $T_{\rm eff}$ a few thousand degrees cooler to match the observed emission lines in all our objects.

In conclusion, of the four atmosphere models tested, WM-basic and SNC02 consistently ionized the model H II regions that matched the observed line emission. Additionally, we find density fluctuations necessary to generate model H II regions that reproduce the observed emission line spectrum.

Acknowledgements

This research is funded by NSF grant AST-0806476. Many thanks to the LOC for the support to attend this conference.

References

Ferland, G.J., Korista, K.T., Verner, D.A., Ferguson, J.W., Kingdon, J.B., Verner, E.M., 1998, PASP, 110, 749
Garnett, D. 1999, IAUS, 190, 266
Hamuy, M., Suntzeff, N.B., Heathcote, S.R., Walker, A.R., Gigoux, P., & Phillips, M.M, 1994, PASP, 106, 566
Lanz, T. & Hubeny, I., 2003, ApJS, 146, 417
Leitherer, C., Schaerer, D., Goldader, J.D., et al. 1999, ApJS, 123, 3L
Martins, F., Schaerer, D., & Hillier, D.J., 2005, A&A, 436, 1049
Pauldrach, A.W., Hoffman, T.L., & Lennon, M. 2001, A&A, 375, 161
Pérez-Montero, E., & Díaz, A.I., 2005, MNRAS, 361, 1063
Schaerer, D., & de Koter, A., 1997, A&A, 322, 598
Smith, R.C., Points, S.D., Chu, Y.-H., Winkler, P.F., Aguilera, C., Leiton, R., & MCELS Team, 2005, AAS, 207, 2507
Smith, L.J., Norris, R.P., & Crowther, P.A., 2002, MNRAS, 337, 1309
Voges, E. S., Oey, M.S., Walterbos, R.A.M., & Wilkinson, T.M., 2008, AJ, 135, 1291

Chapter 4

Future instrumentation and its application to massive star research

Massive stars in the era of ELTs

Christopher J. Evans[1]

[1] UK Astronomy Technology Centre, Blackford Hill, Edinburgh, EH9 3HJ, UK

Abstract: Plans for the next generation of optical-infrared telescopes, the Extremely Large Telescopes (ELTs), are well advanced. With primary apertures in excess of 20 m, they will revolutionise our ground-based capabilities. In this review I summarise the three current ELT projects, their instrumentation plans, and discuss their science case and potential performance in the context of studies of massive stars.

1 Introduction

In many fields of astronomical research we have already approached the sensitivity limits of the 8-10 m class telescopes. Improvements in performance such as better instrument throughputs and further developments in adaptive optics (AO) will likely come in the next few years, but we are fundamentally limited by the collecting areas and (potential) diffraction limits of existing facilities.

The primary motivation to embark on plans for the next generation of ground-based optical and near-IR facilities, the Extremely Large Telescopes (ELTs), is the huge gain from the combination of sensitivity and angular resolution. Large primary apertures will collect more photons from each target and, with correction of atmospheric turbulence via AO, we will achieve angular resolutions beyond our current capabilties (excluding those targets which are bright enough for optical-IR interferometry). The science case for the ELTs is typically split into three areas:

- *Planets & Stars:* including detection and characterization of extra-solar planets, and a broad range of topics relating to solar system science, proto-planetary discs and star formation.
- *Star & Galaxies:* bridging 'local' topics such as the formation and evolution of stellar clusters, out to using stellar populations to study the assembly histories of galaxies beyond the Local Group and, to even larger distances, the study of black holes in active galactic nuclei.
- *Galaxies & Cosmology:* ranging from studies of galaxy evolution at low redshifts, out to characterization of the highest redshift ('first light') systems and studies of cosmic expansion.

Some of the cases relating to ELT studies of massive stars are now discussed, together with a brief consideration of the broader astronomical landscape in the 2020s. Section 2 gives an overview of the three current ELT projects, while Section 3 gives example performances and highlights the need to improve near-IR diagnostics to exploit the ELTs to their best potential. Lastly, Section 4 summarises recent observations with a successful AO pathfinder on the Very Large Telescope (VLT), as an example of the power of 'wide field' AO techniques.

1.1 Star formation

The main thrust of this review is related to extra-galactic studies but it is worth noting the likely contribution of the ELTs toward our understanding of star formation. The tremendous gain here will be the combination of angular resolution with the ability to penetrate the significant optical extinction (typically tens to over a hundred magnitudes) toward ultra-compact H II regions by observing at near- and mid-IR wavelengths (Zinnecker, 2006). Together with other new facilities such as the Atacama Large Millimetre Array (ALMA), we will truly have a multi-wavelength suite of tools to probe the processes at work in the formation of massive stars.

The potential of modern techniques in this area is neatly illustrated by recent observations of W33A by Davies et al. (2010). This is a well-studied massive young stellar object in the Galaxy, at a distance of nearly 4 kpc and with significant extinction at optical wavelengths. Using AO-corrected, K-band observations with the Gemini Near-IR Integral Field Spectrograph (NIFS), Davies et al. were able to investigate the different spatial structures related to W33A. Supported by interferometric results from de Wit et al. (2007, 2010), they conclude that the star is forming via similar processes to those seen in lower mass objects, i.e., accretion from a circumstellar disc, while driving a bi-polar outflow. The collapsed K-band NIFS image is shown in the left-hand panel of Fig. 1, with spectra of selected regions shown in the right-hand panel; note the spatial scales of $\sim$0.″1 in the NIFS image.

With much greater sensitivity, the ELTs will be able to extend studies of ultra-compact H II regions and young stellar objects/clusters to much larger distances and to systems with greater extinction. In this area there will be strong complementarity between the scales probed by the ELTs and by interferometry with, e.g, the Very Large Telescope Interferometer (VLTI). Indeed, the power of VLTI is highlighted by the recent detection of a dusty disc around another very young massive star, IRAS 13481−6124 (Kraus et al. 2010).

Although we are starting to glean some of the first views of the formation of individual massive stars, the majority appear to be in binary/multiple systems (e.g., Mason et al. 2009; Sana & Evans, 2011). The dominant formation mechanism of such systems is still not clear (e.g. Gies, 2008) and, if we want to be able to understand the integrated light populations of distant star-forming galaxies (which are dominated by massive stars), it is clear we still have much to learn.

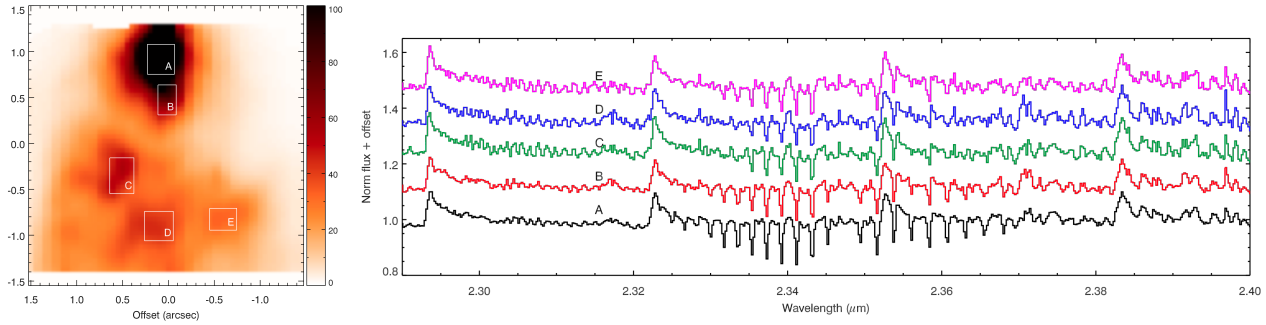

Figure 1: *Left:* Gemini-NIFS K-band image of W33A from Davies et al. (2010). *Right:* K-band spectra of the bright central source (region 'A') and other knots of emission ('B' to 'E'). The variations in the CO spectra were used by Davies et al. to constrain the geometry of material around W33A.

1.2 Stellar spectroscopy beyond the Local Group

One of the big impacts of the 8-10 m telescopes compared to previous facilities has been to obtain high-quality stellar spectroscopy in external galaxies. For example, this gain in sensitivity is evident

for targets in M31, where new Gemini-GMOS spectroscopy of luminous supergiants (Cordiner et al. 2011) makes light work of observations which were challenging with 4 m telescopes (e.g. Bianchi et al. 1994; Herrero et al. 1994). There are two observational regimes in the current 8-10 m era:

- *Fundamental stellar astrophysics in nearby galaxies:* High-quality spectroscopy for quantitative analysis of individual massive stars in the Magellanic Clouds was only possible for selected bright targets with 4 m telescopes. With the advent of multi-object instruments such as FLAMES on the VLT we have been able to obtain large spectroscopic samples of the massive star populations of the Clouds (and the Milky Way) to investigate the role of environment on stellar properties and evolution (e.g. Evans et al. 2005a, 2005b; Martayan et al. 2006, 2007).

- *Stars as tracers of galaxy properties:* Beyond 1 Mpc, we have had our first glimpses of spectra of individual stars in galaxies such as NGC 3109 (Evans et al. 2007) at 1.3 Mpc, and NGC 300 (Bresolin et al. 2002) and NGC 55 (Castro et al. 2008), both of which are spiral galaxies in the Sculptor 'Group' at $\sim$1.9 Mpc (Pietrzyński et al. 2006). Such data can be used to estimate the present-day abundances in these galaxies, to study radial abundance trends in the spirals (Urbaneja et al. 2005), and to help refine our understanding of other diagnostics used in interpretation of more distant systems (Bresolin et al. 2009). The most impressive observations in this context are the VLT spectra of two supergiants in NGC 3621 (Bresolin et al. 2001), at a remarkable distance of 6.7 Mpc.

The arrival of the ELTs will represent an even greater leap forward in our capabilities than that when moving from 4 to 8 m, opening-up an exciting range of options for future study, including:

- *Physics & evolution of massive stars in metal-poor irregulars:* Quantitative analysis of blue supergiants in galaxies such as IC 1613, WLM and NGC 3109 has found oxygen abundances slightly below those found in the Small Magellanic Cloud (Bresolin et al., 2006, 2007; Evans et al. 2007). Determining exact metallicities requires further work, but it is clear that these systems provide an excellent opportunity to expand our studies of massive stars in metal-poor regimes – from the most extreme, luminous phases to main-sequence dwarfs.

- *Massive star populations of nearby spirals:* The full luminosity range of massive stars will also be accessible in local spirals. This includes galaxies such as NGC 55 and NGC 300, but the real prize here is the potential of studying the full age-range of populations in both M31 and M33 – from main-sequence massive stars to the oldest evolved red giants. There is already significant deep imaging in these galaxies, and a new multi-cycle *HST* Treasury Program to image one quadrant of M31 at UV/optical/near-IR wavelengths ('A Panchromatic Hubble Andromeda Survey; PI: J. Dalcanton) will provide rich sources of exciting objects worthy of ELT spectroscopy for quantitative abundances and radial velocities.

- *The most luminous stars in distant galaxies:* As we move beyond the Local Group, there is a rich assortment of galaxy types and environments/groups. Here we can seek to use our understanding of massive stars to learn about the host galaxies. For example, in the starburst galaxy M82, in ellipticals such as Cen A (NGC 5128), NGC 3379 and members of the Virgo Cluster, and in interacting systems such as M51. Looking even further afield, we can exploit the angular resolution of the ELTs to resolve the cluster complexes in the Antennae into their sub-components to assess their ages/populations. Perhaps one of the most compelling targets for further study in terms of its apparently *very* metal-poor population is I Zw 18 (Heap et al. 2011), at a distance 18.2 Mpc (Aloisi et al. 2007). As noted by others in the literature, I Zw 18 could provide important insights into stellar evolution in conditions which are more in keeping with those in the very early universe.

1.3 Synergies with other facilities

The current generation of ground-based, optical-IR telescopes will continue to deliver exciting new results over the coming decade, particularly with the arrival of new instrumentation. However, deep imaging from the 8-10 m telescopes and the *Hubble Space Telescope (HST)* is already revealing targets which are beyond our spectroscopic capabilities. The need for follow-up will become increasingly important, not to mention the potential of combining, e.g, VLTI observations with ELT integral-field spectroscopy.

Such synergies will become even more crucial when looking ahead to ALMA and the *James Webb Space Telescope (JWST)*, both of which will start operations in the coming few years. They will be unique at their respective wavelengths, but supporting ground-based, optical-IR observations will be critical, as exemplified by years of *HST* operations.

Looking further ahead, the impact of other facilities such as the Large Synoptic Survey Telescope (LSST), the Square Kilometre Array (SKA), and the *International X-ray Observatory (IXO*; Rauw & Oskinova 2011) would all benefit hugely from the ability to obtain, e.g., spectroscopic follow-up or diffraction-limited imaging with an ELT.

1.4 Anticipating the unknown

There are a wide range of scientific motivations for the ELTs, all informed by our current research and contemporary understanding; it is harder to plan for the unknown discoveries which await in the coming decade. Harwit (1981) made the point that new discoveries are generally achieved when a new part of parameter space is accessed for the first time. An excellent example of this is provided by the first sub-millimetre observations of distant galaxies (e.g. Smail, Ivison & Blain, 1997). The ELTs will excel in the combination of collecting power and angular resolution so, while we should design the observatories and their instruments to provide the best possible performance for the observations we can contemplate now, we should be wary of focussing those capabilities too much, rendering us unable to investigate future discoveries that we can not even conceive of today.

2 ELTs: Worldwide context

Efforts toward building ELTs are becoming increasingly global, with three projects now in the advanced stages of their design, fund-raising and planning; the top-level details of each observatory are summarised briefly below. While these projects are collectively referred to as 'ELTs', note that there is a large range in the effective areas of their primary apertures.

2.1 GMT: The Giant Magellan Telescope[1]

The GMT employs seven monolithic 8 m mirrors to form the primary aperture. Six of these are off-axis, arranged around the central on-axis mirror (see left-hand panel of Fig. 2). The effective diameter in terms of potential angular resolution is 24.5 m, with an equivalent collecting area of a $\sim$22 m filled-aperture primary. At the time of writing, GMT includes ten partners. These are primarily in the United States, but also include members in South Korea and Australia. The intended GMT site is at the Las Campanas Observatory in Chile, already home to the Magellan, Du Pont and Swope telescopes.

[1] http://www.gmto.org

2.2 TMT: The Thirty Meter Telescope[2]

The initial partners of TMT were Caltech, University of California and Canada. Over the past couple of years this partnership has expanded to include Japan, China and, most recently, India. The effective diameter of the primary is 30 m, comprised of hexagonal segments which are just over 1.4m̀ in diameter (across the corners). This design builds on the considerable experience of the segmented primaries of the Keck telescopes. The TMT will be located on Mauna Kea in Hawaii, with a novel 'Calotte' dome to minimise wind shake (and cost), as shown in the right-hand panel of Fig. 2. An integral part of the project has been to minimise the environmental impact of the observatory on the mountain, including an updated design of the dome and the offices (beyond the one shown in Fig. 2).

Figure 2: *Left:* The GMT in its enclosure (image credit: Giant Magellan Telescope – GMTO Corporation); *Right:* Artist's interpretation of the TMT on Mauna Kea, Hawaii (credit: the Thirty Meter Telescope Project).

2.3 E-ELT: The European Extremely Large Telescope[3]

The E-ELT is under development by the European Southern Observatory (ESO) on behalf of its partners, and features a primary with an equivalent diameter of 42 m (Fig. 3). As with the TMT, the primary is comprised of 1.4 m hexagonal segments. In addition to the primary, secondary and tertiary elements, the telescope design features an adaptive fourth mirror and a fast tip-tilt fifth mirror. The E-ELT site was announced earlier in 2010 to be Cerro Armazones in northern Chile. This is approximately 20 km from Paranal (the site of the VLT), meaning that some of the infrastructure and operations costs can be shared. Armazones is at an altitude of 3060 m, slightly higher than Paranal.

2.4 Instrumentation plans

Detailed overviews of the instrumentation studies completed or underway for each of the three ELT projects were given at the recent SPIE meeting in San Diego (GMT: Jaffe et al. 2010; TMT: Simard et al. 2010; E-ELT: Ramsay et al. 2010). A vast range of parameter space is covered by these studies. This is, in part, to be able to evaluate the relative merits of different capabilities toward each science case, but also to explore the technology readiness/requirements of key components for the future.

[2]http://www.tmt.org
[3]http://www.eso.org/sci/facilities/eelt

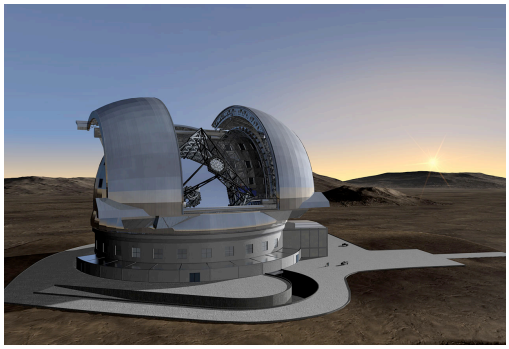

Figure 3: Recent design of the E-ELT in its enclosure (Credit: ESO).

The instrument studies undertaken to date are given in Tables 1, 2, and 3. Part of the motivation for such a comprehensive list is not to dazzle or overwhelm with acronyms and abbreviations, but to illustrate the significant effort that has already gone into these projects from the instrumentation part of the community, in close collaboration with the astronomers who have developed the science cases, undertaken simulations etc.

The first round of studies for TMT were completed in 2008, with three instruments subsequently selected for 'early light' operations, as indicated in Table 2. A similar down-select will form part of the E-ELT construction proposal, to be released in late 2010. The GMT studies will end in July 2011, with a down-select following thereafter.

Table 1: GMT conceptual design studies (Jaffe et al. 2010).

Instrument	Brief description
G-CLEF	High resolving power, high stability, optical spectrograph
GMACS	Multi-slit, seeing-limited, optical spectrograph
GMTIFS	AO-corrected, integral field, near-IR spectrogragh (*à la* GEMINI-NIFS)
GMTNIRS	AO-fed, high resolving power, near-IR spectrograph
NIRMOS	Multi-slit, near-IR spectrograph
TIGER	Mid-IR imager and low-resolution spectrograph

Table 2: TMT capabilities for first decade (Simard et al. 2010).

Instrument	Brief description
IRIS	AO-fed, near-IR, integral field unit (IFU) and imager
IRMS	AO-fed, multi-slit, near-IR spectrograph (clone of Keck-MOSFIRE)
WFOS	Seeing-limited, multi-object, optical spectrograph
HROS	High-resolving power, seeing-limited, optical spectrograph
IRMOS	Multi-IFU, AO-corrected, near-IR spectrograph
MIRES	AO-fed, mid-IR, echelle spectrograph
NIRES	AO-fed, near-IR, echelle spectrograph
PFI	High contrast, near-IR imager
WIRC	'Wide field', AO-corrected imager

The first three instruments (IRIS, IRMS and WFOS) are those planned for 'early light'.

Table 3: E-ELT Phase A studies (Ramsay et al. 2010).

Instrument	Brief description
CODEX	High resolving power, high stability, optical spectrograph
EAGLE	Multi-IFU, AO-corrected, near-IR spectrograph
EPICS	High contrast, near-IR imager/spectro-polarimeter
HARMONI	AO-fed, near-IR, IFU
METIS	AO-fed, mid-IR imager and spectrograph
MICADO	Near-IR, diffraction-limited imager
OPTIMOS	Seeing-limited/ground-layer AO, high-multiplex spectrograph
SIMPLE	AO-fed, near-IR, high resolving power spectrograph

3 Illustrative performances

To illustrate the spectroscopic potential of ELTs, I refer to simulations from the EAGLE Phase A study for the E-ELT (Cuby et al. 2010). EAGLE is a conceptual design for an AO-corrected, near-IR spectrograph with multiple integral field units (IFUs). A key element of its science case is spectroscopy of resolved stellar populations beyond the Local Group, using evolved red giant stars to trace the star-formation histories of their host galaxies. Tools have been developed to simulate EAGLE observations (Puech et al. 2008, Puech, Yang, & Flores 2010), which employ a set of simulated, AO-corrected, point-spread functions (PSFs) for example configurations of natural guide stars (Rousset et al. 2010).

Simulated EAGLE performances for spectroscopy of the calcium triplet (centered at 0.86 μm) were given by Evans et al. (2010). The continuum signal-to-noise (S/N, per pixel) resulting from some of these simulations is summarised in Table 4 for two configurations of guide stars; other relevant parameters were a spectral resolving power, R, of 10000, a total exposure time of 10 hrs (20×1800s) and a seeing of $0\farcs65$. From a stacked 10 hr exposure at $I = 24.5$ (in the Vega System), a continuum S/N ≥ 10 is recovered, some four magnitudes deeper than FLAMES-GIRAFFE on the VLT using the LR08 setting (which is also at a lower resolving power of $R = 6500$), with the same exposure time.

Table 4: Continuum signal-to-noise (S/N, per pixel) obtained for simulated EAGLE observations of the calcium triplet (Evans et al. 2010), with $R = 10000$, $t_{\rm exp} = 10$ hrs, and two configurations of natural guide stars (NGS).

$I_{\rm VEGA}$	S/N [NGS 'Good']	S/N [NGS 'Poor']
22.5	56	48
23.5	28	24
24.5	13	10

These simulations were originally to quantify the performances for red giant stars, but we can also consider their implications in the context of massive stars, where we typically require a S/N ≥ 50. The reach of I-band spectroscopy of different populations is summarised in Table 5. I know the I-band is not exactly replete with useful diagnostics in the spectra of massive stars (!), but these performances are merely to give a feel for the distances to which one can contemplate ELT observations. The bottom-line is that the ELTs will provide spectroscopy of individual stars beyond the Local Group, in the same manner that we have begun to take for granted in nearby galaxies.

3.1 Future diagnostics

An important additional factor in performance calculations for ELTs is the level of AO correction. Seeing-limited spectroscopy in the optical (covering the diagnostic lines with which we have con-

Table 5: Distance moduli (DM) and distances (d) to which I-band spectroscopy could be obtained with EAGLE (at $R = 10000$ and given S/N), assuming the performances from Table 4.

Star	S/N	M_I	DM	d
Tip of red giant branch	≥ 10	-4	28.5	5 Mpc
BA-type supergiants	≥ 50	-7	29.5	8 Mpc
O-type dwarf	≥ 50	-4.5	27.0	2.5 Mpc

siderable experience) could yield spectra of supergiants in the outer halos of distant galaxies, but to probe into the densest regions we will require the best possible contrast from AO, which will be limited to relatively small fields. Moreover, for stellar spectroscopy with the ELTs there will be a fine balance in sensitivity between the improved image quality from adaptive optics as one goes to longer wavelengths (where the wavefront errors become less significant compared to the observational wavelengths) versus the increased background. As an example of the wavelength dependence of the AO correction, Fig. 4 shows results for the encircled energy within a 75 milliarcsecond aperture from the simulated EAGLE PSFs (Rousset et al. 2010).

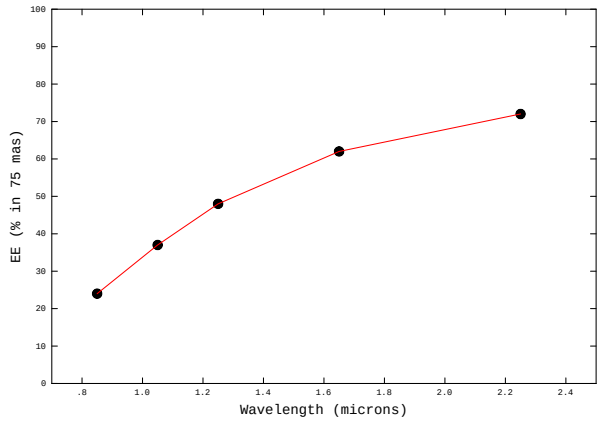

Figure 4: The wavelength dependence of the effective AO correction is shown by the encircled energy (EE) delivered in 75 milliarcseconds by the simulated EAGLE PSFs (Rousset et al. 2010).

Martins (2011) summarised the broad range of diagnostics available to us in our efforts to determine the physical parameters of massive stars. For example, in regions of high extinction such as the Galactic Centre, K-band spectroscopy provides the means to study stellar winds (Martins et al. 2007). Work is already underway to improve our understanding of near-IR diagnostics compared to those in the optical as part of the planning toward ELTs (e.g. Przybilla et al. 2009; Nieva et al. 2009), not to mention compilation of a high-resolution spectral library in the near-IR (Lebzelter et al. 2010; Ramsay et al. 2011).

A more detailed example of exploring alternative diagnostics is the recent study by Davies, Kudritzki & Figer (2010) in which they employ low-resolution ($R \sim$ 2-3000) J-band spectroscopy to determine metallic abundances for red supergiants – this is a relatively unexplored wavelength domain, first considered for this type of abundance work by Origilia et al. (2004). From comparisons with contemporary model atmospheres, the method provides good estimates of stellar metallicities (with a dispersion of $\pm$0.14 dex) for library spectra in the Solar neighbourhood; example fits are shown in Fig. 5. We are now exploring the potential of this method for metal-poor templates in simulated ELT observations, using the tools mentioned earlier that were developed for EAGLE. By their nature, red supergiants are cool (i.e. significant J-band flux in their spectral energy distributions) and

very luminous - when combined with the AO capabilities of the ELTs, this method could provide a probe of stellar abundances out to distances of tens of Mpc.

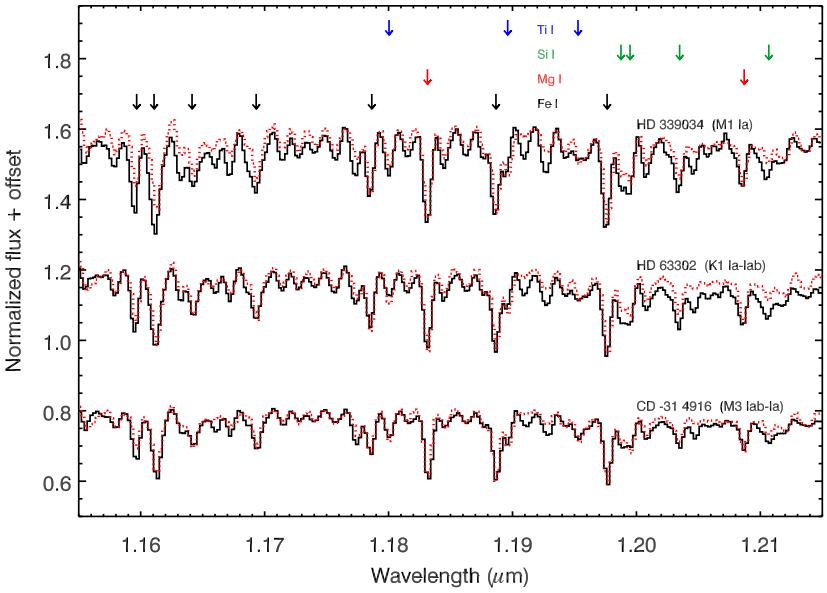

Figure 5: Model atmosphere fits (red lines) to provide metallicities/stellar abundances from J-band spectra of Galactic red supergiants (Davies, Kudritzki & Figer, 2010).

4 MAD: An AO pathfinder for ELTs

Correction for the effects of atmospheric turbulence with AO is a critical ingredient of the plans for ELTs and their instruments. In particular, there is a strong desire for good and *uniform* correction over larger fields-of-view than delivered by, e.g., VLT-NACO (Rousset et al. 2003). A key technical component within ESO's plan toward the E-ELT was an on-sky demonstration of multi-conjugate adaptive optics (MCAO). To this end, the Multi-conjugate Adaptive optics Demonstrator (MAD) was developed (Marchetti et al. 2007) with commissioning at the VLT in early 2007.

MAD employs three wavefront sensors to observe three natural guide stars across a $2'$ circular field, thereby allowing tomography of the atmospheric turbulence. The turbulence is then corrected using two deformable mirrors, one conjugated to the ground-layer (i.e. 0 km), the second conjugated to 8.5 km above the telescope. The MAD near-IR camera critically samples the diffraction-limited PSF at 2.2μm, giving a pixel scale of $0\farcs028$/pixel. With a 2k$\times$2k Hawaii-2 array, this gives a total field-of-view of $57'' \times 57''$.

The commissioning performances were sufficiently compelling that ESO issued a call for Science Demonstration (SD) observations, to which the community responded enthusiastically. As an illustration of the SD programmes I refer to H- and $K_{\rm s}$-band MAD observations of R136 (Fig. 6; Campbell et al. 2010), the dense cluster at the core of 30 Doradus in the Large Magellanic Cloud. Also of direct relevance to the topic of this meeting are the MAD observations of Trumpler 14 (Sana et al. 2010).

The AO correction is such that the mean full-width half-maximum of the PSFs is $\sim 0\farcs10$ in two of the three MAD pointings (the best placed with respect to the guide stars). This provides near-comparable angular resolution to optical imaging with the *HST* (e.g., Hunter et al. 1995). Due to the size of the primaries, the angular resolution from MAD is finer than that from the *HST* at the same wavelength, although the *HST* has a large advantage in terms of sensitivity due to the reduced

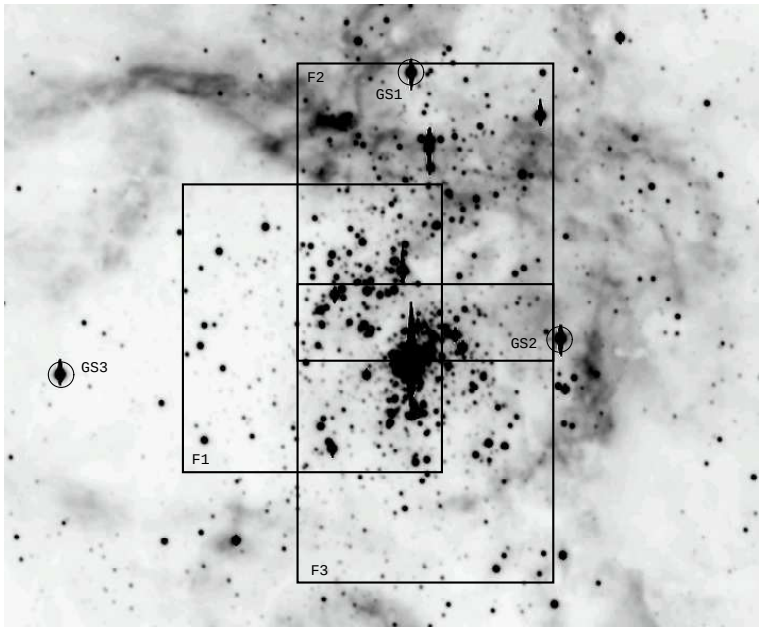

Figure 6: The three MAD pointings overlaid on a V-band image of the central part of 30 Dor. North is at the top, east toward the left. The three reference stars used for the AO correction are shown ('GS#').

sky background (cf. the results of Andersen et al. 2009). Further details regarding calibration and performance are given by Campbell et al. (2010); a combined image of the central region is shown in Fig. 7.

A nice test of the ground-based methods with MAD, compared to the *HST* results from Andersen et al., is provided by the agreement in the derived slopes of power-law fits to the luminosity profile of R136. The MAD data also have the advantage of going out to larger cluster radii than those from Andersen et al., allowing re-investigation of a 'bump' seen in the luminosity profile of R136 from optical *HST* observations (Mackey & Gilmore, 2003). This 'excess light' at large radii has been suggested in the past as perhaps related to the signatures of rapid gas expulsion from young clusters (e.g. Goodwin & Bastian, 2006). In contrast, the MAD data do not reveal an obvious break in the luminosity profile, with Campbell et al. (2010) suggesting that cluster asymmetries are the dominant source. In combination with AO-corrected IFU spectroscopy (Schnurr et al. 2009), the MAD data have since been used to argue that the central stars of R136 have initial masses in excess of 150 $M_\odot$ (Crowther et al. 2010).

The instrumental and scientific experiences of MAD augur well for the AO plans for ELTs. Pathfinders for other AO modes such as Multi-Object Adaptive Optics are underway, for example the CANARY project (Myers et al. 2008; Morris et al. 2010) and plans for RAVEN (Conan et al. 2010). In the shorter term, the Gemini MCAO System (GeMS) is now undergoing its final tests and integration (Neichel et al. 2010), and will offer a unique capability of MCAO with laser guide stars (removing some of the constraints on natural guide stars), for near-IR imaging and multi-object spectroscopy.

5 Summary

The ELTs offer huge potential for studies of massive stars – we will be able to address fundamental questions regarding their formation and evolution (with a particular focus on environmental effects), while also using individual stars as tracers of the stellar populations in galaxies well beyond the Local

Figure 7: Combined mosaic of the central $40'' \times 40''$ MAD images (blue: H; red: K_s; green: interpolated).

Group.

By way of further motivation, consider the ground-breaking study by Swinbank et al. (2010) in which they have used multi-wavelength observations to study a gravitationally-lensed galaxy at a redshift of $z = 2.3$. By virtue of the lens, individual star-forming regions are resolved in sub-millimetre imaging, each $\sim$100 pc in scale – i.e. direct observation of intense regions of star formation with spatial extents comparable to that of 30 Doradus, at a time when the universe was significantly younger. Such an observation is only possible at present due to the magnification of the lens but, with the combined power of ALMA and the ELTs in the future, we can expect comparable observations in unlensed systems. One of the challenges ahead is to improve our models of stellar evolution to the point at which we are confident that we can interpret integrated-light spectroscopy of such distant systems accurately, thereby exploiting our understanding of massive stars to obtain new insights into the processes at work during the critical epoch of galaxy evolution.

Acknowledgements

Thanks to Michael Campbell for his MAD mosaic and to Ben Davies for copies of his figures.

References

Aloisi, A., Clementini, G., Tosi, M., et al. 2007, ApJ, 667, L151

Andersen, M., Zinnecker, H., Moneti, A., McCaughrean, M. J., Brandl, B., Brandner, W., Meylan, G., & Hunter, D. 2009, ApJ, 707, 1347

Bianchi, L., Lamers, H. J. G. L. M., Hutchings, J. B., Massey, P., Kudritzki, R., Herrero, A., & Lennon, D. J. 1994, A&A, 292, 213

Bresolin, F., Kudritzki, R.-P., Mendez, R. H., & Przybilla, N. 2001, ApJ, 548, L159

Bresolin, F., Gieren, W., Kudritzki, R.-P., Pietrzynski, G., & Przybilla, N. 2002, ApJ, 567, 277

Bresolin, F., Pietrzyński, G., Urbaneja, M.A., Gieren, W., Kudritzki, R.-P., & Venn, K. A 2006, ApJ, 648, 1007
Bresolin, F., Urbaneja, M. A., Gieren, W., Pietrzynski, G., & Kudritzki, R.-P. 2007, ApJ, 671, 2028
Bresolin, F., Gieren, W., Kudritzki, R.-P., Pietrzynski, G., Urbaneja, M. A., & Carraro, G. 2009, ApJ, 700, 309
Campbell, M. A., Evans, C. J., Mackey, A. D., Gieles, M., Alves, J., Ascenso, J., Bastian, N., & Longmore, A. J. 2010, MNRAS, 405, 421
Conan, R., Bradley, C., Lardière, O., et al. 2010, SPIE, 7736, 26
Cordiner, M.A., Cox, N.L.J., Evans, C.J., Trundle, C., Smith, K.T., Sarre, P.J., & Gordon, K.D. 2011, ApJ 726, 39
Crowther, P. A., Schnurr, O., Hirschi, R., Yusof, N., Parker, R. J., Goodwin, S. P., & Kassim, H. A. 2010, MNRAS, 408, 731
Cuby, J.-G., Morris, S., Fusco, T., et al. 2010, SPIE, 7735, 80
Davies, B., Kudritzki, R.-P. & Figer, D. F., 2010, MNRAS, 407, 1203
Davies, B., Lumsden, S. L., Hoare, M. G., Oudmaijer, R. D., & de Wit, W.-J. 2010, MNRAS, 402, 1504
de Wit, W. J., Hoare, M. G., Oudmaijer, R. D., & Mottram, J. C. 2007, ApJ, 671, L169
de Wit, W. J., Hoare, M. G., Oudmaijer, R. D., & Lumsden, S. L. 2010, A&A, 515, A45
Evans, C. J., Smartt, S. J., Lee, J.-K., et al. 2005a, A&A, 437, 467
Evans, C. J., Lennon, D. J., Smartt, S. J., & Trundle, C. 2005b, A&A, 456, 623
Evans, C. J., Bresolin, F., Urbaneja, M. A., Pietrzynski, G., Gieren, W., & Kudritzki, R.-P. 2007, ApJ, 659, 1198
Evans, C. J., Yang, Y., Puech, M., et al. 2010, in Clénet, Conan, Fusco & Rousset, eds, *Adaptive Optics for Extremely Large Telescopes*, EDP Sciences, 1004, arXiv:0909.1748
Gies, D. R., 2008, in Beuther, Linz & Henning, eds, *Massive Star Formation: Observations Confront Theory*, ASP Conference Series, 387, p93
Goodwin, S. P. & Bastian, N., 2006, MNRAS, 373, 752
Harwit, M. 1981, *Cosmic Discovery*, Basic Books, New York
Heap, S.R., Hubeny I., Lanz T.,Landsman W., Lindler D., & Malumuth E. 2011, in Proceedings of the 39th Liège Astrophysical Colloquium, eds. G. Rauw, M. De Becker, Y. Nazé, J.-M. Vreux & P. Williams, BSRSL, 80, 149
Herrero, A., Lennon, D. J., Vilchez, J. M., Kudritzki, R. P., & Humphreys, R. H. 1994, A&A, 287, 885
Hunter, D. A., Shaya, E. J., Holtzman, J. A., Light, R. M., O'Neil, E. J., Jr., & Lynds, R. 1995, ApJ, 448, 179
Jaffe, D., Depoy, D. L., Fabricant, D. G., et al. 2010, SPIE, 7735, 72
Kraus, S., Hofmann, K.-H., Menten, K. M., et al. 2010, Nature, 466, 339
Lebzelter, T., Seifahrt, A., Ramsay, S., et al. 2010, Msngr, 139, 33
Mackey, A. D. & Gilmore, G. F., 2003, MNRAS, 338, 85
Marchetti, E., Brast, R., Delabre, B., et al. 2007, Msngr, 129, 8
Martayan, C., Frémat, Y., Hubert, A.-M., Floquet, M., Zorec, J., & Neiner, C. 2006, A&A, 452, 273
Martayan, C., Frémat, Y., Hubert, A.-M., Floquet, M., Zorec, J., & Neiner, C. 2007, A&A, 462, 683
Martins, F., Genzel, R., Hillier, D. J., Eisenhauer, F., Paumard, T., Gillessen, S., Ott, T., & Trippe, S. 2007, A&A, 468, 233
Martins, F. 2011, in Proceedings of the 39th Liège Astrophysical Colloquium, eds. G. Rauw, M. De Becker, Y. Nazé, J.-M. Vreux & P. Williams, BSRSL, 80, 29
Mason, B. D., Hartkopf, W. I., Gies, D. R., Henry, T. J., & Helsel, J. W. 2009, AJ, 137, 3358
Morris, T., Hubert, Z., Myers, R., et al. 2010, in Clénet, Conan, Fusco & Rousset, eds, *Adaptive Optics for Extremely Large Telescopes*, EDP Sciences, 8003
Myers, R. M., Hubert, Z., Morris, T. J., et al. 2008, SPIE, 7015, 6
Nieva, M. F., Przybilla, N., Seifahrt, A., Butler, K., Kufl, H. U., & Kaufer, A. 2009, in Moorwood, ed., *Science with the VLT in the ELT era*, Springer, Netherlands, p499
Neichel, B., Rigaut, F., Bec, M., et al. 2010, SPIE, 7736, 4
Origlia, L., Ranalli, P., Comastri, A., & Maiolino, R. 2004, ApJ, 606, 862
Pietrzyński, G., Gieren, W., Soszyński, I., et al. 2006, AJ, 132, 2556
Przybilla, N., Seifahrt, A., Butler, K., Nieva, M. F., Käufl, H.-U., & Kaufer, A. 2009, in Moorwood, ed., *Science with the VLT in the ELT era*, Springer, Netherlands, p55
Puech, M., Flores, H., Lehnert, M., Neichel, B., Fusco, T., Rosati, P., Cuby, J.-G., & Rousset, G. 2008, MNRAS, 390, 1089
Puech, M., Yang, Y. B., & Flores, H. 2010, SPIE, 7735, 183
Ramsay, S., D'Odorico, S., Casali, M., et al. 2010, SPIE, 7735, 71
Ramsay, S.K., Lebzelter, T., Seifahrt, A., et al. 2011, in Proceedings of the 39th Liège Astrophysical Colloquium, eds. G. Rauw, M. De Becker, Y. Nazé, J.-M. Vreux & P. Williams, BSRSL, 80, 509
Rauw, G., & Oskinova L. 2011, in Proceedings of the 39th Liège Astrophysical Colloquium, eds. G. Rauw, M. De Becker, Y. Nazé, J.-M. Vreux & P. Williams, BSRSL, 80, 475

Rousset, G., Lacombe, F., Puget, P., et al. 2003, SPIE, 4839, 140
Rousset, G., Fusco, T., Assemat, F., et al. 2010, in Clénet, Conan, Fusco & Rousset, eds, *Adaptive Optics for Extremely Large Telescopes*, EDP Sciences, 2008, arXiv:1002.2077
Sana, H., Momany, Y., Gieles, M., Carraro, G., Beletsky, Y., Ivanov, V. D., de Silva, G., & James, G. 2010, A&A, 515, 26
Sana, H. & Evans, C. J., 2011, to appear in *Active OB Stars: Structure, Evolution, Mass loss & Critical Limits*, Proc. IAUS 272, eds. Neiner, Wade, Meynet & Peters, Cambridge University Press
Schnurr, O., Chené, A.-N., Casoli, J., Moffat, A. F. J., & St-Louis, N. 2009, MNRAS, 397, 2049
Simard, L., Crampton, D., Ellerbroek, B., & Boyer, C. 2010, SPIE, 7735, 70
Smail, I., Ivison, R. J. & Blain, A. W., 1997, ApJ, 490, L5
Swinbank, A. M., Smail, I., Longmore, S., et al. 2010, Nature, 464, 733
Urbaneja, M. A., Herrero, A., Kudritzki, R.-P., Najarro, F., Smartt, S. J., Puls, J., Lennon, D. J., & Corral, L. J. 2005, ApJ, 635, 311
Zinnecker, H., 2006, in *The Scientific Requirements for Extremely Large Telescopes*, Proc. IAUS 232, eds. Whitelock, Dennefeld & Leibundgut, Cambridge University Press, 324

Discussion

R. Chini: What will be the contribution of this new generation of ELTs instruments to the investigation of Galactic high-mass (say e.g. $V < 10$ mag) stars? Are there currently any estimates about the brightest stars that can be (are allowed to be) observed, say with the ELT?
C. Evans: You could imagine using a high-spectral resolution instrument to do time resolved studies, but you would have to consider if it's the most efficient telescope if, say, an 8-m class would do. In terms of brightness limits, there are no constraints I know of. Persistance in IR detectors is less of a problem than it used to be but you might have to worry about scattered light issues, for example.

H. Zinnecker: You kindly mentioned ELTs power to penetrate large amounts of extinction ($A_V = 100 - 200$). Indeed, simulations carried out at ESO show that the E-ELT can be used to study the stellar content of very heavily obscured, young protoclusters, in particular the central stellar density of massive young stellar objects. This will be important new information, in order to judge if stellar collisions or interactions are likely to occur in the earliest stages of high-mass star formation found in Galactic Infrared Dark Clouds (IRDCS). Exciting times ahead !
C. Evans: Thanks. I was hoping you would pick-up on this point !

Spectroscopic madness - A golden age for amateurs

Thomas Eversberg

Schnörringen Telescope Science Institute (STScI), Am Kielshof 21a, 51105 Köln, Germany

Abstract: Today, professional instrumentation is dominated by heavily oversubscribed telescopes which focus mainly on a limited number of "fashionable" research topics. As a result, time acquisition for massive star research including extended observation campaigns, becomes more difficult. On the other hand, massive star investigations by amateur astronomers performing spectroscopic measurements are on a level which can fulfil professional needs. I describe the instrumentation available to the amateurs, their observational skills and the potential contribution they can make to the professional community.

1 Introduction

The so-called "Golden Age of Astronomy" not only influences professional scientific work but also the amateur domain. State-of-the-art instrumentation such as 1m class telescopes have reached the amateur domain and optics and CCD detectors are available off-the-shelf for relatively low prices. Today amateurs can accomplish extraordinary spectroscopic results, which would have been impossible a few decades ago.

2 State-of-the-art amateur astronomy

In the past few years, various spectrographs have been successfully designed and constructed by dedicated amateur astronomers using off-the-shelf optics and blazed gratings, and have been properly adapted to respective telescopes. The first generation of instruments delivering a spectral resolution of more than 10.000 are now also available commercially, and after the successful design and construction of various prototypes by some skilled amateurs (fig. 1) the first off-the-shelf Echelle spectrographs are also available, including a complete and tested software routine for a "plug-and-play" data reduction chain (fig. 2)[1]. Amateur and off-the-shelf Echelle spectrographs have the same performance but are often cheaper than similar professional prototypes for small telescopes. This is mainly due to commercial off-the-shelf serial production.

3 Long-term campaigns, surveys, monitoring

Amateur spectroscopic equipment can easily be used for scientific investigations of stellar physics, particularly the study of bright emission line stars where line profile analysis of their often fast varying

[1] www.shelyak.com

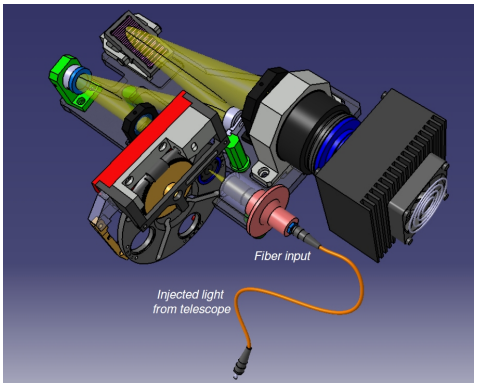

Figure 1: Prototype of an Echelle spectrograph with grating cross-disperser designed by the amateur Tobias Feger. The final device will be mounted in a solid casing.

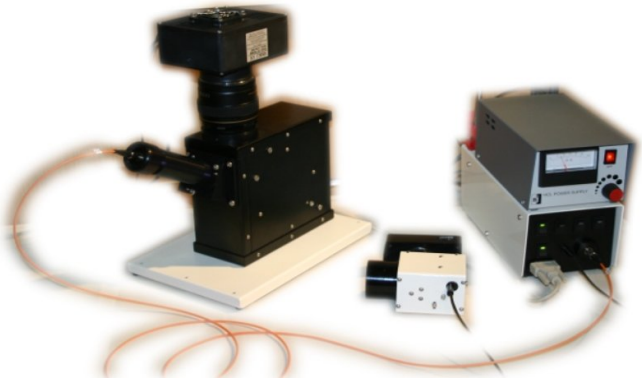

Figure 2: Off-the-shelf fiber-fed Echelle spectrograph with prism cross-disperser from Shelyak.

spectra can be performed. For instance, using a standard 10 inch telescope, a signal-to-noise ratio (S/N) of about 100 can be achieved within 30 minutes for a star of about 8 magnitudes in V and for a two pixel resolution of about 1 Å. Objects of the order of $V = 10$ and fainter are generally excluded due to limited amateur telescope apertures, although with longer exposure times and/or lower S/N this limit can be extended to even fainter stars. Hence, amateur spectroscopists can fill specific gaps for detailed investigations. These are **A) spectroscopic long-term campaigns** monitoring line profiles for periods of the order of months or even years, **B) surveys** to support detailed observations by large or space-based telescopes and **C) monitoring** of specific spectroscopic parameters over many years.

3.1 The long-term ϵ Aurigae campaign

A prominent example of a long-term amateur campaign is the eclipsing binary ϵ Aurigae (F0Ia + companion) with an orbital period of about 27 years[2]. Hα time series, obtained by Christian Buil from his balcony in Marseille using a Shelyak Echelle spectrograph (fig. 2) is shown in fig. 3.

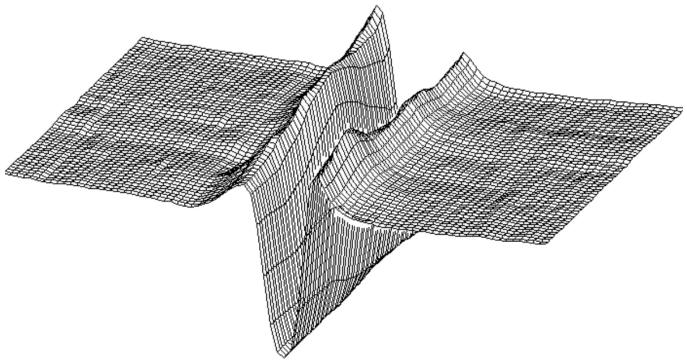

Figure 3: Hα time series for the eclipsing binary ϵ Aur between July 21, 2009 and March 10, 2010 with 3-days increment. Celestron C11, Shelyak Echelle spectrograph, average spectral resolving power R = 11000.

[2]http://www.threehillsobservatory.co.uk/epsaur_spectra.htm

3.2 The long-term MONS campaign

The archetype of colliding-wind binary systems is the 7.9-year period and highly eccentric WR+O binary system WR140 (HD193793, $V = 6.9$). Twenty-six amateurs and professionals from eight countries observed the prominent C III wind line and its excess during periastron passage from Tenerife and from various home observatory in Europe (fig. 4) to estimate the ephemerides of the system. All stations used the LHIRES III spectrograph. As part of this global campaign, Robin Leadbeater obtained spectra during periastron passage from his home observatory (fig. 4). Figure 5 shows his two spectra of C III/C IV before and during periastron passage obtained with his instrumentation. The inset shows the resulting excess emission due to the wind-wind interaction shock cone.

Figure 4: The private Three Hills Observatory of Robin Leadbeater in Cumbria / England consisting of a Vixen 20cm Cassegrain and an off-the-shelf LHIRES III Littrow slit spectrograph

.

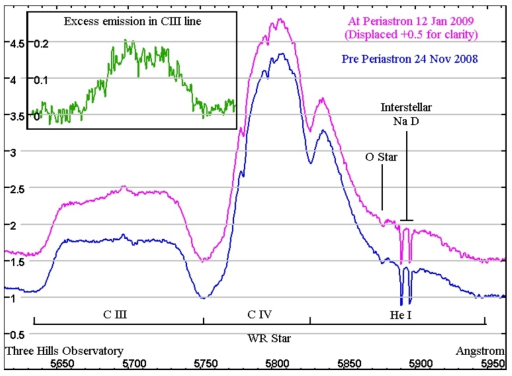

Figure 5: Spectral variability of WR 140 within seven weeks (Robin Leadbeater).

3.3 Surveys

A "classical" example for an astronomical survey, supported by amateur observers, has been the astrometrical High Precision Parallax Collecting Satellite (Hipparcos), launched in 1989. Amateur astrometry has been performed for centuries and dedicated amateurs had already the respective experience to obtain high precision data. As a result, many observers contributed their measurements to perform a successful satellite project. Such ProAm surveys are today possible in spectroscopy, as well. The presently most popular spectroscopic survey is the COROT Be Stars Survey[3] project for the astroseismology satellite COROT (COnvection, ROtation and planetary Transits). A respective amateur COROT survey of bright stars (e.g. Be stars), as performed under professional supervision can help understanding spectral variability like non-radial pulsations or oscillations in the respective Be star disks. An example spectrum, obtained by a French amateur group around C. Buil is shown in fig. 6.

3.4 Monitoring

The most problematic tasks for professional spectroscopy are probably extremely long-term monitoring of specific spectral parameters. Only snapshots within relatively short time-scales are usually

[3] http://www.astrosurf.org/buil/corot/data.htm

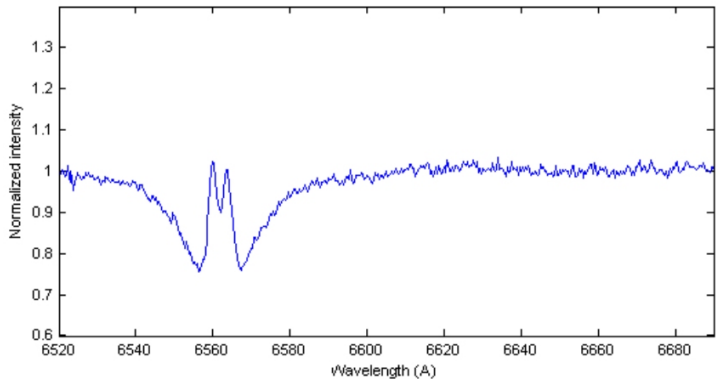

Figure 6: Hα amateur COROT survey spectrum of the $V = 6.14$ B9Ve star HD194244, obtained with a Celestron C11 and an LHIRES III spectrograph with 2700s exposure time.

possible, resulting in large time gaps. The true long-term description of the physical behaviour remains hidden. Delays in publishing results, sometimes for several years do not match the regular needs of a professional astronomer. Continuous monitoring is not a priority in professional spectroscopy. This however, is one of the cornerstones of amateur work using simple standard procedures (e.g., equivalent width and radial velocity measurements) combined with well-known equipment and good routines. An example is shown in fig. 7 for the Be star δ Scorpii.

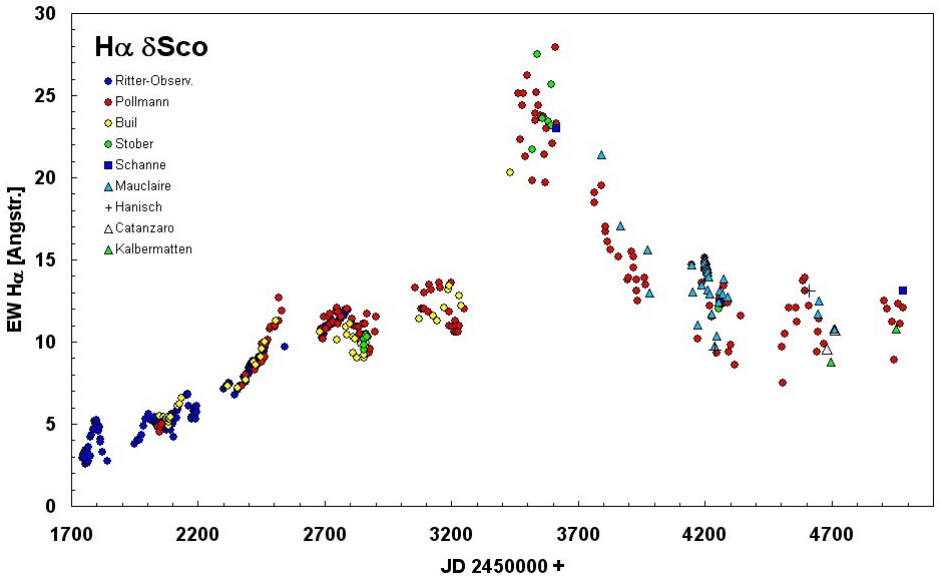

Figure 7: Hα equivalent width measurements for the Be star δ Scorpii over about nine years. Note that the first measurements taken by professionals (blue circles) have been dramatically extended by a group of amateur astronomers.

4 How to establish a ProAm campaign

If the professional community wants to take advantage of amateur measurements one should keep some basic issues in focus. Instrumental knowledge and observational hands-on skills are already present in the amateur domain. On the other hand, scientific knowledge (e.g., physics, procedures,

data interpretation) need to be contributed by those who have a complete university education in this field and already have the relevant experience. The professional community can not expect complete campaign proposals from amateur astronomers but should first take their specific spectroscopic needs to the amateurs and discuss them. For instance, the MONS campaign on WR 140 took only place because of a close contact between a professional scientist (Tony Moffat) and one of his previous students being now active in the German amateur community. The COROT Be stars survey project is mainly driven by a professional group[4] working close together with the amateurs in France[5], Germany[6] and worldwide. Potential ProAm campaigns need some basic details. After an announcement in the respective communities it is essential to give information about the physical background and basic parameters (e.g., S/N, spectral resolution, faq, etc.) to all interested observers. This is best done through a respective website. Unfortunately there are only two well established communities of significant size, namely in France and Germany. In these two communities respective discussion forums are available and it is recommended to use them for proper discussion. For the campaign management it is also recommended to separate science from administration issues. A highlight of each campaign is potential observing time at a professional observatory. Amateurs regularly do not have such access but are generally highly interested to go for it - often even at their own expense (if limited), as happened for the MONS campaign. Finally one should find some minimum financial resources (depending on the observatory site) to cover potential financial deficits (higher equipment transportation costs, unforeseen events, etc.).

5 Future plans and Summary

In May 2010 most of the key players in the WR140 MONS campaign organized a wrap-up meeting at Convento da Arrábida[7] close to Lisbon. The group, now called "ConVento", will establish an informal website covering future ProAm campaigns, respective information about specific stellar targets and a mailing list / discussion forum. Every interested spectroscopist and photometrist is invited to join the group. The link to this website will soon be found at www.stsci.de.

Considering the present situation in astronomy it seems obvious that skilled and sophisticated amateurs equipped with state-of-the art instrumentation in their domain, can successfully contribute their knowledge and enthusiasm to modern spectroscopic campaigns, either at their home observatories or at professional sites. The only obstacle to making continuous observations like those at professional sites is the local weather and the fact that amateur astronomer usually have to work in their daily job. This however can be circumnavigated by joint campaigns, as shown above. It is up to the professional community to uncover this valuable treasure.

Acknowledgements

I thank Tony Moffat, Thierry Morel and Gregor Rauw for their support.

[4] http://www.ster.kuleuven.be/ coralie/members.htm
[5] http://astrosurf.com/aras
[6] http://spektroskopie.fg-vds.de
[7] http://astrosurf.com/joseribeiro/e_arrabida.htm

Discussion

T. Rivinus: Having worked with amateurs I agree this can be a great experience, both teaching- and data-wise. As a word of caution, when working with amateurs you have to take a lot of care about calibration, both in terms of explaining the need for calibrations and their technical implementation. Keep in mind that off-the-shelf instruments often come without a calibration unit, designed for telescopes of 40 cm or less, which is the key of making them affordable for amateur astronomers.
T. Eversberg: First, when using data from other observes, I recommend not to take already reduced data. Do it by yourself, if possible. But, of course, flats, biases and darks should be taken by the observer. Second, standard spectrographs (off-the-shelf) normally come without reduction software. However, Echelle spectrographs are normally delivered including a complete MIDAS reduction loop. Third, a calibration unit (Neon or ThAr) is always included in off-the-shelf spectrographs, at least to my knowledge.

C. Martayan: The experience to work with amateurs was fantastic, for example for the follow-up/long-term monitoring of Be stars. I refer to the papers by Neiner et al. (2005), Thizy (2008)...
My second comment is about δ Sco. I do not know the civilian dates with respect to the JDs on your figure when the outburst occured. However this is a known Be-binary and the outbursts usually occur when the companion is crossing periastron.
My third comment: Currently we are closing the small professional telescopes and let us imagine that η Car explodes as a SN. It will be so bright that its luminosity will prevent the observations with the VLT or future ELTs. This kind of case will give a huge opportunity to amateurs for doing the best observations and provide scientific data of the event(s).
T. Eversberg: I agree.

Studying massive stars with the International X-ray Observatory

Gregor Rauw[1*] and Lida Oskinova[2]

[1] GAPHE, Institut d'Astrophysique & Géophysique, University of Liège,
Allée du 6 Août 17, B-4000, Liège, Belgium
[2] Astrophysik, Universität Potsdam, Am Neuen Palais 10, D-14469 Potsdam, Germany

Abstract: *Chandra* and *XMM-Newton* have deeply changed our view of the X-ray emission of massive stars. However, the majority of the massive stars being rather faint sources, the number of high-resolution X-ray spectra of massive stars remains rather limited and obtaining these spectra requires rather long exposure times. ESA, NASA and JAXA are currently designing the International X-ray Observatory (*IXO*) that will provide a quantum leap in collecting area compared to the current missions. In this contribution, we highlight the capabilities of *IXO* and its instrumentation for the study of massive stars in our Galaxy and beyond.

1 Introduction

X-ray astrophysics is currently in a "golden age" with two major observatories (*XMM-Newton* and *Chandra*) and several other missions (e.g. *Suzaku*, *Swift*,...) flying. These facilities have revolutionized our views of the X-ray universe, including our understanding of massive stars (see e.g. Güdel & Nazé 2009, Oskinova et al. 2011, and Nazé 2011). At the same time, new questions came up, that cannot be addressed with the present generation of X-ray observatories, but require a significant increase in collecting area. The science case for a large collecting area X-ray observatory led to two independent projects. In the USA, the NASA project *Con-X* came up second behind *JWST* in the 2000 Decadal Survey, whilst in Europe, *XEUS* was selected as a candidate mission for the first L-mission launch slot of ESA's Cosmic Vision programme, with contributions from JAXA. In 2008, both concepts were merged into the *International X-ray Observatory* (*IXO*).

In this paper, we first provide a general description of *IXO*, before we describe a few possible studies of massive stars that could be carried out with *IXO*. We conclude by summarizing the current status of the project.

2 The International X-ray Observatory

The key features of the *IXO* project are (Lumb & Bookbinder 2010, see also Fig. 1):

*Honorary Research Associate FRS-FNRS, Belgium

- an effective collecting area of 3 m^2 at 1.25 keV (to be compared to 400 cm^2 and 1400 cm^2 at 1 keV for *Chandra*/ACIS-I and *XMM-Newton*/EPIC-pn respectively),
- an angular resolution (half-energy width) better than 5 arcsec (to be compared to 0.5 arcsec and 15 arcsec for *Chandra* and *XMM-Newton* respectively),
- an unprecedented spectral resolution of 3000 over the 0.3 – 1.0 keV energy domain,
- a focal length of 20 m to be achieved through an extensible optical bench[1],
- a halo orbit around the second Lagrangian point of the Sun - Earth system with a nominal mission lifetime of 5 years and consumables for 10 years.

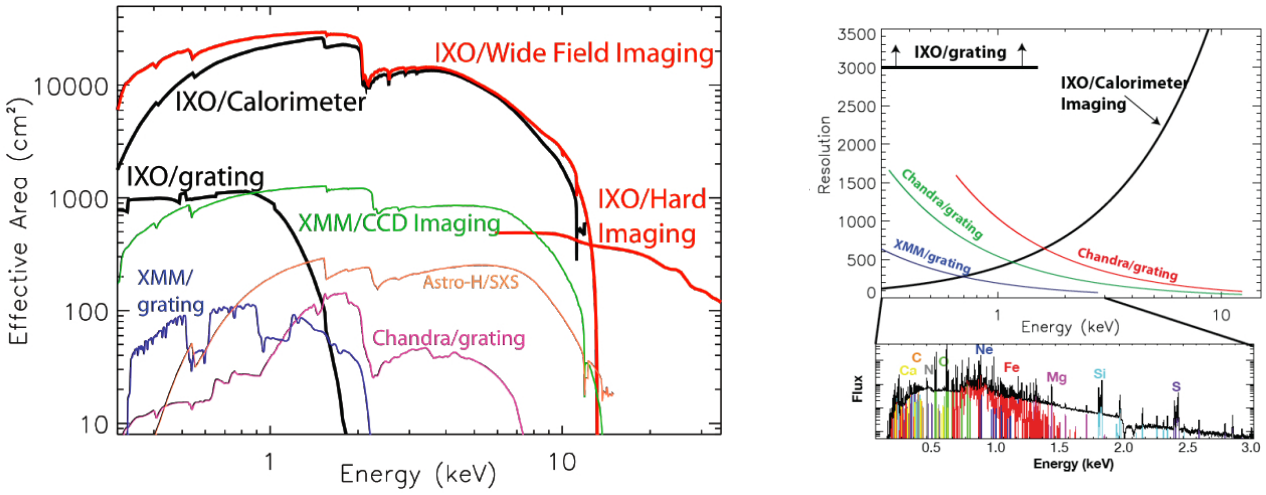

Figure 1: Left: effective collecting area of the *IXO* instruments in comparison to *XMM-Newton* and *Chandra*. Right: same for the spectral resolution. The bottom panel illustrates the emission lines of the various elements in the 0.1 - 3.0 keV energy range. Both figures are taken from the *IXO* website http://constellation.gsfc.nasa.gov/science/performanceRequirements.html

The key ingredients to achieve these performances are the grazing incidence mirrors. They must have a large effective area and a good angular resolution with a mass that should not exceed 2000 kg. This is an extremely challenging requirement. Currently, two technologies are being considered: slumped glass and silicon pore optics. Both technologies represent a quantum leap compared to previous missions, since their mass per unit collecting area is reduced by a factor 10 with respect to the mirrors onboard *XMM-Newton* (Nandra 2010).

The current design of the *IXO* focal plane features several instruments (Martin 2010):

- XGS, the X-ray Grating Spectrometer (0.3 – 1.0 keV, $R \geq 3000$) which is located on a fixed platform and is operated all the time.
- XMS, a cryogenic X-ray Micro-calorimeter imaging Spectrograph (0.2 – 10 keV, with an energy resolution of 2.5 eV over its inner field of view of 2×2 arcmin and 10 eV over the outer field of view of 5×5 arcmin).

[1]Whilst the *XEUS* mission concept was based on two spacecraft operated in formation flight, the *IXO* mission concept features a single spacecraft.

- WFI, a Wide Field Imager (0.1 – 15 keV, with an energy resolution of < 150 eV over a field of view of 18 arcmin), operated in conjunction with HXI, a Hard X-ray Imager (10 – 40 keV, with an energy resolution of < 1 keV).
- HTRS, the High Time Resolution Spectrograph (0.3 – 15 keV, with an energy resolution $<$ 200 eV) which has a time resolution of 10 μs for very bright sources, up to 12 Crab.
- X-POL, an X-ray POLarimeter (2 – 10 keV) able to detect polarization down to the 1% level.

Whilst XGS will be located on a fixed platform and will be operated all the time, the other instruments (XMS, WFI/HXI, HTRS and X-POL) will be on a moveable instrument platform and will observe one at a time.

3 What can we learn about massive stars using *IXO*?

In this section, we highlight a few possible applications of the XGS and XMS instruments to studies of massive stars. We stress that this list is by no means exhaustive.

3.1 Single O and Wolf-Rayet stars

To date, only about a dozen presumably single O-type stars have medium-quality *XMM-Newton* or *Chandra* grating spectra. These are actually the X-ray brightest objects of their class, but they already require minimum exposure times of 100 – 200 ksec. By far, the best quality high-resolution X-ray spectrum of a single O-type is the one of ζ Pup (O4 Ief) which has been observed, as a calibration source, for a total of 700 ksec with the RGS onboard *XMM-Newton* (Nazé et al., in preparation). The mean spectrum has a unique quality and provides the possibility to perform detailed line profile analyses. With *IXO*, we should be able to collect good-quality X-ray spectra for about 100 O-type stars with exposure times of a few 10 ksec. These high-resolution spectra will provide important clues about the properties of clumps in stellar winds, they will allow us to constrain the abundances of the X-ray emitting plasma[2] and to probe the impact of magnetic confinement, etc.

Observations with *IXO* will also open up an entirely new field. Indeed, the individual observations that make up the ζ Pup RGS dataset suggest some low-level line profile variability. However, the present data do not have sufficient statistics to address this issue. With *IXO*, we will be able, for the first time, to study the actual link between wind structures and X-rays through a monitoring of the line profile variability on the relevant time scales.

Since massive stars are usually found in open clusters, often in association with X-ray bright pre-main sequence stars, spatial resolution is important in these studies. The imaging spectrograph XMS will provide an instrument of choice for the investigation of massive stars (see Fig. 2).

Single Wolf-Rayet stars, unlike O-type stars do not exhibit a tight relation between their X-ray and bolometric luminosity. Actually, we currently ignore whether all types of WR stars emit X-rays and if so, by what mechanism. In this context, an interesting result was the detection with *XMM-Newton* of a very faint, but very hard X-ray emission from the WO star WR 142 (Oskinova et al. 2009). With XMS we will be able to collect high-resolution spectra of WR 142 allowing to distinguish between an intrinsically hard emission and a strongly absorbed one.

[2]Lower resolution CCD X-ray spectra frequently suggest sub-solar metal abundances, although the photospheric abundances are essentially consistent with solar metallicity. It remains to be established whether this effect is real, or due to an insufficient spectral resolution in the CCD spectra.

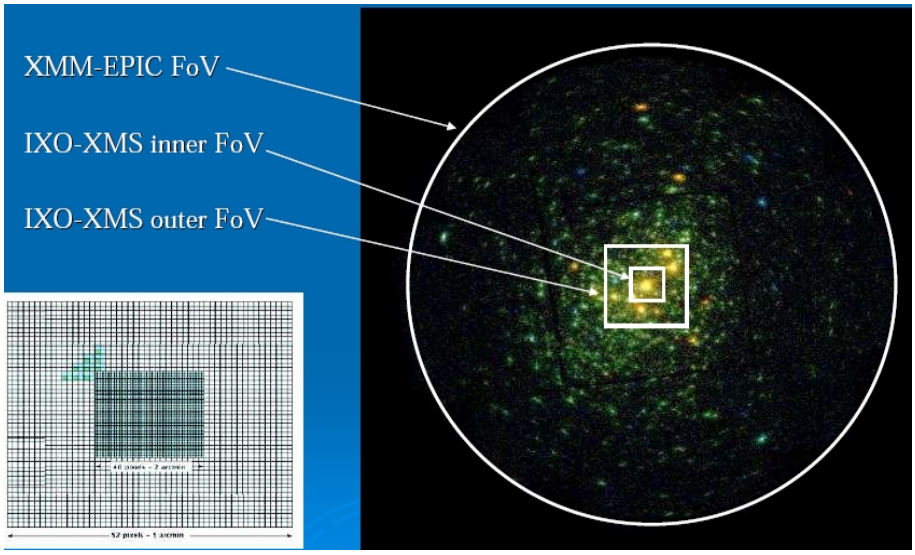

Figure 2: Illustration of the XMS field of view overlaid on an EPIC image of the very young open cluster NGC 6231 (from Sana et al. 2006).

3.2 Massive binary systems

The interactions of stellar winds in massive binary systems can produce a strong X-ray emission due to the heating of the winds in the interaction zone (see e.g. the review in Pittard 2011). Some colliding wind binary systems indeed feature a rather hard X-ray spectrum with a prominent Fe K line which is mainly formed in the wind interaction zone. This line should display profile variations with orbital phase (Henley, Stevens & Pittard 2003). Provided one obtains high-resolution, phase-resolved spectroscopy of this line, one can build a Doppler map of the line emission region. For this purpose, one can use the Doppler tomography technique (Horne 1991, Kaitchuk et al. 1994). The latter uses a reference frame centered on the centre of mass of the binary with the x-axis pointing from the primary to the secondary and the positive y-axis pointing along the direction of the secondary's orbital motion (see Fig. 3). The phase dependence of the radial velocity $v(\phi)$ of any gas flow that is stationary in the rotating frame of reference of the binary can be described by a so-called 'S-wave' relation:

$$v(\phi) = -v_x \cos(2\,\pi\,\phi) + v_y \sin(2\,\pi\,\phi) \tag{1}$$

Here ϕ stands for the orbital phase, whilst (v_x, v_y) are the velocity coordinates of the gas flow. v_x

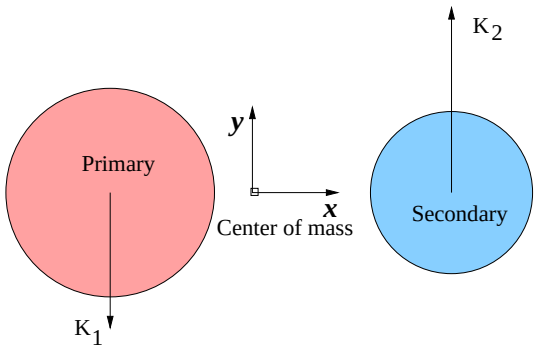

Figure 3: Orientation of the axes used in the Doppler tomography.

and v_y simply reflect the projected velocity components along the x and y axes: $v_x = V_x \sin i$ and

$v_y = V_y \sin i$, where V_x and V_y are the actual velocities in the orbital plane of the binary and i is the orbital inclination. Each pixel in a Doppler map, specified by its velocity coordinates is associated with a particular S-wave (see e.g. Horne 1991 for a detailed discussion of the method).

This technique is already commonly used to study phase-locked profile variations of emission lines (Hα, He II λ4686,...) in the optical spectra of early-type binaries (e.g. Thaller et al. 2001, Rauw et al. 2005). Applying it to the Fe K line in the X-ray spectra will allow to trace the cooling of the material in the wind interaction zones and will thus provide unprecedented insight into the physics of wind-wind interactions.

4 The way forward

Although stars, and massive stars in particular, are not the main science drivers of *IXO*, this high-throughput X-ray observatory will be a tremendously powerful tool to study the physics of massive stars, as we have shown by selecting only a few examples of possible applications.

Pre-phase A studies are under way at ESA and NASA. They indicate that the mission design is feasible, well on track for a launch in 2021 and should be within the budget (Nandra 2010). Recently (August 2010), the Astro2010 Decadal Survey acknowledged that many high-priority science questions require a high-throughput X-ray observatory. Although the ranking of the mission was somewhat ambiguous, its status mainly depends on the outcome of the ESA Cosmic Vision down-selection process that will take place this autumn and during the first half of 2011. Our community needs to support *IXO* to make sure it will indeed be launched in 2021!

Acknowledgements

GR thanks his colleagues from the GAPHE for many fruitful discussions. GR acknowledges support from the Fonds de Recherche Scientifique (FRS/FNRS), through the XMM INTEGRAL PRODEX contract (Belspo) as well as by the Communauté Française de Belgique - Action de recherche concertée - Académie Wallonie - Europe.

References

Güdel, M., & Nazé, Y. 2009, A&ARv 17, 309

Henley, D.B., Stevens, I.R., & Pittard, J.M. 2003, MNRAS 346, 773

Horne, K., 1991, in *Fundamental Properties of Cataclysmic Variable Stars: 12th North American Workshop on Cataclysmic Variables and Low Mass X-ray Binaries*, SDSU Press, ed. A.W. Shafter, 23

Kaitchuck, R.H., Schlegel, E.M., Honeycutt, R.K., Horne, K., Marsh, T.R., White, J.C., & Mansperger, C.S. 1994, ApJS 93, 519

Lumb, D., & Bookbinder, J. 2010, http://ixo.gsfc.nasa.gov/resources/Paris2010/01_Lumb.pdf

Martin, D. 2010, http://ixo.gsfc.nasa.gov/resources/Paris2010/10_Martin.pdf

Nandra, K. 2010, http://ixo.gsfc.nasa.gov/resources/Paris2010/36_Nandra.pdf

Nazé, Y. 2011, in Proceedings of the 39th Liège Astrophysical Colloquium, eds. G. Rauw, M. De Becker, Y. Nazé, J.-M. Vreux & P.M. Williams, BSRSL 80, 109

Oskinova, L.M., Hamann, W.-R., Feldmeier, A., Ignace, R., & Chu, Y.-H. 2009, ApJ 693, L44

Oskinova, L.M., Hamann, W.-R., Ignace, R., & Feldmeier, A. 2011, in Proceedings of the 39th Liège Astrophysical Colloquium, eds. G. Rauw, M. De Becker, Y. Nazé, J.-M. Vreux & P. Williams, BSRSL, 80, 54

Pittard, J.M. 2011, in Proceedings of the 39th Liège Astrophysical Colloquium, eds. G. Rauw, M. De Becker, Y. Nazé, J.-M. Vreux & P. Williams, BSRSL, 80, 555

Rauw, G., Crowther, P.A., De Becker, M., et al. 2005, A&A 432, 985

Sana, H., Gosset, E., Rauw, G., Sung, H., & Vreux, J.-M. 2006, A&A 454, 1047

Thaller, M.L., Gies, D.R., Fullerton, A.W., & Kaper, L. 2001, ApJ 554, 1070

Discussion

M. Corcoran: Can you say something about the use of the polarimeter for massive star research, at least for the brightest systems?
G. Rauw: XPOL should be able to detect polarization down to 1% for 1 mCrab sources in 100 ksec. The possibilities to use it for massive star research will critically depend upon the degree of polarization on the one hand and the brightness of the source on the other.

A. Willis: Can you comment on the drivers in the choice of the angular resolution of *IXO* of around 5 arcsec - 10 times poorer than *Chandra*, with science implications. Is this driven by the cost of mirror fabrication?
G. Rauw: The angular resolution of 5 arcsec is determined by the constraints on the mass of the mirrors and the effective area requirement. To reach the $3m^2$ of effective area, it is mandatory to assemble a large number of smaller elements into the final mirror assembly. Although the metrology of these stacking processes has been greatly improved, they lead eventually to an angular resolution which is poorer than the one of *Chandra*, but still a factor 3 better than the one of *XMM*. The science implications are of course that source confusion in crowded regions such as young open clusters featuring a large number of X-ray emitting PMS stars will be more of an issue than for *Chandra*.

W.R. Hamann: My question is rather a political one. In Potsdam we have a neighbouring Institute for gravitational Physics. Talking with the colleagues there, they seem to be 100% confident that the *LISA* experiment will fly. But as I understand, *LISA* and *IXO* are directly competing within the ESA planning. How optimistic are you that *IXO* will be launched?
G. Rauw: The bottom line of my talk is that there are currently no obstacles (neither technological nor financial) that would render a launch of *IXO* in 2021 impossible within the budgetary framework of an ESA L-type mission. I do not know whether the same statement can be made about *LISA*. In the end, the choice of what mission will fly first, will depend a lot on technological and financial aspects, but it will also be affected by the size of the corresponding community and its enthusiasm for the mission. This is why I think it is important that we support *IXO*.

Spectroscopic binaries as observed by the future Gaia space mission

Yassine Damerdji, Ludovic Delchambre, Thierry Morel, Eric Gosset, Gregor Rauw

Institut d'Astrophysique et de Géophysique, Université de Liège, Belgium

Abstract: The future Gaia satellite will observe a large number of stars through its three main channels: astrometric, photometric and, for the brightest stars, spectroscopic. The satellite is equipped with the RVS spectrograph, which will provide medium-resolution spectra over a small wavelength range. These spectra should allow us to identify stars exhibiting a composite spectrum, either because of a chance alignment or a true binarity. We discuss the various aspects related to the data treatment of the binary candidates and describe the algorithms that are intended to be included in the processing pipeline.

1 Introduction

The aim of the ESA Gaia mission is to chart the Milky Way in its three dimensions. The Gaia astrometric data will provide star positions, proper motions and parallaxes with unprecedented accuracy. The Radial Velocity Spectrograph (hereafter RVS) will provide the third dimension by measuring radial velocities (RVs) using medium-resolution spectra. The characterization of the stellar populations (metallicity, age, masses) will also be made possible thanks to the on-board photometric capabilities. A census of about 1% of the galactic stellar population will be achieved by observing about one billion stars down to V = 20 mag during the 4 years of the mission (e.g., Mignard & Drimmel 2007).

The data processing will be defined and performed under the responsibility of the Data Processing and Analysis Consortium (DPAC), which is split into 9 Coordination Units (hereafter CUs). Each CU is in turn divided into several Development Units (hereafter DUs). We are in charge of DU434, which will derive SB1 and SB2 Keplerian solutions for the candidate spectroscopic variables in the framework of the Non Single Stars branch of CU4 ('Object Processing'). These candidates are either identified by CU6/CU7 (variability detection using RVs obtained within CU6) or by CU8 (stellar classification identifying binary stars using photometric data).

After a description of the specifications of the Gaia RVS experiment, we discuss the algorithms developed for the determination of the orbital parameters and their performance (both deterministic and non deterministic methods have been tested). Finally, we present the current results and discuss our efforts to improve them.

2 RVS specifications

The RVS radial velocities are derived by DPAC/CU6/DU650 (Single Transit Analysis) using single and double star cross-correlation and chi-square minimization techniques (e.g., Tonry & Davis 1979;

Table 1: Typical RVS radial velocity error bars (1σ) for single stars (in km s^{-1}), as a function of the magnitude and spectral type (Viala et al. 2010).

Spectral type	$V = 6$	$V = 9$	$V = 12$	$V = 14$
G5 V	0.4	2	5	15
B5 V	3	10	30	-

Zucker & Mazeh 1994). Each observed spectrum in the RVS spectral range (846–874 nm; chosen to cover the calcium triplet) is cross-correlated with one or two combined synthetic spectra convolved with the instrumental Line Spread Function.

Figure 1 shows that the stars will transit in the RVS field of view on average about 50 times during the mission with values ranging from a minimum of 15 to a maximum of 161 observations.

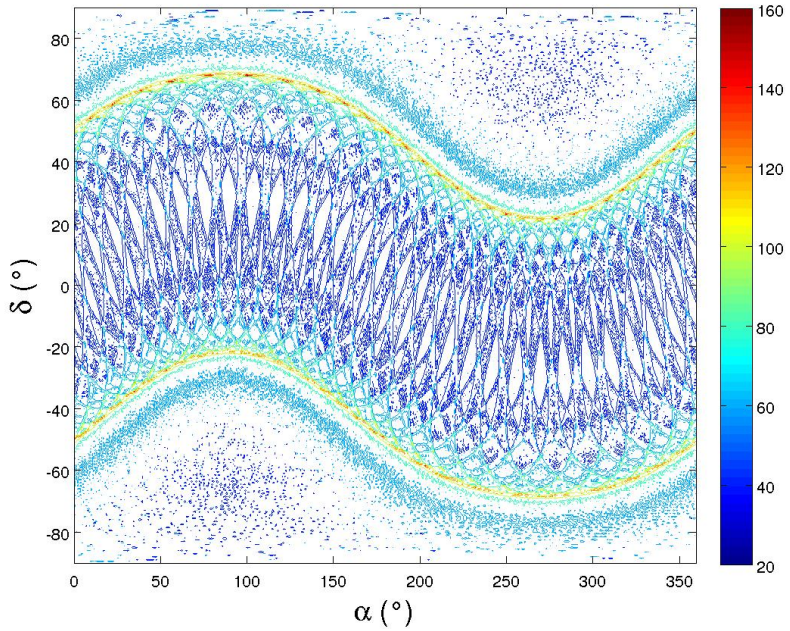

Figure 1: Number of RVS transits in celestial coordinates. The median and mean values are 50 and 51.8, respectively.

Because of the lack for OB stars of metallic lines in the RVS spectral range compared to cooler stars (FGK types), the RV measurements will be much less accurate in this case (besides being more elegant, cross-correlation based algorithms are much more accurate than classical line fit functions because they take all the spectral lines into account). This is illustrated in Table 1, which shows the expected accuracies for a solar-like (G5 V) and a B5 V star.

3 Algorithms

The time series of RVs will be received from DPAC/CU6. They have to be cleaned from inconsistent measurements before starting their processing. The second step consists in searching for a periodicity in the remaining time series. Once this is achieved, an approached orbital solution can be obtained, which is then refined through a global minimization scheme. The final step is to test whether the

obtained eccentric orbit is significant against a circular one. The SB1/SB2 data processing pipeline is mainly composed of 7 sub-pipelines:

- Data cleaning: all bad/unphysical measurements are removed. A check is made to ensure that the remaining data are suitable for further processing.
- Period search: a period is searched using both the time series of RVs and the photometric periodicities provided by CU7. Many algorithms have been tested. We use the fit of a simple sine function in the time or phase space (Heck, Manfroid & Mersch 1985) to preselect the 100 most probable periods. Vr_1 and $|\mathrm{Vr}_2 - \mathrm{Vr}_1|$ are presently used for the SB1 and SB2 cases, respectively.
- Sorting of SB2 data: it is expected that the input velocity data will not necessarily be sorted (i.e., a given velocity will not be assigned either to the primary or to the secondary) because of a confusion in the identification of the spectral types during the computation of the RVs. The procedure used to assign the radial velocities to each binary component is illustrated in Fig.2.
- Determination of the best period and derivation of the approached orbital solution. Many algorithms have been tested (e.g., Russell 1902; Lehmann-Filhès 1894; Monet 1979). We finally decided to use the method proposed by Zechmeister & Kürster (2009) consisting in a fit of a simple sine function in the true anomaly domain.
- Derivation of the final orbital solution using a Levenberg-Marquardt minimization. We use Sterne (1941) and Schlesinger (1910) minimization schemes for low ($e < 0.03$) and high eccentricity solutions, respectively.
- Test the final eccentric solution against the circular one using the test proposed by Lucy & Sweeney (1971).
- The steps (2) and (4) above may be replaced by a genetic algorithm (Haupt & Haupt 2008) combined with Zechmeister & Kürster's Keplerian periodogram. The optimization of the genetic algorithm parameters has to be performed beforehand.

4 Results

The algorithms described above have been tested on purely synthetic time series of RVs. Given the satellite scanning law and the design of the RVS focal plane, 8 sets of $120,000$ RV curves have been simulated, each corresponding to a given number of measurements and noise level. The grid of parameters is as follows:

- $\alpha = 0°$, $\delta = -90°$ (this defines one typical but representative sampling law).
- The number of measurements is 20 or 40.
- The Gaussian noise levels considered are: 0, 15, 30 and 45 km s^{-1}.
- Each set contains a logarithmic grid of 50 periods between 0.2 and 2000 days.
- Each set contains a linear grid of 20 eccentricities between 0 and 0.95.
- Each set contains a linear grid of 12 longitudes of periastron between $0°$ and $180°$ (for the other half of the circle, the RV curves are symmetrical and hence do not need to be simulated).

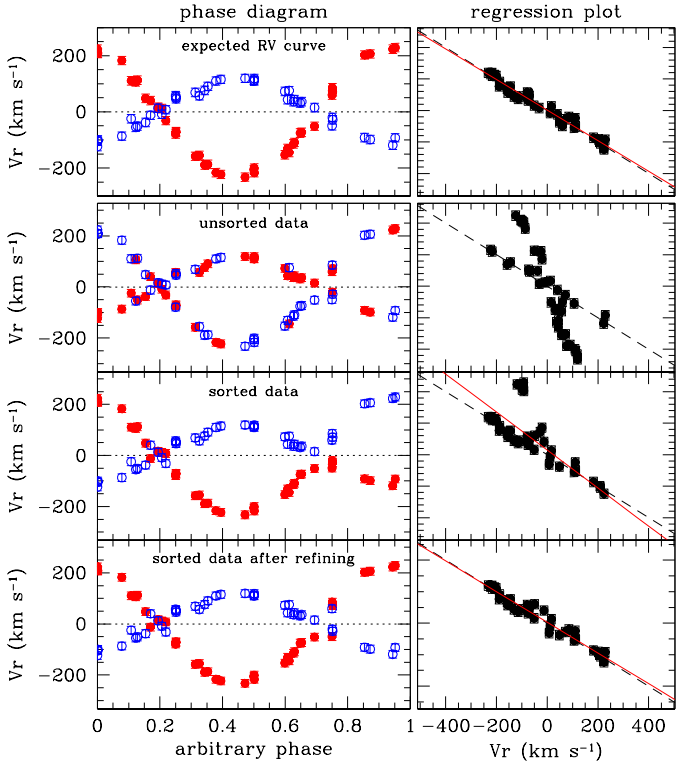

Figure 2: Illustration of the iterative method used to sort the SB2 velocities. The first panel illustrates the true RV curve while the second panel gives the observed wrongly attributed RVs. The open blue and red filled points correspond to the primary and secondary, respectively. The sorting is performed in two steps. The velocities folded in a phase diagram are first assigned to each component based on the identification of the nodes (velocities of the two components both roughly equal to the center-of-mass velocity of the system) in the RV curve (third panels from top). Second, the outliers that are likely not properly assigned after the first step are iteratively identified using a sigma-clipping algorithm in the (Vr_1, Vr_2) plane and their identification permuted (bottom panels).

- Ten noise realisations are made for each combination of period, eccentricity and longitude of periastron.
- The semi amplitude and systemic velocity of all simulated curves are 100 and 0 km s^{-1} respectively.
- For the genetic algorithm, the settings are as follows: selection type = ROULETTE, mutation rate $= 0.15$, population size $= 1000$, number of iterations $= 1000$ and elite number $= 20$.

Figure 3 shows the period search performances in the SB1 case for the deterministic (8 leftmost panels) and genetic algorithms (8 rightmost panels). As expected, the period is more frequently recovered when the number of measurements increases and/or the noise level decreases. The performance of the two algorithms is poor for very noisy data, although the genetic algorithm performs slightly better in this case. Satisfactory results are obtained for both algorithms for RV curves with 40 measurements. Figure 4 shows the performances for the refined eccentricities (without Lucy's correction) for the deterministic (8 leftmost panels) and genetic algorithms (8 rightmost panels). The deterministic algorithm is 15 times faster than the genetic algorithm but seems to be more sensitive to noise. This may be due to the limitations imposed by the user to the genetic algorithm to limit the execution time.

We are planning to test pattern recognition algorithms to determine the approached orbital solution using the folded RV curves. This study will be described in a future paper.

Acknowledgements

This research is supported in part by ESA PRODEX funds, in particular via a Gaia-DPAC contract.

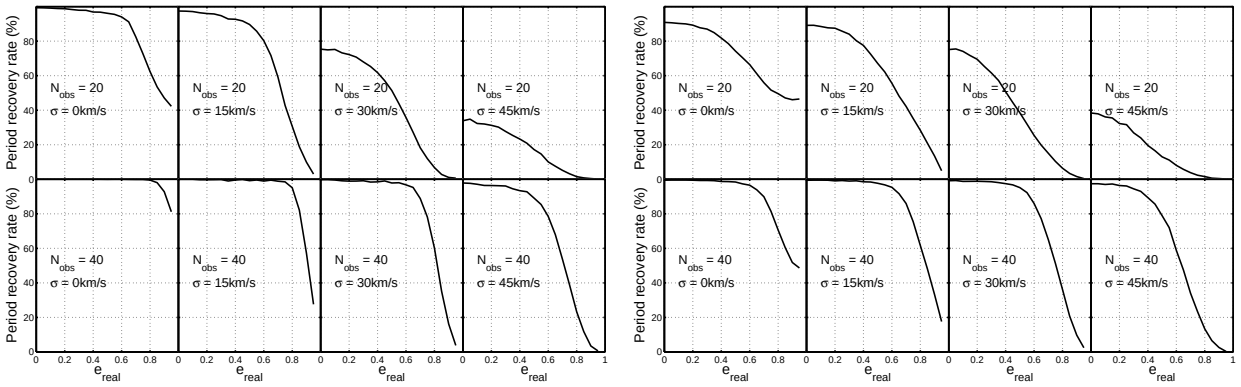

Figure 3: Period search performances for the deterministic (8 leftmost panels) and genetic algorithms (8 rightmost panels) as a function of orbital eccentricity. See text for the description of the input data. The genetic algorithm seems to be less sensitive to noise than the deterministic one.

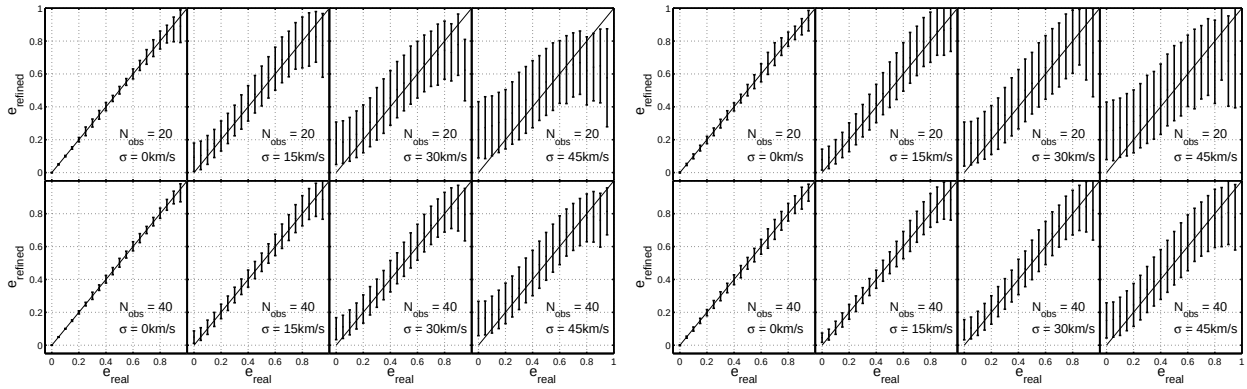

Figure 4: The distribution of the refined orbital eccentricities (without Lucy's correction) for the deterministic (8 leftmost panels) and genetic algorithms (8 rightmost panels) as a function of orbital eccentricity. See text for the description of the input data. Also in this case, the genetic algorithm seems to be less sensitive to noise than the deterministic one. The line on each panel shows the one-to-one aimed at relationship .

.

References

Heck, A., Manfroid, J. & Mersch, G. 1985, A&AS, 59, 63.

Lehmann-Filhès, R. 1894, AN, 136, 17.

Lucy, L.B. & Sweeney, M. A.,1971, AJ, 76, 544.

Mignard, F. & Drimmel, R. (eds), 2007, DPAC Proposal for the Gaia Data Processing, Gaia DPAC Technical note, GAIA-CD-SP-DPAC-FM-030

Monet, D.G. 1979, ApJ, 234, 275.

Haupt, R.L. & Haupt, S.E 1998, in *Practical genetic algorithms*, 2nd ed., ISBN 0-471-45565-2., 27, 150

Russell, H.N. 1902, ApJ, 15, 252.

Schlesinger, F. 1910, Pub. Allegheny Obs. (Pittsburgh), 1, 33.

Sterne, T.E. 1941, Proc. Nat. Acad. Sc. USA, 27, 175.

Tonry, J. & Davis, M. 1979, AJ, 84, 1511.

Viala, Y., Blomme, R., Frémat, Y., et al. 2010, WP650 Software Test Plan and Verification Report - Single Transit Analysis (Cycle 6), GAIA-C6-SP-OPM-YV-007-1.

Zechmeister, M. & Kürster, M. 2009, A&A, 496, 577.

Zucker, S. & Mazeh, T. 1994, ApJ, 420, 806.

Prospects for the multiplicity investigation of massive stars with the CARLINA interferometer

Michaël De Becker[1,2] , Hervé Le Coroller[2] and Julien Dejonghe[2]

[1] Department of Astrophysics, Geophysics and Oceanography, University of Liège, Belgium
[2] Observatoire de Haute-Provence, 04870 Saint-Michel l'Observatoire, France

Abstract: The multiwavelength study of massive stars has revealed many phenomena that are intimately related to their multiplicity. Colliding winds in massive binaries play indeed a significant role in thermal X-ray emission, particle acceleration, or even dust formation in such systems. In this context, the identification of binaries and the determination of their orbital parameters is a pivotal issue. We first briefly describe the CARLINA project. The sensitivity and imaging capability of Carlina are perfectly adapted for the study of binary systems. Considering its expected specifications, Carlina will operate in complementarity with ELTs and kilometer baseline interferometers. Then, we discuss some prospects for the multiplicity investigation of massive stars, on the basis of the expected performances of the prototype currently studied at the Observatoire de Haute-Provence (OHP).

1 The Carlina concept

The Carlina design consists in a diluted aperture of spherical shape, with focal optics mounted in a balloon suspended under a gondola, or suspended under cables between two sides of a valley. One of the main advantages of such a design, with respect to other interferomtric systems, is the absence of delay lines. The apertures are anchored on the ground and positioned to constitute parts of a large spherical surface (curvature radius R=71,2 m for the OHP prototype). The light is reflected up to the focal gondola (at R/2) that contains the sphericity correctors, densified-pupil (Labeyrie 1996) and photon counting camera (Le Coroller et al. 2004). The stability of the position of the gondola is warranted by a tripod of cables whose lenght is accurately controlled by computer-controlled winches and a laser-monitored system (Le Coroller et al. 2011). A schematic view of the prototype installed at OHP is shown in Fig. 1.

1.1 Carlina prototype at OHP

At OHP, a set of three mirrors with a diameter of 25 cm is located on the ground. The 3 baselines have lengths of respectively 5, 9, and 10.5 m. Four waveband filters (width ~ 100 nm) will be available, with central wavelengths respectively of 531, 562, 624 and 692 nm (noted A, B, C, and D, respectively). It is important to emphasize that this prototype operates in the visible domain. The optics mounted in the gondola contains several elements whose individual transmissions are taken into

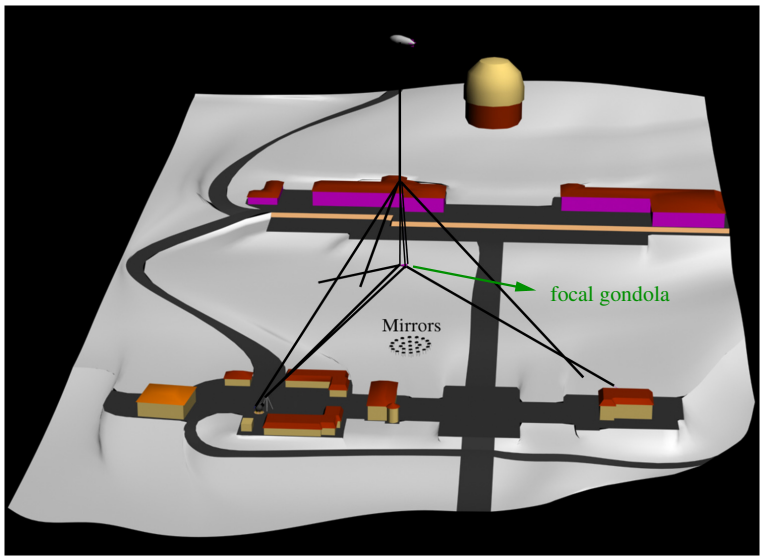

Figure 1: Schematic view of the OHP prototype. The relative position of the balloon and of the main buildings of the observatory are illustrated, along with the position of the mirrors on the ground and the tripod of cables controlling the position of the gondola.

account in order to calculate the efficiency of the design, and convert it into an effective sensitivity as briefly illustrated in Fig. 2. The present design is still in development. First results for technical demonstration are expected in the forthcoming months, and should be followed by a first science observation in 2011 - 2012. In the future, additional mirrors may be installed in order to characterize further the multi-aperture recombination and increase the aperture to 17 m.

1.2 Design for a 100-200 m class Carlina interferometer

Potential sites for future large Carlina interferometers have already been identified. The selection relies mainly on topographic considerations: typically, a valley oriented in the East-West direction is required, with a nearly hemi-cylindrical shape at the bottom. Such a site could be covered by a large number (100 - 1000) of small apertures. Some sites allow the focal optics to be suspended by cables, and not anymore by a balloon. The orientation of the focal optics follows the motion of the target in the East-West direction. In such a site, most of the sky would be accessible, even though the current OHP prototype is limited to a narrow sky band (see Sect. 2).

The replication of a large number of small apertures is much less expensive than the construction a large pieces of mirror. A diluted aperture design such as a Carlina interferometer constitutes an alternative architecture for hypertelescopes able to perform high angular resolution observations in the visible domain (at the sub-mas scale), without the caveat of delay-line designs used in present long baseline interferometric facilities. Carlina should be much more sensitive than conventional interferometers and will be able to obtain complex images of fainter objects ($m_V > 12$).

2 Prospects for the multiplicity study of massive stars

A very important point to consider in the context of massive binaries is the fact that the stellar winds of the components of the system are likely to collide. This phenomenon is a key point in the physics of massive stars. This wind-wind interaction is indeed responsible for several physical processes at the front of modern stellar astrophysics research (De Becker 2010), such as copious high energy emission, particle acceleration, or even dust formation. In addition, high angular resolution techniques turn out to be very valuable in order to investigate the multiplicity of massives stars. Spectroscopic techniques are indeed generally limited to shorter or medium period systems, and are strongly biased to significantly inclined systems (Sana & Le Bouquin 2010). As a complementary technique, inter-

ferometry is worth considering by the massive star community to detect new multiple systems and determine their orbital parameters.

2.1 Science with the OHP prototype

The main goal of the OHP prototype is to test the optical train of an hypertelescope and to show that Carlina will be more sensitive than conventional interferometers. It is a purely technical demonstrator but it is not impossible that we will be able to make some science. To fulfill the requirement for the prototype, potential targets have to meet 4 criteria:

- angular separation: as the resolving capability is directly related to λ/D (where λ is the wavelength considered, and D is the baseline), the prototype is characterized by a well-established angular resolution. Typically, for the longest baseline, i.e. 10.5 m, we may expect an angular resolution of the order of 10 mas. This translates into an orbital separation of 10 AU for a target located at 1 kpc. Only long period systems are thus accessible, considering the typical distance to massive stars (typically a few kpc). This corresponds to a part of the orbital parameter space that is so far not sufficiently investigated by spectroscopic studies.

- brightness ratio: a secondary star in a binary system should not be too faint, with respect to the primary, in order to be detected. Typically in speckle interferometry the contrast should not be larger than 100-1000. Carlina should be able to measure small contrasts but this quantity will be determined with the OHP prototype.

- coordinates: with the present fixed apertures on the flat OHP site, the declination of the targets must lie between +40 and +50 degrees. Such a restriction would of course be lifted in a valley.

- brightness: as a first approach to estimate the sensitivity of the optical design, let us consider that a target is accessible provided that the photon counting camera detects at least one photon in a sub-exposure (typically 0.001 s). Such a criterion is not fully satisfactory, but it gives a first idea of the expected capabilites of this design to detect a target in typical conditions of use.

2.2 Estimation of the photon number

We estimated the number of photons detected by the camera on the basis of synthetic stellar spectra taken from the Kurucz library (Castelli & Kurucz 2004) for a range of spectral types (O3 to O9), using typical fundamental parameters for these stars (Martins, Schaerer & Hillier 2005). In future estimates, once the specifications of the design will be more accurately characterized, more adequate synthetic spectra will be used, at least when massive stars are concerned (e.g. CMFGEN, POWR). However, at the level of accuracy of the present specifications, spectra from the Kurucz library are sufficient. The stellar spectra were corrected for ISM extinction, assuming 1 magnitude of extinction per kpc). The atmospheric extinction has also been taken into account assuming mean atmospheric conditions, i.e. averaged over many locations for moderately good weather conditions. The latter criteria translates into an extinction of 0.28 magnitude for a zenithal direction, at sea level (Green 1992). The complete procedure is summarized in Fig. 2. The aperture diameter considered is 25 cm. Fig. 3 compares the expected results, as a function of the V magnitude of the target, for two filters respectively noted A and D. Fig. 4 plots the number of photons detected for stars of spectral types O3V and O9V as a function of the distance to the target, for two filters. We see that, in typical extinction conditions, O stars might be detected with the OHP prototype provided their distance is not larger than about 4 kpc (with differences depending on the spetral type and the waveband filter used). Note that any

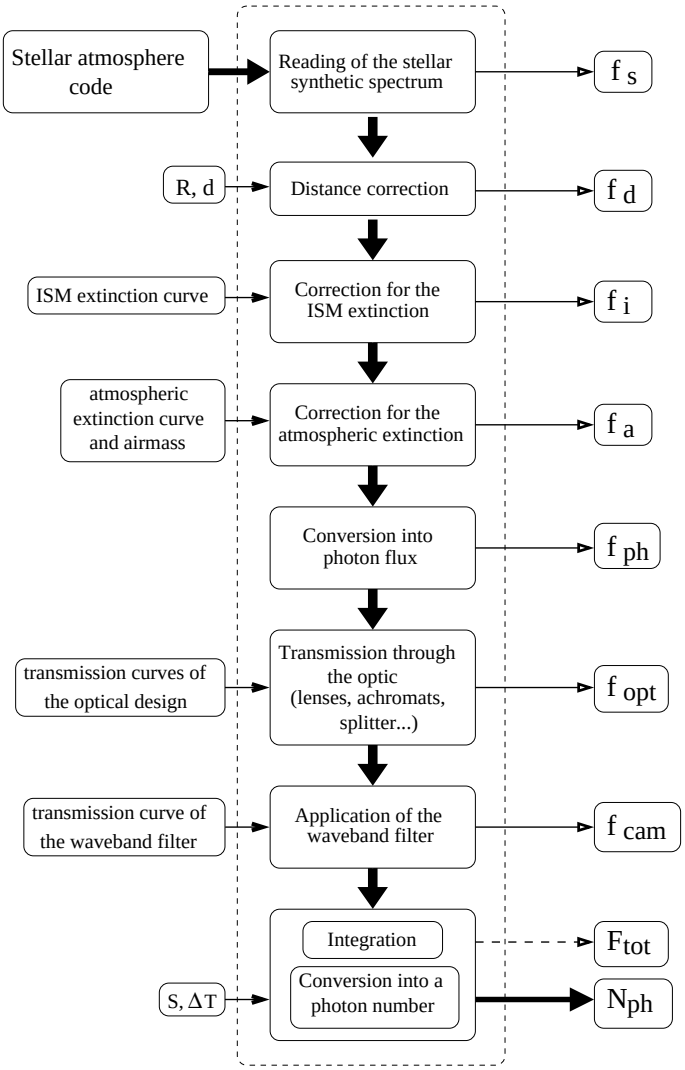

Figure 2: Schematic view of the procedure adopted to estimate the number of photons detected by the photon counting camera, starting from stellar synthetic spectra, and taking into account interstellar and atmospheric extinctions, along with all instrumental transmissions of the optics. The different quantities (noted f_s, f_d, f_i, f_a, f_{ph}, f_{opt}, f_{cam}) on the right correspond to fluxes at each step of the procedure. F_{tot} is the integrated flux (in erg s^{-1} cm^{-2}), and N_{ph} is the number of photons detected for a given collecting area (S) and a given exposure time (ΔT).

additional extinction (due to a potential dusty molecular cloud, or any shell of circumstellar material, depending on individual targets) will affect significantly these limits.

3 Concluding remarks

We have recently succesfully tested the metrology system of Carlina (Le Coroller et al. 2011), and we are integrating the focal gondola. We should be able to observe stars in 2011-2012. Preliminary studies aiming at using the Carlina OHP-prototype are still in progress, and suggest promising results for the multiplicity investigation of massive stars. Potential targets are already identified and should be observed in the forthcoming years. The objective of these preliminary studies is to pave the way for a 100-m class Carlina interferometer, opening a new era for high angular resolution observation techniques, in complementarity with ELTs.

Acknowledgements

MD thanks the Observatoire de Haute-Provence, and especially H. Le Coroller, for his stay at OHP in 2010.

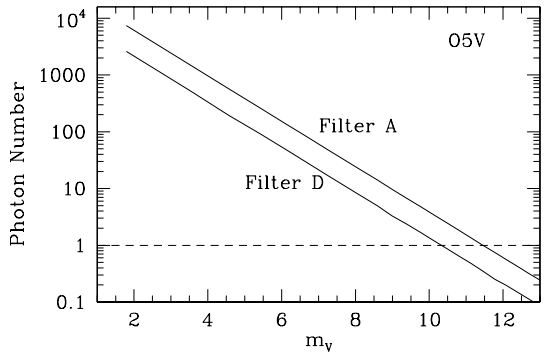

Figure 3: Estimation of the expected number of photons arriving per millisecond at the camera of the OHP prototype for an O5 spectral type, as a function of the visual magnitude (m_V). The results are given for two waveband filters centered respectively at 531 nm (filter A) and 692 nm (filter D).

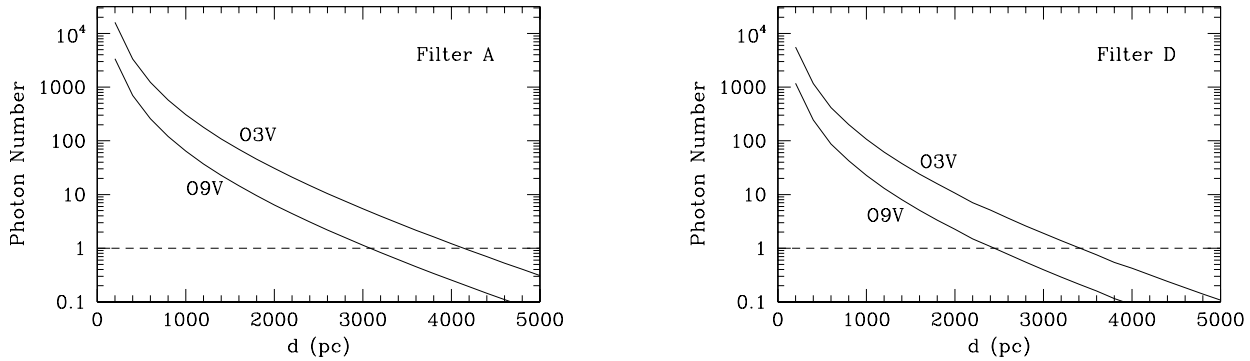

Figure 4: Estimation of the expected number of photons arriving per millisecond at the camera of the OHP prototype for spectral types ranging from O3 to O9, as a function of the distance to the star, assuming a mean extinction law of 1 mag/kpc. The results are given for the two waveband filters A (left panel) and D (right panel).

References

Castelli, F., & Kurucz, R.L. 2004, Proc. IAU Symp. 210 (astro-ph/0405087)
De Becker, M. 2010, RMxAC 38, 35
Green, D.W.E. 1992, International Comet Quarterly 14, 55
Labeyrie, A. 1996, A&AS 118, 517
Le Coroller, H., Dejonghe, J., Arpesella, C., Vernet, D., & Labeyrie, A. 2004, A&A 426, 721
Le Coroller, H., et al. 2011, A&A, in preparation
Martins, F., Schaerer, D., & Hillier, D.J. 2005, A&A 436, 1049
Sana, H., & Le Bourquin, J.-B. 2010, RMxAC 38, 27

The Expanded Very Large Array

S.M. Dougherty[1] and Rick Perley[2]

[1]NRC-HIA, Penticton, Canada
[2]National Radio Astronomy Observatory, Socorro, NM, USA.

Abstract: The Very Large Array is undergoing a major upgrade that will attain an order of magnitude improvement in continuum sensitivity across 1 to 50 GHz with instantaneous bandwidths up to 8 GHz in both polarizations. The new WIDAR correlator provides a highly flexible spectrometer with up to 16 GHz of bandwidth and a minimum of 16k channels for each array baseline. The new capabilities revolutionize the scientific discovery potential of the telescope. Early science programs are now underway. We provide an update on the status of the project and a description of early science programs.

1 Background

The Very Large Array has played a leading role in radio astrophysics over 30 years since it was completed in 1980. Since then, the capabilities of the VLA have changed very little. In order to continue the unparalleled scientific achievements of the telescope, a major expansion of its capabilities is currently nearing completion that improve radically the capabilities of the VLA. The key goals are to attain an order of magnitude improvement in continuum sensitivity (two orders in survey speed), complete frequency coverage from 1 to 50 GHz with vastly increased spectroscopic capability and correlator flexibility. Such improved specifications will greatly enhance the scientific discovery potential of the telescope, particularly in four science areas:

- the magnetic universe - the structure and topology of magnetic fields
- the obscured universe - enable unbiased imaging surveys of dust-enshrouded objects that are obscured at higher frequencies
- the transient universe - enable rapid response to transient events, and
- the evolving universe - tracking the formation and evolution of objects in the universe, from stars to galaxies to magnetic fields.

The key drivers within these broad science themes demand noise-limited, full-field imaging in all Stokes parameters, and point-source sensitivities of a few micro-Jy in an hour, leading to imaging dynamic ranges greater than 10^6, and a wide-range of spectroscopic ability. To attain such demanding specifications, several primary hardware areas have been upgraded:

- new broad-band receiver systems that provide continuous coverage between 1 to 50 GHz in eight different frequency bands, and superior sensitivity compared to the VLA systems (see Figure 1).

- new front-end electronics to digitize four 2-GHz-wide (R and L) frequency pairs at each antenna for a total of up to 8-GHz instantaneous bandwidth per polarization.
- new wide-band fiber-optic data transmission system to carry 16 GHz of signal bandwidth from each antenna to the correlator. This will eliminate stability and calibration challenges imposed by the analogue wave-guides of the VLA e.g. 3 MHz ripple and related spectral baseline instabilities.
- a new, highly-flexible, wide-band, full polarization correlator with at least 16k channels per baseline, and adjustable frequency resolution between 2.0 MHz and 0.12 Hz, using 64 independently tunable sub-bands, leading to an enormous range of potential correlator configurations, especially important for spectroscopy. Additionally, WIDAR has many specialized modes - e.g. phased-array, pulsar gating, pulsar binning etc, that increase greatly its scientific utility.

The EVLA project started in 2001 and is now nearing completion. The upgrade of all front-end electronics in the 27 antennas was completed in July 2009 and the WIDAR correlator began commissioning operations and early science in March 2010. The installation of the new receiver systems is on-going and will be completed in late 2012, and marks the completion of the EVLA. This \$90 Million project is funded jointly by the US National Science Foundation (NSF), the Canadian National Research Council (NRC), and CONACyT, Mexico.

2 EVLA Performance

The upgrades in the EVLA system provide substantial improvement over the performance characteristics of the VLA (Figure 1 and Table 1)

Table 1: Comparison of overall EVLA and VLA performance characteristics

Parameter	VLA	EVLA	Factor
Continuum Sensitivity (1σ, 9 hr)	10 μJy	1 μJy	10
Maximum bandwidth in each polarization	0.1 GHz	8 GHz	80
Number of channels at maximum bandwidth	16	16,384	1024
Maximum number of frequency channels	512	4,194,304	8192
Coarsest frequency resolution	50 MHz	2 MHz	25
Finest frequency resolution	381 Hz	0.12 Hz	3180
Number of full-polarization sub-correlators	2	64	32
log (frequency coverage over 1-50 GHz)	22%	100%	5

A key element of the EVLA is the Wide-band Digital Architecture (WIDAR) Correlator, designed and built by NRC-HIA in Penticton. The major feature of this design is the correlation of the four 2-GHz IF bands (giving 8-GHz of bandwidth in each polarization) via 64 independently tunable sub-band pairs with 16,384 channels per baseline. There are 16 sub-band pairs associated with each 2-GHz IF band. Each pair effectively forms an independent "sub-correlator", and correlator configurations can be assigned to each pair independent of the other pairs. Each sub-band pair can have a sub-band width of any of 128, 64, 32...,0.03125 MHz, and through recirculation the number of spectral channels per baseline can be increased, using certain correlator configurations, up to a maximum of 4.2M channels.

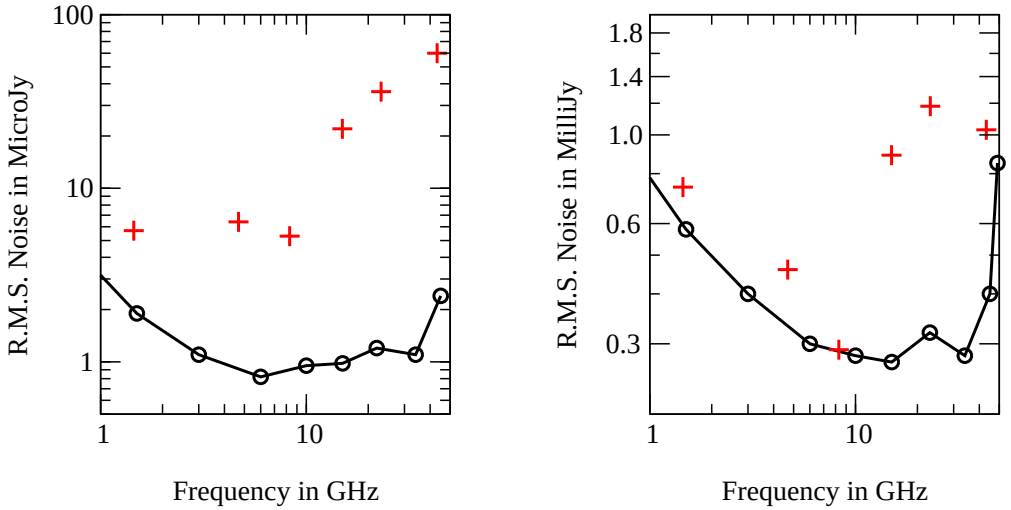

Figure 1: The continuum (left) and line (right) sensitivity of the EVLA (solid lines) compared to the VLA (crosses) (1σ in 12 hours). For the continuum sensitivity, the full available bandwidth at each band is assumed. For the spectral lines, the bandwidth adopted corresponds to a velocity width of 1 km s^{-1}. Note the EVLA will be continuously tunable over the entire frequency range.

2.1 Spectroscopy

The enormous flexibility in the configuration of the WIDAR correlator resources enables the EVLA to meet or exceed the demands of spectroscopic observations, and stands to revolutionize high-resolution centimetre wave spectroscopy.

An example of this flexibility is the simultaneous detection of multiple spectral lines. It is possible to target up to 64 lines simultaneously, and assign different spectral resolutions and sub-band widths for each sub-band pair, if desired. Taking recombination line observing at S band (2-4 GHz) as an example, there are 32 Hydrogen recombination lines that can all targeted independently with 2 kHz resolution and 8 MHz sub-band width (covering 1/8 the total bandwidth at S band), focusing correlator resources on the spectral regions of interest. For weak lines, subsequent stacking can be used to improve the signal-to-noise. More extensive examples of the efficiency of spectral line observing as a result of the WIDAR sub-band design come at K band (18-26.5 GHz), of particular interest to massive star research. Here, the EVLA could target the 32 molecular density and temperature indicator lines with a velocity resolution of 0.2 km s^{-1} e.g. including lines of NH_3, SO_2, H_2CS, H_2O, H_2CO, CH_3OH, OCS (Figure 2). With the remaining resources, 8 sub-bands could be tuned to each of the Hydrogen recombination lines in this frequency range, with the remaining 24 sub-bands covering 24×128 MHz (3 GHz) of continuum. Another advantage of the wide bandwidth, the continuum emission can be readily determined with the abundance of "empty" channels.

There are innumerable variants on the configuration of the WIDAR correlator, and potential users should consult the latest operational status summary for the availability of correlator configurations (http://science.nrao.edu/evla/proposing/obsstatsum.shtml).

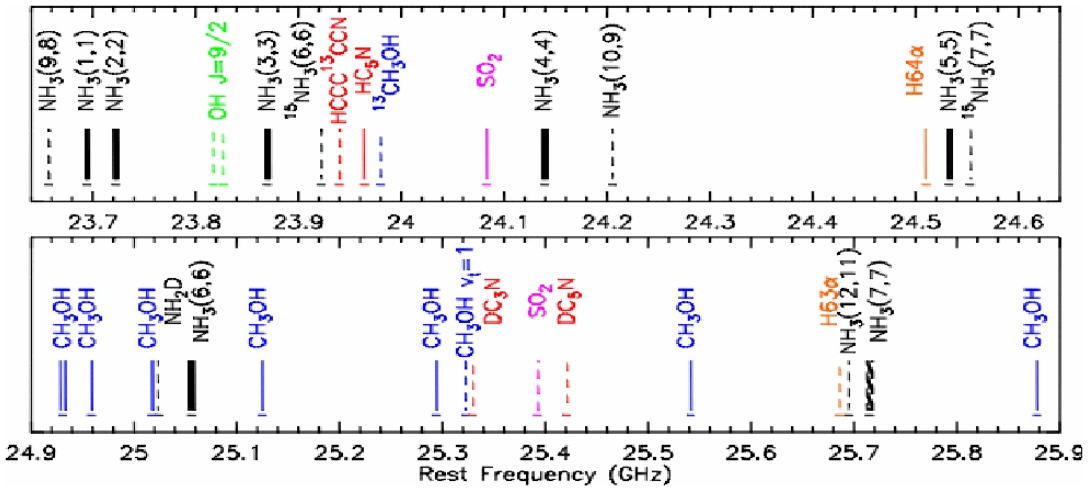

Figure 2: A multi-line spectroscopic setup example that can be attained with the WIDAR correlator, emplacing a sub-band at each of a series of 32 lines at K band (18-26.5 GHz). This example is taken from an RSRO experiment to study the conditions in a massive star forming region (Figure 3).

2.2 Continuum Imaging

The digital data transmission system leads to improved calibration of system gains, and together with the improved sensitivity of the new receivers greatly enhances the continuum capability of the EVLA. Typical image dynamic ranges used to be, at best, approaching 10^5, requiring major post-processing efforts. With the new system, dynamic ranges approaching 10^6 can be readily achieved with little effort, but reveal that more sophisticated processing methods are required to handle the residual image artifacts to attain the goal of greater than 10^6.

The large bandwidth provides two immediate advances of relevance to continuum emission studies. At full bandwidth the EVLA gives a factor of 10 improvement in sensitivity (0.1GHz vs 8 GHz), implying the potential to detect continuum sources out to $3\times$ greater distance at the same noise level, and hence flux limited sample sizes $\sim 30\times$ larger than available with the VLA. For massive stars, higher precision fluxes will lead to more precise mass-loss estimates across the entire range of massive star evolution. Another benefit is the vastly improved ability to determine the continuum spectra as a result of the large number of potential spectral fluxes that an be derived across each observing band and the improved ability to match spectra across adjacent observing bands. For stars, this will lead to improved understanding of, for example, the nature of the underlying emitting particle energy spectrum in non-thermal sources, and circumstellar envelope geometry of thermal emission sources.

3 Early Science programs

To make early and effective use of the new features of the EVLA as they are commissioned, early science with the EVLA is enabled through two observing programs - the Observatory-Shared Risk (OSRO) and Resident-Shared Risk (RSRO) observations.

OSRO: This program provides science capabilities that are similar to those to the VLA, utilizing capabilities in the EVLA system that were commissioned early in 2010, and is possible to access "at-home". Initially, up to 256 MHz of bandwidth is available through two independently tunable 128-MHz bands of 64 channels each, with both co- and cross-polarization products. For higher spectral resolution, the total bandwidth of the sub-bands can be reduced. Alternatively, 256 channels in one

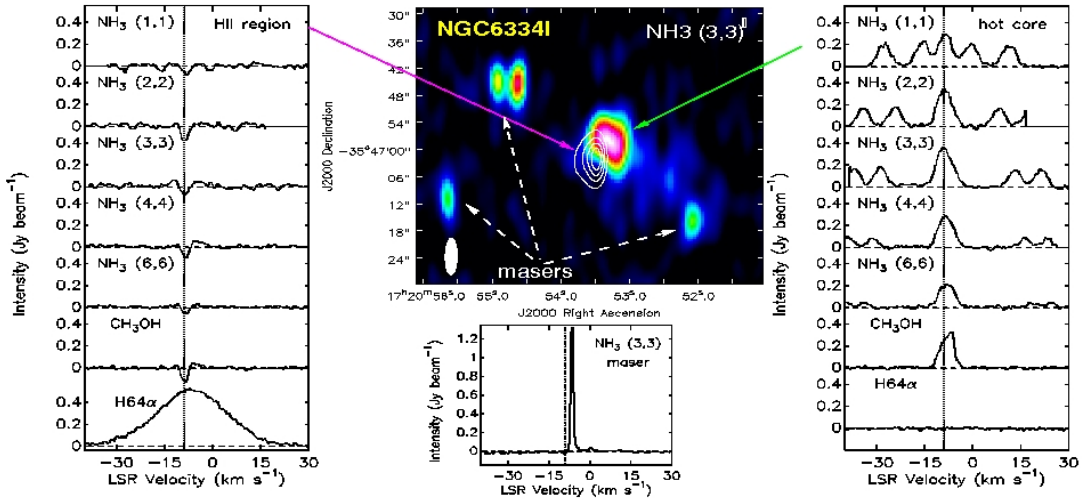

Figure 3: An example of Early Science enabled through the RSRO program, showing a K-band image of Ammonia in a massive star forming region obtained in 10 minutes using 8×8 MHz sub-bands. The contours are continuum emission from an HII region. Ammonia in absorption against the HII region (left panel) and in emission from one of the hot cores (right panel). The panel at bottom-centre shows an ammonia maser line.

128-MHz (or smaller) sub-band is available. The available bandwidth in OSRO is expected to grow in early 2011.

RSRO: Science programs that require access to the more extensive capabilities possible with the EVLA, particularly more sub-bands and broader bandwidths, come under the auspices of the RSRO program. These features are available to users in exchange for a period of residence at the Array Operations Centre to aid in commissioning. The goal is to accelerate the development of the scientific capabilities of the EVLA though the broad expertise of the user community. The current plan is for the RSRO program to run to the end of 2011. For those interested in participating in RSRO, a description of the current status is available at http://science.nrao.edu/evla/earlysicence/rsro.shtml.

4 Summary

Early science is already demonstrating the unprecedented potential of the EVLA system, especially the flexibility and range of configurations of the WIDAR correlator system. The science opportunities are tremendous and ensure the EVLA will be the pre-eminent centimetre-wave radio telescope over at least the next decade. Numerous challenges remain, particularly in data processing and calibration, before the full diversity of science goals can be achieved, but is it is through programs such as RSRO that these challenges can be met in collaboration with the broad community.

Acknowledgments

We would like to thank many people involved in the design and commissioning of the EVLA in providing material for this presentation. In particular, we thank Drs Crystal Brogan and Todd Hunter for permission to present initial results from their RSRO science program.

A focus for hot stars - The German STScI*

Thomas Eversberg[1] & Klaus Vollmann[2]

Schnörringen Telescope Science Institute (STScI) - www.stsci.de
[1] Am Kielshof 21a, D-51105 Köln, Germany
[2] Ringweg 7, D-51545 Waldbröl, Germany

Abstract: The German STScI is re-installing a 1m-class professional telescope for spectroscopic work on massive stars. A combination of scientific investigations and training of young scientists will be the main goal of the newly established institute. Professional equipment (telescope, instrumentation, software and accommodation) and a respective network will not only offer the opportunity for specific long-term campaigns but also for a joint effort to bring together professionals and young scientists.

1 Introduction

The former Wendelstein Telescope operated by the University of Munich has a new home after being replaced by a bigger instrument. The telescope will be installed in a new service building close to the city of Waldbröl, some 50km east of Cologne. The main scientific application will be spectroscopy of massive stars including the visible and near infrared wavelength range. The telescope focus can be used for scientific campaigns and instrumental engineering runs of astronomical institutes. In addition, young scientists (scholars and students) will be trained in the use of astronomical instrumentation.

2 The observatory

The telescope has a 0.8m Ritchey-Chretien primary mirror with an equivalent f-ratio of f/12.5, manufactured by DFM Engineering Inc. / USA (fig. 1). The primary mirror is pneumatically supported and the system focus is thermally stabilized by invar elements. A GUIDE ACQUIRE MODULE offers three different focus positions of the same telescope focal length which allows the use of different instruments without mechanical adjustment (fig. 2). Equipped with a standard spectrograph of spectral resolution of about 10.000, a typical S/N of 100 can be achieved within 30 minutes for a star of about 10mag. We intend to use an infrared focal plane array for imaging and/or spectroscopy between 1 and 2.5 microns (fig. 3). Finally, we will install an Echelle spectrograph with a spectral resolution of at least 20.000 for the complete visual spectra range (fig. 4). For reliability and acceptance in the scientific community, the observatory will operate with professional data processing packages. Figure 5 shows the complete observatory complex. The telescope tower is covered by a dome which houses

*The Schnörringen Telescope Science Institute has no relation with the Space Telescope Science Institute in Baltimore.

the telescope, plus an instrument room in the basement. For optimized seeing conditions the dome itself will be equipped with ventilation flaps and will be actively water cooled according to modern investigations on dome seeing (Zago 1995). A heat exchanger will transfer the heat to the service building for heating and hot water. The service building consists of a control room which houses a series of computers. These computers control all system units (tracking, positioning, data acquisition). An office, seminar room, sanitary, kitchenette and sleeping rooms complete the building, so that proper and independent working conditions are provided (fig. 6). Electrical power will be delivered by photovoltaic cells which will cover the roof of the service building.

Figure 1: The 0.8m DFM telescope with focal ratio f/12.5.

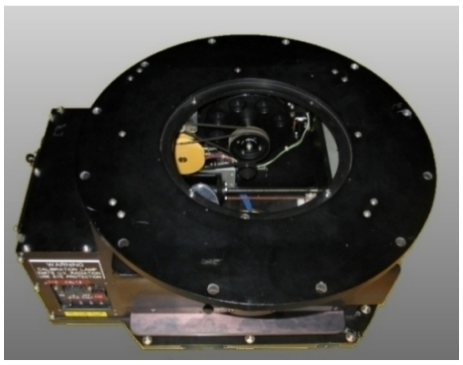

Figure 2: The DFM GUIDE ACQUIRE MODULE (GAM).

3 Site conditions and practical work

The observatory will be erected at 300m altitude, and hence, atmospheric conditions can not compete with professional sites. We expect an average humidity of about 60% during 80 clear nights per year. Average seeing is of the order of 3-4 arcsec. This is an average value, estimated at various sites in western Germany. For professional sites that would be very bad. Our efforts for a better dome and telescope seeing (see above) are nevertheless justified. According to Zago (1995) a cooled and ventilated dome will improve seeing conditions in any case. Note that a warm primary mirror introduces about 0.4 arcsec per degree Celsius above environment temperature. Quick access to a relatively dark and remote site, compensates for these penalties. Regional astronomical institutes can quickly install their instrumentation, which are later used at professional sites.

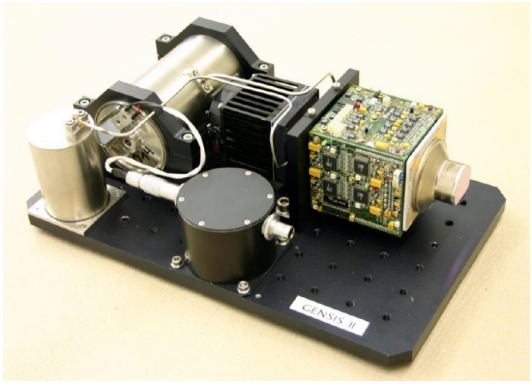

Figure 3: The AIM infrared focal plane array (FPA) with a 256 x 1024 MCT array. The sensor is pulse-tube cooled to 150 K. The quantum efficiency of the chip is about 60% between 1 and 2.5 microns (www.aim-ir.com).

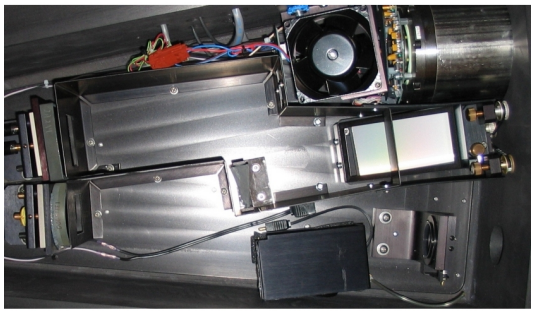

Figure 4: One of the two STScI Echelle spectrographs for the visual spectral range. Collimator and camera (left) consist of off-axis mirrors. The Echelle grating (right) has a size of 100 x 200 mm.

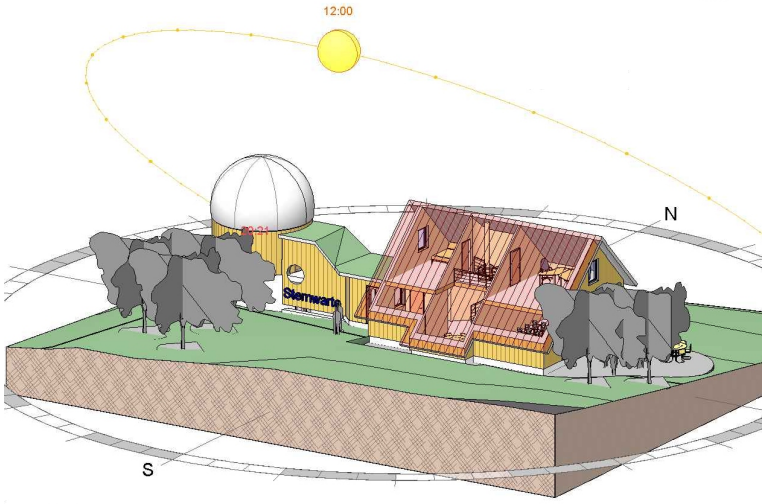

Figure 5: The STScI complex including all necessary equipment for professional work.

3.1 Research and science

Our observatory will be offered to the professional community. We are able to offer long-term campaigns together with other amateur and professional groups (e.g., the MONS campaign - Williams 2011). This is valid for the wavelength ranges covered by our spectroscopic instruments (see above). It will be also possible to perform campaigns in other fields, e.g., deep sky imaging with Johnson filters or in the IR. The telescope can carry heavy instrumentation of the order of 200 kg, as it is often needed in professional astronomy.

3.2 Training the next generation

Our observatory provides excellent training opportunities for young scientists (students), particularly if they are geographically close to their home university. This is especially valid because our training site is equipped with professional hard- and software. We believe in hands-on instrumental experience as it is widely required for modern astronomy with state-of-the-art technology. So, we do not plan

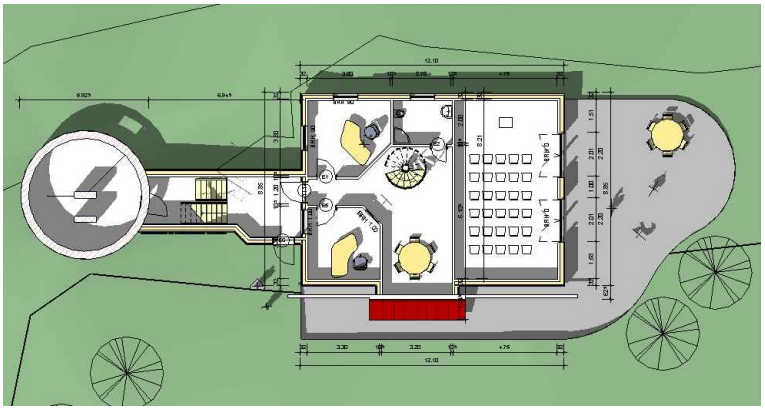

Figure 6: Basement of the service building with control room, office and seminar room.

to offer remote telescope control. A workshop with a lathe and milling machinery completes our technical site equipment.

4 Resume

By combining a professional observatory, the scientific education of the operators (astronomer and atmospheric physicist, both spectroscopists), a good location in Germany, appropriate equipment and an existing network in astrophysics, the STScI has a specific character in Germany. The observatory generally serves two purposes . That are research activities, together with the professional astronomy and training of young scientists from schools and universities.

Acknowledgements

We thank the BUSINESS AND INDUSTRY ASSOCIATION WALDBRÖL (GIV) and all Sponsors out of the region for their generous support.

References

Zago, L. 1995, *"The effect of the local atmospheric environment on astronomical observations"*, PhD thesis, Ecole Polytechnique Federal de Lausanne (EPFL)

Williams, P. 2011, in Proceedings of the 39th Liège Astrophysical Colloquium, eds. G. Rauw, M. De Becker, Y. Nazé, J.-M. Vreux & P.M. Williams, BSRSL 80, 595

Study of a possible X-ray sensor based on the Plasmon Surface Resonance for the next generation of instruments

Anthony Hervé[1], Juriy Hastanin[2], Serge Habraken[3] & Gregor Rauw[1]

[1] GAPHE, AGO, Université de Liège, Allée du 6 Août 17, Bât. B5c, 4000 Liège, Belgium
[2] CSL, avenue Pré-Aily , Bât. B29, 4031 Angleur 4000 Liège, Belgium
[3] Hololab, Université de Liège, Allée du 6 Août 17, Bât. B5a, 4000 Liège, Belgium

Abstract: With the new generation of X-ray space observatories, such as *IXO* in preparation, we explore a new technology in order to improve the spectral resolution and the sensitivity of future instruments. We have studied the possibility to create a sensor based on the Surface Plasmon Resonance (SPR), already used in chemistry and biomedical applications, and have determined the preliminary constraints on its size, energy resolution and working temperature.

1 Introduction

Even though *XMM-Newton* and *Chandra* have deeply modified our view of the X-ray universe, they have also triggered new questions that call for a high sensitivity X-ray observatory offering high energy resolution. Well exposed, higher resolution spectra are indeed needed to confront theoretical models with observations. In this context, we present a new candidate technology for space instrumentation which is currently already used in biomedical and chemistry applications. The Surface Plasmon Resonance (SPR) could be an alternative to calorimeters and other traditional instruments for future X-ray integral field spectrographs.

2 Theory

Surface plasmons are quantized oscillations of free electrons at the interface between a metal (gold, silver or other) and a dielectric material (air for example). In sensing applications, the surface plasmons are commonly excited by evanescent electromagnetic waves at optical frequency. Surface plasmons are excited at a specific incidence angle and result in a sharp and significant reduction of reflected light intensity at this angle (Fig.1). This phenomenon is referred to as "Surface Plasmon Resonance" (SPR). The surface plasmon resonance angle can be calculated via the dispersion relation obtained from Maxwell's equations and the continuity conditions at the interface boundaries (Kretschmann & Raether 1968, Otto 1968).

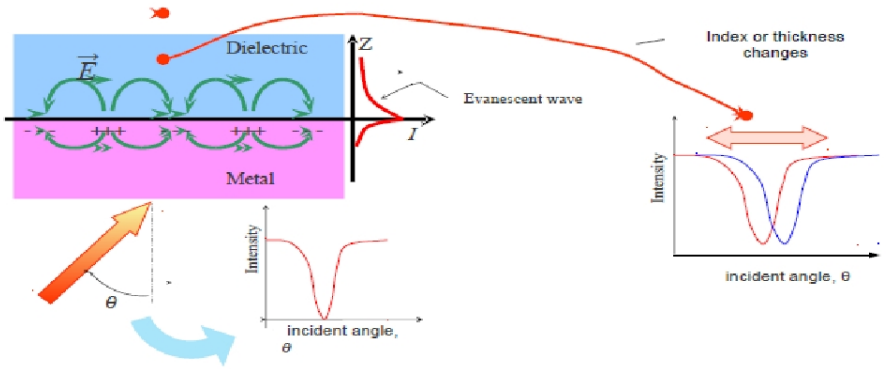

Figure 1: Scheme of the Surface Plasmon Resonance effect.

3 An example of an SPR sensor and first results of a preliminary feasibility study

The concept of the detector is very simple (Fig.2, Hastanin 2009). The cantilever consists of an X-ray absorber fixed on a second non-absorbing material with a different Young module. When a photon is absorbed, the temperature of the absorber increases and leads to a deformation (lengthening) of this part of the cantilever. However, the temperature of the second component of the cantilever is constant. So, the cantilever bends in the direction of the gold layer fixed on the prism surface. The gap of air decreases, modifying the properties of the plasmon surface and accordingly the reflectivity of the prism. The intensity of the reflected light of the laser at the gold/prism interface thus also decreases. From the knowledge of the variation of the intensity of the reflected laser light and the properties of the sensor, we can deduce the energy of the absorbed photon.

In practice, we are confronted to different issues. The main constraint on the future sensor is the working temperature. The thermal noise in the material creates oscillations of the cantilever which lead to fluctuations of the intensity of the reflected laser light. To limit this agitation we have to work at very low temperature to make sure that the variation of the intensity of the laser is truly the result of the absorption of an incoming photon. For example, if we want an accuracy of 1 eV for the sensor we need to work below 1 K.

Assuming the possibility to work at this very low temperature, we now focus on the size of the sensor. In fact, with the future instruments, astronomers want to observe X-rays in the 0.1-10 keV domain with an accuracy of 1eV. The readout system (variation of the intensity of the laser) is very sensitive; a decrease of a few percent in the intensity of the laser is detectable, this corresponds to a motion of the cantiler of a few nanometers. We thus have to adapt the motion of this latter to the accuracy of the detection of a variation on the intensity of the laser. The difference of the bending of the cantilever between two photons the energies of which differ by 1 eV should be around a few nanometers in order for the change of the laser intensity to be detectable. This is our second issue. At room temperature, it is rather easy to find atomic data, and physical properties of the material. However, since we have to work under cryogenic conditions, this is more challenging. The physical behaviour of some of the materials at very low temperature is poorly known and regarding the difficulties to develop experimental studies, we are confronted with a lack of information concerning the absorption capacity, Young module and other properties of the materials. Nevertheless, we have used an extrapolation of the physical laws to low temperatures to estimate the characteristics we need for some materials. Thus, if we use a layer in silicon or bismuth for the absorber, we find that the size of the sensor and especially the cantilever, is compatible with standard micro-manufacturing technology.

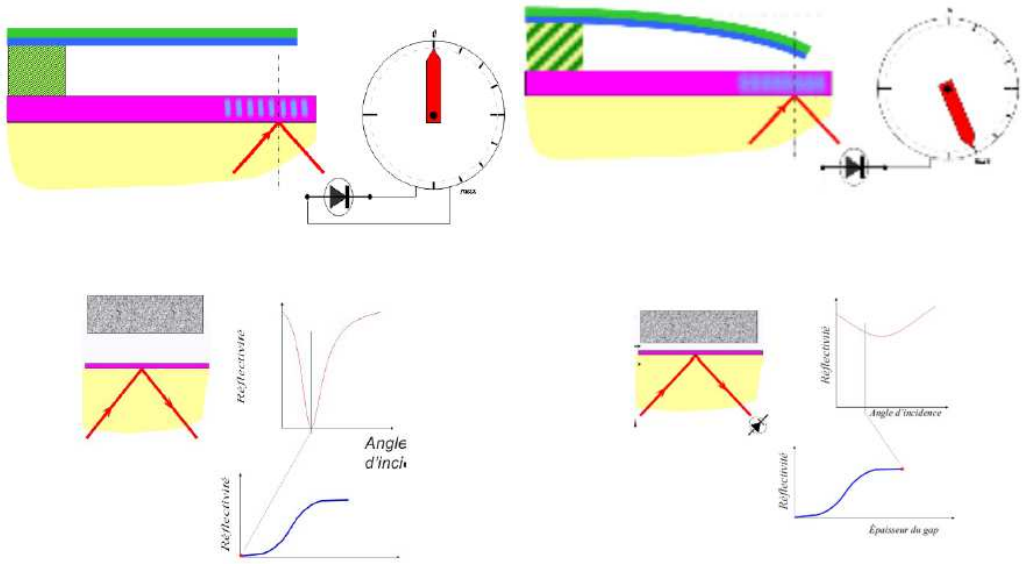

Figure 2: Illustration of an SPR sensor, with the different components. *Left*: At rest. *Rigth*: After the absorption of a photon.

To obtain an SPR effect, the size of the gap between the cantilever and the gold surface is limited (around a few hundred nanometers). In consequence, we need to adjust the dynamical motion of the cantilever and the energy band that we want to observe. Our first results indicate that it is very difficult to measure the full 0.1-10 keV band with an accuracy of 1eV. The design of the detector presented in Figure 2 allows the detection of photons in the 0.1-6 keV band with an accuracy of 1 eV. We are currently working on the design of the sensor to increase the observable energy band. But, our theoretical solution faces manufacturing difficulties. And more important we need to study the impact of the Van der Walls interaction between the cantilever and the gold surface.

The SPR technology has many assets (Hastanin 2009). The measurement of the energy of the absorbed photon is very sensitive. The readout of the global sensor only depends on the capacity to evacuate the heat in the cantilever since the readout of the intensity of the reflected laser light is instantaneous. These features yield an excellent efficiency in the counting of photons. Futhermore, the whole energy of the photons is converted into a mechanical motion of the cantilever and there is no loss in an intermediate system between the absorber and the readout system.

4 Conclusion

A new X-ray sensor based on the SPR technology can be an alternative to other technologies. The readout is very fast and the sensitivity of the measurement is excellent. This yields a very robust behaviour with respect to photon pile-up and a very good accuracy in the measurement of the energy deposited by the photon. The concept which we propose reduces the thermal loss contrary to the other calorimeters. The limitation of this technology is essentially due, as for most other instruments, to the thermal noise. The size and the design of the future detector should allow to design an integral field X-ray spectrograph with good spatial resolution.

Acknowledgements

This research is supported by the FNRS (Belgium) and by the Communauté Française de Belgique - Action de recherche concertée (ARC) - Académie Wallonie–Europe.

References

E. Kretschmann, H. Raether, 1968, Z. Naturforsch., 23A, 2135
A. Otto, 1968, Z. Physik, 216, 398
J. Hastanin, 2009, PhD thesis, Université de Liège

Massive binaries as seen with Gaia

Matthieu Palate, Gregor Rauw, Eric Gosset* and Yaël Nazé†

Institut d'Astrophysique et de Géophysique, Université de Liège, 4000 Liège, Belgium

Abstract: *Gaia*, ESA's forthcoming astrometric observatory, will observe a billion stars of our Galaxy, among which thousands of high-mass stars. In this contribution, we study the capabilities of *Gaia*'s spectrometer (RVS) in the context of massive stars, especially the detectability of lower-mass companions to O-type stars. This preliminary study enables us to estimate to what extent *Gaia* will constrain the distribution of the physical and orbital parameters of massive binaries (luminosity, period, mass ratio, eccentricity...).

1 Introduction

Massive binaries are crucial for a robust determination of fundamental parameters of massive stars. Here, we investigate the detection of massive binaries with the radial velocity spectrograph (RVS) of *Gaia*, ESA's forthcoming astrometric mission. To reach this goal, we have used two approaches: one based on a set of binaries with fixed orbital parameters and a second one based on a larger population with an underlying distribution of orbital parameters. The first gave us specific information on the detection of binaries as a function of spectral class. The second is a more statistical assessment of the detection with respect to the mass ratio. We also simulated the capabilities of the astrometric instrument to quantify the impact of the Lutz-Kelker bias (Lutz & Kelker 1973) that affected the *Hipparcos* parallaxes.

2 Gaia

Gaia is ESA's global astrometry mission due for launch in August 2012 with a nominal lifetime of five years. The goal of this mission is to measure the positions, velocities and distances of about one billion stars to create a 3D map of part of the Milky Way. The satellite has two telescopes that share the same focal plane. The 3-in-1 instrument is placed in the unique focal plane composed of 106 CCDs. This instrument has three channels: astrometric, spectro-photometric and spectrometric. The very high precision of the astrometric instrument (up to 7 μas) will help astrophysicists to improve their knowledge in stellar physics, stellar population distribution, exoplanet systems, galactic structure,... The RVS is a medium-resolution ($R \simeq 11500$) near-infrared spectrograph (see Table 1). Its goal is to measure the radial velocity of stars and therefore complete the information of the astrometric instrument (angular position, angular velocity and parallaxes) to characterize completely the motion

*Senior Research Associate FRS-FNRS (Belgium)

†Research Associate FRS-FNRS (Belgium)

Table 1: Characteristics of the RVS instrument

Wavelength range	$847 - 874$ nm
Accuracy (for late-type stars)	$1 - 10$ kms^{-1}
Resolving power	11500
Spectral resolution	0.075 nm/pixel

of stars. The wavelength range is best suited for G and K stars but includes only a limited number of weak lines in the case of massive (OB-type) stars.

3 Simulations

We simulate the detection of binary systems containing at least one O-star with the RVS. All simulations are done with MATLAB®. We make two distinct simulations but in both cases, the first step is to build synthetic spectra of fake binary systems in the RVS domain. For this purpose, we use a set of eight observed O-star spectra and a grid of thirty-six synthetic spectra of cooler stars from Castelli & Munari (2001) and Munari & Castelli (2000). The spectra are wavelength-shifted according to the orbital elements of the fake binary system. Orbits are supposed circular.

3.1 RVS spectra

In the first case, the orbital elements are fixed. At first, we do not add noise. The masses of the stars are supposed to be known, the inclination of the system takes only three values: $\{0, \pi/4, \pi/2\}$, the period is fixed at ten days and, finally, we only consider the extreme values of the true anomaly[1]. The combination of the spectra of 8 O-stars and 36 non O-stars yields a total of 1440 cases. In the second case, we perform a Monte Carlo simulation for 9 millions binary systems. The latter are generated following the distributions of mass ratios and semi-major axis given by Kobulnicky & Fryer (2007) : $f(q) = C \times q^{0.3}$ where C is a normalization constant. We also assume a uniform distribution of orbital inclinations in the range $[0, \pi]$ radians. The distribution of semi-major axes is also supposed uniform (Kobulnicky & Fryer 2007) and is generated in the range $[13.5R_{\odot}, 3000R_{\odot}]$. Again, we only consider the extreme values of the true anomaly. Finally, we add noise to the synthetic spectra.

3.2 Cross-correlation

The resulting simulated spectra are then cross-correlated with two masks (one for the O-star and another one for its companion) and we consider that the binary nature is successfully detected if the cross-correlation peak yields the right radial velocity within the resolution of the RVS (see Fig. 1). Note that the performance of our method is not as good as the procedure that will eventually be used for *Gaia*. To correct for this lower performance, we adopt a larger tolerance on the radial velocity: in our simulations, this tolerance is 25 km s^{-1}, which corresponds to an error of one pixel (low-sampling mode). Although systems with very low radial velocities (either as a result of a low inclination or an unfavorable orbital phase) generally yield a positive cross-correlation with both masks, we discard these cases from our analysis, since in practice, the binarity of such systems can not be established by

[1]Whilst our simulations consider a "single transit", the results presented below will not change significantly by considering multiple transits, since we have simulated the extreme values of the true anomaly which should provide the best phases for detection of binarity.

Table 2: Characteristics of the ASTRO instrument

Spectral type	Visual Magnitude	Standard deviation of position measurement (μas)
O	< 10	< 7
	< 15	25

these data. Another remark is about the O + O systems. We often found one component of the system but not the second one. This problem comes from the difficulty to find the secondary cross-correlation peak. A more sophisticated method like disentangling could be used to improve the detection of such cases.

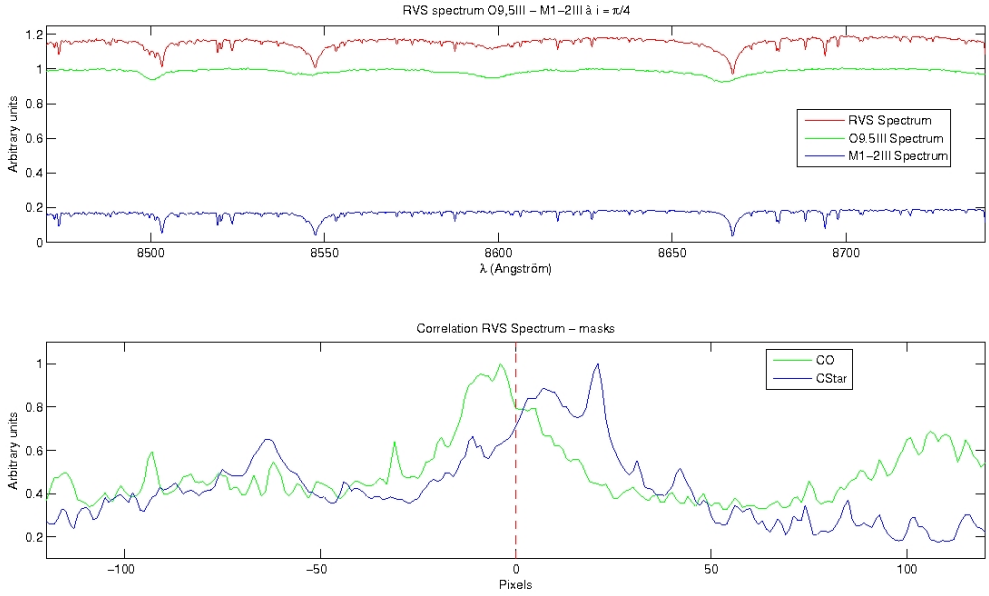

Figure 1: Upper panel: Example of combining spectra of an O9.5 III and an M1-2 pre-main sequence star at an inclination of $\pi/4$. Lower panel: Result of the cross-correlation. The input radial velocities are recovered within the resolution of the RVS.

3.3 Astrometric instrument

Two distinct simulations linked to the astrometric instrument have been done. The first one concerns the calibration of absolute magnitudes. For this purpose, we use the catalogue of Humphreys (1978) of OB-stars and we check whether the error induced by the ASTRO instrument has an impact on the absolute magnitude. The second part of the simulations is linked to the Lutz-Kelker bias (Lutz & Kelker 1973) that affects the *Hipparcos* observations. This bias depends on the ratio σ_{Gaia}/π where σ is the standard deviation of the instrument (see Table 2) and π the observed parallax (we assume that the Humphreys parallaxes are the observed ones). The absolute magnitude and the parallax are connected by the following relation: $M = m - A - d$ with A, the reddening and $d = 5 \times log(1/\pi) - 5$, the distance modulus. For information, the parallaxes given by Humphreys range from 1.5×10^{-4} to 2.9×10^{-3} arcsec.

4 Results and conclusions

The first important result is that the RVS wavelength domain does not allow us to get rid of the common luminosity bias that affects the detection of the companion star. Indeed, binary systems with mass ratios ($M_{companion}/M_O$) below 0.4 will probably not be detected by the RVS, regardless of the luminosity class of the companion (see Fig. 2). The percentages of detections of SB1 and SB2 spectral signatures are given in Fig. 3 below for simulated O + O systems and O + non O systems. As can be seen, the total detection rate will be around 50% (SB1 and SB2 spectral signatures), which is not very good. We also note that high-velocity amplitude systems were actually more difficult to detect. Fortunately these systems are less common than low velocity amplitude systems. The first simulation with a fixed period showed us that the detection rate depends on the luminosity classes of the O-star and its companion. The spectral signatures of O-stars in association with supergiant companions are usually more difficult to detect. The O-star is usually better detected than the companion star. In conclusion, we find that the RVS is not well suited for the study of massive binaries as the near-infrared spectral range, chosen for this instrument, contains only weak lines in the spectra of O-type stars.

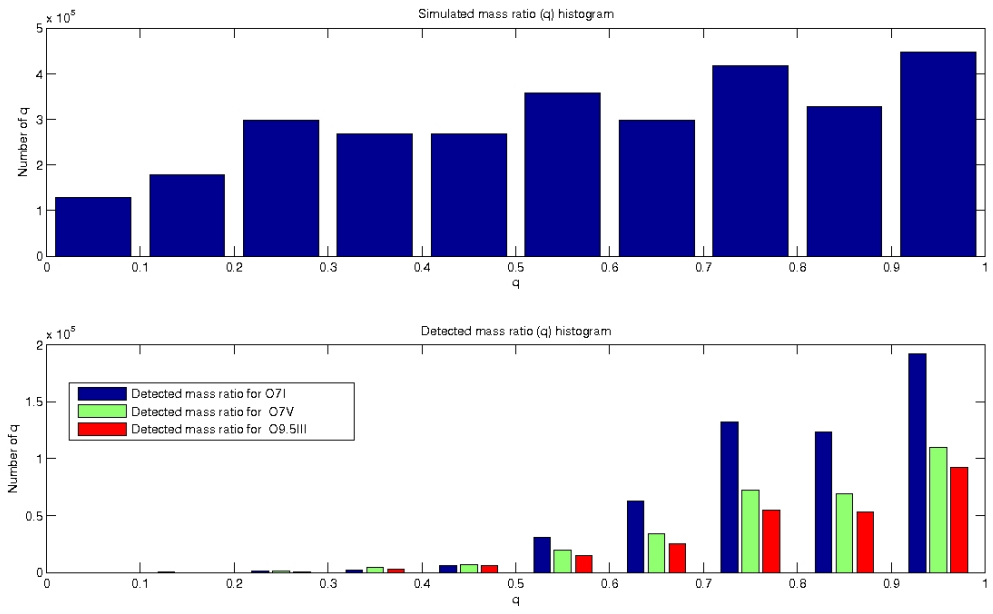

Figure 2: Upper panel: histogram of the simulated mass ratios of the input binary population. Lower panel: histograms of the detected mass ratios for SB2 spectral signatures for three O-star primaries.

The last part of the simulations were related to the astrometric instrument. This instrument will provide parallaxes with unprecedented accuracy that should allow us to obtain a bias-free absolute magnitude calibration for massive stars. For the first part of the simulations, we conclude that the error induced by *Gaia* is indeed negligible. The comparison of our results (catalogue of Humphreys, 1978, + *Gaia*'s error) and the Martins et al. (2005) calibrations showed that the errors introduced by the *Gaia* astrometric instrument are so small that we will be able to distinguish between the different calibrations of O-type star that have been proposed. For the second part of the simulations, the impact of the bias on the determination of the absolute magnitude calibration of O-stars was simulated using the catalogue of Humphreys (1978). We showed that the Lutz-Kelker bias will be negligible (for objects brighter than magnitude 10) thanks to the unprecedented precision of the astrometric instrument. Indeed, the ratio σ_{Gaia}/π is very small, especially for stars brighter than magnitude 10:

Stars	SB1 signatures (%)		SB2 signatures (%)		SB1+SB2 signatures (%)	
	V_O	V_{Star}	V_O	V_{Star}	V_O	V_{Star}
O7I	11.7	40.1	35.5	17.3	47.2	57.4
O7V	21.0	42.1	26.3	16.4	47.3	58.5
O9.5III	19.9	42.3	20.2	14.5	40.1	56.8
Stars	SB1 signatures (%)		SB2 signatures (%)		SB1+SB2 signatures (%)	
	V_{O1}	V_{O2}	V_{O1}	V_{O2}	V_{O1}	V_{O2}
O7I	38.6	9.8	7.2	11.6	45.8	21.4
O7V	32.9	12.2	5.2	5.9	38.1	18.1
O9.5III	27.7	9.5	5.3	7.4	33.0	16.9

Figure 3: Percentages of detections of SB1 and SB2 spectral signatures for three O-star primaries of different luminosity classes. Upper part: O + non O systems. Lower part: O + O systems

the correction on the absolute magnitude is -0.01 at most, and amounts to -0.14 for objects fainter than magnitude 10.

In conclusion, the RVS instrument is not well suited for the study of massive binaries with a detection rate of about 50% even including SB1 signatures. However, the astrometric instrument fulfills its promises to provide a tremendous breakthrough in our understanding of the physics of massive stars.

Acknowledgements

We acknowledge support from the Fonds de la Recherche Scientifique (FRS/FNRS), through the XMM INTEGRAL PRODEX contract and the *Gaia*-DPAC PRODEX contract (Belspo) as well as by the Communauté Française de Belgique - Action de recherche concertée - Académie Wallonie - Europe

References

Castelli, F., & Munari, U., 2001, A&A, 366, 1003
ESA Science & Technology, 2009, *Gaia*, http://sci.esa.int/sciencee/www/area/index.cfm?fareaid=26
Humphreys, R.M., 1978, ApJS 38, 309
Kobulnicky, H.A., Fryer, C.L., 2007, ApJ 670, 747
Lutz, T.E., & Kelker, D.H., 1973, PASP 85, 573
Martins, F., Schaerer, D., Hillier, D.J., 2005, A&A 436, 1049
Munari, U. & Castelli, F., 2000, A&A 141, 141

CRIRES-POP: A library of high resolution spectra in the near-infrared

Ramsay, S.K.[1]*, Lebzelter, T.[2], Seifahrt, A.[3,12], Almeida, P. [4,5],Bagnulo, S.[6], Hartman, H.[7], Hussain, G.[1], Käufl, H.U.[1], Nieva, M.-F.[8], Przybilla, N.[9], Seemann, U.[1,12], Smette, A.[5], Uttenthaler, S.[10], Wahlgren, G.M.[11,13], Wolff, B.[1]

[1] European Southern Observatory, Karl-Schwarschild-Strasse, 2, 85748, Garching, Germany
[2] Institut für Astronomie, Universität Wien, Türkenschanzstr. 17, 1180 Wien, Austria
[3] Physics Department, Univ. of California, One Shields Avenue, Davis, CA 95616 USA
[4] Centro de Astrofísica da Universidade do Porto, Rua das Estrelas, 4150-762 Porto, Portugal
[5] European Southern Observatory, Alonso de Córdova 3107, Vitacura, Santiago, Chile
[6] Armagh Observatory, College Hill, Armagh, BT61 9DG, UK
[7] Lund Observatory, Box 43, SE-221 00 Lund, Sweden
[8] Max-Planck-Institut für Astrophysik, Karl-Schwarzschild-Str. 1, 85741 Garching, Germany
[9] Dr. Karl Remeis-Sternwarte & ECAP, Sternwartstr. 7, 96049 Bamberg, Germany
[10] Institute for Astronomy, Katholieke Universiteit Leuven, Belgium
[11] Catholic University of America, 620, Michigan Ave NE, Washington DC, 20064, USA
[12] Institute for Astrophysics, Göttingen University, Friedrich-Hund-Platz 1, 37077 Göttingen, Germany
[13] NASA Goddard Space Flight Centre, Code 667, Greenbelt, MD 20771, USA

Abstract: We describe an ongoing project to obtain a library of high signal-to-noise, high spectral resolution stellar spectra from ∼1-5μm using CRIRES on the ESO Very Large Telescope (VLT). New instrumental capabilities make the near-infrared an increasingly important wavelength range for high resolution spectroscopy, yet our knowledge of the spectral features in this regions is far from complete. The motivations of our group in conducting this survey are broad, from providing fundamental line data for laboratory spectroscopists, improving wavelength calibration and the removal of telluric lines for CRIRES to applications in astrophysical topics from observations of circumstellar matter to modelling stellar atmospheres. Substantial effort is being invested in producing a library of spectra reduced using a common procedure to ensure homogeneity of the results. So far, we have obtained spectra of 9 sources and hope to complete a sample size of ∼25 to give good coverage of the HR diagram. Most of our targets were selected from the UVES-POP spectral library source list, so that complete coverage of the spectra from the UV to the NIR will be available. An important goal for the project is that the library is public. The data are available at http://www.univie.ac.at/crirespop/.

*sramsay@eso.org

1 Introduction and Motivation

The importance of infrared observations has grown rapidly in recent years thanks to the improvements in instrumentation that is driven partly by the availability of detectors in large formats. Coupled with the increase in telescope aperture from 4-m to 8-m this means that previously photon-starved high spectral resolution observations are now being made routinely at near-infrared wavelengths. This presents us with the opportunity to expand further our understanding of the diagnostics and content of the infrared spectrum and to confront existing models with very high quality infrared spectra. Early high resolution infrared atlases of stellar spectra are from work on the Sun. Examples include the 3–10μm spectrum by Delbouille, Roland & Neven (1973), with extensions to longer wavelengths in later works by this group (e.g. Farmer et al. 1995), and from 0.7–22μm by Wallace et al. 1996. For stars other than the Sun, there are libraries at medium resolving power of around a few thousand (see Rayner, Cushing, & Vacca 2009 for a compilation) but few at higher resolving power. Published examples include the spectrum of the K2 giant Arcturus from 0.9–5.3μm with R$\sim$ 100000 (Hinkle, Wallace & Livingston 1995) and K band spectra of 12 cool stars by Wallace & Hinkle (1996). The CRIRES-POP project (Lebzelter et al. 2010) will greatly advance our knowledge of the high resolution NIR spectra of stars by observing the $\sim$1-5μm spectrum of 25-30 stars over the whole Hertzsprung-Russell diagram at the R$\sim$ 100000 resolving power achievable with the CRIRES spectrometer on the ESO VLT. Stellar spectra are observed at all wavelengths that are not heavily absorbed by the Earth's atmosphere. The library will be made publicly available.

1.1 Science goals of CRIRES-POP

Here we highlight some of the particular science interests and goals of the team working on the project. The identification of molecules in cool stellar atmospheres via their NIR transitions is a major aim of CRIRES-POP. Transitions of either oxygen-bearing molecules (H_2O, SiO) or carbon-bearing molecules (CN-, CH-, C_2-compounds and of course CO, CO_2) will be seen depending on the chemistry of the target. Objects enriched in s-process elements offer a unique opportunity to identify lines of these interesting elements and also of iron-peak elements whose line lists are far from complete in the NIR. We anticipate the identification of new diagnostic features of stellar atmospheres, which will be developed using the CRIRES-POP spectral library through collaboration between the observational astronomers and laboratory spectroscopists in our team.

The spectra of cool stars obtained will also be used to help optimise future exo-planet studies. Nearby M dwarfs are one target sample for searching for planets; the first successful results were recently published (Bean et al. 2010). These low mass stars are potentially good candidates for planet searches using the radial velocity method, as the reflex motion of the star due to a planet is comparatively large, and the NIR wavelength range is potentially optimal as these cool stars are brightest at these wavelengths. However, fully understanding the effectiveness of this approach compared with ongoing searches at optical wavelengths is limited, in part, by a lack of information on the detailed NIR spectrum. A detailed analysis of this and other factors affecting these studies is given in Reiners et al. (2010).

Studies of circumstellar matter in general are expected to benefit from a better understanding of stellar spectra. Systematic errors due to the signature of the stellar atmosphere can effect the accuracy of the results obtained, for example when observing gas emission lines in circumstellar disks. Ramsay Howat & Greaves (2007) published a velocity-resolved emission line spectrum of H_2 from the M3 giant ECHAJ0843.3-7905 from which the stellar continuum was removed. This increased the measured H_2 line flux by 10% with a corresponding effect on the estimated gas mass in the disk. By providing a set of template spectra over different spectral types, such techniques may be

Table 1: Targets observed and pending.

name	Classification	vsini (kms^{-1})	J	H	K	L	M
τ Sco	B0.2V	$\sim$4	+3.30	+3.50	+3.60	+3.6	+3.7
3 Cen A	B5IIIp	2	+4.9	+4.95	+4.97		
e Vel	A6II	6$\pm$1	+3.80	+3.66	+3.60	$\sim$3.5	$\sim$3.4
γ Gem	A0IV	10	+1.73	+1.84	+1.92	+2.06	+1.88
HD 118022	A1 P	10$\pm$1	+5.19	+4.98	+4.88	+4.89	+4.93
LHS 1515	F8IV	5$\pm$1	+2.80	+2.32	+2.40	+2.3	+2.4
τ Leo	G8Iab	4	+3.49	+2.95	+2.83		
HD109379	G5II	6$\pm$1	+1.20	+0.80	+0.70	+0.70	+0.80
HD225212	K3Iab	8	+2.27	+1.61	+1.40		
HD83240	K1III	1$\pm$2	+3.36	+2.80	+2.66	+2.5	+2.6
HD49331	M1I	$\sim$9	+1.70	+0.80	+0.60	+0.40	+0.30
YY Psc	M3III	4$\pm$1	+0.70	-0.25	-0.50	-0.7	-0.5
Barnard's star	M4V	$<$3	+5.24	+4.83	+4.52	+4.2	
X TrA	C5	0$\pm$?	+1.0	-0.0	-0.6	-1.2	-0.8
NZ Gem	S	?	+1.59	+0.64	+0.56		+0.80

more widely used to improve the accuracy of high resolution spectroscopic analyses.

Testing and improving model atmospheres across the complete HRD is one of the goals of CRIRES-POP team members. For hotter stars in particular, the extrapolation of models from the optical to NIR is non-trivial due to the increasing importance of non-local-thermodynamic-equilibirium effects. Only recently has significant progress been made in obtaining a consistent model of the simplest atom, hydrogen, from the optical to the NIR (Przybilla & Butler 2004).

2 Target selection and strategy

At optical wavelengths, the UVES-POP spectral library has been an invaluable resource (Bagnulo et al. 2003). The target list from this programme was therefore used as the starting point when selecting CRIRES-POP sources, so that ultimately the spectrum from $\sim$0.3-5μm will be available for certain stars. CRIRES is a single-order spectrometer (Käufl et al. 2004), therefore we require $\sim$200 grating settings and 10–20 hours per target for our observations. The scope of the programme was set to around 25-30 targets, which provides reasonable coverage of the HR diagram. Table 1 gives details of the targets selected for which observations have been obtained or are scheduled. Stars are selected only if they are slow rotators so that the intrinsic spectrum without rotational broadening is obtained. The CRIRES-POP observations do not require any strong constraints on atmospheric conditions, making it very suitable for execution in service mode and in below average weather conditions.

3 Data reduction and analysis

A strength of the proposed library will be a common data reduction for all spectra. The data are being reduced using the CRIRES data-reduction pipeline. This produces individual spectra for each grating setting. Example spectra of the M3 giant YY Psc in the K and M bands are shown in Figures 1 and 2 respectively. The K band spectrum is centred around the CO Δv = 2–0 overtone bandhead which is seen in great detail and which dominates the spectrum at these wavelengths. In the M band, CO is

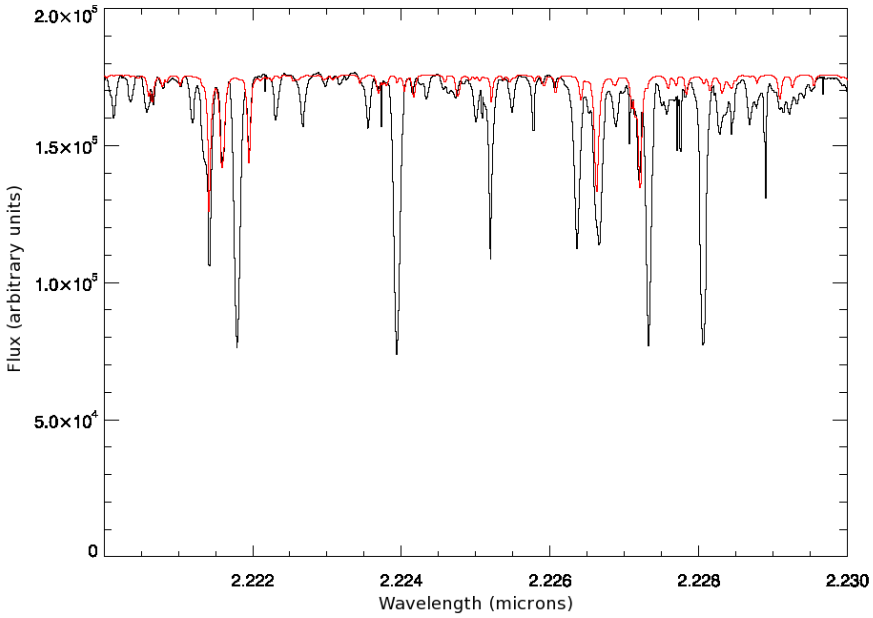

Figure 1: The M3 giant YY Psc in the K band. The star spectrum is in black; the telluric model in red.

also one of the main constituents; isotopic lines of $^{13}C^{16}O$ and $^{12}C^{18}O$ are also detected with a high signal-to-noise ratio. Subsequent to this, the individual spectra will be combined into the complete 0.97–5.26μm spectrum using IDL routines developed by the CRIRES-POP team. This approach was previously successfully used to reduce CRIRES data from single setting observations (Seifahrt & Käufl 2008) and for a more automated approach to the homogeneous reduction of wide wavelength scans (Nieva et al. 2009; Przybilla et al. 2009). An important step is the removal of the telluric absorption lines which are prevalent in the stellar spectra. Standard practice for NIR spectroscopy is to obtain a very high quality spectrum of a spectrally featureless standard star at similiar airmass and close in time to the target. Then the target spectrum is ratioed by the standard star spectrum with the aim of cancelling the telluric absorption lines. This is imperfect - changes in the depth of the telluric lines and the presence of features in the standard star spectrum introduce systematic errors in the target spectrum. At high spectral resolution, obtaining a spectrum of sufficient signal-to-noise that does not degrade the target spectrum can add a substantial overhead. An alternative is to fit and remove the telluric emission features using a model of the Earth's atmosphere. The CRIRES-POP spectra will be used to calibrate these models and then the technique will be used to correct for telluric features in the remainder of the library. Further details can be found in Seifahrt et al. (2010). Also shown with the YY Psc spectra in Figures 1 and 2 is a first attempt to fit a model to the telluric lines.

4 Status

In the first two periods of observations on the VLT, starting in October 2009, 1-5μm data have been obtained of YY Psc, LHS1515, e Vel and HD 83240. At time of writing, partial spectra of τ Sco, X Tra, HD 118022, Barndard's Star and HD 109379 are also available. The raw data are available from the ESO archive immediately (Programme ID 084.D-0912(A)). After a quality check of the pipeline reduced data, they are made available on the CRIRES-POP website: http://www.univie.ac.at/crirespop/. Please reference Lebzelter et al. (2010) when using the data.

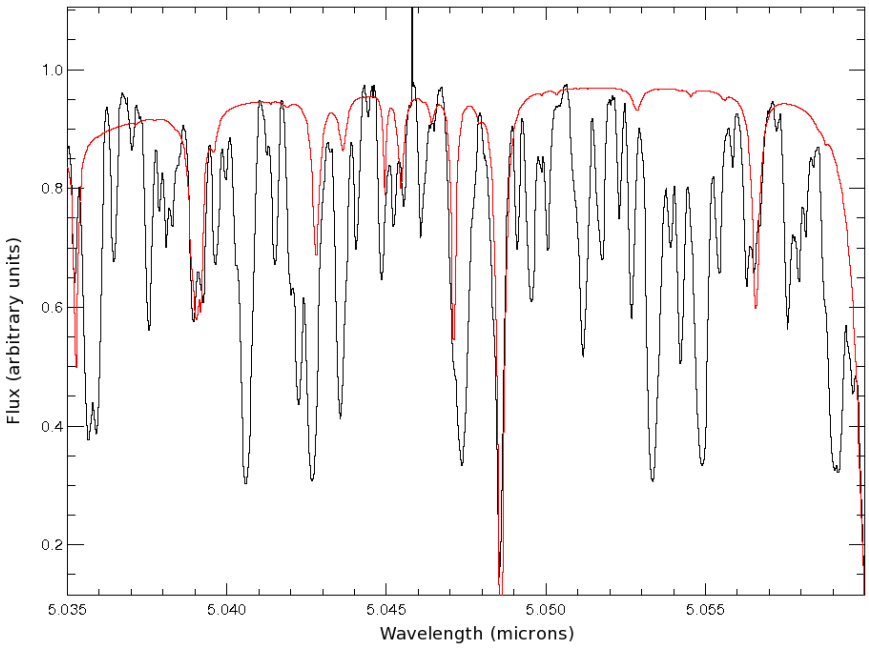

Figure 2: The M3 giant YY Psc in the M band. The star spectrum is in black; the telluric model in red.

Acknowledgements

TL acknowledges support by the Austrian Science Fund FWF under project number P20046-N16. This publication makes use of data products from 2MASS, which is a joint project of the University of Massachusetts and IPAC/CIT, funded by NASA and NSF.

References

Bagnulo, S., Jehin, E., Ledoux, C., Cabanac, R., Melo, C., Gilmozzi, R., & The ESO Paranal Sc. Op. Team 2003, The Messenger, 114, 10

Bean, J. L., Seifahrt, A., Hartman, H., Nilsson, H. Wiedemann, G., Reiners, A., Dreizler, S., & Henry, T. J. 2010, ApJ, 713, 410

Delbouille, L., Roland, G., & Neven, L. 1973, Atlas photometrique du spectre solaire de λ 3000 à λ 10000Å, Liège: Université de Liège – Institut d'Astrophysique.

Farmer, C. B., Delbouille, L., Roland, C., & Servais, C. 1995, Lab. and Astr. High Res. Spectra, 81, 39

Hinkle, K., Wallace, L., & Livingston, W. C., 1995, IR Atlas of the Arcturus Spectrum, 0.9–5.3microns (ASP)

Lebzelter, T., Seifahrt, A., Ramsay, S., et al., 2010, Messenger, 139, 33

Käufl, H.U., Ballester, P., Biereichel, P., et al., 2004, SPIE, 5492, 1218

Nieva, M. F., Przybilla, N., Seifahrt, A., Butler, K., Käufl, H. U. & Kaufer, A., 2009, in "Science with the VLT in the ELT Era", ed. Moorwood, A., 499.

Przybilla, N., Seifahrt, A., Butler, K., Nieva, M. F., Käufl, H. U. & Kaufer, A., 2009, in "Science with the VLT in the ELT Era", ed. Moorwood, A., 55

Przybilla, N. & Butler, K. 2004, ApJ, 610, L61

Ramsay Howat, S. K. & Greaves, J.S., 2007, MNRAS, 379, 1658

Rayner, J., Cushing, M. & Vacca, W. D., 2009, ApJS, 185, 289

Reiners, A., Bean, J. L., Huber, K. F., Dreizler, S., Seifahrt, A. & Czesla, S., 2010, ApJ, 713, 432.

Seifahrt, A. & Käufl, H. U., 2008, A&A, 491, 929

Seifahrt, A., Käufl, H. U., Zängl, G., Bean, J. L., Richter, M. J., & Siebenmorgen, R. 2010, A&A, 524, A11

Wallace, L., Livingston, W., Hinkle, K. & Bernath, P., 1996, ApJS, 106, 165

Wallace, L. & Hinkle, K., 1996, ApJS 107, 312

The IACOB spectroscopic database of Northern Galactic OB stars

S. Simón-Díaz[1,2], N. Castro[1,2], M. Garcia[1,2], A. Herrero[1,2] and N. Markova[3]

[1] Instituto de Astrofísica de Canarias, E-38200 La Laguna, Tenerife, Spain.
[2] Departamento de Astrofísica, Universidad de La Laguna, E-38205 La Laguna, Tenerife, Spain
[3] Institute of Astronomy with NAO, BAS, P.O. Box 136, 4700 Smolyan, Bulgaria

Abstract: We present the IACOB spectroscopic database, an homogeneous set of high quality, high resolution spectra of Galactic O- and B-type stars obtained with the FIES spectrograph attached to the Nordic Optical Telescope. We also present some results from ongoing projects using the IACOB database.

1 Introduction

In an epoch in which we count on a new powerful generation of stellar atmopshere codes that include most of the relevant physics for the modelling of massive OB stars, with (clusters of) high efficiency computers allowing the computation of large grids of stellar models in more than reasonable computational times, and with the possibility to obtain good quality, medium resolution spectra of hundreds O and B-type stars in clusters outside the Milky way in just one snapshot (see e.g. the *FLAMES I & II Surveys of Massive Stars*, Evans et al. 2008, 2010), the compilation of medium and high-resolution spectroscopic databases of OB stars in our Galaxy is becoming more and more important. With this idea in mind, two years ago we began to compile the IACOB spectroscopic database, aiming at constructing the largest database of multiepoch, high resolution, high signal-to-noise ratio (S/N) spectra of Galactic Northern OB-type stars. The IACOB database perfectly complements the efforts also devoted in the last years by the GOSSS (P.I. Maíz-Apellaniz; see also Sota et al. 2011) and the OWN (P.I's Barbá & Gamen, leading a multi-epoch, high-resolution spectroscopic survey of Galactic O and WR stars in the Southern hemisphere; see Barbá et al. 2010) teams.

1.1 Characteristics of the IACOB database and present status

We are using the FIES spectrograph[1] at the 2.56 m Nordic Optical Telescope (NOT) in the Roque de los Muchachos observatory (La Palma, Spain) to compile spectra for the IACOB database. A summary of the instrumental configuration and observing dates (before Sept. 2010) is presented in Table 1. Spectra of $\sim$100 stars with spectral types earlier than B2 and luminosity classes ranging from I (supergiants) to V (dwarfs) have already been compiled. The O-type targets were selected from the

[1] Detailed information about the NOT and FIES can be found in http://www.not.iac.es

Table 1: General characteristics of the IACOB v1.0 spectroscopic database.

Instrumental configuration		Observing run & Dates	
Telesc.: NOT2.56 m	Spect. range: 3800 - 7000 Å	08 A-D: 2008/11/05-08,	10 D: 2010/06/22
Instr.: FIES	Res. power: 46000	09 A-D: 2009/11/09-12,	10 E: 2010/07/15
Fiber: med-res	Sampling: 0.03 Å/pix	10 A-C: 2010/06/05-07,	10 F: 2010/08/07
Spectral types: O4-B2 (I-V)		# stars: 105	# spectra: 720

GOS catalogue (GOSC, Maíz-Apellániz et al. 2004). The main part of the B-type stars sample corresponds to the work presented in Simón-Díaz (2010) and Simón-Díaz et al. (2010). The final spectra usually have S/N $\geq$ 200.

In Fig. 1 we present some examples of spectra in the IACOB database and studies that can be performed with them.

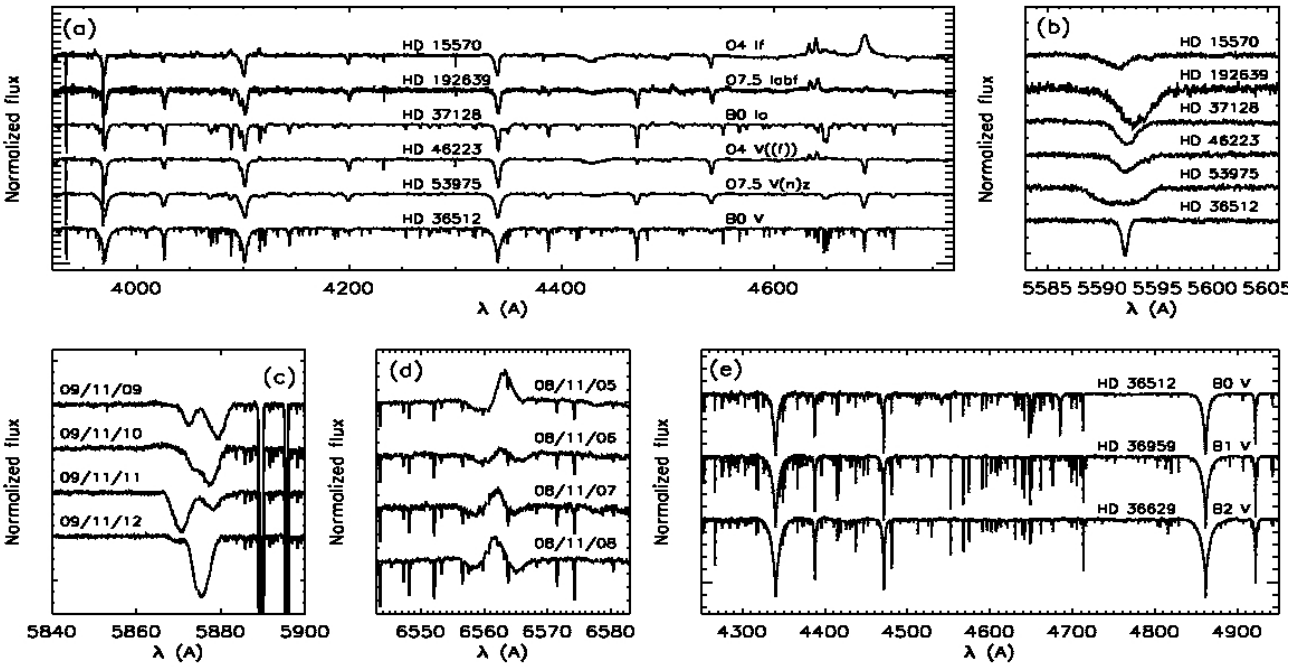

Figure 1: Illustrative examples of studies that can be performed using spectra from the IACOB database. (a) Spectra of a selected sample of MK standard stars centered in the spectral region usually considered for the spectral classifications; (b) same stars in the region where the O III 5592 line is located; this line is well suited to characterize the rotational and macroturbulent broadening in O-type stars, where the Si III 4552 line is no longer available; (c) HD 1337, a double spectroscopic binary, observed in four consecutive nights; (d) HD 37128, a B0 Ia star in which strong variability in the Hα line has been detected; this star is one of the selected targets for the investigation of the macroturbulent broadening-pulsation connection in B supergiants (Simón-Díaz et al. 2010); (e) Three narrow lined B-type stars from the Ori OB1 association, used in the reinvestigation of the chemical composition of young stars in the Orion star forming region (Simón-Díaz 2010).

2 Some ongoing projects using the IACOB spectroscopic database

2.1 Rotational velocities and macroturbulent broadening in OB stars

We used the FT method (viz Gray 1976; see also Simón-Díaz & Herrero 2007, for a recent application to OB stars) to disentangle the rotational and macroturbulent broadening and estimate their values in the whole sample of stars (see Fig. 2). This analysis has allowed us to confirm for the first time in a systematic way the presence of an important non-rotational broadening in O-stars of all luminosity classes. If this effect is not taken into account, it can significantly affect our $v \sin i$ measurements. The origin of this broadening is still not clear and presently under study (see below).

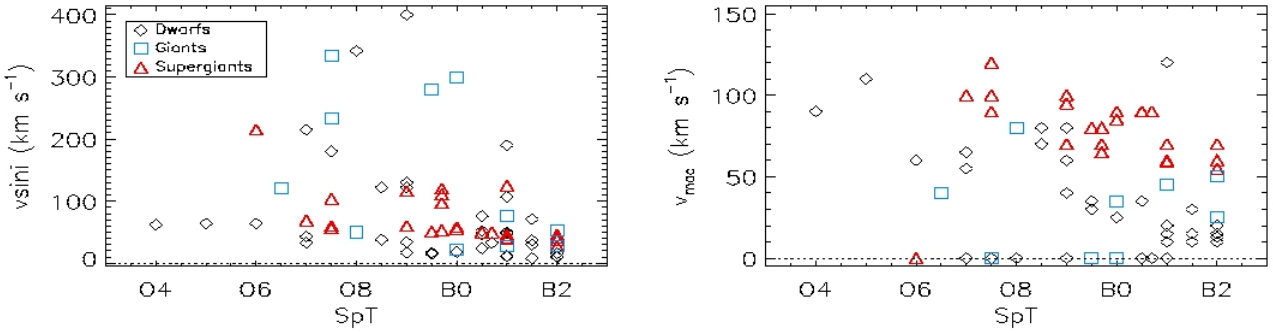

Figure 2: Rotational and macroturbulent velocities measured in the IACOB spectra. Double lined spectra were discarded. Not only the B Supergiants, but also the O-type stars show an important macroturbulent broadening. The increasing trend of $v_{\rm mac}$ with spectral type, previously found for B Supergiants (e.g. Fraser et al. 2010, and references therein), is continued in the O star domain. Note also the increasing trend of $v_{\rm mac}$ with luminosity class for a given spectral type.

2.2 Is macroturbulent broadening in OB stars related to pulsations?

Part of the IACOB database consists of spectroscopic time series of 13 early-B Sgs (+ 2 early-B dwarfs and 2 late-B Sgs). These observations were obtained to investigate the origin of the macroturbulent broadening in OB stars and its possible relation to spectroscopic variability phenomena and stellar pulsations. First results show a tight correlation between the size of macroturbulent broadening and the line-profile variations present in all the early B-Sgs. More details about this investigation can be found in Simón-Díaz et al. (2010), and in Simón-Díaz (2011).

2.3 Increasing the statistics of OB stars with reliable determined stellar & wind parameters

One of the main aims driving the compilation of the IACOB spectroscopic database is to perform a homogenous quantitative spectroscopic analysis of a statistically representative sample of high-resolution, high quality spectra of stars with spectral types ranging from O4 to B2. By means of these data we plan to refine the temperature calibration of Galactic O-type stars and to address important questions such as, e.g. the weak wind problem, the mass discrepancy, etc. The spectra will be analysed using the stellar atmopshere code FASTWIND (Puls et al. 2005), which allows us to create large grids of reliable spherical, NLTE, line blanketed models with winds for O and B stars of all luminosity classes in reasonable computational time-scales. Two examples of results from preliminar analyses of the single lined objects from the IACOB database are presented in Figs 3 and 4. Our

first results indicate important discrepancies with previous SpT - $T_{\rm eff}$ calibrations (Fig. 4). We are investigating the cause of these differences.

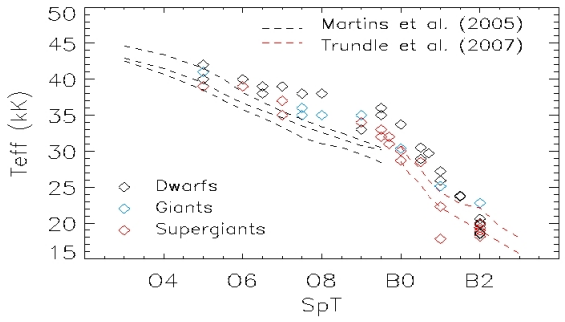

Figure 3: A homogeneous quantitative analysis of the IACOB spectra, accounting for binarity/multiplicity, will help to better define the SpT - $T_{\rm eff}$ calibrations in the O to early-B star domain. Results from the preliminary analyses with FASTWIND, and comparison with two published calibrations.

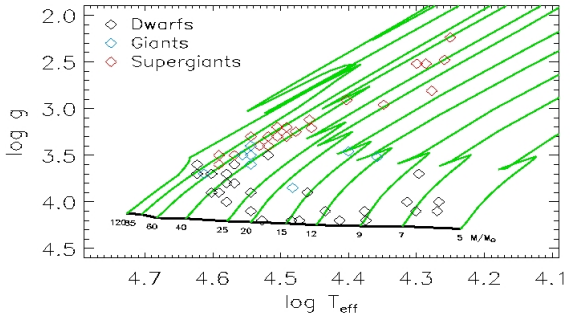

Figure 4: Position of the analyzed stars in the ($\log g$, $\log T_{\rm eff}$) diagram, along with the ZAMS (black, solid line) and evolutionary tracks from Schaller et al. (1992) for stellar masses between 5 and 120 $M_\odot$ (green lines). Our analyses can help to better uncerstand the mass discrepancy problem.

A similar analysis is in progress within the *FLAMES-II Survey of Massive Stars: The Tarantula survey* consortium (P.I. C. Evans). Around 1000 OB stars in 30 Dor will be analyzed to derive their rotational velocities, stellar and wind parameters, and N abundances. The comparison of results from the two samples of stars (born in environments with different metalicity) will be of great importance for our understanding of the physical properties and evolution of massive stars.

2.4 Homogeneity of O and Si abundances in B-type stars in Ori OB1

In Simón-Díaz (2010), we used FASTWIND to perform a self-consistent spectroscopic analysis of a sample of 13 early B-type stars from the Ori OB1 association observed with FIES@NOT. Main results of this study, as part of a series of papers grouped under the title *The chemical composition of the Orion star forming region: stars, gas, and dust* can be found in Simón-Díaz et al. (2011).

2.5 And more ...

- A subsample of spectra from the IACOB (along with UVES and FEROS spectra from the ESO archive) have been recently used within the *FLAMES-II Survey of Massive Stars: The Tarantula survey* consortium to create a template atlas for spectral classification of medium and high resolution spectra of early type stars.

- Following ideas first presented in Markova et al. (2010), the IACOB database will be used (i) to investigate third parameter effects in the classification scheme developed by Walborn and co-authors to type O-stars and (ii) to recalibrate the logarithmic EW ratios underlaying the Conti classification scheme.

- We plan to use some of the IACOB spectra to analyze the feasibility of wavelet filtering to improve the signal-to-noise ratio and, based on the sparsity of the spectra in the wavelet domain, to envision the possibility to do superresolution resting on the compressed sensing theory (Asensio Ramos & López Ariste, 2010).

3 Future of the IACOB

In the next semesters[2], we will continue with the compilation of spectra for the IACOB, observing stars with V$\leq$8 in at least three epochs (more in the case of known or newly detected binaries). Our idea is to make the database public via the Virtual Observatory in the next year. In the meantime, interested people can have access to the database under request to the author (ssimon@iac.es). The complete list of stars will be published in Simón-Díaz et al., in prep.. We will acknowledge any observer who having obtained FIES spectra will like to add the spectra to the IACOB database after scientific exploitation.

Acknowledgements

SSD, NC, MG and AH acknowledge financial support by the Spanish MICINN (AYA2008-06166-C03-01 CSD2006- 00070). NM acknowledge financial support by the IAC and the Bulgarian NSF (DO02-85). We would like to also thank the NOT people for their efficiency and kindness. SSD kindly thanks K. Uytterhoeven, J. Puls, C. Aerts, F. Nieva, and N. Przybilla for their collaboration in some of the studies already published which made use of spectra from the IACOB database.

References

Aerts, C., Puls, J., Godart, M., & Dupret, M.-A., 2009, A&A, 508, 409
Asensio Ramos & López Ariste, 2010, A&A, 509, 49
Barbá, R. H., Gamen, R., Arias, J. I., Morrell, N., Maíz Apellániz, J., Alfaro, E., & Walborn, N., 2010, RMxAC, 38, 30
Evans, C. J., Bastian, N., Beletsky, Y., et al., 2010, *IAU Symposium*, 266, 35
Evans, C. J., Hunter, I., Smartt, S., et al., 2008, *The Messenger*, 131, 25
Fraser, M., Dufton, P. L., Hunter, I., & Ryans, R. S. I., 2010, MNRAS, 404, 1306
Gray, D. F. 1976, *The Observations and Analysis of Stellar Photospheres* (1st ed., New York: Wiley)
Markova, N., Puls, J., Scuderi, S., et al., A&A, submitted
Martins, F., Schaerer, D., & Hillier, D. J., 2005, A&A, 436, 1049
Maíz-Apellániz, J., Walborn, N. R., Galué, H. A.., & Wei, L. H., 2004, ApJS, 151, 103
Puls, J., Urbaneja, M. A., Venero, R., Repolust, T., Springmann, U., Jokuthy, A., & Mokiem, M. R., 2005, A&A, 435, 669
Schaller, G., Schaerer, D., Meynet, G., & Maeder, A. 1992, A&AS, 96, 269
Simón-Díaz , 2010, A&A, 510, 22
Simón-Díaz, S. 2011, in Proceedings of the 39th Liège Astrophysical Colloquium, eds. G. Rauw, M. De Becker, Y. Nazé, J.-M. Vreux & P. Williams, BSRSL, 80, 86
Simón-Díaz & Herrero, 2007, A&A, 468, 1063
Simón-Díaz, S., Herrero, A., Uytterhoeven, K., Castro, N., Aerts, C., & Puls, J., 2010, ApJL, 720, 174
Simón-Díaz, S., Nieva, M.F., Przybilla, N., & Stasińska, G. 2011, in Proceedings of the 39th Liège Astrophysical Colloquium, eds. G. Rauw, M. De Becker, Y. Nazé, J.-M. Vreux & P. Williams, BSRSL, 80, 255
Sota, A., Maíz Apellániz, J., Barbá, R.H., et al. 2011, in Proceedings of the 39th Liège Astrophysical Colloquium, eds. G. Rauw, M. De Becker, Y. Nazé, J.-M. Vreux & P. Williams, BSRSL, 80, 519
Trundle, C., Dufton, P. L., Hunter, I., Evans, C. J., Lennon, D. J., Smartt, S. J., & Ryans, R. S. I., 2007, A&A, 471, 625

[2]The number of observed stars has already increased to $\sim$ 140 between Sept. 2010 and the date of submission of this contribution

The Galactic O-Star Spectral Survey (GOSSS) Project status and first results

Alfredo Sota[1], Jesús Maíz Apellániz[1], Rodolfo H. Barbá[2], Nolan R. Walborn[3], Emilio J. Alfaro[1], Roberto C. Gamen[4], Nidia I. Morrell[5], Julia I. Arias[2] and Miguel Penadés Ordaz[1]

[1] Instituto de Astrofísica de Andalucía-CSIC, Glorieta de la Astronomía s/n, 18008 Granada, Spain

[2] Departamento de Física, Universidad de La Serena, Benavente 980, La Serena, Chile

[3] Space Telescope Science Institute, 3700 San Martin Drive, Baltimore, MD 21218, USA

[4] Instituto de Astrofísica de La Plata-CONICET, Paseo del Bosque s/n, 1900 La Plata, Argentina

[5] Las Campanas Observatory, Observatories of the Carnegie Institution of Washington, La Serena, Chile

Abstract: The Galactic O-Star Spectroscopic Survey (GOSSS) is a project that is observing all known Galactic O stars with $B < 13$ ($\sim$2000 objects) in the blue-violet part of the spectrum with R$\sim$2500. It also includes two companion surveys (a spectroscopic one at R$\sim$1500 and a high resolution imaging one). It is based on v2.0 of the Galactic O star catalog (v1, Maíz-Apellániz et al. 2004; v2, Sota et al. 2008). We have completed the first part of the main project. Here we present results on the first 400 objects of the sample.

1 Description

The Northern part of the survey is being carried out from the Sierra Nevada and Calar Alto observatories (Spain) and the Southern part from Las Campanas (Chile). Although the data have been acquired at three different observatories, they have nearly identical characteristics: uniform and high signal to noise ratio (200-300), same spectral resolution (R $\sim$2500), and similar spectral coverage ($\sim$3900 to 5100 Å). To date, we have completed the first part of the project (observing the first 400 objects of the sample). The main objective is to publish a new Galactic O-Star Atlas as well as the spectrograms for all stars. Figures 1 and 2 show two atlas sheet with the same luminosity class and the same spectral type. We have also observed more than 300 objects from the second part of the project, a number that is increasing in current campaigns. For each star, we typically have two or more epochs. The survey will be used for a number of purposes, such as a precise determination of the IMF for massive stars, the measurement of radial velocities for Galactic kinematical studies, and the detection of unknown massive binaries. Results will be made available through a dedicated web server, will be incorporated into the Virtual Observatory, and will include the most complete spectral library of massive stars to date. A paper with the first $\sim$180 northern stars of the survey, including a new spectral classification atlas, will be presented by Sota et al. (2010, submitted to ApJS). Another paper with $\sim$200 southern stars will follow next year.

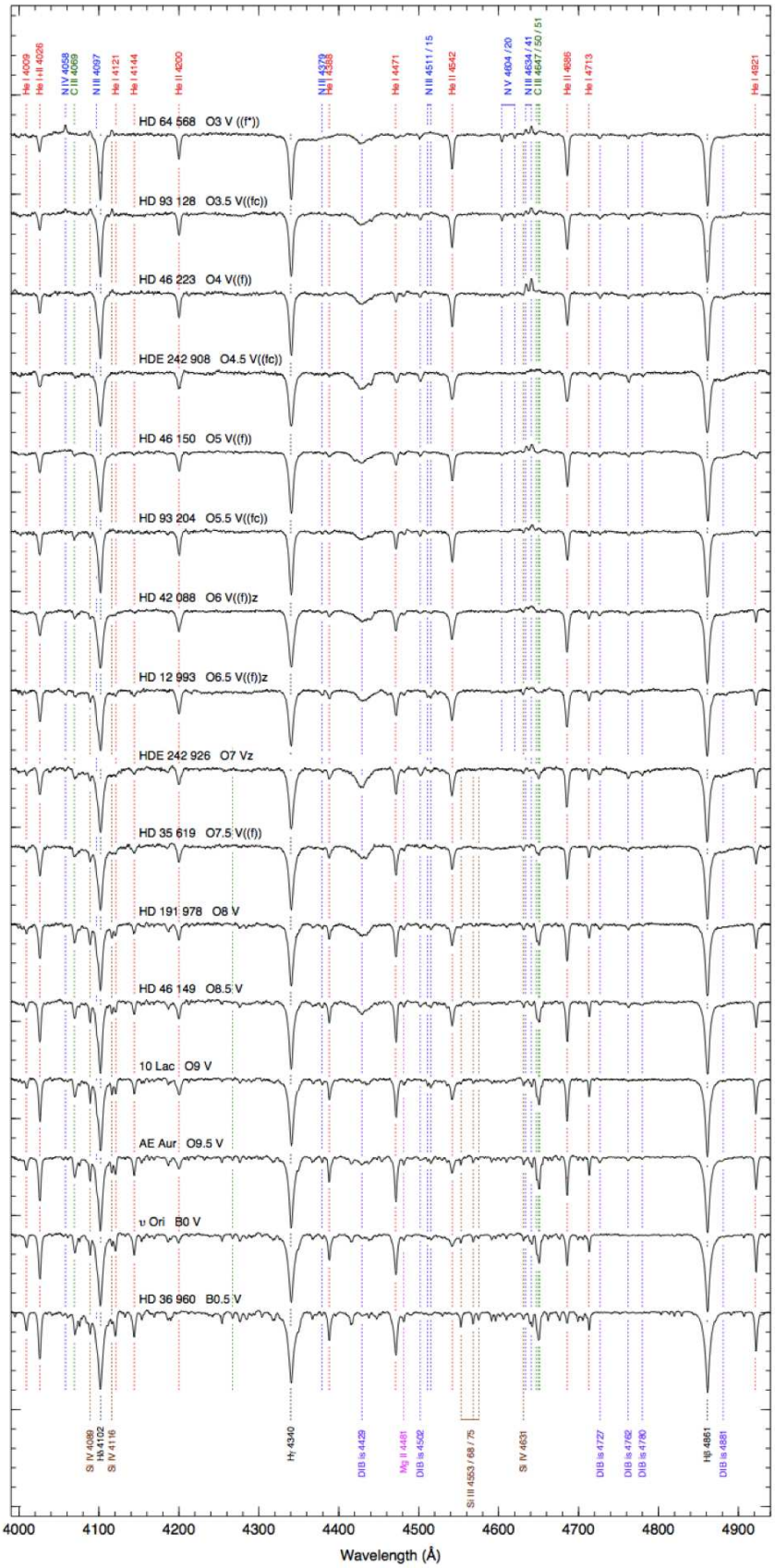

Figure 1: Spectrograms for luminosity class V of Galactic O stars.

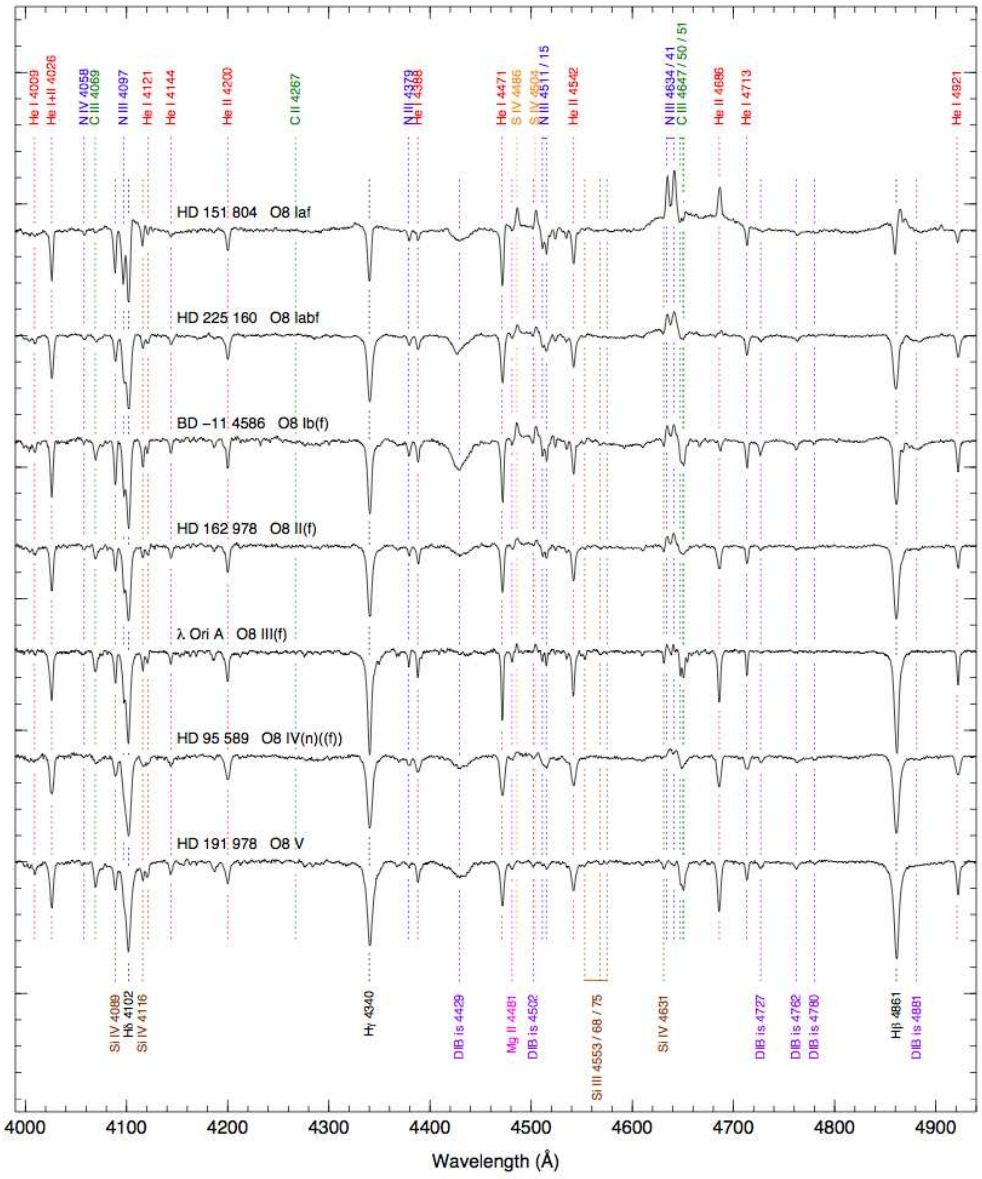

Figure 2: Luminosity effects at spectral type O8.

2 C III Emission Lines in Of Spectra

We introduce the Ofc category, which consists of normal spectra with C III $\lambda\lambda$4647-4650-4652 emission lines of comparable intensity to those of the Of defining lines N III $\lambda\lambda$4634-4640-4642 (Figure 3b). The former feature is strongly peaked to spectral type O5, at all luminosity classes, but preferentially in some associations or clusters and not others. This behavior contrasts with that of the selective C III λ5696 emission, which has a much wider spectral-type distribution. It is also distinct from that of the Of?p stars, which have C III $\lambda\lambda$4647-4650-4652 emission (localized to some particular region of the unknown circumstellar structures), but otherwise peculiar and variable spectra. Magnetic fields have recently been detected on three members of the latter category. We present two new extreme Of?p stars, NGC 1624-2 and CPD -28° 2561, bringing the number known in the Galaxy to five (Figure 3a). Modeling of the behavior of these spectral features can be expected to better define the physical parameters of both normal and peculiar objects, as well as the atomic physics involved (see Walborn, et al. 2010).

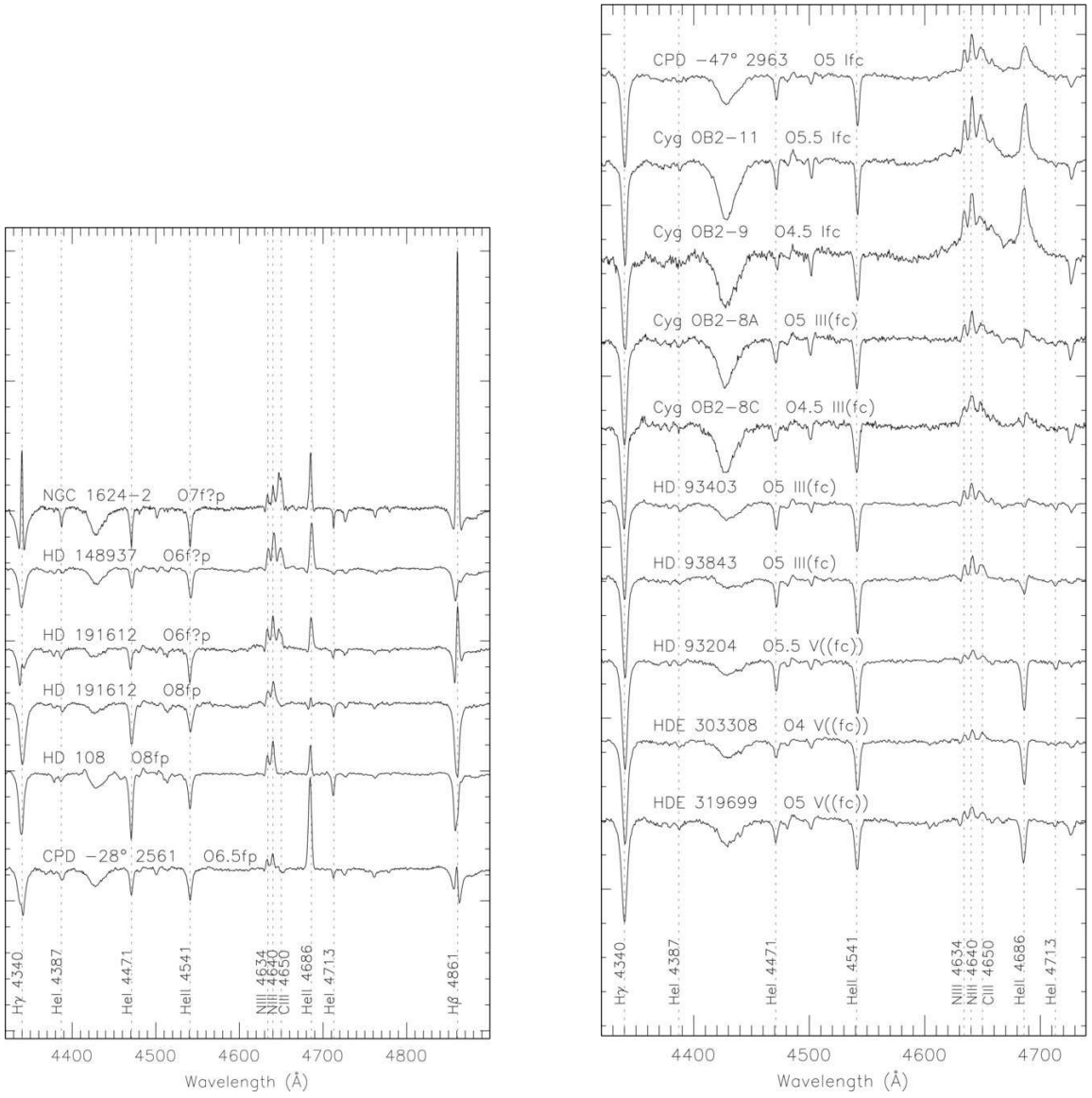

(a) (b)

Figure 3: a) Spectra of the Galactic Of?p stars in the blue-green region, and b) Luminosity sequence of Ofc spectra in the blue-green region.

3 Data Reduction

Due to the large amount of data that we are collecting, we have developed a pipeline for the automatic (quicklook) or semi-automatic (full) data reduction. In quicklook mode, we are able to get the rectified and calibrated spectrograms for all the stars that we have observed in a single night just in a few minutes after the observations. The pipeline can identify every kind of file and apply the standard reduction to the images (bias subtraction, flat-fielding, bad pixel mask, ...). It also extracts the spectrograms from the images (including close visual binaries; see Figure 4), aligns and combines all the spectrogram from the same star (to increase the signal to noise ratio and correct defects like cosmic rays), calibrates in wavelength and rectifies to the continuum. The same operations are performed in full mode with the user being able to tweak the files and parameters used.

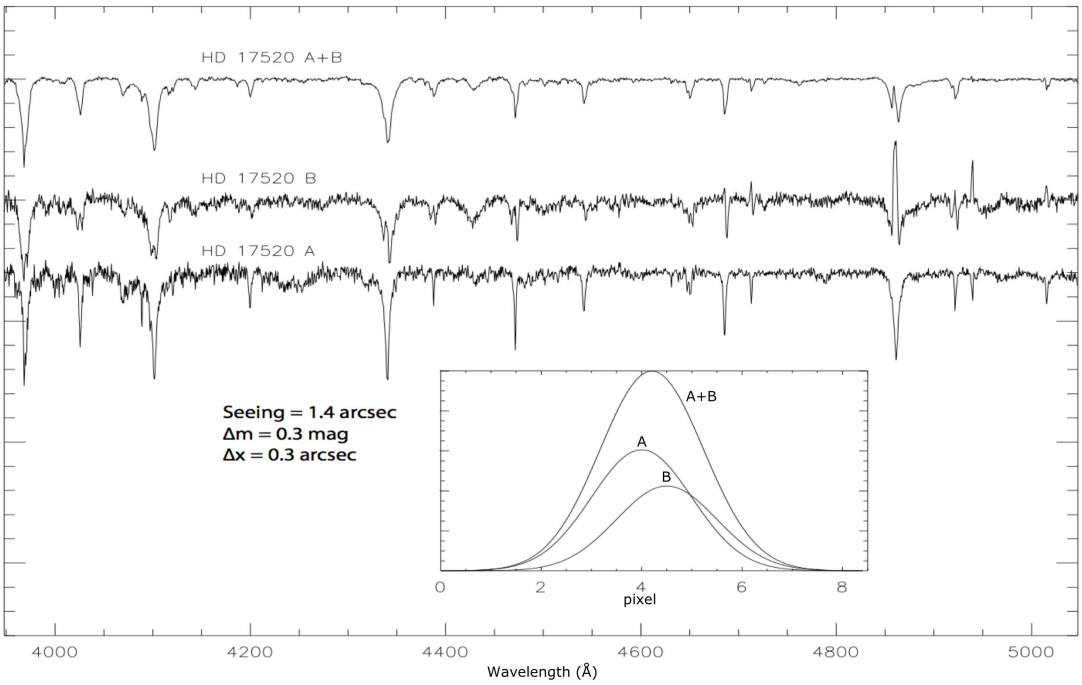

Figure 4: Example of disentangling. The visual binary HD 17520 A+B is separated by only 0.″3, a fraction of the seeing in this exposure. This is the most extreme case in our sample. We are able to disentangle the two pair components to show an O type spectrum and a Be type spectrum (pay attention to the emission lines in the Be star). The inner figure shows the spatial distribution of the combined spectra.

Acknowledgements

Support for this work was provided by [a] the Spanish Government Ministerio de Ciencia e Innovación through grants AYA2007-64052, the Ramón y Cajal Fellowship program, and FEDER funds; [b] the Junta de Andalucía grant P08-TIC-4075; and [c] NASA through grants GO-10205, GO-10602, and GO-10898 from the Space Telescope Science Institute, which is operated by the Association of Universities for Research in Astronomy Inc., under NASA contract NAS 5-26555.

References

Maíz-Apellániz, J., Walborn, N. R., Galué, H. Á., & Wei, Lisa H., 2004, ApJS, 151, 103

Sota, A., Maíz-Apellńiz, J., Walborn, N. R., & Shida, R. Y., 2008, RMxAC, 33, 56

Sota, A., Maíz-Apellániz, J., Walborn, N. R., Alfaro, E. J., Barbá, R. H., Morrell, N. I., Gamen, R. C., & Arias, J. I., 2010, (submitted to ApJS)

Walborn, N. R., Sota, A., Maíz-Apellániz, J., Alfaro, E. J., Morrell, N. I., Barbá, R. H., Arias, J. I., & Gamen, R. C., 2010, ApJ, 711, L143

The e-Merlin Cyg OB2 Radio Survey (COBRaS): Massive and Young Stars in the Galaxy

Allan Willis[1], Raman Prinja[1] and Danielle Fenech[1]

[1] Department of Physics and Astronomy, University College London, UK

Abstract: The e-Merlin Cyg OB2 Radio Survey (COBRaS) will provide targetted deep–field mapping of this extremely rich association in the Galaxy detecting at least 1000 sources. Inter-related core themes of the COBRaS programme include: (i) mass loss and evolution of massive stars, (ii) the formation, dynamics and content of massive OB associations, (iii) frequency of massive binaries and non-thermal radiation and (iv) ongoing and triggered star formation

1 The COBRaS SURVEY

The upcoming enhanced UK radio facility e-Merlin will provide greatly increased sensitivity (about 3 micro-Jy) and high spatial reolution (milli-arcsec) observations at 5 GHz (C-band) and 1.6 GHz (L-band) with bandwiths of 2 GHz and 0.4 GHz respectively. More details of the e-Merlin facility and the COBRaS programme can be found on the website www.homepage.ucl.ac.uk/ ucapwi/cobras. The large bandwidths and size of the e-Merlin network provide for a greatly increased sensitivity over previous radio surveys (eg VLA) which will allow for a huge increase in the numbers of early-type, massive stars with actual radio flux measurements. We are planning a major survey of the tremendously rich Cyg OB2 association using targetted, deep-field mapping of this region to deliver the most detailed radio census for the most massive OB association in the northern hemisphere, offering direct comparison to not only young massive clusters in general, but also young globular clusters and super star clusters. We have been allocated 242 hours at C-band and 42 hours at L-band to conduct this e-Merlin legacy programme, allowing for about 100 pointings at 5 GHz and 20 pointings at 1.6 GHz. We estimate that at least 1000 sources will be detected which will complement other, multi-wavelength surveys of the Cyg-X region (IPHAS, Spitzer, Chandra and JWST). An outline of the major science programmes that will be addressed using this new dataset is given below.

2 Massive Stars: mass loss rates

The mass loss rates for OB (and WR) stars are currently in question at the order of magnitude level (see Fig. 1, Fullerton, Massa & Prinja 2006) with profound implications for stellar evolution, mass loss processes across the HR diagram, and the injection of energy and enriched gas into the ISM. The recognition of clumped and/or porous radiation-driven stellar winds has led to reduced mass loss rate estimates from spectroscopic UV and optical data compared to inferences from past (and very

limited) radio observations. To produce WR stars and neutron stars we may be forced to appeal to episodic mass loss perhaps through numerous LBV stages (eg. Smith & Owocki 2006) rather than continual stellar winds, with major differences in the nature of the energy and enriched gas injected into the ISM.

Radio free-free fluxes from massive stars occur at large radii in the winds where the terminal velocity has been reached and their interpretation is not strongly dependent on details of the velocity law, ionisation conditions, inner velocity field of the photospheric profile etc., which complicates the interpretation of UV P-Cygni profile and H-alpha data. However, the greater geometric region in the radio and density-squared dependence of the free-free flux makes radio data extremely sensitive to clumping in the wind. Thus radio data can be used to constrain wind-clumping and, coupled with H-alpha, near-IR and mm-wave data we can determine the run of clumping as a function of geometrical region in the wind for individual stars.

Based on 2MASS data (Knödlseder 2000) Cyg OB2 contains about 120 O stars and 2600 B stars. We expect the COBRaS survey to increase the number of OB stars detected in the radio by about a factor of 50, including radio mass loss rates for low luminosity stars for the first time. It is anticipated that over 100 OB stars will be detected with sufficient quality to obtain estimates of their mass loss rates. Our e-Merlin data will permit us to: (i) understand how clumping changes as a function of radial distance in the wind, thus providing reliable mass loss rates, (ii) study for the first time how clumping changes as a function of effective temperature, luminosity and rotation in superiants, giants and main-sequence stars. The high quality of the imaging capabilities of e-Merlin will match the 50 mas angular scales marked by the radio "photospheres" of massive stars, which will yield direct evidence of large scale wind structures for OB stars and later evolution stages like LBV and red supregiants.

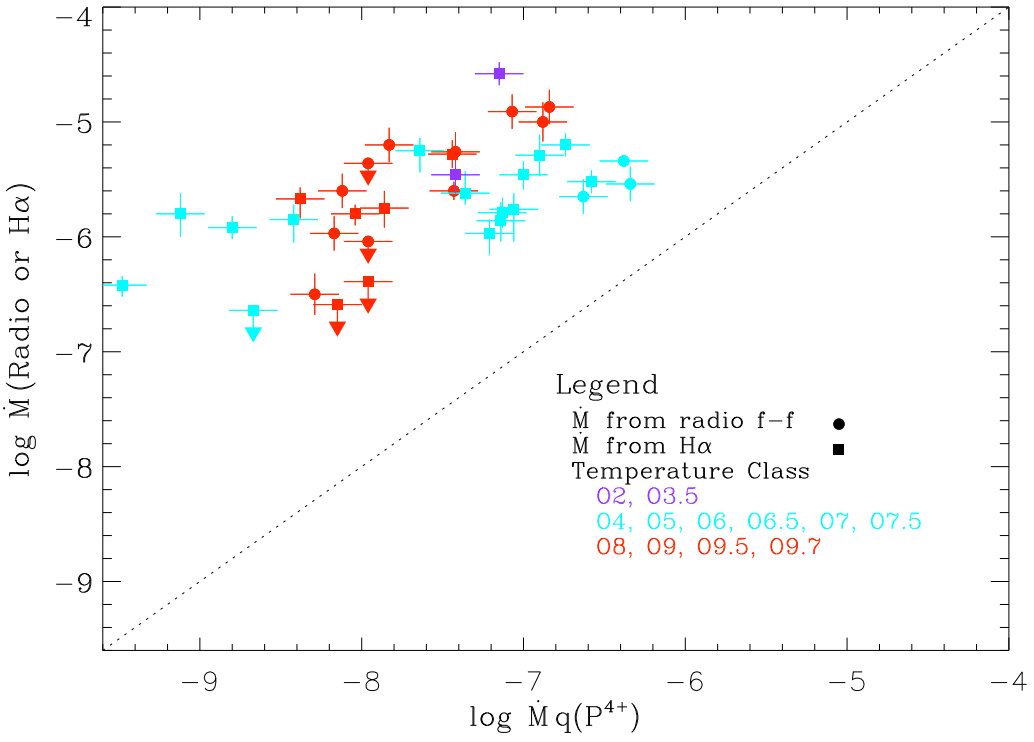

Figure 1: Radio vs. UV mass loss rates for O stars.

3 Cluster Dynamics

We will use e-Merlin to secure milliarcsec accuracy astrometric observations of radio stars in Cyg OB2 at multiple epochs to determine proper motions. Coupled with optical radial velocities this will provide a full 3–D picture of the kinematics of the Cyg OB2 association, its IMF and total mass, and constrain models of cluster formation, together with the star formation history of the region. As part of our consortium we have an ongoing programme of high resolution spectroscopic observations of the massive stellar populations within Cyg OB2 to identify and characterise massive binaries, which provide radial velocity measurements of comparable accuracy. Taken together, these complementary datasets will allow a full 3D picture of the kinematics of Cyg OB2 to be constructed.

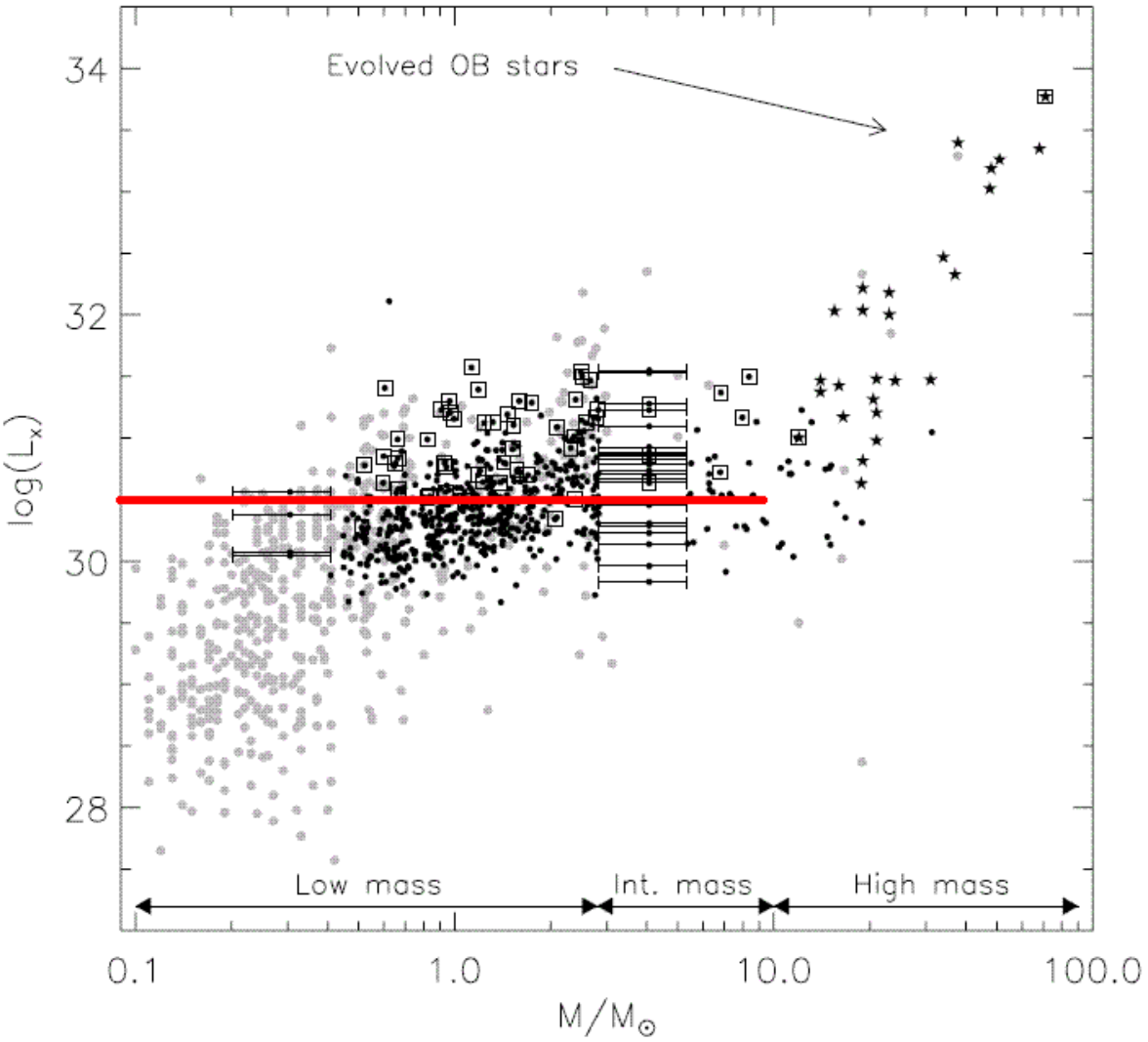

Figure 2: X-ray luminosity vs. Mass for the core of Cyg OB2. The red line is the 3 sigma e-Merlin detection limit.

4 Binarity and non-thermal radiation

In a early-type binary system (e.g. O+O) the two stellar winds collide and electrons are accelerated to relativistic velocities around the shocks in the colliding-wind region. The resulting emission of

synchrotron radiation can be detected at radio wavelengths (Dougherty & Williams 2000), with a characteristic non-thermal radio spectral index. Although at present only a fraction of early-type binaries are quoted as non-thermal radio emitters (De Becker 2007, Benaglia 2010), the COBRaS survey will provide a deeper and more accurate census of the radio emission from massive binaries and provide valuable information on the frequency of non-thermal radio emission amongst colliding-wind binaries which is poorly constrained at present. The broad bandwith of the 5 GHz data will allow us to discriminate between thermal and non-thermal sources and thus identify likely colliding wind binary systems and constrain binary statistics. The e-Merlin data from this project will allow us to: (i) provide a better determined binary frequency in Cyg OB2 which is an important constraint for evolutionary population synthesis models, and hence have a broad impact on our understanding of galactic chemical evolution, (ii) study statistically the colliding-wind phenomenon and better understand its dependence on stellar and binary parameters, and (iii) improve our understanding of the first-order Fermi mechanism responsible for particle acceleration.

5 On-going and Triggered star formation

Until now most pre-main sequence T Tauri ($\sim$ 1 solar mass) and their intermediate ($\sim$ 2-10 solar mass) Herbig Ae/Be counterparts have been found in relatively isolated star-forming regions in the Gould's belt. So far we lack the full picture of star formation in more extreme environments such as in and around the Cyg OB2 association. Recently, Vink et al. (2008) reported the discovery of 50 new PMS candidates towards Cyg OB2, found via their strong H-alpha emission using the IPHAS survey of the northern Galactic Plane. Reipurth & Schneider (2008) discuss current knowledge of the star formation in Cyg OB2. T Tauri stars are traditionally divided into Classical T Tauri stars (CTTS) and Weak line T Tauri stars(WTTS) discriminated by their H-alpha emission equivalent width being greater/lower that 10 Å. The latter population presents a major, perhaps dominant, component of the PMS population in most star forming regions, but it is difficult to find the WTTS population with the H-alpha method alone. However, VLA studies at 5 GHz have shown that WTTS stars have radio emissions a hundred times stronger than that of the Sun, indicating that magnetic activity is much stronger during the PMS phase than at later phases in their evolution. Further, it is known that for low mass stars there is a good correlation between X-ray and radio luminosity (Güdel 2002). Fig. 2 shows the X-ray luminosity vs. mass for the Albacete Colombo et al. (2007) X-ray sources in the core of Cyg OB2 (their Fig. 10) embracing their coverage of T Tauri, Herbig Ae/Be and higher mass stars. Also shown is the 3-sigma e-Merlin detection limit. This shows that we will clearly detect large numbers of T Tauri, Herbig Ae/Be stars. Flaring during the observations will make even more stars detectable, and note also that we plan coverage of Cyg OB2 that is three times larger than that attempted by Albacete Colombo et al. (2007). This will allow us to investigate the Pre-Main-Sequence population in detail and the potential environmental effect of OB stars in the star formation history of the association.

Acknowledgements

The e-Merlin COBRaS legacy project Team is led by Raman Prinja (UCL, P.I.) and comprises: Felix Aharonian (DIAS, Ireland), Mike Barlow (UCL, UK), Ronny Blomme (Royal Obs. Belgium), Ishwara Chandra (GMRT, Tata Isntitute, India), Simon Clark (Open Univ., UK), Paul Crowther (Uni. of Sheffield,UK), Phil Diamond (JBCA, Manchester, UK), Sean Dougherty (NRC, Canada), Jeremy Drake (Harvard CFA, USA), Janet Drew (Univ. of Herts, UK), Stewart Eyres (Univ. of Central Lancashire, UK), Danielle Fenech (UCL, UK), Simon Goodwin (Univ. of Sheffield, UK), Joseph

Hora (Harvard CFA, USA), Ian Howarth (UCL, UK), Dan Kaminki (Univ. of Wyoming, USA), Chip Kobulnicky (Univ. of Wyoming, USA), Derck Massa, STScI, USA), Julian Pittard (Univ. of Leeds, UK), Anita Richards (JBCA, Manchester, UK), Salvo Scuderi(Astron. Obs., Catania), Howard Smith, Harvard CFA, USA), Ian Stevens (Univ. of Birmingham, UK), Joan Vandekerkhove (Royal Obs. Belgium), Jacco Van Loon (Univ. of Keele, UK), Jorick Vink (Armagh Obs., UK), Martin Ward (Univ. of Durham,, UK), Allan Willis (UCL, UK), Dugan Witherick (UCL, UK), Nick Wright (Harvrad CFA, USA), Jeremy Yates (UCL, UK).

We are grateful to the referee for careful reading of the first draft of this paper and for helpful comments to improve it.

References

Albacete Colombo, J.F., Caramazza, M., Flaccomio, E., Micela, G. & Sciortino, S. 2007, A&A, 474, 495
Benaglia, P. 2010, ASP Conf. Ser., Vol. 422, 111
De Becker, M. 2007, A&ARev, 14, 171
Dougherty, S.M., & Williams, P.M. 2000, MNRAS, 319, 1005
Fullerton, A.W., Massa, D.L., & Prinja, R.K. 2006, ApJ, 637, 1025
Güdel, M. 2002 ARA&A, 40, 217
Knödlseder, J. 2000, A&A, 360, 539
Reipurth, B. & Schneider, N. 2008, *Handbook of Star Forming Regions*, Vol. 1, 36
Smith, N. & Owocki, S.P. 2006, ApJ, 645, L45
Vink, J.S., Drew, J.E., Steeghs, D., Wright, N. J., Martin, E. L., Gänsicke, B. T., Greimel, R. & Drake, J. 2008, MNRAS, 387, 308

Chapter 5

Massive binaries: interaction and evolution

Signatures of binary evolution processes in massive stars

Dany Vanbeveren

Astrophysical Institue, Vrije Universiteit Brussel, Pleinlaan 2, 1050 Brussels, Belgium
dvbevere@vub.ac.be
and
GroupT Leuven Engineering College,
Association KU Leuven, Vessaliusstraat 13, 3000 Leuven, Belgium

Abstract: Before binary components interact, they evolve as single stars do. We therefore first critically discuss massive single star processes which affect their evolution, stellar wind mass loss and rotation in particular. Next we consider binary processes and focus on the effect of rotation on binary evolution and on the mass transfer during Roche lobe overflow. The third part highlights the importance of close pairs on the comprehension of the evolution of stellar populations in starburst regions.

1 Introduction

Massive stars are among the most important objects in the Universe and many (most?) of them are formed in binaries. A selection of observational and theoretical facts that illustrate the importance of binaries and the evolution of massive and very massive stars in clusters with special emphasis on massive binaries have been summarized in two recent review papers (Vanbeveren, 2009, hereafter paper I, and Vanbeveren 2010). The present written version of the Liège binary review can be considered as an addendum to both papers.

2 The evolution of massive single stars

Before one or two massive stars in a binary start to interact, they evolve as single stars do. We therefore first discuss briefly massive single star evolution.

2.1 The effect of stellar wind mass loss

The evolution of a massive star depends significantly on its mass loss by stellar wind. We may distinguish 4 stellar wind mass loss phases: the OB-type phase, the luminous blue variable (LBV) phase, the Wolf-Rayet (WR) phase and the red supergiant (RSG) phase. They were discussed in paper I but let me focus a bit more on the RSG-phase.

2.1.1 The RSG stellar wind

Single stars (with Solar metallicity) with an initial mass $\leq$ 30-40 $M_{\odot}$ become RSGs and therefore the RSG stellar wind dominates their further evolution. Most of the stellar evolutionary codes use the RSG wind formalism proposed by de Jager et al. (1988). However this formalism predicts the real RSG wind rates perhaps not better than a factor 5-10. These rates determine whether or not the massive star will lose most of its hydrogen rich layers, e.g. whether or not the massive star will become a WR star. This means that a large uncertainty factor in the RSG rates may seriously affect the theoretically predicted population of WR stars. It was shown in Vanbeveren (1991) that a 35 % increase of the RSG rates (compared to the de Jager rates) is sufficient in order to obtain correspondence between the observed and theoretically predicted WR population in the Solar neighbourhood. This was worked out in more detail in Vanbeveren (1996) and in Vanbeveren et al. (2007). Note that also the Padua group (Salasnich et al. 1999) defended evolutionary computations of massive stars with larger RSG rates.

Interestingly, Yoon & Cantiello (2010) recently studied the evolution of massive stars with pulsation driven super-winds during the RSG phase. As far as the effect on massive star evolution is concerned, they essentially arrive at similar conclusions as in our work.

Let me finally remark that all the massive star population studies performed in Brussels since 1996 account for these higher RSG rates (in particular the population of the different SN types, De Donder & Vanbeveren (2003); the WR population, Vanbeveren et al. (1998a), Van Bever & Vanbeveren (2000, 2003); binaries and the chemical evolution of the Galaxy, De Donder & Vanbeveren (2004), etc.).

2.2 The effect of rotation

The effects of rotation on the evolution of massive single stars has been studied very intensively in the past two decades by the Geneva group (see Meynet et al. 2011). One may distinguish three main effects: rotating stars have larger convective cores than non-rotating stars, rotational mixing is responsible for the transport of interior matter up to the surface, and the faster the rotation the higher the stellar wind mass loss rate.

2.2.1 Rotation, convective cores and rotational mixing

The faster the initial rotation of a massive single star the larger the convective core, e.g. the effect of rotation on massive star cores is similar to convective core overshooting. Based on the observed rotation velocities of galactic O-type stars one concludes that they are born with an initial rotational velocity $\approx$ 200-300 km/s (however see also section 3.1). The calculations of the Geneva team then let us conclude that on average moderate convective core overshooting mimics the average effect of rotation on convective cores.

Due to rotational mixing, matter from the interior may reach the surface layers. This mixing process only slightly modifies the overall evolution of the massive star, but it may alter the chemical abundances of the surface layers and a comparison with observed abundances may decide upon the effectiveness of rotational mixing. Unfortunately the correspondence between theoretical prediction and observations is rather poor (Hunter et al. 2008). Binaries may help (Langer et al. 2008) but magnetic fields may be needed as well. A general warning may be appropriate: comparing the Hunter diagram with theoretical prediction involves population synthesis. In Brussels we have been studying massive star and binary populations for about two decades and we frequently found poor correspondence with observations, but in many cases, after second thoughts we concluded that observational bias was one of the main reasons. Selecting well observed stars/binaries and trying to explain them may be at least as useful as overall population synthesis. OBN binaries are known for quite some time

and I like to call your attention to the interesting system HD 163181. It is a BN0.5Ia + OBN binary (Hutchings 1975; Josephs et al. 2001) with a period P = 12 days and masses 13 $M_\odot$ + 22 $M_\odot$. The 13 $M_\odot$ primary has the luminosity of a 30 $M_\odot$ main sequence star and is at least 1.5 mag brighter than the 22 $M_\odot$ secondary. Binary evolution then reveals that the primary must be a core helium burning star at the end of RLOF (Vanbeveren et al. 1998b). The nitrogen enhancements are most probably due to binary mass exchange and more observations of this system may prove to be very instructive. Interestingly, the 13 $M_\odot$ mass loser has all the properties of WR stars in binaries (except maybe the Teff) but it is not a WR star. We suspect that in the very near future the supergiant will turn into a WR star.

An embarrassing problem of the present rotating massive star evolutionary models is that they produce pulsars that are spinning too fast by at least an order of magnitude (Heger et al. 2000) and also here the coupling between rotation and magnetic fields may be the solution.

Some massive stars are known to rotate very fast, close to break up (the Be stars but also some O-type stars). Due to the combined action of convective core growth and rotational mixing, stars that rotate close to the critical velocity are expected to evolve quasi-homogeneously (Maeder 1987) and their evolution is quite different from the 'normal' evolution of massive stars. An important question is how these stars became extremely rapid rotators. Many rapid rotators are known to be binary components or former binary components and therefore we will come back to this in section 3.1.

2.2.2 Rotation and the stellar wind mass loss rate

One of the main evolutionary effects of rotation is related to the effect of rotation on the stellar mass loss. A first attempt to link rotation and mass loss was proposed by Langer (1997) but Glatzel (1998) showed that the proposed relation may be not correct due to the fact that it does not account for the effect of gravity darkening (von Zeipel 1924). An alternative and attractive formalism has been derived by Maeder & Meynet (2000) where the effect of gravity darkening was taken into account. This relation demonstrate that for most of the massive stars (with an average initial rotational velocity of $\approx$ 200-300 km/s) the increase of the stellar wind mass loss with respect to the non-rotating case is very modest. The increase is significant for stars with a large Eddington factor Γ (e.g., stars with an initial mass $\geq$ 40 $M_\odot$) that are rotating close to critical. However, the following remarks are appropriate: there are no observations yet to sustain the relation proposed by Maeder & Meynet (Puls et al. 2010). Even more, one may wonder whether or not rotation can be a significant mass loss driver, since even at critical rotation, the rotational energy is at most half the escape energy of a massive star (Owocki 2010, private communication).

3 The evolution of massive binaries

The main differences between single star evolution and the evolution of the same star when it is a binary component are related to the Roche lobe overflow (RLOF) process and to binary processes which determine the rotation rate of the star.

3.1 Rotation and binaries

Due to tidal interaction the massive primaries of most of the binaries are expected to be slow rotators. Only in very short period systems (P = 1-2 days) it can be expected that massive primaries are rapid rotators for which the evolution proceeds quasi-homogeneously (De Mink et al. 2009).

In binaries where the RLOF of the primary is accompanied by mass transfer towards and mass accretion onto the secondary, the secondary spins-up and very rapidly rotational velocities are reached

close to the critical one (Packet 1981). This happens in systems where the RLOF occurs when the outer layers of the primary are mainly in radiative equilibrium (Case A / Case Br systems). Population synthesis predicts that many Be stars are formed this way (Pols & Marinus 1994; Van Bever & Vanbeveren 1998). The latter two studies illustrate that one may expect many Be stars with a subdwarf (sdO) or white dwarf (WD) companion. The high temperature of these companions makes them very hard to detect and this may be the reason why so few are known at present (ϕ Per is an exception, see section 3.3.1). The Be-components in Be-X-ray binaries form an interesting subclass of the Be sample because here we have all reasons to believe that binary action has been important in the formation of the Be star. Many Be single stars are also expected to form via binary mass transfer. The reason is that the supernova explosion of a massive primary disrupts the binary in most of the cases. This means that the fact that many Be stars have a neutron star companion means that even more Be single stars have had a similar past as the Be stars in the Be-X-ray binaries.

The optical components of the standard high mass X-ray binaries are former binary secondaries where mass and angular momentum accretion may have occured. The mass and helium discrepancy for single stars discussed by Herrero et al. (1992) is also visible in the optical component of the X-ray binary Vela X-1 (Vanbeveren et al. 1993) and we proposed *the accretion induced full mixing model*. The idea was the following: due to mass and angular momentum accretion, mass gainers spin-up. This may induce efficient mixing. We simulated this possibility with our evolutionary code by fully mixing the mass gainer and, after the mass transfer phase, following the further evolution of the mixed star in a normal way. In this way we were able to explain the helium and mass discrepancy in Vela X-1. The more sophisticated mass gainer models of Cantiello et al. (2007) demonstrate that our simplified models are not too bad.

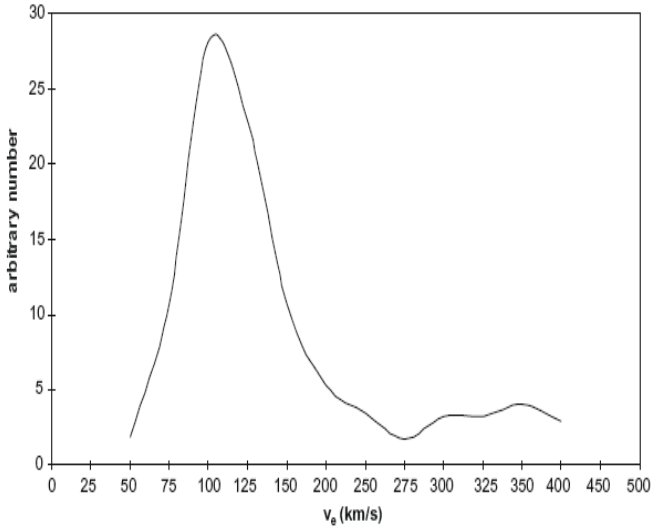

Figure 1: The probable v_{rot} distribution of O-type stars using the data of Penny (1996) (from Vanbeveren et al. 1998).

Starting from the observed $v_{rot}sin$i data of O-type stars of Penny (1996), Figure 1 shows the probable distribution of rotational velocities v_{rot} of O-type stars (from Vanbeveren et al. 1998a) and illustrates that many O-type stars are relatively slow rotators, corresponding to an initial average rotational velocity for O-type stars of $\leq$ 200 km/s for which indeed the effect of rotation on their evolution is rather modest. The figure also shows that there is a subset of very rapid rotators. However, many of these rapid rotators are runaway stars (they have a space velocity $\geq$ 30 km/s) and this may indicate that these stars were former binary components, e.g. they became rapid rotators due to

the mass transfer process in a binary and they became runaways due to the supernova explosion of their companion, or they became rapidly rotating runaways due to stellar dynamics in dense stellar clusters, in which case they were former binary members as well but their formation was governed by star merging. An interesting test bed for this type of process may be ζ Pup which is indeed a rapidly rotating runaway. Note that Mokiem et al. (2006) obtained rotational velocities of 21 OB dwarfs in the SMC and concluded that the average v_{rot}=160-190 km/s. Since massive dwarfs are stars close to the zero age main sequence, this average value is indicative for the average initial rotation velocity of OB-type stars. Remark that this value is not significantly different from the initial average value of Galactic O-type stars whereas, similar as in the Galactic sample, the most rapid rotators in the SMC are runaway stars.

All in all, it looks to me that rotation is important for massive star evolution but perhaps mainly within the framework of binaries in combination with stellar dynamics in young dense clusters.

3.2 The Roche lobe overflow process

When the RLOF starts when the mass loser has a convective envelope (Case Bc and Case C), the mass loss process happens on the dynamical timescale and a common envelope forms. It can be expected that the common envelope is lost as a superwind where most of the energy is supplied by orbital decay and it stops when the two components merge or, when merging of the two stars can be avoided, when most (but not all) of the hydrogen rich layers of the mass loser are removed. This phase is so rapid that it is unlikely that mass accretion plays an important role for the evolution of the secondary star and therefore the latter may not become a rapid rotator.

When the RLOF starts when the mass loser has a radiative envelope (Case A and Case Br), the mass loss process happens on the Kelvin-Helmhotz time scale of the loser and when the initial mass of the gainer is not too much smaller than the initial mass of the loser, mass transfer and mass accretion becomes possible.

The evolution of the mass loser in Case Br and in most of the Case A massive binaries is very straightforward: due to RLOF the redward evolution of the loser is avoided (e.g., massive primaries in Case A or Case Br binaries do not become red supergiants). The RLOF stops when the loser has lost most (but not all) of its hydrogen rich layers and helium starts burning in the core. At that moment the loser resembles a WR-like star (when the mass is large enough the WR-like star is expected to be a guinine WR star with hydrogen in its atmosphere, typically X = 0.2-0.3).

The evolution of the mass gainer in Case A and Case Br binaries is governed by mass and angular momentum accretion and rotation plays a very important role (see the previous subsection).

An important question is whether or not the RLOF in Case A or Case Br binaries is quasi-conservative. Let me first remark that removing matter out of a binary at a rate which is similar to the rate at which the primary loses mass, requires a lot of energy, much more than the intrinsic radiation energy of the two components which is in most cases only sufficient in order to drive a modest stellar wind. The Utrecht group promoted a massive binary model where extensive mass loss from the system happens when the mass gainer has been spun-up by mass and angular momentum transfer and reaches a rotational velocity close to the critical one (Petrovic et al. 2005; De Mink 2010). However, as discussed already in subsection 2.2.2, rotation is not an efficient mass loss driver whereas even at break up, the rotational energy is at least a factor 2 too small compared to the required escape energy. Van Rensbergen et al. (2008) proposed the following model: the gas stream during RLOF forms a hot spot either on the surface of the star when the gas stream hits the mass gainer directly, or on the Keplerian disc when mass transfer proceeds via a disc. The radiation energy of the hot spot in combination with the rotational energy of the spun-up mass gainer can then drive mass out of the binary. The following illustrates that this model is probably not a process that removes from the binary a

significant amount of mass lost by the loser. For the sake of simplicity, let us neglect rotation because as was stated already before, rotation is not an efficient mass loss driver whereas even at critical break up, the rotation energy is too small compared to the escape energy of a massive star. The radiation energy L_{acc} generated by the accretion of the gas stream is given by

$$L_{acc} = G\frac{\dot{M}_{acc}\, M}{R} \tag{1}$$

where we neglect the fact that the gas stream does not originate at infinity but at the first Lagrangian point (it can readily be checked that this assumption does not significantly alter our main conclusions). $\dot{M}_{acc}$ is the mass accretion rate, M and R are the mass and the radius of the gainer. When η is the fraction of L_{acc} that is effectively transformed into escape energy, it follows that

$$\eta\, L_{acc} = \frac{1}{2}\dot{M}_{out} v_{esc}^2 \tag{2}$$

with $\dot{M}_{out}$ the binary mass loss rate and v_{esc} the binary escape velocity. In order to get a first order estimate of the binary mass loss rate, we can replace v_{esc} by the escape velocity of the mass loser only. The foregoing equations then result into

$$\dot{M}_{out} = \eta\, \dot{M}_{acc} \tag{3}$$

Detailed hydrodynamic calculations of stellar winds reveal that the efficiency factor for converting radiation energy into kinetic energy is of the order of 0.01 and 0.001 (Nugis & Lamers, 2002). So, unless the efficiency is much higher, equation (3) then illustrates that in general the accretion energy may cause mass loss out of a binary but this loss is much smaller than the mass accretion rate. Of course when the gainer rotates at the critical velocity, mass accretion on the equator will not happen. Possibly matter will pile up arround the gainer, accretion may happen on the rest of the star, or matter may leave the binary through the second Lagrangian point L2 as illustrated in Figure 2. When this happens the variation of the orbital period can be estimated under reasonable assumptions (e.g. Vanbeveren et al. 1998b). Note that in most of the population studies performed by different groups the effect of a non-conservative RLOF is investigated using this L2 model. Let me finally remark that mass that leaves the binary through the decretion/accretion disk of the gainer when the gainer rotates at the break up velocity, takes with the specific orbital angular momentum of the gainer but also the specific rotational angular momentum of the equator of the gainer. Interestingly, the sum of both momenta is roughly equal to the specific angular momentum of the L2 point.

3.3 Some interesting observed test beds of the Roche lobe overflow process

As discussed in the previous subsection, from theoretical considerations it is unclear whether or not Case A / Case Br evolution in massive binaries is quasi-conservative or not. Are there observed binaries that can be considered as RLOF test beds and allow us to say something about the RLOF? The best candidates are post-RLOF binaries or binaries at the end of RLOF where one can try to fit evolutionary models of binaries where the evolution of both components is followed simultaneously adopting different efficiency values for the mass transfer process. We did this for a number of Galactic massive binaries (Vanbeveren et al. 1998b) and de Mink et al. (2007) for SMC binaries. Here we reconsider two most interesting systems.

3.3.1 ϕ Per

ϕ Per is a sdO6 + B0.5Ve binary with a period = 126 days. It is a post-RLOF binary where the subdwarf O6 star has been the mass loser (thus evolutionary speaking this is the primary although it

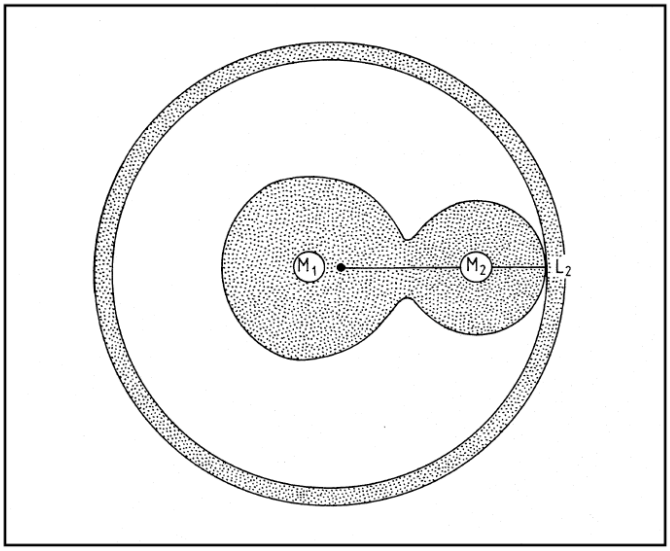

Figure 2: Mass loss from the system through L2 and the formation of a ring around the binary, during the RLOF of the primary in a Case A/ Case Br binary.

is in the visual region by far the less luminous component) and the Be star is the mass gainer (the secondary). The fact that the secondary is a rapidly rotating Be star is indicative that mass transfer has played an important role. There are two different studies where the masses of the components were determined, e.g., 1.7 $M_\odot$ + 17.3 $M_\odot$ (Bozic et al., 1995) and 1.14 $M_\odot$ + 9.3 $M_\odot$ (Gies et al. 1996). Accounting for the period of the binary, both sets of masses imply that the previous RLOF was quasi-conservative (Vanbeveren et al. 1998b).

3.3.2 RY Scuti

The massive binary RY Scuti may be a key system for the discussion whether or not the RLOF in massive binaries is conservative. The spectroscopic study of Grundstrom et al. (2007) reveals that it is a O9.7Ibpe + B0.5I binary with a period = 11.2 days and masses 7 $M_\odot$ + 30 $M_\odot$. The O-type supergiant is the most luminous component and comparison with evolutionary models of binaries reveals that it is most probably a core helium burning star near the end of RLOF with a significantly reduced surface hydrogen content (X = 0.3-0.4). Similarly as the supergiant in HD 163181 (section 2.2.1) we predict that the O-type supergiant will soon become a WR star. If the masses are correct then this system is an illustration of a massive binary where the RLOF was quasi-conservative for the following reasons. From evolution it follows that the 7 $M_\odot$ star comes from a star with initial mass $\leq$ 20 $M_\odot$ that lost $\leq$ 13 $M_\odot$ by RLOF. Since the initial mass of the secondary (mass gainer) must have been $\leq$ 20 $M_\odot$ as well obviously, it must have accreted at least 10 $M_\odot$ of the $\leq$ 13 $M_\odot$ lost by the loser in order to become a 30 $M_\odot$ star, e.g. the mass accretion efficiency must have been at least 80% and we call this quasi-conservative. Note that the observations of Grundstrom et al.(2007) seem to indicate that there is some circum-binary material, but it is clear that the model discussed above does not contradict this fact.

3.3.3 The stellar wind and binaries

Spherically symmetric stellar wind mass loss of one or both components in a binary increases the binary period and decreases the amount of mass lost by RLOF when the stellar wind mass loss hap-

pens before the latter. Stars with an initial mass $\geq$ 30-40 $M_\odot$ are losing their hydrogen rich layers by an O-type wind and by LBV-type mass loss. When a star like that is a binary component with a period that is large enough so that the RLOF would start after these O and LBV type mass loss processes, the RLOF will not happen (the 'LBV scenario' of massive close binaries as it was introduced in Vanbeveren 1991).

Our evolutionary computations of massive single stars but with our preferred RSG wind rates (section 2.1.2) predict that stars in the mass range 15-20 $M_\odot$ up to 30-40 $M_\odot$ lose sufficient hydrogen rich layers so that in the HR-diagram they turn back and become WR or WR-like stars. It is clear that when such a star is a binary member with a period that is large enough so that this RSG mass loss process starts before the Roche lobe overflow (RLOF) starts, the RLOF will be avoided. This means that what is called Case C evolution of binaries does not happen when the primary star has an initial mass $\geq$ 15-20 $M_\odot$ (the 'RSG scenario' of massive binaries, Vanbeveren, 1996).

The evolutionary computations with our preferred RSG rates also predict that stars in the mass range 10 $M_\odot$ and 15-20 $M_\odot$ lose a few $M_\odot$ during the RSG phase. When such a star is the primary of a binary with a period such that it will evolve through a common envelope (CE) phase, the total mass lost due to the latter CE process may be reduced due to the RSG stellar wind mass loss. The binary υ Sgr (Upsilon Sagittarii) may have evolved this way and may be an interesting test bed for the effect of RSG mass loss on binary evolution. It consists of an A-type supergiant + B4-7 main sequence star. The period = 138 days and the present masses are 2.5 $M_\odot$ + 4 $M_\odot$. The A supergiant is extremely hydrogen deficient, core helium/helium shell burning, with $\log L/L_\odot = 4.6$. Evolution predicts that the initial masses were 12 $M_\odot$ + 4 $M_\odot$. The binary is post-common envelope but to understand its evolution (in particular the period evolution) one has to accept that RSG stellar wind mass loss has been important and lowered the importance of common envelope mass loss (see also Vanbeveren et al. 1998b).

4 Close pairs - key to comprehension of the evolution of stellar populations in starburst regions

Mass transfer and mass accretion during a canonical RLOF in Case A/Br binaries is responsible for the formation of a blue straggler sequence in young clusters (Pols & Marinus 1994; Van Bever & Vanbeveren 1998, see Figure 3). Since these blue stragglers are mass gainers or binary mergers, it can be expected that they are rapid rotators, e.g., a cluster of slow rotators but with a significant population of close binaries will become populated with rapid rotators.

Starburst99 (Leitherer et al. 1999) is an interesting spectral synthesis tool to estimate all kinds of properties of starburst regions where only integrated spectra are available. However, it should be noted that this tool only accounts for the properties of single stars. The effects of binaries on the spectral synthesis of starbursts has been studied in Brussels: the effects of binaries on the evolution of $W(H_\beta)$ (Van Bever & Vanbeveren 1999), the effect of binaries on the evolution of UV spectral features in massive starbursts (Belkus et al. 2003), the effect of binaries on WR spectral features in massive starbursts (Van Bever & Vanbeveren 2003), hard X-rays emitted by starbursts with binaries (Van Bever & Vanbeveren 2000). Note that Brinchmann et al. (2008) investigated the spectral properties of WR galaxies in the Sloan Digital Sky Survey and concluded that a comparison with theoretical population synthesis leeds to the conclusion that binaries are necessary.

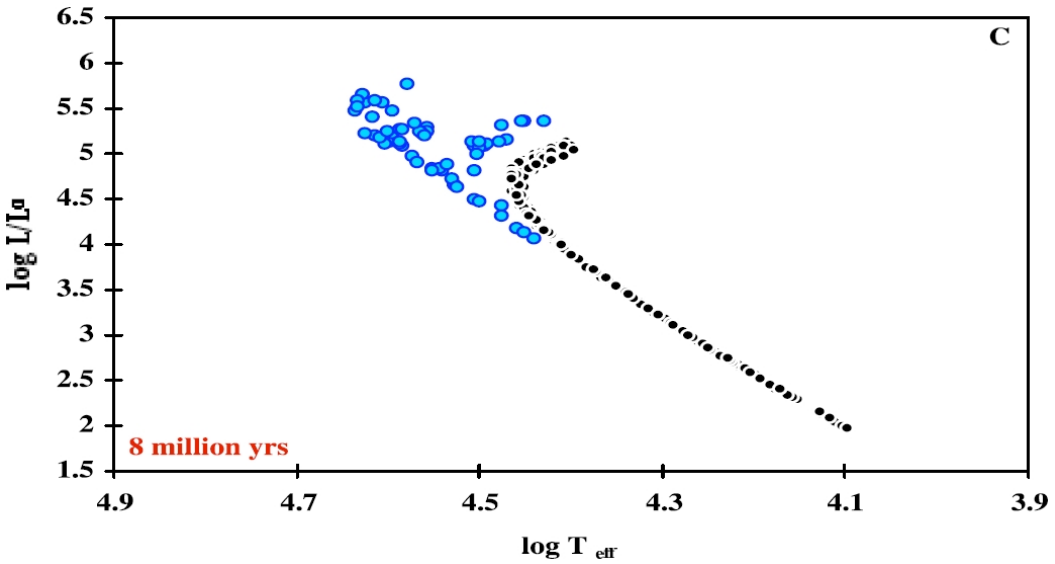

Figure 3: A typical starburst with primordial binaries after 8 Myr; the blue stars are rapidly-rotating mass gainers or binary mergers (from Van Bever & Vanbeveren 1998).

4.1 Intermezzo 1

Vanbeveren (1982) discussed a possible relation between the maximum stellar mass in a cluster and the total cluster mass. It was concluded that *the integrated galaxial stellar IMF should be steeper than the stellar IMF*. This has been worked out in more detail about 20 years later by Kroupa & Weidner (2003) and Weidner & Kroupa (2006) who essentially arrived at the same conclusion.

A consequence of the fact that the mass of the most massive star in a cluster correlates with the cluster mass, is that it is possible that also the mass ratio distribution of the most massive binary population in the cluster correlates with the cluster mass. To illustrate, suppose that the cluster mass indicates that the maximum stellar mass/total binary mass is 50 $M_\odot$, then one may expect binaries like 40 $M_\odot$ + 10 $M_\odot$ or 30 $M_\odot$ + 20 $M_\odot$ etc., but not 40 $M_\odot$ + 30 $M_\odot$.

4.2 Intermezzo 2

Could it be that stars form in isolation? The origin of massive O-type field stars has been studied by De Wit et al. (2004). The authors proposed the following procedure in order to find a candidate O-type star that may have formed in isolation : take a non-runaway O-type field star and look for young clusters within 65 pc from the O-star. The value 65 pc was obtained by assuming that the lifetime of an O-type star is $\leq 10^7$ yr. This is true for single stars however, the lifetime of an O-type star in a binary may be 2-3 times larger and therefore it may be necessary to look for young clusters within 200 pc. The model goes as follows: a 12 $M_\odot$ + 9 $M_\odot$ binary is dynamically ejected from a dense cluster with a velocity of 6 km/s. After 30 million years, when the binary is 200 pc away from its parent cluster, the 12 $M_\odot$ primary starts its RLOF. A quasi-conservative RLOF turns the 9 $M_\odot$ secondary into a 19 $M_\odot$ rejuvenated O-type star. When the primary remnant finally explodes as a supernova, the 19 $M_\odot$ O-type star most likely becomes a single star but the magnitude and direction of its space velocity may have changed completely, even so that its direction does not hit the parent cluster any longer.

4.3 Stellar dynamics in young dense star clusters

Ultra Luminous X-ray sources (ULX) are point sources with X-ray luminosities up to 10^{42} erg s^{-1}. MGG-11 is a young dense star cluster with Solar type metallicity ∼200 pc from the centre of the starburst galaxy M82, the parameters of which have been studied by McCrady et al. (2003). A ULX is associated with the cluster. When the X-rays are due to Eddington limited mass accretion onto a black hole (BH) it is straightforward to show that the mass of the BH has to be at least 1000 $M_\odot$. However how to form a star with Solar metallicity and with a mass larger than 1000 $M_\odot$? Mass segregation in a dense young cluster associated with core collapse and the formation of a runaway stellar collision process was promoted by Portegies Zwart et al. (2004). Note that the latter paper mainly addressed the dynamical evolution of a dense cluster but the evolution of the very massive stellar collision product was poorly described.

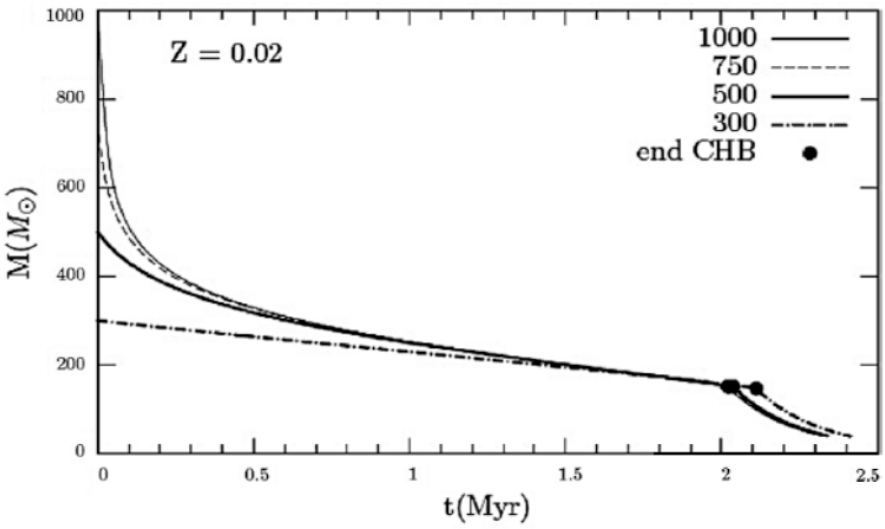

Figure 4: The mass evolution during core-hydrogen-burning and during core-helium-burning of very massive stars (Solar metallicity) with an initial mass 300 $M_\odot$, 500 $M_\odot$, 750 $M_\odot$ and 1000 $M_\odot$ (from Belkus et al. 2007).

The evolution of very massive stars has been studied in detail by Belkus et al. (2007) and Yungelson et al. (2008) and it was concluded that stellar wind mass losses during core hydrogen burning and core helium burning are very important (Figure 4). Belkus et al. presented a convenient evolutionary recipe for such very massive stars, which can easily be implemented in an N-body dynamical code. Our N-body code which includes this recipe has been described in Belkus (2008) and in Vanbeveren et al. (2009) and applied in order to simulate the evolution of MGG-11. In Figure 5 we show the evolution of the runaway stellar collision object for MGG-11 predicted by our code. The blue simulation is performed assuming a similar stellar wind mass loss formalism for very massive stars as the one used by Portegies Zwart et al. (2004). It can readily be checked that our simulation is very similar to the one of the latter paper and this gives some confidence that our N-body-routine is working properly. We then repeated the N-body run but with our preferred evolutionary scheme for very massive stars (the black run in Figure 5). Our main conclusion was the following:

Stellar wind mass loss of massive and very massive stars does not prevent the occurrence of a runaway collision event and the formation of a very massive star in a cluster like MGG-11, but after this event stellar wind mass loss during the remaining core hydrogen burning phase is large enough in order to reduce the mass again and the formation of a BH with a mass larger than ∼75 $M_\odot$ is rather unlikely.

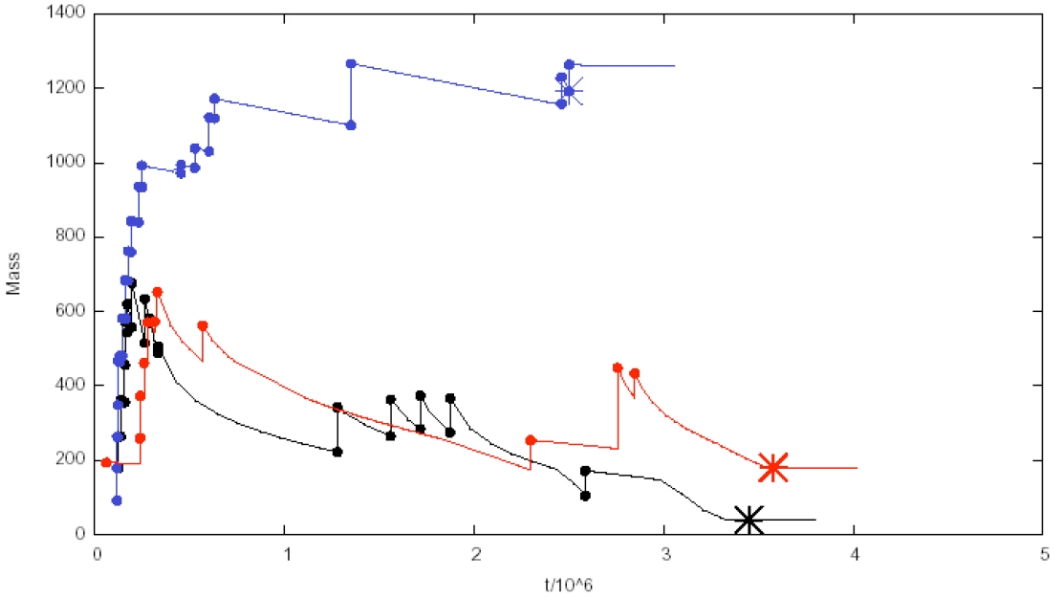

Figure 5: The mass evolution of the collision runaway object in a MGG-11 type cluster. The curve with the largest final mass (blue curve) = simulation with small mass loss, similar to the results of Portegies Zwart and McMillan (2002), the curve with the lowest final mass (black curve) = simulation with the stellar wind mass loss formalism as discussed in Belkus et al. (2007) for Solar type metallicity, the curve with the second largest final mass (red curve) = same as the black curve but for an SMC type metallicity (from Vanbeveren et al. 2009).

Similar conclusions were reached by Glebbeek et al. (2009) for MGG-11 and by Chatterjee et al. (2010) for the Arches cluster, although in both studies cluster dynamics and the evolution of very massive stars are not linked self-consistently.

Our simulations then promote the model for the ULX in MGG-11 where the X-rays are due to super-Eddington accretion onto a stellar mass BH, a model that seems to be a most probable model for many of these systems (Gladstone et al. 2009).

We also made a simulation for an MGG-11 like cluster but where the metallicity is significantly smaller. As can be noticed from Figure 5 (the red simulation) the formation of a BH with a mass of a few 100 $M_{\odot}$ is possible and this is of course a direct consequence of our adopted dependence of the stellar wind mass loss rate on the metallicity. From this simulation we are inclined to conclude that, if the progenitors of globular clusters were massive starbursts in the beginning, it is not unlikely that an intermediate mass black hole formed as a consequence of mass segregation and core collapse in a dense massive cluster.

References

Belkus, H. 2008, PhD Thesis (Vrije Universiteit Brussel)
Belkus, H., Van Bever, J., & Vanbeveren, D. 2007, ApJ 659, 1576
Belkus, H., Van Bever, J., Vanbeveren, D., & van Rensbergen, W. 2003, A&A 400, 429
Bozic, H., Harmanec, P., Horn, J., Koubsky, P., et al. 1995, A&A 304, 235
Brinchmann, J., Kunth, D., & Durret, F. 2008, A&A 485, 657
Cantiello, M., Yoon, S.-C., Langer, N., & Livio, M. 2007, A&A 465, 29
Chatterjee, S., Goswami, S., Umbreit, S., Glebbeek, E., et al. 2009, arXiv0911.1483C
De Donder, E., & Vanbeveren, D. 2003, New Astronomy 8, 817
De Donder, E., & Vanbeveren, D. 2004, New Astronomy Reviews 48, 861

de Jager, C., Nieuwenhuijzen, H., & van der Hucht, K.A. 1988, A&AS 72, 259
de Mink, S.E., Pols, O.R., & Hilditch, R.W. 2007, A&A 467, 1181
De Mink, S.E., Cantiello, M., Langer, N., Pols, O.R., Brott, I., & Yoon, S.-C. 2009, A&A 497, 243
de Wit, W.J., Testi, L., Palla, F., Vanzi, L., & Zinnecker, H. 2004, A&A 425, 937
Gies, D.R., Thaller, M.L., Bagnuolo, W.G.Jr., et al., 1996, BAAS 28, 1373
Gladstone, J., Roberts, T.P., & Done, C. 2009, MNRAS 397, 1836.
Glatzel, W. 1998, A&A 339, L5
Glebbeek, E., Gaburov, E., de Mink, S.E., Pols, O.R., & Portegies Zwart, S.F. 2009, A&A 497, 255
Grundstrom, E.D., Gies, D.R., Hillwig, T.C., et al. 2007, ApJ 667, 505
Heger, A., Langer, N., & Woosley, S.E. 2000, ApJ 528, 368.
Herrero, A., Kudritzki, R.P., Vilchez, J.M., et al. 1992, A&A 261, 209
Hunter, I., Lennon, D.J., Dufton, P.L., et al. 2008, A&A 479, 541
Hutchings, J.B. 1975, ApJ 200, 122
Josephs, T.S., Gies, D.R., Bagnuolo, W.G.Jr., et al. 2001, PASP 113, 957
Kroupa, P., & Weidner, C. 2003, ApJ 598, 1076
Langer, N. 1997, in *Luminous Blue Variables: Massive Stars in Transition*, eds. Nota, A., Lamers, H., ASP Conf. Series 120, p. 83
Langer, N., Cantiello, M., Yoon, S.-C., et al. 2008, IAUS 250, 167
Leitherer, C., et al. 1999, ApJS 123, 3
Maeder, A. 1987, A&A 178, 159
Maeder, A., & Meynet, G. 2000, A&A 361, 159
Meynet, G., Georgy, C., Hirschi, R., Maeder, A., Massey, P., Przybilla, N., & Nieva, M.-F. 2011, in Proceedings of the 39th Liège Astrophysical Colloquium, eds. G. Rauw, M. De Becker, Y. Nazé, J.-M. Vreux & P.M. Williams, BSRSL 80, 266
McCrady, N., Gilbert, A.M., & Graham, J.R. 2003, ApJ 596, 240
Mokiem, M.R., de Koter, A., Evans, C.J., et al. 2006, A&A 456, 1131
Nugis, T., & Lamers, H. 2002, A&A 389, 162
Packet, W. 1981, A&A 102, 17
Penny, L.R. 1996, PhD Thesis (Georgia State University)
Petrovic, J., Langer, N., & van der Hucht, K.A. 2005, A&A 435, 1013
Pols, O.R., & Marinus, M. 1994, A&A 288, 475
Portegies Zwart, S.F., Baumgardt, H., Hut, P., Makino, J., & McMillan, S., L.W. 2004, Nature 428, 724
Puls, J., Sundqvist, J.O., & Rivero Gonzalez, J.G. 2010, arXiv1009.0364P
Salasnich, B., Bressan, A., & Chiosi, C. 1999, A&A 342, 131
Van Bever, J., Belkus, H., Vanbeveren, D., & Van Rensbergen, W. 1999, New Astron. 4, 173
Van Bever, J., & Vanbeveren, D. 1998, A&A 334, 21
Van Bever, J., & Vanbeveren, D. 2000, A&A 358, 462
Van Bever, J., & Vanbeveren, D. 2003, A&A 400, 63
Van Rensbergen, W., De Greve, J.P., De Loore, C., & Mennekens, N. 2008, A&A 487, 1129
Vanbeveren, D. 1982, A&A 115, 65
Vanbeveren, D. 1991, A&A 252, 159
Vanbeveren, D. 1996, in *Evolutionary processes in binary stars*, eds. Wijers, R.A.M.J. and Davies, M.B., ASI Series, vol. 477, Dordrecht: Kluwer Academic Publishers, p. 155
Vanbeveren, D. 2009, New Astron. Reviews 53, 27
Vanbeveren, D. 2010, in *Star clusters: basic galactic building blocks throughout time and space*, IAU Symposium, Volume 266, p. 293
Vanbeveren, D., Belkus, H., Van Bever, J., & Mennekens, N., 2009, Astrophys. Space Sci. 324, 271
Vanbeveren, D., De Donder, E., Van Bever, J., Van Rensbergen, W., & De Loore, C. 1998, New Astronomy 3, 443
Vanbeveren, D., Herrero, A., Kunze, D., & van Kerkwijk, M. 1993, Space Sci. Reviews 66, 395
Vanbeveren, D., Van Bever, J., & Belkus, H. 2007, ApJ 662, 107
Vanbeveren, D., Van Rensbergen, W., & De Loore, C. 1998b, in *The Brightest Binaries*, Kluwer Academic Pub., Dordrecht
von Zeipel, H. 1924, MNRAS 84, 665
Weidner, C., & Kroupa, P. 2006, MNRAS 365, 1333
Yoon, S.C., & Cantiello, M. 2010, ApJ 717, 62
Yungelson, L.R., van den Heuvel, E.P.J., Vink, J.S., et al. 2008, A&A 477, 223

Discussion

N. Smith: I have 2 questions.
In a few places in the talk, in reference to stars that lose their H envelopes in RLOF, you said the star 'has all the properties of a WR star, but it is not'. Could you clarify exactly what you meant by this?
Regarding the mass gainer in RLOF, could you comment on the initial conditions (i.e. mass ratio, initial period) where it may happen that the mass gainer evolves more quickly and explodes first? How often will this happen?
D. Vanbeveren: Question 1: the star is hydrogen deficient, it has a mass that falls within the observed masses of WR binary components, it is core helium burning and it therefore has a M-L relation that is typical for helium burning WR stars
Question 2: the mass ratio of the initial system has to be very close to 1 and the period may not be too large so that mass transfer happens. Realisation frequencies have been calculated in the past (and published in the literature). These frequencies are small but not zero.

C. Martayan: About Be stars and the scenario giving 9-10 single Be stars after the explosion of the companion of the initial binary system in a SN, while 1 system remains bound in a Be X-ray binary, I would expect to see some SN remnants. However, while most of Be stars are in open clusters (no runaway stars) we should see these remnants, which is not the case usually. Do you have some possible observational clues about this scenario?
D. Vanbeveren: Many Be stars are observed as the component of a hard X-ray binary with a neutron star companion. The binary variability of this X-radiation allows us in many cases to estimate the mass of both components.

Binaries are the best single stars

S.E. de Mink[1,2], N. Langer[1,2] and R.G. Izzard[1]

[1] Argelander Institute für Astronomie der Universität Bonn, Germany
[2] Astronomical Institute Utrecht, The Netherlands

Abstract: Stellar models of massive single stars are still plagued by major uncertainties. Testing and calibrating against observations is essential for their reliability. For this purpose one preferably uses observed stars that have never experienced strong binary interaction, i.e. "true single stars". However, the binary fraction among massive stars is high and identifying "true single stars" is not straight forward. Binary interaction affects systems in such a way that the initially less massive star becomes, or appears to be, single. For example, mass transfer results in a widening of the orbit and a decrease of the luminosity of the donor star, which makes it very hard to detect. After a merger or disruption of the system by the supernova explosion, no companion will be present.

The only unambiguous identification of "true single stars" is possible in detached binaries, which contain two main-sequence stars. For these systems we can exclude the occurrence of mass transfer since their birth. A further advantage is that binaries can often provide us with direct measurements of the fundamental stellar parameters. Therefore, we argue these binaries are worth the effort needed to observe and analyze them. They may provide the most stringent test cases for single stellar models.

1 Introduction

"Massive stars appear to love company'.' With this sentence Mason et al. (2009) open and summarize their paper describing a comprehensive compilation of spectroscopic data of close binaries and high angular resolution data of wide binaries. They conclude that more than half of the stars in the Galactic O-star catalogue are spectroscopic binaries. Using a smaller, but homogeneously analyzed data set, Sana & Evans (2010) find a spectroscopic binary fraction of $44 \pm 5\%$ for nearby clusters that are rich in O-stars. As these authors phrase it: "to ignore the multiplicity of early-type stars is equivalent to neglecting one of their most defining characteristics", see also Sana et al. (2008).

Spectroscopic measurements can identify binaries with separations up to a few AU or orbital periods up to a few years. This is of the order of the maximum separation and orbital period for which binaries are close enough to interact by mass transfer. In such close binaries the presence of a nearby companion can drastically alter the further evolution, the observable properties and the final fate of both stars (e.g. Vanbeveren 2011, Kippenhahn & Weigert 1967, Podsiadlowski, Joss & Hsu 1992, Pols 1994, Wellstein & Langer 1999, Eldridge, Izzard & Tout 2008).

Besides the complexity of the physics of binary interaction, we have to face the fact that stellar models of massive single stars are still plagued by major uncertainties. Even during one of the simplest evolutionary phases, the main-sequence evolution, their evolution is strongly affected by poorly

constrained internal mixing processes and mass loss. These uncertainties affect all subsequent evolutionary phases and therefore the large role that massive stars play in the enrichment of the interstellar medium, as sources of ionizing radiation and as progenitors of supernovae and gamma-ray bursts.

Promising opportunities to calibrate and test stellar models come from large, homogeneously analyzed samples. For example, the VLT-Flames survey of massive stars (Evans et al. 2005), quantified the metallicity dependence of stellar winds (Mokiem et al. 2007). It also provided the first homogeneously analyzed data set of surface abundance measurements for stars exhibiting a wide range of rotational velocities, which is crucial for testing the effects of rotationally induced mixing processes (Hunter et al. 2009).

When performing such tests, it is important to consider whether the observed properties are indeed the result of single star evolution or whether they might have been caused by interaction with a binary companion. For example, a rapidly rotating star with peculiar surface abundances can be interpreted as evidence that certain mixing processes operate in rotating single stars (Hunter et al. 2009, Maeder et al. 2009). Alternatively, its properties can be interpreted as a signature of a previous phase of mass accretion from a binary companion (Langer et al. 2008). As this example shows, single stellar physics can in some cases lead to similar observable signatures as expected for binary interaction. Because of this degeneracy it is important to test the physics of single stellar models using observations of stars that have not experienced strong binary interaction such as mass transfer. Identifying such stars is not a simple task because the effects of binary interaction are somewhat counter-intuitive. In Section 2 we explain why stars that have experienced strong binary interaction often appear to be single. In Section 3 we argue that "true single stars", can be found in binaries.

2 Not every single star was always single

Absence of evidence for a companion star does not guarantee that the star has never experienced binary interaction. In fact, a star that has experienced binary interaction in the past will often be – or appear to be – single. To illustrate this we present preliminary results of computations with a rapid binary evolutionary code (Hurley et al. 2002, Izzard et al. 2006, De Mink et al. in prep.). For the purpose of the study of massive binaries we updated the treatment of mass and angular momentum loss and transfer, by implementing an improved Roche-lobe overflow scheme to determine the mass-transfer rate. Furthermore, we include a treatment of the effects of rotation on the stellar structure and the mass-loss rate. We calibrated the code against grids of models computed with the detailed binary evolution codes `STARS` (Eggleton 1971, Pols et al. 1995, De Mink, Pols & Hilditch 2007) and `BEC` (e.g. Wellstein & Langer 1999, Petrovic et al. 2005).

In Figure 1 we depict the evolutionary stages of a massive binary adopting initial masses of 20 and 15 solar masses for the primary and secondary star. We vary the initial orbital period. The evolution of such systems is representative for massive binaries with a primary mass between roughly 10 and 40 solar masses, with not too extreme mass ratios. The figure is intended as illustration of the main argument, not as a quantitative prediction. We discuss different phases for which at least one of the stars is a main-sequence star.

Pre-interaction phase Initially both stars reside within their Roche lobes and the binary system is in a detached configuration (blue area). For systems with orbital periods larger than 4 days, this phase lasts approximately as long as the main-sequence lifetime of the primary star. In tighter systems the initially most massive star fills its Roche lobe before finishing its main-sequence evolution (thick dashed line). During this phase the stars evolve similarly to single stars. Their interaction is limited to interaction via stellar winds and tides. In systems with orbital periods smaller than about 10 days the

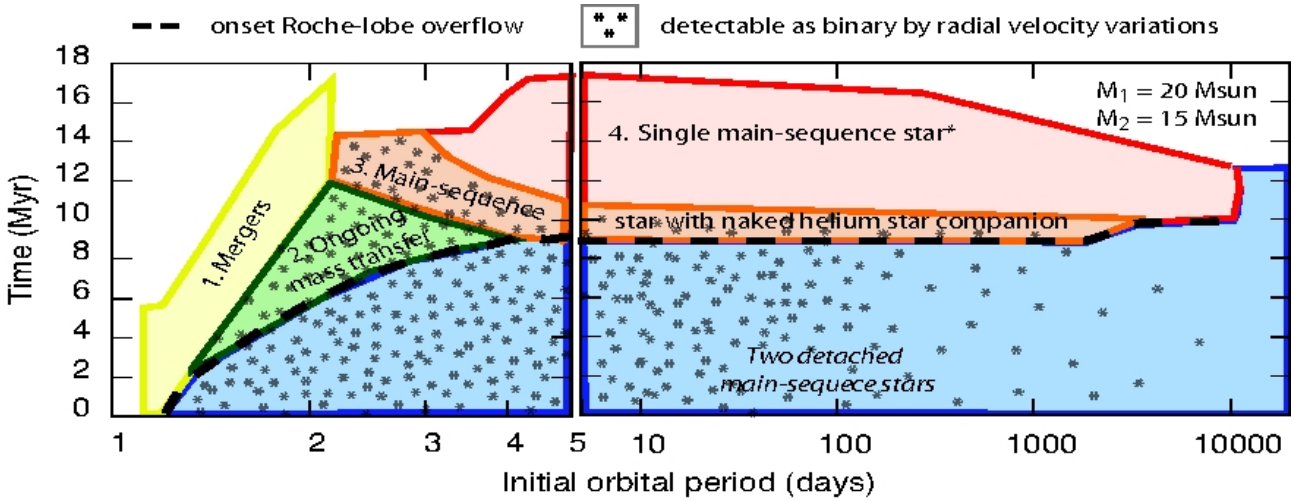

Figure 1: Schematic depiction of the evolutionary stages of a 20+15$M_\odot$ binary as a function of the initial orbital period (x-axis) and time (y-axis). In the left panel we zoom in on very close binaries. We only depict phases in which at least one of the stars is on the main-sequence. The thick dashed line indicates the onset of mass transfer. Plusses indicate qualitatively during which phases systems are detectable as spectroscopic binaries. See text for more explanation.

stars tides will affect their rotation rate. Besides this the physical processes in the star are not expected to differ significantly from those in single stars, assuming that tidally induced mixing processes and angular momentum transport are not very efficient. We refer the reader to De Mink et al. (2009) for a study of the consequences of mixing processes in tidally locked binaries.

These systems can in principle be detected as double-lined spectroscopic binaries, depending on the timing of the observations and on the inclination and eccentricity of the orbit (Sana, Gosset & Evans 2009). A simulation of the detection probability of binaries in the VLT Flames Tarantula survey shows that nearly all binaries with orbital periods up to a 100 days can be identified (>90%). The fraction decreases for wider binaries, but one still expects to recover about half of the binaries with orbital periods between 100 and 1000 days (Evans et al. 2010).

Mergers [1] In the tightest binaries mass transfer will lead to a merger of the two stars (indicated in yellow in Fig. 1). At the moment of contact both stars have only partially burned the hydrogen in their center. The merger product will therefore also be a hydrogen burning, main-sequence star. Although the very tight binaries that lead to these kind of mergers are not very common, there are reasons to believe that mergers can nevertheless not be ignored. In old star clusters mergers can be identified as blue stragglers, being significantly brighter and bluer than stars near the main-sequence turn-off. In young star clusters the turn-off is not well defined and blue stragglers cannot clearly be identified. Given the high fraction of close binaries among massive stars, mergers may constitute a very significant fraction of the stars near the turn-off in young clusters. In regions with continuous star formation mergers will be as bright as newly formed massive single stars. Mergers result from lower mass stars, which are more abundant due to the slope of the initial mass function. Therefore, the fraction of mergers among stars within a given luminosity range may still be significant.

Mergers will have no companion, unless the system was originally a triple. Therefore mergers may be easily mistaken for a primordial single star even though their evolutionary history is completely different. Unfortunately the merger process is poorly understood. In particular, internal mixing, mass and angular momentum loss are uncertain. It is not yet clear whether these mergers demonstrate peculiar observable properties, for example larger rotation rates and enhanced surface nitrogen abun-

dances. Attributing their properties to single star physics might lead to erroneous conclusions.

Semi-detached systems [2] Binary systems in which the primary fills its Roche lobe during its main-sequence evolution experience a long-lasting phase of mass transfer (indicated in green in Fig 1). As these systems are close, tides are efficient in locking the rotation of both stars to the orbit. Large amounts of mass can be accreted onto the companion star, while the transferred angular momentum is quickly converted into orbital angular momentum due to tides (e.g. Petrovic et al. 2005). Because of their geometry and short orbital periods, these systems will show eclipses and radial velocity variations in nearly all cases. They can be useful to test the physics of mass transfer and contact systems (e.g. De Mink et al. 2007, van Rensbergen et al. 2010).

Post-interaction: a stripped helium star companion [3] When the initially most massive star fills its Roche lobe it will continue to lose mass until it has been stripped from its entire hydrogen-rich envelope. For systems with initial orbital periods larger than 4 days, the mass-transfer phase lasts only a thermal timescale. This is short compared to the nuclear timescale and is not visible in Fig. 1. During the mass-transfer phase the orbit widens and the secondary is now the brightest star in the system. The stripped primary star is very hard to detect, due to its low luminosity, low mass and the wide orbit. In addition, the secondary is expected to be rotating rapidly as a result of the accreted angular momentum. Broadening of the spectral lines because of rotation makes it even harder to detect spectral lines of the companion. Therefore, these objects often appear to be single even though their evolution is severely affected by binary interaction.

The duration of this phase, indicated in orange in Fig. 1, is set by the helium burning lifetime of the primary star. This is of the order of one tenth of its main-sequence lifetime, or longer as stellar winds reduce the mass of the helium star. Even though the duration of this phase is considerable, to our knowledge no such massive binary has been detected, which may reflect the difficulty to detect such systems.

Post-interaction: disrupted systems and neutron star companions [4] By the time the initially most massive star explodes, the orbit has become fairly wide due to mass transfer and stellar winds. In most cases, the binary is expected to be disrupted, leaving the secondary behind as a single star. The secondary star may acquire a moderate spatial velocity, although the formation of runaway stars will be the exception rather than the rule. This phase, indicated in red in Fig. 1, lasts as long as the remaining main-sequence lifetime of the secondary.

3 Binaries provide our only chance to identify true single stars

We argued above that many stars are, or appear to be, single after experiencing strong binary interaction. Such stars are expected to constitute a sizable fraction of all single stars and can not be neglected[1]. Searching for stars without a companion is therefore not an effective method to identify "true single stars", i.e. stars that have lived their lives without experiencing strong interacting such as mass transfer. Similarly, removing stars with evidence for binarity from an observed sample will be counter-productive. One would preferentially remove the pre-interaction systems, in which stars have lived their lives similarly to single stars, while post-interaction systems are left in the sample. In other words, excluding detected binaries from a sample increases the relative fraction of stars that have been affected by binary interaction.

[1] As pointed out by the referee this is not a new result, it has been realized by several groups working on binaries. However, a full review of the literature is beyond the scope of this contribution.

Fortunately, binaries provide us with an opportunity to identify stars that have not suffered from strong binary interaction. Evolutionary models show that binary interaction by Roche-lobe overflow strips the donor star from its hydrogen-rich envelope. When one of the stars fills its Roche lobe, it does not detach again until the entire envelope has been removed. Therefore, in a close binary system containing two detached main-sequence stars, we can exclude the occurrence of mass transfer since their birth as hydrogen burning stars.

Such binaries often provide us with a unique method to measure the fundamental stellar parameters directly. For this reason they have been used successfully by various authors to test evolutionary models of single stars (e.g. Schröder, Pols & Eggleton 1995, Pols et al. 1995, Pavlovski & Southworth 2009, Pavlovski et al 2009). Therefore we advocate that, in order to increase our understanding of single stars, binaries provide one of our best opportunities.

Acknowledgements

We acknowledge the members of the VLT Flames consortium of massive stars and the stellar evolutionary groups in Bonn and Utrecht for fruitful discussions.

References

De Mink, S.E., Pols, O.R., Hilditch, R.W. 2007, A&A 467, 1181
De Mink, S.E., Cantiello, M., Langer, N., Pols, O.R., Brott, I., & Yoon, S.-C. 2009, A&A 497, 243
Eggleton, P.P. 1971, MNRAS 151, 351
Eldridge, J.J., Izzard, R.G., & Tout, C.A. 2008, MNRAS 384, 1109
Evans, C.J., Smartt, S.J., Lee, J.-K., et al. 2005, A&A 437, 467
Evans, C.J., Bastian, N., Beletsky, Y., et al. 2010, IAU Symposium 266, 35
Hunter, I., Brott, I., Langer, N., et al. 2009, A&A 496, 841
Hurley, J.R., Tout, C.A., & Pols, O.R. 2002, MNRAS 329, 897
Izzard, R.G., Dray, L.M., Karakas, A.I., Lugaro, M., & Tout, C.A. 2006, A&A 460, 565
Kippenhahn, R., & Weigert, A. 1967, ZAP 65, 251
Langer, N., Cantiello, M., Yoon, S.-C., Hunter, I., Brott, I., Lennon, D., De Mink, S.E., & Verheijdt, M. 2008, IAU Symposium 250, 167
Maeder, A., Meynet, G., Ekström, S., & Georgy, C. 2009, CoAst 158, 72
Mason B.D., Hartkopf W.I., Gies D.R., Henry T.J., & Helsel J.W. 2009, AJ 137, 3358
Mokiem, M.R., de Koter, A., Vink, J.S., et al. 2007, A&A 473, 603
Pavlovski, K., & Southworth, J. 2009, MNRAS 394, 1519
Pavlovski, K., Tamajo, E., Koubský, P., Southworth, J., Yang, S., & Kolbas, V. 2009, MNRAS 400, 791
Petrovic, J., Langer, N., Yoon, S.-C., & Heger, A. 2005, A&A 435, 247
Podsiadlowski, P., Joss, P.C., & Hsu, J.J.L. 1992, ApJ 391, 246
Pols, O.R. 1994, A&A 290, 119
Pols, O.R., Tout, C.A., Eggleton, P.P., & Han, Z. 1995, MNRAS 274, 964
Pols, O.R., Tout, C.A., Schröder, K.-P., Eggleton, P.P., & Manners, J. 1997, MNRAS 289, 869
Sana, H., Gosset, E., Nazé, Y., Rauw, G., & Linder, N. 2008, MNRAS 386, 447
Sana, H., Gosset, E., & Evans, C.J. 2009, MNRAS 400, 1479
Sana, H., & Evans, C.J. 2010, arXiv:1009.4197
Schröder, K.-P., Pols, O.R., & Eggleton, P.P. 1997, MNRAS 285, 696
Vanbeveren, D. 2011, in Proceedings of the 39th Liège Astrophysical Colloquium, eds. G. Rauw, M. De Becker, Y. Nazé, J.-M. Vreux & P.M. Williams, BSRSL 80, 530
van Rensbergen, W., De Greve, J.P., Mennekens, N., Jansen, K., & De Loore, C. 2010, A&A 510, A13
Wellstein, S., & Langer, N. 1999, A&A 350, 148

Discussion

N. Evans: Is there any way you can detect merger products through Asteroseismology (CoRoT, Kepler, Most)?
S. De Mink: Possibly. The internal structure of a star that resulted from the merger of two less massive stars will be very different from that of a star that has lived its live as a single star. The differences in internal structure wil give rise to other oscillation modes.
However, I think what the interior of stellar mergers will look like is still very poorly known compared to the extreme sensitivity of oscillation modes to even minor changes in the stellar structure. My feeling is that measuring something that is highly uncertain with a very accurate measurement tool will not give you the insight you want.

D. Gies: I am curious about your treatment of angular momentum loss through winds (for example, if mass loss in rapid rotators is preferential at poles).
S. De Mink: We are currently implementing latitude dependent winds using prescriptions from the Geneva Group. The models presented here assume spherically symmetric mass loss. However, the effect of polar winds on the rotation rates is limited. Due to the deformation of the star, most of the mass is still lost at intermediate latitudes (Georgi, C. et al. in prep.).

H. Zinnecker: Can you give us an example of an initial configuration (component masses, typical separation) that leads to a low-mass X-ray binary (with a neutron star, say)?
S. De Mink: This is not my expertise, but I guess one would need a primary star that is massive enough to become a neutron star, say 15 solar masses, and a low mass companion of say 1 solar mass in an orbit so wide that the stars start to interact in an advanced state, say several hundred solar radii. Unfortunately, this type of binaries is very hard to detect: they are wide and the companion star will be faint. The number of progenitor systems for such systems is still poorly constrained from observations.

N. Smith: In your models for stars that result from mergers, you showed that it typically takes at least 1-2 Myr for the rapidly rotating merger to spin down. I am wondering what determines this timescale or how it may be shortened. The reason I ask is because there are several blue supergiants surrounded by equatorial rings (e.g. SN1987A's progenitor) where the nebular ring is only $\sim 10^4$ year old but the central star is not a particularly fast rotator. Could you please comment?
S. De Mink: How stellar mergers (or stars that gained mass from a companion) get rid of their excess angular momentum and spin down is still an open question. In these preliminary models I assumed that the mergers rotate initially at their break up limit and I only considered spin down as a result of their radiatively driven winds. There are mechanisms we can think about that will help the star to spin down more quickly, for example magnetic fields or mass loss while the star is still in its inflated stage trying to restore its thermal equilibrium. Nevertheless, the low rotation rates for blue supergiants are intriguing.

Solving light curves of WR+O binaries: the regularization approach

Igor I. Antokhin

Sternberg State Astronomical Institute, Moscow State University, Moscow, Russian Federation

Abstract: Extended semi-transparent atmospheres of WR stars in eclipsing WR+O binaries present some difficulties for analysis of their light curves. We present an approach to the problem based on solving the most general form of integral equations describing a light curve of a WR+O binary: Fredholm's equations of the first kind. The unknown functions are the brightness and opacity distributions across the disk of the WR component. The equations represent an ill-posed problem. To get a stable, unique solution one needs to impose some *a priori* constraints on the solution. We review various physically justified sets of constraints and, using artificially simulated light curves with known solutions, show how these constraints and the so-called regularization technique work to retrieve the functions of interest. The influence of errors in the input light curve on the solution is shown and discussed. The algorithms and the corresponding computer programs are open to the scientific community.

1 Introduction

Eclipsing binaries containing a WR component provide a potential possibility to directly probe WR winds and to get important clues about their structure. However, strong semi-transparent WR winds make parametric modeling in binaries rather problematic. In the most general case the light loss during an eclipse in a binary is described by the equation

$$1 - l(\Delta) = \iint\limits_{S(\Delta)} I_c(\vec{\rho}) I_a(\vec{r})\, d\sigma \tag{1}$$

where l is the normalized flux (maximal flux outside of eclipses is equal to 1), $I_c(\vec{\rho})$ is the brightness distribution across the disk of the eclipsed component, $I_a(\vec{r})$ is the opacity distribution across the disk of the component in front, S is the eclipsed area, Δ is the projected distance between the centers of the stellar disks (normalized by the orbital separation), i is the orbital inclination angle. For simplicity, in the rest of the paper we assume a circular orbit, although the method outlined below can be easily generalized to elliptical orbits. For a circular orbit, $\Delta = \sqrt{\cos^2 i + \sin^2 i\, \sin^2 \theta}$, where θ is the orbital phase. In case of spherical stars with thin atmospheres the function I_a for a given component is simply

$$I_a(\vec{r}) = \begin{cases} 1, & |\vec{r}| < r_* \\ 0, & |\vec{r}| \geq r_* \end{cases}, \tag{2}$$

while I_c may be parametrized e.g., by the linear darkening law

$$I_c(s) = I_0 \left(1 - x + x\sqrt{1 - \frac{s^2}{r_*^2}}\right) \tag{3}$$

With these assumptions, equation (1) becomes a parametric problem which can be solved by e.g. minimizing χ^2 error between the model and observed light curves. Many minimization techniques have been proposed in the literature (see e.g. the semi-analytical approach by Russell & Merrill (1952) for classical binaries or the purely numerical method of Wilson (1979) for close binaries with tidally distorted components). In case of WR+O binaries the functions I_a and I_c for the WR component cannot be easily represented by any parametric expressions. In the present paper we implement a method for directly solving (1) without making any strong assumptions about I_a and I_c for the WR component.

In Section 2 we describe the method itself. In Section 3 we show how the method works on artificially simulated light curves of a WR+O binary and discuss the influence of errors in the input data on the solution. We discuss the results and potential application of the method to other problems in Section 4.

2 Method: model assumptions and basic equations

The method outlined below follows the approach first suggested by Cherepashchuk and his co-authors (see e.g., Goncharsky, Cherepashchuk & Yagola 1985, Antokhin & Cherepashchuk 2001 and references therein). To simplify the problem, we make the following assumptions: (i)the binary components are spherical, the functions I_a and I_c are axially symmetrical; (ii)the O component is a "normal" main-sequence star so its I_a and I_c functions can be represented by the equations (2) and (3) respectively. With these assumptions, equation (1) written for both eclipses, becomes

$$1 - l_1(\Delta) = \int_0^{R_\mathrm{w}} K_1(s, \Delta) I_0 I_a(s)\, ds \tag{4a}$$

$$1 - l_2(\Delta) = \int_0^{R_\mathrm{w}} K_2(s, \Delta) I_c(s)\, ds \tag{4b}$$

$$L_\mathrm{O} + L_\mathrm{WR} = I_0 \pi r_\mathrm{O}^2 (1 - \frac{x}{3}) + 2\pi \int_0^{R_\mathrm{w}} I_c(s) s\, ds = 1, \tag{4c}$$

where indexes 1 and 2 refer to the primary (WR star in front) and secondary (O star in front) eclipses respectively, K_1 and K_2 are the equation kernels describing the geometry of the eclipsed areas, I_0 is the brightness of the O component in the center of its disk, I_a and I_c are opacity and brightness functions for the WR component, R_w is the radius of the WR disk (wind), r_O is the radius of the O star, L_O and L_WR are the luminosities of the O and WR stars respectively. The third equation is the normalization condition on the luminosities of the binary components. Expressions for K_1 and K_2 will be given in the detailed forthcoming paper (Antokhin 2011).

The unknown quantities in (4) are the I_a and I_c functions, the orbital inclination angle i and the radius of the O star r_O. At any given pair of i and r_O, (4) can be solved as follows: (i)solve (4b) and obtain I_c; (ii)substitute I_c to (4c) and obtain I_0; (iii)substitute I_0 to (4a) and solve it to obtain I_a. The equations(4a,b) have the form of the well known Fredholm's integral equation of the first kind

$$Az = \int_a^b K(x,s)z(s)ds = u(x), x \in [c,d] \quad (5)$$

Such equations present a so-called ill-posed problem, that is, infinitely small perturbations in the input data may result in arbitrarily large fluctuations in the solution. Obtaining a unique stable solution requires some *a-priori* knowledge about the unknown function. According to Tikhonov et al. (1995), there are two possible approaches to the problem: (i)to solve Fredholm's equation on a so-called compact set of unknown functions; (ii)to use some sort of regularization technique. We consider these two approaches below.

2.1 Solving (4) on a compact set

A set Y of a metric space Z is said to be compact if from any infinite sequence of its elements one can extract a sub-sequence converging to some element $y \in Y$. Considering our particular problem, the examples of the compact sets are (i)non-negative monotonically non-increasing functions; (ii)non-negative convex functions; (iii)non-negative convex-concave functions. It can be demonstrated (see, e.g. Tikhonov et al. 1995) that Fredholm's equation of the first kind has a unique solution if the latter is searched for on a compact set. The above examples of compact sets seem to be quite reasonable assumptions about the unknown brightness and opacity distributions across the disk of the WR component. They are loose enough to not restrict the functions by any parametric form like the linear limb darkening. Solving (4a), (4b) consists in minimizing the residual (the norm) squared $||Az - u||^2$, $z \in S$ (see (5)). Here u is the observed light curve $(1 - l_{1,2}(\Delta))$, Az is the model light curve (the elements of the matrix A are constructed in such a way that the product Az is the numerical approximation of the integral in (5)). A particular expression for the norm depends on the metric used to measure the distance between the model and the input light curve. This approach was used in Antokhin & Cherepashchuk (2001) and other previous papers.

2.2 Regularization approach

One problem with solving (4) on a compact set is that it does not require the solution to be smooth. As we will see below, this leads to unrealistic solutions. One can stabilize the solution and require it to be smooth by using the regularization technique developed by Tikhonov (Tikhonov et al. 1995). The basic idea is very simple: instead of minimizing the residual, one has to minimize the function $||Az - u||^2 + \alpha||z||^2$. The second term in this expression is the so-called stabilizing term. It is small when z is smooth and large when z is oscillating. Thus, minimizing this function one can minimize the residuals while keeping z smooth. The regularization parameter α controls the relative weight of the stabilising term.

The central question in this technique is how to choose α. Tikhonov et al. (1995) showed that there exists a way of choosing α based on the uncertainty of the input data δ such that the resulting approximate solution converges to the true solution as long as $\delta \to 0$. In case the A operator is known exactly, α must be chosen in such a way that $||Az_\delta^\alpha - u_\delta|| = \delta$, where u_δ is the input data set containing some noise, and z_δ^α is the approximate solution obtained with this data set.

In its original form the regularization technique requires the solution to be smooth and does not impose other constraints. The technique can, however, be combined with some *a priori* constrains on the unknown functions like those listed in the previous subsection.

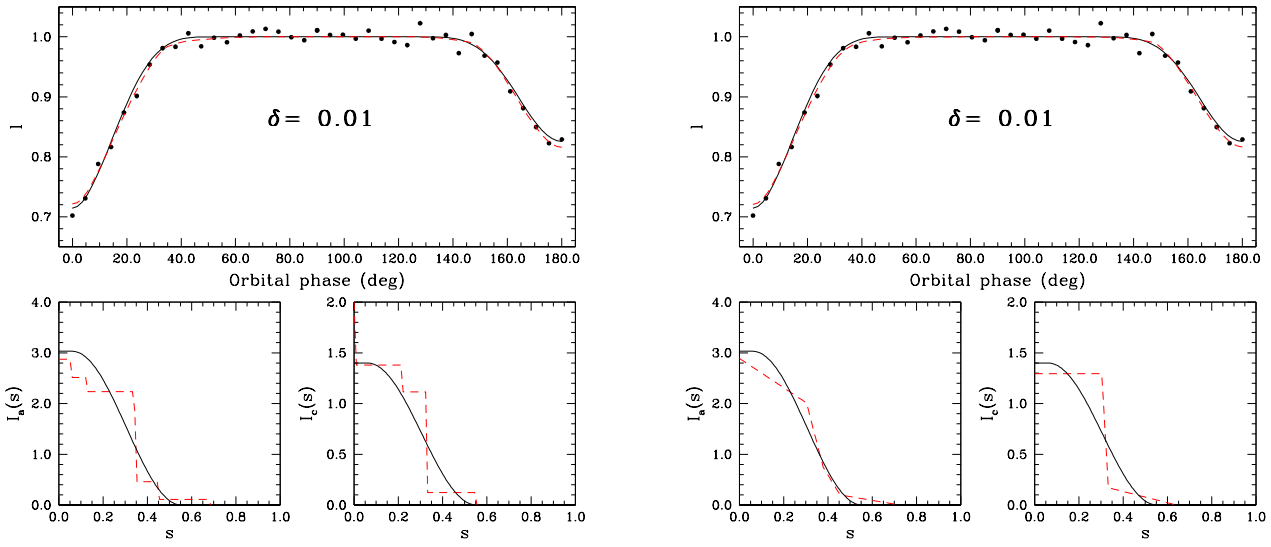

Figure 1: Solution of (4) on compact sets. Left: assumption (i) of section 2.1. Right: assumption (iii). Solid lines represent the exact I_a and I_c (bottom plots) and the exact light curve (top plots). Dots on the top plots show the simulated light curve with added noise. Dashed lines represent approximate solutions (bottom plots) and model light curves (top plots).

3 Simulated light curves

To demonstrate how various approaches to solving (4) work, we created a simulated light curve of a WR+O binary using smooth convex-concave functions I_a and I_c. Gaussian noise with various standard deviations was then added to the exact light curve to produce several simulated light curves used as input in (4). The values of i and $r_{\rm O}$ were set to $i = 78^\circ$, $r_{\rm O} = 0.2$.

In Fig.1 two examples of solving (4) on compact sets are shown. The approximate solutions (dashed lines) demonstrate some characteristic features: stair-like structures in the left hand plot, broken lines in the right hand plot. The reason for these structures is that in an attempt to minimize the residual (recall that input data contain noise), the algorithm always uses as much flexibility as it is allowed to. In model (i) the solution must be non-increasing. This means that it *may* be non-decreasing in some parts. Similarly, in the convex (concave) part of the model (iii) the second derivative of the solution must be non-positive (non-negative); this means that it *may* be equal to zero. It is important to note that the above structures will *always* be present in approximate solutions of this kind, as long as the data contain some noise. Clearly, such brightness and opacity distributions are not very meaningful.

In Fig.2 the regularization approach is shown. In the left hand plot, the input light curve is the same as in Fig.1. The unknown functions are assumed to be non-negative, convex-concave, smooth (the functions themselves and their first derivatives continuous). The right-hand plot shows how the approximate solution approaches the true solution if the error of the input data decreases.

4 Discussion

Provided that an input light curve has sufficiently good accuracy ($\delta = 0.001$ seems to be a reasonable expectation from modern photometry), the regularization technique allows one to obtain empirical distributions of brightness and opacity across the disk of the WR component in an eclipsing WR+O binary. I_c can be used to estimate, e.g., the brightness temperature of the WR star. More inter-

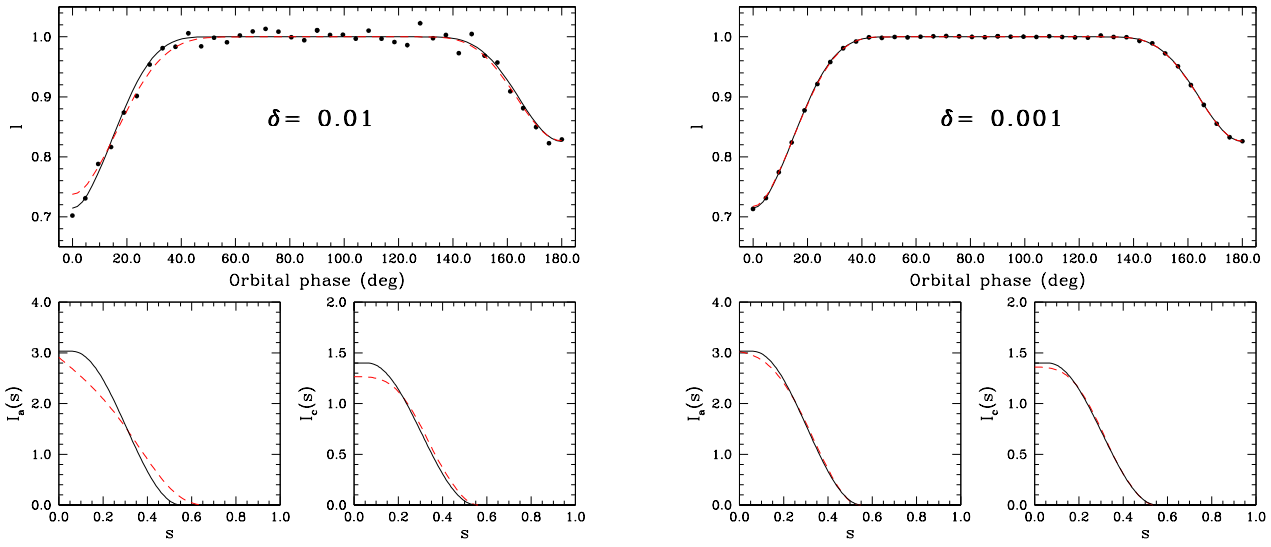

Figure 2: Regularization approach. I_a and I_c are assumed to be convex-concave.

estingly, I_a allows one to get an empirical distribution of the velocity in the WR wind. Indeed, $I_a(s) = 1 - e^{-\tau(s)}$, where τ is the optical depth of the WR wind along the line of sight at the impact distance s. In turn,

$$\tau(s) = 2 \int_s^\infty \frac{\epsilon(r) r dr}{\sqrt{r^2 - s^2}}, \tag{6}$$

where ϵ is the linear absorption coefficient. Recalling that the main absorption agent in the WR wind in the optical continuum is electronic scattering and using the continuity equation, we get $\epsilon(r) = \sigma_T n_e = \frac{k \sigma_T \dot{M}}{4\pi m_p v(r) r^2}$, where $k \simeq 0.5$ if helium is fully ionized, $k \simeq 0.25$ in the He II zone[1], σ_T is the scattering cross section, $\dot{M}$ is the mass loss rate, m_p is the proton mass, $v(r)$ is the velocity law. Thus, from the empirical $I_a(s)$ one can obtain $\tau(s)$, and, solving (6), called Abel's equation, obtain $\epsilon(r)$ and hence $v(r)$. Such an empirical velocity law can be used as a constraint in any self-consistent theory of WR winds. Solving Abel's equation as well as application of the technique presented in the current paper, to real objects, will be a subject of forthcoming papers.

Potential applications of the regularization technique are much wider than the particular problem discussed in the present paper. This technique can be used whenever a problem can be described by Fredholm's equation of the first kind (CoRoT observations of exoplanets, lunar occultations of stars, correction of observational data for the response function of the receiver being a few examples of its use). The computer code for solving light curves of WR+O binaries and the underlying libraries for solving Fredholm's equation using non-trivial *a priori* constraints on the solution are freely available to all interested sides on request.

Acknowledgements

This research is supported by the Russian Foundation for Basic Research through the grants No 08-02-01220 and 11-02-00940.

[1]Helium is the most abundant element in WR winds.

References

Antokhin, I.I., & Cherepashchuk, A.M. 2001, Astronomy Reports 45, 517
Antokhin, I.I. 2011, MNRAS, in preparation
Goncharsky, A.V., Cherepashchuk, A.M., & Yagola, A.G. 1985, *Ill-posed problems of astrophysics*, Moscow, Nauka
Russell, H.N., & Merrill, J.E. 1952, Contrib. Princeton Univ. Obs., No. 26
Tikhonov, A.N., Goncharsky, A.V., Stepanov, V.V, & Yagola, A.G. 1995, *Numerical methods for the solution of ill-posed problems*, Kluwer Academic Publishers, Dordrecht
Wilson, R.E., 1979, ApJ 234, 1054

Discussion

G. Rauw: You mentioned the impact of the errors on the data on the stability of your solution. One can of course reduce these errors by using e.g. CoRoT, but what about the intrinsic variability of the WR star that will also appear in the light curve?
I. Antokhin: As long as you use a regularization technique, the stability of the solution is not a problem. You need good accuracy of the data to get an accurate estimate of the "exact" brightness and opacity distributions. As for the intrinsic irregular variability, one should obtain as much data (long runs) as possible so these variations will be smoothed in the mean light curve. Filtering based on e.g. Fourier decomposition is also possible.

Theoretical Models of Interacting Winds in Massive Binaries

Julian Pittard[1]

[1] School of Physics and Astrophysics, University of Leeds, United Kingdom

Abstract: Massive binary systems are excellent laboratories for studying stellar winds. The powerful collision of the winds unleashes a broad spectrum of emission revealing the interesting physics of high Mach number shocks, including the acceleration of a small proportion of particles to relativistic energies. The wind-wind collision is also useful for probing the underlying wind and stellar parameters. This paper reviews our current understanding of the dynamics of such systems and models of (predominantly) the non-thermal emission, finishing with a brief note on possible future advances.

1 The Dynamics of Colliding Wind Binaries

1.1 Instabilities

In binary systems, the winds collide between the stars (or the stronger wind overwhelms its companion's wind, and crashes directly onto its surface). Therefore, it should come as no surprise that colliding wind binaries (CWBs) are an extremely diverse class of systems, with a very wide range of properties. To zeroth order, the nature of a particular CWB depends on the orbit of its stars. In short period systems, where the two stars are very close together, the wind-wind collision is likely to be highly radiative. The shock-heated gas therefore cools very rapidly, and a geometrically thin and dense region of gas forms which is prone to severe, and perhaps disabling, non-linear thin-shell instabilities (NTSI, Vishniac 1994) [1]. On the other hand, if the orbital period is long, the shocked gas may behave largely adiabatically, flowing out of the system while still hot. In this case the wind-wind collision region (WCR) stays thick and "puffed-up", and is far less affected by instabilities. Kelvin-Helmholtz instabilities, due to a velocity shear at the contact discontinuity between the winds, may occur in this case. Where one wind is radiative and the other largely adiabatic, a thin dense layer of cooled gas abuts a thicker, hotter, but more rarefied layer which acts like a "cushion" to damp out thin shell instabilities occuring in the dense layer (Vishniac 1983). These differences were illustrated by Stevens et al. (1992), and are reproduced in Fig. 1.

The transition between radiative and adiabatic post-shock regions is conveniently estimated using the value of $\chi \equiv t_{\rm cool}/t_{\rm dyn} \approx v_8^4 D_{12}/\dot{M}_{-7}$, where $t_{\rm cool}$ is the cooling time of the gas, $t_{\rm dyn}$ is a dynamical flowtime which is rather loosely defined but can be taken as either the time for shocked

[1] This is the conventional wisdom, but in fact it is not clear exactly what occurs between the stars - e.g. even whether two "winds" are produced - in such an extreme and hostile environment.

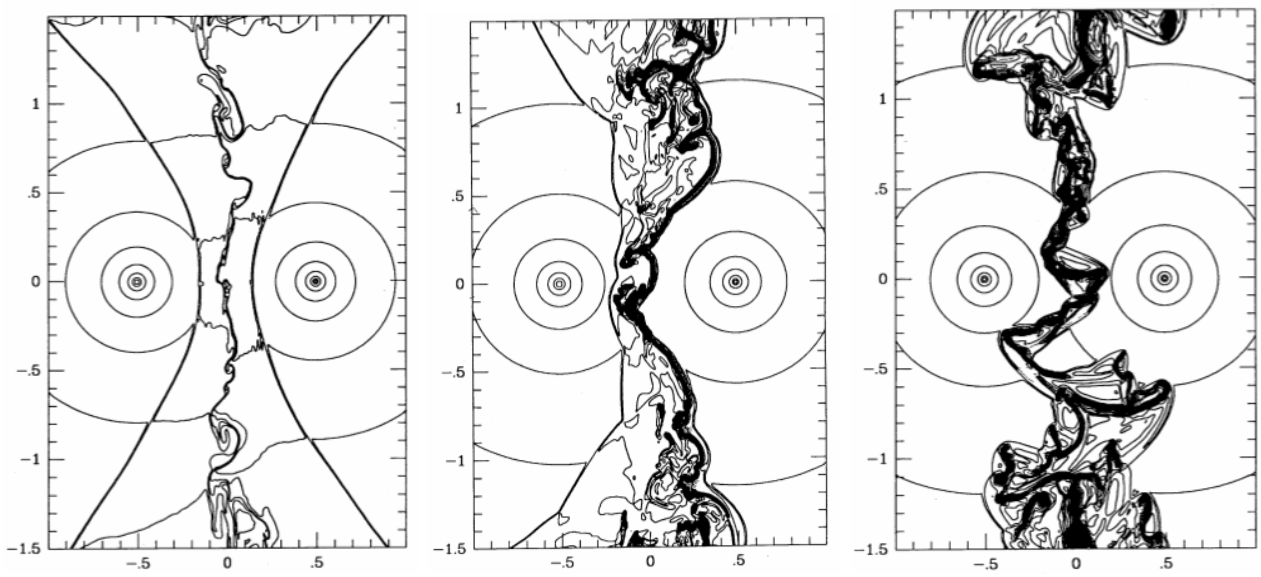

Figure 1: Instabilities in the WCR of CWBs. Left: When both sides of the contact discontinuity are largely adiabatic, the WCR is very smooth. Center: When one side is radiative thin shell instabilities occur, but are somewhat limited by the "cushioning" of the hot gas (Vishniac 1983). Right: When both sides are radiative, the much stronger and highly non-linear thin shell instability occurs (Vishniac 1994). Adapted from Stevens et al. (1992).

gas at the apex of the WCR to flow a distance $D_{\rm sep}$ downstream, or for the shocked gas from the weaker wind to flow a distance $r_{\rm OB}$ downstream (see Stevens et al. (1992) for these definitions). In the above, v_8 is the wind speed normalized to $1000\ {\rm km\,s^{-1}}$, D_{12} is the stellar separation normalized to $10^{12}\,{\rm cm}$, and $\dot{M}_{-7}$ is the mass-loss rate normalized to $10^{-7}\ {\rm M_\odot\,yr^{-1}}$. Note that this formalism for χ depends on specific assumptions about the post-shock temperature and the morphology of the cooling curve at this point (see Pittard & Stevens 2002). By specifying appropriate values for $\dot{M}_{-7}$, etc., it is possible to determine a separate value of χ for each shocked wind. Values of χ in several key systems are listed in Pittard et al. (2005a).

1.2 Radiative Driving Effects

Early hydrodynamical models of the WCR were 2D, axisymmetric, and ignored orbital motion and radiative driving. The self-consistent transition between adiabatic and radiative behaviour was a key improvement in Stevens et al. (1992) compared to earlier work (e.g. Luo et al. 1990). Up until this point, all works modelled the winds as colliding at their terminal speed (or some fraction of this), and conveniently ignored the acceleration of the winds. This assumption is valid in long period systems, where the winds have room to accelerate before colliding, but is clearly not so when the stars are relatively close together. The effect of a nearby opposing radiation field was first explored by Stevens & Pollock (1994), where an effect termed "radiative inhibition" was noted. In this scenario the acceleration between the stars of one wind is inhibited by the radiation field of the other star, thus reducing the speed of the wind. A complementary effect, termed "radiative braking", was studied by Gayley et al. (1997). This effect comes into play in systems where the stronger wind closely approaches the more luminous star. This condition is met in many Wolf-Rayet (WR) + O-star binaries. The stronger radiation field may then efficiently couple to the more powerful wind, causing a sudden deceleration or braking. The effect is highly non-linear, and the braking can be so severe that the stronger wind can be prevented from colliding with the surface of the more luminous star even in

cases where a normal ram-pressure balance between the winds would not be possible.

1.3 Orbital Effects

The first 3D models of CWBs published in a refereed journal were presented by Lemaster et al. (2007), with a focus on the effect of orbital motion. This causes the WCR to twist as the hot gas flows out of the system, creating an effect which resembles an Arcimedian spiral. However, this investigation was highly simplified in that it lacked several key processes which are important in the short-period systems where the effects of orbital motion are greatest. The most notable omissions were the lack of any treatment for the acceleration of the winds and the cooling of the shocked gas. Shortly afterwards, 3D smoothed-particle-hydrodynamics (SPH) simulations of the WCR in the massive binary system η Carinae were presented (Okazaki et al. 2008). Though these models were isothermal, and did not solve for the temperature structure behind the shock, they provided much insight into the dynamics of the WCR in this highly eccentric ($e \approx 0.9$) system.

At about the same time, a "dynamic" model was presented by Parkin & Pittard (2008). This model did not solve the hydrodynamic equations, but instead mapped the apex of the WCR (given by the equations in Stevens et al. 1992) into a 3D space. The apex was provided with a time-dependent skew which aimed to reflect the ratio of the wind to orbital speeds, and the gas was assumed to behave ballistically further downstream. Though the resulting dynamics are only representative of the true situation, a comparison against results from a full hydrodynamical calculation revealed that this approach does a more than adequate job in many situations. Its great power, of course, is its speed, with a full 3D orbital calculation taking only seconds to run. It is then a simple matter to map appropriate emissivities onto the contact surface of the winds and perform ray-tracing through the volume. This method was also applied to a study of η Carinae, and revealed that contrary to the conclusion of Okazaki et al. (2008), the observed X-ray minimum could not be explained by an increase in absorption as the denser wind of the LBV primary moves in front of the apex of the WCR (Parkin et al. 2009). In fact, it now seems that the action of instabilities like those shown in Fig. 1 may play a key role in explaining the minimum (Parkin et al. 2011, submitted).

The first 3D simulations of CWBs to include orbital motion, the radiative driving of the winds and cooling of the shocked gas were presented by Pittard (2009). Focusing on O+O-star systems, this work showed that in a short period (3 d) system, the low speed of the winds between the stars prior to their collision ($730\,\mathrm{km\,s^{-1}}$) led to rapid cooling ($\chi << 1$) and the generation of a cold dense sheet of compressed gas. This sheet is susceptible to instabilities, and dense clumps break-off which are surrounded by bowshocks and hot shocked gas. However, the instabilities develop slightly differently from the equivalent case without orbital motion. This is because the high inertia of the dense shell causes it to move to the trailing edge of the WCR as the stars move around on their orbits. This curvature means that downstream the leading edge becomes quite rarefied and remains hot, such that this gas acts as a cushion against run-away development of the NTSI. It will be interesting to see if the NTSI occurs in systems which are even more radiative.

A system with the same stars as the previous case but where the orbital period was increased to 10 d displays totally different behaviour. This is due to the increased distance between the stars which allows the winds to accelerate to higher speeds before they collide ($1630\ \mathrm{km\,s^{-1}}$), and for the shocked gas to be hot and rarefied enough for it to remain largely adiabatic ($\chi \sim 40$) as it flows out of the system. The WCR is now very smooth, with small Kelvin-Helmoltz instabilities along the contact surface the only disturbance. The twisting of the WCR due to orbital motion is also less severe.

The most interesting dynamics occurred in an eccentric system ($e = 0.36$) where the periastron and apastron separations were chosen to match the orbital separations in the two previous simulations. The WCR displays a strong hystersis through the orbit (see Fig. 2), with marked differences

in its properties when the stars are at identical stellar separations but approaching or receding from periastron. For instance, the gas in the WCR remains hot until near phase 0.9, after which it collapses into a thin dense sheet which is torn apart by instabilities. However, it is not until after apastron that the cold clumps are cleared away from the stars. This is again due to their high inertia relative to the rarefied gas which flows past them. During the transition between a radiative and largely adiabatic WCR (as χ goes from $<< 1$ to ~ 40), the radiative overstability (e.g. Strickland & Blondin 1995; Pittard et al. 2005b) is seen. More recently, the dynamics of WR+O-star binaries have been investigated by Parkin et al. (2011, submitted - see also this volume).

Studies of how wind clumping affects the WCR have been presented by Walder (1998), who showed that dense clumps can tip an otherwise marginally adiabatic WCR into a radiative regime. Pittard (2007) examined the effect of clumps on an adiabatic WCR. If the clumps are not too dense or large (so that they do not punch through the WCR), they can be rapidly destroyed by the vorticity created during their passage through the shocks bounding the WCR. Although the WCR becomes highly turbulent as a result, the overall effect is to smooth out the flow. Thus determinations of the stellar mass-loss rates using the emission from a WCR may be relatively insensitive to clumping, and thus offer a useful alternative to other methods where this is not the case. The strong turbulence occuring within the WCR also has implications for particle acceleration and the mixing of the winds.

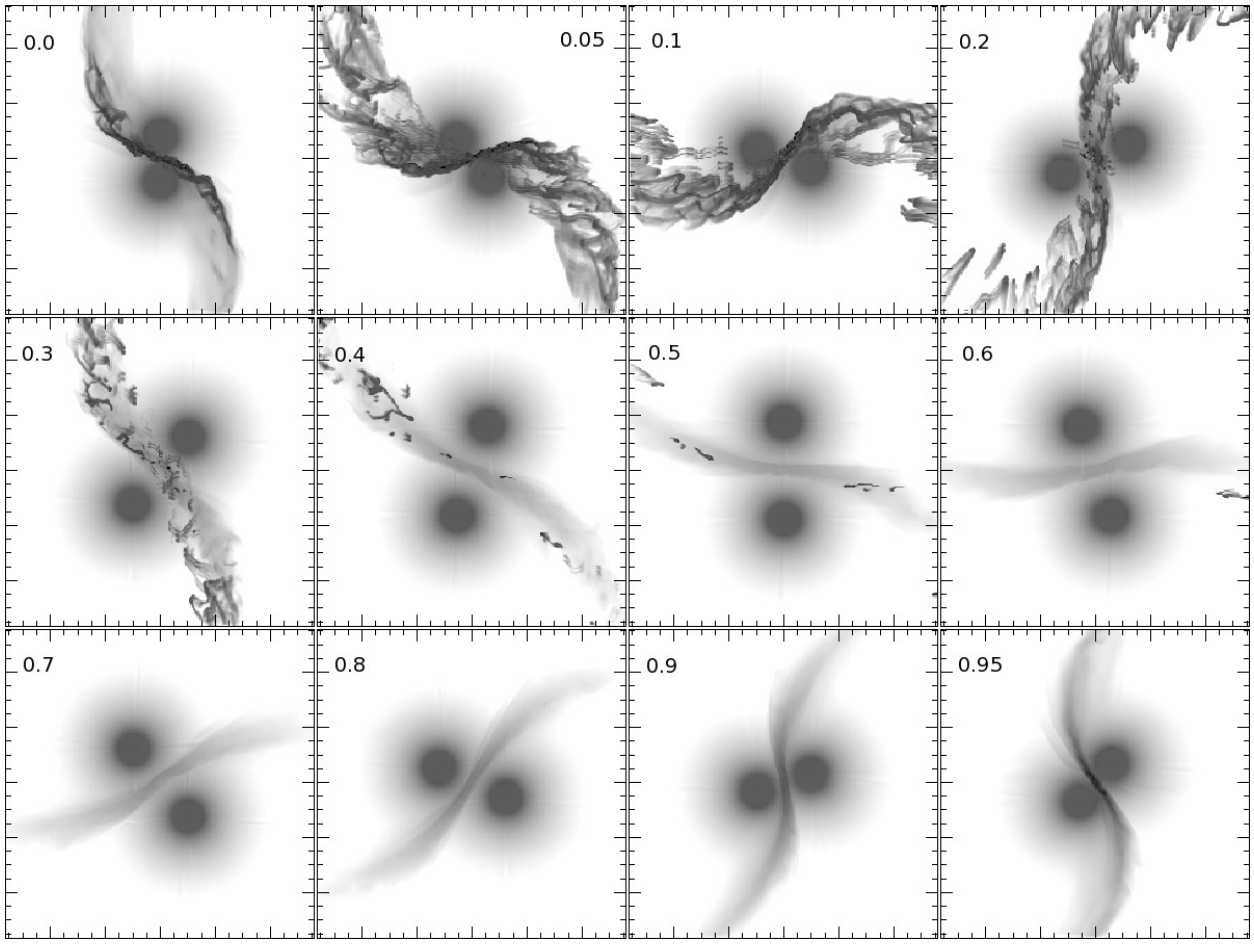

Figure 2: Intensity images at 1000 GHz for an observer viewing an eccentric ($e = 0.36$) O+O-star system with an orbital period of 6.1 d (see Pittard (2009) for details of the hydrodynamical model).

2 Modelling CWB Phenomena

Models of the WCR in CWBs can help to determine:

1. The mass-loss rate and wind speed (for instance from the X-ray emission - see e.g. Stevens et al. 1996 and Pittard & Corcoran 2002). The thermal radio emission from close binaries may also be used to determine the mass-loss rates.

2. The wind momentum ratio and flow speed in the WCR (the latter as measured from line-profiles).

3. The ionization timescale of the shock-heated gas (from X-ray line profiles - see Pollock et al. 2005).

4. The particle acceleration efficiency and the magnetic field strength (by comparing against the non-thermal emission - see Pittard et al. 2006).

To model the emission from the WCR with hydrodynamic codes, one must resolve the cooling length behind the shock. This is a difficult task when the cooling is very rapid. To overcome this problem, Antokhin et al. (2004) developed a model which decoupled the small-scale post-shock cooling from the large-scale structure of the collision region. This was subsequently employed to intrepret data on HD 159176 (De Becker et al. 2004). However, a central assumption is that the global structure is stable, but as we have seen in Fig. 1, when the cooling is rapid the action of instabilities becomes dynamically important.

One of the most important models in the last decade or so is the Lührs model (and its subsequent improvements) for fitting the profile variability of IR, optical and UV lines (Lührs 1997). In this model it is assumed that the excess emission on top of flat-topped emission lines is from material flowing along the shock cone (i.e. the WCR). This excess can be parameterized by two quantities: the full width of the excess emission (at some suitable height), and the mean radial velocity of the excess. Lührs (1997) derived simple relationships between these quantities and values for the orbital inclination, the half-opening angle of the WCR, and the skew of the WCR due to orbital effects. Fitting the model to the observed phase-dependent profiles yields for these parameters. However, its application to systems with highly eccentric orbits should be made with care, because significant orbit induced curvature of the WCR can be misinterpreted as a large opening angle, and therefore the wind momentum ratio can be wrongly inferred. In such cases, a model which accounts for curvature of the WCR (and not just its skew angle) is needed. Models of X-ray line profile formation in the WCR have been presented by Henley et al. (2003, 2005, 2008).

2.1 Models of the Non-thermal Radio Emission

Direct evidence for non-thermal emission from a CWB was presented by Williams et al. (1997). UKIRT shift-and-add IR images overlaid on radio images of WR 147 revealed that when the southern (WR) star was aligned with the southern (thermal) radio source, the northern (non-thermal) radio source was found to lie just south of the northern (O) star, in a position consistent with the point of ram-pressure balance between the winds. Further support for this picture has been provided by direct imaging of the WCR in WR 146 and WR 140 (Dougherty et al. 2000, 2005). While there are many possible mechanisms for accelerating particles, it is normally assumed that diffusive shock acceleration (DSA) is the dominant process. A detailed discussion of other possibilities can be found in Pittard & Dougherty (2006).

The non-thermal radio emission from the WCR escapes easily from WR 146 and WR 147, which are both very wide and likely have orbits with periods of thousands of years, but has a much harder

job escaping from WR 140, due to its much tighter, highly eccentric, orbit of 7.94 yr period where the stellar separation varies between $\approx 1.5 - 28$ AU. The radio emission shows dramatic, phase-repeatable, modulations, at least part of which can be expected to be caused by variable circumstellar extinction to the source of the non-thermal emission as the O star orbits in and out of the radio photosphere in the dense WR wind. More recently, this system has been imaged with the VLBA, yielding a full orbit definition, including, most importantly, the inclination of the system (Dougherty et al. 2005). A pro-Am campaign to monitor WR 140 through periastron passage has further tightened the orbital elements (Fahed et al. 2011). However, while these studies have helped to provide some of the best modelling constraints of any system, relatively little is known about the wind of the O-star, and the wind momentum ratio remains ill-constrained.

Early models of the non-thermal radio emission from CWBs were very simple. It was usually assumed that the observed flux ($S_\nu^{\rm obs}$) was a combination of the free-free flux from the spherically symmetric winds ($S_\nu^{\rm ff}$), plus the flux from a point-like non-thermal source located at the stagnation point of the winds ($S_\nu^{\rm nt}$). In this model the non-thermal emission is then attenuated by free-free absorption (optical depth $\tau_\nu^{\rm ff}$) through the surrounding winds:

$$S_\nu^{\rm obs} = S_\nu^{\rm ff} + S_\nu^{\rm nt}\, {\rm e}^{-\tau_\nu^{\rm ff}}. \quad (1)$$

While this approach allows simple solutions to the radiative transfer equation (e.g. Williams et al. 1990; Chapman et al. 1999), such models fail to reproduce the spectral variation of the emission with orbital phase. Clearly their level of realism needed to be improved. Williams et al. (1990) therefore proposed that in future models of WR 140 the low-opacity "hole" in the dense WR wind created by the O-star's wind should be accounted for. However, White & Becker (1995) pointed out that in WR 140, even the O-star's wind has significant opacity. Together, these works demonstrated the need for more realistic models which account for the spatial extent of the emission and absorption from the circumbinary envelope and the WCR. More realistc models should also account for the effects of various cooling mechanisms (e.g. inverse Compton, adiabatic, etc.) on the non-thermal electron distribution, and also additional absorption mechanims (e.g. the Razin effect).

Major improvements in the modelling of the radio emission were made by Dougherty et al. (2003), where key assumptions in previous models, such as a point-like source of non-thermal emission, and a spherically symmetric, single temperature, surrounding envelope, were removed. Models of the thermal and non-thermal radio emission were instead based on 2D, axisymmetric, hydrodynamical simulations, allowing a more accurate description of the density and temperature structure of the system. This meant that sight-lines to the observer can pass through regions of both high and low opacity. The assumption of a point-source of non-thermal emission was also removed, by treating the emission in a phenomenological way. Accelerated electrons were assumed to be present within the WCR, with an energy density ($U_{\rm rel,e}$) proportional to the local thermal energy density ($U_{\rm th}$) i.e. $U_{\rm rel,e} = \zeta_{\rm rel,e} U_{\rm th}$. The magnetic field energy density was specified in a similar manner: $U_{\rm B} = \zeta_{\rm B} U_{\rm th}$. The non-thermal electrons were further assumed to have a power-law distribution, $N(\gamma)d\gamma = C\gamma^{-p}d\gamma$, where γ is the Lorentz factor, C is proportional to $\zeta_{\rm rel,e}$, and it was assumed that $p = 2$ (suitable for test particle DSA, with strong shocks and an adiabatic index equal to $5/3$).

Although this model introduced its own set of assumptions, it provided a great deal of new insight into the nature of the radio emission from CWBs. An immediate realization was the potential importance of the Razin effect in attenuating the low frequency synchrotron emission within the WCR. Several key scaling relationships were also established. For instance, the total synchrotron emission from the entire WCR in adiabatic systems was found to scale as $D^{-1/2}\nu^{-1/2}$, where D is the separation of the stars (for comparison, the X-ray emission in the optically thin, adiabatic limit, scales as D^{-1}). The importance of IC cooling was also highlighted, having been shown to be a significant effect even in wide systems. In fact, the neglect of IC cooling in this work resulted in an overestimate

of the high frequency synchrotron flux from WR 147.

Pittard et al. (2006) addressed the IC cooling of the downstream non-thermal electron distribution in a follow-up paper, and discovered that non-thermal electrons located near the contact discontinuity of the WCR suffered the greatest amount of IC cooling, leading to a dearth of emission from this region. Not suprisingly, the addition of IC cooling led to a significantly better fit between models and observations of WR 147. It also broke the previously identified relationship between the total synchrotron luminosity and the stellar separation noted by Dougherty et al. (2003). Instead, the *intrinsic* luminosity was now observed to *decline* with stellar separation as IC cooling became increasingly strong. The effect of the stellar separation on the *thermal* radio flux was also explored. It was discovered that the *thermal* radio emission from the WCR scales as D^{-1}, in an identical way to the thermal X-ray emission. Since this emission is optically thin in systems with an adiabatic WCR, it can mimic a synchrotron component, so that one should rather cautiously interpret data with a spectral index $-0.1 \lesssim \alpha \lesssim 0.5$ (Pittard et al. 2006).

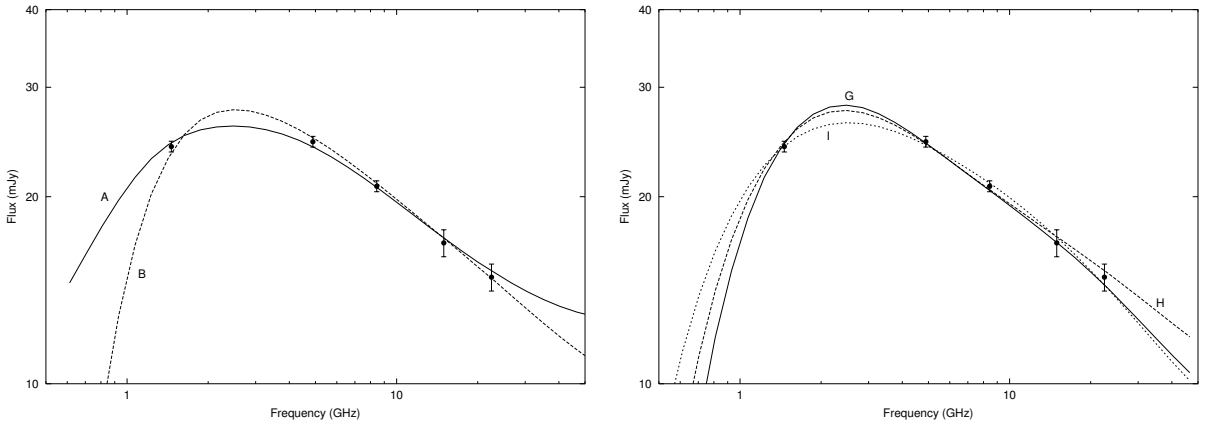

Figure 3: Model fits to the radio data of WR 140 at $\phi = 0.837$. Left: Fits where the low-frequency turndown is due to free-free absorption. Models A and B span plausible values of the wind momentum ratio, η. Right: Fits where the Razin effect is responsible for the turndown. For further details of the models see Pittard & Dougherty (2006).

The improved model was applied to WR 140 in Pittard & Dougherty (2006), with X-ray data further helping to constrain the mass-loss rates. Fits were obtained to data at orbital phase 0.837, which is around the peak of the non-thermal radio lightcurve and also when an *ASCA* dataset is available. It was discovered that the low frequency turndown in the radio spectrum could be explained as either free-free absorption through the surrounding stellar winds, or the Razin effect (see Fig. 3). In the former case it proved impossible to obtain a good fit to the data with $p = 2$. The best fit was obtained with $p = 1.4$, though changes to the assumed magnetic field strength allow this value to move slighty. Such indices can result from the shock re-acceleration process, whereby the non-thermal particles pass through a sequence of shocks (Pope & Melrose 1994), or from 2nd order Fermi acceleration. Either of these processes may be significant in CWBs, since the clumpy nature of the winds means that the WCR is likely to be highly turbulent, with weak shocks distributed throughout it (Pittard 2007). In contrast, fits with the Razin effect dominant do allow $p = 2$, though require a worryingly high efficiency of electron acceleration. For this reason, fits with free-free absorption dominant were preferred. A wide range of wind momenta could fit the data in this case, though it might be possible to constrain the models with future, high sensitivity VLBA observations. It might also be necessary to apply a rather extreme taper to better emphasize the lower spatial frequency content of the visibility data to tease out structure further downstream of the WCR apex where the opening angle of the WCR has reached its asymptotic limit.

2.2 Models of the Non-thermal X-ray and γ-ray Emission

In recent years there has been a revival of interest in non-thermal X-ray and γ-ray emission from CWBs, as the dramatic sensitivity gains achieved by space-based satellites and ground-based arrays of Cerenkov telescopes have raised the tantalizing prospect of the first detections. This, in turn, has led to new theoretical predictions. Amongst the first was a work by Bednarek (2005), who calculated the expected γ-ray emission from WR20a, a rare WR+WR binary. The short orbital period of this system means that the optical depth to electron-positron pair creation is high enough to initiate electromagnetic cascades. Due to this system's high optical depth to TeV photons, it cannot be directly responsible for nearby TeV emission (Aharonian et al. 2007), which more likely is the result of acceleration processes within the collective wind of the nearby cluster Westerlund 2.

A two-zone model for the non-thermal emission from CWBs was presented by Reimer et al. (2006). In their model, particles are accelerated in an inner zone where their spatial diffusion exceeds their motion due to advection with the background fluid. Relevant gain and loss mechanisms are considered in the computation of the energy distribution. Particles leave this region once the timescale for their diffusion exceeds their advection timescale. The particles are then assumed to move into an outer advection region where they suffer further losses as they flow downstream.

The anisotropic nature of the IC process is considered in the calculation of the expected flux, though the weaker of the two stellar radiation fields is ignored. Reimer et al. (2006) conclude that GLAST/Fermi should easily detect WR 140, though they expect that the large variation in the energy density of the stellar radiation fields resulting from the high orbital eccentricity is likely to obscure the effect of the change in the IC flux with viewing angle due to anisotropic scattering. However, Reimer & Reimer (2009) demonstrate that it is possible to constrain the orbital inclination of colliding wind systems through their nonisotropic IC emission.

A complementary model of the X-ray and γ-ray emission from WR 140 was presented by Pittard & Dougherty (2006). This work built on the phenomenological model developed previously by Dougherty et al. (2003) and Pittard et al. (2006) to explore the non-thermal radio emission. Here the energy spectrum is assumed rather than calculated, but the model benefits from a more realistic description of the density and temperature distribution within the system. Although Pittard & Dougherty (2006) adopt an isotropic treatment of the IC emission, they find that other uncertainities, such as the particle acceleration efficiency and the spectral index of their energy distribution (both of which remain ill-constrained from fits to radio data - see the previous section), have at least as much influence on the predicted flux as the angle-dependence of the IC emission. A key issue is that the degeneracy which exists between the models in the radio is broken at MeV-TeV energies, raising the possibility of future γ-ray detections allowing one to distinguish the nature of the low-frequency turndown, the acceleration efficiency of the non-thermal electrons, and the strength of the magnetic field. Several of the Razin fits have since been ruled out by the upper limits to the INTEGRAL emission obtained by De Becker et al. (2007).

Fits to the WR 140 radio data at other phases have been performed, and a good match to the radio lightcurve is now obtained (Pittard, in preparation). However, the fitted parameters change with orbital phase in a relatively complicated fashion which defies easy explanation.

2.3 Models of the Thermal Radio Emission

The effect of binarity on the thermal radio emission was investigated by Stevens (1995), who found that at a given orbital separation, the 2 cm radio flux increased as the wind momenta ratio became more uniform, and could exceed the single star value by up to 50%. More recently, Pittard (2010) showed that in short period O+O-star systems with a radiative WCR, the thermal emission from the WCR becomes optically thick, and can dominate the total radio flux from the system, exceeding

the combined flux from identically typed single stars by over an order of magnitude. This clearly would have a large impact on the derived stellar mass-loss rates in cases where the emission from the WCR is ignored. Radio lightcurves and spectra were also obtained. A strong hystersis is seen in the synthetic lightcurve of a simulated eccentric system, reflecting the underlying hystersis of the dynamics. Similar behaviour is seen in simulated X-ray observations (Pittard & Parkin 2010).

3 Future Research

3D models of the dynamics of the WCR have provided useful new insight into the nature of colliding wind systems. A full investigation of possible orbit and stellar parameters will undoubtedly occur over time. The continuing progress in computational power is making fully 3D simulations possible, though they are a long way from being routine.

In modelling non-thermal emission, a key area for progress will involve abandoning phenomenological models of the non-thermal emission in favour of a model in which the acceleration of the particles and their effect on the shock structure are self-consistently obtained. To develop such models will require the integration of an advection-diffusion equation for the non-thermal particles into the hydrodynamical codes. The advent of radio interferometers with increased sensistivity (e.g. the EVLA and e-MERLIN) will add significant numbers of newly detected radio CWBs, which will allow better comparison to the new models in progress.

Acknowledgements

I would like to express my sincere gratitude to the organizers for the invitation to present a review talk. I would also like to thank Sean Dougherty for many stimulating discussions, and the Royal Society for funding a University Research Fellowship which allowed the development of some of the research covered in this review.

References

Aharonian, F., Akhperjanian, A. G., Bazer-Bachi, A. R., Beilicke, M., Benbow, W., Berge, D., Bernlöhr, K., Boisson, C., et al. 2007, A&A, 467, 1075
Antokhin, I. I., Owocki, S. P. & Brown, J. C. 2004, ApJ, 611, 434
Bednarek, W. 2005, MNRAS, 363, L46
Chapman, J. M., Leitherer, C., Koribalski, B., Bouter, R. & Storey, M. 1999, ApJ, 518, 890
De Becker, M., Rauw, G., Pittard, J. M., Antokhin, I.I., Stevens, I. R., Gosset, E. & Owocki, S. P. 2004, A&A, 416, 221
De Becker, M., Rauw, G., Pittard, J. M., Sana, H., Stevens, I. R. & Romero, G. E. 2007, A&A, 472, 905
Dougherty, S. M., Beasley, A. J., Claussen, M. J., Zauderer, B. A. & Bolingbroke, N. J. 2005, ApJ, 623, 447
Dougherty, S. M., Pittard, J. M., Kasian, L., Coker, R. F., Williams, P. M. & Lloyd, H. M. 2003, A&A, 409, 217
Dougherty, S. M., Williams, P. M. & Pollacco, D. L. 2000, MNRAS, 316, 143
Fahed, R., Moffat, A. F. J., Zorec, J., et al. 2011, in Proceedings of the 39th Liège Astrophysical Colloquium, eds. G. Rauw, M. De Becker, Y. Nazé, J.-M. Vreux & P.M. Williams, BSRSL 80, 668
Gayley, K. G., Owocki, S. P., Cranmer, S. R. 1997, ApJ, 475, 786
Henley, D. B., Corcoran, M. F., Pittard, J. M., Stevens, I. R., Hamaguchi, K. & Gull, T. R. 2008, ApJ, 680, 705
Henley, D. B., Stevens, I. R. & Pittard, J. M. 2003, MNRAS, 346, 773
Henley, D. B., Stevens, I. R. & Pittard, J. M. 2005, MNRAS, 356, 1308
Lemaster, M. N., Stone, J. M. & Gardiner, T. A. 2007, ApJ, 662, 582
Lührs, S. 1997, PASP, 109, 504
Luo, D., Mc Cray, R. & Mac Low, M.-M. 1990, ApJ, 362, 267
Okazaki, A. T., Owocki, S. P., Russell, C. M. P. & Corcoran, M. F. 2008, MNRAS, 388, L39

Parkin, E. R. & Pittard, J. M. 2008, MNRAS, 388, 1047
Parkin, E. R., Pittard, J. M., Corcoran, M. F., Hamaguchi, K. & Stevens, I. R. 2009, MNRAS, 394, 1758
Pittard, J. M. 2007, ApJ, 660, L141
Pittard, J. M. 2009, MNRAS, 396, 1743
Pittard, J. M. 2010, MNRAS, 403, 1633
Pittard, J. M., Corcoran, M. F. 2002, A&A, 383, 636
Pittard, J. M., Dobson, M. S., Durisen, R. H., Dyson, J. E., Hartquist, T. W. & O'Brien, J. T. 2005b, A&A, 438, 11
Pittard, J. M. & Dougherty, S. M. 2006, MNRAS, 372, 801
Pittard, J. M., Dougherty, S. M., Coker, R. F. & Corcoran, M. F. 2005a, in "X-Ray and Radio Connections", eds. L.O. Sjouwerman and K. K Dyer, published electronically by NRAO, http://www.aoc.nrao.edu/events/xraydio
Pittard, J. M., Dougherty, S. M., Coker, R. F., O'Connor, E. & Bolingbroke, N. J. 2006, A&A, 446, 1001
Pittard, J. M. & Parkin, E. R. 2010, MNRAS, 403, 1657
Pittard, J. M. & Stevens, I. R. 2002a, A&A, 388, L20
Pollock, A. M. T., Corcoran, M. F., Stevens, I. R. & Williams, P. M. 2005, ApJ, 629, 482
Pope, M. H. & Melrose, D. B. 1994, PASA, 11, 175
Reimer,A., Pohl, M., Reimer, O. 2006, ApJ, 644, 1118
Reimer, A. & Reimer, O. 2009, ApJ, 694, 1139
Stevens, I. R. 1995, MNRAS, 277, 163
Stevens, I. R., Blondin, J. M. & Pollock, A. M. T. 1992, ApJ, 386, 265
Stevens, I. R. & Pollock, A. M. T. 1994, MNRAS, 269, 226
Stevens, I. R., Corcoran, M. F., Willis, A. J., Skinner, S. L., Pollock, A. M. T., Nagase, F. & Koyama, K. 1996, MNRAS, 283, 589
Strickland, R. & Blondin, J. M. 1995, ApJ, 449, 727
Vishniac, E. T. 1983, ApJ, 274, 152
Vishniac, E. T. 1994, ApJ, 428, 186
Walder, R. 1998, Ap&SS, 260, 243
White, R. L. & Becker, R. H. 1995, ApJ, 451, 352
Williams, P. M., Dougherty, S. M., Davis, R. J., van der Hucht, K. A., Bode, M. F. & Setia Gunawan, D. Y. A. 1997, MNRAS, 289, 10
Williams, P. M., van der Hucht, K. A., Pollock, A. M. T., Florkowski, D. R., van der Woerd, H. & Wamsteker, W. M. 1990, MNRAS, 243, 662

Discussion

P. Williams: Many of the colliding wind systems with carbon-rich Wolf Rayet stars have dust. Chemical models for dust formation require overdensities of many orders of magnitude. Are you seeing these in your models?
J. Pittard: Yes, if there is strong cooling, it is in principle very easy to obtain large overdensities. One may first obtain a factor of 4 increase in density at the shock, and then as gas cools from $\sim 10^4$K to $\sim 10^3$K one can get up to another factor of $\sim 10^4$ increase in overdensity. Having said this, as the gas cools and is compressed, the magnetic field may start to exert a significant pressure and thereby moderate the overall increase in density to some extent.

J. Groh: Related to Prof. Williams' question, what's the minimum temperature you achieve in the overdense regions of your simulations?
J. Pittard: All our simulations have a floor temperature of 10^4K, which is also assumed to be the wind temperature. However, in reality the temperature will be set by the balance between photoionization heating and radiative cooling. We do not include photoionization in our current models. In principle, we should be able to reach temperatures $\sim 10^3$K as indeed is observed when dust forms.

A Multiwavelength Study of the Runaway Binaries HD 14633 and HD 15137

M. Virginia McSwain[1*], Michaël De Becker[2], Mallory S. E. Roberts[3], and Tabetha S. Boyajian[4]

[1] Department of Physics, Lehigh University, USA
[2] Department of Astrophysics, Geophysics and Oceanography, Université de Liège, Belgium
[3] Eureka Scientific, Inc., USA
[4] Department of Physics and Astronomy, Georgia State University, USA

Abstract: The runaway O-type binaries HD 14633 and HD 15137 were likely ejected from the cluster of their birth by supernovae explosions in close binaries. Here we present recent optical spectra to update the orbital solutions of the binaries and study the physical parameters of the O star primaries. We also present *XMM-Newton* observations of both systems that attempt to detect hard power-law emission from compact companions. EPIC spectra of HD 14633 at periastron and apastron reveal a non-thermal X-ray flux component that is variable during the orbit. Our EPIC spectra of HD 15137 indicate thermal X-ray emission consistent with an isolated O star. We provide an upper limit on the emission from a compact companion in HD 15137.

1 Introduction

There are two accepted mechanisms to explain the origin of runaway O-type stars: close multi-body interactions in a dense cluster environment (Poveda, Ruiz & Allen 1967), or a supernova explosion within a close binary (Zwicky 1957). Binary runaways such as HD 14633 and HD 15137 offer the potential to study the companion star and distinguish between these ejection scenarios, providing valuable insight into the evolution of open clusters and close binary stars.

The optical properties and space velocity of HD 14633 have been studied by Boyajian et al. (2005) and McSwain et al. (2007a). HD 14633 is an ON8.5 V star with effective temperature $T_{\rm eff} = 35100$ K, surface gravity $\log g = 3.95$, and projected rotational velocity $V \sin i = 138$ km s^{-1}. The short orbital period ($P = 15.4$ d) and very high eccentricity ($e = 0.70$) suggest a disruptive supernova origin for the runaway. The very low mass function likewise supports a low mass, neutron star (NS) companion. The enriched nitrogen and relatively fast rotation observed in HD 14633 may be due to a mass transfer episode prior to the supernova in a close binary. With a peculiar space velocity $V_{\rm pec} = 71$ km s^{-1} and

*Based partly on observations collected at the Observatoire de Haute-Provence (France) and on observations obtained with XMM-Newton, an ESA science mission with instruments and contributions directly funded by ESA Member States and NASA.

distance of 2040 pc, this runaway single-line spectroscopic binary (SB1) system was likely ejected from the open cluster NGC 654 about 14 Myr ago (Boyajian et al. 2005).

HD 15137 has many optical and orbital properties similar to HD 14633 (Boyajian et al. 2005, McSwain et al. 2007a, McSwain et al. 2010). It is slightly more evolved with spectral type O9.5 III(n), $T_{\rm eff} = 29700$ K, $\log g = 3.50$, and $V \sin i = 234$ km s^{-1}. The star may also be N rich, and it is also an SB1 with a highly eccentric orbit and a very low mass function. It is located at a distance of 2420 pc and has $V_{\rm pec} = 63$ km s^{-1}. Coincidentally, HD 15137 was also traced back to the open cluster NGC 654, with a travel time of about 10 Myr since its ejection (Boyajian et al. 2005).

In this work, we present updated orbital solutions for HD 14633 and HD 15137 to refine their orbital geometry and study the potential for binary interactions. We also present the results from the first *XMM-Newton* observations of both systems in an attempt to detect compact companions.

2 Optical Observations and Radial Velocity Measurements

We obtained 34 spectra of HD 14633 and 44 spectra of HD 15137 at the Observatoire de Haute-Provence (OHP) during several observing runs from 2005 October to 2007 November. We used the 1.52m telescope with the Aurélie spectrograph with grating #3 and the 2048×1024 CCD EEV 42-20#3 detector with a pixel size of 13.5 μm. These spectra cover a wavelength range between 4460–4890 Å with a resolving power of $R = \lambda/\Delta\lambda \approx 8000$.

We also obtained 32 spectra of HD 14633 and 47 spectra of HD 15137 at the KPNO coudé feed (CF) telescope over 35 consecutive nights during 2008 October and November. We used grating B in third order with the 4-96 order-sorting filter and the F3KB detector. This instrumental configuration resulted in a wavelength range of 4130–4570 Å with $R \approx 9000$ across the chip.

For both datasets, we obtained ThAr comparison spectra for wavelength calibration shortly before or after each observation. The OHP data were bias corrected, flat fielded, cleaned for cosmic rays, and extracted using the MIDAS software developed at the European Southern Observatory. The CF spectra were reduced using standard procedures in IRAF. Both datasets were rectified to a unit continuum using line-free regions and interpolated onto a log wavelength scale using a common heliocentric wavelength grid. Our observations are described in more detail by McSwain et al. (2010).

To measure the radial velocities, V_r, of both stars, we used a cross correlation procedure described by McSwain et al. (2010). The orbital period of HD 14633 is well known at $P = 15.4$ d from our previous spectroscopic studies (Boyajian et al. 2005, McSwain et al. 2007a), and our new V_r measurements allow us to refine the orbital parameters of this system here. For HD 15137, we initially proposed an orbital period $P \sim 30$ d for the system, but our new V_r measurements exclude this value. From our new period search, there was no one clear signal that stands out from any of the resulting periodograms, so we inspected each candidate frequency carefully. We used each proposed period to solve for the resulting orbital elements. After ruling out all resulting V_r curves with poor fits and extremely large scatter, any $P < 35$ d, and an alias frequency, we adopt an orbital period $P = 55.4$ d for HD 15137.

We present the final orbital solutions for HD 14633 and HD 15137 in Table 1, and the corresponding radial velocity curves in Figure 1. Both orbits are highly eccentric with low velocity semiamplitudes and very low mass functions, suggesting low mass companions. Based on the runaway nature of the binaries and their orbital parameters, Boyajian et al. (2005) proposed a supernova ejection scenario and a NS companion for both stars, even though they were not known X-ray sources. They proposed that HD 14633 and HD 15137 may be "quiet" HMXBs, too widely separated for the NS to accrete a significant mass of stellar winds to produce the bright X-ray flux commonly associated with X-ray binaries (Liu, van Paradijs & van den Heuvel 2006). To investigate this scenario, we describe *XMM-Newton* observations of both systems below.

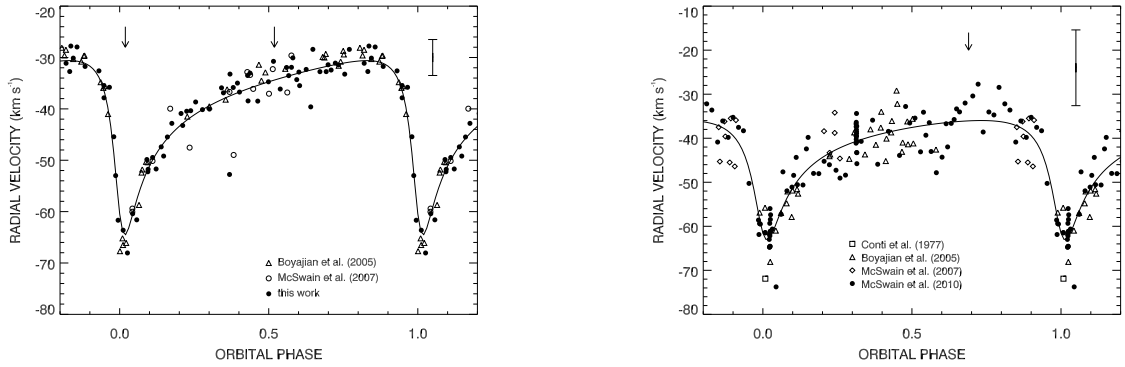

Figure 1: *Left:* Radial velocity curve of HD 14633. A typical error bar assuming the standard deviation $\sigma = 4.3$ km s^{-1} is also shown. Arrows mark the orbital phases of our *XMM-Newton* observations of HD 14633. *Right:* Radial velocity curve of HD 15137. The error bar includes $\sigma = 7$ km s^{-1} in addition to the intrinsic V_r error of ± 5 km s^{-1} due to rapid line profile variations. The arrow marks the orbital phase of the single *XMM-Newton* observation of HD 15137.

Table 1: Orbital Elements

	HD 14633	HD 15137
P (days)	15.40825 ± 0.00024	55.3957 ± 0.0038
T (HJD–2,400,000)	44227.297 ± 0.099	54421.991 ± 0.064
e	0.677 ± 0.035	0.6239 ± 0.0088
ω (deg)	139.2 ± 6.5	152.17 ± 0.86
K_1 (km s^{-1})	17.0 ± 1.3	13.56 ± 0.15
γ (km s^{-1})	-38.88 ± 0.55	-42.06 ± 0.11
$f(m)$ ($M_\odot$)	0.00312 ± 0.00080	0.00685 ± 0.00030
$a_1 \sin i$ ($R_\odot$)	3.80 ± 0.33	11.60 ± 0.17
σ (km s^{-1})	7.13	4.28

3 XMM-Newton Observations

We observed HD 14633 twice with *XMM-Newton* on 2009 July 23 and July 31. We denote these two observations as A and B, respectively, and further details are summarized in Table 2. We observed HD 15137 once on 2008 August 3, observation ID 0553810201, for approximately 20 ks. Based on the orbital solution above, these observations took place at orbital phase $\phi = 0.69$. The EPIC Observation Data Files and event lists were provided by the standard XMM Pipeline Processing System, and we filtered the event lists and extracted the source spectra using standard analysis threads.

3.1 Spectral Fits of HD 14633

For each observation of HD 14633, we fit the two MOS spectra simultaneously over the range 0.5–5.0 keV by grouping the data to a minimum of 5 photons per energy bin. Obs. A was fit using two absorption components: the ISM (model *tbabs* with Wilms abundances; Wilms, Allen & McCray 2000) and a second warm absorber from the N-rich stellar wind (model *vphabs*). The *tbabs* component

Table 2: XMM-Newton Observations and Spectral Fits of HD 14633

Parameter	Obs. A	Obs. B	Notes
Observation ID	0603570301	0603570401	
Good time interval	27 ks	33 ks	
Orbital phase, ϕ	0.519	0.019	
$nH_{\rm tbabs}$ (cm^{-2})	7.50×10^{20}	7.50×10^{20}	a
$nH_{\rm vphabs}$ (cm^{-2})	$2.2^{+0.09}_{-1.0} \times 10^{21}$	$2.20^{+0.13}_{-0.07} \times 10^{21}$	
N abundance ($\times$ solar)	15^{+12}_{-11}	15	b
$kT_{\rm vapec,1}$ (keV)	0.27	0.27	b, c
norm$_{\rm vapec,1}$ (cm^{-5})	$8.2^{+13}_{-3.6} \times 10^{-3}$	8.2×10^{-3}	b, d
$kT_{\rm vapec,2}$ (keV)	0.56	0.56	b, c
norm$_{\rm vapec,2}$ (cm^{-5})	$1.2^{+2.0}_{-0.8} \times 10^{-3}$	1.2×10^{-3}	b, d
Γ	–	$1.46^{+0.75}_{-0.83}$	
norm$_{\rm power}$ (keV cm^{-2} s^{-1})	–	$3.3^{+2.7}_{-2.0} \times 10^{-6}$	
Reduced χ^2	1.33	1.29	
Degrees of Freedom	78	103	
Absorbed flux (erg cm^{-2} s^{-1})	$5.7^{+9.4}_{-3.4} \times 10^{-14}$	$7.9^{+11.1}_{-4.7} \times 10^{-14}$	
Unabsorbed flux (erg cm^{-2} s^{-1})	$9.4^{+15.5}_{-5.4} \times 10^{-14}$	$1.1^{+1.7}_{-0.7} \times 10^{-13}$	e
$L_X/L_{\rm bol}$	1.3×10^{-7}	1.5×10^{-7}	

a: Fixed, see text. b: The value for Obs. B was fixed using the value from Obs. A. c: Not constrained according to *steppar*. d: The $nH_{\rm vphabs}$ and N abundances were frozen to determine errors with *steppar*. e: The unabsorbed flux neglects only the interstellar absorbing column.

was fixed using the observed $E(B-V) = 0.13$ (McSwain et al. 2007a) and the relation $nH/E(B-V) = 5.8 \times 10^{21}$ atoms cm^{-2} mag^{-1} (Bohlin, Savage & Drake 1978). For the X-ray source, the best fit was achieved with a two-temperature (2-T) thermal model (*vapec*) with the N abundances fixed to the value from *vphabs*. We used the *steppar* routine separately for each parameter to investigate the 90% confidence limits. No additional components were necessary to fit obs. A, and the fit results are provided in Table 2.

Obs. B has a slightly higher observed count rate than A, especially at higher energies. We attempted to fit obs. B using the same model *tbabs*vphabs(vapec + vapec)* used for A, but none of the results were well constrained with *steppar*. Thus we chose to fix the N abundance and *vapec* values to those from obs. A, and we investigated whether an additional flux component was required. Adding a hard powerlaw component produced a significant improvement according to a statistical F-test. These results are summarized in Table 2, and the spectral fits are shown in Figure 2.

We derived the ratio of the X-ray to bolometric luminosity, $L_X/L_{\rm bol}$, using the unabsorbed flux with the measured effective temperature and distance to HD 14633 ($T_{\rm eff} = 35100$ K, $d = 2.150$ kpc; McSwain et al. 2007a). The compact companion contributes a flux $F_X = 1.6 \times 10^{-14}$ erg cm^{-2} s^{-1} at periastron. Assuming that this flux is due to wind accretion onto a neutron star, we used the stellar wind properties (McSwain et al. 2007b), physical parameters of the optical star (McSwain et al. 2007a), and the orbital elements above to determine the Bondi-Hoyle accretion rate $S_a \sim 9 \times 10^{-11}\ M_\odot$ yr^{-1} near periastron (Lamers, van den Heuvel & Petterson 1976). Given the observed F_X, this implies a low efficiency $\zeta \approx 10^{-5}$ of converting accreting matter into X-ray luminosity.

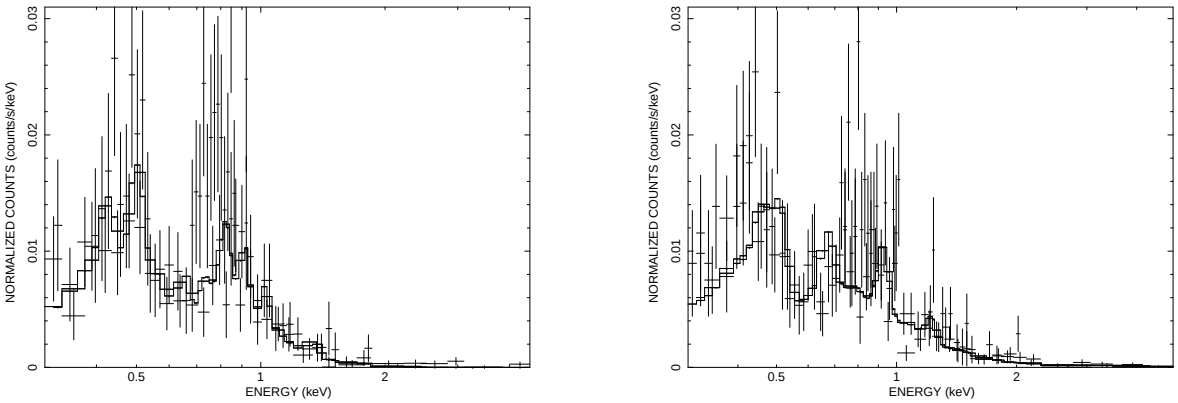

Figure 2: *Left: XMM-Newton* MOS spectra of HD 14633 (obs. A) performed near apastron. *Right: XMM-Newton* MOS spectra of HD 14633 (obs. B) performed near periastron.

3.2 Spectral Fit of HD 15137

Our *XMM-Newton* observation of HD 15137 is described in detail by McSwain et al. (2010), and we summarize the key results here. The EPIC spectra of HD 15137 are consistent with a soft thermal source typical of isolated O-type stars (Sana et al. 2006). We fit the MOS spectra simultaneously over the range 0.5–2.3 keV, using a variety of warm absorbed, single temperature (1-T) and 2-T thermal models, and we repeated our fits for the pn spectrum. The resulting fits were equally good for the 1-T and 2-T models, but a statistical F-test reveals that the second temperature does not significantly improve the fits. We also cannot distinguish between the quality of the various 1-T model fits due to the low signal-to-noise. We weakly constrain the temperature to $0.10 \leq kT \leq 0.25$ keV, and the neutral hydrogen column density to $2.8 \times 10^{21} \leq nH \leq 8.6 \times 10^{21}$ atoms cm^{-2}. We find an absorbed flux $F_{abs} \sim$ 1–2 $\times$ 10^{-14} erg cm^{-2} s^{-1} and unabsorbed flux $F_{unabs} \sim$ 2–4 $\times$ 10^{-14} erg cm^{-2} s^{-1} (0.2–10 keV) depending on the model. There is no evidence of any hard X-ray photons.

In order to place an upper limit on any hard power law component that may originate from an accreting compact companion, we repeated the 1-T models with an additional power law component with photon index $\Gamma = 2$ (fixed). All of the best fit parameters from the 1-T fits, including nH, kT, and their normalizations, were fixed in Xspec. We then refit each model, allowing only the normalization of the power law component to vary. We then used the *steppar* routine to investigate the 90% confidence limit for the power law normalization. Upon removing the thermal component from the models, we used the fixed Γ and the upper limit for its normalization in the remaining absorbed power law model to determine the upper limit for the X-ray flux, F_X, of the putative compact object. Our fits indicated an unabsorbed $F_X < 10^{-14}$ erg cm^{-2} s^{-1} (0.2–10 keV). At a distance of 2.42 kpc, this corresponds to an X-ray luminosity $L_X < 10^{31}$ erg s^{-1} for any hard power law component.

4 Conclusions

We have detected a hard X-ray component from the proposed NS companion in HD 14633. Due to its very high eccentricity, the binary separation in that system varies by a factor of 7 during the orbit. The lack of detection near apastron suggests that stellar wind interactions with the NS produce a modulated X-ray emission during the orbit, and we recommend further observations throughout the orbit to study the interaction region and variability.

The longer orbital period and greater system separation of HD 15137 is not favorable for wind interactions, hence our non-detection of a NS. Our observation was also not performed at an optimal orbital phase. Further observations near periastron may identify a compact companion in this system.

Acknowledgements

We are grateful to Drs. G. Rauw and N. Linder for taking some of the OHP spectra, the staff at KPNO and OHP, and the Ministère de l'Enseignement Supérieur et de la Recherche de la Communauté Française de Belgique for financial support for the OHP observing runs. This work is also supported by NASA DPR numbers NNX08AX79G, NNG08E1671, and NNX09AP86G and Lehigh University.

References

Bohlin, R. C., Savage, B. D., & Drake, J. F. 1978, ApJ 224, 132
Boyajian, T.S., Beaulieu, T.D., Gies, D.R., Huang, W., McSwain, M.V., Riddle, R.L., Wingert, D.W., & De Becker, M. 2005, ApJ 621, 978
Lamers, H.J.G.L.M., van den Heuvel, E.P.J., & Petterson, J.A. 1976, A&A 49, 327
Liu, Q.Z., van Paradijs, J., & van den Heuvel, E.P.J. 2006, A&A 455, 1165
McSwain, M.V., De Becker, M., Roberts, M.S., et al. 2010, AJ 139, 857
McSwain, M.V., Boyajian, T., Grundstrom, E., & Gies, D.R. 2007a, ApJ, 655, 473
McSwain, M.V., Ransom, S.M., Boyajian, T., Grundstrom, E., & Roberts, M.S.E. 2007b, ApJ, 660, 740
Poveda, A., Ruiz, J., & Allen, C. 1967, Bol. Obs. Tonantzintla Tacubaya 4, 86
Sana, H., Rauw, G., Nazé, Y., Gosset, E., & Vreux, J.-M. 2006, MNRAS 372, 661
Wilms, J., Allen, A., & McCray, R. 2000, ApJ 542, 914
Zwicky, F. 1957, Morphological Astronomy (Berlin: Springer)

Discussion

L. Oskinova: Two questions. (1) Did you check the X-ray images for the presence of some diffuse emission? (2) Did you estimate the X-ray luminosity of these objects?
M.V. McSwain: Visual inspection of the *XMM-Newton* images did not indicate any diffuse emission. Given the close orbits that should truncate any diffuse gas, we do not expect to resolve any diffuse emission. The unabsorbed X-ray luminosity of HD 14633 ranges from $1.3 - 2.1 \times 10^{32}$ erg/sec. The unabsorbed X-ray luminosity of HD 15137 is about 2×10^{31} erg s^{-1}.

I. Antokhin: I have a question about your fit of the X-ray spectrum of HD 14633. Maybe I missed something, but why do you attribute a lower temperature component of your 2T-fit to the shock?
M.V. McSwain: Our initial fits of HD 14633 data with `xspec` suggest a 2 component model: a thermal component associated with the O star, and a plane-parallel shock. The HD 14633 spectra are significantly softer than the HD 15137 spectrum. Therefore our preliminary analysis attributes the soft X-ray excess to the shock component. However, different models of interstellar absorption treat the soft components differently, and we are currently exploring further models to better account for the two components.

I. Negueruela: You mentioned that the two objects that you studied were likely runaways from the open cluster NGC 654. How was this determined and how certain is it? The brightest stars in NGC 654 have rather later spectral types than your targets. If they are really runaways, their present day spectral types (O types) would be strong indication of mass transfer in a binary, making them very important

objects to test models for the creation of early-type blue stragglers.

M.V. McSwain: The cluster of origin was determined by Boyajian et al. (2005), who traced their positions back in time by integrating a model of the Galactic potential. Based on their present day space velocities, the runaways were ejected 10-14 Myr ago, which is no longer than the expected lifetime of these O-type stars. And as you mentioned, the earliest spectral types remaining in NGC 654 are B0 - 1 V. Therefore we suspect that HD 14633 and HD 15137 were rejuvenated by prior mass transfer. HD 15137 does show evidence of CNO-enriched gas at its surface.

D. Gies: I'd like to comment on this point. Boyajian et al. (2005) used proper motions and radial velocities to trace back the motion of stars and of cluster NGC 654 in the Galactic potential. A common origin is suggested but not proven.

Cyg OB2 #5: When three stars are just not enough.

M. Kennedy[1], S.M. Dougherty[2,3], P.M. Williams[4] and A. Fink[2]

[1] University of Victoria, BC, Canada
[2] NRC-HIA DRAO, Penticton, BC, Canada
[3] Institute for Space Imaging Science, University of Calgary, AB, Canada
[4] Institute for Astronomy, Royal Observatory, Blackford Hill, Edinburgh, Scotland

Abstract: Archival observations from the Very Large Array (VLA) at frequencies between 1.4 GHz and 43 GHz of the 6.6-day O6.5-7+O5.5-6 binary Cyg OB2 #5 over 20 years are re-examined. The aim is to determine the location and character of its known variable radio emission. The radio emission consists of a primary component associated with the binary, and a non-thermal source (NE), $0.8''$ to the NE. This work reveals that NE shows no evidence of variation demonstrating that the variable emission arises in the primary component. With NE constant, the radio flux from the primary can now be well determined for the first time, especially in observations that do not resolve both the primary and NE components. The variable radio emission from the primary has a period of 6.7 ± 0.3 years which is described by a simple model of a non-thermal source orbiting within the stellar wind envelope of the binary. Such a model implies the presence of a third, unresolved stellar companion (Star C) orbiting the 6.6-day binary with a period of 6.7 years. The non-thermal emission arises from either a WCR between Star C and the binary system, or possibly from Star C directly. Examination of radial velocity observations suggests reflex motion of the binary due to Star C, for which a mass of 23^{+22}_{-14} $M_\odot$ is deduced. Together with the star associated with NE, this implies that Cyg OB2 #5 is a quadruple system.

1 Introduction

Cyg OB2 #5 (V729 Cyg, BD $+40\,4220$) is an eclipsing binary system consisting of two O-type supergiants orbiting in a 6.6-day period (Hall 1974; Leung & Schneider 1978; Rauw, Vreux & Bohannan 1999). This system is one of several luminous O-star systems in the Cyg OB2 association that shows evidence of variable radio emission (Persi, Ferrari-Toniolo & Grasdalen 1983, Persi et al. 1990; Bieging, Abbott & Churchwell 1989). The radio emission has two states: a low-flux state of $\sim$ 2 mJy at 4.8 GHz where the spectral index is consistent with thermal emission from a stellar wind, and a high-flux state of $\sim$ 8 mJy at 4.8 GHz, where the spectral index is flatter than in the low state. The variations appear to have a $\sim$ 7-year period (Miralles et al. 1994) and have been attributed to variable non-thermal emission from an expanding plasmon arising in the binary (Bieging et al. 1989; Persi et al. 1990; Miralles et al. 1994).

Observations by Abbott, Bieging & Churchwell (1981) with the VLA revealed a primary component associated with the binary and a second component (hereafter NE) $\sim 0.8''$ to the NE of the primary radio source. NE appears non-thermal and Contreras et al. (1997) argue it is the result of a wind-collision region (WCR) between the stellar wind of the binary and that of a B0-2 V star, $0.9''$ from the binary to the NE (Contreras et al. 1997).

The previous analyses of the radio emission from Cyg OB2 #5 are based on observations from the Very Large Array (VLA), obtained in all the different configurations of the array. Hence, the observations may

or may not resolve the emission from both the primary and NE components. In this work, all VLA archive radio observations of Cyg OB2 #5 are re-examined to produce a consistently calibrated data set. This analysis accounts for changes in the resolution of the observations and presents a consistent treatment of the emission from both the primary and NE sources in each observation. For the first time, the nature and evolution of the emission of both the primary and NE are determined. Kennedy et al. (2010) provide a more complete description of the work highlighted here.

2 Observations

A total of 50 VLA observations of Cyg OB2 #5 obtained between 1983 and 2003 were extracted from the NRAO archive, re-calibrated and analysed. Examples of the resulting deconvolved images at 8.4 GHz are shown in Fig. 1.

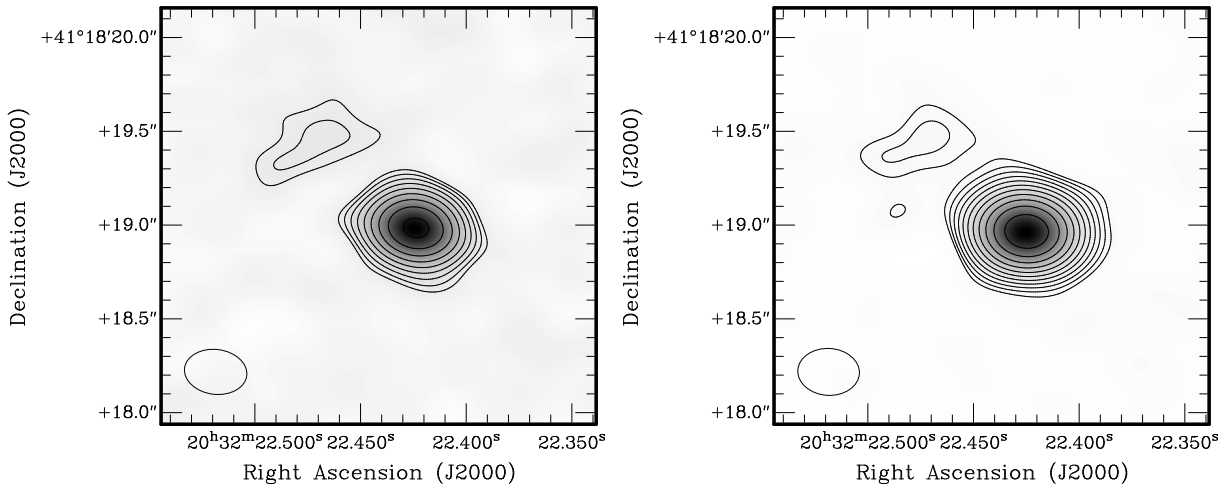

Figure 1: Two examples of the deconvolved VLA images at 8.4 GHz that show the primary and NE sources. The left image is from 1992 December 19 during a low emission state and the right image is from 1996 December 28 during a high emission state.

At 8.4 GHz, the two components were readily resolved in all observations obtained with A and B configuration of the VLA, whereas at 4.8 GHz the two components were only resolved in A-configuration observations. In all of these observations, NE was always detected. In C and D configurations, the two components are not resolved separately at any of the observing frequencies, with only a single unresolved source being observed. Higher resolution MERLIN observations at 1.4 GHz resolve the two radio components separately giving a 1.4-GHz flux for NE and confirming its non-thermal nature with a negative spectral index..

3 Analysis: variations in Radio Emission

The fluxes of Cyg OB2 #5 at both 4.8 GHz and 8.4 GHz as a function of time are shown in Fig. 2. Through the 20 years of observations it is evident that the 4.8-GHz emission from Cyg OB2 #5 has cycled through three cycles of high and low emission with an approximate period of ~ 7 yrs. It is also clear that the radio emission from NE shows no variation and the primary radio component is the source of the variations in Cyg OB2 #5.

At both 4.8 GHz and 8.4 GHz there were 12 and 11 epochs of VLA observations respectively where NE was resolved separately from the primary and a flux could be measured directly. These observations of NE have a weighted-mean flux at 4.8 GHz of 0.83 ± 0.11 mJy and 0.50 ± 0.12 mJy at 8.4 GHz. The flux of NE is statistically constant. This implies the variations arise exclusively in the primary radio source.

Knowing that NE is constant enables the flux of the primary to be determined for all observations where the two radio components are not spatially resolved. The period of the flux variations in the primary emission

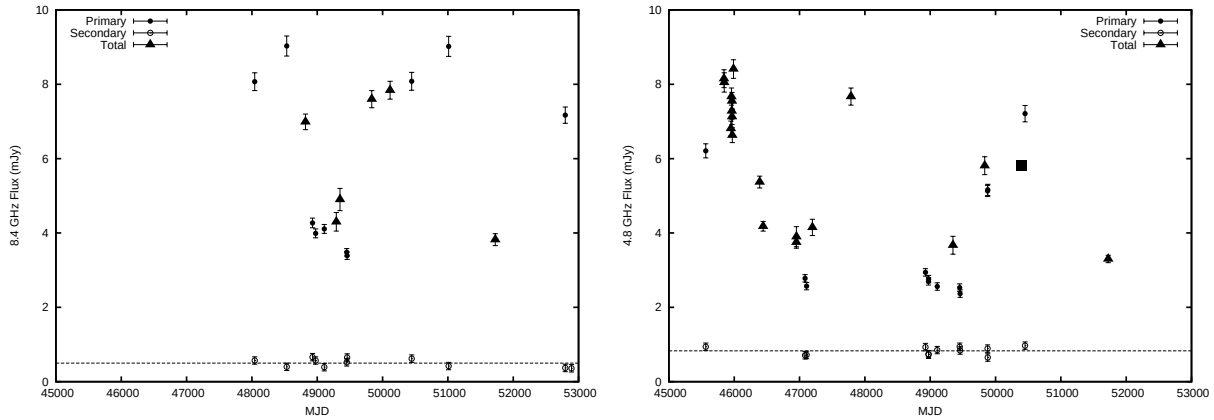

Figure 2: The fluxes of Cyg OB2 #5 between 1983 and 2003 at 8.4 GHz (left) and 4.8 GHz (right), with the primary (solid circles) and NE (open circles) and total i.e. when the components were *not* resolved as separate sources (solid triangles). The mean fluxes of NE are shown (dashed line). The MERLIN 4.8-GHz observation is shown as a square.

was determined using a string-length technique (van Loo et al. 2008, and references therein), and found to be 6.7 ± 0.3 years, remarkably similar to the "eyeball" period derived in previous works.

4 Discussion

4.1 The Primary and Variable Emission

The primary emission component is associated with the O-star binary system and is the source of all the observed variations in the radio emission. In the low state the primary radio emission is found to have a spectral index of 0.60 ± 0.04, consistent with that expected for thermal emission arising in a steady-state radially symmetric stellar wind. The thermal emission must be reasonably constant since 350-GHz JCMT observations obtained away from radio minimum are consistent with the stellar wind spectrum deduced from the radio observations at radio minimum, with a best-fit spectral index 0.63 ± 0.04 across this broad frequency range.

During the high state, the spectral index is much flatter, with an index of $0.24 \pm \pm 0.01$. A model for the primary radio emission component is proposed, where the lower spectral index during high emission is the result of the addition of a non-thermal component to the thermal emission from the binary system that leads to a "composite" spectrum. Such a model has been successfully applied to describe the relatively flat continuum spectra of some Wolf-Rayet stars (e.g. Chapman et al. 1999) where the non-thermal emission arises in a WCR between the wind of the WR star and that of a massive companion star.

For a non-thermal source embedded in a thermal stellar wind plasma, the total observed flux as a function of frequency ν and at epoch t is the sum of the thermal and non-thermal fluxes, given by:

$$S_{obs}(\nu, t) = 2.5 \left(\frac{\nu}{4.8}\right)^{0.6} + S_{4.8}(t) \left(\frac{\nu}{4.8}\right)^{\alpha} e^{-\tau(\nu,t)} \quad \text{mJy},$$

where it is assumed the thermal emission component is constant with a spectral index of $+0.6$ and 4.8 GHz flux of 2.5 mJy measured in the low, thermal emission state, and $S_{4.8}(t)$ is the intrinsic 4.8-GHz flux of the non-thermal source at epoch t, α is the spectral index of the intrinsic non-thermal emission assumed to be constant. $\tau(\nu, t)$ is the line-of-sight free-free opacity through the stellar wind to the non-thermal source at frequency ν and epoch t, approximated by

$$\tau(\nu, t) \approx \tau_{4.8}(t) \left(\frac{\nu}{4.8}\right)^{-2.1}$$

where $\tau_{4.8}(t)$ is the 4.8-GHz line-of-sight free-free opacity at epoch t. The line-of-sight opacity is dependent on the geometry of the line-of-sight to the non-thermal emission. Here, the case of a non-thermal source in a 6.7-yr

orbit about the binary is considered. Williams et al. (1990) derived the varying free-free opacity along a line-of-sight to a non-thermal source orbiting in the circumbinary wind of the massive WR+O binary WR 140. The opacity is dependent on the orbit inclination (i), argument of periastron (ω), as well as the eccentric anomaly (e) and the time of periastron passage (T_0), hence

$$\tau_{4.8}(t) = \tau_{4.8}(t, i, \omega, e, T_0)$$

The intrinsic non-thermal flux $S_{4.8}(t)$ is expected to depend on the local conditions e.g. electron density, which will vary as the source moves through the dense circumbinary wind. This may be approximated by assuming a simple power-law relation with separation, namely

$$S_{4.8}(t) = S'_{4.8} r^{-s},$$

where $S'_{4.8}$ is the non-thermal flux when the separation is equal to a, and s is a power-law index. These definitions, along with the analytic form for $\tau_{4.8}(t)$ (cf. Williams et al. 1990), allow $S_{obs}(\nu, t)$ to be determined as a function of the orbital phase of the non-thermal source orbiting the binary system. The resulting light curves arising from these models are plotted in Fig. 3 for four different model parameter sets, showing excellent agreement with the observations.

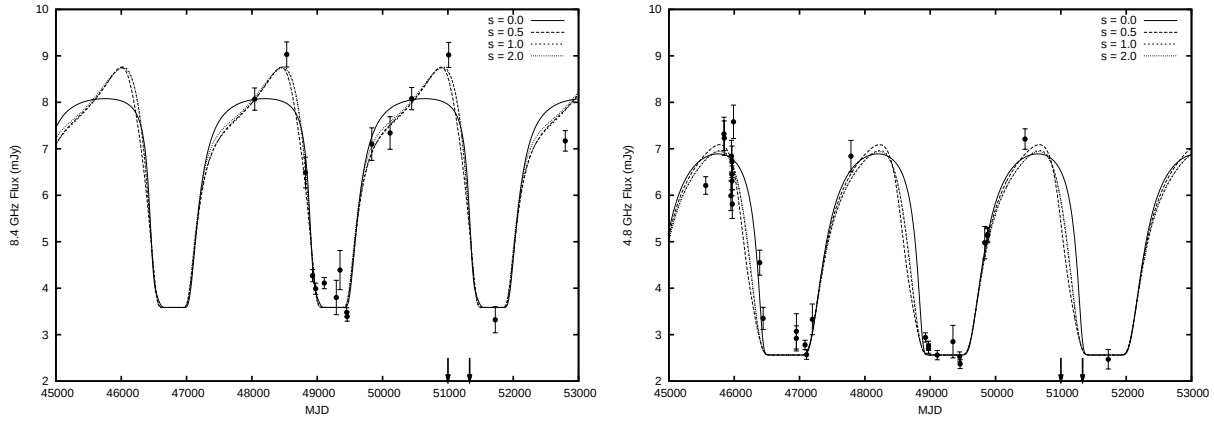

Figure 3: The best-fit orbiting non-thermal source model against the observed fluxes of the primary (slid circles) at 8.4 GHz (left) and 4.8 GHz (right) for the $s = 0, 0.5, 1$, and 2 models.

4.2 Evidence for a Third Star?

A non-thermal source orbiting the O+O binary system requires a star (hereafter Star C) to be in a 6.7-year orbit around the binary. This star may contribute to the non-thermal radio emission via a WCR arising from the collision of its own stellar wind with the wind from the O+O star binary. Such WCRs have been observed directly in some WR+O star and O+O star binary systems (e.g. Dougherty & Pittard 2006, and references therein). Alternatively, the non-thermal emission may arise from the putative third star directly, e.g. a compact object.

Given the high luminosities of the two supergiants in the binary and emission from circumstellar material, it will be very hard to detect the proposed third star directly, let alone measure its orbit. Instead, the radial velocities (RVs) of the O+O binary from Rauw et al. (1999) and Bohannan & Conti (1976) are examined to search for reflex motion due to its putative orbit with Star C. For each RV observed from the primary, the residual (O–C) was calculated from the orbit by Rauw et. al. (1999) and formed the average (O–C) for each run. A systematic increase of RV between phases 0.26 and 0.89 is seen, implying that the O+O binary moves away from us more rapidly. This implies that Star C moves towards us more rapidly in this phase interval so that the circumbinary extinction to the non-thermal radio source diminishes, consistent with it brightening during this orbital phase interval.

The run of mean (O–C) with phase is compared with the reflex motion of the O+O binary in orbit with Star C following the orbital elements of the embedded non-thermal radio source from the $s = 0$ case (see Fig. 4). Fitting

$$\mathrm{v}_r = \gamma + K_{\mathrm{O+O}}(e\cos\omega + \cos(f+\omega))$$

for $K_{\mathrm{O+O}}$ and systemic velocity γ, gives $K_{\mathrm{O+O}} = 32 \pm 17$ km s^{-1} and $\gamma = -5.9 \pm 4.7$ km s^{-1}. This leads to a mass function $f(m)$ derived from P (in days) and K (in km s^{-1}) from

$$f(m) = \frac{m_{\mathrm{C}}^3 \sin^3(i)}{(m_{\mathrm{O+O}} + m_{\mathrm{C}})^2} = 1.036 \times 10^{-7} \left(1 - e^2\right)^{3/2} K^3 P,$$

giving an estimate of the mass, m_{C}, of Star C. From the data here, $f(m) = 3.2^{+8.2}_{-2.8}$ M$_\odot$. Assuming $\sin(i) = 1$ and adopting $m_{\mathrm{O+O}} = 41.5 \pm 3.4$ M$_\odot$ from Linder et. al. (2009), this gives $m_{\mathrm{C}} = 23^{+22}_{-14}$ M$_\odot$ for Star C.

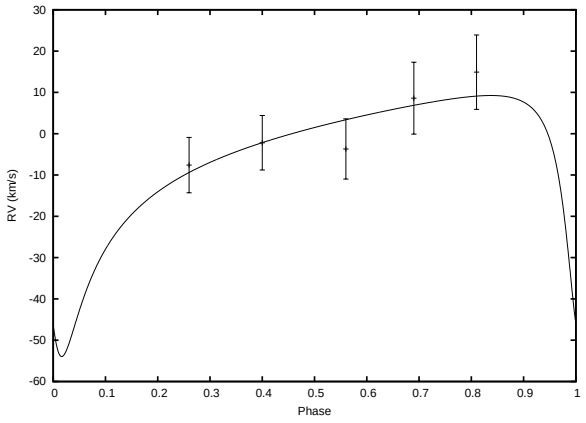

Figure 4: Observed (O–C) residuals and the RV curve for the reflex motion for the elements of the $s = 0$ model with $K = 32 \pm 17$ km s^{-1} and $\gamma = -5.9 \pm 4.7$ km s^{-1}.

References

Abbott, D.C., Bieging, J.H., & Churchwell, E.B. 1981, ApJ 250, 645

Bieging, J.H., Abbott, D.C., & Churchwell, E.B. 1989, ApJ 340, 518

Bohannan, B., & Conti, P.S. 1976, ApJ 204, 797

Chapman, J.M., Leitherer, C., Koribalski, B., Bouter, R., & Storey, M. 1999, ApJ 518, 890

Contreras, M.E., Rodriguez, L.F., Tapia, M., Cardini, D., Emanuele, A., Badiali, M., & Persi, P. 1997, ApJ 488, L153

Dougherty, S., & Pittard, J.M. 2006, in Proceedings of the 8th European VLBI Network Symposium, arXiv:astro-ph/0611088

Hall, D.S. 1974, Acta Astronomica, 24, 69

Kennedy, M., Dougherty, S.M., Williams, P.M., & Fink, A. 2010, ApJ 709, 632

Leung, K.-C., & Schneider, D.P. 1978, ApJ 224, 565

Linder, N., Rauw, G., Manfroid, J., Damerdji, Y., De Becker, M., Eenens, P., Royer, P., & Vreux, J.-M. 2009, A&A 495, 231

Miralles, M.P., Rodriquez, L.F., Tapia, M., Roth, M., Persi, P., Ferrari-Toniolo, M., & Curiel, S. 1994, A&A 282, 547

Persi, P., Ferrari-Toniolo, M., & Grasdalen, G. L. 1983, ApJ 269, 625

Persi, P., Ferrari-Toniolo, M., Tapia, M., Rodriguez, L. F., & Roth, M. 1990, A&A 240, 93

Rauw, G., Vreux, J.-M., & Bohannan, B. 1999, ApJ 517, 416

van Loo, S., Blomme, R., Dougherty, S.M., & Runacres, M.C. 2008, A&A 483, 585

Williams, P.M., van der Hucht, K.A., Pollock, A.M.T., Florkowski, D.R., van der Woerd, H., & Wamsteker, W.M. 1990, MNRAS 243, 662

Discussion

D. Gies: A question to G. Rauw. Is there any evidence of a third star in your spectra of Cyg OB2 #5?
G. Rauw: There is so far no direct evidence for the presence of a fourth component (actually counting the visual component as the third star of the system). This being said, whilst the spectral lines display phase-locked variability on the period of the close binary system, we noted that there are also longer-term variations that might actually be linked to the 6.8 years radio period (Rauw et al. 1999). However, this needs to be checked with additional data. If confirmed, these variations could be linked to blending with absorption lines of the fourth component. Finally, let me stress that the analysis of the light curve of Cyg OB2 #5 performed by Linder et al. (2009) did not account for the presence of third light. Including third light might actually bring our distance determination into better agreement with conventional values of Cyg OB2.

M. De Becker: We have also another indication for the presence of a fourth star in the system in X-rays. The results of the analysis of the *XMM-Newton* spectra cannot be explained only by the presence of the short period binary and that of the other star located far away to the NE direction.

P. Williams: Determination of the long period orbit from reflex motions of the central binary looks like an attractive project for the amateur spectroscopists described by Thomas Eversberg. From new sets of observations one can re-determine the 6-day orbit at different epochs to determine the γ-velocity with other parameters fixed and so measure long-term velocity variations.

The Eta Carinae 2009 Campaign

M. F. Corcoran[1,2]

[1] CRESST/NASA-GSFC, Greenbelt MD USA
[2] Universities Space Research Association, Columbia, MD USA

Abstract: In January 2009, the enigmatic, extremely massive and luminous star η Car went through one of its periodic "minimum" states in which the excitation of its circumstellar nebula, along with the 2–10 keV emission from the star, collapses for a brief period. Current understanding associates this minimum state with the occurrence of periastron passage of a massive, unseen hot companion star around the much more luminous, much more massive η Car. These events offer a direct probe of the mass loss from η Car and the system as a whole, with circumstantial evidence tying these events to the spectacular "Great" and "Lesser" eruptions of the 19^{th} century. As such these events have attracted the interest of a broad community of stellar and nebular astrophysicists. I report here on the results obtained during a nearly pan-chromatic campaign of observations of the January 2009 minimum, with some emphasis on the unique aspects of this particular minimum.

1 Introduction

Eta Car (η Car) is the closest example of a superluminous, supermassive star near $100 M_{\odot}$ (Davidson & Humphreys 1997, Hillier et al. 2001). The star is near the Eddington limit and the Humphreys-Davidson limit, and as such it is very unstable. During the "Great Eruption" around 1843, η Car generated massive ejecta at speeds of up to 6000 km s^{-1}, producing almost as much kinetic energy as a low-luminosity supernova (Smith 2008) and producing the enormous bipolar circumstellar shell around the star, the so-called Homunculus Nebula. The star underwent a smaller, though still spectacular "Lesser" eruption in 1890. The physical cause of these eruptions is still not understood after 150 years of study. Nor is it understood what role such sporadic, large-scale eruptions play in driving the ultimate evolution of η Car, and those extremely massive objects like it, through hypernova and black hole formation.

Understanding these sporadic variations is difficult without identifying any type of underlying periodic phenomena. Astronomers have long sought periodicities in η Car's observable behavior ever since the Great Eruption. Shortly after the Great Eruption, Rudolf Wolf and Elias Loomis suggested recurrence cycles of 46 and 67 years (Wolf 1863, Loomis 1869); more recently, shorter cycles of 15–16 years (Payne-Gaposchkin 1957) to 3 years (Feinstein & Marraco 1974) were also suggested. The complex behavior of η Car's observed variations in broad-band photometry and in spectrographic observations made determination of any true period difficult, and none of these suggested periods had much predictive power.

The discovery of η Car's first confirmed period depended on observations spanning twenty years or more. This began with the recognition of a so-called "spectroscopic event" by Zanella, Wolf and

Table 1: System parameters for the η Car binary system. Personal estimates for the types of observations providing the firmest estimates of these paramters are given: X=X-ray, U=ultraviolet, V=visible-band, I=IR.

Parameter	Value
P	2024 ± 2 days (X, U, V, I)
V_∞ (η Car)	500 km s^{-1}(U,V)
V_∞ (Companion)	3000 km s^{-1}(X)
$\dot{M}_{\eta\ Car}$	10^{-3} to 10^{-4} (U,V; X)
$\dot{M}_{companion}$	10^{-5} (X)
e	0.9 (X,U,V)
a	15 AU? (X, U, V)
ω	$270°?, 90°?, 180°? \cdots$ (X,U,V)
$\theta = 0$ (periastron passage)	$\phi = 0$ (start of X-ray minimum)
i	$45°$–$55°$? (U,V)

Stahl in 1981 (Zanella et al. 1984). These "events" represent a dramatic and complex change in η Car's visible-band spectrum in which high-excitation He I and [Ne III] emission lines abruptly fade, then recover. Similar changes happened in 1948 and 1965, which suggested to them a recurrence timescale of 17 years (Zanella et al. 1984). We now recognize that other such events had occurred in 1953, 1959, 1970, and 1975. Near-infrared photometry from South Africa obtained by Patricia Whitelock and her collaborators (Whitelock et al. 1994) over 156 nights in 1975-1994 showed a significant 5–6 year cycle, but this cycle was confused with other near-infrared variations on other timescales. Meanwhile new spectroscopic events occurred in 1986 and in 1992, though the former was not widely reported.

The breakthrough was provided by a set of 27 measurements of the He I 10830Å emission line obtained by Augusto Damineli at Brazil's National Astrophysical Laboratory. These observations, augmented by 4 additional measures from other observers from 1981–1995, showed a clear, rapid weakening of the 10830Å line every 5.5 years, lasting only for a few weeks (a duty cycle of $< 5\%$). Damineli (1996) also showed the fading of the 10830Å line occurred at nearly the same time as brightening of the system in the near IR, and that the 5.5 year period recovered not only the "spectroscopic event" seen by Zanella, Wolf and Stahl in 1981, but also all other "spectroscopic events" observed in the previous 50 years, and perhaps even the Great Eruption in the 1840's and the Lesser Eruption of 1890. Serendipitous observations of η Car during 1992–1993 at the Australian Telescope National Facility (Duncan et al. 1995) and by the Röntgen Satellite (Corcoran et al. 1995) confirmed the presence of a minimum state in the radio and X-ray bands. Damineli's period (which has now been refined to $P = 2024 \pm 2$ days, Damineli et al. 2008) successfully predicted the occurrence of the next minimum at the end of 1997, an event which was observed in the radio to optical through the UV up to the X-ray regime.

Orbital motion of one star around another provides the simplest interpretation of this strict, panchromatic period. The long period and short duty cycle of the minimum suggests that the orbit is highly eccentric ($e \sim 0.8$–0.9), and further suggests that the minima occur near periastron passage when the stars are moving most rapidly. The response of the circumstellar Homunculus nebula around the cycle suggests variable photo-excitation and photo-ionization conditions in the nebula. This is now attributed to photospheric radiation from a companion star much hotter than η Car, whose radiation gets funneled by a "bow shock" produced by the collision of the companion's wind with the stronger wind of η Car. The minimum state occurs as the companion's emission is blocked by the inner wind of

η Car near periastron passage. A simulation of the expected density distribution of the two interacting winds at certain key times in the orbit is shown in Figure 1.

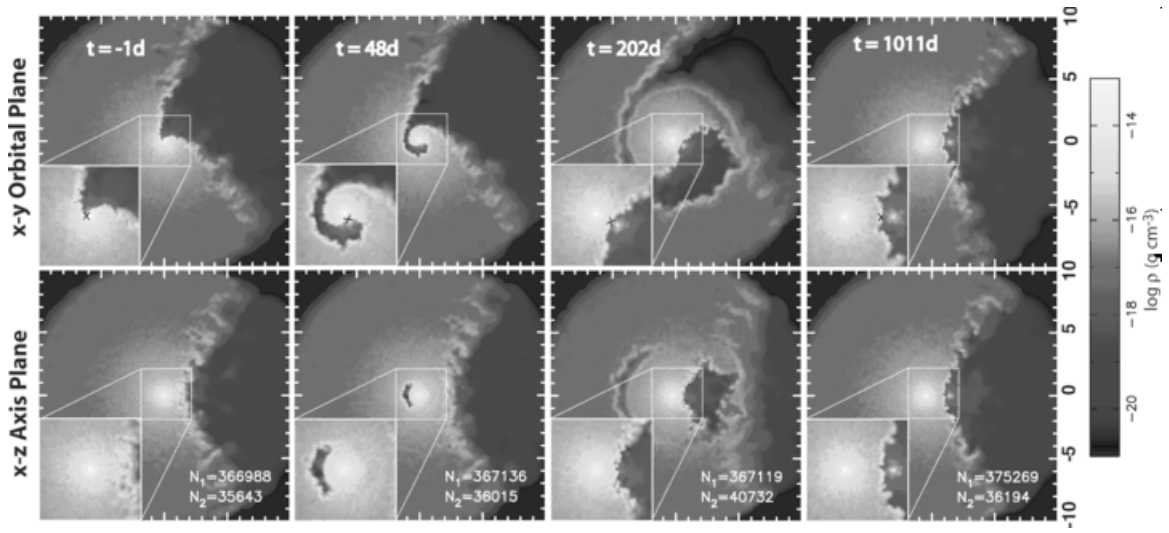

Figure 1: "Snapshots" of the wind density distribution in and perpendicular to the orbital plan from a 3-D smoothed particle hydrodynamics (SPH) simulation by Okazaki et al. (2008) for selected times in the 2024-day orbit. The "bow shock" is concave around the weaker-wind companion star. X-ray emission originates along the bow shock on the side of the companion star, and most of the far UV photospheric radiation from the companion star can only escape through the lower-density companion wind bounded by the bow shock.

We note that there is as yet no widely accepted direct evidence of the companion star (however, see for example, Iping et al. 2005). Arguably, the best evidence of the presence of a companion star in orbit around η Car comes from study of the 2–10 keV X-ray emission variations. Detailed X-ray observations (Ishibashi et al. 1999, Corcoran 2005) document a variation that is most easily explained as originating in shock-heated gas produced where a fast ($V \approx 3000$ km s^{-1}), less dense wind of a companion star slams into the slow ($V \approx 500$ km s^{-1}), dense wind from η Car. The parameters of the system are given in Table 1, along with a personal estimate of the wavebands used to derive these parameters. The first three parameters are rather firmly established, while there is some uncertainty in the remainder.

2 The 2009 Minimum

Damineli's ephemeris predicted a minimum on January 16, 2009 (oddly enough, just days after a similar event in WR140, another long-period highly eccentric massive binary, which is the topic of a review by Williams 2011). In anticipation of this event, observations spanning almost the entire electromagnetic spectrum were planned. Although a number of observers frequently monitor η Car whenever feasible, we consider the observing campaign as beginning roughly one year before the predicted minimum (January 2008), when most of the new observations began in earnest. Although much progress had been made from prior observations, especially during the 2003 July minimum (which included detailed observations with the Hubble Space Telescope obtained as part of the HST η Car Treasury Program[1]) there were a number of key issues left unresolved. What actually causes the "event" (an eclipse?; cooling/"discombobulation" of the shock?; phase-dependent mass loss?; jet

[1]http://etacar.umn.edu/

formation?), and is the wind-wind collision region stable? Do the stars interact near periastron, and if so how? How is the geometry of the inner wind of η Car altered by the passage of the companion through it, and how does this geometry propagate outwards? What is the actual density profile of η Car's wind? And most importantly, what are the stellar radial velocities and what is the system mass ratio? Addressing these questions was a main goal of the 2009 η Car observing campaign, with the hope of reconstructing the full 3-D geometry of the wind-driven mass loss from the system.

3 The Campaigners

Table 2 gives a list of participants in the 2009 observing campaign. This list is incomplete, because it's impossible to identify everyone who made significant contributions in the space allotted, but hopefully, it captures much of the observational effort. It's divided by energy band and since it's observationally biased, it ignores the significant modelling efforts of Pittard, Parkin, Okazaki, Madura, Russell, Soker, Kashi and Akashi. Some of the modeling work is described elsewhere in this volume.

Table 2: An (incomplete) list of Participants in the η Car 2009 Observing Campaign

Regime	Observatory	Observers
Hard X-ray/ Gamma Ray ($>$ 10 keV - 300 GeV)	INTEGRAL, Fermi, AGILE, Suzaku	Leyder et al., Takahasihi/Fermi Team, Tavani et al., Hamaguchi et al., Russell et al.
X-ray (1-10 keV)	RXTE, Chandra, Suzaku, XMM, Swift	Corcoran, Hamaguchi et al., Pian et al.
UV/Optical	OPD-LNA/Brazil, SOAR, HST, OALP, CASLEO, SMARTS/CTIO, Monash, VLT/UVES, Magellan	Damineli, Mairan et al., Mehner, Davidson et al., Gull, Madura et al., Fernandez-Lajus et al., Gies, Richardson et al., Landes & Fitzgerald, Bomans, Weis, Stahl
IR	VLTI/AMBER, VLT/CRIRES, VLTI/VINCI	Weigelt et al., Groh et al.
(sub)mm	Itapetinga, APEX	Abraham et al., Gomez et al.
Radio	ATNF	White

4 Results

In the following section we highlight some of the main observational results.

4.1 Broad-Band Monitoring in the Optical and X-ray Bands

Figure 2 compares photometry of the system in two wavebands: ground-based V-band photometry from the LaPlata group (Fernández-Lajús et al. 2010) and space-based 2–10 keV X-ray photometry from the *RXTE* satellite (Corcoran et al. 2010). Both the optical and X-ray monitoring have similar sampling and similar spectral sensitivity. Nominally, the optical data has much better spatial resolving power compared to the X-ray data ($12''$ vs. 1° for the *RXTE* Proportional Counter Array), but the X-ray

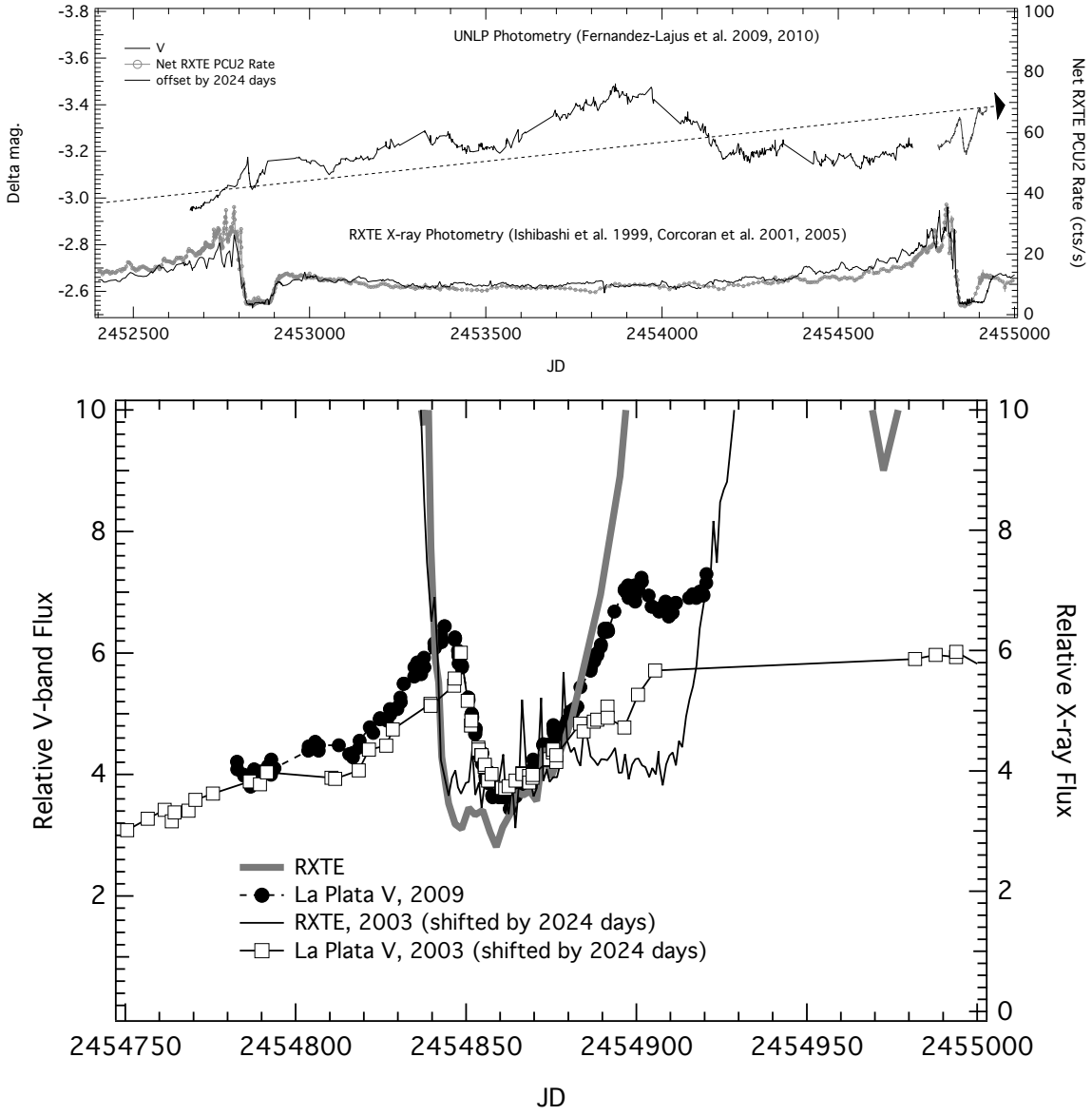

Figure 2: Top: Comparison of V-band photometry by the La Plata group from the Virpi S. Niemela telescope at LaPlata and at CASLEO covering the 2003.5 and 2009 minima, compared to the 2–10 keV band X-ray photometry from *RXTE*. The dashed arrow represents the general brightening trend at V seen in recent years. Both the V-band and 2–10 keV emission show evidence of "eclipse-like" minima, though the relative depth is much more pronouncedd in the X-ray band. Bottom: A detailed comparison of the V-band and X-ray flux variations for both minima. The 2003.5 data for both the X-ray and V photometry has been progressed forward by 2024 days for comparison with the 2009 minimum.

emission arises in a limited volume in the bow shock where the winds collide and so should sample a much smaller region of variability than the optical photometry does. As can be seen in the figure, an "eclipse-like" minimum is apparent from both ground and space, though the relative variation is larger in the X-ray data than in the optical. The optical emission is confused between real intrinsic changes in stellar brightness and circumstellar changes in the environment of the Homunculus. This confusion accounts for some of the large-scale variations seen in the V-band lightcurve. A particularly interesting feature is the large "hump" between JD 2453500 and 2454200. No such change is seen

in the X-ray lightcurve during this interval. The bottom panel of Figure 2 shows a detailed view of the two minima sampled by the X-ray and optical monitoring. Both show good reproducibility in the decline to the minimum, particularly impressive in light of the relative lack of correlation between the X-ray and V band outside of the minimum. The comparison of the 2003 and 2009 X-ray minima show that the 2009 minimum was substantially shorter than the 2003 minimum by about 1 month. There is also some evidence that the optical "eclipse" was also shorter in 2009 than in 2003, as indicated in Figure 2. The question is, what caused the minima (so stable in 1998 and 2003) to be so much shorter in 2009?

4.2 A Sea Change?

Since the minimum is strongly influenced by the density of η Car's wind, it's perhaps reasonable to suggest that shorter minimum duration means that the density of the wind has changed (Kashi & Soker 2009, Corcoran et al. 2010). One way to determine the overall mass loss rate from η Car is to examine the strengths of Hα and other strong emission lines. Mehner et al. (2010) compared a set of strong emission lines from η Car (particularly Fe II, [Fe II], Cr II, [Cr II] and Hα) obtained at approximately the same phase in the 5.5-year cycle but separated by 2 cycles. They found that, compared to 1999, the continuum-normalized emission lines decreased by factors of order 2 in 2010, (for example, see the Hα profiles in Figure 3). The simplest explanation of this large scale decrease in emission line strength is a recent, significant decrease in the density of the wind from η Car. Preliminary modeling of the X-ray data suggests that a large change in wind density (equivalent to a factor of 2 or more decline in η Car's mass-loss rate) is necessary to explain the narrow 2009 X-ray minimum. It's unclear if the decline in emission line strength documented by Mehner et al. is consistent with so large a change in wind density. Nevertheless these data do suggest some type of large intrinsic change in η Car is occurring.

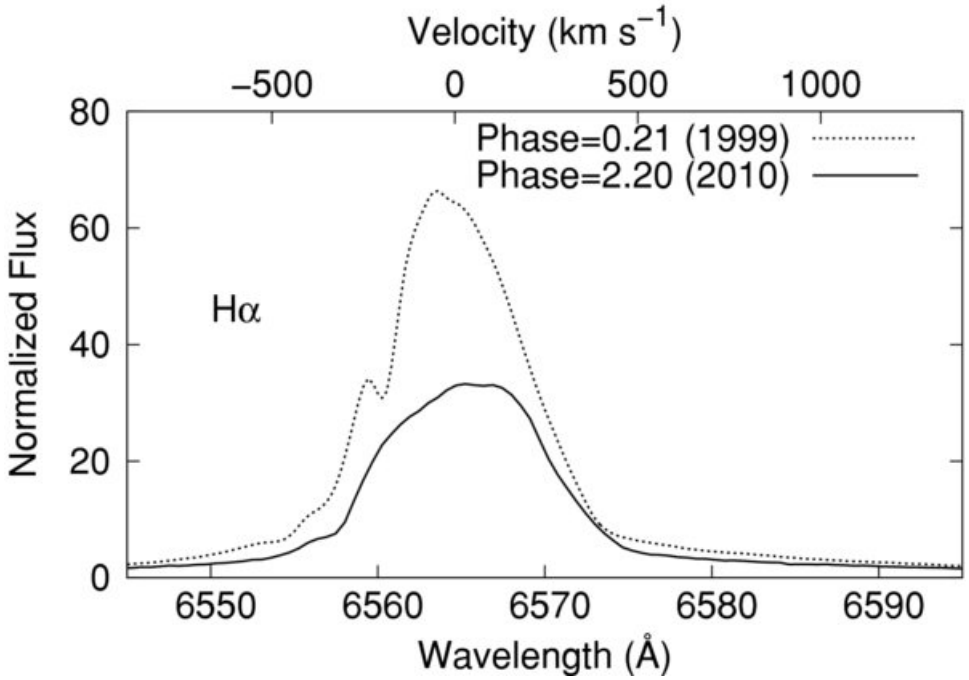

Figure 3: Comparison of the Hα line profile from η Car 1999 & 2010 (Mehner et al. 2010).

4.3 High-Velocity Outflows

The appearance of high velocity emission in the X-ray emission line spectrum was noted by Behar et al. (2007) and Henley et al. (2008) using *CHANDRA* grating observations obtained just prior to the X-ray minimum in 2003. X-ray line profiles showed emission at velocities $V \approx -2000$ km s^{-1}. Such velocities are about a factor of 2–4$\times$ higher than the wind speed of η Car, but somewhat lower than the deduced companion wind speed (speeds of ≈ 3000 km s^{-1}are necessary to produce the observed X-ray emission at energies above 3 keV, Pittard & Corcoran 2002). The 2003 observations left unclear whether this high velocity emission represented a transient jet from the poles of the companion or the projected outflow from the wind-shock region. The upper panel of Figure 4 compares the Lyα profiles from the strong hydrogenic Si XIV line obtained between 20–40 days before the X-ray minima in 2003 and 2009, along with the same line at apastron. In contrast to the apastron profile, the profiles of the Si XIV emission near both the 2000 and 2009 minima are broader and show blue-shifted emission to velocities of ≈ -2000 km s^{-1}. However, the centroid velocity peak in 2009 is at a substantially lower velocity compared to the 2003 profile.

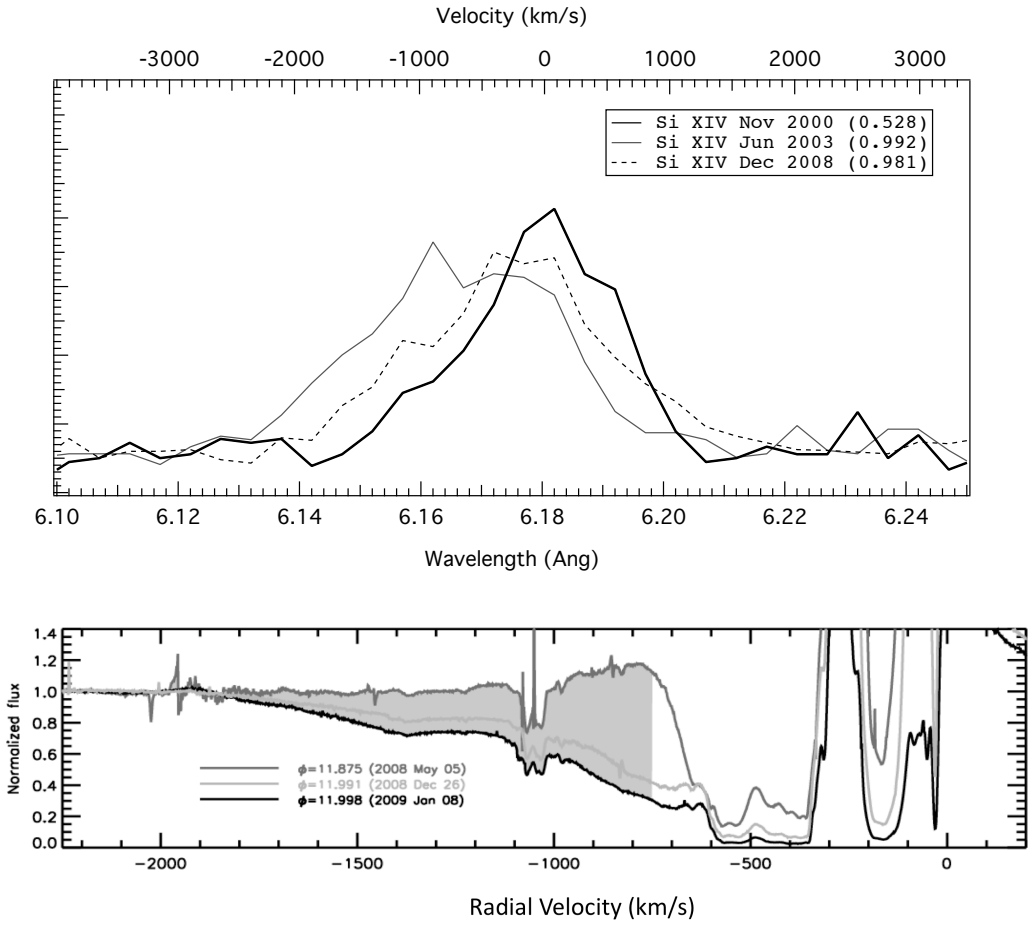

Figure 4: Top: comparison of Lyα Si XIV line profiles from *CHANDRA* High Energy Transmission Grating spectra just prior to X-ray minimum in 2003 (thin solid line) and 2008 (dashed line); the thick line shows the Si XIV Lyα line near apastron from 2000 November for reference. Bottom: variation of the He I 10830Å line from CRIRES spectra (Groh et al. 2010) in 2008-2009.

Similar changes can be seen at lower energies. Groh et al. (2010) obtained a detailed series of measures of the He I 10830Å line from 2008 through 2009 with the CRyogenic high-resolution InfraRed Echelle Spectrograph (CRIRES). These observations clearly showed the appearance, in absorption,

of high velocity material appearing about 1 month prior to the 2009 X-ray minimum, i.e. consistent with the appearance of the high-velocity X-ray emission. The lower panel of Figure 4 shows the development of the high velocity absorption component in 2008 December and 2009 January from Groh et al. (2010). They also noted the appearance in HST/STIS data from 2003 of high velocity absorption in the Si IV resonance doublet at 1400Å in a similar interval prior to the 2003 minimum. They further showed that no such high-velocity emission was seen in lower ionization species. This is strong evidence that the high-velocity features seen in the X-ray, near-IR and UV regions trace the outflow along the wind-wind shock, and thus can be used to constrain models of velocity and ionization changes with distance along the wind-wind bow shock. Such information is crucial to understanding the geometry of the bow shock and the relative strength of the stellar winds from the two stars.

4.4 The Shape of Things – To Come?

As the bow shock swings around following the companion star in its orbit, the companion's far UV photospheric radiation variably illuminates the circumstellar gas and dust like a cosmic searchlight. This variable illumination in principle constrains the shape of the bow shock, the orbital motion and also the geometric distribution of the outer wind and ejecta around η Car. This can provide information about the mass-loss rates of both stars, help constrain the mass ratio, and refine our understanding of the sporadic large-scale ejection events. Therefore this is a dynamic area of current research. Figure 5 shows a simulation of a spatially-resolved [Fe III] emission line at 4659Å based on the distorted outer wind of η Car from a 3-D SPH simulation (Madura, 2010, PhD thesis; see also the discussion by Madura et al. 2011). This simulation is then compared to the same line profile as observed by HST/STIS (Gull et al. 2009).

Madura found that the simulation which best matched the observed STIS profile had $i \approx 40° \pm 10°$, $\omega \approx 255° \pm 15°$, with the orbital axis projected on the sky at a position angle $\Theta \approx 312° \pm 15°$. This implies that the orbital angular momentum vector is closely aligned with the symmetry axis of the Homunculus, with the resulting projected orbit on the sky having the companion star moving clockwise around η Car, with apastron on the observer's side of the system. This orientation is shown on the bottom panel of Figure 5.

The size of the emitting region has been imaged interferometrically at 2 microns by Weigelt and collaborators using the Very Large Telescope Interferometer. During the 2009 minimum, the size of the He I emitting region collapsed from 17.4 mas (39 AU) to only 5.7 mas (13AU) on 5 Jan 2009 (see Figure 6) before recovering in 2009 March to 11 mas (25 AU). Even at minimum, the size of the emitting region is apparently still comparable to the size of the orbital semi-major axis ($\sim$ 16 AU). Throughout this interval, the size of the Br-γ and continuum-emitting region stayed almost constant. On 2009 March 3 the size of the He I emitting region recovered to 11.4 mas (25 AU).

4.5 Even Higher Energy Emission

Studies of η Car at hard X-ray and Gamma-ray energies have been made using *INTEGRAL*, *AGILE*, *Suzaku*, and *Fermi*. At these energies emission is dominated by non-thermal processes like inverse Compton scattering or synchrotron emission. *INTEGRAL*, *AGILE*, and *Fermi* all have directly imaged a strong source within a few arcminutes of η Car (see Figure 7). The source is rather luminous with $L_\gamma \approx 10^{34}$ ergs s^{-1} in the 20-100 keV band, increasing to $\approx 10^{36}$ ergs s^{-1} in the 1-300 GeV band. There is as yet no strong suggestion that the Gamma-ray source varies through the minimum, though the statistical significance of the observations are not exceedingly high. Tavani et al. (2009) reported the occurrence of a Gamma-ray flare by *AGILE* which was not however confirmed by contempora-

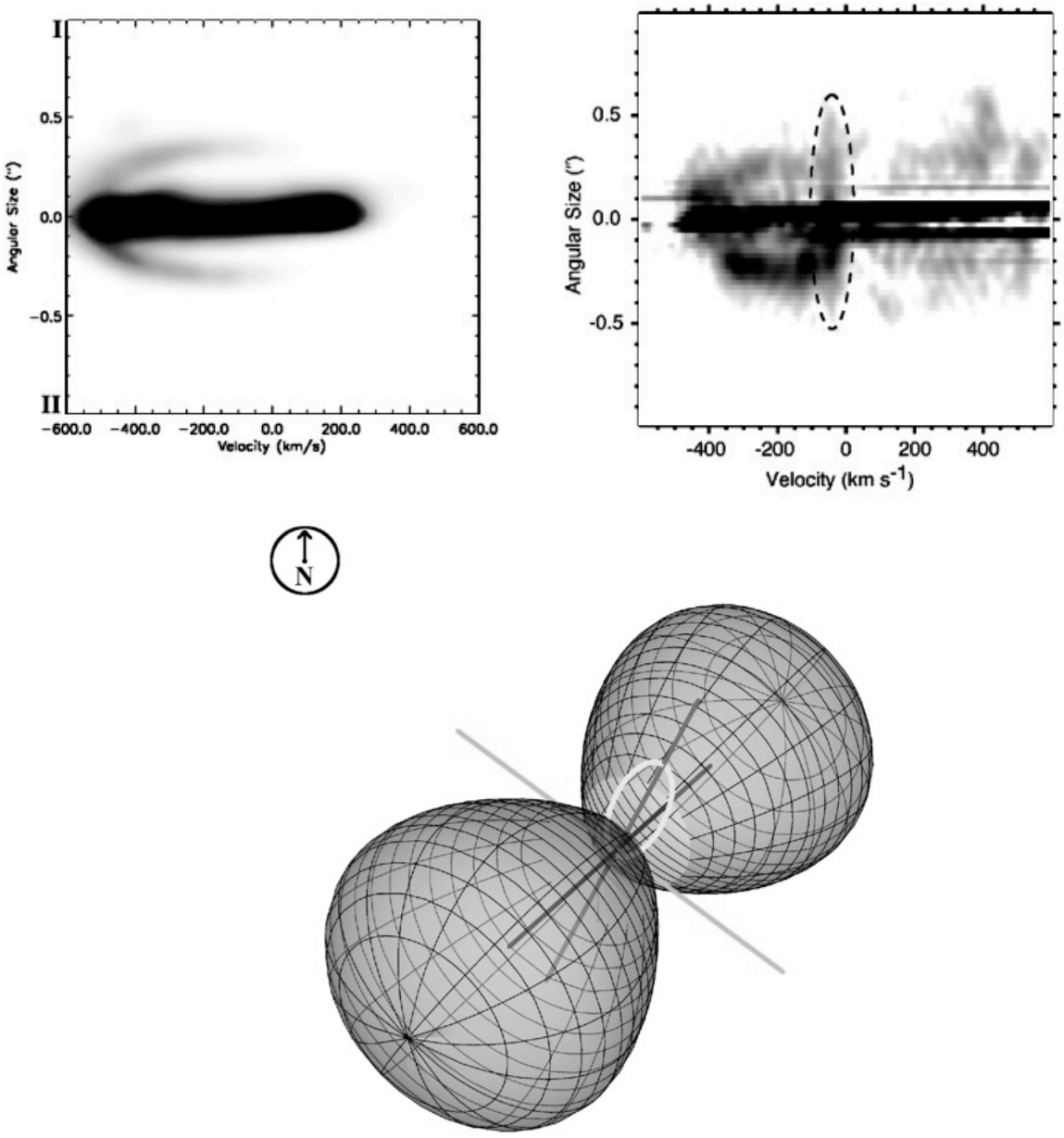

Figure 5: Top left: simulated spatially resolved [Fe III] line profile by Madura et al. (2011) for a particular slit orientation based on a 3-D SPH model. Top right: Observed spatially-resolved line profile as observed by HST/STIS for the same slit orientation (Gull et al. 2009). The simulation successfully reproduces the overall shape and orientation of the [Fe III] emission line as observed by STIS for the particular slit position and orbital phase of the observation. The dotted oval shows the region of emission produced by one of the "Weigelt knots" (a dense nebulosity ejected from the star in the 19^{th} century) and is not included in the model simulation. Bottom: a "dressmaker's dummy" model of the orbital orientation based on the line profile simulation showing the relation of the derived orbit relative to the orientation of the bipolar lobes of the Homunculus (not to scale).

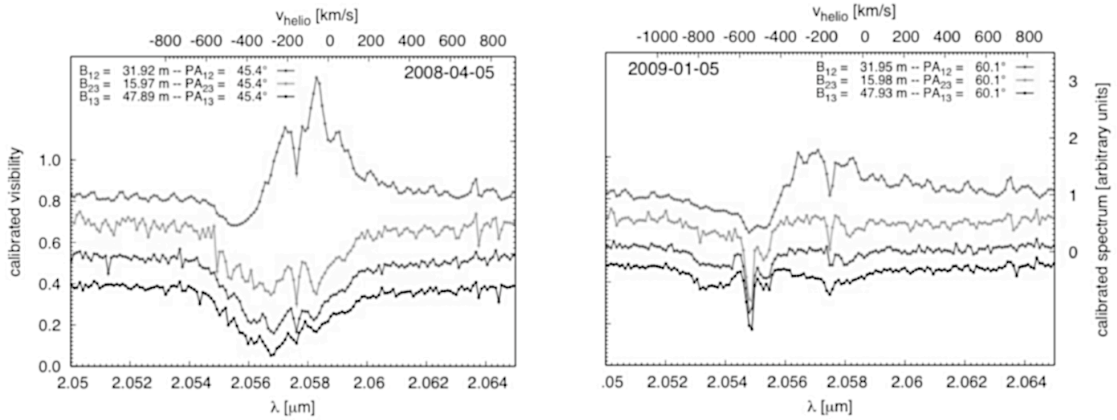

Figure 6: Visibilities at He I 2.06μm obtained at the VLTI from 2008 (*left*) and in 2009 January (*right*). The He I emitting region collapsed from 17.4 mas (39 AU) to 5 mas (11 AU) in 2009 January, and grew to 11 mas by 2009 March.

neous observations with *Fermi*. It is possible that the observed Gamma-ray source is not directly associated with the stellar source; perhaps it's associated somehow with the ejecta (see, for example, Ohm et al. 2010), or perhaps arises from an unrelated background object (though the almost perfect coincidence with η Car seems to rule out a chance alignment with a background source).

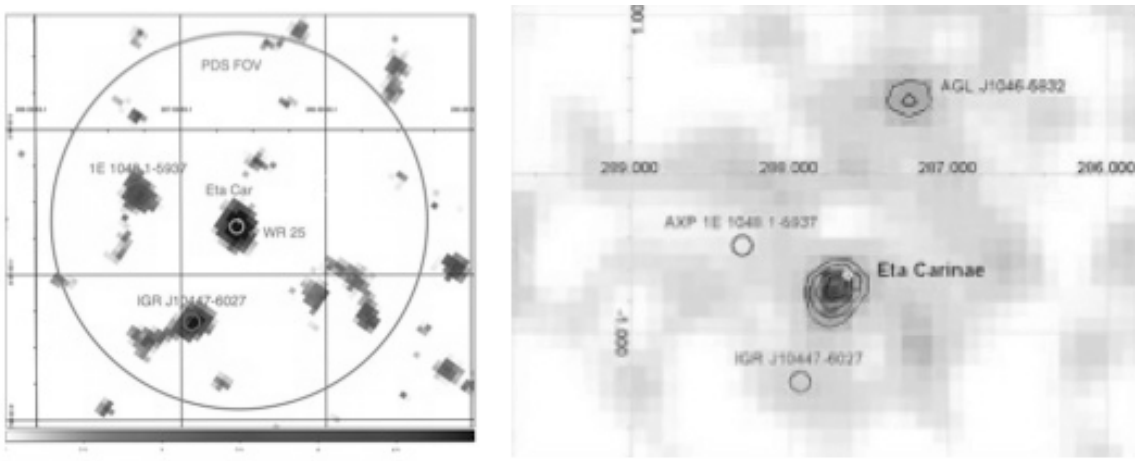

Figure 7: Left: an *INTEGRAL*-ISGRI image of the field around η Car, in the 20-100 keV band (Leyder et al. 2008). A significant source is detected near η Car. Right: an *AGILE* observation of η Car in the 30 MeV–30 GeV band (Tavani et al. 2009).

5 Conclusions and Possible Directions for Future Work

Arguably the most surprising result of the 2009 observing campaign was the rapid recovery from the minimum state seen most prominently at X-ray energies, along with the decline in emission line strength seen in the optical. The cause of these changes is still not well understood, although a decline in the mass loss rate from η Car itself likely plays a significant role. But if so then preliminary modeling of the X-ray minimum duration suggests a large change in mass loss rate (by a factor of 2–4 or so) is required. It remains to be seen if such a large change is consistent with the decline in emission line strength reported by Mehner et al. (2010); if not this either means that the emitting

material producing the optical emission lines and the 2–10 keV X-rays may originate in different volumes with different densities, or something even stranger is going on. But if the mass loss rate really declined by a factor of 2 or more, then this must be driven by some fundamental, underlying change in the photospheric radiation field of the star itself. What this could be remains to be examined.

Attempts to image the system, either interferometrically or by examining the response of the distorted wind to illumination by the far UV of the companion via spatially-resolved spectrometry and 3-D modeling, hold great hope to advance our understanding of the physical parameters of the stars and to refine the orbital elements. This work already supports a fundamental correlation between the orbit of the system and the ejection of the material that formed the Homunculus, helping to strengthen ties between periastron passage and the mechanism producing (or at least shaping) the Great Eruption.

Clearly, new observations are needed to understand the future evolution of mass loss from the system and to understand fully the mass-loss history. Modeling efforts, especially in 3-D, including realistic heating and cooling mechanisms, and including adaptive methods to try to resolve the structure of the bow shock, also provide an important key for interpreting the anticipated wealth of new data (and to better understand the legacy data residing in the η Car Treasury Program archives and in the high energy archives). One wonders what changes 2014 will bring.

Acknowledgements

I'd like to acknowledge the immense efforts of this world-wide group in carrying out this observing campaign and the extraordinary efforts undertaken in order to increase our understanding of this peculiar and spectacular object.In particular I need to gratefully thank those observers and modelers who have graciously shared their results, in many cases prior to publication. I'd also like to acknowledge the contributions of all those who were not specifically noted in this report due to space limitations. The *CHANDRA* η Car program has been supported by *CHANDRA* grants GO0-11039A, G07-8022A, G09-0016A, and G08-9018A. This support is gratefully acknowledged. This work has also been supported in part by NASA Cooperative Agreement NNG06EO90A. This research has made use of NASA's Astrophysics Data System Bibliographic Services, an indispensable tool. This research has made use of data obtained from the High Energy Astrophysics Science Archive Research Center (HEASARC), provided by NASA's Goddard Space Flight Center, also an indispensable resource for the high energy astrophysicist.

References

Behar, E., Nordon, R., & Soker, N. 2007, ApJL, 666, L97
Corcoran, M. F. 2005, AJ, 129, 2018
Corcoran, M. F., Rawley, G. L., Swank, J. H., & Petre, R. 1995, ApJL, 445, L121
Corcoran, M.F., Hamaguchi, K., Pittard, J.M., Russell, C.M.P., Owocki, S.P., Parkin, E.R., & Okazaki, A. 2010, ApJ, 725, 1528
Damineli, A. 1996, ApJL, 460, L49
Damineli, A., Hillier, D. J., Corcoran, M. F., et al. 2008, MNRAS, 386, 2330
Davidson, K., & Humphreys, R. M. 1997, ARAA, 35, 1
Duncan, R. A., White, S. M., Lim, J., Nelson, G. J., Drake, S. A., & Kundu, M. R. 1995, ApJL, 441, L73
Feinstein, A., & Marraco, H. G. 1974, A&A, 30, 271
Fernández-Lajús, E., Fariña, C., Calderón, J. P., et al. 2010, New Astronomy, 15, 108
Groh, J. H., Nielsen, K. E., Damineli, A., et al. 2010, A&A, 517, A9+
Gull, T. R., Nielsen, K. E., Corcoran, M. F., et al. 2009, MNRAS, 396, 1308
Henley, D. B., Corcoran, M. F., Pittard, J. M., Stevens, I. R., Hamaguchi, K., & Gull, T. R. 2008, ApJ, 680, 705
Hillier, D. J., Davidson, K., Ishibashi, K., & Gull, T. 2001, ApJ, 553, 837

Iping, R. C., Sonneborn, G., Gull, T. R., Massa, D. L., & Hillier, D. J. 2005, ApJL, 633, L37
Ishibashi, K., Corcoran, M. F., Davidson, K., et al. 1999, ApJ, 524, 983
Kashi, A., & Soker, N. 2009, ApJL, 701, L59
Leyder, J.-C., Walter, R., & Rauw, G. 2008, A&A, 477, L29
Loomis, E. 1869, MNRAS, 29, 298
Madura, T.I., Gull, T.R., Owocki, S.P., Okazaki, A.T., & Russell, C.M.P. 2011, in Proceedings of the 39th Liège Astrophysical Colloquium, eds. G. Rauw, M. De Becker, Y. Nazé, J.-M. Vreux & P.M. Williams, BSRSL 80, 694
Mehner, A., Davidson, K., Humphreys, R. M., et al. 2010, ApJL, 717, L22
Ohm, S., Hinton, J. A., & Domainko, W. 2010, ApJL, 718, L161
Okazaki, A. T., Owocki, S. P., Russell, C. M. P., & Corcoran, M. F. 2008, MNRAS, 388, L39
Payne-Gaposchkin, C. 1957, The Galactic Novae (Amsterdam: North-Holland Pub. Co.)
Pittard, J. M., & Corcoran, M. F. 2002, A&A, 383, 636
Smith, N. 2008, Nature, 455, 201
Tavani, M., Sabatini, S., Pian, E., et al. 2009, ApJL, 698, L142
Whitelock, P. A., Feast, M. W., Koen, C., Roberts, G., & Carter, B. S. 1994, MNRAS, 270, 364
Williams, P.M. 2011, in Proceedings of the 39th Liège Astrophysical Colloquium, eds. G. Rauw, M. De Becker, Y. Nazé, J.-M. Vreux & P.M. Williams, BSRSL 80, 595
Wolf, R. 1863, Astronomische Nachrichten, 60, 59
Zanella, R., Wolf, B., & Stahl, O. 1984, A&A, 137, 79

Discussion

N. Smith: From the near-IR SED, we see that the new dust forming in the wind collision is very hot - about 1700 K. That means it can't be silicates (which form at $\leq$ 1000 K) like the dust in the Homunculus. The hot dust could be carbon-rich, except that we think Eta Car's wind is N-rich and C/O-poor. Thus, the newly forming dust is probably corundum (Al_2O_3) or something similar, which can condense at high temperatures.

D. Gies: Would the general brightening taking place at the current epoch be inconsistent with a decrease in the LBV mass loss rate?
M. Corcoran: Not necessarily. The extinction is decreasing mostly caused by the expansion of the Homunculus.

Multi-wavelength diagnostics of massive binary interaction in Eta Carinae

Jose Groh[1*]

[1]Max-Planck-Institut für Radioastronomie, Auf dem Hügel 69, D-53121 Bonn, Germany

Abstract: Eta Car is generally accepted to be a binary system comprised of two massive stars with a total luminosity of $L_{\rm tot} \geq 5 \times 10^6$ L$_\odot$ and total mass of at least 110 M$_\odot$. Most authors agree on a high eccentricity ($e \sim 0.9$) and an orbital period of 2022.7 ± 1.3 days, but light from the companion star has never been unambiguously observed, causing a large uncertainty in the individual masses and in the other orbital parameters such as the orbital inclination and longitude of periastron. We developed two-dimensional radiative transfer models of Eta Car which account for the presence of the low-density cavity and wind-wind interaction zone created by the rarified, fast wind of the companion, as predicted by hydrodynamical simulations. By comparing synthetic line profiles with available observations, we show that the cavity in the dense wind of the primary star strongly affects multi-wavelength diagnostics such as the ultraviolet spectrum, the optical hydrogen lines, and the shape of the near-infrared continuum region. All these diagnostics have been previously interpreted as requiring a latitude-dependent wind generated by a fast-rotating primary star. Ultimately we found that the presence of the companion hampers the determination of the rotational velocity of the primary.

1 Introduction

Eta Carinae is one of the most luminous objects in the Galaxy, and its study provides crucial constraints on massive stellar evolution under extreme conditions. Extensive monitoring of the optical spectrum of Eta Car showed that the spectroscopic events repeat periodically every 5.54 yr (Damineli 1996). This led to the suggestion that Eta Car is a binary system (Damineli et al. 1997) consisting of two very massive stars, $\eta_{\rm A}$ (primary) and $\eta_{\rm B}$ (secondary), with a total system mass amounting to at least 110 M$_\odot$ (Hillier et al. 2001). The spectroscopic events are related to the periastron passage of $\eta_{\rm B}$, and the binary scenario is supported by numerous multi-wavelength observations as summarized by M. Corcoran (2011). Although most orbital parameters of the Eta Car system are uncertain, the wealth of multi-wavelength observations are consistent with a high eccentricity ($e \sim 0.9$) and an orbital period of 2022.7 ± 1.3 d (Damineli et al. 2008).

1.1 Is $\eta_{\rm A}$ a rapid rotator?

$\eta_{\rm A}$ is an LBV star with a high mass-loss rate of $\dot{M} \simeq 10^{-3}$M$_\odot$yr^{-1} and wind terminal velocity of $v_\infty \simeq 500 - 600$ km s^{-1} (Hillier et al. 2001). Based on the variations of Hα absorption line

*email: jgroh@mpifr.de

profiles in scattered light from the Homunculus, which provide us with different viewing directions to the star, and assuming that the rotation axis of $\eta_{\rm A}$ and the Homunculus axis are aligned, Smith et al. (2003) suggested that $\eta_{\rm A}$ has a latitude-dependent wind, with faster, denser outflow in polar directions. Interferometric measurements obtained with VLTI/VINCI (van Boekel et al. 2003; Kervella 2007) and VLTI/AMBER (Weigelt et al. 2007) in the near-infrared K-band continuum are consistent with an ellipsoidal shape projected on the sky, and were interpreted as evidence for a dense prolate wind generated by fast rotation, as theoretically predicted by Owocki et al. (1996). In Groh et al. (2010a) we employed 2-D radiative transfer models of prolate winds generated by rapid rotation to analyze the interferometric observations and obtained that $\eta_{\rm A}$ is spinning at $\sim 80-90\%$ of its critical velocity for break-up. Interestingly, our 2-D models suggest that the rotation axis of the primary star is not aligned with the Homunculus polar axis.

The results described above ignore any possible effects of $\eta_{\rm B}$ on the wind of $\eta_{\rm A}$. However, recent 3-D numerical simulations show that the wind of $\eta_{\rm B}$ significantly influences the geometry of the very dense wind of $\eta_{\rm A}$ via the creation of a cavity and dense wind-wind collision zone (Pittard & Corcoran 2002; Okazaki et al. 2008; Parkin et al. 2009). Here we discuss the influence of $\eta_{\rm B}$ on the optical spectrum and on the geometry of the K-band emission, which are the key diagnostics supporting the fast rotation of $\eta_{\rm A}$.

2 Radiative transfer model

Our models are based on the spherically symmetric models of $\eta_{\rm A}$ (Hillier et al. 2001, 2006), but use the 2-D code of Busche & Hillier (2005) to study the influence of the low-density cavity, and dense interaction-region walls, on the spectrum. Further details are given in Groh et al. (2010a) and Groh et al. (2011, in preparation), and here we outline only the main characteristics of our implementation.

We approximate the cavity as a conical surface with half-opening angle α and interior density 0.0016 times lower than that of the spherical wind model of $\eta_{\rm A}$. We include cone walls of angular thickness $\delta\alpha$ and, assuming mass conservation, a density contrast in the wall of $f_\alpha = [1 - \cos(\alpha)]/[\sin(\alpha)\delta\alpha]$ (Gull et al. 2009) times higher than the wind density of the spherical model of $\eta_{\rm A}$ at a given radius. The conical shape is justified since the observations we model here were taken at orbital phases sufficiently before periastron, when such a cavity has an approximately 2-D axisymmetric conical form (Okazaki et al. 2008). Based on the expected location of the cone apex during these phases (Cantó et al. 1996; Okazaki et al. 2008), we place the cavity at a distance $d_{\rm apex}$ from the primary star. We assume that the material inside the cavity and along the walls has the same ionization structure as the wind of $\eta_{\rm A}$. Thus, at this point we explicitly neglect the ionization changes that might occur in the wind-wind interacting region. We also do not account for the ionizing flux of $\eta_{\rm B}$. Despite these limitations, our implementation should be adequate for understanding how the line profiles of $\eta_{\rm A}$ are modified by the carving of its wind by $\eta_{\rm B}$.

3 Effects of the companion on the optical spectrum of Eta Car

The optical spectrum of Eta Car has been monitored by the Eta Car HST Treasury Project from 1998 to 2004 (Davidson et al. 2005), encompassing slightly more than one orbital cycle. Assuming a single-star scenario with a spherically-symmetric stellar wind, Hillier et al. (2001) obtained a reasonable fit to the observed optical spectrum obtained right after periastron, at orbital phase $\phi \sim 0.05$. The CMFGEN model spectrum from Hillier et al. (2001) reproduced well the emission line profiles of H, Fe II, and N II lines (Fig. 1), yielding the following stellar parameters: stellar temperature $T_\star$ = 35,310 K

(at Rosseland optical depth $\tau_{\rm Ross} = 150$), effective temperature $T_{\rm eff}$= 9,210 K (at $\tau_{\rm Ross} = 2/3$), luminosity $L_\star = 5 \times 10^6$ L$_\odot$, mass-loss rate $\dot{M} = 10^{-3}$ M$_\odot$yr^{-1}, wind terminal velocity $v_\infty = 500$ km s^{-1}, a clumping volume-filling factor $f = 0.1$, and distance $d = 2.3$ kpc.

However, when compared to observations taken at $\phi \sim 0.05$, the spherically-symmetric CMFGEN model overestimates the amount of P-Cygni absorption. The comparison is even worse as one moves toward apastron, when the observations show little or no P-Cygni absorption components in H and Fe II lines (Fig. 1; see also Nielsen et al. 2007). A possible explanation for absence of P-Cygni absorption in the H lines is that the wind of $\eta_{\rm A}$ is latitude dependent (Hillier et al. 2001; Smith et al. 2003).

Using our 2-D radiative transfer model, which takes into account the cavity in the wind of $\eta_{\rm A}$ caused by $\eta_{\rm B}$, we computed the synthetic optical spectrum of Eta Car at $\phi \sim 0.6$ (Fig. 1). We assumed the same parameters described above for $\eta_{\rm A}$ (Hillier et al. 2001) and a standard geometry of the cavity at apastron as predicted by 3-D hydrodynamical simulations (Okazaki et al. 2008; Parkin et al. 2009): $d_{\rm apex} = 19$ AU, $\alpha = 54°$, $\delta\alpha = 3°$ (i.e., $f_\alpha = 9.7$), $b = 0.0016$. For a viewing angle of $i = 41°$ and longitude of periastron of $\omega = 270°$, the 2-D model produces a much better fit to the P-Cygni absorption line profiles of H and Fe II lines than the 1-D CMFGEN model, while still fitting the emission line profiles. The improved fit to the P-Cygni absorption line profiles yielded by the 2-D model is due to the cavity in the wind of $\eta_{\rm A}$, which reduces the H and Fe II optical depths in the line-of-sight to $\eta_{\rm A}$ when the observer looks down the cavity.

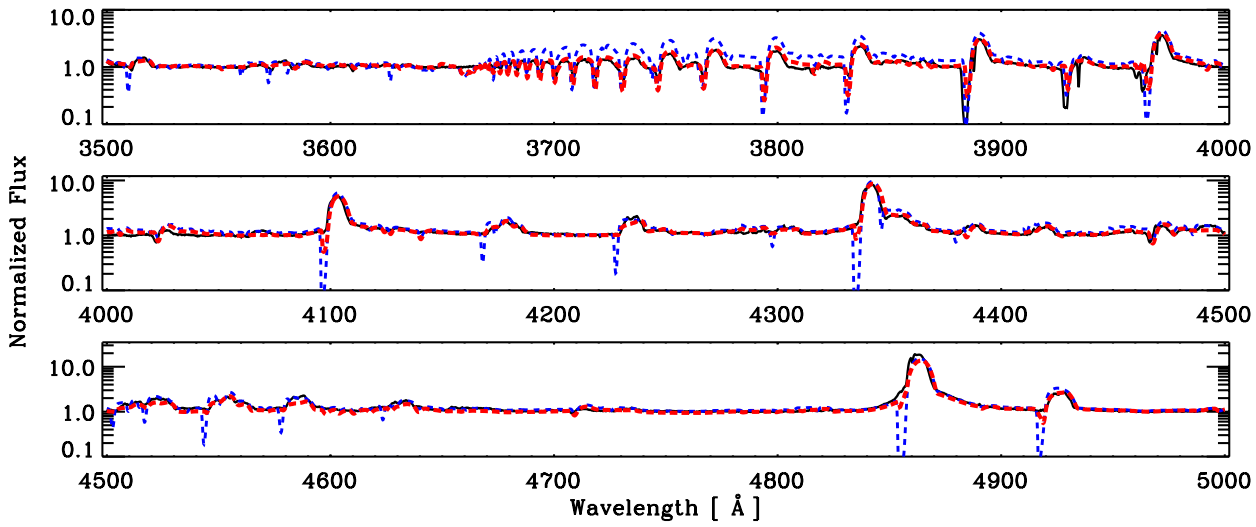

Figure 1: Optical spectrum of $\eta_{\rm A}$ observed with *HST/STIS* at $\phi \sim 0.6$ (solid black line) compared to the spherically-symmetric CMFGEN model from Hillier et al. (2001) (blue dashed line) and with our 2-D model including a cavity and compressed walls created by the wind of $\eta_{\rm B}$ (red dashed line). See text for the model parameters.

4 Effects of the companion on the geometry of the K-band emission

The advent of near-infrared long baseline interferometry has allowed one to spatially resolve the wind of Eta Car using ESO's VLTI/VINCI and VLTI/AMBER instruments (van Boekel et al. 2003; Weigelt et al. 2007). Previously the observations have been interpreted assuming a single-star, latitude-dependent wind generated by rapid rotation. Here we analyze how our 2-D model of the binary

system affects this interpretation. We investigate the influence of $\eta_{\rm B}$ on the inner wind of $\eta_{\rm A}$ through the presence of a low-density cavity and density enhanced wind-wind collision zone, with the goal of determining how these may affect the interpretation of the VLT/VINCI dataset obtained relatively close to periastron. We apply, for the first time for Eta Car, 2-D radiative transfer models with the same parameters as described in Section 3, except for a different orbital phase ($\phi \sim 0.93$).

The amount of influence of the wind-wind interaction on the observables depends on two factors: how close the cavity gets to the K-band emitting region of $\eta_{\rm A}$ ("bore hole effect", Madura & Owocki 2010), and how much free-free radiation is emitted by the dense walls of the shock cone ("wall effect"). According to our models, the main effect from the wind-wind collision zone at the orbital phases analyzed is extended free-free emission from the compressed walls. Such an effect may influence the geometry of the K-band emitting region even at orbital phases far from periastron, depending on the observer's location, geometry of the cavity, i, α, and f_α.

We found that a model with $\alpha = 54°$, $f_\alpha = 9.7$ (i. e., $\delta\alpha = 3°$; Gull et al. 2009), and $i = 41°$ shows significant wall emission and is able to produce a significant elongation of the K-band continuum (Fig. 2). To explain the VLTI/VINCI observations, the symmetry axis of the cavity has to be oriented along PA$\simeq 35° - 45°$ (i.e., SW-NE axis; Fig. 2), which is roughly consistent with that expected from a longitude of periastron of $\omega = 243°$ (e.g., Okazaki et al. 2008; Parkin et al. 2009; Gull et al. 2009, Groh et al. 2010b) and a counterclockwise motion of $\eta_{\rm B}$ on the sky. The $\dot{M}$ of $\eta_{\rm A}$ needs to be slightly reduced to 8×10^{-4} M$_\odot$yr^{-1} to compensate for the extra extension in the K-band emitting region caused by the wall effect.

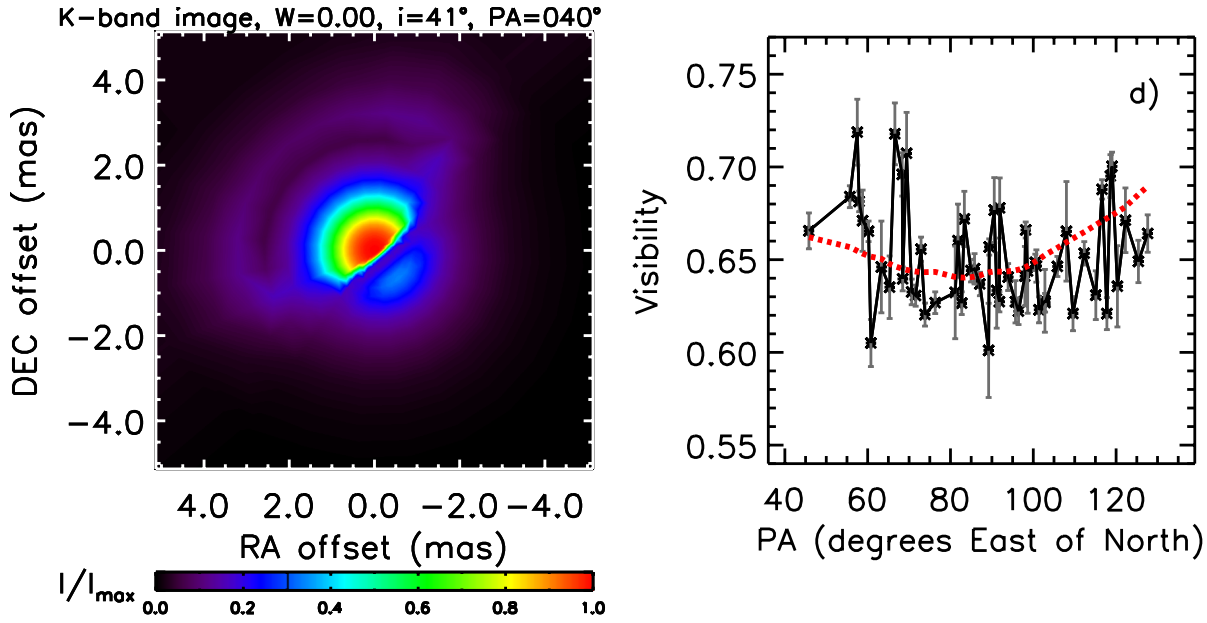

Figure 2: *Left:* Synthetic K-band image predicted by the best-fitting 2-D model of $\eta_{\rm A}$ including a cavity and compressed walls created by the wind of $\eta_{\rm B}$. The model is appropriate for the VINCI observations ($\phi = 0.93$) and assumes $i = 41°$, PA $= 40°$, $d_{\rm apex} = 10$ AU, $\alpha = 54°$, and $\delta\alpha = 3°$. *Right:* Observed VLTI/VINCI visibilities for the 24 m baseline as a function of telescope PA (connected black asterisks) compared to the 2-D cavity model prediction (red dotted line). Note that the projected baseline length of the VINCI measurements changes as a function of PA.

5 Short summary

How much does $\eta_{\rm B}$ affect the H line profiles and the K-band emitting region of $\eta_{\rm A}$, which are the two diagnostics of rapid rotation in $\eta_{\rm A}$? Here we showed that both are *strongly* affected by the presence of $\eta_{\rm B}$, which carves a significant cavity in the wind of $\eta_{\rm A}$. Therefore, an intrinsic latitude-dependent wind produced by fast rotation may not be the only explanation for existing observations, but this does not mean that $\eta_{\rm A}$ is not a rapid rotator. Three-dimensional radiative transfer models will be needed to properly account for both the presence of the cavity and a latitude-dependent wind generated by rapid rotation.

As discussed in Groh et al. (2010a), the presence of the cavity and walls have an effect on the available interferometric observables that is as large as that due to a latitude-dependent wind caused by rapid rotation, although the morphology of the K-band images is noticeably different in the two scenarios. Our 2-D model, in combination with milliarcsecond-resolution images reconstructed from interferometric observations which will be available in the near future, will be the key for probing the effects of the companion and rapid rotation in Eta Car.

Acknowledgements

Many thanks to my collaborators in this project: T. Madura, S. Owocki, J. Hillier, and G. Weigelt. I am grateful to the referee Peredur Williams for the useful comments on the manuscript. I appreciate financial support from the Max-Planck-Society. I would like to congratulate the organizers for putting together a very nice meeting with a fantastic scientific atmosphere. I also appreciate the tasteful prize awarded during the conference dinner, and I think I should thank a *certain* couple of stars for that.

References

Busche, J. R. & Hillier, D. J. 2005, AJ, 129, 454
Cantó, J., Raga, A. C., & Wilkin, F. P. 1996, ApJ, 469, 729
Corcoran, M.F. 2011, in Proceedings of the 39th Liège Astrophysical Colloquium, eds. G. Rauw, M. De Becker, Y. Nazé, J.-M. Vreux & P.M. Williams, BSRSL 80, 578
Damineli, A. 1996, ApJL, 460, L49
Damineli, A., Conti, P. S., & Lopes, D. F. 1997, New Astronomy, 2, 107
Damineli, A., Hillier, D. J., Corcoran, M. F., et al. 2008, MNRAS, 384, 1649
Davidson, K., Martin, J., Humphreys, R. M., et al. 2005, AJ, 129, 900
Groh, J. H., Madura, T. I., Owocki, S. P., Hillier, D. J., & Weigelt, G. 2010a, ApJL, 716, L223
Groh, J. H., Nielsen,K. E. ,Damineli, A., et al. 2010b, A&A, 517, A9
Gull, T. R., Nielsen, K. E., Corcoran, M. F., et al. 2009, MNRAS, 396, 1308
Hillier, D. J., Davidson, K., Ishibashi, K., & Gull, T. 2001, ApJ, 553, 837
Hillier, D. J., Gull, T., Nielsen, K., et al. 2006, ApJ, 642, 1098
Kervella, P. 2007, A&A, 464, 1045
Madura, T. I., & Owocki, S. P. 2010, Rev. Mex. de Astronomia y Astrofisica Conf. Series, 38, 52
Nielsen, K. E., Corcoran, M. F., Gull, T. R., et al. 2007, ApJ, 660, 669
Okazaki, A. T., Owocki, S. P., Russell, C. M. P., & Corcoran, M. F. 2008, MNRAS, 388, L39
Owocki, S. P., Cranmer, S. R., & Gayley, K. G. 1996, ApJL, 472, L115
Parkin, E. R., Pittard, J. M., Corcoran, M. F., Hamaguchi, K., & Stevens, I. R. 2009, MNRAS, 394, 1758
Pittard, J. M. & Corcoran, M. F. 2002, A&A, 383, 636
Smith, N., Davidson, K., Gull, T. R., Ishibashi, K., & Hillier, D. J. 2003, ApJ, 586, 432
van Boekel, R., Kervella, P., Schöller, M., et al. 2003, A&A, 410, L37
Weigelt, G., Kraus, S., Driebe, T., et al. 2007, A&A, 464, 87

Results from the 2009 campaign on WR 140

Peredur Williams

Institute for Astronomy, Royal Observatory, Edinburgh, UK

Abstract: The archetypal Wolf-Rayet + O star colliding-wind binary WR 140 has a very elliptical orbit, so that maximum interaction between the WR and O winds, and the most rapid changes in configuration, occur around periastron passage. To exploit this laboratory for studying wind-collision and high-energy phenomena, several groups mounted campaigns to observe WR 140 intensively around the most recent (2009) periastron passage. These included multi-site optical spectroscopy to refine the radial velocity orbit and study anomalous emission from the shock-compressed wind, infrared spectroscopy to study related features and map the wind-collision region, high-resolution radio imaging of the wind-collision shock, and X-ray observations with *RXTE*, *XMM-Newton*, *Chandra* and *Suzaku* to study physical conditions in the shocks. Some preliminary results from these campaigns will be surveyed and the synergy of multi-wavelength observations considered.

1 Context: A multi-wavelength history of WR 140

The WC7+O5 Wolf-Rayet system WR 140 (HD 193793, BD +43°3571; all three designations are used at different times in the literature but, for simplicity, only the first will be used here despite the anachronisms) is the archetypal WR colliding-wind binary (CWB). It shows anomalously strong X-ray emission, non-thermal radio emission, infrared emission from condensation of carbon dust and conspicuous variation of spectral line profiles. These phenomena all vary round the $P \simeq 8$-year binary orbit, partly because of our changing viewing angle, but mostly because the orbit of WR 140 is very elliptical ($e > 0.88$), so that the interaction of the stellar winds varies hugely as the separation of the stars varies by a factor of ~ 18 round the orbit. The high eccentricity of the orbit may have contributed to the delay in recognition of WR 140 as a binary. On the basis of nine discordant radial velocities (RVs) measured in 1921–22, Plaskett (1924) suggested that WR 140 was a spectroscopic binary but, although many more RVs were measured in subsequent studies over six decades, no RV orbit was found (e.g. McDonald 1947, Conti et al. 1984). It was the observation of a second dust-formation episode in the infrared that allowed Williams et al. (1987) to suggest a period (7.9 y.) for these events and demonstrate that the RVs could be fit with a high-eccentricity orbit having the same period and going through periastron passage shortly before dust formation. This was probably the first, but certainly not the last, instance of multi-wavelength synergy in the study of CWBs. The multi-wavelength infrared photometry continued, and a long-term light curve in L' (3.8μm) is shown in Fig. 1.

Another wavelength region where WR 140 showed unexpected behaviour was in the radio. In 1975, Florkowski & Gottesman (1977) observed radio emission having a spectrum, $S_\nu \propto \nu^{-0.2}$, which differed from that expected from a stellar wind, suggesting variable mass loss. The emission

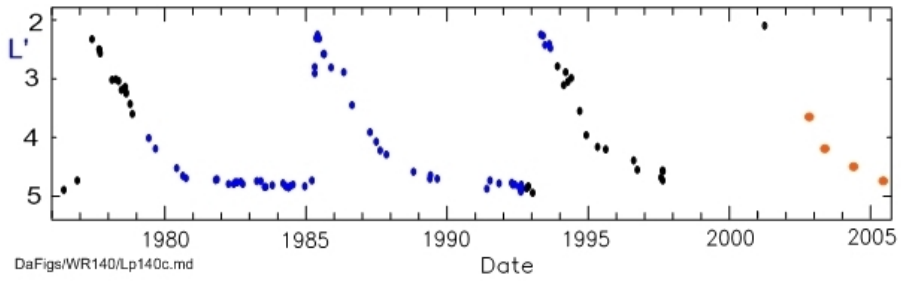

Figure 1: Long-term light curve of WR 140 in L' (3.8 μm) from photometers on UKIRT (blue points), the IRFC/TCS and other telescopes (black), or derived from images (orange). The maxima occur immediately after the 1977, 1985, 1993 and 2001 periastron passages.

was observed to fade significantly at the time of the 1977 dust-formation episode (Florkowski 1982). Fortunately, the unresolved radio emission from WR 140 allowed its position to be measured precisely, so that it was one of 20 stars observed in a programme to link the radio and optical reference frames – and observations in 1982–83 (Florkowski et al. 1985) showed the emission brightening again, ensuring further observations.

The link between these unexpected phenomena observed from WR 140 and the effects of colliding stellar winds was provided by the X-ray emission. The significance of colliding winds in massive binaries can be said to date from the recognition (e.g. Prilutskii & Usov 1976) that collision of a WR stellar wind with that from a companion OB star could be a significantly stronger source of X-rays than collision of the WR wind with the OB star itself. The WC7 and O5 winds of WR 140 are fast, v_∞ = 2860 and 3100 km^{-1}, and carry $\sim 2 \times 10^{-5}$ and $\sim 2 \times 10^{-6} M_\odot$ y^{-1} mass-loss respectively, giving them kinetic powers ($0.5 \dot{M} v_\infty^2$) in excess of 10^4 and $10^3 L_\odot$. Of this power, $\sim 3 \times 10^3 L_\odot$ is dissipated where the winds collide, leading to shock-heating of the plasma to $T_{ion} > 10^7$ K and thermal X-ray emission. The first X-ray observation of WR 140 (Pollock 1987a, with *EXOSAT*) showed it to be exceptionally luminous in X-rays; while a survey of the WR stars observed with *Einstein* showed that the WR+O binaries were generally more luminous in X-rays than single WR stars (Pollock 1987b).

These several strands were pulled together in the multi-frequency study by Williams et al. (1990), who modelled the infrared variations in terms of the formation and dissipation of circumstellar dust and derived a high-eccentricity (e = 0.84$\pm$0.04) orbit for WR 140 adopting the period (2900 d.) from the dust-formation episodes. They developed simple models for the radio and X-ray variations in terms of the varying circumstellar extinction through the WC7 or O5 stellar winds to the wind-collision region (WCR) as the orbit progressed.

The phenomena shown by WR 140 were soon examined in terms of colliding wind theory. Usov (1991) showed that part of the WC7 stellar wind entering the wind-collision shock between the stars could cool very efficiently, and reach a density $\simeq 10^3$ times its pre-shock value, providing cool, dense material within which dust could condense. Usov (1992) developed analytical models of the colliding winds and X-ray emission of massive binaries, and showed that the observed X-ray luminosity of WR 140 was consistent with the parameters of its winds. Non-thermal radio emission from colliding-wind binaries, and WR 140 in particular, was modelled by Eichler & Usov (1993). Stevens, Blondin & Pollock (1992) also developed models of colliding winds, drawing attention to the ratio, χ, of the cooling to escape times of the shocked gas, which determined whether the shocks were adiabatic or isothermal. When cooling is significant, thermal instabilities in the WCR become important. On account of the separation of the stars in WR 140, the post-shock regions of its winds were considered to be close to adiabatic throughout the orbit. Under these conditions, the geometry is scale-free and X-ray luminosity should vary as $1/D$, where D is the separation of the stars.

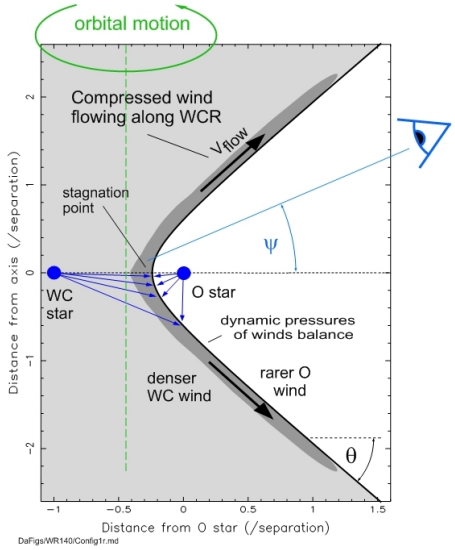

Figure 2: A slice through the WCR perpendicular to the orbital plane; the stars and WCR rotate about the vertical axis.

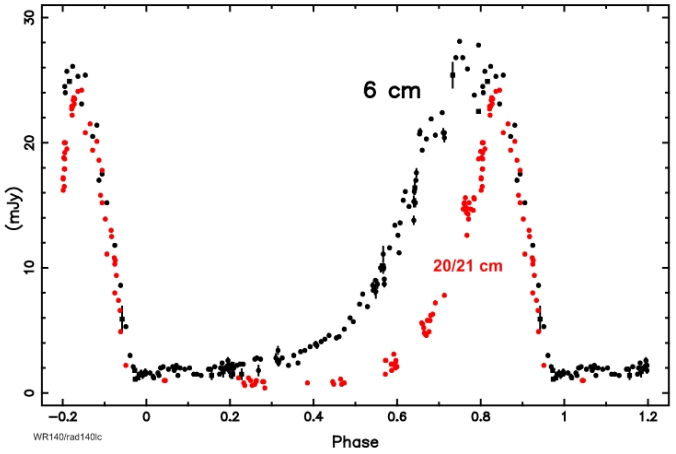

Figure 3: Phased 6-cm and 20/21-cm flux densities showing maxima well before O5 star conjunction (ϕ = 0.95).

Theoretical work on colliding winds is becoming ever more sophisticated, as described by Pittard (2011), so a very simple model will be used here for illustration. The WCR (Fig. 2) lies where the dynamic pressures of the WC7 and O5 stellar winds balance. Its shape can be calculated from the ratio of the momenta of the two stellar winds, $\eta = (\dot{M}v_\infty)_{O5}/(\dot{M}v_\infty)_{WC7}$, which does not change round the orbit if the winds collide at their terminal velocities. The WCR is closer to the O5 star because its mass-loss rate and wind momentum are much lower than that of the WC star. At large distances from the stars, the WCR can be approximated by a cone (opening angle θ) symmetric about the axis. This is twisted to form a spiral in the orbital plane by the motion of the stars in their orbit. The pitch angle of the spiral depends on the ratio of the transverse velocity of the stars in their orbit relative to stellar wind velocities. Given the fast winds and long period of WR 140, this ratio is small but it does vary significantly (factor > 15) near periastron, so the breadth of the spiral varies hugely round the orbit — like a badly filled sausage.

The WC7 and O5 stellar winds are shocked on each side of the WCR in regions which are wide if the shocks are adiabatic but thin and distorted by instabilities (not shown in Fig. 2) if the shocks are radiative. These shocks compress the winds, which flow along the WCR (only that of the WC7 star is shown in the figure). The compressed winds accelerate from the stagnation point on the axis (the line of centres) between the stars to reach an asymptotic value, V_{flow}, on the 'conical' region of the WCR, which can be calculated from the stellar winds following Cantó, Raga & Wilkin (1996). It is within the compressed, carbon-rich WC7 stellar wind that the dust is believed to condense, sufficiently down-wind to escape immediate destruction by the harsh stellar radiation. The orbital motion spreads it around in a plume whose dimensions depend on θ and the angular movement of the WCR during dust formation. On the other hand, the X-ray emission is more likely to arise near the stagnation point, where the winds collide head-on and the post-shock temperature is highest. A goal of the observing campaigns is to use the variations to locate the different sources of emission in the WCR.

The rotation of the WCR with the stars causes our viewing angle, ψ, to vary with phase, modulating the extinction to the stars and WCR and also the observed RV of compressed wind flowing in the WCR. The angle ψ is related to the true anomaly, f, of the stars in the orbit via $\cos\psi = -\sin i \sin(f + \omega)$, where i is the orbital inclination and ω the argument of periastron. If i is not known, it can in principle be determined from the variations of ψ inferred from motion of the com-

pressed wind or varying extinction and a model for the WCR — but if we want to use the observations to study the WCR, we need an independent determination of the inclination.

The brightness of WR 140 ensured its observation with most X-ray missions: twice with *Ginga* (Koyama et al. 1990), five times with *ROSAT* before the 1993 periastron, twice with *ASCA* after the 1993 periastron, and six further observations with *ASCA* between the 1997 apastron and the radio maximum in 1999 (Koyama et al. 1994, Zhekov & Skinner 2000, Pollock, Corcoran & Stevens 2002). Like the *EXOSAT* spectra taken immediately after the 1985 periastron, the two *ASCA* spectra taken immediately after the 1993 periastron showed strong circumstellar absorption. The X-ray spectra could be reproduced with CWB shock models and reasonable wind parameters. The observations covered a sufficiently wide range of orbital phase and stellar separation, D, that it was possible to test the $1/D$-dependence of the X-ray flux expected from adiabatic shocks. Both Zhekov & Skinner and Pollock et al. (2002) found that the flux levels of the 1993 spectra taken near periastron were lower than expected than from the $1/D$-dependence and those of the other spectra, and proposed changes to the RV orbital elements – proposals not supported by existing or subsequent (Marchenko et al. 2003, hereafter MM03) orbital analyses. For the 2001 periastron passage, Pollock et al. (2005) secured *Chandra* spectra at ϕ = 0.99, near X-ray maximum, and ϕ = 0.03, when the flux had recovered to about half its maximum after the deep minimum near conjunction, when the WCR was observed through the densest region of the WC7 stellar wind. The flux level itself was monitored with weekly observations with *RXTE*, which showed a well defined minimum at 2001.13. The velocity widths and shifts of the spectral lines measured in the high-resolution *Chandra* spectra indicated where in the WCR they were formed and the relevant ions located. The ϕ = 0.99 spectrum showed blue-shifted motion of $\sim$ 600 km s^{-1}, while the ϕ = 0.03 spectrum showed red-shifted motion of $\sim$ 400 km s^{-1}, consistent with their formation in the accelerating wind region of the WCR (Fig. 2) and its rotation with the orbital motion.

The early radio observations were extended with WSRT observations of the 1991–92 radio maximum at 6 cm and 21 cm (Williams, van der Hucht & Spoelstra 1994) and VLA observations by White & Becker (1995) at monthly intervals around the whole orbit at 2 cm and 6 cm, together with observations at 20 cm for two years near maximum. The full light curves (Fig 3) showed that the radio maximum occured much earlier ($\phi \simeq 0.8$) than conjunction ($\phi \simeq 0.95$), when the non-thermal source was viewed through the lower-density O5 stellar wind, requiring abandonment of the simple model. White & Becker developed a new model in which the wind of the WC7 star was mostly flattened into a disk inclined to the orbital plane, and this extinguished the non-thermal radio flux until the O5 star and wind-collision region (WCR) passed through it in the observer's direction. The intrinsic non-thermal emission depended on the distance from the disk, and passage through the disk near phase 0.7 accounted for the maximum intrinsic emission at that phase. This model was criticised by Pollock et al. (2002) on the basis of the X-ray observations. Also, Marchenko et al. (2003) modelled the polarization from the flattened WC7 stellar wind and showed it to be higher than the upper limits observed, unless the orientation was very contrived. *The radio flux variations remain to be explained.*

In the ultraviolet, Setia Gunawan et al. (2001) used *IUE* SWP spectra to determine the orbit of the O5 star, also adopting the 2900-d dust-formation period, and derived an eccentricity (e = 0.87$\pm$0.05) close to that (e = 0.84) found in the optical. The profiles of the UV resonance lines varied with phase as the sight lines to the two stars passed through different regions of the winds. In particular, absorption at velocities up to 400 km s^{-1} higher than v_∞ were observed near periastron, possibly due to observation through a turbulent region of the wind or the WCR. These results should be re-examined using the latest RV orbital elements to help determine the location of the high-velocity absorption.

For their determination of the RV orbit, MM03 observed over 100 new spectra of WR 140. They derived the first RV period, 2899 d., in good agreement with the dust-formation period (2900 d.), and

a higher eccentricity (e = 0.881) than previous solutions. They observed the appearance of sub-peaks on the low-excitation 5696-Å C III and 5876-Å He I emission lines near periastron ($\phi \sim 0.995$–1.015), similar to those shown by shorter period WR+O systems with circular orbits like WR 79 (Lührs 1997). The sub-peaks were blue-shifted before periastron and red-shifted afterwards, consistent with formation in the compressed He- and C-rich WR stellar wind flowing at V_{flow} in the WCR, and its rotation with the stars in their orbit (Fig. 2). MM03 used these variations and a Lührs model of the WCR to determine V_{flow} and i. The flux in the sub-peak varied rapidly with phase, and more steeply with stellar separation than the $1/D$-dependence expected from optically thin emission from shocked gas in an adiabatic WCR. This led MM03 to suggest that the shock conditions switched from abiabatic to radiative for a short time around periastron.

A stronger sub-peak was observed on the flat-topped emission profile of the 1.083-μm He I line between phases 0.96 and 1.019 (Varricatt, Williams & Ashok 2004). This also moved from the blue to the red part of the profile as WR 140 went through periastron and the RVs were consistent with a Lührs model with V_{flow} calculated from the stellar winds following Cantó et al. (1996). Varicatt et al. measured the radiative fluxes in the sub-peak to be $\sim 10^{-13}$ Wm^{-2} near periastron, and pointed out that this was a significant coolant, exceeding the X-ray fluxes, $\sim 2.5 \times 10^{-14}$ Wm^{-2} observed with *EXOSAT* (2–6 keV) and *ASCA* (1–10 keV) shortly after the 1985 and 1993 periastron passages, and supported the departure from adiabatic conditions near periastron.

The most recent radio and infrared observations have been direct imaging of the non-thermal radio emission and circumstellar dust.

Dougherty et al. (2005) imaged the non-thermal radio emission during ϕ = 0.74–0.95 with the VLBA, observing a bow-shaped ridge of emission identified with non-thermal emission from the WCR. This was observed to rotate clockwise on the sky. The axis of symmetry was taken to represent the axis of the WCR projected on the sky, with the open end of the bow giving the position angle (P.A.) of the O5 star relative to the WC7 star. From this motion, the RV orbit from MM03 and the P.A. of the stars observed by Monnier et al. (2004) at ϕ = 0.297, Dougherty et al. derived the orbital inclination, i = 122°, and longitude of ascending node, Ω = 353°, thereby completing the definition of the orbit in three dimensions. They also used the stellar separation measured by Monnier et al. and the orbital parameters to derive a distance of 1.85 kpc to WR 140.

The dust emission from WR 140 was first imaged in 2001 (ϕ = 0.039 and 0.055) by Monnier, Tuthill & Danchi (2002) with the Keck telescope. More images were observed between 2001 and 2005 (ϕ = 0.06–0.56) in a multi-site campaign by Williams et al. (2009) at wavelengths between 2.2 μm and 12.5 μm; as the dust cooled, it was necessary to observe it at longer wavelengths. The dust features were observed to expand at constant rates. Extrapolation back to the star gave 'start' times very close to the 2001 periastron. The deepest long-wavelength images showed faint dust features at the same position angles as the brightest dust features from the 2001 dust, but at greater distances, consistent with their formation during the 1993 periastron and subsequent movement with constant proper motion. Relation of the dust maps to the projected orbit is difficult. After deriving the complete orbit, Dougherty et al. (2005) noted that the O5 star and base of the WCR were NW of the WC7 star at the time of periastron, and commented on the paucity of dust in that direction. Owing to the high orbital eccentricity, however, the position angle of the WCR changes very rapidly around periastron passage (e.g. the P.A. of the O5 star relative to the WC star moves through *three-quarters* of its orbit in only 0.04P), accounting for the spreading of the dust around much of the orbit despite the short duration of dust formation — nucleation occurred for only $\simeq$ 0.025 P. The detailed comparison of the dust images, photometry and orbit give information on the azimuthal distribution (leading *vs.* following edge in the orbital plane) of matter in the WCR (Williams et al. 2009), but need re-examination with the new orbital parameters derived in the Campaign.

Table 1: Critical orbital phases and their dates in 2008–2009.

Phenomenon	Phase	JD	Date
Conjunction: O5 star in front	0.956	245 4719	2008 Sep 9
Quadrature	0.996	245 4834	2009 Jan 2
Periastron	0.000	245 4846	2009 Jan 14
Conjunction: WC7 star in front	0.003	245 4855	2009 Jan 23
Quadrature	0.038	245 4956	2009 May 4

1.1 The need for an intensive observing campaign

These different studies drew on and illustrated the value of WR 140 as a laboratory of wind-collision phenomena. Many other systems show one or more of the trademark wind-collision effects: X-rays, non-thermal radio emission or dust formation. These include well known systems such as WR 19, WR 125, WR 137, WR 146 and WR 147 and newly discovered WR stars in massive, obscured clusters. The presence of one or more of these observable effects in some systems has led to their consideration as CWBs (e.g. the WR stars in Westerlund 1 proposed as binaries from their X-ray emission by Skinner et al. 2006). These systems are fainter and more difficult to observe than WR 140, which is the prime target for detailed observations of wind-collision effects at all wavelengths. Another advantage of WR 140 is its proximity, which has allowed the orbit to be determined in three dimensions and the distribution of dust to be compared directly with the orbit.

Generally, the wind-collision effects show maximum activity around the time of periastron when the stars are closest and the pre-collision density of the stellar winds is greatest. At the same time and shortly afterwards, between periastron and conjunction (critical phases are given in Table 1), the circumstellar extinction to the WCR is greatest because of the orientation of the orbit. Accurate knowledge of the configuration at the time of an observation, whether for planning or interpreting an existing observation, is always important but especially in WR 140 around periastron, because the configuration changes so quickly. The eccentricity is so high that a small uncertainty in the orbit can make a significant difference to the stellar configuration on a particular date.

In preparation for the 2009 periastron, a number overlapping groups prepared observing campaigns. The goals can be divided into three categories, although the division between the second and third is artificial and should vanish as more sophisticated models are developed:

- Refinement of the orbit
- Determination of the geometry of the WCR
- Determination of physical conditions in the WCR

To tackle the problem of rapidly changing configurations, intensive observations, often daily, were sought to capture rapid changes in observable wind-collision phenomena. First results were reported at a workshop[1] held at Convento da Arrábida in 2010 May-June

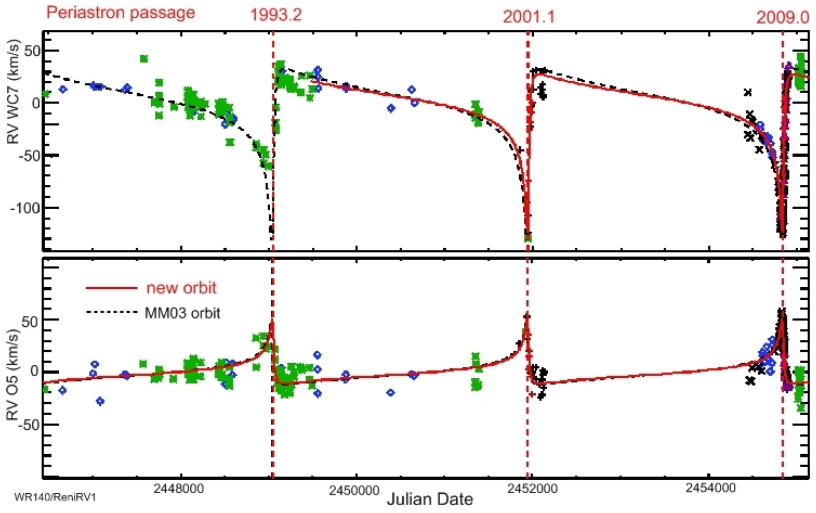

Figure 4: Three orbital cycles of RV observations showing critical requirement for intensive coverage of periastron passage and its achievement in the 2009 Campaign (adapted from Fahed et al. 2011)

2 Refinement of the Orbit

2.1 Radial velocity orbit

The first determinations of the RV orbit of WR 140 used available observations, and the study by MM03 included many more observations to provide good coverage around the orbit, but it was evident from the RV curves (Fig. 4) that the periastron passage required more intensive observations. Accordingly, Tony Moffat and Thomas Eversberg organized an observing campaign drawing on professional and amateurs. The advantage of the multi-site nature of the campaign was demonstrated when spectra were observed at the Three Hills Observatory in Cumbria (a relatively wet part of England), while poor weather was preventing observations at the usually better site on Tenerife. All the data were reduced in a consistent way and a new orbit derived by Fahed et al. (2011). The new orbital elements (Table 2) differ from those derived by MM03 in having a slightly shorter period, higher eccentricity, lower K_{WC}, and smaller uncertainties on all elements. The change in e looks small, but it makes a significant difference to the configuration near periastron, e.g. a change of 9° to the true anomaly at ϕ = 0.01. This feeds through to comparable changes in the viewing angle, ψ, and the projected position angle of the stars at critical phases, significantly affecting the interpretation of observations. For dates near 2009, the changes in P and T_0 work in opposite senses, so phases are smaller by less than 0.001 for a given date, but the differences are greater for earlier observations. The RV orbital parameters underpin the interpretation of all the other observations.

2.2 Astrometric orbit from radio images

Dougherty, Trenton & Beasley (2011) continued the VLBA imaging of the radio emission from WR 140, extending the phase coverage to ϕ = 0.43–0.96. Two of the new 8.4-GHz images are shown in Figs 5 and 6. They show the bow-shaped emission consistent with a source in the curved region of the WCR, and comparison of the two shows both proper motion of the WR 140 system and rotation of the emission, taken to be rotation of the axis of the WCR projected on the sky. As before, Dougherty et al. used the P.A. of the stars observed at ϕ = 0.297 by Monnier et al. (2004) together with the

[1] http://astrosurf.com/joseribeiro/e_arrabida.htm

Table 2: The RV orbital elements of WR 140

	Fahed et al. (2011)	MM03
Period (d)	2896.52±0.70	2899.0±1.3
eccentricity	0.8962±0.0015	0.881±0.005
T_0 (JD)	2446156.2±2.2	2446147.4±3.7
ω (°)	44.6±1.1	46.7±1.6
K_{O5} (km/s)	-30.87±0.58	-30.5±1.9
K_{WC} (km/s)	75.48±0.73	82.0±2.3

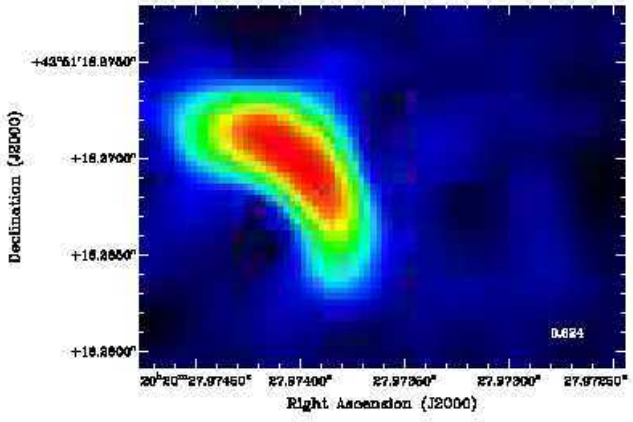

Figure 5: VLBA image of WR 140 observed at ϕ = 0.62 from Dougherty et al. 2011

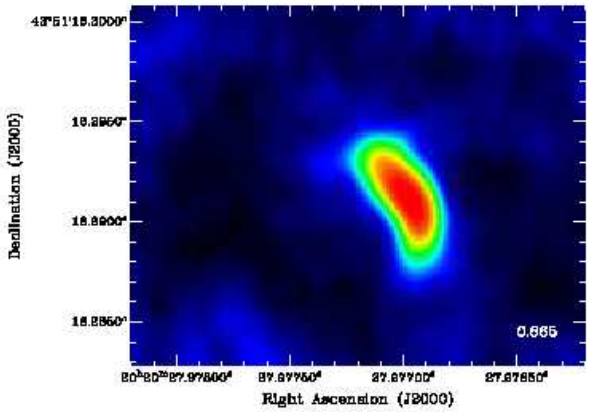

Figure 6: VLBA image observed at ϕ = 0.87

P.A.s measured from the axes of symmetry of the bow-shaped sources to determine the inclination, i = 120°, and longitude of ascending node, Ω = 352°. Comparison with the separation observed by Monnier et al. with the parameters allowed refinement of the distance to 1.81 kpc.

These results are close to those found previously, and still depend on the single interferometric observation of the stars by Monnier et al. (2004). Further such observations, which have been taken, will strengthen the results. Direct comparison of the stellar position angles with the radio images will provide a valuable test of the location of the non-thermal radio emission in the WCR, including examination of its symmetry about the axis (e.g. leading *vs* following edges) in the orbital plane.

With the geometric distance, extinction $A_V = 2.9$ (Morris et al. 1993), equivalent to $A_v = 3.2$, and the O5 star 0.6 mag. brighter than the WC7 star in this wavelength region (van der Hucht 2001), we have $M_v(O5) = -6.9$ and $M_v(WC7) = -6.3$. The luminosity and radius of the O5 star can be determined by fitting $M_v(O5)$ with the 5160-Å flux from a 35-kK WM-Basic model appropriate to an O5 star (Smith, Norris & Crowther 2002), which gives $R(O5) \simeq 35\ R_\odot$ and log ($L/L_\odot$) = 6.20. Fitting the flux from the WC7 star to a 70-kK CMFGEN model flux (Smith et al.) gives log ($L/L_\odot$) = 5.73. The luminosity of the O5 star is very close to that adopted by Pittard & Dougherty (2006) but that of the WC7 star is greater by 0.23 dex. Both are rather luminous for their spectral types (cf. Repolust, Puls & Herrero 2004 and van der Hucht 2001 respectively), suggesting that the O5 star is a supergiant, and strengthening the view that the WC7 component is an unusual WC7 star. The complete orbit has a = 12.6 AU and D ranging from 1.3 AU at periastron to 23.9 AU at apastron. Colliding wind theory gives the distance, r_{O5}, of the WCR from the O5 star in terms of the wind-momentum ratio, η: $r_{O5} = \sqrt{\eta}/(1+\sqrt{\eta})D$. For η = 0.1, this gives $r_{O5} \simeq 0.24D$ which, at periastron, is only 2.2 $R(O5)$, probably too close to allow the O5 wind to have accelerated to its terminal velocity

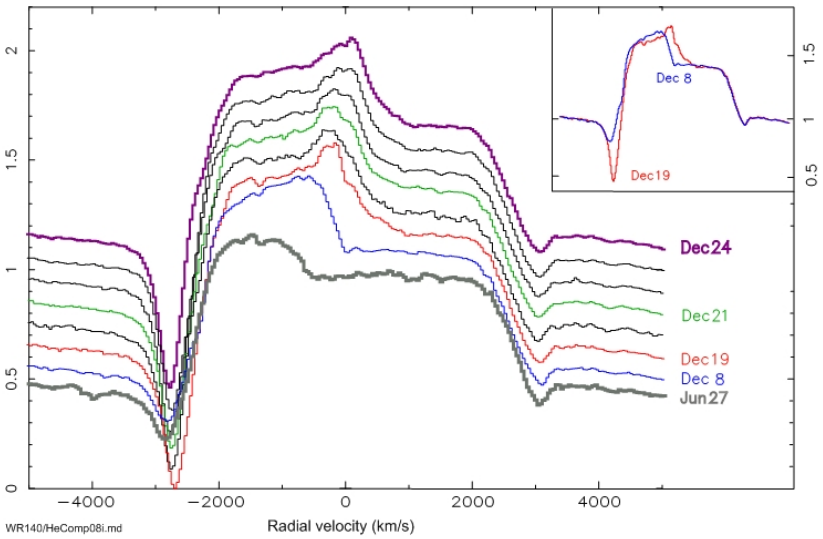

Figure 7: Profiles of 1.083-μm line on 2008 Jun 27, Dec 8 and nightly Dec 19–24. Inset: Dec 8 and 19 spectra overplotted to show abrupt change of absorption component between these dates.

before reaching the WCR, making for a smaller WCR located even closer to the O5 star.

In reply to the question "Are we there yet?" regarding the orbit, we can answer that we are very close to having a secure orbit with all parameters — which could be nailed down with an astrometric orbit from interferometric measures of the stars.

3 Geometry of the Wind-collision region

3.1 The absorption component of the 1.083-μm He I line profile

Whatever the detailed structure of the WCR, it separates two stellar winds of different chemical composition and very different density, providing a significant contrast in absorption, especially of He and C features. Varricatt et al. (2004) used the variation of the absorption component of the 1.083-μm He I profile with orbital phase to constrain the opening angle, θ of the WCR 'cone' as a function of inclination.

For the Campaign, Varricatt, Adamson and Williams extended this work with further observations of the 1.083-μm line. The new observations were taken during 2008 with UIST on the United Kingdom Infrared Telescope (UKIRT) at a resolution of 200 km s^{-1} and comprise five spectra extending the coverage to earlier phases (ϕ = 0.93–0.95) than Varricatt et al. and nine spectra, some at daily intervals, near ϕ = 0.99, when the configuration of the binary was changing very rapidly. A selection of line profiles is presented in Fig. 7 to show the difference between that near conjunction (June; spectra observed in July and August were very similar) and during December shortly before periastron, when the profile was changing rapidly.

The strength of the 1.083-μm absorption varies significantly (Figs 7 and 8), and most of the absorption must arise in the WC7 stellar wind. The underlying continuum comes from both the WC7 and O5 stars. The WC7 star is always seen through at least some of the WC7 wind (cf. Figs 2 and 9), the densest region near the star. It is also expected to be fainter than the O5 star in the one-micron region, so most of the variation observed in the 1.083-μm line absorption component must come from the variation in absorption to the O5 star. When the viewing angle, ψ, is small, the O5 star is seen through its own wind only, which has one-tenth the density of the WC7 wind and a significantly lower

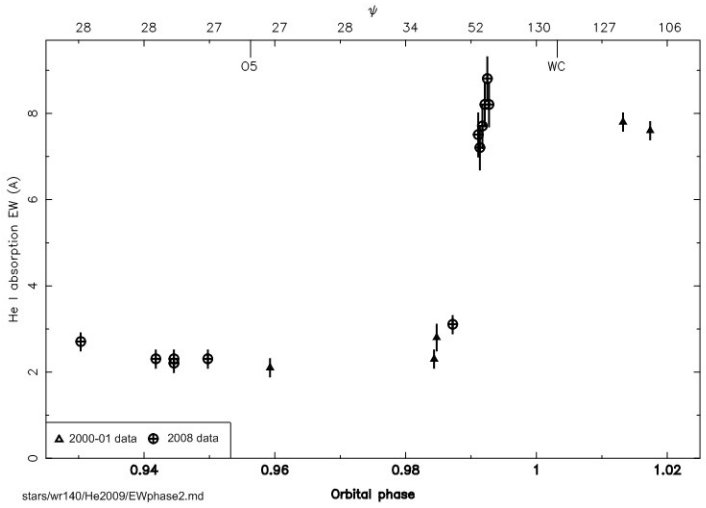

Figure 8: EW of absorption component as a function of phase near periastron. On top are the viewing angle, ψ, and phases of conjunction, 'O5' and 'WC', in front.

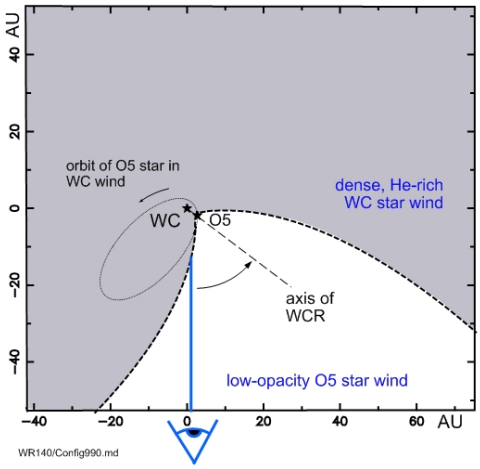

Figure 9: Sketch of the system in the plane of the orbit for the beginning of the WC7 wind 'eclipse' at $\phi = 0.99$.

helium abundance, so the absorption is at its lowest. This can be seen in Fig. 8, where the absorption is least near conjunction (O5 star in front) and barely changes while we observe the O5 star through its own wind between the first observation and $\phi = 0.985$, when it suddenly rises sharply. This must be the phase at which the following edge of the WCR crosses our sightline to the O5 star (Fig. 9). At this phase, the viewing angle, ψ, approaches the WCR cone angle θ, and we begin to observe the O5 star through the more opaque WC7 stellar wind. Modelling the sharp increase of absorption ('eclipse') must account for the twisting of the WCR from the orbital motion, but we have a measure of the opening angle: $\theta \simeq 40°$ using the new orbital elements from Fahed et al. (2011), and i from Dougherty et al. (2011). This is 10° smaller than the value derived using the MM03 RV orbit and a stark illustration of the sensitivity of the configuration to the orbital elements. It implies a smaller value of the wind-momentum ratio, $\eta = 0.05$, locating the WCR closer to the O5 star.

3.2 Observations of the He I and C III line profiles

The sub-peaks observed on the 1.083-μm He I (Fig. 7) and optical He I and C III line profiles (Fahed et al.) are believed to form in the compressed He- and C-rich WC stellar wind flowing in the WCR (MM03). The two datasets are complementary: the infrared observations cover a greater phase range (ϕ = 0.93–1.019) than the optical (ϕ = 0.99–1.015), and the sub-peaks are stronger; but the optical spectra were observed more frequently and cover crucial phases at periastron. The IR spectra were not observed often enough to pinpoint the phases at which the emission started (it was not present at $\phi = 0.86$) and stopped (it had vanished by $\phi = 0.29$). Fahed et al. confirmed and strengthened the result from MM03 that the flux in the 5696-Å C III subpeak varied more steeply than $\propto 1/D$ near periastron.

Detailed comparison of the profiles of the 1.083-μm and 5696-Å lines observed on the same dates will test whether the subpeaks are formed in the same region of the WCR. If they are, we will have relatively straightforward information on the geometry of the WCR; but if it is evident that they form in different regions, we will need models of the conditions including emissivity in the lines to identify where in the WCR they form.

In both cases, following the earlier studies by MM03 and Varricatt et al., the variations of the RVs and widths of the sub-peaks with phase were examined using the Lührs model. In this model, all the

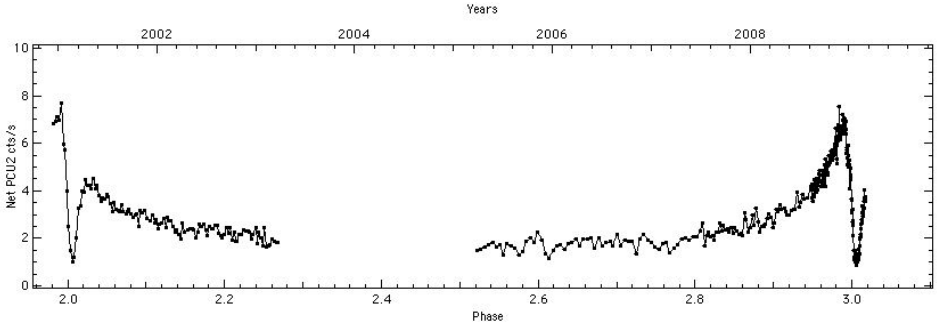

Figure 10: *RXTE* 2–10-keV count rate from WR 140 as a function of date and phase (Corcoran).

sub-peak emission arises in the 'conical' section of the WCR defined by the opening angle θ, and flows with constant V_{flow}. The twisting of the WCR from orbital motion is described with a third constant ($\delta\phi$), the deviation of the axis of the WCR from the line of centres of the stars. This has the virtue that it is not necessary to know the distribution of emissivity along the WCR, either radially or azimuthally around the cone: the RV and width of the sub-peak can be derived using simple analytic relations from the orbit and the model constants. The observed variations in the RVs and widths of the 1.083-μm and 5696-Å lines were recovered, supporting their formation in the rotating WCR, but proper account has still to be taken of twisting of the WCR from orbital motion. As noted above, this depends on the ratio of the tranverse velocity of the WCR to the wind velocity, which in WR 140 is small but varies significantly near periastron. The complex line profiles (Fig. 7 and Fahed et al. 2011) are not fully described by RV and line width, and require to be modelled. To date, this has not been successful with reasonable geometric parameters, and it will be necessary to consider formation over a greater range of the WCR including a ranges of angles, flow velocities and spatial variation of emissivity. The spectral sub-peaks have the promise of being a powerful diagnostic, bridging the gap between geometry and physical conditions in the WCR, especially where they can be compared with the profiles of lines observed in high-resolution X-ray spectra at the same phases.

4 Physical conditions in the WCR

4.1 Intensive X-ray monitoring with *RXTE*

For the Campaign, Corcoran et al. extended the *RXTE* Proportional Counter Array (PCA) observation set by resuming bi-weekly observations from 2005.2 (near apastron), increasing the frequency to daily from ϕ = 0.94 to cover the periastron. The flux curve from PCU2 is shown in Fig. 10. Matching of the two minima gives a period of 2897 d., in excellent agreement with the new RV period (Fahed et al. 2011). Comparison with a $1/D$-variation shows the flux falling below it between phases $\simeq$ 0.93 and 1.07. The hardness ratio was found to be constant, implying the same value of kT ($\simeq$3–4 keV) and collision at the same, presumably terminal velocities until near conjunction, when, from ϕ = 0.99, the hardness ratio rose owing to rising extinction through the WC stellar wind. Detailed examination of the flux minimum shows that it is not wholly caused by circumstellar extinction: the *intrinsic* flux fades to a minimum near $\phi \simeq$ 1.003–1.008. The reduced emissivity could be caused by another source of cooling or weakening of the wind collision, but the continued emission in the 5696-Å C III sub-peak through periastron (Fahed et al. 2011) argues against failure of the wind collision. Occultation is also possible as the minimum occurs near conjunction (Table 1), but probably not by the WC7 star itself given the orbital inclination.

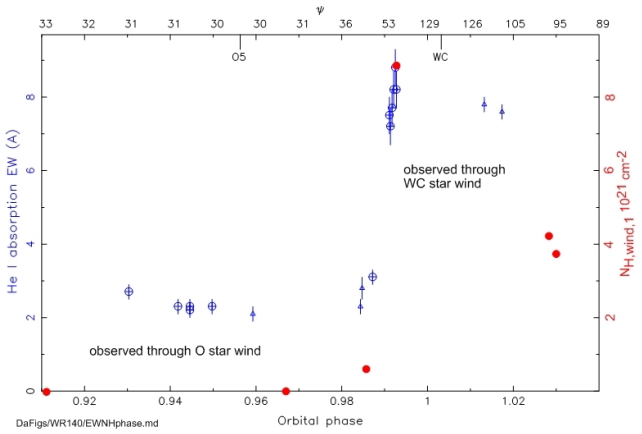

Figure 11: Comparison of onset of 1.083-μm (blue $\oplus$, $\triangle$) and X-ray (red $\bullet$, *XMM-Newton* EPIC spectra) absorption in the WC7 wind.

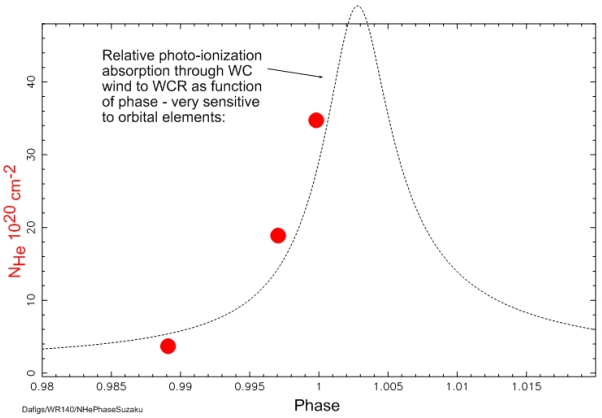

Figure 12: Inner wind extinction probed by *SUZAKU* compared with model.

4.2 X-ray spectroscopy using *Suzaku*, *XMM-Newton* and *Chandra*.

De Becker et al. (2011) used *XMM-Newton* to observe four spectra before periastron (ϕ = 0.91–0.99) and two afterwards (ϕ = 1.029–1.031). The 0.3–10-keV EPIC spectra were fitted with three-component (T $\sim$ 5, 15, and 50 MK) thermal models giving normalisation parameters and wind extinctions for each. The normalisation parameter of the first component does not fit the $1/D$-dependence, e.g. rising by 5% in ϕ = 0.987–0.994 while $1/D$ rises by 60%. The extinction to this component, $N_{H,wind,1}$, shows a rapid increase near ϕ = 0.99 as the sightline to the X-ray source moved from the O5 stellar wind to the WC7 wind. Fig. 11 shows $N_{H,wind,1}$ plotted against phase, alongside the 1.083-μm absorption equivalent widths. The similarity of the 'eclipses' of the X-ray source and O5 star suggests that the X-ray source is not greatly extended. The relative values of $N_{H,wind,1}$ in the last three spectra are well fit with the absorbing column densities calculated following Williams et al. (1990) and the modern orbit (De Becker et al. 2011). The RGS spectra observed when the absorption was lower are dominated by Ne X Lyα and the spectra are still being analysed e.g. the *fir* ratios in the Ne IX triplet.

Sugawara et al. (2010, 2011) observed four spectra with *Suzaku* XIS and HXD-PIN at phases ϕ = 0.90–1.00, giving an unprecendented view of the system at periastron. The dominant X-ray component could be fit with a $kT \sim 3$ keV model with varying emission measure and circumstellar absorption. The variation of absorption with phase is consistent with expected variation (Williams et al. 1990) of wind extinction to the WCR moving in the WC7 wind (Fig. 12) but the emission measure, after rising as $1/D$ between phases 0.903 and 0.989, then falls in the ϕ = 0.997 and periastron spectra. This is presumably related to the fading close to periastron seen in the *RXTE* data. Sugawara et al. attribute the fading to the failure of the O5 wind to reach its terminal velocity before collision when the stars are very close, leading to a smaller WCR and θ. Sugawara et al. discovered two further components of the X-ray emission: a hard X-ray component observed at ϕ = 0.989 in the HXD-PIN ($>$ 10keV) band, which could be fit with a power law ($\Gamma \simeq 1.9$ photon index), and a soft ($E \sim 1$ keV) component at phases 0.997 and periastron which was not affected by circumstellar wind absorption.

Pollock et al. observed a further high-resolution spectrum with *Chandra* ACIS at ϕ = 0.951, O5 star conjunction. Its shape was very similar to that of the ϕ = 0.65 spectrum, differing only in intensity and wavelength shift of the lines: the profile of Ne X was blue-shifted to ~ -1400 km s^{-1} as expected from the orientation of the WCR. The spectra should yield abundances of O, Ne, Mg and other elements in the WC wind for comparison with evolutionary models.

These studies are currently being worked up, together with others, e.g. optical photometry and

polarimetery (P.I. Moffat), *SWIFT* XRT spectroscopy (P.I. Corcoran), and radiometry at a wide range of frequencies (P.I. Dougherty). Each will shed light on conditions and processes in the wind collision in WR 140, but the goal must be the development of *consistent models able to explain all the processes together*: heating, cooling, particle acceleration, and dust formation. For example, the appearance of the sub-peak on the profile of the 1.083-μm He I line occurs between phases 0.86 and 0.93, close to the phase ($\phi \simeq 0.93$) when the X-ray emission begins to deviate from a $1/D$-dependence: are both these phenomena related to departure from adiabatic conditions, and is the 'deficit' in X-ray flux made up in IR and optical sub-peak line emission? And, closer to periastron, for about $0.025P$, the intrinsic X-ray flux falls, emission in the C III sub-peak reaches its maximum, and dust nucleates in the wind; are these connected? Can they be explained *simultaneously?*. The multi-wavelength observations will continue to provide a fuller picture of processes in WR 140, particularly near periastron, and colliding winds in any other systems, including those for which it is more difficult to obtain such full datasets, e.g. η Carinae and more distant massive binaries.

Acknowledgements

The campaign was stimulated and organized by the "Getting-to-Grips with WR 140" group comprising Andy Pollock, Julian Pittard, Kenji Hamaguchi, Mike Corcoran, Sean Dougherty, Tony Moffat, and the author. My thanks to Sean Dougherty, Rémi Fahed and Mike Corcoran for figures. I am grateful to the Institute for Astronomy for hospitality and continued access to facilities of the Royal Observatory, Edinburgh.

References

Cantó, J., Raga, A. C. & Wilkin, F. P. 1996, ApJ, 469, 729
Conti, P. S., Roussel-Dupré, D., Massey, P. & Rensing, M. 1984, ApJ 282, 693
De Becker, M., Pittard, J. M., Williams, P. M., et al. 2011, in Proceedings of the 39th Liège Astrophysical Colloquium, eds. G. Rauw, M. De Becker, Y. Nazé, J.-M. Vreux & P.M. Williams, BSRSL 80, 653
Dougherty, S. M., Beasley, A. J., Claussen, M. J., Zauderer, A. & Bolingbroke, N. J. 2005, ApJ 623, 447
Dougherty, S. M., Trenton, V. & Beasley, A. J. 2011, in Proceedings of the 39th Liège Astrophysical Colloquium, eds. G. Rauw, M. De Becker, Y. Nazé, J.-M. Vreux & P.M. Williams, BSRSL 80, 658
Eichler, D. & Usov, V. V. 1993, ApJ 402, 271
Fahed, R., Moffat, A. F. J., Zorec, J., et al. 2011, in Proceedings of the 39th Liège Astrophysical Colloquium, eds. G. Rauw, M. De Becker, Y. Nazé, J.-M. Vreux & P.M. Williams, BSRSL 80, 668
Florkowski, D. R. 1982, in: C. W. H. de Loore & A. J. Willis, eds, Wolf-Rayet Stars: Observations, Physics, Evolution, IAU Symposium 99, 63
Florkowski, D. R. & Gottesman, S. T. 1977, MNRAS 179, 105
Florkowski, D. R., Johnston, K. J., Wade, C. M. & de Vegt, C. 1985, AJ 90, 2381
Koyama, K., Kawada, M., Takano, S. & Ikeuchi, S. 1990, PASJ 42, L1
Koyama, K., Maeda, Y., Tsuru, T., Nagase, F. & Skinner, S. 1994, PASJ 49, L93
Lührs, S. 1997, PASP 109. 504
McDonald, J. K. 1947, Pubs Dominion Astrophysical Obs. 7, 311
Marchenko, S. V., Moffat, A. F. J., Ballereau, D., Chauville, J., Zorec, J., Hill, G. M., Annuk, K., Corral, L. J., et al. 2003, ApJ, 596, 1295 (MM03)
Monnier, J. D., Tuthill, P. G. & Danchi, W. C. 2002, ApJ, 567, L137
Monnier, J. D., Traub, W. A., Schloerb, F. P., Millan-Gabet, R., Berger, J.-P., Pedretti, E., Carleton, N. P., Kraus, S., et al. 2004, ApJ 602, L57
Morris, P. W., Brownsberger, K. R., Conti, P. S., Massey, P. & Vacca, W. D. 1993, ApJ, 412, 324
Pittard, J.M. 2011, in Proceedings of the 39th Liège Astrophysical Colloquium, eds. G. Rauw, M. De Becker, Y. Nazé, J.-M. Vreux & P.M. Williams, BSRSL 80, 555
Pittard, J. M. & Dougherty, S. M. 2006, MNRAS, 372, 801
Plaskett, J. S. 1924, Pubs Dominion Astrophysical Obs. 2, 287

Pollock, A. M. T. 1987a, A&A 171, 135
Pollock, A. M. T. 1987b, ApJ, 320, 283
Pollock, A. M. T., Corcoran, M. F. & Stevens, I. R. 2002, in: A. F. J. Moffat & N. St-Louis, eds, Interacting Winds from Massive Stars, ASP Conf. Series 260, 537
Pollock, A. M. T., Corcoran, M. F., Stevens, I. R. & Williams, P. M. 2005, ApJ 629, 482
Prilutskii, O. F. & Usov, V. V. 1976, Soviet Ast., 20, 2
Repolust, T., Puls, J. & Herrero, A. 2004, A&A, 415, 349
Setia Gunawan, D. Y. A., van der Hucht, K. A., Williams, P. M., Henrichs, H. F., Kaper, L., Stickland, D.J. & Wamsteker, W. M. 2001, A&A 376, 460
Skinner, S. L., Simmons, A. E., Zhekov, S. A., Teodoro, M., Damineli, A. & Palla F. 2006, ApJL 639, L35
Smith, L. J., Norris, R. P. F. & Crowther, P. A. 2002, MNRAS 337, 1039
Stevens, I. R., Blondin, J. M. & Pollock, A. M. T. 1992, ApJ 386, 265
Sugawara, Y., Maeda, Y., Tsuboi, Y. & Hamaguchi, K. 2010, AIP Conf. Procs, 1248, 9
Sugawara, Y., Maeda Y., Tsuboi Y., et al. 2011, in Proceedings of the 39th Liège Astrophysical Colloquium, eds. G. Rauw, M. De Becker, Y. Nazé, J.-M. Vreux & P.M. Williams, BSRSL 80, 724
Usov, V. V. 1991, MNRAS, 252, 49
Usov, V. V. 1992, ApJ 389, 635
van der Hucht, K. A. 2001, New Astron. Rev., 45, 135
Varricatt, W. P., Williams, P. M. & Ashok, N. M. 2004, MNRAS, 351, 1307
White, R. L. & Becker, R. H. 1995, ApJ 289, 698
Williams, P. M., van der Hucht, K. A., van der Woerd, H., Wamsteker, W. M., Geballe, T. R., Garmany, C. D. & Pollock A. M. T. 1987, in: H. J. G. L. M. Lamers & C. W. H. de Loore, eds, Instabilities in Luminous Early Type Stars, D. Reidel, 221
Williams, P. M., van der Hucht, K. A., Pollock, A. M. T., Florkowski, D. R., van der Woerd, H. & Wamsteker, W. M. 1990, MNRAS, 243, 662
Williams, P. M., van der Hucht, K. A. & Spoelstra, T. A. Th. 1994, A&A 291, 805
Williams, P. M., Marchenko, S. V., Marston, A. P., Moffat, A. F. J., Varricatt, W. P., Dougherty, S. M., Kidger, M. R., Morbidelli, L., et al. 2009, MNRAS 395, 1749
Zhekhov, S. A. & Skinner, S. L. 2000, ApJ 538, 808

Discussion

J. Groh: Concerning the He I 10830 line profile, I have two questions:

1. Do you see variations in the maximum velocity of the P-Cygni absorption profile?
2. Apparently there is red shifted He I 10830 absorption at $+3000\,\mathrm{km\,s^{-1}}$. Is that real or due to blends?

P. Williams:

1. No, there are no conspicuous changes in the width of the absorption component.
2. I expect it is due to the gap between the He I line and a He II line in the WR star (at the position of $Pa\gamma$).

S. Owocki: Regarding the disappearance of X-rays near periastron, I would again note that the severe thin-shell instabilities that occur in radiatively cooled shocks make it essentially impossible for any numerical code (even with AMR) to give reliable X-ray fluxes, because of numerical diffusion and/or mixing of hot and cold material. But such mixing seems likely also to be physically possible in nature, and if it is efficient enough, this could effectively soften or even quench the X-rays, by shifting the radiative emission to EUV and UV from the cool or warm material. This could well be a key point of the explanation for the sharp X-ray minima in WR 146 and other eccentric wind collision systems.

L. Oskinova: In conjuction, when the WC star was in front, did you detect intrinsic X-ray emission from the WC star wind?
P. Williams: No, I don't think so.

3D modelling of the massive star binary systems Eta Carinae, WR 22, and WR 140

E. R. Parkin[1,2], J. M. Pittard[2], M. F. Corcoran[3,4], K. Hamaguchi[3,5], I. R. Stevens[6], E. Gosset[1], G. Rauw[1], and M. De Becker[1]

[1] Institut d'Astrophysique et de Géophysique, Université de Liège, Belgium
[2] School of Physics and Astronomy, The University of Leeds, UK
[3] CRESST and X-ray Astrophysics Laboratory, NASA/GSFC, USA
[4] Universities Space Research Association, USA
[5] Department of Physics, University of Maryland, USA
[6] School of Physics and Astronomy, University of Birmingham, UK

Abstract: Massive stars possess powerful stellar winds. Wind-wind collision in a massive star binary system generates a region of thermalized plasma which may emit prolifically at X-ray wavelengths. Results are presented from 3D adaptive-mesh refinement (AMR) hydrodynamical models which include radiative cooling and the radiative driving of the stellar winds. The models provide an exceptional insight into the turbulent nature of the wind-wind interaction regions. The X-ray emission from the hydrodynamical models is then calculated, allowing detailed comparisons with observational data. Preliminary results from investigations of Eta Carinae, WR 22, and WR 140 are discussed.

1 Introduction

In a binary system consisting of two hot massive stars the collision of the hypersonic winds generates a region of thermalized plasma which emits at X-ray wavelengths (e.g. Stevens, Blondin & Pollock 1992). X-ray observations therefore provide a direct probe of the wind-wind collision region (WCR) and can be used to infer details about the pre-shock winds (e.g. Pittard & Corcoran 2002). Depending on the parameters of the winds and the orbit, the dynamics of the post-shock gas in the WCR can cover a diverse range (Stevens et al. 1992). For instance, in long-period binaries (i.e. on the order of years) the post-shock gas is expected to be quasi-adiabatic for the most part, whereas in short-period (i.e. $\sim$ few days) systems the post-shock gas is expected to be highly radiative. Highly eccentric systems, such as η Car, WR 140, and WR 22, provide the interesting prospect of transitioning between these two extremes as, given the relatively small separation of the stars at periastron, the WCR may reside deep in the wind-acceleration regions. Considering that the pre-shock wind velocity strongly influences the stability of the WCR through the effectiveness of radiative cooling, periastron passage in these systems may also be chaotic. Furthermore, the high contrast in wind ram pressures characteristic of WR+O binary systems (e.g. WR 140 - Williams et al. 1990; Zhekov & Skinner 2000; Pollock

Table 1: Adopted system and stellar parameters. P is the orbital period, e is the orbital eccentricity, a is the semi-major axis of the orbit, and $\dot{M}_i$ and $v_{\infty i}$ are the mass-loss rate and terminal wind speed for star i. References are noted in parentheses, and are as follows: 1 = Damineli et al. (2008), 2 = Hillier et al. (2001), 3 = Parkin et al. (2009), 4 = Pittard & Corcoran (2002), 5 = Rauw et al. (1996), 6 = Rauw (1997), 7 = Crowther et al. (1995), 8 = Gosset et al. (2009), 9 = Williams et al. (1990), 10 = Marchenko et al. (2003), 11 = Pittard & Dougherty (2006).

System	P (d)	e	a (AU)	$\dot{M}_1$ ($\mathrm{M_\odot\ yr^{-1}}$)	$v_{\infty 1}$ ($\mathrm{km\ s^{-1}}$)	$\dot{M}_2$ ($\mathrm{M_\odot\ yr^{-1}}$)	$v_{\infty 2}$ ($\mathrm{km\ s^{-1}}$)
η Car	2024 (1)	0.9 (1)	16.64 (2)	4.8×10^{-4} (3)	500 (4)	1.4×10^{-5} (3)	3000 (4)
WR 22	80.325 (5)	0.559 (5)	1.68 (5)	1.6×10^{-5} (6)	1785 (7)	2.8×10^{-7} (8)	2100 (8)
WR 140	2900 (9)	0.881 (10)	16 (10)	4.33×10^{-5} (11)	2860 (11)	8.0×10^{-7} (11)	3100 (11)

et al. 2005; Pittard & Dougherty 2006) places the WCR close to the O star, and a stable wind-wind momentum balance may not occur. In such cases the WR wind may be radiatively braked prior to reaching the O star (Gayley, Owocki & Cranmer 1997).

Here we present preliminary results from hydrodynamic models aiming to explore the aforementioned possiblities. The remainder of this work is structured as follows: in Sect 2 we describe the model, results are presented in Sect. 3, followed by conclusions in Sect. 4.

2 The model

We model the colliding winds by numerically solving the time-dependent equations of Eulerian hydrodynamics in a 3D Cartesian coordinate system. For this purpose we use the AMR hydrodynamics code FLASH (Fryxell et al. 2000) into which we have implemented customized units for radiative driving, gravity, orbital motion, and radiative cooling. A description of the numerical methods used can be found in Pittard (2009) and Parkin et al. (2010, in prep). The adopted system and stellar parameters are listed in Table 1.

3 Results

3.1 η Carinae

Possibly the largest and finest example of a pre-hypernova candidate, η Car presents a rare but exceptional opportunity to test our current understanding of stellar evolution in the upper Hertzsprung-Russell diagram. X-ray emission from η Car is indicative of a highly eccentric, long-period binary system (Table 1). The binary model is relatively successful in explaining the majority of the X-ray lightcurve (e.g. Okazaki et al. 2008, Parkin et al. 2009). However, when the spatial extent of the X-ray emission region and energy dependence of the emission and absorption are taken into consideration (Parkin & Pittard 2008, Parkin et al. 2009), the width of the observed X-ray minimum cannot be reproduced by an eclipse of the X-ray emitting plasma alone. Furthermore, the observed X-ray emission in the 7-10 keV band was over-estimated by an order of magnitude if the pre-shock winds were assumed to be at terminal velocity. One potential cure for this discrepency would be a disruption of the WCR apex, initiated by effective radiative cooling of the companion's wind (Davidson 2002, Parkin et al. 2009, Parkin et al. 2010, in prep).

In our recent work, tests with static stars at a periastron separation and radiatively-driven stellar winds reveal that the companion star's pre-shock wind speed is reduced from $3000\ \mathrm{km\ s^{-1}}$ to $\simeq$

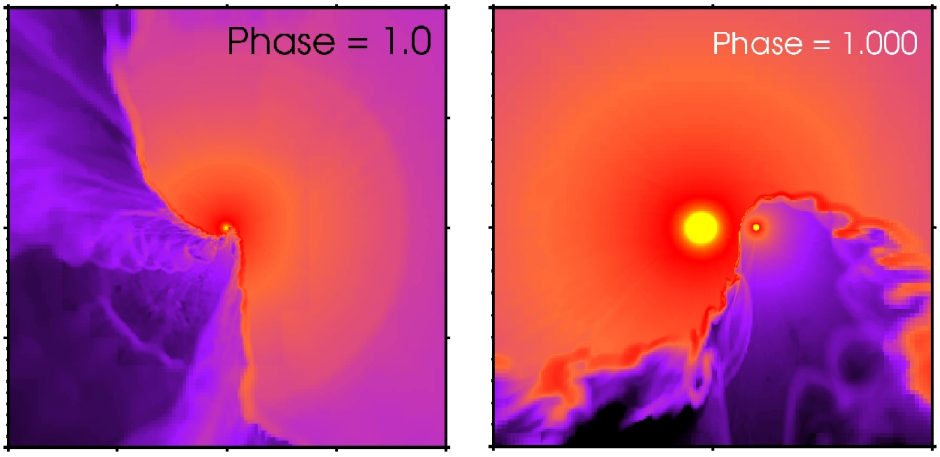

Figure 1: Snapshots of the gas density in the orbital $(x - y)$ plane from the radiatively-driven winds simulation of η Car at $\phi = 1.0$. At periastron ($\phi = 1.0$) the primary is to the left, and the companion is to the right, of the image centre. The plots show a region of $\pm 2 \times 10^{15}$ cm (left panel) and $\pm 5 \times 10^{14}$ cm (right panel).

2200 km s^{-1} by radiative inhibition (Stevens & Pollock 1994). Consequently, radiative cooling in the post-shock gas becomes important, driving the runaway growth of non-linear thin-shell instabilities (NTSI - Vishniac 1994) which massively distort the WCR. Subsequent vigorous oscillations lead to the collision of dense fragments of the WCR against the companion star. Compared to a simulation with terminal velocity winds, the aforementioned disruption leads to a reduction in the 7-10 keV X-ray flux by a factor of 8, thus providing a plausible explanation for the observed X-ray minimum.

However, in large-scale simulations (Fig. 1), the inclusion of orbital motion of the stars reduces the impact of radiative inhibition and increases the acquired pre-shock velocities. As such, the post-shock gas temperature and cooling time see a commensurate increase, and sufficient gas pressure is preserved to stabilize the WCR against catastrophic instability growth.

3.2 WR 22

The eccentric intermediate period system WR 22 contains one of the most massive Wolf-Rayet stars ever weighed (Rauw et al. 1996 - see also Schweickhardt et al. 1999). A recent analysis of *XMM-Newton* observations of WR 22 by Gosset et al. (2009) characterised the X-ray emission as a two-component spectrum with a soft component at ~ 0.6 keV and a harder component at $\sim 2 - 4.5$ keV, consistent with the colliding winds binary hypothesis. However, difficulties were encountered as wind-wind collision models were found to over-predict the observed X-ray flux by more than two orders of magnitude. The parameters of WR 22 provide the interesting prospect of a transition in the state of post-shock gas between quasi-adiabatic at apastron to highly radiative at periastron, which will considerably affect the resulting X-ray emission. Furthermore, a stable wind-wind momentum balance may be lost leading to a catastrophic reduction in X-ray flux.

Our simulations of WR 22 reveal that when the stellar winds are assumed to be instantaneously accelerated, a stable WCR is established throughout the orbit. In this case the model over-predicts the observed X-ray flux by more than two orders of magnitude. However, when the acceleration of the winds is considered, the character of the WCR changes dramatically between apastron and periastron. As radiative cooling becomes effective in the post-shock O star's wind, the growth of powerful NTSIs massively disrupts the WCR. Shortly before periastron the WCR collapses onto the O star (Fig. 2), and the over-estimate of the observed X-ray flux by the model is reduced to a factor of ~ 4, massively

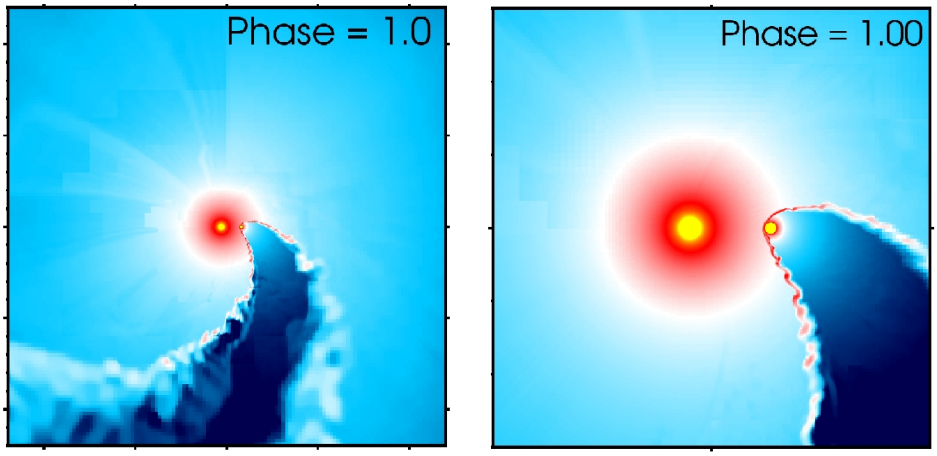

Figure 2: Snapshots of the gas density in the orbital ($x - y$) plane from the radiatively-driven winds simulation of WR 22 at $\phi = 1.0$. At periastron ($\phi = 1.0$) the WR star is to the left, and the O star is to the right, of the image centre. The plots show a region of $\pm 1.2 \times 10^{14}$ cm (left panel) and $\pm 3 \times 10^{13}$ cm (right panel).

improving the agreement[1].

3.3 WR 140

WR 140 represents the archetypal colliding winds binary system: it is a well known non-thermal radio emitter (Dougherty & Williams 2000), an exceptionally bright X-ray source (Pollock et al. 2005; De Becker et al. 2010, in prep), and an episodic dust producer (Williams et al. 2009).

The rapid motion of the stars around periastron contorts the WCR into a spiral structure (Fig. 3). Both winds remain quasi-adiabatic and a stable WCR is established at all orbital phases. Preliminary results of X-ray calculations show that the model provides a reasonable match to the majority of the X-ray lightcurve. However, the rise in X-ray flux prior to periastron is not well matched, and the model lightcurve exhibits no X-ray minimum at periastron. This could be due to our adopted wind parameters - for hydrodynamic models which adopt slightly different wind parameters see the contribution by Russell et al. (2011).

We note that currently we have only explored models of WR 140 with instantaneously accelerated (i.e. terminal velocity) winds. Considering the ratio of wind ram pressures, the wind acceleration regions may become important for a brief period around periastron passage. As we have seen from our simulations of WR 22, effective radiative cooling of both winds post-shock can jeopardise the stability of the WCR and considerably affect the emergent X-ray flux. Furthermore, rapid radiative cooling of post-shock gas around periastron could provide a means for forming dust. Hence, the importance of the wind-acceleration regions will be explored in future models.

4 Conclusions

Preliminary results from 3D hydrodynamic simulations of the massive star binary systems η Car, WR 22, and WR 140 have been presented which include the radiative driving of the stellar winds,

[1]The approach to radiatively driving the stellar winds in the hydrodynamic simulations is based on the formalism of Castor, Abbott & Klein (1975); a $\beta-$velocity law with $\beta = 1$. Therefore, aspects of WR wind acceleration are not accounted for, e.g. an inner, and outer, wind acceleration region (Hillier & Miller 1999, Gräfener & Hamann 2005). However, the wind-wind collision generally occurs close to the O star, and our conclusions remain uneffected.

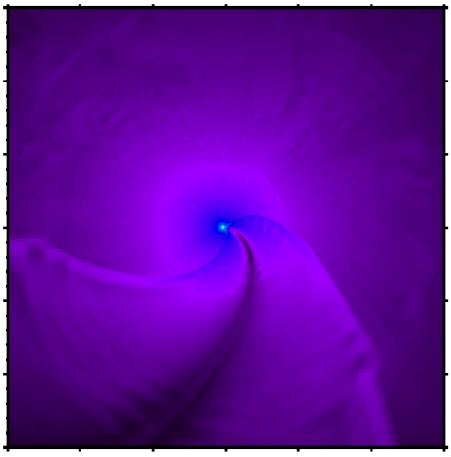

Figure 3: Snapshot of the gas density in the orbital $(x-y)$ plane from the instantaneously accelerated winds simulation of WR 140 at $\phi = 1.0$. At periastron ($\phi = 1.0$) the WR star is to the left, and the O star is to the right, of the image centre. The plot shows a region of $\pm 1.5 \times 10^{15}$ cm - large axis tick marks correspond to a distance of 5×10^{14} cm.

gravity, orbital motion, and radiative cooling. In the systems explored the post-shock gas in the WCRs exhibits a breadth of interesting dynamics. For instance, in WR 22 the transition of the post-shock gas from quasi-adiabatic at apastron to radiative at periastron brings about a dramatic change in the stability of the WCR. Interestingly, transitions in the character of post-shock gas seem to be characteristic of the highly eccentric systems examined.

An extensive study of the dynamics in these systems will be presented in a series of forthcoming papers, along with a detailed comparison between X-ray calculations performed on the models and observations (see e.g. Pittard & Parkin 2010).

Acknowledgements

ERP was suported in part by a Henry Ellison Scholarship from The University of Leeds and by a PRODEX XMM/Integral contract (Belspo).

References

Castor, J. I., Abbott, D. C., & Klein, R. I. 1975, ApJ, 195, 157
Crowther P. A., Hillier D. J., & Smith L. J. 1995, A&A, 293, 403
Damineli A., et al. 2008, MNRAS, 384, 1649
Davidson K. 2002, ASPC, 262, 267
Fryxell B. et al. 2000, ApJS, 131, 273
Gayley K. G., Owocki S. P., Cranmer S. R. 1997, ApJ, 475, 786
Gosset E., Nazé Y., Sana H., Rauw G., & Vreux J. 2009, A&A, 508, 805
Gräfener, G. & Hamann, W. 2005, A&A, 432, 633
Hillier, D. J. & Miller, D. L. 1999, ApJ, 519, 354
Hillier D. J., Davidson K., Ishibashi K., & Gull T. 2001, ApJ, 553, 837
Marchenko S. V., et al. 2003, ApJ, 596, 1295
Okazaki A. T., Owocki S. P., Russell C. M. P., & Corcoran M. F. 2008, MNRAS, 388, L39
Parkin E. R., & Pittard J. M. 2008, MNRAS, 388, 1047
Parkin E. R., Pittard J. M., Corcoran M. F., Hamaguchi K., & Stevens I. R. 2009, MNRAS, 394, 1758
Pittard J. M. 2009, MNRAS, 396, 1743

Pittard, J.M. 2011, in Proceedings of the 39th Liège Astrophysical Colloquium, eds. G. Rauw, M. De Becker, Y. Nazé, J.-M. Vreux & P.M. Williams, BSRSL 80, 555
Pittard J. M. & Corcoran M. F. 2002, A&A, 383, 636
Pittard J. M. & Dougherty S. M. 2006, MNRAS, 372, 801
Pittard J. M. & Parkin E. R. 2010, MNRAS, 403, 1657
Pollock A. M. T., Corcoran M. F., Stevens I. R., & Williams P. M. 2005, ApJ, 629, 482
Rauw G. 1997, PhD Thesis, University of Liège, (1997)
Rauw G., Vreux J., Gosset E., et al. 1996, A&A, 306, 771
Russell, C.M.P., Corcoran, M.F., Okazaki, A.T., Madura, T., & Owocki, S.P. 2011, in in Proceedings of the 39th Liège Astrophysical Colloquium, eds. G. Rauw, M. De Becker, Y. Nazé, J.-M. Vreux & P.M. Williams, BSRSL 80, 719
Schweickhardt J., Schmutz W., Stahl O., Szeifert T., & Wolf B. 1999, A&A, 347, 127
Stevens I. R. & Pollock A. M. T. 1994, MNRAS, 269, 226
Stevens I. R., Blondin J. M., & Pollock A. M. T. 1992, ApJ, 386, 265
Vishniac E. T. 1994, ApJ, 428, 186
Williams P. M., van der Hucht K. A., Pollock A. M. T., Florkowski D. R., van der Woerd H., & Wamsteker W. M. 1990, MNRAS, 243, 662
Williams P. M., et al. 2009, MNRAS, 395, 1749
Zhekov S. A. & Skinner S. L. 2000, ApJ, 538, 808

Discussion

I. Stevens: Would you expect to see any observational consequences of wind collapse in, say, the spectrum of the O star, i.e. WR material being dumped onto the surface?
E.R. Parkin: I would expect that there will be some consequence but it will strongly relate to the mixing of the WR wind into the inner wind of the O star. We do not currently resolve the wind acceleration region sufficiently well to examine this effect.

T. Madura: Could you comment on how a latitude-dependent primary wind might affect your results for η Car?
E.R. Parkin: The X-ray emission predominantly originates from the apex of the wind-wind collision region which is close to the orbital plane. Therefore, a latitude dependent primary star wind should not have a considerable effect on the shocks which emit the X-rays. However, the inclination angle of the orbital plane is $\sim$42°, so X-rays may pass through denser gas towards the pole of the star, thus affecting the degree of attenuation.

W.-R. Hamann: As we had discussed a lot on Monday, mass-loss rates of WR and O stars are still uncertain to some factor 2 or 3, depending on the degree of clumping and the clump sizes. How sensitive are your hydrodynamical simulations to the mass-loss rate, and to possible large-scale wind clumping?
E.R. Parkin: The importance of radiative cooling for the dynamics of postshock gas is directly related to the stellar wind mass-loss rates. Therefore, if you change the mass-loss rates you could significantly change the character of the wind-wind collision region. There is also the effect of clumps in the wind on the shocks. For instance, the processing of clumps in the wind-wind collision region can introduce a large amount of vorticity (Pittard 2011).

Cygnus OB2: A Laboratory for Massive Binaries, Runaway Stars, and Triggered Star Formation

Henry A. Kobulnicky[1] and Daniel C. Kiminki[1]

[1] Department of Physics & Astronomy, University of Wyoming, Laramie, WY 82072, USA

Abstract: The Wyoming Cygnus OB2 Radial Velocity Survey has identified dozens of new OB stars in this region while measuring orbital parameters for 15 binary systems, bringing the known total to 20. From these data we have modeled the distribution of binary parameters. We conclude that the slope of the distribution of periods is approximately flat in log space and that the slope of the distribution of mass ratios is either flat or slightly favoring larger q. However, there appears to be an excess of systems with 3–5 day periods and a deficit of systems with 7–14 day periods. From among $\sim$120 systems surveyed we find only one radial velocity runaway —a binary system! A Search of *Spitzer Space Telescope* images of the Cygnus X region reveals several bowshocks from high-velocity early type stars. We use the principles of bowshock physics to derive a novel technique for estimating the mass loss rates of runaway stars.

1 Introduction to the Cygnus OB2 Radial Velocity Survey

Herein we present results from a 10-year spectroscopic campaign on massive stars in Cygnus OB2. This is primarily the work of PhD student Daniel Kiminki supported by a big team of students at the University of Wyoming using data from the Wyoming Infrared Observatory 2.3 m telescope. The title doubles as my outline. Most of this contribution will focus on the emerging statistics of massive binaries. The remainder will report on searches for runaway stars in this region.

Cyg OB2 is home to one of the largest collections of OB stars in the Milky Way, and it is also one of the nearest. Odenwald & Schwartz (1993) presented a beautiful overview of the busy 5x5 degree region known as Cygnus X toward Galactic longitude l=80°. Their annotated 100 micron map shows the plethora of star forming complexes, molecular clouds, and OB associations as we look several kpc along the local spiral arm. Cyg OB2 sits in the middle of this region and is thought to be located at a distance of 1.4 – 1.7 kpc (Massey & Thompson 1991; Hanson 2003).

Since 1999 we have been conducting a radial velocity survey of $\sim$120 probable Cyg OB2 members using a variety of telescopes and optical spectrographs in order to improve upon the statistics regarding massive binary frequency, period, and mass ratio. Our goal is to improve upon the pioneering work of Garmany, Conti & Massey (1980) who performed a similar survey but over a shorter duration, drawing their sample from bright O stars all over the sky. Our sample is photometrically selected from the survey of Massey & Thompson (1991, MT91), and the sample is supplemented by additional OB stars from the imaging study of Comerón et al. (2002). Our survey was conducted at four major observatories between 1999 and the present, but most of the observations were made at the WIRO 2.3 m telescope with the longslit spectrograph at a resolving power of R$\simeq 4000$. Details

of observations and analysis may be found in Kiminki et al. (2007, 2008, 2009, 2011) and Kiminki & Kobulnicky (2011).

Figure 1 shows the portion of orbital parameter space to which our survey is sensitive. The blue shaded region at upper left indicates sensitivity to primaries with velocity amplitudes greater than about 15 km s^{-1}. As such, our survey will detect binaries with periods of days to perhaps several years, beginning to probe the interesting region of this diagram populated by the progenitors of low-mass X-ray binaries under some standard formation scenarios described by van den Heuvel (1983). Imaging surveys (speckle and interferometric; see e.g. Caballero-Nieves et al. 2011) are complementary in that they probe periods >10 yr.

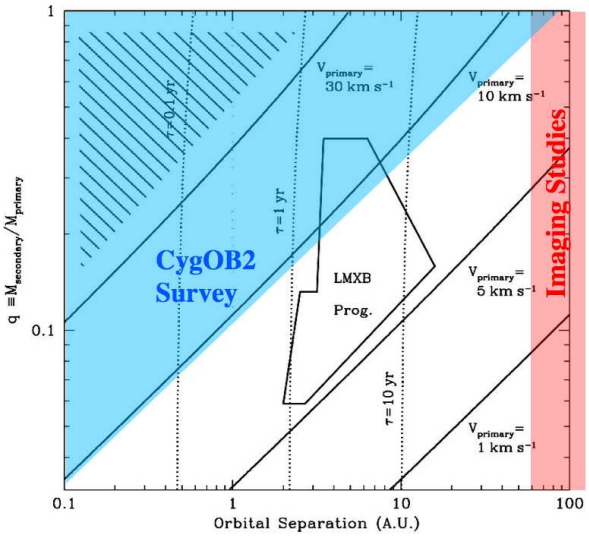

Figure 1: The survey is sensitive to primaries with velocity amplitudes of greater than about 15 km s^{-1}, shown by the shaded region in the upper left. Speckle and interferometric imaging surveys are sensitive to companions with separations greater than ∼100 A.U., shown by the red shaded region. This figure assumes a primary mass of 10 M$_\odot$ and circular orbits at inclination 90°.

2 Results on Binary Parameters

The Wyoming Cygnus OB2 Radial Velocity Survey has detected and/or measured orbital parameters for 15 binaries. When added to known systems already in the literature (famous examples such as the non-thermal radio emitters Schulte #5, #8a, #9 (Schulte 1958), see Nazé et al. (2010) for recent results on #9), the number of known massive binaries stands at 20, the largest number in any one cluster or association to-date. Of course, there is no guarantee that they are all members, but they are likely to lie within Cyg OB2 based on their photometric properties (magnitude and reddening) as measured by MT91 and Hanson (2003) and our systemic radial velocity results. We note, furthermore, that information about higher order systems (triples, etc.) is not easily extracted from our data, so we refer to all multiples herein as binaries. A table of the orbital elements for all systems is included in Kiminki et al. (2009) and Kiminki et al. (2011). Finally, there are an additional ∼20 systems for which we detect radial velocity variability, suggesting the presence of additional binaries that will require further observations to refine their orbital elements.

Figure 2 shows the plot of eccentricity versus period and mass ratio, $q \equiv M_2/M_1$, versus period. Filled circles show double-lined spectroscopic binaries (SB2s) and open circles show single-lined spectroscopic binaries (SB1s). As might be expected, the shortest period systems have low eccentricities. At periods longer than a few days, the range of eccentricities increases to cover the range 0 – 0.5. The distribution of Cyg OB2 stars appears similar to the OB stars drawn from the 9th Catalog of Spectroscopic Binary Orbits (Pourbaix et al. 2004). The lower panel shows that the distribution of q spans the full range from 1 to the detection limit of ∼0.1 for all periods between 1.5 and 25 days. The perceptive eye will also notice a dearth of systems with periods between about 7 and 14 days.

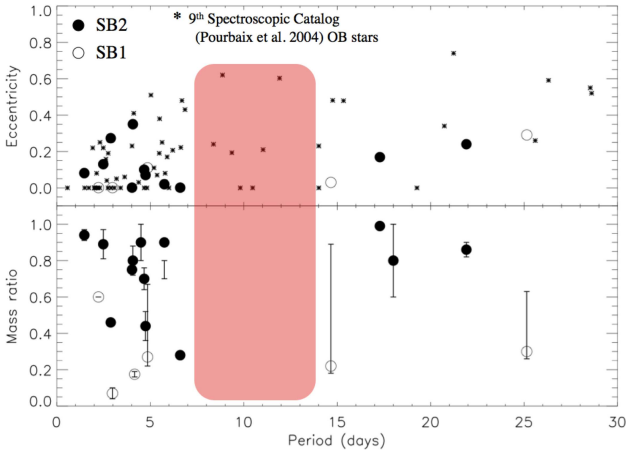

Figure 2: Eccentricity and mass ratio versus period for the massive binaries in Cyg OB2.

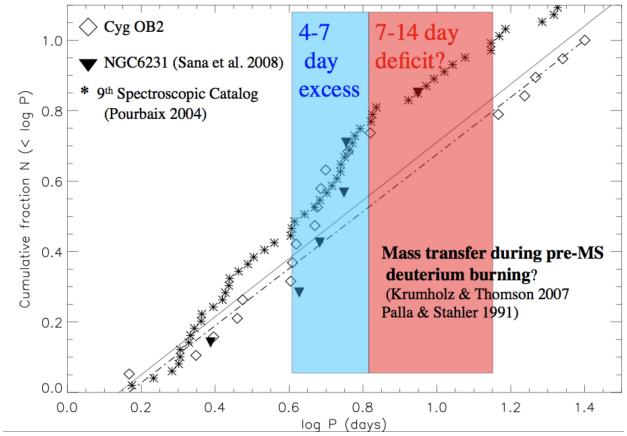

Figure 3: Cumulative distribution of orbital periods in this and other surveys.

The distribution of orbital periods is better seen in Figure 3 where we show the cumulative period distribution (diamonds and left abscissa) versus log(period) in days. Diamonds again show the Cyg OB2 sample. The cumulative distribution rises rapidly over the range 3–5 days, while there are no systems with periods between 7 and 14 days. The solid and dash-dot lines show (with slightly different normalization) a power law given by $f(logP) \propto (logP)^{\beta}$, where $\beta \simeq 0.2$. However no power law is consistent with the observed distribution given the large gap in the period distribution.

One possible explanation for the excess of short-period systems and simultaneous lack of systems in the 7–14 day range is Roche-lobe overflow and mass transfer/loss during the pre-main-sequence deuterium burning phase of the primary star. Such a scenario was proposed by Krumholz & Thompson (2007) following Palla & Stahler (1991) in order to produce copious numbers of "twin" systems with mass ratios near unity that binary studies in the SMC seemed to demand (Hilditch, Howarth & Harries 2005; Pinsonneault & Stanek 2006). A mass-losing primary and mass-gaining secondary (possibly coupled with mass lost from the system) would also serve to reduce the orbital period of systems that were (even briefly) close enough to interact. If this is the operative mechanism, then we would expect to see an excess of high q systems having short periods. Such a feature is not obvious, but might be present.

Figure 4 show the distributions, cumulative on the left abscissa and conventional histogram on the right abscissa, for the mass ratios observed in Cyg OB2. Although the bin between q=0.8 and q=0.9 is the most populated, the overall distribution is not far from flat and is roughly characterized by a power law of slope α=0.3 where f(q)$\propto q^{\alpha}$. We find no significant population of "twins" having q>0.9. The survey becomes increasingly incomplete at q<0.3, so it is likely that there are additional systems in this mass range. Full details of the analysis, completeness limits, and results regarding massive binary parameters may be found in Kiminki et al. (2009) and Kiminki et al. (2011).

Velocities of the Cyg OB2 Systems

The mean heliocentric radial velocity for Cyg OB2 stars in our survey is -15.6 km s^{-1} with a dispersion smaller than our typical measurement uncertainty (i.e., <9 km s^{-1}). We find only one system, A36 in the notation of Comerón et al. (2002), that differs by more than 30 km s^{-1} from the mean, the canonical space velocity adopted to designate stars as runaways (Gies & Bolton 1986). A36 has a heliocentric radial velocity of -47 km s^{-1}, making it a probable runaway system—one of only three known runaway binary systems having non-degenerate components (D. Gies, private communi-

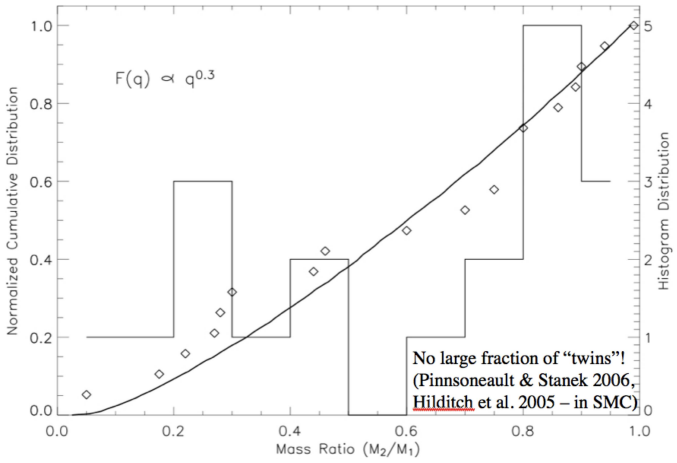

Figure 4: Cumulative (left) and histogram (right) distribution of mass ratios.

cation). Gies & Bolton (1986) find that ∼10% of all O stars are runaways. This would predict ∼12 runaways from Cyg OB2.

We conducted a search for runaways with space motions tangent to the line of sight using data from the *Spitzer Space Telescope* Cygnus X Legacy Survey (Hora et al. 2009) to identify bowshocks, one signpost of a massive star traveling at supersonic speeds. A visual search for arc-like objects within about two degrees of Cyg OB2 revealed 10 candidate bowshocks. Followup spectroscopy from the Wyoming Infrared Observatory confirmed that all 10 contained an object with the spectra and spectral energy distributions of late-O and early-B stars near their centers. However, many other types of astrophysical objects may superficially resemble bowshocks, such as the heads of gaseous pillars illuminated from the outside. We compared the candidate bowshocks to analytical models of Wilkin (1996) and found three of the objects have strong morphological similarity to the theoretical shape of shocks resulting from the supersonic motions of a massive star. We classified the remaining objects as either young stellar objects with surrounding interstellar material (3) or unknown/ambiguous in nature (4). We add BD+43°3654, a known high-velocity runaway and probable escapee from Cyg OB2 (Comerón & Pasquali 2007) to our list, bringing the number of probable runaways to four.

The analytical theory for stellar wind bowshocks has been developed by many authors, including Baranov et al. (1971) and more recently by van Buren et al. (1990) and Wilkin (1996). Working from their derivations and extending the terminology of Povich et al. (2008), we find that the mass loss rate of a star seen as a stellar wind bowshock object can be expressed as

$$\dot{M}_{w,-6} = \frac{0.67[R_0(pc)]^2[V_a(km/s)]^2 n_{a,3}}{V_{w,8}} \, . \tag{1}$$

R_0 is the "standoff" distance between the star and bowshock apsis which can readily be measured from images given the known distance to Cyg OB2. V_a is the velocity of the star, which, while unmeasured, can safely be assumed to be in the vicinity of 30 km s^{-1} based on other observed runaways. $V_{w,8}$ is the velocity of the stellar wind in units of 10^8 cm s^{-1}, which can be adopted from the known spectral type of each star and published wind speeds (e.g., Mokiem et al. 2007). The least certain parameter is $n_{a,3}$, the ambient interstellar density in units of 10^3 cm^{-3}. We estimate this parameter from the measured size and luminosity of each bowshock nebula, in conjunction with dust emissivity models of Draine & Li (2007). The derived mass loss rates are broadly consistent with, but slightly higher than measurements from other methods such as Hα, radio, and UV absorption line studies. Details of this approach, along with images and results may be found in Kobulnicky, Gilbert & Kiminki (2010).

Figure 5 compares the results for bowshock nebula analyzed in this manner (skeletal symbols) to results from other methods (open and filled symbols). There is a clear trend toward higher mass loss

rates for the earlier and more evolved stars, and the overall zero point is in reasonable agreement with data from the Mokiem et al. (2007) and Fullerton, Massa & Prinja (2006). While this novel approach is unlikely to supplant more established techniques of mass loss determination, it provides a novel and independent estimate for a select subclass of high-velocity stars evincing bowshocks.

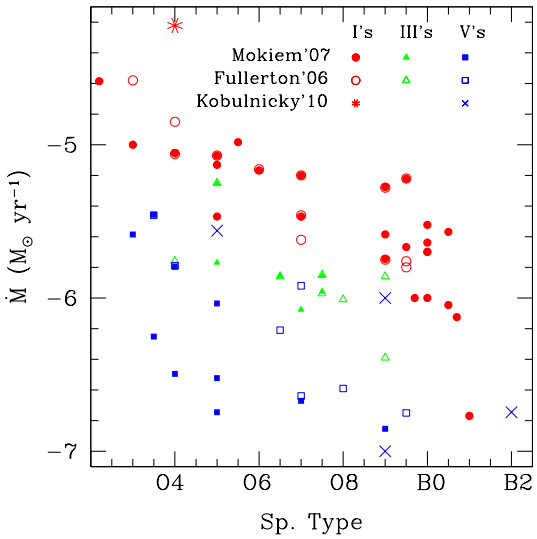

Figure 5: Mass loss rate as a function of stellar type for stars from the literature (open and filled symbols) and the runaway bowshock sample (skeletal symbols).

In conclusion, the Wyoming Cygnus OB2 Radial Velocity Survey is an ongoing observational program that will continue to measure massive binary parameters for additional systems in the coming years. The program also provides science training for many students. A new direct distance measurement to Cyg OB2 using eclipsing systems is now underway. The time-domain nature of the survey leads us to expect additional serendipitous discoveries, and we invite collaborations with astronomers interested in the Cygnus X region.

References

Baranov, V. B., Krasnobaev, K. V., & Kulikovskii, A. G., 1971, Sov. Phys. — Dokl, 15, 791

Caballero-Nieves, S.M., Gies, D.R., Roberts, L.C., & Turner, N.H. 2011, in Proceedings of the 39th Liège Astrophysical Colloquium, eds. G. Rauw, M. De Becker, Y. Nazé, J.-M. Vreux & P.M. Williams, BSRSL 80, 639

Comerón, F., & Pasquali, A., 2007, A&A, 467, L23

Comerón, F. Pasquali, A., Rodighiero, G., et al., 2002, A&A, 389, 874

Draine, B. T., & Li, A., 2007, ApJ, 657, 810

Garmany, C. D., Conti, P. S., & Massey, P., 1980, ApJ, 242, 1063

Gies, D. R., & Bolton, C. T., 1986, ApJS, 61, 419

Fullerton, A. W., Massa, D. L., & Prinja, R. K., 2006, ApJ, 637, 1025

Hanson, M. M., 2003, ApJ, 597, 957

Hilditch, R. W., Howarth, I. D., & Harries, T. J., 2005, MNRAS, 357, 304

Hora, J. L., Bontemps, S., Megeath, S. T., et al., 2009, BAAS 41, 498

Kiminki, D. C., Kobulnicky, H. A., Kinemuchi, K., et al., 2007, ApJ, 664, 1120

Kiminki, D. C., McSwain, M. V., & Kobulnicky, H. A., 2008, ApJ, 679, 1478

Kiminki, D. C., Kobulnicky, H. A., Gilbert, I., Bird, S., & Chunev, G., 2009, AJ, 137, 4608

Kiminki, D. C., et al., 2011, ApJ, in prep

Kiminki, D. C. & Kobulnicky, H. A., 2011, ApJ, in prep

Kobulnicky, H.A., Gilbert, I. J., & Kiminki, D. C., 2010, ApJ, 710, 549

Krumholz, M. & Thompson, I., 2007, ApJ, 661, 1034
Massey, P., & Thompson, A. B., 1991, AJ, 101, 1408
Mokiem, M. R., de Koter, A., Vink, J. S., et al., 2007, A&A, 473, 603
Odenwald, S. F., & Schwartz, P. R., 1993, ApJ, 405,706
Nazé, Y., Damerdji, Y., Rauw, G., et al., 2010, ApJ, 719, 634
Palla, F. & Stahler, S., 1991, ApJ, 375, 288
Pinsonneault, M. H., & Stanek, K. Z., 2006, ApJ, 639, L67
Pourbaix, D., Tokovinin, A. A., Batten, A., et al., 2004, A&A, 424, 727
Povich, M. S., Benjamin, R. A., Whitney, B. A., Babler, B. L., Indebetouw, R., Meade, M. R., Churchwell, E., 2008, ApJ, 689, 242
Schulte, D. H., 1958, AJ, 128, 41
van Buren, D., Mac Low, M.-M., Wood, D. O. S., & Churchwell, E., 1990, ApJ, 353, 570
van den Heuvel, E. P. J., 1983, in Accretion-Driven Stellar X-ray Sources, 303
Wilkin, F. P., 1996, ApJ, 459, L31

Discussion

N. Evans: We are using a photometric technique (X-rays) to look for small q systems. Preliminary results confirm your flat q distribution. As challenge of the well studied 5 $M_{\odot}$ systems (P $>$ 1 year) we find half of the binaries are triples.

R. Chini: What is the minimum mass ratio that you are able to detect? You cannot detect "face-on" orbits. To what inclinations can you detect binaries?
C. Kobulnicky: We have simulated the completeness levels of the survey as part of our Monte Carlo analysis; I'll include those in future publications.

The multiplicity of O-type stars in NGC 2244

L. Mahy[1], G. Rauw[1], F. Martins[2], E. Gosset[1], Y. Nazé[1], M. Godart[1], H.Sana[3], M. De Becker[1] and P. Eenens[4]

[1] Institute of Astrophysics and Geophysics, University of Liège, Belgium
[2] GRAAL, Université Montpellier II, CNRS, France
[3] Sterrenkundig Instituut "Anton Pannekoek", Universiteit van Amsterdam, The Netherlands
[4] Departamento de Astronomía, Universidad de Guanajuato, Mexico

Abstract: The investigation of the multiplicity of massive stars is crucial to determine a robust binary fraction but also for understanding the physical properties of these objects. In this contribution, we will present the main results from our long-term spectroscopic survey devoted to the young open cluster NGC 2244. We discuss the spectral classification, the projected rotational velocity ($v \sin i$) and the multiplicity of O-stars. The stellar and wind parameters of each star, obtained using the CMFGEN atmosphere code, help us to better constrain the individual properties of these objects. Several of these stars were observed by the CoRoT satellite (SRa02) in the Asteroseismology channel. This intensive monitoring and the unprecedented quality of the light curves allow us to shed a new light on these objects.

1 Introduction

O-type stars play a key role in the ecology of galaxies but the knowledge of their formation is still fragmented. In this context, the study of massive stars in clusters is interesting in order to discriminate between the different formation scenarios since they constitute a homogeneous population (same age, distance and chemical composition).

The study of the multiplicity of early-type stars in galactic young open clusters through extensive spectroscopic campaigns unveils an average binary fraction of 0.44±0.05 (Sana & Evans 2011). These investigations led to serious corrections of the binary fractions in the rich-open clusters quoted by Garcìa & Mermilliod (2001). However, numerous observational biases prevent the detection of all spectroscopic binaries such as e.g., a very long-term period, a large mass ratio or too low an inclination (for details, see Sana & Evans 2011, Sana, Gosset, & Evans 2009 or Mahy et al. 2009).

In order to extend these studies, we have undertaken a detailed investigation of the young open cluster NGC 2244, situated in the core of the Rosette Nebula and aged between 2 and 3 Myr (Chen, de Grijs, & Zhao 2007, and references therein). We establish the binary fraction amongst O-type stars in the cluster, present the preliminary wind and stellar parameters of all these stars and summarise the preliminary results of the analysis of the CoRoT data devoted to 4 O-stars in NGC 2244.

2 Spectroscopic campaign

Garcia & Mermilliod (2001) listed 6 O-type stars as belonging to NGC 2244 whilst Ogura & Ishida (1981) reported a seventh O star (HD 258691), fainter than the others ones, and which is located outside of the field of view used by Wang et al. (2008). The question of the membership of this latter is thus open. As a consequence, our multiplicity investigation focused on the same stars as taken into account by Garcia & Mermilliod (2001) to establish the binary fraction of NGC 2244.

Our spectroscopic dataset thus contains a total of 136 spectra for 6 O-type stars. These spectra were taken with different instruments which implies different resolutions. The data were spread over a timescale of 9 years, allowing us to search for the short as well as the long-period binaries. The details and results of the spectroscopic investigation of O-type stars are reported in Mahy et al. (2009).

Among the 6 O-type stars in NGC 2244, only one has been detected, for the first time, as a spectroscopic binary: HD 46149. The signature of the secondary component is clearly visible (see Mahy et al. 2009) and we have estimated its orbital period to be close to 800 days. However, it is difficult to be more accurate because our data do not cover the entire orbital cycle. From the least blended spectrum, we estimated spectral types of O8V and early B (B0–1) for the primary and the secondary, respectively. We also classified HD 46150 as a binary candidate since small variations, at the limit of being significant, have been detected and the Temporal Variance Spectrum (TVS, Fullerton, Gies, & Bolton 1996) exhibited profiles with double or triple peaks. Although HD 46056 and HD 46485 present broad and shallow lines, their line widths did not change as a function of time, supporting the idea that both stars are fast rotators rather than binary systems. In general, the 4 remaining stars, HD 46056, HD 46202, HD 46223 and HD 46485, did not show any significant variations in their radial velocities and were, accordingly, classified as presumably single stars.

The spectroscopic investigation thus reveals a binary fraction of O-type stars in NGC 2244 in the range of 17–33% while the previous estimate (Garcìa & Mermilliod 2001) put this value at 50%, based on a very heterogeneous dataset i.e., radial velocities taken from the literature.

3 Determination of stellar and wind parameters

We have used the CMFGEN atmosphere code (Hillier & Miller 1998) for the analysis of the optical and UV spectra of the 6 O-type stars in NGC 2244. The luminosity was computed supposing a distance of 1.55 kpc for the young open cluster, i.e., the mean value in the range estimated by Hensberge, Pavlovski, & Verschueren (2000). On the one hand, the stellar parameters such as the surface gravity ($\log g$) or the effective temperature ($T_{\rm eff}$) were determined from the optical domain. We used the wings of Balmer absorption lines H_β, H_γ and H_δ as indicators of $\log g$ whilst the classical ratio between the equivalent widths of the He I λ 4471 and He II λ 4542 lines provided a good estimate of the $T_{\rm eff}$. Other lines of He I and He II, such as He I λ 4026, He I λ 5876, He II λ 4200 and He II λ 5412 were used as additional diagnostics to determine $T_{\rm eff}$.

On the other hand, the wind parameters were derived from the IUE spectra. The wind terminal velocity (v_∞) was estimated from the absorption part of the P Cygni lines observed in the UV domain. The UV P Cygni and emission lines also served as main indicators of the mass-loss rate ($\dot{M}$).

The $v \sin i$ were directly estimated by comparison of our synthetic spectra to the observed line profiles. A macroturbulence component has to be introduced to correctly reproduce the line profiles (e.g., for the He I λ 4713, C IV λ 5812 and He I λ 5876 lines).

The preliminary wind and stellar parameters of the 6 O-type stars (Martins et al., in prep) are reported in Table 1. However, the results concerning the secondary component of HD 46149 are uncertain. Indeed, our sample of spectra does not cover the entire orbital cycle, it is thus difficult to correctly disentangle the individual spectra of both components of HD 46149. From these parameters,

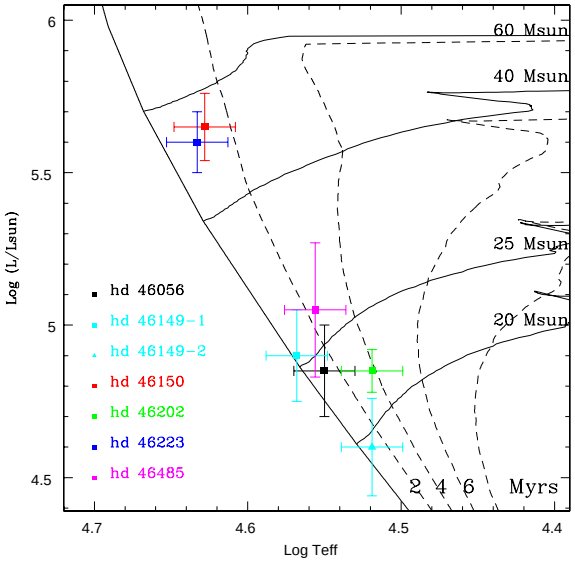

Figure 1: HR diagram showing the position of the O-type stars in NGC 2244. Evolutionary tracks are from Meynet & Maeder (2003) computed with an initial rotational velocity of about 300 km s^{-1}. The dotted lines indicate the isochrones of 2, 4, 6 and 8 Myr.

we put all the stars on a HR diagram (Fig. 1), implying an age of less than 5 Myr for all the O-type stars investigated in Sect. 2. The two hottest stars, HD 46150 and HD 46223, are found to be of the same age (i.e., 0–2 Myr old). A previous study of NGC 2244, by Wang et al. (2008) in the X-ray domain, revealed the existence of X-ray sources, associated to PMS stars, around HD 46150 but not around HD 46223. Two explanations were advanced by these authors. The first one assumes that dynamical interactions in NGC 2244 would be responsible for the ejection of HD 46223 from the central part of the cluster. The second scenario considers that HD 46223 might actually be younger than HD 46150 and would not be part of the same population as the core of the cluster. Our results favor the former explanation based on dynamical interactions inside the cluster since the two hottest stars appear to have a similar age.

Table 1: Preliminary stellar and wind parameters of the 5 O-type stars and both components of HD 46149. The different columns indicate the stars, the spectral type (derived in Mahy et al. 2009), the effective temperature, the luminosity, the surface gravity, the mass-loss rate, the terminal velocity, the projected rotational velocity and the macroturbulence velocity, respectively.

Target	Spectral type	$T_{\rm eff}$ (kK)	$\log(\frac{L}{L_\odot})$	$\log g$	$\log(\dot{M})$ ($M_\odot$ yr^{-1})	v_∞ (km s^{-1})	$v \sin i$ (km s^{-1})	$v_{\rm mac}$ (km s^{-1})
HD 46056	O8V	35.5±2.0	4.85	3.75±0.10	–9.0	1500±100	330	0
HD 46149-A	O8V	37.0±2.0	4.90	4.25±0.10	≤–9.0	1800±100	∼0	24
HD 46149-B	B0–1	33.0±2.0	4.60	3.50±0.10	–	–	100	27
HD 46150	O5.5V	42.5±2.0	5.65	4.00±0.10	–7.2	2800±100	100	37
HD 46202	O9V	33.0±2.0	4.85	4.00±0.10	–8.9	1200±100	20	17
HD 46223	O4((f$^+$)) V	43.0±2.0	5.60	4.00±0.10	–7.2	2800±100	100	32
HD 46485	O8V	36.0±2.0	5.05	3.75±0.10	–8.1	1700±100	300	0

4 The CoRoT photometric data

The CoRoT satellite (Auvergne et al. 2009) has observed 4 O-type stars in NGC 2244 (HD 46149, HD 46150, HD 46202 and HD 46223) during the second short run (SRa02, ∼34 days) with the Asteroseismology channel. The sampling of the obtained data is of one point every 32 s, providing light curves of an unprecedented quality.

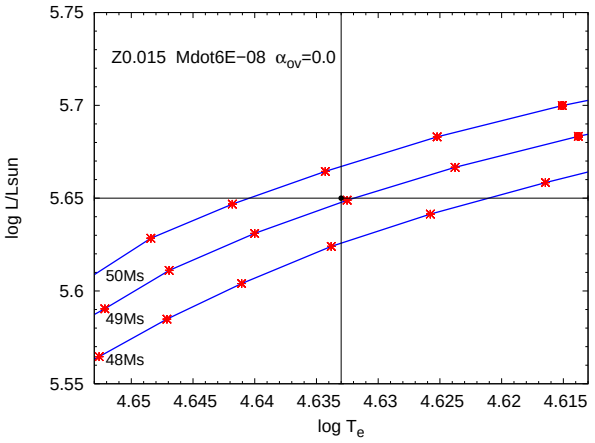

Figure 2: Evolutionary tracks of HD 46223 in the error box computed from the parameters estimated by CMFGEN (Table 1). The red crosses correspond to models computed with ATON and red points correspond to models with excited modes. No overshooting is included in the models.

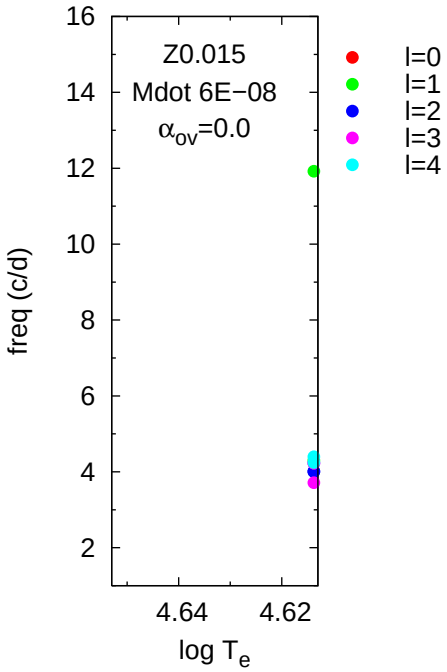

Figure 3: Frequencies computed for the models with excited modes (l) on the tracks of 49 $M_\odot$.

Degroote et al. (2010) claimed the presence of solar-like oscillations in the CoRoT light curve of HD 46149. However, it is currently not possible to attribute these oscillations to the late O-type primary or to the early B-type secondary star of the binary system. Another intensive asteroseismological activity is also detected from the CoRoT light curve of HD 46202 (Briquet et al., in prep).

However, from a general point of view, all O-type stars in the sample observed by CoRoT are affected by the presence of red noise. The parallelism with the helioseismology could indicate that this red noise is linked to something similar to granulation. The work of Cantiello et al. (2009) suggested that a sub-surface convection zone, induced by the iron opacity bump, could affect the stellar surface behaviour through, e.g., the microturbulence or the clumping and could be responsible for the red noise. Furthermore, Belkacem, Dupret, & Noels (2010) suggested that this convection zone could generate stochastically excited oscillations in massive stars.

We have established a first preliminary theoretical asteroseismological analysis of HD 46223. We have determined an error box (Fig. 2) on the HR diagram from the stellar parameters derived with the CMFGEN code (Hillier & Miller 1998, Table 1). Several models have been computed using the ATON evolution code (Ventura, D'Antona, & Mazzitelli 2008) to determine the possible existence of excited modes in this star. Among the 17 different models (red crosses in Fig. 2), computed in the error box, only two present excited modes. If we consider the associated frequencies (Fig. 3), we should detect frequencies close to 4 d^{-1} and 12 d^{-1}. However, no outstanding peak is visible around these frequencies in the semi-amplitude spectrum (Fig. 4) of HD 46223, which implies that this star

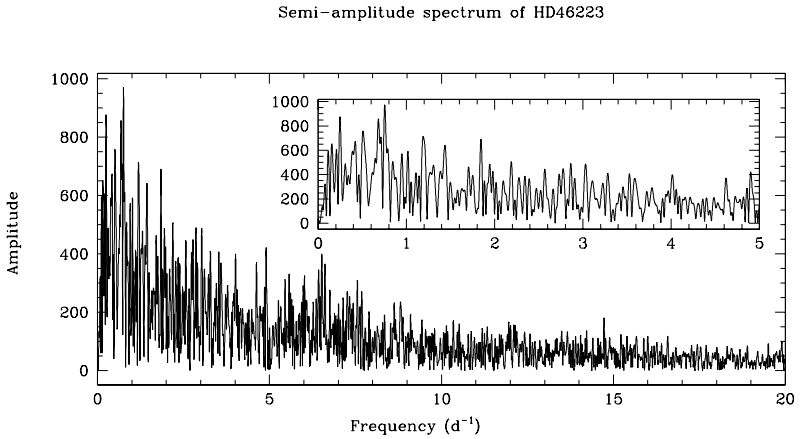

Figure 4: Semi-Amplitude spectrum of the CoRoT light curve of HD 46223 computed with the Heck, Manfroid & Mersch method (Heck, Manfroid, & Mersch 1985; revised by Gosset et al. 2001). The inset shows a zoom-in on the low-frequency domain.

would only be affected by red noise. However, we present here only preliminary results of the analysis of these CoRoT data. A more detailed analysis will be presented in a forthcoming paper (Blomme et al., in prep).

Acknowledgements

This research is supported by the FNRS (Belgium), by a PRODEX XMM/Integral contract (Belspo) and by the Communauté Française de Belgique-Action de Recherche Concertée (ARC)-Académie Wallonie-Europe. We acknowledge the Ministère de l'Enseignement Supérieur et de la Recherche de la Communauté Française for supporting our travels to O.H.P. We also thank the staff of Observatoire de Haute-Provence and of La Silla ESO Observatory for their technical support. F.M. thanks John Hillier for making his code available and for assistance. P.E. acknowledges support through CONACyT grant 67041.

References

Auvergne, M., Bodin, P., Boisnard, L., et al., 2009, A&A, 506, 411
Belkacem, K., Dupret, M. A., & Noels, A., 2010, A&A, 510, A6
Cantiello, M., Langer, N., Brott, I., et al., 2009, A&A, 499, 279
Chen, L., de Grijs, R., & Zhao, J. L., 2007, AJ, 134, 1368
Degroote, P., Briquet, M., Auvergne, M., et al., 2010, A&A, 519, A38
Fullerton, A. W., Gies, D. R., & Bolton, C. T., 1996, ApJS, 103, 475
Garcìa, B., & Mermilliod, J. C., 2001, A&A, 368, 122
Gosset, E., Royer, P., Rauw, G., et al., 2001, MNRAS, 327, 435
Heck, A., Manfroid, J., & Mersch, G., 1985, A&AS, 59, 63
Hensberge, H., Pavlovski, K., & Verschueren W., 2000, A&A, 358, 553
Hillier, D. J., & Miller, D. L., 1998, ApJ, 496, 407
Mahy, L., Nazé, Y., Rauw, G., Gosset, E., De Becker, M., Sana, H., & Eenens, P., 2009, A&A, 502, 937
Meynet, G., & Maeder, A., 2003, A&A, 404, 975
Ogura, K., & Ishida, K., 1981, PASJ, 33, 149
Sana, H. & Evans, C. J., 2011, IAUS 272, in press (arXiv:1009.4197)
Sana, H., Gosset, E. & Evans, C. J., 2009, MNRAS 400, 1479

Ventura, P., D'Antona, F., & Mazzitelli, I., 2008, Ap&SS, 316, 93
Wang, J., Townsley, L. K., Feigelson, E. D., Broos, P. S., Getman, K. V., Román-Zúñiga, C. G., & Lada, E., 2008, ApJ, 675, 464

Discussion

W.R. Hamann: I am really excited by your discovery of "red noise" as an indication of granulation on O star surfaces. The iron opacity bump, which is expected from theory to cause an outer convection zone, also plays an important role for initiating radiation-driven winds. Therefore I think that both phenomena - convection and wind initialization - are in fact closely interwoven, although we don't have an idea how this looks like in detail.

S. Heap: How did you distinguish between physical red noise and instrumental red noise?
L. Mahy: We have just assumed that the instrumental noise has to be the same for all the stars in the field of view of the CoRoT satellite. However, all the CoRoT light curves of O stars have a different trend which tends to favor the physical red noise and not an instrumental one.

The massive binary population of the starburst cluster Westerlund 1*

B.W. Ritchie[1], J.S. Clark[1] and I. Negueruela[2]

[1] Department of Physics and Astronomy, The Open University, Walton Hall, Milton Keynes, U.K.
[2] Departamento de Física, Ingeniería de Sistemas y Teoría de la Señal, Universidad de Alicante, Apdo. 99, 03080 Alicante, Spain

Abstract: We present initial results from a long-baseline radial velocity survey for massive binaries in the cluster Westerlund 1. Four systems are examined: the dust-producing WC binary W239, the double-lined eclipsing binary W13, and the single-lined B0 supergiants W43a and W3003. Finally, the evolutionary implications for the population of massive stars in Westerlund 1 are discussed.

1 Introduction

The galactic starburst cluster Westerlund 1 (hereafter Wd1; Westerlund 1987; Clark et al. 2005) contains a rich, coeval population of massive stars that trace both the hot (OB supergiant, Wolf-Rayet) and cool (yellow hypergiant, red supergiant) phases of post-Main Sequence evolution. Motivated by X-ray, infra-red and radio observations that show Wd1 to be binary-rich (Crowther et al. 2006; Clark et al. 2008; Dougherty et al. 2010), we have undertaken an intensive multi-epoch radial velocity (RV) survey of Wd1 in order to obtain a census of massive binaries amongst both the highly-luminous transitional supergiants and the lower-luminosity stars just evolving off the main sequence. In these proceedings we discuss four massive binary systems identified by our survey, along with the possible implications of these objects for binary-mediated evolution in Wd1.

2 Observations

A list of targets discussed here is given in Table 1. With the exception of W3003, which is a newly-identified cluster member (Ritchie et al. 2009a), designations are from Westerlund (1987); alternate *WR* designations for the Wolf-Rayet population from Clark & Negueruela (2002) and Crowther et al. (2006) are also given in the text where appropriate. Data were obtained on 11 nights between 20/06/2008 and 20/08/2009, using the FLAMES multi-object spectrograph on VLT UT2 *Kueyen* at Cerro Paranal, Chile. Setup HR21 was used to cover the 8484-9001Å range with a resolving

*Based on observations collected at the European Southern Observatory under programmes ESO 81.D-0324 and 383.D-0633

Table 1: List of targets.

ID	Spectral Type	Period (days)	RA (J2000)	Dec (J2000)	R[a]	I[a]	Notes[b]
W13	B0.5 Ia$^+$+OB	9.27	16 47 06.45	-45 50 26.0	14.63	12.06	X, E
W43a	B0 Ia	16.27	16 47 03.54	-45 50 57.3	15.22	12.26	A
W239 (F)	WC9d	6.5	16 47 05.21	-45 52 25.0	15.39	12.90	X, A
W3003	B0 Ib	11.12	16 47 11.60	-45 49 22.4	16.21	13.31	A

[a]Photometric *R* and *I*-band magnitudes are taken from Clark et al. (2005) or Bonanos (2007).
[b]**X**-ray sources (Clark et al. 2008), **E**clipsing or **A**periodic variables (Bonanos 2007).

power ∼16200; target selection, data acquisition and reduction are described in detail in Ritchie et al. (2009a).

Radial velocities were measured by fitting Gaussian profiles to the cores of strong absorption and/or emission lines using the IRAF *ngaussfit* routines, with the derived velocity an error-weighted average of individual lines. The Paschen 11-15 lines were used to obtain radial velocities for W13, W43a and W3003, with the Pa16 λ8502 line that also falls within our coverage excluded due to blending with an adjacent C III λ8500 line that strengthens rapidly at B0.5 and earlier (Negueruela, Clark & Ritchie 2010). In the case of the dusty Wolf-Rayet W239 (WR F; Clark & Negueruela 2002), strong C III $\lambda\lambda$8500, 8664 emission lines were used for radial velocity measurement (see Clark et al. 2010). A well-defined diffuse interstellar band (DIB) at ∼8620Å provides a serendipitous check for zero-point errors in our data, with spectra showing epoch-to-epoch variability of well under 1 km s^{-1}.

3 Results

3.1 The double-lined eclipsing binary W13

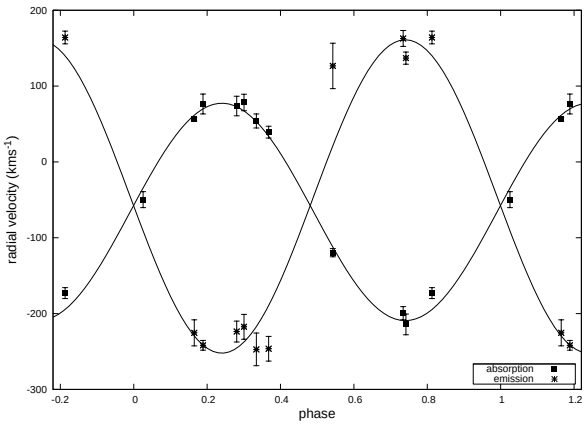

Figure 1: RV curve for the double-lined eclipsing binary W13. T_0 is at MJD=54643.080, which corresponds to the eclipse of the B0.5Ia$^+$ emission-line star.

W13 was identified as an eclipsing binary system by Bonanos (2007), with Ritchie et al. (2009a, 2010) finding it to be a double-lined system consisting of a peculiar O9.5-B0.5 supergiant and an B0.5 Ia$^+$ emission-line object. The strong similarities in spectral morphology between W13, the

WN9h star W44 (WR L) and the WN10-11h star W5 (WR S) suggest that the B0.5 Ia$^+$ star is an immediate evolutionary precursor to the Wolf-Rayet phase, although the weakness of the He I emission lines and absence of N II λ6611 emission make it the least-evolved member of the WNL population in Wd1.

Results from our full FLAMES dataset presented by Ritchie et al. (2010) show W13 to have an orbital period of 9.2709±0.0015 days, with lower limits for the masses of the emission-line object and supergiant companion of $21.4 \pm 2.6 M_\odot$ and $32.8 \pm 4.0 M_\odot$ respectively, rising to $23.2^{+3.3}_{-3.0} M_\odot$ and $35.4^{+5.0}_{-4.6} M_\odot$ for our best-fit inclination 62^{+3}_{-4} degrees. The evolved state, short orbital period and near-contact configuration all suggest strong interaction during the evolution of the system, with comparison with the evolutionary models of Petrovic, Langer & van der Hucht (2005) suggesting highly non-conservative late-Case A/Case B mass transfer and an initial mass for the emission-line object of $\sim 40 M_\odot$. This implies that the magnetar CXOU J164710.2-455216 formed from an even more massive progenitor, with close binary evolution apparently instrumental in shedding sufficient mass to avoid formation of a black hole (Clark et al. 2008; Ritchie et al. 2010).

3.2 The WC9d binary W239 (WR F).

The dust-forming WC9 star W239 (WR F) was noted by Ritchie et al. (2009a) as showing RV changes consistent with binarity, and our full FLAMES dataset confirms a period of ∼6.5 days and a semi-amplitude of ∼45 km s^{-1} that is consistent with a WR+O binary viewed at i∼10–20°. W239 shows strong near-mid IR excess and dilute K-band spectrum, both indicative of hot circumstellar dust (Crowther et al. 2006). However, the ∼6.5d orbital period is a factor of ∼5 shorter than any other known dust-forming WC star, and implies likely Case A or contact evolution in a very close binary (∼4 days) with subsequent wind-driven mass loss widening the orbit (Petrovic et al. 2005). W239 is examined in detail by Clark et al. (2010).

3.3 The B0 supergiant binaries W43a and W3003.

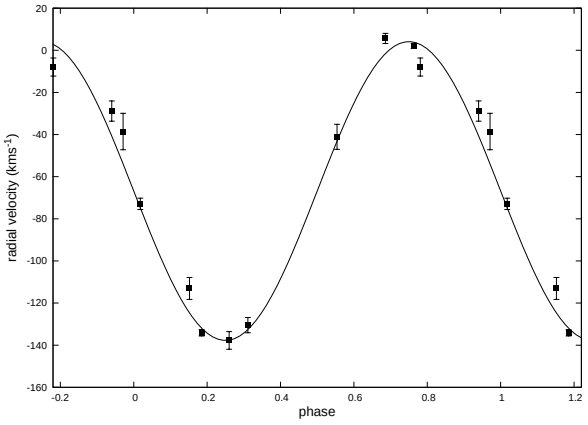

Figure 2: RV curve for the single-lined binary W43a (B0 Ia), with T_0 corresponding to the start of our observations at MJD=54646.185

W43a (B0 Ia; Negueruela et al. 2010) displays an unremarkable R-band spectrum with weak wind emission lines from Hα and C II, and He I in absorption. The star is not detected at X-ray or radio wavelengths (Clark et al. 2008, Dougherty et al. 2010), and no eclipses are apparent in the photometry of Bonanos (2007). Nevertheless, the I-band FLAMES data reveal significant RV changes on a timescale of a few days, although no indication of a companion is seen in the spectrum. A fit to

eleven epochs of RV data gives a period of 16.266 ± 0.005 days, a semi-amplitude of 71 ± 6 km s^{-1} and a systemic velocity of -67 ± 4 km s^{-1}; the latter is somewhat blueshifted with respect to other members of Wd1, but this effect is seen also in the OB supergiant companion in W13 and discrepant systemic velocities are commonly observed in early-type spectroscopic binaries (see Ritchie et al. 2010 and refs. therein).

The B0 Ib supergiant W3003 (Ritchie et al. 2009a), located to the north-east of the cluster, appears a similar system to W43a. Our RV data find a period of 11.12 ± 0.01 days and a slightly eccentric orbit ($e \lesssim 0.05$), with a systemic velocity of -39 ± 8 km s^{-1} and a semi-amplitude of 38 ± 5 km s^{-1}. Once again, no indications of binarity are found in other observations[3]. These two supergiants are therefore of interest as the first examples that previous estimates of the binary fraction of Wd1 based on the signature of colliding-wind systems (in which *both* components must be sufficiently massive to support a powerful stellar wind) are incomplete. In the case of W43a, assuming a $\sim$35M$_\odot$ primary and an inclination of $\sim$35–45° implies a main sequence secondary with a mass $\sim$15–21M$_\odot$; lower inclinations would suggest a higher-mass secondary that should be directly visible in our spectra, while higher inclinations would result in a detectable eclipsing system. Similarly, the low semi-amplitude of W3003 suggests either a very low inclination and/or a low-mass companion. The intrinsic X-ray luminosity of individual OB supergiants in Wd1 ($L_x \lesssim 10^{32}$ erg s^{-1}; Clark et al. 2008) is insufficient for direct detection, and unequal-mass OB supergiant+main sequence binaries such as W43a and W3003 will lack the strong wind interaction required to significantly raise their X-ray luminosities. Neither system is expected to have begun strong binary interaction, but once shell burning commences the primary will rapidly lose its Hydrogen envelope via Case B mass transfer, leaving a WR+O binary with an orbital period of a few weeks (Petrovic et al. 2005).

4 Evolutionary implications

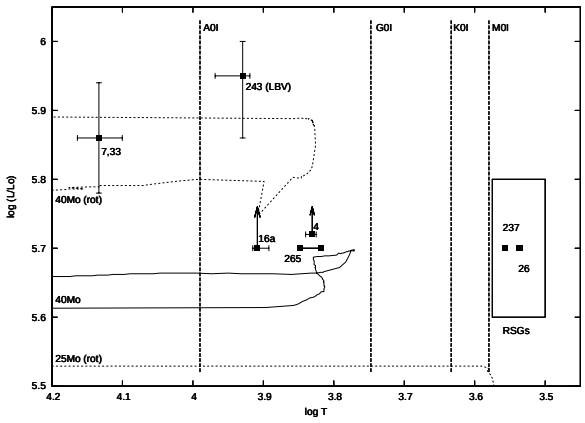

Figure 3: Location of luminous hypergiants and red supergiants in Wd1 compared to evolutionary tracks with and without rotation (Meynet & Maeder 2003).

The OB supergiant population of Wd1 suggests a single burst of star formation lasting less than 1 Myr and a cluster age of $\sim$5 Myr (Negueruela et al. 2010). The $\sim$40M$_\odot$ main sequence mass of the emission-line object in W13 and lack of evidence for significant non-coevality in the cluster therefore suggests that the ten highly-luminous B5-F8 Ia$^+$ hypergiants in Wd1 all evolved from progenitors with $M_{\rm ini} \gtrsim$35M$_\odot$. Although these objects appear to be in good agreement with evolutionary tracks

[3]Both W43a and W3003 are identified as aperiodic variables in the photometry of Bonanos (2007), but this likely reflects pulsational instability seen in all stars later than $\sim$B0 in Wd1 (Ritchie et al. 2009a).

including rotation (Meynet & Maeder 2003), these models do not predict further evolution to the red supergiant (RSG) phase for stars in this mass range. In contrast, the transitional population in Wd1 also contains four RSGs (see Figure 3), while the early-A LBV W243 (Ritchie et al. 2009b) also displays nitrogen enrichment and oxygen and carbon depletion suggestive of CNO-processed material 'dredged up' during a previous RSG phase.

Lack of contemporaneous spectroscopy and photometry means that the luminosities of the Wd1 RSGs are somewhat uncertain, although the spectral types, derived from TiO bandhead strengths, are secure. Estimates of the luminosity of the RSG W26 (M1–6 Ia) suggest $\log(L/L_{\odot})\sim5.8$, and a consequent radius possibly as large as $\sim$2000 $R_{\odot}$, while non-LTE modelling of the LBV W243 yields $R \sim 450(d/4.5\mathrm{kpc})$ $R_{\odot}$. Such objects are clearly incompatible with close binary evolution channels in which stars are separated by $\lesssim 100$ $R_{\odot}$, and the distribution of Wolf-Rayets and cool hypergiants in Wd1 therefore hints at a split evolutionary sequence in which the close binary population undergo strong interaction as the primary evolves off the main sequence, becoming WR+O binaries like W13 and W239, while isolated (or long-period binary) stars become B–F hypergiants en route to the RSG phase. Further observations of the transitional hypergiant, RSG and Wolf-Rayet populations will allow this hypothesis to be tested directly, and this topic is explored further in Clark et al. (2010).

Acknowledgements

We thank the referee for a thorough reading of this manuscript and helpful comments.

References

Bonanos, A.Z., 2007, AJ, 133, 2696
Clark J.S. & Negueruela, I., 2002, A&A, 396, L25
Clark J.S., Negueruela I., Crowther P.A. & Goodwin, S.P., 2005, A&A, 434, 949
Clark J.S., Muno M.P., Negueruela I., et al., 2008, A&A, 477, 147
Clark J.S., Ritchie B.W., Negueruela I., et al., 2010, A&A, submitted
Crowther P.A., Hadfield L.J, Clark J.S., et al., 2006, MNRAS, 372, 1407
Dougherty S.M., Clark J.S., Negueruela I., et al., 2010, A&A, 511, A58
Meynet, G. & Maeder, A., 2003, A&A, 404, 975
Negueruela I., Clark J.S. & Ritchie B.W., 2010, A&A, 516, A78
Petrovic J., Langer N. & van der Hucht, K.A., 2005, A&A, 435, 1013
Ritchie B.W., Clark J.S., Negueruela, I. & Crowther, P.A., 2009a, A&A, 507, 1585
Ritchie B.W., Clark J.S., Negueruela, I. & Najarro, F., 2009b, A&A, 507, 1597
Ritchie B.W., Clark J.S., Negueruela, I. & Langer, N., 2010, A&A, 520, A48
Westerlund, B.E., 1987, A&AS, 70, 311

Discussion

A. Lobel: Radial velocity changes are often hard to measure in emission lines because the lines are so broad. Do you observe the entire emission line core to shift? Are there profile changes in the emission lines of the binaries?

B. Ritchie: Although the emission lines can be very broad (Hα, for example, has a FWHM of $\sim 500\,\mathrm{km\,s^{-1}}$) the higher Paschen series emission lines are relatively narrow and well defined. We see shifts in the entire emission line profile, with two spectra taken at phase 0.32 – 0.33 showing very little variability in profile despite being separated by 45 orbits (417 days). The consistency of line

profiles can be seen in Figure 1 of Ritchie et al. (2010).

G. Meynet: Can we imagine, is it reasonable, that at least some of the red supergiants which are observed in Wd1 are some kind of disguised red supergiants, in the sense that they would be yellow supergiants having undergone an outburst making the star to be surrounded by an opaque extending and dusty envelope?
B. Ritchie: Long-term observations ($>$ 5 yr) of Westerlund 1 are sparse, but the RSGs appear to be a long-lived phase (at least, in the canonical YHG outburst sense) and the same objects are identified as RSGs in the observations of Westerlund (1961, 1987) and Koorneef (1977).
An outburst scenario from evolved YHGs or BHGs/LBVs is hard to rule out, but these objects appear to be bona fide RSGs; see further discussion in Clark et al. (2010).

The peculiar O9.5V star BD+53°2790, the massive counterpart to the X-ray binary system 4U 2206+54

Pere Blay[1] and Víctor Reglero[1]

[1] IPL, University of Valencia, PO BOX 22085, 46071 Valencia, Spain

Abstract: The X-ray binary system 4U 2206+54 hides many mysteries. Among them, the surprising behavior of both of its components: the O9.5 dwarf star BD+53°2790 and a slowly rotating neutron star. BD+53°2790 misled the astronomers, exhibiting characteristics reminiscent of Be stars. However, a deeper spectral analysis and more intense monitoring revealed that the real picture was a bit more complicated: a) Although it shows evidence of a circumstellar envelope, its observable properties differ from those typical of envelopes in Be stars. b) Comparison with spectral standards and models indicates a possible over-abundance in He. This would open the possibility to link the behavior of BD+53°2790 to the He-rich class of stars. c) UV spectra show an abnormally slow and dense wind for an O9.5V star. d) Spectral classification in the IR wavelength region suggest a more likely supergiant nature of the source, in contradiction with the optical classification. e) The presence of an intense magnetic field is under investigation. BD+53°2790 stands as a perfect laboratory for testing stellar structure, as well as wind and evolutionary theories. The observable properties of this source in a wide range of spectral bands are discussed, and some interpretations outlined.

1 Introduction

X-ray binary systems consist of two stellar bodies orbiting each other and emitting high energy photons as the result of mass transfer from one onto the other. BD+53°2790 is the massive companion of one of such systems, namely 4U 2206+54. Although initially BD+53°2790 was mis-classified as a Be star, Negueruela & Reig (2001) and Blay et al. (2006) show reasons to discard this classification and suggest that BD+53°2790 is instead a very peculiar main sequence O9.5 star. We will briefly review its peculiarities, from a wide point of view only achieved with a multiwavelength approach. In X-ray binary systems, each part of the electromagnetic spectrum gives us information from a very specific part of the system. While optical data show us what kind of massive companion is contained in 4U 2206+54, as well as its stellar parameters and properties, infrared data indicate the properties of the very close neighborhood of this massive star, UV bands tell us how the mass-transfer takes place, and high energy and radio data helps to unveil what kind of accretor is hosting 4U 2206+54. Only a complete multiwavelength approach will help to comprehend BD+53°2790 and its compact companion.

2 High energy data: The compact companion

X and γ-ray measurements lead to the conclusion that 4U 2206+54 hosts a neutron star. Its pulse period has only been determined recently, by Reig et al. (2009) and Finger et al. (2010), to be 5560s. It is one of the longest pulse periods for a High Mass X-ray Binary System (HMXRB). INTEGRAL detection of the pulse period is shown on the two plots of Figure 1. The high energy light-curve of 4U 2206+54 (Figure 2) is reminiscent of that of a HMXRB hosting a supergiant star and a wind-fed accreting compact companion (see Ribó et al. 2006).

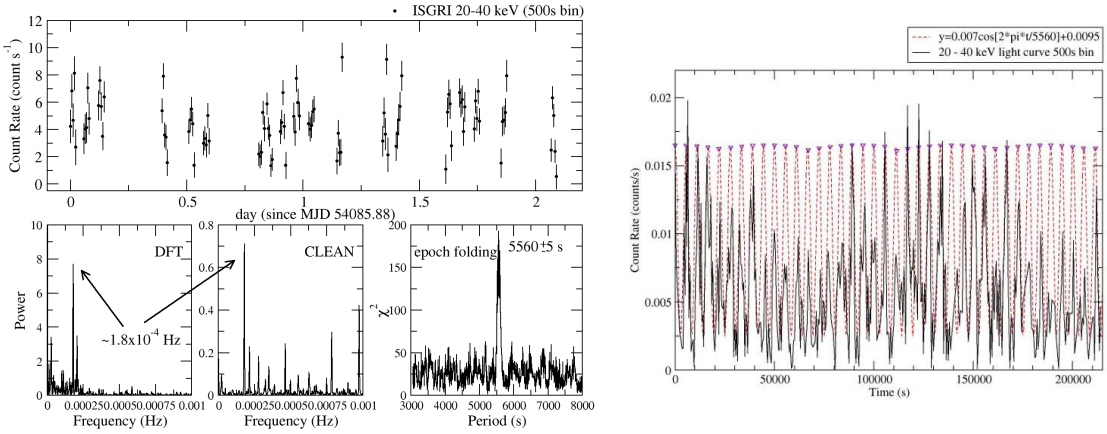

Figure 1: Left panels: 500s binned light curve (upper plot) and periodograms (lower plots) showing the pulse period detection from 4U 2206+54 by INTEGRAL/ISGRI data in the 20-40 keV energy range. A clear periodic variation at $1.8\,10^{-4}$ Hz (5560s) is shown. Right panel: Pulsed emission from 4U 2206+54 compared to a sinusoidal-like variation with a 5560s periodicity. The irregularity of the pulse profile is evident and striking.

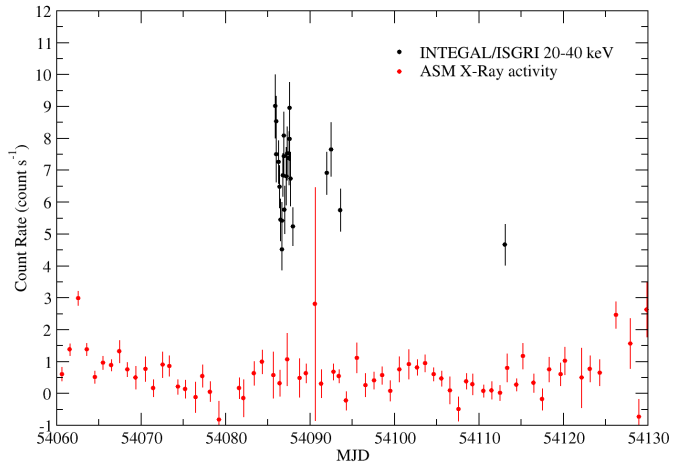

Figure 2: X-ray light curve of 4U 2206+54 in the 2-10 keV (RXTE/ASM) and 20-40 keV (INTEGRAL/ISGRI) energy ranges. The flaring-like variability typical of wind fed HMXRBs is shown in both energy ranges.

Although a 9.56d periodicity was previously considered as the orbital period of the system (see Ribó et al. 2006), more recent high energy data indicate that most likely the orbital period is almost double this value, namely 19.25d (see Corbet, Markwardt, & Tueller 2007).

3 UV data

There are very few data in the UV range for BD 53°2790. Two low resolution and one high resolution spectra are available in the IUE (International Ultraviolet Explorer) database. They are described in

detail in Negueruela & Reig (2001) and Blay, Ribó & Negueruela (2009). Ribó et al. (2006) found that the stellar wind from BD+53°2790 was slower and denser than expected for a O9.5V star. However, this peculiar wind could explain the observed behavior in the X-ray ranges if wind-fed accretion takes place in an moderately eccentric (e∼0.15) orbit.

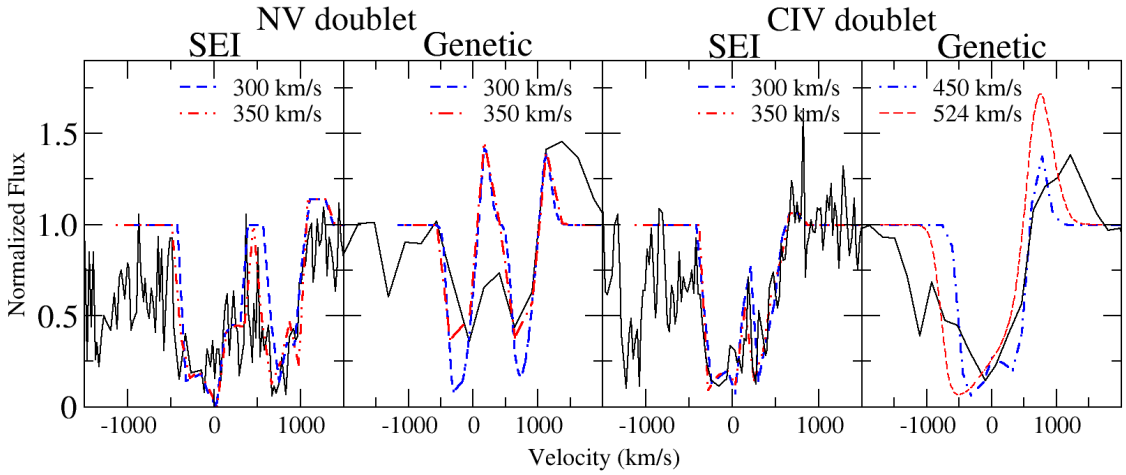

Figure 3: Fit to the observed N V and C IV doublets profiles by using a genetic algorithm and the SEI code as explained in the text. All fits yield terminal wind velocities in the range 300-500 kms^{-1}. The two fits shown in each plot represent the lower and upper limits of the range of possible solutions (see Ribó et al. 2006).

Figure 3 shows the result of fitting the IUE high resolution spectrum by using the SEI code (Sobolev with Exact Integration, Lamers, Cerruti-Sola & Perionotto 1987) and a genetic algorithm developed by Georgiev & Hernández (2005). Terminal wind velocities in the range 300-500 kms^{-1} are found, as explained in more detail in Ribó et al. (2006) and Blay et al. (2009).

4 Optical data: a very intriguing star

Negueruela & Reig (2001) and Blay et al. (2006) describe the optical peculiarities of BD +53°2790. The adopted spectral type and luminosity for this massive star are O9.5Vp. There are still some peculiarities to be explained in the optical spectra of BD +53°2790: a) the presence of metallic lines which is reminiscent of those of later types (see Negueruela & Reig 2001); b) when compared to standard stars of the same or very similar spectral type, BD +53°2790 seems to be overabundant in He (Blay et al. 2006 suggest the possibility to link BD +53°2790 to the group of He-rich stars). When comparing the He profiles to those of standard stars which are broadened rotationally, a rotational velocity of 315 kms^{-1} is found for this object. Figure 4 depicts the variability of the Hα line. Although the double peaked profile is always present, with the red peak always higher than the blue one, the variability is evident on short and long time scales. V magnitude variability is shown in Figure 5. The average V magnitude remains fairly constant over time, but on shorter time scales it is clearly variable, with no coherent variability detected so far.

5 IR data: the circumstellar environment

Infrared magnitudes and colors obtained during a long-term monitoring campaign (1987-2001) are described and analyzed in Blay et al. (2006). No coherent variability is shown by the IR data. However

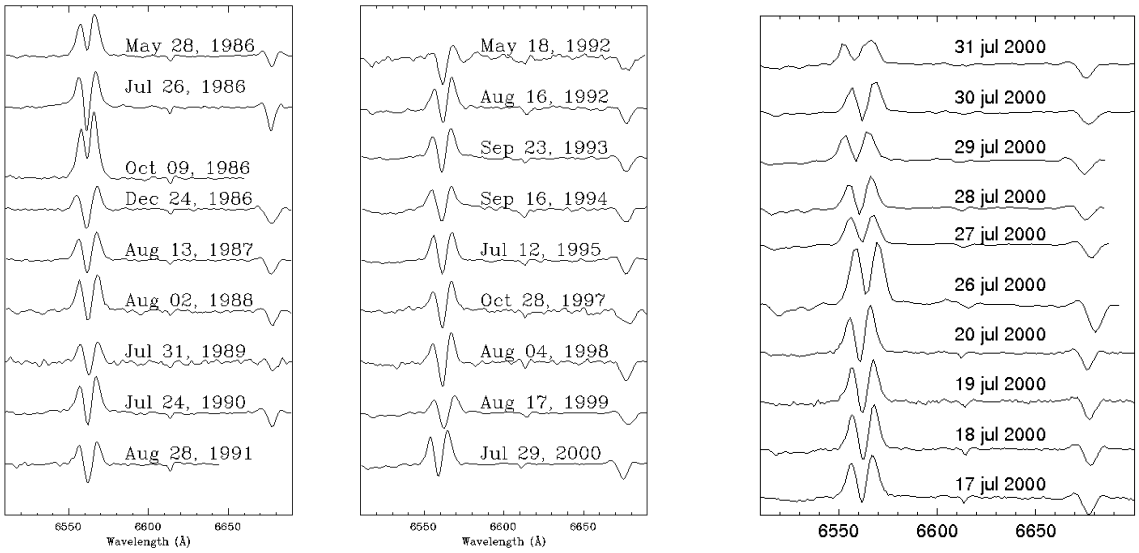

Figure 4: Hα line variability on long time scales (left panels) and shorter time scales (right panel). See Blay et al. (2006).

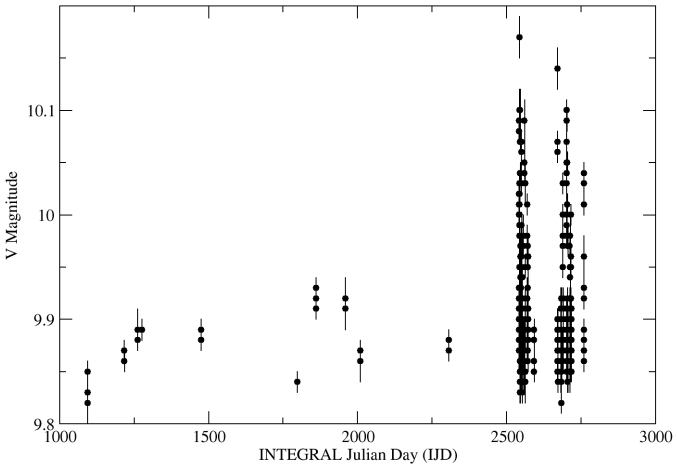

Figure 5: V magnitude observations of the OMC (Optical Monitoring Camera) on board the high energy satellite INTEGRAL. The OMC works in the V filter range. Large amplitude variability is seen at some epochs, however, in the long term, the V magnitude average remains fairly constant.

a long-term trend seems to be present in the J and H magnitudes, but not shared by the K magnitude. On the other hand, as shown in Figure 6, the (J-H), (J-K) and (H-K) colors show a long-term trend which seems to be correlated with RXTE/ASM X-ray data (in the 2-10keV energy range) in the case of the two former colors, but not so well correlated when the latter colour is considered. This is an indication that X-ray emission could be proportional to the IR excess, i.e., to the amount of available circumstellar matter. Spectroscopic classification in the IR band indicates a more evolved nature of BD+53°2790 (see Negueruela & Reig, 2001).

6 Radio data: as expected for a neutron star.

Radio emission from 4U 2206+54 was analyzed in Blay et al. (2005). An image was obtained with the VLA at 8.4 GHz after concatenation of observations from 2 runs during May 2003, with no radio emission detected at a significant level. According to Gallo, Fender & Pooley (2003) the presence of a Black Hole would imply radio emission in the 4-15 GHz frequency range. As stated by Blay et al. (2005), the expected radio emission from 4U 2206+54 (if hosting a black hole) would be 60 times greater than the 3σ upper limit given by the VLA observation.

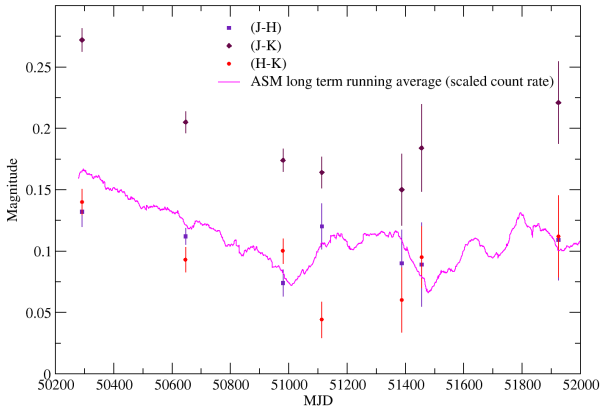

Figure 6: Comparison of the long term IR colours (J-H), (J-K) and (H-K) with the long-term trend of the RXTE/SAM count rate as a running average over 300 days. RXTE/ASM count rate has been scaled for plotting purposes.

7 Conclusions

Given the peculiarity of both of its components, 4U 2206+54 shows up as a unique type of X-Ray binary system. There are only two known High Mass X-Ray Binary systems showing wind-fed accretion from a main sequence star. One of them is 4U 2206+54, the other system is the microquasar LS 5039, which hosts a black hole and a O6.5V star. These systems are of great importance as they are presumably the progenitors of Supergiant HMXRBs. 4U 2206+54 also shows similarities with the supergiant systems 2S 0115+54, which also hosts a slowly rotating Neutron Star (2.78 h), and IGR J16358-4726, with a 1.6 h X-ray pulsar. BD+53°2790 is a very active peculiar star, possibly belonging to the class of He rich stars. It very likely hosts a magnetically driven equatorial disk-like envelope, but its existence is still to be confirmed by the detection of intense magnetic field, by magnitude variations modulated by its rotational motion, or both.

Acknowledgements

This research is supported by the Spanish MCINN, poject 20071152/ASIM-GRI. This work is a compilation of the results from the collaboration with I. Negueruela, P. Reig, M. Ribó and a large number of observers.

References

Blay, P., Ribó M., Negueruela, I., Torrejón, J. M., Reig, P., Camero, A., Mirabel, I. F., & Reglero, V., 2005, A&A, 438, 963

Blay, P., Negueruela, I., Reig, P., Coe, M. J.,; Corbet, R. H. D., Fabregat, J., & Tarasov, A. E., 2006, A&A, 446, 1095

Blay, P., Ribó, M.,& Negueruela I., 2009, Ap&SS, 320, 145

Corbet, R.H.D., Markwardt, C.B., & Tueller, J. 2007, ApJ, 655, 458

Finger, Mark H., Ikhsanov, Nazar R., Wilson-Hodge, C. A., & Patel, S. K., 2010, ApJ, 709, 1249

Gallo, E., Fender, R.E., & Pooley, G.G., 2003, MNRAS, 344, 60

Georgiev, L., Hernández, X., 2005, RMAA, 41, 121

Lamers, H.J.G.L.M., Cerruti-Sola, M., & Perionotto, M., 1987, ApJ, 314, 726

Negueruela, I., & Reig, P., 2001, A&A, 371, 1056

Reig, P., Torrejón, J. M., Negueruela, I., Blay, P., Ribó, M., & Wilms, J., 2009, A&A, 494, 1073

Ribó, M., Negueruela, I., Blay, P., Torrejón, J. M., & Reig, P., 2006, A&A, 687, 698

Cyg OB2 Unveiled: The Search for Astrometric Companions

S. M. Caballero-Nieves[1], D. R. Gies[1], L. C. Roberts[2], and N. H. Turner[3]

[1] Georgia State University, Atlanta, GA, USA
[2] JPL/California Institute of Technology, Pasadena, CA, USA
[3] GSU CHARA Array, Mount Wilson, CA, USA

Abstract: We present results from a high angular resolution survey of the most massive stars in the nearby Cygnus OB2 association. Using the NIRI instrument and ALTAIR AO system on Gemini North, we obtained J, H and K band observations of 75 O- and B-type association members to search for astrometric companions. This search is sensitive to companions in the separation range of 0.08 - 10″ with a magnitude difference less than 11 mag. The detected sample begins to fill in the period gap between astrometric and spectroscopic binaries. From photometric colors, we find that many of these companions appear to be very young, red stars. Using a statistical method to estimate field contamination, 42% of our targets have at least one highly probable companion.

1 Introduction

Massive stars have a higher frequency of multiplicity than cooler, less massive stars, especially when they are found in clusters (Mason et al. 2009). At a distance of 1.7 kpc (Massey & Thompson 1991), Cygnus OB2 provides a nearby, young stellar environment, rich in high-mass stars. The association is close enough, that with modern-day adaptive optics (AO), we are able to resolve wide companions. Due to extinction towards the cluster, the cluster begins to be unveiled in the infrared (IR).

2 Observations

Our observations were part of three queue observing programs at the Gemini North Observatory during the 2005B, 2008A and 2008B semesters. Using the Near Infrared Imager and Spectrograph (NIRI) with the Altair AO system, we collected high resolution images (0.022″/pixel) of 75 O- and B-type stars in Cyg OB2 with a field of view of approximately $22'' \times 22''$ (Hodapp 2003). Every target was observed in the K-band to detect possible companions. Most of those with a star detected in the field were followed up with J-band observations. The seven targets observed during the 2005B semester were also imaged in the H-band.

In addition to the NIRI K-band observation, MT421, was observed with the Palomar High Angular Resolution Optics (PHARO) AO system on the 200-in Hale telescope during an engineering night in

2009 July. We were able to get observations in all three IR bands, J, H, and K_S, with a comparable field of view as NIRI.

3 Results

In every K-band frame, we identified at least one candidate companion near our target. We determined that 32 out of our 75 targets or 42% have at least one statistically probable companion. The statistical probability for each object was calculated using the Correia et al. (2002) equation:

$$P(\Sigma_K, \Omega) = 1 - e^{-\pi \Sigma_K \Omega^2} \quad (1)$$

Here P is the probability of a star being a chance alignment at a separation of Ω, in arcseconds, from the target. Σ_K is the surface density of stars in the surrounding field down to a magnitude of K. The stellar field density was determined using a combination of data from 2MASS (Skrutskie et al. 2006) and UKIDSS (Lawrence et al. 2007). A star with $P(\Sigma_K, \Omega) < 0.01$ has a very high probability of being a physical companion. In Table 1 we list the number of stars found with $P(\Sigma_K, \Omega) < 0.01$. Of note are MT465 and WR145 that have more companions in the Washington Double Star Catalog (WDS; Mason et al. 2001) than we detected in our study. This is due to the fact that the additional companions detected in the WDS fall outside our field.

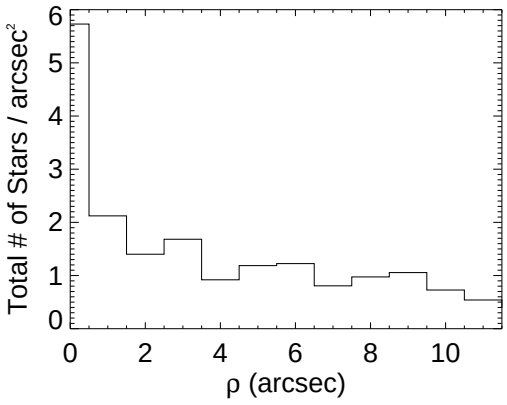

Figure 1: The graph shows how the number density of stars falls with angular separation but levels off at larger distances. At a distance of $1.7kpc$, the distance to Cyg OB2, $1''$ corresponds to a projected size of $121AU$.

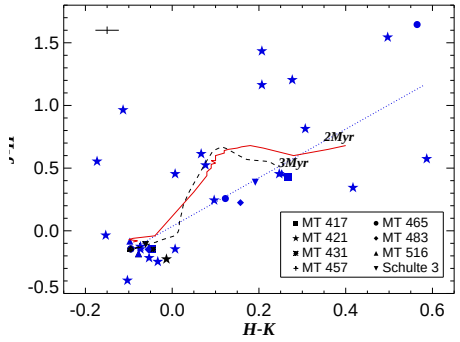

Figure 2: Intrinsic color-color diagram of a few of our targets and their companions (blue symbols), dereddened according to estimates from Negueruela et al. (2008). Overlaid are a ZAMS isochrone at 3 Myr (dashed, black line) from Girardi et al. (2006), a Pre-MS track at 2 Myr (solid, red line) from Siess et al. (2000) and standard reddening vector (dotted, blue line) from Fitzpatrick (1999), the length shows the amount of extinction for $E(B-V) = 4$ mag. Top left is a representative error bar.

In Figure 1 we show the number density of the entire sample over square area as a function of separation. At larger separations, the density levels off. This very likely corresponds to the average number density of the association. Stars found at these separations are more likely to be chance alignments (see above equation). The number density per area increases greatly with $\rho < 1''$ and stars found within this separation are more likely to be physical companions.

Cyg OB2's high content of massive stars indicates that it is a relatively young association. The color-color diagram (Fig. 2) plots the intrinsic color in JHK of eight of our targets and their respective companions. Overlaid are a 2 Myr Pre-Main Sequence track (Siess, Dufour & Forestini 2000) and a 3 Myr Zero-Age Main Sequence isochrone (Girardi et al. 2006). In determining the intrinsic color, we assumed that all stars in a frame were at the same distance and had the same reddening as the target star. The empirical data follows the Fitzpatrick (1999) reddening vector (dotted blue line) but the fact that we see a large scatter implies that our assumption might not be true for all the stars in the field. This may be due to circumstellar reddening for young stars or they may be foreground objects or reddened early type stars. Further color and spectroscopic information is needed to determine the nature of these objects. However, the position of the target stars with respect to the isochrones indicates that these stars are at the same distance, young and coeval.

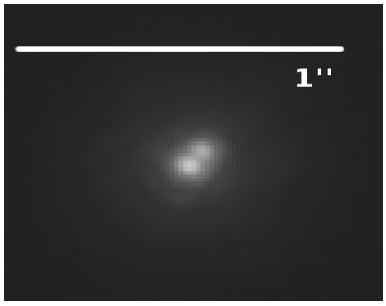

Figure 3: NIRI AO, K-band image of MT429, the closest pair ($\rho = 0.08''$) found in our survey.

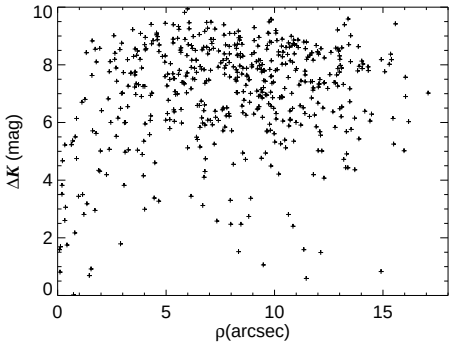

Figure 4: This figure shows the dynamic range of our observation as a function of projected radius. Within $0.5''$ we are still able to detect objects with $\Delta K \approx 5$ mag.

The closest, resolved pair found in our survey, MT 429A and MT429B (see Fig. 3) have a ΔK = 1.59 mag and are at a separation of $0.08''$, which is at the limits of the AO capabilities. Figure 4 shows the dynamical range of the AO system as a function of separation for our sample. We detected stars with a magnitude difference as large as $\Delta K \approx 5$ mag even with small separations of $\rho < 0.5''$ from the target. This figure demonstrates the sensitivity and completeness of our survey.

We detected 47 objects in the $22''$ area around the star MT421, significantly the most stars detected in our sample. Statistically, only 3 stars are likely to be gravitationally bound to MT421. They are the three brightest stars within the 10 000 AU circle in Figure 5. The 10 000 AU radius is approximately the radius where the orbital speed is on the order of the random motion in a cluster. Companions found at separations larger than this are easily disrupted in dense clusters. We found that 65 stars in our sample had at least one star within that radius. While all of our statistically probable companions are within that projected radius, they constitute 55% of the 65 stars.

Figure 5 is a false-color image composed of the J, H, K_S images taken with the PHARO AO. Many of the fainter objects are much brighter in the K_S band due their red color, the high extinction towards Cyg OB2, and/or contamination by foreground, cooler stars.

4 Summary

We made one epoch imaging of 75 O- and B-type stars in Cyg OB2 with high angular resolution methods in the infrared JHK bands. We found that:

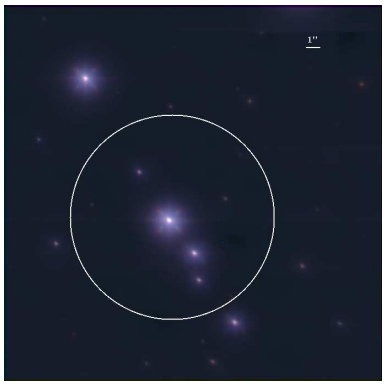

Figure 5: False color Palomar image (J=blue, H=green, K=red) of MT421, the most populated field with 47 sources detected. The circle is at a projected radius of 10 000 AU (5.88″).

- 87% of our sample has another star within 10 000 AU, the nominal distance for two objects to be gravitationally bound, about half of which are statistically significant
- 42% of stars have a statistically probable companion, based on magnitude, separation and surrounding stellar density
- several stars have companions near the 0.08″ angular resolution limit of the AO that span a large differential magnitude range
- the presence of O- and B-type stars supports the idea that Cyg OB2 is a young association, but some of the fainter, redder stars detected may be foreground objects.

Future observations would be useful to detect orbital motion and to further establish the true binarity of some of these systems.

Acknowledgments

We would like to especially thank Ellyn K. Baines for her tremendous help in the reduction process. This material is based upon work supported by the National Science Foundation under Grant AST-0606861.

References

Comerón F., Pasquali A., Rodighiero G., et al., 2002, A&A, 389, 874
Correia S., Zinnecker H., Ratzka Th., Sterzik M. F., 2006, A&A, 459, 909
Fitzpatrick, E. L., 1999, PASP, 111, 63
Girardi L., Bertelli G., Bressan A., Chiosi C., Groenewegen M. A. T., Marigo P., Salasnich B., Weiss A., 2003, Mem. Soc. Astronom. Italiana, 74, 474
Hodapp K. W., Jensen J. B., Irwin E. M, .et al., 2003, PASP, 115, 1388
Lawrence A., Warren S. J., Almaini O., et al., 2007, MNRAS, 379, 1599
Massey P., Thompson A. B., 1991, AJ, 101, 1408
Mason B. D., Hartkopf W. I., Gies D. R., Henry T. J., Helsel J. W., 2009, AJ, 137, 3358
Mason B. D., Wycoff G. L., Hartkopf W. I., Douglass G. G., Worley C. E., 2001, AJ, 122, 3466
Negueruela I., Marco A., Herrero A., Clark J. S., 2008, A&A, 487, 575
Schulte, 1958, ApJ, 128, 41
Siess L., Dufour E., Forestini M., 2000, A&A, 358, 593
Skrutskie M.F., Cutri R.M., Stiening R., et al., 2006, AJ, 131, 1163

Table 1: Multiplicity properties of stars in Cyg OB2

Star[a]	No. of stars in field[b]	$P(\Omega,\Sigma)$[c]	WDS[d]	Star[a]	No. of stars in field[b]	$P(\Omega,\Sigma)$[c]	WDS[d]
A11	6	3	...	**MT421**	47	3	...
A12	2	...	...	**MT429**	8	1	...
A15	3	...	...	**MT431**	1	...	...
A18	11	...	...	**MT448**	16	...	...
A20	5	1	...	**MT455**	19	...	...
A23	1	...	...	**MT457**	1	...	...
A24	2	...	...	**MT462**	11	3	...
A25	7	1	...	**MT465**	6	3	7
A26	6	1	...	**MT470**	11	...	...
A27	2	...	...	**MT473**	15	...	...
A29	1	...	...	**MT480**	10	...	...
A32	6	...	...	**MT483**	4	...	...
A37	5	...	...	**MT485**	9	...	...
A38	11	1	...	**MT507**	6	...	...
A41	2	1	...	**MT516**	3	2	2
A46	3	...	...	**MT531**	5	1	...
B17	4	...	...	**MT534**	5	...	...
MT5	14	1	...	**MT555**	3	...	...
MT59	3	1	...	**MT556**	5	1	...
MT70	8	...	...	**MT588**	10	...	...
MT83	2	...	...	**MT601**	11	1	...
MT138	8	1	...	**MT605**	8	1	...
MT140	8	...	...	**MT611**	8	1	...
MT145	13	...	...	**MT632**	3	2	...
MT213	6	...	...	**MT642**	4	1	...
MT217	5	1	...	**MT692**	9	...	...
MT227	6	...	...	**MT696**	7	1	...
MT250	21	...	...	**MT716**	16	...	...
MT258	15	1	...	**MT734**	1	...	...
MT259	15	...	...	**MT736**	2	...	...
MT299	8	1	...	**MT745**	2	...	...
MT304	2	1	...	**MT771**	4	1	...
MT317	3	...	...	**MT793**	6	...	...
MT339	10	...	...	**S03**	3	1	...
MT376	7	...	...	**S05**	2	1	2
MT390	9	...	...	**S73**	12	1	...
MT403	10	1	...	**WR145**	1	...	2
MT417	11	2	2				

[a] Names of the stars. *A#* or *B#* use nomenclature from Comerón et al. (2002). *MT#* designations are from Massey & Thompson (1991). *S#* are stars named according to their Schulte (1958) designation.

[b] Total number of the stars found in the field around the target.

[c] Number of stars that have a high probability of being real companions.

[d] Number of companions listed in the Washington Double Star Catalog.

Multiwavelength study of the intriguing massive star CPD–59 2629 (Tr 16-22)

J. A. Combi[1,2,3], J. F. Albacete-Colombo[2], P. L. Luque Escamilla[3], G. E. Romero[1], R. Gamen[4], P. Benaglia[1], J. Martí[3], J. López-Santiago[5], E. Sánchez-Ayaso[3], A. J. Muñoz-Arjonilla[3], and J. R. Sánchez-Sutil[3]

[1] Instituto Argentino de Radioastronomía, Buenos Aires, Argentina
[2] Centro Universitario Regional Zona Atlántica (CURZA), Viedma, Argentina
[3] Departamento de Física, Universidad de Jaén, Jaén, Spain
[4] Instituto de Astrofísica de La Plata, CONICET, UNLP, Argentina
[5] Departamento de Astrofísica y CC. de la Atmósfera, UCM, Madrid, Spain

Abstract: We report preliminary results of a multi-wavelength (radio–optical–X-ray) study of the massive star CPD $-59\,2629$ (Tr 16-22) in the Carina Nebula (NGC 3372). This star has historically shown a large X-ray excess (log $L_X/L_{bol} < -6$ or even larger), which is one order of magnitude larger than expected from single massive O-type stars. A colliding wind scenario is a plausible explanation. On this subject, we searched for non-thermal radio emission and used high-resolution optical spectroscopy to check for multiplicity and investigate the nature of the stars as well as the origin and excess of the X-ray emission. We detected long-term radial-velocity and X-ray variability. Both results suggest that Tr 16-22 is a long-term massive binary system and a variable colliding wind shock scenario.

1 Introduction

Trumpler 16 is one of the most massive young open clusters in the Carina Nebula (NGC 3372). It is located at about 2250 pc (Davidson et al. 1997). Among the large population of O-type stars emitting in X-ray, CPD $-59\,2629$ (Tr 16-22) displays an unusually high X-ray luminosity in comparison with its bolometric luminosity $L_X/L_{bol} \cong -5.8$, -5.3 and -5.2 (Evans et al. 2003; Sanchawala et al. 2007; Albacete-Colombo, Méndez & Morrell 2003, respectively). Furthermore, it shows a large average absorption with an unusual characteristic beyond simple foreground reddening. The X-ray luminosity of the source seems to be variable, i.e. $L_X = 7.9 \pm 0.5 \times 10^{31}$ erg s^{-1} (Evans et al. 2003); log $L_X = 32.83$ erg s^{-1} (Sanchawala et al. 2007); log L_X = 33.30 and 32.8 erg s^{-1} (Albacete-Colombo et al. 2003, 2008; respectively), but also converts this star in one of the brightest O-type stars observed, i.e. approximately a factor of 5-20 larger than other known O8.5 V stars in massive clusters. In addition, Tr 16-22 presents a hard X-ray spectrum, that could be indicative of strong colliding stellar winds processes in a massive binary system (Corcoran 2003). All these issues make Tr 16-22 a somewhat more peculiar object, different from other known O-type stars.

2 Radio observations

The field of the massive star Tr 16-22 was observed at 4.8 and 8.64 GHz with ATCA, as part of the RMS campaigns (Lumsden et al. 2002, Urquhart et al. 2007). The field center at (FK5 J2000) = (10:45:00.90, -59:47:1) corresponds to a MSX source (G287.6393-00.7219). The synthesized beams (RA,Dec,P.A) resulted in 1.9 x 1.2, -23.9 deg (at 8.64 GHz) and 3.0 x 1.8, -21.2 deg (at 4.8 GHz). The rms attained were 0.12 mJy/beam, and 4.99 mJy/beam, at 8.64 and 4.8 GHz respectively. Unfortunately, no radio continuum source was found at the position of the star.

3 Optical observations

We compiled a set of spectrograms obtained in three different runs from CASLEO, Argentina, and LCO, Chile. From CASLEO, we obtained 5 echelle spectra ranging from 3800 Å to 6100 Å with a typical dispersion of 0.3 Å pix^{-1}. The three spectra obtained from LCO have a coverage of 3500-9800 Å and a dispersion of 0.1 Å pix^{-1}. We measured the radial velocities (RV) of He II and He I absorption lines, as well as the Na II interstellar lines and some nebular emission lines to check the stability of both echelle spectrographs. We obtained that Tr 16-22 is a radial-velocity variable. We determined a significant ($\sim$50 km s^{-1}) difference between the most extreme spectra. The mean RV obtained in each epoch could be due to a long period system. And also, some profiles suggest the presence of a secondary companion. This star is now included in the OWN survey (Barbá et al. 2010).

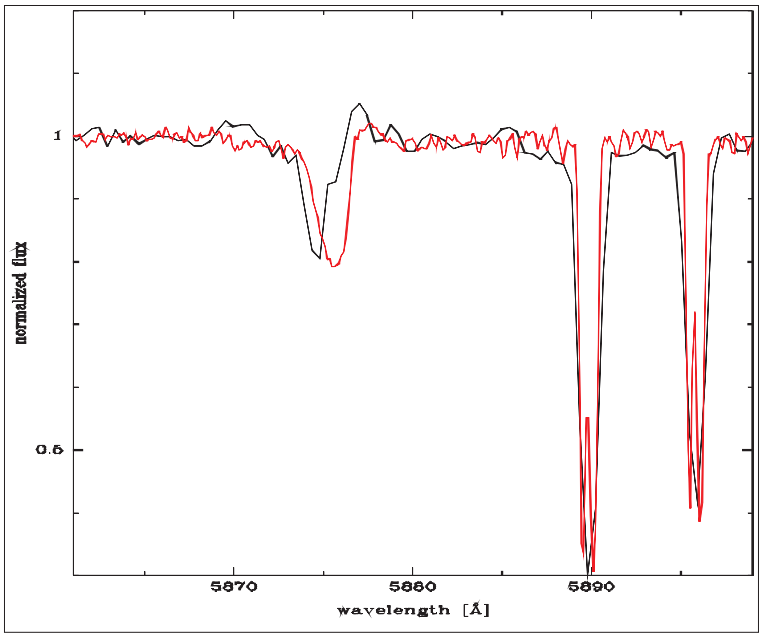

Figure 1: Two optical spectra of Tr 16-22, in the region of He I 5875 Å. Note the wavelength shift between He I absorption lines, but not between the Na I interstellar (IS) lines.

4 X-ray observations

The field of the Carina nebula, locus of the massive star Tr 16-22, was observed, more than 20 times over 10 years, by the *Newton* X-ray Multi-Mirror Mission (*XMM*) observatory with the EPIC-PN and MOS. For this work, we use a preliminary set of seven available *XMM-Newton* observations of the

region. Further analysis with the remaining available *XMM-Newton* and *Chandra* observations will be published soon. Detailed information of the observations used is given in Table 1. The data were analyzed with the XMM Science Analysis System (SAS) version 9.0.0 and the latest calibrations files.

The results show that the X-ray light curve of Tr 16-22 displays a significant variability (see Fig. 2, left panel), which covers a factor 30 over the time-scale of about 3 years. Moreover, we found time-dependent N_H variations (see Fig. 2, right panel), which confirm that the bulk of absorption comes from Tr 16-22, not the ISM. Otherwise, two thermal components are necessary to fit the X-ray spectra. While the soft component at about 0.5 keV does not show significant variations, the hard component of the spectrum varies with some dispersion between 1.5 and 2.5 keV. If it were a long-term binary as suggest our optical data, (i.e. probably an eccentric orbit), at some orbital phases, stellar winds would collide at velocities near the wind escape velocity (i.e. 2000 to 3000 km/s), which implies post-shock temperatures over 1 to 3 keV (Stevens et al. 1992). These results mean that the hard part of the X-ray spectrum would come from the colliding wind region (CWR) at the different orbital configurations of the system.

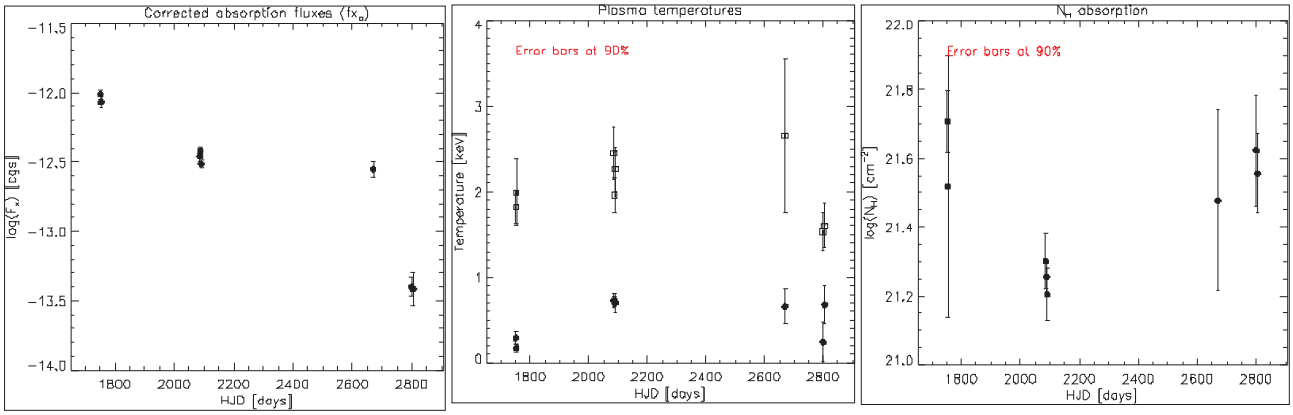

Figure 2: Left: Total absorption corrected X-ray flux as a function of time. X-ray fluxes were computed in the 0.5-8.0 keV energy band. It is clear that f_x varies over a factor 31. Center: The first and second temperature components show a slight variation in time. Right: Time-dependent N_H variations. Changes of the N_H could be due to different orbital configurations of the system. N_H^{ISM} was fixed to 5.8×10^{21} cm^{-2} (A_v=3.6; Albacete-Colombo et al. 2008.)

5 Discussion and conclusions

In massive early O-type stars, X-ray emissions are observed as a natural consequence of multiple small-scale shocks in the inner layers of their radiation-driven stellar winds (e.g. Feldmeier, Puls & Pauldrach 1997). However, in the case of O+OB binary systems, wind-wind interaction produces a hot shocked gas region with temperatures that exceed one million degrees (few keV), but also produce an increment in the observed X-ray emission from the star. Such X-ray emission is observed to be variable according to the different orbital phases, i.e. density and relative velocity of the winds of the CWR and the wind absorption along the line of sight.

Besides the observed X-ray excess of the Tr 16-22 star (e.g. Albacete-Colombo et al. 2003, 2008), its X-ray light curve shows a significant variability with time (a factor 31 in 3 years). Such a behavior cannot be explained in terms of the line-driven stellar wind shocks. The most plausible explanation of the observed flux variability and high kT values is that Tr 16-22 is an O+OB interacting wind binary system, which produces an excess X-ray emission at the CWR. Previous works suggested this

Table 1: Detailed information of the used X-ray observations

Obs-Id	Date	Exp (ks)
0112580601	2000-07-26	36509
0112560101	2001-06-25	37052
0112560201	2001-06-28	40092
0112560301	2001-06-28	37714
0160160901	2003-06-30	38352
0160160901	2003-06-13	31655
0112580701	2000-07-27	12425

scenario (e.g. Albacete Colombo et al. 2008), but this work constitutes the first report of a long-term X-ray variability in the Tr 16-22 star.

Complementary analysis of available *XMM-Newton* and *Chandra* data are in progress, and also future spectroscopic optical observations are scheduled to improve these results. These information could help to reveal more details of the interesting star Tr 16-22.

Acknowledgements

The authors acknowledge support by grant AYA2007-68034-C03-02 from the Spanish government, and FEDER funds. This work has been also supported by the Consejería de Innovación, Ciencia y Empresa (CICE) of Junta de Andalucía as research group FQM-322 and excellence fund FQM-5418. J.A.C., J.F.A.C. and G.E.R are researchers of CONICET. J.F.A.C was suportes by grant PICT 2007-02177 (SecyT). G.E.R. and J.A.C. were supported by grant PICT 07-00848 BID 1728/OC-AR (ANPCyT) and PIP 2010-0078 (CONICET). J.L.S. acknowledges support by the Spanish Ministerio de Innovación y Tecnología under grant AYA2008-06423-C03-03.

References

Albacete-Colombo, J.F., Méndez, M., & Morrell, N.I. 2003, MNRAS 346, 704

Albacete-Colombo, J.F., Damiani, F., Micela, G., Sciortino, S., & Harnden, F.R.Jr. 2008, A&A 490, 1055

Barbá, R.H., Gamen, R., Arias, J.I., Morrell, N., Maíz Apellániz, J., Alfaro, E., Walborn, N., & Sota, A. 2010, RMxAC 38, 30

Corcoran, M.F. 2003, IAU Symp. 212, 130

Davidson, K., Ebbets, D., Johansson, S., Morse, J.A., & Hamann, F.W. 1997, ApJ 113, 335

Evans N.R., Seward F.D., Krauss M.I., Isobe T., Nichols J., Schlegel E.M., & Wolk S.J. 2003, ApJ 589, 509

Feldmeier, A., Puls, J., & Pauldrach, A.W.A. 1997, A&A 322, 878

Lumsden, S.L., Hoare, M.G., Oudmaijer, R.D., & Richards, D. 2002, MNRAS 336, 621

Sanchawala, K., Chen, W.-P., Lee, H.-T., Chu, Y.-H., Nakajima, Y., Tamura, M., Baba, D., & Sato, S. 2007, ApJ 656, 462

Stevens, I.R., Blondin, J.M., & Pollock, A.M.T. 1992, ApJ 386, 265

Urquhart, J.S., Busfield, A.L., Hoare, M.G., et al. 2000, A&A 461, 11

First results on the optical campaign devoted to the gamma-ray binary candidate HD259440

Michaël De Becker[1,2] , M. Virginia McSwain[3], and Christina Aragona[3]

[1] Department of Astrophysics, Geophysics and Oceanography, University of Liège, Belgium
[2] Observatoire de Haute-Provence, Saint-Michel l'Observatoire, France
[3] Department of Physics, Lehigh University, USA

Abstract: Quite recently, a very high-energy gamma-ray source has been detected in the Monoceros region. This source belongs to the category of TeV emitters with no identified counterpart at other wavelengths, even though it may be coincident with other high-energy sources detected with other observatories (ROSAT, CGRO). However, it is interesting to note that the error box of this TeV source admits the possibility that the Be star HD259440 is at the origin of the high-energy emission. This may be possible only if that Be star is member of a still undetected binary system including a compact (neutron star or black hole) companion, therefore belonging to the very scarce category of gamma-ray binaries. We describe here the first results of the optical campaign devoted to HD 259440, with emphasis on the investigation of its multiplicity, using spectra obtained at the Observatoire de Haute-Provence (OHP) and at the Kitt Peak National Observatory (KPNO).

1 Scientific context

Recently, a TeV source has been detected by HESS in the Monoceros region: HESS J0632+057 (Aharonian et al. 2007). This region is rather complex, and several associations with objects known at other wavelengths seem plausible. In the context of the VHE emission from astronomical sources, binary systems made of an early-type star and of a neutron star/black hole are particularly important. Along its orbit, the compact star is likely to accrete material from the wind of the early-type star on its surface. Such an accretion process is known to be very efficient at producing high-energy photons. Among these high-mass X-ray binaries (HMXB), one can distinguish the sub-class of microquasars, which are considered as good candidates for the production of VHE γ-rays. Microquasars are X-ray binaries which produce jets. In this category, LS 5039 and LSI +61° 303 have been identified as VHE γ-rays sources, although their classification as microquasars is still somewhat controversial (Romero et al. 2007). On the other hand, Cygnus X-3 has been detected both by Fermi (Abdo et al. 2009) and AGILE (Tavani et al. 2009), and is an uncontroversial high-mass microquasar. Cygnus X-1 has also been detected in the very high energy gamma-ray domain with MAGIC (Albert et al. 2007). In the context of such binaries including a compact object, VHE γ-rays may be produced by synchrotron self-Comptonization, where a hard-X-ray photon produced by the synchrotron mechanism is up scattered up to much higher energies through a Comptonization mechansim, in the presence of relativistic electrons accelerated in the jets. External Compton emission can be important as well, since the stars

are quite luminous, therefore providing the wealth of photons likely to be upscattered up to very high energies. According to these scenarios, microquasar-like objects are good candidates for a γ-ray emission in the TeV domain likely to be detected with an observatory such as HESS. Another possiblity comes from the high density of the stellar winds of HMXBs. The dense matter fields in the region where the jets exists can lead to strong collisions between jets and wind material. The collisions can therefore lead to neutral pion production and decay, and hence to production of VHE γ-rays and neutrinos (Romero et al. 2003). It should be noted that, in the case of these accreting γ-ray binaries, the orbital period is generally not very long (at most several weeks), except in some cases where an accreting neutron star in a long orbit might produce VHE gamma-rays (Orellana & Romero 2005, Orellana et al. 2007).

Beside these accreting binaries, we may also consider the case of non-accreting longer period binaries where the secondary turns out to be a pulsar. This is the case of the 3.4-year Be + pulsar binary PSR B1259-63, whose TeV emission was detected by HESS during periastron passage (Aharonian et al. 2005). In this scenario, the interaction of the relativistic wind from the pulsar with the stellar wind of the primary constitutes a viable scenario to explain the detected VHE emission (see Dubus 2006 for a discussion of this scenario). Here again, the presence of a compact companion in HD 259440 – even though on a wider orbit – constitutes a valuable working hypothesis to interpret the nature of HESS J0632+057.

In both cases, if HD 259440 is a still undetected binary system whose secondary is a neutron star – or even a black hole – it could be the counterpart of HESS J0632+057. A multiplicity investigation of this star is therefore needed in order to check this interpretation, and we describe here the first results obtained in this context.

2 Observations

We observed the target 7 times with the SOPHIE échelle spectrograph mounted on the 1.93 m telescope at the Observatoire de Haute-Provence (OHP, France) using the high efficiency mode (R=40000). Two observations occurred in March 2009, and five in October 2009. The data consist in 39 orders covering the wavelength range 3872-6943 Å . The spectra were corrected for the blaze and flat-fieded, before being wavelength calibrated using Th/Ar spectra obtained maximum 2 hours before or after the sky exposure. We used exposure times between 45 and 90 minutes. The spectra present an average S/N ratio ranging between 80 and 220, depending on the exposure time and on weather conditions. We also retrieved archive SOPHIE spectra of the same target obtained between October 2007 and February 2008, with exposure times of 5 to 15 minutes. We note however that the S/N ratio of the latter is generally significantly lower than those obtained in 2009 (i.e. down to about 40 in the worst cases).

We also observed HD 259440 using the Kitt Peak National Observatory (KPNO) Coudé Feed (CF) telescope with the F3KB detector between 2008 October 17 and November 21. We used both blue and red spectral setups each night and generally obtained two spectra of HD 259440 in each. The blue spectra (R=9500) cover a wavelength range 4130–4570 Å , and have a S/N ratio of 50–140. The red spectra (R=12000), span a wavelength range of 6400–7050 Å , and have a S/N of 100–250. The spectra were zero corrected, flat-fielded, and wavelength calibrated using standard procedures in IRAF1. Two blue optical spectra were finally obtained at the KPNO 2.1m telescope using the GoldCam Spectrograph on 2008 December 12–13, with a resolving power of 2100–3100. These observations cover a wavelength range of 3700–4900 Å and a S/N ratio of 125–150. For details on the data set and on the data processing procedure, we refer to Aragona et al. (2010).

3 The multiplicity of HD259440

3.1 Searching for a companion

We measured the radial velocity of the star using first the KPNO time series, on the basis of the He I line at 4471 Å . These measurements did not lead to any detection of a significant radial velocity shifts during the 35 nights of the KPNO campaign. We obtained a standard deviation of the radial velocities of 20.1 km s^{-1}. We note that we did not notice any slow trend of increasing or decreasing radial velocities across the time series, likely to reveal a putative variation on a time basis much longer than that of the time series.

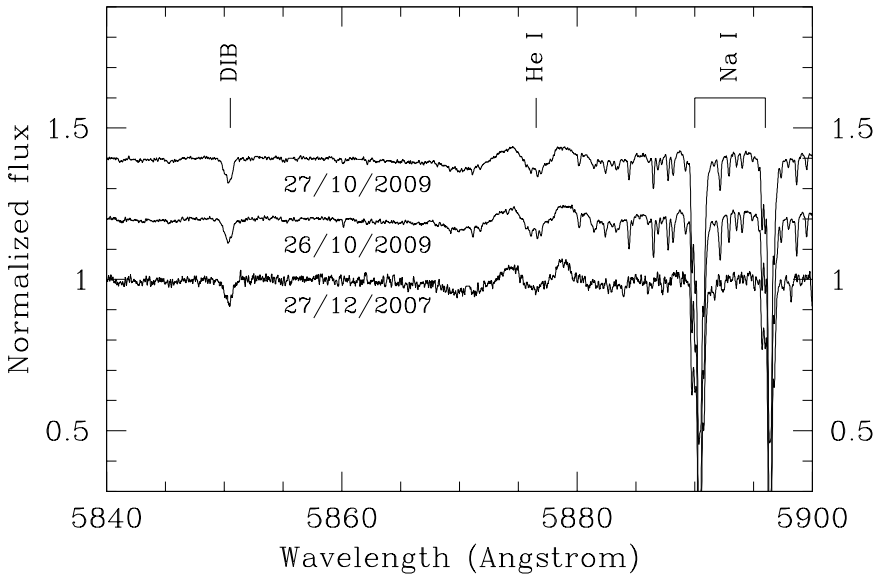

Figure 1: Spectrum of HD 259440 between 5840 and 5900 Å obtained with the SOPHIE spectrograph at three different epochs.

We also estimated the radial velocities on the basis of the OHP data set. Considering the rather low signal to noise ratio of the blue part of the échelle spectra, we refrained from using blue lines to measure radial velocities. Considering the shape of the line profile and the overall signal to noise ratio of the time series, we focused on the He I line at 5876 Å (see Fig. 1). We measured the radial velocity by fitting Gaussians to the central absorption component of the profile. These measurements led to a standard deviation of the radial velocities of 6.7 km s^{-1}. Considering the natural width and shape of the spectral lines used for these measurements, such a value is rather close to the expected accuracy on the radial velocities of the target. We therefore did not detect any significant radial velocity variation on the basis of our time series.

3.2 Constraints on the multiplicity

In the absence of evidence for the presence of a companion, we can only conjecture on the probability to have missed the binary, provided HD 259440 is not single. We adopted the procedure described by Garmany et al. (1980), and more recently used by Mahy et al. (2009).

The mass function of the primary component is given by:

$$f(m) = \frac{M_1 \ \sin^3 i}{q \ (1+q)^2} = 1.0355 \times 10^{-7} \ K^3 \ P \ (1-e^2)^{3/2} \tag{1}$$

where M_1 is the primary mass (in $M_\odot$), K is expressed in km s^{-1}, e represents the orbital eccentricity, $q = M_1/M_2$ and P defines the orbital period (in days).
Equation 1 is transformed on $\sin i$, we insert $2\sigma_{RV}$ as an upper limit on K and assume a zero eccentricity. Therefore, we obtain:

$$\sin i \ \leq \ 9.392 \ \times \ 10^{-3} \ \sigma_{RV} \ (1-e^2)^{1/2} \ \left(\frac{P \ q \ (1+q)^2}{M_1} \right)^{1/3} \tag{2}$$

Making the assumption of a random distribution of the orbital directions in space, we can write the probability that the orbital inclination is smaller than the value obtained from Equation 2 as:

$$\int_0^{i_{up}} \sin i \ di \ = \ 1 - \cos i_{up} \tag{3}$$

This approach requires the knowledge of several quantities. First, we need an upper limit on the variation of the radial velocities. The strongest constraint comes from the OHP data, and we will consider the 6.7 km s^{-1} value. For the mass ratio, we need the value of the primary mass. We used the KPNO spectra to estimate the effective temperature and the gravity of the primary, through line fitting of a TLUSTY BSTAR2006 model (Lanz & Hubeny 2007). We then confronted the best-fit parameters to evolutionary tracks from Schaller et al. (2002), yielding a mass of about 16 M$_\odot$. Details on the adopted procedure are given in Aragona et al. (2010).

On the basis of these numbers, we computed the probability to have missed the putative binary because of a too low orbital inclination, for different assumed secondary masses (assuming a neutron star as the secondary, we considered values of 1.5, 2.0 and 2.5 M$_\odot$). We assumed also different values for the eccentricity (0.0, 0.2, 0.4 and 0.6), and in each case we computed the probability for a range of period values. The results are plotted in Fig. 2. We see in these plots that the present data can not reject that HD 259440 might be a still undetected binary system, mostly if we are dealing with a long period eccentric binary system.

4 Concluding remarks

Our multiplicity study of the Be star HD 259440 did not reveal any hint for the presence of a companion. However, our analysis put constraints on the probability to have missed a putative binary because of a too low inclination of the system: we may still be dealing with an undetected long period eccentric binary. In such a scenario, HD 259440 could belong to the class of non-accreting gamma-ray binaries like PSR 1259-65, or possibly harbour an accreting neutron star in a long-period orbit.

Acknowledgements

We thank the staff and observers at the Observatoire de Haute-Provence for the service mode observations, and especially Dr. H. Le Coroller for the scheduling of the observations. Our thanks go also to Yves Gallant, Bertrand Plez, and Guillaume Dubus for the obtaining of the archive SOPHIE data we used in this study.

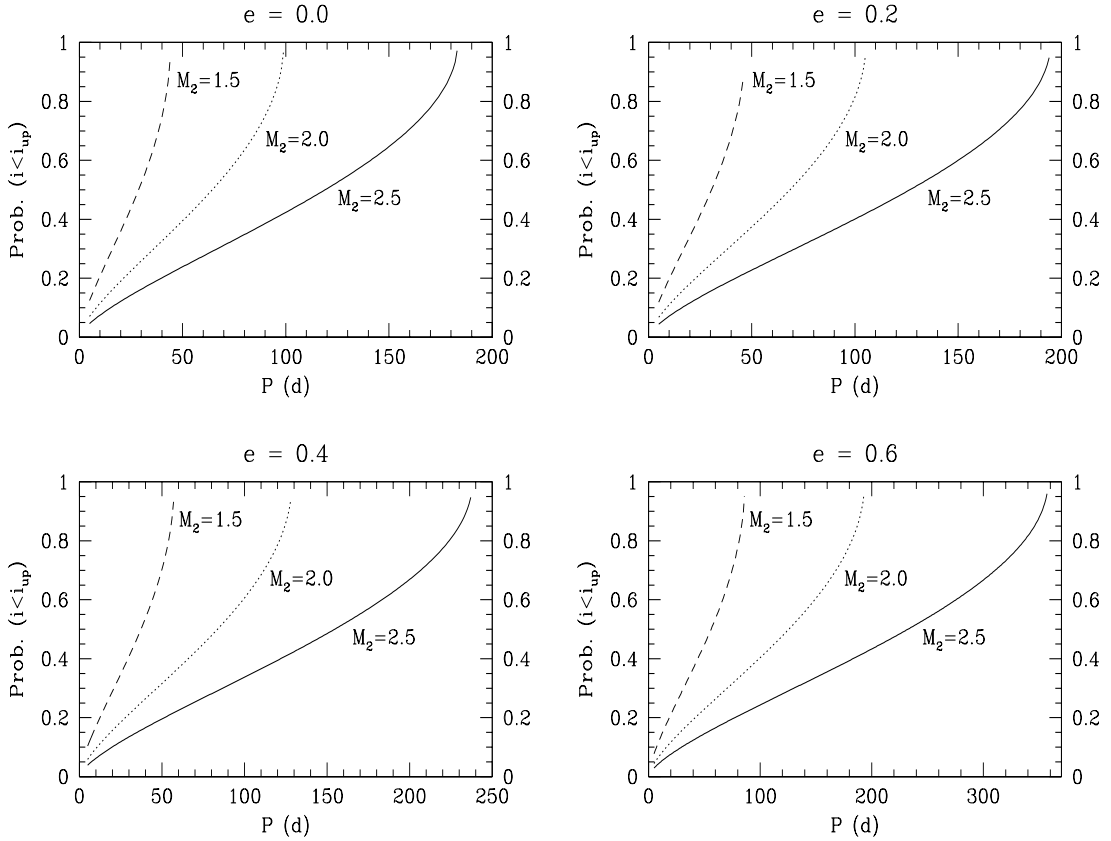

Figure 2: Probability to have missed the binary because of a too low inclination angle as a function of the orbital period, for eccentricities equal to 0.0, 0.2, 0.4, and 0.6, respectively. In each panel, three different secondary masses have been assumed.

References

Abdo, A.A., Ackermann, M., & Ajello, M. 2009, Science 326, 1512
Aharonian, F.A., Akhperjanian, A.G., Aye, K.-M., et al. 2005, A&A 442, 1
Aharonian, F.A., Akhperjanian, A.G., Bazer-Bachi, A.R., et al. 2007, A&A 469, L1
Albert, J., Aliu, E., Anderhub, H., et al. 2007, ApJ 665, 51
Aragona, C., McSwain, M.V., & De Becker, M. 2010, ApJ 724, 306
Dubus, G. 2006, A&A 456, 801
Garmany, C.D., Conti, P.S., & Massey, P. 1980, ApJ 242, 1063
Lanz, T. & Hubeny, I. 2007, ApJS 169, 83
Mahy, L., Nazé, Y., Rauw, G., et al. 2009, A&A 502, 937
Orellana, M., & Romero, G.E. 2005, Ap&SS 297, 167
Orellana, M., Romero, G.E., Pellizza, L.J., & Vidrih, S. 2007, A&A 465, 703
Romero, G.E., Torres, D.F., Kaufman Bernadó, M.M., & Mirabel, I.F. 2003, A&A 410, L1
Romero, G.E., Okazaki, A.T., Orellana, M., & Owocki, S.P. 2007, A&A 474, 15
Schaller, G., Schaerer, D., Meynet, G., & Maeder, A. 1992, A&AS 96, 269
Tavani, M., Bulgarelli, A., Piano, G., et al. 2009, Nature 462, 620

The XMM-Newton view of the X-ray spectrum of WR140 across periastron passage

Michaël De Becker[1,2] , Julian M. Pittard[3], Peredur M. Williams[4]
for the WR140 consortium

[1] Department of Astrophysics, Geophysics and Oceanography, University of Liège, Belgium
[2] Observatoire de Haute-Provence, Saint-Michel l'Observatoire, France
[3] Department of Physics and Astronomy, University of Leeds, UK
[4] Institute for Astronomy, Royal Observatory, Edinburgh, UK

Abstract: An XMM-Newton campaign dedicated to the study of the X-ray emission of the colliding wind massive binary WR140 across its 2009 periastron passage has been undertaken. The high quality EPIC spectra revealed a strong phase-locked variability both in flux and in spectral shape. The observed variations are consistently explained by the varying emission measure of the emitting plasma along the eccentric orbit, and by the changing absorption column density along the line of sight. Our results are first interpreted in the context of simple multi-temperature thermal emission models, and prospects for more sophisticated modelling are discussed.

1 Scientific context

WR 140 (HD 193793, HIP 100287) is undoubtedly one of the most studied WR+O massive binaries. It is a long period system (7.9 yr) consisting of a WC7 + O5 pair (Williams et al. 2009). This system turns out to be an especially relevant astrophysical laboratory for the study of colliding stellar winds. First, radio observations of this system revealed a non-thermal nature of its spectrum pointing to its capability to accelerate particles up to relativistic energies (e.g. Williams, van der Hucht & Spoelstra 1994, White & Becker 1995, Dougherty et al. 2005). Second, the wind-wind interaction region of WR 140 is known to be a nucleation site for dust particles (Monnier, Tuthill & Danchi 2002). Finally, previous soft X-ray observations (ASCA: Koyama et al. 1994, Zhekov & Skinner 2000; Chandra: Pollock et al. 2005) revealed a strong thermal emission spectrum dominated by the hot plasma expected to be present in such a colliding wind massive binary. Until recently, visibility constraints prevented any observations of WR 140 with the highly sensitive XMM-Newton satellite. This paper presents some first results obtained in the framework of the XMM-Newton campaign devoted to this target, especially across its periastron passage that motivated a multi-wavelength/multi-observatory effort among the massive star community (see Williams 2011 for a review).

Table 1: Journal of observations. The columns include respectively the number of the observation in our series, the observation identifier, the Julian date at mid exposure, and the orbital phase as computed from the ephemeris of Marchenko et al. (2003).

ID	Obs. ID	JD	ϕ
obs.1	0555470701	2 454 589.443	0.912
obs.2	0555470801	2 454 751.110	0.968
obs.3	0555470901	2 454 806.553	0.987
obs.4	0555471001	2 454 826.651	0.994
obs.5	0555471101	2 454 928.462	0.029
obs.6	0555471201	2 454 934.275	0.031

2 XMM-Newton observations

XMM-Newton observed WR 140 six times in AO7, across its 2009 periastron passage, with exposure times of 20 ks (proposal ID055547). Unfortunately, pointing constraints of the satellite did not allow us to observe the target at periastron. The aim-point was set to the position of the target in order to obtain simultaneously high resolution RGS spectra. For EPIC instruments, we used the thick filter to reject optical light. Data were processed with SASv8.0. We extracted the events from the sources and the background separately, using spatial filters devoid of any detectable point source. For details on the data set and on the reduction procedure, we refer to De Becker et al. (2011). EPIC-MOS1 spectra are shown in Fig. 1.

3 General X-ray properties and broadband spectral variability

We fitted various composite models prepared with the XSPEC software (v.12.5.1)[1] to spectra from every observation. The models were made using different components for the X-ray emission and for the absorption in order to represent the observed spectra between 0.3 and 10.0 keV. We achieved a good description of the X-ray spectrum of WR 140 using a 3-T thermal emission model with varying abundances, along with photoelectric absorption components representing the interstellar and wind absorption. Best-fit parameters were obtained for a model of the following form:

`tbabs*(vphabs*vapec+vphabs*vapec+vphabs*vapec)`

where `tbabs` is a model for the interstellar extinction taking into account updated abundances, along with the impact of hydrogen molecules and dust particles (Wilms, Allen & McCray 2000). We fixed the interstellar hydrogen column density to a value of 0.59×10^{22} cm^{-2} (see Pollock et al. 2005), but we left the local absorbing columns as free parameters. The plasma temperatures have values of the order of 5, 15 and 50 MK. We note that even though some spectra of the series could at first sight be fitted by a 2-T model, we refrained to do so mainly for one reason: we adopted the same model for the complete time series in order to discuss consistently the variability of the X-ray spectrum, and this could not be done with a heterogenous modelling. Our results point to a significant overabundance in C, in agreement with the WC type of the primary (see De Becker et al. 2011 for a more detailed discussion). This approach provides a rather good representation of the X-ray emission and of its phase-locked variability (see De Becker et al. 2011), but a more appropriate modelling of the X-ray

[1] http://heasarc.gsfc.nasa.gov/docs/xanadu/xspec/.

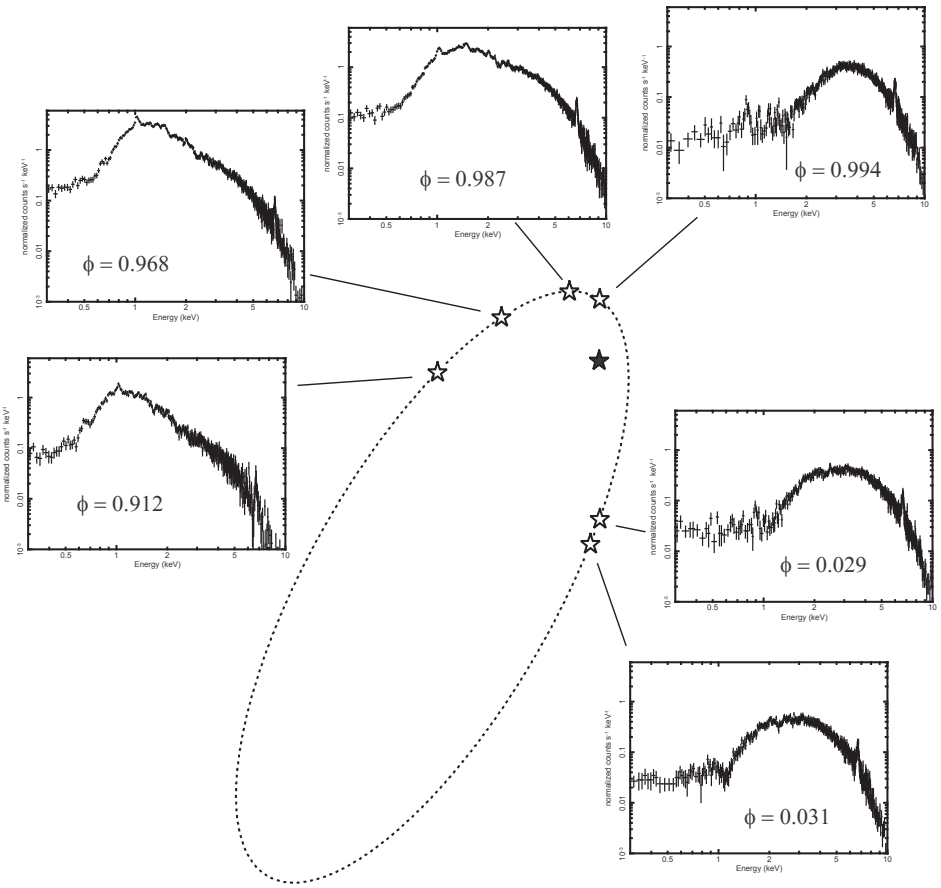

Figure 1: Variability of the EPIC-MOS X-ray spectrum (between 0.3 and 10.0 keV) of WR 140 as a function of the orbital phase. The spectra are identified with the projected positions of the O5 star (open symbols) at the phases of the observations in its orbit around the WR star (filled symbol) projected on the sky.

emission is in preparation.

On the other hand, RGS data reveal several spectral lines, including the dominating Ne X Lyα line, along with the rather strong He-like triplet of Ne IX (see Fig. 2). The global shape of the RGS spectrum changes significantly along the orbit, with the most striking variation observed when the wind-wind interaction region is occulted by the dense WC wind: starting from phase 0.994, the X-rays are almost completely absorbed. A net increase in the line strength is observed when approaching periastron, in agreement with the expected increase of the emission measure. This is especially obvious for instance when looking at the Ne X Lyα line, going from phase 0.912 to 0.968.

4 Phase-locked variability interpretation

We measured the count rates in different energy bands in order to investigate in more detail the variability of WR 140 in X-rays. The count rate in the hard part of the spectrum (mostly unaffected by absorption) has its maximum close to periastron. This is interpreted in terms of variations of the emission measure of the emitting plasma, that changes along the eccentric orbit. In the soft part of the spectrum, the variations are at least qualitatively interpreted as the result of a competition between an emission measure effect (as the separation, D, of the WR and O5 stars varies as a function of the orbital phase) and an orientation effect (as the line of sight crosses absorbing material with changing

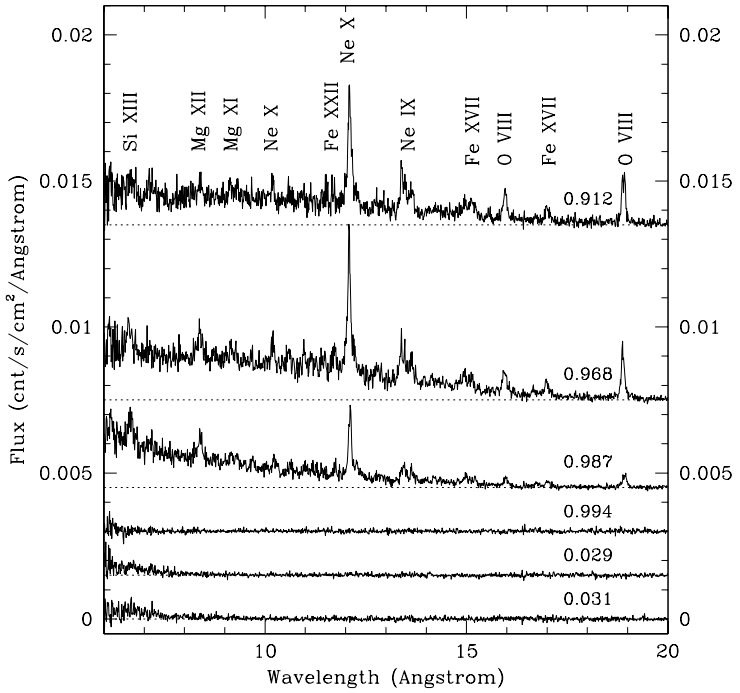

Figure 2: Fluxed RGS spectra of WR 140 for the six observations plotted between 6 and 20 Å. The spectra have been vertically shifted by an arbitrary value for clarity, and the zero-flux level for each spectrum is represented by the horizontal dotted lines. The most prominent spectral lines are labelled.

column density as a function of the orbital phase). Such measurements constitute valuable constraints for models currently in development aiming at a good 3-dimensional description of the physics of the colliding winds in WR140 (Parkin et al. 2011, and future developments).

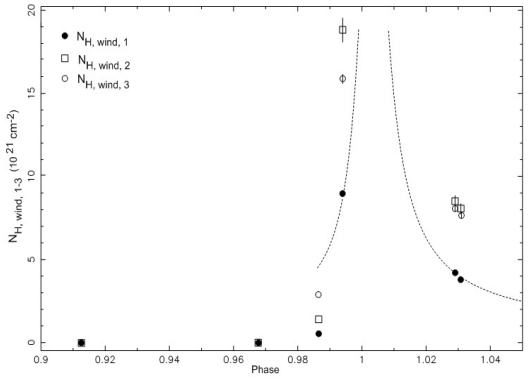

Figure 3: Variation of the local column densitites as a function of the orbital phase. The values obtained from our simple modelling fit quite well the expected trend for WR140 illustrated by the two curves, calculated following an integration through the WC wind to a source moving along the eccentric orbit (see equations A16 and A17 in Williams et al. 1990). Orbital parameters from Marchenko et al. (2003) were used.

The stellar winds have reached their terminal velocity before colliding, so to first order the plasma temperature is expected to be constant with orbital phase (in fact, there will be small changes in the pre-shock velocities due to the expansion and contraction of the system (see, e.g. Pittard & Parkin 2010), plus possible changes near periastron due to increased cooling). We therefore assume that the global shape of the unabsorbed spectrum is constant, with variations in (i) the total emission measure due to the varying orbital separation, and (ii) the wind absorption. We fixed the ratio of the vapec normalization parameters, and we fixed the temperatures to the best fit values (along with the element abundances). The evolution of the normalization parameter of the first emission component shows that emission measure does not follow the $1/D$ trend expected for adiabatic cases (Stevens, Blondin & Pollock 1992). On the other hand, the absorbing column densities could be plotted to check their evolution as a function of the orbital phase, in order to be confronted to the expected trend described for instance by Williams et al. (1990). Fig. 3 shows that we find a fairly good agreement between the measured quantities and the expected ones, though ultimately the spectra should be

compared against more realistic models (e.g. Pittard & Parkin 2010).

5 Concluding remarks

At this stage of the analysis, we can formulate the following conclusions:

1. The XMM-Newton spectra obtained across periastron passage reveal a spectacular phase-locked variability, qualitatively explained in terms of varying emission measure and absorbing wind column densities.

2. The unabsorbed X-ray flux does not follow the simple $1/D$ trend expected for a self-similar adiabatic wind-wind collision region.

3. This first approach is severely limited by the capabilities of the simple models we used. Dedicated opacity tables have been prepared to improve the modelling of the absorption by the wind material (in progress).

4. In order to describe adequately the X-ray emission from WR 140, state-of-the-art models which are as realistic as possible are needed. Such models will have to deal with the 3D hydrodynamics and radiative transfer as a function of the orbital phase (e.g. Pittard 2009), and take into account more detailed physics such as non-equilibrium ionization, or the possible feedback of particle acceleration on shock properties.

Acknowledgements

Financial support from FRS-FNRS and XMM/INTEGRAL PRODEX contracts is acknowledged by MDB. Our thanks go also to the Science Operation Center (SOC) team for the scheduling of the XMM-Newton observations.

References

De Becker M. et al. 2011, A&A, in preparation
Dougherty, S.M., Beasley, A.J., Claussen, M.J., Zauderer, B.A., & Bolingbroke, N.J. 2005, ApJ, 623, 447
Koyama K., Maeda Y., Tsuru T., Nagase F., Skinner S. 1994, PASJ, 46, L93
Marchenko S., Moffat A.F.J., Ballereau D. et al. 2003, ApJ, 596, 1295
Monnier J.D., Tuthill P.G. & Danchi W.C. 2002, ApJ, 567, L137
Parkin E.R., Pittard J.M., Corcoran M.F., Hamaguchi K., Stevens I.R., Gosset E., Rauw G., & De Becker M. 2011, in Proceedings of the 39th Liège Astrophysical Colloquium, eds. G. Rauw, M. De Becker, Y. Nazé, J.-M. Vreux & P. Williams, BSRSL, 80, 610
Pittard J.M. 2009, MNRAS, 396, 1743
Pittard J.M. & Parkin E.R. 2010, MNRAS, 403, 1657
Pollock A.M.T., Corcoran M.F., Stevens I.R., & Williams P.M. 2005, ApJ, 629, 482
Stevens I.R., Blondin J.M. & Pollock A.M.T, 1992, ApJ, 386, 265
White R.L. & Becker R.H. 1995, ApJ, 451, 352
Williams P.M., van der Hucht K.A., Pollock A.M.T., Florkowski D.R., van der Woerd H., Wamsteker W. M. 1990, MNRAS, 243, 662
Williams P.M., van der Hucht K.A., & Spoelstra T.A.T. 1994, A&A, 291, 805
Williams P.M., Marchenko S.V., Marston A.P. et al. 2009, MNRAS, 395, 1749
Williams P.M. 2011, in Proceedings of the 39th Liège Astrophysical Colloquium, eds. G. Rauw, M. De Becker, Y. Nazé, J.-M. Vreux & P. Williams, BSRSL, 80, 595
Wilms J., Allen A. & McCray R. 2000, ApJ, 542, 914
Zhekov S.A. & Skinner S.L. 2000, ApJ, 538, 808

The Orbit and Distance of WR 140

S.M. Dougherty[1,2], V. Trenton[1,3], A.J. Beasley[4]

[1] NRC-HIA DRAO, Penticton, BC, Canada
[2] Institute for Space Imaging Science, University of Calgary, AB, Canada
[3] University of Prince Edward Island, Charlottetown, PEI, Canada
[4] National Ecological Observatory Network, Boulder, Colorado, USA

Abstract: A campaign of 35 epochs of milli-arcsecond resolution VLBA observations of the archetype colliding-wind WR+O star binary system WR 140 show the wind-collision region (WCR) as a bow-shaped arc of emission that rotates as the highly eccentric orbit progresses. The observations comprise 21 epochs from the 1993-2001 orbit, discussed by Dougherty et al. (2005), and 14 epochs from the 2001-2009 orbit, and span orbital phase 0.43 to 0.95. Assuming the WCR is symmetric about the line-of-centres of the two stars and "points" at the WR star, this rotation shows the O star moving from SE to E of the WR star between these orbital phases. Using IR interferometry observations from IOTA that resolve both stellar components at phase 0.297 in conjunction with orbital parameters derived from radial velocity variations, the VLBA observations constrain the inclination of the orbit plane as $120^\circ \pm 4^\circ$, the longitude of the ascending node as $352^\circ \pm 2^\circ$, and the orbit semi-major axis as 9.0 ± 0.1 mas. This leads to a distance estimate to WR 140 of 1.81 ± 0.08 kpc. Further refinements of the orbit and distance await more IR interferometric observations of the stellar components directly.

1 Introduction

The 7.9-year period WR+O system WR 140 (HD 193793) is the archetype of CWB systems. It is comprised of a WC7 star and an O4-5 star in a highly elliptical orbit ($e \approx 0.88$), where the stellar separation varies between $\sim$ 2 AU at periastron to $\sim$ 30 AU at apastron. This highly eccentric orbit clearly modulates the dramatic variations observed in the emission from the system, from X-ray energies to radio wavelengths (Williams et al. 1990). Perhaps the most dramatic variations are observed at radio wavelengths, where there is a slow rise from a low state close to periastron of a few mJy, to a frequency-dependent peak in emission of 10's of mJy between orbital phase 0.65 to 0.85, before a precipitous decline immediately prior to periastron (see Fig 1). A number of attempts to model these variations have been made (e.g. Williams et al. 1990, White & Becker, 1995) with limited success, though advances in our understanding of WCRs are being made (e.g. Pittard & Dougherty 2006; Pittard 2011). Accurate orbital parameters are critical inputs to these models.

Many of the orbital parameters in WR 140, in particular the orbital period (P), epoch of periastron passage (T_o), eccentricity (e), and the argument of periastron (ω) have been established by others (see Marchenko et al. 2003 and references therein), and refined most recently in an extensive observing campaign during the 2009 periastron passage. However, the orbital inclination (i), semi-major axis

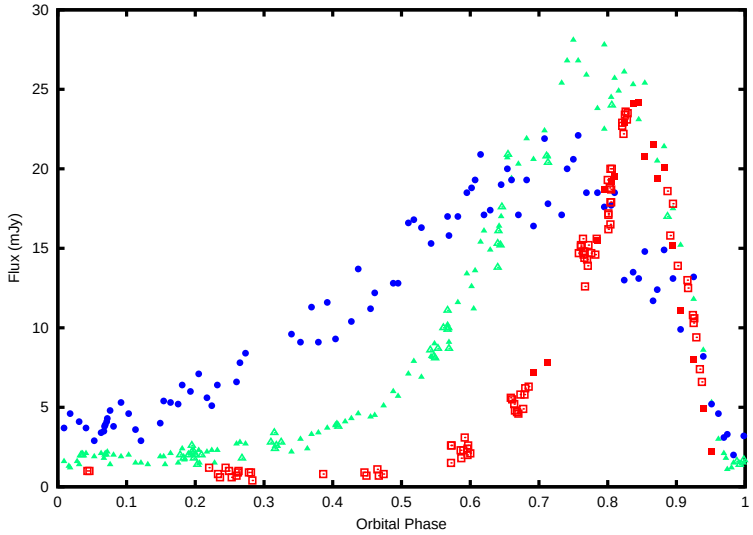

Figure 1: Radio emission from WR 140 at 15 GHz (blue circles), 5 GHz (green triangles), and 1.6 GHz (red squares) as measured with the VLA (solid) and WSRT (open). Data are from Williams et al. (1990) and White & Becker (1995).

(a), and the longitude of the ascending node (Ω) require the system to be resolved into a "visual" binary. The two stellar components in WR 140 have been resolved using the Infra-red Optical Telescope Array (IOTA) interferometer at a single epoch (Monnier et al. 2004). This single observation sets the scale and orientation of the orbit since it constrains potential families of solutions for (i, a, Ω). Further epochs of IOTA observations have been completed, but until analysis is complete, the VLBA observations of the WCR offer the only means to determine the orbit direction and constrain i, and hence Ω and a.

An initial analysis of 21 epochs of VLBA observations taken between 1999 and 2000 (orbital phase 0.74 to 0.95) was described in Dougherty et al. (2005). The work presented in this paper is an amalgamation of those observations with an additional 14 observations obtained between 2004 to 2008, that extended the orbital phase coverage from 0.43 to 0.96. A re-analysis of the earlier observations with the new data leads to tighter constraints on the derived orbit parameters.

2 VLBA observations of WR 140

WR 140 was observed with the VLBA at 8.4 GHz at 35 epochs between orbital phase 0.43 and 0.97. A selection of images are shown in Fig. 2. The 8.4-GHz emission is clearly resolved, with a bow-shaped emission region observed at many epochs. This shape is anticipated for a WCR from model calculations (e.g. see Eichler & Usov 1993, Dougherty et al. 2003, Pittard et al. 2006). The WCR rotates from "pointing" NNW to W over the observed orbital phases. This rotation is key to determining the orbit of WR 140. Assuming the arc of emission is symmetric about the line-of-centres and points towards the WR star, the O star is to the SSE of the WCR at epoch 0.43, and approximately to the E at phase 0.96.

Deriving the Orbit

On June 17, 2003 Monnier et al. (2004) observed WR 140 to have a separation of $12.9^{+0.5}_{-0.4}$ mas at a position angle of $151.7^{+1.8}_{-1.3}$ degrees east of north. Using $P = 2896.6$ days, $T_o = 2446156.3$,

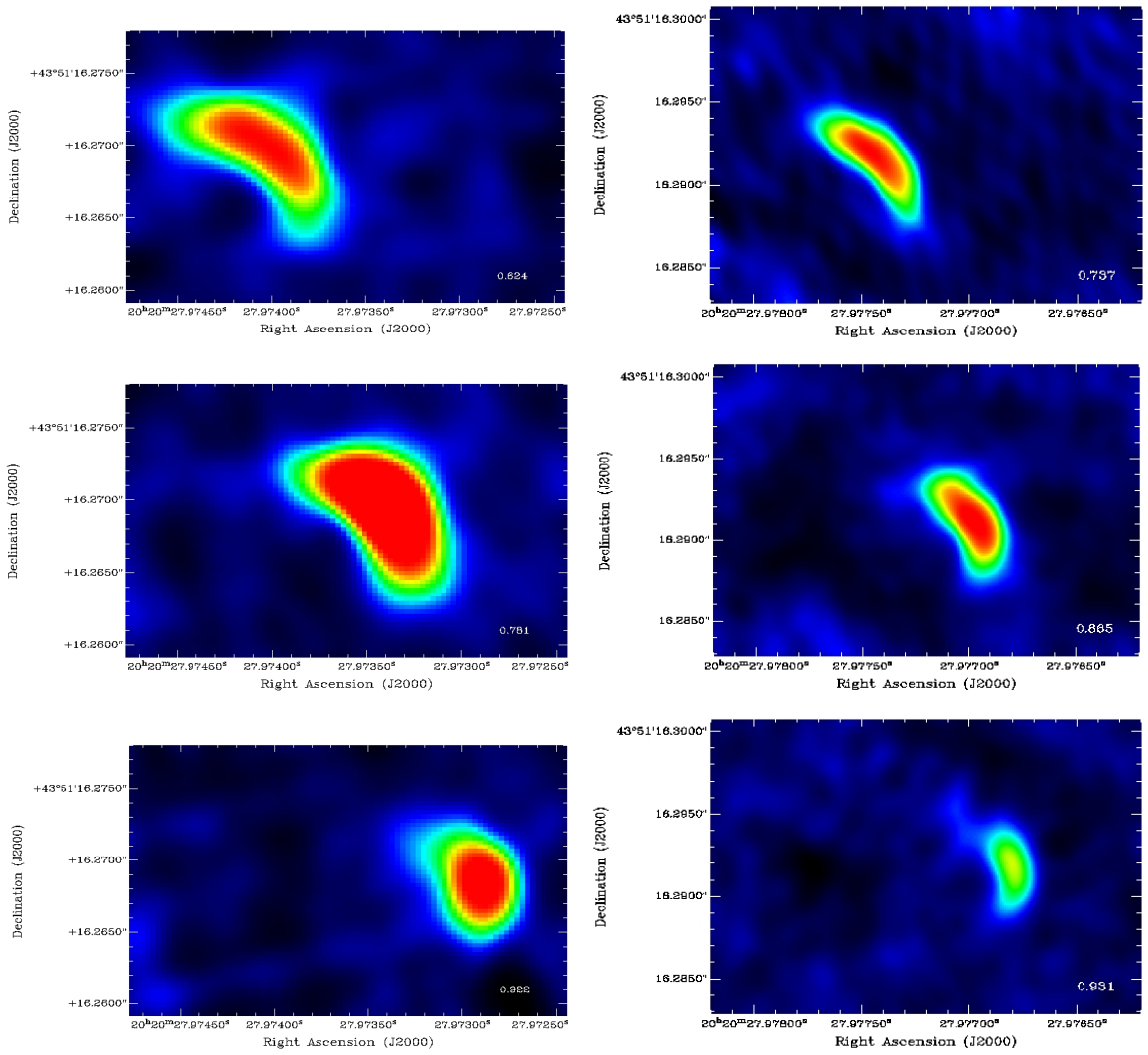

Figure 2: VLBA 8.6-GHz images of WR140 at phases 0.62, 0.74, 0.78, 0.87, 0.92, and 0.93 from the 1993-2001 orbit (phases 0.74, 0.87 and 0.93 - taken from Dougherty et al. 2005) and the 2001-2009 orbit. The synthesized beam is 2.0×1.5 mas^2 in the 1993-2001 orbit, and approximately $1.3\times$ that for the latest observations. Note change in RA and Dec between the images taken from the 1993-2001 orbit and the recent orbit. Rotation and proper motion of the WCR are evident during both orbits.

$e = 0.897$ and $\omega = 46.8°$ determined from analysis of observations during the 2009 periastron (Fahed et al. 2010), the observation at orbital phase 0.296 restricts potential sets of solutions for i, a and Ω to those shown in Fig. 3 for inclinations in the range $0° < i < 180°$.

The change in the orientation of the WCR with orbital phase gives the inclination since each (i, Ω) solution family provides a unique set of position angles as a function of orbital phase. A weighted minimum χ^2 measure between the observed position angle of the line of symmetry of the WCR, and by proxy the line-of-centres of the stars, as a function of orbit phase determined for different sets of (i, Ω) leads to a best-fit solution of $i = 120° \pm 4°$ and $\Omega = 352° \pm 2°$ (Fig. 4). These values lead to a semi-major axis of $a = 8.97 \pm 0.13$ mas.

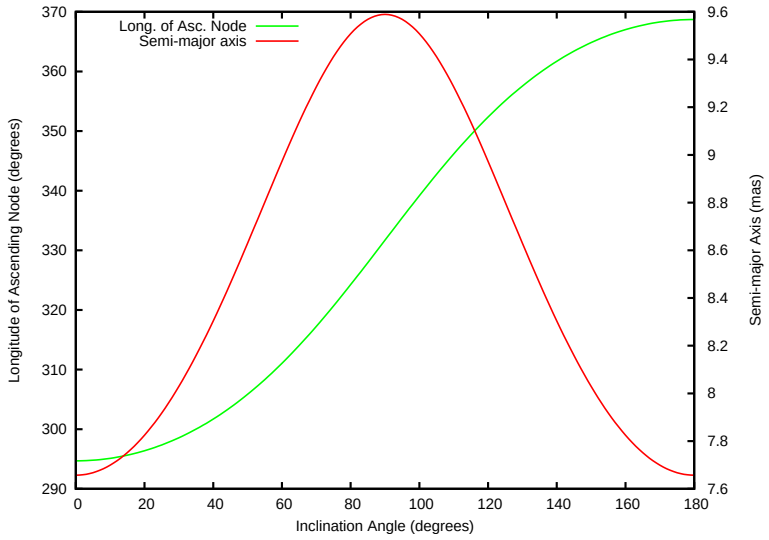

Figure 3: Solutions for the longitude of the ascending node (red line) and orbit semi-major axis (green line) as a function of orbit inclination, derived from an IOTA separation and a position angle of the stellar components at orbit phase 0.296 (Monnier et al. 2004).The uncertainty in the IOTA observation gives an error in Ω of closely $\pm 1°$, and in the semi-major axis of ± 0.3 mas.

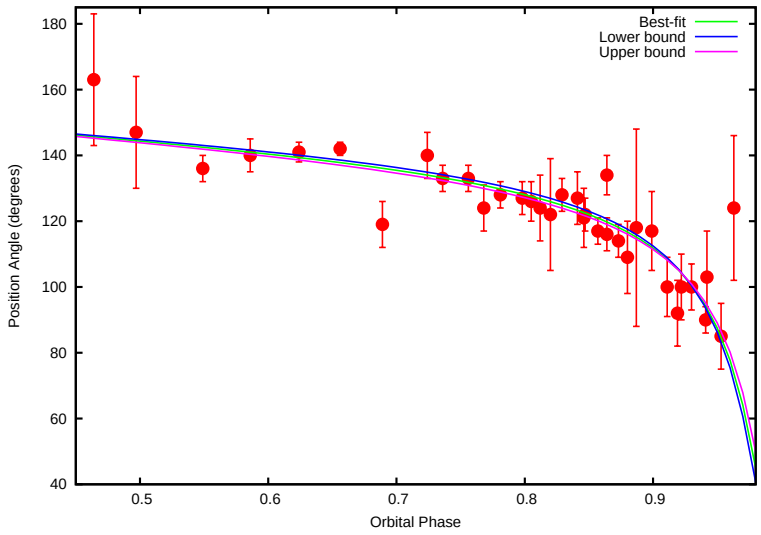

Figure 4: The change in the position angle of the axis of symmetry of the WCR as a function of orbital phase. The green line is the weighted best-fit curve of the position angle of the line-of-centres of the two stars as a function of phase, corresponding to $i = 120°$ and $\Omega = 352°$. The other two lines show the fits for $\Delta\chi^2 = \pm 1$, showing the range of potential fits for the quoted uncertainties.

Distance of WR 140

Stellar distance is one of the more difficult parameters to determine for stars. Marchenko et al. (2003) determined $a \sin i = 14.10 \pm 0.54$ AU from radial velocity observations. From our estimate of i, this gives $a = 16.28 \pm 0.81$ AU. A semi-major of $a = 8.97 \pm 0.13$ mas then gives a distance estimate of 1.81 ± 0.09 kpc, consistent with the previous estimate of 1.85 ± 0.16 kpc by Dougherty et al. (2005).

Summary

High-resolution radio observations of the WCR in WR140 have provided, to date, the only way to determine the direction and orientation of the orbit, starting from the scale of the orbit as deduced from IR interferometry and orbital parameters from optical spectroscopy. From this work it is possible to determine a precise, and hopefully accurate, distance to WR140.

WR140 is the best colliding-wind binary system for attempts to understand the underlying particle acceleration processes and physics in wind-collision regions, in large part due to the wealth of observational constraints. However, the orbit and distance are critical to modelling the WCR, and further refinements of these parameters await further IR interferometric observations that will resolve the stellar components directly.

Acknowledgments

We are grateful to Peredur Williams for many useful discussions related to this work. The work has been supported by the National Research Council of Canada, and the University of Prince Edward Island Co-op programme. The observations presented here were obtained from the Very Long Baseline Array, operated by the National Radio Astronomy Observatory (NRAO).

References

Dougherty, S.M., Beasley, A.J., Claussen, M.J., Zauderer, B.A., & Bolingbroke, N.J. 2005, ApJ, 623, 447
Dougherty, S.M., Pittard, J.M., Kasian, L., Coker, R.F., Williams, P.M., & Lloyd, H.M. 2003, A&A, 409, 217
Eichler, D., & Usov, V. 1993, ApJ, 402, 271
Fahed, R., Moffat, A. F. J., Zorec, J., et al. 2011, in Proceedings of the 39th Liège Astrophysical Colloquium, eds. G. Rauw, M. De Becker, Y. Nazé, J.-M. Vreux & P.M. Williams, BSRSL 80, 668
Marchenko, S.V., Moffat, A.F.J., Ballereau, D., et al. 2003, ApJ, 596, 1295
Monnier, J.D., Traub, W.A., Schloerb, F.P., et al. 2004, ApJ, 602, L57
Pittard, J.M. 2011, in Proceedings of the 39th Liège Astrophysical Colloquium, eds. G. Rauw, M. De Becker, Y. Nazé, J.-M. Vreux & P.M. Williams, BSRSL 80, 555
Pittard, J.M., Dougherty, S.M., Coker, R.F., O'Connor, E., & Bolingbroke, N.J. 2006, A&A, 446, 1001
Pittard, J.M., & Dougherty, S.M. 2006, MNRAS, 372, 801
White, R.L., & Becker, R.H. 1995, ApJ, 451, 352
Williams, P.M., van der Hucht, K.A., Pollock, A.M.T., Florkowski, D.R., van der Woerd, H., & Wamsteker, W.M. 1990, MNRAS, 243, 662

Multiplicity in 5 $M_\odot$ Stars

Nancy Remage Evans[1]

[1] Smithsonian Astrophysical Observatory

Abstract: Multiwavelength opportunities have provided important new insights into the properties of binary/multiple 5 $M_\odot$ stars. The combination of cool evolved primaries and hot secondaries in Cepheids (geriatric B stars) has yielded detailed information about the distribution of mass ratios. It has also provided a surprisingly high fraction of triple systems. Ground-based radial velocity orbits combined with satellite data from Hubble, FUSE, IUE, and Chandra can provide full information about the systems, including the masses. In particular, X-ray observations can identify low mass companions which are young enough to be physical companions. These multiwavelength observations provide important tests for star formation scenarios including differences between high and low mass results and differences between close and wide binaries.

1 Introduction

The multiplicity of stars provides important clues to star formation processes, and in some cases is the most important determinant of their future. For 5 $M_\odot$ stars, multiwavelength observations have provided detailed information about their multiplicity and also their binary/multiple properties. Specifically Cepheids (post-main sequence He burning stars in the "blue loop" phase of evolutionary tracks) can be used to provide such information in novel ways.

1.1 Multiplicity

Because these cool supergiants often have hot main sequence companions, ultraviolet spectra (HST and IUE) provide a spectrum of the companion uncontaminated by the light of the primary (Evans 1995). This has been used to determine Cepheid masses (Evans et al. 2005, and references therein). It has also been a particularly valuable way to identify systems which are not simply binaries, but triple systems (Evans, et al. 2005). In fact, without some direct information about the secondary, one cannot be confident in general that a system contains only two stars.

Triple systems among Cepheids have been identified in many ways (see Evans, et al. 2005). W Sgr provides one example. It was known both to be a binary system with an orbit (Babel et al. 1989) and to have a hot companion (Böhm-Vitense & Proffitt 1985; Evans 1991). However, the combination was not consistent with a reasonable mass for the Cepheid (see Evans, Massa & Proffitt 2009). The solution came from an HST STIS (Space Telescope Imaging Spectrograph) spectrum (Fig 1). The hottest star in the system is resolved from the Cepheid and its spectroscopic binary companion. This new insight results in a reasonable upper limit to the Cepheid mass from the astrometric orbit of the Cepheid (Benedict et al. 2007).

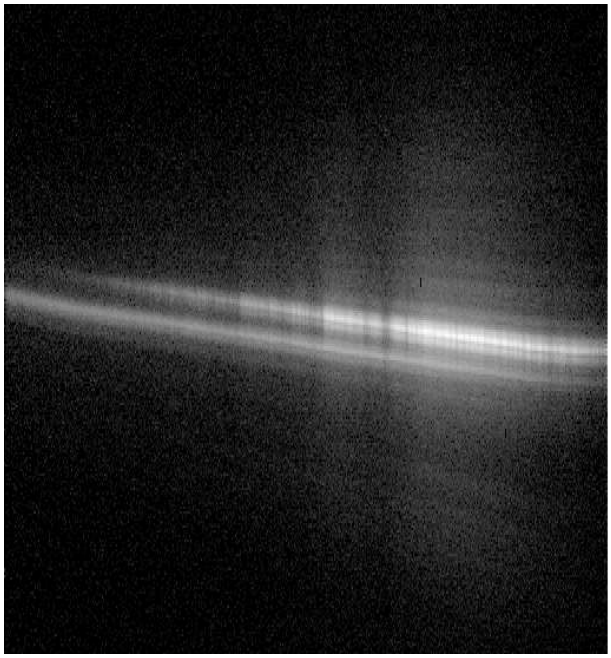

Figure 1: The flat-fielded HST STIS image of W Sgr. Wavelength increases to the right from about 1796 to 3382 Å. The cooler component (Cepheid + spectroscopic binary companion) is the upper one in the image and clearly separated from the hotter component below which extends much further toward shorter wavelengths. The spectrum flux is on a log scale. The strongest feature in the Cepheid spectrum is Mg II 2800Å. Reprinted from Evans, et al. (2009).

Another example of the detection of a third star from a spectrum of the secondary is provided by SU Cyg. The hot companion of the Cepheid is known to be a binary from ultraviolet velocities. However, in addition, it has a strong Ga II feature at 1414 Å, indicating that it is a HgMn star (Wahlgren & Evans 1998). Since these chemically peculiar stars require very slow rotation to facilitate element diffusion, they are found in short period binaries, whose orbit and rotation have been tidally locked. The Ga II feature is easily identifiable on a low resolution spectrum, indicating that the companion is itself a binary.

In order to determine the fraction of well-studied binary Cepheid systems which are in fact triple, we (Evans et al. 2005) have compiled a list of 18 Cepheids with orbits which have an ultraviolet spectrum of the companion. Of these, 44% (possibly 50%) are triples, a very high fraction for 5 $M_{\odot}$ stars.

1.2 Mass Ratio Distribution

Ultraviolet spectra also provide very precise spectral types of the companion, from which masses can be inferred. The mass ratios from the companion mass and a mass inferred for the Cepheids are shown in Fig. 2. (See Evans (1995) for a full discussion of Cepheid mass ratios and completeness.) Note that the Cepheid sample includes only systems with orbital periods longer than a year, since shorter period systems would have undergone Roche lobe overflow before the primary became a supergiant. For comparison, the mass ratio distribution of solar mass stars from Duquennoy and Mayor (1991, hereafter referred to as DM) is shown. The distributions are very similar, despite the fact that the Cepheid primaries are 5 times as massive as the DM primaries. For comparison, the mass ratio distribution of O stars from recent studies is shown (Rauw et al. 2009; Sana et al. 2008; Sana, Gosset & Evans 2009; Kiminki et al. 2009). It contains a population of equal mass binaries and falls off

for low mass companions. This poses the question of whether the mass ratio (q) distribution is a function of separation and/or mass, and also the role of incompleteness. That is, one explanation for the difference in Fig. 2 between Cepheids and O stars may be that short period binaries in the O star sample are more likely to have equal mass binaries than the remaining longer period (wider separation) binaries in the Cepheid sample.

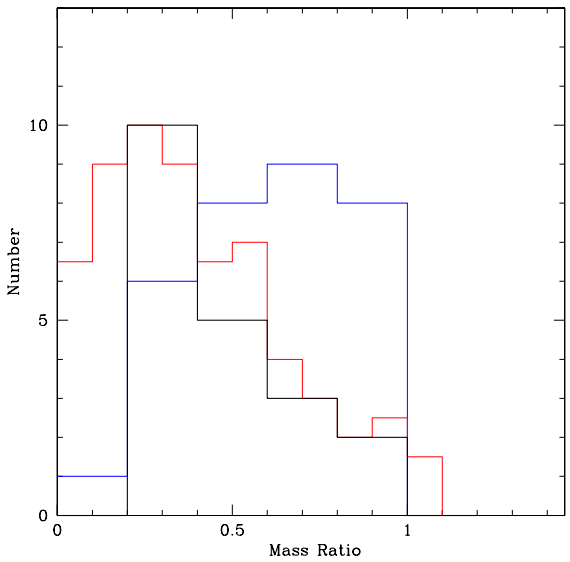

Figure 2: The distribution of mass ratios q = M_2/ M_1. The black line is the Cepheid sample (Evans 1995); the red line is the solar mass sample from DM; the blue line is the O star sample.

1.3 Low Mass Companions

One important aspect of binary properties is the prevalence of low mass companions for 5 $M_\odot$ primaries. These are, of course, the most difficult to detect both by photometric and spectroscopic (radial velocity) techniques. We are exploring the use of X-rays to improve this situation. Comparable mass main sequence stars (late B stars) do not in general produce X-rays. Low mass stars (spectral types mid F through K) young enough to be Cepheid/late B star companions (typically 50 Myr old) produce copious X-rays. M stars are weaker X-ray sources; older field stars are also much weaker X-ray sources. A list was drawn up of B3 to A0 stars in Tr 16 with proper motions indicating cluster membership (Cudworth, Martin & DeGioia-Eastwood 1993). Fig. 3 shows the sample with X-ray detections from a Chandra image (Evans et al. 2011; Townsley et al. 2011; Albacete-Colombo et al. 2008). Lines show the ZAMS for 2.3 kpc with E(B-V) = 0.45, 0.55, and 0.65 mag. 39% of the late B stars are detected as X-ray sources, indicating that they have low mass companions. See Evans, et al. (2011) for a complete discussion, including the X-ray detection fraction.

1.4 Discussion

As shown in the previous sections, multiwavelength observations have provided considerable new insight into the binary/multiple properties of 5 $M_\odot$ stars. Here we discuss some remaining issues about multiplicity.

Direct observations of companions, provided particularly in ultraviolet studies by HST and IUE, find a high fraction of triple systems (at least 44%). Even this, however, may not be the total count of

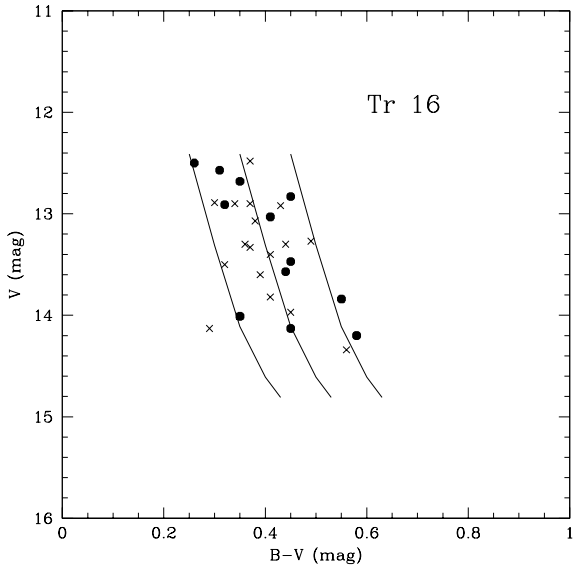

Figure 3: Late B stars in Tr 16 (from Evans, et al. 2011). Dots are detected in X-rays; x's are not detected. The lines are the ZAMS for 2.3 kpc and an appropriate range of B-V corresponding to E(B-V) = 0.45, 0.55, and 0.65 mag.

system members. For instance, in some systems with low mass companions, the low mass companion might itself be a binary.

The distribution of mass ratios (Fig. 2) strongly favors unequal mass companions. This pertains, however, only to Cepheids with separations ($a \sin i$) larger than about 0.4 AU and periods longer than a year (Sugars & Evans 1996). This is at least part of the reason for the difference between Cepheid mass ratios and those of O stars in Fig. 2.

A way to identify low mass companions of late B stars (comparable in mass to Cepheids) using X-ray images is shown in Fig. 3. How complete is our knowledge of the total binary/multiple fraction for 5 $M_\odot$ stars? The fraction Cepheids with companions hotter than mid A spectral type is known from an IUE survey of the 76 Cepheids brighter than 8^{th} mag (Evans 1992). 21% were found to have companions (which rises to 34% after a statistical correction was included based on stars with known orbital motion). The "Chandra fraction" of low mass companions and the "IUE fraction" should have relatively little overlap, and hence are approximately additive. Furthermore, the results tentatively suggest that the steep rise in secondary mass frequency seen in the DM solar mass stars from 1 to 0.2 $M_\odot$ stars is mimiced in the $5M_\odot$ mass ratio distribution. However, a drop off at the lowest mass ratios for the O stars (if confirmed) would imply only a very small fraction companions of 1 $M_\odot$ or less, as compared to a very large fraction for solar mass stars. That is, the *mass ratio* not the *mass* may be the important parameter at the time in star formation scenarios when the q distribution is determined.

For comparison, the recent study by Mason et al. (2009) of combined spectroscopic binary velocity results with interferometry for O and B stars[1]. They find a binary fraction of 66% for O stars. Their lists, of course, are not likely to contain low mass companions since small mass ratios and large magnitude differences make these companions very difficult to detect.

[1]X-ray identification of young companions cannot be used, since O and early B stars in this sample are intrinsic X-ray producers.

Acknowledgements

Funding for this work was provided by Chandra X-ray Center NASA Contract NAS8-39073.

References

Albacete-Colombo, J. F., Damiani, F., Micela, G., Sciortino, S., and Harnden, F. R., Jr. 2008, A&A, 490, 1055
Babel, J., Burki, G., Mayor, M., Waelkens, C., and Chmielewski, Y. 1989, A&A, 216, 125
Benedict, G. F., McArthur, B. F., Feast, M. W., et al. 2007, AJ, 133, 1810
Böhm-Vitense, E. and Proffitt, C. 1985, ApJ, 296, 175
Cudworth, K. M., Martin, S. C., and DeGioia-Eastwood, K. 1993, AJ, 105, 1822
Duquennoy, A. & Mayor, M. 1991, A&Ap, 248, 485 (DM)
Evans, N. R. 1991, ApJ 372, 597
Evans, N. R. 1992, ApJ, 384, 220
Evans, N. R. 1995, ApJ, 445, 393
Evans, N. R., Carpenter, K. G., Robinson, R., Kienzle, F., and Dekas, A. E. 2005, AJ, 130, 789
Evans, N. R., Massa, D., and Proffitt, C. 2009, AJ, 137,3700
Evans, N. R., DeGioia-Eastwood, K, Gagne, M., et al. 2011, ApJS, preprint
Kiminki, D. C., Kobulnicky, H. A., Gilbert, I., Bird, S., and Chunev, G. 2009, AJ, 137, 4608
Mason, B. D., Hartkopf, W. I., Gies, D. R., Henry, T. J., and Helsel, J. W. 2009, AJ, 137, 3358
Rauw, G. Nazé, Y., Fernández Lajús, E., Lanotte, A. A., Solivella, G. R., Sana, H., and Gosset, E. 2009, MNRAS, 398, 1582
Sana, H., Gosset, E., Nazé, Y., Rauw, G., and Linder, N. 2008, MNRAS, 386, 447
Sana, H., Gosset, E., and Evans, C. J. 2009, MNRAS, 400, 1479
Sugars, B. J. A. and Evans, N. R. 1996, AJ, 112, 1670
Townsley, L. K., Broos, P. S., Corcoran, M. F. et al. 2011, ApJS, preprint
Wahlgren, G. M. and Evans, N. R. 1998, A&A, 332, L33

Spectroscopic follow-up of the colliding-wind binary WR140 during the 2009 January periastron passage

R. Fahed[1], A. F. J. Moffat[1], J. Zorec[2], T. Eversberg[3], A. N. Chené[4],
F. Alves*, W. Arnold*, T. Bergmann*, L. F. Gouveia Carreira*, F. Marques Dias*,
A. Fernando*, J. Sanchez Gallego*, T. Hunger*, J. Knapen*, R. Leadbeater*, T. Morel*,
G. Rauw*, N. Reinecke*, J. Ribeiro*, N. Romeo*, E. M. dos Santos*, L. Schanne*,
O. Stahl*, Ba. Stober*, Be. Stober*, N. G. Correia Viegas*,
K. Vollmann*, M. F. Corcoran, S. M. Dougherty, J. M. Pittard, A. M. T. Pollock,
and P. M. Williams

[1] Université de Montréal, Montréal, Canada
[2] Institut d'Astrophysique de Paris, Paris, France
[3] Schnörringen Telescope Science Institute, Köln, Germany
[4] Herzberg Institute of Astrophysics, Victoria, Canada
* MONS pro-am collaboration

Abstract: We present the results from the spectroscopic follow-up of WR140 (WC7 + O4-5) during its last periastron passage in January 2009. This object is known as the archetype of colliding wind binaries and has a relatively large period ($\simeq$8 years) and eccentricity ($\simeq$0.9). We provide updated values for the orbital parameters, new estimates for the WR and O star masses and new constraints on the mass-loss rates.

1 Introduction

WR140 is a very eccentric WC7+O5 colliding-wind binary (CWB) system with an eccentricity of nearly 0.9 (Marchenko et al. 2003 (= M03) and this paper) and a long period of about 7.9 years. It is also the brightest Wolf-Rayet star in the northern hemisphere and is considered as the archetype of CWB. We present here the results from a spectroscopic follow-up, unique in time coverage and resolution. The observation campaign was a worldwide collaboration involving professional and amateur (pro-am) astronomers and took place during a period of 4 months around periastron passage in January 2009.

2 Observations

A list of the sources of the campaign is presented in Table 1.

Table 1: List of the different sources in the 2009 campaign. Names marked with an asterisk are amateur astronomers/organisations equipped with their personal instrumentation.

Observatory / Telescope	Dates	Wavelength Range (Å)	Resolution (Å/ pixel)	Nb. of spectra
IAC / MONS 50 cm	1.12.08 - 23.03.09	5530-6000	0.35	34
OHP / 193 cm	12.12.08 - 23.3.09	4000-6800	0.01	63
DAO / 120 cm	22.4.08 - 9.1.09	5350-5900	0.37	13
OMM / 160 cm	5.7.09 - 8.8.09	4500-6000	0.63	18
Three Hills* (UK) Amateur telescope	10.12.07 - 20.3.09	5600-6000	0.68	38
Berthold Stober* (Germany) Amateur telescope	26.8.08 - 29.2.09	5500-6100	0.53	12

3 Radial velocities

The WR star radial velocities were estimated by cross correlation with a reference spectrum and the O star radial velocities by measuring the centroid of the photospheric absorption lines (see Fig. 1a). We notably find a higher eccentricity than previously published (e=0.896 $\pm$ 0.002 cf. 0.881 $\pm$ 0.005 from M03) and an updated value for the period (2896.5 $\pm$ 0.7 d instead of 2899.0 $\pm$ 1.3 d).

4 Excess emission

The presence of a shock cone around the O star induces an excess emission that we measured on the C III 5696 flat top line. This excess emission appears first, just before periastron passage, on the blue side of the line, and then moves quickly to the red side and grows, just after periastron passage, before it disappears (Fig.2). We fitted the radial velocity and the width of this excess as a function of orbital phase using a simple geometric model (Luehrs 1997) which enables us to constrain the half opening angle of the shock cone θ, the velocity of the fluid along the cone $v_{\rm strm}$, the orbital inclination i and an angular shift due to Coriolis forces $\delta\phi$ (see Fig.3). To be able to use the Luehrs model, which is originally designed for circular orbits, we fitted the excess as a function of the true anomaly instead of phase. By doing this, we implicitly assume that the $\delta\phi$ parameter stays constant throughout the periastron passage. This hypothesis is of course questionable and a more general model would be needed. Meanwhile, the resulting fit (shown in Fig. 4) seems quite good. We find a value for the inclination of 52$\pm$8° (cf. 58$\pm$5° from Dougherty et al. 2005) which gives the following estimation for the stellar masses : M_{WR} = 18.4$\pm$1.8 $M_\odot$ and M_O = 45.1$\pm$4.4 $M_\odot$ (cf. 19 $M_\odot$ and 50 $M_\odot$ from M03). From the half opening angle of the shock cone (Canto, Raga & Wilkin 1996), we also find a wind momentum ratio η = 0.028$\pm$0.009 (cf. 0.045 from M03 and 0.22 from Dougherty et al. 2005).

5 Conclusion

The 2009 periastron campaign on WR140 provided updated values for the orbital parameters, new estimates for the WR and O star masses and new constraints on the mass-loss rates. It is also a very encouraging success in term of professional-amateur collaboration and we hope it will give rise to similar initiatives in the future. However, our capability to measure the shock cone parameters with confidence and to understand its underlying physics is limited by the over simplistic approach

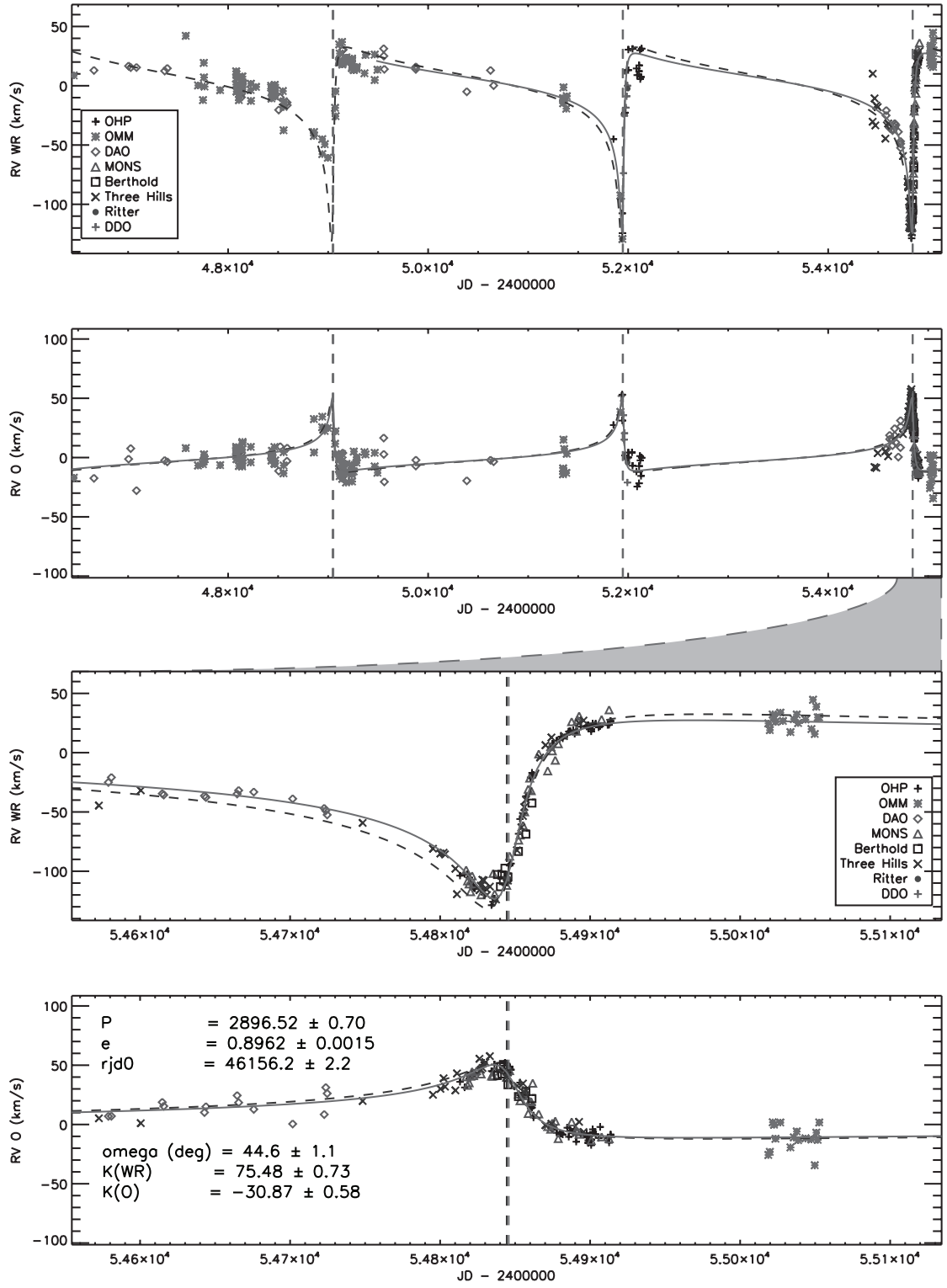

Figure 1: Top two panels: measured radial velocities of the WR star and of the O star together with the fit for the orbital solution (full line). We included data from the last periastron campaigns in 1993-2001 (M03), taken at David Dunlap Observatory (DDO), OHP, Ritter Observatory, DAO and OMM. The black dashed line is the orbital solution from M03. The dashed vertical lines show the position of the periastron passage. Bottom two panels: same plots but zoomed on the 2009 campaign (the filled curve between panel 2 and 3 illustrates the X axis expansion). The best fit parameters are indicated in panel 4.

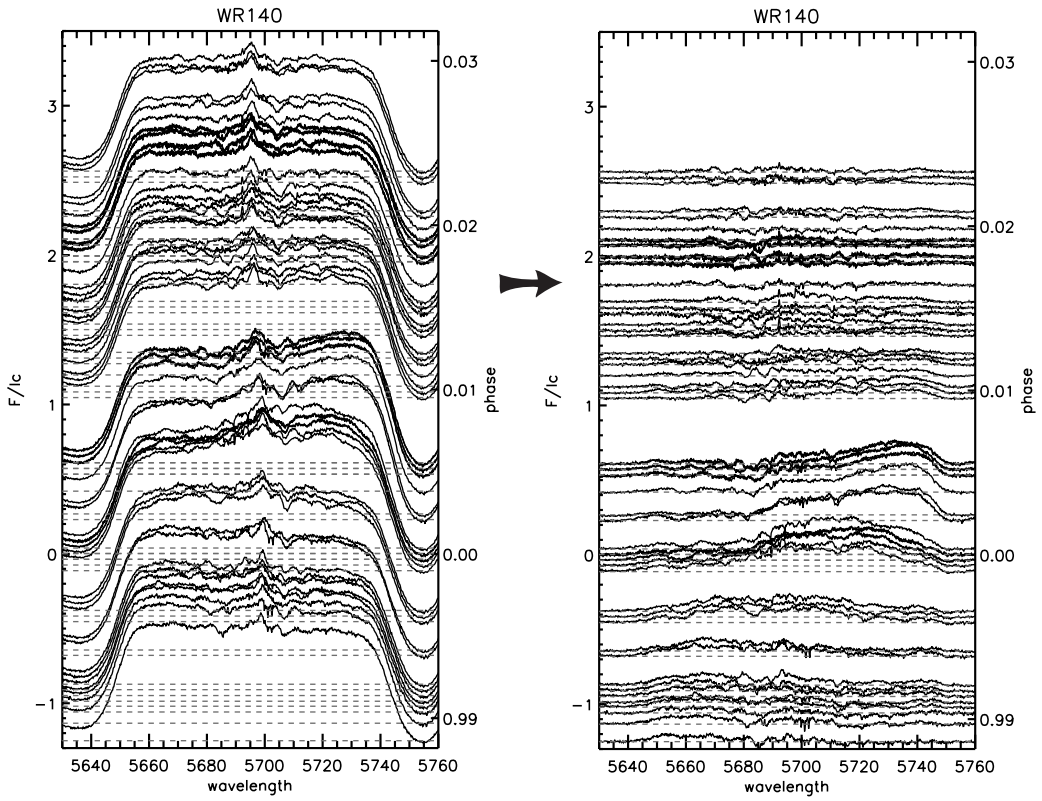

Figure 2: Left: the C III 5696 flat top line as a function of the orbital phase (OHP data). Right: excess emission as a function of the phase, obtained by substraction of a reference profile, unaffected by wind collision.

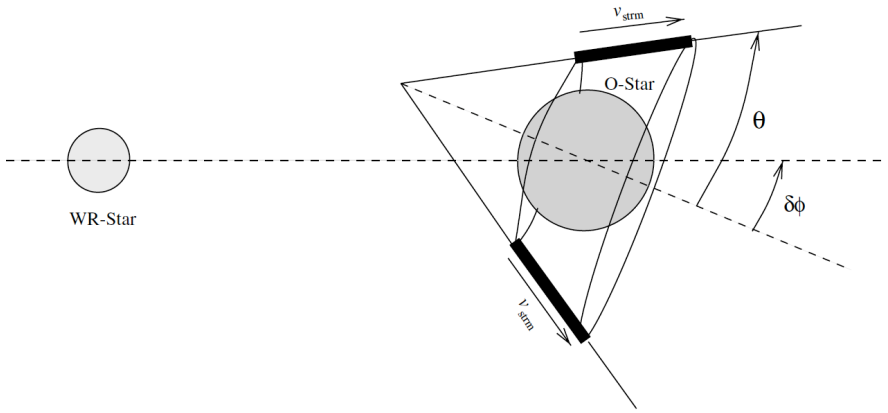

Figure 3: Schematic view of the geometric model by Luehrs (1997). The full width and radial velocity of the excess will then be given by : $FW_{ex} = C_1 + 2\,v_{\rm strm}\,\sin(\theta)\sqrt{1-\sin^2(i)\,\cos^2(\phi-\delta\phi)}$ and $RV_{ex} = C_2 - v_{\rm strm}\,\cos(\theta)\,\sin(i)\,\cos(\phi-\delta\phi)$

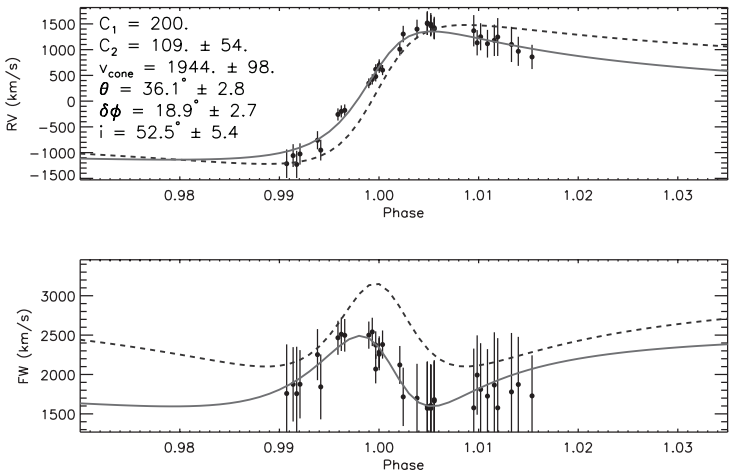

Figure 4: Fit of the radial velocity and width of the excess using the Luehrs model (full grey line). The black dashed line shows the solution from M03.

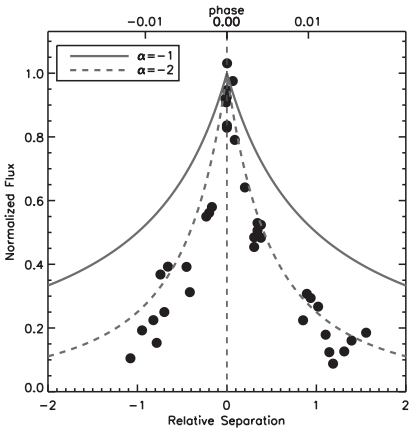

Figure 5: Normalized flux of the excess as a function of the relative separation of the two stars ($[d - d_{min}]/d_{min}$). The full line shows a d^{-1} dependence, expected for an adiabatic emission process. The dashed line shows a d^{-2} dependence, possibly more in line with an isothermal process.

of our model. A more sophisticated theoretical investigation should be done. Meanwhile, the d^{-2} dependence of the excess, shown in Fig. 5, strongly suggests that some kind of isothermal process is involved here. Links with observations in other spectral domains (X-ray, IR and radio) will certainly provide valuable clues about the physics. Finally, we will attempt to isolate the WR spectrum from the O-star spectrum from our data in order to identify the spectral type of the latter more precisely. We also have some photometric and spectropolarimetric data to analyse to complete our view of this system.

References

Canto, J., Raga, A.C. & Wilkin, F.P., 1996, ApJ, 469, 729
Dougherty, S.M., Beasley, A.J., Claussen, M.J., Zauderer, B.A. & Bolingbroke, N.J., 2005, ApJ, 623, 447
Luehrs, S., 1997, PASP, 109, 504
Marchenko, S.V., Moffat, A.F.J., Ballereau, D. et al. 2003, ApJ, 596, 1295 (M03)

The X-ray emission of the colliding wind binary V444 Cyg

Thomas Fauchez[1], Michaël De Becker[1,2] & Yaël Nazé[1]

[1] Department of Astrophysics, Geophysics and Oceanography, University of Liège, Belgium
[2] Observatoire de Haute-Provence, Saint-Michel l'Observatoire, France

Abstract: This paper presents the analysis of six *XMM-Newton* observations of the colliding wind system V444 Cyg. Unlike what one might have expected at first, it appears that the O star wind most probably dominates the WN wind: the bow shock is wide open, with the hard X-ray emission arising close to the WN star. An important radiative braking could partly explain this situation but revising the wind parameters may also prove necessary. Furthermore, we have probably observed for the first time an occultation of the colliding wind zone by the binary components.

1 Scientific context

V444 Cyg is a close colliding wind binary system made up of an O6 star and a WN5 star. It is a double eclipse system with a period of ∼4.2 days. The physical parameters are summarized in Table 1. Using these parameters, we have calculated the pre-shock velocities of both winds, assuming that the winds obey the following velocity law: $v_j(r) = v_{\infty,j}(1-\frac{R_j}{r_j})^{\beta_j}$, with j indicating the number of the star (1 for the WN and 2 for the O-star), $v_{\infty,j}$ being the terminal wind speed of the jth star, R_j the stellar radius of the jth star, r_j the radial distance to star j and β being equal to 1 for both stars (Hamann & Schwarz 1992). We obtained a pre-shock velocity value of 2204 km s^{-1} for the WN wind and 441 km s^{-1} for the O star wind. These velocities result in post-shock temperatures of about 9 keV. Note that this value is an upper limit since the Rankine-Hugoniot equations do not take into account the phenomenon of radiative braking.

2 Observations

For our study of the V444 Cyg system, six exposures taken by *XMM-Newton* in 2004 (Obs. ID 020624) were available. These observations covered half an orbit (i.e. they were taken at phases 0.02, 0.12, 0.28, 0.39, 0.49, and 0.51) with a nominal exposure time by observation of 10 ks. Note that phase 0 corresponds to the phase where the WR is in front of the O-star.

	WR star	O star	Ref
P_0 [days]	4.212450 ± 0.000048		1
T_0 [julian days]	2438636.867		2
Incl. angle [deg]	78		3
Distance[kpc]	1.7		4
$f(m)[M_\odot]$	12.9 ± 0.3	1.1 ± 0.1	5
$M[M_\odot]$	12.4 ± 0.5	28.4 ± 0.6	5
$\dot{M}[M_\odot\ yr^{-1}]$	4.6×10^{-6}	5.8×10^{-7}	5
$R[R_\odot]$	2.9	10	6
$a[R_\odot]$	26.2 ± 0.3	11.5 ± 0.3	5
$\gamma[km\ s^{-1}]$	45 ± 1	-26 ± 2	5
$K[km\ s^{-1}]$	309 ± 2	136 ± 3	5
$\omega[deg]$	268.6 ± 0.4	88.0 ± 1.0	5
$v_\infty[10^3 km\ s^{-1}]$	2.5	1.7	7

Table 1: Physical parameters of V444 Cyg. References are (1) Pelt (1992); (2) Underhill et al. (1990); (3) Cherepashchuk, Eaton & Khaliullin (1984); (4) Forbes (1981); (5) Hirv et al. (2006); (6) Corcoran et al. (1996); (7) Stevens et al. (1992)

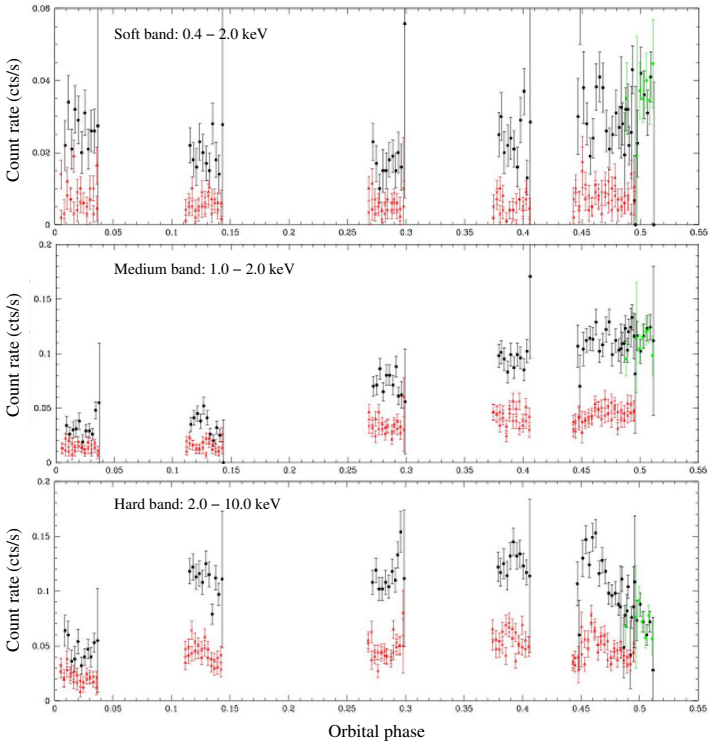

Figure 1: Variations of the count rates in three energy bands. The black and green circles correspond to EPIC-pn data, while crosses and red triangles indicate EPIC-MOS data.

3 Light curve analysis

Figure 1 shows the evolution of the EPIC count rates with orbital phase for three different energy bands. In the soft band (0.4-2 keV), the count rate is always significantly low because the absorption is particularly strong in this system, thus it shows only weak variations (not statistically significant) over the orbit. The medium band (1-2 keV) count rate decreases when

the system is seen through the opaque wind of the WN. However, this flux decrease occurs only over a short phase interval, implying that the O-star wind dominates that of the WN and that the bow shock is probably wide open. This can probably be explained by the phenomenon of radiative braking. Indeed, simulations of Owocki & Gayley (1995) showed that, provided radiative braking is strong enough, the bow shock could be widely open. By contrast, the hard band (2-10 keV) count rate remains stable over the orbit, except at the phases corresponding to the optical eclipses. Indeed, a large decrease of the count rate is observed between the phases $\phi = 0.00$ and $\phi = 0.04$ and between the phases $\phi = 0.45$ and $\phi = 0.50$. This could be easily explained if the stars occult the zone emitting the hard X-rays at these phases. In this case, a sketch of the system (Fig. 2) suggests that the allowed position of the hot plasma (green hatched area) is close to the WN star, in other words far from the theoretical stagnation point (black dot). This difference is probably due to radiative braking, but not only, as simulations by Owocki & Gayley (1995) do not result in a colliding-wind zone wrapped around the WN star. Therefore, a revision of the system's physical parameters (mass-loss rate, wind velocity) is probably needed.

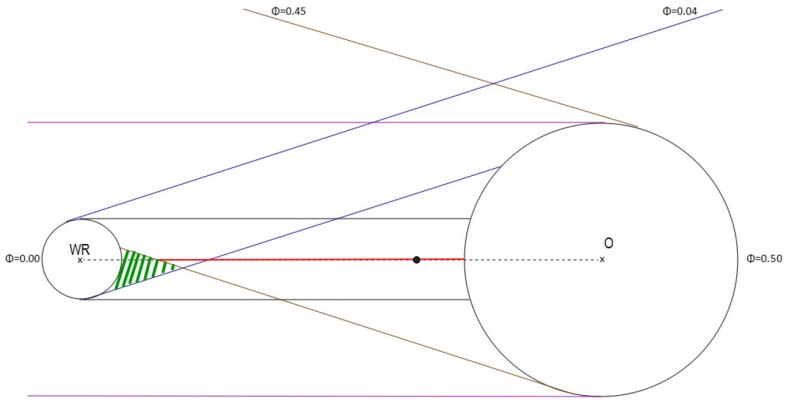

Figure 2: Sketch to scale of the V444 Cyg system (assuming an inclination of 90°). The dotted line joins the stars' centers; the black dot on this line represents the theoritical position of the stagnation point when solely considering ram-pressure balance. The grey and blue parallel lines bound the zone eclipsed by the WN at phases $\phi = 0.00$ and $\phi = 0.04$, respectively; the purple and brown parallel lines bound similar zones, but eclipsed by the O-star at phases $\phi = 0.45$ and $\phi = 0.50$, respectively. The green hatched area corresponds to the area eclipsed during both phase intervals $0 < \phi < 0.04$ and $0.45 < \phi < 0.5$. If the occultation hypothesis is correct, then a significant fraction of the hot plasma due to the colliding winds should be located there.

4 Spectral analysis

The spectral fitting was done using a progressive approach, i.e. we freed one physical parameter at a time. This careful approach allowed us to obtain physically realistic spectral parameters. First of all, we used a very simple model with one global absorption component and two optically-thin thermal plasma emission components, i.e. $wabs \times (apec + apec)$. Next, we associated an individual absorption component to each emission component and used a global absorption component fixed to the interstellar value of 0.32×10^{22} cm^{-2} (Oskinova 2005), i.e. the model has the form $wabs_{ISM} \times (wabs \times apec + wabs \times apec)$. In this case, whatever the orbital phase, we obtained temperatures of the order of ∼0.6 keV and ∼2.0 keV for the thermal

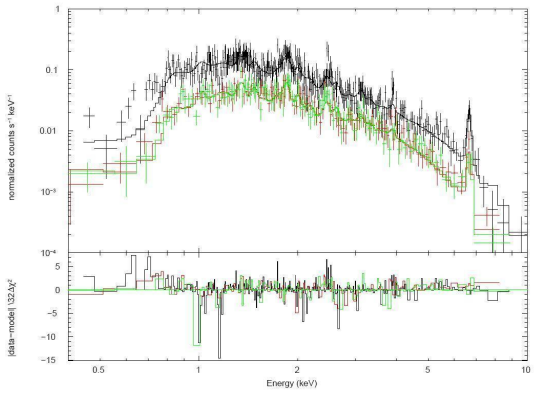

Observation	n_{H1} $[10^{22} cm^{-2}]$	norm 1 $[10^{-3} cm^{-5}]$	n_{H2} $[10^{22} cm^{-2}]$	norm 2 $[10^{-3} cm^{-5}]$	reduced χ^2 dof	absorbed flux unabsorbed flux $[erg\ cm^{-2}\ s^{-1}]$
Obs 1	$0.67^{0.77}_{0.58}$	$0.52^{0.63}_{0.43}$	$7.11^{7.67}_{6.60}$	$3.74^{4.01}_{3.48}$	1.03 306	1.15×10^{-12} 1.26×10^{-12}
Obs 2	$0.49^{0.57}_{0.43}$	$0.45^{0.53}_{0.38}$	$11.81^{13.90}_{9.99}$	$2.41^{2.83}_{2.03}$	1.20 264	0.62×10^{-12} 0.76×10^{-12}
Obs 3	$0.77^{0.92}_{0.58}$	$1.47^{2.12}_{0.83}$	$2.10^{3.17}_{1.31}$	$1.14^{1.35}_{0.95}$	0.96 141	0.87×10^{-12} $1,10 \times 10^{-12}$
Obs 4	$1.12^{1.22}_{1.02}$	$2.07^{2.51}_{1.68}$	$3.51^{3.98}_{3.09}$	$2.69^{2.89}_{2.51}$	1.05 447	1.36×10^{-12} 1.54×10^{-12}
Obs 5	$1.09^{1.23}_{0.94}$	$1.45^{1.90}_{1.05}$	$3.19^{3.68}_{2.77}$	$2.23^{2.40}_{2.08}$	1.08 346	1.14×10^{-12} 1.28×10^{-12}
Obs 6	$0.99^{1.06}_{0.91}$	$2.04^{2.39}_{1.70}$	$2.69^{3.04}_{2.38}$	$2.04^{2.24}_{1.87}$	1.01 617	1.24×10^{-12} 1.46×10^{-12}

Figure 3: *Left*: Best-fit model superimposed on the observed spectra (MOS 1 & 2 data shown in green and red, respectively, pn data in black) of the 6th observation (i.e. ϕ=0.51). *Right*: Best-fit spectral parameters for the final model. n_{H1} and n_{H2} represent the column densities in front of the first and second emission component, respectively, and $norm_1$ and $norm_2$ represent the normalization parameters of the first and second emission component. The plasma temperatures were fixed to the values of 0.59 and 2.01 keV, respectively, for the two emission components. The nitrogen abundance was fixed to 101.3 (best-fit value for the 6th observation), while those of carbon and oxygen were fixed to 0. Other abundances were frozen to solar values.

components. Since these temperatures did not seem to vary with phase, we froze them and then successively allowed the abundances of nitrogen, carbon, oxygen and iron of the emission components to vary. The abundances of some elements deviate significantly from the solar values: N presents a significant overabundance, while abundances of C and O are compatible with a null value. We did not notice any significant deviation from the solar value for the iron abundance. Our best-fit parameters were obtained when we fixed the plasma temperatures and abundances to the values for the highest quality observation (ϕ=0.51), allowing only local absorbing columns and normalization parameters to vary from one observation to the other. This approach was necessary to achieve a consistent modelling of the EPIC spectrum of V444 Cyg as a function of the orbital phase. The results are shown in Fig. 3.

The absorption and normalization factors of the cooler thermal component appear constant over the orbit. Moreover, the column density is quite small (with regard to the high density of the WN wind). This can be explained if the soft emission is intrinsic to the stellar winds and takes place far from the two stars. The normalization factor of the hotter emission component varies only slightly but its absorption varies strongly with orbital phase. It should indeed reach its maximum when the system is seen through the WN wind. This situation occurs between the phases $\phi = 0.00$ and $\phi = 0.12$. It is a surprisingly short phase interval, implying that the O-star wind clearly dominates the WN wind. Therefore, the bow shock should be wide open and may even wrap around the WN star.

5 Comparison with previous studies

V444 Cyg has been a target for several X-ray observatories: EINSTEIN (Moffat et al. 1982; Pollock 1987), ROSAT (Corcoran et al. 1996), ASCA (Maeda, Koyama & Yokogawa 1999). These campaigns already pointed out the presence of a probable contribution of the X-rays coming from colliding winds. The analysis of ASCA data led to a global description of the

X-ray spectrum in good agreement with ours: the spectrum is of thermal origin, with typical temperatures of the order of 0.6 and 2.0 keV. Maeda et al. (1999) also detected some variations in the X-ray spectrum as a function of the orbital phase (in particular in the hard part), but did not interpret them in terms of a potential occultation of the colliding-wind region.

More recently, the same *XMM-Newton* data set as presented here was analyzed by Bhatt et al. (2010). These authors obtained comparable lightcurves but do not interpret them. Furthermore, their spectral analysis was made in a very different manner: a complex model, with many free parameters, was used right away. This resulted in erratic results, sometimes unphysical, without satisfactory coherence between the results obtained at different orbital phases.

6 Concluding remarks

Our spectral and lightcurve analyses of the *XMM* data of V444 Cyg provided unexpected results. First, the evolution of the medium-band count rate and of the fitted absorption shows that the observed flux decreases when the system is seen through the WN wind. As this occurs over a short phase interval, this implies that the bow shock is widely open, maybe even folded around the WN star. In addition, the evolution of the flux observed in the hard band strongly suggests the occultation of a significant fraction of the hard X-ray emitting region, at orbital phases close to conjunctions. If confirmed, this result would constitute the first detection of occultations by stars of the hot plasma produced by a wind-wind collision. It must be noted that, in this framework, the hard X-ray emission should arise close to the WN star. These two results may be explained if one takes into account a strong radiative braking, perhaps combined to a revision of the wind parameters.

Acknowledgements

The authors acknowledge support from the XMM+INTEGRAL PRODEX contracts (Belspo) and the FRS/FNRS (Belgium). Our thanks go also to the referee for useful comments that significantly improved the present manuscript.

References

Bhatt, H., Pandey, J.C., Kumar, B., Singh, K.P. & Sagar, R. 2010, MNRAS 402, 1767
Cherepashchuk, A., Eaton, J., & Khaliullin, K. 1984, ApJ 281, 774
Corcoran, M.F., Stevens, I.R., Pollock, A.M.T., Swank, J.H., Shore, S.N. & Rawley, G.J. 1996, ApJ 464, 434
Forbes, D. 1981, PASP 93, 441
Hamann, W.-R., & Schwarz, E. 1992, A&A 261, 523
Hirv, A., Annuk, K., Eenmäe, T., Liimets, T., Pelt, J., Puss, A. & Tempel, M. 2006, Baltic Astronomy 15, 405
Maeda, Y., Koyama, K. & Yokogawa, J. 1999, ApJ, 510, 967
Moffat, A.F.J, Firmani, F., McLean, I.S., & Seggewiss, W. 1982, in *Wolf-Rayet Stars: Observations, Physics, Evolution*, IAU Symp 99, eds. de Loore, C.W.H. & Willis A.J., 577
Oskinova, L. 2005, MNRAS 361, 679
Owocki, S.P., & Gayley, K.G. 1995, ApJ 145, 148
Pollock, A.M.T. 1987, ApJ, 320, 283
Pelt, J. 1992, in *Irregular Spaced Data Analaysis - User Manual*, Helsinki University Press
Stevens, I.R., Blondin, J.M., & Pollock, A.M.T. 1992, ApJ 265, 287
Underhill, A.B., Grieve, G.R., & Louth, H. 1990, PASP 102, 749

Combined Spectroscopic and Interferometric Orbits for HD 193322

D. Gies[1], T. ten Brummelaar[1], D. O'Brien[1], G. Schaefer[1], E. Grundstrom[2], M. V. McSwain[3], C. Farrington[1], N. Turner[1], R. Matson[1], and S. Williams[1]

[1] CHARA, Georgia State University, Atlanta, GA, U.S.A.
[2] Department of Physics and Astronomy, Vanderbilt University, Nashville, TN, U.S.A.
[3] Department of Physics, Lehigh University, Bethlehem, PA, U.S.A.

Abstract: The star HD 193322 is a remarkable multiple system that lies at the heart of the cluster Collinder 419. Here we report on a new spectroscopic orbit for the central binary ($P = 312$ d) based on spectra collected over the last decade. We have also obtained long baseline interferometry of the target in the K'-band with the CHARA Array, and the fringe packet from the nearby companion was used to calibrate the visibility of the fringes of the shorter period binary. We performed an analysis of the fringe visibilities from many epochs, position angles, and baselines to obtain an astrometric orbit for the inner binary. We discuss the masses and other properties of the binary from the combined spectroscopic and astrometric results.

1 Introduction

The massive O-type stars are usually found with one or more nearby companions (Mason et al. 2009). Most of these luminous stars are very distant, and consequently, we generally only detect their very nearby companions (through Doppler shifts) or very distant acquaintances (angularly resolved). We must rely on high angular resolution observations of the few nearby cases to detect those elusive, mid-range separation, binary stars. One of the most revealing examples is HD 193322 (O9 V:((n)); Walborn 1972), the central star in the sparse open cluster Collinder 419. The distance to the cluster is 741 ± 36 pc according to the recent study by Roberts et al. (2010). The first hint of the star's multiplicity came with the discovery of a companion Ab through speckle interferometry observations by McAlister et al. (1987), and subsequent speckle measurements detected its orbital motion (Hartkopf et al. 1993). The optical spectrum is dominated by a relatively narrow-lined component Ab1, and Fullerton (1990) discovered significant radial velocity variations in this component indicative of a spectroscopic binary. The first spectroscopic orbit for Ab1 was presented by McKibben et al. (1998), who determined an orbital period of 311 d. In addition to the close Ab spectroscopic pair and the speckle Aa,Ab pair, there is another wider companion B at an angular separation of 2.6 arcsec. A mobile diagram presenting the known components of this multiple system is illustrated in Figure 1.

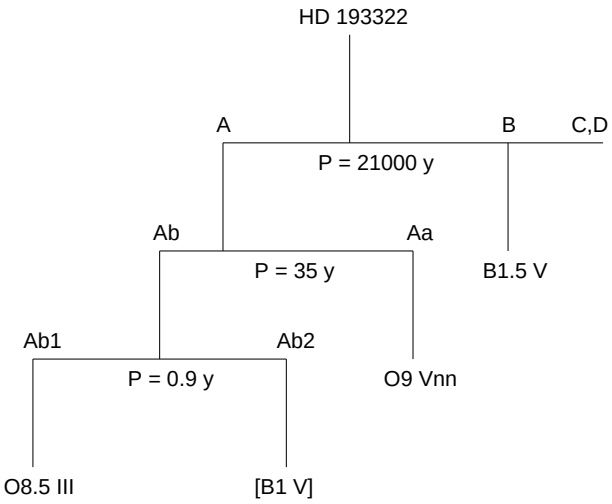

Figure 1: A mobile diagram of the components of the multiple star HD 193322.

2 Resolved Astrometric Orbits

The orbital motion of the Aa-Ab pair has been followed since its discovery by Mason and Hartkopf (USNO) through continued speckle interferometry observations (Mason et al. 2009) and new separated fringe packet observations with the CHARA Array long baseline interferometer (Farrington et al. 2010). The CHARA Array is an optical/infrared system consisting of six 1 m aperture telescopes in a Y-shaped configuration with baseline separations of 30 to 330 m (ten Brummelaar et al. 2005). We observed HD 193322 with the CHARA "Classic" beam combiner in the near-IR K'-band using a variety of telescope pairs over the period from 2005 to 2010. These observations always separated the Aa and Ab fringe packets of the speckle binary, and in the best circumstances we were able to measure the projected separation for several, near-orthogonal baselines. These were combined to obtain the separation and position angle of the Aa,Ab pair (see details of the method in Farrington et al. 2010). Mason and Hartkopf (priv. communication) have made a new orbital solution based on the full data set that is illustrated in Figure 2. The orbital period is 34 y, and using the cluster distance from Roberts et al. (2010), the period and semimajor axis yield a total mass (of Aa, Ab1, and Ab2) of $59 \pm 13 M_{\odot}$.

The interferometric visibility of a very close binary is modulated as a sinusoid with increasing baseline, where the cycle length is related to the projected separation on the sky (Raghavan et al. 2009). The calibration of visibility is aided when the signal of a nearby star produces a separated fringe packet that can be used to calibrate the visibility of the central binary. We have used this self-calibration method with the set of CHARA Array observations of HD 193322. We fit these calibrated visibilities with a relative orbit for Ab1,Ab2 by performing a grid search for the semimajor axis, inclination, longitude of the ascending node, and the magnitude differences of the Aa,Ab and Ab1,Ab2 pairs (the orbital period and epoch were set from the spectroscopic results for the circular orbit of Ab1; see §3). The preliminary solution for the angular orbit of Ab1,Ab2 is shown in Figure 3. Again adopting the distance from Roberts et al. (2010), the derived total mass of the Ab1,Ab2 pair is $43 \pm 7 M_{\odot}$. The difference in the mass sums for the Aa,Ab and Ab1,Ab2 orbits yields an approximate mass estimate of Aa of $15 M_{\odot}$, which is close to the nominal mass of $17 M_{\odot}$ for a typical O9 V star

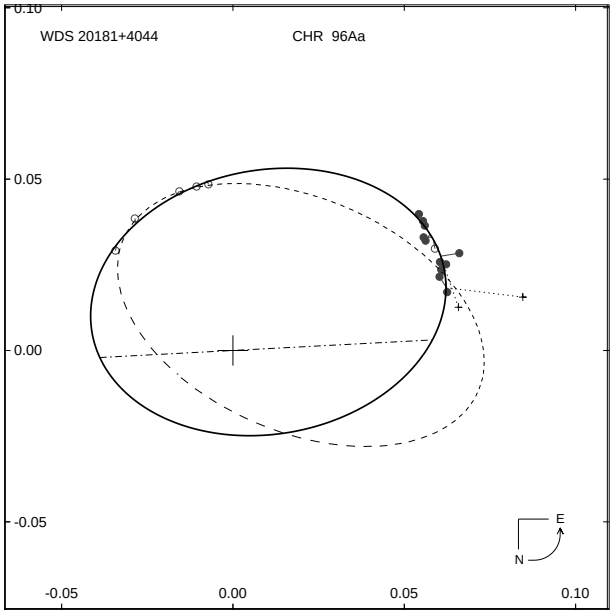

Figure 2: The astrometric orbit of the Aa,Ab pair (in units of arcsec). The dashed curve represents the first solution (Hartkopf et al. 1993) while the solid curve is the new solution from Mason and Hartkopf. The dot-dash line shows the line of the nodes. The filled circles represent the CHARA Array separated fringe packet results. The reliable speckle observations are displayed as open circles, while the poorer speckle points are zero weighted and are shown as plus signs connected to the calculated positions by dashed $O-C$ lines. Note that north is down and east to the right in this figure, and the directional arc in the lower right corner shows the counter-clockwise sense of orbital motion.

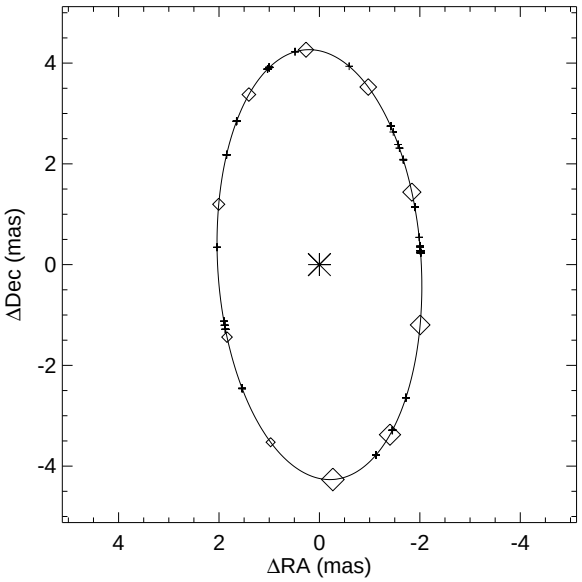

Figure 3: The astrometric orbit of the Ab1,Ab2 pair (in units of milli-arcsec = mas) based upon new CHARA Array visibility measurements. The sense of the orbit progresses counter-clockwise from the largest diamond (at the crossing of the ascending node of Ab1) through smaller symbols for steps of $0.1P$. Plus signs indicate the calculated positions at the times of observation. Note the much smaller angular scale and the different orientation compared to the Aa,Ab orbit shown in Figure 2.

(Martins et al. 2005). This suggests that Aa consists of only one star as indicated in Figure 1.

3 Spectroscopic Orbit

Spectroscopy potentially holds the key to determine the mass ratio of the Ab1,Ab2 pair, and hence, to find the masses of all three of the central stars. Furthermore, the spectral lines associated with each component can help us determine the temperature and relative flux of each star. This is a difficult task, however, because the stars are so close that conventional, ground-based spectroscopy will record the flux of all three stars (as well as the flux of component B in many cases) and because their Doppler shifts are comparable to the line widths so that line blending is severe. Nevertheless, we have started this task by analyzing a set of new moderate and high dispersion optical spectra of HD 193322. Most of these spectra were obtained with the Kitt Peak National Observatory 0.9 m coudé feed telescope, with resolving powers around $R = 10000$. This set was augmented with several higher resolving power spectra ($R = 75000$) from the Canada-France-Hawaii Telescope and ESPaDOnS spectrograph and the Nordic Optical Telescope and FIES spectrograph. We show an example of the CFHT spectra

in Figure 4. We focus here on the spectrum of Ab1 that is a major flux source, has narrow spectral lines, and displays Doppler shifts over the shorter orbit of Ab1,Ab2. The spectral lines of the narrow-lined component are consistent with those of a hot star ($T_{\rm eff} \approx 33$ kK) that contributes about 40% of the optical flux. There is also a very broad-lined component that contributes about the same flux fraction. This component does not participate in the short period orbital motion of Ab1,Ab2, but does show the long term variation expected for the Aa component. The much fainter Ab2 and B components account for the remaining flux.

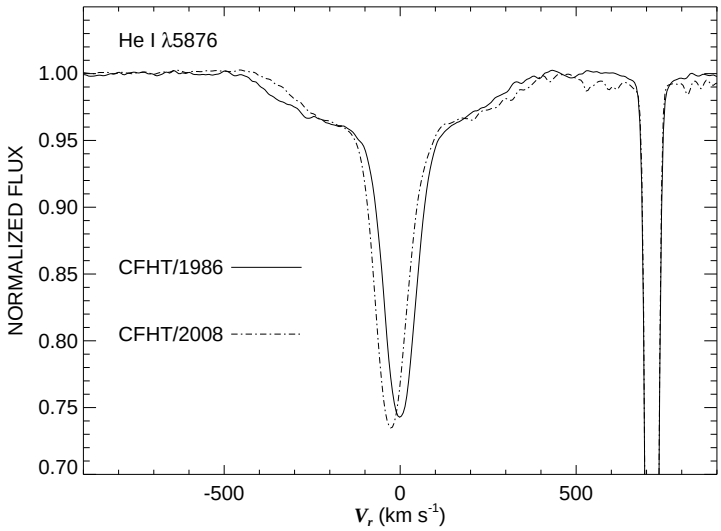

Figure 4: CFHT spectroscopy of the He I λ5876 line profile from two epochs. The narrow-lined component is associated with Ab1, while the broad-lined component corresponds to Aa.

Since the Ab1 component is so dominant in the spectrum, it is relatively straight forward to measure its orbital Doppler shifts. We measured radial velocities by cross-correlating the observed spectra with a model absorption line spectrum for Ab1 (from the grid of Lanz & Hubeny 2003). The velocities of Ab1 must be adjusted for the motion of the Ab1,Ab2 center of mass in the orbit of Aa,Ab (which depends on the mass ratios). We made this correction by an iterative method to determine the orbital motion of Ab1 in both the short and long period binaries. This was done by fitting the residuals from the short period orbit with the period P, eccentricity e, and longitude of periastron ω fixed from the astrometric orbit for the long period binary Aa,Ab, and with the systemic velocity γ, semiamplitude K, and epoch of periastron T as parameters to be determined. The resulting solution of the long period orbit was then used to correct the observed velocities for motion in the wide orbit, and a new solution was found for the short period orbit. This procedure quickly converged to the orbital solution shown in Figure 5 (for a circular orbit).

These kinds of observations hold significant promise for the determination of the masses and dynamical evolution of this remarkable multiple star system. For example, the semiamplitude of the spectroscopic orbit of Ab1 can be combined with the semimajor axis and inclination from the angular orbit and with the distance from the cluster to estimate the mass ratio of the Ab1,Ab2 pair and, hence, their individual masses. Furthermore, continuing high resolving power spectroscopy will yield an accurate, double-lined orbit for the Aa,Ab pair to provide an independent estimate of their masses. Once reliable orbital solutions are known, Doppler tomography reconstructions of the spectra will help us assign the other physical parameters of the stars. These data will shed light on the dynamical formation processes of massive, multiple star systems like HD 193322 that are often found at the centers of dense clusters.

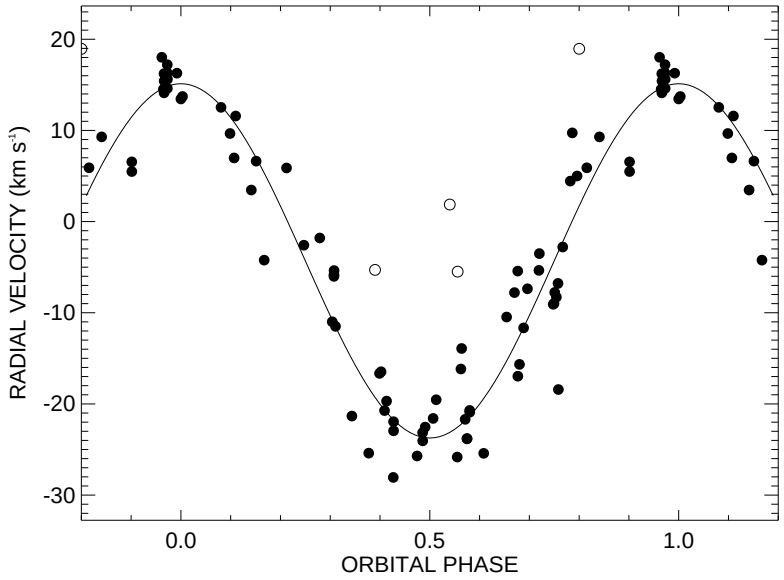

Figure 5: The derived radial velocity curve of Ab1 (solid line) in the 312 d orbit based upon the corrected radial velocity measurements. Open circles indicate those measurements assigned zero weight in the solution. Phase zero corresponds to the time of maximum radial velocity (star crossing the ascending node) in this circular orbit.

Acknowledgements

We are grateful to our colleagues Brian Mason and William Hartkopf (USNO), Lewis Roberts (JPL), Alexander Fullerton (STScI), and Sergio Simón-Díaz (IAC) for sharing their observations and analyses in advance of publication. This material is based upon work supported by the National Science Foundation under grants AST-0606861 and AST-1009080.

References

Farrington, C. D., ten Brummelaar, T. A., Mason, B. D., Hartkopf, W. I., McAlister, H. A., Raghavan, D., Turner, N. H., Sturmann, L., et al. 2010, AJ, 139, 2308

Fullerton, A. W. 1990, Ph.D. dissertation, Univ. of Toronto

Hartkopf, W. I., Gies, D. R., Mason, B. D., Bagnuolo, W. G. Jr. & McAlister, H. A. 1993, BAAS, 25, 872

Lanz, T. & Hubeny, I. 2003, ApJS, 146, 417

Martins, F., Schaerer, D. & Hillier, D. J. 2005, A&A, 436, 1049

Mason, B. D., Hartkopf, W. I., Gies, D. R., Henry, T. J. & Helsel, J. W. 2009, AJ, 137, 3358

McAlister, H. A., Hartkopf, W. I., Hutter, D. J., Shara, M. M. & Franz, O. G. 1987, AJ, 92, 183

McKibben, W. P., Bagnuolo, W. G. Jr., Gies, D. R., Hahula, M. E., Hartkopf, W. I., Roberts, L. C., Jr., Bolton, C. T., Fullerton, A. W., et al. 1998, PASP, 110, 900

Raghavan, D., McAlister, H. A., Torres, G., Latham, D. W., Mason, B. D., Boyajian, T. S., Baines, E. K., Williams, S. J., et al. 2009, ApJ, 690, 394

Roberts, L. C., Gies, D. R., Parks, J. R., Grundstrom, E. D., McSwain, M. V., Berger, D. H., Mason, B. D., ten Brummelaar, T. A., et al. 2010, AJ, 140, 744

ten Brummelaar, T. A., McAlister, H. A., Ridgway, S. T., Bagnuolo, W. G. Jr, Turner, N. H., Sturmann, L. , Sturmann, J., Berger, D. H., et al. 2005, ApJ, 628, 453

Walborn, N. R. 1972, AJ, 77, 312

The X-ray emission of the WR+O binary WR 79

Eric Gosset[1] , Hugues Sana[2] , Gregor Rauw[1] and Yaël Nazé[1]

[1] Institut d'Astrophysique et de Géophysique, Université de Liège, Belgium
[2] Sterrenkundig Instituut Anton Pannekoek, Universiteit van Amsterdam, The Netherlands

Abstract: In the framework of our multiwavelength study of the open cluster NGC 6231, we observed the colliding-wind WR+O binary WR 79 at six different epochs with the *XMM-Newton* observatory. These pointings offer the possibility to study the X-ray spectrum of WR 79 and its possible variability. Our results are briefly discussed and compared with the X-ray characteristics of other similar objects.

1 Introduction

1.1 An X-ray survey of NGC 6231

In the context of our scientific program on massive stars proposed for guaranteed time observations with the *XMM-Newton* satellite, we acquired several pointings aiming at the detailed analysis of the massive binary system HD 152248, an object located at the centre of the rich open cluster NGC 6231 in the Sco OB1 association. These X-ray pointings associated with an extensive ground-based spectroscopic support in the visible domain led to a multi-wavelength study of a palette of massive O-type binary stars, covering a wide range of configurations of colliding-wind binary (CWB) systems (see Sana et al. 2004, 2005, 2006a, 2007a, 2008). The same pointings were combined to perform an unprecedentedly deep X-ray survey of the cluster and a catalogue (see Sana et al. 2006b, 2006c, 2007b). The false-colour X-ray image of the central part of the cluster is reproduced in Fig. 1. One object appears light-blue and is thus a relatively hard source: it has been identified with WR 79, a well-known WC+O binary system. In the present work, we take the opportunity of the existing data to investigate the X-ray spectrum of this particular object and its possible variability.

1.2 The Wolf-Rayet star WR 79

In their study of NGC 6231, Shapley & Sawyer (1927) detected an extreme Oa spectral type for HD 152270 (≡WR 79), and Payne (1928) reported the existence of Wolf-Rayet (WR) emission bands in addition to an O-type absorption spectrum (central reversal of the lines). Payne (1933) identified a WC spectrum with superimposed absorption lines. Swings (1942) further refined the classification to WC6+ and discussed the origin of the absorption spectrum. Struve (1944a) reported conspicuous radial velocity variations but could not discern between profile variations and pure velocity shifts. One had to wait for Struve (1944b) to turn HD 152270 into the first WC star recognized to belong to a binary system. The derived period was 8.82 days and the mass ratio q turned out to be in favour of

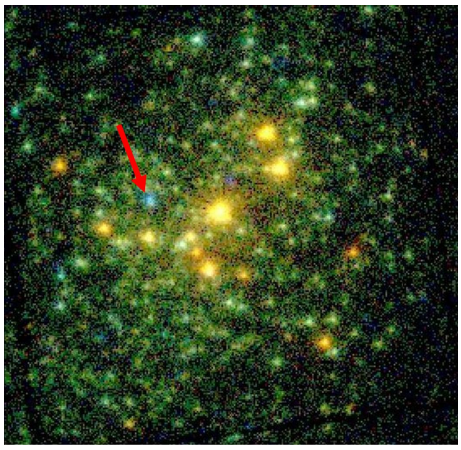

Figure 1: X-ray image of the core of the NGC 6231 cluster based on the combined MOS1 and MOS2 detectors. This is a false-colour image using three energy ranges: Soft (0.5-1.0 keV) represented in red, Medium (1.0-2.5 keV) in green and Hard (2.5-10.0 keV) in blue (Sana et al. 2006b). The yellow-orange objects are associated to the massive OB stars. Numerous greenish objects are harder sources believed to essentially be constituted of pre-main sequence stars. WR 79 appears as a much harder (blue) object (see the red arrow).

the O star. Seggewiss (1974) performed the first extensive study of the WC6-7+O5 binary system and reported a P=8.893 d circular system with q=2.8. He also described a strong emission line at C III λ5696, flat-topped with a superimposed pair of emission peaks, suspected to arise from gas streams within the shell. The dramatic changes of this structure were analysed by Schumann & Seggewiss (1975). These enigmatic variations, first attributed to a stream, were subsequently modelled as being due to an extended optically thin shell around the WR star (emitting the flat-topped component) from which some matter has been removed, due to an interaction with the O-type star (see Neutsch et al. 1981 and references therein). Along the rim of the matter-free hole, enhanced density and thus emission generate the additional sub-peaks. The distance between the two sub-peaks varies with half the orbital period. The configuration proposed by Neutsch et al. (1981) allowed them to constrain the inclination of the system to a value of 35°. Additional works in photometry (Lamontagne et al. 1996), in polarimetry (St-Louis et al. 1987) and in spectroscopy (Smith et al. 1990) suggested a spectral type WC7+O5-8 and an inclination angle of 33.6–44.8°. After the pioneering work of Neutsch et al. (1981), the next important step was the paper by Lührs (1997) that interpreted the C III λ5696 line-profile variations with a colliding-wind model where the extra emission over the main flat-topped profile was actually shaped like a saddle with the two above-mentioned sub-peaks at both limits. The extra emission was interpreted as recombination light emitted on the surface of the cone that is created by the collision between the WR wind and the O one. Lührs (1997) favoured an inclination of i=28.0°$\pm$1.1° and a half opening angle of the cone of 39.8°$\pm$0.8°. Hill et al. (2000, 2002) further refined the work and the CWB model of Lührs. They converged to an inclination of 29°$\pm$5°, and to a half opening angle of 29°$\pm$4°. Therefore, WR 79 turns out to be a CWB and should emit in the X-ray domain. In this domain, Pollock (1987) reported a first tentative 2σ-detection with the *EINSTEIN* satellite. Owing to the crowding of the field, the first convincing detection necessitated the HRI instrument on-board *ROSAT*; Pollock (1995) listed a surprisingly weak source with a luminosity of 5.9$\pm$1.1 $\times$ 10^{31} erg s^{-1} for a distance of 2 kpc. Corcoran (1999) confirmed the anomalous faintness of WR 79 for a CWB and attributed a lower luminosity of 2.3 $\times$ 10^{31} erg s^{-1} and a $\log(L_{\rm X}/L_{\rm bol})$ below -8.0.

2 Observations

2.1 Visible domain

We acquired several optical spectra of WR 79 in March 2006 and June 2006 with the FEROS spectrograph at the ESO/MPI 2.2m telescope (La Silla). The main aim was to ascertain the phase of the binary system during the *XMM-Newton* observations. We measured the positions of the He II

Table 1: List of the pointings involved in the present study along with the phases computed for the binary system WR 79. Phase zero corresponds to conjunction with the WR star in front. Individual count rates for WR 79 and their $\pm 1\sigma$-errors are also given.

Obs.	Exposure ID	JD	Exposure Time (ks)		Phase	Count rates (10^{-3} cts/s)	
		(JD−2400000)	MOS1	MOS2		MOS1	MOS2
1	109490101	52158.214	33.1	33.2	0.12	7.55±0.62	8.50±0.65
2	109490201	52158.931	19.8	19.8	0.20	7.96±0.82	8.99±0.87
3	109490301	52159.796	33.7	33.9	0.30	8.58±0.67	9.13±0.69
4	109490401	52160.925	26.0	24.3	0.43	7.59±0.71	7.64±0.72
5	109490501	52161.774	30.9	31.0	0.52	8.02±0.67	8.06±0.65
6	109490601	52162.726	32.9	32.8	0.63	8.75±0.67	9.24±0.67

Table 2: Measured mean count rates in various energy ranges and the corresponding hardness ratios.

Detector	Total (10^{-3} cts/s)	Soft (10^{-3} cts/s)	Medium (10^{-3} cts/s)	Hard (10^{-3} cts/s)	HR1	HR2
MOS1	8.08 (0.29)	0.45 (0.09)	3.23 (0.19)	4.40 (0.20)	0.76 (0.05)	0.15 (0.04)
MOS2	8.60 (0.30)	0.72 (0.10)	3.50 (0.19)	4.38 (0.20)	0.66 (0.04)	0.11 (0.04)

absorption lines of the O star and tried to reconnect them with the data of Hill et al. (2000, 2002). We confirmed the circular character of the orbit and computed the phase with, as a convention, the phase zero corresponding to the conjunction with the WR star being in front. The phases are given in Table 1 for epochs of interest and with a precision of a very few percent.

2.2 XMM-Newton data

Six pointings were acquired in the framework of the NGC 6231 study. They are summarized in Table 1 along with the derived phase of the WC+O binary WR 79. These data constitute a homogeneous coverage of half an orbital cycle, which certainly could represent a constraining data set. Individual pointings have exposure times of about 30 ks (see Table 1). These individual pointings were combined to build a total image (see Fig. 1). The X-ray count rates were measured in several energy ranges, namely the 'Total' band (0.5-10.0 keV), and the 'Soft' (0.5-1.0 keV), the 'Medium' (1.0-2.5 keV), and the 'Hard' (2.5-10.0 keV) ones, from individual data sets but also on the basis of the combined data set (resulting from the merging of the six individual data sets; the details of the reduction are identical to those given in Sana et al. 2006b). The individual count rates in the Total band are given in Table 1. The combined count rates in various ranges and the hardness ratios are given in Table 2. The latter are defined as HR1=(Medium–Soft)/(Medium+Soft) and HR2=(Hard–Medium)/(Hard+Medium). The X-ray spectra were also extracted from individual data sets and from the combined ones (see also Sana et al. 2006b). WR 79 was always falling very close to a CCD gap on the pn detector and we preferred to discard these data.

3 Results

3.1 Mean characteristics

The hardness ratios are very similar to those of V444 Cyg at quadrature (Fauchez et al. 2011). From Fig. 1 and from the hardness ratios, it is clear that WR 79 presents a luminosity in the Hard band that is high compared to those in other ranges, making WR 79 an interesting object. The X-ray spectrum

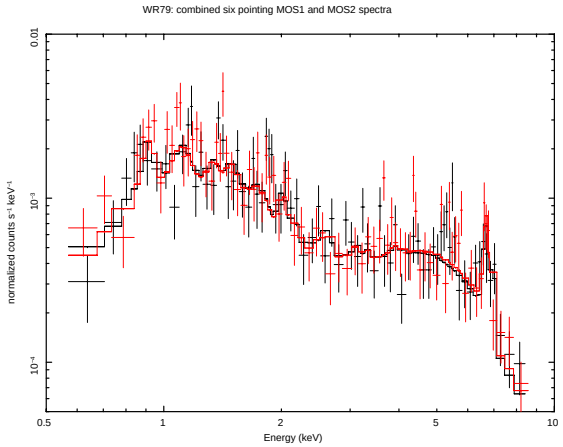

Figure 2: Observed X-ray mean spectra (MOS1, black; MOS2, red) along with the best-fitted three-temperature `mekal` model (no.2 in Table 3). The hard emission component is obvious including the Fe-K line. On the other hand, the parameters of the cooler component could be strongly correlated, implying a degeneracy of the fitted values.

of the binary system, extracted from the full combined event lists, is presented in Fig. 2 and confirms the above-mentioned results with its apparently flat nature, particularly on the hard side. The flux depression around 2-3 keV is reminiscent of the post-periastron spectrum of WR 140 (Pollock et al. 2005) and of the low-state spectrum of γ^2 Vel (Schild et al. 2004). The mean spectrum was studied using the XSPEC software. We essentially fitted it with optically thin thermal plasma emission models of the type `mekal`. One and two-temperature `mekal` components are not able to fit the observed data. Actually, the spectrum from 3 to 9 keV is difficult to fit. We needed three-component models to reach a reasonable level of fitting. Table 3 gives the results of the fits for various models. The 3-9 keV region necessitates a power law (neglecting the Fe-K line) or a very hot component with, in front, a huge column density (both being probably unphysical). Solar abundances and WC-type abundances were selected for the emitting plasma; we give in Table 3 the results for the best fits. The selected abundances have very small effect on the fitted temperatures. The absorbing column densities are free parameters except the ISM one fixed at $N_{\rm H} = 0.27 \times 10^{22}$ cm^{-2} (Sana et al. 2006c). The fluxes observed and corrected for the ISM are also given. Adopting the same distance as in the rest of the study (DM=11.07; 1.64 kpc), the corrected flux (2.10×10^{-13} erg cm^{-2} s^{-1}) corresponds to a luminosity $L_{\rm X}$(0.5-10.0 keV) = 6.7×10^{31} erg s^{-1}. This value is rather low (but larger than the expected intrinsic emission of the companion) and gives a ratio $\log(L_{\rm X}/L_{\rm bol})$ of -7.3. This flux value is also rather low. The dereddened flux in the *ROSAT* band is still five times lower, giving a $L_{\rm X}$(0.2-2.4 keV) = 2.1×10^{31} erg s^{-1} (at 2 kpc) in good agreement with the one quoted by Corcoran (1999). The column density in front of the soft component is in the range $N_{\rm H}$ = 0.8-1.2 10^{22} cm^{-2} and is similar to the estimation of the WC wind absorption in γ^2 Vel (Schild et al. 2004). Further progress necessitates a full hydrodynamical study of the colliding-wind structure and of its emission.

3.2 Variability

The Total count rates of WR 79 corresponding to the individual pointings (see Table 1) give a mean of 8.08 (MOS1) and 8.59 (MOS2) as well as a dispersion σ = 0.50 (MOS1) and σ = 0.64 (MOS2) corresponding to χ^2(d.o.f.=5) values of 3.02 (MOS1) and 5.06 (MOS2). The dispersions are lower than the individual errors and the χ^2-tests indicate that these count rates are thus compatible with constancy. In Fig. 3, we present the six pairs of spectra corresponding to the different pointings along with the model fitted (no.2 in Table 3) on the combined data set. From these individual spectra, we can conclude that, within the errors, the star is not varying in the X-ray domain over the orbital cycle (at least for phases 0.12 to 0.63). *Chandra* observations show that WR 79 corresponds to CXO J165419.7–414911 and has two X-ray emitting neighbours at 4.8″ and 5.9″. The three objects are not resolved by *XMM-Newton*. WR 79 itself represents 70 % of the count rates of the blend and even if one of the

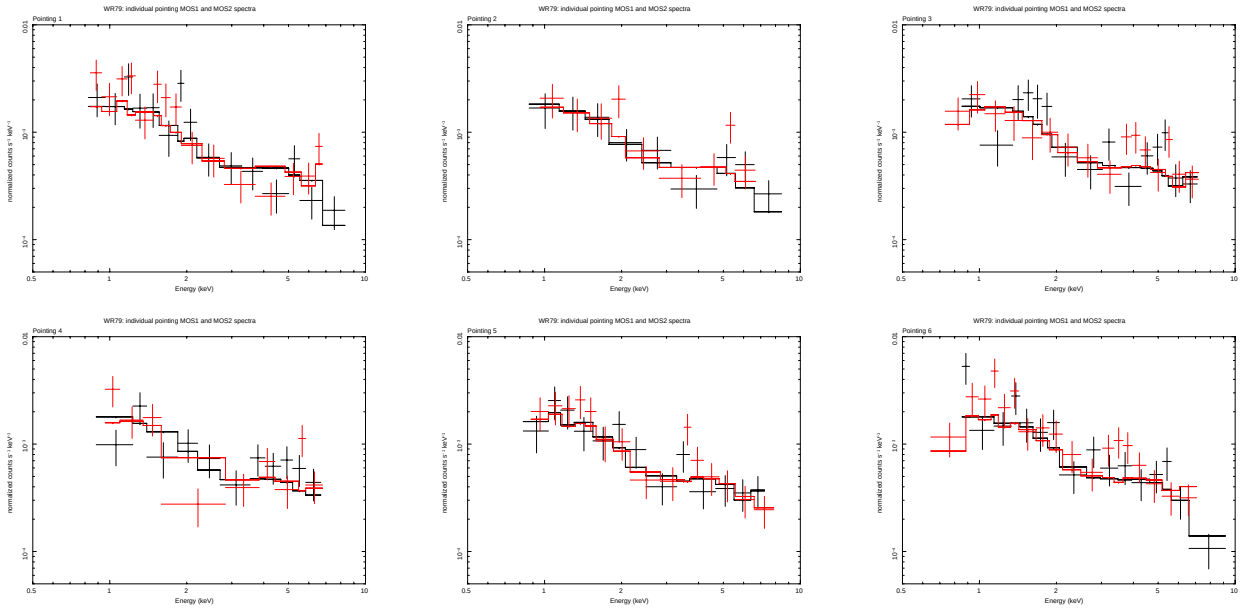

Figure 3: The six individual X-ray spectra (one per pointing) MOS1 (black) and MOS2 (red) of WR 79. We also show the above-mentioned model that has been fitted to the combined spectra. None of the individual spectra deviates significantly from the model, illustrating the constancy of the X-ray emission.

objects could be variable, this has no deep impact on our conclusions: WR 79 is, in the X-ray domain, constant to about 10-15 %.

4 Conclusion

The circular nature of the orbit of WR 79 suggests that the only possible variability, in the X-ray domain, induced by the orbital variation must arise from a varying absorbing column density along the line of sight to the observer. This variability is not detected whereas it is observed in other similar systems (Schild et al. 2004). Usually, the variability is interpreted as being due to the fact that, at one moment, the hot plasma due to the wind collision and situated near the binary axis between the two stars, is visible through a region of lower opacity corresponding to a line of sight going through the shock cone generated by the O star wind (Willis, Schild & Stevens 1995). Indeed, when the line of sight to the emitting plasma goes through the WC wind, the absorption is larger and the received flux is lower. The opacity being higher in the soft X-ray domain, the emerging X-ray radiation is hard. Such variations are observed in WR 140 and in γ^2 Vel. Concerning V444 Cyg, Maeda et al. (1999) reported a constant soft X-ray component and a varying hard component, the latter variability being due to a varying absorption over the orbital cycle. In this case also, the lowest absorption corresponds to the O star being in front of the WR (but see Fauchez et al. 2011). The absence of such variations in WR 79 (variations that should occur at about phase 0.5, corresponding to the conjunction with the O star in front) suggests that the absorbing column density remains about stable over the orbital cycle. The rather hard emission, the rather strong absorbing column involved and the constant nature of the X-ray emission and its low flux suggest that we are permanently looking at the emitting plasma through the WC wind. This implies a rather small inclination of the system (or alternatively a strong Coriolis effect due to the comparatively short period). If the half opening angle derived by Hill et al. (2002) is correct, this means that the inclination must be lower. This low value is in fair agreement with the results deduced from the extra emission over the C III λ5696 line.

Table 3: Result of the fit of the observed X-ray spectrum with various models. The superscripts and subscripts correspond to the permitted range at the 90 % confidence level. The ISM contribution is fixed whereas all the other parameters were left free. Fluxes are expressed in 10^{-13} erg cm^{-2} s^{-1} and correspond to the Total band. PhI is the photon index for model 1. kT_3 remains undefined.

Model	$N_{\rm H,1}$ (10^{22} cm^{-2})	kT_1 (keV)	$N_{\rm H,2}$ (10^{22} cm^{-2})	kT_2 (keV)	$N_{\rm H,3}$ (10^{22} cm^{-2})	PhI or kT_3 (keV)	χ^2_ν (d.o.f.)	Flux Obs.	Flux Dered.
1	$\texttt{wabs}_{\rm ISM}$*$\texttt{wabs}_1$*(mekal$_1$+mekal$_2$+powerlaw)								
	$0.15^{0.40}_{0.00}$	$0.70^{0.80}_{0.62}$	-	$4.70^{6.20}_{3.10}$	-	$-0.83^{-0.47}_{-1.40}$	1.22(149)	2.37	2.52
2	$\texttt{wabs}_{\rm ISM}$*(wabs$_1$*(mekal$_1$+mekal$_2$)+wabs$_3$*mekal$_3$)								
	$0.80^{0.98}_{0.65}$	$0.14^{0.17}_{0.09}$	-	$2.81^{4.44}_{2.07}$	$26.4^{33.4}_{20.8}$	$>10.$	1.22 (149)	1.83	2.00
3	$\texttt{wabs}_{\rm ISM}$*(wabs$_1$*mekal$_1$+wabs$_2$*mekal$_2$+wabs$_3$*mekal$_3$)								
	$1.15^{1.46}_{0.86}$	$0.10^{0.12}_{0.08}$	$0.21^{0.41}_{0.02}$	$5.00^{7.43}_{3.39}$	$31.6^{42.0}_{23.0}$	$>10.$	1.16(148)	1.96	2.13

References

Corcoran M.F., 1999, Rev. Mex. A. A. (Ser. Conf.), 8, 131
Fauchez, T., De Becker, M., & Nazé, Y. 2011, in Proceedings of the 39th Liège Astrophysical Colloquium, eds. G. Rauw, M. De Becker, Y. Nazé, J.-M. Vreux & P.M. Williams, BSRSL 80, 673
Hill G.M., Moffat A.F.J., St-Louis N., Bartzakos P., 2000, MNRAS, 318, 402
Hill G.M., Moffat A.F.J., St-Louis N., 2002, MNRAS, 335, 1069
Lamontagne R., Moffat A.F.J., Drissen L., et al., 1996, AJ, 112, 2227
Lührs S., 1997, PASP, 109, 504
Maeda Y., Koyama K., Yokogawa J., Skinner S., 1999, ApJ, 510, 967
Neutsch W., Schmidt H., Seggewiss W., 1981, Acta Astronomica, 31, 197
Payne C.H., 1928, Harvard College Obs. Bull., 855, 1
Payne C.H., 1933, Zeitsch. f. Astr., 7, 1
Pollock A.M.T., 1987, ApJ, 320, 283
Pollock A.M.T., 1995, IAU Symp. No.163, eds. K.A. van der Hucht & P.M. Williams, p.429
Pollock A.M.T., Corcoran M.F., Stevens I.R., Williams P.M., 2005, ApJ, 629, 482
Sana H., Stevens I.R., Gosset E., et al., 2004, MNRAS, 350, 809
Sana H., Antokhina E., Royer P., et al., 2005, A&A, 441, 213
Sana H., Gosset E., Rauw G., 2006a, MNRAS, 371, 67
Sana H., Gosset E., Rauw G., et al., 2006b, A&A, 454, 1047
Sana H., Rauw G., Nazé Y., et al., 2006c, MNRAS, 372, 661
Sana H., Rauw G., Gosset E., 2007a, ApJ, 659, 1582
Sana H., Rauw G., Sung B., et al., 2007b, MNRAS, 377, 945
Sana H., Nazé Y., O'Donnell B., et al., 2008, New Ast., 13, 202
Schild H., Güdel M., Mewe R., et al., 2004, A&A, 422, 177
Schumann J.D., & Seggewiss W., 1975, IAU Symp. No.67, p.299
Seggewiss W., 1974, A&A, 31, 211
Shapley H., & Sawyer H.B., 1927, Harvard College Obs. Bull., 846, 1
Smith L.F., Shara M.M., Moffat A.F.J., 1990, ApJ, 358, 229
St-Louis N., Drissen L., Moffat A.F.J., et al., 1987, ApJ, 322, 870
Struve O., 1944a, ApJ, 100, 189
Struve O., 1944b, ApJ, 100, 384
Swings P., 1942, ApJ, 95, 112
Willis A.J., Schild H., Stevens I.R., 1995, A&A, 298, 549

Spectropolarimetry of Beta Lyrae: Constraining the Location of the Hot Spot and Jets

Jamie R. Lomax[1] and Jennifer L. Hoffman[1]

[1] University of Denver, Denver, CO, USA

Abstract: Beta Lyrae is an eclipsing, semi-detached binary system whose state of active mass transfer can reveal details of the nonconservative evolution of binary stars. Roche lobe overflow has caused the system to evolve to a complex state. A thick accretion disk almost completely obscures the secondary, mass-gaining star while the rapid mass transfer likely drives mass loss through the system's bipolar outflows. Polarimetry can provide important information about the physical structure of complex systems; in fact, the discovery of bipolar outflows in beta Lyrae was confirmed through polarimetry. Here we present results from 6 years of new and recalibrated spectropolarimetric data taken with the University of Wisconsin's Half-Wave Spectropolarimeter (HPOL). We discuss their implications for our current understanding of the system's disk-jet geometry. Using both broadband and line polarization analysis techniques, we derive new information about the structure of the disk, the presence and location of a hot spot, and the distribution of hot line-emitting gas.

1 Introduction

Beta Lyrae (hereafter β Lyr) is a semi-detached, eclipsing binary star system. The primary star is a B6-8 II giant, while the secondary star is likely a B0.5 V main-sequence star (Hubeny & Plavec 1991). Mass loss from the primary via Roche lobe overflow has caused a thick accretion disk to surround and obscure the secondary. A bipolar flow or jet has also been detected in the system through interferometric (Harmanec et al. 1996) and spectropolarimetric (Hoffman, Nordsieck & Fox 1998) methods. The jets may originate from a hot spot (Harmanec 2002) caused by the impact of the mass stream on the disk. See Harmanec (2002) for a comprehensive overview of our current understanding of the system.

Since the stars in β Lyr are hot, the material in the disk is at least partially ionized. Therefore, the observed polarization is primarily caused by electron scattering. Analyzing the polarization behavior allows us to extract geometric information about the system. Thus we can use polarimetry to probe the location of the hot spot and jets. There is no evidence of a hot spot in β Lyr's light curve. However, since the hot spot is a local disruption in the disk, which is the primary scattering region for visible light, we expect it may act as a depolarizing region whose effects would be detectable in the polarization light curve. As long as the hot spot does not lie on the line connecting the centers of mass of the two stars, its depolarizing effect should result in a phase difference between the minimum flux and minimum polarization.

If the jets originate from the hot spot, we expect to see eclipse effects at phases in the polarized light that do not match those in total light. For the case where the hot spot leads the primary star in

phase, the eclipse of the jets would occur after the secondary minimum in scattered visible light.

2 Observations

We investigated these predictions by analyzing six years of newly calibrated and previously unpublished spectropolarimetric β Lyr data taken with the University of Wisconsin's Half-Wave Spectropolarimeter (HPOL). These data consist of 69 observations taken between the years of 1992 and 1998, the first 29 of which were presented in Hoffman et al. (1998). To calculate the phase of each observation, we have used the quadratic ephemeris given by Harmanec & Scholz (1993). We used eight observations of β Lyr *B*, an unpolarized star physically associated with β Lyr and located $45''$ away, to establish a new interstellar polarization (ISP) estimate. We subtracted the Serkowski law fit of the mean β Lyr *B* polarization spectra from each β Lyr observation to correct for ISP effects.

2.1 *V* Band Polarimetry

To look for effects of the hot spot, we constructed a projected polarized flux light curve (Figure 1). We did this by rotating the Stokes parameters to the system axis ($164°$) so that the average *%u* value is zero and multiplying the rotated *%q* value by the normalized *V* band light curve (Harmanec et al. 1996). The resulting light curve represents only the scattered light. As shown in Figure 1, the *V* band data display a shift in secondary minimum when compared to the total light curve. An error-weighted Fourier fit to the projected polarized flux data, represented by a red line in Figure 1, has a minimum at phase 0.487, while the secondary eclipse occurs at phase 0.5. This matches our prediction of how a hot spot would manifest itself in polarimetric data and provides evidence for its presence. Based on the offset between the secondary eclipse minima, the maximum size of the hot spot across the disk edge visible to the observer is approximately $26.5R_{\odot}$ at phase 0.487. This is comparable in size to the disk radius, $30R_{\odot}$, and its large size may be due to contributions from the mass stream to this effect. The large fluctuations in the position angle near secondary eclipse also seen in Figure 1 are consistent with this interpretation, as the hot spot should disrupt the disk edge, causing a randomization of the position angle of light scattered from the hot spot's location.

We also note that the two maxima in the Fourier-fit *V*-band projected polarized flux curve are slightly unequal in magnitude. This effect decreases at longer wavelengths, demonstrating that the polarized spectrum is bluer before secondary eclipse than after. This effect is consistent with a hot spot model, as we expect the disk temperature to be higher near the spot than on the opposite side.

2.2 Hα Line Polarimetry

We performed a similar analysis to investigate the polarization behavior of the strong Hα (6562.8 Å) emission line. As Figure 2 shows, its position angle is aligned nearly $90°$ away from that of continuum and is therefore likely scattered in the jets. The Hα polarization curve shows two eclipses, suggesting that the scattering regions in the bipolar jets are comparable in size to the disk height. The eclipse centered on phase 0.5 indicates, in contradiction to previous models of β Lyr, that the jets do not originate from the hot spot. Instead, they are likely centered between the stars near the surface of the secondary, perhaps forming as disk material accretes onto the secondary. However, the large errors and scatter of the data shown in Figure 2 make the exact phase of the secondary eclipse and the jet's location considerably uncertain.

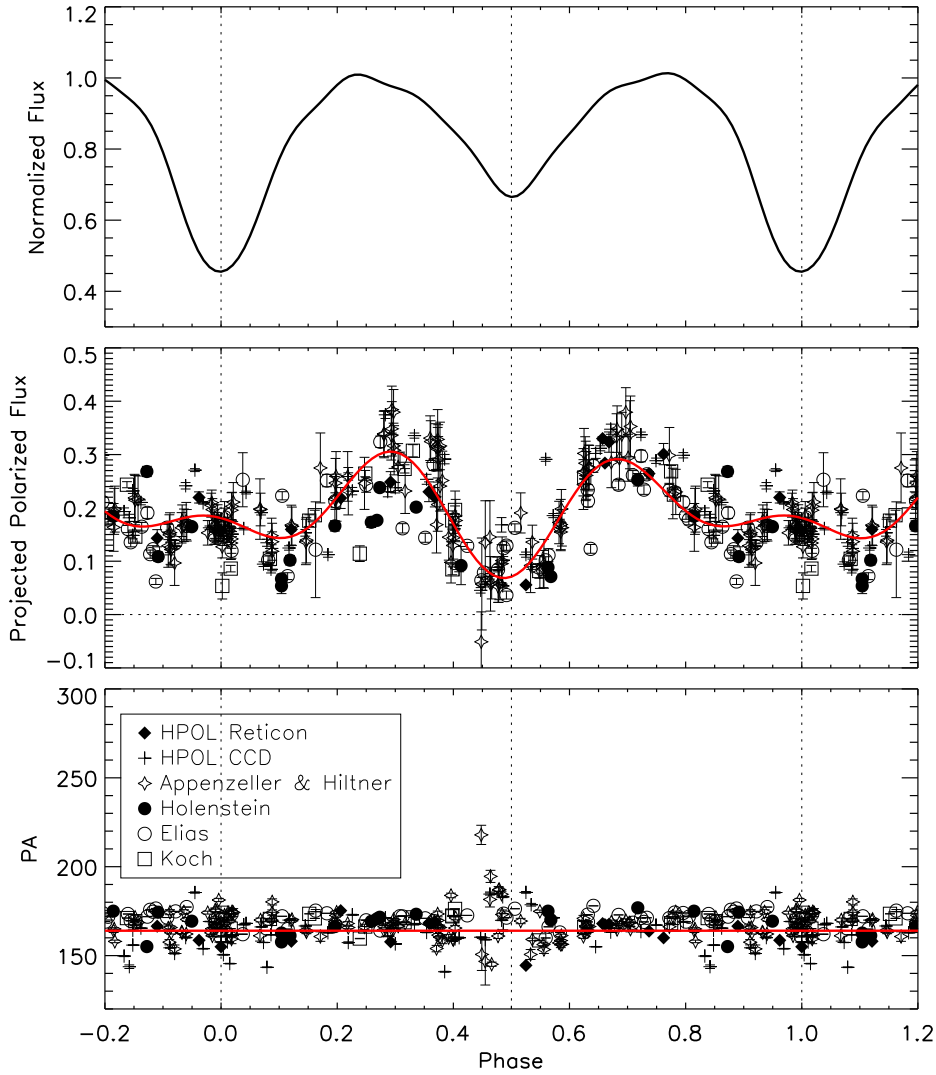

Figure 1: The top panel shows the V band Fourier fit light curve of β Lyr (Harmanec et al. 1996). The middle panel shows the V band projected polarized flux curve and a Fourier fit to the data. The bottom panel shows the phase variation of the position angle, with the average position angle of $164°$ indicated. Filled diamonds represent HPOL Reticon data, crosses represent HPOL CCD data, open diamonds are data from Appenzeller & Hiltner (1967), open circles represent data taken with the Flower and Cook Observatory (FCO) by N.M. Elias II, closed circles represent FCO data taken by B.D. Holenstein and open squares represent FCO data taken by R.H. Koch (Elias, Koch & Holenstein 1996). Both the polarized flux and the position angle show effects just before secondary eclipse that suggest a hot spot influences the disk polarization.

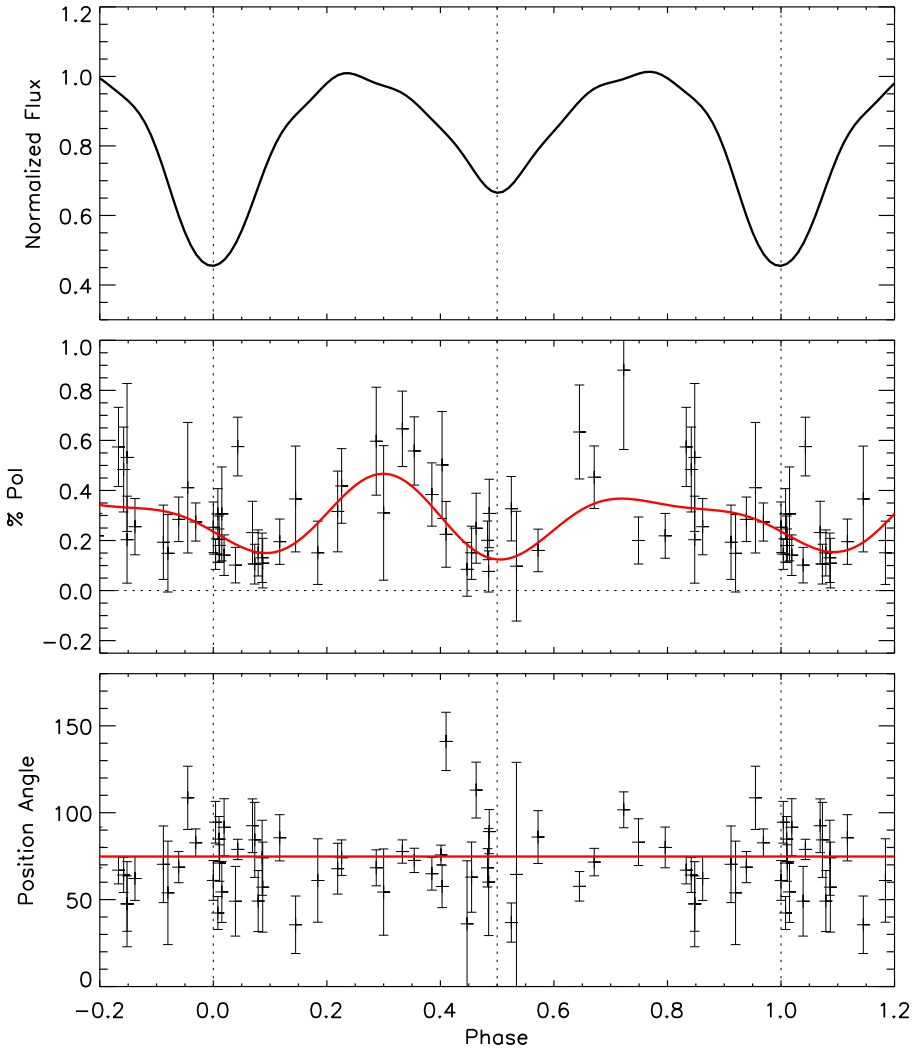

Figure 2: The top panel shows the *V* band Fourier fit light curve (Harmanec et al. 1996). The middle panel shows how the polarization of the Hα line changes with phase. The curve is a Fourier fit to the data. The bottom panel shows the position angle with the mean value of 75° indicated. Only HPOL CCD data are shown. The presence of an eclipse centered on phase 0.5 suggests, contrary to previous models of β Lyr, that the jets are not centered on the hot spot.

2.3 New Model of the β Lyr System

The *V* band and Hα polarimetry indicate that a new model of the system is needed. The *V* band result suggests the hot spot begins its transit across the disk before the loser eclipses the disk. As seen in Figure 3, this model produces a minimum in polarization when the area of the disk covered by the primary star and hot spot is maximized. As minimum flux approaches, the area covered by the hot spot decreases as seen by the observer because it is rotating to the far side of the disk. Figure 4 shows an illustration of our new model that includes the jet location implied by the Hα polarimetry results. Improved line polarization observations will help us refine our current model of the system.

3 Future Work

Future analysis of these data will provide quantitative constraints on the size and location of the hot spot and line scattering regions. We plan on improving the line polarization results with new observations using HPOL at the Mount Lemmon Observing Facility to improve the constraints on the properties of the jets. We will present a more detailed analysis of the results of the line and *U,B,R* and *I* band polarimetry in full in a future paper. In order to detect the mass stream and confirm the existence of the hot spot, we plan to conduct future observations in both the infrared and X-ray regimes.

While previous studies have detected phase variations on timescales longer than the orbital period of the system, preliminary period analysis of the polarimetric data presented here do not reveal any of these variations. However, this analysis is still ongoing and will be presented in a future paper.

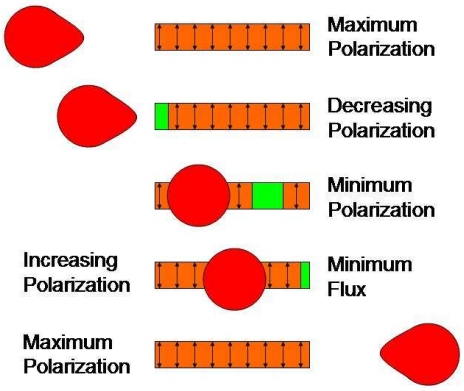

Figure 3: This cartoon shows our interpretation of the results presented in Figure 1. The vectors indicate the relative strength of the polarization signal at the given phases. Minimum polarization occurs before minimum flux because this is when the disk area eclipsed by the primary and disrupted by the hot spot (highlighted in green) is the largest. This drawing is not to scale.

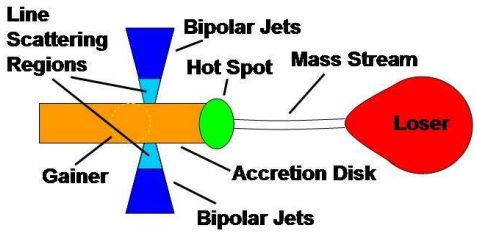

Figure 4: This cartoon shows our interpretation of the results presented in Figure 2. The location of the jets must be near the center of the disk and the sizes of their scattering regions (highlighted in light blue) must be smaller than the height of the primary star to produce the eclipses seen in the Hα line polarization.

Acknowledgements

Lomax acknowledges the support of the 39th Liège International Astrophysical Colloquium's Organizing Committee in the form of a travel grant, which enabled her to attend this conference. This research is supported by NASA ADP award NNH08CD10C and NSF award AST0807477. A special thanks to Marilyn R. Meade, Petr Harmanec, Kenneth Nordsieck, Richard Ignace and Nicholas M. Elias II for their continued help with this project.

References

Appenzeller, I., & Hiltner, W.A., 1967, ApJ, 149, 353
Elias II, N.M., Koch, R.H., and Holenstein, B.D., 1996, BAAS, 28, 913
Harmanec, P., 2002, Astron. Nachr., 323, 87
Harmanec, P., Morand, F., Bonneau, D., et al., 1996, A&A, 312, 879
Harmanec, P., & Scholz, G., 1993, A&A, 279, 131
Hoffman, J.L., Nordsieck, K.H., and Fox, G.K., 1998, AJ, 115, 1576
Hubeny, I., & Plavec, M.J., 1991, AJ, 102, 1156

Constraining the Properties of the Eta Carinae System via 3-D SPH Models of Space-Based Observations: The Absolute Orientation of the Binary Orbit

Thomas I. Madura[1], Theodore R. Gull[2], Stanley P. Owocki[1], Atsuo T. Okazaki[3], and Christopher M.P. Russell[1]

[1] University of Delaware, Newark, DE, USA
[2] NASA Goddard Space Flight Center, Greenbelt, MD, USA
[3] Hokkai-Gakuen University, Sapporo, Japan

Abstract: The extremely massive (> 90 $M_\odot$) and luminous ($= 5 \times 10^6$ $L_\odot$) star Eta Carinae, with its spectacular bipolar "Homunculus" nebula, comprises one of the most remarkable and intensely observed stellar systems in the Galaxy. However, many of its underlying physical parameters remain unknown. Multiwavelength variations observed to occur every 5.54 years are interpreted as being due to the collision of a massive wind from the primary star with the fast, less dense wind of a hot companion star in a highly elliptical ($e \sim 0.9$) orbit. Using three-dimensional (3-D) Smoothed Particle Hydrodynamics (SPH) simulations of the binary wind-wind collision, together with radiative transfer codes, we compute synthetic spectral images of [Fe III] emission line structures and compare them to existing *Hubble Space Telescope*/Space Telescope Imaging Spectrograph (*HST*/STIS) observations. We are thus able, for the first time, to tightly constrain the absolute orientation of the binary orbit on the sky. An orbit with an inclination of $i \sim 40°$, an argument of periapsis $\omega \sim 255°$, and a projected orbital axis with a position angle of $\sim 312°$ east of north provides the best fit to the observations, implying that the orbital axis is closely aligned in 3-D space with the Homunculus symmetry axis, and that the companion star orbits clockwise on the sky relative to the primary.

1 Introduction

The direct detection of the hot companion star Eta Car B has proven to be quite difficult, especially since at UV, Visible, and IR wavelengths the extended wind of the primary star Eta Car A dominates the spectrum. Given the lack of direct signatures of Eta Car B, the focus has recently shifted to examining spectral features formed in the wind-wind collision region and circumstellar ejecta near Eta Car A (Verner et al. 2005; Nielsen et al. 2007; Mehner et al. 2010). In a further attempt to spatially characterize the wind-wind interaction region, Gull et al. (2009) presented an analysis of *HST*/STIS observations obtained between 1998 and 2004, identifying spatially extended, velocity-resolved forbidden emission lines from low- (IP $<$ 13.6 eV) and high- (IP $>$ 13.6 eV) ionization species. More importantly, Gull et al. (2009) show how proper modeling of the *HST*/STIS slit spectra, which provide valuable spatial *and* velocity information, has the potential to constrain the absolute orientation and direction of the binary orbit on the sky by removing the ambiguity inherent to models based solely

on the observed RXTE X-ray light curve or other point-source data. As an extension of the work in Gull et al. (2009), we present a 3-D dynamical model for the high-ionization forbidden line emission observed in Eta Car with *HST*/STIS. This model is based on the results of 3-D SPH simulations of the colliding winds and radiative transfer calculations performed with a modified version of the SPLASH (Price 2007) code. Synthetic spectro-images are generated from the models and compared to the observations with the goal of constraining the absolute orientation and direction of the binary orbit.

2 Observations

Observations of high- and low-ionization forbidden emission lines were obtained from March 1998 to March 2004 with the *HST*/STIS (0.1″ angular resolution, $R \sim 8000$), and are described in detail in Gull et al. (2009). Figure 1 presents sample spectro-images of resolved, broad forbidden lines of both high and low ionization. The leftmost panel is an *HST*/ACS HRC image of the central 2″ of Eta Car with a 2″ × 0.1″ portion of the STIS aperture shown at position angle (PA) = +38°. The three black dots correspond to Weigelt blobs B, C, and D, while the direction of north is shown in the top left corner. For an adopted distance of 2.3 kpc to Eta Car, 0.1″ = 230 AU. The middle two panels of Figure 1 are spectro-images of [Fe III] and [N II] (IP's = 16.2 & 14.5 eV) recorded May 5, 2003 (orbital phase $\phi = 0.976$) at this same STIS PA. In both cases the emission structures appear as well-defined blue-shifted rings that extend spatially up to $\sim 0.35''$ from the central source. For comparison, a spectral image of [Fe II] (IP = 7.9 eV) is presented in the rightmost panel. Notice the slightly more spatially extended, red- *and* blue-shifted double-ring emission structures. As noted in Gull et al. (2009), the observed emission features change with both orbital phase and STIS PA (Figure 2), providing further insights into the geometry and physics of Eta Car's extended wind structure.

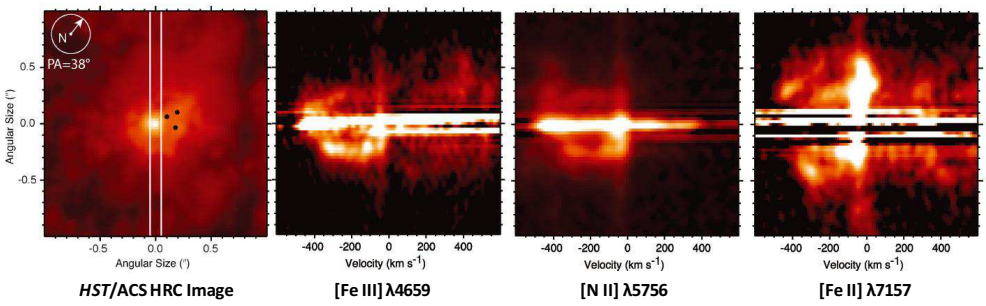

Figure 1: Leftmost panel: *HST*/ACS HRC image of the central 2″ of Eta Car with the 0.1″ wide STIS aperture at PA = +38°. Middle 2 panels: Spectro-images of the high-ionization lines of [Fe III] and [N II] (IP's = 16.2 & 14.5 eV) recorded at orbital phase $\phi = 0.976$. Rightmost panel: Spectro-image of the low-ionization line of [Fe II] (IP = 7.9 eV), taken at the same phase and STIS PA (+38°).

3 A 3-D Dynamical Model for the Forbidden Line Emission

The 3-D dynamical model for the high-ionization, forbidden line emission is based on the results from 3-D SPH simulations of the binary colliding winds in the Eta Car system. SPH model parameters are similar to those of Okazaki et al. (2008), except that the new simulations assume a factor of four higher mass-loss rate for the primary star (10^{-3} $M_\odot$/yr), use adiabatic cooling, and have a 10× larger computational domain (corresponding to a box size of $\sim \pm 1550$ AU). For a desired orbital phase, the volume of material ionized by Eta Car B, assuming that it is an O5 giant with $10^{49.48}$ H ionizing photons/second (Mehner et al. 2010; Martins, Schaerer & Hillier 2005), is found, followed by a

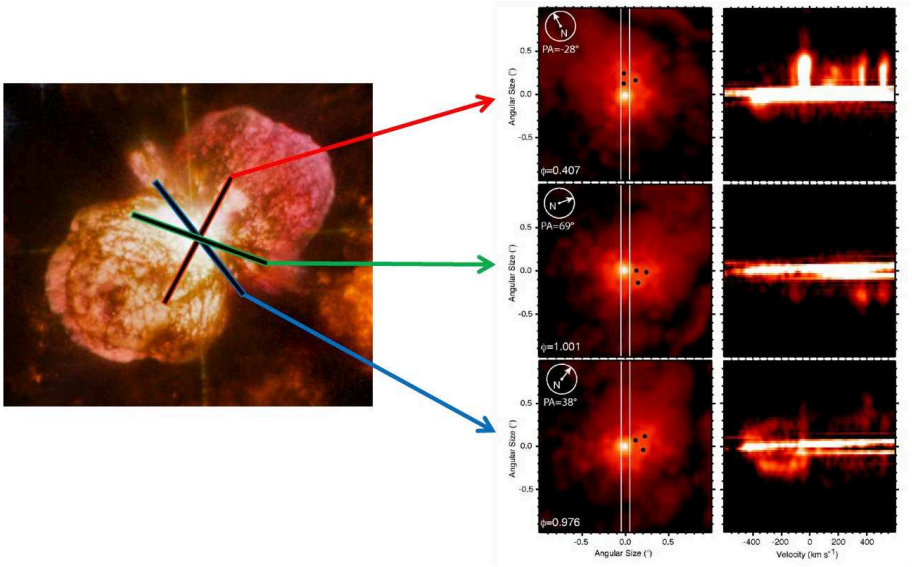

Figure 2: Left: *HST*/WFPC2 image of Eta Car with the STIS aperture shown at PAs of $-28°$ (red), $+69°$ (green), and $+38°$ (blue). Right: Corresponding ACS HRC image (left column) and observed spectro-image (right column, from top down) at phases $\phi = 0.407$, 1.001, and 0.976.

computation of the emissivity in the [Fe III] 4659Å line (IP = 16.2 eV) assuming a 2-level atom and collisional ionization equilibrium. A synthetic spectral image is made by orienting the 3-D binary wind structure on the sky at a specific PA and sampling the [Fe III] emissivity in the spatial/velocity plane of the *HST*/STIS long slit. The synthetic spectro-images are then convolved with a Gaussian ($0.1''$ and $\lambda/\Delta\lambda = 8000$) to better match the spatial and spectral resolutions of *HST*/STIS. For details on the modeling, see Madura (2010).

4 Results

The blue-shifted, ring-like emission feature shown in the middle panels of Figure 1 was modeled first since it represents a well-defined structure observed at a specific orbital phase and STIS PA. A parameter study was performed where the orbital inclination i, argument of periapsis ω, and position angle of the projected (on the sky) orbital axis of the system were varied in $10°$, $15°$, and $10°$ increments, respectively. Figure 3 helps illustrate the main results of this parameter study, assuming $i = 45°$ and an orbital axis at the same PA on the sky as the Homunculus symmetry axis ($312°$), at four values of the argument of periapsis $\omega = 0°$, $90°$, $180°$, and $270°$. It was found that only orbital orientations with values of ω near $270°$ are able to reproduce the observations, regardless of the assumed value of i or position angle of the projected orbital axis. Moreover, only orientations with $i \sim 40° - 60°$ and a projected orbital axis that is closely aligned with the Homunculus symmetry axis yield results that closely match the observed ring-like emission structure in both velocity and spatial extent.

The orbital orientation was further constrained by modeling a variety of observations obtained at different STIS PAs and orbital phases. In order to simultaneously reproduce the observed blue-shifted, ring-like emission feature at phase 0.976 and STIS PA = $+38°$, and the temporal variations in emission seen at other phases and STIS PAs, the binary system needs to have $i \approx 40° \pm 10°$, $\omega \approx 255° \pm 15°$, and an orbital axis projected on the sky with a PA $\approx 312° \pm 15°$ (Figure 4). This implies that the orbital axis is closely aligned in three-dimensional space with the symmetry axis of the Homunculus, with the resulting projected orbit on the sky having Eta Car B moving clockwise relative to Eta Car A, and apastron on the observer's side of the system (Figure 5).

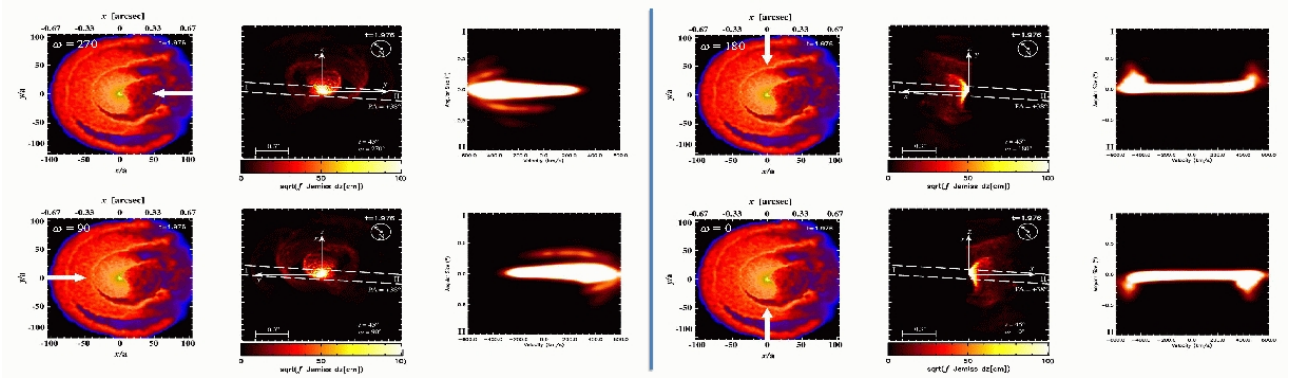

Figure 3: Illustration showing how the synthetic spectro-images depend on the orientation of the binary orbit. Each set of three images corresponds to a different value of ω. Left: $\omega = 270°$ (top) and $90°$ (bottom). Right: $\omega = 180°$ (top) and $0°$ (bottom). The 1st and 4th columns show slices of log density in the orbital plane from the 3-D SPH simulation at phase 1.976. The white arrow indicates the direction of the observer's line-of-sight. The 2nd and 5th columns show the 2-D projection on the sky of the square root of the intensity in the [Fe III] λ4659 line, assuming $i = 45°$ and a projected orbital axis that is aligned with the Homunculus symmetry axis. The projected semi-major (x), semi-minor (y), and orbital (z) axes are shown, as is the direction of north. Overlaid is the $0.1''$ wide STIS aperture at PA = $+38°$. Roman numerals I and II indicate the tops and bottoms of the slits, respectively. The 3rd and 6th columns show the corresponding synthetic slit spectro-images.

5 Conclusions

The 3-D dynamical model and observations tightly constrain, for the first time, the absolute orientation of the binary orbit, implying an orbital axis that is closely aligned in 3-D space with the Homunculus symmetry axis, and a companion star that orbits clockwise on the sky. The observations are best fit assuming an inclination $i \approx 40°$, argument of periapsis $\omega \approx 255°$, and a projected orbital axis with a position angle on the sky of $\sim 312°$. The modeling shows that most of the high-ionization forbidden line emission originates in the inner $\pm 0.1''$ of the system and is due to the unresolved current-day wind-wind interaction region excited by the far-UV of the hot companion star Eta Car B. The blue-shifted, spatially extended ring-like emission structures observed at phase 0.976 and STIS PA = $+38°$ originate in the dense, compressed shells of the outflowing wind-wind interaction region created during the previous orbital cycle. Spectral variations in emission with orbital phase are due to orbital motion of Eta Car B, which causes different portions of the extended wind structures to be ionized. The disappearance of the high-ionization forbidden emission during periastron is attributed to the wrapping of the dense primary wind around the binary system, trapping the far-UV radiation from Eta Car B. Finally, observed variations in the emitting structures with STIS PA are due to the narrow STIS aperture sampling different specific regions of the projected wind structures.

The derived alignment of the orbital and Homunculus axes, if confirmed, could have important implications for theories governing the formation of the Homunculus and/or the present shape of Eta Car A's wind. Binarity may turn out to have played an important role in the Great Eruption of the 1840s, and possibly the smaller eruption that later formed the Little Homunculus. If the orbital axis and rotation axis of Eta Car A are also aligned, this could provide support for theories of the Homunculus' formation that are based on radiation-driven mass loss from a rapidly rotating primary star. Further modeling and observations will help test the above conclusions.

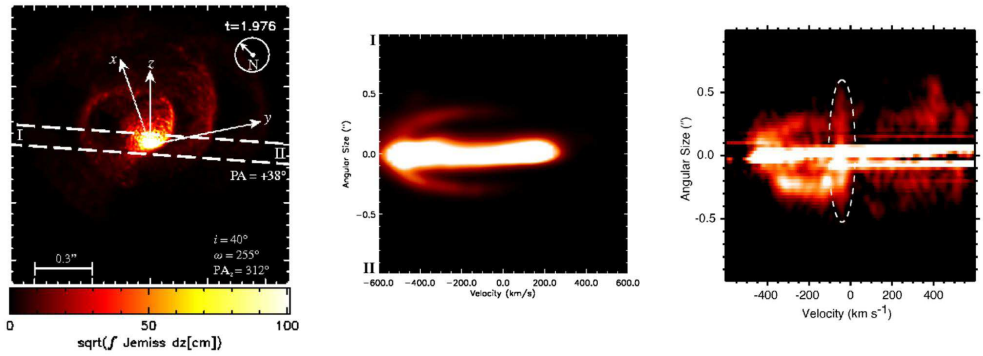

Figure 4: Best-fit model for matching the ring-like emission feature at phase 0.976 and STIS PA = $+38°$. Left: 2-D projection of the square root of the intensity of the [Fe III] line for $i = 40°$, $\omega = 255°$, and a projected orbital axis aligned with the Homunculus symmetry axis. Overlaid is the $0.1''$ wide STIS slit. Middle: Resulting synthetic spectro-image. Right: Observed spectro-image. The emission feature circled in white originates in the dense, slow-moving Weigelt blobs and should be ignored.

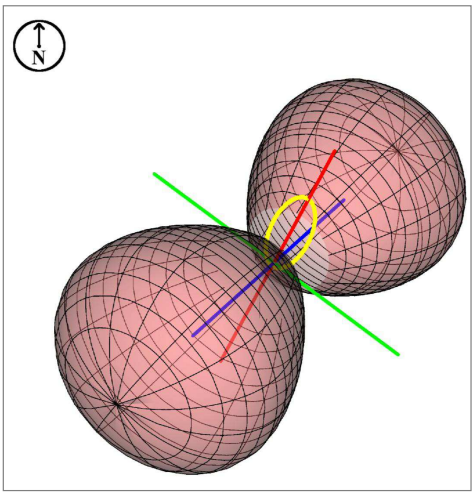

Figure 5: Illustration of the derived binary orbit (yellow) relative to the Homunculus (not to scale), projected on the sky, for $i = 40°$, $\omega = 255°$, and an orbital axis (blue) that is aligned with the Homunculus polar axis. The projected semi-major (red) and semi-minor (green) axes are also shown.

Acknowledgements

Observations were accomplished using *HST*/STIS observations from programs 9420, 9973, 11506, and archival research under 11273 and 10955. This work was funded by a NASA GSRP Fellowship.

References

Gull, T.R., Nielsen, K.E., Corcoran, M., et al., 2009, MNRAS, 396, 1308
Madura, T.I., 2010, Ph.D. Dissertation, University of Delaware
Martins, F., Schaerer, D., & Hillier, D.J., 2005, A&A, 436, 1049
Mehner, A., Davidson, K., Ferland, G.J., & Humphreys, R.M., 2010, ApJ, 710, 729
Nielsen, K.E., Corcoran, M., Gull, T., Hillier, D.J., Hamaguchi, K., Ivarsson, S., Lindler, D. 2007, ApJ, 660, 669
Okazaki, A.T., Owocki, S.P., Russell, C.M.P., & Corcoran, M., 2008, MNRAS, 388, L39
Price, D.J., 2007, Publications of the Astronomical Society of Australia, 24, 159
Verner, E., Bruhweiler, F., & Gull, T., 2005, ApJ, 624, 973

High Mass X-ray Binaries in the NIR: Orbital solutions of two highly obscured systems. *

A.B. Mason[1]†,A.J. Norton[1],J.S. Clark[1],P. Roche[1],I. Negueruela[2]

[1] The Open University, Milton Keynes, UK

[2] Universidad de Alicante, Alicante, Spain

Abstract: The maximum mass of a neutron star (NS) is poorly defined. Theoretical attempts to define this mass have thus far been unsuccessful. Observational results currently provide the only means of narrowing this mass range down. Eclipsing X-ray binary (XRB) pulsar systems are the only interacting binaries in which the mass of the NS may be measured directly. Only 10 such systems are known to exist, 6 of which have yielded NS masses in the range 1.06 - 1.86 $M_{\odot}$.We present the first orbital solutions of two further eclipsing systems, OAO 1657-415 and EXO 1722-363, whose donor stars have only recently been identified. Using observations obtained with the VLT/ISAAC NIR spectrograph, our initial work was concerned with providing an accurate spectral classification of the two counterpart stars, leading to a consistent explanation of the mechanism for spin period evolution of OAO 1657-415. Calculating radial velocities allowed orbital solutions for both systems to be computed. These are the first accurate determinations of the NS and counterpart masses in XRB pulsar systems to be made employing NIR spectroscopy.

1 Introduction

Despite extensive and ongoing theoretical work on the NS equation of state (EOS), the precise nature of the fundamental physical properties of NS matter is still poorly defined. Observational work can assist in reducing the number of contending theories by eliminating those that place unrealistic constraints on the mass range of observed NS. NS masses may only be determined from binary systems. Within this paper we consider a specific class of these objects, those containing an eclipsing X-ray binary pulsar. At present only 10 such systems are known within our Galaxy. Prior to this work 6 of the NS in these systems had mass determinations, with the donor star in each observable optically. Within this paper we discuss the first mass estimates found for NS employing near-infrared (NIR) spectroscopy. We have studied two eclipsing X-ray pulsar systems containing a High Mass donor, OAO 1657-415 and EXO 1722-363. Initially an accurate spectral classification for each of the donor stars was conducted utilising observations made using the VLT/ISAAC NIR spectrograph and current NIR spectral atlases. Using multi-epoch NIR spectra of each system we were able to determine the radial velocity of the donor star in each of the two systems thus enabling the construction of an orbital solution. This solution was then employed in calculating the mass estimate of each NS and the

*Based on observations carried out at the European Southern Observatory under programmes 081.D-0073(A), 077.B-0872(A) and 081.D-0073(B).

†a.mason@open.ac.uk

corresponding high mass donor, placing constraints upon the system inclination and separation of the binary system.

2 Spectral classification

2.1 Spectral classification of EXO 1722-363

EXO 1722-363 (alternatively designated IGR J17252-3616) was discovered in 1984 by *EXOSAT* Galactic plane observations (Warwick et al. 1988). *XMM-Newton* observations narrowed down the source position location to 4″. This allowed the identification of an IR counterpart 2MASS J17251139-3616575 (with magnitude J = 14.2, H = 11.8 and K_s = 10.7, Zurita Heras et al. 2006). Examining Fig.1 we can see that all absorption lines in this spectrum are narrow, indicative of the object being a supergiant. EXO 1722-363 shows the singlet He I 2.058 μm line in emission, this line being highly sensitive to wind and temperature properties. The N III 2.115 μm emission line is a common feature in B0-B1 supergiants. The absence of strong Brγ 2.1655 μm emission features implies that EXO 1722-363 does not exhibit a strong stellar wind. From a qualitative comparison of spectra from Hanson et al. 2005, we identify EXO 1722-363 as being of spectral type B0-B1 Ia (Mason et al. 2009). By comparison with evolutionary rotational massive star models (Meynet & Maeder, 2000) we find an initial progenitor mass for EXO 1722-363 in the range 30$M_\odot$ - 40$M_\odot$. Following the method for determining spectroscopic distance as detailed in Bibby et al. (2008), we determined a distance for EXO 1722-363 of $8.0^{+2.5}_{-2.0}$ kpc which is comparable within errors to the distance deduced in Thompson et al. (2007). Comparing our calculated distance with model fluxes derived from spectral fits to EXO 1722-363 (Corbet et al. 2005), we found that EXO 1722-363 has an intrinsic X-ray flux variability (in the range 2-60 keV) such that $F_{\rm min}$ = 0.78 $\times 10^{-10}$ erg cm^{-2} s^{-1} and $F_{\rm max}$ = 12.2 $\times 10^{-10}$ erg cm^{-2} s^{-1}. We derive X-ray luminosities for EXO 1722-363 such that $L_{X_{\rm min}}$ = 3.4 $\times 10^{35}$ erg s^{-1} and $L_{X_{\rm max}}$ = 1.6 $\times 10^{37}$ erg s^{-1}. We find this luminosity range entirely consistent with EXO 1722-363 being the donor within an SGXRB system.

2.2 Spectral classification of OAO 1657-415

OAO 1657-415 was first detected over 30 years ago by the *Copernicus* X-ray satellite. From an examination of the orbital parameters of the X-ray pulsar it was determined that OAO 1657-415 was a high-mass system, indicating the mass of the donor lay between 14-18 $M_\odot$ with a corresponding radius range of 25-32$R_\odot$. Determination of these stellar parameters led to a suggested classification of B0-6 I (Chakrabarty et al. 1993).The correct identification of the donor in this system required the precise location of OAO 1657-415 to be accurately made. This was achieved by the *Chandra X-Ray Observatory* narrowing the X-ray location error radius down to 0.5″. Optical imaging of this position did not detect any donor candidates down to a magnitude of V>23. Near infrared imaging was employed to overcome significant levels of interstellar reddening, resulting in the identification of a donor located within the *Chandra* error radius. A corresponding IR counterpart was located in the *2MASS* catalogue, 2MASS J17004888-4139214 (with magnitudes J = 14.1, H = 11.7 and K_s = 10.4) with A_V = 20.4 ± 1.3, located at a distance of 6.4 ± 1.5 kpc (Chakrabarty et al. 2002). NIR K_s band spectroscopy of the donor obtained in 2008 (Mason et al. 2009) led to a re-evaluation of the spectral classification. Close examination revealed that OAO 1657-415 shared a similar spectral morphology with that of Ofpe/WNL stars. These are stars in transition between the OB main sequence and hydrogen depleted Wolf-Rayet stars, whose evolution follows from a wide range of progenitor masses. The spectrum of the mass donor in OAO1657-415 is presented in Fig. 1, and is dominated by He I 2.058 μm and Brγ emission, the former stronger than the latter. We find a poor correspondence

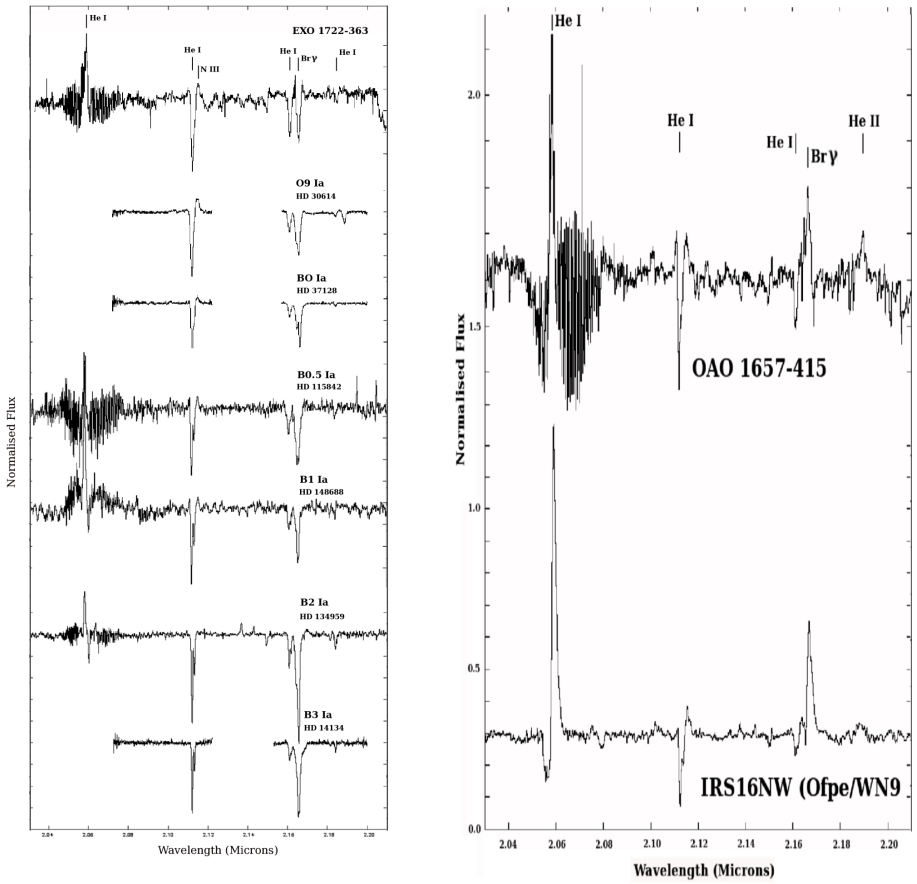

Figure 1: Left: Comparison of EXO 1722-363 and template O9-B3 Ia spectra from Hanson et al. (2005). Right: Topmost shows a spectrum of OAO1657-415 compared with a Ofpe/WNL spectrum of IRS16NW from Martins et al. (2007).

with the spectra of B0-6 supergiants (Hanson et al. 1996, Hanson et al. 2005) - as suggested for the mass donor by Chakrabarty et al. (2002) on the basis of a combination of photometric and X-ray data. However, comparison with the spectra of massive transitional objects presented by Morris et al. (1996) is more encouraging. In particular OAO 1657-415 shows pronounced similarities to the hot Ofpe/WNL stars. Consequently we may not *a priori* determine a unique distance to OAO 1657-415 on the basis of this classification. We thus find inevitably unconstructive limits of $4.4\,\mathrm{kpc} < d < 12\,\mathrm{kpc}$. In turn this results in $1.5 \times 10^{36}\,\mathrm{erg}\,s^{-1} < L_{\mathrm{X}} < 10^{37}\,\mathrm{erg\,s^{-1}}$, also entirely consistent with observed luminosities of SGXRBs. Adopting the distance derived by Audley et al. (2006) leads to $\log\left(L/L_{\odot}\right) \sim 5.7$. For such a luminosity, comparison to the evolutionary tracks for massive stars (Meynet & Maeder 2000) implies an initial mass of $\sim 40\,\mathrm{M}_{\odot}$.

3 OAO 1657-415 : A mechanism for spin-period evolution

We now turn to the implications of the Ofpe/WNL classification for the X-ray properties of OAO 1657-415. The anomalous position of OAO 1657-415 within the Corbet diagram (Figure 2) (Corbet et al. 1986), is then naturally explained in terms of the properties of its stellar wind. Compared to normal OB supergiants (Crowther et al. 2006), Ofpe/WNL stars typically demonstrate systematically lower wind velocities and higher mass loss rates (Martins et al. 2007). This combination of wind properties permits a higher accretion rate and hence transfer of angular momentum to the NS, in turn

leading to a smaller (instantaneous) equilibrium spin period with respect to normal OB supergiants ($P_{\rm spin} \propto \dot{\rm M}^{-3/7} v_{\infty}^{12/7}$ from Eqn. 12 of Waters et al. (1989), where $P_{\rm spin}$, $\dot{\rm M}$ and v_{∞} are the spin period of the NS and the mass loss rate and terminal velocity of the mass donor wind respectively).

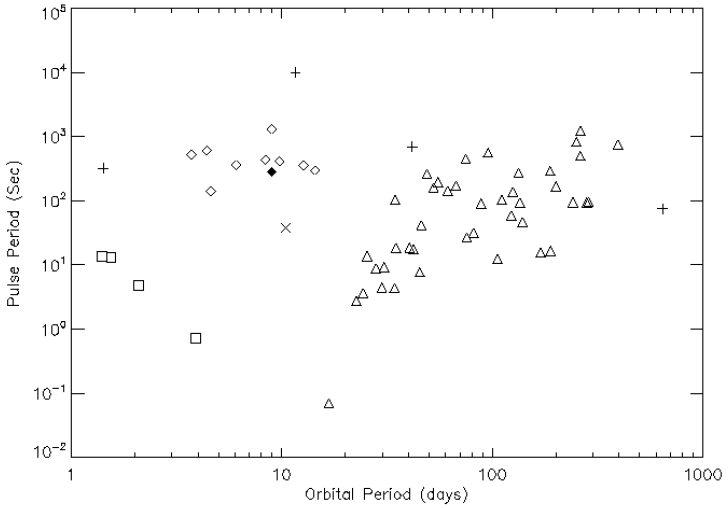

Figure 2: Corbet diagram marking position of OAO 1657-415 and other HMXBs. OAO 1657-415 is marked by an X, EXO 1722-363 by a filled diamond. SGXRB Roche-Lobe Overflow systems (Squares), Be/X binaries (Triangles), SGXRB Wind-fed systems (Diamonds) and anomalous systems (+)

4 Orbital solution for EXO 1722-363

The orbital solution we have calculated was obtained from archival ESO VLT data. Using a small subset of the available archive data, (11 spectra taken at different epochs spanning a wide range of orbital phase, from a set of 104 in total) we were able to measure radial velocities and construct the orbital solution shown in Fig. 3 (left). These spectra were centered on 2.1μm, having an integration time of 700s, and were obtained using the SW MRes mode with a 0.6$''$ slit. This resulted in high S/N spectra at a resolution R $\approx$ 4200. The resulting NS mass that we have determined from our orbital solution for EXO 1722-363 is consistent with the canonical mass of 1.4 $M_{\odot}$ measured in most other eclipsing HMXBs, except for that in Vela X-1, (Quaintrell et al. 2003). The NS mass range we have determined stems from a lower and upper limit obtained using the following constraints - *Lower* : the system is viewed edge on (i.e. $i = 90^{\circ}$), *Upper* : the donor star fills its Roche lobe. Utilising this orbital solution we find a NS mass range of 1.5 - 1.6 $M_{\odot}$ (Mason et al. 2010). In a similar way the measured mass and radius of the supergiant donor, $M \sim 13 - 15$ $M_{\odot}$ and $R \sim 25 - 28$ $R_{\odot}$ is determined, and this lends support to the B0-1 Ia spectral classification that we previously found (Mason et al. 2009).

5 Orbital solution for OAO 1657-415

As the mass donor in OAO 1657-415 is faint (H $\sim$ 11.7) we employed the NIR spectrometer ISAAC on the VLT to obtain high resolution (R $\sim$ 3000) and S/N spectra in the H band. Observations were conducted between 2008 May 13th and 2008 September 25th in the SW MRes mode with an 0.8$''$ slit. Cross-correlation was performed using the standard IRAF routine *fxcor*. Twelve high quality spectra were obtained that covered a wide range of orbital phase, sufficient to determine a dynamical mass solution for OAO 1657-415 (Fig. 3). Utilising this orbital solution we find a NS mass range of $\approx$ 1.4 - 1.7 $M_{\odot}$ with a corresponding mass range for the counterpart star of $\approx$ 14 - 17 $M_{\odot}$. For a more precise mass determination please refer to Mason et al. (2011).

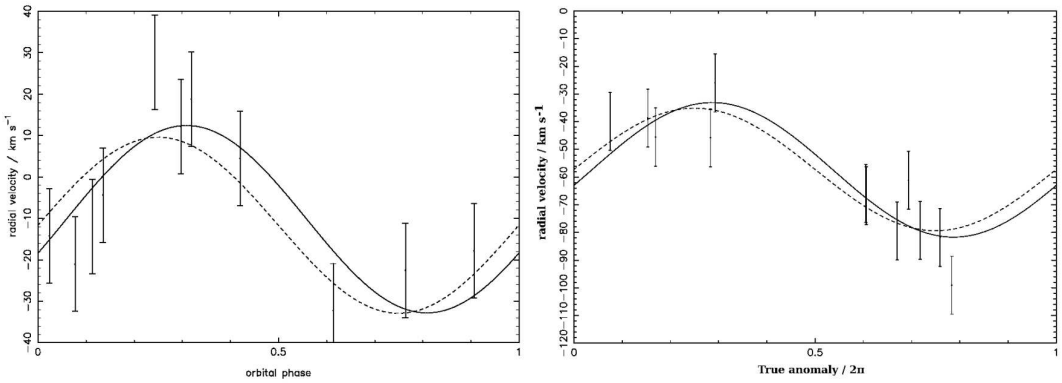

Figure 3: Left : Radial velocity data for the donor in EXO 1722–363. Right : Radial velocity data for the donor in OAO 1657-415. In both cases the solid line is the best fitting sinusoid with three free parameters, the dashed line is that with a fixed zero phase in line with the published ephemeris. In the case of EXO 1722–363 the orbital phase is based upon the ephemeris of Thompson et al. (2007). For OAO 1657-415 the orbital phase is based upon the ephemeris of Bildsten et al. (1997).

Acknowledgements

ABM acknowledges support from an STFC studentship. JSC acknowledges support from an RCUK fellowship. This research is partially supported by grants AYA2008-06166-C03-03 and Consolider-GTC CSD-2006-00070 from the Spanish Ministerio de Ciencia e Innovación (MICINN). Based on observations carried out at the European Southern Observatory, Chile through programmes 081.D-0073(A and B) and 077.B-0872(A) .

References

Audley, M.D., Nagase, F., Mitsuda, K., et al. 2006, MNRAS 367, 1147
Bibby, J.L., Crowther, P.A., Furness, J.P., et al. 2008, MNRAS 386, 23
Bildsten, L., Chakrabarty, D., Chiu, J., et al. 1997, ApJS 113, 367
Chakrabarty, D., Grunsfeld, J.M., Prince, T.A., et al. 1993, ApJ 403, L33
Chakrabarty, D., Wang, Z., Juett, A.M., et al. 2002, ApJ 573, 789
Corbet, R.H.D., Thorstensen, J.R., Charles, P.A. et al. 1986, MNRAS 220, 1047
Corbet, R.H.D., Markwardt, C.B., & Swank, J.H., 2005, ApJ 633, 377
Crowther, P.A., Lennon, D.J., & Walborn, N.R. 2006, A&A 446, 279
Hanson, M.M., Conti, P.S., & Rieke, M.J. 1996, ApJS 107, 281
Hanson, M.M., Kudritzki, R.P., Kenworthy, M.A., et al. 2005, ApJS 161, 154
Martins, F., Genzel, R., Hillier, D.J., et al. 2007, A&A 468, 233
Mason, A.B., Clark, J.S., Norton, A.J., et al. 2009, A&A 505, 281
Mason, A.B., Norton, A.J., Clark, J.S. et al. 2010, A&A 509, 79
Mason, A.B., Norton, A.J., Clark, J.S. et al. 2011, submitted.
Meynet, G., & Maeder, A. 2000, A&A 361, 101
Morris, P.W., Eenens, P.R.J., Hanson, M.M., et al. 1996, ApJ 470, 597
Quaintrell, H., Norton, A.J., Ash, T.D.C., et al. 2003, A&A 401, 313
Thompson, T.W.J., Tomsick, J.A., in 't Zand, J.J.M., et al. 2007, ApJ 661, 447
Warwick, R.S., Norton, A.J., Turner, M.J.L., Watson, M.G., & Willingale, R. 1988, MNRAS 232, 551
Waters, L.B.F.M., & van Kerkwijk, M.H. 1989, A&A 223, 196
Zurita Heras, J.A., de Cesare, G., Walter, R., et al. 2006, A&A 448, 261

Thermal Radio Emission from Radiative Shocks in Colliding Stellar Winds

Gabriela Montes[1*], Ricardo F. González[2], Jorge Cantó[3], Miguel A. Pérez-Torres[1] and Antonio Alberdi[1]

[1] Instituto de Astrofísica de Andalucía, IAA-CSIC, Granada, Spain
[2] Centro de Radioastronomía y Astrofísica, CRyA-UNAM, Morelia, Mexico
[3] Instituto de Astronomía, IA-UNAM, Mexico, D.F., Mexico

Abstract: We present a semi-analytic model for computing the thermal radio continuum emission from radiative shocks within colliding wind binaries. Assuming a thin shell approximation, we determine the contribution of the wind collision region (WCR) to the total thermal emission for close binaries. We investigate the effect of the binary separation and the stellar wind parameters on the total spectrum. In addition, we point out the relevance of taking into account this contribution for the correct interpretation of the observations, and the accuracy of the stellar wind parameters derived from them.

1 Introduction

Stellar winds from hot massive stars, OB and Wolf-Rayet (WR) type stars, emit free-free thermal emission detectable at radio frequencies. For a steady, isothermal, and radially symmetric wind, the radio spectrum is characterized by a spectral index, $\alpha \sim 0.6$ ($S_\nu \propto \nu^\alpha$; Wright & Barlow, 1975; Panagia & Felli, 1975). However, deviations from these assumptions, such as variations in the wind parameters at injection, might alter the value of α (Leitherer & Robert, 1991; González & Cantó 2008). Furthermore, in binary systems, the stellar winds of both stars might collide, resulting in a WCR between the stars (Eichler & Usov 1993). This WCR might also affect the radio spectrum, since its structure might i) alter the symmetry of stellar wind, and, ii) contribute with an extra emission component, which could be thermal and/or non-thermal emission.

Theoretical studies suggest that for wide systems (orbital periods, P ∼years) the thermal emission from the WCR might have an important but not dominant contribution to their total emission (see Stevens 1995), being more important for close systems (Pittard et al. 2006). Pittard et al (2006) analyzed the thermal emission arising from an adiabatic WCR, and found that the hot gas within the WCR remains optically thin, with a thermal component of emission with an spectral index ∼-0.1. Recently, Pittard (2010) studied the emission from radiative shocks in O+O type systems. They found that the thermal emission from the material within this kind of shocks remains optically thick with spectral indices up to ~ 1.5 for frequencies ~ 50 GHz. Such steep tendency for the spectral index

*gmontes@iaa.es

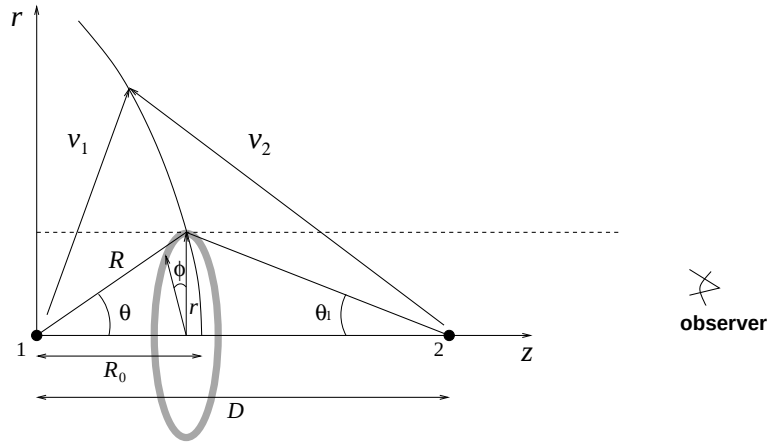

Figure 1: Schematic diagram of the two symmetric winds from stars 1 and 2, having velocities v_1 and v_2, and the thin shell resulting from their interaction. Dotted line represent the line of sight from the observer through the stellar winds, which intersects the thin shell at the impact parameter r.

were reported for WR systems in Montes et al. 2009, which suggest that a thermal component from a radiative WCR could also be taking place in WR stars.

2 Thermal radio-continuum emission from the WCR

2.1 The analytical model

Using the formalism developed by Cantó, Raga, & Wilkin (1996) and Cantó, Raga, & González (2005) we obtain semi-analytic solutions (Montes et al. 2010) from which the free-free thermal emission arising from the interaction region, and its dependence with the stellar wind parameters, can be obtained.

We assume two symmetric and stationary outflows, and use a thin shell approximation to describe their interaction. We define $\dot{m}_1$ and v_1 as the mass loss rate and the velocity of the wind source at the origin of the spherical coordinate system (R, θ, ϕ), and $\dot{m}_2$ and v_2 as the corresponding quantities for the wind from the source located at a distance D. The position of the thin shell can be approximated by the momentum balance curve described by,

$$R(\theta) = D \sin\theta_1 \csc\left(\theta + \theta_1\right), \tag{1}$$

(Cantó et al. 1996). Additionally, the distance to the stagnation point is $R_0 = \beta^{1/2} D/(1+\beta^{1/2})$, where $\beta = (\dot{m}_1\, v_1)/(\dot{m}_2\, v_2)$ (see Figure 1).

These assumptions allow us to find an analytic expression for the emission measure of the WCR as a function of θ and θ_1, $EM(\theta, \theta_1)$. In this way, the optical depth of the WCR, in the direction perpendicular to the thin shell, can be written as $\tau_{WCR,\perp}(\theta, \theta_1) = EM(\theta, \theta_1)\, \chi(\nu)$, where $\chi(\nu)$ =8.436 $\times 10^{-7}\, \nu^{-2.1}$, where ν is the frequency in Hz.

2.2 The radio spectra of binary systems

The radio continuum flux from a system located at a distance L from the observer can be calculated by,

$$S_\nu = 2\pi B_\nu \left(\frac{R_0}{L}\right)^2 \int_0^{\tilde{r}(\theta_\infty)} [1 - \mathrm{e}^{-\tau(\theta,\theta_1)}]\, \tilde{r}\, d\tilde{r} \tag{2}$$

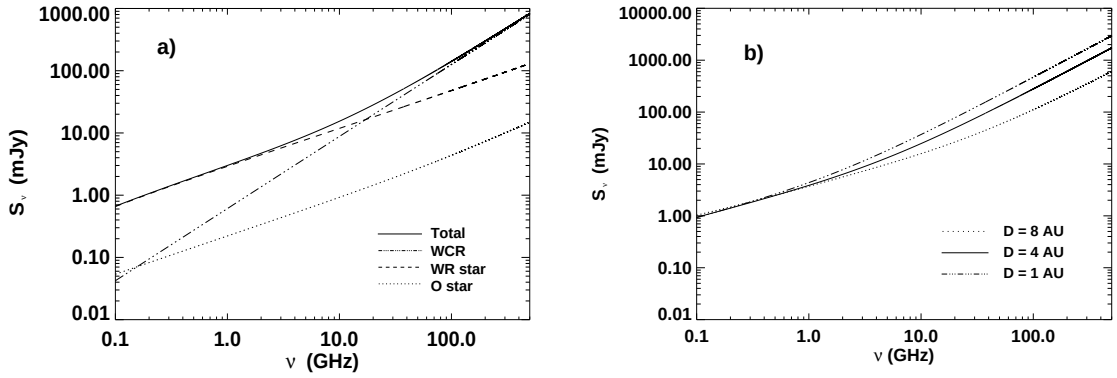

Figure 2: a) Predictions from the analytical model presented in Section 2 of the thermal radio spectrum of a binary system with $\beta = 0.25$, $D = 4$AU, $v_1 = v_2 = 10^3 \mathrm{km\,s^{-1}}$, $\dot{M}_1 = 1.25 \times 10^{-5}\,\mathrm{M_\odot\,yr^{-1}}$, and $\dot{M}_2 = 5 \times 10^{-5}\,\mathrm{M_\odot\,yr^{-1}}$. All the emission components, and the total spectrum are plotted. b) Total thermal emission for systems at different separation D, considering the terminal wind velocities $v_1 = v_2 = 10^3 \mathrm{km\,s^{-1}}$, and mass loss rates $\dot{M}_1 = \dot{M}_2 = 5 \times 10^{-5}\,\mathrm{M_\odot\,yr^{-1}}$ ($\beta = 1$).

where $\tau(\theta, \theta_1) = \tau_{WCR}(\theta, \theta_1) + \tau_{w,1}(\theta) + \tau_{w,2}(\theta)$ is the total optical depth along the line of sight, $B_\nu = 2kT\nu^2/c^2$ (being k the Boltzmann's constant, and c the speed of light) is the Planck function in the Rayleigh-Jeans approximation, and $\tilde{r}(\theta_\infty)$ is the impact parameter at the asymptotic angle θ_∞ of the thin shell, which corresponds to $R \rightarrow \infty$.

In Figure 2-a we show the total thermal spectrum from a binary system with typical WR+O type star parameters. All the individual contributions to the emission are plotted. The shock emission remains optically thick with $\alpha_{WCR} \sim 1.1$, and the stellar wind components shows the expected $\alpha \sim 0.6$ behavior. In this way, the total spectrum shows a stellar wind behavior at low frequencies, changing to one dominated by the shock at high frequencies. Therefore, the impact of the WCR over the total spectrum is seen as an excess of emission at high frequencies (with respect to that expected for a single stellar wind spectrum). This result is similar to that found by Pittard (2009) from hydrodynamic simulations for radiative O+O systems.

From equation (3), for the case $\tau_{WCR} >> 1$ it can be seen that $S_\nu \propto R_0^2 \propto D^2$, in contrast with the D^{-1} dependence for adiabatic shocks (Pittard et al. 2006). Figure 2-b shows the increase of the WCR contribution when the distance between the stars D is increased.

3 Applicability of the model

This model can be applied to WR binary systems that satisfy $P > 15$ days, where the wind acceleration region and braking effect, which could be relevant in shorter period systems (Gayley, Owocki, & Cranmer, 1997), can be neglected. On the other hand, Parkin & Pittard (2008) found, for a WR system, that the cooling is important for orbital periods $\lesssim 1$ year. Thus, the systems we are considering have a period between 15 days and 1 year.

3.1 The case of WR 98

WR 98 (HD 318016) is a system identified as a double-line binary (WN7o/WC+O8-9) with an orbital period, $P = 47.8$ days (Gamen & Niemela 2002). Montes et al. (2009) reported variability in both flux density and spectral index, which they interpreted as the result of a WCR contribution. We apply our model and fit the flux densities obtained for which their determination of the spectral index

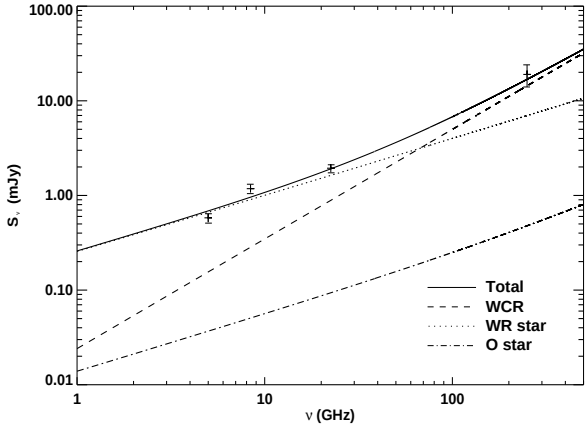

Figure 3: Fit of the radio observations of the binary system WR 98 including the WCR thermal component. Flux densities, $S_{5\,\mathrm{GHz}} = 0.58 \pm 0.06$ mJy, $S_{8.4\,\mathrm{GHz}} = 1.18 \pm 0.05$ mJy, $S_{23\,\mathrm{GHz}} = 1.94 \pm 0.05$ mJy from Montes et al. (2009), and $S_{250\,\mathrm{GHz}} = 19 \pm 5$ mJy from Altenhoff et al. (1994) are plotted.

suggest a thermal spectrum, with $\alpha \sim 0.64$ (see Figure 3). For the WR star, we have assumed a mass loss rate $\dot{M}_{WR} = 3.0 \times 10^{-5}\,\mathrm{M_\odot\,yr^{-1}}$ (upper limit derived by Montes et al. 2009), and a terminal velocity $v_{WR} = 1200\,\mathrm{km\,s^{-1}}$ (Eenens & Williams, 1994). The best fit to the observations was found using the O star parameters $\dot{M}_O = 4.0 \times 10^{-6}\,\mathrm{M_\odot\,yr^{-1}}$ and $v_O = 1800\,\mathrm{km\,s^{-1}}$, which are reasonable values for an O type star. We assume a separation, $D = 0.5$AU (see Gamen & Niemela 2002), and calculate $\beta = 0.2$, and $R_0/D = 0.3$. From our model we predict that the WCR might start to contribute to the spectrum at a frequency of $\nu \sim 70$ GHz, and reach an excess of emission at 250 GHz of a factor of 2 that from the stellar winds (~ 7 mJy), which is similar to the flux density at 250 GHz, $S_{250\,\mathrm{GHz}} = 19 \pm 5$ mJy, reported by Altenhoff, Thum, & Wendker (1994).

4 Discussion and Conclusions

Steep spectral indices in both WR and O type stars have been observed (Montes et al. 2009; Benaglia 2010). In particular, for WR stars, Nugis, Crowther, & Willis (1998) analyzed their spectrum from mm to IR frequencies, finding spectral indices between 0.6-1.0, with cases where α increases at high frequencies. Although several processes have been used to explain such behavior, our model predicts the WCR to have a similar impact over the radio-mm spectrum.

At this time, the impact of the WCR over the radio spectrum has only been inferred from the analysis of non-thermal emission, detectable mainly at low frequencies. In this way, for those close systems where the non-thermal emission is expected to be absorbed and only the thermal stellar wind emission is thought to be detected, this model also predicts an impact from a WCR contribution. Furthermore, as well as in the case of the non-thermal emission, the thermal contribution from the WCR is expected to be modulated by the orbital motion (Pittard 2010), resulting in this way in a variable thermal contribution. Therefore, observational studies to identify a modulated thermal excess of emission might represent a new method to unveil close binary systems from radio observations, this time at high radio frequencies (a few cm down to a few mm). Those close systems like WR 113, and WR 141, where steep spectral indices have been observed (Montes et al. 2009), are excellent candidates for this kind of study.

On the other hand, in order to compare the spectrum behavior in close systems with respect to

those in wide systems and single stars, a statistical study of the emission at frequencies ($\gtrsim 50$ GHz) is required. This study might reveal a steep tendency for the spectral index in close systems, unveiling in this way a binary influence as result of the process described here. However, at this moment there is a poor sample of O and WR stars (those with the strong winds) observed at high frequencies, so that this kind of study is not possible to perform, and high-frequency observations are required.

Furthermore, as was pointed out for WR 98 in Section 4, the total flux density at 250 GHz was estimated to be a factor of 2 higher than that from a single stellar wind, as result of the WCR contribution. Therefore, this possible extra contribution must be taken into account for a mass loss rate determinations from these frequencies. This effect could be even higher than in the example of WR 98, as was pointed out by Pittard (2010) from his estimates of the WCR contribution in radiative O+O systems.

Acknowledgments

G.M. acknowledges financial support from CSIC predoctoral JAE fellowship. This research was partially supported by the Spanish MICINN through grant AYA2009-13036-CO2-01. RFG has been partially supported by DGAPA (UNAM) grant IN117708. We acknowledge to the referee and the editor P.W. for their suggestions and careful reading of this work.

References

Altenhoff, W. J., Thum, C., & Wendker, H. J. 1994, A&A, 281, 161
Benaglia, P. 2010, Astronomical Society of the Pacific Conference Series, 422, 111
Cantó, J., Raga, A. C., & Wilkin, F. P. 1996, ApJ, 469, 729
Cantó, J., Raga, A. C., & González, R. 2005, RMxAA, 41, 101
Eenens, P. R. J., & Williams, P. M. 1994, MNRAS, 269, 1082
Eichler, D., & Usov, V. 1993, ApJ, 402, 271
Gamen, R. C., & Niemela, V. S. 2002, New Astronomy, 7, 511
Gayley, K. G., Owocki, S. P., & Cranmer, S. R. 1997, ApJ, 475, 786
González, R. F., & Cantó, J. 2008, A&A, 477, 373
Leitherer, C., & Robert, C. 1991, ApJ, 377, 629
Nugis, T., Crowther, P. A., & Willis, A. J. 1998, A&A, 333, 956
Montes, G., Pérez-Torres, M. A., Alberdi, A., & González, R. F. 2009, ApJ, 705, 899
Montes, G., González, R. F., Cantó, J., Pérez-Torres, M. A., & Alberdi, A., 2010, A&A, submited
Panagia, N., & Felli, M. 1975, A&A, 39, 1
Parkin, E. R., & Pittard, J. M. 2008, MNRAS, 388, 1047
Pittard, J. M. 2009, MNRAS, 396, 1743
Pittard, J. M. 2010, MNRAS, 403, 1633
Stevens, I. R. 1995, MNRAS, 277, 163
Wright, A. E., & Barlow, M. J. 1975, MNRAS, 170, 41

A first orbital solution for the non-thermal radio emitter Cyg OB2 #9*

Y. Nazé[1]†, Y. Damerdji[1], G. Rauw[1], D.C. Kiminki[2], L. Mahy[1], H.A. Kobulnicky[2], T. Morel[1], M. De Becker[1], P. Eenens[3], C. Barbieri[4]

[1] GAPHE, Institut d'Astroph. et Géoph., Dépt AGO, Université de Liège, Allée du 6 Août 17, Bât B5C, B4000-Liège, Belgium

[2] Dep. of Physics & Astronomy, University of Wyoming, Laramie, WY 82070, USA

[3] Dep. de Astronomia, Univ. de Guanajuato, Apartado 144, 36000 Guanajuato, GTO, Mexico

[4] Dip. di Astronomia, Univ. degli studi di Padova, vicolo Osservatorio 2, 35122 Padova, Italy

Abstract: We reported in 2008 the first detection of the binary nature of Cyg OB2 #9. Since then, we have continued our spectroscopic monitoring of this object, doubling the number of available spectra of the star while covering a second periastron passage. Using a variety of techniques, the radial velocities were estimated and a first, preliminary orbital solution was derived (P=2.4 yrs). The mass ratio appears close to unity and the eccentricity is large, 0.7-0.75.

1 Introduction

Non-thermal radio emission is a rare phenomenon among massive stars, with fewer than 40 cases known in our Galaxy (see e.g. De Becker 2007). It requires two ingredients, magnetic fields and relativistic electrons. Magnetic fields have long been searched for in massive stars, but it is only in the last decade that the first direct detections were finally obtained from sensitive spectropolarimetric observations (e.g. Donati et al. 2002, Hubrig et al. 2008). A population of relativistic electrons can be generated from shocks through the first-order Fermi mechanism and the stellar winds of massive stars are good places to find such shocks. Indeed, on the one hand, the line-driving mechanism at the origin of the wind acceleration is intrinsically unstable; on the other hand, shocks can also appear when winds collide in massive binaries. Theoretical modelling showed that the observed non-thermal radio emission can be reproduced only in the second case, i.e. in colliding wind binaries (Van Loo et al. 2005). Dedicated observational campaigns confirm this view by revealing signatures of multiplicity in most non-thermal radio emitters — only 3 of the 17 WRs and 3 of the 16 O stars listed by De Becker (2007) totally lacked evidence for binarity.

One of these remaining cases is Cyg OB2 #9, though it was one of the first O-stars detected as a non-thermal radio emitter (Abbott et al. 1984). It was only in 2008 that two pieces of evidence finally

*Based on data obtained with XMM-Newton (ESA) and at the OHP (France).

†Research Associate FNRS

pointed towards a binary scenario. The first one was indirect: a long-term (2.355 yrs) modulation of the radio emission was detected by Van Loo et al. (2008). The second piece of evidence was the unambiguous detection of double line profiles in the optical spectrum of Cyg OB2 #9 by Nazé et al. (2008). However, no orbital solution could then be derived and the direct detection of wind-wind collision (e.g. through X-ray data) was still lacking.

2 Optical data

2.1 Observations

In the last decade, we began an intensive spectroscopic monitoring of Cyg OB2 #9. To investigate the binarity of the star, spectral resolving powers of at least 3500 (and maximum 35 000) were required and the yellow-red domain was favored due to the high interstellar extinction. These data were obtained at the Asiago observatory (AFOSC in echelle mode), San Pedro Mártir Observatory (Espresso), Wyoming Infrared Observatory (WIRO-Longslit spectrograph), and the Haute-Provence Observatory (Aurélie and Sophie spectrographs). Exposure times of several hours were often needed to reach typically signal-to-noise ratios of 50–100. The wavelength calibration was improved by using strong and narrow diffuse interstellar bands close to stellar lines, remaining errors on the radial velocities (RVs) being reduced to $<$5–10 km s^{-1}. A full journal of the observations can be found in Nazé et al. (2008, 2010).

2.2 A preliminary orbit

Cyg OB2 #9 is not an easy star to analyse since it is strongly absorbed. The star therefore appears faint and its optical spectrum is filled with strong interstellar lines, often more intense than the stellar lines. To get reliable RVs, the best choice is He I λ 5876 since it is a stellar line which is both strong and uncontaminated by interstellar components (there is a caveat, though, since this line sometimes appears polluted by emission in some extreme O-type stars but we do not see obvious emission in our dataset). In total, our monitoring provided 34 observations of that line.

Another problem is that the stellar lines appear blended during 80% of the orbit. Several ways to determine the RVs were therefore tested. Cross-correlations, line disentangling, and 2-Gaussian fitting throughout the whole orbit give poor results, due to the strong line blending. Reliable RVs could then be found from two methods only. The first one is to find the individual line properties from a 2-Gaussian fitting when the lines are at maximum separation and then to fix the line characteristics (width, intensity), shifting the resulting Gaussians until the χ^2 is minimized (case A in Table 1 below). The second method is to perform 2-Gaussian fitting when the lines appear somewhat deblended (20% of the orbit) and 1-Gaussian fitting otherwise (case B in Table 1 below). This latter solution is probably less reliable than the former one, but it relies on fewer assumptions and thus represents a "minimalistic" approach.

Once a reliable set of RVs was available, a period search was performed using the Heck et al. (1985) Fourier method. The SB2 dataset was then converted into an equivalent SB1 dataset (cf. Liège Orbital Solution Package, Sana & Gosset, A&A, submitted). A first guess of the orbital solution was then derived from the Wolfe et al. (1967) or Lehmann-Filhés (1894) methods, the final solution being found after a Levenberg-Marquardt minimization. An independent check was made using the method of Zechmeister & Kurster (2009). Table 1 provides the orbital solutions derived from the two RV datasets considered above.

The period derived from the optical data is fully compatible with the timescale derived from the recurrent radio variations. The mass ratio is close to unity, confirming the preliminary results of

Table 1: Preliminary orbital solution of Cyg OB2 #9. Solution A uses RVs determined using the χ^2 method, solution B uses 2 RVs only when the lines are clearly deblended. Note that T_0 is expressed as HJD - 2 450 000 and that the preferred inclination is $\sim$50° for case A and $\sim$70° for case B (if both stars are supergiants and the "typical" masses of O5–7 stars from Martins et al. 2005 are assumed).

Parameter	A	B
P(d)	852.9±4.3	852.8±4.4
T_0	4036.8±3.69	4030.9±3.9
e	0.744±0.0304	0.708±0.027
$\omega(^\circ)$	−164.4±4.19	−175.1±4.4
M_1/M_2	1.17±0.22	1.10±0.17
γ_1(km s^{-1})	−40.6±3.23	−28.1±3.4
γ_2(km s^{-1})	16.6±3.5	1.2±3.5
K_1(km s^{-1})	53.0±7.0	63.2±6.8
K_2(km s^{-1})	62.1±8.1	69.4±7.4
$a_1 \sin i$(R$_\odot$)	598.0±84.4 7	752.1±86.0
$a_2 \sin i$(R$_\odot$)	699.3±97.7 3	825.9±93.7
$M_1 \sin^3 i$(M$_\odot$)	21.7±7.2	38.0±10.1
$M_2 \sin^3 i$(M$_\odot$)	18.6±6.1	34.6±9.1
rms(km s^{-1})	14.5	16.3

Nazé et al. (2008), who proposed spectral types of O5 and O6–7 for the binary components. The eccentricity is large, but is not the main cause of the poor deblending. In fact, the non-crossing of the RV curves (see Fig. 1) comes mostly from the large asymmetry in the center-of-mass velocities (often attributed to wind asymmetries and/or illumination effects on the side of the star facing its companion, see Rauw et al. 1996 and references therein). While non-equal γ are often observed in massive binaries, Cyg OB2 #9 clearly appears as an extreme case, at least as far as O-type binaries are concerned.

3 X-ray data

The Cyg OB2 association was observed six times with the XMM-Newton observatory: four pointings (with a separation of 10 days) were obtained in Oct.-Nov. 2004 and two pointings, separated by 4 days, were taken in May 2007. The data reduction and instrumental configuration were similar in all cases. The stellar data were always extracted in a circle of at least 23″ in radius while the background was estimated from a nearby source-free region some $50'' \times 20''$ in size. Considering the ephemeris of Cyg OB2 #9 derived above, these X-ray data correspond to orbital phases of 0.14–0.18 for the 2004 data and of 0.21–0.22 for the 2007 data.

The X-ray spectrum of Cyg OB2 #9 appears thermal in nature, as evidenced by the presence of several X-ray lines (notably the iron line at 6.7 keV, Fig. 2). No trace of non-thermal emission is detected but this is not surprising, as the strong thermal emission can easily hide any non-thermal X-ray emission in the 1–10 keV range (see e.g. De Becker et al. 2009).

Good fits are obtained with models using two thermal components, both being absorbed by the (fixed) interstellar absorption and an additional wind component let free to vary. In all six cases, the derived spectral parameters are rather similar: the wind absorbing column amounts to $\sim 5 \times 10^{21}$ cm^{-2}, while the two temperatures are 0.6 keV and $\sim$2.4 keV. In fact, the spectrum is similar to that of HD168112, another non-thermal radio emitter. The $\log(L_X/L_{BOL})$ ratio amounts to −6.3

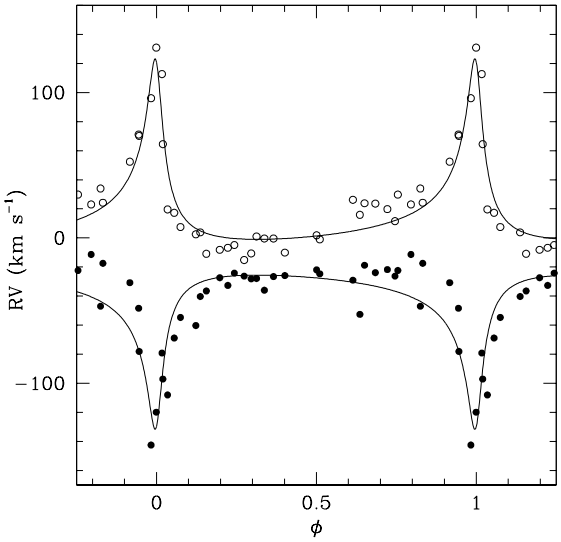

Figure 1: RV curves superimposed on the best SB2 solution (case A). Figure reproduced from Nazé et al. (2010).

and the average temperature $< kT >$ is 1.2 keV. Comparing with the results from the 2XMM survey (Nazé 2009), Cyg OB2 #9 therefore appears slightly overluminous (it is on the luminous edge of the $\log(L_X/L_{BOL})$ dispersion for O-type stars) and somewhat hot (in the 2XMM, 83% of the O-type stars display $< kT >$ below 1 keV). However, there is no strong signature of colliding winds in our XMM data.

Nonetheless, an intriguing fact is the detection of some variability between exposures (Fig. 2). There is notably a 10% decrease of the flux between 2004 and 2007, i.e. as the stars get further away from each other. This flux decreases towards apastron and the lack of strong colliding winds signature in the available data may be reconciliable with a colliding winds scenario — there would be an intense brightening near periastron, followed by a decrease and a minimum contamination of the wind-wind collision emission near apastron. However, this needs to be ascertained by securing data near periastron.

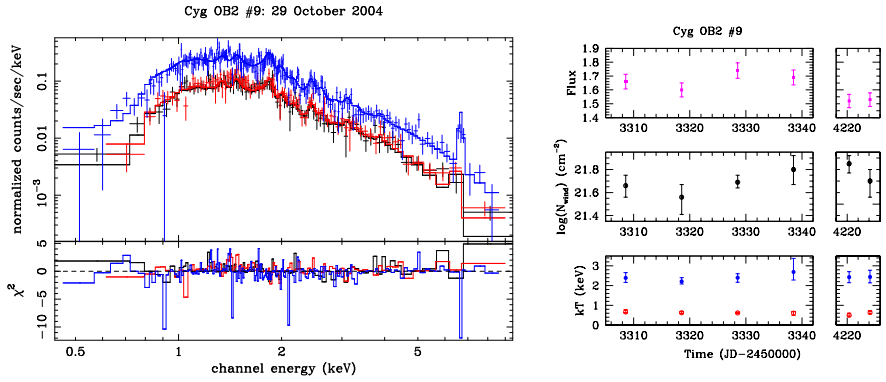

Figure 2: Left: EPIC spectra of Cyg OB2 #9 with best-fit model superimposed (lower/upper data points correspond to EPIC-MOS/pn, respectively). Right: Variations of the fitted parameters through the observations. Figure reproduced from Nazé et al. (2010).

4 Conclusions

Thanks to an intensive optical spectroscopic monitoring, we have obtained the first orbital solution for Cyg OB2 #9. This system has a long period ($\sim$850d), a mass ratio close to unity, and a large eccentricity ($\sim$0.7). It is a difficult system to study, as the lines are deblended only in a small window of the orbit, implying that the center-of-mass velocities are very different from each other, which could be linked to the illumination of one star by the other and/or wind asymmetries.

In the X-ray domain, Cyg OB2 #9 is only slightly harder and brighter than "normal" O-type stars, i.e. no strong emission from the expected wind-wind collision is detected. Some low-amplitude (10%) flux variability is however detected, but its origin is uncertain without additional data (it must be noted that the observations were all taken quite close to each other and relatively far from periastron).

The next periastron passage should occur in mid-2011. We plan to perform a multiwavelength monitoring (from X-ray to radio) at that time, in order to ascertain the full geometry of the colliding winds' zone and the full orbital characteristics. Only then will a detailed hydrodynamical modelling be possible, which should shed new light on non-thermal emission processes in O-type stars.

Acknowledgements

The authors acknowledge support from the Scient. Coop. prog. 2005-2006 between Italy and the Belgian "Communauté Française" (project 05.02), the "Communauté Française" (travels to OHP), the Gaia-DPAC and XMM+INTEGRAL PRODEX contracts (Belspo), the 'Action de Recherche Concertée' (CFWB-Académie Wallonie Europe), the EC's 7th Framework Prog. (FP7/2007-2013, RG226604-OPTICON), the "Crédit d'impulsion ULg no. I-06/13" (ULg), the FRS/FNRS (Belgium), and the Conacyt (Mexico).

References

Abbott, D. C., Bieging, J. H., & Churchwell, E. 1984, ApJ, 280, 671
De Becker, M. 2007, A&AR, 14, 171
De Becker, M., Blomme, R., Micela, G., Pittard, J. M., Rauw, G., Romero, G. E., Sana, H., & Stevens, I. R. 2009, American Institute of Physics Conference Series, 1126, 347
Donati, J.-F., Babel, J., Harries, T. J., Howarth, I. D., Petit, P., & Semel, M. 2002, MNRAS, 333, 55
Heck, A., Manfroid, J., & Mersch, G. 1985, A&AS, 59, 63
Hubrig, S., Schöller, M., Schnerr, R. S., González, J. F., Ignace, R., & Henrichs, H. F. 2008, A&A, 490, 793
Lehmann-Filhés, R. 1894, Astronomische Nachrichten, 136, 17
Martins, F., Schaerer, D., & Hillier, D. J. 2005, A&A, 436, 1049
Nazé, Y., De Becker, M., Rauw, G., & Barbieri, C. 2008, A&A, 483, 543
Nazé, Y. 2009, A&A, 506, 1055
Nazé, Y., Damerdji, Y., Rauw, G., Kiminki, D.C., Mahy, L., Kobulnicky, H.A., Morel, T., De Becker, M., Eenens, P., & Barbieri, C. 2010, ApJ, 719, 634
Rauw, G., Vreux, J.-M., Gosset, E., Hutsemékers, D., Magain, P., Rochowicz, K. 1996, A&A, 306, 771
van Loo, S., Runacres, M. C., & Blomme, R. 2005, A&A, 433, 313
van Loo, S., Blomme, R., Dougherty, S. M., & Runacres, M. C. 2008, A&A, 483, 585
Wolfe, R. H., Jr., Horak, H. G., & Storer, N. W. 1967, Modern astrophysics. A memorial to Otto Struve, 251
Zechmeister, M., & Kürster, M. 2009, A&A, 496, 577

Observational approach to the chemical evolution of high-mass binaries

K. Pavlovski[1,2], J. Southworth[2], E. Tamajo[1], and V. Kolbas[1]

[1] Department of Physics, University of Zagreb, Croatia
[2] Astrophysics Group, Keele University, Staffordshire, UK

Abstract: The complexity of composite spectra of close binaries makes the study of the individual stellar spectra extremely difficult. For this reason there exists very little information on the chemical composition of high-mass stars in close binaries, despite its importance for understanding the evolution of massive stars and close binary systems. A way around this problem exists: spectral disentangling allows a time-series of composite spectra to be decomposed into their individual components whilst preserving the total signal-to-noise ratio in the input spectra. Here we present the results of our ongoing project to obtain the atmospheric parameters of high-mass components in binary and multiple systems using spectral disentangling. So far, we have performed detailed abundance studies for 14 stars in eight eclipsing binary systems. Of these, V380 Cyg, V 621 Per and V453 Cyg are the most informative as their primary components are evolved either close to or beyond the TAMS. Contrary to theoretical predictions of rotating single-star evolutionary models, both of these stars show no abundance changes relative to unevolved main sequence stars of the same mass. It is obvious that other effects are important in the chemical evolution of components in binary stars. Analyses are ongoing for further systems, including AH Cep, CW Cep and V478 Cyg.

1 Introduction

In the last decade theoretical stellar evolutionary models, particularly for higher masses, were improved considerably with the inclusion of additional physical effects beyond the standard ingredients. It was found that rotationally induced mixing and magnetic fields could cause substantial changes in the resulting predictions (Meynet & Maeder 2000, Heger & Langer 2000). Some of these concern evolutionary changes in the chemical composition of stellar atmospheres. Due to the CNO cycle in the core of high-mass stars some elements are enhanced (such as helium and nitrogen), some are depleted (e.g. carbon), whilst some (e.g. oxygen) are not affected at all. The rotational mixing predicted by stellar models is so efficient that changes in the atmospheric composition should be identifiable whilst the star is still on the main sequence.

On the observational side, substantial progress has also been made. The VLT/FLAMES survey (Evans et al. 2005) produced CNO abundances for a large sample of B stars in the Milky Way, and the Magellanic Clouds. This survey has opened new questions since a large population of slow rotators have shown an enhancement of nitrogen (Hunter et al. 2009). Also, important empirical constraints

on models arose from the observational study performed by Morel, Hubrig & Briquet (2008) who found that magnetic fields have an important effect on the atmospheric composition of these stars.

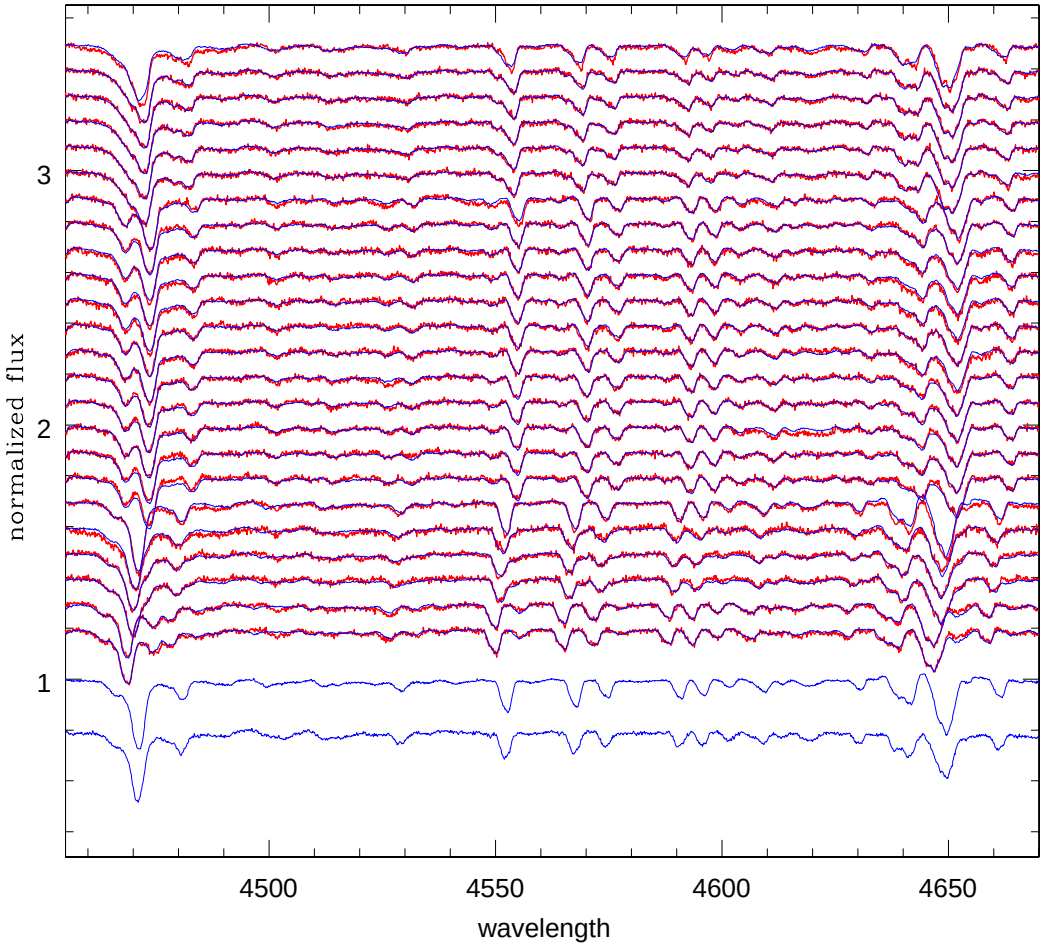

Figure 1: Time series of observed composite spectra (red lines) of the B0 V + B1 V close eclpsing binary system V453 Cyg (Pavlovski & Southworth 2009). This is a portion of échelle spectra secured with the FIES spectrograph at the Nordic Optical Telescope (La Palma). The individual disentangled spectra of the two stars, which have very similar effective temperatures, are shown at the bottom of the plot (blue lines, secondary offset by -0.2) with their correct continuum levels. The disentangled spectra have been adjusted with the appropriate Doppler shifts and relative intensities to reproduce the observed spectra, and are overlaid on them using blue lines.

Detached eclipsing binaries are fundamental objects for obtaining empirical constraints on the structure and evolution of high-mass stars, and are the primary source of directly measured stellar properties. Accurate physical properties are available for fewer than a dozen high-mass binaries, and most have no observational constraints on their chemical composition (Torres, Andersen & Giménez 2010). The aim of our projects is to obtain a sample of high-mass binaries both with accurate parameters and, for the first time, with detailed abundance studies of the individual stars. We aim to gain insight into the chemical evolution of high-mass stars in close binary systems. The close proximity of the components leads to strong tidal forces, which may be an important additional effect on the internal and chemical structure of the stars, beside rotation and magnetic fields.

2 Sample and Method

The complexity of the composite spectra of close binaries makes studying the spectra of the individual stars extremely difficult. For this reason there exists very little information on the chemical composition of high-mass stars in close binaries, despite its importance for understanding the evolution of both massive stars and close binaries. A way around this problem exists: spectral disentangling. This technique allows a time-series of composite spectra to be decomposed into their individual components whilst preserving the total signal-to-noise ratio in the input spectra, and without the use of template spectra (Simon & Sturm 1994). An overview of almost a dozen methods for spectral disentangling has been given by Pavlovski & Hensberge (2010). For our work we use the FDBINARY Fourier-space code (Ilijić et al. 2004). Synthetic spectra are generated using ATLAS9 with non-LTE model atoms (see Pavlovski & Southworth 2009 and Pavlovski et al. 2009 for details).

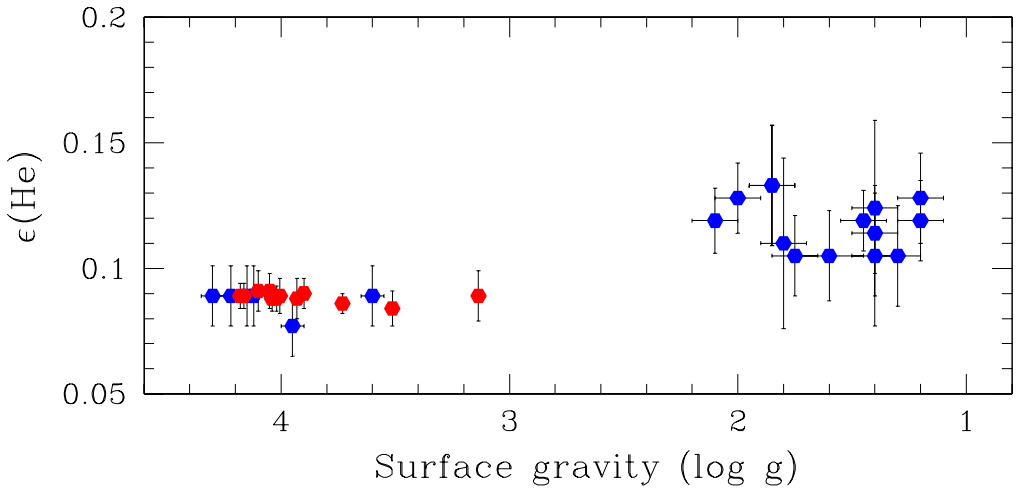

Figure 2: Helium abundances for high-mass stars in close binaries from our sample (red symbols) compared to single sharp-lined B-type main sequence stars and BA supergiants in the Przybilla et al. (2010) sample (blue symbols). ϵ(He) is the fractional helium abundance by number of atoms.

A vital step in a spectroscopic abundance study is precise determination of the stellar atmospheric parameters (effective temperature, surface gravity, microturbulence velocity, etc). When reconstructing the separate spectra of the components their individual light contributions have to be obtained either from the disentangled spectra itself, or from some other source such as a complementary light curve analysis (c.f. Pavlovski & Hensberge 2010).

So far, we have performed detailed abundance studies for 14 components in eight eclipsing binaries. In many cases we have also reanalysed existing or new light curves. Of the systems studied, V380 Cyg (Pavlovski et al. 2009), V453 Cyg (Pavlovski & Southworth 2009, Southworth, Maxted & Smalley 2004a) and V621 Per (Southworth et al. 2004b, 2011 in prep.) are the most informative as their primary components are evolved either close to or beyond the terminal-age main sequence (TAMS). Other binaries studied include V578 Mon (Pavlovski & Hensberge 2005, see also Hensberge, Pavlovski & Verschueren 2000), AH Cep, CW Cep, Y Cyg and V478 Cyg [helium abundances have also been measured from disentangled spectra for DH Cep (Sturm & Simon 1994), Y Cyg (Simon, Sturm & Fiedler 1994) and DW Car (Southworth & Clausen 2007)]. These objects mostly contain stars at the beginning of their main sequence lifetimes, so are important for calibrating theoretical models near their initial conditions.

3 The quest for surface helium enrichment

Theoretical stellar evolutionary models which include rotational mixing predict an enrichment of helium at the stellar surface, even during a star's main sequence lifetime. Extensive observational studies comprising B-type stars in the field (Lyubimkov, Rostophchin & Lambert 2004), and in stellar clusters (Huang & Gies 2006) yield evidence for this enrichment, but with a very large scatter in the individual measurements. An unexpectedly large fraction of both helium-rich, and helium-weak stars were detected by Huang & Gies (2006), who included only three helium lines in their analysis.

The results of our detailed abundance determinations in the sample of 14 components of close binary stars are shown in Fig. 2 (red symbols). The results of a recent study of helium abundances in the sample of sharp-lined main sequence and BA supergiants (Przybilla et al. 2010) are also plotted (blue symbols). It is interesting that no helium abundance enrichment has been detected in these studies, either for single stars (Przybilla et al. 2010) or the components of close binaries (this work). The studies therefore do not support a large spread in helium abundance, as found by other authors, with the caveat that the sample of main sequence stars studied is limited.

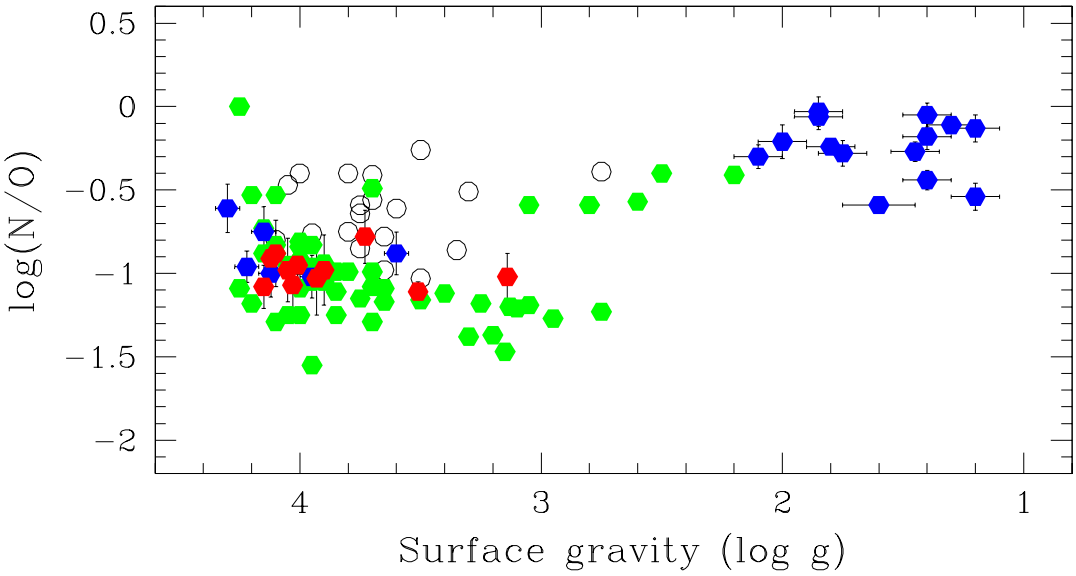

Figure 3: Evolution of nitrogen in high-mass MS stars to supergiants. The close binary systems in our sample are represented by red symbols. Other symbols represent single stars as follows: blue symbols the VLT/FLAMES survey of B stars in Milky Way (Hunter et al. 2009); green symbols the results of an abundance study for a sample of B stars with detected magnetic fields (Morel et al. 2008); and open symbols a study of sharp-lined stars (Przybilla et al. 2010).

4 The evolution of nitrogen in high-mass binaries

In close binary stars, both fast rotation and tidal forces due to the proximity of the components play an important role in stellar evolution. Tides spin up (or spin down) the stars until their rotation period synchronises with the orbital period. The effects of tides, rotational mixing and magnetic fields were studied by de Mink et al. (2009). Their model calculations indicate a significant dependence of the surface helium and nitrogen abundances for short-period systems ($P < 2$ days) for a considerable

fraction of their MS lifetime. The best candidates for testing these concepts contain more massive components, in advanced phases of the core hydrogen-burning phase, with significantly less massive and less evolved companions. V380 Cyg, V621 Per and V453 Cyg fit this bill well, but have longer orbital periods (3.9 d to 25.5 d) so are not predicted to show significant abundance enhancements. This is illustrated in Fig. 3 in which the abundance ratio N/O is plotted against $\log g$, which is a good indicator of evolutionary stage. The N/O ratios for the evolved stars in our sample are consistent with ZAMS values, like many of the stars in the VLT/FLAMES sample of Hunter et al. (2009). The evolutionary enhancement of nitrogen is only clearly present in the sample of supergiants observed by Przybilla et al. (2010). On average the magnetic B-type stars (Morel et al. 2008) have large nitrogen abundances, but definitive conclusions on the role of magnetic fields on nitrogen enrichment are still not possible (Morel 2011). The large spread in nitrogen abundances for MS stars is obvious.

Since the enhancements of helium and nitrogen are larger at lower metallicity, the best candidates for detailed study would be close binaries in the Magellanic Clouds. However, these are challenging objects for accurate abundance determination due to their high rotational velocities (resulting in line blending) and relative faintness.

Acknowledgements

KP acknowledges receipt of the Leverhulme Trust Visiting Professorship which enables him to work at Keele University, UK, where this work was performed. This research is supported in part by a grant to KP from the Croatian Ministry of Science and Education.

References

De Mink, S., Cantiello, M., Langer, N., Pols, O.R., Brott, I., & Yoon, S.-Ch. 2009, A&A 497, 243
Evans, C.J., Smartt, S.J., Lee, J.-K., et al. 2005, A&A 437, 467
Heger, A., & Langer, N. 2000, ApJ 544, 1016
Hensberge, H., Pavlovski, K., & Verschueren, W. 2000, A&A 358, 553
Huang, W., & Gies, D.R. 2006, ApJ 648, 591
Hunter, I., Brott, I., Langer, N., et al. 2009, A&A 496, 841
Ilijić, S., Hensberge, H., Pavlovski, K., & Freyhammer, L.M., 2004, in *Spectroscopically and Spatially Resolving the Components of Close Binary Systems*, eds. Hilditch R.W., Hensberge H., Pavlovski K., ASP Conf. Ser. 318, 111
Lyubimkov, L.S., Rostophchin, S.I., & Lambert, D.L. 2004, MNRAS 351, 745
Meynet, G., & Maeder, A. 2000, A&A 361, 101
Morel, T. 2011, in Proceedings of the 39th Liège Astrophysical Colloquium, eds. G. Rauw, M. De Becker, Y. Nazé, J.-M. Vreux & P.M. Williams, BSRSL 80, 405
Morel, T., Hubrig, S., & Briquet, M. 2008, A&A 481, 453
Pavlovski, K., & Hensberge, H. 2005, A&A 439, 309
Pavlovski, K., & Hensberge, H. 2010, in *Binaries - Key to Comprehension of the Universe*, eds. A. Prša and M. Zejda, ASP Conference Series (in press), arXiv:0909.3246
Pavlovski, K., & Southworth, J. 2009, MNRAS 394, 1519
Pavlovski, K., Tamajo, E., Koubsky, P., Southworth, J., Yang, S., & Kolbas, V. 2009, MNRAS 400, 791
Przybilla, N., Firnstein, M., Nieva, M.F., Meynet, G., & Maeder, A. 2010, A&A 517, 38
Simon, K.P., & Sturm, E. 1994, A&A 281, 286
Simon, K.P., Sturm, E., & Fiedler, A. 1994, A&A 292, 507
Southworth, J., & Clausen J.V. 2007, A&A 461, 1077
Southworth, J., Maxted, P.F.L., & Smalley, B. 2004a, MNRAS, 351, 1277
Southworth, J., Zucker, S., Maxted, P.F.L., & Smalley, B. 2004b, MNRAS 355, 986
Sturm, E., & Simon, K.P. 1994, A&A 282, 93
Torres, G., Andersen, J., & Giménez, A. 2010, ARA&A 18, 67

X-ray Modeling of η Carinae & WR140 from SPH Simulations

Christopher M. P. Russell[1], Michael F. Corcoran[2], Atsuo T. Okazaki[3], Thomas I. Madura[1], and Stanley P. Owocki[1]

[1] University of Delaware, Newark, DE, USA
[2] NASA GSFC, Greenbelt, MD, USA
[3] Hokkai-Gakuen University, Sapporo, Japan

Abstract: The colliding wind binary (CWB) systems η Carinae and WR140 provide unique laboratories for X-ray astrophysics. Their wind-wind collisions produce hard X-rays that have been monitored extensively by several X-ray telescopes, including RXTE. To interpret these RXTE X-ray light curves, we model the wind-wind collision using 3D smoothed particle hydrodynamics (SPH) simulations. Adiabatic simulations that account for the emission and absorption of X-rays from an assumed point source at the apex of the wind-collision shock cone by the distorted winds can closely match the observed 2-10keV RXTE light curves of both η Car and WR140. This point-source model can also explain the early recovery of η Car's X-ray light curve from the 2009.0 minimum by a factor of 2-4 reduction in the mass loss rate of η Car. Our more recent models relax the point-source approximation and account for the spatially extended emission along the wind-wind interaction shock front. For WR140, the computed X-ray light curve again matches the RXTE observations quite well. But for η Car, a hot, post-periastron bubble leads to an emission level that does not match the extended X-ray minimum observed by RXTE. Initial results from incorporating radiative cooling and radiatively-driven wind acceleration via a new anti-gravity approach into the SPH code are also discussed.

1 Point-Source Emission Model

η Carinae and WR140 are long period, highly eccentric colliding wind binaries (CWBs) that provide unique laboratories for X-ray astrophysics. Their wind-wind collisions produce hard X-rays that are strongly phase dependent; the wide range in stellar separation from the high eccentricity affects the X-ray emission, and the severe distortion in the wind geometry from significantly high orbital speeds around periastron affects the X-ray absoprtion. Our initial attempts to model the 2-10 keV RXTE light curves of both η Car and WR140 have applied a simple model of point-source emission plus line-of-sight wind absorption to 3D, adiabatic, smoothed particle hydrodynamics (SPH) simulations of the binary wind-wind interaction (see Okazaki et al. 2008 for details). To match the recent shorter minimum of η Car (Corcoran et al. 2010), the primary mass loss rate is reduced by a factor of 2.5 at phase 2.2. Many of the light curve's features are reproduced, including the shorter recent minimum. The WR140 light curve matches remarkably well (see Fig. 1 for the light curves and Table 1 for the parameters of the SPH simulations).

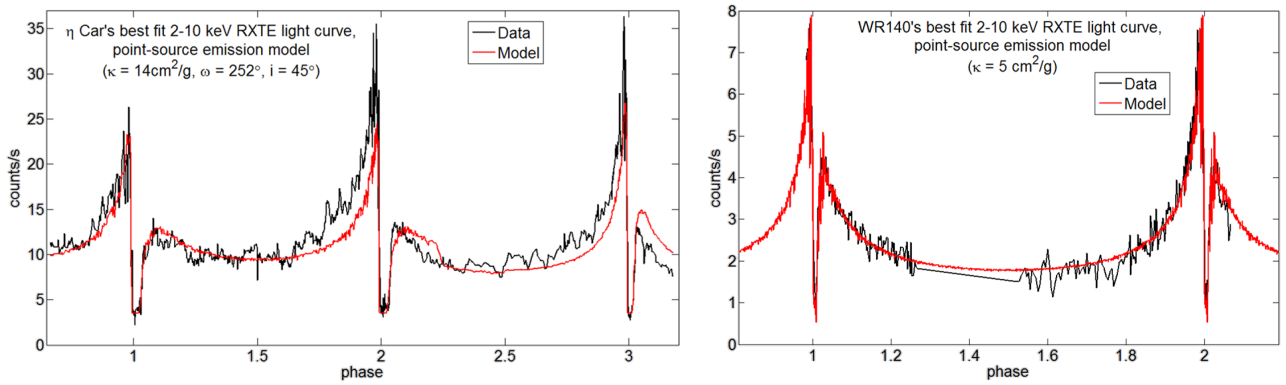

Figure 1: Best-fit RXTE light curves using the point-source emission model for η Car (left) and WR140 (right). The model light curves are normalized to match the average maximum just before the first periastron passage (phase $\sim$0.98) and the following apastron (phase 1.5). The free parameters of the model - opacity κ, argument of periastron ω, and inclination i - are shown for the relevant models.

Table 1: Parameters used in the adiabatic SPH simulations of η Car and WR140.

Parameter	η Car	WR140	References
Primary Mass ($M_\odot$)	90^a	50^b	a: Hillier et al. 2001
Secondary Mass ($M_\odot$)	30^c	19^b	b: Marchenko et al. 2003
Primary Radius ($R_\odot$)	$90^\dagger$	12^d	c: Verner, Bruhweiler & Gull 2005
Secondary Radius ($R_\odot$)	$30^\dagger$	13^e	d: Williams et al. 1990
Primary Mass Loss Rate ($M_\odot$ yr^{-1})	2.5×10^{-4} ^{f}	1.2×10^{-6} ^{g}	e: Pollock et al. 2005
Secondary Mass Loss Rate ($M_\odot$ yr^{-1})	1.0×10^{-5} ^{f}	3.8×10^{-5} ^{g}	f: Pittard and Corcoran 2002
Primary Wind Velocity (km s^{-1})	500^a	3200^g	g: Zhekov and Skinner 2000 (Model A)
Secondary Wind Velocity (km s^{-1})	3000^f	2860^g	h: Corcoran 2005
Orbital Period (d)	2024^h	2899^b	i: Corcoran et al. 2001
Semi-major Axis (au)	15.4^i	16.3^b	j: Dougherty et al. 2005
Orbital Eccentricity	0.9^i	0.88^b	
Inclination (deg)	??	122^j	†: assumed M($M_\odot$)/R($R_\odot$) =1
Argument of Periastron (deg)	??	46.7^b	

2 Extended Emission Model

Our more recent efforts to model the RXTE light curves of η Car and WR140 relax the point-source approximation (e.g. Parkin et al. 2009). The emission now originates from spatially extended post-shock gas in the wind-wind collision region according to $\rho^2\Lambda(E,T)$, where ρ is the density and $\Lambda(E,T)$ is the emissivity as a function of energy E and temperature T obtained from the MEKAL code (Mewe, Kaastra & Liedahl 1995). The extended wind absorption is now also energy dependent. We then use the SPH visualization program SPLASH (Price 2007) to calculate the ray-tracing through the system, which generates images in various X-ray bands that combine to make a 2-10 keV X-ray light curve. Once again, the WR140 light curve matches well (assuming the opacity is 10$\times$ the opacity of an O star wind at solar abundances, an assumption that will be relaxed in future work). The same is not true for η Car, however, where a hot, post-periastron bubble blown into the slow, dense primary wind by the much faster companion wind prevents the reproduction of the extended X-ray minimum (see Fig. 2).

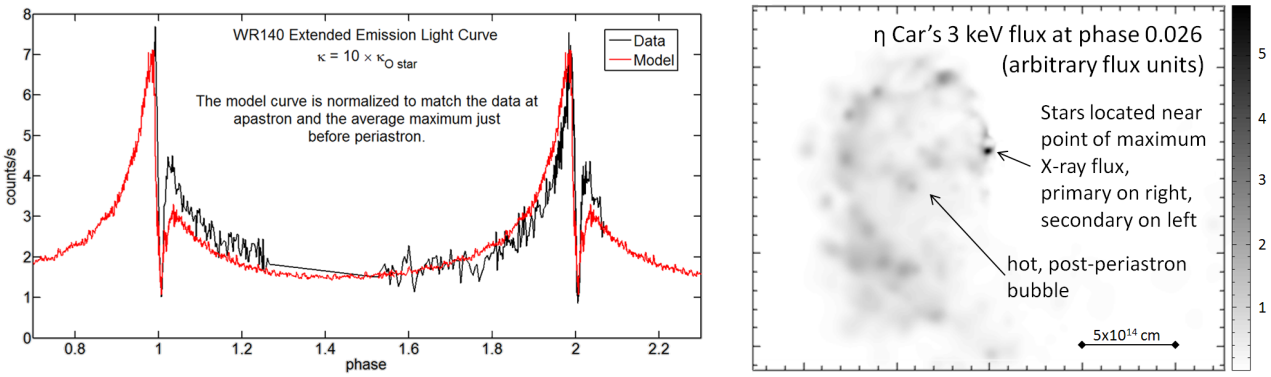

Figure 2: WR140 RXTE light curve using the extended emission model (left) and the post-periastron bubble of η Car (right).

Radiative cooling, via the Exact Integration Scheme (Townsend 2009), and the radiative driving of the stellar winds, via an anti-gravity approximation (an assumed outward acceleration that competes with gravity instead of the full Castor-Abbott-Klein calculation), have been implemented. The acceleration of the secondary wind towards the primary star drastically decreases around periastron due to radiative inhibition, where the radiation from one star provides enough force on it's companion's wind to inhibit it's acceleration (Stevens & Pollock 1994). This leads to the secondary's wind colliding with the primary's wind at a much lower speed directly between the stars, so the high temperature shock cone of η Car collapses, as was proposed by Parkin et al. (2009). However, there is still a high temperature shock on the backside of the secondary, the side opposite the primary star. The high orbital speed at periastron essentially causes the secondary to become buried in the primary's wind, so the secondary wind on the backside will collide with primary wind material. Since the acceleration of the backside's secondary wind is not affected by radiative inhibition, this portion of the wind still collides at a high speed (although the collision is co-moving instead of head-on) to create a high temperature, post-periastron bubble. The hard X-rays produced in this post-periastron bubble prevent the reproduction of the minimum of the RXTE light curve with the extended emission model. Outside the minimum, the model matches fairly well (see Fig. 3).

3 Conclusions & Future Work

The results of using 3D SPH simulations to model the wind-wind interaction of the CWBs η Carinae and WR140 have been presented, as well as our attempts to model these systems' RXTE light curves. Although the point-source emission model produces remarkably good results for both systems when applied to the adiabatic SPH simulations, this model is clearly an approximation that needs to be relaxed. Upon doing this by implementing an extended emission model, the resultant X-ray light curve for WR140 matches pretty well, while η Car's light curve does not match well during the X-ray minimum. A hot, post-periastron bubble forms in η Car from the fast companion wind blowing into the slow primary wind just after periastron, and this large emitting region creates a significant digress from the point-source result. On the other hand, the similar wind speeds in WR140 prevent a post-periastron bubble from forming, so the emission is approximately point-like throughout the orbit, and hence in good agreement with the point-source emission model results.

To improve the match of the extended emission model during η Car's RXTE X-ray minimum, radiative cooling and radiative driving of the winds via an anti-gravity approach were added to the SPH code (previous SPH simulations were adiabatic and had the winds leave their star at terminal

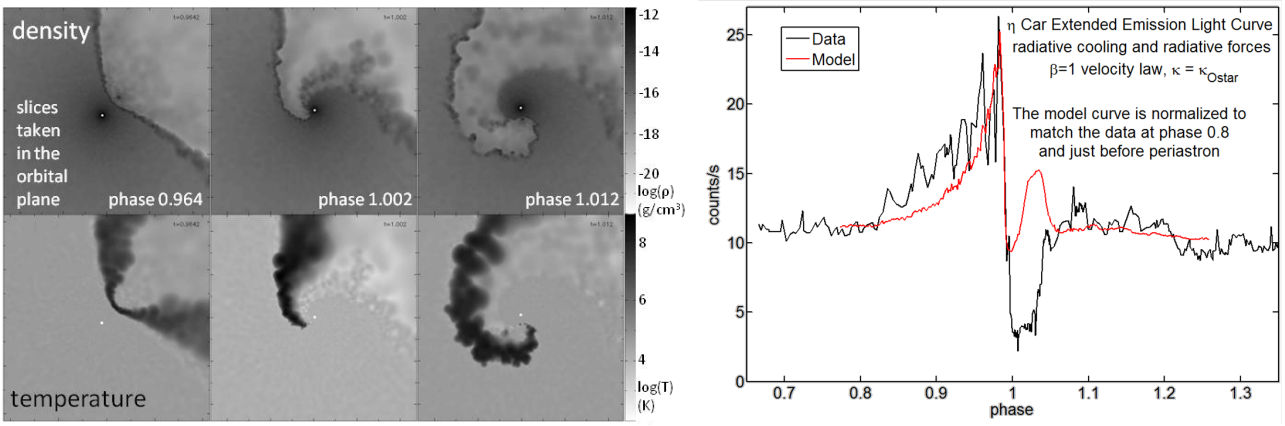

Figure 3: Density and temperature snapshots of an SPH simulation of η Car that includes radiative forces and radiative cooling (left) and the resulting RXTE model light curve using the extended emission model (right). In the SPH snapshots, η Car is the white dot, while the companion is shown by the black dot in the left density panel and then orbits counterclockwise. The snapshots show that hot material exists between the stars before periastron (left panels), vanishes at periastron (center panels) from radiative forces and radiative cooling, and begins to reappear after periastron (right panels). The right panels also shows the hot, post-periastron bubble that forms below both stars, which prevents the matching of the RXTE light curve during the X-ray minimum.

speed). While this leads to the collapse of the high temperature shock between the stars at periastron due to radiative inhibition, it does not affect the hot gas in the remainder of the post-periastron bubble. Therefore, there is still excess X-ray emission at periastron compared to the RXTE observations.

At the time of this conference, the results from the SPH simulations with radiative cooling and radiative driving are relatively new, so our immediate future work will be to further explore and understand these results. Of particular interest is the post-periastron bubble, which appears to be preventing the matching of the RXTE light curve during the X-ray minimum. Furthering the intrigue about this bubble are the results of Parkin et al. (2011) where a 3D grid-based hydrodynamics code was used to model η Car, and although the density and temperature structures compare very well from the grid-based code to the SPH code, and they too have excess emission during the X-ray minimum, the authors do not claim to see a post-periastron bubble. Other future work will include modeling WR140 with the radiative cooling and radiative driving improvements to the SPH code, modeling other CWBs such as HD5980, and improving the resolution of the extended emission model to begin modeling the X-ray spectra of CWBs.

Acknowledgements

CMPR and TIM acknowledge support from NASA GSRP Fellowships.

References

Corcoran M.F., 2005, AJ, 129, 2018
Corcoran M.F., Ishibashi K., Swank J.H., Petre R., 2001, ApJ, 547, 1034
Corcoran M.F., Hamaguchi K., Pittard J.M., Russell C.M.P., Owocki S.P., Parkin E.R., Okazaki A.T., 2010, ApJ, 725, 1528
Dougherty S.M., Beasley A.J., Claussen M.J., Zauderer B.A., Bolingbroke N.J., 2005, ApJ, 623, 447

Hillier D.J., Davidson K., Ishibashi K., Gull T., 2001, ApJ, 553, 837
Marchenko S.V., Moffat A.J., Ballereau D., et al., 2003, ApJ, 596, 1295
Mewe R., Kaastra J.S., Liedahl D.A., 1995, Legacy, 6, 16
Okazaki A.T., Owocki S.P., Russell C.M.P., Corcoran M.F., 2008, MNRAS, 288, L39
Parkin E.R., Pittard J.M., Corcoran M.F., Hamaguchi K., Stevens I.R., 2009, MNRAS, 394, 1758
Parkin E.R., Pittard J. M., Corcoran M. F., Hamaguchi K., Stevens I.R., Gosset E., Rauw G., & De Becker M., 2011, in Proceedings of the 39th Liège Astrophysical Colloquium, eds. G. Rauw, M. De Becker, Y. Nazé, J.-M. Vreux & P. Williams, BSRSL, 80, 610
Pittard J.M., Corcoran M.F., 2002, A&A, 383, 636
Pollock A.M.T., Corcoran M.F., Stevens I.R., Williams P.M., 2005, ApJ, 629, 482
Price D.J., 2007, PASA, 24, 159
Stevens I.R., Pollock A.M.T., 1994, MNRAS, 269, 226
Townsend R.H.D., 2009, ApJS, 181, 391
Verner E., Bruhweiler F., Gull T., 2005, ApJ, 624, 973
Williams P.M., van der Hucht K.A., Pollock A.M.T., Florkowski D.R., van der Woerd H., Wamsteker W.M., 1990, MNRAS, 243, 662
Zhekov S.A., Skinner S.L., 2000, ApJ, 538, 808

The variable X-ray spectrum of the Wolf-Rayet binary WR140 with Suzaku

Yasuharu Sugawara[1], Yoshitomo Maeda[2], Yohko Tsuboi[1], Kenji Hamaguchi[3,4], Michael Corcoran[3,5], Andy Pollock[6], Anthony Moffat[7], Peredur Williams[8], Sean Dougherty[9] and Julian Pittard[10]

[1] Department of Physics, Chuo University, Japan
[2] Department of High Energy Astrophysics, ISAS/JAXA
[3] CRESST and X-ray Astrophysics Laboratory NASA/GSFC
[4] Department of Physics, University of Maryland
[5] Universities Space Research Association
[6] European Space Agency, XMM-Newton Science Operations Centre
[7] D*é*partement de Physique, Universit*é* de Montr*é*al
[8] Institute for Astronomy, Royal Observatory Edinburgh
[9] National Research Council of Canada
[10] School of Physics and Astronomy, The University of Leeds

Abstract: We report the preliminary results of the Suzaku observations of the W-R binary WR 140 (WC7+O5I). We executed the observations at four different epochs around periastron passage in Jan. 2009 to understand the W-R stellar wind as well as the wind-wind collision shocks. The total exposure was 210 ks. We detected hard X-ray excess in the HXD band ($>$ 10 keV) for the first time from a W-R binary. Another notable discovery was a soft component which is less absorbed even by the dense wind. The spectra can be fitted by three different components; one is for the cool component with kT=0.1–0.6 keV, one for a dominant high-temperature component with kT $\sim$3 keV, and one for the hardest power-law component with the photon index of $\sim$2. As periastron approached, the column density of the high-temperature component increased, which can be explained as self-absorption by the W-R wind. The emission measure of the dominant, high-temperature component is not inversely proportional to the distance between the two stars.

1 Introduction

The Wolf-Rayet binary WR140 (WC7+O5I) has an extremely eccentric (e =0.88) orbit with long orbital period (P=7.94 yrs; Marchenko et al. 2003). The Suzaku AO-3 cycle covered the periastron passage, when physical parameters change the most dramatically. We executed X-ray monitoring observations around periastron passage to measure the change of the conditions in the hot post-shock gas.

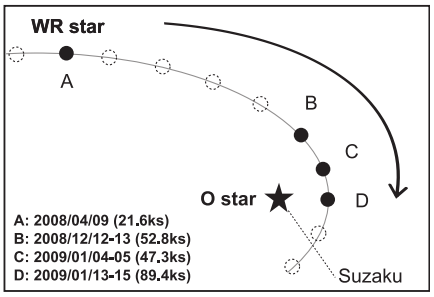

Figure 1: The geometry at the epochs of the four observations.

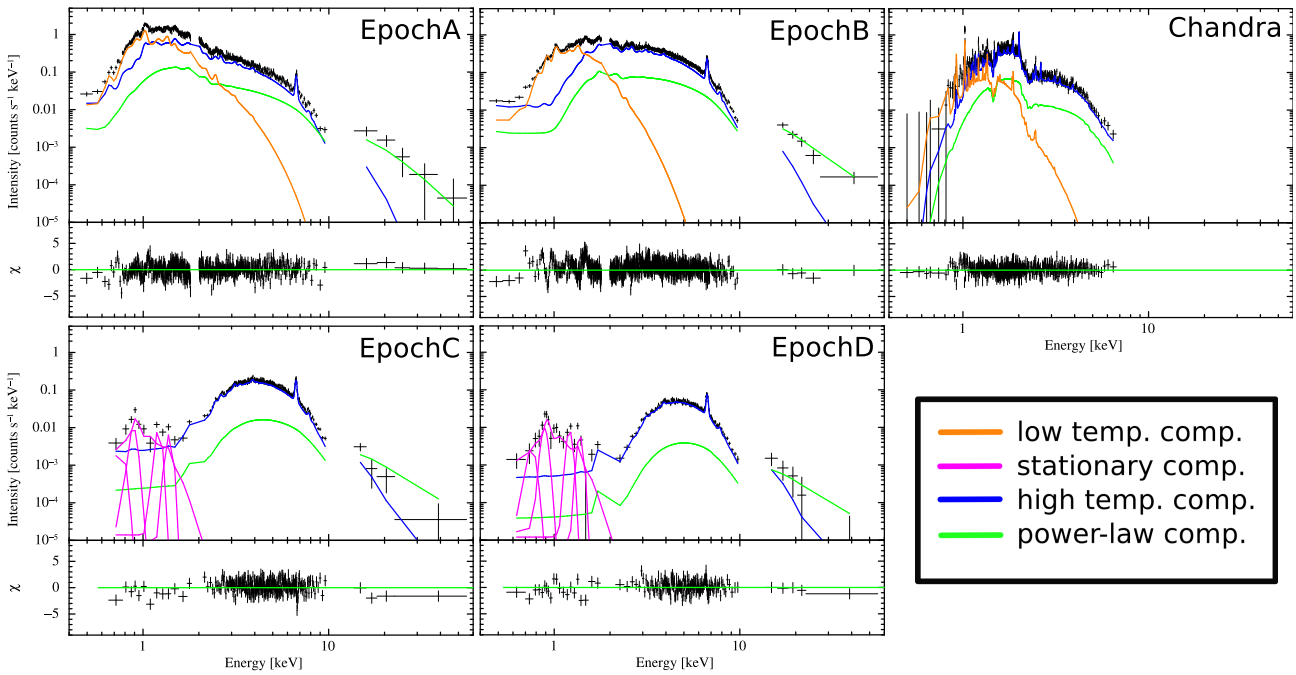

Figure 2: The XIS and HXD-PIN spectra of WR140 at each epoch. Backgrounds are subtracted. The model components are separately indicated in the upper panels. Lower panels show the residuals of the data from the best-fit model(Table 1). We fitted simultaneously the spectra of the epoch A and B, together with those of Chandra.

2 Observations & Analysis

We observed WR140 with Suzaku at four different epochs around periastron passage in Jan. 2009. The total exposure time was 210 ks. Figure 1 shows the observational geometries and the X-ray spectra at the four epochs, respectively. We adopted the orbital solution in Marchenko et al. (2003). The spectra below $E = 10$ keV were obtained with XIS, and those above 10 keV were with HXD-PIN. The flux and spectral shape of the X-ray spectra varied with the epochs. In spite of the variation, lines from highly ionized ions of oxygen, neon, magnesium, silicon, sulphur, argon, calcium, iron and nickel are detected. They are attributed to the emission from the optically thin thermal plasma as seen in the previous satellite observations.

Figure 2 shows that soft X-ray absorption varied with phase and is lowest at epoch A (phase=2.904) and largest at epoch D (phase=3.000). It is naturally explained that the main component of the X-ray emission is deeply embedded in the WR 140 binary system and is self-absorbed by the WR-wind (cf., Zhekov & Skinner 2000). We modeled the WR-wind absorption with a photoelectric absorption code with variable abundances, varabs. XSPEC package version 12.5 is used in the analysis of the spectra. We also added an absorption model, TBabs (Wilms, Allen & McCray 2000) to take into account the

interstellar absorption. The solar abundances by Wilms et al. (2000) were adopted. The interstellar absorption column density was determined from the spectrum at epoch A.

In addition to the Suzaku data, we used archived Chandra data. WR 140 was observed with the Chandra HETGS on 2000 December 29 beginning at 10:13:28 (ObsID 2337), with a total integration time 45.5 ks. Pollock et al. (2005) reported the results of this spectral analysis. The HETG spectra are very sensitive to the line emission and works to constrain the abundance of the plasma. Since this Chandra observation (phase=1.987) was made at the similar epoch of the Suzaku epoch B (phase=2.989), the spectra of the Suzaku epoch A, B and the 2000 Chandra were simultaneously fit to the same models with the some parameters allowed to vary (Table 1). But, this method may require validation to consider the variable nature of X-ray emission.

Table 1: Results of spectral fitting with the three components of models. Errors and upper limits are at 90% confidence level.

Epoch	A	B	Chandra	C	D
Orbital phase	2.904	2.989	1.987	2.997	3.000
interstellar absorption (TBabs)					
$N_{\rm H}$ (10^{21} cm^{-2})		$8.59^{+0.02}_{-0.01}$		8.59(fixed)	
low-temperature component (varabs*vpshock)					
$N_{\rm He}^{\rm LT}$ (10^{19} cm^{-2})	–	2.5±0.1	2.2±0.4	–	–
$k_{\rm B}T_{\rm LT}$ (keV)	$0.656^{+0.007}_{-0.010}$	$0.3511^{+0.0002}_{-0.0006}$		–	–
τ_u($\times 10^{12}$ s cm^{-3})	$4.1^{+0.4}_{-0.3}$	$3.9^{+0.6}_{-0.3}$		–	–
norm [1]($\times 10^{-3}$)	$7.4^{+0.1}_{-0.4}$	$14.5^{+0.2}_{-0.7}$	10^{+2}_{-1}	–	–
$L_{\rm X}$ [2]($\times$ 10^{34} erg s^{-1})	2.32	6.11	4.33	–	–
high-temperature component (varabs*vpshock)					
$N_{\rm He}^{\rm HT}$ (10^{20} cm^{-2})	≤ 0.006	$1.74^{+0.03}_{-0.01}$	5.3±0.4	$12.6^{+0.2}_{-0.1}$	$23.1^{+0.6}_{-0.2}$
$k_{\rm B}T_{\rm HT}$ (keV)	$2.73^{+0.03}_{-0.06}$	$3.03^{+0.02}_{-0.03}$		$2.60^{+0.08}_{-0.06}$	$2.73^{+0.07}_{-0.13}$
τ_u($\times$ 10^{12} s cm^{-3})	4.1^{4}	3.9^{4}		$1.8^{+1.0}_{-0.5}$	$1.7^{+1.4}_{-0.8}$
norm [1]($\times 10^{-2}$)	$1.09^{+0.04}_{-0.01}$	$2.97^{+0.03}_{-0.05}$	$3.54^{+0.05}_{-0.06}$	$3.57^{+0.11}_{-0.07}$	$1.89^{+0.10}_{-0.09}$
$L_{\rm X}$ [2]($\times$ 10^{34} erg s^{-1})	2.01	5.57	6.68	8.23	4.44
power-law component					
Γ		$1.93^{+0.02}_{-0.03}$		1.93(fixed)	
norm [5] ($\times$ 10^{-3})	$1.98^{+0.06}_{-0.02}$	$4.69^{+0.01}_{-0.04}$		2.3±0.4	$1.0^{+0.3}_{-0.5}$
$L_{\rm X}$ [2]($\times$ 10^{33} erg s^{-1})	0.71	1.67		0.79	0.34
stationary component (varabs*(apec+5redge))					
$N_{\rm He}^{\rm S}$ (10^{19} cm^{-2})	–	–	–	1.4(fixed)	
$k_{\rm B}T_{\rm S}$ (keV)	–	–	–	0.13(fixed)	
norm [1]($\times 10^{-3}$)	–	–	–	14(fixed)	
$k_{\rm B}T_{\rm RRC}$ (eV)	–	–	–	12(fixed)	
norm$_{\rm C\,VI}$ [3]($\times 10^{-2}$)	–	–	–	1.6(fixed)	
norm$_{\rm O\,VII}$ [3]($\times 10^{-4}$)	–	–	–	3.1(fixed)	
norm$_{\rm O\,VIII}$ [3]($\times 10^{-4}$)	–	–	–	1.5(fixed)	
norm$_{\rm Ne\,IX}$ [3]($\times 10^{-5}$)	–	–	–	1.5(fixed)	
norm$_{\rm Ne\,X}$ [3]($\times 10^{-6}$)	–	–	–	7.4(fixed)	
$L_{\rm X}$ [2]($\times$ 10^{35} erg s^{-1})	–	–	–	1.1	
χ^2/dof		4424.50/3230		619.95/499	338.48/292

[1] Normalization constant defined as EM $\times$ $10^{-14}(4\pi {\rm D}^2)^{-1}$, where EM is the emission measure in cm^{-3} and D is the distance in cm.

[2] The absorption-corrected luminosity (0.5–50.0 keV) was calculated assuming a distance of 1.85 kpc.

[3] Normalization constant of the redge model defined as total photons cm^{-2} s^{-1} in the line.

[4] Ionization timescale of high temperature component is linked to that of low temperature component.

[5] Normalization constant of the power-law model defined as photons keV^{-1} cm^{-2} s^{-1} at 1 keV.

2.1 Spectral fit at epoch A, B and the 2000 Chandra observation

The single-temperature plane-parallel shock model (vpshock) shows a good fit in the energy band higher than 4 keV. However, the model can not reproduce the line and edge structures which appeared in the soft energy band below $\sim$3 keV. So we adopted a two-temperature plane-parallel shock model suffering two different absorption column densities. We found that the fitting is significantly improved in the XIS spectra.

At epochs A and B, there further exist residuals in the HXD/PIN data above 10 keV. We then introduce the power-law model as an additional component. The power-law component is only significant in the epoch A spectra. The best-fit power-law index at the epochs A and B is $\Gamma \sim 1.9$. We assumed the same value for the other epochs of C (phase=2.997) and D. The emission may originate from inverse Compton interactions between relativistic electron and stellar UV photons or from thermal bremsstrahlung of higher temperature shock plasma.

No emission lines from helium and carbon ions were identified in the data. For the vpshock models, we assumed the abundance ratio C/He $= 0.4$ by number, which was taken from Hillier & Miller (1999). Other abundance value except helium, carbon, neon, magnesium and iron were fixed the best-fit values of Pollock et al. (2005). The abundance for the absorption model of $N_{\rm He}$ is linked to that of the vpshock model.

2.2 Spectral fit at epoch C and D

The single-temperature vpshock model shows a good fit in the energy band higher than 2 keV. However, the model can not reproduce the soft excess seen below 2 keV. We then add another soft component of an absorbed single-temperature model. Since the statistics are limited, we assume a plasma in the collisional ionized equilibrium (APEC). Since no significant change in X-ray flux below 1.6 keV were detected, we further assumed the same parameters for this stationary component at both epochs C and D.

The soft component can be fitted with a single-temperature model of $k_{\rm B}T_{\rm S} \sim 0.15$ keV with an absorption column of $N_{\rm He}^{\rm S} \sim 1\times 10^{20}$ cm^{-2}, but some line-like residuals still remained (χ^2/dof of 198/56). We found that the residuals are consistent with those of the recombination edges. So, we introduce the five RRC (redge) models at the energy of C VI(0.499 keV), O VII(0.739 keV), O VIII(0.871 keV), Ne IX(1.196 keV), and Ne X(1.362 keV). The fit was improved to an acceptable χ^2/dof of 68/50. After checking the significance of an F-test for an additional recombination edge model, the RRC structure of Ne IX is the most significant. At the epochs A and B, emissions of a soft component are virtually undetectable due to dominant emissions of other high-temperature component. Therefore, we didn't add a soft component to these best-fit models at epoch A, B and the 2000 Chandra observation.

3 The variation of emission measure

From epoch A to C, the emission measure increased along with the inversely proportional correlation with the separation, d, of two stars. This is consistent with the prediction in the simple colliding wind theory (Usov 1992), which is usually used. On the other hand, from epoch C to D, toward periastron, the emission measure decreased against the prediction. This would mean that we need to introduce one more parameter R, wind momentum flux ratio, $R = \left((\dot{M}v)_{\rm WR}/(\dot{M}v)_{\rm O}\right)^{1/2}$. According to Stevens, Blondin & Pollock (1992), EM can be written as ${\rm EM} \propto d^{-1}\ (1+R)/R^4$.

At periastron, the momentum flux of the O-type star becomes smaller, since the O-star wind cannot reach terminal velocity because of the small distance from the O-star to the shock region, while that

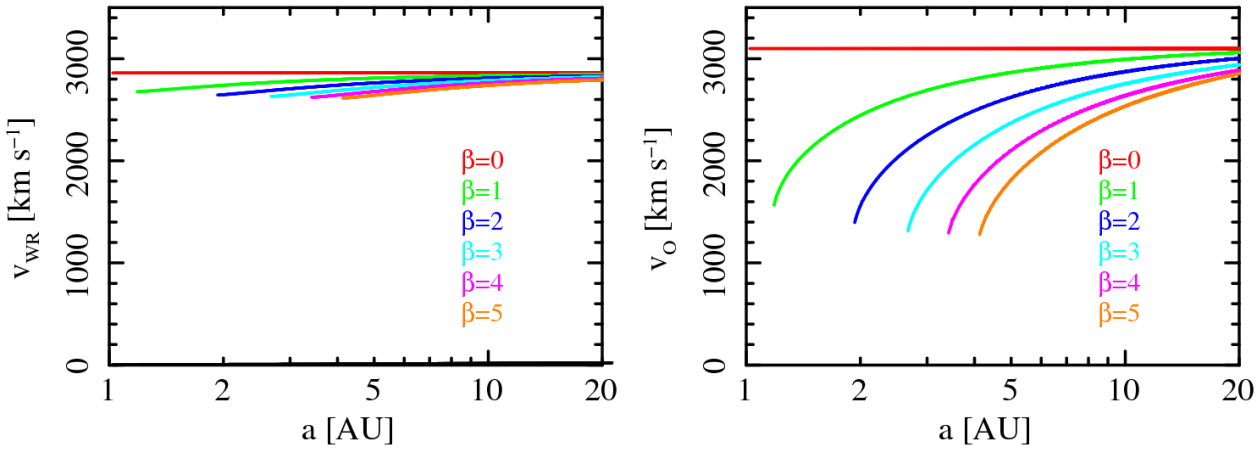

Figure 3: The wind velocity vs. distance (left;W-R star, right;O star).

of the W-R star changes less. In Figure 4, we show the pre-shock stellar wind velocities of the W-R and O stars at a given binary separation. We adopted a simple beta law for the wind acceleration: $v(r) = v_\infty(1 - R_*/r)^\beta$. Here, r, v_∞, and R_* are the distance from stellar surface to shock region, terminal velocity, and stellar radius, respectively. We used the value of $R_*^{\rm WR} = 13\ R_\odot$ (Williams et al. 1990), $R_*^{\rm O} = 26\ R_\odot$ (cf., Williams et al. 2009), $\dot{M}({\rm WR}) = 4.3\times10^{-5}{\rm M}_\odot{\rm yr}^{-1}$ and $\dot{M}({\rm O}) = 8.7\times10^{-6}{\rm M}_\odot{\rm yr}^{-1}$ (Dougherty et al. 2005). The W-R wind reaches near the terminal velocity in any assumption for β while the O-star is far below its terminal value for a large value of β.

In Figure 4, we plot the normalized X-ray emission measure calculated using the equation (EM $\propto d^{-1}\ (1 + R)/R^4$). The emission measure is normalized at the separation of epoch A (15 AU). The wind momentum flux ratio rapidly becomes large near the periastron for the large β. The calculation is truncated near the periastron since the stagnation point reaches the surface of the O star. The sudden drop of the emission measure near epoch D is visible for the case of a slow wind acceleration of $\beta \approx 2$–3.

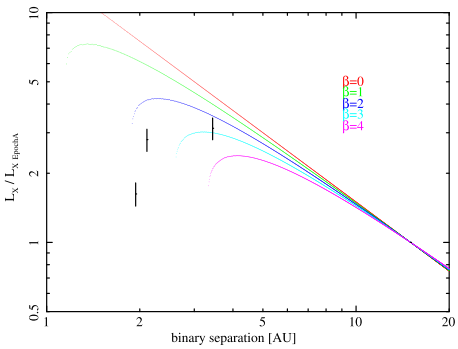

Figure 4: The binary separation vs. normalized X-ray luminosity. Black shows emission measure of a dominant high-temperature component with kT ∼3 keV.

References

Dougherty, S.M., Beasley, A.J., Claussen, M.J., Zauderer, B.A., & Bolingbroke, N.J. 2005, ApJ 623, 447

Hillier, D.J., & Miller, D.L. 1999, ApJ 519, 354

Marchenko, S.V., Moffat, A.F.J., Ballereau, D., et al. 2003, ApJ 596, 1295

Pollock, A.M.T., Corcoran, M.F., Stevens, I.R., & Williams, P.M. 2005, ApJ 629, 482

Stevens, I.R., Blondin, J.M. & Pollock, A.M.T. 1992, ApJ 386, 265

Usov, V.V. 1992, ApJ 389, 635

Wilms, J., Allen, A., & McCray, R. 2000, ApJ 542, 914

Williams, P.M., van der Hucht, K.A., Pollock, A.M.T., Florkowski, D.R., van der Woerd, H., & Wamsteker, W.M. 1990, MNRAS 243, 662

Williams, P.M., Marchenko, S.V., Marston, A.P., et al. 2009, MNRAS 395, 1749

Zhekov, S.A., & Skinner, S.L. 2000, ApJ 538, 808

The most massive eclipsing binary with apsidal motion

Francesc Vilardell[1,2], Ignasi Ribas[3], Carme Jordi[2], Yevgeny Tsodikovich[4], Tsevi Mazeh[4], Edward F. Guinan[5] and Edward L. Fitzpatrick[5]

[1] Departament de Física, Enginyeria de Sistemes i Teoria del Senyal, Universitat d'Alacant, Alacant, Spain

[2] Departament d'Astronomia i Meteorologia (ICC-IEEC), Universitat de Barcelona, Barcelona, Spain

[3] Institut de Ciències de l'Espai (CSIC-IEEC), Campus UAB, Bellaterra, Spain

[4] School of Physics and Astronomy, Raymond and Beverly Sackler Faculty of Exact Sciences, Tel Aviv University, Tel Aviv, Israel

[5] Department of Astronomy and Astrophysics, Villanova University, Villanova, USA

Abstract: The fundamental properties of a detached and eccentric eclipsing binary (EB) with apsidal motion are presented (M31V J00442326+4127082). The system is composed by two very massive stars (with masses over 40 $M_{\odot}$). An additional third light is observed that could be the responsible of the discrepancy between the observed apsidal motion (of 2.4 ± 1.0 deg yr^{-1}) and the value predicted by stellar interior models (5.4 ± 0.8 deg yr^{-1}). However, the observed apsidal motion could be more easily explained if the stellar cores were larger than currently predicted. Therefore, additional observations of the EB presented here could be used to test the internal structure of very massive stars.

1 Introduction

Eclipsing binaries (EBs) are powerful tools to determine the fundamental properties of massive stars (masses, radii, temperatures, etc). Specially valuable are those systems displaying apsidal motion, since they can be used to test general relativity and the internal distribution of matter. During the course of a project aimed at finding suitable EBs for a distance determination to M31 (Ribas et al. 2005, Vilardell, Ribas & Jordi 2006, Vilardell et al. 2010), a very massive (with masses over 40 $M_{\odot}$), detached and eccentric EB showing evidence of apsidal motion (M31V J00442326+4127082) was discovered. The fundamental properties of M31V J00442326+4127082 are presented here.

2 Masses and radii

The combination of light and radial velocity curves in EBs provides the masses and the radii of the components. In our case, Johnson B and V time series photometry was obtained from Vilardell et al.

(2006) and from the DIRECT V band photometry (Macri 2004, and references therein). Radial velocities were derived by applying a three dimensional cross-correlation algorithm (TRIMOR, Mazeh et al. 2009) to a set of spectra obtained with GMOS at the Gemini North telescope. The analysis of light and radial velocity curves with the 2003 version of the Wilson & Devinney (1971) algorithm (Fig. 1) revealed a detached EB system composed by two very massive stars (49 ± 6 $M_\odot$ for the primary component and 46 ± 5 $M_\odot$ for the secondary) and an important tertiary light source (Table 1). The derived properties (see Vilardell 2009, for further details[1]) place M31V J00442326+4127082 among the few known EBs with very massive components (Bonanos 2009).

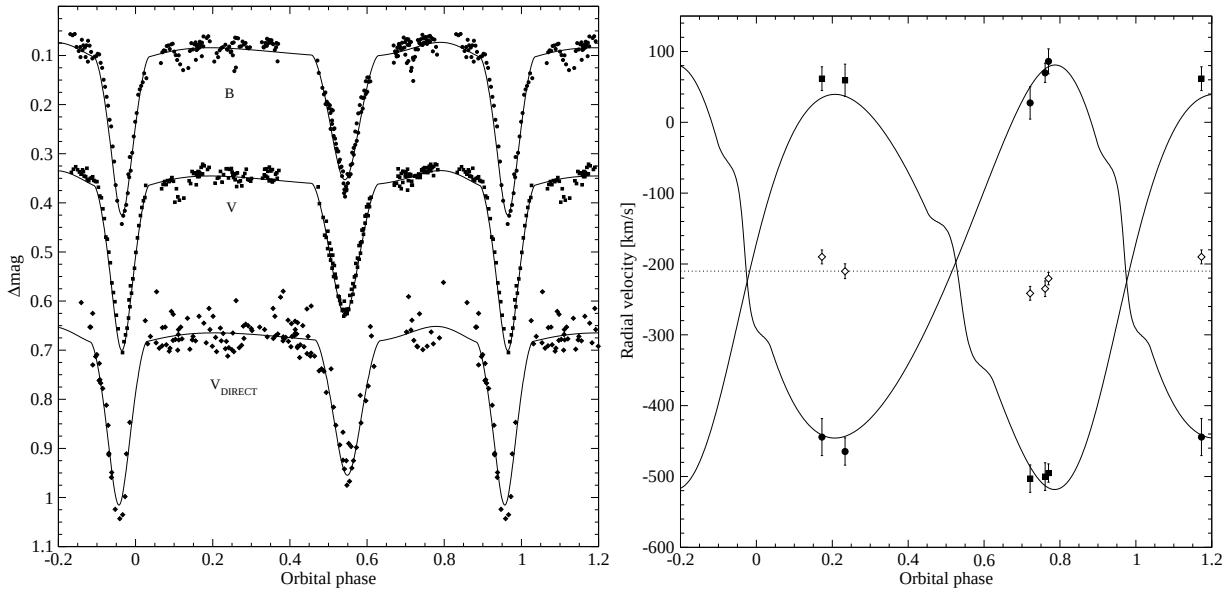

Figure 1: Observations for M31V J00442326+4127082 with the corresponding fits. Left: B, V, and DIRECT V light curves with arbitrary offsets for clarity. Right: Radial velocity curves

3 Radiative properties

The detached nature of M31V J00442326+4127082 allowed the comparison of the derived masses and radii with the Geneva stellar evolutionary models of Lejeune & Schaerer (2001). As a first step, the mass-radius diagram was used to infer suitable evolutionary tracks (Fig. 2, left). The resulting most likely models were used to determine the temperature and luminosity of both components (Fig. 2, right). The derived properties are fully compatible with a coeval system having an age of 2.2 ± 0.5 Myr (Table 2). In addition, by assuming that the tertiary light source is a single coeval component (either belonging to the same stellar association or forming a triple system), its physical properties could also be determined. The derived properties (with a mass of 36 ± 6 $M_\odot$ and a radius of 10.8 ± 1.7 $R_\odot$) reveal that the tertiary component could also be massive.

Once the intrinsic properties of the three components were derived, their combined absolute magnitudes in B and V, together with the distance to M 31 (Vilardell et al. 2010) and the observed photometry, could be used to derive a line-of-sight absorption and a color excess. The assumption of a tertiary coeval component is useful to illustrate that, even with a hot tertiary component, the total-to-selective extinction ratio is far from the mean value of $\mathcal{R}_V = 3.1$ usually adopted ($\mathcal{R}_V = 4.2 \pm 0.6$). GALEX photometry (Thilker et al. 2005) confirms that the extinction law is non-standard, but additional observations in the infrared are required to confirm the value of $\mathcal{R}_V$.

[1] Accessible online at: http://www.tdx.cat/TDX-0526109-091957

Table 1: Properties of M31V J00442326+4127082 derived from the analysis with the Wilson & Devinney code.

System properties				
B magnitude at maximum light[a]	19.284±0.017			mag
V magnitude at maximum light[a]	19.195±0.014			mag
Period	5.75268±0.00005			days
Time of minimum	2 452 546.586±0.008			HJD
Eccentricity	0.17±0.02			
Argument of periastron	45±7			deg
Apsidal motion	2.4±1.0			deg yr^{-1}
Inclination	81.3±1.9			deg
Systemic velocity	-210±11			km s^{-1}
Semi-major axis	62±2			$R_\odot$
Third light contribution in B	0.21±0.08			
Third light contribution in V	0.20±0.09			
Component properties	Primary		Secondary	
Mass	49±6	$M_\odot$	46±5	$M_\odot$
Radius	15.3±1.3	$R_\odot$	14.7±1.3	$R_\odot$

[a] Out of eclipse average: $\Delta\phi = [0.04 - 0.45, 0.63 - 0.88]$

4 Apsidal motion

The combination of the DIRECT V band photometry (Macri 2004, and references therein) with our obtained data provides a time baseline of ∼7 years (1996-2003) and allowed the detection of an apsidal motion of 2.4 ± 1.0 deg yr^{-1}. M31V J00442326+4127082 is, therefore, the most massive EB system with measured apsidal motion ever reported. The deformation of the components (dependent

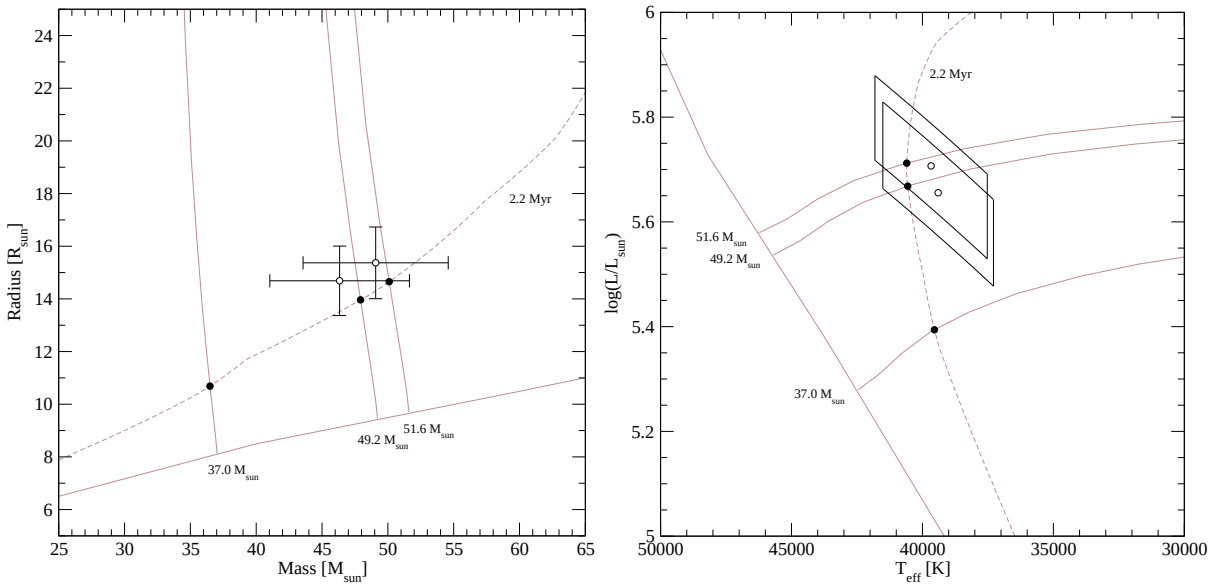

Figure 2: Best fitting stellar evolutionary tracks (solid lines) and isochrone (dashed line) to the observed properties of M31V J00442326+4127082. Left: Mass-radius diagram. Right: Hertzsprung-Russel diagram.

Table 2: Properties of M31V J00442326+4127082 derived from comparison with stellar evolutionary models and assuming that the three components are coeval.

System properties						
Age				2.2±0.5		Myr
Absolute V magnitude				-6.86±0.19		mag
Color excess in $B-V$				0.40±0.02		mag
Line-of-sight absorption in V^a				1.7±0.2		mag
Total-to-selective extinction ratio				4.2±0.6		mag
Component properties	Primary		Secondary		Tertiary	
Mass	50±5	$M_\odot$	48±5	$M_\odot$	36±6	$M_\odot$
Radius	14.8±1.4	$R_\odot$	14.1±1.4	$R_\odot$	10.8±1.7	$R_\odot$
Effective temperature	40 000±2 000	K	40 000±2 000	K	39 000±2 000	K
Intrinsic luminosity in $\log L/L_\odot$	5.71±0.08	mag	5.67±0.08	mag	5.37±0.20	

[a] Adopting a distance modulus of 24.36 ± 0.08 mag (Vilardell et al. 2010)

on the internal structure of the stars) seems to be the most likely explanation. However, the observed apsidal motion rate is discrepant (at the 1.5σ level, the predicted value is 5.4 ± 0.8 deg yr^{-1}) with current stellar interior models (Claret 2004). Although similar results have also been obtained for other B-type EBs (e.g., V380 Cyg), where stellar interior models for massive stars predict cores that are too small when compared with observations, the possible presence of a tertiary massive companion could also be affecting the observed apsidal motion. Therefore, additional observations of the EB presented here are required to determine the possible effect of the tertiary component on the observed apsidal motion and to test whether current stellar interior models correctly predict the internal structure of very massive stars.

Acknowledgements

This program was supported by grant AYA2006-15623-C02-01/02 of the Spanish Ministerio de Ciencia e Innovación (MICINN). F.V. acknowledges support from MICINN through a Consolider-GTC (CSD-2006-00070) fellowship.

References

Bonanos, A.Z. 2009, ApJ 691, 407
Claret, A. 2004, A&A 424, 219
Lejeune, T., & Schaerer, D. 2001, A&A 366, 538
Macri, L.M. 2004, in *Variable Stars in the Local Group*, eds. D.W. Kurtz & K.R. Pollard, ASP Conference Proceedings, 310, 33
Mazeh, T., Tsodikovich, Y., Segal, Y., Zucker, S., Eggenberger, A., Udry, S., & Mayor, M. 2009, MNRAS 399, 906
Ribas,I., Jordi, C., Vilardell, F., Fitzpatrick, E.L., Hilditch, R.W., & Guinan, E.F. 2005, ApJ 635, L37
Thilker, D.A., Hoopes, C.G., Bianchi, L., et al. 2005, ApJ 619, L67
Vilardell, F. 2009, PhD thesis, Departament d'Astronomia i Meteorologia, Universitat de Barcelona
Vilardell, F., Ribas, I., & Jordi C. 2006, A&A 459, 321
Vilardell, F., Ribas, I., Jordi, C., Fitzpatrick, E.L., & Guinan E.F. 2010, A&A 509, A70
Wilson R.E., & Devinney E.J. 1971, ApJ 166, 605

Modelling the synchrotron emission from O-star colliding wind binaries

Delia Volpi[1]

[1] Royal Observatory of Belgium, Ringlaan 3, 1180 Brussels, Belgium

Abstract: Many early-type stars are in binary systems. A number of them show radio emissivity with periodic variability. This variability is associated with non-thermal synchrotron radiation emitted by relativistic electrons. The strong shocks necessary to accelerate the electrons up to high energies are produced by the collision of the radiatively-driven stellar winds. A study of the non-thermal emission is necessary in order to investigate O-star colliding wind binaries. Here preliminary results of our modeling of the colliding winds in Cyg OB2 No. 9 are presented.

1 Introduction

Many OB stars show non-thermal radio emission together with the thermal free-free radiation in the same band. The non-thermal emissivity is thought to be due to synchrotron radiation emitted by relativistic electrons spiraling around the dipole magnetic field lines of the star. The electrons are accelerated up to high energies by strong shocks.

In recent years a number of early-type stars radiating non-thermal radio emission have been discovered to be binary systems. This discovery supports the hypothesis of colliding winds from the primary and the secondary as the origin of the strong shocks (see Eichler & Usov 1993, Dougherty et al. 2003, Pittard et al. 2006). The observed synchrotron emissivity is characterized by a periodic variability directly connected with the orbital phase of the binary system.

One of these binary systems is Cyg OB2 No. 9, which was detected as a non-thermal emitter in 1984 (see Abbott et al. 1984). By studying the observed VLA (Very Large Array) radio fluxes at 3.6, 6 and 20 cm from Cyg OB2 No. 9, Van Loo and collaborators found a variability with a period of 2.35 yr (Van Loo et al. 2008). This periodicity confirmed the presence of radio non-thermal emission suggesting also a binarity of this system. At the same time Nazé et al. (2008) discovered its binarity after a long-term spectroscopic monitoring. The observed 6 cm radio flux is shown in Fig. 1. The orbital parameters of Cyg OB2 No. 9 were derived for the first time by Nazé et al. (2010).

The study of the synchrotron emission at different orbital positions is relevant to constrain stellar, orbital and wind parameters, such as the mass loss rates from the stars and the clumping/porosity, and in general to investigate the nature of the stellar winds. As a matter of fact the mass loss rate determination in massive stars is presently one of the main problems. This problem has become relevant due to the clumping/porosity of the stellar winds which affects the estimation of the mass loss rate. To determine the emitted synchrotron radiation and its absorption by the stellar wind plasma permits to estimate the amount of porosity in the wind.

In order to better understand the physics of the non-thermal emission and to constrain the model parameters we developed a numerical code. Here the simulated model for Cyg OB2 No. 9 is presented. The theoretical results are compared with the corresponding observations.

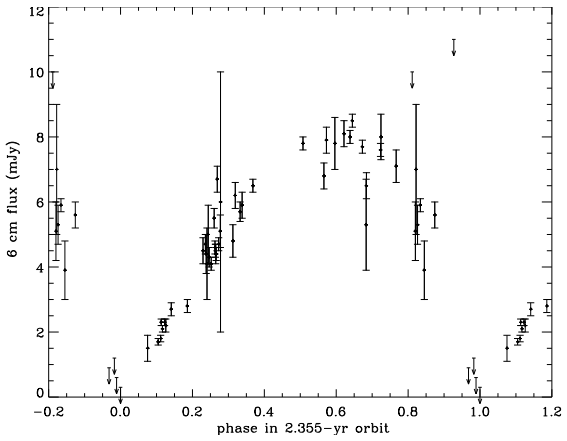

Figure 1: Cyg OB2 No. 9. Observed VLA 6 cm radio emission (from Van Loo et al. 2008).

2 Modeling

In this section the theoretical model used to obtain the simulated results is described. A first version of this model was developed by R.Blomme. The details of the model can be found in Blomme et al. (2010).

The two winds are considered to collide at the contact discontinuity. Its position is assumed to be coincident with the two shocks and it is calculated using the Anthokin et al. (2004) equations. The electrons accelerated at the shock are followed as they advect away and cool down along the post-shock streamlines. We stop following the electrons when their momentum falls below a minimum value (see Van Loo et al. 2004), or when they leave the simulation volume. Adiabatic and inverse Compton losses are both taken in account. The momenta follow a modified power-law distribution.

The synchrotron emissivity from the relativistic electrons is calculated along the post-shock streamlines in the orbital plane. The Razin effect is also included. The formula of the emissivity $j_\nu(r)$ is reported below as in Van Loo (2005):

$$j_\nu(r) = \frac{1}{4\,\pi}\int_{p_0}^{p_c} dp\, N(p,r)\int_0^\pi \frac{d\theta}{4\pi} 2\pi\sin\theta \frac{\sqrt{3}\,\mathrm{e}^3}{\mathrm{m_e\,c^2}} B\, f(\nu,p)\sin\theta\, F\left(\frac{\nu}{f^3(\nu,p)\,\nu_\mathrm{s}(p,r)\sin\theta}\right) \qquad (1)$$

where ν is the frequency, r is the radial position, p_0 is the minimum momentum, p_c is the maximum one, p is the particle momentum, $N(p,r)$ is the modified power-law distribution of the electrons, θ is the pitch angle, e and $\mathrm{m_e}$ are the electron charge and mass, c is the velocity of light, B is the magnetic field at a distance r, ν_s is the critical frequency, and $f(\nu,p)$ takes into account the Razin effect.

The synchrotron emission is calculated in the orbital plane. The third dimension is recovered by rotating the orbital plane along the line which connects the two stars. The free-free opacity and emission due to the ionized wind material are also included using the Wright & Barlow (1975) equations. The theoretical fluxes are obtained at different orbital phases using Adam's method (Adam 1990) that solves the radiative transfer equation in a very simple way.

The orbital parameters are provided by Nazé et al. (2010) observations, the stellar parameters by Martins et al. (2005) theoretical models and the wind parameters by Vink et al. (2001) theoretical

Table 1: Stellar, orbital and wind parameters for Cyg OB2 No. 9.

	primary star	secondary star
P (days)	860.2 ± 5.5	
e	0.744 ± 0.030	
i (deg)	48.59 ± 7.45	
ω (deg)	-164.4 ± 4.1	
d (pc)	1820 ± 200	
ν_0 (km/s)	0.1	
$M_\star$ ($M_{\rm sun}$)	50.72	44.10
a ($R_{\rm sun}$)	797.34 ± 203.95	932.40 ± 237.17
R ($R_{\rm sun}$)	19.45	19.95
L (erg s^{-1})	$2.85{\cdot}10^{39}$	$2.48{\cdot}10^{39}$
$T_{\rm eff}$ (K)	38612	36801
v_∞ (km/s)	2050	1850
$\dot{M}$ ($M_{\rm sun}/yr$)	5.79d-06	4.86d-06

Note. P and d are the orbital period and the distance from the Earth (Van Loo et al. 2008), e and ω are the eccentricity and the angle of the periastron (Nazé et a. 2010), $M_\star$, R, L, $T_{\rm eff}$ are the mass, the radius, the luminosity, and effective temperature for the star (Martins et al. 2005), i is the inclination angle (obtained from a comparison between the theoretical mass $M_\star$ calculated in Martins et al. 2005 and the projected observed one $M_\star \sin i^3$ from Nazé et al. 2010), a is the semi-major axis of the orbit, ν_0 is the velocity of the wind at the surface of the star (Blomme et al. 2010), v_∞ and $\dot{M}$ are the velocity of the wind at large distance from the star and the mass loss rate (Vink et al. 2001).

models. We choose spectral type O5I+O6I: the Martins' stellar parameters for this spectral type are consistent with the spectroscopic observations and the chosen spectral type is in agreement with the O5+O6-7 spectral types suggested by Nazé et al. (2008). Current spectroscopic information does not allow a reliable determination of the luminosity class.

The knowledge of the spectral type is necessary to select the values of parameters that cannot be obtained by the observations. These parameters are used as input to our model. The chosen values of the parameters are reported in Table 1.

3 Theoretical results: the emissivity and model light curve at 6 cm

The 6 cm emissivity images at periastron and apastron are shown in Fig. 2. The 6 cm emissivity at periastron is much more concentrated around the contact discontinuity than at apastron mainly because the Razin effect is more important in the periastron high-density region. The synchrotron radiation is however not negligible in both cases due to the extension of the emitting area. This extended region explains the synchrotron emission that was observed in OB stars systems during the last years.

In Fig. 3 the preliminary 6 cm light curve from our modeling is presented. The variability in the radio flux is clearly visible as observed with VLA. This variability linked to the orbital period is the fingerprint of the non-thermal radiation. Compared to the observations (see Fig. 1), the theoretical fluxes are much too high and the maximum occurs too early. This overestimate of the flux could

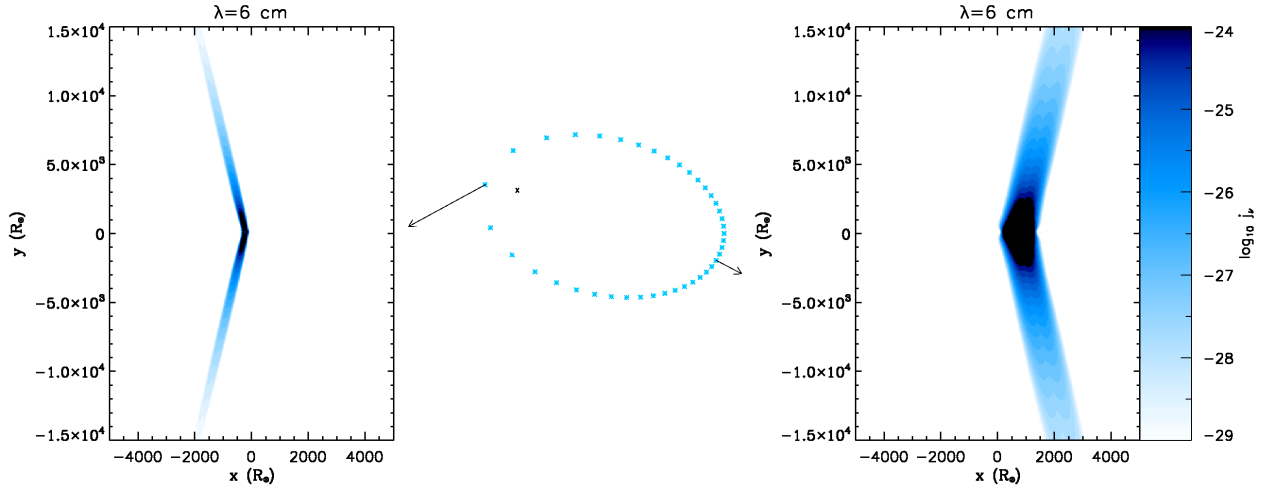

Figure 2: Cyg OB2 No. 9 simulated results. Left panel: the 6 cm emissivity at periastron. Middle panel: the eccentric orbit of the binary system. Right panel: the 6 cm emissivity at apastron. Along the axis the distances from the apex are in unit of $\mathrm{R_{Sun}}$. The color bar represents the emissivity in $\mathrm{erg/cm^3\ s\ Hz}$ with a logarithmic scale. The arrows link respectively the periastron and apastron positions with the corresponding emissivity pictures.

be produced by too high a number of particles being taken into account. In order to reduce the theoretical fluxes we could decrease the fraction of energy transferred from the shock to the relativistic particles. In the present work the assumed value was the typical 0.05 accepted for a strong shock following Eichler & Usov (1993). Another option could be to increase the index n of the p^{-n} particle momentum distribution function and thus to decrease the shock strength, or even to diminish the star surface magnetic fields that we assumed to be 100 Gauss. Before tuning these model parameters it is however more urgent to evolve directly the hydrodynamical equations in order to correctly position the shocks and obtain a realistic value for their strengths, and to take into account the instabilities and inhomogeneities that influence both the thermal and non-thermal emission. Then it would be relevant to include the orbital motion.

Further investigation and changes in the model will thus be necessary to improve quantitatively the simulated results.

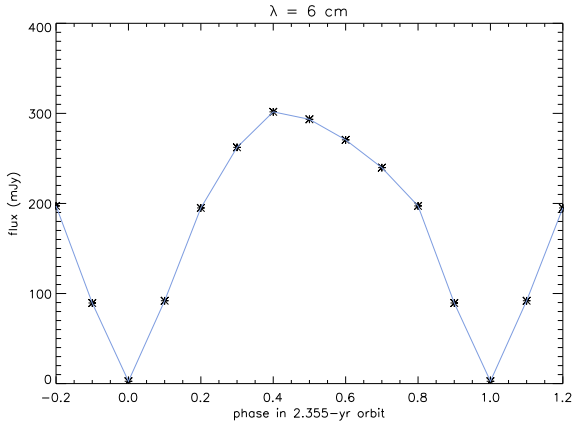

Figure 3: Cyg OB2 No. 9. Simulated 6 cm light curve.

4 Future work

Future work will consist first of all in solving directly the hydrodynamical equations and including the orbital motion. Then it will be necessary to explore the parameter space of our model to obtain a better agreement with the corresponding observations (including the stellar spectral types).

Acknowledgments

This research is supported by contract Action 1 project MO/33/024 (Colliding winds in O-type binaries).

References

Abbott, D. C., Bieging, J. H. & Churchwell, E. 1984, ApJ, 280, 671
Adam, J., 1990 A&A, 240, 541
Anthokin, I. I., Owocki, S. P. & Brown, J. C. 2004, ApJ, 611, 434
Blomme, R., De Becker, M., Volpi, D. & Rauw, G. 2010, A&A, 519, A111
Dougherty, S. M., Pittard, J. M., Kasian, L., Coker, R. F., Williams, P. M. & Lloyd, H. M. 2003, A&A, 409, 217
Eichler, D. & Usov, V. V. 1993, ApJ, 402, 271
Martins, F., Schaerer, D. & Hillier, D. J. 2005, A&A, 436, 1049
Nazé, Y., De Becker, M., Rauw,G. & Barbieri, C. 2008, A&A, 483, 543
Nazé, Y., Damerdji, Y., Rauw, G., Kiminki,D.C., Mahy, L., Kobulnicky, H. A., Morel, T., De Becker, M., et al. 2010, ApJ, 719, 634
Pittard, J. M., Dougherty, S. M., Coker, R. F., O'Connor, E. & Bolingbroke, N. J. 2006, A&A, 446, 1001
Van Loo, S., Runacres, M. C. & Blomme, R. 2004, A&A, 418, 717
Van Loo, S. 2005, PhD Thesis, KULeuven,Leuven, Belgium, http://hdl.handle.net/1979/53(VL)
Van Loo, S., Blomme, R., Dougherty, S. M. & Runacres, M. C. 2008, A & A, 483, 585
Vink, J. S., de Koter, A. & Lamers, H. J. G. L. M. 2001, A&A, 369, 574
Wright, A. E. & Barlow, M. J. 1975, MNRAS, 170, 41

Concluding remarks

The multi-wavelength view of Hot, Massive Stars: Concluding remarks

D. Gies[1]

[1] CHARA, Georgia State University, Atlanta, GA, U.S.A.

Abstract: The papers in this volume demonstrate the importance of adopting a multi-wavelength approach to understanding hot, massive stars and their environments. They also reflect an excitement about recent developments in the field of massive star research that was so clearly evident during the meeting in Liège. Here I review some of the topics and results that were presented at the meeting that capture a sense of the emerging issues and opportunities in massive star studies.

1 Multi-wavelengths and multi-processes

We are truly living in the Golden Age of Astronomy, seeing for the first time the appearance of the sky across the electromagnetic spectrum. The profound influence of multi-wavelength observations is particularly evident in massive star research, and the work presented at this meeting dramatically illustrated the new insights we have gleaned from Earth-based and space-borne telescopes that give access to almost all wavelength bands. The second theme that resonated through the meeting was the importance of high angular resolution observations in illustrating the interaction between stars and their immediate environments. Table 1 (loosely borrowed from the presentation by Zinnecker) outlines in very broad terms the kinds of radiation sources we detect in different spectral bands, and it reminds us that we need to look beyond the optical band in order to discover the thermal and non-thermal emission from gas and to detect the radiation from the cooler dust component.

Table 1: Radiation Sources

Wavelength region	Physical origin
gamma-ray	winds, gas/cosmic rays
X-ray	hot gas, winds
UV/optical	stars, winds, H II regions
near-IR	stars, winds, embedded protostars
thermal-IR	disks in young stars
far-IR	warm dust
submillimeter/radio	cold dust, gas

A visually and scientifically beautiful example is the composite image of the RCW 49 H II region and embedded cluster Westerlund 2 shown in Figure 1. The black and white image shows the dust and line emission in the near-IR from *Spitzer* while the false colour inset shows the *Chandra* image of the young star cluster. The point sources include the very massive binary system WR 20a, a dozen early O-type stars, and a large number of pre-main sequence stars (Nazé, Rauw & Manfroid 2008). The central region surrounding the massive stars has been swept clear of dust by their radiation and winds. Images like this remind us of the profound interactions between massive stars and their surroundings, and it is through multi-wavelength investigations that we can begin to understand the co-evolution of stars and their environments. In this review, I will highlight some of the remarkable discoveries and insights that were presented at this meeting. Rather than cite each individual paper, I will simply refer to the lead author's name in my discussion of selected topics, and I hope this will encourage readers to seek out these contributions elsewhere in this volume.

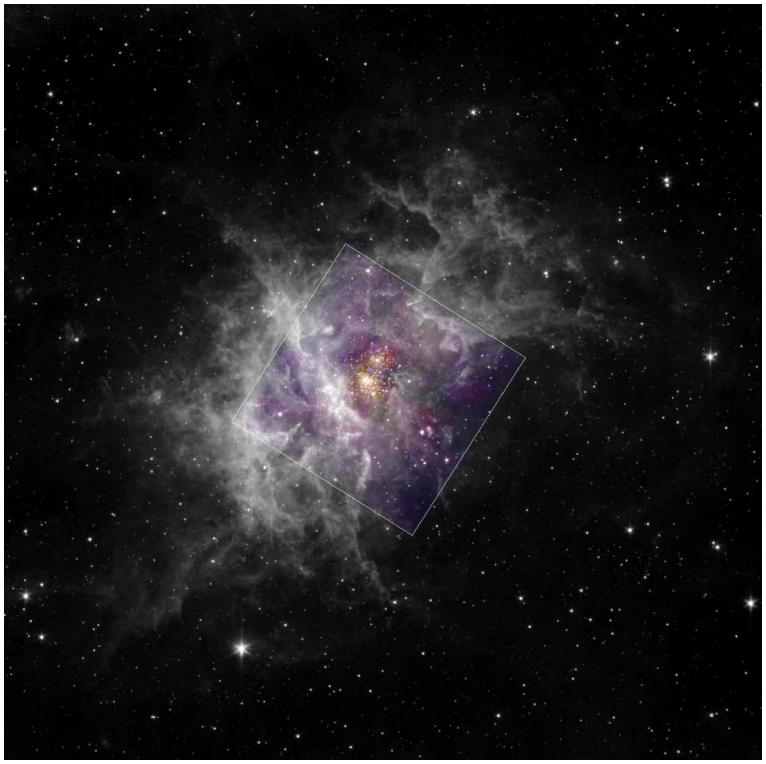

Figure 1: The young star cluster Westerlund 2 as seen in the infrared (*Spitzer Space Telescope*; shown in black and white) and in X-rays (*Chandra X-ray Observatory*; shown in false color). The hot stars and pre-main sequence objects within the cluster's central region shine brightly in X-rays. (Courtesy of Y. Nazé, G. Rauw, J. Manfroid, and E. Churchwell.)

2 Making massive stars

The primary sequence in the creation of a massive star includes the fragmentation of a giant molecular cloud, collapse and formation of an ultra-compact H II region, disk accretion onto a protostar, and dispersal of the remnant gas (Beuther). The theory of massive star formation has had to confront two fundamental problems: how gas accretion can occur in the presence of the radiation pressure and winds of a luminous protostar and how the natal gas angular momentum can be redistributed to permit accretion. We learned at this meeting of the substantial progress made through detailed magneto-

hydrodynamic simulations of the star formation process (Kuiper), its consequences for the surrounding nebula (Mackey), and the interaction between the winds of the disk and protostar (Parkin). Figure 2 shows an example of a recent three-dimensional simulation of the star formation process from Krumholz et al. (2009). This and other simulations show that massive accretion disks tend to fragment and form massive companions, so that much of the angular momentum is transformed into stellar orbital motion. Furthermore, gas accretion can occur despite radiation pressure through Rayleigh-Jeans instabilities that occur near the inner disk boundary. Such models suggest that effective gas accretion can form stars as large as $140 M_{\odot}$ (Kuiper).

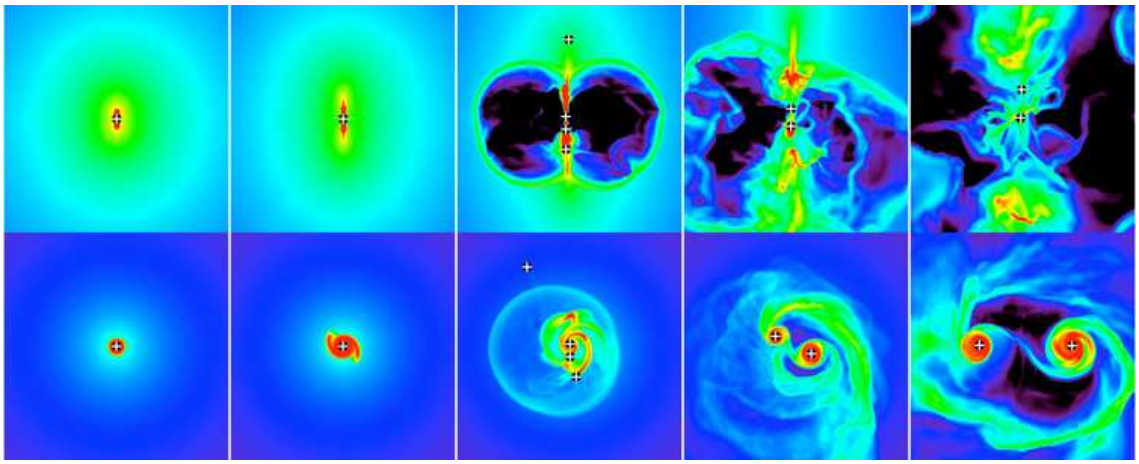

Figure 2: A simulation of the formation of a massive star (colour representing density) from Krumholz et al. (2009). Time progresses from left to right over an interval of 4×10^4 y. The top panels show an equatorial view, while a polar view appears in the lower panels. Plus signs indicate the projected positions of stars, and the two survivors had masses of $41.5 M_{\odot}$ and $29.2 M_{\odot}$ at the conclusion of the simulation. (Courtesy of M. Krumholz.)

Confronting the models with observations is particularly challenging, because most of the accretion onto massive protostars occurs while the young star is still deeply embedded in its very opaque natal cloud. Nevertheless, progress is being made in identifying objects with specific stages in the formation process and in understanding the consequences of these processes for the natal gas cloud. For example, Robitaille et al. (2006) and others suggest that young objects may be assigned to perhaps three evolutionary stages in a sequence of decreasing accretion rate: Stage I objects have infalling clouds and possibly disks, Stage II objects have optically thick disks with a continuing rain of infalling gas, and Stage III objects have optically thin disks. Individual massive young stellar objects (YSOs) can be related to these stages based upon criteria associated with their spectral energy distributions and spectral features (Chen). There is abundant indirect evidence of the predicted disks around massive YSOs from observations of bipolar outflows and IR excesses, and of the consequences of their radiation output in superbubbles, H II regions, X-ray heating, and maser emission (Beuther, Chini, Chu, Clark, Hummel, Hénault-Brunet, Ramsey, Selier, van der Walt). Direct evidence of disks may soon be forthcoming through long baseline interferometry methods. For example, Kraus et al. (2010) recently reported on VLTI/AMBER observations a $20 M_{\odot}$ YSO with a flattened appearing circumstellar envelope.

3 Evolution and clusters

The story of how massive stars evolve from their birth in a dense cloud to death in a supernova explosion is assembled largely through detailed stellar interior models and their interpretation through the distributions of different kinds of stars in star clusters of different ages. The evolutionary models from the Geneva group (Meynet) are particularly successful in reproducing the primary features of stars in clusters. The main issues remaining concern the assignment of realistic mass loss rates at different stages of evolution and the treatment of the angular momentum redistribution in the interiors of rapidly rotating stars (Ekström et al. 2008). It is now clear that the evolutionary path of a single massive star depends fundamentally on its initial mass, metallicity, and rotation rate. Ekström et al. (2008), for example, show that the ratio of the equatorial to critical rotational velocities increases as a star evolves away from the zero-age main sequence. Luminous stars will probably encounter the so-called $\Omega\Gamma$-limit (Maeder & Meynet 2000) at even lower rotational velocities earlier in their lives, and such cases may correspond to the Luminous Blue Variables (LBVs), stars that experience large scale, eruptive, mass loss episodes. The mass and angular momentum consequences for the evolution of the star depend critically on the assumptions made about the variation in mass loss rate between the equator and poles of rapidly rotating, luminous stars (Lovekin, Meynet, Owocki).

A large fraction of massive stars are members of binary systems (Mason et al. 2009), and consequently, it is vitally important to consider how the presence of a close companion can alter a star's evolutionary path. Now, in addition to the fundamental parameters of the single star case, one must specify the binary properties of orbital period (or separation), mass ratio, and orbital eccentricity (De Mink, Vanbeveren). The evolutionary path of the binary will depend on both mass and angular momentum loss and transfer, so it is important to account for changes in rotation caused by tidal locking, Roche lobe overflow, and mergers (De Mink). It is helpful for investigating such a large parameter space to create distributions for all these input parameters and then to combine binary evolutionary codes with sampling of these distribution functions to perform a numerical population synthesis (De Mink, Vanbeveren). There are such diverse stages and outcomes for binary evolution that it is difficult to make comparisons with observational properties. For example, is a single, rapidly rotating star spun up by a change in the internal moment of inertia or by mass transfer from a companion lost by a supernova explosion? In such circumstances, it may be that stars in wide binaries offer the best examples of single star evolution, because we can reasonably conclude that they have not experienced mass exchange (De Mink).

The Conti-scenario (Conti 1976) for the formation of Wolf-Rayet (WR) stars through mass loss by stellar winds has stood the test of time, but there is now a realization that the WR phenomenon may represent more the state of a stellar atmosphere rather than a specific evolutionary stage. For example, there are now many known cases of WNL stars (those with some hydrogen in their atmosphere) among the most luminous stars in very young and massive clusters. These are probably extremely massive stars ($60-120M_{\odot}$) that are "born evolved", i.e., without experiencing a prior red supergiant phase (Hamann, Liermann). Lower mass WR stars may have lost their H-envelopes by winds or Roche lobe overflow in a binary, but it appears that the wind loss rates are sufficient to create a WR star even at the low metallicity of the Small Magellanic Cloud (Pasemann).

A critical test of stellar evolutionary models is to consider the numbers and kinds of supernovae predicted based upon an assumed Initial Mass Function for massive stars (Smith). This approach shows some disagreements with our simple expectations (Smith et al. 2011). For example, the mass range of WR stars that lose their H envelopes by winds makes up less than half the observed fraction of SNeIbc, those supernova lacking H but otherwise occurring among massive populations. This suggests that a significant fraction of SNeIbc progenitors lost their H-envelopes through binary mass transfer.

Star clusters remain the fundamental means to test the evolutionary tracks for populations with a well defined age and to search for evidence of dynamical processes such as mass segregation and the ejection of runaway stars. Observational programs on clusters are well advanced and have focused on very young and dense clusters like 30 Dor (Hénault-Brunet, Taylor), the Quintuplet Cluster near the Galactic center (Liermann), Westerlund 1 (Dougherty, Ritchie), the Cyg OB2 association (Caballero-Nieves, Kobulnicky, Willis), M17 (Chini), and the Carina region (Kumar). Surveys, particularly in the infrared, have led to significant progress on other clusters in the Galaxy (Clark, Edwards, Mahy, Marco, Ramírez Alegría) and beyond (Bomans, Bonanos, Sholukhova, Wofford).

4 Winds and outflows

The CAK theory of the radiatively driven winds of luminous stars (Castor, Abbott & Klein 1975) remains central to our understanding of mass loss, and we are still exploring its ramifications for wind structure (Owocki). Radiatively driven winds are inherently susceptible to a line-shadowing instability that leads to the formation of small dense clumps in the wind, and the presence of wind clumping can radically influence the mass loss rates derived from diagnostics based upon density-squared. In some circumstances, large scale, optically thick structures may form in the wind, and the resulting "porosity" affects diagnostics that depend linearly on density. The challenge ahead is to develop time-dependent dynamical wind models to study the development of structure in the wind and to determine how such structures influence different measurements of the mass loss rate (Hamann, Lobel, Owocki, Sundqvist, van Marle). Puls et al. (2006) found that the clumping factor may have a radial density dependence, so a single value of the clumping factor may be inadequate to describe the whole wind. Models were presented at the meeting that describe how clumping affects the interpretation of optical and UV features (Sundqvist) and X-ray diagnostics (Hervé, Oskinova).

Rotation plays an important role in the mass loss rates, and current models suggest that in a rapid rotator, the wind is slower and less dense at the equator and is faster and more dense at the poles (Lovekin, Meynet, Owocki). The fact that we often observe dense equatorial outflows around luminous stars (for example, the skirt region in η Car) indicates that other mechanical processes are at work in addition to radiative driving. One explanation for the ejection of equatorial disk gas in Be stars is the combined action of rapid rotation and stellar pulsation (Cranmer 2009). Pulsations or other azimuthally distributed perturbations may create Corotating-Interaction Regions that alter the wind velocity law and lead to accelerating Discrete Absorption Components in spectral lines formed in the wind (Lobel).

We now have a very rich set of observational results on mass loss diagnostics based upon the spectral line shapes and spectral energy distributions (Gräfener, Martins, Pasemann, St-Louis, Sander, Williams). X-ray measurements of the mass loss rate have assumed a new importance (Nazé, Oskinova) especially since there are now large samples of OB stars in the Second XMM-Newton serendipitous source catalogue (Watson et al. 2009) and the Carina complex survey (Gagné et al. 2010). Radio flux measurements are available for many stars, but these may be complicated by the presence of a non-thermal component from colliding winds in binaries (Blomme, Dougherty, Romero). Intrinsic polarization estimates are needed to study departures from spherical symmetry in the wind (Hoffman, Lomax).

A number of investigators have monitored selected sources to follow the photometric and spectroscopic variations due to clumping and other structural changes in the circumstellar environment (Buemi, Burggraf, Clark, David-Uraz, Grundstrom, Morel). These studies indicate a great deal of diversity in atmospheric and mass loss properties, but it may well be that deep seated photospheric changes may ultimately drive structure in the wind. For example, pulsational modes in rotating stars (Englebrecht) may attain large amplitude near the equator and promote mass loss there. More gen-

erally, higher order, multi-mode pulsations may increase the turbulence in the photosphere (Simon-Diaz), and turbulence may help seed instabilities in the wind that drive clumping.

The radiation and winds of luminous stars will help sculpt the ionization zones and density variations in the surrounding medium (Mackey, Pellegrini, Zastrow). The mass loss effects on the environment are most striking in more evolved, luminous stars where we observe the results from an entire stellar lifetime and we can study "mass loss archeology" from the radial distribution of the ejected gas (Hoffman, Smith, Umana). Wind gas may be swept up into a dense shell if a fast wind develops after a slow wind episode (van Marle, Smith), and we observe such shells in many LBV, WR, and B[e] stars (Bomans, Chu, Stock, Umana, Vamvatira-Nakou, Wachter, Weis). These shells are especially prominent in *Spitzer* 24μm images of evolved, massive stars (Wachter et al. 2010). Multiple outer shells and dust disks may also be detected when the star explodes as a supernova and first illuminates them and then sweeps them up as the blast wave moves outwards (Hoffman, Smith).

5 Rotation and magnetism

The fastest rotating massive stars are generally found among the emission line Be stars, where the equatorial velocities are perhaps $70-90\%$ of the critical velocity (Grundstrom, Martayan). If these stars are able to maintain some fraction of their angular momentum up to the time of the supernova, then it is possible that the core collapse will result in a short phase of disk and relativistic jet formation that is associated with long duration gamma-ray burst sources (Martayan).

On the other hand, we often find that slow rotators are stars with measurable magnetic fields (Morel). The number of magnetic detections is growing thanks to the concerted observational effort of the consortium on *Magnetism in Massive Stars (MiMeS)* [2] (Wade et al. 2008). Magnetic fields in early-type stars apparently act like those in late-type stars to spin down stars over their lifetime. A noteworthy example is HD 191612, a magnetic star and spectrum variable with a rotation period of 538 d (Howarth et al. 2007). Magnetic fields may also alter the star's wind properties (sometimes in spectacular ways; Townsend, Owocki, & Groote 2005). If magnetic reconnection acts to increase the X-ray generation, then the wind gas may appear overionized for the star's temperature and be classified as a "weak wind star" (Austin, Garcia). Curiously, a few magnetic stars are rapid rotators, and these must either be very young or recently spun-up stars.

6 Individual and binary stars

The fundamental parameters of many massive stars are now well established thanks to very careful spectroscopic analyses (Doran, Martayan, Martins, Przybilla, Simon-Diaz). These investigations yield the stellar effective temperature, mean gravity, projected rotational velocity $V \sin i$, and estimates of the photospheric micro- and macroturbulence. Macroturbulence may be a manifestation of multi-mode pulsations that are too complex to detect in the integrated stellar flux or spectral lines (Simon-Diaz). Surprisingly, the most massive stars ($50-200 M_{\odot}$) all tend to have similar spectral types (O2-3 or possibly WNL) and may appear as luminosity class III or I objects even when very young (Doran).

With reliable fundamental parameters in hand, it is possible to obtain good estimates for the photospheric abundances of He, C, N, O, and other elements (Heap, Nieva, Pavlovski, Przybilla, Simon-Diaz). The measurements are especially useful for the reconstructed spectra of eclipsing binary stars, where independent estimates of stellar mass and radius are available (Pavlovski). Internal mixing in

[2] http://www.physics.queensu.ca/~wade/mimes/MiMeS__Magnetism_in_Massive_Stars.html

massive stars should bring CNO-processed gas into the photosphere causing the [N/C] ratio and He abundance to increase with time (Przybilla). Naively, we would expect mixing to be more vigourous in rapidly rotating stars, but there is no obvious correlation between [N/C] and $V \sin i$ in observational data from the VLT FLAMES survey. This diversity in abundance patterns hints that processes related to magnetism and binarity are at work (Morel).

The determination of stellar masses from binary orbits continues to be of central importance (Antokhin, N. Evans, Gies, Kobulnicky, Mahy, Nazé, Pavlovski, Vilardell). The current record holder is NGC 3603 A1a with a mass of $116 \pm 31 M_{\odot}$ (Schnurr et al. 2008), although there are a number of candidates with even larger mass based upon luminosity estimates and evolutionary models (Crowther et al. 2010). There are a number of impressive studies in these proceedings of selected "extreme stars" including supergiant B[e] types, hypergiants, and massive X-ray binaries (Aragona, Blay, De Becker, Martayan, Mason, McSwain).

The power of stellar winds assumes new forms in colliding wind binaries that offer us an extraordinary laboratory to study wind physics (Williams). Both analytical and smoothed-particle hydrodynamic models are now available that are valuable guides to the observations of colliding wind systems (Montes, Parkin, Pittard, Volpi). These models predict the spectral features and X-ray and radio emission as a function of orbital phase for eccentric orbit systems. One of the more remarkable predictions is that energies in the collision zone may be sufficient to create very high energy gamma-rays through π^0-decay of accelerated hadrons interacting with the dense stellar wind gas, and such a high energy component has now been identified in *Fermi* data on η Car, announced as a "very large hadron collider" in the sky (Farnier, Walter & Leyder 2011). It is now well established that η Car is a binary of two massive stars in a 5.54 y eccentric orbit. The two stars recently attained closest approach during a periastron passage in early 2009, and the colliding winds model appears to be consistent with most of the optical and X-ray spectral variations observed around that time (Corcoran, Groh, Madura, Parkin, Russell). The other famous colliding winds binary is WR 140, which also has an eccentric orbit, in this case with a period of 8 yr (De Becker, Dougherty, Fahed, Morel, Parkin, Sugawara, Williams). The colliding winds zone is a strong radio source in this binary and its positional variation with the orbit is detected in VLBA observations (Dougherty). There are many more colliding wind systems that are now under investigation in different wavelength bands (Blomme, Combi, Dougherty, Fauchez, Gosset, Nazé, Williams).

7 Future opportunities

We are entering a new era of extremely large, optical/IR telescopes (LSST, GMT, TMT, ELT) that will have superb instrumentation and extraordinary capabilities (C. Evans). They will help us find and characterize Galactic massive stars with large extinction and will make possible detailed studies of individual stars in nearby low metallicity galaxies (Bomans, C. Evans, Heap). At longer wavelengths there will be many new opportunities with ALMA, SKA, EVLA (Dougherty), and e-merlin (Willis). Among space missions, some of the first and very promising results are now available from Herschel (Vamvatira-Nakou), and we can anticipate future missions including JWST, GAIA (Damerdji, Palate), IXO (Hervé, Rauw), and BRITE (microvariations of bright stars; Chené). Many of the special targets among the massive stars are relatively bright and can be observed even with small aperture telescopes with good instrumentation (such as the spectrographs for small telescopes built by Shelyak Instruments). Professional – amateur collaborations hold great promise for extended observing campaigns on selected targets (Eversberg), such as the recent ConVento group collaboration on WR 140[3]. We are also entering an era of large scale surveys, and we will need to develop tools to present and mine

[3] http://www.stsci.de/convento/

databases (Nieva, Ramsay, Simon-Diaz, Sota) and to create and distribute software to deal with the interpretation of vast new data sets (Garcia, Hanson).

Beyond the new multi-wavelength dimension, we now have the means to explore the spatial characteristics of massive stars and their environments at very high angular resolution thanks to developments in optical long baseline interferometry[4] (VLTI, Keck, NPOI, CHARA; plus future instruments like MRO and CARLINA; De Becker). Figure 3 shows a remarkable example of results from high resolution work, images of the components of the interacting binary β Lyr from H-band interferometry with the CHARA Array (Zhao et al. 2008). This binary consists of an evolved, B-type star (darker component) that is actively transferring mass to a companion, hidden in an extended accretion disk (lighter component), and these images probably represent our first resolution of an accretion disk in a Roche lobe overflow binary.

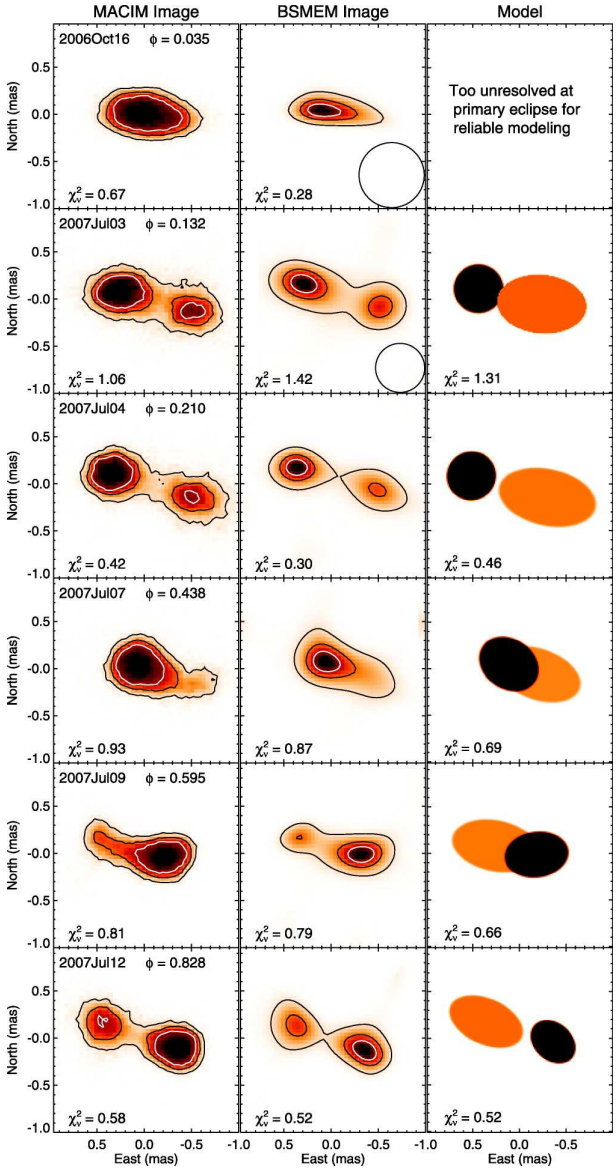

Figure 3: Image reconstructions of the interacting binary β Lyr from CHARA Array observations (Zhao et al. 2008). The six rows show the results from different binary phases while the three columns indicate two image reconstruction methods and a geometrical model fit. (Courtesy of M. Zhao.)

[4]http://olbin.jpl.nasa.gov/

8 A word of thanks

This meeting was a huge success in providing us with a venue to compare research results from across the spectrum and to better appreciate the methods and opportunities available at other wavelengths. The meeting brought together some 138 astrophysicists from around the globe, and I think that its impact will be significant and widespread (following in the tradition of earlier Liège astrophysical colloquia). The participants will long remember how we enjoyed World Cup football, the dramatically changing weather, and the companionship of colleagues and excellent hosts. This success was due to the support of the Université de Liège and other sponsors, the commitment of the Scientific Organizing Committee, and the hard work of the Local Organizing Committee. I would like to express my gratitude to all the meeting organizers and especially to the chairmen of the meeting, Gregor Rauw and Peredur Williams, for their vision and leadership. Finally, I extend our thanks to Yaël Nazé and Gregor Rauw's baby[5] who delayed her arrival until after the conclusion of the meeting.

Acknowledgements

I am grateful to the organizers of this Colloquium for travel support. This material is based in part upon work supported by the National Science Foundation under Grant No. AST-0606861.

References

Castor, J.I., Abbott, D.C., & Klein, R.I. 1975, ApJ 195, 157
Conti, P.S. 1976, Mém. Société Royale des Sciences de Liège, 9, 193
Cranmer, S.R. 2009, ApJ 701, 396
Crowther, P.A., Schnurr, O., Hirschi, R., Yusof, N., Parker, R.J., Goodwin, S.P., & Kassim, H.A. 2010, MNRAS 408, 731
Ekström, S., Meynet, G., Maeder, A., & Barblan, F. 2008, A&A 478, 467
Farnier, C., Walter, R., & Leyder, J.-C., 2011, A&A 526, A57
Gagné, M., Townsley, L., Corcoran, M., et al. 2010, BAAS 41, 684
Howarth I.D., Walborn N.R., Lennon D.J., et al. 2007, MNRAS 381, 433
Kraus S., Hofmann K.-H., Menten K.M., et al. 2010, Nature 466, 339
Krumholz M.R., Klein R.I., McKee C.F., Offner S.S.R., & Cunningham A.J. 2009, Science 323, 754
Maeder, A., & Meynet, G. 2000, A&A 361, 159
Mason, B.D., Hartkopf, W.I., Gies, D.R., Henry, T.J., & Helsel J.W. 2009, AJ 137, 3358
Nazé, Y., Rauw, G., & Manfroid, J. 2008, A&A 483, 171
Puls, J., Markova, N., Scuderi, S., Stanghellini, C., Taranova, O.G., Burnley, A.W., & Howarth, I.D. 2006, A&A 454, 625
Robitaille, T.P., Whitney, B.A., Indebetouw, R., Wood, K., & Denzmore, P. 2006, ApJS 167, 256
Schnurr, O., Casoli, J., Chené, A.-N., Moffat, A.F.J., & St-Louis, N. 2008, MNRAS 389, L38
Smith, N., Li, W., Filippenko, A. V., & Chornock R. 2011, MNRAS, in press (arXiv:1006.3899)
Townsend, R.H.D., Owocki, S.P., & Groote, D. 2005, ApJ 630, L81
Wachter, S., Mauerhan, J.C., Van Dyk, S.D., Hoard, D.W., Kafka, S., & Morris, P.W. 2010, AJ 139, 2330
Wade, G.A., Alecian, E., Bohlender, D.A., et al. 2008, in *Cosmic Magnetic Fields: From Planets, to Stars and Galaxies*, eds. G. Bruzual and S. Charlot, Proc. IAU Symp. 259, 333
Watson, M.G., Schröder, A.C., Fyfe, D., et al. 2009, A&A 493, 339
Zhao, M., Gies, D., Monnier, J.D., et al. 2008, ApJ 684, L95

[5] Anaïs, born 2010 August 4.